Huaqun Guo
Hongliang Ren
Noori Kim *Editors*

IRC-SET 2020

Proceedings of the 6th IRC Conference on Science, Engineering and Technology, July 2020, Singapore

Springer

IRC-SET 2020

Huaqun Guo · Hongliang Ren · Noori Kim
Editors

IRC-SET 2020

Proceedings of the 6th IRC Conference on Science, Engineering and Technology, July 2020, Singapore

Springer

Editors
Huaqun Guo
International Researchers Club
Singapore, Singapore

Noori Kim
Newcastle University in Singapore
Singapore, Singapore

Hongliang Ren
Department of Biomedical Engineering
National University of Singapore
Singapore, Singapore

ISBN 978-981-15-9471-7 ISBN 978-981-15-9472-4 (eBook)
https://doi.org/10.1007/978-981-15-9472-4

This Springer imprint is published by the registered company Springer Nature Singapore Pte Ltd.
The registered company address is: 152 Beach Road, #21-01/04 Gateway East, Singapore 189721, Singapore

Organizing Committee

General Chair

Prof. Maode Ma, Nanyang Technological University (NTU), Singapore

General Co-chair

Dr. Liuqun Gu, National University of Singapore (NUS), Singapore

Technical Program Chair

Dr. Umayal Lakshmanan, EDDC, A*STAR, Singapore

Technical Program Co-chairs

Dr. Aishwarya Bandla, NUS, Singapore
Prof. Chau Yuen, Singapore University of Technology and Design (SUTD)
Prof. Bharadwaj Veeravalli, NUS, Singapore
Dr. Victor Peng Cheng Wang, Singapore Institute of Technology (SIT)
Dr. Aldy Gunawan, Singapore Management University (SMU)
Dr. Noori Kim, Newcastle University in Singapore
Dr. Boon Seng Chew, Singapore Polytechnic
Dr. Yu Wang, A*STAR Research Entities, Singapore

Dr. Guang Chen, Singapore
Dr. Xingjie Yu, Singapore
Dr. Mandar Godge, Temasek Polytechnic, Singapore

Publicity Chairs

Dr. Yongqing Zhu, Singapore University of Social Sciences
Ms. Jeilene Ho, National Junior College, Singapore

ePoster Chairs

Mr. Peng Liu, A*STAR Research Entities, Singapore
Ms. Jeilene Ho, National Junior College, Singapore

Sponsorship Chair

Dr. Victor Peng Cheng Wang, SIT, Singapore

Publication Chairs

Dr. Noori Kim, Newcastle University, Singapore
Dr. Hongliang Ren, NUS, Singapore

Steering Committee

Prof. Lawrence Wai Choong Wong, NUS, Singapore
Dr. Huaqun Guo, A*STAR Research Entities, Singapore
Dr. Bhojan Anand, NUS, Singapore

International Advisory Panel

Prof. Jianying Zhou, SUTD, Singapore
Prof. Chip Hong Chang, NTU, Singapore

Prof. Robert H. Deng, SMU, Singapore
Prof. Janina Mazierska, James Cook University, Australia
Prof. Yong-Jin Park, Universiti Malaysia Sabah, Malaysia
Prof. Kristin L. Wood, SUTD, Singapore

TPC Members

Dr. Chris Choy, StarHub
Dr. Claus Muschallik, Coffee Electronics Pte. Ltd.
Mr Dajun Wu, Institute for Infocomm Research
Dr. Dexin Xiong, NauticAWT Limited
Dr. Guisheng Zeng, Institute of Molecular and Cell Biology
Dr. Guoxian Tan, Raffles Institution
Dr. Jien Wu, Institute of Molecular and Cell Biology
Dr. Jizhong Luo
Dr. Kasthurirengan Sampath, JOil (s) Pte. Ltd.
Dr. Keyu Gu, Temasek Life Sciences Laboratory, NUS
Mr. Krishnamoorthy Baskaran, Energy Research Institute [ERIAN], NTU
Dr. Muthu Sebastian, Environment Water Technology Center of Innovation
Dr. Rong Li, National Anti-Doping Laboratory, Shanghai University of Sport
Ms. Wai Ee Wong, WD Media (S) Pte. Ltd.
Dr. Yi Zhou, Singapore Institute of Technology
Dr. Yvonne Chow, Singapore Institute of Food and Biotechnology Innovation
Dr. Zaiqun Yu, Institute of Chemical and Engineering Sciences

Preface

International Researchers Club (IRC) (www.irc.org.sg) was set up in 2001. The vision of IRC is to create a vibrant and innovative research community for Singapore, through contributions of technical specialties and occupational experiences from its members, and fostering strong networking and social interactions of expatriates and new citizens with the local community.

With the vision of IRC, it is our great pleasure to organize IRC conference on science, engineering and technology (IRC-SET, www.ircset.org) for the younger talents and researchers. IRC-SET 2015 is the inaugural conference of IRC and IRC-SET 2020 is the sixth conference. IRC-SET conference aims to provide a platform for young researchers to share fresh results, obtain comments and exchange innovative ideas in the multi-discipline areas. The students from universities, junior colleges, polytechnics and top secondary schools are invited to participate in this conference to showcase and present their research projects, results and findings. Unlike other academic conferences, this conference focuses specifically on education and youth development and has officially been given technically sponsorship from six universities, namely National University of Singapore (NUS), Nanyang Technological University (NTU), Singapore University of Technology and Design (SUTD), Singapore Management University (SMU), Singapore Institute of Technology (SIT) and Newcastle University in Singapore. IRC-SET 2020 conference is also supported by IEEE Intelligent Transportation Systems Society (ITSS) Singapore Chapter, IEEE Broadcast Technology Society (BTS) Singapore Chapter and IEEE Singapore Section Women in Engineering (WIE) Affinity Group

The program of IRC-SET 2020 advocates the importance of innovative technology backed by the strong foundation of science and engineering education. By exposing students from universities, junior colleges, polytechnics and top secondary schools to the key technology, enablers will encourage more interest into the fields of science, engineering and technology. To select students, the IRC-SET 2020 Call for Papers is broadcast to universities, junior colleges, polytechnics and top secondary schools according to our plan. The students then submit their technical papers to the conference online system. For the criteria that papers have to meet, firstly, the submitted papers should follow the standard template. Secondly,

the conference technical program committee has allocated each paper to several reviewers from IRC researchers, professors, lecturers and teachers to review the paper and give the comments and recommendations based on novelty of the work, scientific, engineering and technology relevance, technical treatment plausible and clarity in writing, tables, graphs and illustrations. Based on the review results, the technical program committee has selected number of papers to present in the IRC-SET 2020 conference and publish in this proceeding.

IRC-SET 2020 conference is held online and consists of the opening speech by Prof. Sir John O'REILLY (Chairman of A*STAR Science and Engineering Research Council), introduction of International Researchers Club by Dr. Huaqun GUO (President, IRC), a poster session, and nine presentation sessions. The nine presentation sessions include physics, chemical engineering, biomedical science, ITSS session, BTS session, WIE session, mechanical engineering, material science and life sciences. In the closing ceremony, Prof. Maode Ma (General Chair) and Dr. Huaqun GUO (President, IRC) announce the winners of best paper awards, best poster awards and best presenter awards.

Finally, this proceeding is dedicated to International Researchers Club and its members.

Singapore
July 2020

Huaqun Guo
Hongliang Ren
Noori Kim

Acknowledgements

We would like to extend our utmost gratitude to the people who have, in one way or other, inspired, aided and contributed to the successful completion of this book.

First of all, we would like to thank all members of conference organizing committee to contribute their time and professional knowledges to make the conference a big success.

Special thanks to all reviewers for their expertise, time, effort and timely response throughout the peer evaluation process.

We would also like to take this opportunity to thank Newcastle University in Singapore to sponsor the Zoom accounts for the online conference and ten IRC Junior Memberships and Chairman Dr. Anthony Yee of the Royal Commonwealth Society Singapore to provide three mathematics books as winner prizes for the conference.

Last but not least, the heartiest gratitude is given to IRC members for their unity.

Contents

Investigating the Efficacy of *Magnetite* as a Sedative in *Drosophila Melanogaster*

Evangeline Enbei Chen, Dawn Lok, and Jui Chin Lee

Abstract Sedatives are a category of drugs that modulates the response of the Central Nervous System, thus slowing the normal brain function. At higher doses it may result in slurred speech, staggering gait; poor judgment; slow, uncertain reflexes. Currently, many sedatives ingested by humans have side effects including depression, aggression and hallucinations. Magnetite, a potential sedative in the domain of Traditional Chinese Medicine (TCM) with little known side effects poses as a possible alternative sedative option. Furthermore, it is cheap and easily obtainable. Hence, this project aims to investigate the efficacy of Magnetite as a sedative using Drosophila melanogaster as a model system. Magnetite was fed to fruit flies in varying doses and its efficacy was assessed based on the flies' responses in physiological assays, namely phototaxis, smell chemotaxis and taste chemotaxis. Our preliminary study showed that treatment with a dosage as low as 0.01 g/L was capable of dampening the flies' responses towards light, taste, smell, indicating that Magnetite functions as a sedative. A greater percentage of flies treated with Magnetite failed to respond to light, taste and smell as compared to the untreated flies. 46% of flies treated with Magnetite failed to respond to light stimulus, as compared to the 10% of untreated flies that failed to respond to light; 74% of treated flies failed to respond towards the taste stimulus as compared to the control flies, 35%; and 85% of treated flies failed to respond to smell stimulus while 25% of control flies failed to do so.

Keywords Efficacy · Magnetite · Sedative · Drosophila melanogaster

1 Introduction

E. E. Chen · D. Lok · J. C. Lee (✉)
Raffles Institution, Singapore, Singapore
e-mail: 20YLEEJ308D@student.ri.edu.sg

E. E. Chen
e-mail: evangeline.chen02@gmail.com

D. Lok
e-mail: dawnlok9@gmail.com

H. Guo et al. (eds.), *IRC-SET 2020*,
https://doi.org/10.1007/978-981-15-9472-4_1

A. *Sedatives*

Sedatives are a category of drugs that modulates the response of the Central Nervous System, thus slowing the normal brain function. At higher doses it may result in slurred speech, staggering gait; poor judgment; slow, uncertain reflexes [1]. Currently, many sedatives ingested by humans have indisposable side effects including depression [2], aggression [3] and hallucinations [2].

B. *Magnetite as a potential sedative*

With that in mind, *Magnetite*, a drug commonly used in Traditional Chinese Medicine (TCM) poses as an alternative to current sedatives in the market. *Magnetite* (Fig. 1). *Magnetite*, with the chemical formula Fe_3O_4, is known to be a mineral that brings about sedation and tranquilization, and is primarily used in the domain of TCM to clear the mind and produce a calming sensation [4].

TCM is based on the concept of *Qi*, a universal form of energy that manifests itself in various forms. In TCM, the theory of *Yin* and *Yang* states that they are two opposite but complementary energies that are present in all matter in the universe. While *Yin* refers to aspects or manifestations of *Qi* that are material, cool, solid and heavy, *Yang* refers to aspects or manifestations of *Qi* that are immaterial, warm, hollow and light. When there is a balance of *Yin* and Yang, they are said to be in harmony. In the practice of TCM, a state of wellness in patients can be attained by balancing the *Yin* and *Yang* in one's body [5].

Magnetite is a *Yin* herb that covers three different meridians—the kidney, liver and lungs. Its main functions are to soothe the liver, suppress *Yang*, calm one's nerves, improve hearing and vision as well as to relieve asthma. Its main uses and indications include dizziness, dim eyesight, deafness, tinnitus, palpitation, insomnia, asthma, and reverse flow of *Qi* due to deficient kidneys. It is often used alongside Cinnabar, Rehmannia, Schisandra, Dragon Bone, Dogwood and Oyster Shell for enhanced effect. Lastly, *Magnetite* also has a sedative and anticonvulsant effect [5].

Fig. 1 Picture of *Magnetite*, a traditional Chinese medicine (TCM) drug that is commonly used for sedation and tranquilization

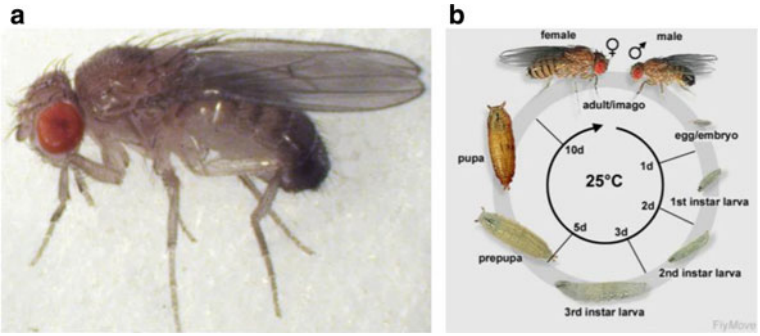

Fig.2 **a** *Drosophila melanogaster*, red eyed male, used in our research as model organisms [6]. **b** Life cycle of *Drosophila* [7]

C. *Drosophila as a model organism*

Drosophila melanogaster, the common fruit fly (Fig. 2), is used as the model organism in our experiments as it is inexpensive to obtain and easy to manage in labs. *Drosophila* has a short life cycle of 10–14 days, allowing research to progress rapidly and pedigrees over several generations can be easily planned and monitored. *Drosophila* also produce large numbers of externally laid embryos, making the management and culture of these organisms easy in laboratories [6].

Virtually every gene of *Drosophila* is amenable to targeted manipulations, rendering this system ideal to perform reverse genetics. The genetic makeup of the *Drosophila* is somewhat similar to that of the human. Furthermore, the fundamental biological mechanisms and pathways that control development and survival are well-conserved across evolution between these species [6]. A huge body of knowledge and rich resources regarding *Drosophila* have been accumulated and this enormously facilitates our research [8].

Hence, *Drosophila melanogaster* was used as a model organism in our biological research.

D. *Effects of stimulus on Drosophila melanogaster*

Recent articles have reported the suitability of the use of *Drosophila* to examine the effects of sedatives. In addition, past studies have shown that Drosophila respond to different stimulants such as lithium carbonate, theobromine, valproic acid and caffeine [9]. Depending on the nature of the stimulus, *Drosophila* will exhibit behavioural response, either as a form of attraction or repulsion. Behaviour responses towards light [10–12], volatile chemicals [13–15] and temperature [9, 16, 17] are commonly used to test the efficacy of a sedative.

E. *Purpose of research*

As of today, there has been no detailed reports on the use of *Magnetite* as a sedative. Yet, it is plausible that *Magnetite* could potentially serve as an effective sedative. In this study, we aimed to establish the efficacy of *Magnetite* as a sedative through observing its effect on the behavioural responses of *Drosophila* towards various stimuli. To do so, *Magnetite* was fed to fruit flies in varying doses and its efficacy was assessed based on the flies' responses in physiological assays, such as phototaxis, taste chemotaxis and smell chemotaxis assays.

2 Hypothesis

Magnetite functions effectively as a sedative in adult *Drosophila melanogaster* by dampening its response to light, taste and smell.

3 Materials and Methods

A. *Drug preparation*

50 g of *Magnetite* was boiled in 100 ml of distilled water for an hour and topped up constantly to maintain the original water level of around 125 ml. The mixture was then filtered and the filtrate was mixed with 1 g yeast paste to obtain final concentrations of 0, 0.01, 0.02, 0.03, 0.04, 0.05 g/L.

The respective yeast paste was spread evenly around the walls of food vials containing standard cornmeal medium.

10d old male Oregon-R (Bloomington Stock Centre) were used for all drug treatments and all experiments were performed at 25 °C.

B. *Phototaxis assay* [18]

With reference to Fig. 3, two identical vials, each 9.5 cm in length, were held together by a transparent connector tape and four quarters, 4.25 cm apart, were marked. The vials were placed in a shoebox to minimise background light. A flap, 23 cm by 13 cm, was cut out at the top of the box and covered with red cellophane tape to facilitate counting of the flies. A piece of red cellophane was also used to cover the opening of the flap so as to prevent sudden stray light from alarming the flies. A circular hole with a diameter of 0.9 cm was made and the light source was inserted. The light source produced a light intensity 495 lx, with a gradient of 175, 45, 15 and 5 lx at quarters 4, 3, 2 and 1 respectively. This light source acted as an attractant for fruit flies.

20 male flies were first placed in the vials and pounded down to the quarter of the vial that is furthest away from the light source, marked 1. The light source was then

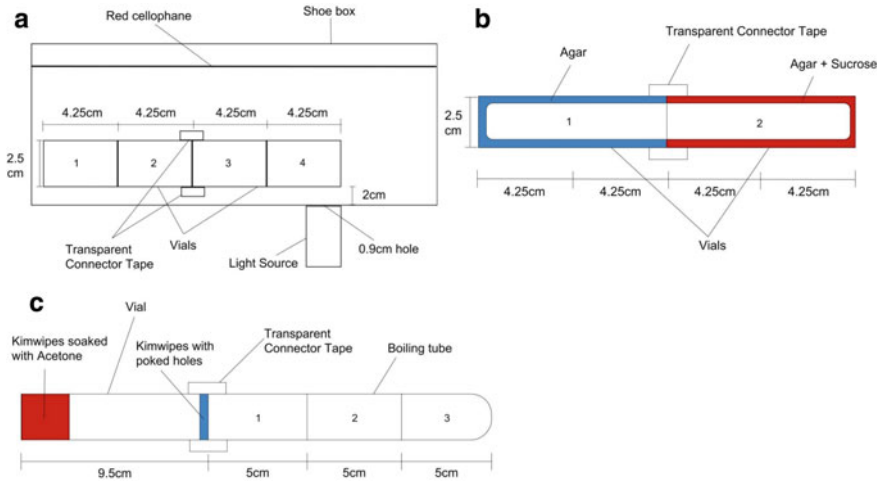

Fig. 3 Schematic diagrams of experimental set-ups for the behavioural assays [18]

turned on and the timer was started once all the flies regained consciousness. The number of flies in each quarter was counted every 2 min over a duration of 10 min.

C. *Taste Chemotaxis assay* [18]

With reference to Fig. 3, 20 male fruit flies were first starved by keeping them in 5% agar for 20 h. The agar containing sucrose was made by dissolving 10 g of sucrose in 100 ml of 5% agar. A vial 9.5 cm in length was coated with 3 ml of the agar and sucrose mixture. This was done by placing melted agar into the vial and rotating the vial horizontally, ensuring that there is an even coating. The exterior of the vial was then placed in the fridge until the agar hardened. The same method was used to coat another identical vial with only 1 ml of 5% agar. The 20 male flies were placed into the non sucrose vial and pounded down to the end of the vial. The two vials were connected with transparent tape. The timer was started when the flies regained consciousness and the number of flies in each vial was counted every 2 min over a duration of 10 min.

D. *Smell Chemotaxis assay* [18]

With reference to Fig. 3, a piece of Kimwipes was soaked in 3 ml of Acetone, folded and placed to the end of a 9.5 cm vial. The Acetone acted as a repellent. The vial was then covered by half a piece of Kimwipes poked with holes. 20 male flies were then placed into a boiling tube of 15 cm, which was plugged with cotton. Once conscious, the boiling tube was connected to the vial with transparent tape and the flies were then pounded down to the piece of Kimwipes. The number of flies in each third of the boiling tube was counted every 2 min over a duration of 10 min.

4 Results and Discussion

A. *Results*

Magnetite, a potential sedative, was tested for its effectiveness as a sedative on *Drosophila melanogaster*. To investigate its efficacy, phototaxis, taste chemotaxis and smell chemotaxis assays were performed to assess the fruit flies' responses towards light, taste and temperature respectively (Figs. 4–6).

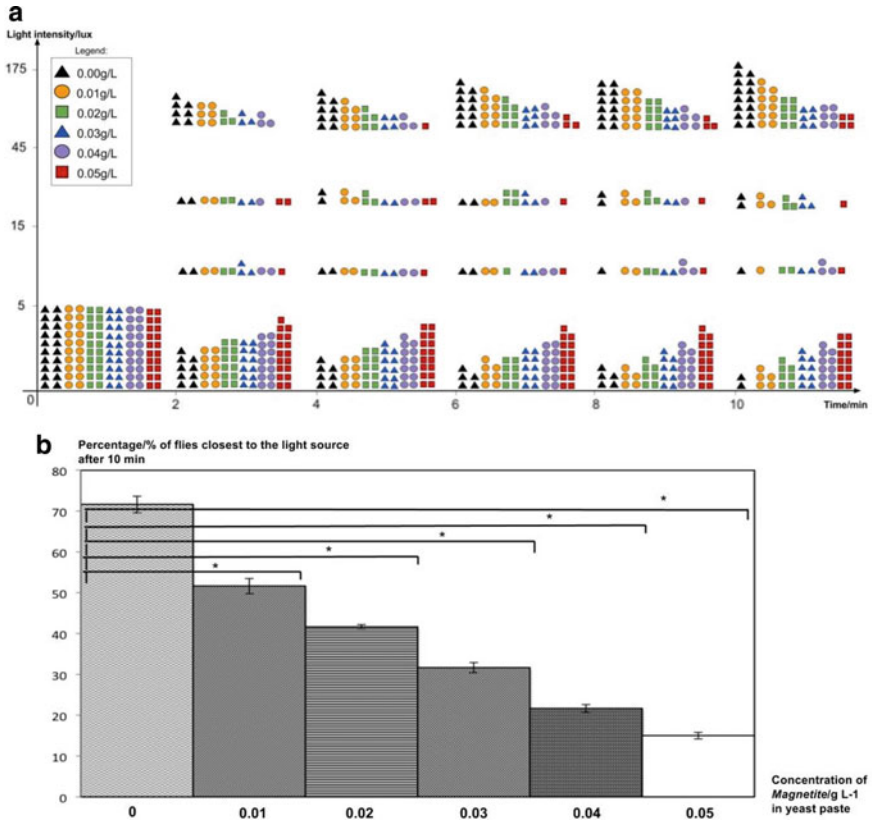

Fig. 4 Fruit flies treated with *Magnetite* failed to respond to the light stimulus. **a** Graph exhibiting the mean number of flies at the four quarters of different light intensities over a period of 10 min, with the first quarter exposed to the lowest light intensity, 5 lx. Flies were treated with 0.01 g/L, 0.02 g/L, 0.03 g/L, 0.04 g/L, 0.05 g/L of *Magnetite* for 10 days are represented with the symbols, black triangle, orange circle, green square, blue triangle, purple circle and red square respectively. Control flies were fed with yeast paste containing no *Magnetite* for the same duration. $n = 20$. **b** Bar graph exhibiting the percentage of flies closest to the light source at the end of the 10 min phototaxis assay. *$p < 0.05$

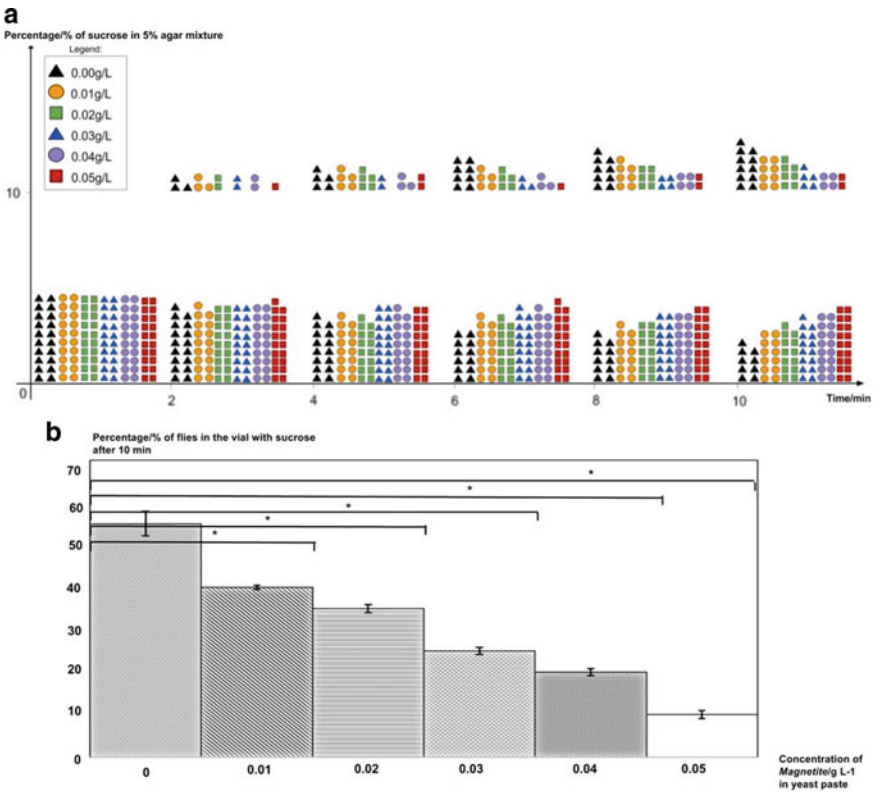

Fig. 5 Fruit flies treated with *Magnetite* failed to respond to sucrose. **a** Graph exhibiting the mean number of flies at two vials, with one containing agar and sucrose, and the other containing agar only, over a period of 10 min. Fruit flies were treated with 0.01 g/L, 0.02 g/L, 0.03 g/L, 0.04 g/L, 0.05 g/L of *Magnetite* for 10 days, represented by the symbols black triangle, orange circle, green square, blue triangle, purple circle, red square respectively. Control flies were fed with yeast paste containing no *Magnetite* for the same duration. n = 20. **b** Bar graph exhibiting the percentage of flies in the vial containing sucrose at the end of the 10 min taste chemotaxis assay. *$p < 0.05$

In the phototaxis assay, it was observed that an increasing *Magnetite* concentration from 0.00 to 0.05 g/L resulted in a decrease in the number of flies moving away from the light source. 17 untreated flies were in the quarter with the highest light intensity while only 4 flies treated with 0.05 g/L of *Magnetite* were in the same quarter at the end of 10 min. (Fig. 4a) Hence, it was observed that increasing *Magnetite* concentration from 0.00 to 0.05 g/L resulted in a decrease in the percentage of average number of flies that reacted to the light stimulus across the three repeats, from 72 to 15% (Fig. 4b).

This indicated that *Magnetite* results in the flies a slower response to the light stimulus, and thus an effective sedative while 0.01 g/L of *Magnetite* solution is the minimum concentration for effective sedation of the flies.

In the taste chemotaxis assay, it was observed that an increasing *Magnetite* concentration from 0.00 to 0.05 g/L resulted in a decrease in the number of flies moving towards the taste stimulus. 11 untreated flies were in the vial with sucrose while only 2 flies treated with 0.05 g/L of *Magnetite* were in the same vial at the end of 10 min. (Fig. 5a) Hence, it was observed that as the concentration of *Magnetite* increased from 0.00 to 0.05 g/L, the percentage of the average number of flies that reacted to the taste stimulus decreased from 55 to 10% (Fig. 5b).

This indicated that *Magnetite* results in the flies a slower response to the taste stimulus, and thus an effective sedative while 0.01 g/L of *Magnetite* solution is the minimum concentration required for effective sedation of the fruit flies.

In the smell chemotaxis assay, it was further observed that an increase in *Magnetite* concentration from 0.00 to 0.05 g/L resulted in a decrease in the number of flies moving away from the vial containing the repellent, acetone. 15 untreated flies responded to the smell stimulus by moving into the third furthest from the repellent while only 3 flies treated with 0.05 g/L of *Magnetite* were in the same third at the end of the 10 min (Fig. 6a). Hence, it was observed that as the concentration of *Magnetite* increased from 0.00 to 0.05 g/L, the percentage of the average number of flies that reacted to the smell stimulus across the three repeats decreased from 75 to 15% (Fig. 6b).

This indicated that *Magnetite* results in the flies a slower response to the smell stimulus, and thus an effective sedative while 0.03 g/L of *Magnetite* solution was the minimum concentration required for effective sedation of the flies and a concentration of less than 0.02 g/L fails to enact a significant behavioural change in the flies.

B. *Discussion*

Many sedatives that are currently in use result in a plethora of side effects. However, *Magnetite*, a TCM herb is not known to have any life threatening side effects upon consumption, and has been used in the field of Chinese Medicine for its sedative and anticonvulsant properties, this research aims to investigate if *Magnetite* is effective as a sedative using three behavioural assays, namely phototaxis, taste chemotaxis and smell chemotaxis assays using *Drosophila melanogaster* as a model organism.

In the phototaxis assay, it was observed that a higher percentage of fruit flies, 46%, failed to respond towards the light stimulus following drug treatment, which is significantly higher as compared to the control flies (10%, Fig. 4). Treatment with *Magnetite* concentration as low as 0.01 g/L was sufficient to elicit a significant sedation in the flies (Fig. 4b).

Similarly, from the taste chemotaxis assay, it was observed that a higher percentage of fruit flies (74%) failed to respond towards the taste stimulus following drug treatment as compared to the control flies (35%, Fig. 5). Treatment with *Magnetite* concentration as low as 0.01 g/L was sufficient to elicit a significant sedation in the flies (Fig. 5b).

From the smell chemotaxis assay, it was evident that a higher percentage of fruit flies treated with 0.05 g/L of *Magnetite* (85%) failed to respond to the smell stimulus

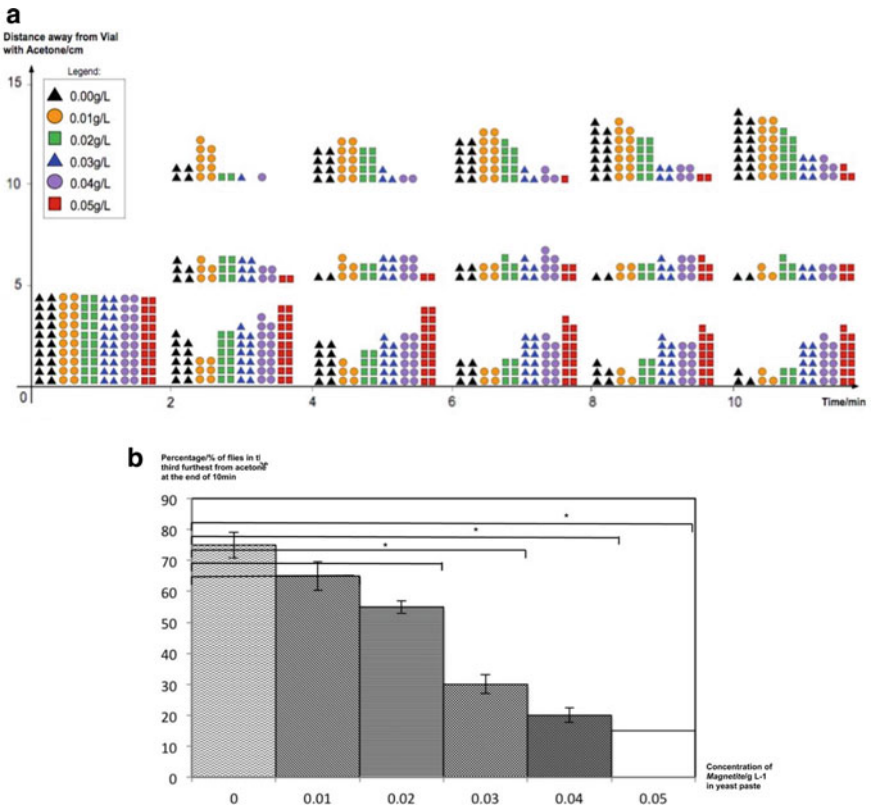

Fig. 6 Fruit flies treated with *Magnetite* failed to respond to acetone. **a** Graph exhibiting the mean number of flies at the three thirds of the boiling tube, each third is 5 cm long, with the first third being nearest to the vial containing acetone, a repellent for fruit flies. Flies were treated with 0.01 g/L, 0.02 g/L 0.03 g/L, 0.04 g/L, 0.05 g/L of *Magnetite* for 10 days, indicated by black triangles, orange circles, green squares, blue triangles, purple circles, red squares respectively. Control flies were fed with yeast paste containing no *Magnetite* for the same duration. n = 20. **b** Bar graph exhibiting the percentage of flies in the third furthest away from the repellent at the end of the 10 min smell chemotaxis assay. *p < 0.05

as compared to the control flies (25%, Fig. 6). Treatment with *Magnetite* as low as 0.01 g/L was also sufficient to elicit sedation in the flies (Fig. 6b).

Since the lowest dosage, 0.01 g/L, examined in this study was sufficient to sedate the flies, future experiments should test lower concentration of drug to establish the minimum dosage required for treatment. Nevertheless, in this current work, it was clearly established that *Magnetite* functions effectively as a sedative.

Magnetite can be considered as a mild sedative as flies were not completely unconscious after the drug treatment. Hence, *Magnetite* can possibly bring about sedation and tranquilization, further substantiating claims in past research papers where it was stated that *Magnetite* was used in the domain of TCM to clear the mind

and produce a calming sensation [4]. As a mild sedative, *Magnetite* can also be used to reduce anxiety to treat claustrophobia and other anxiety-related disorders [19].

Although cytotoxicity of *Magnetite* has yet to be established, past articles have shown that *Magnetite* is not known to cause any harm to human organs, with the capacity to penetrate in liver and kidneys with no significant morphological alterations in both organs [20]. Furthermore, *Magnetite*, a form of Traditional Chinese medicine, is a naturally occurring mineral and hence able to work in harmony with the human system when ingested properly [21]. On the other hand, Western pharmaceutical drugs commonly used for sedation have numerous negative side effects, such as depression [2], aggression [3] and hallucinations [2]. In subsequent experiments, cytotoxicity assays should be performed to ensure that *Magnetite* is safe for consumption. *Magnetite*, commonly known as Iron oxide, contains elements such as Fe, O, Mg, Al, Si, P, Ca, Sc, Ti, V, Cr, Mn, Co, Ni, Cu, Zn, Ga, Ge, Y, Zr, Nb, Mo, Sn, Hf, Ta, W, Pb [22]. Among these elements, it is highly plausible that eleven of which have a potential sedative effect on organisms: Mg, Sc, Ti, Mo, V, Mn, Zn, Ge, Ga, Y, and O. Mg was suggested to be a useful adjunct to CNS depressants traditionally used, inducing a sedative effect on humans [23]; Sc induces symptoms of sedation [24]; Ti potentially induces a sedation effect as it does in titanium dioxide [25]; Mo suppresses pain [26] and is stated to have sedative effect along with V, Mn, Zn [27]; Ge has a sedative effect as investigated in rats [28]; Ga and Y are effective as a sedative in Erbium Chromium Yttrium Scandium Gallium Garnet (Er, Cr: YSGG) which is a form of sedative [29]; O also has sedative effects and can be used as a sedative in minor surgery in the form of Nitrous Oxide [30]. It is possible that these elements work in isolation or in specific dosage combinations to achieve sedation in the fruit flies.

Indeed, Calcium, another element present in the *Magnetite* extract, may be responsible for sedation [31]. Chan et al. (2018) demonstrated that *Drosophila* KCNQ potassium channels were involved in *Magnetite* sedation. KCNQ channels have been reported to regulate neuronal excitability in humans [32]. A ubiquitous calcium sensor, calmodulin (CaM), plays a major role in KCNQ function and channel trafficking [31]. In *Drosophila*, loss of KCNQ function increases neural excitability [32]. Hence it is likely that Calcium acts through CaM to reduce KCNQ function, causing a loss in neural excitability and hence, achieving sedation.

In order to elucidate the mechanism by which sedation is achieved through the use of *Magnetite*, in the fruit flies, elemental depletion can be performed. Taken together, this current work has established the effectiveness of *Magnetite* as a sedative in *Drosophila melanogaster*.

5 Conclusion and Recommendations for Future Work

In conclusion, *Magnetite* is effective as a sedative by suppressing *Drosophila melanogaster* response to light, taste and smell. However, the minimum dosage for *Magnetite* to achieve its effect can be further explored. Future work should also

explore the duration of treatment to achieve the optimal sedation. As the fly gene sequences are evolutionarily well-conserved in the human genome, the findings from this research can be extended to improve our understanding of how *Magnetite* can function in the human body. Subsequent work should also establish the safe use and effectiveness of this drug in humans.

Acknowledgements We would like to thank our teacher mentors, Dr. Lim Ai Khim and Mr. Chan Sau Siong as well as our lab technician, Ms. Wong whose unwavering support and guidance were valuable to the completion of this project.

References

1. Montenegro, M., Veiga, H., Deslandes, A., Cagy, M., McDowell, K., Pompeu, F., Piedade, R., Ribeiro, P. (2005). Neuromodulatory effects of caffeine and bromazepam on visual event-related potential (P300): a comparative study. Arq Neuropsiquiatr 63(2B): 410–5.
2. American Psychiatric Association (2013). Diagnostic and statistical manual of mental disorders, 5th edition, 155–88. Arlington, VA: American Psychiatric Association.
3. Editorial: Tranquilizers Causing Aggression. (1975). British medical Journal, 1(1590): 113–4.
4. O'Brien, K. A., Xue, C. C. The theoretical framework of Chinese medicine. In: Leung P-C, Xue CC, Cheng Y-C, eds. A Comprehensive Guide to Chinese Medicine. River Edge, NJ: World Scientific Publishing Co.; 2003., in press.
5. Hall, J. (2000). The illustrated guide to crystals, 97–125. New York: Sterling Pub. Co.
6. Jennings, B. (2011). *Drosophila* – a versatile model in biology & medicine. Materials Today 14(5): 190–5.
7. Roote, J., and Prokop, A. (2013). How to design a genetic mating scheme: a basic training package for Drosophila genetics. G3 (Bethesda) 3, 353–8.
8. Katz, B., Minke, B. (2009). *Drosophila* photoreceptors and signaling mechanisms Front Cell Neurosci 3: 1–18.
9. Rosenzweig, M., Kang, K., Garrity, P. (2008). Distinct TRP channels are required for warm and cool avoidance in *Drosophila melanogaster*. P Natl Acad Sci U S A 105: 14668–73.
10. Hardie, R. C. (2012). Phototransduction mechanisms in *Drosophila* microvillar photoreceptors. WIREs Membr Transp Signal 1: 162–87.
11. Vosshall, L. B., Stocker, R. F. (2007). Molecular architecture of smell and taste in *Drosophila.* Annu Rev Neurosci (2007).30: 505–33.
12. Su, C. Y., Menuz, K., Carlson, J. R. (2009). Olfactory perception: receptors, cells, and circuits. Cell 139: 45–59.
13. Benton, R., Vannice, K. S., Gomez-Diaz, C., Vosshall, L. B. (2009). Variant ionotropic glutamate receptors as chemosensory receptors in Drosophila. Cell 136: 149–62.
14. Montell, C. (2009). A taste of the *Drosophila* gustatory receptors. Curr Opin Neurobiol 19: 345–53.
15. Weiss, L. A., Dahanukar, A., Kwon, J. Y., Banerjee, D., Carlson, J. R. (2011). The molecular and cellular basis of bitter taste in *Drosophila.* Neuron 69: 258–72.
16. McKemy, D. D. (2007). Temperature sensing across species. Eur J Physiol 454: 777–91.
17. Hamada, F. N., Rosenzweig, M., Kang, K., Pulver, S. R., Ghezzi, A., Jelga, T. J., Garrity, P. A. (2008). An internal thermal sensor controlling temperature preference in *Drosophila.* Nature 454: 217–22.
18. Vang, L. L., Medvedev, A. V., Adler, J. (2012). Simple Ways to Measure the Behavioural Responses of *Drosophila* to Stimuli and Use of these Methods to Characterize a Novel Mutant. PLoS ONE 7(5): e37495, in press.

19. Francis, J. M., Pennell, D. J. (2000). Treatment of Claustrophobia for Cardiovascular Magnetic Resonance: Use and Effectiveness of Mild Sedation. Cardiovascular Magnetic Resonance 2(2): 139–41.
20. Jalil, W. B. F., Pentón-Madrigal, A., Mello, A., Carneiro, F. A., Soares, R. M., Baptista, L. S., Sinnecker, J. P., de Oliveira, L. A. S. (2017). Low toxicity superparamagnetic magnetite nanoparticles: One-pot facile green synthesis for biological applications. Materials Science and Engineering C 78: 457–66.
21. Harvey, A. L. (2008). Natural products in drug discovery. Drug Discovery Today 13(19–20): 894–901.
22. Dare, A. S. S., Barnes, S. J., Beaudoin, G., Meric, J., Boutroy, E., Potvin-Doucet, C. (2014). Trace elements in *Magnetite* as petrogenetic indicators. Mineralium Deposita 49(7): 785–96.
23. Lipman, J., James, M. F., Erskine, J., Plit, M. L., Eidelman, J., Esser, J. D. (1987). Autonomic dysfunction in severe tetanus: magnesium sulfate as an adjunct to deep sedation. Critical Care Medicine 15(10): 987–8.
24. Horovitz, C. T. (2012). Scandium Its Occurrence, Chemistry Physics, Metallurgy, Biology and Technology, 535–47. Amsterdam, Netherlands: Elsevier.
25. Vries, J. (2011). The Pharmacy Guide to Herbal Remedies, 10–1. USA: Random House.
26. Moss, M. (2009). Effects of Molybdenum on Pain and General Health: A Pilot Study. Journal of Nutritional & Environmental Medicine 5(1): 55–61.
27. Pfeiffer, C. C. (2013). International Review of Neurobiology: Supplement 1, 149–50. Cambridge: Academic Press.
28. Cupp, M. J., Tracy, T. S. (2002). Dietary Supplements: Toxicology and Clinical Pharmacology, 199–207. Berlin, Germany: Springer Science & Business Media.
29. Poli, R., Parker, S. (2015). Achieving Dental Analgesia with the Erbium Chromium Yttrium Scandium Gallium Garnet Laser (2780 nm): A Protocol for Painless Conservative Treatment. Photomedicine and Laser Surgery 33(7): 364–71.
30. Griffin, G. C., Campbell, V. D., Jones, R. (1981). Nitrous Oxide—Oxygen Sedation for Minor Surgery: Experience in a Pediatric Setting. JAMA 1981 245: 2411–4.
31. Chan, K. M. C., Tay, Y. K. M., Toh, R. (2018). Investigating the role of *Magnetite* as a sedative in *Drosophila melanogaster*. Unpublished.
32. Jentsch, T. J. (2000). Neuronal KCNQ potassium channels:physiology and role in disease. Nature Reviews Neuroscience 1: 21–30.

Improving the Workflow of Chemical Structure Elucidation with Morgan Fingerprints and the Tanimoto Coefficient

Cheng Zhi Ying, Chieu Hai Leong, Liew Wen Xing Alvin, and Chua Jing Yang

Abstract Chemical structure elucidation (CSE) is useful in identifying unknown chemical threats. However, manual CSE has been a notoriously challenging process till today. As a result, a viable workflow has been developed by DSO National Laboratories to automate CSE. However, inaccuracies in predicting the correct structure with computer assisted CSE will be counterproductive for chemists as they would be verifying a multitude of inaccurate structures. This research thus investigates a way to identify potential compounds whose exact structure would be less accurately predicted. We calculated the Tanimoto distance of the predicted compounds using Morgan Fingerprints and from our investigation, there appears to be an inverse correlation between the diversity of the predicted compounds and the accuracy of its postulated structures. With this finding, future development of a scoring matrix using the Tanimoto distances could help to improve the use of the workflow at the chemist's end.

Keywords Chemical structure elucidation · Tanimoto coefficient · Morgan fingerprints

C. Z. Ying (✉)
Raffles Institution, 1 Raffles Institution Ln, Singapore 575954, Singapore
e-mail: zhi.ying252@gmail.com

C. H. Leong
Department of Information, DSO National Laboratories, 12 Science Park Dr, Singapore 118225, Singapore

L. W. X. Alvin
Department of Chemistry, DSO National Laboratories, 12 Science Park Dr, Singapore 118225, Singapore

C. J. Yang
National University of Singapore, 21 Lower Kent Ridge Rd, Singapore 119077, Singapore

H. Guo et al. (eds.), *IRC-SET 2020*,
https://doi.org/10.1007/978-981-15-9472-4_2

1 Introduction

Chemical structure elucidation (CSE) is the process of deducing the structural formula of an unknown chemical compound through mass spectroscopy. By identifying the fragments produced when the unknown chemical compound undergoes fragmentation inside the mass spectrometer, chemists can piece together the structure of the parent molecule. However, manually carrying out this process is known to be a challenging task in the field of analytical chemistry. Even with the knowledge of a chemical compound's mass spectrum and molecular formula, determining its structural formula remains arduous for chemists due to isomerism [1]. As there are many different forms of isomorphism, from stereoisomerism to constitutional isomerism, numerous isomers can exist for a single chemical compound. Unexpectedly, this holds true for compounds with a smaller chemical formula as well. For instance, a simple molecule like benzene (C6H6) has 217 possible structural formulas [1]. For more complicated chemical compounds, the number of conceivable isomers even goes into the millions [1]. In addition, rearrangement reactions such as McLafferty's also significantly hampers the work of chemists [2].

Hence, computer assisted CSE has been increasingly well-received in recent years as it is notably easier for chemists than manual CSE [3]. Using machine learning and subgraph isomorphism, a promising computer assisted CSE workflow has been developed to predict the top 20 structural formulas of an unknown chemical given its molecular formula and mass spectrum [4]. Despite the workflow's high accuracy of 88% and 71% respectively in identifying the compound classes of phosphonothionates (PPTN) and phosphonates (PPN), the workflow still has room for improvement as its inaccuracies will pose as a double-edged sword for chemists. On one hand, it could save chemists a lot of time. Should the correct structural formula be found within the neural network's top 20 predictions, verifying the predictions will result in the efficient identification of the structure. On the other hand, should the top 20 predictions be false, it will be counterproductive for chemists to verify a multitude of inaccurate structures. Since achieving 100% accuracy with machine learning is almost impossible, this project investigates a way to identify the potential compounds that would be less accurately predicted to improve the use of the current workflow from the chemists' point of view.

2 Materials and Methods

A. Error analysis with Marvin View

We first conducted an error-analysis on the chemical compounds that were used to test the workflow. The test cases for both the PPTN and PPN compounds were sorted according to the rank in which their correctly predicted structure was found. For example, test cases with the correct structure found in the top 1 position were

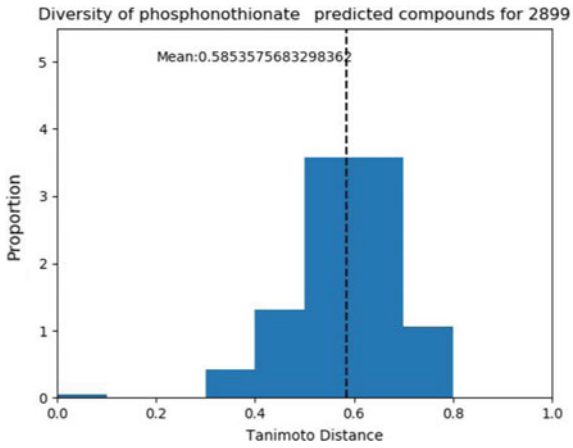

Fig. 1 An example of the histogram plotted by the script

grouped together. As the workflow aims to generate the correct structure in the top 20 positions, test cases where the workflow failed to predict the correct structure in the top 20 positions were labelled as anomalies (Figs. 1, 2, 3, 4 and 5).

MarvinView was then utilised to sketch the predictions of each test case. Upon inspecting the predicted structures, we noticed that the top 20 predicted structures for the better performing test cases were relatively similar since they were found to be mostly chain isomers or positional isomers of the correct structure (Annex Fig. 5). On the other hand, the top 20 predicted structures for the anomalous cases appeared to be more diverse, with a number of its predicted structures being functional group isomers (Annex Fig. 6).

With this initial analysis, we came up with the hypothesis that there is a relationship between these two variables, whereby the lower the performance of the workflow in predicting the structure, the greater the diversity of the predicted compounds.

B. Experimentation with Morgan Fingerprints and Tanimoto similarity from RDkit

To test our hypothesis, a total of 49 PPTN and 285 PPN test cases were used. As our aim was to investigate the diversity of the predicted compounds for each test case, we took a common cheminformatic approach of conducting similarity searches with molecular fingerprints. The molecular fingerprint chosen for this project was the Morgan Fingerprint as it is well-established and widely used in encoding the identity of chemical compounds to calculate their chemical similarity [5]. One of the requirements to generate the Morgan fingerprint was selecting the fingerprint radius, which refers to the number of neighbouring atoms taken into account when the fingerprint is encoded (Annex Fig. 4). Since the typical radius used is a radius from 1 to 3, a radius of 3 was selected as PPN and PPTN compounds are relatively large in size [6].

An appropriate similarity index had to be chosen as well to measure the chemical distance between the molecular fingerprints. As such, the Tanimoto similarity coefficient was employed, being one of the most reliable metrics of similarity [7].

PPTN compounds	
Group	Median
Top 1	0.630
Top 2-20	0.676
Anomalies	0.778

PPN compounds	
Group	Median
Top 1	0.588
Top 2-3	0.598
Top 4-20	0.613
Anomalies	0.654

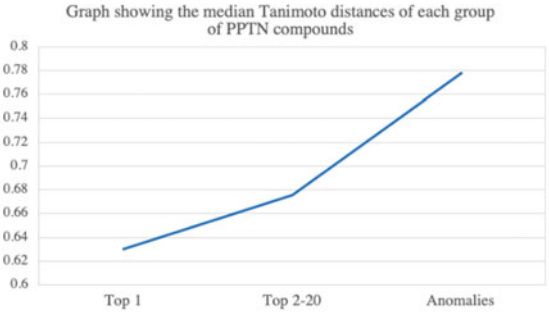

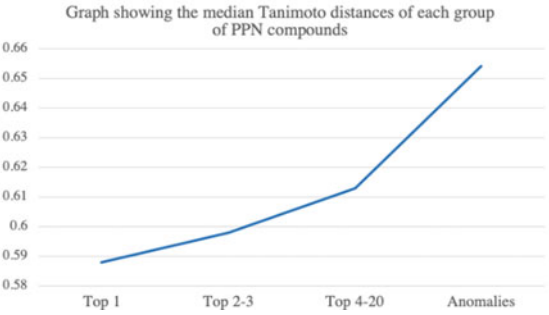

Fig. 2 Table and graph showing the median Tanimoto distances between the predicted compounds for each test case group

	Between the top 1 and anomaly groups	Between the remaining top 20 and anomaly groups	Between the top 20 groups
P-values	0.00489	0.214	0.0194
H_0 Rejection	Yes	No	Yes

Fig. 3 Table showing the p-values and the conclusion of the statistical tests for the PPTN compounds

	Between the top 1 and anomaly groups	Between remaining the top 20 and anomaly groups		Between the top 20 groups		
		Top 2-3	Top 4-20	Top 1 vs 4-20	Top 1 vs 2-3	Top 2-3 vs 4-20
P-values	0.0124	0.000348	0.00449	0.275	0.328	0.0886
H_0 Rejection	Yes	Yes	Yes	No	No	No

Fig. 4 Table showing the p-values and the conclusion of the statistical tests for the PPN compounds

$$\text{Tani}(Vi, Vj) = \frac{Vi \cdot Vj}{\sum_b Vi + \sum_b vjb - Vj \cdot Vj}$$

To test the hypothesis, a script was coded using suitable packages from a cheminformatics software known as RDkit (Annex Figs. 7 and 8). A breakdown of how the script runs is as follows. Firstly, Morgan fingerprints of the compounds' top 20 predictions will be generated from their MOL files (Annex Fig. 9). The fingerprints of the top 20 predictions for each compound are then compared in a pairwise manner and similarity scores for each pair of fingerprints will be calculated using the Tanimoto similarity coefficient. The similarity scores are referred to as the Tanimoto distance where Tanimoto distance = 1 – Tanimoto similarity. The Tanimoto distance ranges from values of 0 to 1, with 0 indicating that the two fingerprints were completely identical and 1 indicating that they were most dissimilar. Lastly, suitable histograms are plotted to represent this data. The histograms show the proportion of fingerprint pairs for the Tanimoto distances recorded and a line indicating the average Tanimoto distance is featured in the histogram as well (Fig. 1). Observing that most of the histograms did not show a skewed distribution, the mean was used over the median or mode as it would account for all values in the data, making the mean a more representative measure of central tendency [8].

Following which, the mean values for the test cases were recorded in a table and likewise, the data was grouped according to the rank in which the test case's correctly predicted structure was found. Due to smaller sample sizes in some of the group rankings, which may cause inaccuracies in identifying a trend in the data, certain groups of test cases were aggregated. For the PPTN compounds, the data was regrouped into three umbrella groups. The three groups consisted of the anomaly test cases, test cases with their correctly predicted structure found in the top 1 position and test cases with their correctly predicted structure found in top 2–20 positions. For the PPN compounds, the data was regrouped into four umbrella groups. Namely, the anomaly test cases, test cases with their correctly predicted structure found in the top 1 position, test cases with their correctly predicted structure found in top 2–3 positions and test cases with their correctly predicted structure found in top 4–20 positions.

Lastly, the median Tanimoto distance for each of the above groups were calculated. The median rather than the mean or mode was used due to potential outliers in the data that could skew the results. Using the median of each group, we could observe for the presence or absence of a trend in the data and hence reach a preliminary conclusion about our hypothesis.

3 Results

From the consistent results of both the PPTN and PPN compound classes (Fig. 2), the values appeared to agree with the hypothesis that there is an inverse correlation between the diversity of the predicted compounds and the rank or accuracy of its correctly predicted structure.

However, as the values only deferred by a few decimal places, statistical tests had to be carried out to prove that there was a significant difference between the means of the Tanimoto distances for each group before we accepted our hypothesis. The independent sample T-test and the Z-test were thus chosen for this purpose as they are often used to determine if there is a significant difference between two samples of data [9].

The reason for using both the T-test and Z-test was because our data had varying sample sizes and the T-test could only be used for samples sizes of 30 and below. Hence, the Z-test was used when the sample sizes exceeded 30 (Annex Figs. 10 and 11).

In view that there were two types of independent sample T-tests, we had to decide whether to carry out the T-test assuming equal variance or unequal variance. Since the general rule of thumb states that the variances of both samples are considered equal so long as one is four times less than the other, we chose the T-test assuming equal variance [10]. We also had to select a significance level for our T-test and choose between a two-tailed or one-tailed T-test. For this research, we used a significance level of 0.05 [11] and we ran a one-tailed T-test as we only required to test the statistical significance in one and not both directions of interest [12]. In other words, we chose the one-tailed T-test because in the case of our hypothesis, we were not interested in knowing that the Tanimoto distances of the better performing test cases were merely different from those of the poorer ones, where the difference could either be lower or higher Tanimoto distances. Rather, we were only specifically interested if the Tanimoto distances of the better performing test cases were lower than those of the poorer performing test cases.

After defining the variables and parameters of our statistical tests, a null hypothesis (H0) and an alternative hypothesis (H1) were written prior to the tests. For the objective of our project, we identified them as H0: The two samples do not have a significant difference between the mean diversity scores and H1: The two samples have a significant difference between the mean diversity scores and the mean diversity scores of the poorer performing test cases is larger. Depending on whether the p-values fall below 0.05, H0 would be rejected and H1 would be accepted.

Looking at the p-values of our statistical tests (Figs. 3 and 4), for both the PPTN and PPN compounds, there was a significant difference between the mean Tanimoto distance of the top 1 and anomaly groups.

For the PPTN compounds (Fig. 3), there was a significant difference between the top 1 and top 2–20 groups as well. However, the top 2–20 group did not have significantly different Tanimoto distances as compared to the anomalies.

Meanwhile, for the PPN compounds (Fig. 4), there were significant differences between the anomaly groups and the different top 20 groups but between the top 20 groups themselves little significant difference was shown between their Tanimoto distances. It is worth noting though that the p-value for the test between the top 2–3 and top 4–20 groups was 0.0886, which meant that it was only slightly bigger than of 0.05 and H_0 was marginally not rejected.

4 Discussion

Hence from the above results, we can conclude that the results mostly follow the hypothesis.

With regards to the PPTN compounds, although the difference between the top 2–20 groups and the anomalies was not very significant, this could be due to a shortage of test cases causing poor representation of the data for those in the top 2–20 category. We noted that the sample size of the test cases in the top 1 group was about twice the size of that of the top 2–20 group. In relation to the PPN compounds, whilst the Tanimoto distances of the test cases in the top 20 groups were not clearly differentiated, it can be ascertained that the anomalies do have a significantly higher diversity score than the test cases in the top 20 groups. When the anomalies were compared to the top 1, top 2–3 and top 4–20 groups, the p-values were notably smaller than 0.05, allowing H0 to be rejected and H1 to be accepted. Moreover, in both compounds, the top 1 and anomaly groups showed significantly different Tanimoto distances.

Due to time constraints, we were unable to conduct a k-fold cross validation test to increase the sample size of the test cases used to validate the hypothesis. In future however, this test can be performed to obtain more data and thus more accurate results as the number of groups of data will not be limited to three or four umbrella groups with a larger data set. The chances of anomalies occurring will also be reduced. For future development, the findings of this experiment could be used to create a scoring matrix for the chemist's reference. With this scoring matrix, when chemists test for an unknown chemical, they will be able to have a rough sensing on which of the predicted structures in the top 20 should they be looking at depending on the Tanimoto distance of the predicted compounds as the predicted structures are not always found in the top 1 position. In the event of anomalous cases where the correct structure is not predicted in the top 20, they can also save the time of verifying 20 incorrect structures.

Acknowledgements I would like to express my gratitude to my mentor Dr Chieu for his patience and understanding throughout the project. I am also really appreciative of his help in clarifying my misunderstandings about the project and for allowing me to have this opportunity to learn more about coding and cheminformatics. I would also like to express my gratitude to Alvin for his invaluable guidance and for always going the extra mile to help me with the issues that I was having with project. I am utmost grateful for his understanding and unwavering support. Last but not least,

I would like to thank Jing Yang for teaching me how to code and for always willing to lend me a helping hand despite his ongoing project. This project would not have been possible without them.

Appendix

See Figs. 5, 6, 7, 8, 9, 10, 11 and 12.

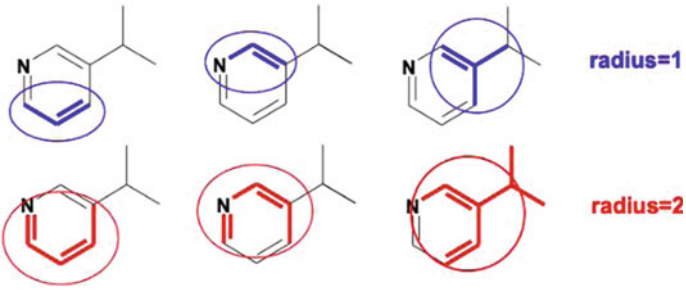

Fig. 5 Diagram explanation of RDKit's Morgan fingerprint radius [4]

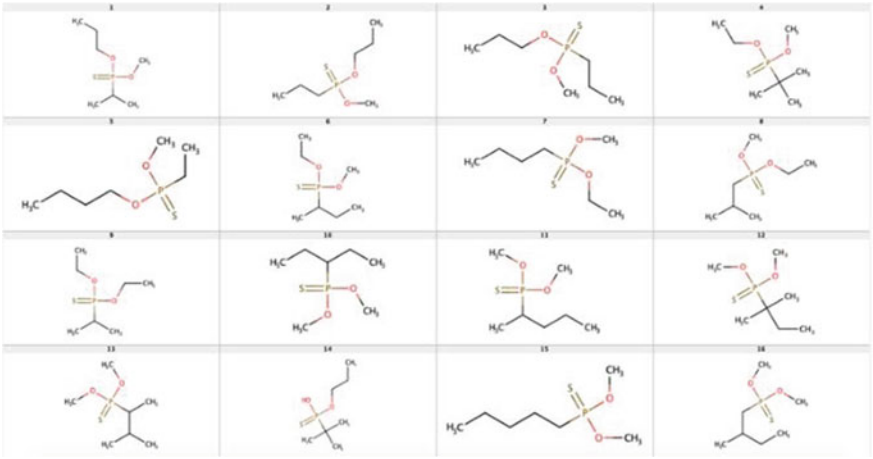

Fig. 6 An example of the predicted compounds for the better performing test case, compound 1076, with the correct structure found in the top 2 positions

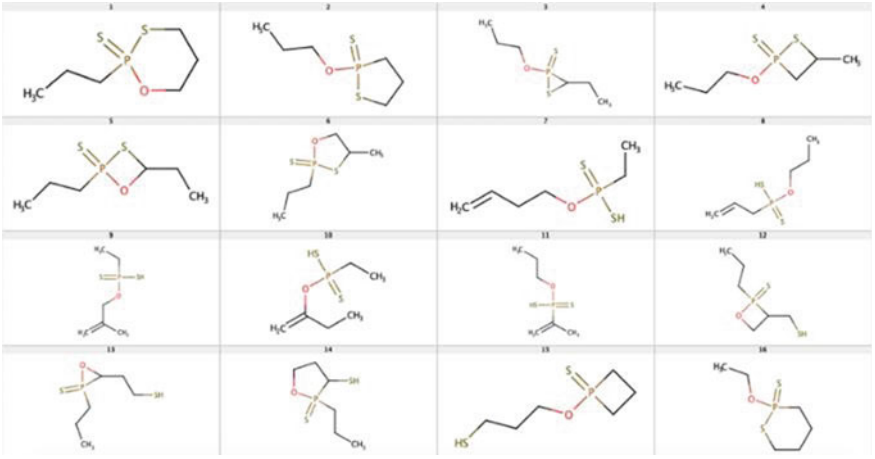

Fig. 7 An example of the predicted compounds for the poorer performing test case, compound 3499, with the correct structure not found within the top 20 positions

```
from argparse import ArgumentParser
from rdkit import Chem
from rdkit.Chem.rdMolDescriptors import GetMorganFingerprint
from rdkit import DataStructs
import numpy as np
import matplotlib
import matplotlib.pyplot as plt
import sys

def dist(i, j, fps):
    return 1- DataStructs.TanimotoSimilarity(fps[i], fps[j])

def main(args):
    path = "phosphonates_predicted/" + args.fileid + ".sdf"
    supplier = Chem.SDMolSupplier(path)

    mols = []
    for mol in supplier:
        mols.append(mol)

    fps = [GetMorganFingerprint(x, 2) for x in mols]

    similarities = []

    for i in range(len(mols)):
        for j in range(i+1, len(mols)):
            similarities.append(dist(i, j, fps))

    matplotlib.use('Agg')
    plt.hist(similarities, np.arange(0, 1.1, 0.1), density=True)
    plt.xlabel('Tanimoto Distance')
    plt.ylabel('Proportion')
    plt.axvline(x = np.mean(similarities), color = 'black', linestyle = '--', )
    plt.text(x = 0.2, y = 5, s = 'Mean:{}'.format(np.mean(similarities)))
    plt.title('Diversity of {} predicted compounds for {}'.format(args.dataset, args.fileid))
    plt.axis([0, 1.0, 0, 5.5])
    plt.savefig('histograms/predicted_similarity_histograms/radius_2/anomaly/similarity_{}.png'.format(args.fileid))
    plt.clf()
    plt.cla()
    plt.close()

if __name__ == '__main__':
    parser = ArgumentParser()
    parser.add_argument('dataset', help="phosphononate")
    parser.add_argument('fileid', help="4083")
    args = parser.parse_args()
    main(args)

print()
```

Fig. 8 Script coded to test the hypothesis

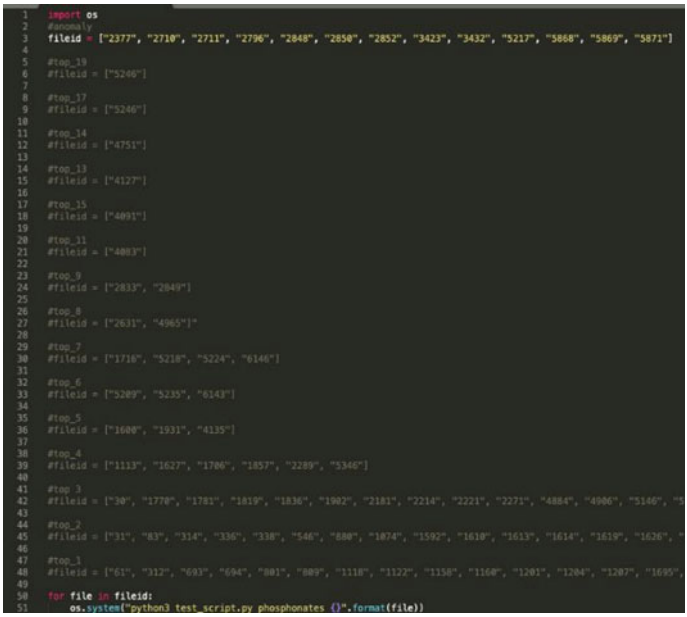

Fig. 9 Script coded to automate repetitive running of the script to test other test cases

```
O-SEC-BUTYL O-CYCLOHEXYL PROPYLPHOSPHONOTHIONATE

Library ID = 3689
 17 17  0  0  0  0  0  0  0  0999 V2000
   -1.0292    0.5250    0.0000 C   0  0  3  0  0  0  0  0  0  0  0  0
   -0.6208   -0.1875    0.0000 C   0  0  0  0  0  0  0  0  0  0  0  0
    0.1958   -0.1901    0.0000 C   0  0  0  0  0  0  0  0  0  0  0  0
    0.6104    0.5181    0.0000 C   0  0  0  0  0  0  0  0  0  0  0  0
    0.2020    1.2306    0.0000 C   0  0  0  0  0  0  0  0  0  0  0  0
   -0.6208    1.2349    0.0000 C   0  0  0  0  0  0  0  0  0  0  0  0
   -2.4334    1.1106    0.0000 P   0  0  3  0  0  0  0  0  0  0  0  0
   -1.8500    1.6981    0.0000 S   0  0  0  0  0  0  0  0  0  0  0  0
   -3.0209    1.6940    0.0000 C   0  0  0  0  0  0  0  0  0  0  0  0
   -3.0209    0.5269    0.0000 O   0  0  0  0  0  0  0  0  0  0  0  0
   -1.8500    0.5227    0.0000 O   0  0  0  0  0  0  0  0  0  0  0  0
   -3.8500    0.5292    0.0000 C   0  0  3  0  0  0  0  0  0  0  0  0
   -4.2667    1.2458    0.0000 C   0  0  0  0  0  0  0  0  0  0  0  0
   -5.0917    1.2458    0.0000 C   0  0  0  0  0  0  0  0  0  0  0  0
   -4.2667   -0.1833    0.0000 C   0  0  0  0  0  0  0  0  0  0  0  0
   -3.8500    1.7000    0.0000 C   0  0  0  0  0  0  0  0  0  0  0  0
   -4.2667    2.4167    0.0000 C   0  0  0  0  0  0  0  0  0  0  0  0
  9  7  1  0  0  0  0
  7 10  1  0  0  0  0
 11  7  1  0  0  0  0
  2  3  1  0  0  0  0
  3  4  1  0  0  0  0
  4  5  1  0  0  0  0
 10 12  1  0  0  0  0
 11  1  1  0  0  0  0
  5  6  1  0  0  0  0
 12 13  1  0  0  0  0
  7  8  2  0  0  0  0
 13 14  1  0  0  0  0
 12 15  1  0  0  0  0
  1  2  1  0  0  0  0
  9 16  1  0  0  0  0
  1  6  1  0  0  0  0
 16 17  1  0  0  0  0
M  END
$$$$
```

Fig. 10 An example of the MOL file of compound 3689

	Anomaly	*Top 1*
Mean	0.815	0.7831
Variance	0.003580182	0.001903334
Observations	12	30
Pooled Variance	0.002364468	
Hypothesized Mean Difference	0	
df	40	
t Stat	1.92066054	
P(T<=t) one-tail	0.030961554	
t Critical one-tail	1.683851013	
P(T<=t) two-tail	0.061923109	
t Critical two-tail	2.02107539	

Fig. 11 An example of the data collected from the T-test and its sample size (observations)

	Top 2-3	*Anomaly*
Mean	0.66425	0.579247312
Known Variance	0.00507423	0.01320525
Observations	12	93
Hypothesized Mean Difference	0	
z	3.576582382	
P(Z<=z) one-tail	0.000174058	
z Critical one-tail	1.644853627	
P(Z<=z) two-tail	0.000348116	
z Critical two-tail	1.959963985	

Fig. 12 An example of the data collected from the Z-test and its sample size (observations)

References

1. Elyashberg, M. E., Williams, A., & Blinov, K. (2011, November 30). Contemporary Computer-Assisted Approaches to Molecular Structure Elucidation New Developments in NMR, 253–299. doi: https://doi.org/10.1039/9781849734578-00253
2. 2. Mclafferty, F. W. (1959). Mass Spectrometric Analysis. Molecular Rearrangements. Analytical Chemistry, 31(1), 82–87. doi: https://doi.org/10.1021/ac60145a015
3. Béni, Z., Szakács, Z., & Sánta, Z. (2015). Computer-Assisted Structure Elucidation in NMR. *Anthropic Awareness*, 317–354. doi: https://doi.org/10.1016/b978-0-12-419963-7.00009-2
4. Lim, Jing, Wong, Joshua, Wong, Xuan, M., … Nigel, N. K. (2018, November 17). Chemical Structure Elucidation from Mass Spectrometry by Matching Substructures. arXiv:1811.07886
5. Apodaca, R. L. (n.d.). Computing Extended Connectivity Fingerprints. Retrieved December 29, 2019, from https://depth-first.com/articles/2019/01/11/extended-connectivity-fingerprints/.
6. Landrum, greg. (n.d.). Open-Source Cheminformatics Software. Retrieved December 19, 2019, from https://www.rdkit.org/.
7. Bajusz, D., Rácz, A., & Héberger, K. (2015). Why is Tanimoto index an appropriate choice for fingerprint-based similarity calculations? *Journal of Cheminformatics*, *7*(1). doi: https://doi.org/10.1186/s13321-015-0069-3
8. Frost, J. A., Rubel, J. A., Rubel, M. undefined, Frost, M. undefined, Memon, O. undefined, Memon, O. undefined, … Shams, undefined undefined. (2019, October 1). Measures of Central Tendency: Mean, Median, and Mode. Retrieved December 20, 2019, from https://statisticsbyjim.com/basics/measures-central-tendency-mean-median-mode/.
9. Kenton, W. (2019, November 18). T-Test Definition. Retrieved December 29, 2019, from https://www.investopedia.com/terms/t/t-test.asp.
10. Zaiontz, C. (n.d.). Two Sample t Test: unequal variances. Retrieved December 29, 2019, from https://www.real-statistics.com/students-t-distribution/two-sample-t-test-uequal-variances/.
11. Glen, S. (2019, August 8). Alpha Level (Significance Level): What is it? Retrieved December 29, 2019, from https://www.statisticshowto.datasciencecentral.com/what-is-an-alpha-level/.
12. Glen, S. (n.d.). One Tailed Test or Two in Hypothesis Testing: How to Decide in Easy Steps. Retrieved December 29, 2019, from https://www.statisticshowto.datasciencecentral.com/probability-and-statistics/hypothesis-testing/one-tailed-test-or-two/.

Transport and Optical Studies of Two-Dimensional Electron Gas in AlN/$SrTiO_3$ Heterostructure

Junyao Floria Wang

Abstract Emerging phenomena discovered at the interface between two adjacent layers, such as two-dimensional electron gas (2DEG) and spin–orbit coupling (SOC) provides promising building blocks for future novel electronics. To exploit these phenomena, it is necessary to modulate and harness them via electric, magnetic, and optical stimuli. This study presents an emergent two-dimensional electron gas at the interface between amorphous aluminium nitride (a-AlN) and single crystal strontium titanate ($SrTiO_3$), i.e. the a-AlN/$SrTiO_3$ interface. The amorphous 2DEG system is powerful, controllable, and easily manufactured, demonstrating great potential for nanoelectronics. First, while applying back and top gate, we show that the 2DEG exhibits high mobility and a transition from weak localisation to weak anti-localisation, where weak anti-localisation indicates the appearance of SOC. The carrier mobility and SOC at the 2DEG are highly tunable upon applying gate electric field, which is useful for future oxide electronics. Second, via applying optical stimuli, we modulated the resistance/conductivity of the 2DEG according to key parameters including backgate voltage, wavelength and power of visible-light illumination. We notice an illumination-enhanced gating effect, due to the migration of oxygen vacancies under electrical field and light illumination, and a highly tunable photoconductivity of 2DEG under visible light illumination and electrostatic gating. This work demonstrates the tunability of amorphous two-dimensional electron gas under magnetic, electrical, and optical stimulation, which could pave the way for next-generation electronic devices.

Keywords Amorphous two-dimensional electron gas · Material science · Nanoelectronics

J. F. Wang (✉)
Hwa Chong Institution (College), Singapore, Singapore
e-mail: floriawang777@gmail.com

H. Guo et al. (eds.), *IRC-SET 2020*,
https://doi.org/10.1007/978-981-15-9472-4_3

1 Introduction

Research in oxide interfaces, formed by transition-metal oxide compounds, has flourished over the past decade [1, 2], owing to tremendous advancements in the atomic-scale synthesis of oxide heterostructures, such as pulsed laser deposition and molecular beam epitaxy [3, 4]. Investigating such structures bears great potential for the development of next-generation electronic devices. Oxide interfaces are strongly correlated electron systems, characterised by higher areal carrier densities and much shorter electron confinement lengths than conventional semiconductor interfaces. Such interfaces offer tremendous flexibility in terms of their interfacial properties, and are therefore highly exploitable for the fabrication of a multitude of potentially useful structures, which exhibit properties not shown in conventional semiconductors. Such properties include interface superconductivity, magneto-electric coupling, and the quantum Hall effect, which could greatly enhance future technology.

The two dimensional electron gas (2DEG) is a phenomenon found at oxide interfaces that displays enormous potential for application. There are two types of 2DEG—crystalline *c*-2DEG, and amorphous *a*-2DEG. The former occurs in oxide heterostructures consisting a compound with charge-neutral layers and a compound with charged polar layers, where polar discontinuity occurs. The formation of polar discontinuity generates or removes charge carriers at the interface, driving the formation of 2DEG at the crystalline/crystalline interface. For the latter, past research has suggested a dipole model as the explanation, where the 2DEG is formed due to charge transfer induced by oxygen vacancies that form in the substrate near the interface [5].

Amorphous *a*-2DEG differs greatly from crystalline *c*-2DEG in various areas. Despite having similar physical properties in terms of superconductivity, potential-well depth, and so on, a-2DEG has less lattice strain at the interface, a higher interface carrier density, and fewer requirements for growth [6–8]. Thus, these differences make *a*-2DEG a powerful, controllable, and easily manufacturable 2DEG system. Extensive investigation is necessary for the exploitation of the potential of such a system.

2 Research Objectives

Applying electrostatic gating field and visible-light illumination are two of the commonly used stimuli for semiconductor devices [9]. Via capacitive effect, a gate field modifies the carrier density of the devices, and illumination generates extra carriers at the interface by exciting trapped electrons.

The selected material for this study is *a*-AlN/$SrTiO_3$. As studies on the optoelectrical properties of a-2DEG are scarce at present, with more focus given to *c*-2DEG in past research.

This study aims to comprehensively understand the a-AlN/SrTiO3 interfacial phenomena related to spin–orbit coupling and its tunability via electrostatic gating field stimulation with the aid of backgating and dual-gating. It also aims to study the photoresponse of the a-2DEG under visible-light illumination.

3 Theoretical and Experimental Background

A. *The Drude Model*

The Drude model, proposed by Paul Drude in 1900, systematically analyses the electrical transport characteristics of metals by considering electrons the reason for their conductive properties [10, 11].

From the Drude model, we obtain the following equation, which suggests the Hall Effect for longitudinal current flow j_x and induced electric field along the *y*-direction:

$$\begin{pmatrix} E_x \\ E_y \end{pmatrix} = \frac{1}{\sigma_0} \begin{pmatrix} 1 & -\frac{qB\tau}{m} \\ \frac{qB\tau}{m} & 1 \end{pmatrix} \begin{pmatrix} j_x \\ j_y \end{pmatrix} \tag{1}$$

where $\boldsymbol{E}_x$ and $\boldsymbol{E}_y$ are electric fields in the x- and y-directions respectively, σ_0 is the conductivity, q is the elementary charge of an electron, τ is the mean free time between ionic collisions (i.e. relaxation time), $\boldsymbol{B}$ is the applied magnetic field, and j is current density.

The Hall field may be represented by:

$$E_y = R_H j_x,\ R_H = \frac{B}{nq} \tag{2}$$

where R_H is the Hall coefficient and n is the charge density. We observe from this that $\boldsymbol{E}_y$ has a linear proportional relationship with the applied magnetic field $\boldsymbol{B}$.

The conductivity obtains from (1) as such:

$$\sigma_{xx} = \frac{\rho_{xx}}{\rho_{xx}^2 + \rho_{xy}^2} = \frac{n\tau q^2}{m} \frac{1}{1 + \omega_c^2 \tau^2}$$

$$\sigma_{xy} = \frac{\rho_{xx}}{\rho_{xx}^2 + \rho_{xy}^2} = \frac{n\tau q^2}{m} \frac{\omega_c^2 \tau^2}{1 + \omega_c^2 \tau^2}$$

where $\omega_c = \frac{q\boldsymbol{B}}{m}$.

Where $\sigma = mq\mu$, we derive the carrier mobility at zero magnetic field:

$$\mu = \frac{\sigma_{xx}}{nq} = \frac{1}{nq\rho_{xx}} = \frac{q\tau}{m}$$

The Drude model is very effective in describing the direct current and alternating current conductivity, the Hall effect, and the magnetoresistance of metals near room temperature. However, it is insufficient for modelling materials with more than one type of carriers, or more than one conductive channels, which is common in doped materials and complex heterostructures. This is because it assumes that all carriers move in a single conduction band. Thus, in order to obtain a suitable model for the multi-carrier material used in this study, we must modify the Drude model to better describe this circumstance.

B. *Two Band Model and Non-linear Hall effect*

The Drude model assumes a linear Hall effect, where all electrons move in one conduction band, and fails to account for cases where there are more than one conduction band due to doping or the construction of heterostructures. However, there are typically two or more conduction bands in heterostructures, which may be considered parallel conduction channels. Revising the representation of the Hall Effect as described by the Drude model, the carrier conductivity rewrites as such:

$$\sigma_{xx} = \sigma_{xx_1} + \sigma_{xx_2}$$

$$\sigma_{xy} = \sigma_{xy_1} + \sigma_{xy_2}$$

and the carrier resistivity as such:

$$\begin{aligned}\rho &= \begin{pmatrix} \rho_{xx} & -\rho_{xy} \\ \rho_{xy} & \rho_{xx} \end{pmatrix} \\ &= \begin{pmatrix} \sigma_{xx_1} + \sigma_{xx_2} & -(\sigma_{xy_1} + \sigma_{xy_2}) \\ \sigma_{xy_1} + \sigma_{xy_2} & \sigma_{xx_1} + \sigma_{xx_2} \end{pmatrix}^{-1}\end{aligned}$$

The two-carrier model successfully describes the mechanism of the nonlinear Hall effect and provides a mathematical form of transverse resistance R_{xy} as a function of magnetic field $\boldsymbol{B}$ perpendicular to the plane:

$$R_{xy} = -\frac{1}{q}\frac{\left(\frac{n_1\mu_1^2}{1+\mu_{1B^2}^2} + \frac{n_2\mu_2^2}{1+\mu_{2B^2}^2}\right)B}{\left(\frac{n_1\mu_1}{1+\mu_{1B^2}^2} + \frac{n_2\mu_2}{1+\mu_{2B^2}^2}\right)^2 + \left(\frac{n_1\mu_1^2}{1+\mu_{1B^2}^2} + \frac{n_2\mu_2^2}{1+\mu_{2B^2}^2}\right)^2}$$

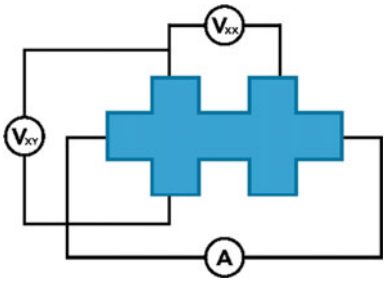

Fig. 1 Schematic diagram of 6-contact hall bar

where q is the elementary charge, n_i, μ_i $(i = 1, 2)$ are the sheet carrier densities and mobilities of two different conduction bands, respectively. This equation is written assuming that $n_1 + n_2 = n_{total}$, and $\mu_1 n_1 + \mu_2 n_2 = \sigma$.

C. *Hall Bar Measurement Method*

The Hall bar geometry is a commonly used method to measure the Hall effect. By applying a current and magnetic flux, the Hall voltage is induced in the perpendicular direction, which we may measure using a 6-contact Hall bar, as illustrated in the Fig. 1.

A Hall bar with 6 contacts shows an ideal symmetrical geometry. Each contact pair is designed symmetrically over the mid-point of the major axis. The symmetrical 1-2-2-1 Hall bar device grants the possibility of measuring both resistivity and Hall coefficient [12].

The sheet resistance for Hall bar measurement may be calculated using the equation

$$R_s = \frac{\text{thickness}}{\text{length}} R$$

where $R = \frac{V}{I}$.

D. *Van der Pauw Measurement Method*

The van der Pauw [13] method is another common way to measure electrical transport and Hall effect. For this method, the sample has a square geometry, and we connect four leads with the four corners of the sample, as shown in the Fig. 2.

The equation $R_S = \frac{\pi}{ln2} R_{vdP}$ obtains the sheet resistance, where $R_{vdP} = \frac{V}{I}$.

4 Results and Discussion

A. *Magnetoresistance Dependent on Spin–Orbit Coupling*

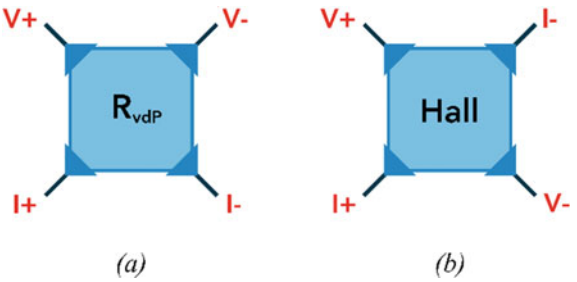

Fig. 2 Van der Pauw method for measuring transport properties: **a** sheet resistance; **b** Hall effect

The 2DEG at the *a*-AlN/$SrTiO_3$ interface is strongly confined within the transverse direction. Its electrical transport properties were measured using Hall-bar patterned samples.

By applying backgate voltage of various magnitudes, we successfully achieved the gate tuning transition from weak localisation to weak anti-localisation, which suggests the significance of spin–orbit coupling in impacting the electrical properties at the 2DEG interface.

From Fig. 3, there is a notable negative magnetoresistance at 14 V gating voltage, which is 20 times greater than that in the original state with 0 V gating voltage at 8 T applied magnetic field. By varying the gating voltage within the range of −10 to 14 V, we note a transition from weak localisation (in the negative voltage range) to weak anti-localisation (in the positive voltage range). This gate-tunability of magnetoresistance strongly indicates the presence of spin–orbit interaction, resulting in weak anti-localisation in the 2DEG.

The Hall measurement verifies the above interpretation.

From Fig. 3, the nonlinear Hall effect is observed when the backgating voltage is increased past 4 V (as the graphs become concave upwards). This suggests greater interaction at the 2DEG interface which affects the magnetoresistance in a larger magnetic field, where spin–orbit coupling no longer dominates in influence. In the high-field ($\boldsymbol{B} \geq 1.0$ T), the presence of multiple carriers intensify the decline of conductivity, which matches the data shown in Fig. 4, where it drops dramatically at high-field with backgate voltage of 4 V and above.

B. *Dual-gate modulation on Carrier Density and Mobility*

We also studied the effect of backgate voltage on carrier density and mobility—two significant factors which determine the performance of devices. High-performance devices mostly require high carrier density and mobility.

First, we studied sheet resistance at the 2DEG interface as a function of backgate voltage. Figure 4 demonstrates that resistance decreases as voltage varies from −10 to 10 V.

Figure 5 demonstrates the change in carrier density n_{2D} and carrier mobility μ, which both increase generally when backgate voltage is increased from −4 to 14 V.

Notably, when backgate voltage increases from 2 to 16 V, the carrier density quickly plateaus above 10 V, which indicates that it has reached saturation point.

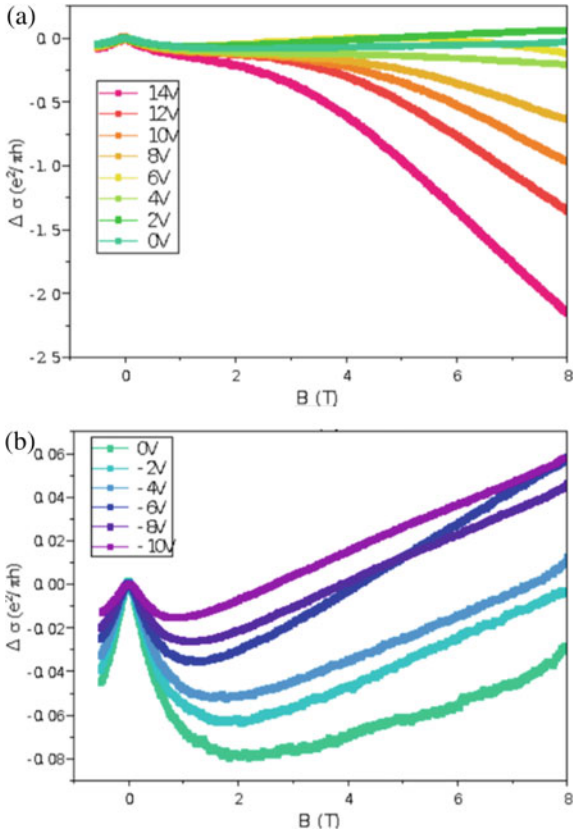

Fig. 3 Magnetoresistance as a function of magnetic field (x-axis) under varied gating voltage from −10 to 14 V

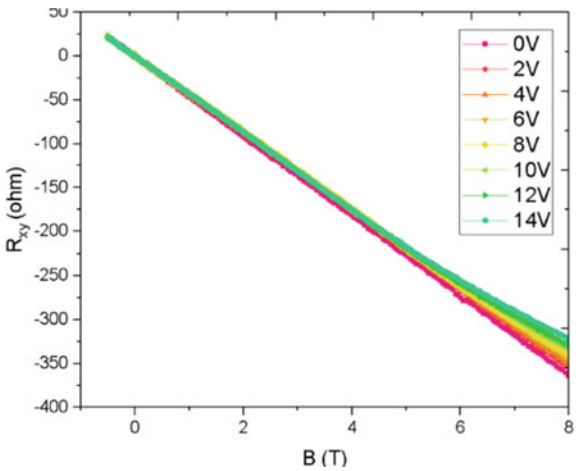

Fig. 4 Hall measurement demonstrating non-linear Hall effect

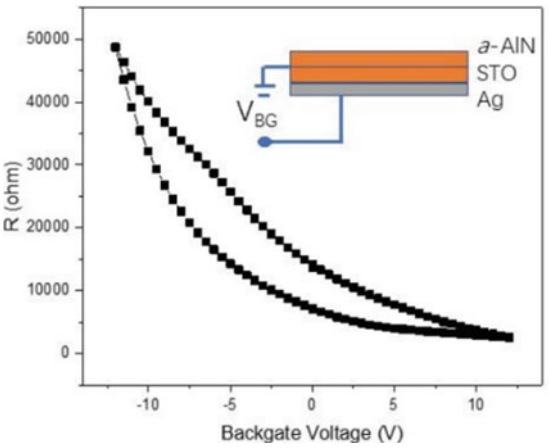

Fig. 5 Resistance as a function of backgate voltage

Furthermore, this carrier density is 2–3 orders of magnitude lower than the high carrier density of a-AlN/$SrTiO_3$ itself. Despite this, the corresponding carrier mobility above 10 V backgate voltage continues to increase gradually. This suggests that backgating is potentially limiting in allowing the 2DEG interface to reach higher performance (Fig. 6).

To address the issue regarding the plateauing of carrier density, we design a dual-gate device by applying electrostatic gating from the top of the amorphous AlN (topgate) and from the back of the $SrTiO_3$ substrate. The topgate is applied via ionic liquid, which has been proven, in past studies, to tune carrier density effectively [14–16].

In doing so, we replace the dielectric device (achieved via backgate method) to a field-effect device (via topgating through the ionic liquid). The resulting device is somewhat like a nanoscale capacitor, which allows for a significantly greater range for tuning carrier density.

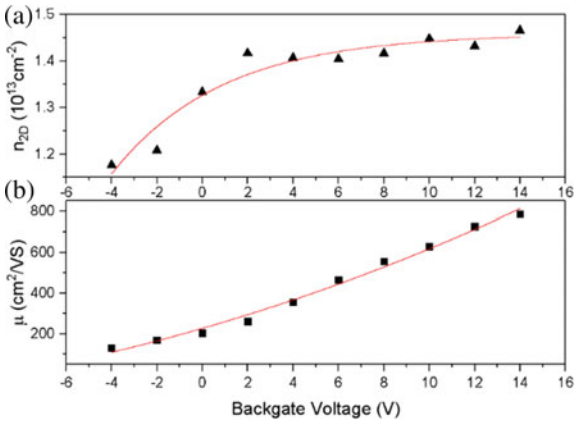

Fig. 6 **a** Carrier density, and **b** carrier mobility as modulated by varied backgate voltage

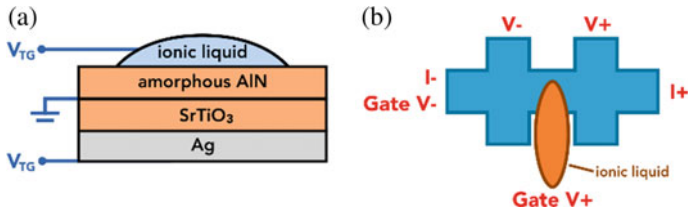

Fig. 7 Schematic diagram of **a** 2DEG heterostructure, **b** Hall bar, with applied with ionic liquid topgate

To prevent excessive current leakage, we apply ±0.4 V topgate voltage to the sample at 270 K, then cool the sample down to 1.5 K to measure its carrier properties.

Figure 7 shows the results of this measurement.

Note that carrier density n_{2D} is considerably stable for topgate voltage (ILG) of 0.4 V, at a significantly greater carrier density beyond the range achieved by only applying backgate voltage. For topgate voltage (ILG) of −0.4 V, varied backgate voltage modulates carrier density over a large range, indicating that topgate successfully tuned carrier density to a significantly greater, and more practical range for high-performance devices.

For carrier mobility, we observe a similar result. Remarkably, where carrier density is lower with topgate voltage (ILG) of −0.4 V, the carrier mobility is tuned to 2 orders of magnitude greater than that in original state. To this, we ascribe the large dielectric constant of $SrTiO_3$, which gives rise to relatively weak confinement of electrons, thus resulting in a high carrier mobility at the 2DEG interface.

C. *Gate Modulation of Photoresponse*

We achieved basic knowledge of the 2DEG photoresponse by shining light of different wavelengths on the sample with backgating. We obtain the Fig. 8 for the relationship between sheet resistance and backgate voltage from −50 to 50 V.

Interestingly, the graph of sheet resistance against backgate voltage for $\lambda = 635$ nm presents an asymmetrical change in resistance when backgate voltage varies, similar to that shown in Fig. 4, where no optical stimulus is present, suggesting that $\lambda = 635$ nm is ineffective in inducing a significant photoresponse at the 2DEG interface, to be further confirmed.

In Fig. 10, we present results of experiments using illumination by the three different lasers, with backgate voltage switched from 0 to ±40 V at regular time intervals.

Remarkably, the sample illuminated by $\lambda = 409$ nm has a different photoresponse to that of $\lambda = 519$ nm and $\lambda = 635$ nm. This can be understood through comparing photoconductivity of the sample under different electrical stimuli.

When backgating voltage is 0 V, the sheet resistance of 2DEG decreases only for lasers $\lambda = 409$ nm and $\lambda = 519$ nm, with a greater change under illumination by $\lambda = 409$ nm laser. It remains relatively stable under illumination by $\lambda = 635$ nm. This difference may be attributed to the lower photon energy for $\lambda = 635$ nm laser,

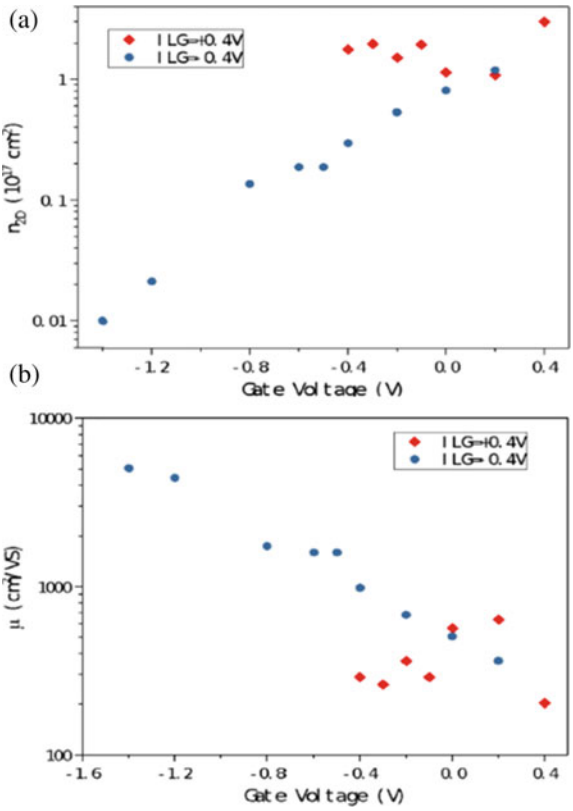

Fig. 8 **a** Carrier density, **b** carrier mobility, as modulated by varied backgate voltage for ±0.4 V topgate voltage

insufficient to excite electrons across the $SrTiO_3$ bandgap. As photon energy increases as wavelength decreases, the greatest photoresponse is observed with $\lambda = 409$ nm.

Then, we look at the photoresponse of 2DEG under no optical stimulus, and illuminated by $\lambda = 519$ nm and $\lambda = 635$ nm. We note that sheet resistance increases when backgate voltage is negative (−40 V), which is likely due to a decrease in carrier density. Conversely, when positive (+40 V) backgate voltage is applied, sheet resistance decreases in general. Surprisingly, this is not the case for $\lambda = 409$ nm.

Figure 10 results match with Fig. 9. It also shows that sheet resistance is lowest when backgate voltage is negative, for the sample illuminated by $\lambda = 409$ nm. We identify this as a significant difference, which requires further investigation, as there is no conclusive justification for this phenomenon that we can present at this moment.

D. *Illumination Power Modulation of Photoresponse*

The photoresponse of the 2DEG interface was also studied through varying illumination power, using lasers with different wavelengths and applying backgate voltage of ±40 V.

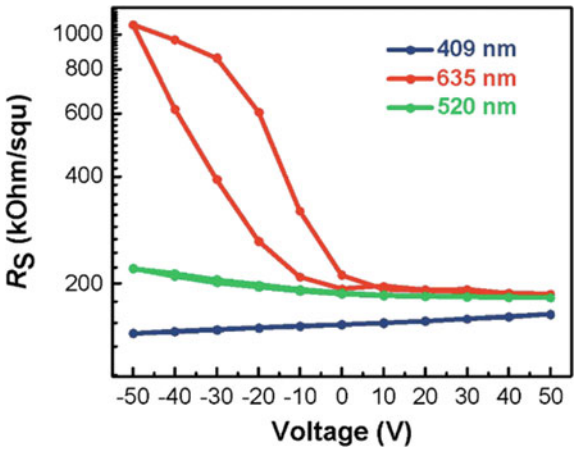

Fig. 9 Sheet resistance of 2DEG with backgate voltage

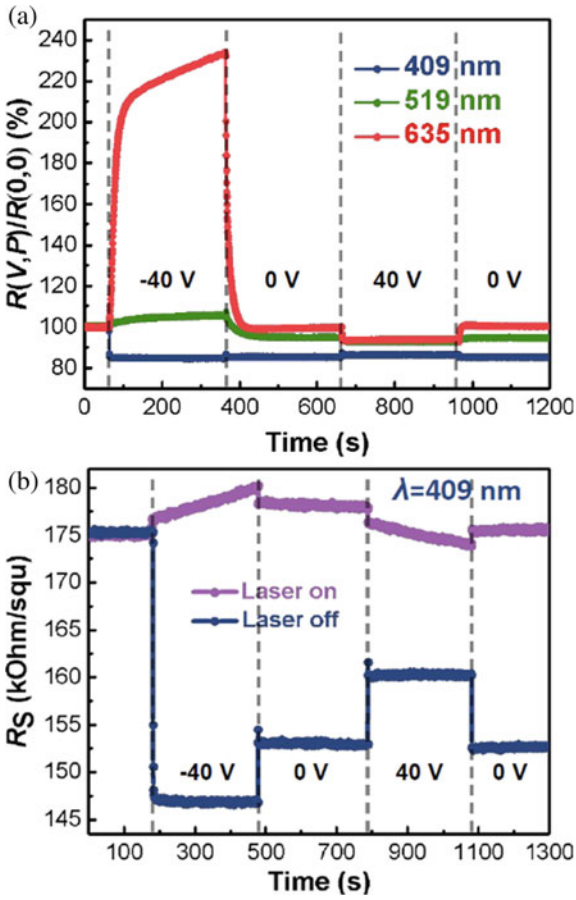

Fig. 10 **a** Sheet resistance modulated by backgate voltage; **b** sheet resistance with on/off illumination of $\lambda = 409$ nm

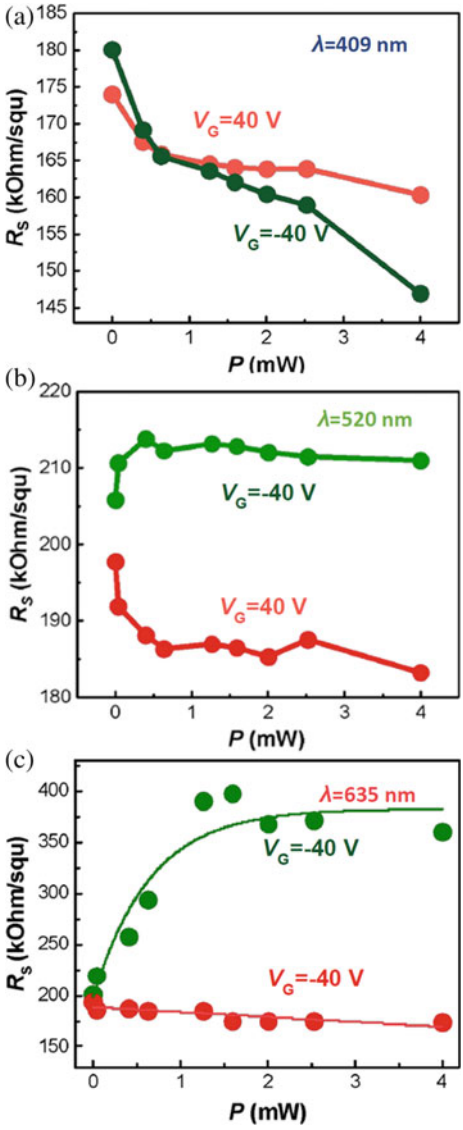

Fig. 11 Sheet resistance modulated by varying illumination power for **a** λ = 409 nm, **b** λ = 519 nm, **c** λ = 635 nm

We note that for λ = 519 nm, 635 nm, the general relationship between sheet resistance and illumination power are similar—sheet resistance increases and stabilizes as illumination power increases from 0 to 4 mW with negative backgating. Sheet resistance decreases and stabilizes as illumination power increases with positive backgating. This can be explained by the enhancement of the photoelectric effect when illumination power is increased, causing more electrons to be excited at the 2DEG interface, therefore decreasing sheet resistance.

For $\lambda = 409$ nm, the trend differs greatly from the other experiments once more. This corresponds to our observations from Figs. 9 and 10, and requires further study (Fig. 11).

E. *Summary and Future Work*

By using *a*-AlN/$SrTiO_3$ as the research sample, we realised the formation of 2DEG at the interface and successfully tuned it to high carrier density similar to the typical *c*-$LaAlO_3$/$SrTiO_3$ system. This was done by tuning spin–orbit interaction via gating, which enhanced weak anti-localisation at the interface. Further, we applied dual-gating on the sample and successfully modulated both carrier density and mobility of the 2DEG. In the future, it could be valuable to enhance carrier mobility, and study the Fermi surface of the 2DEG interface. To do so, we may examine the quantum Hall effect, arising from quantisation of the cyclotron motion of charge carriers in a normal magnetic field, only occurring when electrons are not scattered.

We also studied the photoresponse of *a*-AlN/$SrTiO_3$ to optical and electrical stimuli, and observed its photoconductive behaviour. A remarkable result of the photoresponse at 409 nm illumination was observed, for which no theoretical explanation has been formulated at the time of writing. To understand it, we may further research the interfacial properties of AlN/$SrTiO_3$ heterostructure through a combination of electrical, magnetic, and optical stimuli. This helps to develop a photoelectric-gating tunable photodetector based on 2DEG, valuable to the future development of high-performance photodetectors and next-generation photoelectrical devices.

Acknowledgements The author thanks Asst. Prof. Wang Xiao, Renshaw, Ye Chen, and Jin Mengjia of the School of Physical and Mathematical Sciences, Nanyang Technological University, for their advice, support, and guidance through this project.

References

1. Mannhard, J., *et al*. (2008) Two-Dimensional Electron Gases at Oxide Interfaces. *MRS Bulletin, 33*(11), 1027-1034. doi: https://doi.org/10.1557/mrs2008.222
2. Hwang, H. Y., *et al*. (2012). Emergent phenomena at oxide interfaces. *Nature Material, 11*(2), 103-113. doi: https://doi.org/10.1038/nmat3223
3. Eason, R. (2007). *Pulsed laser deposition of thin films: applications-led growth of functional materials*. Hoboken, NJ: Wiley-Interscience.
4. Chambers, S. A. (2000). Epitaxial growth and properties of thin film oxides. Surface Science Reports, 39(5-6), 105–180. doi: https://doi.org/10.1016/s0167-5729(00)00005-4
5. Li, C., *et al*. (2018). Formation of Two-dimensional Electron Gas at Amorphous/Crystalline Oxide Interfaces. *Scientific Reports, 8*(1). doi: https://doi.org/10.1038/s415980-17-18746-4
6. Liu, Z., *et al*. (2013). Origin of the Two-Dimensional Electron Gas at $LaAlO_3$/$SrTiO_3$ Interfaces: The Role of Oxygen Vacancies and Electronic Reconstruction. *Physical Review X, 3*(2) doi: https://doi.org/10.1103/physrevx.3.021010
7. Chen, Y., Christensen, D., Trier, F., Pryds, N., Smith, A., & Linderoth, S. (2012). On the origin of metallic conductivity at the interface of LaAlO3/SrTiO3. Applied Surface Science, 258(23), 9242–9245. doi: https://doi.org/10.1016/j.apsusc.2012.01.117

8. Beyreuther, E., Paparo, D., Thiessen, A., Grafstr öm, S., & Eng, L. M. (2013). Conducting and insulating LaAlO3/SrTiO3 interfaces: A comparative surface photovoltage investigation. Journal of Applied Physics, 114(24), 243709. doi: https://doi.org/10.1063/1.4858376
9. Lei, Y., *et al*. (2014). Visible-light-enhanced gating effect at the $LaAlO_3/SrTiO_3$ Interface. *Nature Communications, 5*(1) doi: https://doi.org/10.1038/ncomms6554.
10. Drude, P. (1900). Zur Elektronentheorie er Metalle; II. Teil. Galvanomagnetische und thermomagnetische Effecte. *Annalen Der Physik, 308*(11), 369–402 doi: https://doi.org/10.1002/andp.19003081102.
11. Sommerfeld, A. (1928). Zur Elektronentheorie er Metalle. *Die Naturwissenschaften, 16*(21), 374-381 doi: https://doi.org/10.1007/bf01508000
12. Schroder, Dieter K. (2006). *Semiconductor Material and Device Characterization.* Hoboken: Wiley.
13. Pauw, L. J. V. D. (1991). A Method of Measuring Specific Resistivity And Hall Effect of Discs of Arbitrary Shape. *Semiconductor Devices: Pioneering Papers*, 174-182 doi: https://doi.org/10.1142/9789814503464
14. Gallagher, P., *et al*. (2015) A high-mobility electronic system at an electrolyte-gated oxide surface. *Nature Communications, 6*(1) doi: https://doi.org/10.1038/ncomms74
15. Ueno, K., Nakamura, S., Shimotani, H., Ohtomo, A., Kimura, N., Nojima, T, … Kawasaki, M. (2008). Electric-field-induced superconductivity in an insulator. Nature Materials, 7(11), 855–858. doi: https://doi.org/10.1038/nmat2298
16. Ye, J. T., Inoue, S., Kobayashi, K., Kasahara, Y., Yuan, H. T., Shimotani, H., & Iwasa, Y. (2009). Liquid-gated interface superconductivity on an atomically flat film. Nature Materials, 9(2), 125–128. doi: https://doi.org/10.1038/nmat258

A Comprehensive Study into the Magnetic Levitation of a Magnetic Stirrer

M. Abdul Jabbar and J. W. Tan

Abstract The magnetic stirrer is a common science laboratory equipment, typically used for the mixing of a solution. It is observed that under certain circumstances, the flea of a magnetic stirrer lags behind the driver magnets sufficiently, to the point that it is able to levitate. For this research, we study the onset of this levitation, and quantify the flea's motion, finding excellent agreement between our analytical model and the flea's motion. We also study the stability of the levitation, attributing it to the fluid flow, which provides the restoring force for radial stability. These results provide a novel method by which magnetic levitation can be stabilised, allowing for the development of passive magnetic bearings that work at low angular velocity, as well as bidirectional fluid pumps.

Keywords Magnetism · Levitation · Dipoles · Mechanics

1 Introduction

Levitation is the process by which an object is held afloat in a stable position, without the need for mechanical support. Magnetic Levitation, specifically, is a method by which repulsive forces between magnets are able to counteract the effects of gravitational acceleration, such that it is able to levitate at a height above the dipole. The two key aspects of magnetic levitation are firstly, the lifting forces, where a magnetic force needs to be able to provide an upward force sufficient to counteract gravity, and stability: ensuring that the system does not spontaneously move out of the levitation state.

In this research, we build on the work of [1] and conduct an investigation into a unique phenomenon that is observed at times in a laboratory, that being the phenomenon whereby a magnetic flea, often used to mix a combination of liquids,

M. Abdul Jabbar (✉)
Raffles Institution, One Raffles Institution Lane, Singapore, Singapore
e-mail: firasjabbar03@gmail.com

J. W. Tan
NUS High School of Mathematics and Science, 20 Clementi Ave 1, Singapore, Singapore

H. Guo et al. (eds.), *IRC-SET 2020*,
https://doi.org/10.1007/978-981-15-9472-4_4

Fig. 1 Flea in levitation

is able to levitate as seen in Fig. 1, when placed in a viscous fluid and spun at high angular velocities, contrary to its function of mixing a liquid when placed at the base of the container.

We first begin by explaining qualitatively why it should levitate, followed by quantitatively modelling the motion of the flea. We then experimentally verify the liftoff conditions, heights of levitation and the motion during levitation across varying the drive angular velocity and the initial height of the base.

These results can possibly be applied to the development of magnetic bearings. Current methods of building passive magnetic bearings are mostly based on spin-stabilised magnetic levitation [2]. However, such bearings require high spin in order for gyroscopic stability. For example, in reference [2] the top stopped levitating once its angular velocity went below 1000 rpm. The results of this paper allow for a levitation setup to be built, such that the rotating object (in our case the flea) can rotate at relatively low angular velocities, possibly as low as 400 rpm.

In addition, the reversal of flow direction that we observe can be used to build fluid pumps that can cause fluid to move in both directions, without having to make any changes to the mechanism by which the pump works.

2 Experimental Setup

To allow us to vary properties of the magnetic stirrer easily, we opted to build our own magnetic stirrer, comprising of a 3D-printed mould which holds the driving motor magnets in place. The mould is attached to a motor, and the angular velocity of the motor is adjusted through the use of a potentiometer.

The driving motors magnets are two cylindrical magnets, polarized along their axes. They are placed side by side on a plate, with their axes vertical and their magnetizations antiparallel, such that one north pole and one south pole face upwards.

We can treat this system of two magnets as being similar to that of one magnet polarized along an axis in the *xy*-plane—the *drive magnet*.

In addition, as seen in Fig. 2, the glass beaker is placed on an acrylic plate held up by two lab jacks. The lab jacks enable us to vary the distance between the base of the beaker and the drive magnet, and hence the initial magnetic coupling. We shall denote this distance as z_b.

It is experimentally observed that the motion of the flea is only along the axis of the drive magnet, and it rotates only about a vertical axis. As such, unless explicitly stated otherwise, from now on references to quantities such as *force* will implicitly refer to their vertical component, and quantities such as *angular velocity* shall refer to that about the vertical axis.

In Fig. 3, we observe that the angular displacement of the flea can be given by (1), where ω_s and ω_w are known as the spin and waggle frequencies.

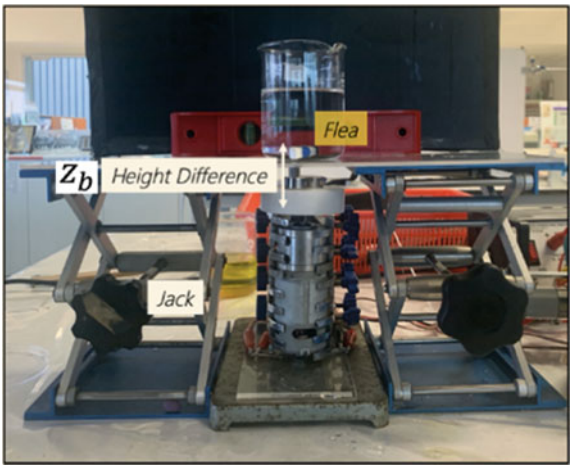

Fig. 2 Experimental set-up

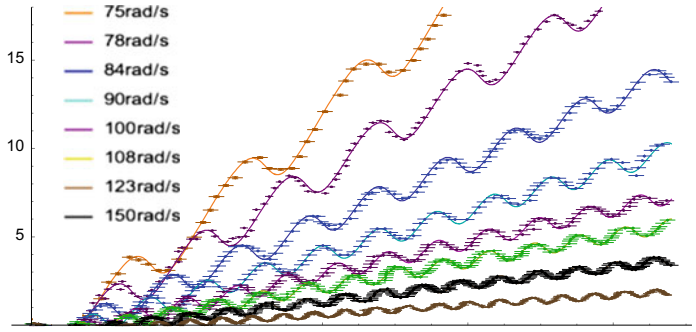

Fig. 3 Angular displacement of flea in levitation

$$\phi = \omega_s t + A_w \sin\omega_w t \tag{1}$$

Two cameras were placed at the side and top of the beaker, allowing for both the rotational motion of the flea about the vertical axis and the vertical motion to be captured. From this, the velocity and the acceleration can be easily determined. To determine $\omega_s t$, we time average the angular velocity, while to determine $\omega_w t$, we perform a Fast-Fourier Transform on the velocity and take the peak frequency.

3 Qualitative Account for the Phenomenon

When the flea is first placed in the container it aligns antiparallel to the driving motor magnets at the base of the container. When spun at low angular velocities, experimentally, the flea behaves just as we would expect—the flea sticks to the drive magnet and spins at a constant angular velocity $\Omega\omega_d$. We call this motion *synchronous*.

This synchronous spinning is maintained by the magnetic torque—when the drive magnet spins, it drags the flea along with it, resulting in this synchronous spinning observed. However, the magnetic torque is not the only torque acting on the flea—the drag torque opposes the synchronous spinning, creating a phase lag, where the flea lags slightly behind the drive magnet, as shown in Fig. 4.

As we increase the drive angular velocity, the magnetic torque stays constant. However, the drag torque, which is proportional to angular velocity, increases. This increases the phase lag between the drive and the flea.

As the phase lag increases, the north pole of the flea get further away from the south poles of the drive magnet, while getting closer to the north pole of the drive. Hence, the magnetic force is steadily decreasing. When the phase lag goes past a value of $\frac{\pi}{2}$ radians, as seen in Fig. 4 where the flea is perpendicular to the drive, the net magnetic force becomes repulsive. The phase lag continues to decrease until it

Fig. 4 Flea on the verge of levitation

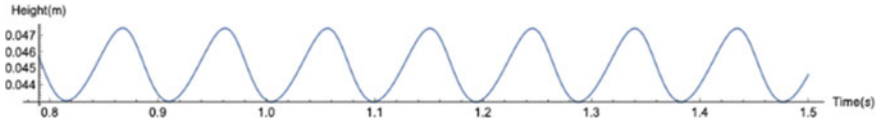

Fig. 5 Vertical displacement of flea during levitation

reaches a point where the magnetic force in the vertical direction is able to overcome the apparent weight of the flea, and thus, lift-off and levitate.

When in levitation, as seen in Fig. 5, the flea is observed to have a sinusoidal vertical motion, with the frequency of this oscillation being identical to the waggle frequency ω_w. This implies that the vertical motion is coupled to the rotational motion, where the rotational motion provides the vertical stability.

With that in mind, let us consider the condition for levitation to be maintained. This is that the average force must be equal to gravity

$$\langle F_{mag} \rangle = mg \tag{2}$$

However, if we were to allow the flea to spin at a constant angular velocity, the force would time average to zero by symmetry. Thus, the waggling motion provides for an imbalanced time average of the force.

Now it has been established why there is an imbalanced time average, the question of how remains. To do so, let us consider the motion in the rotating frame, where the drive magnet is stationary. We shall assume that the north pole of the drive magnet is on the right, and the flea is on average rotating clockwise.

The positions of the flea can be divided into four quadrants, as seen in Fig. 6, depending on the angle of the north pole of the flea.

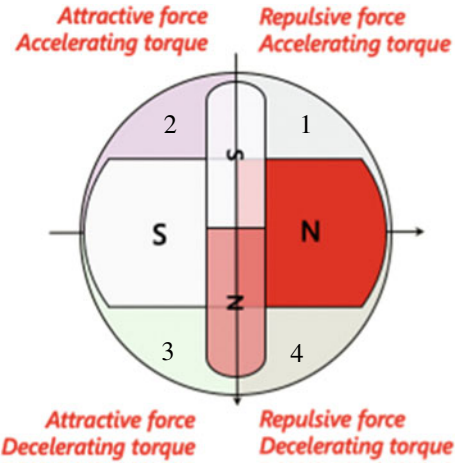

Fig. 6 Four quadrants of flea's motion

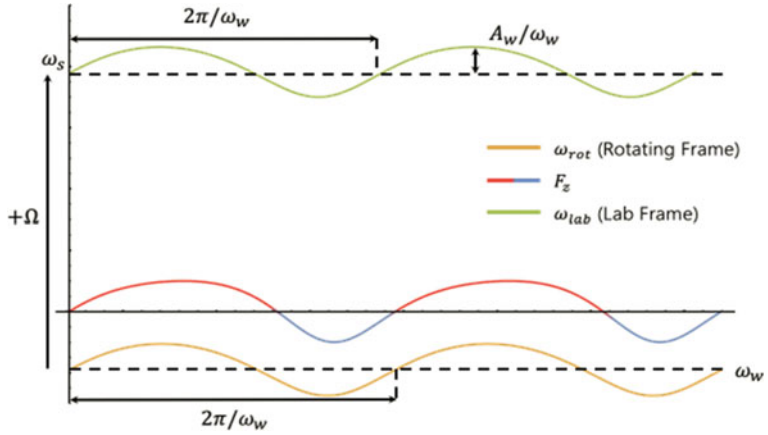

Fig. 7 Angular velocity of the flea

Let us begin by considering a flea in the 3rd quadrant where the force is attractive, while the torque is decelerating. This causes a decrease in the angular velocity. The flea then rotates to the 4th quadrant.

In the 4th and 1st quadrant, the force is repulsive. Since the angular velocity is low in these regions, this means that the time spent in the repulsive regions is longer than the time spent in the attractive regions. This results in the force being on average repulsive, which is required to maintain levitation against gravity.

We now proceed to discuss the angular motion of the flea in levitation. Figure 7 shows a graph of the angular velocity against time, with the orange line being the angular velocity in the rotating frame. We note that since the torque fluctuates as a function of the angle, the frequency at which the velocity oscillates is also the frequency of oscillation, $\omega_w \omega_\mathrm{w}$.

Converting this from the rotating frame to the lab frame, we add the velocity of the frame of reference, which is $\Omega\omega_\mathrm{d}$. The final velocity fluctuates with frequency $\Omega\omega_\mathrm{w}$, which we shall call the waggle frequency, and a mean $\omega_s \omega_\mathrm{s}$, the spin frequency. The amplitude of this fluctuation is given by A_w/ω_w where A_w $\mathrm{A_w}$ is the waggle amplitude.

As for the vertical motion of the flea, we observe experimentally that the flea oscillates about a mean height. From the discussion earlier, the force will oscillate with frequency ω_w. As seen in Fig. 8, this leads to a similar oscillation of the vertical position of the flea, π radians out of phase with the force. Thus, the flea will reach its lowest height when the force is most repulsive. Since the force is also inversely dependent on the height, this can possibly result in further amplification of the oscillation.

Now, that we have qualitatively accounted for the phenomenon, we proceed to establish a rigorous theoretical account for the phenomenon and verify its validity against experimental data obtained from our experiments.

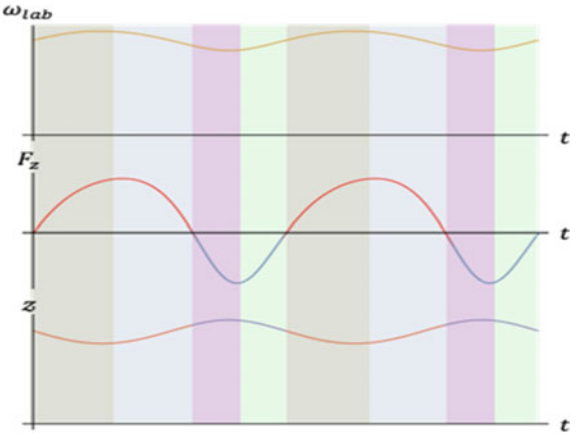

Fig. 8 Oscillation of flea

4 Force Analysis of the Flea

A force analysis, as seen in Fig. 9, shows that the forces acting on the flea are the magnetic, drag and gravitational forces. The torques are the magnetic and drag torques.

Hence, the equations of motion are given by

$$m\ddot{z} = F_{mag}(z, \phi - \Omega t) - mg' - k\dot{z} \tag{3}$$

$$I\ddot{\phi} = \tau_{mag}(z, \phi - \Omega t) - k_2\dot{\phi} \tag{4}$$

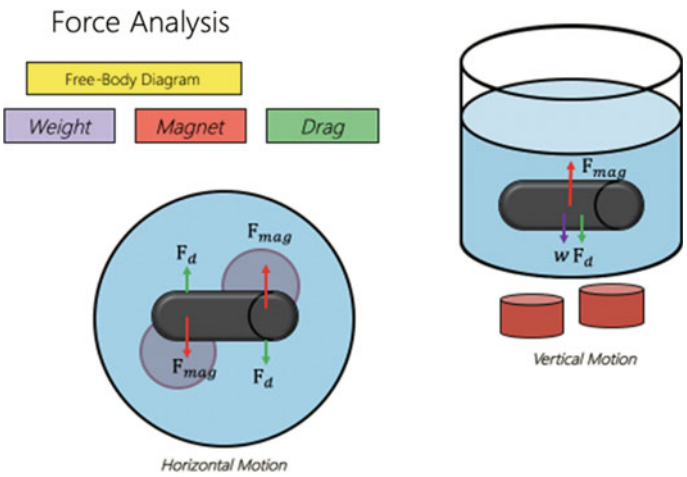

Fig. 9 Force analysis of flea in levitation

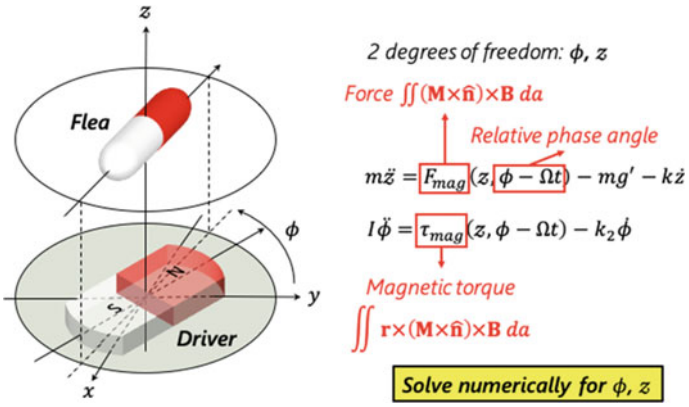

Fig. 10 Solving for motion of flea

where $F_{mag}F_{mag}$ and τ_{mag} are the magnetic forces and torques respectively, g' is the buoyancy-corrected gravitational acceleration, and k and k_2 are drag coefficients. The magnetic force was characterised using the Biot-Savart Law. Full characterisations of the coefficients can be found in the Appendix. We then solve this equation numerically for the two degrees of freedom ϕ and ‡ as functions of time, as shown in Fig. 10.

5 Verification of Theoretical Model

For the verification of our model, we begin by examining the levitation height. Figure 11 shows the mean height of the flea, z, against the drive angular velocity omega.

Initially, when we increase the drive angular velocity, the flea spins synchronously on the base with an increasing relative phase angle. Eventually, when the angular velocity reaches a critical value, the force will then be repulsive enough to cause the flea to lift off.

In addition, we note that there is a decreasing trend in the average height as the drive frequency is increased. This is since when the drive angular velocity is increased, the relative angular velocity is increased.

We recall that the magnetic force providing for levitation is caused by fluctuations in the angular velocity, and hence an uneven time average. When the relative angular velocity is increased, the fluctuations will then be smaller compared to the mean relative angular velocity, as shown in Fig. 12.

Hence, there will be a lower difference between time spent in the repulsive regions and time spent in the attractive regions and thus a lower average magnetic force.

Interestingly, we note that when decreasing the angular velocity, the flea becomes unstable and falls at an angular velocity omega down that is smaller than the angular velocity for lift-off omega up. This is due to the conditions for lift-off and falling

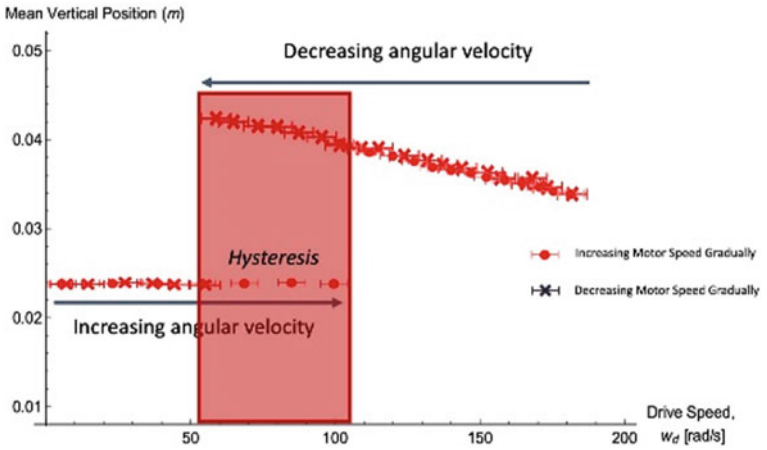

Fig. 11 Mean vertical position of flea in levitation across multiple drive speeds

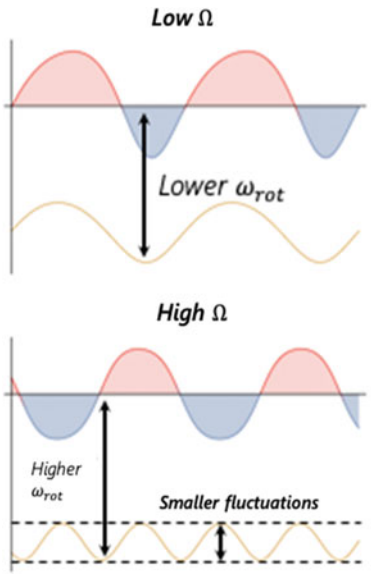

Fig. 12 Rotational motion of flea

being different. For the flea to fall, the time averaged magnetic force only needs to be slightly lower than the gravitational force, and the flea will fall.

However, for lift-off to occur, the time averaged magnetic force needs to be higher. For a certain value of the drive angular velocity, there is only one stable levitation height, and the flea needs to lift off until it reaches this height. If it does not reach that height, it will simply fall back down. Hence, the phase lag needs to be high enough such that it can push the flea to this stable levitation height.

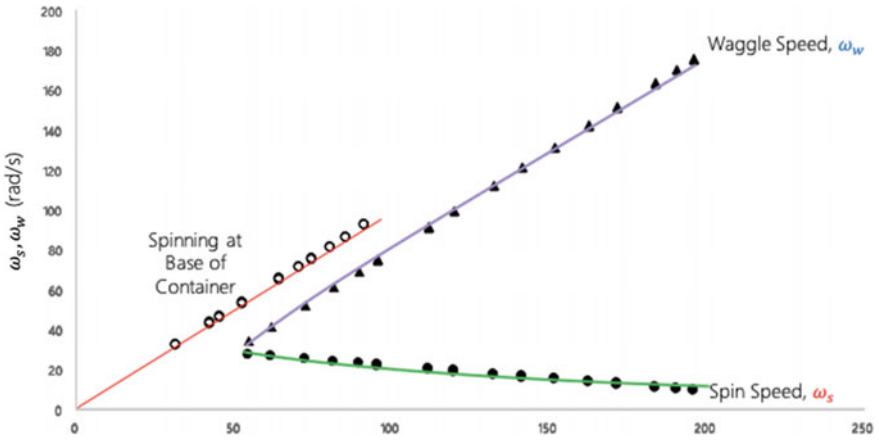

Fig. 13 Frequencies of spin and waggle against drive angular velocity

Thus, the angular velocity for levitation is higher than the angular velocity for it to fall, and this creates a region in the middle, where the state of the system depends on whether the angular velocity is increased or decreased.

In addition, we can plot the frequencies of spin and waggle against the drive angular velocity, as shown in Fig. 13. Initially, we notice that they follow a linear trend, where the flea spins synchronously at the same angular velocity as the drive magnet. This continues until $\omega_{\uparrow}\omega_{\uparrow}$, where the flea starts levitating.

We also note that the frequency of waggle, ω_w asymptotically approaches the drive frequency while the spin speed approaches 0. This is because when the drive angular velocity is extremely large, the fleas angular velocity will be much smaller than that of the drive magnet, and thus it will barely move when compared to the drive. Hence, the torque will oscillate approximately at Ω, resulting in a waggle frequency $\omega_w = \Omega$.

We can also plot the angular velocity required for lift-off, $\omega_{\uparrow}\omega_{\uparrow}$ against the initial height difference z_b, as seen in Fig. 14. As the height of the base $z_b z_b$ increases, the angular velocity required for levitation omega up decreases. This happens since the base is closer to the stable levitation height, and hence a lower angular velocity is required to cause the flea to jump up to that height.

In addition, there is a region where erratic behavior occurs in Fig. 15. This erratic behavior occurs when $\omega_{\uparrow} < \omega_{\downarrow}$. When this occurs, the flea will simply fall down after lifting up, resulting in the erratic behavior mentioned earlier.

6 Radial Stability

Now that we have talked about and modelled the vertical motion of the flea, we must explain the radial stability of its motion. Let us first hypothesize that the radial

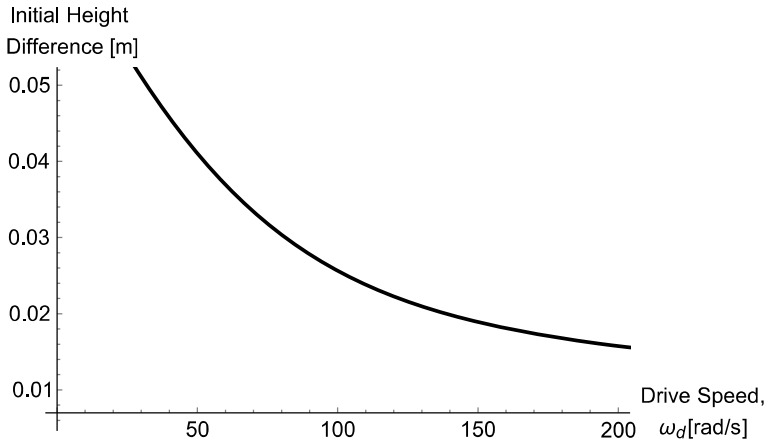

Fig. 14 Angular velocity for liftoff as a function of base height

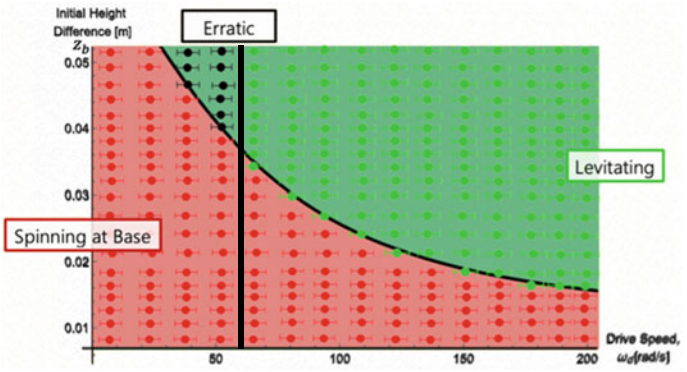

Fig. 15 Origins of levitation of the flea

stability is similarly provided by the magnetic force. In Fig. 16, we consider a flea that is radially perturbed. In this case, we note that since in this region the force is repulsive, the radial component of the force will point outwards. We note from the earlier discussion that the force is on average repulsive. Hence, we conclude that the magnetic force is destabilizing. The stabilizing force must thus be the fluid force.

In literature [1], it is observed that the radial stability is provided by outward flowing fluid flow, with the flow switching direction when the Reynolds Number is increased, and we now attempt to understand why. To do so, we start with the Navier–Stokes equation, following the first few steps of a derivation given in [3].

$$\frac{\partial \mathbf{u}}{\partial t} + (\mathbf{u} \cdot \nabla)\mathbf{u} = \frac{1}{\rho}\nabla P + \eta \nabla^2 \mathbf{u} + \mathbf{g} \tag{5}$$

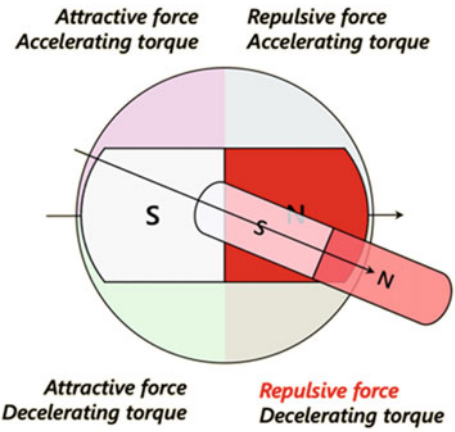

Fig. 16 Radially perturbed flea

For small oscillations, the second term is 2nd order in the velocity and is thus negligible. We then take the curl of the resultant equation, giving

$$\frac{\partial \boldsymbol{\omega}}{\partial t} = \eta \nabla^2 \boldsymbol{\omega} \tag{6}$$

where $\boldsymbol{\omega} \equiv \nabla \times \mathbf{u}$ is the vorticity of the flow. This is analogous to a heat conduction equation, where the conductivity is replaced by the viscosity. This means that the vorticity diffuses further away as the viscosity is increased. As such, when we have a body moving through a fluid, at high viscosity the vortices will diffuse away and this results in the flow following at the body, while at low viscosity the vortices will be confined to the body, resulting in the flow seeming to reverse direction (Fig. 17).

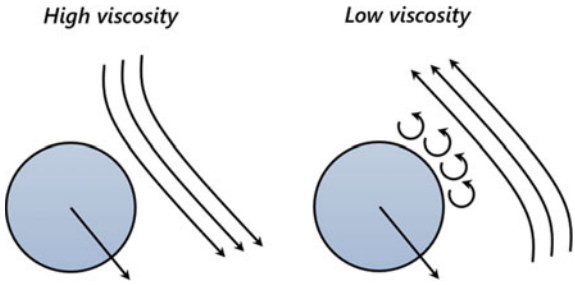

Fig. 17 Flow reversal due to vorticity

7 Further Insights

When we decrease the fluid height and making the fluid extremely shallow or decrease the viscosity of the liquid. We observe that there is little inertia and the fluid is easily moved. At very low liquid levels or low viscosities, the fluid moves along with the flea, forming a vortex. The vortex decreases the relative velocity between the flea and the fluid, decreasing the drag force acting on the flea. This decreased drag force then causes the levitation height to decrease, keeping the flea within the fluid.

8 Conclusion and Future Work

In conclusion, we have qualitatively explained the conditions for lift-off due to the phase lag, the asynchronous motion causing dynamic stabilisation of the vertical motion, and the flow switching due to presence and vortices of motion (Fig. 18).

We have also numerically modelled the levitating states, and we see that the model has predictive power over the frequencies of motion, lift-off conditions and levitation heights.

Future work could involve experimental verification of the radial stability, as well as numerically modelling the exact boundary at which the flow will reverse and the flea will lose stability.

Acknowledgements We would like to thank Mr. Sze Guan Kheng, Mr. Harapan Ong, Dr. Wang Guanquan and Mr. Tan Weng Seng from Raffles Institution, Mr. Joel Tan Shi Quan from Yong Loo Lin School of Medicine, Mr. Poh Boon Hor, Mr. Tan Guan Seng and Ms. Yenny Wijaya from NUS High School of Mathematics and Science for their invaluable guidance and support. We would also like to thank the Laboratory Staff at the Cluster Labs for their assistance.

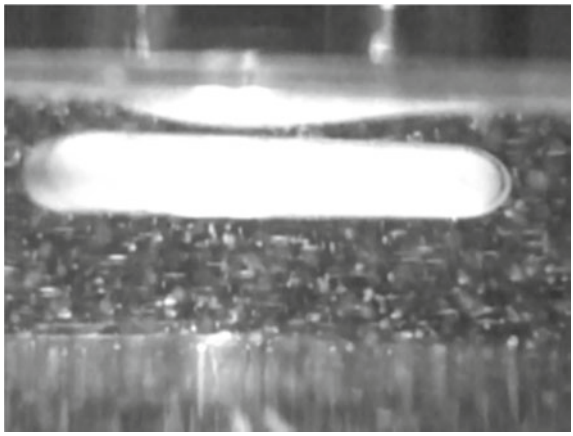

Fig. 18 Induced vortex flows

References

1. K. A. Baldwin, J.-B. de Fouchier, P. S. Atkinson, R. J. A. Hill, M. R. Swift, and D. J. Fairhurst. Magnetic Levitation Stabilized by Streaming Fluid Flows, Phys. Rev. Lett. 121, 064502 – Published 8 August 2018. https://journals.aps.org/prl/abstract/https://doi.org/10.1103/PhysRevLett.121.064502
2. 1. Simon, Martin D., Heflinger,Lee O., Ridgway,S. L. (1997), Spin stabilized magnetic levitation, American Journal of Physics https://doi.org/10.1119/1.18488, https://doi.org/https://doi.org/10.1119/1.18488
3. L. D. Landau, E. M. Lifshitz (1959). Fluid Mechanics. Vol. 6

3D Printed Prosthetic Hand

Hemadri Rajam Ramkumar, Wan Ni Nicole Tay, Ying Lin Valeska Tan, and Guoxian Tan

Abstract Upper limb deficiency is a widespread issue around the world today. While there are numerous prostheses available, they currently fail to meet all the major consumer-base requirements simultaneously. Bionic limbs are highly advanced but extremely expensive to the normal person; consequently, most patients end up using cosmetic prostheses that have little to no functionality. This paper describes the development of a low-cost, highly functional and cosmeticised prosthetic hand. It discusses a 3D printed prosthetic design that consists of a flexible palm, cable-mechanism actuated fingers and a user-friendly Myoelectric control system. The hand also features a conductive matrix capable of supporting sensory feedback and touchscreen compatibility for greater user satisfaction.

Keywords Prosthetic · 3D printing · Upper limb deficiency · Myoelectric

1 Introduction

Upper limb deficiency is a prevailing problem worldwide, with the market for upper limb prosthetics valued at more than USD$200 million in 2019 [1]. However, current prostheses lie on two extremes; they are either highly functional but extremely expensive, or low-cost but lacking in functionality. As a result, the rejection of prostheses use was observed in 1 out of 5 people with upper limb deficiency [2]. This project hence aims to develop a prosthetic hand that is able to achieve both a high degree of functionality as well as remain low-cost, thus plugging the gap in the market and addressing the needs of all patients.

Current prosthetics can be grouped into three categories: cosmetic, body-powered and myoelectric. Cosmetic prosthetics have limited functionality, with the lifelike appearance of the prosthetic being prized over its efficiency. Despite this, such prosthetics are unreasonably expensive - a purely cosmetic socket from Tan Tock Seng Hospital is priced at $5000.

H. R. Ramkumar (✉) · W. N. N. Tay · Y. L. V. Tan · G. Tan
Raffles Science Institute, Raffles Institution (RI), Singapore, Singapore
e-mail: adrirajam@gmail.com

H. Guo et al. (eds.), *IRC-SET 2020*,
https://doi.org/10.1007/978-981-15-9472-4_5

Some of the most advanced myoelectric models available for purchase include the Michelangelo and Bebionic hands, both developed by Ottobock and priced at $60,000 and $11,000 USD respectively [3, 4]. These models are motorised and highly efficient; however, their steep price tag means that they are inaccessible to a large majority of patients.

Much of the efforts to reduce the cost price of such prosthetics have centered around 3D printing, as this provides a much quicker, cheaper alternative to current production methods in the market. This would include the Victoria Hand Project [5] and the Raptor Hand [6], which costs USD$320 and USD$200 respectively. Current literature has proposed that the 3D printed hand be driven by a cable mechanism; these are largely body-powered prosthetics which utilise a harness attached to another body part. These systems are actuated via movement of the shoulder [7] and are thus inconvenient and difficult to use. An alternative pneumatic mechanism was proposed but poses an additional difficulty in manufacturing due to its airtight requirement. We thus propose the usage of a cable mechanism in our prototype, and have evaluated a second alternative coupling mechanism below.

In recent years, prosthetics have become even more functional through the incorporation of sensory feedback into their designs [10]. Sensory feedback is instrumental as it allows the user to 'feel' the amount of force acting on the prosthetic and vice versa, thus allowing for a more intuitive and natural experience. This can be implemented in three ways: direct neural stimulation, targeted muscle reinnervation or sensory substitution. Direct neural stimulation works via the implantation of electrodes within the nerve stumps of amputees while targeted muscle reinnervation involves the transfer of residual nerves within the stump to new intact muscles, resulting in sensation. In comparison, sensory substitution is a preferred method as it is non-invasive and easier to implement.

Given this background, we aim to develop a prosthetic hand that is able to meet the following criteria: (1) low-cost, (2) highly functional and (3) cosmeticised. 3D printing was selected as the method of production as this brings down the cost of the prototype and also results in minimal assembly for the user, thus making the prosthetic more accessible to patients and easily repairable [8].

2 Materials and Methods

Our research aimed to create a 3D printed prosthetic hand with the following functionalities and features:

1. Myoelectric-controlled
2. Cable mechanism actuated by servos and motors
3. Conductive matrix capable of supporting sensory feedback mechanism

A. **Myoelectric-Controlled**

Our design utilises the Myoware Armband from Thalmic Labs together with an Arduino Uno to effect the servo motors within the hand. The Myoware armband consists of EMG sensors which detect signals from the muscle groups within the arm. These signals are processed and sent as an output to the Arduino, which sends a specific command to the servo motor depending on the muscle activity detected. This then results in a movement of the thumb and fingers. The Myoware armband is to be worn on the transradial suspension area of the stump of the user as it contains the greatest number of muscle groups and thus allows for a greater range of movement of the prosthetic [9]. The Arduino and breadboard will be located in the socket of the prosthetic. The usage of the Myoware Armband (instead of the shoulder harness that is popular among current 3D printed prostheses) allows for greater user compatibility by removing the need to learn specialised motions to use the prosthesis.

B. **Cable mechanism actuated by servos and motors**

The fingers and thumb are attached to cables via holes in the phalanxes, which are then attached to DC servo motors located within the body of the hand. Upon actuation, a force is exerted onto the cables which results in flexion of the fingers. This mechanism is chosen as it has proven to be more feasible than the pneumatics system which is not suited for 3D printing.

C. **Conductive Feedback Matrix**

Our proposed form of sensory substitution would be vibrotactile stimulation through the use of a piezoelectric sensor and coin vibration motor. The piezoelectric sensor reads the force exerted by the object on the hand and converts it into a voltage for the Arduino to send to the motor. The motor will then vibrate accordingly, allowing the user to gauge the amount of force being used to grip the object. However, the incorporation of such a feedback mechanism would require an extensive wiring system which may not be able to fit within the hand due to size constraints. To solve this problem, it is thus proposed that these wires be replaced by a conductive matrix of Acrylonitrile Butadiene Styrene/Carbon-Nanotubes (ABS/CNT).

ABS/CNT is a conductive composite material synthesised by solution processing which has good mechanical and electrical properties. The material has good dispersion and retains the aspect ratio of CNT, allowing for the direct printing of complex embedded conductive structures and making it a suitable material for our conductive matrix. The printing of this material onto the fingertips will also facilitate touchscreen usage [11].

D. **3D Printing**

The designs were modelled using the CAD software Autodesk Fusion 360 and printed using Fused Deposition Modelling through the Flashforge Dreamer 3D printer. The materials used in the prints were Polylactic Acid (PLA), NylonFlex and the ABS/CNT composite.

The models were qualitatively analysed with respect to print quality and functionality, and improved upon based on the limitations identified. Finally, a series of tests were conducted to evaluate the effectiveness of our final prototype.

3 Results and Discussion

After the text edit has been completed, the paper is ready for the template. Duplicate the template file by using the Save As command, and use the naming convention prescribed by your conference for the name of your paper. In this newly created file, highlight all of the contents and import your prepared text file. You are now ready to style your paper; use the scroll down window on the left of the MS Word Formatting toolbar.

A. **Prototypes**

1. Prototype 1

Prototype 1 (refer to Fig. 1) served as a proof-of-concept of the cable mechanism and featured rudimentary, hollow PLA fingers. The fingers were individually attached to cables via holes in the first phalanx, then tied together to a servo. Upon exertion of a force onto the cables, all four fingers would flex towards the palm, thus allowing for the gripping of an object.

The one-way flexion meant that the fingers had only one degree of freedom, thus limiting the range of motion of the hand. As the fingers were hollow and lightweight, the centre of gravity was located near the palm and resulted in decreased grip strength.

The PLA palm was designed with grooves to enclose each cable and prevent entanglement; however, this inefficiently utilized space as actuators could not be fitted into the palm.

2. Prototype 2

Prototype 2 aimed to test the dual printing mechanism of the 3D printer while improving upon the previously identified flaws. The fingers were dual-printed with an ABS/CNT pathway running through them and ending on the fingertip to allow for touchscreen usage as well as provide potential for the utilisation of a conductive matrix embedded within the hand structure. The fingers were also connected to the cables via two sets of holes which translated into two degrees of freedom.

As seen in Fig. 2, the dual printing resulted in an unclean finish that resulted in weak conductivity in the ABS/CNT; the ooze shield had caught much of the extra waste but the raft was hard to remove, thus causing further damage to the print. It was also difficult to perfectly align the two materials, and the ABS/CNT did not adhere as well to the rest of the print. Lastly, the ball-and-socket design ABS/CNT embed was very small and thus extremely fragile and not durable.

The guiding pipes in the palm were removed (refer to Fig. 3) resulting in a hollow and lightweight palm. The palm shape was also modified to better resemble that of

a human palm, thus improving the aesthetic of our hand. However, the rigid design of the PLA palm meant that it was unable to curve around an object for better grip.

3. Prototype 3

Prototype 3 was targeted at improving the design flaws of the earlier prototypes.

Palm Design

The palm was first fully printed using the flexible material NylonFlex (refer to Fig. 4) in order to achieve the curvature necessary to effectively wrap around objects. The thickness and infill of the palm wall was varied to optimise the curvature of the palm—an overly thin palm tended to collapse onto itself when force was exerted by the cable system, whereas an excessively thick palm was unable to curve to fit around an object.

To solve this problem, 'ribs' were introduced to form a guide along which the flexible palm would fold similar to that in the human hand. Three variations of ribbed palms were designed and tested:

1. Flexible Palm with Rigid Ribs (refer to Fig. 5),
2. Rigid PLA Palm with Flexible NylonFlex Ribs (refer to Fig. 6), and
3. Flexible Palm with indented Flexible Ribs (refer to Fig. 7).

Palm (3) had a slightly unclean finish, but was highly flexible. It had the best curvature around an object and performed better than its fully flexible counterpart. Palm (1) had a rough, unclean finish and the materials failed to adhere well to each other upon printing, thus requiring more assembly from the user who would have to assemble the different components of the palm. Palm (2) was highly rigid and unable to fold along the ribs; this is because the thickness of the NylonFlex strips compromised their flexibility. Therefore, Palm (3) was identified as the best design.

Finger Design

In place of the embedded ABS/CNT design, slots are printed on the tips of the distal phalanxes, and ABS/CNT disks are printed separately and inserted into the slots (refer to Fig. 8). Wires are thereafter soldered to the disk inside the phalanx to create a similar conductive pathway. This results in a much cleaner finish and durable design. Rubber banding was added to the tips of the fingers, mimicking fingerprints, so as to increase traction in gripping between the fingers and object. Elastic was also added onto the back of the fingers to allow them to snap back to their original positions and release their grip on an object.

Thumb Design

This prototype featured a 'ball-and-socket' thumb design (refer to Fig. 9). The thumb was connected to two sets of cables positioned at right angles from each other to allow the thumb to pivot 360°. The print had a clean finish and the minimal contact area between the ball and the socket reduced friction upon motion, allowing for

easy manipulation of the thumb. However at least 2 servos are needed for 360° actuation—a tight fit for a standard human sized palm.

4. Prototype 4

This prototype aimed to test out an alternative finger mechanism in place of the cable system. The approach used was that of a four-bar linkage mechanism similar to that proposed by Zhang et al. [12]. This design featured fingers with three degrees of freedom, with its joints locked temporarily by spring elements to prevent unwanted motion. Unlike the cable mechanism fingers, this functioned directly as a skeletal mechanism which would achieve individual dexterity of the fingers.

Using a similar approach, we designed and printed a finger with the four-bar links as its backbone, with the individual bars printed using PLA and assembled together using a 3D-printed nut-and-bolt mechanism (refer to Fig. 10). This mechanism allowed for more freedom of movement of the finger; however, it was difficult to restrict the motion of the finger with torsion springs of the appropriate tension. This prototype was also much more fragile due to the thinness (2 mm) of the arms and broke when minimal force was applied as compared to the cable mechanism fingers.

B. **Evaluation of Designs**

A number of tests were conducted on our chosen design to quantify its effectiveness and useability in practical application, and then compared to that achieved in current market prosthetics. Parameters such as grip strength and maximum tensile force withstood by the hand were not tested as these would relate directly to the power of the motor connected to the prosthetic rather than be a product of the improved cable design.

1. Impact Test

This experiment aimed to investigate the durability of the prototypes by dropping varying weights onto the phalanxes of Prototype 3 (refer to Fig. 8) from a fixed height until significant damage to the finger was observed (refer to Fig. 11). Significant damage refers to any sustained, observable impact which would affect the functionality of the prosthetic or suggest that the structural integrity had been compromised, such as deformation or cracking. This simulates a situation where the prosthetic hand collides into another object. From this experiment, it was observed that the PLA finger design could withstand the impact of a 4 kg mass dropped from a height of 0.45 m (refer to Figs. 11 and 12), thus indicating that the prosthetic is extremely durable and is suitable for everyday usage. This is comparable to existing research prototypes which failed at drop weights and heights of 3.34 kg and 20 mm [13].

2. Minimum Force Test and Finger Joint Angles

This test aimed to find the minimum force required in the cables to achieve complete flexion of the fingers in Prototype 2 (refer to Figs. 2 and 3). Weights were incrementally added to the cables (refer to Fig. 13) while measuring the angle of the phalanxes

from the horizontal (refer to Fig. 14) until no further flexion was observed (refer to Fig. 15). The angle of flexion of the proximal phalanx (PAF/°) is equal to the angle of displacement of the phalanx from horizontal (PAH/°). The angle of flexion of the distal phalanx (DAF/°) on the other hand is the difference between the angle of displacement of the distal phalanx (DAH/°) and PAH, where DAH ≥ PAH. Based on this test, a force of 1.72 N is required to achieve proximal flexion of 94.01° and distal flexion of 81.29°(refer to Fig. 16), which can easily be achieved through the use of a standard DC motor. This thus confirms the feasibility of our hand design in our proposed cable mechanism assembly. The range of motion of the prosthetic hand is very close to that of a normal human finger, where $0° \leq \text{PAF} \leq 80°$ and $-10° \leq \text{DAF} \leq 90°$ [15]. This indicates that our hand design has great potential to be harnessed for a large range of motions, allowing the user to carry out more complex actions.

3. Maximum Object Size

Prototype 2 Palm (refer to Fig. 3) with Prototype 3 fingers (refer to Fig. 8) was used to hold balls of various sizes. The contact angle between the middle finger's distal phalanx and the balls was then measured to identify the grip quality. It was found that the larger the object, the smaller the contact angle and thus the better the grip as a larger angle would mean that the object is more likely to slip out of the hand's grasp.

Our prosthetic fingers have two phalanges as opposed to the three phalanges of a human hand; however, the angles measured are similar to that of the distal and proximal phalanges of the human hand in existing literature. This shows that having two phalanges instead of three in our prototype is sufficient to achieve a secure grip on an object.

A separate test was then conducted to determine the upper limit of the object size capable of being gripped by the hand. A constant force was exerted on the cables and the four fingers of the hand were used to pick up spherical objects of increasing sizes from a flat surface. The maximum object size was taken to be the maximum diameter of the sphere that can be lifted by the hand for five seconds without slipping out of its grasp. It was found that the prototype is able to pick up an object of 33 mm in diameter. This could be due to insufficient friction between the fingers and the smooth object, as well as the thick and chunky palm which restricts the hand from holding larger objects.

The maximum size could be greatly increased if the grip was conducted with the usage of an antagonistic thumb as designed in Fig. 9. The thumb provides an opposing force to that exerted by the fingers on the objects [16], thus preventing sliding of the object along the palm and allowing for a stronger precision grip of a much larger object.

4 Further Work

The MyoArmband is preset to recognise four default hand gestures [14]. However, gesture classification could be carried out beyond these preset gestures so as to allow for an even greater range of motion of the hand. This would result in greater functionality of the prosthetic, and further exploit the full potential of the design.

A 3D scanner could be used to scan and model the amputee's stump so that the socket can be customised for a better fit and greater comfort for the patient.

5 Conclusion

The proposed 3D printed, myoelectric-controlled prosthetic hand design is able to achieve our original goals of functionality, low cost and cosmetic appeal (refer to Fig. 17). It is also estimated to cost less than $200, making it more affordable than currently available models.

Acknowledgements We would like to express our gratitude to our research mentor and our senior for their invaluable guidance. The lab staff are greatly appreciated for their assistance with 3D printing. Thank you to our seniors for allowing us to access their past research. Lastly, we thank our peers for giving us crucial feedback that helped us improve.

Appendix

See Figs. 1, 2, 3, 4, 5, 6, 7, 8, 9, 10, 11, 12, 13, 14, 15, 16 and 17.

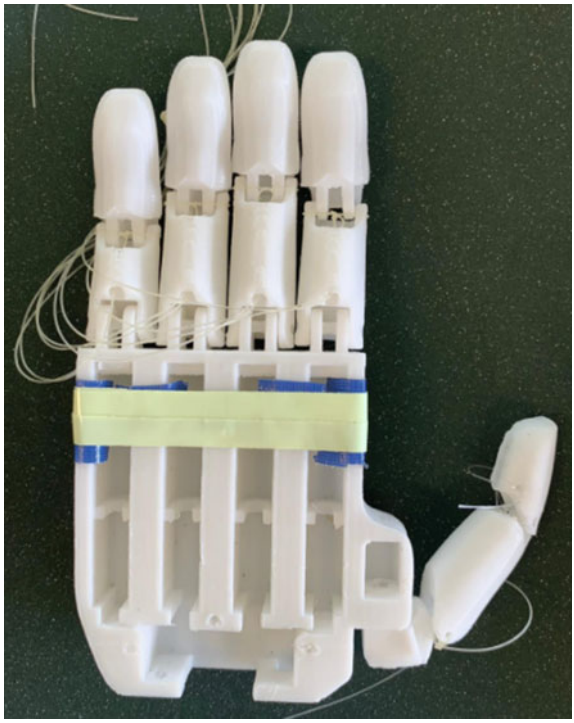

Fig. 1 Assembled prototype 1

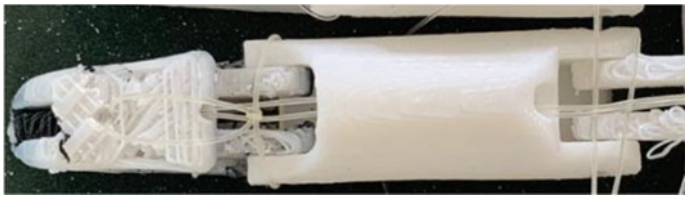

Fig. 2 Prototype 2 finger

Fig. 3 Prototype 2 palm

Fig. 4 Flexible palm design (prototype 3)

Fig. 5 Flexible palm with rigid ribs (prototype 3)

Fig. 6 Rigid palm with flexible ribs (prototype 3)

Fig. 7 Flexible palm with indented ribs (prototype 3)

Fig. 8 ABS/CNT slotted finger design (prototype 3)

Fig. 9 Ball and socket thumb (prototype 3)

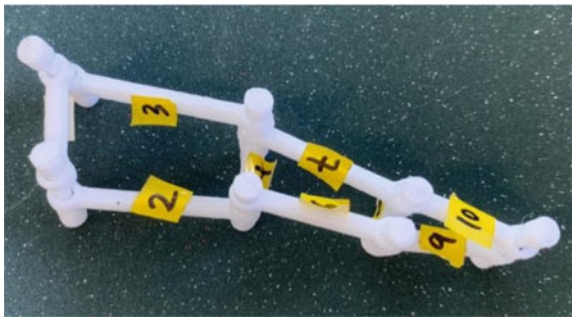

Fig. 10 Four bar linkage mechanism finger (prototype 4)

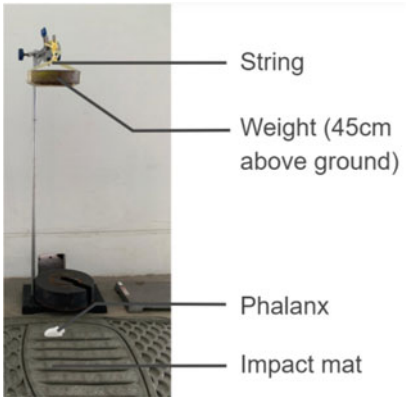

Mass/kg	Deformation
1	No deformation
2	Cracks formed after repeated drops
3	No significant additional crack
4	2.5mm depression Joints are broken
5	Crushed

Fig. 11 Impact test experiment set-up and results

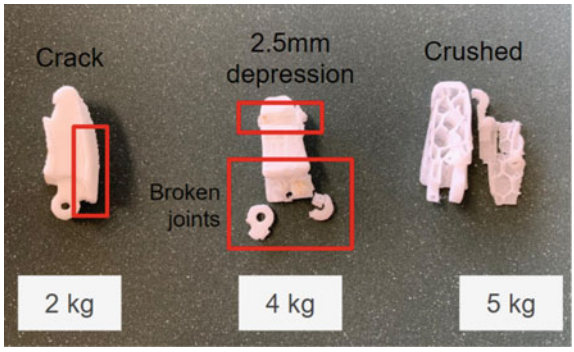

Fig. 12 Phalanges after impact test

Fig. 13 Minimum force test set-up

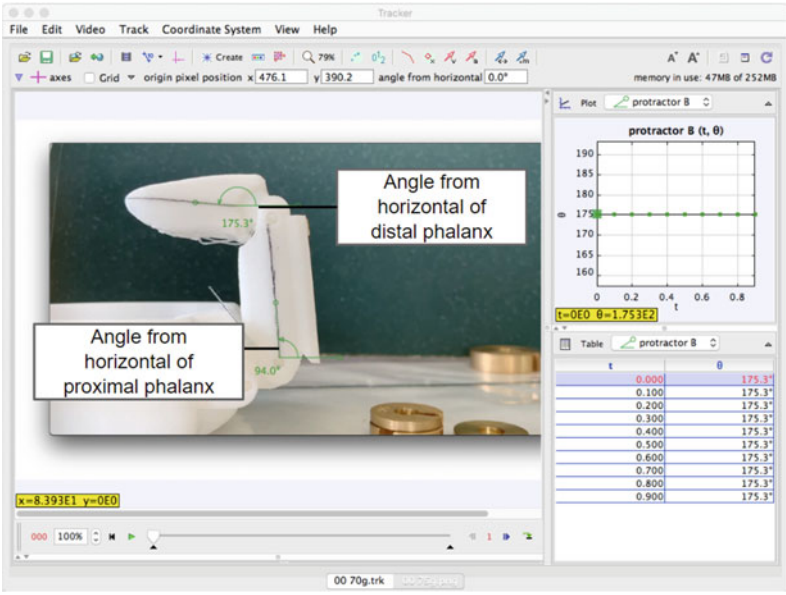

Fig. 14 Measurement of angle from horizontal of distal and proximal phalanges

Fig. 15 Minimum force test results

Mass/g	PAF/°	DAH/°	DAF/°
50	8.68	14.41	5.73
60	91.5	171.4	79.9
65	93.9	174.2	80.3
70	93.0	174.5	81.5
75	94.01	175.3	81.29
80	94.01	175.3	81.29
85	94.01	175.3	81.29
90	94.01	175.3	81.29

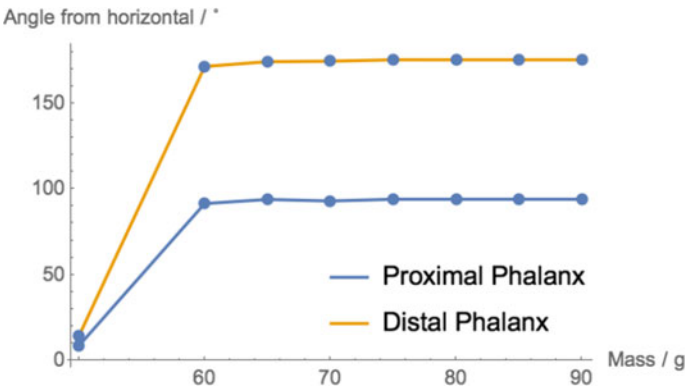

Fig. 16 Minimum force test (maximum flexion results)

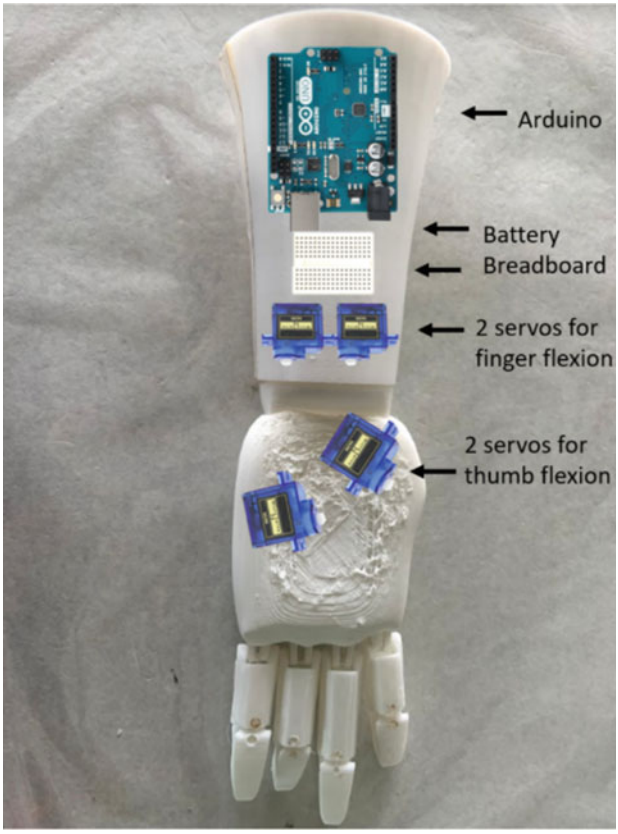

Fig. 17 Assembled prototype

References

1. Global Upper Limb Prosthetics Market Size, Market Share, Application Analysis, Regional Outlook, Growth Trends, Key Players, Competitive Strategies and Forecasts, 2018 to 2026
2. A. Biddiss and T. T. Chau, "Upper limb prosthesis use and abandonment: A survey of the last 25 years," Prosthetics and Orthotics International, vol. 31, no. 3, pp. 236–257, 2007.
3. Birnbaum, I. (2016, September 28). The 'Maserati of Microprocessor Prosthetics' Costs $120,000. Retrieved from https://www.vice.com/en_us/article/jpgagx/luxury-prosthetics.
4. Saenz, A., Saenz, A., Aaron, A. S. L. M. F., & Aaron, M. F. (2018, November 30). How Much is the Newest Advanced Artificial Hand? $11,000 USD (video). Retrieved from https://singularityhub.com/2010/06/30/how-much-is-the-newest-advanced-artificial-hand-11000-usd-video/.
5. Hall, S. (2018, November 18). Victoria Hand Project: Applying 3D Printing to Prosthetics. Retrieved from https://thenewstack.io/victoria-hand-project-applying-3d-printing-to-prosthetics/.
6. Schwartz, J. (2016, June 27). The future of 3D-printed prosthetics. Retrieved from https://techcrunch.com/2016/06/26/the-future-of-3d-printed-prosthetics/.
7. Kulkarni T. and Uddanwadiker R. (2016). Overview: Mechanism and Control of a Prosthetic Arm by Tushar Kulkarni and Rashmi Uddanwadiker. Retrieved from https://www.researchgate.net/publication/291274244_Overview_Mechanism_and_Control_of_a_Prosthetic_Arm
8. Dipaola, M., & Wodajo, F. M. (2019). 3D printing in orthopaedic surgery. St. Louis, MO: Elsevier.
9. R. Barański and A. Kozupa, "Hand grip-EMG muscle response," Acta Physica Polonica A, vol. 125, no. 4A, 2014
10. 10. J. T. Kate, G. Smit, and P. Breedveld, "3D-printed upper limb prostheses: a review," *Disability and Rehabilitation: Assistive Technology*, vol. 12, no. 3, pp. 300–314, Feb. 2017.
11. S. Zhong, H. J. Lin, and C. Y. T. Chor, "Synthesis of a conductive polymer for potential use in printing prosthetic hands using FDM technique," *Proceedings of the 2nd International Conference on Progress in Additive Manufacturing (Pro-AM 2016)*, 2016.
12. Zhang, Y., Duan, X., & Deng, H. (2017). Kinematic analysis of a novel couple-adaptive underactuated finger mechanism. *DEStech Transactions on Computer Science and Engineering*, (iccae). doi: https://doi.org/10.12783/dtcse/iccae2016/7215
13. Mio, R., Sanchez, M., & Valverde, Q. (2018). [Regular Paper] Mechanical testing methods for body-powered upper-limb prostheses: A Review. *2018 IEEE 18th International Conference on Bioinformatics and Bioengineering (BIBE)*. doi: https://doi.org/10.1109/bibe.2018.00040
14. Liew L. R., Jin M., Zhang K. W. & Tan G., "Low-cost 3D printed prosthetic hand," unpublished
15. Peña-Pitarch, Esteban & Falguera, Neus & Yang, Jingzhou. (2012). Virtual human hand: model and kinematics. Computer methods in biomechanics and biomedical engineering. 17. https://doi.org/10.1080/10255842.2012.702864
16. To Grip and Not to Slip. (2006, October 10). Retrieved from https://www.hsimagazine.com/article/to-grip-and-not-to-slip-499/

NLP in Fake News Detection

An Ensemble Deep Learning Approach in Style Based and Truth Based Detection

Fanghe Ma and Guoxian Tan

Abstract Given the ubiquity of fake news online, a reliable mechanism for automated detection is needed. This project proposes a new end-to-end detection pipeline, which uses Natural Language Processing (NLP) techniques for automated evidence extraction from online sources given an input claim of arbitrary length. This project also compiles a dataset of input claims and evidence larger than state of the art datasets. Distant supervision is used to generate weakly labelled training data and increase sample size. The resultant dataset displays topical variation and variations in length and features. The final ensemble models demonstrate high detection accuracy and micro-average F1 scores. The results validate distance supervision as a viable strategy for model training and data collection. A ConvNet-RNN hybrid was found to be the best performing style based model, while a Siamese LSTM with layer-weights sharing was found to be the best performing truth based model. Generally, truth based models outperformed style based models, and ensembling different models leads to performance gains over any single classifier.

Keywords Fake news detection · Deep learning · Natural language processing

1 Introduction

A. *Background Information*

The growing ubiquity of the internet and social media has led to the increased propagation of fake news, defined as news that were deliberated created with the intention to mislead or manipulate [1]. The democratization of content creation online and the ease by which information can be spread has resulted in the unprecedented dissemination of fake news [2]. Given the sheer volume of fake news present, an efficient

F. Ma (✉) · G. Tan
Raffles Science Institute, Raffles Institution, Singapore, Singapore
e-mail: 20ymafa048z@student.ri.edu.sg

G. Tan
e-mail: guoxian.tan@ri.edu.sg

H. Guo et al. (eds.), *IRC-SET 2020*,
https://doi.org/10.1007/978-981-15-9472-4_6

and reliable framework for fake news detection and news verification is needed [3]. Current credible news-checking outlets, such Snopes and Politifact.com, employ experts to manually verify and identify fake news articles. While extremely reliable and accurate, such methods are limited in efficiency, require significant human effort and are very time consuming. To ensure the timely detection of fake news, there is a need for an automated detection and debunking mechanism.

B. *Literature Review*

The problem of automated fake news detection falls under the umbrella of Natural Language Processing (NLP) and machine learning. State-of-the-art implementations use one, or a combination of the following categories of strategies, namely style based, context based and truth based.

Style based approaches assert that there are linguistic features that are common to all fake news articles, such as the use of emotive language, increased occurrences of spelling mistakes and informal language [4, 5]. Examples include N-grams, Parts of Speech Tagging, etc. [4, 6]. However, such approaches are extremely context specific, and do not fully exploit complex semantic dependencies and relationships [4]. Recent development has seen deep learning models replacing human feature engineering [7], where language styles can be captured via word embeddings and recurrent networks.

The second category of approaches consider information external to the input claim or news article [8]. Such meta-data include the author, the source, the time of posting as well as the propagation path of an article on social media over time. While this approach has shown promise by characterizing propagation trends of fake news online [9–11], such meta data are rarely homogeneous or readily available for most news sources, and this approach has yet to been proven to be more than platform specific [4], and its generalizing ability is very limited.

The last category deals with the veracity of news content [3, 5]. This type of 'evidence aware' approach employs secondary information retrieved from other sources in order to verify the truth of a given label or article. Current criticism of such approaches mainly point out the need for structured data. Previous attempts have employed the use of human engineered lexicons or subject-predicate-object triplets for stance analysis for example [12, 13].

C. *Hypotheses*

This project aims to develop an ensemble approach that employs both style based and truth based models. More specifically, this project proposes a fake-news detection pipeline that consists of two separately trained classifiers, and a mechanism for automated evidence collection.

When given an input claim, the proposed model employs NLP techniques to extract salient external evidence from the web. The input claim is fed through a classifier that considers solely the input claim and extracts linguistic features and word choice for classification. Both the input claim and the extracted evidence are also fed into a separate classifier that maps each input to a hidden state representation

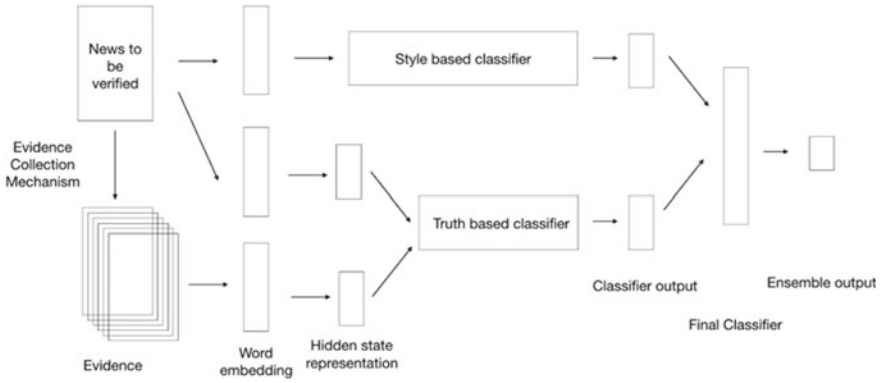

Fig. 1 Proposed fake news detection pipeline

before performing a comparison for classification. The separate decisions of each classifier are then aggregated for the final output of the classifier pipeline.

In coming up with the proposed approach, this project hypothesizes that

1. The comparison of a piece of news claim or article with external evidence could lead to a reliable conclusion regarding the veracity of given news.
2. Such comparison process could be learned, without human feature engineering, by a deep learning network trained with an appropriate dataset
3. A pipeline of trained classifiers that employs an ensemble approach leads to more reliable and generalisable fake news detection (Fig. 1).

2 Dataset

D. *Rationale*

The performance and viability of deep learning models are largely dependent on the dataset with which they are trained. Hence the dataset used in this project was collected to fit the desired traits of the final model. The model was intended to be firstly generalisable across different contexts or domains, and secondly to be able to perform fact-checking regardless of the length of the input article or claim, nor the length of the evidence collected. Therefore, the dataset contains a mix of different combinations of input length and evidence length, as well as information from different domains. The aggregate dataset consists of the following.

E. *Snopes.com*

Snopes (www.snopes.com) is a well known fact checking website that verifies and validates news and information from a variety of sources, ranging from Internet rumours to urban legends and email chains. Each piece of information is mapped

to a single claim and a manually assigned credibility verdict. This project uses the version of Snopes dataset distributed by Popat [1]. Each training instance consists of: a claim, the ground-truth label, and a reporting article that verifies said claim. The dataset contains 4341 claims and 29,242 reporting articles.

F. *PolitiFact*

PolitiFact is a famous fact checking website that deals specifically with online falsehoods in the domain of US politics. Claims made by political figures are verified and assigned a credibility label manually. This project uses the version of PolitiFact compiled by Popat [1]. Each training instance shares the same format as that of Snopes dataset. 29,556 such training instances were used with 3568 claims.

G. *Liar Dataset*

The Liar dataset was developed and collected by Wang [2] as a new benchmark dataset for automated fake news detection research. The dataset was collected to mitigate the lack of reliable and sufficiently large training data, which was identified to be a key restraint on classifier performance by Wang [2]. The Liar dataset contained manually fact checked labels based off the pre-2017 PolitiFact database. For this project, duplicates found in both Liar dataset and PolitiFact dataset provided by Popat et al. 2018 were dropped. Each training instance contained the claim, the ground truth label and automatically collected external evidence. The process by which evidence was collected will be elaborated upon below.

H. *Popat et al.* [3] *extended*

To introduce variety to the dataset in terms of input article length, the Snopes and PolitiFact dataset provided by Popat 2018 is extended via distant supervision using a dataset of weakly labelled training data. In the Popat 2018 dataset, each claim C_i has a list of reporting articles $\{A_0, A_1, \ldots, A_j\}$, and label L_i. For the extended dataset, each article $A_{i,j}$ is then used as a separate input article, and the original label, L_i is given to the new training instance. The input article is then used to retrieve external evidence to form one complete training instance. 58,796 articles were successfully used to extract external evidence.

I. *Evidence collection process*

External evidence used in this project came in two varieties: those already collected by the Snopes and PolitiFact dataset by Popat et al. [3], as well as those that were manually collected during this project. While [3] entered hand crafted claims into Google and crawled top webpages for their new articles, this project proposes an automated, NLP based evidence collection mechanism. The process is as follows

1. Given an input claim, the sequence is first tokenized, splitting by whitespaces and punctuation.
2. The statistical model 'en_core_web_lg' provided by spaCy is loaded and fit onto the input stream.

Dataset	Popat 2018		Popat 2018 extended	Liar
	Snopes.com	PolitiFact		
Labeling	Manually labelled		Weakly labelled	Manually labelled
Evidence collection	Precompiled		Automatically collected	Automatically collected
Input length	Short		Long	Short
Topics & Domains	Varied	Politics	Varied	Politics
Size	29,242	29,556	58,796	12,786

Fig. 2 Dataset overview

3. Parts of Speech (POS) tagging is performed on input sequence.
4. Each token is stemmed and lemmatized.
5. Stop words are removed from the sequence.
6. Dependency parsing is performed for noun phrases identification, which are then preserved.
7. Named entities are identified are preserved.
8. The noun phrases, named entities, and verbs are returned as the final sequence. These salient words are assumed to serve as a summary of the intial input.

Each summary is then entered into the Google search engine. Webpages are crawled via the BeautifulSoup Python Library, where all texts from span tag of class 'st' were returned. Regular expression was used to sieve out date and time data to prevent the model from possibly overfitting on features that were not meaningful.

The final dataset had a total number of training instances of 130, 380 (Fig. 2).

3 Methdology

J. *Problem statement and metrics*

This project set out to investigate the initial hypotheses by validating three different aspects of the proposed approach. Firstly, to verify the automated evidence collection mechanism, models were trained on compiled evidence only and tested against those trained on all data. Secondly, to validate the use of distant supervision to generate more training samples models were trained on manually labelled dataset as well as weakly labelled dataset and compared. Lastly, to validate the deep learning ensemble approach, numerous model architectures were tested and trained and their performance was evaluated.

As a summary of the testing process, the problem statement for each training instance is as follows

Style based: Given input claim or article, C_i, predict its truth probability $L_{\text{pred style}}$.

Truth based: Given input claim C_i and external evidence, A_i predict its truth probability $L_{\text{pred truth}}$.

Ensemble model: Given claim, C_i and truth probability $L_{\text{pred style}}$ and $L_{\text{pred truth}}$, predict the truth probability $L_{\text{pred final}}$.

The models were evaluated based on their micro and macro-average accuracy, as well as F1-score, precision and recall.

K. *Control variables and text vectorization*

To keep other variables constant, models were set to minimize binary cross entropy during training, and were trained for as many epochs as validation loss is decreasing, using callback utilities provided by Keras. Training batch size of 512 was found during pre-testing to be a satisfactory compromise between training speed and generalizing ability of final model. To compensate for data imbalance, each instance of real news was given a 2.5× class weight.

The vectorization process was also held constant as a control variable, and all models were trained with fine-tuned GloVe embedding. Text vectorization was handled by the Keras text-preprocessing utilities. A Tokenizer class object is instantiated and fitted on the entire text corpus from the dataset, associating each word with an integer index. Since indices are assigned depending on the order in which the input sequence is passed to the fit_on_texts method of the Tokenizer instance, the method is called under the same conditions for all testing and training. Each integer is then associated with a dense, floating point word vector via the embedding layer. During training, the word vectors are adjusted until the final embedding vector space displays structure and reflects semantic relationship.

While the embedding layer can be trained from scratch, a powerful strategy is to use pretrained word embeddings. In particular, Global Vectors for Word Representation (GloVe) is a commonly used word embedding developed by Stanford researchers. A key feature of such embedding pretrained on a large corpus is that in the embedding vector space, geometric transformations can reflect semantic relationships, improving the representational power of the model.

Another strategy commonly used when a large dataset is present is to allow the embedding layer to be unfrozen such that they may be adjusted during training, thereby resulting in a context-specific word embedding space. In this project, the GloVe layer was allowed to be fine-tuned during training.

4 Results and Discussion

L. *Distant Supervision*

This project firstly validates distant supervision as a viable strategy for improving model performance by extending upon existing datasets. Models trained on directly labelled training data underperforms not only in terms of the micro-average metrics across all test datasets, but also on the very data it was trained on (Liar Dataset). The better performance of models trained via both direct and distant supervision is likely due to the much greater number of training instances. As discussed below, the aggregate dataset using both methods of supervision produced deep learning models with outstanding performance (Fig. 3).

M. *Automated Evidence Collection*

The automated data collection process too was proven to be viable for fake news detection. While models trained on precompiled evidence was unable to produce meaningful results when tested on automatically collected data, this is likely due to the differences in dataset. Precompiled evidence were generally much longer and consisted of full sentences while automatically collected evidence contained salient words only. However, by introducing variety into the dataset with a combination of both evidence sources, the final model as discussed below was able to judiciously output accurate truth labels for all datasets (Fig. 4).

N. *Style Based Models*

Five different model architectures were trained and evaluated, namely Long Short Term Memory (LSTM) network, 1D convolutional network (ConvNet), Gated Recurrent Network (GRU), a bidirectional LSTM (BiLSTM) and a ConvNet Recurrent Network hybrid. All models were supplied with a first layer embedding, and testing results can be found in Figure X. Firstly, all five were proven to be viable model

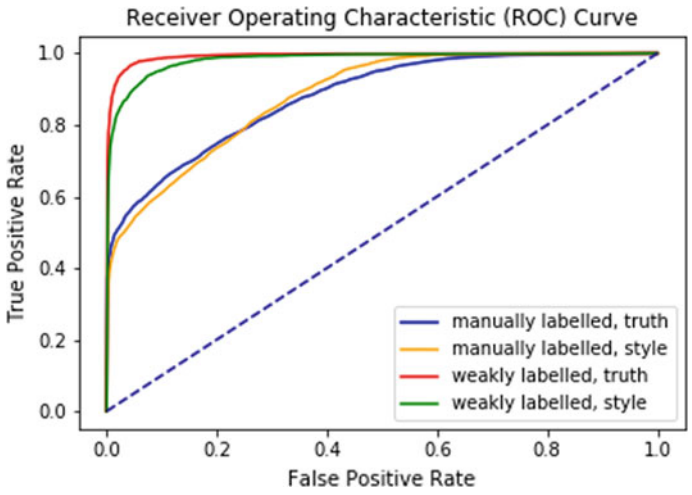

Fig. 3 ROC, distant supervision

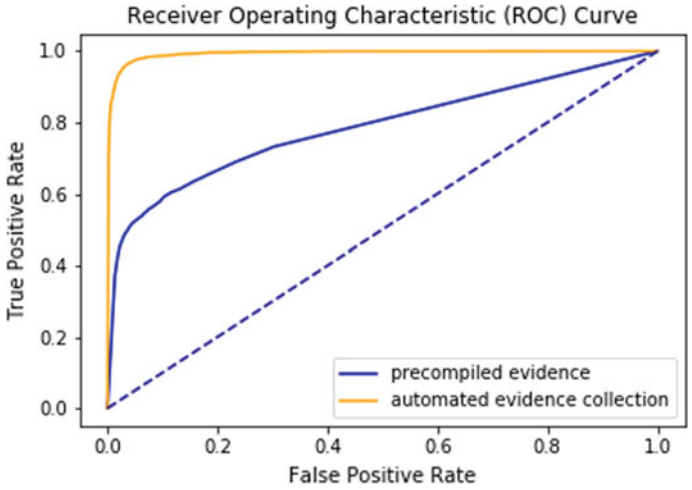

Fig. 4 ROC, automatic evidence collection

architectures for style based fake news recognition, as almost all received an accuracy of around 90%. Judging by the high scores received across all four metrics (accuracy, F1, precision and recall), all five were deemed to have sufficient representational power for the task of fake news detection. In particular, BiLSTM and ConvRNN hybrid were found to outperform other model architectures. The high performance of BiLSTM corroborates with existing literature that recurrent networks which processes sequence data in a stateful manner are order-invariant and can receive performance gains when trained in both directions [11]. As argued by Cholet, it is possible that training in the reverse direction allows the network to increase its representational capacity (Fig. 5).

Among the models tested were two convolutionary variants. In particular, a pure ConvNet and a ConvNet stacked with RNN. 1D ConvNet has shown significant promise in the field of machine translation and other sequence-oriented tasks, being able to capture translation invariant patterns [7]. Compared with their recurrent counter parts, 1D ConvNets result in much smaller models that have theoretically also recognises sequence features without heavy computational costs. However, when tested, ConvNet greatly underperforms other models and has exceedingly low precision, showing a tendency to blindly classify inputs as the positive class. This could be due to the fact that the ConvNet is trained to recognise features in a given kernel size of 7, which closely approximates the length of short claims in the test data set, resulting in limited effectiveness. This is supported by the relatively better performance of ConvNet on the extended dataset, where input lengths are longer. Compared to the pure ConvNet, the ConvNet-RNN hybrid has much better performance. The hybrid architecture is a novel approach proposed by Cholet [7] where a feature map returned by convolutionary network is then fed into a recurrent layer. At the cost of

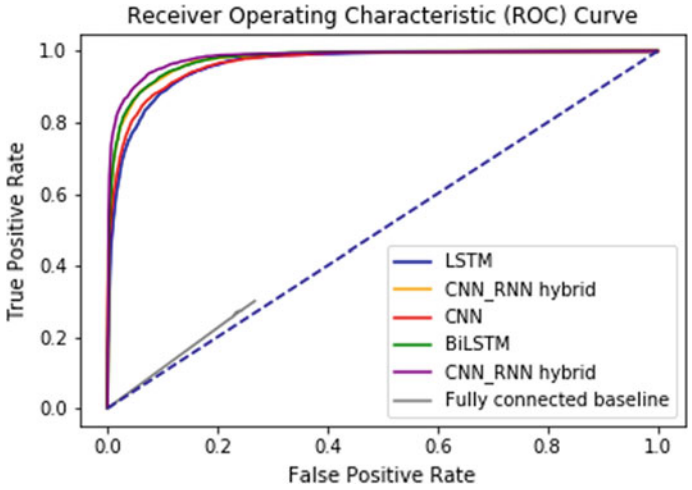

Fig. 5 ROC, style based models

heavy computation, this approach empirically grants better performance across all test datasets.

However, it must be noted that a densely connected baseline performs style based classification just as well, and even better than the ConvNet and GRU. A possible reason that accounts for this is use of GloVe word embeddings. Hence when a densely connected baseline without GloVe embedding was trained, the model reached an accuracy of 47% before overfitting, showing essentially no representational power. GloVe massive boosts the performance of such networks because of its ability to capture semantic relationships. Hence, even without consideration of data in a sequential manner, GloVe embedded word vectors already encapsulate enough information for a style based classifier to work satisfactorily, although no style based approach exceeded an F1 score of more than 0.85.

O. *Truth Based Models*

The truth based model used different model architectures to generate a hidden state representation for both the input article and the external evidence, and a classifier is then trained on the concatenated representations. To test different architectures for representation generation, the final classifier is kept constant as a densely connected layer. The different architectures include: parallel recurrent networks and its bidirectional variant, a conditionally encoded sequential recurrent network, as well as a Siamese recurrent. To reduce the number of variables tested, all recurrent networks were chosen to be LSTM, which was the best performing pure recurrent network from style based testing (Fig. 6).

All four truth based models not only outperformed their densely connected baselines, but also all style based models, validating the approach of considering external

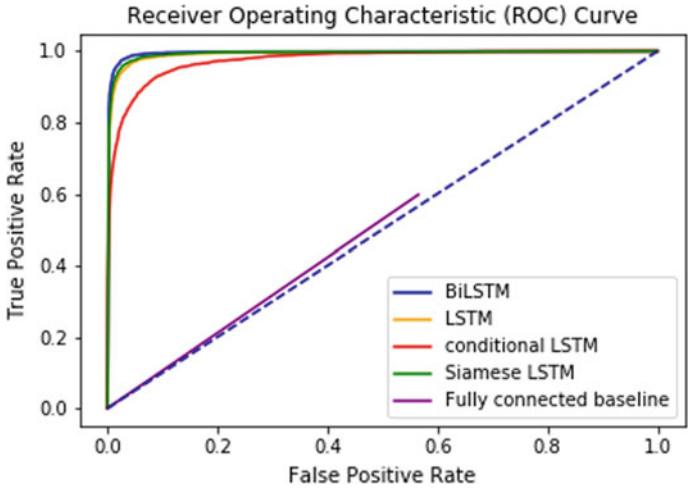

Fig. 6 ROC, truth based models

evidence. Comparing the different model architectures, it is apparent that conditionally encoded sequential LSTM underperforms all other truth based approaches. Compared to other architectures where LSTMs run in parallel, conditional LSTM borrows from the encoder-decoder framework currently used in state of the art machine translation models, where LSTMs are chained together. The encoder LSTM maps the first input to a higher dimensional representation, which is then used to initialize the second LSTM. In abstract terms, this can be described as processing the second input with regards to the first input. In this context, conditional LSTM generally underperforms, but its performance especially deteriorates for short input sequences, likely because the resulting initializing matrix is unable to discern useful information from short input sequences.

Comparing the other models, bidirectional networks marginally outperform their single direction counter parts, however at the cost of significant computational power. Siamese LSTMs were surprisingly found to have the greatest performance among all truth based models. Siamese LSTM employs the layer weight sharing technique [7]. The same LSTM layer is used to operate on both inputs to reach a higher dimensional hidden representation. Intuitively, this approach which works well in determining the semantic similarity between texts should also work well in determining the veracity of news articles when compared with external evidence, given the symmetry in manipulating input data to a higher dimensional space.

P. *Ensemble Approach*

To test the validity of the ensemble approach, the best performing style based model, ConvNet-RNN hybrid was joined with the best performing truth based model, Siamese LSTM. The output from both models were then fed into a fully connected dense classifier. The last node functions as a weighted mean. The weights were then

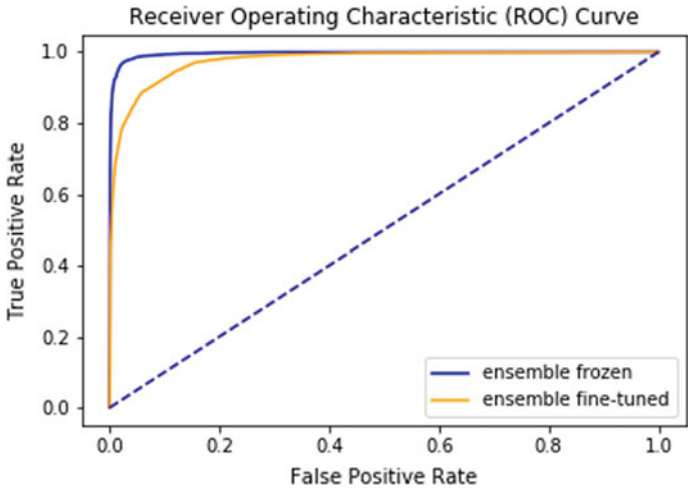

Fig. 7 ROC, ensemble models

adjusted during training. The final ensemble model outperforms both the truth based and style based models, proving the hypothesis that an ensemble model leads to performance gains. However it should be noted that performance gains were only achieved when the initial style based and truth based models were frozen during final training. When allowed to vary, the model proved too large to be trained effectively, training time increased by an order of magnitude over style based models, and the final model performance dipped below the top performing truth based model. This could be due to the vanishing gradient problem, where large models eventually become untrainable as the feedback signal during backpropagation no longer adjusts model weights accurately [7] (Fig. 7).

5 Concluding Remarks

Q. *Limitation and Future Words*

The scope of this study was targeted at verifying the validity of deep learning models in fake news detection and the validity of the proposed dataset. While the dataset was much larger than that found in current literature, there was no attempt made in this project to investigate the validity of the proposed pipeline in a local context.

The project also did not test every combination of possible architecture. For example, when testing different models for hidden state representation, LSTM was used for all to reduce the number of independent variables. However, GRU, which underperformed for the style based model could very possibly outperform LSTM for hidden state representation.

Given the validity of the automated evidence collection mechanism and distant supervision, future work could extend upon datasets found in other domains, such as the local context, and generate more training instances with their corresponding evidence retrieved from the web.

R. *Conclusion*

This project establishes distant supervision as a valid approach for enlarging existing datasets. This project also proposes and validates a fake news detection pipeline that performs truth based and style based fake news detection with no feature engineering or human intervention required. The pipeline is able to extract salient words and retrieve evidence given an input claim or news article, and then judiciously generate a credibility label.

References

1. Pathak, A., & Srihari, R. (2019). BREAKING! Presenting Fake News Corpus For Automated Fact Checking. *Proceedings of the 57th Annual Meeting of the Association for Computational Linguistics: Student Research Workshop*, 357–362.
2. Wang, W. Y. (2017). "Liar, Liar Pants on Fire": A New Benchmark Dataset for Fake News Detection. *Proceedings of the 55th Annual Meeting of the Association for Computational Linguistics (Volume 2: Short Papers)*, *2*, 422–426.
3. Popat, K., Mukherjee, S., Yates, A., & Weikum, G. (2018). DeClarE: Debunking Fake News and False Claims using Evidence-Aware Deep Learning. *Proceedings of the 2018 Conference on Empirical Methods in Natural Language Processing,* 22–32.
4. Sharma, K., Qian, F., Jiang, H., Rachansky, N., Zhang, M., & Liu, Y. (2018). Combating Fake News: A Survey on Identification and Mitigation Techniques. *ACM Trans. Intell. Syst. Technol. 37, 4, Article 111 (August 2018)*
5. Parikh, S. B., & Atrey, P. K. (2018). Media-Rich Fake News Detection: A Survey. *IEEE Conference on Multimedia Information Processing and Retrieval (MIPR).*
6. Rayson, P., Wilson, A., & Leech, G. (2001). Grammatical word class variation within the British NationalCorpus sampler. *New Frontiers of Corpus Research*, 295–306
7. 7. Chollet François. (2018). *Deep learning with Python.* Shelter Island, NY: Manning Publications Co.
8. Bunntain, C., & Golbeck, J. (2017). Automatically Identifying Fake News in Popular Twitter Threads. *2017 IEEE International Conference on Smart Cloud (SmartCloud)*, *1*, 208–215.
9. Shu, K., Mahudeswaran, D., Wang, S., Lee, D., & Liu, H. (2019). FakeNewsNet: A Data Repository with News Content, Social Context and Dynamic Information for Studying Fake News on Social Media. *Association for the Advancement of Artificial Intelligence* (www.aaai.org).
10. Ma, J., Gao, W., Mitra, P., Kwon, S., Jansen, B. J., Wong, K.-F., & Cha, M. (2016). Detecting Rumors from Microblogs with Recurrent Neural Networks. *IJCAI'16: Proceedings of the Twenty-Fifth International Joint Conference on Artificial Intelligence*, 3818–3824.
11. Ma, J., Gao, W., & Wong, K.-F. (2017). Detect Rumors in Microblog Posts Using Propagation Structure via Kernel Learning. . *Proceedings of the 55th Annual Meeting of the Association for Computational Linguistics*, 708–717.
12. Popat, K., Mukherjee, S., Strotgen, J., & Weikum, G. (2017). Where the Truth Lies: Explaining the Credibility of Emerging Claims on the Web and Social Media. *2017 International World Wide Web Conference Committee (IW3C2).*

13. Popat, K., Mukherjee, S., Strotgen, J., & Weikum, G. (2016). Credibility Assessment of Textual Claims on the Web. *CIKM'16*. doi: http://dx.doi.org/https://doi.org/10.1145/2983323.2983661
14. Chen, W.-F., & Ku, L.-W. (2016). UTCNN: a Deep Learning Model of Stance Classification on Social Media Text. *Proceedings of COLING 2016, the 26th International Conference on Computational Linguistics: Technical Papers*, 1635–1645
15. Chaudry, A. K., Baker, D., & Thun-hohenstein, P. (n.d.). Stance Detection for the Fake News Challenge: Identifying Textual Relationships with Deep Neural Nets. Retrieved from https://web.stanford.edu/class/archive/cs/cs224n/cs224n.1174/reports/2760230.pdf
16. Dey, K., Shrivastava, R., & Kaushik, S. (2018). Topical Stance Detection for Twitter: A Two-Phase LSTM Model Using Attention. *Accepted at the 40th European Conference on Information Retrieval (ECIR), 2018*. Retrieved from https://arxiv.org/abs/1801.03032
17. Rajendran, G., Chitturi, B., & Poornachandran, P. (2018). Stance-in-Depth Deep Neural Approach to Stance Classification. *International Conference on Computational Intelligence and Data Science (ICCIDS 2018)*, *132*, 1646–1653.
18. Zhang, J., Dong, B., & Yu, P. S. (2018). FakeDetector: Effective Fake News Detection with Deep Diffusive Neural Network.

Automatic Grading of Online Formative Assessments Using Bidirectional Recurrent Neural Networks and Attention Mechanism

Advay Pakhale, Xavier Lien, and Tan Guoxian

Abstract Formative assessments have been shown to be highly beneficial for students' learning processes due to their ability to provide feedback to both teachers and students. However, the marking of short-answer questions in formative assessments is a tedious task for teachers. The advent of online learning platforms, however, has allowed for the digitalisation of student answers which opens up opportunities for automatic grading. We propose novel automatic grading architectures that (1) produce an accurate quantitative score in order to expedite the marking process and (2) provide qualitative feedback to teachers and students in terms of the key areas of improvement. These architectures consist of bidirectional long short-term memory and gated recurrent unit networks with an attention mechanism for quantitatively scoring answers, and a cosine similarity-based model that provides qualitative feedback based on a simple marking scheme comprising marking points. We evaluate these architectures across different metrics on two datasets collected from an online physics quiz, consisting of two short-answer physics questions on the topic of thermodynamics. We show that our architectures achieve reasonable accuracy on the scoring task and provide useful feedback to teachers and students, thus successfully aiding in automatically grading formative assessments.

Keywords Automatic grading · Machine learning · Online learning · Bidirectional recurrent neural networks · Attention mechanism · Formative assessments

A. Pakhale (✉) · X. Lien · T. Guoxian
Raffles Science Institute, Raffles Institution, Singapore, Singapore
e-mail: advay.pakhale@gmail.com

X. Lien
e-mail: xavilien@gmail.com

T. Guoxian
e-mail: guoxian.tan@ri.edu.sg

H. Guo et al. (eds.), *IRC-SET 2020*,
https://doi.org/10.1007/978-981-15-9472-4_7

1 Introduction

Formative assessments place a primary focus on providing qualitative feedback for both teachers and students. Such feedback not only allows teachers to monitor their students' progress and evaluate the effectiveness of their own instruction, but also provides insight as to how the teaching and learning process can be optimised going forward [1]. Formative assessments have been shown to produce a much greater impact on student learning as compared to summative assessments when administered frequently and in a timely manner [2]. Hence, formative assessments clearly play a beneficial role in today's modern classrooms.

However, grading certain forms of formative assessments such as short-answer questions is a complex task that requires significant human intervention and input. Furthermore, valuable feedback needs to be produced that is beneficial to both students and teachers, which is a time-consuming and tedious task for teachers. The automation of this task would allow open-ended formative assessments to be administered more frequently and easily, greatly easing the workload of teachers and allowing both students and teachers to reap their benefits through the frequent and timely report of progress that they would receive.

The advent of online learning platforms has made administering formative assessments more convenient and more importantly, has allowed for the digitalisation of student answers which opens up opportunities for automatic grading that are explored in the following sections.

2 Literature Review

Much progress has been made in developing different approaches to the automatic grading of open-ended questions. Reference [3] showed that a system utilising multiple linear regression with a combination of hand-crafted features and probabilistic models, such as Bayesian classifiers and k-nearest-neighbour algorithms, can give results comparable with human graders. Reference [4] developed CarmelTC, a rule-based approach, combining both features obtained from deep syntactic functional analyses of texts and a "bag-of-words" classification extracted from Rainbow Naive Bayes, outperforming Latent Semantic Analysis, Rainbow Naive Bayes and a purely symbolic approach. Reference [5] used a deep learning approach for essay grading while [6] used hand-picked features with linear regression on the same dataset. The former performed significantly better, demonstrating the superiority of deep learning approaches over classic Natural Language Processing (NLP) methods.

However, much of the literature focuses on grading summative assessments; the only objective is to produce an accurate quantitative prediction of the score. This is arguably easier and less complex than grading formative assessments which involves producing feedback for both teachers and students on top of merely providing a quantitative score. Thus, there is a need for new automatic grading architectures that can fulfil the aims of formative assessments.

3 Methodology

3.1 Datasets

An online physics quiz was conducted on 292 Raffles Institution Secondary 2 students, comprising two short-answer physics question on the topic of thermodynamics. Thermodynamics was chosen as it is an important topic in mainstream schools which students have many misconceptions about, and this topic is typically tested using qualitative short-answer questions. The first question is a simple recall question, while the second question is a more complex application question, designed to have more variance in answers. The answers were then graded by an entire level of 3 physics teachers based on a marking scheme comprising different marking points. Student answers were then pre-processed by tokenising and converting to lowercase while punctuation, non-alphabetical characters and stop words were also removed. The answers and scores from question 1 and question 2 are denoted dataset 1 and dataset 2 respectively.

3.2 Components of Architecture

We aim to design an architecture (Fig. 1) that automatically grades short-answer formative assessments by **(1)** providing an accurate quantitative score for student answers in order to expedite the marking process and **(2)** providing qualitative feedback to teachers and students in terms of the key areas of improvement. We evaluated different qualitative and quantitative models that attempt to achieve these two aims.

3.2.1 Quantitative Component

We propose a neural network model for the quantitative component. In order to design the best performing architecture, we propose different types of models below. Firstly, we compare the use of different word embeddings. Secondly, we fix our baseline model to be a simple feedforward neural network. Thirdly, we compare two types of Recurrent Neural Networks (RNNs), Long Short-Term Memory (LSTM) networks and Gated Recurrent Unit (GRU) networks. Fourthly, we compare the use of

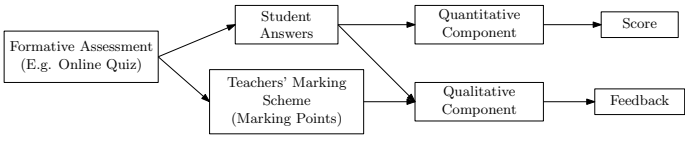

Fig. 1 Outline of architecture

bidirectional RNNs (BiRNNs) and their unidirectional variants. Finally, we propose an attention mechanism.

(a) Word Embeddings Within the neural networks, the answers are first represented in terms of word vectors that can encode meaningful semantic relationships between words. We compare 2 types of word embeddings—GloVe [7] and fastText [8], both of which are 300 dimensional.

(b) Feedforward Neural Network (Baseline) We chose a simple feedforward neural network as our baseline. This network is trained on an "answer vector" for each answer, which is simply the sum of the word vectors for each word in the answer. While this approach does not preserve sequential information, word vectors have been shown to be able to meaningfully encode linearities such as *king* − *man* + *woman* = *queen* and *Paris* − *France* + *Italy* = *Rome* [9]. Thus, we hypothesise that the answer vectors will nevertheless be able to encode meaningful information about the answers to a certain degree. The architecture of the baseline and non-baseline models can be found in Fig. 2.

(c) LSTM and GRU Networks LSTM networks [10] preserve long-distance dependencies, making them ideal for processing text sequences [11]. On the other hand, GRU networks were developed as an alternative to LSTM networks and are computationally less complex [12], yet perform comparably to LSTM net-

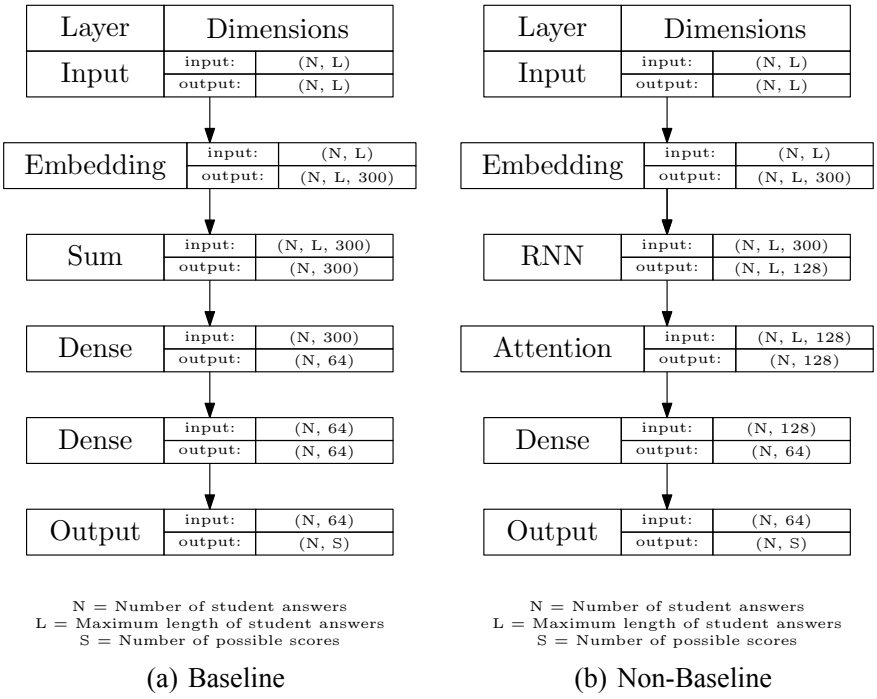

Fig. 2 Model architectures

works in sequence processing tasks [13]. We chose to work with RNNs as they have demonstrated excellent performance in sequence processing tasks, including sequence classification, due to their ability to account for sequential information [14], making them applicable to our task of grading short-answer physics questions.

(d) Bidirectional Recurrent Neural Networks BiRNNs [15] such as BiLSTM networks aim to improve upon RNNs by processing the same input sequence twice, forwards and backwards. This allows the BiRNN to retain contextual information in both directions and has led to an improvement in performance in various sequence processing tasks [16, 17]. Hence, we compare the performance of BiLSTM and BiGRU models with that of regular LSTM and GRU models.

(e) Attention Mechanism Recently, the attention mechanism has been developed for sequence processing tasks such as machine translation and sequence classification [18, 19]. Since not all words in a sentence contribute equally to its meaning, attention is used to place more weight on more important words while placing less weight on less important words. We hypothesise that attention would be able to extract keywords from answers to aid in marking them more effectively, similar to how a teacher might mark answers. A detailed diagram showing the architecture of the attention layer on top of a BiRNN layer can be found in Fig. 3.

3.2.2 Qualitative Component

We propose a few different methods to provide qualitative feedback to students and teachers using the marking schemes in our datasets by capturing common strengths and weaknesses in student answers. We mainly adapt and draw inspiration from classic probabilistic topic models such as Latent Dirichlet Allocation [20], which produces sparse and low-dimensional interpretations of topic memberships in documents. These are highly interpretable, allowing humans to gain high-level insight and intuition from them, which is especially necessary in the field of formative assessment where human understanding and feedback is key.

(a) Vector Decomposition Our datasets provide us with marking points and student answers. In order to manipulate these mathematically, a vector representation first needs to be defined for them. Motivated by the fact that word vectors can meaningfully encode linearities, as mentioned in Sect. 3.2.1b, we initialise the marking point vectors to be the sum of the words in each marking point, so that they capture the meaning of the marking points:

$$\mathbf{t_k} = \sum_{i \in T_k} \mathbf{w_i}, \tag{1}$$

where $\mathbf{t_k}$ and T_k are the marking point vector and the set of words in the kth marking point out of n marking points respectively, and $\mathbf{w_i}$ is the word vector for

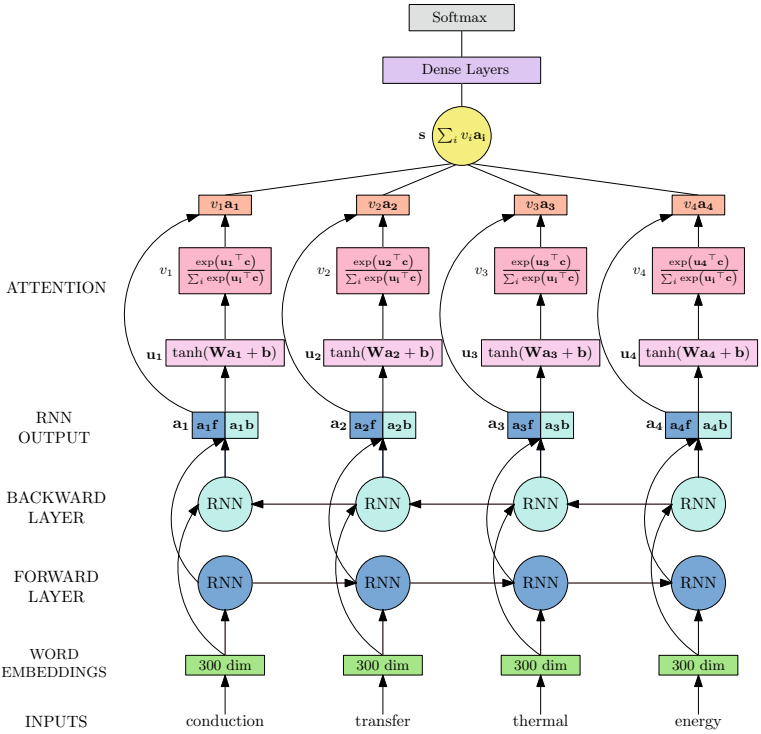

Fig. 3 Attention mechanism on top of a BiRNN

the *i*th word. The GloVe word vectors are used for the purposes of the qualitative experiments.

A similarly suitable vector representation of student answers, is simply the sum of all the word vectors for each word in the answer:

$$\mathbf{a_j} = \sum_{i \in A_j} \mathbf{w_i}, \tag{2}$$

where $\mathbf{a_j}$ and A_j are the answer vector and the set of words in the jth answer respectively. However, an answer can also be represented as a complete or incomplete combination of the marking points.

Thus, we hypothesise that the answer vector $\mathbf{a_j}$ can be decomposed into a linear combination of marking point vectors:

$$\hat{\mathbf{a_j}} = \sum_{k=1}^{n} p_{jk} \mathbf{t_k} = \sum_{k=1}^{n} p_{jk} \sum_{i \in T_k} \mathbf{w_i}, \tag{3}$$

where p_{jk} is the proportion of a marking point k in answer j and $p_{jk} \in [0, 1]$. $p_{jk} = 0$ would mean that a marking point is completely not within the student's answer, while $p_{jk} = 1$ would mean otherwise. Let $\mathbf{T}$ be the matrix whose columns are $\mathbf{t_1}, \ldots, \mathbf{t_k}, \ldots, \mathbf{t_n}$. Then $\hat{\mathbf{a}}_\mathbf{j}$ is an element of the column space of $\mathbf{T}$, and can be equivalently expressed as $\hat{\mathbf{a}}_\mathbf{j} = \mathbf{T}\mathbf{p_j}$. In order to then find an accurate decomposition of the answer vector, the optimal proportion vector $\hat{\mathbf{p}}_\mathbf{j}$ can be found by optimising the mean squared error between $\hat{\mathbf{a}}_\mathbf{j}$ and $\mathbf{a_j}$:

$$\hat{\mathbf{p}}_\mathbf{j} = \arg\min_{\mathbf{p_j}} \|\hat{\mathbf{a}}_\mathbf{j} - \mathbf{a_j}^2\| \tag{4a}$$

$$= \arg\min_{\mathbf{p_j}} \|\mathbf{T}\sigma(\mathbf{p_j}) - \mathbf{a_j}^2\|. \tag{4b}$$

The logistic function $\sigma(x) = \frac{1}{1+e^{-x}}$ is applied element-wise on $\mathbf{p_j}$ to enforce the constraint $0 \leq p_{jk} \leq 1$.

(b) Cosine Similarity Under this method, the marking point proportions p_{jk} are defined as the cosine similarity [21] between the student answer vector and each marking point vector:

$$p_{jk} = \cos\theta_{jk} = \frac{\mathbf{a_j} \cdot \mathbf{t_k}}{\|\mathbf{a_j}\|\|\mathbf{t_k}\|}. \tag{5}$$

These p_{jk} values are collected into a vector, $\mathbf{p_j} = \big((p_{j0}\ p_{j1}\ \ldots\ p_{jk})\big)$, for each answer j.

(c) Euclidean Distance p_{jk} can also defined as the Euclidean distance [21] between the student answer vector and each marking point vector:

$$p_{jk} = \|\mathbf{a_j} - \mathbf{t_k}\|. \tag{6}$$

Similarly, we define $\mathbf{p_j} = \big((p_{j0}\ p_{j1}\ \ldots\ p_{jk})\big)$.

4 Data and Discussion

4.1 Evaluation Methodology

The datasets are split into training and validation sets, with a proportion of 0.8 and 0.2 respectively. Each model is evaluated using 5-fold cross-validation on 3 metrics. Firstly, accuracy checks to see whether the model is able to give each student answer a correct score. Such a metric is useful for teachers and students as an ideal model would be able to mark all student answers exactly like a teacher would. Secondly, categorical cross-entropy loss is used to compare the different models as this the loss function that they were trained using. Lastly, weighted F1 score takes into consideration the unequal distribution of scores for the student answers as there are very few students who received full marks for each question. The hyperparameters used for the quantitative models can be found in Table 1.

Table 1 Hyperparameters for quantitative models

GloVe dimensions	300d
Number of hidden layers (without attention)	2
Number of hidden layers (with attention)	3
Number of units per hidden layer	64
Activation	ReLu
Optimizer	Adam
Learning rate	0.001
Dropout	0.1
Loss	Categorical cross-entropy

4.2 Evaluation of Quantitative Component

4.2.1 Comparison of Models

(a) LSTM versus GRU From Tables 2 and 3, the GRU models performed better than the LSTM models on dataset 1, while the opposite is true for dataset 2. We hypothesise that this is the case because of the difference in complexity of the two questions. Since question 1 is less complex than question 2, the simpler GRU models with fewer parameters are likely to have less overfitting than the LSTM models. Likewise, the LSTM models are likely able to better capture the complexities of the second questions, giving them better performance. As shown by [22], LSTM networks are "strictly stronger" than GRU networks as they can easily perform unbounded counting, which GRU networks cannot, further supporting the hypothesis that LSTM networks are better suited for more complex questions. The difference in question complexity is likely also the reason for the disparity in performances between the two datasets for all models.

(b) Attention In addition, attention significantly improved the performance of the models, supporting our initial hypothesis. This is likely because physics answers are marked based on keywords, which is suited for attention as it is able to place weight on more important words and extract keywords. This is further corroborated by the attention weights extracted from the layer, visualised in Fig. 4, which shows that attention places more weight on keywords such as "gases", "solids", and "states".

(c) Word Embeddings GloVe performed better for the first dataset while fastText performed better for the second dataset. We hypothesise that this performance disparity could be to the fact that fastText was better able to capture the more complex nature of the second question, due to the "subword" information captured by fastText [8].

(d) Baseline Contrary to our initial hypothesis, the baseline performed surprisingly well and outperformed many of the more complex models, despite having a major disadvantage due to the fact that it does not preserve sequential informa-

Table 2 Performance of quantitative models on dataset 1

Models	Accuracy	Loss	F1 score
Feedforward neural network (Baseline)	0.733	0.849	0.719
LSTM with GloVe	0.702	0.780	0.660
BiLSTM with GloVe	0.705	0.837	0.699
BiLSTM with GloVe and attention	0.760	0.698	0.750
BiLSTM with fastText and attention	0.716	0.741	0.696
GRU with GloVe	0.715	1.050	0.701
BiGRU with GloVe	0.709	0.909	0.692
BiGRU with GloVe and attention	*0.781*	*0.701*	*0.775*
BiGRU with fastText and attention	0.726	0.715	0.692

Table 3 Performance of quantitative models on dataset 2

Models	Accuracy	Loss	F1 score
Feedforward Neural Network (Baseline)	0.472	1.354	0.433
LSTM with GloVe	0.428	1.840	0.399
BiLSTM with GloVe	0.432	1.546	0.394
BiLSTM with GloVe and Attention	0.520	1.530	0.500
BiLSTM with fastText and attention	*0.541*	*1.157*	*0.506*
GRU with GloVe	0.414	1.658	0.373
BiGRU with GloVe	0.421	1.459	0.392
BiGRU with GloVe and Attention	0.462	1.435	0.447
BiGRU with fastText and attention	0.496	1.265	0.465

tion. We conjecture that this could be due to two possible reasons. The more complex models have a significantly greater number of parameters compared to the baseline. This, combined with the relatively small datasets, could have led to overfitting in these models [23], preventing them from generalising their classification task to the validation set as well as the baseline model, leading to the latter having a better performance. The baseline could have also outperformed the other models due to poor hyperparameter tuning in the more complex models, causing them to be stuck in poor local minima [24]. If this is the case, then there is a possibility that performance can be significantly improved with a more careful hyperparameter search.

4.2.2 Performance Across Different Data Environments

We explored how the number of training samples affects the models' performance. 42 student answers were put aside to be the validation set. The size of the training

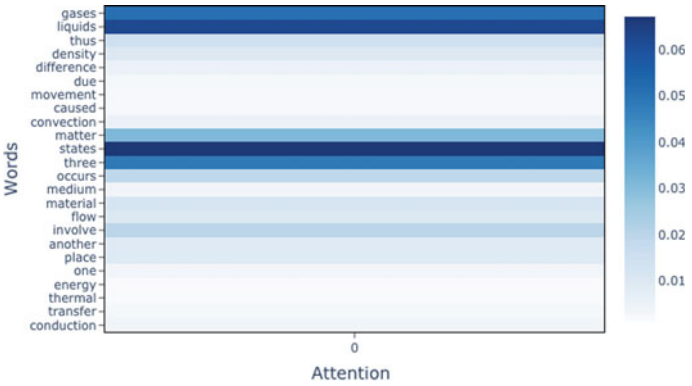

Fig. 4 Attention weights of answer sample from dataset 1

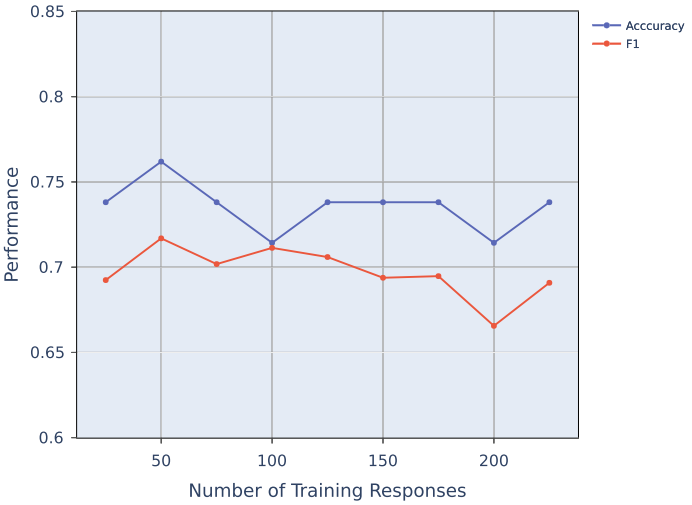

Fig. 5 Performance of dataset 1 best model (BiGRU with GloVe and attention) against size of training set

set was varied from 25 samples to 250 samples in increments of 25 samples and the performance of the model was monitored. The detailed results, which can be found in Figs. 5 and 6, show that our best models perform well even in low data environments. Since one of the intended aims of our models is to reduce the marking load for teachers, this demonstrates their utility as teachers only need to mark a small proportion of the dataset for the models to perform well.

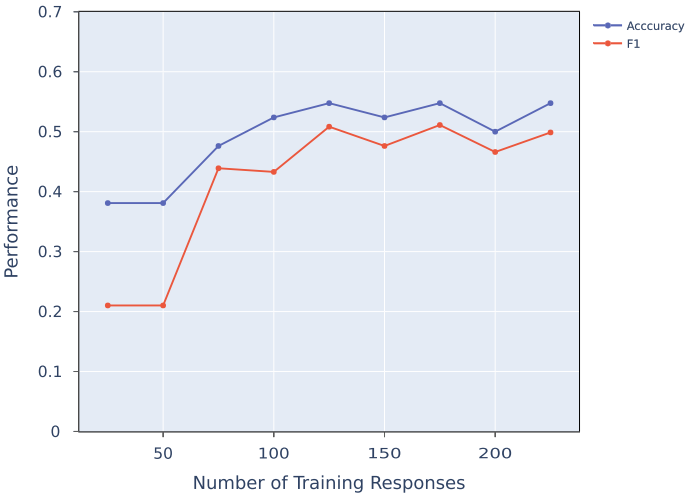

Fig. 6 Performance of dataset 2 best model (BiLSTM with fastText and attention) against size of training set

4.3 Evaluation of Qualitative Component

4.3.1 Comparison of Models

To test how accurate the set of $\mathbf{p_j}$ vectors generated by each qualitative model is, we trained a simple feedforward neural network to predict the scores based on $\mathbf{p_j}$ as the input. This is based on the assumption that accurate proportions of each marking point should be correlated to the score of the answers, since these marking points are used by teachers to mark the answers. The results are summarised in Tables 4 and 5. It can be seen that the cosine similarity model clearly outperforms the rest and the results achieved by it are even comparable to our best quantitative models despite the relative simplicity of this approach. This could be due to the same reasons our baseline quantitative model outperformed more complex models, as highlighted in Sect. 4.2.1d. This good performance also shows that the proportions generated are accurate.

4.3.2 Producing Feedback

The $\mathbf{p_j}$ vectors can be used to produce feedback for both teachers and students. Upon some basic visualisation, students can view their own $\mathbf{p_j}$ vector and observe which marking points they managed to incorporate into their answer and which marking points were missed out, to give them an indication of their areas for improvement. Furthermore, an average $\mathbf{p_j}$ vector across all answers can also be calculated and visu-

Table 4 Performance of qualitative models on dataset 1

Models	Accuracy	Loss	F1 score
Vector decomposition	0.591	0.931	0.552
Cosine similarity	*0.716*	*0.652*	*0.713*
Euclidean distance	0.648	0.769	0.608

Table 5 Performance of qualitative models on dataset 2

Models	Accuracy	Loss	F1 score
Vector decomposition	0.455	1.251	0.438
Cosine Similarity	*0.541*	*1.128*	*0.527*
Euclidean distance	0.534	1.165	0.493

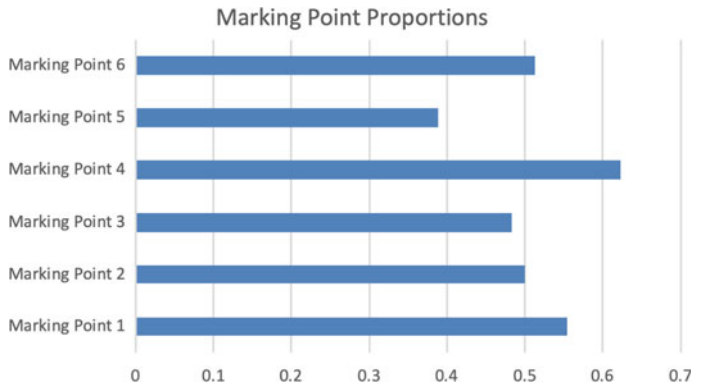

Fig. 7 Marking point proportions

alised for teachers' analysis, as seen in Fig. 7. Figure 7 was produced by averaging the $\mathbf{p_j}$ vectors from the cosine similarity model run on dataset 1. From this, teachers can immediately observe which marking points most students wrote in their answers and which they failed to incorporate. This would provide feedback to teachers about which parts of their teaching were well understood by the students and likewise, which parts might need review. We can thus see how the qualitative feedback produced by the model aids in the task of formative assessment.

4.4 Final Architecture

Based on our results, we recommend two separate architectures for different types of questions. For the quantitative component, we recommend a BiGRU network with GloVe embeddings and an attention mechanism for simple recall style questions but

a BiLSTM network with fastText embeddings and an attention mechanism for more complex application-based questions. For the qualitative component, we recommend the cosine similarity model for both types of questions.

5 Conclusion and Future Work

In this work, we proposed a novel approach to grading short-answer physics questions. Both the qualitative and quantitative components are shown to perform well, especially in low data conditions, which is important in order to reduce the marking workload of teachers. Furthermore, the architectures also provide interpretable feedback for both teachers and students, aiding in the task of formative assessment.

Given such promising results, these architectures can be applied to online learning portals where teachers can deploy a system for each short-answer question they create and feed the system a small amount of marked answers as training data along with a simple marking point-based marking scheme.

In future works, we propose exploring different word embeddings such as ELMo [25], which could yield a performance upgrade. Additionally, to tackle the problem of overfitting we identified, dropout layers [26] could be employed in our models. Thirdly, more careful hyperparameter optimisation using comprehensive methods such as randomised search [27] and sequential search [28] on our current models could yield better results. Considering the good performance of the qualitative models, it may be possible to increase performance by incorporating the marking points as features to the quantitative models. Lastly, the models could also be evaluated on other datasets, such as larger datasets and datasets from different domains such as other sciences, to test its scalability and adaptability.

References

1. P. Black and D. Wiliam, "Developing the theory of formative assessment," *Educational Assessment, Evaluation and Accountability (formerly: Journal of Personnel Evaluation in Education)*, vol. 21, no. 1, p. 5, 2009.
2. P. Black and D. Wiliam, "Assessment and classroom learning," *Assessment in Education: Principles, Policy & Practice*, vol. 5, no. 1, pp. 7–74, 1998.
3. L. S. Larkey, "Automatic essay grading using text categorization techniques," in *Proceedings of the 21st Annual International ACM SIGIR Conference on Research and Development in Information Retrieval*, ser. SIGIR '98. New York, NY, USA: ACM, 1998, pp. 90–95.
4. C. P. Rosé, A. Roque, D. Bhembe, and K. VanLehn, "A hybrid approach to content analysis for automatic essay grading," in *Companion Volume of the Proceedings of HLT-NAACL 2003 - Short Papers*, 2003, pp. 88–90. [Online]. Available: https://www.aclweb.org/anthology/N03-2030
5. H. Nguyen and L. Dery, "Neural networks for automated essay grading," 2018.
6. Y. Zhang, R. Shah, and M. Chi, "Deep learning+ student modeling+ clustering: A recipe for effective automatic short answer grading." *International Educational Data Mining Society*, 2016.

7. J. Pennington, R. Socher, and C. Manning, "Glove: Global vectors for word representation," in *Proceedings of the 2014 Conference on Empirical Methods in Natural Language Processing (EMNLP)*, 2014, pp. 1532–1543.
8. P. Bojanowski, E. Grave, A. Joulin, and T. Mikolov, "Enriching word vectors with subword information," *Transactions of the Association for Computational Linguistics*, vol. 5, pp. 135–146, 2017.
9. T. Mikolov, K. Chen, G. Corrado, and J. Dean, "Efficient estimation of word representations in vector space," 2013.
10. S. Hochreiter and J. Schmidhuber, "Long short-term memory," *Neural computation*, vol. 9, no. 8, pp. 1735–1780, 1997.
11. S. Hochreiter and J. Schmidhuber, "Lstm can solve hard long time lag problems," in *Proceedings of the 9th International Conference on Neural Information Processing Systems*, ser. NIPS'96. Cambridge, MA, USA: MIT Press, 1996, pp. 473–479.
12. K. Cho, B. Van Merriënboer, C. Gulcehre, D. Bahdanau, F. Bougares, H. Schwenk, and Y. Bengio, "Learning phrase representations using rnn encoder-decoder for statistical machine translation," 2014.
13. J. Chung, C. Gulcehre, K. Cho, and Y. Bengio, "Empirical evaluation of gated recurrent neural networks on sequence modeling," 2014.
14. J. Y. Lee and F. Dernoncourt, "Sequential short-text classification with recurrent and convolutional neural networks," 2016.
15. M. Schuster and K. K. Paliwal, "Bidirectional recurrent neural networks," *IEEE Transactions on Signal Processing*, vol. 45, no. 11, pp. 2673–2681, 1997.
16. A. Graves, S. Fernández, and J. Schmidhuber, "Bidirectional lstm networks for improved phoneme classification and recognition," in *International Conference on Artificial Neural Networks*. Springer, 2005, pp. 799–804.
17. M. Sundermeyer, T. Alkhouli, J. Wuebker, and H. Ney, "Translation modeling with bidirectional recurrent neural networks," in *Proceedings of the 2014 Conference on Empirical Methods in Natural Language Processing (EMNLP)*, 2014, pp. 14–25.
18. D. Bahdanau, K. Cho, and Y. Bengio, "Neural machine translation by jointly learning to align and translate," 2014.
19. Z. Yang, D. Yang, C. Dyer, X. He, A. Smola, and E. Hovy, "Hierarchical attention networks for document classification," in *Proceedings of the 2016 Conference of the North American Chapter of the Association for Computational Linguistics: Human Language Technologies*. San Diego, California: Association for Computational Linguistics, Jun. 2016, pp. 1480–1489. [Online]. Available: https://www.aclweb.org/anthology/N16-1174
20. D. M. Blei, A. Y. Ng, and M. I. Jordan, "Latent dirichlet allocation," *Journal of Machine Learning Research*, vol. 3, pp. 993–1022, Mar. 2003. [Online]. Available: http://dl.acm.org/citation.cfm?id=944919.944937
21. A. Huang, "Similarity measures for text document clustering," in *Proceedings of the 6th New Zealand Computer Science Research Student Conference*, vol. 4, 01 2008, pp. 9–56.
22. G. Weiss, Y. Goldberg, and E. Yahav, "On the practical computational power of finite precision rnns for language recognition," 2018.
23. D. M. Hawkins, "The problem of overfitting," *Journal of Chemical Information and Computer Sciences*, vol. 44, no. 1, pp. 1–12, 01 2004.
24. N. Reimers and I. Gurevych, "Optimal hyperparameters for deep lstm-networks for sequence labeling tasks," 2017.
25. M. E. Peters, M. Neumann, M. Iyyer, M. Gardner, C. Clark, K. Lee, and L. Zettlemoyer, "Deep contextualized word representations," 2018.
26. N. Srivastava, G. Hinton, A. Krizhevsky, I. Sutskever, and R. Salakhutdinov, "Dropout: A simple way to prevent neural networks from overfitting," *Journal of Machine Learning Research*, vol. 15, pp. 1929–1958, 2014. [Online]. Available: http://jmlr.org/papers/v15/srivastava14a.html

27. J. Bergstra and Y. Bengio, "Random search for hyper-parameter optimization," *Journal of Machine Learning Research*, vol. 13, no. Feb, pp. 281–305, 2012.
28. J. S. Bergstra, R. Bardenet, Y. Bengio, and B. Kégl, "Algorithms for hyper-parameter optimization," in *Advances in Neural Information Processing Systems 24*, J. Shawe-Taylor, R. S. Zemel, P. L. Bartlett, F. Pereira, and K. Q. Weinberger, Eds. Curran Associates, Inc., 2011, pp. 2546–2554. [Online]. Available: http://papers.nips.cc/paper/4443-algorithms-for-hyper-parameter-optimization.pdf

An Evaluation of the Presence, Type and Suggestions About the Mechanisms of Drug Interaction Between Venetoclax and GSK595 in Multiple Myeloma

Eileen Yu Ling Wong, Darren Qiancheng Tan, and Toshio Suda

Abstract Multiple myeloma (MM) is the second most prevalent blood cancer in Singapore. Although the BH3-mimetic Venetoclax is effective against MM, acquired drug resistance occurs due to a shift in the balance between the activities of pro- and anti-apoptotic Bcl-2 family proteins towards survival. Here, we investigate whether the protein arginine methyltransferase 5 (PRMT5) inhibitor GSK3326595 can synergise with Venetoclax by modulating the activities of pro- and anti-apoptotic Bcl-2 family proteins. Using the Zero interaction potency (ZIP) model, we demonstrate the potential synergy between Venetoclax and GSK3326595 on several MM cell lines. Using flow cytometry and gene expression analysis, we also elucidated possible mechanisms of synergy and a seemingly counterintuitive gene expression pattern, which collectively suggest that both drugs likely induce apoptosis at the post-translational level.

Keywords Multiple myeloma (MM) · Venetoclax · Arginine methyltransferase 5 (PRMT5) inhibitor · GSK3326595 · Bcl-2 · Synergise

1 Introduction

Multiple myeloma (MM) is a plasma cell malignancy within the bone marrow that causes numerous complications including cytopenia, lytic bone lesions, renal impairment and hypercalcaemia. Notably, MM is the second most prevalent blood cancer in Singapore, with increasing occurrence in Asia [1]. More importantly, MM patients

E. Y. L. Wong (✉)
Raffles Institution, Singapore, Singapore
e-mail: wongylei@gmail.com

D. Q. Tan · T. Suda
Cancer Science Institute of Singapore, NUS, Singapore, Singapore
e-mail: darrentanqc@gmail.com

T. Suda
e-mail: sudato@z3.keio.jp

H. Guo et al. (eds.), *IRC-SET 2020*,
https://doi.org/10.1007/978-981-15-9472-4_8

typically cannot recover from MM due to acquired drug resistance, which results in relapse [2].

The BH3-mimetic Venetoclax (ABT-199), which specifically inhibits the anti-apoptotic protein BCL2, is known to be effective against MM but susceptible to acquired drug resistance [2]. BCL2 is one of several anti-apoptotic Bcl-2 family proteins, along with BCL-X_L and MCL1 [3], which inactivate pro-apoptotic proteins of the same family by binding to their BH3 motifs [2]. Death by the intrinsic pathway of apoptosis largely depends on the balance between the activities of both pro-apoptotic and anti-apoptotic Bcl-2 family proteins. Hence, the inhibition of multiple anti-apoptotic Bcl-2 family proteins is needed to trigger apoptosis [4], and shift the balance towards death. Consequently, Venetoclax is only mildly effective against cell lines that have large quantities of both BCL2 and MCL1, with Venetoclax-resistant cells relying on MCL1 for survival [2]. Therefore, to completely eradicate MM cells, it is important to inhibit both BCL2 and MCL1. Additionally, there is a need to discover which drug combinations are synergistic in treating MM, where synergism is defined as multiple drugs having an effect stronger than if individual effects were simply added up, in order to lessen toxicity while being effective. Conversely, antagonism is when the combination is weaker than the sum of individual drugs. Additivity is defined as each drug not affecting the potency of the others [5].

GSK3326595 (GSK595) is a competitive inhibitor of protein arginine methyltransferase 5 (PRMT5), and functions by binding the active site of PRMT5 to displace substrate peptides [6]. PRMT5 depletion has been reported to inhibit growth in various MM cell lines and upregulates p53 activity [7]. This is relevant as p53 has been shown to inhibit MCL1. For instance, p53 activation in acute myeloid leukaemia (AML), leads to upregulation of PUMA (encoded by *BBC3*), BAX and BAK, which bind and inhibit MCL1 [8]. Therefore, we hypothesize that Venetoclax has synergistic effects with GSK595, where GSK595 increases the activity of p53 to reduce the amount of MCL1, which serves to overcome resistance to Venetoclax. Moreover, since p53 also increases the expression of the pro-apoptotic Bcl-2 family proteins PUMA, BAX and BAK, inhibiting PRMT5 to increase the activity of p53 may further shift the balance between pro-and anti-apoptotic Bcl-2 family proteins in favour of apoptosis. In this study, we analysed drug combinations between Venetoclax and GSK595 on the MM cell lines KMS11, KMS12BM and OPM2. We also evaluated apoptosis in OPM2 and changes in the mRNA expression of pro- and anti-apoptotic Bcl-2 family proteins. This paper presents our results on the presence of drug interaction between Venetoclax and GSK595, and proposes a mechanism on how these drugs function together.

2 Materials and Methods

A. *Cell lines*

The cell lines KMS11, KMS12BM and OPM2 were cultured in RPMI 1640 medium with L-Glutamine (Biowest) supplemented with 10% FCS (Biowest).

B. In vitro*proliferation/viability assay*

ABT-199 (Venetoclax; Aobious) and GSK3326595 (GSK595; MedChemExpress) stock solutions were prepared and diluted in sterile-filtered cell culture-grade DMSO (Sigma).

To evaluate cell response to monotherapy or combination therapy, cells were seeded in 96-well white plates (Greiner BioOne) at a density of 6×10^4 cells/ml in 100 μl, treated with either or both compounds at the indicated concentrations, and incubated for 6 days at 37 °C, 5% CO_2 under humidified conditions. Technical duplicates were performed for each independent experiment, using drug concentrations of GSK595 from 0 to 5 μM, and concentrations of venetoclax from 0 to 5 μM. The drugs were mixed at varying ratios in a 6 × 6 checkerboard in a 96-well plate with each drug increasing in concentration along each axis. On day 6 post-treatment, cell viability was determined using CellTiter-Glo® Luminescent Cell Viability Assay (Promega) and the most synergistic concentrations of both compounds and synergy scores were quantified using SynergyFinder using the Zero interaction potency (ZIP) model.

C. *Annexin-V/Hoechst flow cytometry assay*

For analysis of apoptosis by Annexin-V/Hoechst flow cytometry assay, OPM2 cells were seeded in 6-well plates at a seeding density of 2×10^5 cells/ml in 2.9 ml. Each well was treated with either DMSO, GSK595 (0.04 μM), Venetoclax (0.04 μM), or both drugs (0.04 μM each). 2.5×10^5 cells were harvested 4 days post-treatment, washed and resuspended in Annexin-V binding buffer (BD Bioscience). The cells were then labelled with APC-conjugated annexin-V (Thermo Fisher Scientific) and Hoechst 33258 (Thermo Fisher Scientific). Flow cytometric analysis was performed on a FACSAria II (BD Biosciences), and the data analysed using FlowJo 10.1 (Treestar).

D. *RNA extraction*

For gene expression analysis, total RNA was first extracted from cells (treated as indicated above), harvested on day 4 post-treatment, using the RNeasy Mini Kit (Qiagen) as per manufacturer's instructions. In brief, OPM2 cells (no more than 4 $\times 10^6$ cells) were first lysed and homogenised using a highly denaturing guanidine-thiocyanate-containing buffer to immediately inactivate RNases. The lysate was then homogenised using a QIAshredder spin column. RNeasy spin columns were then used to bind mRNA to a silica-based membrane. On-column DNase digestion was also performed with the RNAse-Free DNase Set (Qiagen) to prevent the carryover of genomic DNA in subsequent qRT-PCR steps. The purified mRNA was finally eluted in 30ul of RNase-free water.

E. *qRT-PCR*

For gene expression analysis, cDNA was synthesized from total RNA by reverse transcription (RT) using the EvoScript Universal cDNA Master (Roche) in accordance with manufacturers' instructions.

Quantitative PCR (qPCR) was performed using the QuantStudio™ 5 Real-Time PCR system (Thermo Fisher Scientific). Taqman™ Fast Universal PCR master mix (Thermo Fisher Scientific) was used with PrimeTime® qPCR Probe Assays (Integrated DNA Technologies) according to manufacturers' instructions. Gene list and PrimeTime® qPCR primers and probes sequences are provided in Appendix Table 1. The thermal cycling parameters used are: 1 cycle of 95 °C for 10 min, followed by 45 cycles at 95 °C for 15 s and 60 °C for 1 min. Technical duplicates were performed for each independent experiment. Amplification of the housekeeping genes *GAPDH* and *B2M* was conducted for each sample used as an endogenous control and to normalize levels of all target genes.

3 Results

A. *Interaction between Venetoclax and GSK595*

To identify the type and presence of drug interaction between Venetoclax and GSK595, we exposed several MM cell lines (KMS11, KMS12BM and OPM2) to increasing concentrations of either drug combined at different ratios. We then assessed potential drug interactions using the ZIP model, where delta scores (δ) >0, <0 or =0 indicate synergy, antagonism or a lack of interaction, respectively [9].

The interaction between Venetoclax and GSK595 are generally synergistic in the cell lines tested; with average synergy scores of 3.27, 2.76 and 4.39, and the most synergistic areas having scores of 7.39, 4.26 and 8.09 for OPM2, KMS12BM and KMS11 respectively. For KMS11 and KMS12BM, we observed synergy along a single axis (Fig. 1a, b). In contrast, we observed synergy along both axes for OPM2. Synergy in OPM2 was most pronounced at lower concentrations of both Venetoclax and GSK595, while antagonism was seen at higher concentrations of Venetoclax and moderate concentrations of GSK595 (Fig. 1c). Overall, the evidence suggests that Venetoclax and GSK595 are likely to produce a synergistic effect, with OPM2 displaying a wider variety of concentration ratios which are synergistic.

B. *Monotherapy and Combination Therapy*

To confirm the presence of drug synergy in OPM2, we compared the degree of apoptosis between monotherapy and combination therapy. Based on the ZIP model data (Fig.1), we chose drug concentrations which produced significant synergism. Consistent with previous reports where tumor cell killing by GKS595 was generally

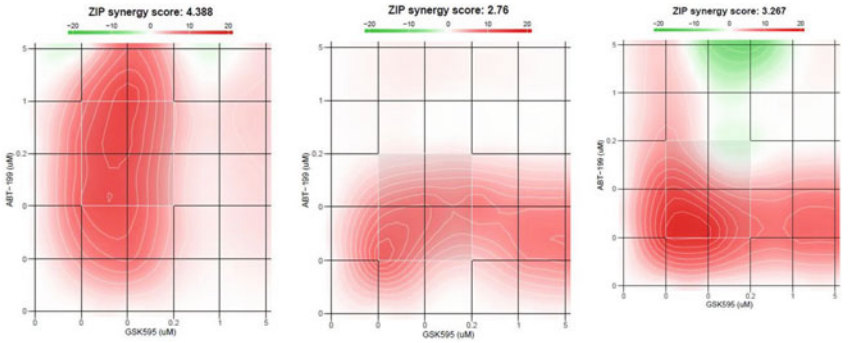

a: Synergy scores at each concentration ratio as measured by ZIP model in SynergyFinder in KMS11 when treated with 0 to 5 μM of Venetoclax and GSK595 for 6 days as measured by CellTiter-Glo cell viability assay

b: Synergy scores at each concentration ratio as measured by ZIP model in SynergyFinder in KMS12BM when treated with 0 to 5 μM of Venetoclax and GSK595 for 6 days as measured by CellTiter-Glo cell viability assay

c: Synergy scores at each concentration ratio as measured by ZIP model in SynergyFinder in OPM2 when treated with 0 to 5 μM of Venetoclax and GSK595 for 6 days as measured by CellTiter-Glo cell viability assay.

Fig. 1 ZIP synergy score maps of MM cell lines to venetoclax and GSK595

observed after 6 days [6, 7], we observed no apparent change in the proportion of apoptotic cells (Annexin V^+ $Hoechst^-$) in GSK595-treated OPM2 cells compared to DMSO-treated controls 4 days post-treatment (Fig. 2). In contrast, we observed a twofold increase in the proportion of apoptotic OPM2 cells upon Venetoclax treatment compared to DMSO-treated controls 4 days post-treatment (Fig. 2); which is consistent with the rapid cell killing action of Venetoclax previously documented [2]. With combination treatment, the proportion of apoptotic OPM2 cells was very similar to that of Venetoclax monotherapy (Fig. 2). Therefore, these results suggest that Venetoclax contributes to early eradication of MM cells, and that the observed synergy with GSK595 could occur after 4 days of treatment.

C. *mRNA Levels of Pro- and Anti-apoptotic Bcl-2 Family Members*

To understand the molecular mechanisms underlying synergism between Venetoclax and GSK595, we next performed gene expression analysis to evaluate the mRNA levels of pro- and anti-apoptotic Bcl-2 family members. Unexpectedly, we found that the mRNA of pro-apoptotic Bcl-2 members decreased while the mRNA of anti-apoptotic members increased. Specifically, *BAK1* and *BBC3*, which encode pro-apoptotic BAK and PUMA proteins respectively, showed a notable decrease upon combination therapy (Fig. 3). Similarly, *BAK1* and *BBC3* expression decreased in response to Venetoclax; but remained relatively unchanged with GSK595 treatment (Fig. 3). The expression of *BAX*, which encodes the pro-apoptotic protein BAX, remained unchanged under all treatment conditions compared to the DMSO-treated control (Fig. 3). Meanwhile, the mRNA of anti-apoptotic Bcl-2 members increased to different extents. *BCL2* expression increased after GSK595 treatment and combination therapy, while *BCL2L1* (encodes for BCL-X_L) and *MCL1* expression did not change appreciably during treatment (Fig. 3). Conversely, we observed a consistent and obvious increase in *PRMT5* expression after any treatment; where the largest increase was seen upon combination therapy (Fig. 3). Taken together, our data suggests that the synergistic cell killing effect of the Venetoclax-GSK595

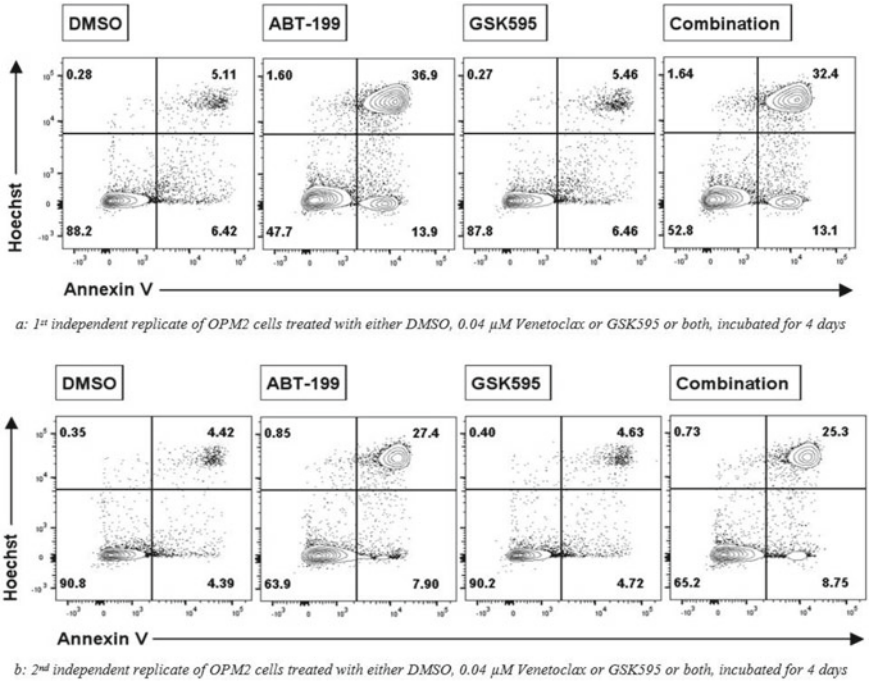

Fig. 2 Flow cytometry assays on OPM2. The bottom left, bottom right and top right gates indicate live, apoptotic and dead cells respectively

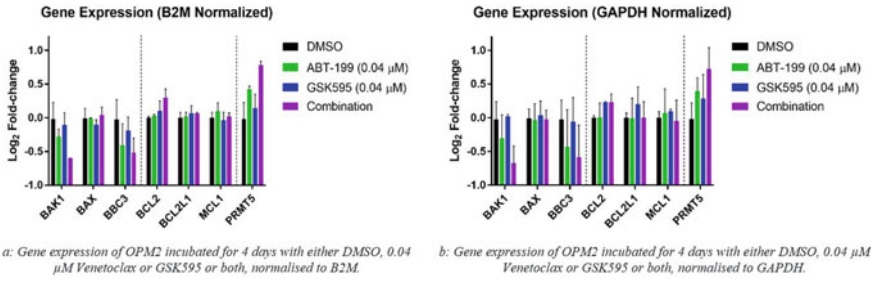

Fig. 3 Gene expression profiles of *BAK1, BAX, BBC3, BCL2, BCL2L1, MCL1, PRMT5* normalized to *B2M* or *GAPDH*. Results shown are the average (±SEM) of two independent experiments

combination in MM cells is unlikely to involve regulation of Bcl-2 family proteins at the transcriptional level.

4 Discussion

MM cells are highly dependent on anti-apoptotic Bcl2 family proteins to evade apoptosis [2], and the current drug Venetoclax targets the anti-apoptotic protein BCL2 to induce cell death via the intrinsic pathway of apoptosis [4]. However, Venetoclax can be resisted by cells that overexpress MCL1 [2]. Fortunately, MCL1 can be inhibited by p53 activation, which leads to transcriptional upregulation of pro-apoptotic Bcl-2 family proteins that inhibit MCL1 [8]. Thus, activating p53 is a potential strategy to overcome Venetoclax resistance by tipping the balance between pro- and anti-apoptotic proteins towards cell death. Hence, we evaluated the effects of Venetoclax in combination with the PRMT5 inhibitor GSK595, which competitively inhibits PRMT5 to increase the activity of p53 [6, 7], to check for the presence of any interactions, especially synergistic effects to minimise toxicity and maximise efficacy in vivo.

In this study, we discovered synergy between Venetoclax and GSK595 in MM cells. Interestingly, our observations in OPM2 are inconsistent with previous reports, which suggest that OPM2 is relatively insensitive to Venetoclax [2]. In addition, the presence of a p53 mutation in OPM2 has been proposed to render OPM2 resistant to another PRMT5 competitive inhibitor functioning similar to GSK595, EPZ015666 [7]. Hence, either drug can only be expected to have minimal effect on OPM2. Instead, Venetoclax and GSK595 showed evident growth inhibition activity against OPM2 individually, and to a greater extent, in combination 6 days post-treatment based on the CellTiter-Glo cell viability assay (Fig. 1). Therefore, while Venetoclax and GSK595 generally appear to elicit a synergistic effect on MM cell lines, the results for OPM2 should be interpreted with caution.

We chose to further investigate Venetoclax-GSK595 synergism in OPM2 as it showed a wider range of synergistic concentration ratios than the other cell lines tested. We found that while Venetoclax substantially elevated the proportion of apoptotic cells, GSK595 resulted in no apparent change in the proportion of apoptotic cells, and contributed little towards apoptotic cell killing in combination with Venetoclax at least at 4 days post-treatment (Fig. 2). One possible interpretation is that a time point of 4 days post-treatment for the apoptosis assay was too early and insufficient for the effect of GSK595 to manifest. Unlike Venetoclax, which acts by directly inhibiting BCL-2 [2], GSK595 inhibits PRMT5 to reduce arginine methylation and promote p53 activation [6, 7], which subsequently leads to transcriptional upregulation of pro-apoptotic Bcl-2 family proteins [8]. As cellular processes involving changes to pre-existing proteins take a shorter time to be effected than processes that need new proteins to be transcribed and then translated [10], the time required for GSK595 to initiate apoptosis may be greater than 4 days. This may explain why a synergistic effect could be observed 6 days post-treatment (CellTiter-Glo cell viability assay, Fig. 1) but not at 4 days post-treatment with the apoptosis assay (Fig. 2). As such, we propose that further investigation should be performed on days 2 and 6 to account for the potential time-dependent effects of drug synergism. Taken together, the type of interaction between GSK595 and venetoclax requires further clarification.

An important part of our findings was the gene expression analysis. While the proportion of live cells always decreased after drug treatment (Fig. 2), there was a counterintuitive change in the ratio of pro- to anti-apoptotic gene expression. Thus, it is likely that the observed cell death is not regulated at the transcriptional or post-transcriptional level, but rather at the post-translational level. Indeed, Venetoclax directly inhibits BCL2 [2], while GSK595 directly inhibits PRMT5 [6]. Since these inhibitory activities occur at the protein level, the mRNA levels of *BCL2* and *PRMT5* would not be expected to decrease. Interestingly, the pro-apoptotic p53 target genes *BAK1*, *BBC3* and *BAX* remained relatively unchanged despite GSK595 treatment, which has been reported to activate p53 [6]. However, this is consistent with previous reports that OPM2 cannot upregulate these genes via p53 due to a mutation in codon 175 of p53 [7], which causes the DNA-binding surface to lose its conformation, resulting in non-functional p53 [11]. Although Venetoclax appears to decrease the expression of pro-apoptotic Bcl-2 members *BAK1* and *BBC3*, antagonism is unlikely to occur as studies conducted in AML cells resistant to p53 activation have shown that Venetoclax is able to significantly counteract resistance to p53 activation [8]. Therefore, further tests involving protein quantification and activity must be carried out to confirm if regulation occurs at the post-translational level to determine the mechanism of any interaction between Venetoclax and GSK595 in MM cells.

5 Conclusion

In conclusion, our data suggests that the interaction between GSK595 and Venetoclax is potentially synergistic, although further tests are required to exclude an additive effect. Moreover, our data suggests that both drugs likely regulate cell death at the post-translational level, rather than at the transcriptional or post-transcriptional level. Importantly, we have not fully elucidated whether the drug synergy between Venetoclax and GSK595 is applicable across MM, or whether the synergistic effect is limited to specific MM subtypes (e.g. with functional p53). Therefore, future work should explore drug interactions between both drugs using a wider panel of cell lines, as well as analyze protein levels in addition to mRNA levels, to further clarify the mechanisms involved.

Acknowledgements I would like to thank my mentors Dr. Darren Tan and Professor Toshio Suda from the Cancer Science Institute of Singapore for their constant guidance, support and encouragement. In addition, I would like to thank Dr. Abigayle Ng from Raffles Institution for her support, the National University of Singapore (NUS) for the valuable opportunity to participate in the Science Research Programme (SRP).

Appendix

Table 1 Gene list, PrimeTime® qPCR primers and probes sequences

Gene	*BAK1*
Probe	5′-/56-FAM/TCAGAGTTC/ZEN/CAGACCATGTTGCAGC/3IABkFQ/-3’
Primer 1	5′-CGACATCAACCGACGCTAT-3’
Primer 2	5′-CAGAAGAGCCACCACACG-3’
Gene	*BAX*
Probe	5′-/56-FAM/TTTCCGAGT/ZEN/GGCAGCTGACATGTT/3IABkFQ/-3’
Primer 1	5′-AGTTGAAGTTGCCGTCAGAA-3’
Primer 2	5′-GGAGCTGCAGAGGATGATTG-3’
Gene	*BBC3*
Probe	5′-/56-FAM/TGCTCCTCT/ZEN/TGTCTCCGCCG/3IABkFQ/-3’
Primer 1	5′-ACGACCTCAACGCACAGTA-3’
Primer 2	5′-CACCTAATTGGGCTCCATCT-3’
Gene	*BCL2*
Probe	5′/56-FAM/CAGGATAAC/ZEN/GGAGGCTGGGATGC/3IABkFQ/-3’
Primer 1	5′-GATGACTGAGTACCTGAACCG-3’
Primer 2	5′-AGCCAGGAGAAATCAAACAGAG-3’
Gene	*BCL2L1*
Probe	5′-/56-FAM/AAGTATCCC/ZEN/AGCCGCCGTTCTC/3IABkFQ/-3’
Primer 1	5′-GCCACTTACCTGAATGACCAC-3’
Primer 2	5′-GCATTGTTCCCATAGAGTTCCA-3’
Gene	*MCL1*
Probe	5′-/56-FAM/TCCACAAAC/ZEN/CCATCCCAGCCTC/3IABkFQ/-3’
Primer 1	5′-CATTAGCAGAAAGTATCACAGACG-3’
Primer 2	5′-ACATTCCTGATGCCACCTT-3’
Gene	*PRMT5*
Probe	5′-/56-FAM/CATCGCCAG/ZEN/AAACGCACACAGAT/3IABkFQ/-3’
Primer 1	5′-GTTTCCCATCCTCTTCCCTAT-3’
Primer 2	5′-CCCACTCATACCACACCTTC-3’
Gene	*GAPDH*
Probe	5′-/56-FAM/AAGGTCGGA/ZEN/GTCAACGGATTTGGTC/3IABkFQ/-3’
Primer 1	5′-ACATCGCTCAGACACCATG-3’
Primer 2	5′-TGTAGTTGAGGTCAATGAAGGG-3’
Gene	*B2M*
Probe	5′-/56-FAM/CCTGCCGTG/ZEN/TGAACCATGTGACT/3IABkFQ/-3’
Primer 1	5′-GGACTGGTCTTTCTATCTCTTGT-3’
Primer 2	5′-ACCTCCATGATGCTGCTTAC-3’

References

1. "Home > Cancer Information > About Cancer > Multiple Myeloma." National University Cancer Institute Singapore NCIS. https://www.ncis.com.sg/Cancer-Information/About-Cancer/Pages/Multiple-Myeloma.aspx
2. E.A. Punnoose *et al.*, "Expression profile of BCL-2, BCL-XL, and MCL-1 predicts pharmacological response to the BCL-2 selective antagonist Venetoclax in multiple myeloma models," in *Molecular Cancer Therapeutics,* vol.15, no. 5, pp.1132–1144, Apr.2016. [Online]. Available: doi: https://doi.org/10.1158/1535-7163.MCT-15-0730
3. A. Shamas-Din, J. Kale, B. Leber and D.W. Andrews, "Mechanisms of action of Bcl-2 family proteins," in *Cold Spring Harbour Perspectives in Biology*, vol.5, no. 4, Apr.2013. [Online]. Available: doi: https://doi.org/10.1101/cshperspect.a008714
4. Alberts *et al.* "Cell Death," In *Molecular Biology of The Cell*, New York, United States: Garland Science, Taylor and Francis Group, LLC, 2015, ch.18, pp.1026–1027
5. T. Pemovska, J.W. Bigenzahn and G. Superti-Furga, "Recent advances in combinatorial drug screening and synergy scoring," in *Current Opinion in Pharmacology,* vol.42, pp.102–110, Oct.2018, [Online]. Available: https://doi.org/10.1016/j.coph.2018.07.008
6. Gerhart *et al.*, "Activation of the p53-MDM4 regulatory axis defines the anti-tumour response to PRMT5 inhibition through its role in regulating cellular splicing," in *Sci. Rep.,* vol.8, Jun.2018. [Online]. Available: https://doi.org/10.1038/s41598-018-28002-y
7. Gullà *et al.*, "Protein arginine methyltransferase 5 has prognostic relevance and is a druggable target in multiple myeloma" in *Leukemia*, vol.32, pp.996–1002, Apr.2018. [Online]. Available: doi:https://doi.org/10.1038/leu.2017.334
8. Pan *et al.*, "Synthetic lethality of combined Bcl-2 inhibition and p53 activation in AML: mechanisms and superior antileukemic efficacy," in *Cancer cell*, vol.32, no.6, pp.748–760.e6, Dec.2017. [Online]. Available: doi:https://doi.org/10.1016/j.ccell.2017.11.003
9. B. Yadav, K. Wennerberg, T. Aittokallio and J. Tang, "Searching for drug synergy in complex dose–response landscapes using an Interaction Potency Model" in *Computational and structural biotechnology journal*, vol.13, pp.504–513, Sep.2015. [Online]. Available: doi:https://doi.org/10.1016/j.csbj.2015.09.001
10. Alberts *et al.*. "Cell signalling," In *Molecular Biology of The Cell*, New York, United States: Garland Science, Taylor and Francis Group, LLC, 2015, ch.15, pp. 825
11. Liu, X.Y.; Pestka, S.; Shi, Y.F., "Can p53 act as a biomarker in cancer management and therapy?" In *Recent Advances in Cancer Research and Therapy*, Amsterdam, Netherlands: Elsevier: Amsterdam, 2012, ch.9.2

Lasing in Chlorophyll

A Theoretical Investigation

K. Sarvesha and Derrick Yong

Abstract This project aims to come up with a theoretical framework to accurately describe lasing in chlorophyll, in particular, chlorophyll a (Chla). Extensive literature review was conducted to find variables pertaining to lasing parameters and constants to adapt it for lasing in Chla. An energy level system of Chla with the primary processes involved was come up with to model for single-mode lasing with a lasing output at 730 nm and pump absorption at 430 nm and 660 nm. From this a system of differential rate equations was developed to complete our theoretical framework which models and describes lasing in Chla.

Keywords Lasing · Chlorophyll · Energy level system · Differential rate equations

1 1. Introduction

A. *Laser*

A laser is a source of coherent light. It achieves this through light amplification by stimulated emission of radiation, thus the acronym LASER. A laser has 3 essential components: a pump, a gain medium and an optical resonator.

B. *Spontaneous Emission*

Quantum mechanics states that all matter has discrete energy levels, and that it can exchange energy with light in discrete packets. Let us consider a 2-level energy system. When light is introduced to the system, it interacts with the matter. Electrons in the E_1 energy level absorb photons which have an energy equivalent to the energy difference between the E_1 and E_2 energy levels, given by hf. This excited electron moves into the E_2 energy level, forming a non equilibrium system. The instability

K. Sarvesha
Raffles Institution, Singapore, Singapore

D. Yong (✉)
Precision Measurements Group, Singapore Institute of Manufacturing Technology, A*Star, Singapore, Singapore
e-mail: derrick-yong@simtech.a-star.edu.sg

H. Guo et al. (eds.), *IRC-SET 2020*,
https://doi.org/10.1007/978-981-15-9472-4_9

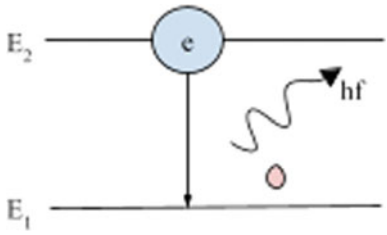

Fig. 1 Spontaneous emission

causes it to decay and as it falls back to the E_1 energy level, it emits a photon with the same energy as before. This is known as spontaneous emission (Fig 1) and the light produced has the same wavelength but not the same phase. The light produced is thus incoherent.

C. *Stimulated Emission*

A laser operates by the principle of stimulated emission (Fig. 2). All electrons are already excited at E_2 and the incoming photon forces the electron down to a lower energy state, E_1. This results in the formation of another photon that is identical to the incoming photon in the sense that has the same wavelength and phase. Thus the light produced is coherent.

D. *Pump*

A pump is an external source of energy that is required for population inversion in a laser. It can be either optical or electric in nature. Population inversion is the state in which majority of the matter is at excited states. This cannot be achieved in a 2-level energy system. Even with heating or optical pumping, the best we can achieve is a state in which $N_2 = N_1$, that is, the number of electrons in energy level 2 is equal to that in energy level 1. This is because quantum mechanics states the rate at which the electrons get excited is the same as the rate at which they come down. The probability of going up or down is equal and so population inversion cannot be achieved, and exciting the system more will cause the system to become optically transparent. However in a 3-level energy system, the rates of excitation and decay can be manipulated to achieve population inversion and overcome the constraints of a 2-level energy system. This provides for gain in a laser.

E. *Optical Resonator*

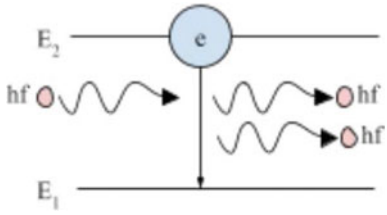

Fig. 2 Stimulated emission

An optical resonator, also known as an optical cavity, in the simplest context is a cavity in which light bounces back and forth between 2 mirrors. This sustains a singular frequency and oscillation for a period of time. Only a discrete number of wavelengths is allowed inside the resonator to produce different modes of light. For example, the longest wavelength that fits between the 2 mirrors is a half wavelength and subsequent wave of shorter wavelengths are an integral multiple of half wavelengths, all of which are referred to as different modes. There are different types of optical resonators, which include the basic 2 mirror resonator and a ring resonator.

F. *Gain Medium*

To prevent decay, gain provides the system with energy to drive it after each cycle and the driving force is kept in phase with the system. The gain medium is placed between the mirrors of an optical resonator to amplify light. Each gain medium has its own gain spectra and bandwidth and it can be used to select a specific mode of light. The specific frequency that is required gets amplified by the gain and becomes even sharper while the other modes die out due to energy loss. For lasing to occur, the net round trip gain must be greater than or equal to 1.

G. *Biolasers*

Lasing has been realised in various organic mediums by integrating microfluidics, optical resonators, and gain medium in liquid environments to produce optofluidic biolasers. These biolasers are highly sensitive and can thus measure and quantify changes in biological molecules and processes in the gain medium using the amplification that occurs during lasing [4].

H. *Lasing in Chlorophyll*

In this project we are concerned with lasing in chlorophyll a (Chla). Chlorophylls are the principal photoreceptors for photosynthesis in green plants, algae, and bacteria as well as the electron donors in photosynthesis and are very abundant on earth [5]. Chla is one form of chlorophyll and it is the primary photosynthetic pigment used in oxygenic photosynthesis. Chla is used as the gain medium by being dissolved in ethanol solvent. A thin walled glass capillary based optofluidic ring resonator (OFRR) serves as our optical cavity (Fig. 3) and it is used to contain the Chla in

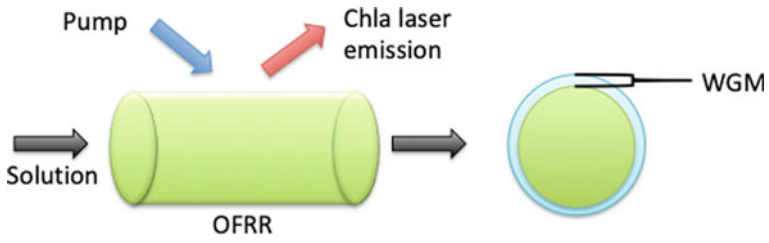

Fig. 3 Chla in ethanol solution in OFRR and cross section of OFRR with WGM [2]

ethanol solution. The OFRR makes use of Whispering Gallery Mode (WGM), in which light from the pump is incident to the wall of the OFRR and specific modes of light are confined inside the OFRR due to continuous total internal reflection. This system is optically pumped to produce an optofluidic chlorophyll laser.

2 Materials and Methods

A. *Energy levels for Chla*

Since we are interested in single-mode lasing, we will only take the lasing output at 730 nm into consideration and neglect the lasing output at 680 nm, though Chla has 2 lasing outputs at 680 and 730 nm (Fig. 4).

Pump Absorption is depicted by the blue arrows in which electrons are excited from the ground state either at 430 nm or 660 nm to the N_5 and N_3 energy levels respectively by absorbing energy from the external energy source.

Lasing Re-absorption is depicted by the red arrow in which electrons which have been excited and decayed back to the ground state through stimulated emission at 680 nm are once again excited to N_2 due to it falling within the same range as the 660 nm pump absorption (Fig. 5).

Non Radiative Transitions are depicted by curly arrows and refer to electrons relaxing from a higher energy state to a lower energy state with the excitation energy being dissipated as vibrations (heat) in the organic medium instead of being emitted as photons. This process occurs between all pairs of adjacent energy levels. Intersystem crossing (isc) is when the electron crosses over from a singlet state to a triplet state and vice versa, given by the curly arrows marked τ_{isc} and τ_t. Photobleaching refers to the permanent loss of electrons from the triplet state and this is shown by the curly arrow marked τ_{bleach}. Intersystem crossing and photobleaching both take place at slower rates that are of a different magnitude to that of the processes which occur

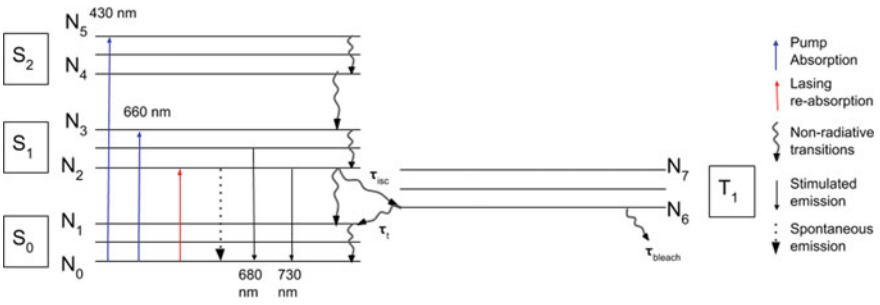

Fig. 4 Energy level diagram of Chla with singlet states S0, S1, and S2 and triplet state, T1 showing the primary energy conversions. Sx are the energy levels of the entire Chla molecule whereas Nx are the energy levels of electrons

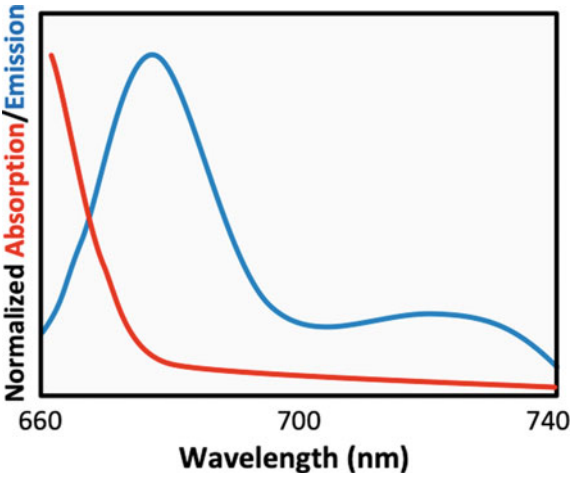

Fig. 5 Absorption cross sections (red curve) and emission cross sections (blue curve) of Chla in ethanol from 660 nm to 745 nm

between singlet states so electrons are largely trapped in the triplet states while the primary processes such as spontaneous and stimulated emission occur.

3 Results

Using the energy level diagram above, the system of differential rate equations (Fig. 6) was come up with to model the primary energy conversions between the different energy states and levels. The model accounts for all the inputs and outputs for each energy level by each process.

$$\frac{dN_0}{dt} = -\frac{P_{src}}{hf_{P,430}} n^{S_0S_2} \frac{(N_0-N_2)}{N_{total}} - \frac{P_{src}}{hf_{P,660}} n^{S_0S_1} \frac{(N_0-N_1)}{N_{total}} - v_g \sigma_{abs}^{S_0S_2} T_s \Phi_s \frac{(N_0-N_2)}{V} + F_P \frac{\beta}{\tau_{spont}} T_s \Phi_s (N_2-N_0) + F_P \frac{\beta}{\tau_{spont}} T_s N_2$$

$$\frac{dN_1}{dt} = +\frac{N_2}{\tau_{21}} - \frac{N_1}{\tau_{10}} + \frac{N_6}{\tau_t}$$

$$\frac{dN_2}{dt} = +v_g \sigma_{abs}^{S_0S_2} T_s \Phi_s \frac{(N_0-N_2)}{V} - F_P \frac{\beta}{\tau_{spont}} T_s \Phi_s (N_2-N_0) - F_P \frac{\beta}{\tau_{spont}} T_s N_2 - \frac{N_2}{\tau_{21}} + \frac{N_3}{\tau_{32}} - \frac{N_2}{\tau_{isc}}$$

$$\frac{dN_3}{dt} = +\frac{P_{src}}{hf_{P,660}} n^{S_0S_1} \frac{(N_0-N_3)}{N_{total}} + \frac{N_4}{\tau_{43}} - \frac{N_3}{\tau_{32}}$$

$$\frac{dN_4}{dt} = +\frac{N_5}{\tau_{54}} - \frac{N_4}{\tau_{43}}$$

$$\frac{dN_5}{dt} = +\frac{P_{src}}{hf_{P,430}} n^{S_0S_2} \frac{(N_0-N_5)}{N_{total}} - \frac{N_5}{\tau_{54}}$$

$$\frac{dN_6}{dt} = +\frac{N_2}{\tau_{isc}} - \frac{N_6}{\tau_t} - \frac{N_6}{\tau_{bleach}}$$

$$\frac{d\Phi}{dt} = -v_g \sigma_{abs}^{S_0S_2} T_s \Phi_s \frac{(N_0-N_2)}{V} - \frac{\Phi_s}{\tau_{loss}} + F_P \frac{\beta}{\tau_{spont}} T_s \Phi_s (N_2-N_0) + F_P \frac{\beta}{\tau_{spont}} T_s N_2$$

Fig. 6 Differential rate equations for Chla

A. *Rate Equations for Lasing in Chla*

Tau (τ), known as lifetime, is the inverse of rate, given by $\frac{1}{\text{rate}}$ and can thus be taken to be a measure of rate. The superscripts indicate the energy levels or the process involved and the inverse of the term gives the rate of electrons moving from one energy level to another. For example, $\frac{N_2}{\tau_{21}}$ indicates that electrons are moving non-radiatively from N_2 to N_1 at a rate of $\frac{1}{\tau_{21}}$. τ_{bleach} refers to the photobleaching lifetime and $\frac{N_6}{\tau_{bleach}}$ refers to the rate at which electrons are lost from N_6 through photobleaching. τ_{isc} and τ_t refer to the intersystem crossing lifetimes for their respective energy levels involved. $\frac{\Phi_s}{\tau_{loss}}$ is the rate of passive photon decay.

P_{src} is the power from the pump. hf_p is the energy of one photon, since $E = hf$. In this case the frequency of the photon is either 430 or 660 nm depending on the transition. $n^{S_0S_1}$ is the fraction of the pump power that is absorbed by electrons transiting from one energy state to another, in this case from S_0 to S_1. N_{total} refers to the total number of electrons. $\frac{P_{src}}{hf_p} n^{S_0S_1} \frac{(N_0-N_5)}{N_{Total}}$ thus refers to the rate of pumping for electrons transitioning from one energy state to another, in this case N_0–N_3.

v_g is the group velocity of the lasing mode [1]. $\sigma^{S_0S_1}$ is the cross section absorption area, which is also a measure for the probability of an absorption process. Ts is the fractional energy of the lasing mode contained in the organic region [1]. Φ_s is the lasing photon number. V is the volume of the organic medium. $V_g \sigma^{S_0S_1} T_s \Phi_s \frac{(N_0-N_5)}{V}$ refers to the rate of lasing absorption from one energy state to another, in this case N_0–N_2.

Fp is the Purcell factor. It is the spontaneous emission modification factor, that is the modification to the spontaneous emission rate of the gain medium, $\frac{1}{\tau_{spoint}}$, in the presence of a cavity [1]. β is the spontaneous emission coupling factor, which is the spontaneous emission rate into the lasing modes divided by the total spontaneous emission rate [3]. T_{spont} is the spontaneous emission lifetime. $F_p \frac{\text{B}}{\tau_{spoint}} T_s \Phi_s (N_2 - N_0)$ refers to the rate of stimulated emission, in this case from N_2 to N_0. $F_p \frac{\text{B}}{\tau_{spoint}} T_s \Phi_s N_2$ refers to the rate of spontaneous emission, from N_2.

4 Discussion

These are some of the possible pathways that can be taken by an electron that is excited from the ground state. The electron can either reach back the ground state or be lost from the system. The abovementioned electron transitions result in a shift of the entire electron cloud for complex molecules such as Chla molecules when they get excited, causing them to transit between different singlet and triplet energy states.

A. *Direct pathways*

The most direct pathways are shown below. Electrons are excited from the ground state either at 430 nm (Fig. 7) or 660 nm (Fig. 8) to the N_5 and N_3 energy levels

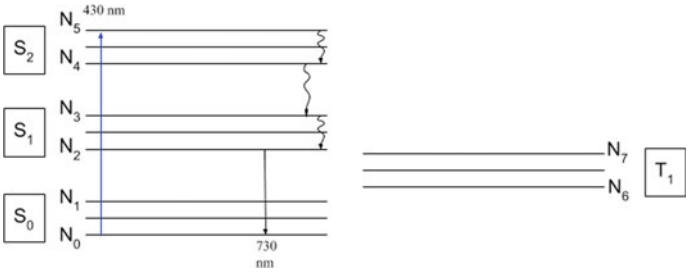

Fig. 7 Direct pathway for lasing, 430 nm

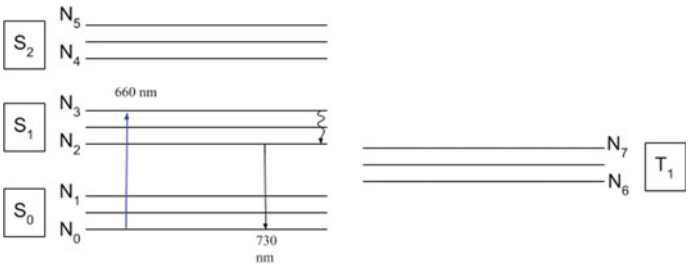

Fig. 8 Direct pathway for lasing, 660 nm

respectively through pump absorption. From there the electron decays back to the ground state through non radiative transitions. The Chla molecule is excited from S_0 to S_2 or S_1 and decays back to S_0, resulting in lasing emissions.

B. *Pathways involving Intersystem Crossing*

These are alternative pathways to reach the ground state via triplet states. Electrons are once again excited from the ground state either at 430 nm (Fig. 9) or 660 nm (Fig. 10) to the N_5 and N_3 energy levels respectively. From there the electron decays through non radiative transitions until the N_2 energy level. From there intersystem crossing (isc) takes place from the N_2 to N_6, after which the electron crosses back

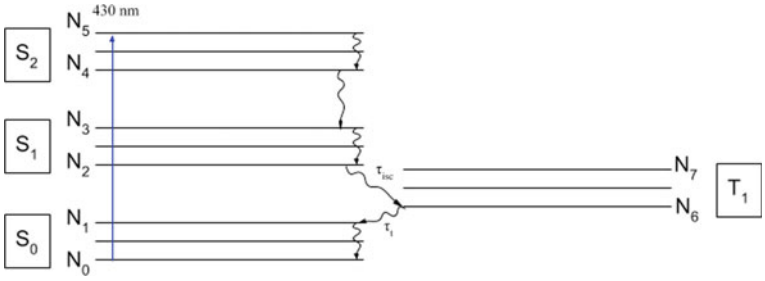

Fig. 9 Pathway for lasing involving intersystem crossing, 430 nm

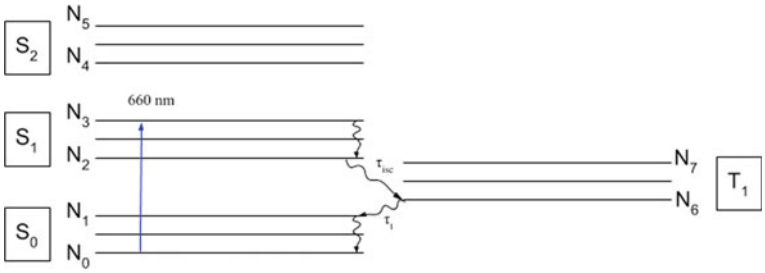

Fig. 10 Pathway for lasing involving intersystem crossing, 660 nm

to N_2 once again before decaying back to the ground state non radiatively. The Chla molecule has crossed to and back from the triplet state T_1 and decays back to S_0, resulting in lasing emissions.

C. *Photobleaching pathways*

Alternatively, the electron can be lost from the system from N6 through the process of photobleaching after going through the 430 nm (Fig. 11) or 660 nm (Fig. 12) pumping pathway. This reduces the total number of photons in the system. The Chla molecules become radicalised as they can react with each other or other molecules

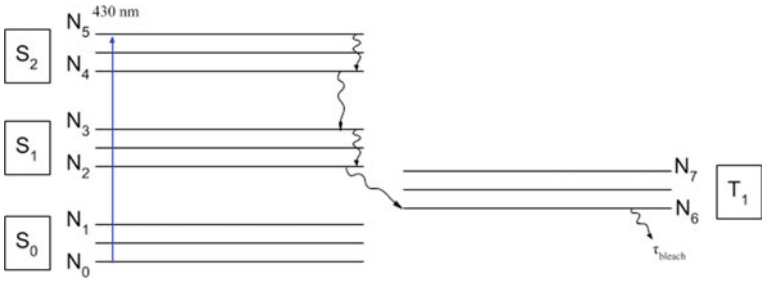

Fig. 11 Photobleaching pathway, 430 nm

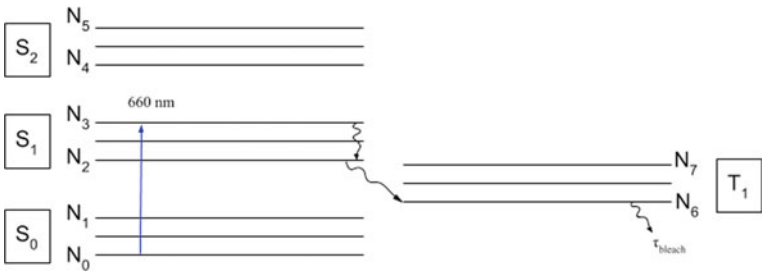

Fig. 12 Photobleaching pathway, 660 nm

to become radicals, before eventually photobleaching and degrading. This leads to a loss of lasing emission intensity.

5 Conclusion

We have come up with a theoretical framework comprising an energy level system and its corresponding system of differential rate equations to describe single mode lasing in Chla.

A. *Suggestions for future work*

Given that the 680 nm lasing pathway is significant in Chla, a double-mode lasing framework ought to be considered to more accurately model lasing in Chla in future works. The 680 nm lasing pathway starts from an energy level that is between N2 and N3 and the inclusion of an additional energy level would require the inclusion of all other processes which are inputs and outputs for that energy level. This was omitted in our model as insufficient data was found pertaining to these processes.

Moreover, there was only one triplet state included in the energy level system. The number of triplet states in Chla has not ben determined, but their presence can be determined experimentally. These results can be incorporated through the addition of higher energy triplet states in our energy level system.

Acknowledgements I would like to thank my teacher-mentor, Dr. Derrick Yong, for his constant help, feedback and advice throughout this project and for not giving up on me, my teacher advisor Dr. Abigayle Ng for providing timely guidance, A*Star for allowing me to work on this project and Dr. Yu-Cheng Chen for clarifying doubts and showing me around his labs.

References

1. Chen, Y.-C., Chen, Q., & Fan, X. (2016, May 12). Optofluidic chlorophyll lasers. Retrieved from https://pubs.rsc.org/en/content/articlelanding/2016/lc/c6lc00512h#!divAbstract.
2. Chen, Y.-C., Chen, Q., & Fan, X. (2016, May 12). Supplementary Information for "Optofluidic chlorophyll lasers." (n.d.). Retrieved from http://www.rsc.org/suppdata/c6/lc/c6lc00512h/c6lc00512h1.pdf.
3. Chin, M. K.,Chu, D. Y., & Ho, S. (1993, November 18). Estimation of the spontaneous emission factor for microdisk lasers via the approximation of Whispering gallery modes. Retrieved from http://users.ece.northwestern.edu/~sth/HO%20JAP%20p3302%2094.pdf
4. Fan, X., & Yun, S.-H. (2014, January 30). The potential of optofluidic biolasers. Retrieved from https://www.nature.com/articles/nmeth.2805.
5. Hindman, J. C., Kugel, R., Svirmickas, A., & Katz, J. J. (1977, January 1). Chlorophyll lasers: Stimulated light emission by chlorophylls and Mg-free chlorophyll derivatives. Retrieved from https://www.pnas.org/content/74/1/5.

Machine Learning of Biological Data in Cell Manufacturing

Suan Enhui and Derrick Yong

Abstract A program was developed to stitch the cell images with their corresponding spectrophotometer readings. These stitched images will be sent to an artificial intelligence interface to be analysed so as to predict the cell states and suggest ways to maximise the number of cells during the cell manufacturing process. In addition, a CellProfiler pipeline has been made to count the number of cells and predict the amount of mitochondrial activity present in the cell as this would also help to predict the confluency and mitochondrial networks of the cell. This would be significant in ensuring that the cells present in the cell culture are respiring and a larger interconnected network of cells show that there are more cells respiring and that the confluency of the cells present in the cell culture is higher, leading to a better cell culture. These can be predicted using machine learning of biological data in the cell manufacturing process by extracting and analyzing part of the cell culture to aid in growing more healthy cell cultures with higher confluency.

Keywords Machine learning · Biological data · Cell manufacturing · Mitochondrial activity

1 Introduction

A. *Machine Learning*

(1) *What is Machine Learning?*
Machine Learning is a way to analyse data through automation. It is a branch of artificial intelligence based on the concept of having systems learn from data, identify patterns and making the decisions needed completely free from the restrictions of their human counterparts. In addition, machine

E. Suan
Raffles Institution, Singapore, Singapore
e-mail: suanenhui@gmail.com

D. Yong (✉)
Singapore Institute of Manufacturing Technology, a*STAR, Singapore, Singapore
e-mail: derrick-yong@SIMTech.a-star.edu.sg

H. Guo et al. (eds.), *IRC-SET 2020*,
https://doi.org/10.1007/978-981-15-9472-4_10

learning can be used to reduce the time and errors needed and create through human work, increasing the efficiency of work given to the system.

(2) *How does Machine Learning work?*
A set of algorithms are used to determine the principles which the rule of the program would follow to learn how to classify and cluster the data according to their similarities. This set of algorithms form a computer model which will be used in the classification of data input. Data input can range from text and images to sound and numbers.

B. *Deep Learning*

(1) *What is Deep Learning?*
Deep Learning is a branch of Machine Learning in Artificial Intelligence. Deep Learning has networks which are capable of learning unsupervised from data that is unstructured or unlabeled through learning by example. These networks are more commonly known as neural networks [3]. Deep Learning can be found being used in driverless cars, voice control in devices such as Siri or Google Home and more [5]. In this project, a deep learning model was trained to classify images and the spectrometer data to its different confluencies. Such models are trained through these many hidden layers to be able to classify the numbers, text and images given to them without the need of manual feature extractions. Deep Learning has been shown to be able to give extremely accurate classifications and can sometimes exceed the accuracy of humans [6].

C. *Neural Networks*

(1) *What are Neural Networks?*
Inspired by the way the human brain functions, neural networks function in a similar manner. A Neural Network is a set of algorithms which are designed to recognise patterns. They interpret sensory data, similar to a human brain through a kind of machine perception by labelling or clustering the raw input. Neural Networks allow for numerical, images, sounds, text or time series to be input as data into the Neural Network, though they would all be translated into numerical data so that the Neural Network may recognise them since they are only able to recognise the patterns if they are in their numerical form. Neural Networks are used as a way to classify and cluster data according to their similarities among the example inputs which they have been trained on, for easy storage and management. In addition, as the performance of neural networks improves, they grow bigger and are able to work with more and more data, unlike other Machine Learning algorithms which will reach a plateau after a certain point.

(2) Types of Neural Networks
There are many types of neural networks. Each different type of neural network uses a different set of principles to determine their rules which they will follow. Due to this difference in principles and rules, each neural network will have their individual strengths and weaknesses. However, for

this research, we have narrowed down to using the convolutional neural networks (CNN) and Artificial Neural Networks (ANN) [2].

D. *CellProfiler*

(1) *What is CellProfiler?*
CellProfiler is an open-source software used to quantitatively analyse biological images. It was started in 2003 by Anne E. Carpenter and Thouis (Ray) Jones in the Sabatini Laboratory and Golland Laboratory. CellProfiler is being maintained and improved in the project team in the Carpenter Lab at the Broad Institute of Harvard and MIT. It allows users to construct their own pipelines to extract and manipulate data from the inputted biological images [1].

E. *Research Scope and Purpose*
It is a known fact that counting and monitoring cells can be very tedious as one needs to check their confluency and be able to predict the different ways as to which the cell culture can be changed so that the confluency of cells and number of cells being cultured will be higher. A higher cell count and better cell quality in the cell culture would be representative of a better cell culture during the cell manufacturing process.
As cells are living beings and their growth and reaction of their growth mediums can be unpredictable, this would provide cell manufacturers with a better way to consistently grow cell cultures through understanding the confluency and possible ways to improve cell growth through non-invasive means of analysing the cells in the cell culture, thereby reducing the waste which invasive methods of analysing cells.

F. *Real Life Applications*
Currently, in cell manufacturing it is difficult to ensure and maintain the consistent quality and quantity of cells grown in a cell culture. This is due to the fact that cells may respond differently to the same medium, making it difficult for manufacturers to predict the response of the cell culture to a medium and properly determine if the medium is best for the cell to grow in.
Therefore, through this project, we hope to be able to find a way to aid in analysing the cell culture through non-invasive methods like spectrophotometry, before suggesting changes to improve the medium of the cell culture to aid in encouraging better quality and quantity of the cells manufactured.

G. *Other Similar Technologies*
As of now, there are neural networks which are able to count cells. However, no model is currently available to form the correlation of the confluency of the cells, which is related to the number of cells in the cell culture, to the health of the cells. Therefore, this machine learning would be the first of its kind.
In addition, current CellProfiler pipelines monitoring cell activity are not mainly focused on mitochondrial interconnected networks or activity in the cells. Although there has been a pipeline [4] made concerning analyzing mitochondrial activity, it measures this by average intensity per square pixel. This is extremely

inaccurate as the average can be vastly affected by bright spots present in certain cells if some cells have higher activity than others or if only one cell is alive. Thus, this machine learning would provide a better and more accurate way to measure the interconnectedness and intensity of the mitochondrial networks and mitochondrial activity of a cell respectively.

2 Hypothesis

As previous research has shown that making such a pipeline and stitching images together is possible, we hypothesise that it is possible to construct the pipeline and stitch the images together. In addition, we also hypothesise that the greater the fluorescence of the cytoplasm, the higher the confluency of the cell culture.

3 Materials and Methods

A. *Materials and Software Used*

1. Python version 2.7.
2. CellProfiler 3.
3. Cell images obtained from an Olympus microscope.
4. Spectrophotometer data from the cell culture.

B. *Procedure for Stitching Images*

1. Import numpy, pandas, matplotlib.pyplot, cv2, os, sys, Image from PIL, splittext os.path, Counter from collections, tkinter, filedialog from tkinter for the Python operating system version 2.7.
2. Checking the filenames in the directory, extract the files with the spectrophotometer data using their file extensions.
3. Using matplotlib.pyplot, plot a graph of the reading against the wavelength on a black background and black axes.
4. Save the graph using the same filename as the spectrophotometer data.
5. Using the filename of the data, search the relevant directory for the filename for the microscope image of the cell culture.
6. Stitch the two images together by plotting the two images using matplotlib.pyplot and cv2.
7. Save the image under desired name in the specified directory.

C. *Procedure for CellProfiler Pipeline Construction*

1. Set up a new pipeline for CellProfiler.
2. Under Metadata, ensure that Metadata is not extracted from the images.

3. Under Names and Types, assign a name to images matching the file extension of the images. They can be assigned the names OrigDAPI, OrigMito, OrigActin, IllumDAPI, IllumMito and IllumActin.
4. Select all image types to Grayscale Image and do not process them as 3D.
5. Set all intensity ranges to be from Image Metadata.
6. Set image set matching method to Order.
7. Under Groups, ensure that the inputted images are not grouped.
8. Add a EnhanceorSuppressFeatures module, enhancing the speckles from the input image OrigMito with feature size of 20 and fast speed and accuracy.
9. Add two modules of IdentifyPrimaryObjects and input the images OrigDAPI and OrigActin to identify the nuclei and fluorescence reading of the cells.
10. Add a module of IdentifySecondaryObject to identify the cells present in the image.
11. Add a module of IdentifyTertiaryObjects to identify the cytoplasm of the cells around the nuclei.
12. Add a module of Threshold, using the OrigMito image, change the correction factor to 0,9 and bounds on threshold to 0.0–1.0.
13. Add two modules of MeasureObjectIntensity to measure the intensity of the cytoplasm and nuclei of the cells in the image.
14. Add a module of MeasureObjectSizeShape to measure the cytoplasm while ensuring that the Zernike features are not being calculated.
15. Measure the average intensity per square pixel and the standard deviation using CalculateMath and MeasureImageIntensity modules.
16. Export the data to a spreadsheet using the ExportToSpreadsheet module.

K. *Procedure to test Hypothesis of relationship between mitochondrial networks and confluency*

1. From the spreadsheet obtaind from the CellProfiler pipeline, extract the data of the intensity per square pixel of the cells' cytoplasm
2. Draw a graph of average intensity per square pixel against confluency of the cell.

4 Results

See Figs. 1, 2, 3 and 4.

5 Discussion

A. *Analysis*

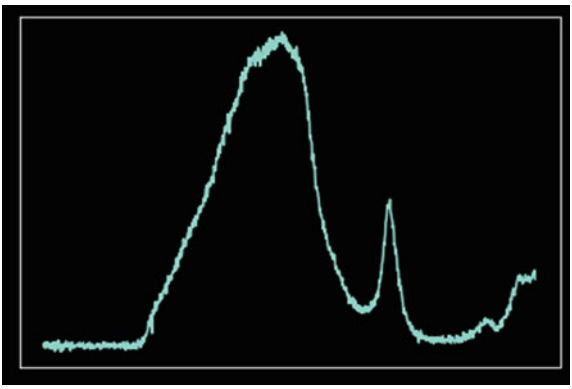

Fig. 1 Image of graph generated from spectrophotometer data

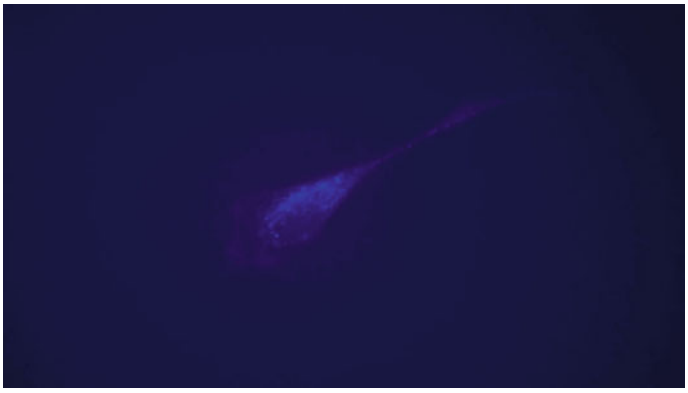

Fig. 2 Image of graph generated from spectrophotometer data

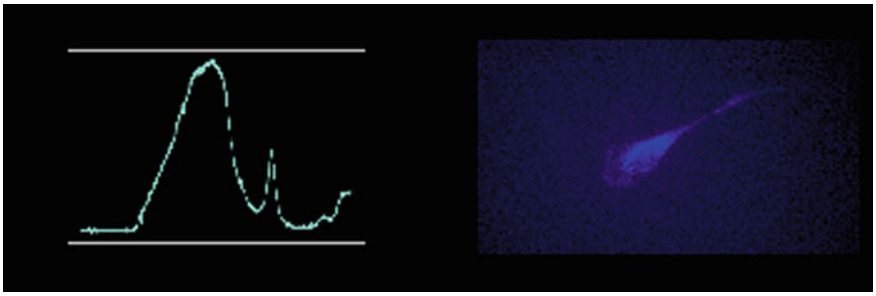

Fig. 3 Stitched image generated from python code

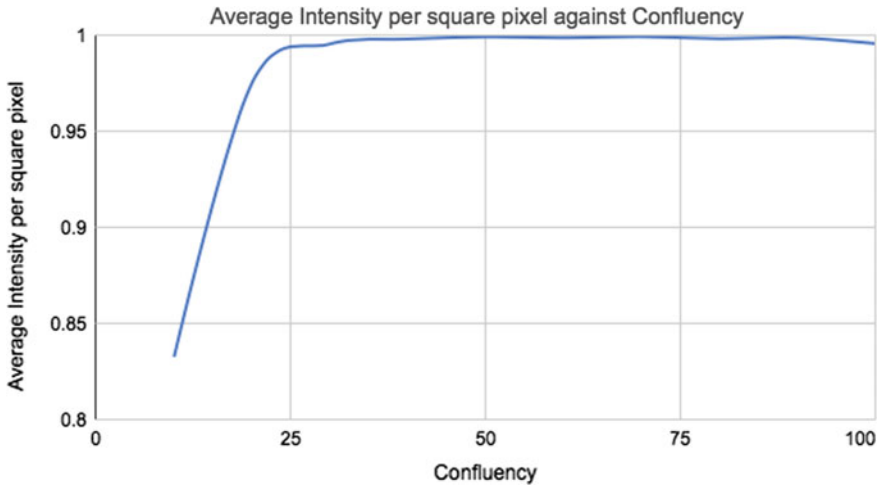

Fig. 4 Graph of average intensity per square pixel against confluency

It has to be noted that there are no axes on the graphs generated, such as in Fig. 1, since the presence of extra features in the graph would cause the neural network model to be incorrectly trained in recognising the keywords in the axes instead of the plot itself. This is due to the fact that features in white, like the axes headings, would be read by the neural network as having a reading of 255, causing it to disrupt the reading of the graph since computers read by taking the colour values of the pixels. However, the x-axis is wavelength (nm) and the y-axis is the fluorescence intensity. All cell images, like Fig. 2, are images of fibroblast cells from different cell cultures with different confluencies taken from the Olympus Microscope by connecting the laptop to the microscope. For all stitched images generated, such as Fig. 3, it was generated uniformly with the graph generated from the spectrophotometer data (Fig. 1) on the right and the cell image on the left (Fig. 2).

The stitching of images causes no significant difference in the accuracy of the results, the results stay between 90 and 95%. This means that the stitching of the images alone does not provide an aid to the neural networks to increase the accuracy of the classification of confluencies of cell cultures. Despite this, the hypothesis that the images could be stitched together through a Python code was confirmed.

However, since no research has been done on the effect of the stitching of images on improving the accuracy of neural networks, there are unfortunately no studies to compare this against.

The CellProfiler pipeline has confirmed the hypothesis that the higher the average intensity of the cytoplasm fluorescence of the cells present in the microscope image, the higher the confluence of the cell culture. It has done this by showing a positive trend between confluency and intensity of cytoplasm fluorescence, as seen in Fig. 4. Detailed values of the average intensity of the fluorescence of the cells' cytoplasmis in the Appendix (Table 1). This indicates that the higher the confluency of the cell

culture, the healthier the cells in the cell culture. These mitochondrial networks arise from mitochondrial fusion and fission [8]. Mitochondrial fusion is extremely important in living cells as it allows the spreading of metabolites, enzymes and mitrochondrial gene products through the mitochondrial network. It can optimise mitochondrial function and counteract the accumulation of mitochondrial mutations due to aging. Fragmented mitochondrial networks are more commonly found in resting cells. However, mitochondrial fission aids in the removal of damaged organelles [7]. Thus, it can be said that the intensity of the cytoplasm fluorescence of cell cultures with a higher confluence is indeed expected since it would indicate that the cells have a high respiration activity and are alive. This would therefore provide a more accurate insight on the interconnectedness, activity and quality of the cell culture, thereby making it more able to provide better feedback on changing the medium to suit the cell culture and manufacture better cells. This can be done since it has been found that healthy mitochondria and thus healthy cell cultures have mitochondrial networks between being highly fragmented and completely fused.

B. *Conclusion*

Stitching the spectrum together with the microscopy cell image does improve the classification accuracy of the machine learning method. Although this was not a significant improvement because of the already high accuracy of the spectrum-only machine learning method, it does indicate a potential in using both spectrum and image for classification. However, the CellProfiler pipeline would be able to serve as another way to predict and classify the confluence of the cell while checking the activity levels of the mitochondria to ensure that the cells within the culture are healthy and alive.

C. *Suggestions for Future Work*

Perhaps it could be future researched to find out if other features indicating the health of the cell can be found so that it would be possible to rely on more than one feature to determine the health of the cells in the cell culture. In addition, as it is currently not fully known how fluorescence intensity of a cell's cytoplasm relates to the health of a cell, it could also be further researched upon in order to give a better understanding and narrowing of the range of values possible for a cell culture to be considered healthy.

Additionally, it is possible that by stitching the graph of the spectrophotometer data and corresponding cell images together in addition to using the average intensity per square pixel of the cell's cytoplasm in the cell image through the Python code and CellProfiler pipeline, it would be possible to aid in increasing the accuracy of the neural network closer to 100% accuracy. This would be extremely useful in cell manufacturing to give feedback, analyse and predict the confluencies of the cells as well as to aid in suggesting adjustments in the medium to ensure better manufactured cells.

D. Contriution to Cell Manufacturing through Machine Learning

Machine Learning is able to classify features without manually extracting them, allowing for a hands-off classification of images, text and sounds. In addition, machine learning allows for extremely complex features to be recognized by the computer models allowing for classification of much higher accuracy than that of their human counterparts.

Cell Manufacturing is made up of many components. These include cell counting and checking if the cells in the cell culture vessel are healthy. These are labour-intensive tasks which generate a lot of data for which labour can be reduced if machine learning was used in cell manufacturing by feeding the Neural Network images of the cells in the cell culture vessel to measure the number of cells and the health of the cells in the cell culture vessel so that proper adjustments to the cell culture vessel can be suggested to improve the health and growth of the cells in the cell culture vessel. In this case, to reduce the manpower and time needed for the monitoring of cells in the cell culture vessels during cell manufacturing, machine learning is essential.

Acknowledgements I would like to thank my teacher-mentor, Dr Derrick Yong for his help, advice and feedback throughout the duration of the project, Singapore Institution of Manufacturing Technologies for being supportive of this project, Afif for working on the neural networks to analyse and predict the confluency of the cell culture from the images presented.

Appendix

See Table 1.

Table 1 Table of detailed results of results of cell image intensity

Confluency	Average intensity of cytoplasm per square pixel normalized to 255
10	0.8325654260
20	0.9753729186
30	0.9957051161
40	0.9983172165
50	0.9994269522
60	0.9989359418
70	0.9995384679
80	0.9984812932
90	0.9990185786
100	0.9959462322

References

1. CellProfiler. (2003). Retrieved from https://www.cellprofiler.org/.
2. Chauhan, N. S. (2019, October 10). Introduction to Artificial Neural Networks(ANN). Retrieved from https://towardsdatascience.com/introduction-to-artificial-neural-networks-ann-1aea15775ef9.
3. Hargrave, M. (2019, November 18). Deep Learning. Retrieved from https://www.investopedia.com/terms/d/deep-learning.asp.
4. Kitami, T., Logan, D. J., Negri, J., Hasaka, T., Tolliday, N. J., Carpenter, A. E., … Mootha, V. K. (2012). A Chemical Screen Probing the Relationship between Mitochondrial Content and Cell Size. *PLoS ONE*, *7*(3). https://doi.org/10.1371/journal.pone.0033755.
5. MathWorks. (n.d.). What Is Deep Learning?: How It Works, Techniques & Applications. Retrieved from https://www.mathworks.com/discovery/deep-learning.html.
6. pathmind. (n.d.). A Beginner's Guide to Neural Networks and Deep Learning. Retrieved from https://pathmind.com/wiki/neural-network.
7. Westermann, B. (2012). Bioenergetic role of mitochondrial fusion and fission. Biochimica Et Biophysica Acta (BBA) - Bioenergetics, 1817(10), 1833–1838. https://doi.org/10.1016/j.bbabio.2012.02.033.
8. Zamponi, N., Zamponi, E., Cannas, S. A., Billoni, O. V., Helguera, P. R., & Chialvo, D. R. (2018). Mitochondrial network complexity emerges from fission/fusion dynamics. *Scientific Reports*, *8*(1). https://doi.org/10.1038/s41598-017-18351-5.

Automation of Precision Ellipsometry System

Jerald Siah Chi Ming, Samuel Foo Enze, and Nikolai Yakovlev

Abstract Precision ellipsometry (PREL) is an optical technique used to measure changes in the thickness of surfaces or thin films. With a sensitivity of up to 0.01 nm, it is used in studies of molecular layers. A compact, low-cost and portable computer-driven system was developed to automate the fluidic processes of PREL. Two fluidic components were designed and built—a syringe pump to control the injection of liquid reagents and a valve to regulate the flow of rinsing liquid for washing. Motors were used to control the flow of liquids with pipes, syringes and other low-cost materials. Circuit networks, as well as programmes in Arduino and Python, were developed and integrated together to provide computer control through a graphic user interface and to simplify setting operation parameters. The automated system reduces operational fatigue and removes inaccuracies in data collection due to human error. It also enables multiple PREL set-ups to be run simultaneously by a single operator. The system can be incorporated into the existing PREL set-up easily, thus allowing PREL to be applied in a research or industrial environment.

Keywords Engineering mechanics · Industrial engineering-processing · Precision ellipsometry · Automation · Valve · Syringe pump · Fluidic control

1 1. Research Problem

A. *Precision Ellipsometry*

Precision ellipsometry (PREL) is an optical technique used to determine changes in the thickness of surfaces or thin films. With a sensitivity of up to 0.01 nm, it is used

J. S. C. Ming · S. F. Enze (✉)
Raffles Institution, Singapore, Singapore
e-mail: fooenzesamuel@gmail.com

J. S. C. Ming
e-mail: jeraldsiahchiming9876@gmail.com

N. Yakovlev
Institute of Materials Research and Engineering, Agency for Science, Technology and Research, Singapore, Singapore

H. Guo et al. (eds.), *IRC-SET 2020*,
https://doi.org/10.1007/978-981-15-9472-4_11

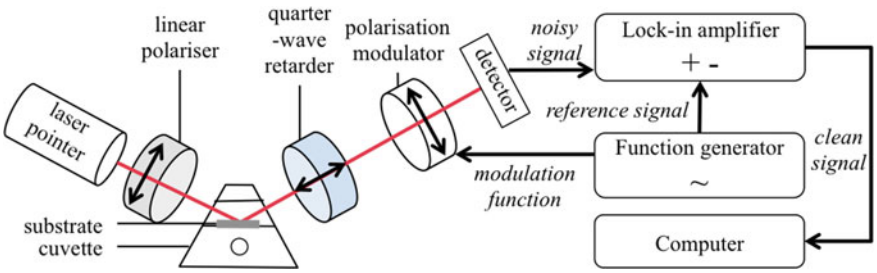

Fig. 1 Electro-optical set-up of liquid-phase precision ellipsometry

in the study of molecular layers and the adsorption and desorption of molecules [1]. It has a wide range of practical applications, including bio-sensors, protein detection systems, the real-time monitoring of materials growth and reaction kinetics.

Presently, a portable and versatile PREL set-up has been developed [2] and used in the study of biomolecules [3]. This project shall focus on automating this set-up.

In PREL, the substrate is placed into the cuvette, which has two transparent sides. The laser pointer shines polarised light onto the substrate. During an experiment, liquid reagents are injected into the cuvette. When the reagent molecules are adsorbed onto the surface of the substrate, there will be a change in the polarisation of the light reflected off the substrate. This change in polarisation is recorded by the modulator, photo-detector and lock-in amplifier, Fig. 1. Washing is then carried out by passing rinsing liquid through the cuvette to remove any reagents that have not attached to the substrate. Each layer to be deposited on the substrate involves one cycle of injection and washing. Presently, a pipette is used to inject reagents manually and manual clamp is used to control the flow of the rinsing liquid. This has several disadvantages.

Firstly, it is labour-intensive, especially since a typical experiment involves multiple cycles of injection and washing. Secondly, manual operation increases noise in data acquisition. As the PREL set-up is sensitive, any vibrations caused by the operator may affect the accuracy of data collected. Thirdly, it is imprecise. Due to human reaction time, it is impossible for fluids to be added to the cuvette at the precise moment when they are needed. Also, with manual operation, the rate at which fluids are added will be different each time. In time-sensitive experiments, this may lead to errors calculating the rate of change of film thickness, which is crucial in kinetics studies.

Automation of the fluidic processes of PREL is beneficial. Firstly, it allows the operator to multitask, since he or she no longer needs to focus entirely on the set-up during an experiment. Secondly, it allows for multiple PREL set-ups to be run by a single operator simultaneously, reducing the duration of experimentation.

B. *Engineering Goal*

This project aims to automate the fluidic components of the present PREL set-up by building a compact syringe pump to inject reagents, and an automated valve

without moving parts in liquid to control the flow of rinsing liquid. The new system will combine fluidic control and the respective electronics with the existing data acquisition system. It will be designed such that it can be integrated with the existing set-up easily, to allow PREL to be applied in a research and industrial environment.

2 Design of System

The development of fluidic control will consist of an automated valve and a syringe pump controlled by the same Arduino that is used for data acquisition. The syringe pump and the automated valve were designed to make the system as compact, low-cost and portable as possible (Fig. 2).

C. *Design of Syringe Pump*

Conventional syringe pumps have polished rails for a sliding mechanism to push the plunger, making these syringe pumps complicated and expensive. A pump without rails would usually be three times the distance travelled by the piston (Fig. 3, top). We took a novel approach and designed a pump without rails which is only two times the travel of the piston (Fig. 3, bottom), by incorporating the screw into the plunger (Fig. 4).

When the motor rotates clockwise, the long screw will rotate as well. Since the slider is unable to rotate, it will move forward, pushing the plunger flange of the syringe inwards. Conversely, when the motor rotates counter-clockwise, the slider

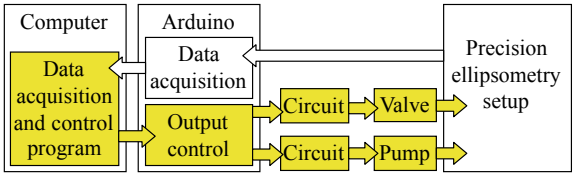

Fig. 2 Schematic of proposed system. The yellow boxes show the components built for fluidic control

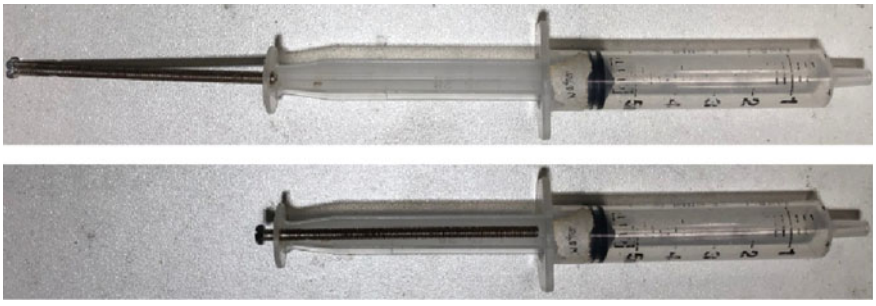

Fig. 3 Length of conventional syringe pumps without rails (top), and our design (bottom)

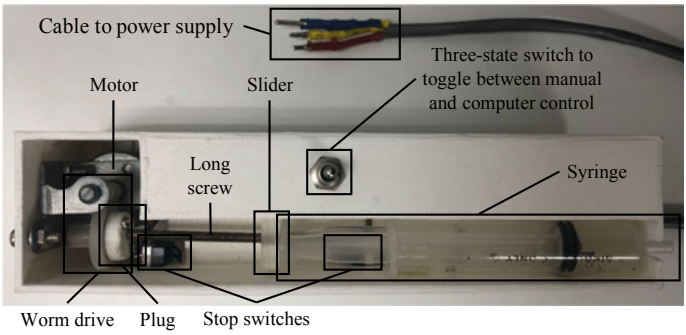

Fig. 4 Diagram of syringe pump

will move back to its original position near the motor, allowing the syringe to be replaced.

The three-state switch allows the operator to choose between manual operation or computer control. In the side positions, the switch applies +5 V power in forward or reverse polarity to the motor for the slider to move forwards or backwards respectively. The transistors are connected with their collector to the three-state switch, so that they are both closed when it is in the side positions. In the middle position, the motor will be controlled by the Arduino. With 5 V at control, both transistors are open and apply voltage to the motor for the slider to move forward; with 0 V at control, no voltage is applied. In this case, the operator's only role is to flick the switch backward to move the slider back to its original position after each syringe has been emptied. The circuit (Fig. 5) has been designed such that manual operation always overrides computer control, without creating any short circuits.

The stop switches break the circuit when pressed by the slider, preventing it from moving towards them any further. However, the motor will still be able to rotate in the opposite direction for the slider to move away from the stop switch being pressed. This allows the motor to be used continuously without needing to be reset each time the slider moves forward or backward.

D. *Design of Valve*

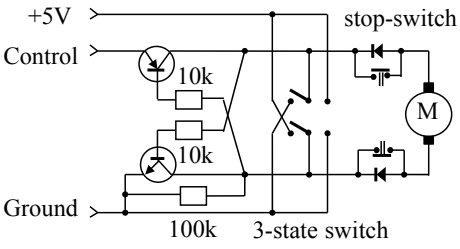

Fig. 5 Diagram of control circuit of syringe pump

A valve was developed to regulate the flow of rinsing liquid into the cuvette. It has no moving parts in the liquid, to prevent any contamination of the rinsing liquid from the moving parts (Fig. 6).

The rotation of the motor was used to twist the pipe, since the motor is not strong enough to close the pipe by pressing it. A customised 3D-printed accessory was attached onto the main gear of the motor. It includes a holder to clamp the pipe to the motor, as well as a finger to press the stop switches at the sides. The ends of the pipe are held in place by clamps, so that the pipe does not shift when it twisted. When the motor rotates clockwise, the pipe is open (Fig. 7, left). When it rotates counter-clockwise, the pipe is closed (Fig. 7, right) (Fig. 8).

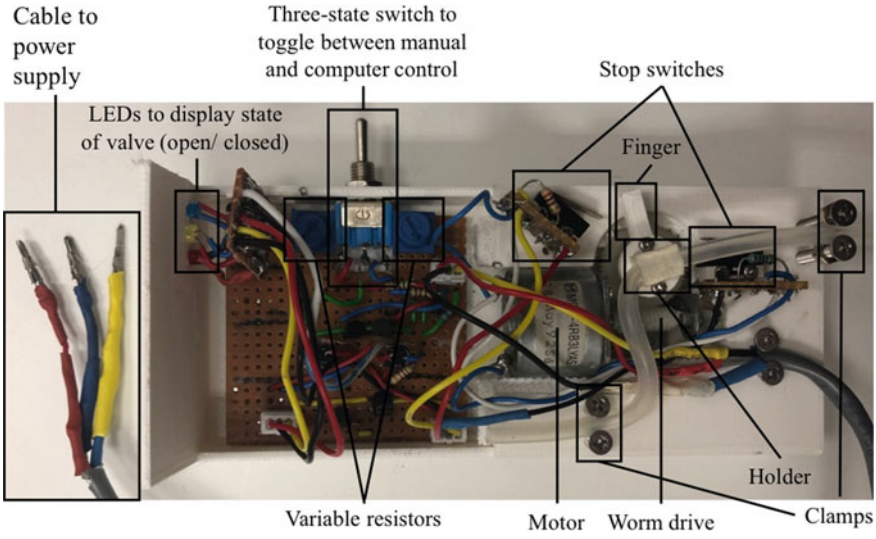

Fig. 6 Diagram of valve

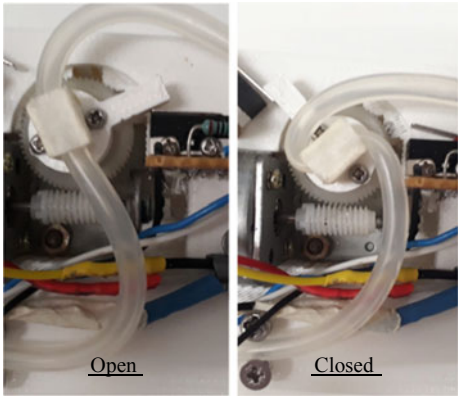

Fig. 7 Shape of pipe when water can flow (left) and cannot flow (right)

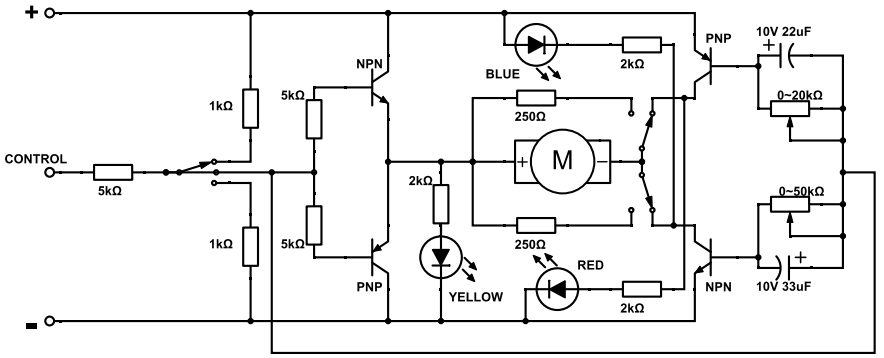

Fig. 8 Control circuit for valve

A circuit was designed to control the rotation of the motor. Stop switches at the side of the motor are used to break parts of the circuit, to stop the motor at the precise position where the pipes are opened or closed. If the motor rotates clockwise to press the switch on the right, only the circuit responsible for clockwise rotation will be broken. Thus, the motor can still rotate counter-clockwise. The same is true for the opposite direction. This feature allows the device to be used continuously without the need to reset it after each rotation.

The three-state switch allows the operator to toggle between manual operation and computer control. When the switch is at the centre, the device is controlled by the computer. When the switch is flicked to the left or right, the motor rotates clockwise or counter-clockwise respectively.

E. *Integration with Computer*

To allow the operator to control the syringe pump and valve with the computer, a graphic user interface (GUI) was built using Python. In the GUI, the operator inputs a schedule for injection and washings, with a time specified for the start and end of each. When it is time to perform an action, Python will send a byte to Arduino through serial communication. Four different bytes are defined in both the Python and Arduino code for each of the four actions—start injection, stop injection, start washing and stop washing (Figs. 9 and 10).

After receiving the byte from Python, Arduino will change the voltage supplied by the ports. Three Arduino ports are used, one for the valve and two for syringe pumps. Each port can either be set to high voltage or low voltage. The six possible Arduino controls are each represented by the six bytes.

The syringe pump and the valve were designed to respond to the Arduino controls. Injection begins when the Arduino port the syringe pump is connected to supplies a high voltage. Similarly, washing begins when the Arduino port the valve is connected to supplies a high voltage. The reverse is true when injection and washing ends. For data acquisition, the sensors connected to Arduino writes back to Python, which saves the data. In this way, the system simultaneously records data and performs actions.

Fig. 9 GUI upon entering the system

Fig. 10 GUI for scheduling of tasks

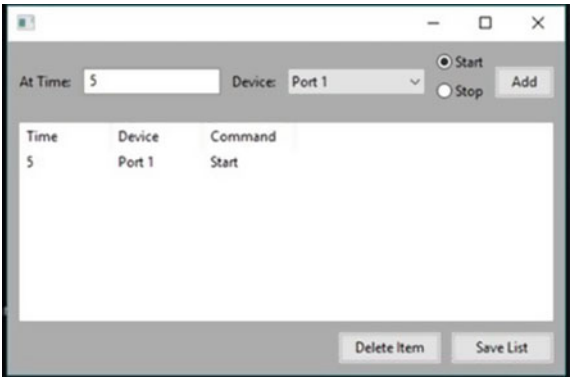

3 Evaluation

Our automated system was evaluated by deposition of poly-electrolyte multilayers from water solutions onto silicon substrate and simultaneous recording of deposited thickness. The molecules used here were: poly-allylamine-hydrochloride (PAH), which is positively charged in water solution, and sodium poly-styrene-sulfonate (PSS), which is negatively charged. Thus depositing one above the other creates a stable film by electrostatic attraction.

The process of multilayer deposition was as follows: silicon substrates were cleaned by wet chemistry installed into optical cuvette and optical system was aligned. While rinsing water was flowing through the cuvette, data acquisition started. At 590 s after the start, the valve was closed, and at 600 s, the syringe pump injected 1 ml of PAH solution; it is seen that the thickness gradually increased to around 0.5 nm, Fig. 11. At 1000 s, the valve was opened and the solution was rinsed away, but the thickness did not change; it shows that the attachment was permanent. The same process was repeated with PSS solution at 1200 s, then again PAH at 1800 s and so on. The measurement shows that PSS consistently gives increments of around

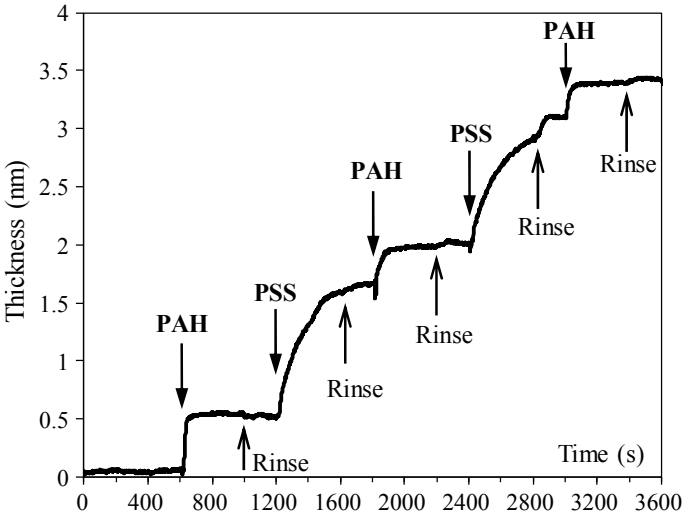

Fig. 11 Example of PREL measurement of sequential attachment of poly-electrolyte layers PAH and PSS on oxidised silicon substrate

1 nm and PAH around 0.5 nm. This proves reproducibility of control and acquisition and confirms stability of the whole system even during the whole hour of the process.

Our automated system brings about several advantages. Firstly, our system is easy to use, with the GUI being the sole interface the operator has to work with. With the syringe pump and valve in place, the operator simply schedules the time for injection and washing. Secondly, the programme designed brings computer precision to the PREL set-up, for injection and washing to be performed on time. With the system, there will no longer be any more mistimed addition of chemicals. Thirdly, our system is portable because it takes power only from a USB power supply, and USB ports are readily available. It is also compact, as the components can be fit into two small 3D-printed boxes—one for the syringe pump and one for the valve, with a total space of 40 mm wide, 165 mm long and 60 mm high. Fourthly, the cost of the system is low. While commercial peristaltic pumps or a standard syringe pumps can cost up to $500, our system was built with low-cost materials, such as relatively cheap motors, circuit boards and 3D-printed bodies. Lastly, the automated system can be easily modified to be compatible with other techniques as it does not have requirements specific to PREL (Fig. 12).

4 Conclusion

We have developed a flow control system to automate the fluidic components of the present PREL set-up. It consists of a syringe pump to inject reagents, and a valve

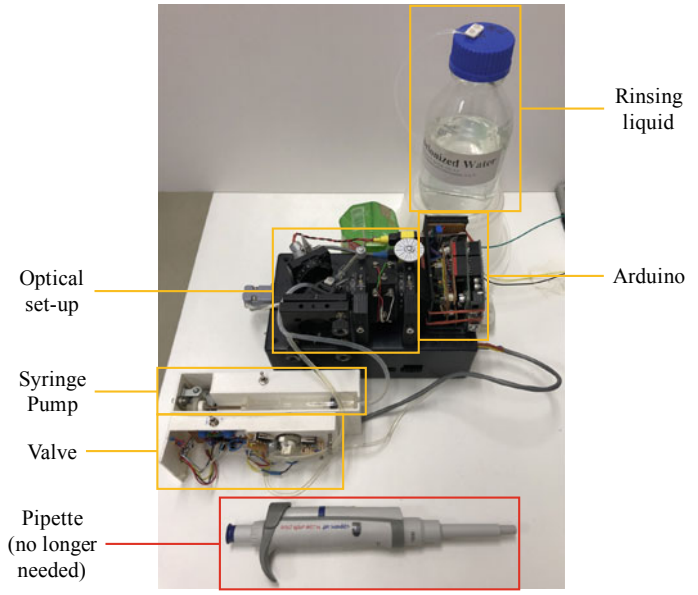

Fig. 12 Automated system developed in this project, integrated with the existing PREL set-up

to regulate the flow of rinsing liquid, respective electronic circuits and software to control the system simultaneously with data acquisition. The specialised automation system can be integrated easily into the existing PREL set-up. Furthermore, the compact, low-cost and portable nature of the system allows it to be used efficiently in a research or industrial environment. Most importantly, it works.

References

1. S. N. Jasperson, S. E. Schnatterly, "An Improved Method for High Reflectivity Ellipsometry Based on a New Polarisation Modulation Technique". The Review of Scientific Instruments, v.40 (6), 761–767 (1969).
2. N. L.Yakovlev, Hou Chin Quek, Karol M. Dabrowski , William R Birch, Kinetics of Small Molecule Adsorption Studied Using Precision Ellipsometry, Surface and Interface Analysis, v.51(7), p.697 (2019).
3. Lau, H., Murney, R., Yakovlev, N., Novoselova, M., Lim, S., Roy, N., Singh, H., Sukhorukov, G., Haigh, B. and Kiryukhin, M. (2017). Protein-tannic acid multilayer films: A multifunctional material for microencapsulation of food-derived bioactives. Journal of Colloid and Interface Science, 505, pp. 332–340.

The Influence of Transfection Methods on the Molecular Dynamics of the Cell Plasma Membrane

Guo Meihui, Thorsten Wholand, and Sapthaswaran Veerapathiran

Abstract Lipofection is an example of transfection, where foreign nucleic acids are coupled with cationic lipids and delivered into the cell via endocytosis [16]. However, lipofection is a traumatic event for the cells. Due to the lack of elucidation on how lipofection affects cell membrane dynamics and the duration for the cell to recover, this study aims to elucidate the duration of membrane re-organization. To achieve the aims of this study, CHO-K1 are transfected with Glycosylphosphatidylinositol tagged Green Fluorescent Protein (GPI-GFP) and exposed to 488 nm laser light, leading to GFP fluorescent emission (510 nm), which is subsequently recorded on a fast camera. The fluctuations in fluorescence intensity in each pixel are measured by Imaging Fluorescent Correlation Spectroscopy (ImFCS), which correlates the fluctuations in the fluorescent intensity to obtain the diffusion coefficient of GPI-GFP. The results of determining the diffusion coefficient over different length scales (by 21 × 21 pixel binning) are used in the FCS Diffusion law to produce a diffusion law plot, where the y-intercept values of the plots give insights on the modes of diffusion. This experiment showed that plasma membrane recovery post lipofection is surprisingly robust, with no significant membrane perturbations observed.

Keywords Transfection · Lipofection · Fluorescent microscopy

1 Introduction

Transfection is the process of introducing foreign nucleic acids into eukaryotic cells. It is a fundamental technique for the study of biochemical and physiological processes of cells and has been applied to genetically manipulate mammalian cells to express high levels of selected proteins [15]. Such technology is an important area in healthcare as it could enable large-scale production of desired products such as insulin,

G. Meihui (✉)
Hwa Chong Institution, Singapore, Singapore
e-mail: guomeihui50@gmail.com

T. Wholand · S. Veerapathiran
BioImaging Sciences, NUS, Singapore, Singapore

H. Guo et al. (eds.), *IRC-SET 2020*,
https://doi.org/10.1007/978-981-15-9472-4_12

interferon, and even viral vaccines [3, 13, 18]. Common transfection methods include electroporation, microinjection, viral transfection and lipofection. All transfection procedures are traumatic events for the cells, as the membrane porosity required for deliverance of foreign genes into the cell inevitably creates micropores that severely disrupts membrane integrity. Previous studies have shown that the cellular responses to such membrane perturbations contributed to the differential expression of the gene of interest, which not only pose difficulty in understanding which effects are the true biological responses to the specific gene, but also negatively impacts the identification and production of desired proteins for clinical use [6–8]. As a result, various studies have been conducted to investigate the effects of transfection on cell membrane. However, there is a lack of elucidation on how lipofection, a process by which foreign nucleic acids are coupled with cationic lipids delivered into the cell via endocytosis and phagocytosis, in particular, affects cell membrane dynamics [16]. Since this process requires extensive interactions between the cationic DNA-lipid complexes and the cell membrane, it is expected that lipofection would cause observable cell membrane perturbations and result in temporary or permanent membrane changes. Therefore, the aim of this study is fill in the gap in our understanding of how lipofection affect cell membrane organization and experimentally elucidate the duration for the cell membrane to recover after lipofection.

To elucidate how lipofection affect cell membrane dynamics, a fundamental understanding of the cell membrane is necessary. The cell plasma membrane is a biological barrier that covers the cell surface, separates the cell from its extracellular environments and ensures proper cellular functioning by regulating cellular interactions between adjacent cells and the extracellular environment. Recent studies have shown that the cell membrane is non-homogenous and highly segregated into compartmentalized microdomains, also known as lipid rafts [14]. Lipid rafts are distinct regions on the cell membrane with a higher concentration of cholesterol, glycosphingolipids, and glycosylphosphatidylinositol (GPI)-anchored proteins. There is now increasing evidence suggesting that lipid rafts are instrumental in regulation of important cellular processes such as cell polarity, protein trafficking, and signal transduction [4, 5]. For example, cell membrane surface receptors such as the epidermal growth factor receptor are known to be involved in cell proliferation, differentiation and survival [1, 10]. In addition, lipid rafts are also known as the modulator of sensitivity of cell signaling during tissue morphogenesis [9]. Studies have also revealed that confinement by lipid rafts allows for the receptors and cofactors to meet at an increased rate and hence speed up cell responses. Together, these reports point to the fact that lipid rafts influence an array of critical biological events and play crucial roles in the plasma membrane organization. Given the significant role of lipid rafts in cell membrane organization, GPI-anchors, which are known to be associated with lipid rafts, are therefore chosen as the marker for cell membrane organization. GPI-anchors and tagged with Green Fluorescent Protein (GPI-GFP) to enable monitoring of GPI-GFP fluorescence and hence localizations of GPI anchors, thereby giving insights on the cell membrane organization post lipofection.

Conventionally, the study of diffusion modes of fluorescent molecules is conducted via Fluorescent Correlation Spectroscopy (FCS), an analytical tool that

performs statistical analysis of fluctuation data to give diffusion coefficients and diffusion times of fluorescent molecules in femtoliter volumes. However, due to interference between neighboring confocal volumes, conventional FCS requires a minimum distance 10–15 confocal diameters between focal volume elements, hence limiting the confocal spots in FCS experiments [17, 19]. To improve on the conventional FCS technique, Total Internal Reflection FCS (TIRF-FCS), which selectively illuminating only a thin layer of the sample that lies in the focal plane of the detection objective and thus reduces interferences between the detection elements, is used in this experiment to obtain more measurements per sample per time interval with less phototoxicity. Nevertheless, TIRF-FCS is still constrained by the Abbe diffraction limit, which states that regardless of how an optical instrument is manufactured, its resolving power will always be diffraction-limited to scales of 200–360 nm for optical wavelengths [2, 11, 12]. Lipid rafts, typically around 20-100 nm are well below this fundamental limit of diffraction. Therefore, the diffusion behavior of lipid rafts and the raft-associated proteins cannot be observed directly. To resolve this challenge, FCS diffusion law, an analytical technique that plots the diffusion time (τ_d) against the observation area (A_{eff}), was used in conjunction of TIRF-FCS to deduce the mode of diffusion of GPI-GFP. Extrapolation of the diffusion law plot gives the y-intercepts, which provide insights on the diffusion mode of fluorescent molecules. For freely diffusing molecules, the y intercept is zero as τ_d is directly proportional to A_{eff}. For raft-associated molecules, y intercept is positive as the diffusing molecules are obstructed and slowed down by the presence of lipid rafts. For hop diffusion due to meshwork confinement, y intercept is negative (Fig. 1).

Continuous monitoring of the mode of diffusion of GPI-GFP post lipofection provides answers to the state of cell membrane reorganization, and the duration for the cell membrane to recover after lipofection.

1.1 Methods and Results

A. *Cell culturing*

CHO-K1 cells were cultivated in Dulbecco's Modified Eagle Medium (DMEM; Invitrogen, Singapore), a liquid medium with high concentration of amino acids and vitamins, to achieve sustained cell growth. Fetal Bovine Serum (FBS), which has high content of embryonic growth factors, was added at 10% concentration to promote cell growth. 1% Penicillin-Streptomycin (PS) was added to control gram-positive and gram-negative bacterial contamination and the cells were maintained at 37 °C and 5% v/v CO_2 to create optimum growth conditions. When the cells covered 90% surface area of a T75 flask (90% confluent), the DMEM was removed, 3 ml of Phosphate Buffered Saline (PBS) was added to rinse the flask, and 2 ml of trypsin was subsequently added to detach the cells from the flask. 10 ml of DMEM was added 2 min after trypsinization to neutralize the effects of trypsin. The detached cells were then seeded on 35 mm glass-covered dishes (No. 1.0 cover glass 0.13-0.16 mm,

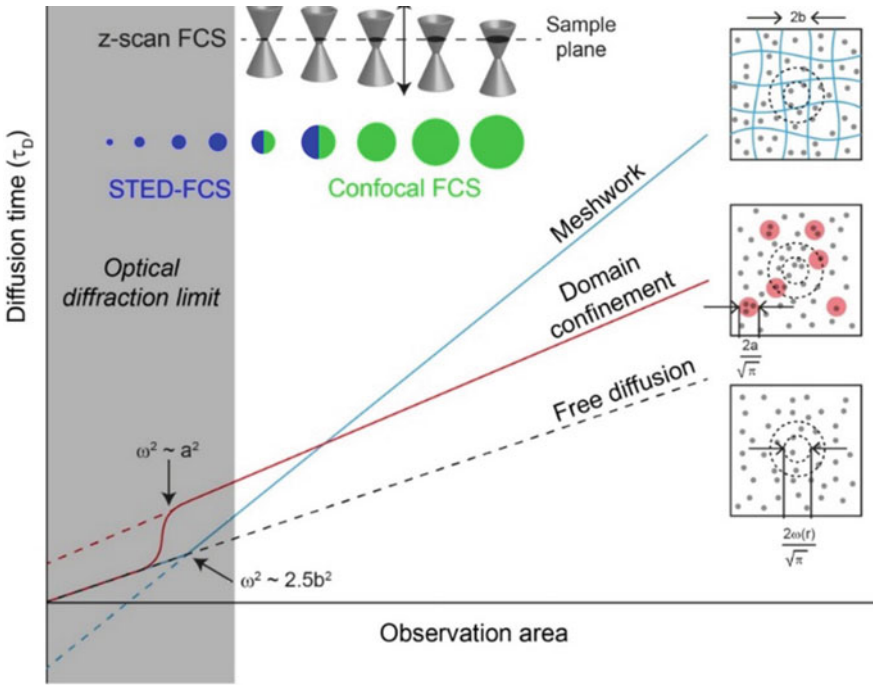

Fig. 1 FCS diffusion law plots for various diffusion modes in the membrane: free diffusion (black dotted line), hindered diffusion in domain confinement (red line) and hop diffusion in meshwork compartmentalization (light blue line) are illustrated. Reprinted from X. Ng et al. (2015)

Matek Corporation, US) with fresh DMEM, 10% FBS and 1%PS and incubated at 37% °C and 5% v/v CO_2 for 48 h to achieve 90% confluence.

B. *Lipofection procedure*

In a sterile Eppendorf tube, 6 microliters of Lipofectamine 3000™ reagent (L3000; Invitrogen, Singapore) was diluted in 125 microliters of Opti-MEM Reduced Serum Media (Opti-MEM, Invitrogen, Singapore). In another sterile Eppendorf tube, 2 microliters of GFP-GPI plasmid (Anovasia Pte Ltd, Singapore) and 4 microliters of P3000™ reagent (Invitrogen, Singapore) was diluted in 125 microliters of Opti-MEM. The diluted GFP-GPI plasmid was added to the diluted L3000 reagent and the resulting complex was incubated for 10 min at room temperature. After incubation, the complex was added to the 90% confluent CHO-K1 cells for transfection. The transfected cells were incubated at 37 °C and 5% v/v CO_2 and fluorescent expression was monitored every 30 min post transfection up to 10 h, at which fluorescent expression could be observed under a 4X light microscope. The transfected cells were then washed with Hank's Balanced Salt Solution (HBSS; Invitrogen, Singapore) and maintained in Phenol red-free DMEM and 10% FBS at 37 °C and 5% v/v CO_2.

C. *TIRF FCS instrumentation*

A Total Internal Reflection Fluorescence (TIRF) microscope (IX83, Olympus, Singapore) was equipped with an Electron Multiplying Charge Coupled Device (EMCCD) camera (Andor iXon2 X-9388, 128 × 128 pixels; Andor Technology, US), a 488 nm excitation laser (Olympus Cell Lasers 488; Olympus, Singapore), and a oil-immersion objective (UApoN100x, Olympus, Singapore). The principal attribute of a TIRF microscope is the utilization of evanescent wave to excite the fluorescent molecules, as opposed to excitation via direct laser light. The energy of the evanescent wave is concentrated in the vicinity of the glass-specimen interface, and therefore the penetration depth into the specimen is limited to a few hundred nanometers. This spatially limited excitation range allows for exclusive excitation of fluorescent particles in a small observation area located close to the interface and significantly increases signal-to-noise ratio, making the TIRF microscope ideal for imaging of fluorescent-tagged dynamic reactions in the cell membrane. The transfected cell cultures were maintained at 37 °C and 5% v/v CO_2 by an incubator with an objective heater (Live Cell Instruments, CU-109, Chamlide, Seoul, Korea) and a CO2 gas chamber (Live Cell Instruments, FC-05, Chamlide, Seoul, Korea). The 488 nm excitation beam was focused on the sample by a tilting mirror and a dichromic mirror. The Olympus Xcellence software was used to achieve total internal reflection via automatic calibration of the incident angle of the laser beam. The signal reflected by the objective was filtered by an emission filter (ZET405/488561/647 m, Chroma Technology, USA) and directed to the EMCCD camera.

D. *Data collection*

A 21 × 21 pixels (5 × 5 μm^2) region of interest on the cell was captured by 30 000 frames at 3 ms exposure. The Kinetic image acquisition mode was utilized with a readout rate of 10 MHz, a vertical shift speed of 45 μs and an electron multiplier gain level of 300 (in a scale of 6–1000). The recorded image stacks were processed with ImFCS 1491 plugin from ImageJ. Correlation of the intensity fluctuations of each pixel by ImFCS 1491 provides autocorrelation function (ACF) curves according to Eqs. (1)–(2), and subsequently gives a plot of diffusion time against the observation area, from which the diffusion coefficient (D) and the number of particles (N) could be obtained.

$$G(\tau) = \sum_{i}^{N_d} \alpha_i \left[\frac{erf(p(\tau)) + \frac{-(p(\tau))^2 - 1}{\sqrt{\pi}\, p(\tau)}}{erf(p(0)) + \frac{e^{-(p(0))^2} - 1}{\sqrt{\pi}\, p(0)}} \right] \left[1 + \left(\frac{F_t}{1 - F_t} \right) \exp\left(-\frac{\tau}{t_f} \right) \right] + G_\infty \tag{1}$$

$$p(\tau) = \frac{a}{\sqrt{4D\tau_o^2}} \tag{2}$$

$$\alpha_i = \frac{B_i^2 \langle N_i \rangle}{(B_i \langle N_i \rangle)^2} \tag{3}$$

In the equations above, $G(\tau)$ represents ACF model as a function of time (τ). The pixel length is denoted by a, and the Gaussian approximation of microscope point spread function, which is the three-dimensional image of a point-like fluorescent molecule under the microscope, is denoted by ω_o. The average number of fluorescent molecules is denoted by $\langle N_i \rangle$ and the brightness of the fluorescent molecules is denoted by B_i. The proportion of fluorescent particles in the triplet state and the duration spent in the triplet state are denoted by F_t and t_f respectively. The convergence value after a long lag time is denoted by G_∞.

The ImFCS diffusion law is the plot of τ_d against A_{eff}, according to Eqs. (4)–(5)

$$\left(A_{eff}\right) = \tau_o + \frac{A_{eff}}{D} \tag{4}$$

$$A_{eff}(\tau) = \frac{a^2}{\frac{\omega_0}{\left[a\sqrt{\pi}\left(e^{-\frac{a^2}{\omega_o^2}-1}\right)+\mathrm{erf}\left(\frac{a}{\omega_o}\right)\right]^2}} \tag{5}$$

2 Results

A TIFR-FCS microscope is used to record the intensity fluctuations of the GPI-GFP fluorescence, which are subsequently autocorrelated by software ImFCS 1491 to give a graph of $G(\tau)$ against τ, also known as an ACF curve (Fig. 2). From the ACF curve, the diffusion coefficient (D) and the number of particles (N) could be obtained. D is then feed into the diffusion law to produce a graph of τ_o against observation area (Fig. 3), from which the duration for the cell membrane to recover to its native state could be deduced.

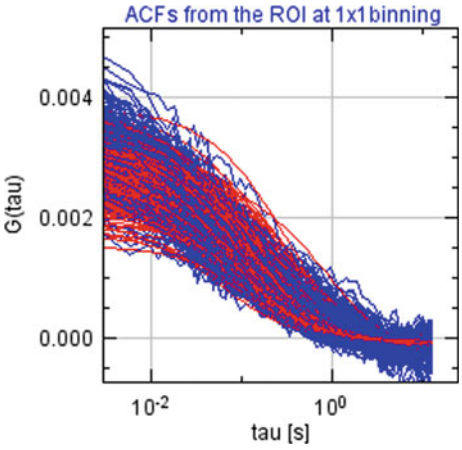

Fig. 2 Representative experimental auto correlation function (ACF) curve for CHO-K1 cells transfected with GPI-GFP

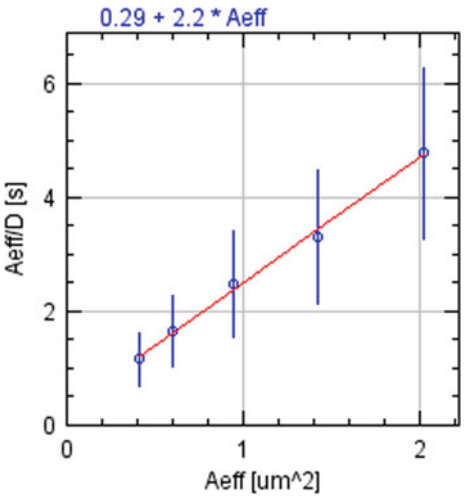

Fig. 3 Representative diffusion law plot for CHO-K1 cells transfected with GPI-GFP with a τ_o of 0.29

Interestingly, D shows no significant fluctuations as time progresses (Fig. 4). D remains relatively constant at 0.34 $\mu m^2/s$, with a D value of 0.40 ± 0.07 $\mu m^2/s$ at the 10th hand a D value of 0.31 ± 0.02 $\mu m^2/s$ at the end of the 24th h. Similarly, average τ_o show no significant fluctuations (Fig. 5). τ_o remains relatively constant at 0.67 *s*, with a τ_o value of 0.63 ± 0.26 *s* at the start of 10th h to 0.78 ± 0.21 *s* at end of the 24th h. Since all τ_o values are positive, it can be inferred that GPI-GFP molecules are undergoing domain confined diffusion.

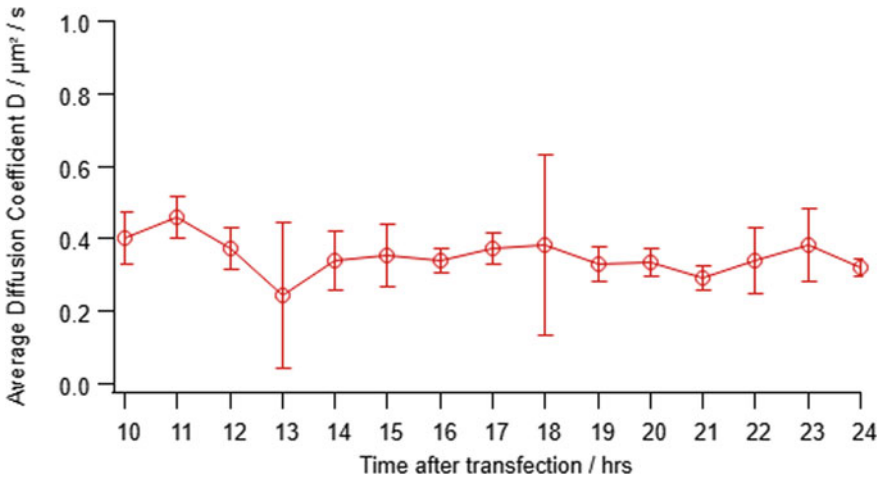

Fig. 4 Graph of average diffusion coefficient (D) against time after transfection

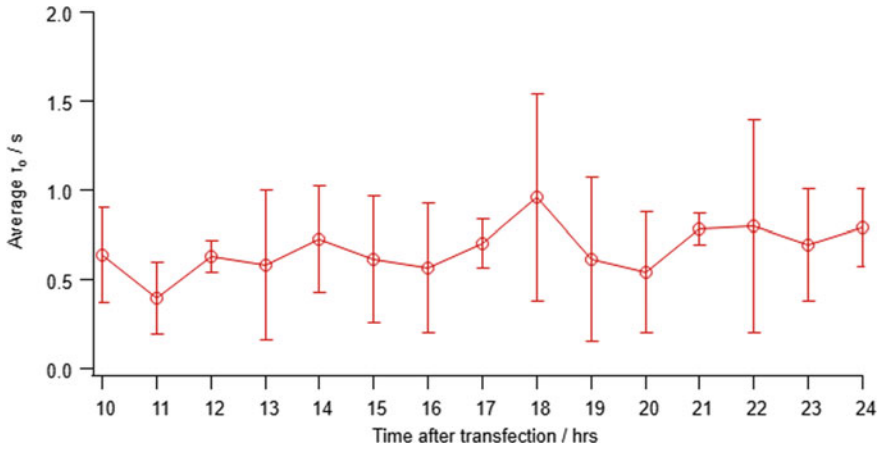

Fig. 5 Graph of average τo against time after transfection

3 Discussion

The stability of D and τ_o is surprising as it is expected that the lipofection procedure would cause observable cell membrane perturbations. The relative stability of D and τ_o suggest that the cell membrane recovered significantly by the 10th h post transfection. This is in stark contrast to previous electroporation experiments done by other members of our lab, which showed that both D and τ_o values stabilize only after the 13th h. This suggests that lipofection is not only a less invasive transfection method as compared to electroporation, but also do not significantly disturb cell membrane organizations. Another possible explanation for the apparent stability of D and τ_o values could be that by the time fluorescent expressions are observable, the membrane perturbations caused by lipofection have attenuated significantly. Following cellular internalization of GFP-GPI via endocytosis, the GFP-GPI would appear in the endosomes and later in the nucleus. It is still unclear how the GFP-GPI are released from the endosomes and traverse the nuclear membrane. After reaching the nucleus, the integration of GFP-GPI into the DNA of host cells and the eventual fluorescent expressions requires yet more time. These series of events ultimately result in a observable time lag between actual membrane perturbations immediately after lipofection and the first expression of fluorescence after 10 h. Therefore, the relative stability of membrane organizations post lipofection could be explained by the fact that the any actual perturbations of cell membrane immediately post lipofection are not captured due to the inherent limitation of the lipofection technique used in this experiment.

4 Conclusion

The results suggest that the duration for the cells to recover after lipofection is less than 10 h. This observation would be useful for future researchers seeking to perform various kinds of transfection on cells to study expression of desired proteins. Nevertheless, more question regarding the membrane perturbances caused by lipofection immediately after lipofection procedures are generated. Further elucidation on the duration of recovery of cell membrane post lipofection would fill in the gap in our understanding of the effects of lipofection of cell membrane organization, hence helping researchers performing the procedure to better understand the differential expressions of gene of interest post lipofection, which ultimately results in better identification and production of desired proteins for clinical use. Further research could be performed with probes targeting other regions, such as the non-raft regions and the actin cytoskeleton meshwork, to investigate if similar results would be obtained. Moreover, temporal study of other transfection methods such as sonoporation, microinjection and viral transduction could be conducted to investigate how other transfection methods affect membrane dynamics.

Acknowledgements I would like to thank Professor Thorsten Wohland for providing mentorship and support throughout my project. I would also like to express my gratitude to my mentor Sapthaswaran Veerapathiran, who has kindly assisted me throughout the project, particularly in the learning of how to use equipment stated in the methodology, growing of CHO-K1 samples, and guiding the analysis of the experiments.

References

1. Hoeller D, Volarevic S, and Dikic I. (2005), "Compartmentalization of growth factor receptor signalling," Current Opinion in Cell Biology. 17, 107–111. https://doi.org/10.1016/j.ceb.2005.01.001
2. Baddeley D, Jayasinghe D, Lam L, Rossberger S, Cannell M. B, and Soeller C. (2009). "Optical single-channel resolution imaging of the ryanodine receptor distribution in rat cardiac myocytes," Proceedings of the Natural Academy of Sciences. U.S.A. 106, 22275–22280. https://doi.org/10.1073/pnas.0908971106
3. Roca-Cusachs P, Gauthier N. C, Del Rio A, and Sheetz M. P. (2009). "Clustering of alpha (5) beta (1) integrins determines adhesion strength whereas alpha (v) beta (3) and talin enable mechanotransduction," Proceedings of the Natural Academy of Sciences. U.S.A. 106, 16245–16250. https://doi.org/10.1073/pnas.0902818106
4. Singer S. J., Nicolson L. (1972). "The Fluid Mosaic Model of the Structure of Cell Membranes," Science. Feb: Vol. 175, Issue 4023, pp. 720–73. https://science.sciencemag.org/content/175/4023/720/tab-pdf
5. Simons K, Ikonen E. (1997). "Functional rafts in cell membranes," Nature. 387. 569–72.
6. Simons K, Vaz W L. (2004). Annual Review of Biophysics and Biomolecular Structure. 33:269–95.
7. Klaasse E C, Ijzerman A P, and Beukers M W. (2008). Internalization and desensitization of adenosine receptors. Purinergic Signal. 4, 21–37. https://doi.org/10.1007/s11302-007-9086-7

8. Batada N, Shepp L A, and Siegmund D O. (2004). “Stochastic model of protein–protein interaction: why signaling proteins need to be colocalized,” Proceedings of the Natural Academy of Sciences. Sci. U.S.A. 101, 6445–6449. https://doi.org/10.1073/pnas.0401314101
9. Catherine S. (2011). “In DNA transfection, efficiency and cytotoxicity are two sides of the same coin,” Biocompare. https://www.biocompare.com/Editorial-Articles/41821-In-DNA-Transfection-Efficiency-and-Cytotoxicity-Are-Two-Sides-of-the-Same-Coin/
10. Prevette L. E, Mullen, D. G, Holl M. (2010). “Polycation-induced cell membrane permeability does not enhance cellular uptake or expression efficiency of delivered DNA,” Molecular pharmaceutics, 7(3), 870–883. https://www.ncbi.nlm.nih.gov/pmc/articles/PMC2882516/
11. Stelzer E. “Beyond the diffraction limit,” Nature 417, 806–807 (2002) https://doi.org/10.1038/417806a
12. Jagadish S, Andreas K, Scott A. R, Thorsten W. (2018). “Quantitative imaging and spectroscopic technologies for microbiology,” FEMS Microbiology Letters. Volume 365, Issue 9, May, fny075. https://doi.org/10.1093/femsle/fny075
13. Sapthaswaran V, Thorsten Wohland. (2018). “The imaging FCS law in the presence of multiple diffusive modes,” Methods. May 1;140–141:140-150.
14. Lingwood D, Kaiser HJ, Levental I, Simons K. (2009) “Lipid rafts as functional heterogeneity in cell membranes,” Biochemical Society Transactions. Oct;37(Pt 5):955–60.
15. Kusumi A, Sako Y. (1996). “Cell surface organization by the membrane skeleton,” Current Opinion in Cell Biology. Aug, 8(4), 566–74
16. Kim T K, & Eberwine J H. (2010). “Mammalian cell transfection: the present and the future,” Analytical and bioanalytical chemistry, 397(8), 3173–3178, https://www.ncbi.nlm.nih.gov/pmc/articles/PMC2911531/
17. Linda B Jacobsen, Susan A Calvin, Edward K. Lobenhofer (2018). “Transcriptional effects of transfection: the potential for misinterpretation of gene expression data generated from transiently transfected cells,” Biotechniques. VOL. 47, NO. 1. https://doi.org/10.2144/000113132
18. Griffiths AJF, Miller JH, Suzuki DT. “An Introduction to Genetic Analysis,” 7th edition. New York: W. H. Freeman; 2000. Recombinant DNA technology in eukaryotes. https://www.ncbi.nlm.nih.gov/books/NBK22002/
19. Elson E L. (2011). “Fluorescence correlation spectroscopy: past, present, future,” Biophysical,journal, 101(12),2855–2870. https://doi.org/10.1016/j.bpj.2011.11.012

Engineering of a Novel Inhibitor of Factor XIa with Better Stability and Inhibitory Efficiency

Tasha Annakin S. Idnani and Yong Hsuen Wei Melissa

Abstract Thrombosis is the cause of many cardiovascular diseases, which accounts for 29.2% of deaths in 2018 locally [1]. Current treatment options for it include heparin, warfarin and new oral factor Xa or thrombin inhibitors. However, prevalent limitations have been associated with these drugs, with the most significant being excessive bleeding. This study seeks to target Factor XIa (FXIa), an enzyme in the intrinsic pathway of coagulation. Inhibitors of FXIa have shown to effectively prevent pathological thrombus formation, without increasing bleeding risks in patients [2]. P1395, a putative FXIa inhibiting 77-residue peptide sequence, has been identified from the salivary gland of deer tick [3]. In its wildtype (WT) form, P1395 is able to inhibit FXIa at sub-nanomolar level. Still, its development in therapeutics is severely limited due to two inherent issues. First, the presence of seven cysteine(C) residues results in a free C with a free reactive thiol group after formation of disulfide bonds, reducing the stability of the peptide and increases the possibility of alternative disulfide pairings which are undesirable. Consequently, C was mutated to serine. An enzymatic assay analysis showed that P1395 mutant possesses similar activity to P1395 WT. Therefore, we have successfully eliminated the reactive thiol group to improve the stability of P1395 to be further developed as a drug candidate. Second, P1395 WT folds into a monomeric domain capable of binding to a single FXIa active site, which is a dimer. Given that two P1395 WT molecules are required for complete inhibition of one FXIa molecule, the overall inhibition efficiency of P1395 monomer is halved. This study sought to utilise the free thiol to engineer a dimeric P1395 linked through a peptide linker to improve inhibitory efficiency. However, in our preliminary assessment, the P1395 and peptide linker did not conjugate. Further optimisations of the conjugation are to be conducted.

National University of Singapore, School of Biological Sciences, S2.

T. A. S. Idnani (✉) · Y. H. W. Melissa
NUS High School of Mathematics and Science, Singapore, Singapore
e-mail: petlovertasha@gmail.com

Y. H. W. Melissa
e-mail: melloyoong@gmail.com

H. Guo et al. (eds.), *IRC-SET 2020*,
https://doi.org/10.1007/978-981-15-9472-4_13

Keywords Anticoagulant · Factor XIa · SDS-PAGE · Gene cloning · Protein synthesis · LC-MS · HPLC · Enzymatic assay

1 Introduction

A. *Excessive Blood Coagulation Predicament*

Blood coagulation is an imperative process in averting excessive bleeding upon the rupture of endothelium of blood vessels. Clots typically materialise in veins and arteries, which constitute the circulatory system of mammalian bodies. Given the necessity of blood coagulation systems for survival, the system is highly conserved in most species of Mammalia organisms.

Excessive blood clotting, or thrombophilia, could nevertheless occur, resulting in severely restricted blood flow. Vascular injury due to coagulation is a normal physiological response to imbalance in coagulation, which emanates from pathological clot formation, otherwise known as thrombosis. Thrombophilia has ensued an array of disorders, which comprise of deep vein clotting. The primary distinctive symptoms of deep vein clotting are swelling, throbbing pain and skin decolourisation. When blood flow is obstructed in arteries, tissues such as the heart and brain have a reduced blood supply, leading to a heart attack or stroke. It was reported that, in 2018, 17 individuals died per day from cardiovascular diseases in Singapore alone, accounting for 29.2% of all deaths in that year [1].

B. *Anticoagulants*

Anticoagulants are chemical substances developed to reduce coagulation of blood in order to prolong clotting time. Elongation of clotting time could eminently impede the progression of various diseases, such as myocardial infarction [4] and coronary heart disease [5], consequently saving abundant lives. It is, hence, notable that the capability of anticoagulation mechanisms to suppress clotting factors is indispensable to the survival of humans.

Numerous naturally-occurring anticoagulants are present within blood-sucking animals such as leeches, mosquitoes and ticks. These anticoagulants equip these animals to keep the bite area unclotted for an extended period, therefore allowing the animal to feed continuously. Thrombin, in particular, plays a vital role in blood coagulation by promoting platelet aggregation and by converting fibrinogen to form the fibrin clot in the final step of the coagulation cascade. To date, hirudin is the one and only thrombin inhibitor adopted in clinical agent development. Hirudin was originally isolated from the salivary glands of the medical leech *Hirudo medicinalis* [6].

Given the potency of anticoagulants in resolving multitudes of cardiovascular diseases, there exists an urgent need to develop new anticoagulants, particularly those with high potency and specificity yet minimal bleeding risk.

C. *Factor XIa (FXIa): Prospective Anticoagulant Drug Target*

In this project, we aim to target factor XIa (FXIa), a keenly pursued anticoagulant drug target. It has been shown to effectively prevent pathological thrombus formation, without significantly increasing bleeding risks in patients. P1395, a putative FXIa inhibiting 77-residue peptide sequence, has been identified from the salivary gland of the black-legged tick Ixodes scapularis [3]. *Even though it is able to inhibit FXIa at sub-nanomolar concentrations, several issues hindered the prospect of developing the peptide into a therapeutics. Firstly, the presence of seven cysteine (C) residues resulted in one free cysteine after the formation of three disulfide bridges. The free cysteine results in the presence of a reactive free thiol group, which significantly reduces the stability of the peptide and complicates purification process. It also results in alternative disulfide pairings during folding of the peptide which are undesirable. Hence, a sequence was purchased with the Cys73 mutated into Ser73. Another issue present with P1395 Wild Type (WT) protein is that it folds into a single, monomeric domain capable of binding to a single FXIa active site. However, FXIa is a dimer, thus two P1395 molecules are needed for complete inhibition of every one FXIa molecule, reducing overall efficiency of the inhibition by P1395. Thus, in this study, an attempt was made to evaluate the thiol mutant as well as engineer a dimeric P1395 linked through a peptide linker.*

2 Primary Research Objectives

This study primarily seeks to analytically deduce the best possible efficiency of the bivalent P1395 inhibitor by varying the lengths of protein involved in the formation of this bivalent inhibitor. The Cys73 to Ser73 mutation performed was to increase P1395's stability. This study primarily obtained P1395 from the salivary gland of *Ixodes scapularis*, an inhibitor of factor XIa utilised to prevent blood coagulation. The possibility of P1395 being used as a putative inhibitor with heightened efficiency and fewer harmful side effects was evaluated.

3 Hypotheses

Given the similarity in size between Serine and Cysteine, the hypothesis for Part One is that Serine can replace Cys73 without affecting the overall folding, structure and activity of P1395.

In addition, peptide linkers of different lengths can react with P1395 through the free thiol to form dimers, which can subsequently be assayed to select for the most efficient inhibitor of FXIa.

4 Procedure

A. *Part One: Cloning of P1395*

Cloning of P1395 WT and P1395 mutant (M) were performed by members of our host laboratory.

B. *Part One: Recombinant Expression of P1395 WT and Mutant In Bacterial*

Firstly, the recombinant AVA0421 plasmid containing the P1395 Wild Type(WT) gene was transformed into SHuffle® T7 Competent *E.coli* cells (New England Biolabs) following the manufacturer's instructions and protocol. After heat-shock transformation, 950 μl of Luria broth(LB) was added to the bacteria cell and grown in a 30 °C incubator for 60 min at 200 rpm. 100 μl of the bacterial suspension was plated onto LB plate supplemented with kanamycin. This plating was repeated with 200 μL of bacterial suspension. The plates were incubated overnight at 30 °C.

Next, starter cultures consisting of the transformed SHuffle cells with 50 μg/mL kanamycin and 10 mL of LB were prepared. Thereafter, they were incubated for 18 h at 250 rpm at 30 °C.

Each starter culture was then added into a 2.8 L conical flask containing 1L of LB broth and 50 μg/mL of kanamycin. The cultures were incubated at 30°C at 250 rpm until their optical density(OD) at 600 nm was 0.6–0.8. The cultures were then induced with 0.5 μM of Isopropyl β-d-1-thiogalactopyranoside (IPTG) and further incubated for 16 h and 16 °C at 150 rpm.

The 4 l of recombinant SHuffle T7 cell culture was centrifuged for 30 min at 6000 rpm. The pellet was then resuspended in 25 ml of 1 × Phosphate-buffered saline(PBS) with 8 M urea. The solution was incubated on ice for two hours with rocking before it was sonicated for a total of 22 min, with a pulse setting of 5 s on and 5 s off. Then, the product was centrifuged for 30 min at 4 °C at 10,000 rpm. The supernatant containing the P1395WT protein was kept.

Then, metal affinity chromatography column was prepared by adding 4 ml of Ni-NTA agarose beads into the column. The beads were washed with 8 ml of milli Q water twice before 8 ml of 1XPBS with 8 M urea was added to the column. All the supernatant from the previous step was poured into the column. The column was capped and incubated for 30 min. The column was washed with the following solutions in sequence: 8 ml of 1XPBS with 8 M urea, 8 ml of 1X PBS with 160 μM NaCl and 8 ml of 1XPBS. Thereafter, the Ni-NTA beads were incubated with 1X PBS with 1 mg/mL 3C protease for 16–18 h overnight at room temperature. After that, the protein was eluted out and cleaved by 3C protease. 250 μM of Imidazole was added to the Ni-NTA agarose beads and the eluate was collected immediately. A 10X dilution of the eluent was done using 1X PBS buffer.

The sample was then filtered using a 0.45 μM pore size filter. High Performance Liquid Chromatography(HPLC) and mass spectroscopy(MS) were run. HPLC was ran with an ACE 5 C18-300 250 × 4.6 mm for eluate one and Jupiter 5u C18 300A New Column 250 × 10 mm for eluate two.

C. *Part One: Sodium Dodecyl Sulfate-Polyacrylamide Gel Electrophoresis (SDS-PAGE)*

10 µl of sample was taken after each extraction or purification step, mixed with 2.5 µl of 6 × Purple Loading Dye from NEB, and pipetted into a 12-well SDS-PAGE gel. 10 µl of Precision Plus Protein™ Standards (Dual Colour) ladder and Buffer tris-glycine Sodium dodecyl sulfate (SDS) were used. Gel electrophoresis was then run for 45 min at 150 V. After confirmation of the positive gel results, we freeze dry the proteins from the pure HPLC fractions.

D. *Part One: Enzymatic Assay*

An enzymatic assay was conducted on P1395 WT and P1395 mutant proteins.

Firstly, a reaction buffer of 50 µM Tris pH 7.4, 0.15 µM NaCl, 0.002 nM $CaCl_2$ was prepared and used to dilute the concentrations of the proteins.

Then, ten wells in a 96-well plate were loaded with different concentrations, in nM, of P1395 proteins, at 300, 90, 30, 9, 3, 0.9, 0.3, 0.09, 0.03and 0.009. Another two wells were loaded with only FXIa and S2366 and served as a control. To each well, 0.75 nM of Factor XIa(FXIa) was added. P1395 and FXIa were then incubated for 45 min. After 45 min, a substrate, S2366, of concentration 3 µM was added. Immediately, OD_{405} of each of the wells were recorded and plotted on a graph of absorbance against time. From there, the Vmax (OD/hr) numerical values and subsequent percentage of inhibition, which corresponds to the effectiveness of the inhibitor, were computed.

E. *Part Two: Synthesis Of Linker Peptides*

Different lengths of linker peptides were synthesized to bind two P1395WT monomers together, forming a dimeric inhibitor. Firstly, 0.10-Resin Swelling(HS) was adopted. Amino acids were subsequently added in the respective sequence using 0.10-Single Coupling(HS), followed by 0.10-Final deprotection(HS). Addition of Cysteine via 0.10-Single 50 °C 10 min Coupling (HS) was then performed. For L25 onwards, the addition of cysteine was performed via 0.10-Double 50 °C 10 min Coupling (HS). For the last 20 amino acids of each sequence, the amino acids were added using 0.10-Double Coupling(HS).

10 ml of Dichloromethane(DCM) was added to the resin transferred into a filter tube. The accent system was then adopted for drainage of the DCM. The process was repeated with 10 ml of methanol.

For each protein, 5 ml of cleavage cocktail was prepared using TFA, milliQ water, TIS and DODT in the ratio of 37:1:1:1. A magnetic stirrer was added to the cocktail and resin and left to spin for three hours. The system was adopted to drain the cocktail into a tube, which facilitated collecting of the desired protein.

After 3 h, 40 ml of cold diethyl ether was added for the peptide to precipitate out. It was centrifuged at 3000 rpm for 3 min, which allowed for the collection of the peptide as a pellet at the bottom. HPLC analysis using ACE C18 5µ 300 Ångstrom 4.6 × 250 µM reverse phase column and MS was then conducted using a similar mechanism as above, keeping the relevant HPLC fractions.

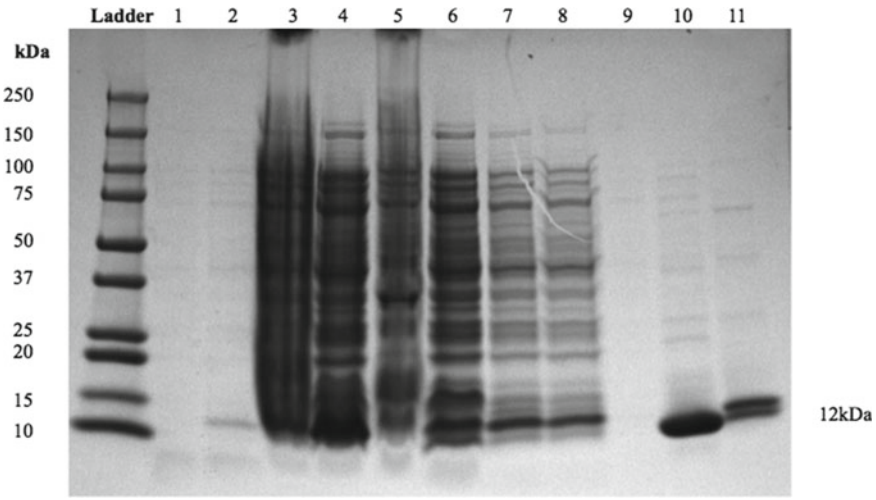

Fig. 1 .

F *Part Two: Conjugation Of Linker Peptides To P1395 WT*

The linker peptides with varied lengths, which were synthesized previously, were mixed. These linker peptides included L19, L13, and L17, with FXIa and P1395 proteins in a buffer solution. For this step, 120 nM of each length of protein was incubated, together with 60 nM of FXIa and 240 nM of P1395WT for 48 h at room temperature. The buffer used was 50 μM Tris pH 7.4, 0.15 μM NaCl, 0.002 nM $CaCl_2$. Finally, an analysis by LC-MS using a reverse-phase C18 Accucore RP column was conducted.

5 Results

A. *P1395 Sequence AVA0421-P1395 (WT)*[1]
B. P1395 Sequence AVA0421-P1395 (Mutant)[b]:
MAHHHHHHMGTLEAQTQ/ [1] GP…**S**…TY
C. *SDS-PAGE*
Figure 1 shows the successful expansion and purification of P1395 WT protein was purified and observed as the 12 kDa bands in the eluate(lane 10) and imidazole(lane 11) fractions. Lane 1 and 2 shows that there is no protein present before and after induction respectively. Lane 3 was taken after sonication, releasing all protein products present in the cell. Lane 4 shows most protein was present in the soluble fraction after centrifugation, and this is supported by lane 5 which shows

[1] sequence of the protein is not disclosed as intellectual property is pending:
MAHHHHHHMGTLEAQTQ/[2]GP…**C**…TY

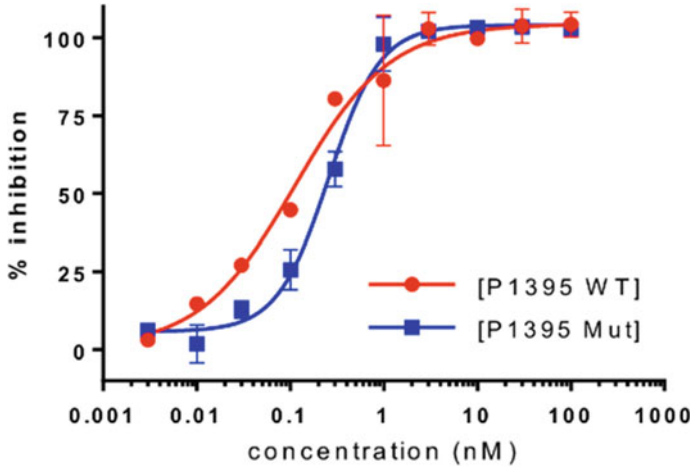

Fig. 2 Dose response curve of the percentage inhibition of FXIa against the concentration of P1395WT and mutant

minimal protein loss in the insoluble fraction. Lane 6 is the flow through during metal affinity chromatography, where non-P1395WT proteins are removed from the column. Lane 7–9 are the washes conducted.

D. Enzymatic Assay
Figure 2 shows the IC_{50} value of P1395 WT is 0.112 and IC_{50} value of P1395 Mutant is 0.257, which is a two-fold drop in activity of P1395. The values of Vmax are the same as the OD_{405} per hour, which is the reaction rate when the enzyme FXIa is fully saturated by substrate S2366, over time (OD_{405}/hour). The percentage inhibition was calculated by using the following formula- $z\frac{V\max(control)-V\max(sample)}{V\max(control)}\times 100\%$. The percentage inhibition against the various concentration of P1395 was plotted using the calculated values to obtain the dose response curve.

E. *PEPTIDE LINKER SYNTHESIS*
Table 1.

6 Discussion

A. *Successful Extraction Of P1395 WT Protein*

SDS-PAGE analysis revealed that P1395 WT was successfully expressed. The successful expression of P1395 was evident in the heightened thickness of the band on the gel at the expected 12 kDa size upon induction by IPTG, which demonstrates overexpression of the P1395 WT protein (Fig. 1). As such, it can be concluded that expression and purification of P1395 WT was successful.

B. *Enzymatic Assay Revealed Two-Fold Drop In FXIa Activity*

Table 1 Success rate of the linker protiens synthesized, ans tested for successful conjugation with the P1395 inhibitor[a]

Name	Molecular weight (g/mol)	Successful synthesis
L9[d]	767.79	No
L13[d]	1026.02	No
L17[d]	1284.84	No
L21[d]	1542.50	No
L25[d]	1800.72	No
L29[d]	2059.00	No
L33[d]	2317.20	No
L9[e]	809.87	Yes
L13[e]	1082.13	Yes
L17[e]	1354.39	Yes
L21[e]	1626.65	Yes (minute)
L25[e]	1898.91	No
L29[e]	2171.18	No
L33[e]	2443.44	No
L25[f]	1989.00	No
L29[f]	2291.28	No
L33[f]	2563.55	No

[a]Fmoc-based solid phase peptide synthesis(gly) was done with 0.17 substitution
[b]Fmoc-based solid phase peptide synthesis(ala) was done with 0.69 substitution
[c]Fmoc-based solid phase peptide synthesis(ala) was done with 0.48 substitution

As evident from the P1395 WT and mutant sequence, the only distinction observed is the last cysteine in the sequence, which was modified into a serine, resulting in merely six cysteines present in the mutant sequence. The presence of six cysteines facilitated the formation of three disulphide bridges, therefore increasing the stability of the inhibitor. In the enzymatic assay, FXIa catalysed the hydrolysis of S2366 into para nitroaniline, which was detected at 405 nm absorbance. From the IC_{50} value, a two fold drop of activity from 0.112 to 0.257 nM from the WT to mutant sequence was observed (Fig. 2). This indicates that the P1395WT is more effective at inhibiting FXIa when compared to P1395 Mutant. However, even though there is a drop in the P1395 Mutant activity, the IC_{50} value of 0.257 nM still suggests a strong inhibiting nature of the mutant. Hence, P1395 Mutant which should be further pursued as a possible anticoagulant drug.

Further analysis on the stability of the P1395 mutant and subsequent contrasting with P1395 WT could be conducted. This would provide firm justification that P1395 mutant is more stable than P1395WT as was inferred from the removal of the thiol group. Further stability analysis via LCMS analysis of both inhibitors over time could

be performed to observe degradation or formation of side products. More extensive enzymatic assays could be conducted to ensure reliable, consistent results.

C. *Unsuccessful Peptide Linker Synthesis*

Initially, it can be seen that the repeating sequence used was "GSGG" across the linker peptides from L9 to L33. However, when HPLC and MS were ran, the purity of the product was extremely low (less than 30% of overall proteins present). It was deduced that this was possibly due to the fact that the repeating sequences caused the probability of the addition of the next amino acid to be significantly lowered. Hence, we introduced alanine into the sequence to increase the sequence variability. We also used a resin with a higher substitution value of 0.69, to increase the probability of a correct sequence being synthesized. This resulted in the successful synthesis of L9–L21. For the larger peptide linkers, the product purity was still low(less than 40% of overall proteins present). Since these peptides are longer, more variability was included in the 3rd run, by alternating "SAGG" and "SASG" sequences until it reached the desired length. The resin was also changed to one with a lower substitution value of 0.48 to prevent inter-peptide interactions. However, the HPLC and MS results still showed low purity levels. In the future, perhaps more unique amino acids are needed for longer sequences or different resins should be used to optimize the conditions.

D. *HPLC Analysis Indicated Unsuccessful Conjugation*

The HPLC analysis observed after mixing revealed negative results. There are two major peaks, which correspond to the mass of a P1395 monomeric inhibitor and dimeric inhibitor without the linker peptide, of 8728 and 17,456 molecular weight respectively, in that order. We were unable to form a dimeric inhibitor with the linker peptide and hence unable to test which peptide length will best to form a dimeric inhibitor for factor XIa. To increase the likelihood of conjugation of the linker peptide and P1395 WT, conditions need to be further optimized. This could possibly be done by altering the pH, temperature or by adding oxidizers and redox shufflers to make the formation of disulphide bonds more kinetically and thermodynamically favourable.

Finally, even though these solutions are mutually exclusive at this stage, the potential for the two approaches to converge through further engineering solutions remains. It is very highly probable that after finding out the optimum peptide linker length, we could clone the P1395WT gene and add residues within the two domains. This allows for the transcripted protein to be a dimer with the peptide linker, so there is no need for conjugation afterwards. Hence, a dimeric, bivalent inhibitor of FXIa that is stable and efficient could be formed.

7 Applications

This study has prominent applications to coagulation disorders.

Quantitative results revealed that in the case of the P1395 mutant inhibitor, stability is marginally improved from the mutation which resulted in removal of the free thiol group. In the case of the P1395 WT, even though P1395 WT was unable to conjugate successfully with the linker peptide currently, with optimized conditions it could be completed to form a dimeric, bivalent inhibitor. This inhibitor could potentially be highly efficient since FXIa is also dimeric.

In both cases, the P1395 inhibitor could be adopted to inhibit FXIa. Hence, when adopted as an anticoagulant drug, minimal bleeding risk would be present, which is critical for drugs used over long time periods. This is an important step forward in cardiology and therapeutics, for the development of the first anticoagulant drug with low bleeding risks.

8 Conclusion

A. *Part One*

As seen from the IC_{50} value, even though there is a two fold drop of activity from the WT to mutant sequence, this drop is very minimal. Thus, this indicates that the mutant is still indeed a strong inhibitor and we could pursue this as a possible anti-coagulant drug provided the compromise between activity and stability of inhibitor is insignificant.

B. *Part Two*

We were unable to test which linker protein will best form a dimeric inhibitor for factor XIa, owing to the fact that the linker protein was not compatible with the P1395 monomers due to difference in size. However, we understand that changing the concentration ratio of P1395 monomers or linker proteins could produce better results. Finally, we believe that if P1395 were to dimerize successfully and effectively inhibit FXIa, it could prove to be more cost-effective as compared to warfarin and heparin, opening up many possibilities in the healthcare industry in the aspects of medical devices and coagulation disorders.

Acknowledgements T. I. and M. Y. thank Professor Koh Cho Yeow and his lab for mentoring us throughout our research journey. We also thank the National University of Singapore, School of Biological Sciences, S2, for providing us with the resources to carry out this project.

References

1. Singapore Statistics. (n.d.). Retrieved from https://www.myheart.org.sg/my-heart/heart-statistics/singapore-statistics/.
2. Al-Horani R. A. and Desai R.U. (2017) Factor XIa inhibitors: A review of patent literature, pg 1–2

3. VectorBase. Ixodes scapularis. (2019, June 25). Retrieved from https://www.vectorbase.org/organisms/ixodes-scapularis.
4. WebMD. Myocardial Infarction (Heart Attack) Causes and Warning Signs. (2019, July 2). Retrieved from https://www.webmd.com/heart-disease/understanding-heart-attack-basics#1.
5. Sig, A. K., Guney, M., Guclu, A. U., & Ozmen, E. (2017). Medicinal leech therapy—an overall perspective. *Integrative Medicine Research*, *6*(4), 337–343.
6. Boston Scientific. What is coronary artery disease and what causes it? (n.d.). Retrieved from https://www.bostonscientific.com/en-US/patients/health-conditions/coronary-artery-disease.html.
7. Weber M., Steinle H., Golombek S., Hann L., Schlensak C., Wendel H. P. and Avci-Adali M. (2018) Blood-Contacting Biomaterials: *In Vitro* Evaluation of the Hemocompatibility, Frontiers in Bioengineering and Biotechnology, Volume 6:99.
8. Rosano, G.L and Ceccarelli, E.A (2014) Recombinant protein expression in *Escherichia coli*: advances and challenges, Frontiers in Microbiology, Volume 5:172.
9. Tanaka-Azevedo A. M., Morais-Zani K.,Torquato R. J. S., and Tanaka A. S. (2010) Thrombin Inhibitors from Different Animals, Journal of Biomedicine and Biotechnology, Volume 2010:641025.
10. Wilson A. C., Neuenschwander P. F. and Chou S. F. (2019) Engineering Approaches to Prevent Blood Clotting from Medical Implants, Archives in Biomedical Engineering & Biotechnology, Volume 1:2.

Computational Studies of Cell Durotaxis on Extracellular Matrix Rigidity Gradients as a Model for Wound Healing and Fibrosis

Chieng Ling Poh

Abstract Durotaxis is the phenomenon where cells migrate towards stiffer regions on a substrate surface, and has important significance in biological processes and diseases such as wound healing or fibrosis, where rigidity gradients of the extracellular matrix may influence cell migration. However, studies on durotaxis are often limited by the difficulty in creating substrates with smooth stiffness gradients or creating very soft substrates and gels for experimentation, hence the need for a computational model. In this study, we developed a computational model for simulation of cell durotaxis, and analysed the behaviour of durotactic efficiency in response to varying stiffness gradients, and the dependence of durotaxis on absolute rigidity of substrates. The model involves a cell consisting of ordered or randomly aligned actin filaments, which exert traction forces on the substrate causing cell migration. It was found that durotactic efficiency increases with increasing substrate stiffness gradient, and there exists a threshold stiffness gradient required in order to induce effective durotaxis. Besides rigidity gradient, absolute rigidity also affects durotaxis. As absolute rigidity increases, efficiency of durotaxis first increases then decreases, with durotaxis being the most efficient on substrate of intermediate stiffness. Increased extracellular matrix rigidity is correlated with increased severity of disease, thus increased durotactic efficiency leads to increased number of cells migrating to the area for healing and repair. A threshold gradient for durotaxis may be necessary to prevent a noisy substrate of fluctuating rigidity from being interpreted as a rigidity gradient, thus gradient needs to be high enough for durotaxis.

Keywords Durotaxis · Rigidity gradient · Computational model

1 Introduction

Cells have long been demonstrated to migrate towards stiffer regions on a substrate surface in a phenomenon known as durotaxis [1, 2]. Such cell migration has important

C. L. Poh (✉)
NUS High School of Mathematics and Science, Singapore, Singapore
e-mail: h1510105@nushigh.edu.sg

H. Guo et al. (eds.), *IRC-SET 2020*,
https://doi.org/10.1007/978-981-15-9472-4_14

biological significance, as rigidity of the extracellular matrix (ECM) may influence cell migration in biological processes such as wound healing and diseases such as fibrosis. Increase in rigidity of the ECM during wound healing [3] may influence the migration of cells necessary for wound healing towards the site of the wound, which may in turn influence the healing process and formation of new tissue. Stiffening of tissue and the ECM in fibrosis [4] may also influence migration of cells involved in fibrosis. Although the exact mechanisms involved in cell durotaxis are still unknown, substrate rigidity has been known to influence various aspects of the cell, including actin polymerization [5, 6], focal adhesion stability [2, 5–7], and ability to generate traction forces [2, 5]. Stiffer substrate is known to correlate with increased ordering of actin filaments [5], higher actin polymerization [6, 8], more stable focal adhesions [5–8] and increased traction forces [2, 5]. These responses can be used to construct a computational model for cell durotaxis. The cell can be modelled as a circle containing many rods representing actin filaments. On stiff substrates, actin filaments are increasingly ordered in one direction, while on softer regions, the actin filaments are less ordered and arranged randomly in different orientations. The cell exerts traction forces on the substrate through actomyosin contractions through the actin filaments, and by Newton's third law, the substrate exerts an equal and opposite force on the cell. As the actin filaments are more ordered in a single direction on stiff substrates, the traction forces from each actin filament add up to produce a large net force, while on softer substrate, the force vectors in different directions cancel out to produce a small net force. The greater force experienced by the cell on the stiff region allows the cell to be pulled towards the stiffer region on the substrate. A schematic diagram of the cells and actin filaments can be found in Figs. 2 and 3 in the appendix. Though cells have been known to migrate towards stiffer substrate along rigidity gradients [1, 7, 9], little has been done to analyse the behaviour of durotactic efficiency in response to varying gradients, such as investigating the existence of a threshold gradient or the rate of change of durotactic efficiency in response to changing rigidity gradients. In addition, not many studies have been done to investigate the dependence of durotaxis on the absolute rigidity of substrates, instead of just considering the rigidity gradient. Even so, the scope of these studies are usually limited by the difficulty in creating substrates with completely smooth stiffness gradients [10], or creating very soft substrates and gels for experiments, thus not much analysis is done on very soft substrates. Hence, a computational model is relevant and necessary for us to predict the results of these experiments that are difficult to replicate in real life. In this study, we evaluated a durotactic index (DI) to represent the durotactic efficiency of cells on a substrate, and used our computational model to investigate the behaviour of DI with changing substrate stiffness gradients, and dependence of DI on absolute rigidity of the substrate (Fig. 1).

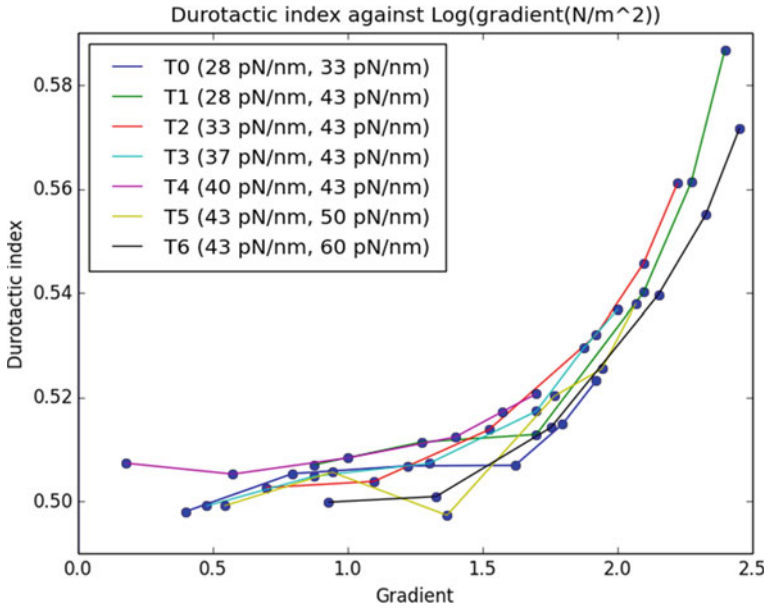

Fig. 1 Summary graph of Durotactic index against rigidity gradient at different absolute rigidities. The softest and stiffest stiffnesses of the gradients for each condition T0–T6 are shown. Each data point is the average DI of 2000 simulated cells

2 Methods

We modelled a cell as a circle of radius 30 μm on a substrate consisting of a soft and stiff region located a horizontal distance away from each other, with a uniform stiffness gradient between the two regions. The position of the cell is represented in a coordinate system with x = 0 equidistant from both regions. The stiff region is always on the right of the soft region. Let x1 and x2 be the x-coordinates of the boundaries of the soft and stiff regions respectively in μm, so that $x1 = -x2$ (x2 is positive and x1 is negative). Let E1 and E2 be the stiffness of the soft and stiff regions respectively in pN/nm, let x be the x-coordinate of a point and let E be the stiffness at that point. When $x < x1$, $E = E1$. When $x > x2$, $E = E2$. When $x1 < x < x2$, stiffness varies linearly with x, so $E = \frac{E2-E1}{x2-x1}x + \frac{E1+E2}{2}$. $\frac{E2-E1}{x2-x1}$ gives the magnitude of the stiffness gradient in kN/m^2.

A. *Generation of rod filaments*

Each cell has 35 rods of length 15 μm each, representing actin filaments. The centre of each rod is positioned randomly within the cell. The circle formed by the rod when rotated 360° about its centre should be completely within the cell.

B. *Generation of rod filament angles*

Substrate stiffness E at the rod centre is used to calculate an order parameter S of the rod. Actin filaments are more ordered on stiffer substrate, so S increases as E increases [5]. From experimental data from Fig. 4e of Gupta et al. [5], we approximate a function of S against E that fits the experimental data [5]. Thus we define the order parameter S to be increasing linearly from 0 at 30 pN/nm to 0.65 at 100 pN/nm, with S = 0 for E below 30 pN/nm. S at any E above 30 pN/nm can be obtained by $S = \frac{13}{1400}E - \frac{39}{140}$. A graph of S against E can be found in Fig. 4 in the appendix. The angle for each rod is sampled from a von Mises distribution with $\mu = 0$ and $\frac{1}{\kappa} = 9.841e^{-28.79S} + 2.324e^{-4.183S}$. This is the angle between the rod and the positive x-axis. Output angles above 90° or below −90° are adjusted by subtracting the angle from 90° and −90° respectively, so that all angles are adjusted to be within −90° to 90°.

C. *Generation of traction forces*

E at the rod is now defined as the stiffness at the end of the rod further away from the cell centre, instead of at the rod centre. Using experimental data from Fig. 4g of Gupta et al. [5], we approximate a function of traction force against E that fits the experimental data obtained [5]. From the data, we can define the traction force as

$$\begin{aligned} F_{traction} = &\left(-2.998 \times 10^{-10}\right)E^6 + \left(9.941 \times 10^{-8}\right)E^5 \\ &- \left(1.297 \times 10^{-5}\right)E^4 + 0.0008521E^3 - 0.03028E^2 \\ &+ 0.6138E + 0.02629 \end{aligned}$$

where E is in pN/nm and force is in pN. A graph of this function can be found in Fig. 5 in the appendix. This is the traction force associated with that actin filament, exerted by the cell on the substrate. It points from the end of the rod further away from the cell centre to the end of the rod closer to the cell centre. The x- and y- components of the force vectors from all 35 rods are summed to obtain the total force by the cell in the x and y directions.

D. *Generation of random forces*

A random force adds random motion to the cell. A θ is sampled from a von Mises distribution with $\mu = 0$ and $\kappa = 10^{-5}$. The x- and y-components of the force (in pN) are defined as $Fx_{random} = 18.648cos(\theta)$ and $Fy_{random} = 18.648sin(\theta)$ respectively.

E. *Moving the cell*

The total force exerted by the cell consisting of the traction forces and random force are summed to obtain the total force F_{total} in the x and y directions. The force exerted on the cell by the substrate is of equal magnitude but opposite in direction. By manipulation of Eq. (2) of Zeng et al. [11], we obtain an equation describing the displacement of the cell depending on force exerted [11]. Reducing the equation, we define the displacements in the x- and y-directions, Δx and Δy to be $\Delta x =$

$-0.3Fx_{total}$, and $\Delta y = -0.3Fy_{total}$ respectively. The negative signs reflect the fact that the force exerted on the cell is in the opposite direction to the force the cell exerts.

F. *Calculation of durotactic index, DI*

The entire process was repeated 72 times for each cell for a total of 72 time steps. If the position of the cell centre at the start of a time step is within the stiffness gradient range ($x1 \leq x \leq x2$), that time step is included in calculation of DI. The time step is durotactic if the angle of the displacement vector of the cell relative to the positive x-axis, α, falls within a predetermined range of angles. When $0 < cos(\alpha) \leq 1 (-90° < \alpha < 90°)$ as in our model, the time step is durotactic as long as displacement is in the positive x-direction (towards stiffer region). However, a narrower range of values of α can be used if a stricter requirement for durotaxis is desired. The DI of the cell is defined as ratio of number of durotactic time steps divided by total number of time steps (where $x1 \leq x \leq x2$). Greater extent of durotaxis corresponds to higher DI. Since $0 < cos(\alpha) \leq 1$, the expected DI for random motion is 0.5.

G. *Dependence of DI on gradient*

A substrate of some E1 and E2 was subjected to 6 sets of values of x1 and x2 in Figure A2d in the appendix to obtain 6 different rigidity gradients but same rigidity on the soft and stiff regions. x1 and x2 were restricted such that $x2 - x1 \geq 60\ \mu m$, as diameter of the cell is 60 μm and it would be difficult for the cell to feel the change in stiffness along the gradient if one end of the cell reaches the stiff side before the other leaves the soft side and vice versa. For each gradient, 2000 cells were simulated with half starting at x1 and half at x2. The DI of this gradient is the average DI of all 2000 cells. DI was plotted against log (gradient). A logarithmic scale is used for gradients as skewness in values makes the results hard to visualize together. The above was repeated for different E1 and E2 in Figure A2c in the appendix. Thus we obtain 7 plots of DI against log(gradient), each corresponding to a condition T0–T6.

3 Results

A. *Durotactic efficiency increases with rigidity gradient*

Based on the graph obtained, the DI showed a general increasing trend as gradient increases for all conditions. Analysing the cell trajectories of cells in condition T2 on gradients of 167 N/m^2 (DI 0.56, Fig. 6) and 5 N/m^2 (DI 0.50, Fig. 7), cell trajectories on the 167 N/m^2 gradient show migration towards the stiffer region of the substrate (towards the right) compared to cells on the 5 N/m^2 gradient, which showed roughly equal movement of cells in both directions. This confirms that the extent of durotaxis of cells on the substrate did indeed increase due to the increase in gradient.

B. *Existence of threshold gradient required to induce durotaxis*

The different values of E1 and E2 used in the different conditions allow us to compare substrates with same or similar gradients but of different absolute rigidity. From T0 to T6, the absolute rigidity of the substrate becomes stiffer as the average rigidity of the substrate increases. For all conditions, DI stays relatively constant at about 0.5 (indicating random motion) for a range of gradients before it starts to increase exponentially past a certain gradient value. This suggests the existence of a threshold rigidity gradient required for durotaxis to occur.

C. *Durotaxis is most optimal on intermediate stiffness*

Past the threshold, DI generally increases with gradient, but at different rates for different conditions. Substrates of the same gradient but different absolute rigidity have different DI. Thus other than rigidity gradient, absolute rigidity is also a factor in determining the durotactic efficiency of cells on the substrate. For gradients past the threshold, T2 is observed to have the highest DI when compared to other substrates at the same gradient, followed by T4, T3, T1, T5, T6 then T0. Since average rigidity of the substrate increases from T0–T6, durotaxis is most efficient on substrate of intermediate stiffness, and cells on substrates that are softer or stiffer than the optimal stiffness range do not exhibit efficient durotaxis. Generally, the observed trend is that as substrate stiffness increases, durotactic efficiency first increases until an optimal stiffness then decreases as the substrate becomes stiffer. A substrate with higher durotactic efficiency would also be expected to have lower threshold gradient, which is identified by the point where DI starts to increase exponentially after staying constant at about 0.5. From the graph, T2 has the lowest threshold gradient of 12.5 N/m^2 where DI starts increasing, which confirms that T2 has the greatest extent of durotaxis out of all the conditions and that durotaxis is indeed most efficient on substrate of intermediate stiffness. The threshold gradients for the other conditions do not strictly follow the general trend that durotactic efficiency increases then decreases as stiffness increases, but these anomalies may be attributed to random variation.

4 Discussion

Since a greater rigidity difference correlates with increased extent of durotaxis, it is expected that DI increases as gradient increases [1]. For substrates with the same rigidity gradient but different absolute rigidity, we found that as absolute rigidity increases, the general trend is that durotactic efficiency first increases then decreases, with most efficient durotaxis occurring on substrate of intermediate stiffness. To understand this phenomenon, we can look at the functions of the order parameter, S (Fig. 4) which determines how aligned the direction of the traction forces are, and magnitude of traction force, $F_{traction}$ (Fig. 5) against substrate stiffness. On a gradient, the two ends of the cell experience different substrate stiffness, so the different forces experienced in two ends of the cell determines the net force on the cell and thus the direction of cell migration. Since the graph of traction force is concave downwards, as rigidity increases, the difference in the magnitude of traction force decreases for

the same difference in substrate stiffness. Thus the net force on the cell decreases and the DI decreases as absolute rigidity of the substrate increases for the same rigidity gradient. At low substrate stiffness, S stays constant at 0 before it starts increasing linearly at E = 30 pN/nm. Thus for substrate at low rigidities below 30 pN/nm, the reduced difference in the order parameter values leads to decreased extent of durotaxis. Thus for substrates of the same rigidity gradient, durotaxis is most efficient on substrate of intermediate absolute stiffness and efficiency is reduced if the substrate is too soft or too stiff. As substrate rigidity increases, DI first increases until an optimum stiffness, then decreases as the substrate becomes stiffer. The latter trend was also observed by DuChez et al. [9] and Moriyama and Kidoaki [7], when durotaxis was observed to become more efficient as the substrate becomes softer [7, 9]. Due to the different cell types used, the range of substrate stiffness used in observing this trend in their experiments may not overlap with the range used in our simulation, however the trend of durotactic efficiency increasing with decreasing substrate stiffness was still observed. However, the trend observed in our simulation that durotactic efficiency decreases when substrate rigidity further decreases beyond an optimum stiffness was not observed in both of the above mentioned experiments done by DuChez et al. [9] and Moriyama and Kidoaki [7]. This may be due to the difficulty in making soft substrates and gels compared to hard substrates, thus experimentation was not done on soft substrates that are softer than the stiffness ranges used in these experiments, so durotactic efficiency was not observed to decrease when substrate becomes even softer. If further experimentation was done on even softer substrates softer than those used in these experiments, this additional trend may also be observed. However, due to the difficulty in creating these very soft substrates soft enough to observe this trend, we can only use the results from our computational model to predict the results of these real-life experiments.

Our results can also be explained by considering their biological implications in diseases such as fibrosis or wound healing. Increased stiffness gradient of the extracellular matrix is likely to be correlated with increased severity of disease, such as more scarring or having more stiff fibrotic tissue. Hence, more cells are needed to migrate to the area for increased formation of new healthy tissue for healing and repair, so durotactic efficiency increases on higher rigidity gradients. The existence of a threshold gradient to induce durotaxis ensures that a noisy substrate with randomly fluctuating rigidity will not be misinterpreted as a substrate with a low rigidity gradient, thus gradient needs to be of a high enough value in order to induce durotaxis.

5 Conclusion

In conclusion, we have confirmed the existence of a threshold rigidity gradient that is required in order to induce effective durotaxis. Cells undergo random motion at low rigidity gradients, and past a certain threshold gradient, durotactic efficiency starts to increase with gradient. Absolute rigidity of the substrate also affects the

extent of durotaxis of cells. As absolute rigidity increases, efficiency of durotaxis first increases then decreases, with durotaxis being the most efficient on substrate of intermediate stiffness. Increase of durotactic efficiency with gradient can be correlated with increased number of migratory cells needed for repair due to increased severity of disease, while a threshold gradient for durotaxis may be necessary to prevent a noisy substrate from being interpreted as a rigidity gradient, thus gradient needs to be high enough.

Acknowledgements Thanks to Dr Chiam Keng-Hwee and Dr Yip Ai Kia from Bioinformatics Institute, A*STAR for the constant guidance and support.

Appendix

See Figs. 2, 3, 4, 5, 6 and 7, Tables 1 and 2.

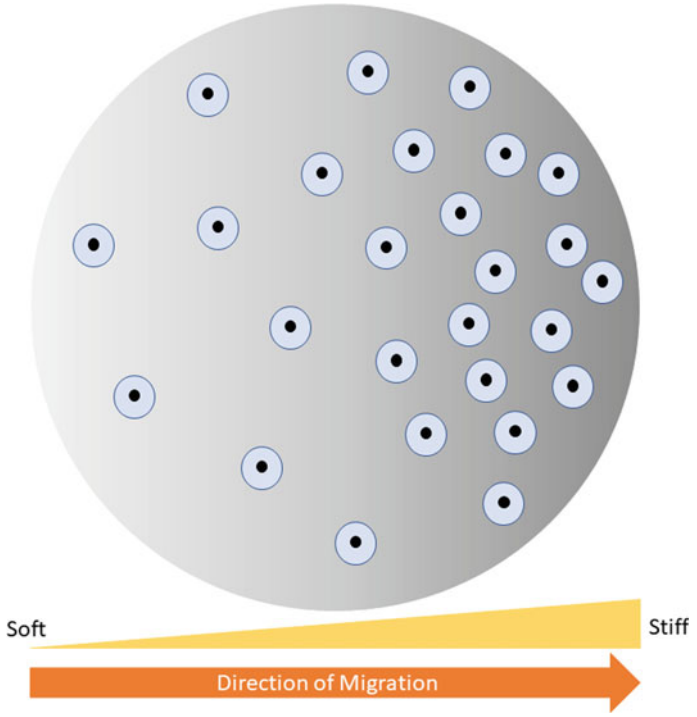

Fig. 2 Schematic diagram of durotactic cell migration of cells towards stiffer substrate on a substrate rigidity gradient

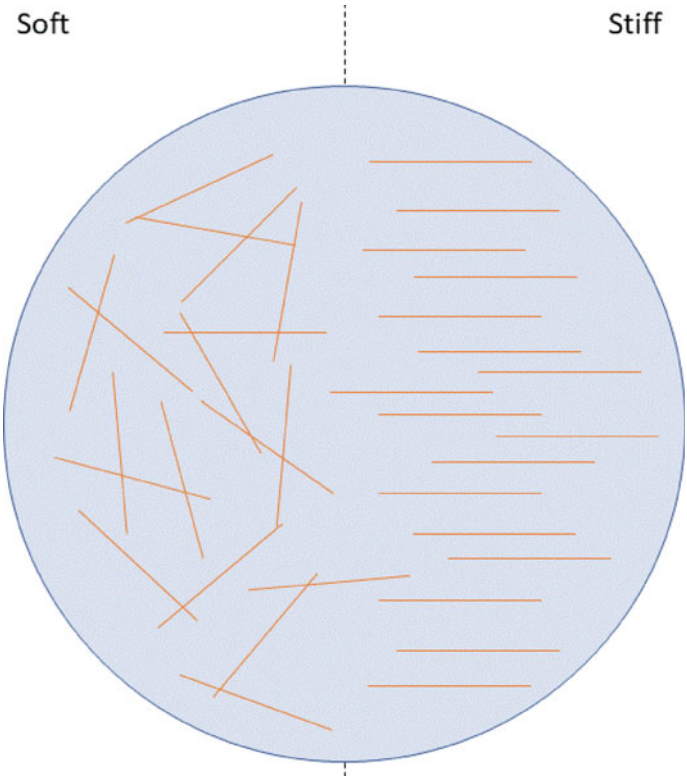

Fig. 3 Schematic of cell and actin filaments. Actin filaments are more ordered on stiff substrate, leading to greater net force on stiffer substrate causing cell migration

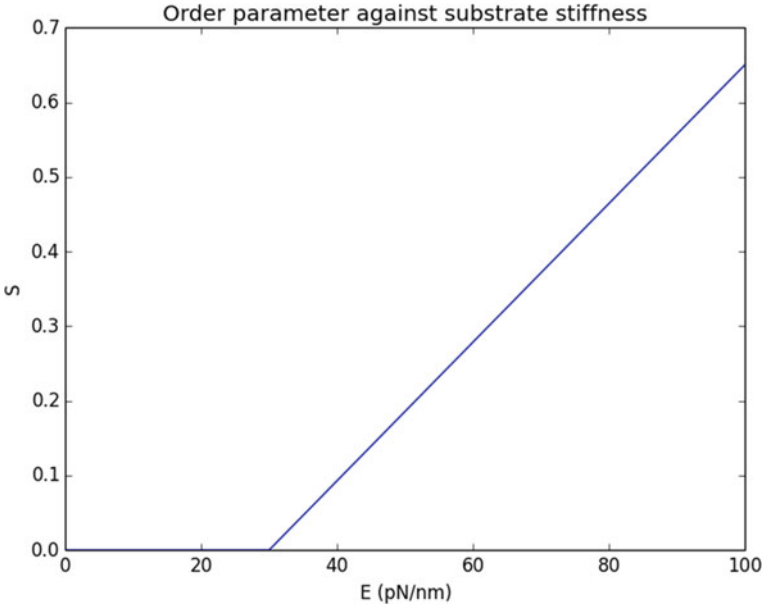

Fig. 4 Graph of order parameter of cell actin filaments against substrate stiffness at cell centre

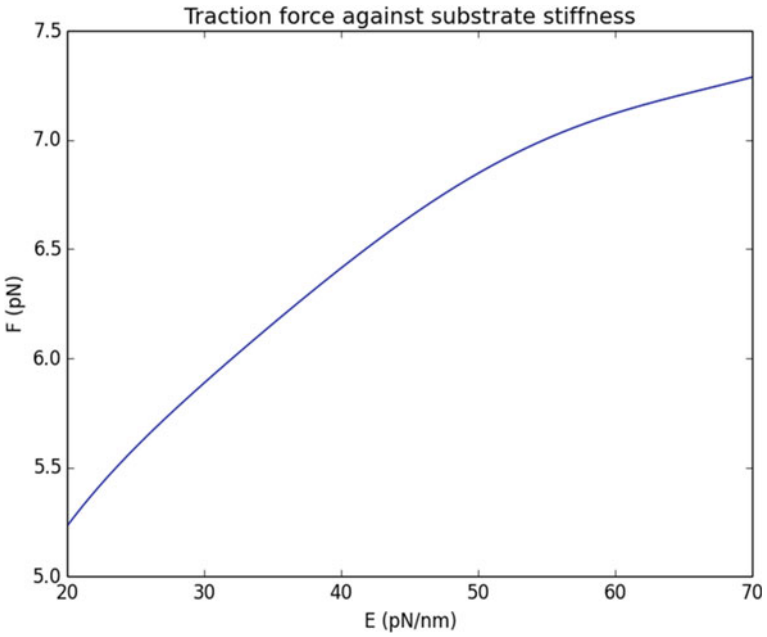

Fig. 5 Graph of traction force exerted by each actin filament against substrate stiffness at actin filament

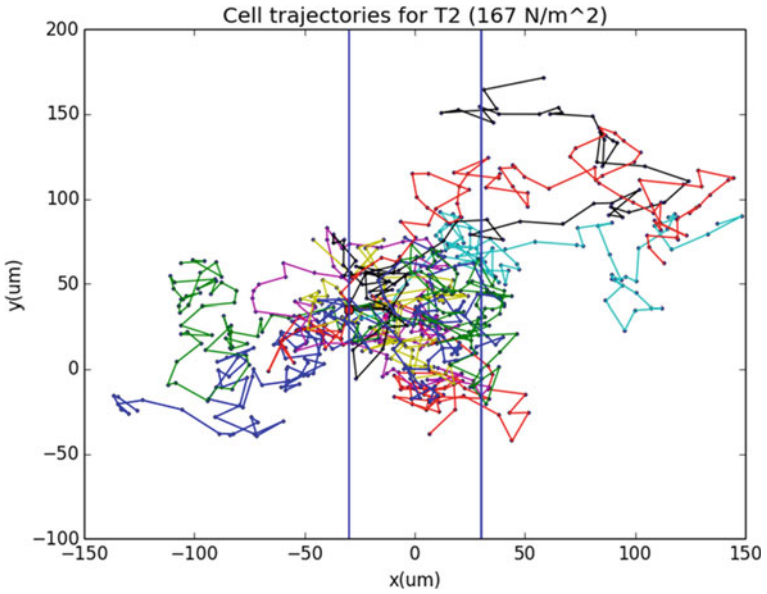

Fig. 6 10 cell trajectories for cells on T2 (between 33 pN/nm and 43 pN/nm) at gradient of 167 N/m^2 starting at x1 (-30 μm). The red circle represents the starting position of all the cells. Durotactic migration towards stiffer region (right side) can be seen

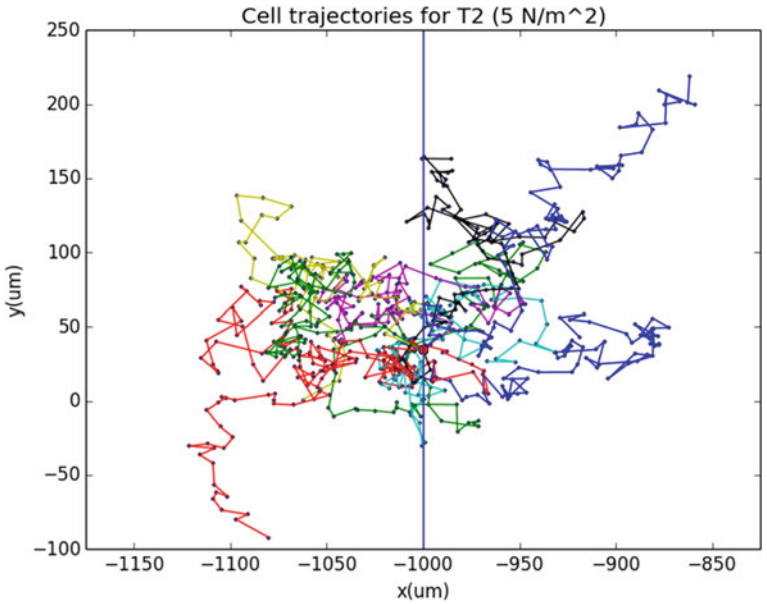

Fig. 7 10 cell trajectories for cells on T2 (between 33 pN/nm and 43 pN/nm) at gradient of 5 N/m^2 starting at x1 (-1000 μm). The red circle represents the starting position of all the cells. Equal migration of cells in both directions towards both soft and stiff regions, so no durotaxis observed

Table 1 E1 and E2 (softest and stiffest rigidities) used for the rigidity gradients at each condition

Condition	E1 (pN/nm)	E2 (pN/nm)
T0	28	33
T1	28	43
T2	33	43
T3	37	43
T4	40	43
T5	43	50
T6	43	60

Table 2 Values of x1 and x2 used (x-coordinates of boundaries of the substrate stiffness gradient region)

x1 (μm)	x2 (μm)
−30	30
−40	40
−60	60
−150	150
−400	400
−1000	1000

References

1. Hassan, A. R., Biel, T., & Kim, T. (2018). Mechanical Interactions between a Cell and an Extracellular Environment Facilitate Durotactic Cell Migration. bioRxiv, 460170.
2. Lo, C. M., Wang, H. B., Dembo, M., & Wang, Y. L. (2000). Cell movement is guided by the rigidity of the substrate. Biophysical journal, 79(1), 144–152.
3. Rosińczuk, J., Taradaj, J., Dymarek, R., & Sopel, M. (2016). Mechanoregulation of wound healing and skin homeostasis. BioMed Research International, 2016, 1–13.
4. Herrera, J., Henke, C. A., & Bitterman, P. B. (2018). Extracellular matrix as a driver of progressive fibrosis. The Journal of clinical investigation, 128(1), 45–53.
5. Gupta, M., Sarangi, B. R., Deschamps, J., Nematbakhsh, Y., Callan-Jones, A., Margadant, F., … & Ladoux, B. (2015). Adaptive rheology and ordering of cell cytoskeleton govern matrix rigidity sensing. Nature communications, 6, 7525.
6. Geiger, B., Spatz, J. P., & Bershadsky, A. D. (2009). Environmental sensing through focal adhesions. Nature reviews Molecular cell biology, 10(1), 21–33.
7. Moriyama, K., & Kidoaki, S. (2018). Cellular durotaxis revisited: Initial-position-dependent determination of the threshold stiffness gradient to induce durotaxis. Langmuir, 35(23), 7478–7486.
8. Hirata, H., Tatsumi, H., & Sokabe, M. (2008). Mechanical forces facilitate actin polymerization at focal adhesions in a zyxin-dependent manner. Journal of cell science, 121(17), 2795–2804.
9. DuChez, B. J., Doyle, A. D., Dimitriadis, E. K., & Yamada, K. M. (2019). Durotaxis by human cancer cells. Biophysical journal, 116(4), 670–683.
10. Sunyer, R., Jin, A. J., Nossal, R., & Sackett, D. L. (2012). Fabrication of hydrogels with steep stiffness gradients for studying cell mechanical response. PloS one, 7(10), e46107.
11. Zeng, Y., Yip, A. K., Teo, S. K., & Chiam, K. H. (2012). A three-dimensional random network model of the cytoskeleton and its role in mechanotransduction and nucleus deformation. Biomechanics and modeling in mechanobiology, 11(1–2), 49–59.

Effects of Hand Soap, Detergent and Dishwashing Soap on Bacterial Microbiome, Sebum and pH of Skin

Kalyani Palaniappan, Li Yu Xin Karin, and Medha Shridharan

Abstract Investigation on the effects of different types of soap (hand soap, detergent and dishwashing soap) on our skin was done to test the effects of different soaps on the density of bacteria commonly found on our skin and how sebum [1] and pH are affected by the microfauna. The research question was "Is it healthy to use laundry detergent or dish soap instead of hand soap/body foam to wash our hands? How does washing hands with different types of soap affect your skin—specifically its bacterial microbiome, sebum and pH?" Experimental results found that dish soap was the most effective in killing *Escherichia coli* (E. coli) bacteria, while laundry soap was the most effective in killing *Bacillus subtilis*; Hand soap B removes the least sebum and that dish soap has the pH closest to skin pH. Dish soap is the healthiest soap to wash our hands with by the criteria we have studied.

1 Introduction

Many people of today's world regularly wash their hands with specialised soaps, designed to moisturise and gently clean their skin. However, some occasionally wash their hands with other soaps such as dish soap and detergents for convenience. We wanted to find out if this will affect the health of our skin in the long term, and if so, how it does.

A microbiome is defined as the community of microorganisms inhabiting a particular environment. The bacterial microbiome on our skin is the community of bacteria commonly inhabiting human skin. We wanted to investigate a particular species of bacteria, *Escherichia coli,* on the skin [2, 3] We also wanted to test the effects of these

K. Palaniappan · L. Y. X. Karin · M. Shridharan (✉)
NUS High School, Singapore, Singapore
e-mail: h1810105@nushigh.edu.sg

K. Palaniappan
e-mail: h1810064@nushigh.edu.sg

L. Y. X. Karin
e-mail: h1810080@nushigh.edu.sg

H. Guo et al. (eds.), *IRC-SET 2020*,
https://doi.org/10.1007/978-981-15-9472-4_15

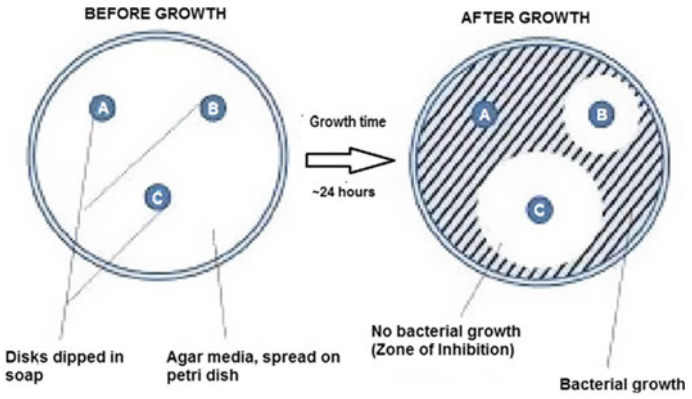

Fig. 1 Experimental design of Phase 1

soaps on a strain of bacteria, *Staphylococcus epidermidis,* which has been found to protect against certain forms of skin cancer [4–6]. However, as this particular species of bacteria was unavailable, we decided to test the effects of these soaps on another type of gram positive bacteria, *Bacillus subtilis* as we thought the soaps would have similar effects on both.

2 Materials and Methods

2.1 Phase 1

Dilute the body foam, dish soap and laundry detergent with DI water in a 1:5 soap to DI water ratio. Wet the punched disks of filter paper with the diluted soaps and DI water. Divide an agar-coated petri dish into 4 sections with permanent marker. In the laminar flow, use the micropipette to pipette 100 μl of the bacteria sample into the agar-coated petri dish. Use an L-shaped spreader to spread liquid *Escherichia coli* sample over the agar. Repeat 6 more times. Make 7 samples with *Bacillus subtilis* instead of *Escherichia coli.* Place the petri dishes in an incubator. Wait for 24 h. Measure the furthest distance from the edge of the stain to the centre of the disk using a ruler. Record results in table [7] (Fig. 1).

2.2 Phase 2

Dilute the body foam, dish soap and laundry detergent with DI water in a 1:5 soap to DI water ratio in a beaker. Use a dropper to add 1 ml of jojoba oil and 1 ml of diluted

body foam to an empty test tube. Shake the test tube for 5 s. Repeat 6 times. Repeat with dish soap, detergent and DI water (negative control), 7 times each. Record results in table.

2.3 Phase 3

Measure the pH of each liquid 7 times using a pH meter connected to a data logger.

2.4 Assumptions Made

We took the longest diameter of zone inhibition. This could indicate a bias if the zone was more of an oblong, irregular shape instead of a circular shape. Thus, we made the assumption that the zone of inhibition is circular in shape. We also made the assumption that there is a negligible amount of foam in the dropper when we measured out the soap for our phases. Due to fungal contamination of Hand A in phase 1.1, Hand B was used for phases 1.2, 2 and 3.

3 Results, Discussions & Implications

3.1 Phase 1.1

Figure 2 shows pictures of two of the results obtained for the *Escherichia coli (E.coli)* bacteria. As shown in Figs 2 and 3 above, dish soap had the largest diameter of the zone of inhibition, with a mean of 19.9 mm and median of 20.0 mm. The mean diameters for laundry, hand A and DI water were 11.6 mm, 11.0 mm and 8.7 mm respectively.

However, the results for dish soap also had the largest standard deviation of 7.180 mm and the largest interquartile range of 13.0 mm. Thus, due to this large variation and range of results, the results can be considered inconsistent. The laundry soap had the smallest standard deviation of 4.686 mm while hand A had the smallest interquartile range of 7.5 mm. From this, we can conclude that the dish soap had the greatest effect on the *E.coli* bacteria and is thus most effective in this phase. However, the inconsistency in the results might indicate possible contamination. The DI water, a negative control, showed some antibiotic properties, which is false. It is also important to take into consideration that the results for the hand soap may not be accurate due to possible fungal contamination.

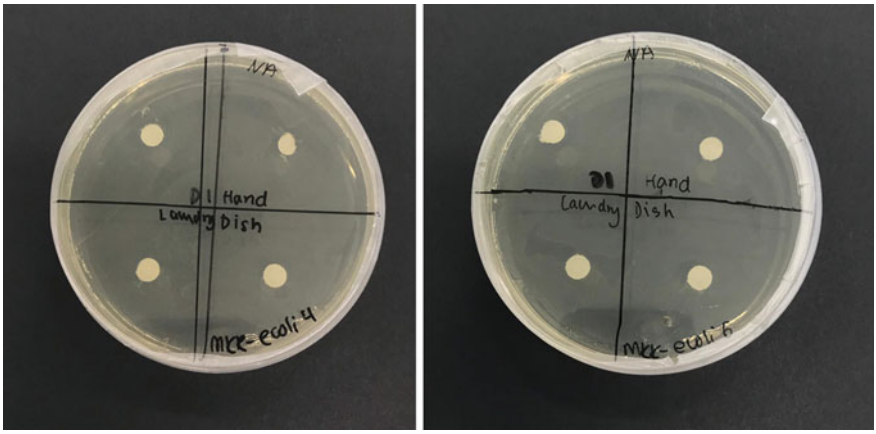

Fig. 2 Results obtained for Escherichia coli bacteria in Trials 4 and 6

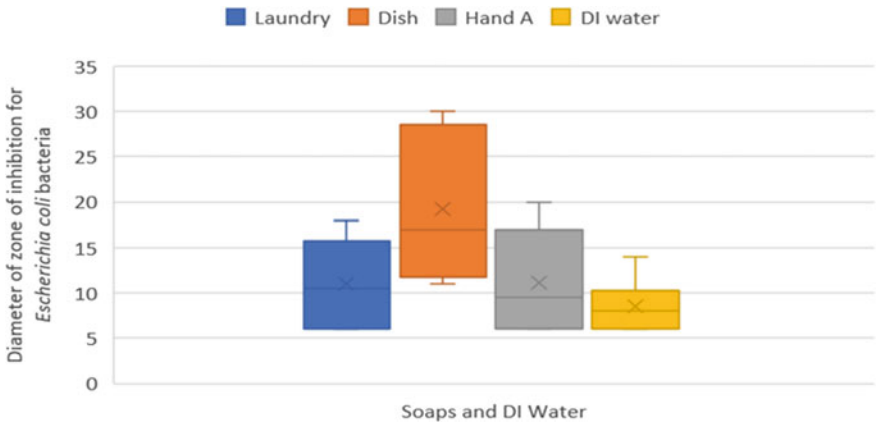

Fig. 3 Box and whisker plot of diameter of zone of inhibition/mm for Escherichia coli bacteria in laundry dish, hand A and DI water

3.2 Phase 1.2

Figure 4 shows the results obtained in trials 5 and 6. Figure 5 shows the results of trial 3, which was nulled during data collection due to the bacteria being improperly spread. As shown in Table 1.2 and Fig. 6 above, hand soap B had the lowest mean and median diameters of their zones of inhibition, at 22.2 mm and 22.0 mm respectively. Hand soap B had the smallest standard deviation of 1.951 mm, followed by laundry soap at 2.115 mm and dish soap at 3.145 mm. Dish soap had the smallest interquartile range of 2.5 mm, followed by laundry at 3.0 mm and hand soap B at 3.8 mm. As the hand soap is shown to have the smallest diameter of the zones of inhibition and has

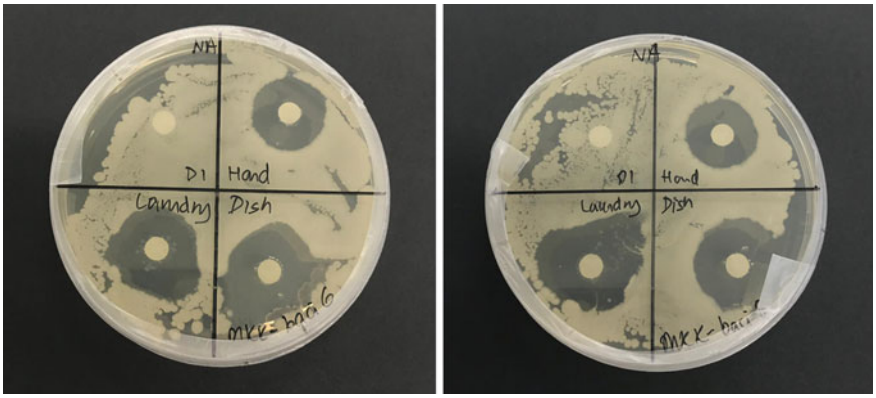

Fig. 4 Results obtained for Bacillus subtilis bacteria in Trials 5 and 6

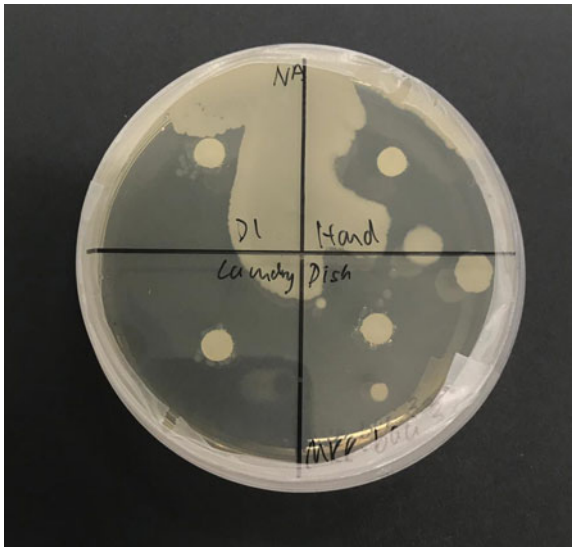

Fig. 5 Nulled results obtained in Trial 3 (Bacteria not spread properly)

a relatively small interquartile range and standard deviation, it is the least effective soap at killing *Bacillus subtilis* bacteria. Additionally, as the negative control of DI water yielded the expected results, the results obtained are reliable. As the hand soap is shown to be the least effective at killing *Bacillus subtilis* bacteria, it is likely to be similarly ineffective at killing other gram positive bacteria, such as *Staphylococcus epidermidis.* If applied directly to the skin, the hand soap B is least likely to affect the bacterial microbiome of *Staphylococcus epidermidis* on the skin. Thus, it would inflict the least negative consequences. This is due to the fact that *Staphylococcus epidermidis* helps to protect the skin from solar ultraviolet (UV) radiation and other harmful bacteria, such as *Staphylococcus aureus.*

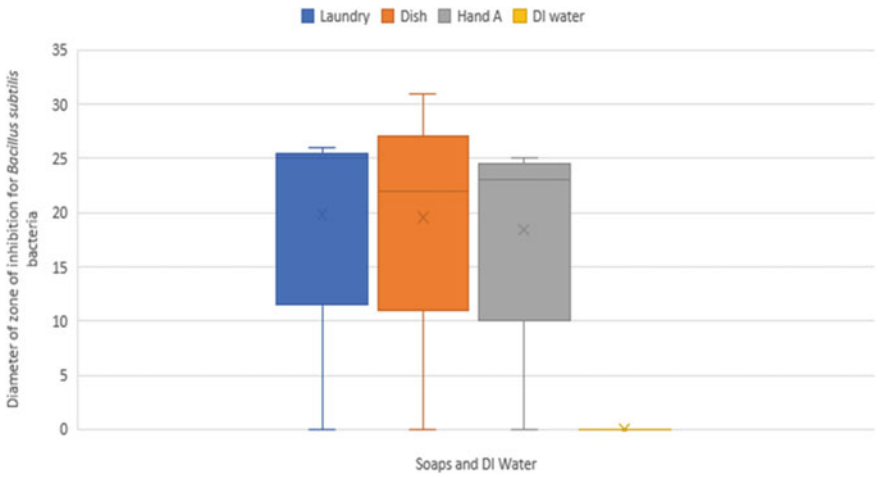

Fig. 6 Box and whisker plot of diameter of zone of inhibition/mm for Bacillus subtillis bacteria in laundry, dish handA and DI water

3.3 Phase 2

For the soaps, the jojoba oil becomes slightly foamy and settles on top of the mixture. For the DI water, jojoba oil remains clear and settles on top of the mixture.

As shown in Fig 7, hand B has the longest median column of foam at 16.0 mm. Laundry, dish and DI water have column lengths of 10.0, 15.0 and 0.0 mm.

Dish soap has the longest mean column of foam at 14.4 mm, closely followed by hand B which has a mean column length of 14.3 mm. Laundry and DI water have mean foam column lengths of 10.0 mm and 0.0 mm respectively. The median is used to compare results to avoid outliers, and there is also a large interquartile range

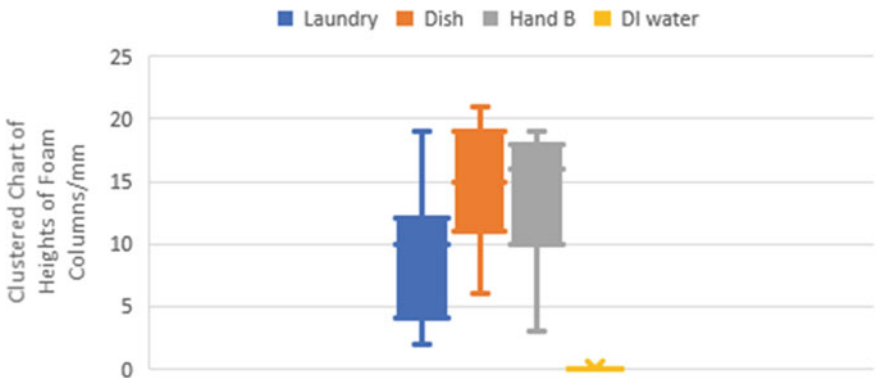

Fig. 7 Clustered chart of heights of foam columns/mm

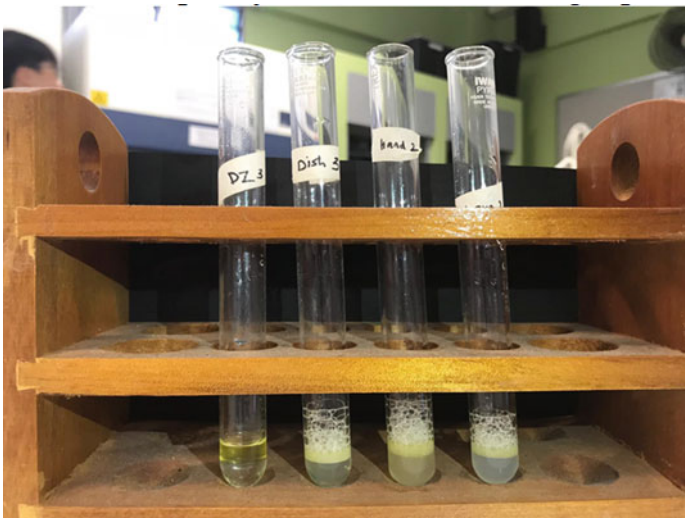

Fig. 8 Examples of results obtained during experiment

for the 3 soaps which shows that the results are quite inconsistent. The jojoba oil in the experiment is used to simulate the sebum found on human skin [8], and the length of the foam column corresponds to how ineffective the soap is at removing the jojoba oil. Thus, the longer the foam column, the lesser the oil removed; therefore, the longest column would be the healthiest to wash hands with. Thus, hand B would be the healthiest to wash hands with (Fig. 8).

3.4 Phase 3

As shown in the results above, laundry detergent has the highest pH, with a mean and median of pH 8.4. The mean pH for dish, hand soap and DI water are pH 5.2, pH 3.5, and pH 6.0 respectively. But as the aim for this phase is to find out the soap whose pH is closest to the skin's pH, which has a pH of 4.0–5.0. Thus, from Fig. 9, we can see that the dish soap has the closest pH to the skin's pH, with a pH of 5.2 [9]. All of the soaps have a small standard deviation that does not exceed 0.1 and a small interquartile range that does not exceed 1, which means that the results gotten are quite consistent. From this, we can conclude that out of all four soaps and DI water, laundry has the highest pH, but dish soap has the closest pH to the skin's pH.

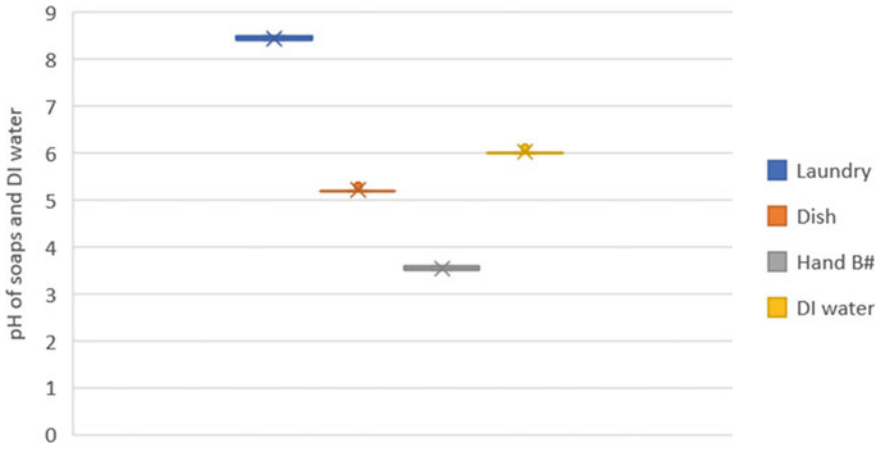

Fig. 9 Box and whisker plot of pH of soaps and DI water

3.5 Limitations and Future Work

We switched hand soap halfway through the experiment as hand soap A had been contaminated by fungi. We could have been more consistent in which hand soap we use. Secondly, the bacteria could have been spread more evenly in Phase 2, and lastly, more samples can be prepared so that more accurate results can be obtained, and attempt to achieve a smaller interquartile range and standard deviation. The small sample size of 7 may not provide the necessary consistency of results needed, thus a larger sample size would make the results of the analysis more reliable.

As dish soap yielded the best results in both phases 1 and 3, we believe this shows that **dish soap** is the healthiest to wash hands with.

References

1. Philip WW (2009) Sebum—an overview. Retrieved 10 July 2019, from https://www.sciencedirect.com/topics/medicine-and-dentistry/sebum
2. Alisa M, Allison M The ABCs of our body bacteria. Retrieved 10 July 2019, from https://www.livescience.com/19913-body-microbiome-nigms.html
3. Regina B (2018) 5 Types of bacteria that live on your skin. Retrieved July 10, 2019, from https://www.thoughtco.com/bacteria-that-live-on-your-skin-373528
4. Atlas of Oral Microbiology (2015) *Staphylococcus epidermidis*. Retrieved 10 July 2019, from https://www.sciencedirect.com/topics/medicine-and-dentistry/staphylococcus-epidermidis
5. Teruaki N, Tiffany HC, Anna MB, Lynnie LT, Sang-Jip N, Karina TS, Wei Z, Julia O, Michael O, William F, Richard LG (2018) A commensal strain of *Staphylococcus epidermidis* protects against skin neoplasia. Retrieved 13 July 2019, from https://www.ncbi.nlm.nih.gov/pmc/articles/PMC5834004/

6. Sabia R, Shahida H, Abeel A (2009) Antibacterial activity of soaps against daily encountered bacteria. Retrieved 9 September 2019, from https://www.researchgate.net/publication/237255933_Antibacterial_activity_of_soaps_against_daily_encountered_bacteria
7. Narang A (2018). Comparing the effectiveness of various hand-sanitizers against *E.coli*. Int J Pharm Sci Res 3(4):16–18
8. Keen S Which oil is closest to body oil? Retrieved 10 July 2019, from https://www.leaf.tv/articles/which-oil-is-the-closest-to-body-oil/
9. Blaak J, Staib P (2018). The relation of pH and skin cleansing. Retrieved 17 July 2019, from https://www.ncbi.nlm.nih.gov/pubmed/30130782

Achieving Low Resistance Ohmic Contacts to Transition Metal Dichalcogenides (TMDCs)

Anirudh Gajula, Wes Wen Jun Lee, Calvin Pei Yu Wong, and Kuan Eng Johnson Goh

Abstract Transition metal dichalcogenides (TMDCs) harbor great potential for use in high performance electronic devices. However, their practical usage has been hindered by a lack of suitable low resistance ohmic contacts, resulting in high contact resistances and low electron mobilities. Our study aims to investigate the performances of alternative contacts strategies such as exfoliated graphite contacts, bottom-up gold (Au) contacts and evaporated gold-capped indium (In-Au) contacts to exfoliated tungsten disulfide (WS_2) by first fabricating field-effect transistors (FET) and later, conducting transfer line measurements (TLM). Our results show that evaporated gold-capped indium/WS_2 contacts achieved the best ohmic performance out of the three contact strategies with a significantly higher field effect electron mobility of 114 cm^2V^{-1} s^{-1} and a lower contact resistance of 462 k Ω μm to few layer WS_2 and a mobility of 5.45 cm^2V^{-1} s^{-1} and contact resistance of 169 M Ω μm to monolayer WS_2 at room temperature, while graphite/WS_2 contacts and bottom up Au/WS_2 contacts yielded poor non-ohmic characteristics with a field effect electron mobility of 0.0409 and 0.00542 cm^2V^{-1} s^{-1} respectively. Our results also show that low resistance ohmic contacts for WS_2 can be achieved through the direct evaporation of gold-capped indium (In–Au) contacts. This is of current relevance and importance as WS_2 has been found to have a plethora of applications from high mobility field-effect transistors to quantum information processing and the formation of the low resistance ohmic contact is a fundamental step towards achieving these goals.

A. Gajula (✉) · W. W. J. Lee
School of Mathematics and Science, NUS High, Singapore, Singapore
e-mail: h1510040@nushigh.edu.sg

W. W. J. Lee
e-mail: h1510150@nushigh.edu.sg

C. P. Y. Wong · K. E. J. Goh
Institute of Materials and Research Engineering (IMRE), Agency for Science, Technology and Research (A*STAR), Singapore, Singapore
e-mail: calvin_wong@imre.a-star.edu.sg

K. E. J. Goh
e-mail: gohj@imre.a-star.edu.sg

H. Guo et al. (eds.), *IRC-SET 2020*,
https://doi.org/10.1007/978-981-15-9472-4_16

Keywords Electrical properties · Van der waals contacts · Nanomaterials · 2D materials · Transition metal dichalcogenides · Tungsten disulfide

1 Introduction

Tungsten disulfide (WS_2), a transition metal dichalcogenide (TMDC), has recently shown great promise in the pioneering field of ultrathin 2D semiconductors. Bulk WS_2 has an appreciable band gap of 1.32 eV, which increases to 1.8 eV for monolayer WS_2 [1] and contributes significantly to its distinct electronic properties and potential to act as ultrathin transistors in various digital circuits. For example, WS_2 has been shown to work as a high mobility field effect transistor [2, 3] and also shown promise in quantum information processing, with the tunable valley polarization that provides an opportunity to control the valley pseudospin [4].

Despite the great promise brought about by the advent of TMDCs, the field remains plagued by significant challenges in the largely unexplored field of solid-state physics. The contacts between 2-dimensional monolayer TMDCs and 3-dimensional metal contacts are known to have high contact resistance, which hinders their potential for practical usage in high-performance devices and microelectronics [5, 6]. Thus, some studies have attempted alternative methods, such as chemical doping methods using lithium fluoride or F4TCNQ to successfully reduce the contact resistance by an order of magnitude [7, 8]. However, it is not clear if these dopants are stable in the long term upon device fabrication.

Recently, it has been shown that weakly interacting van der Waals contacts to TMDC have low contact resistances [5, 9]. Hence, the objective of this study is to investigate van der Waals contacts to WS_2 devices fabricated using 3 different strategies (1) bottom-up graphite contacts, (2) bottom-up gold (Au) contacts, and (3) top-down (evaporated) gold-capped indium (In–Au) contacts. We analyzed these fabrication methods using electron mobilities extracted from field effect transistor measurements and contact resistance extracted from the transfer line measurements. We found that the top-down gold-capped indium (In–Au) contacts resulted in the best device performance with an electron mobility of 114 cm^2V^{-1} s^{-1} and a contact resistance of 462 k Ω μm for few layer WS_2, and an electron mobility of 5.45 cm^2V^{-1} s^{-1} and a contact resistance of 169 M Ω μm for monolayer WS_2.

2 Experimental Design

The first method to achieve van der Waals contacts to WS_2 involves the positioning of the exfoliated WS_2 on top of the two graphite contacts, which are contacted using chromium palladium gold (Cr-Pd-Au) contacts. We expect to have a low contact resistance van der Waals contact between the WS_2 monolayer and the graphite contact. We exfoliated WS_2 monolayers onto Polydimethylsiloxane (PDMS) and transferred

them onto the graphite contacts using a microscope transfer station. The second method involves the direct contact of the monolayer WS_2 on the gold contacts, also using the microscope transfer station. The third method involves the direct metallization of gold-capped indium (In–Au) contacts onto the wafer, using In as a soft non-invasive contacting metal, which has been shown to have a lower contact resistance than directly evaporated titanium gold (Ti–Au) contacts [5]. The direct metallization of gold-capped indium (In-Au) contacts allows for a simple fabrication method for multiple contacts of different channel lengths for the transfer length measurements, which are difficult to achieve using bottom up contacts.

3 Methodology

Figure 1 above shows the device fabrication process for the three types of devices. The exfoliation of WS_2 monolayer flakes was carried out using an adhesive tape (Ultron) onto a polymer layer of polydimethylsiloxane (PDMS, Gelpak X4) from a WS_2 crystal (2D semiconductors, Inc). The identification of the WS_2 monolayers was carried out with an optical microscope (Olympus BX60) using the optical contrast method. Graphite flakes were exfoliated from highly oriented pyrolytic graphite (SPI) onto a 285 nm SiO_2 coated silicon wafer and similarly identified through an optical microscope (Olympus BX60).

Contacts to the graphite flakes were fabricated using electron beam lithography (EBL). First, Polymethyl methacrylate (PMMA) A5 was spin coated onto the exfoliated flakes at 4000 rpm for 90 s. Next, the PMMA was patterned by electron beam lithography (EBL), using an ELS-7000 Elionix at 100 kV, and developed in a 1:3 ratio of methyl isobutyl ketone (MIBK) and isopropyl alcohol (IPA) for 70 s. Then, Cr-Pd-Au contacts were deposited using a Denton Explorer 14 e-beam evaporator at a base pressure of 2E-7 mbar. Lift off was carried out in acetone for 2 h. The graphite break junction of 5 μm for contacting WS_2 was fabricated by etching the exfoliated graphite flake. The exposed areas of the graphite flakes through the PMMA mask were etched off via oxygen-plasma etching at 50 W and 50 mTorr for 60 s. This created graphite contacts that were separated by a 5-micron gap.

The transfer of the WS_2 flakes from the PDMS polymer to the silicon wafer or the graphite break junction was done through a PDMS dry transfer method [10], which involved the mounting of the glass slide containing the WS_2 flakes onto a micromanipulator. The receiving substrate was then heated to a temperature of 80 °C, and the glass slide was carefully lowered down onto the silicon wafer to initiate the transfer process. Lastly, electrical measurements were carried out in a Janis vacuum probe station (pressure 5E-5 mbar), using two Keithley 2450 for the source-drain-gate measurements, as illustrated in Fig. 2.

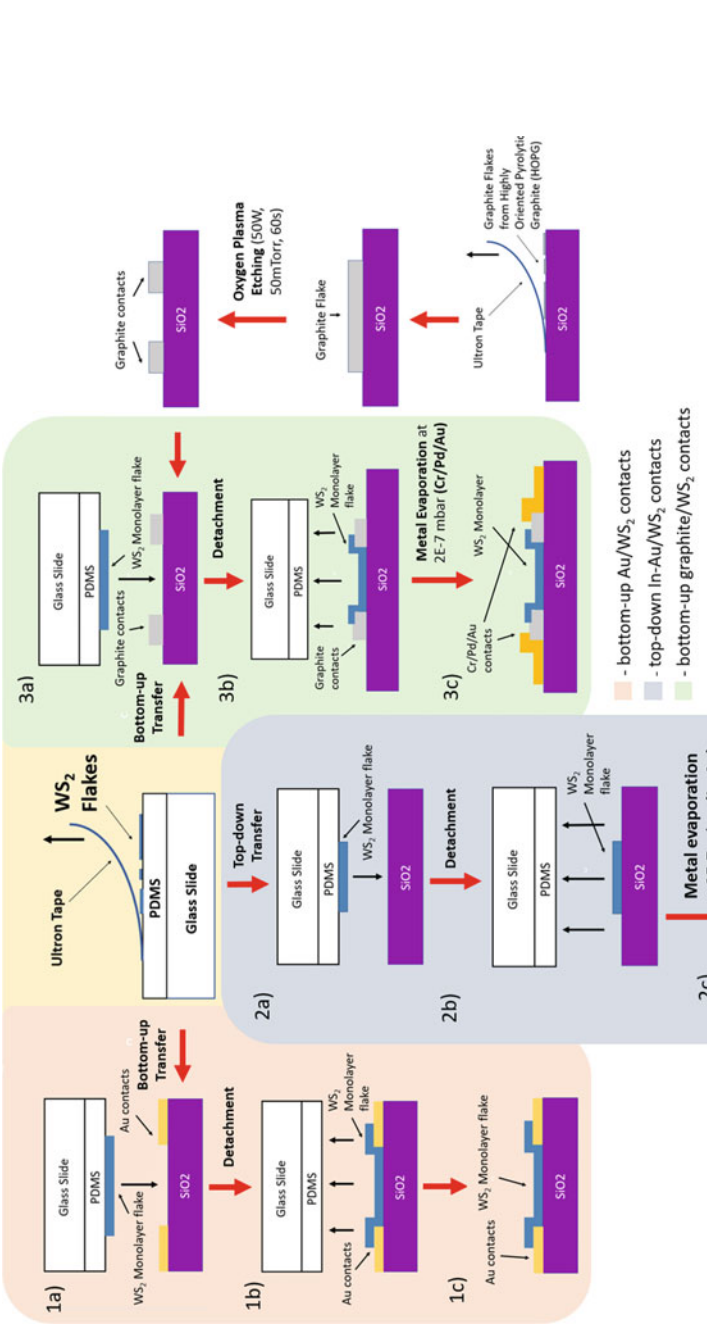

Fig. 1 A schematic diagram representation of the device fabrication process. Process 1, denoted by **a**, **b** and **c**, depicts the fabrication process of the bottom-up gold/WS_2 contacts. Process 2, denoted by **a**, **b** and **c**, depicts the fabrication process of the top-down gold-capped indium/WS_2 contacts. Process 3, denoted by **a**, **b** and **c**, depicts the fabrication process of the bottom-up graphite/WS_2 contacts

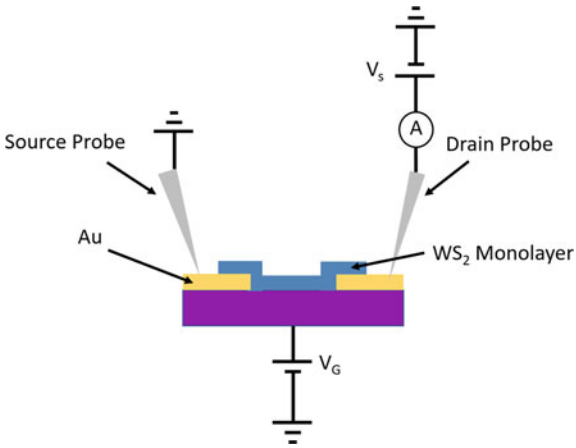

Fig. 2 A schematic diagram representation of the electrical measurement process. Conventional current flows from the source probe to the drain probe

4 Results and Discussion

4.1 Optical Images

Figure 3 shows the optical micrographs of the fabricated devices. For the bottom-up gold (Au) contacts (Fig. 3a), the few layer exfoliated WS_2 was placed onto the contacts across the 5 μm gap, achieving a 2-terminal contact. The thickest regions of the WS_2 were not contacted, so current is flowing through the few layer regions in the device in Fig. 3a. For the bottom-up graphite contacts (Fig. 3b), the exfoliated monolayer WS_2 was placed across the 5um gap between the 2 graphite contacts, similarly achieving a 2-terminal contact. The top-down gold-capped indium (In-Au) contacts (Fig. 3c) are placed across multiple contacts exfoliated WS_2 to obtain the results for the transfer line measurement analysis.

4.2 Carrier Mobilities

Figure 4 shows the transfer curves (I_s–V_g) of the fabricated devices, from which the field effect mobility is extracted from. The field effect mobility is extracted from (Eq. 1), where μ_{FE} refers to the field-effect carrier mobility, L_{CH} refers to the channel length, g_m refers to the intrinsic transconductance, W_{CH} refers to the channel width, C_G refers to the gate capacitance per unit area, and V_S refers to the source voltage. C_G can be further calculated from $C_G = \varepsilon_0 \varepsilon_r / d_{ox}$, where ε_0 is the permittivity of free space, ε_r represents the relative dielectric constant of 3.8 for SiO_2, and the thickness of the oxide layer, $d_{ox} = 285$ nm.

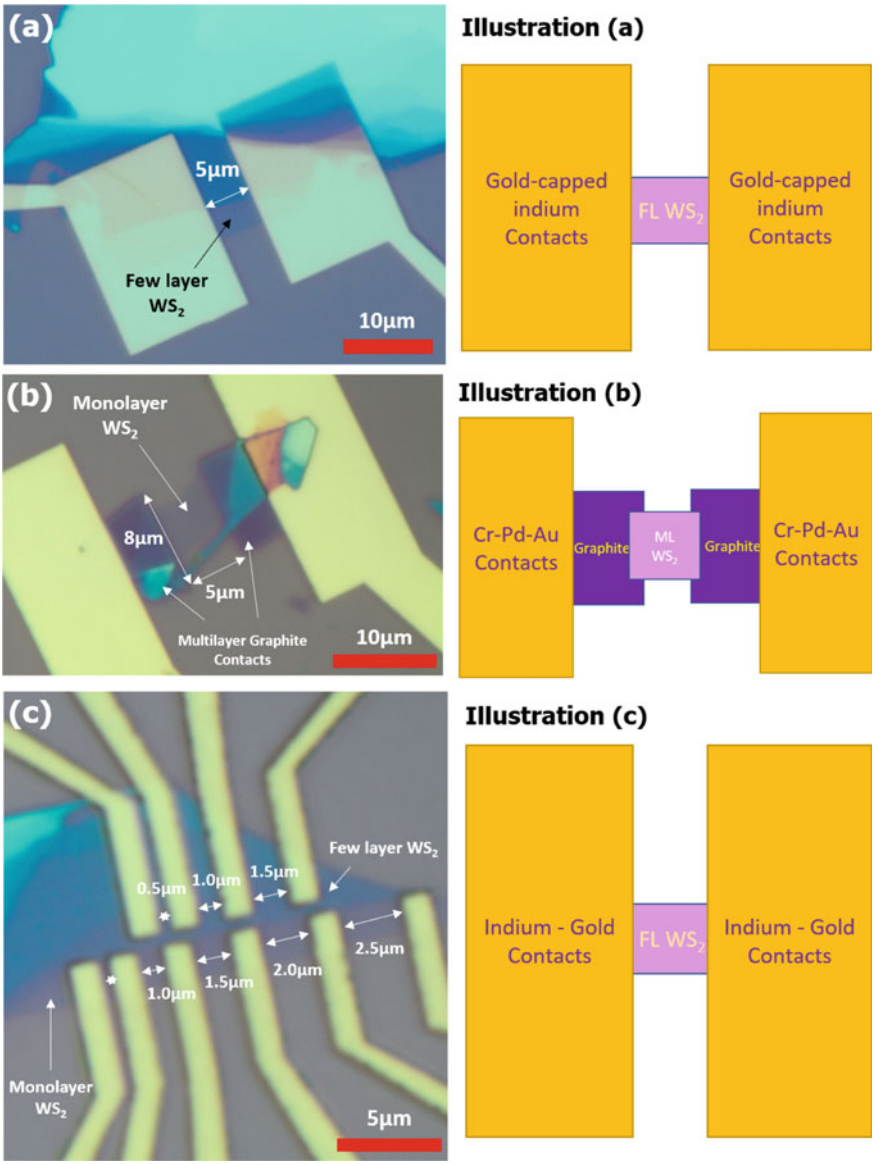

Fig. 3 Optical microscopy images of the devices. **a** Optical image of bottom-up gold contacts to WS_2 (gold/WS_2). The WS_2 monolayer was 6um by 12um. **b** Optical image of bottom-up chromium palladium gold (Cr–Pd–Au) contacts to WS_2 (graphite/WS_2). The WS_2 monolayer was 5 by 8 um. **c** Optical image of evaporated gold-capped indium contacts to few layer & monolayer WS_2 (gold-capped indium/few layer WS_2 and gold-capped indium/monolayer WS_2) for transfer line measurements. The lengths ranged from 0.5 to 2.5 um for the WS_2 monolayer; the lengths ranged from 0.5 to 1.5 um for the WS_2 few layer

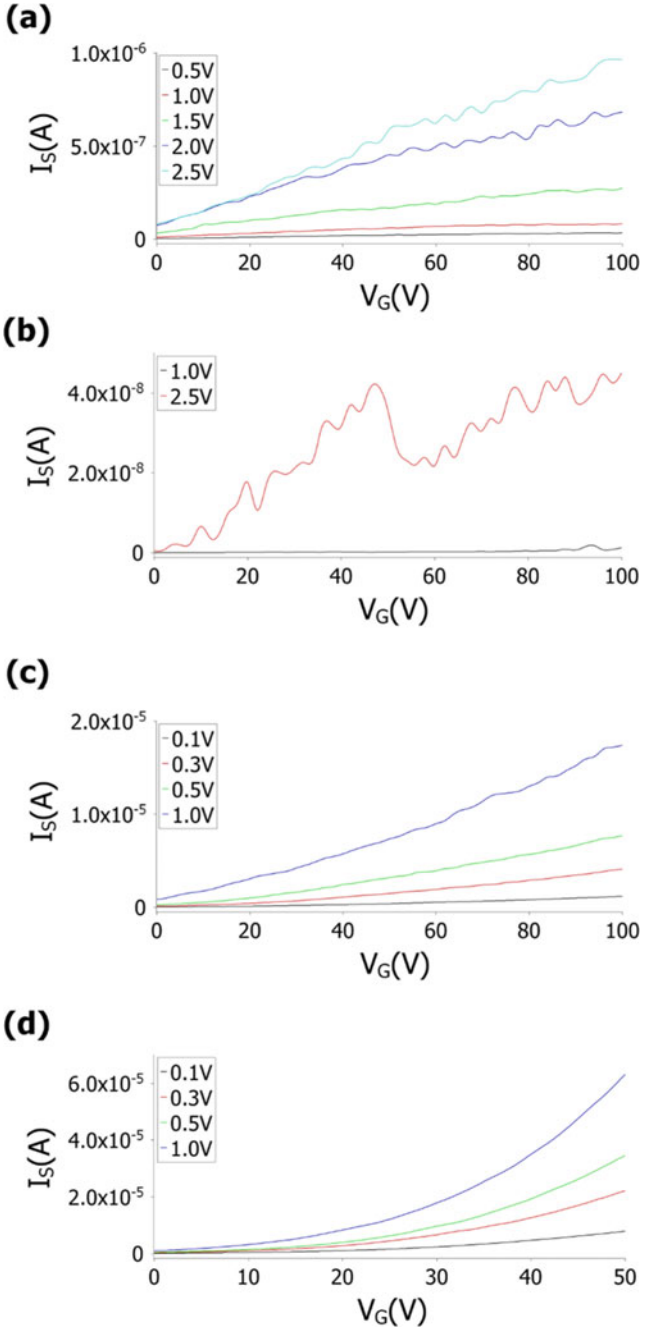

Fig. 4 Graphs of source current (I_S) against gate voltage (V_G) used to determine the field-effect mobilities for each of the devices. **a** Graph of I_S against V_G for gold/WS_2. The extracted electron mobility was 0.00542 cm^2V^{-1} s^{-1}. **b** Graph of I_S against V_G for graphite/WS_2. The extracted electron mobility was 0.0409 cm^2 V^{-1} s^{-1}. **c** Graph of I_S against V_G for gold-capped indium/monolayer WS_2. The extracted electron mobility was 5.45 cm^2 V^{-1} s^{-1}. **d** Graph of I_S against V_G for gold-capped indium/few layer WS_2. The extracted electron mobility was 114 cm^2 V^{-1} s^{-1}

$$\mu_{FE} = \frac{L_{CH} g_m}{W_{CH} C_G V_S}. \tag{1}$$

The gate voltage induced carrier density, n_{2D}, was extracted using the parallel-plate capacitor model from (Eq. 2), where C_G refers to the gate capacitance per unit area, V_G refers to the gate voltage, $V_{G,th}$ refers to the threshold voltage, and e refers to the unit charge (Fig. 4).

$$n_{2D} = \frac{C_G\left(V_G - V_{G,\text{th}}\right)}{e}. \tag{2}$$

The electron mobilities were computed and compared at carrier densities of approximately 2.2×10^{12} cm^{-2}. Thus, the derivative of the I_S against V_G curve (g_m) was taken at V_G values which corresponded to the carrier density of 2.2×10^{12} cm^{-2} for each of the devices. This is to conduct a valid comparison between the electron mobilities that were obtained for each of the devices.

The gold-capped indium (In–Au) contacts to few layer WS_2 yielded the highest electron mobility of 114 cm^2V^{-1} s^{-1}, 5 orders of magnitude larger than the electron mobility of the gold/WS_2 contacts. Other studies have also found that evaporated gold-capped indium (In-Au) contacts offer higher electron mobilities than pure gold (Au) or gold-capped titanium (Ti-Au) contacts for TMDCs [5]. However, the graphite contacts to WS_2 yielded lower than expected electron mobilities of 0.0409 cm^2V^{-1} s^{-1}, even though they were shown to form low resistance contacts to TMDCs [11]. Nonetheless, the electron mobility of WS_2 with the graphite contact was nearly 10 times that of bottom-up gold (Au) contact even though the graphite/WS_2 device is a monolayer device which has typically shown lower mobilities than the few layer WS_2 devices. Since only one graphite contact was functional, of the 11 graphite contacts produced, fabrication of more graphite contacts to WS_2 is required to confirm if graphite contacts indeed offer, on average, higher electron mobilities than gold (Au) contacts.

4.3 Contact Resistance Determination

Figure 5 shows the output curves (I_s–V_s) of the bottom-up gold/WS_2 contacts, gold-capped indium (In–Au) contacts to monolayer WS_2, and gold-capped indium (In–Au) contacts to few layer WS_2. The output curves of the gold/WS_2 contacts (Fig. 5a) are not linear, from which we can conclude that the contact is not ohmic, and a large Schottky barrier exists at the interface. The output curves of (Fig. 5b) is approximately linear, implying that a small Schottky barrier exists for the gold-capped indium/monolayer WS_2 contact. The linear output curves of gold-capped indium/few layer WS_2 (Fig. 5c) shows that the contact is ohmic.

Using the transfer line measurement readings, the contact resistance and sheet resistance for the gold-capped indium (In–Au) contacts to WS_2 were determined by

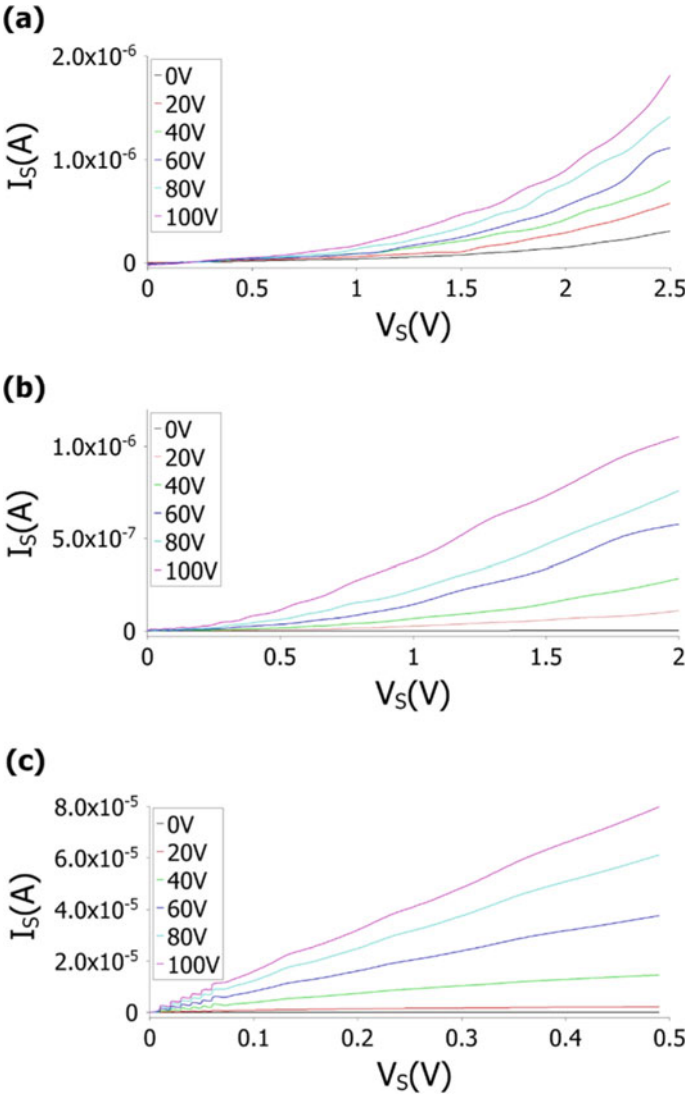

Fig. 5 Graphs of source current (I_S) against source voltage (V_S) for devices at constant gate voltage (V_G). **a** Graph of I_S against V_S for gold/WS_2. It is evident that the gold/WS_2 contact does not display ohmic behavior, and a large Schottky barrier exists at the interface. **b** Graph of I_S against V_S for gold-capped indium/monolayer WS_2. It is evident that the gold-capped indium/monolayer WS_2 contact displays slight Schottky behavior. **c** Graph of I_S against V_S for gold-capped indium/few layer WS_2. The linear behavior shows that the gold-capped indium/few layer WS_2 contact displays extensive ohmic behavior

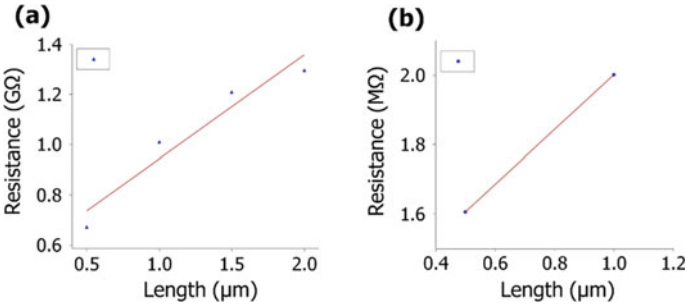

Fig. 6 Graphs of resistance against channel length (obtained from transfer line measurements). **a** Graph of resistance against channel length for gold-capped indium/monolayer WS_2. The extracted contact resistance was 169 M Ω μm. **b** Graph of resistance against length for gold-capped indium/few layer WS_2. The extracted contact resistance was 462 k Ω μm

taking the limit of the trend lines in the graphs of Fig. 6a and Fig. 6b to a zero-length resistor. We obtain the contact resistances for the gold-capped indium/monolayer WS_2 and the gold-capped indium/few layer WS_2 as 169 M Ω μm and 462 k Ω μm respectively.

The contact resistance of 462 k Ω μm for the gold-capped indium/few layer WS_2 is much higher than those obtained in the latest studies, where Yan Wang et al. reported low contact resistances of 2.4 k Ω μm [5]. They used Ar/H_2 gas annealing to reduce the Schottky barrier and interface contamination. We did not subject our samples to Ar/H2 annealing due to the lack of facilities. Hence the higher contact resistances could arise either from the current having to tunnel through a wider Schottky barrier or scattering by the contaminants.

Only 2 terminal measurements were taken for gold/WS_2 and graphite/WS_2 contacts as the WS_2 flakes obtained from exfoliation are typically very small, ranging from 10 to 20 μm in length. Since it is much more difficult to align flakes of such small structures under the microscope, this method was not attempted for gold/WS_2 and graphite/WS_2 contacts. Nonetheless, as we used WS_2 flakes that were exfoliated from the same bulk crystal, it can be inferred from the lower field-effect mobilities for gold/WS_2 and graphite/WS_2 contacts that gold/WS_2 and graphite/WS_2 have significantly higher contact resistances than gold-capped indium/WS_2. Our 2D transfer yield for the bottom up graphite and gold (Au) contacts was poor (only 1 out of 10 devices work), showing the difficulty of this fabrication method. Although an experienced and well-trained practitioner can have higher fabrication yield, this method is not suitable for scaling up and the top down (evaporation) method is preferred.

5 Summary of Values

See Table 1.

Table 1 Summary of values obtained for each device

Device	Electrical properties			
	Electron mobility (cm^2V^{-1} s^{-1})	Contact resistance (M Ω μm)	Sheet resistance (M Ω)	Contact resistivity (Ω cm^2)
Gold/WS_2	0.00542	–	–	–
Graphite/WS_2	0.0409	–	–	–
Gold-capped Indium/WS_2 monolayer (ML)	5.45	169	580	2.36
Gold-capped Indium/WS_2 few layer (FL)	114	0.462	1.11	0.00647

6 Future Work

To further improve the reliability of the results, the monolayer WS_2 and few layer WS_2 should be etched into rectangular strips, so that the widths and lengths are well defined. This would also enable the isolation of the monolayer regions from the few later WS_2 and ensure that current is passing through the monolayer WS_2 or few layer WS_2 only. Next, more data points should be collected for the transfer line measurements of gold-capped indium/few layer WS_2. In addition, temperature dependent measurements can be carried out to determine the Schottky barrier height, which would further validate our claim that In-Au contacts offer the lowest contact resistance and highest mobilities of the 3 methods proposed. Lastly, contact resistances and carrier mobilities may be improved by conducting a hydrogen annealing step together with h-BN capping [5, 12].

7 Conclusion and Applications

We have shown that low resistance ohmic van der Waals contacts for the TMDC WS_2 can be achieved using the direct metallization of gold-capped indium (In-Au) contacts onto WS_2. In contrast, the transfer of the few layer WS_2 on pure gold (Au) contacts or graphite contacts produced poorer contacts, which we attribute mainly to gold (Au) having a higher work function than Indium (In) by 1.38 eV, or by the presence of more contamination on the gold (Au) or graphite surface. Our findings are of current relevance and importance as electrical metal contacts formed are known to strongly affect device performance and the successful development of a low contact resistance van der Waals contact is imperative for the next-generation development of energy-efficient electronics and opto-electronics applications of WS_2.

Acknowledgements A.G. and W.W.J.L. thank the Institute of Materials Research and Engineering and the Agency for Science, Technology and Research (A*STAR) for providing the facilities for the

successful completion of this project. This research was supported by A*STAR under its A*STAR 2D PHAROS Grant No. 1527000016 and A*STAR QTE Grant No. A1685b0005.

References

1. A. Kuc, N. Zibouche, and T. Heine. "Influence of quantum confinement on the electronic structure of the transition metal sulfide TS_2." *Phys. Rev. B* 83, 245213, (2011).
2. D. Ovchinnikov, A. Allain, Y. S. Huang, D. Dumcenco, & A. Kis. "Electrical Transport Properties of Single-Layer WS_2." *ACS Nano*, 8(8), 8174–8181, (2014).
3. X. Liu, J. Hu, C. Yue, N. Della Fera, Y. Ling, Z. Mao, & J. Wei. "High Performance Field-Effect Transistor Based on Multilayer Tungsten Disulfide." *ACS Nano*, 8(10), 10396–10402, (2014).
4. T. Norden, C. Zhao, P. Zhang, R. Sabirianov, A. Petrou, & H. Zeng. "Giant valley splitting in monolayer WS_2 by magnetic proximity effect." *Nature Communications*, 10(1), (2019).
5. Y. Wang, J. C. Kim, R.J. Wu, J. Martinez, X. Song, J. Yang, F. Zhao, A. Mkhoyan, H. Y. Jeong, M. Chhowalla. "Van der Waals contacts between three-dimensional metals and two-dimensional semiconductors." *Nature*, 568(7750), 70–74, (2019).
6. A. Allain, J. Kang, K. Banerjee, & A. Kis. "Electrical contacts to two-dimensional semiconductors." *Nature Materials*, 14(12), 1195–1205, (2015).
7. D. Kiefer, R. Kroon, A. I. Hofmann, H. Sun, X. Liu, A. Giovannitti, D. Stegerer, A. Cano, J. Hynynen, L. Yu, Y. Zhang, D. Nai, T. F. Harrelson, M. Sommer, A. J. Moulé, M. Kemerink, S. R. Marder, I. McCulloch, M. Fahlman, S. Fabiano, C. Müller. "Double doping of conjugated polymers with monomer molecular dopants." *Nature Materials*, 18(2), 149–155, (2019).
8. H. M. W. Khalil, M. F. Khan, J. Eom, H. Nom. "Highly Stable and Tunable Chemical Doping of Multilayer WS_2 Field Effect Transistor: Reduction in Contact Resistance." *ACS Applied Materials & Interfaces*, 7(42), 23589–23596, (2015).
9. Y. Liu, J. Guo, E. Zhu, L. Liao, S. J. Lee, M. Ding, X. Duan. "Approaching the Schottky–Mott limit in van der Waals metal–semiconductor junctions." *Nature*, 557(7707), 696–700, (2018).
10. A. C. Gomez, M. Buscema, R. Molenaar, V. Singh, L. Janssen, H. S. J van der Zant, G. A. Steele. "Deterministic transfer of two-dimensional materials by all-dry viscoelastic stamping." *2D Materials*, 1(1), 011002, (2014).
11. Y. Liu, H. Wu, H. C. Cheng, S. Yang, E. Zhu, Q. He, M. Ding, D, Li, J. Guo, N. O. Weiss, Y. Huang, and X. Duan. "Toward barrier free contact to molybdenum disulfide using graphene electrodes." *Nano Lett*. 15, 3030–3034 (2015).
12. M. W. Iqbal, M. Z. Iqbal, M. F. Khan, M. A. Shehzad, Y. Seo, J. H. Park, C. Hwang, J. Eom. "High-mobility and air-stable single-layer WS2 field-effect transistors sandwiched between chemical vapor deposition-grown hexagonal BN films." *Scientific Reports*, 5(1), (2015).

Smart Surgical Tools Checker

Vinamr Athavle and Tang Kok Zuea

Abstract According to Singapore Health Services, the largest healthcare group in Singapore, they perform approximately 479 surgeries daily (SingHealth (2018) About us. https://www.singhealth.com.sg/PatientCare/Overseas-Referral/En/AboutUs/Introduction/Pages/Home.aspx. Retrieved, 12 June 2018). Multiple requirements and steps are also involved in instrument processing, including preparation, cleaning, and packaging (Even Cuny and Fiona M. Collins (May 2010). Instrument Processing, Work Flow and Sterility Assurance. Retrieved June 12, 2018). These factors increase the stress that instrument processing department staff face and the propensity of human errors, as most hospitals check surgical tools with their own eyes. The Smart Surgical Tools Checker (SSTC) is an intelligent scanner that will identify the tool on the platform and tally it with a reference toolset. If there is a wrong tool placed, or if there are missing tools, the software, using image processing algorithms and artificial intelligence (AI), will warn the user about the error. This reduces the occurrence of incomplete surgical sets and missing tools in the inventory.

Keywords Artificial intelligence · Machine learning · Image processing · Surgical tools · VGG16 neural network · Surgical tool checker

1 Introduction

The World Health Organization (WHO) released the WHO Safe Surgery Checklist which has played a major role in preventing errors [1, 2] caused by the usage of wrong tools during operations [3]. However, there are many disadvantages of the checklist, such as the duplication of existing checklists which leads to 'checklist fatigue' [4]. Another product is the Ultra High-Frequency Radio Frequency Identification (RFID),

V. Athavle (✉)
NUS High School of Mathematics and Science, 20 Clementi Avenue 1, Singapore 129957, Republic of Singapore
e-mail: h1610153@nushigh.edu.sg

T. Kok Zuea
Faculty of Engineering, National University of Singapore, 9 Engineering Drive 1, #07-26 EA, Singapore 117575, Republic of Singapore

H. Guo et al. (eds.), *IRC-SET 2020*,
https://doi.org/10.1007/978-981-15-9472-4_17

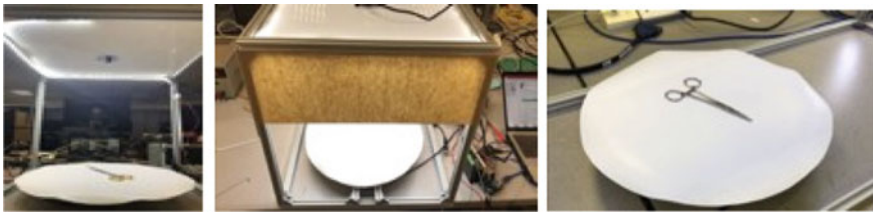

Fig. 1 Images of hardware set-up of surgical tool checker

which keeps track of surgical tools. While it reduces the time wasted and is cost-efficient [5], the signal produced may interfere with sensitive medical equipment.

Previous prototypes from NUS students [6] have been rejected. These systems involved a push-in-pull-out closed system tray, which was hard to sterilize. The SSTC built upon these limitations and thus the system had been made semi-open for ease in sterilization, while preventing ambient lighting from affecting the images captured of the surgical tools.

The SSTC will benefit hospital staff and patients by reducing human errors affecting the surgery and packaging staff can work in less stressful environments and more efficiently.

2 Materials and Methods

2.1 Phase 1—Building of Prototype

The setup used an acrylic sheet ceiling to attach an 8-megapixel camera, and the underside was lined with LED lights along the aluminium rods. To support the structure, aluminium rods were attached to the sheet. A circular rotating disc was placed at the bottom of the structure (with a stepper motor) and covered with a non-slip medical cloth (Fig. 1).

2.2 Phase 2—Coding (Image Processing and Machine Learning)

Turntable: After connecting the stepper motor to the Arduino Uno Microcontroller, we used the Arduino Genuino IDE [7] software to code a program allowing for the turning of the mechanism.

Image Capturing: Using OpenCV [8] and NumPy libraries in Python, we connected the camera to the computer and obtained one picture. A high-resolution red–green–blue (RGB) image was captured by altering external factors such as lighting around

the tool. The image capturing was then adjusted such that 1 picture was taken per 1-degree rotation of the turntable. Image processing tools and variation in lighting intensity, opaqueness etc., were used to create 2 or more copies of the same image allowing for a larger dataset for training the model.

Neural Network: We used a VGG16 neural network model to construct a deep learning model. To test the accuracy of the network, we trained it with pictures from Kaggle [9]. We then trained with real surgical tools and improved the accuracy such as by improving the picture resolution.

2.3 Obtaining Data

Experiments were done using a macOS High Sierra with a 2.9 GHz Intel Core i5 processor 64 bit installed with Python version 3.6, without GPU acceleration. We applied the VGG16 neural network and Keras software (with TensorFlow backend) to train the computer using data (pictures of tools) gathered from Phase 2. The accuracy of the model was tested before more functions were applied to improve the accuracy of the computer with more data of tools.

2.4 Getting Accuracy of Model

Given N training samples, x represents the annotated parts of the model while y represents the labels given to the images. After training, the VGG16 model can approximate a model F by mapping out the relationship between the input vectors x and output vectors y. During the forward propagation phase, when a training sample (x_i, y_i) is taken in by the neural network, x_i is fed-forward from the input layer to the output layer. Finally, we get the output o_i. This process can be formulated as, where L is the number of layers in the sequential model, w_j is the weight vector of the jth layer F_j. We define F_j as the convolutional layer which performs operations. After a series of operations by the convolutional layers, estimating the weight vectors w_1, w_2, …, w_L can be solved with the following optimization problem, where is usually defined as cross-entropy loss function.

3 Results and Discussion

We implemented a method of saving the bottleneck features of the image taken by using a data flow generator to convert the images into a NumPy array and a VGG16 Neural Network without the fully-connected top layer to train with the images initially. The second part of the program involved a bottleneck model with

two dense layers, and a dropout of 50% to achieve a greater generalization across all convolutional layers for them to be independent of each other and generate a higher validation accuracy. The *sigmoid* activation was used on the last dense layer to generate the predictions of the images we put into the bottleneck model. The model was compiled with the *RMSProp* optimizer and the *binary cross entropy* loss function. Table 1 shows the results of our training and validation at the 100th epoch of two of the runs in our experiments.

From our results in Table 1, the training accuracy was higher than the validation accuracy in the 1st and 2nd runs, indicating that we had overfitted the neural network. This caused the model to learn the specific details of the pictures and random fluctuations in the training data as new concepts such that the performance was negatively affected. This affected the validation as these concepts did not apply to new data and affected the model's ability to generalize. While we achieved a 90% accuracy in both runs, our results improved after replacing the images from Kaggle with surgical tools (Table 2).

This could be due to the effect of generalization, where in the case of the training images, all training data varied a lot from each other in terms of shape, colour and features; whereas for the images of the tools we had taken with the SSTC, it was limited to a small set of images where all the images were similar. As such, the trained model would be able to pick up the salient differences in the images and learn how to differentiate between the tools, thus giving the high training and validation accuracy [10, 11]. However, the accuracy started to decrease significantly when more tools were added for training (Tables 3 and 4).

To improve the accuracy of our model, we adapted multiple functions and physical changes to our program and set-up respectively. We worked with different optimizers to compile the Keras model and different activations for the last and dense layers of the model to obtain a better differentiation curve where the mapping of the given data sets can be separated clearly. We worked on more aggressive dropout and batch normalization to generalize the model as much as possible to prevent complex co-adaptations on training data. Physical changes we made include the usage of better lighting and better internal reflection of the internal setup such that a clearer image is used by the model. We also took more pictures to enlarge our limited dataset, and train the model to pick up changes in the images.

Using our original data and bottleneck model (Table 1) as a benchmark, we made alterations to the code. The original bottleneck model utilized a flattening layer, followed by a dense layer of output size 256, data dropout of 50%, and finally a dense layer of output size 1 with a *sigmoid* function. In the first test, two tools, the crab-claw tool (CCT) and golden scissors (GS) were used. In the second, the CCT, GS and length-one scissors (L1S), and for the third, the CCT, GS and pincer tool (PT). As seen from the results of the first three tests, we can conclude that as the number of images and number of classes put into the model increased, the accuracy of the model decreased.

In test 4, the dropout layer was removed. The accuracy was lower as overfitting had occurred and the neurons in test 3 were able to be co-dependent of each other during training and curb the individual power of each neuron. In test 5, a few more

Table 1 Results of training and validation with VGG16 neural network using pictures from Kaggle

	Training images	Saving time/s	Validation images	Saving time/s	Training time/s	Training loss/%	Training accuracy/%	Validation loss/%	Validation accuracy/%
1st run	10,000	1859.83	5000	925.605	531.106	8.51	0.9750	69.8	88.92
2nd run	10,000	1805.74	5000	916.176	537.016	3.79	0.9910	65.9	90.80

Table 2 Results of training and validation with VGG16 neural network using two tools taken by the tool checker

Training images	Validation images	Training loss/%	Training accuracy/%	Validation loss/%	Validation accuracy/%
10,800	3600	208.56e−07	100.00	109.60e−07	100.00

Table 3 Results of training and validation with VGG16 neural network using four tools (crab-claw tool, golden scissors, length-one scissors and pincer tool) taken by the tool checker

Training images	Validation images	Training loss/%	Training accuracy/%	Validation loss/%	Validation accuracy/%
37,800	12,600	199.02	25.00	196.59	25.00

Table 4 Comparison of results of training and validation with VGG16 neural network using two, three and four tools taken by the Tool Checker at the last (50th) epoch

Number of tools	Training loss/%	Training accuracy/%	Validation loss/%	Validation accuracy/%
2	208.56e−07	100.00	109.60e−07	100.00
3	327.83e−09	33.33	397.36e−08	33.33
4	199.02	25.00	196.59	25.00

dense and dropout layers were added, but the model was slightly less viable. In tests 6 and 7, different amounts of dropout (75% and 25% respectively) caused underfitting of the model, resulting in lower accuracies recorded. In test 8, the size of the output dense layer was modified from 8 to 32 to check if it had an effect on the predictions that were obtained from the final dense layer. However, the accuracy was lower, indicating that too many parameters were present for the prediction layer to have a conclusive accurate classification.

From tests 10 to 13, we tested to see if the size of the output dense layer had an effect on the model again, but using the original model (from test 1). As the size increased from 8 to 32, the accuracy increased from 43 to 63%. However, as the size increased further from 32 to 64 and 512, the accuracy dropped from 63 to 59 and 33%.

From test 14 to 16, we worked with various activation functions of the final prediction layer. With softmax, the accuracy was 33%. With tanh, the accuracy dropped from 59% in epoch 1–37% in epoch 50. With the linear function, the accuracy was at 0.00% indicating that the model was unable to differentiate the tools from each other. As such, the sigmoid function was still the most viable activation function.

Through these results, we concluded that for this specific dataset of tools, the dense layer with an output size of 32 and data dropout of 50% with the sigmoid activation function would be the most efficient and reliable model.

Increasing epoch number and decreasing batch size proved to yield a lower accuracy as seen from test 17, and limits in computational power increase the training time

required significantly. Increasing dense and dropout layers with the current model as in test 18 decreased model accuracy (like in test 3 and 4) to 33.33%, and decreasing batch size in test 19 and an intermediate dense layer was added in test 20 with a SoftMax activation function provided negligible change to the accuracy from test 18. Increasing the number of epochs to 1000 (like in test 17) lead to higher accuracy as more time was provided for training, so accuracy increased to 62%.

A method we finally utilized was a data augmenter. We conducted vigorous data augmentation of the images by changing the images' zoom range, flipping the image, altering the RGB channels etc. This yielded an accuracy of about 75%, which was a significant improvement from the previous sets of results, as the more varied set of images present prevented the model from picking up random fluctuations.

Another method was the use of multi-label instead of multi-class classification. This means each image can be grouped together under the same class so the model can identify similar aspects in tools for faster classification as well as higher accuracy due to the neurons learning to focus only on specific parts of the image. We also made the VGG16 smaller by decreasing the convolutional layers in each convolution. More vigorous batch normalization was used to provide better generalization as proven from the tests. This smaller VGG16 also allowed us to save training time, allowing for more efficient, practical usage of the model. With all 3 methods implemented, the results improved significantly (Table 5).

In our machine learning program, a support vector machine (SVM) [12] was being built. Using an SVM classifier enabled classification of data into two or more classes. When training, the SVM builds a model before mapping the decision boundary for each class, and specifies the hyperplane that separates the classes. Increasing the hyperplane margin improves the classification accuracy. As such, SVM can be used to effectively perform non-linear classification. The model needs to know what input shape it should expect. Thus, the first layer in a sequential model needs to receive information about its input shape. This input image is a placeholder tensor that contains generated images and will be put into the network for training. A convolutional neural network (CNN) is comprised of one or more convolutional layers, followed by one or more fully connected layers as in a standard multilayer neural network.

First, we know that deep learning needs a large amount of labelled training data, and second, the surgical tools are very similar to each other and in order to differentiate them, a high-resolution image would be preferred such that the hyperplane margin can increase in distance. Ambient lighting as well as reflectivity of the turntable play an essential role in ensuring the correct identification of the tools into their classes.

Table 5 Results of training and validation with VGG16 neural network using seven tools at the last (75th) epoch with data augmentation and multi-label classification

Number of tools	Training loss/%	Training accuracy/%	Validation loss/%	Validation accuracy/%
7	0.44	99.84	27.25	92.05

As such, we need to find the optimum point at which both lighting and reflectivity can be balanced to ensure a high-quality image produced. Our final model was also able to balance the resolution of the image by altering the RGB channels of the image such that it would be optimized for input into the neural network model. Our dataset this time consisted of 7 tools, length-0 scissors (L0S), L1S, length-2 scissors (L2S), GS, PT, ST and CCT.

4 Conclusion and Future Work

The SSTC is able to identify tools accurately with a low-cost production. By minimizing human errors, it will greatly reduce the time wasted that will affect the surgery being carried out. Unlike similar projects, the SSTC will enable the streamlining of hospital procedures in a more efficient manner. Some improvements for the future include creating a larger platform such that more tools can fit onto it such that the speed of processing and registering the tools will be increased. Some factors that we did not work on would be the use of a different table below the setup, as that could affect the image taken by the camera. We could have adapted a Faster R-CNN model which would be able to bypass the problem of having to select a huge number of regions for identification. Finally, we also hope to work on a Graphical User Interface (GUI) such that the SSTC can be more user-friendly and catered to the hospital staff, rather than be hindered by complicated lines of codes which may be irrelevant to them.

Acknowledgements We would like to thank Dr. Tang Kok Zuea for his constant guidance throughout this project. This project would not have been successful without his patient understanding and guidance.

We would also like to acknowledge Ms. Winni Valentina and Mr. Jonathan, graduates from NUS, for providing us with deep insight into the project, and guiding us on how to sieve out ideas for a better prototype.

Next, we would like to thank Mr. Lim Teck Choow, the teacher-in-charge for all SMP teams in NUS High. Without his dedication and constant reminders of the many deadlines, we would not have been able to achieve success in this project. A special thanks to our lab officers, Mr. Tan Chee Siong, who provided us with space in the lab for us to do our research and the necessary resources required to conduct our experiments, as well as Mr. Richard Yip and Mr. Justin Yip for the help and advice they have given us on the design of our prototype.

Lastly, we would like to acknowledge our family members for their support while we worked on this project. Their support has given us the motivation to continue to work hard and strive for the best.

References

1. SingHealth (2018) About us. https://www.singhealth.com.sg/PatientCare/Overseas-Referral/En/AboutUs/Introduction/Pages/Home.aspx. Last retrieved, 12 June 2018.

2. Even Cuny and Fiona M. Collins (May 2010). Instrument Processing, Work Flow and Sterility Assurance. Retrieved June 12, 2018.
3. World Health Organisation (2018) WHO surgical safety checklist and implementation manual. https://www.who.int/patientsafety/safesurgery/ss_checklist/en/. Last retrieved, 13 June 2018.
4. Dr. Natasha Woodman (5 February 2016) 325 WHOSurgical Safety Checklist. Retrieved June 12, 2018.
5. Xerafy (2018) Usage of RFID Surgical Instruments Tracking Established to Increase Patient Safety. https://www.xerafy.com/blog/usage-of-rfid-surgical-instruments-tracking-established-to-increase-patient-safety/. Last retrieved, 12 June 2018.
6. SmartSurgicalTool Checker(2017),SohWJ,NUSSchoolOf Engineering. Retrieved June 12, 2018.
7. Arduino (n.d.). https://www.arduino.cc/. Last retrieved, 12 June 2018.
8. OpenCV library. (n.d.). https://opencv.org/. Last retrieved, 13 June 2018.
9. Kaggle: Your Home for Data Science.(n.d.). https://www.kaggle.com/. Last retrieved, 12 June 2018.
10. Kim et al. Performance analysis of CNN frameworks forGPUs. in Proceedings of 2017 IEEE International Symposium on Performance Analysis of Systems and Software (ISPASS), 2017, pp 10–13. Last retrieved, 16 June 2018
11. Li, Hailiang, et al. An improved deep learning approachfor detection of thyroid papillary cancer in ultrasound images. *Scientific Reports*, 26 Apr. 2018. Last retrieved, 12 June 2018
12. Lin, Y. et al. Large-scale image classification: Fast feature extraction and svm training. in Computer Vision andPattern Recognition, 1689–1696 (2011).

Magnetisation Transport in XXZ Spin Chains

Akshat Chaudhary, Christophyr Yeoh Kai Xiang, Vinamr Athavle, Xing Bo, and Dario Poletti

Abstract At the macroscopic scale we observe that transport between two regions is proportional to the difference of concentration between them, otherwise known as Fick's law. It is however not trivial to understand how this macroscopic and phenomenological law emerges from the microscopic laws of nature. Here, by studying the magnetization transport in one-dimensional quantum spin chains, we show two effects that contribute to the emergence of this law: interaction between the constituting elements as well as the presence of decohering processes. This is important for better understanding the behavior of transport at the nanoscale and to produce novel nano/quantum transport devices.

1 Introduction

The macroscopic world we are more familiar with is well described by phenomenological laws like Fourier's law [1],

$$\dot{Q} = -k\nabla T \tag{1}$$

where $\dot{Q}$ is the heat flow, k is the conductivity, ∇T is the temperature gradient. A mathematically analogous relation is Fick's law [2] which relates the current of a quantity, J^s, with the gradient of the concentration of this quantity, s,

$$J^s \propto \nabla s \tag{2}$$

A. Chaudhary · C. Yeoh Kai Xiang · V. Athavle (✉)
NUS High School of Mathematics and Science, Singapore, Singapore
e-mail: h1610153@nushigh.edu.sg

X. Bo · D. Poletti
Science and Mathematics Cluster, Singapore University of Technology and Design, Singapore, Singapore

H. Guo et al. (eds.), *IRC-SET 2020*,
https://doi.org/10.1007/978-981-15-9472-4_18

It is however not obvious how these laws are derived from microscopic principles, especially considering the fact that the laws of nature at the microscopic scale are fundamentally quantum mechanical [3–5]. From a technological point of view, and for the design of future nano-devices, it is also important to understand how transport occurs at the quantum scale [6–8]. Subatomic particles have properties that are very different from classical, macroscopic properties of everyday objects. An example of this is superposition (being in two places at the same time). Electrons, in particular have a property known as "spin", and in materials, the spin of the electrons in the outer orbitals plays an important role in the magnetic properties of the materials. Here we consider a system in which the outer electrons are localized to each atom (e.g. they cannot tunnel or jump to other atoms), but the character of the spin can be influenced by the spins nearby, or it can be swapped with its neighbours. The particular model we will consider is known as an XXZ Heisenberg spin chain, and this system is a good approximation of the magnetic properties of real materials like copper pyrazine dinitrate $Cu(C_4H_4N_2)(NO_3)_2$ [9], or it can be constructed artificially with surface adatoms [10] or Rydberg atoms [11, 12]. Fundamental studies which show the emergence of Fourier's law were done in 1984 for classical systems [13], and in 2004 for quantum systems [14] like the one we consider here. Here we aim to study at magnetization current, or spin current, in a scenario in which one side of the Heisenberg spin chain is driven to a certain concentration of spin (or magnetization) [15], and the other end of the spin chain to a different magnetization. The fact that the two edges of the spin chains are driven to different magnetization will induce a spin current through the chain. In this research project we show that both the interaction between the spins and the presence of decoherence can induce the emergence of Fick's law. In particular we show that for non-interacting and non-decohering system the transport is ballistic, i.e. the current is independent of the system size, while transport becomes diffusive with the current being inversely proportional with the system size, i.e. Fick's law, in presence of strong enough interactions, and/or of decoherence. Moreover we show other interesting effects of the interaction on transport, for instance we show that for large concentration differences and large interactions, the current decreases for increasing concentration differences, which is very different from Fick's law. In this case, decoherence again allows the emergence of Fick's law.

The report is organized in the following way. In Sect. 2 we give some basic introduction of the quantum mechanics needed for this project, and we also describe the model used and the observables studied. In Sect. 3 we describe briefly the numerical implementation of the problem we study. In Sect. 4 we describe our results, first only considering the role of interactions, and then the combined role of interactions and decoherence. In Sect. 5 we draw our conclusions.

2 Tools and System

Here, we discuss the basic elements in quantum mechanics that are fundamental to our understanding of the phenomena studied in this paper.

2.1 Basic Elements of Quantum Mechanics

(1) *Vector Space:* In order to define the conditions of the spin-half particles that we study in this paper, it is necessary for us to define a space in which these particles are located and where they are given the relevant properties. This manifests itself in the form of a vector space, which we define as the complex 2-dimensional Hilbert space. Since we use this space to determine our quantum states and hence where our state vectors are located, we can then define our basis as all the possible quantum states the system can have. The overall dimension of the system will then be equal to 2^N where N is the number of spins.
A Hilbert space is a generalisation of normal, everyday Euclidean space, expanding it to the complex realm as well. Since a spin-half particle can only be spin-up or spin-down, (more formally in the form of $a + b$ where a and b represent the probability of being either spin-up or down) we only need a 2-dimensional complex space to conduct our modelling of a single electron, i.e. C^2. As we expand the system to N particles, a 2-dimensional space is not sufficient to describe all N particles. Hence, we expand the Hilbert space such that our total space becomes N tensor products of C^2 with total dimension 2^N. We connect this to the fact that there are 2^N possible states for an N-particle system, hence a 2^N dimensional space is needed.
Writing these vector spaces, we have operators. Operators, when acting upon the wave function or a density matrix (see Sect. 2.1) allow us to measure the observable it corresponds to by solving for its eigenvalues, a process we will touch upon later.

(2) *Pauli Matrices:* There are certain important operators that we use in order to determine the magnetisation of a particle. We call these matrices the Pauli matrices, denoted by σ^x, σ^y and σ^z. We use these matrices to find the magnetisation of the particle in a specific direction, in this case the x, y and z axes respectively. These matrices have constant values and are as such:

$$\sigma^x = \begin{pmatrix} 0 & 1 \\ 1 & 0 \end{pmatrix} \sigma^y = \begin{pmatrix} 0 & -i \\ i & 0 \end{pmatrix} \sigma^z = \begin{pmatrix} 1 & 0 \\ 0 & -1 \end{pmatrix} \tag{3}$$

These matrices have certain special properties. For example, these matrices are Hermitian (i.e. the conjugate transpose of the matrix is equal to itself) and unitary (i.e. the matrix multiplied by its conjugate transpose is the identity matrix).

(3) *Density Matrix:* The density matrix represents the statistical state of a system in quantum mechanics. It is generally defined as

$$\rho = \sum_i p_i |\psi_i\rangle\langle\psi_i| \tag{4}$$

where ρ refers to the density matrix, ψ_i refers to the quantum state of that particular particle and p_i refers to the probability that the particle is in the state ψ_i. Since p_i is a probability, all instances of p_i adds up to 1. For a mixed state, $i > 1$ since a mixed state is a mixture of 2 pure states with a probability of the system being in each particular state. This is formally known as a statistical ensemble of pure states. Each pure and mixed states can be represented by one density matrix, which makes it very useful due to the simplification it brings to our calculations. Another crucial reason for the importance of these matrices is that we can deduce the probability of virtually any outcome from a defined measurement of the system from the density matrix. This makes it of paramount importance for us to understand this concept. In a pure state, density matrices have certain additional special properties. These include: Tr $\rho = 1$, $\rho \in \mathrm{R}^+$ and $\rho = \rho^2$.

2.2 Model

(1) *Heisenberg Hamiltonian:* In this paper, we consider an XXZ spin chain with nearest neighbour interactions and a homogeneous magnetic field. This means that any particle i is affected only by the particles adjacent to it, i.e. $i + 1$ and $i - 1$.

In order to represent the energy of the system, we introduce an operator we call the Hamiltonian, represented as H. It acts as a representation of the sum of kinetic, potential and interactive energies of the system. This means that the Hamiltonian represents the total energy of the system. The eigenvalues of H are the energies of the system. The following equation represents the computation of the Hamiltonian:

$$H = h\sum_j \sigma_j^z + \Delta \sum_{\langle i,j\rangle}^{n} \sigma_i^z \sigma_j^z + J_z \sum_{\langle i,j\rangle}^{n} (\sigma_i^+ \sigma_j^- + \sigma_i^+ \sigma_j^-).$$

where σ^z is the aforementioned Pauli matrix, $\sigma^+ = (\sigma^x + i\sigma^y)/2$ and $\sigma^- = (\sigma^x - i\sigma^y)/2$. h, Δ and J_z are amplitudes of the magnetic field term, interaction term, and spin of the system respectively, and $<i, j>$ represents the nearest neighbour term.

The Hamiltonian is important for us to conduct time-evolution of quantum states, represented by $\psi(t)$ as per the Schrödinger Equation which is as follows:

$$H|\psi(t)\rangle = i\hbar\frac{\partial}{\partial t}|\psi(t)\rangle \tag{5}$$

This makes the Hamiltonian indispensable to our calculations. To measure the system, we apply the Time-Independent Schrödinger's equation to find its steady state, as all observables are independent of time in the steady state.

$$H|\psi\rangle = E|\psi\rangle \tag{6}$$

where H is the Hamiltonian and E is a constant equal to the energy level of the system. This equation is an eigenvalue equation, and the corresponding right eigenvector to the eigenvalues E is the steady state of the system.

(2) *Lindbladian:* In an ideal environment with no dissipation, we can use the von Neumann equation to model the time evolution of the density matrix, which is as follows:

$$i\hbar\dot{\rho} = [H, \rho] \tag{7}$$

Solving this differential equation allows us to find ρ as a function of time. However, we want to study systems that are non-ideal, which are exposed to some sort of environment. Then, in order to mathematically model ρ as a function of time in such a non-ideal situation, we describe the outside environment as a dissipator, denoted by $_D(\rho)$. Under these conditions, in order to observe spin transport in XXZ spin chain systems, we use the Gorini-Kossakowski-Sudarshan-Lindblad master equation (GKSL master equation) [16, 17], alternatively called the Lindbladian master equation. The equation is as follows:

$$\dot{\rho} = \frac{i}{\hbar}[H, \rho] + L_D(\rho) \tag{8}$$

where ρ refers to the density matrix, H refers to the Hamiltonian, and $\mathrm{L}_D(\rho)$ refers to the dissipator environment. We define the Dissipator environment $\mathrm{L}_D(\rho)$ as follows [18],

$$L_D(\rho) = \sum_{ij}(L_i \rho L_j^+ - \frac{1}{2}\Big[L_j^+ L_i, \rho\Big])$$

(3) *Boundary driving:* We attach the XXZ spin chain to dissipator environments on the left and right. This allows us to observe how the system behaves under dephasing, as well as diffusive and ballistic spin transport. We expose the system to outside interference, to observe a reduction in the wave-like properties of the elections, thus dephasing the system to recover classical behaviour. For an XXZ spin chain with N spins, the Dissipator on the left is [18],

$$L_{\mathrm{D,L}} = \lambda_L^+\left(\sigma_1^+ \rho \sigma_1^- - \frac{1}{2}\{\sigma_1^- \sigma_1^+, \rho\}\right) + \lambda_L^-\left(\sigma_1^- \rho \sigma_1^+ - \frac{1}{2}\{\sigma_1^+ \sigma_1^-, \rho\}\right)$$

where $L_{\mathrm{D,L}}$ refers to the dissipator function, λ_{L}^{-} refers to the left boundary driver, which drives the spin up or down on the left depending on the superscript and $\sigma_1^{+/-}$ refers to the matrices outlined in Sect. 2.2 for the first particle. The expressions of the left boundary drivers with relation to the amplitude, represented by Γ and imbalance, represented by μ. Γ affects the overall magnitude of the boundary driving, and μ relates to the ratio between the positive and negative boundary driving. When imbalance is at 0, the positive and negative driving values are the same. Varying this will vary the ratio of the positive and negative driving values, and hence affect the dissipator function and the regime of spin transport.

$$\lambda_L^+ = \Gamma(1+\mu)\lambda_L^- = \Gamma(1-\mu) \tag{9}$$

Similarly, we have a dissipator environment on the right as well [18].

$$L_{\mathrm{D,R}} = \lambda_R^+\left(\sigma_N^+\rho\sigma_N^- - \frac{1}{2}\{\sigma_N^-\sigma_N^+,\rho\}\right) + \lambda_R^-\left(\sigma_N^-\rho\sigma_N^+ - \frac{1}{2}\{\sigma_N^+\sigma_N^-,\rho\}\right)$$
$$\lambda_L^+ = \Gamma(1+\mu)\lambda_L^- = \Gamma(1-\mu) \tag{10}$$

The symbols here refer to the same things as they do in Eqs. (10) and (11).

(4) *Dephasing:* A result of dissipation is that we observe dephasing, which means that the system loses its quantum behaviour as it transitions to classical-esque behaviour. Resulting which, we will be unable to observe properties such as wave-particle duality that we usually ascribe to quantum systems. In a more mathematical form, a result of dephasing is that ρ transitions into a diagonal matrix, and all non-diagonal elements of the matrix go to zero. By solving Eq. (7), we can find ρ as a function of time [18].

$$L_{\mathrm{Dephasing}}(\rho) = \lambda_z \sum_l (\sigma_l^z \rho \sigma_l^z - \rho) \tag{11}$$

2.3 Observables: Magnetization and Current

(1) *Obtaining the steady state:* Observables are essentially the properties of the system we are studying. Such observables are characterised by corresponding operators. For example, energy, an observable, has the Hamiltonian as its corresponding operator. Finding the eigenvalues of the operator yields the amplitude of the observable. This is obtained by passing the eigenvalue equation with the state function through an eigensolver. Alternatively, the trace function and density matrix can be used in its place, which we demonstrate in Eq. (13).

We have previously discussed the need to obtain the state function, or equivalently the density matrix, at steady state in Sect. 2.1. To solve for the density matrix at the

steady state, we apply the Lindbladian discussed in Eq. (8) in Sect. 2.2. We vectorise this equation such that we obtain a super where $L_{D,L}$ refers to the dissipator function, $\lambda^{+/-}$ refers to

$$\dot{\rho} = \frac{-i}{\hbar}[H, \rho] = M\rho \tag{12}$$

At steady state, $\rho^{\cdot} = 0$, hence we solve for the smallest absolute eigenvalues of M, as they equate to the magnitude of $\rho^{\cdot}$. The corresponding eigenvector is the density matrix at steady state in column vector form.

(2) *Characterizing the steady state:* By reshaping the density matrix and applying the following relation, we obtained our desired observables.

$$\langle A \rangle = Tr(\rho A) \tag{13}$$

where A is any arbitrary observable and A is the corresponding operator. In our study of XXZ spin chains, the observables of our interest are particle magnetisation σ^z and spin current J^s, the transfer of spin. The magnetisation operator is simply the Pauli matrix σ^z at site i, while the spin current operator is.

For site i and N sites, where $0 \leq i \leq (N-1)$.

$$J_i^s = \frac{-i}{\hbar}\left[H, \sigma^z\right] = \frac{2}{\hbar}\left(\sigma_i^x \sigma_{i+1}^y - \sigma_i^y \sigma_{i+1}^x\right) \tag{14}$$

3 Numerical Implementation

In order to implement this modelling, we used computational software, including the num.py and sci.py libraries of Python as well as eigensolvers in MATLAB. We initially generated a Hamiltonian of the system, following which we generated a superoperator that when acting upon the various operators, can form a series of matrix equations that we export from Python to MATLAB. In MATLAB, we use the eigensolver to then solve the equations, yielding the values for our observables. We export the raw solutions back to Python in order to plot it.

We inputted initial values of h, J_z, Δ, Γ, μ as well as λ_z in order to output our observables. From the aforementioned quantities, we computed ρ (see Eq. (4)) and the Hamiltonian (see Eq. (1)) as previously described. From Eq. (11), we generated our superoperator M. Following the procedures gone through previously in the paper, we solved for the eigenvalues of the superoperator and solved for the steady-state density matrix, from which we measured all our observables.

We investigated systems of up to 8 spin-half particles. Recall from II-A.1 that the dimension of the matrices we work with is 2^{16}. If we were to use standard eigensolvers with normal, unchanged matrices, the amount of computing power

needed is extremely high, with computing times of over 10^3 s. In order to increase the efficiency of computing, we used algorithms made specially for sparse matrices instead, which take advantage of the fact that there happen to be many zero elements in the matrices we work with, significantly reducing CPU processing time.

4 Results

4.1 Transport in Absence of Dephasing

In Fig. 1, it can be observed that changing the value of Δ can change the properties of magnetization transport. With smaller values for Δ resulting in ballistic transport properties, with $\Delta = 0.1$ showing ballistic properties, mid-range values of Δ showing diffusive transport properties, and higher values of Δ exhibiting progressively more insulating behaviour. Also, notice that the strong boundary driving results in ballistic and insulating regimes for low and high values of Δ respectively. We can observe that spin current is symmetric about $\Delta = 0$, this means that only the magnitude of Δ influences the spin current. We also notice that as Δ increases, J^s tends to 0.

In Fig. 2, we observe that lower Δ values present us with ballistic magnetisation regimes. However, there is diffusive behavior observed in $\Delta = 1$, which is very different from the insulating behavior observed with strong boundary driving. Hence with smaller driving μ, even strong interaction cannot induce an insulating behavior. Similarly, the sign of Δ does not affect magnitude of J^s and we observe that J^s is greatest at $\Delta = 0$, exactly as seen in Fig. 1. However, J^s tends to 0 more slowly with increasing Δ, unlike the observation made in Fig. 2.

Overall, we can notice that the effects of varying Δ are effectively the same regardless of boundary driving on J^s. However, lower boundary driving values result in a reduction of insulating behavior and, instead, diffusive properties.

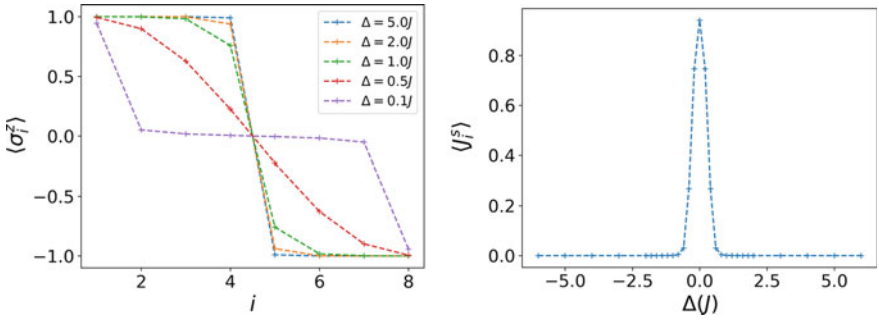

Fig. 1 Left: Magnetisation $\langle \sigma_i^z \rangle$ versus site i in presence of strong boundary driving: $\Gamma = 4J/\hbar$, $\mu = 1$. Right: Spin current versus Δ in the presence of strong boundary driving

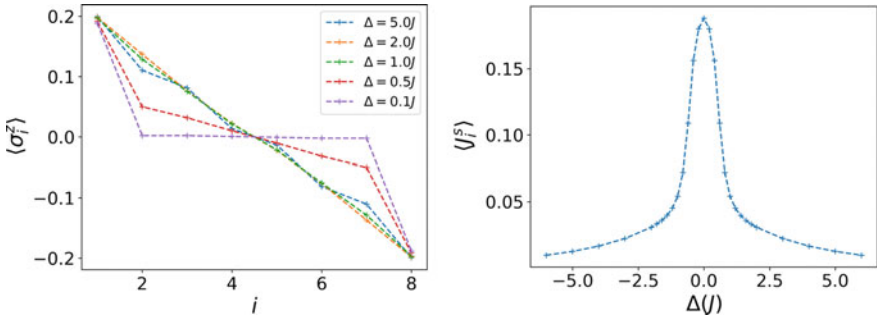

Fig. 2 Left: Magnetisation $\langle \sigma_i^z \rangle$ versus site i in presence of weak boundary driving: $\Gamma = 4J/\hbar$, $\mu = 0.2$. Right: Spin current versus Δ in the presence of weak boundary driving

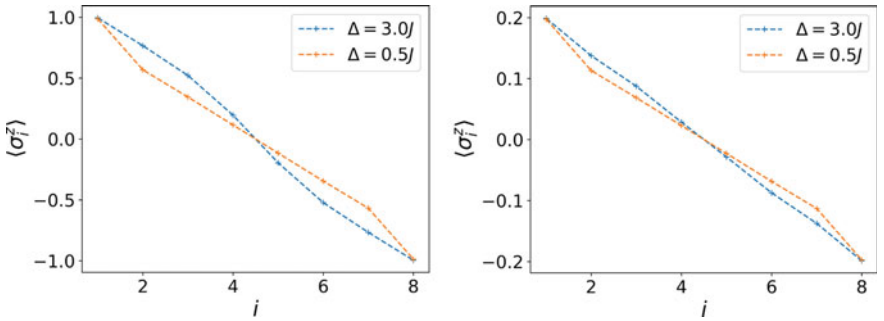

Fig. 3 Magnetisation $\langle \sigma_i^z \rangle$ versus site i in presence of strong and weak boundary driving: $\Gamma = 4J/\hbar$, $\mu = 1$ (left), $\mu = 0.2$ (right)

4.2 Transport with Dephasing

In the presence of dephasing, Fig. 3, $\lambda_Z = 1J/\text{n}$, there is significant difference from the behavior of systems that are not exposed to dephasing. We observe more generally diffusive properties, even at large, or very small, values of Δ.

The effects of changing Δ is very similar to that of the previous figures, with an increased delta giving rise to an increase in diffusive properties. Furthermore, notice that the effects of weak boundary driving has led to comparatively more diffusive properties.

In Fig. 4, the spin current varies with the value of λ_z in different ways with different boundary driving magnitudes. Notice that although we observe that J^s reduces across the board with increasing λ_z for a lower Δ value, we see that J^s in fact increases with increasing λ_z only for strong boundary driving with high Δ values, but remains fairly constant with a slight downward trend for systems with low boundary driving.

Figure 5 has been added to show more clearly the emergence of diffusive behavior in the form of Fick's Law. Notice from Eq. (2) that

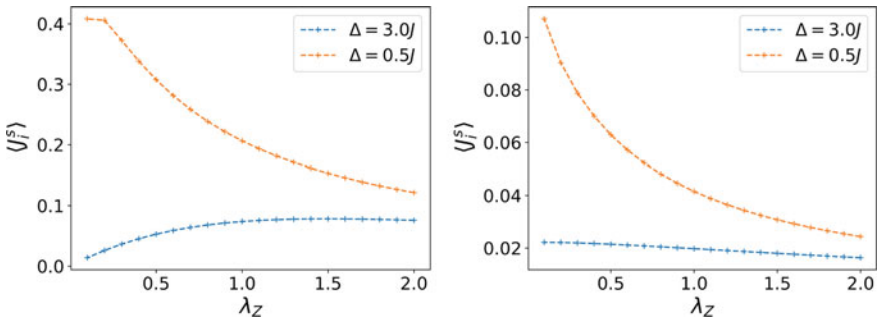

Fig. 4 Spin current $\langle J_i^s \rangle$ versus λ_Z in presence of strong and weak boundary driving: $\Gamma = 4J/\hbar$, $\mu = 1$ (left), $\mu = 0.2$ (right)

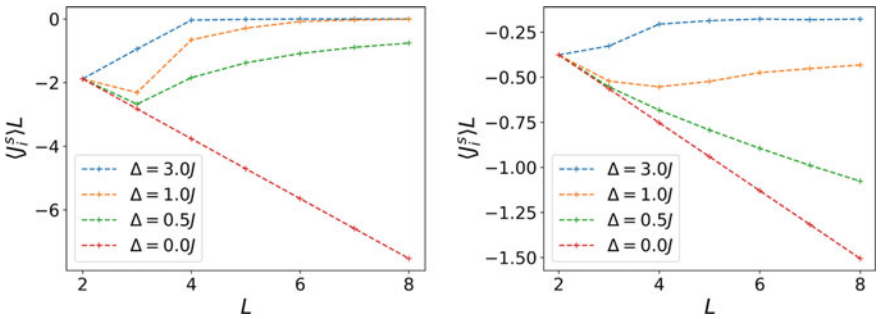

Fig. 5 Spin Current times Length $\langle J_i^s \rangle L$ versus length L in presence of strong (left) and weak (right) boundary driving, absence of dephasing: $\Gamma = 4J/\hbar$, $\mu = 1$ (left), $\mu = 0.2$ (right)

$$J^s \propto \nabla s = -k\frac{\Delta s}{L} J^s L = -k\Delta s \tag{15}$$

Given the coupling of the system to the spin baths, we can assume that Δs is constant in both the strong and weak coupling scenario. Therefore, $J^s L$ is expected to be constant if the system obeys Fick's Law.

In the absence of dephasing, Fig. 5, there is an emergence of Fick's Law in systems for large values of Δ. As suggested previously in Figs. 1 and 2, the transport is diffusive in these scenarios. In the case of ballistic transport, Fick's Law is not observed. In the presence of dephasing, Fig. 6, Fick's Law is observed for all Δ values. The presence of dephasing recovers the classical behaviours from the quantum system and results in diffusive transport for all Δ values. This is again in agreement with the observation in Fig. 3.

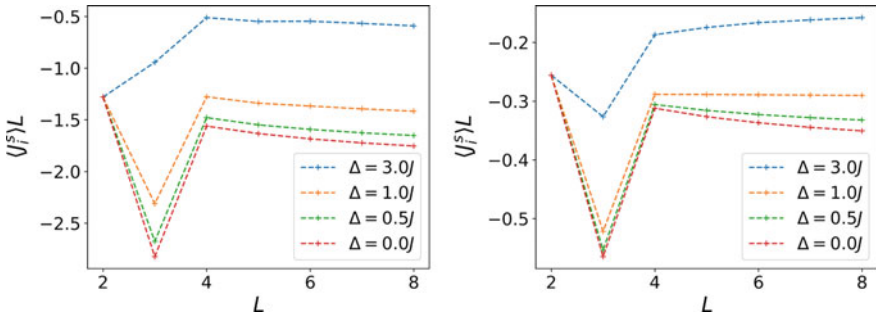

Fig. 6 Spin current times length $\langle J_i^s \rangle L$ versus Δ in presence of dephasing, strong (left) and weak (right) boundary driving $\Gamma = 4J/\hbar$, $\mu = 1, 0.2$, $\lambda_Z = J/\mathrm{n}$

5 Conclusion

We have numerically studied the magnetization transport in a spin-1/2 XXZ chain for various Δ, dephasing, and system sizes. By studying the magnetization profile and calculating the steady-state spin current, we have found that that the system behaves differently due to the presence of Δ and dephasing.

As a main result, we have found that an increase in the magnitude of interaction, Δ, causes the transport property of the system to change from ballistic to diffusive. Interestingly, when $\mu = 1$, a high Δ value can tune the system towards an insulator. Furthermore, we have demonstrated that the presence of dephasing can recover the classical behaviours of the system, regardless of the strength of Δ. This is confirmed by the observation of Fick's law in the system, ignoring the anomaly caused by the finite system size when L is smaller than 4.

Understanding the transport property at the quantum scale for magnetization is important for applications such as spintronics, where one cannot, in general, assume the validity of Fick's law. The application of such XXZ Heisenberg spin chains also lies in approximating the magnetic properties of materials such as copper pyrazine dinitrate to a good degree.

References

1. Fourier, J. (2009). Equation of the Movement of Heat. In A. Freeman (Trans.), The Analytical Theory of Heat (Cambridge Library Collection—Mathematics, pp. 85–130). Cambridge: Cambridge University Press.
2. Fick, A. (1855). "Ueber Diffusion". Annalen der Physik (in German). 94 (1): 59–86.
3. G.T. Landi, E. Novais, M.J. de Oliveira, and D. Karevski, Phys. Rev. E **90**, 042142 (2014).
4. L. Zhang, Y. Yan, C.-Q. Wu, J.-S. Wang, and B. Li, Phys. Rev. B **80**, 172301 (2009).
5. T. Werlang, M. A. Marchiori, M. F. Cornelio, and D. Valente, Phys. Rev. E **89**, 062109 (2014).
6. M. Terraneo, M. Peyrard, and G. Casati, Phys. Rev. Lett. **88**, 094302 (2002).
7. N. Li, J. Ren, L. Wang, G. Zhang, P. Hänggi, and B. Li, Rev. Mod. Phys. **84**, 1045 (2012).

8. G. Benenti, G. Casati, C. Mejía-Monasterio, and M. Peyrard, *From thermal rectifiers to thermoelectric devices*, in *Thermal transport in low dimensions*, S. Lepri (Ed.), Lecture Notes in Physics **921** (Springer, 2016).
9. Breunig, O., Garst, M., Klümper, A., Rohrkamp, J., Turnbull, M. and Lorenz, T., Science Advances, 3(12), sp.eaao3773. (2017)
10. R. Toskovic, R. van den Berg, A. Spinelli, I. S. Eliens, B.van den Toorn, B. Bryant, J.-S. Caux, and A. F. Otte, Nat. Phys. 12, 656 (2016).
11. M. Endres, H. Bernien, A. Keesling, H. Levine, E. R.Anschuetz, A. Krajenbrink, C. Senko, V. Vuletic, M. Greiner, and M. D. Lukin, Science 354, 1024 (2016).
12. D. Barredo, S. de Leseleuc, V. Lienhard, T. Lahaye, and A. Browaeys, Science 354, 1021 (2016).
13. Giulio Casati, Joseph Ford, Franco Vivaldi, and William M. Visscher, Phys. Rev. Lett. **53**, 1120 (1984)
14. B. Li, L. Wang, and G. Casati, Phys. Rev. Lett. **93**, 184301 (2004).
15. V. Balachandran, G. Benenti, E. Pereira, G. Casati, and D. Poletti, Phys. Rev. Lett. **120**, 200603 (2018).
16. G. Lindblad, Commun. Math. Phys. **48**, 119 (1976).
17. V. Gorini, A. Kossakowski, and E.C.G. Sudarshan, J. Math. Phys. **17**, 821 (1976).
18. H.-P. Breuer, and F. Petruccione, *The theory of open quantum systems*, (Oxford University Press, Oxford, 2002)

Graphene and Montmorillonite-Enabled Ultrastretchable Integrated Chemical Barriers and Fire Retardant Nanocoatings for Next-Generation Protective Clothing

Pei Yi Loh, Sean Kar Weng Leong, Chi Zhang, and Po-Yen Chen

Abstract The ideal next-generation protective clothing would confer three main properties: stretchability, flame resistance and chemical retardancy. However, conventional materials render these properties mutually exclusive—as an effective barrier involves closely packed structures while stretchable materials are associated with sparsely packed molecules and considerable free space. In this study, we seek to bridge the gap between retardancy (chemical and fire) and stretchability, by developing a synthetic process allowing both to coexist rather than compromise one another. The fabrication utilised graphene oxide (GO) and montmorillonite (MMT), which are known chemical and flame retardants respectively. These were dispersed onto shrink film templates, before undergoing heat-induced deformation to form a crumpled nanocoating. Additional elastomer curing and shrink film removal programmed the crumpled architecture to unfold under tensile stress, improving final stretchability. Various conditions such as the chemical environment of dispersion and method of integrating GO and MMT were investigated to maximise flexibility and stretchability. It was found that GO-elastomer prepared via aqueous GO solution withstood up to 180% linear strain before fracturing, while the GO-MMT-elastomer hybrid can be elongated by 160% of its original length. Furthermore, an easily upscaled process was facilitated by doctor blade coating, complementing the optimal synthetic pathway. Finally, the barrier properties of the integrated MMT-GO-elastomer were verified via flame tests and gas chromatography tests. Therefore, this study has successfully developed a scalable fabrication pathway for an ultrastretchable, versatile, flexible material that can also slow down chemical and flame penetration, paving the way for the manufacturing of next-generation protective clothing.

Keywords Graphene oxide · Montmorillonite · Ultrastretchable · Fire retardant · Chemical retardant · Protective clothing

P. Y. Loh · S. K. W. Leong · C. Zhang
NUS High School of Mathematics and Science, Singapore, Singapore

P.-Y. Chen (✉)
Department of Chemical and Biomolecular Engineering, National University of Singapore (NUS), Singapore, Singapore
e-mail: checp@nus.edu.sg

H. Guo et al. (eds.), *IRC-SET 2020*,
https://doi.org/10.1007/978-981-15-9472-4_19

1 Introduction and Literature Review

The need for next-generation protective clothing is becoming increasingly salient, in today's volatile, complex, uncertain and ambiguous world. Demand for protective clothing has surged at a compound annual growth rate of 6.1% [1], with the burgeoning of various industries such as manufacturing, construction, and oil and gas. Naturally, the onset of greater workplace risks arises—Singapore alone has experienced more than 10,000 cases of workplace injuries in a year [2]. Of these, chemical and fire hazards are named among the top 10 hazards in the workplace [3], culminating in endeavours in the field of protective clothing which attempt to address these risks.

Protective clothing seeks to strike a balance between protection (effective barrier properties) and human comfort (stretchability of the material) [4]. This has traditionally been perceived as a trade-off between the two: barrier properties often stem from tightly packed structures which prevent the penetration of various substances, whilst stretchability tends to be a property of loosely packed molecular chains with significant, compressible free space. This is a cause of concern in the context of manufacturing protective clothing, as movements by the wearer demand a reasonable degree of flexibility and stretchability [5], whilst still maintaining the protective properties without significant abrasions or cracks forming. Conventional protective clothing have yet to integrate all of the following three desirable properties into a single protective fabric—stretchability, flame retardancy and chemical impermeability (Fig. 1). Common chemical barriers such as elastomers [6], carbon coatings [7, 8] and ceramics [9] are hardly stretchable, while recent attempts at stretchable barriers [10] (we denote in this paper as "competitor") are not geared to provide fire

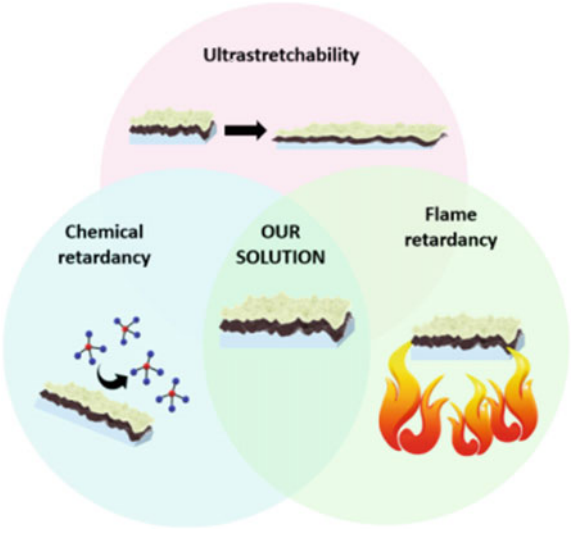

Fig. 1 A Venn diagram depicting the novel intersection between ultrastretchability, chemical and flame retardancy in our protective material

retardancy. Typical fire-resistant protective clothing are also unable to resist chemical penetration when in direct contact [11]. This presents a dilemma to consumers—wearing two layers of clothing would be unfeasible, on the grounds of cost, thickness of the material and discomfort to the wearer. On the other hand, choosing one of the clothings would compromise on functionality, risking ignition or chemical injury.

This study thus addresses the imperative for designing a versatile solution which can be applied to produce and manufacture all-in-one, multipurpose protective clothing. We explore and optimise the synthesis process for a graphene oxide (GO) and montmorillonite (MMT) based material, which are known to be chemical barriers and flame retardants respectively. Studies in the field have revealed that GO is impermeable to almost all gases and liquid [12], while MMT significantly improves flame retardancy and lowers heat release rates of materials [13]. We leverage on the highly folded 3D crumpled GO and MMT nanostructures (Fig. 9 in appendix), which is capable of undergoing programmed unfolding when functionalized on a stretchable elastomeric surface, which also provides structural support. By bridging the gaps between the properties of stretchability, fire retardancy and chemical impermeability, this study aims to minimise the impact of chemical and fire hazards, whilst improving user comfort by stretching and compressing to a suitable degree in accordance to their day-to-day movements.

2 Methodology

We seek to develop a methodology to integrate the three main components for our final product—GO, MMT, and a silicon-based elastomeric layer. Given that previous literature has determined the optimal conditions in which MMT can adhere to the elastomer (7 mg/ml, with MMT:PVA ratio of 3:1) [14], our first step is to establish how various factors can be optimised to allow GO to adhere to the elastomer and maximise stretchability. Thereafter, the GO and MMT are integrated with the elastomer, and we investigate the most optimal method to do so. At the same time, we upscale our production procedure for versatile application to the industrial world. Finally, we verify the barrier properties of our final product using stretching, flame and gas chromatography (GC) tests (Fig. 2).

2.1 Fabrication of GO-Elastomer Bilayer

Our methodology utilises plastic shrink films as a template for GO solution to be dispersed on, as after coating a planar GO layer, heat-induced shrinking of the films can guide it to form the desired crumpled architecture. Stock 5 mg/ml GO solution was diluted to 0.75 mg/ml for the dispersion, using either water or ethanol (95%, Sigma). 5 by 5 cm shrink films were first prepared and rinsed thoroughly with DI water and ethanol and treated with pure oxygen plasma for 5 min. Next, 20 ml of GO

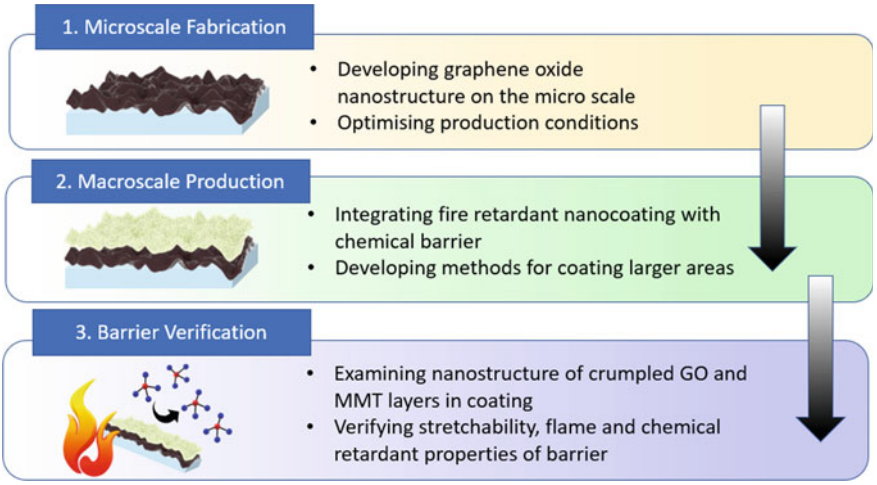

Fig. 2 The overarching methodology in this study, which aims to first optimise the conditions in which crumpled GO should be produced, before moving on to integrate both the fire retardant and chemical barrier properties together and investigating means for easy upscaling. Lastly, the crumpled nanostructures of the GO and MMT layers were verified by observation under the scanning electron microscope, and the barrier properties of our material were cross-checked via flame and chemical testing

solution in various chemical environments was dropcast and added in excess to a 5 by 5 cm shrink film in petri dish (10 cm diameter). The GO water solution was left to dry overnight, forming a planar coating. Afterwards, the GO coated shrink film was heated in the oven at 140 °C for 15 min to undergo heat-induced deformation, shrinking to about 2 by 2 cm. The shrunk GO coated film was coated with liquid elastomer and left to cure for 4 h, before it was immersed in dichloromethane (DCM) (≥99.8%, Sigma) for 2 h to dissolve the shrink film layer, leaving the final material to dry in the fumehood (Fig. 3).

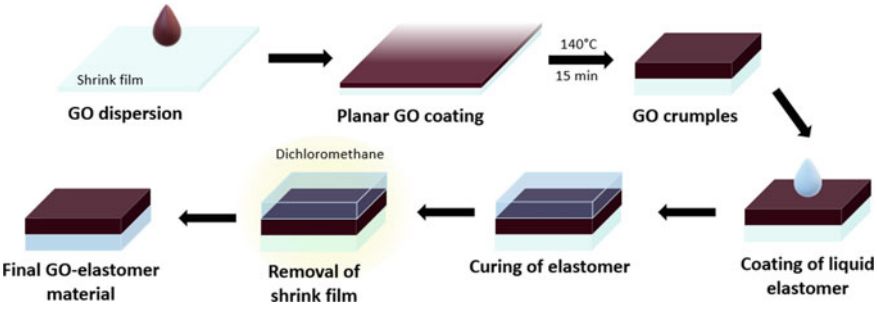

Fig. 3 A schematic diagram illustrating the methodology behind synthesizing the GO-elastomer bilayer, by dispersing a planar layer of GO onto shrink film and using heat deformation to induce the crumpled architecture, and curing with elastomer

Via this methodology, we aim to maximise the degree that the GO-elastomer complex can be stretched before surface fracturing, and therefore investigated the effect of different parameters on the stretchability. For the solvent in which the stock GO was dissolved, water and ethanol were chosen—the former was decided under the consideration that the stock GO was already suspended in water, while the latter was selected as alcohol is highly polar and could possibly aid the dispersion of GO on the nonpolar shrink film surface. However, initial experimentation found that alcohol-diluted GO prevented the planar GO coating from being evenly distributed due to the formation of coffee-ring effect. Hence, the stock GO solution was diluted with water for the rest of the procedure and experimentation.

Several other variables were also looked into. For the GO dispersion step, we explored incorporating hydrogels into the GO layer, as the hydrophilic groups in its constituent polymer network could possibly enhance the adhesion of GO to the elastomer, improving stretchability without fracturing. In this study, aqueous 0.75 mg/ml GO solution was incorporated with three different hydrogels—sodium alginate, polyvinyl alcohol (PVA) and polyvinyl pyrrolidone (PVP). These were chosen based on literature, since sodium alginate is a known low-cost and non-toxic hydrogel [15]; PVA is able to act as a good adhesive [16] and is chemical resistant [17]; PVP has previously been used for enhancing liquid dispersion in other contexts. [18] For each hydrogel, different GO:hydrogel ratios were also used, namely 2:1, 4:1 and 9:1 to represent a range of GO concentrations, which is proportional to the thickness of the GO layer. A negative control was also used, by diluting the stock GO solution with water only, to ensure that any variations in the final stretchability is solely due to the presence of polymers.

As for the elastomeric layer, we used three different types of elastomer with varying hardness, to represent those in the extra soft, soft and medium soft range (Fig. 10 in appendix). Platinum cure silicone (Ecoflex 00–20 and Ecoflex 00–50) and polydimethylsiloxane (PDMS) were chosen due to their relative softness and flexibility, as well as the relatively fast curing time. The way in which the elastomer was also coated was also varied; particularly, both spin coating and petri dish curing were used. However, spin coating at high speeds (500–600 rpm) resulted in elastomer layers that were too thin (1–2 mm), while spin coating at low speeds (100–300 rpm) started to compromise on the uniformity of distribution. Overall, spin coating was unable to give the desired thickness of about 5–6 mm to achieve a balance between flexibility and durability. Hence, the various liquid elastomers were decanted into 10 cm diameter petri dishes and placed into the vacuum chamber for 5 min to remove air bubbles, before leaving to cure for 4 h.

2.2 *Production of GO-MMT Hybrid and Manufacturing Approach*

Once we have determined the optimal chemical environment for GO to maximise stretchability, we subsequently proceed to integrate the MMT, enabling the material to slow down the penetration of both fire and chemicals. For this step, rectangular and longer shrink films, in this case 16 by 4 cm, were used to mimic the rectangular fabrics that are produced in mass manufacturing, allowing us to better simulate the process. Doctor blading was chosen as our approach for manufacturing our hybrid GO-MMT-elastomer material in the large scale, as it is capable of coating controlled thin layers on our shrink film template, and can produce relatively uniform coatings in short amounts of time.

The procedure of producing the GO-MMT hybrid is largely similar to the previous section. However, we note that there fumehood. (For a detailed schematic, see Fig. 11 in the appendix).

3 Results and Discussion

Given the existing knowledge on the efficacy of GO and MMT as barrier materials, the synthetic procedure that we optimise in this study thus focuses on maximising the stretchability. To find the stretchability, we linearly stretch the GO-elastomer and GO-MMT hybrid materials which synthetic procedures were described earlier, until the surface begins to fracture. The initial and final lengths of the GO surface, which we denote as L_i and L_f respectively, were measured and recorded. are different ways in which GO and MMT could be integrated onto the same surface of the elastomeric materials. We set MMT to be either on the same plane, or overlapping the GO, as fire protection would prevent the material from being burnt first, in order for the chemical protection layer to function smoothly even while burning. After narrowing down the most plausible ways in which this could be incorporated with doctor blading, we performed three distinct methods to integrate GO and MMT (Fig. 4).

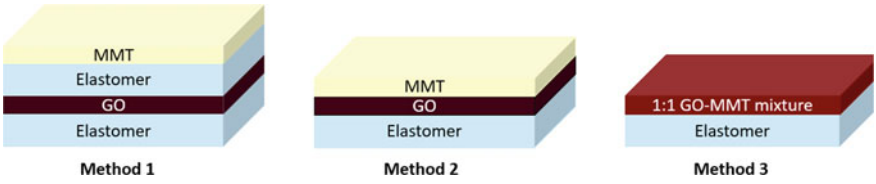

Fig. 4 The three different methods in which GO and MMT can be integrated with the elastomer to form a versatile chemical barrier and fire retardant nanocoating. Method 1 involves making separate GO-elastomer and MMT-elastomer layers and attaching them afterwards. Method 2 involves coating a layer of GO and MMT respectively and Method 3 coats a mixture of both on elastomer

We first prepared a 4 by 16 cm shrink film and treated it with pure plasma oxygen for 5 min, before coating with 3 ml of 10 mg/ml MMT-water solution using an automatic film coater machine, to coat the solution on the shrink film with a pre-set thickness of 120 μm. The MMT coated shrink film was left overnight to dry. We then coated this MMT-coated shrink film with another 3 ml of GO, once again dried overnight. The resulting material was heated at 140 °C to induce shrinking, before liquid Ecoflex 00–20 elastomer was coated on and left to cure for 4 h. Finally, the shrink film layer was dissolved by immersing in dichloromethane for another 4 h, giving the final product upon drying in the fumehood.

These were used to compute the percentage elongation of the material as shown in the following equation. This in turn reflects the linear strain exerted and the overall stretchability.

$$\text{Percentage Linear Strain} = \frac{L_{\text{f}} - L_i}{L_i} \times 100$$

3.1 Optimising Stretchability of GO-Elastomer Bilayer

For determining the type of elastomer that is most suitable for fabrication of our ultrastretchable material, aqueous tandard oxide with a concentration of 0.75 mg/ml was tandardized for dispersion, to ensure that the outcome would not be skewed by any chemical interactions of polymeric hydrogels. Out of the three types of elastomer used, Ecoflex 00–20 was chosen as most optimal, as the GO layer had the best adherence to its surface as opposed to PDMS, and allowed air bubbles trapped in the liquid elastomer to escape easily via vacuum suction before it begins to cure, giving rise to a desirable uniform elastomer layer.

Figure 5 illustrates the effect of various hydrogels mixed with GO in different ratios on the stretchability of the GO-elastomer bilayer. Surprisingly, while the addition of hydrogels was expected to promote hydrophilicity and adherence of GO to

Type of hydrogel used (if any)	Percent elongation of GO-elastomer before surface fracture		
	GO: hydrogel = 2:1	GO: hydrogel = 4:1	GO: hydrogel = 9:1
GO-sodium alginate	GO unable to adhere	GO unable to adhere	GO unable to adhere
GO-PVA	5%	5-10%	10%
GO-PVP	50%	50%	20-25%
No hydrogel (GO-water)	80%		

Fig. 5 Table showing the effect of various types of hydrogels used in the GO dispersion stage, and the relative ratios between the GO and hydrogel, on the overall stretchability of the material. This is determined by ascertaining the percent elongation of the GO-elastomer surface before cracks and fractures appear

the elastomer, this caused the stretchability to decrease instead of increase compared to aqueous GO.

GO-water exhibited the highest percent elongation before surface fracture, at 80% of its original length, as compared to a maximum stretchability of 50% for PVP and 10% for PVA. When mixed with sodium alginate, the GO layer was unable to adhere well to the elastomer and became very brittle, possibly because the heat-induced deformation of the shrink film has also broken the cross-links within the alginate hydrogel. For PVP, stretchability is higher in the lower GO:PVP ratios (2:1 and 4:1) than higher ratios (9:1), which suggests that though the presence of PVP decreases overall stretchability, increasing PVP proportions still reduces it to a smaller extent. This might be due to higher concentrations PVP inducing more crumpling effect of the GO nanostructure during heat-induced deformation, which increases stretchability. As for PVA, this trend is reversed, with stretchability generally increasing as the GO:PVA ratio increases. This suggests that the more PVA added, the lower the stretchability, which can be attributed to the intermolecular interactions from PVA's hydroxyl groups reducing the extent of GO crumpling during heating, lowering the threshold that the GO layer can unfold before cracking. Hence, aqueous GO was chosen for the next step which integrates the fire retardant MMT and devises a viable method for large-scale production of our material. Figure 12 in the appendix illustrates the adherence of the GO layer to the elastomer via snapshots of each resulting material.

3.2 Large-Scale Fabrication of GO-MMT Hybrid

Figure 6 shows the relative stretchability of the GO-MMT hybrid using each possible method of integrating the two barriers together, used in conjunction with the doctor blading approach for large scale synthesis. Method 2, which coats the elastomer with a layer of GO, then a layer of MMT on the exterior, fares the best in terms of stretchability, elongating by 60% before first experiencing fractures. Method 3, where 1:1 GO-MMT mixture is coated comes in second, at 55% percent stretchability, while Method 1, which attaches a GO-elastomer bilayer with another MMT-elastomer bilayer, has the lowest percentage elongation. This could be because with increased number of layers, the product of Method 1 has a higher Young's modulus, leading to greater shear stress in the nanocoatings per unit deformation. Moreover, it is expected that using a GO-MMT mixture would decrease the stretchability, as the MMT solution had also incorporated PVA (in a ratio of 3:1) in our preparation stage, and from our previous experiments, mixing GO with PVA had decreased the stretchability of the GO nanocoating. There are also concerns that Method 1 would give rise to a fabric that is too thick for user comfort, posing the risk of overheating; while Method 3 would result in compromised flame retardancy properties, since both GO and MMT would be on the same plane. Taking into account all of these results and considerations, Method 2 was thus chosen as the method to be adopted when

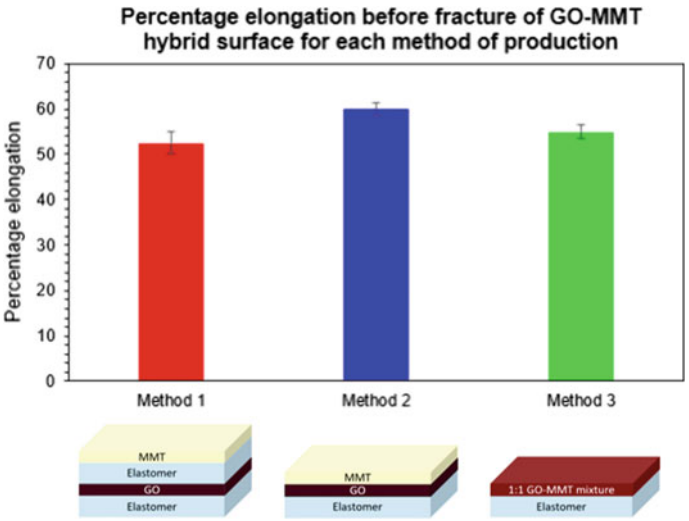

Fig. 6 Bar graph showing how the different possible ways of integrating the chemical barrier (GO) with fire retardant (MMT) fare in terms of the stretchability of the eventual material without the formation of cracks. It was found that stacking distinct GO and MMT layers on a single layer of elastomer gave rise to the highest percentage elongation among the three methods

manufacturing our integrated protective material. The flexibility of our material is also verified as shown in Fig. 13 (in appendix).

3.3 Barrier Properties of GO-MMT Hybrid

To verify the fire retardancy properties of our material, a GO-elastomer layer (without MMT) and our hybrid material were both exposed to an open flame. Within 20 s, the GO-elastomer layer ignited and undergone severe deformation while the hybrid material had negligible deformation, and did not ignite throughout. (Fig. 7). This is consistent with the findings from previous literature, about the fire retardant properties of MMT [13, 14].

As for the chemical retardancy properties of our material, literature has previously rigorously and extensively proven the chemical barrier properties for GO against almost all liquid and gas chemicals. Hence, gas chromatography tests were only conducted on DCM and acetone (≥97%, Sigma). DCM was selected as it was a part of the synthesis procedure, and we intended to verify that long hours of DCM exposure would not compromise the barrier's ability to slow down its penetration; and acetone was selected due to its ubiquity as chemicals and solvents. Figure 14 in the appendix illustrates the GC test results from DCM and acetone with hexane (≥95%, Sigma) as a solvent, showing that both DCM and acetone were able to be resisted from penetration for at least 10–20 min, reinforcing findings from existing

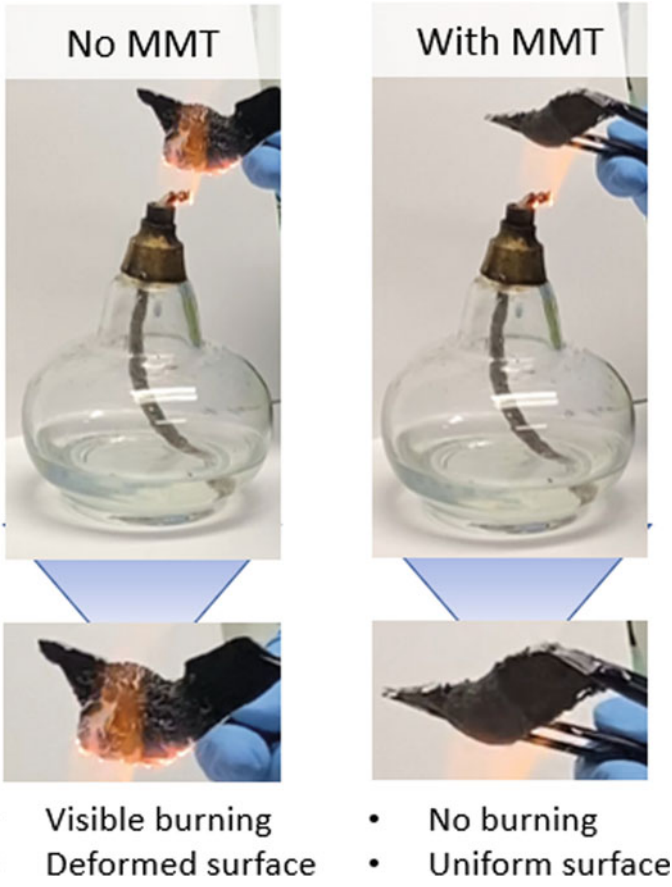

Fig. 7 Comparison pictures showing the effect of an open flame on GO-elastomer versus the GO-MMT hybrid, which proved MMT effective in conferring fire retardancy

literature [12], and buying users crucial time to seek help in the event of direct chemical contact.

Figure 8 provides a comparison of the overall efficacy of our solution in stretchability, chemical and fire retardancy, put into perspective with existing barrier materials and conventional fabrics used in clothing (nylon, polyester, cotton) [19–21].

In the future, we aim to continue developing our protective material in the following areas—firstly, we will further upscale our GO-MMT-elastomer hybrid from our current A4-size to a size that is suitable for producing a full-body suit. We will also seek to test biocompatibility by testing the comfort levels of the suit over extended periods of time. Through this progressive framework, we endeavour to develop an easily usable and comfortable protective suit that embodies all desired characteristics—stretchability, chemical retardancy and fire retardancy.

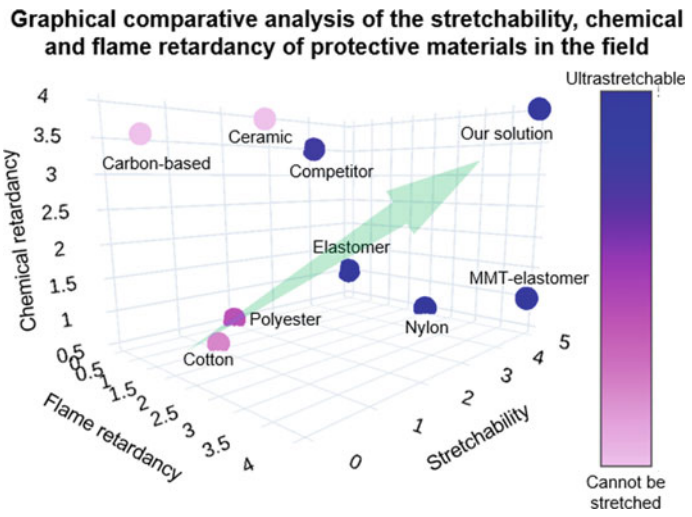

Fig. 8 A graphical perspective on the overall efficacy of our integrated protective barrier versus others in the field. The green arrow points towards the direction of the desirable material which is effective in every aspect

4 Conclusion

In this project, a novel versatile material for next-generation protective clothing was successfully produced, which seamlessly integrates ultrastretchability, flame retardancy and chemical barrier properties. This was achieved by fabricating crumpled GO and MMT nanostructures which were functionalised on a stretchable elastomer layer, designed to undergo programmed unfolding upon undergoing tensile stress. A rigorous approach was taken not only to optimise the stretchability of our material, but also devise a feasible and sustainable process to manufacture our material on the large scale. Our solution thus demonstrates the potential for valuable applications for revolutionising the production and synthesis of protective clothing in various industrial settings, alleviating the pervasive workplace chemical and fire hazards, and reducing the avoidable injuries and deaths in consequence.

Acknowledgements We would like to sincerely thank our external mentor, Asst Prof Chen Po-Yen from Department of Chemical and Biomolecular Engineering, NUS, for offering us this project opportunity and for his valuable insights. We would also like to thank our teacher-mentor, Mr Murali Krishnaswamy from NUS High School of Mathematics and Science, for his unwavering guidance and support throughout this journey.

Appendix

All diagrams were self-created.
See Figs. 9, 10, 11, 12, 13, and 14.

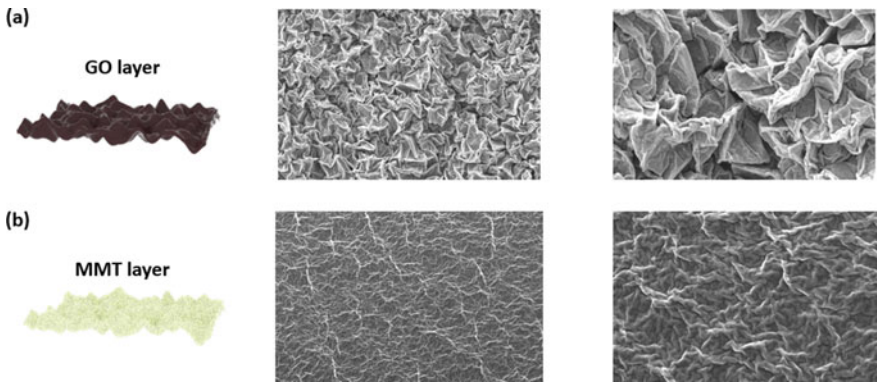

Fig. 9 Diagrams versus scanning electron micrographs of each layer of crumpled nanostructure in our barrier material. **a** From left to right, the figure shows a schematic of the GO layer's architecture, followed by SEM images at 300 × and 1000 × magnification respectively. **b** The same is presented for the MMT layer

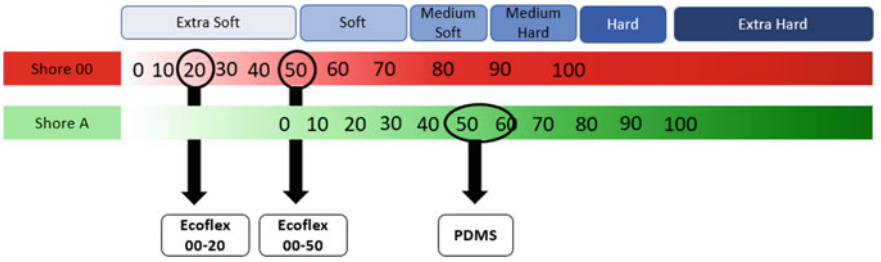

Fig. 10 A depiction of the spectrum of material hardness on the Shore scales, for both the Shore 00 and Shore A scales. Ecoflex 00–20 has a Shore 00 reading of 20, and is considered an extra soft material; while Ecoflex 00–50 has a Shore 00 reading of 50, and is considered as a soft material. Research has shown that PDMS has a Shore A reading of about 46–61 [22], making it a medium soft elastomeric material

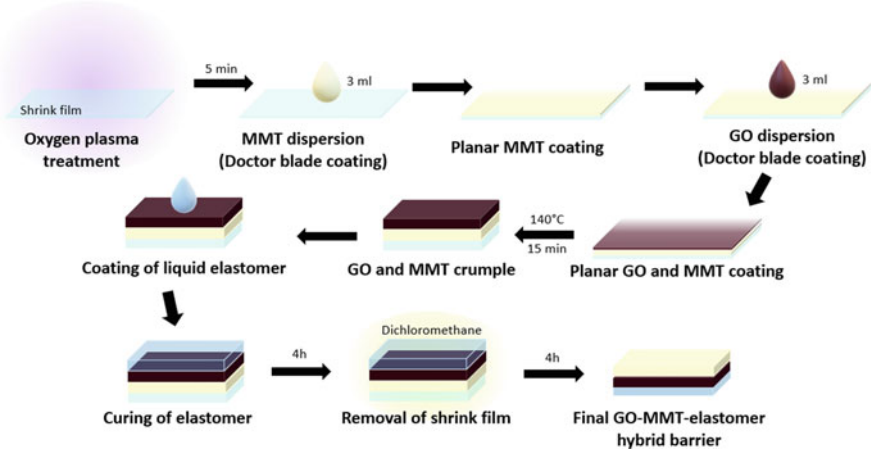

Fig. 11 A schematic diagram showing the detailed synthetic process for the GO-MMT hybrid material, which coats a layer of MMT and GO on top of the elastomer, to confer both chemical retardant and fire retardant barrier properties, in addition to ultrastretchability

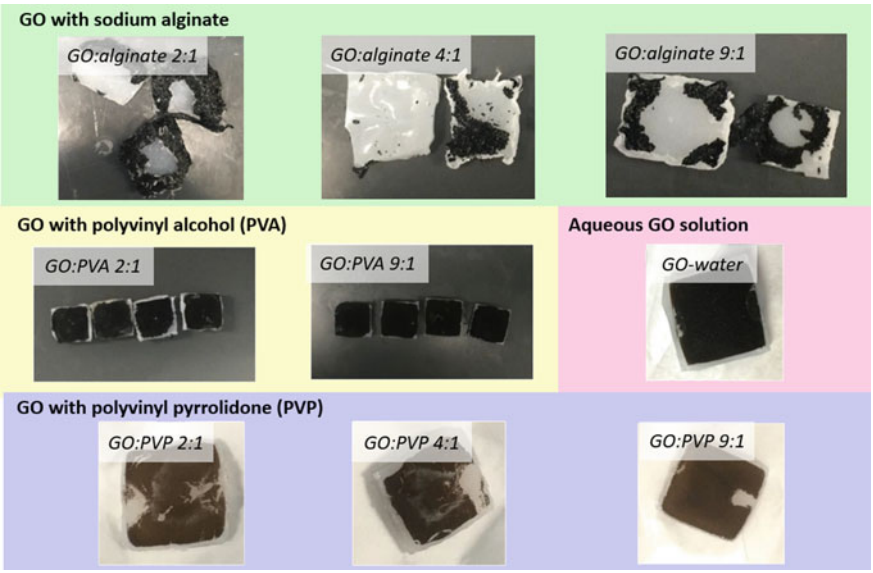

Fig. 12 Photographs of the GO-elastomer bilayers that result from each dispersion condition, where the GO is dissolved either in water or with various hydrogels as well. For all ratios involving GO and alginate, the adhesion of the GO layer to the elastomer is poor, and GO-PVP adheres moderately well to the surface. GO-PVA and GO-water both adhere well to the surface, however, GO-water had the best stretchability

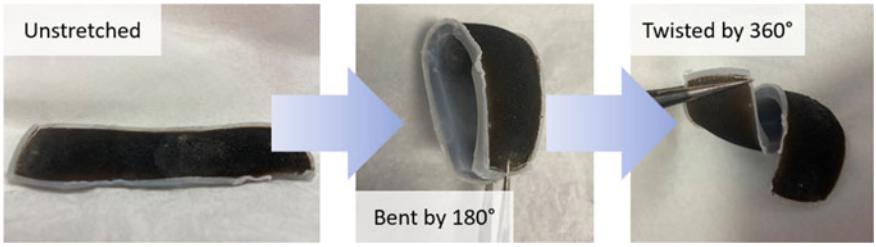

Fig. 13 Our material is not only ultrastretchable but also flexible, as shown by how it can be bent by 180° and twisted by 360° while being able to return to its original shape, without undergoing any damage. This reinforces the suitability of this material for application in protective clothing

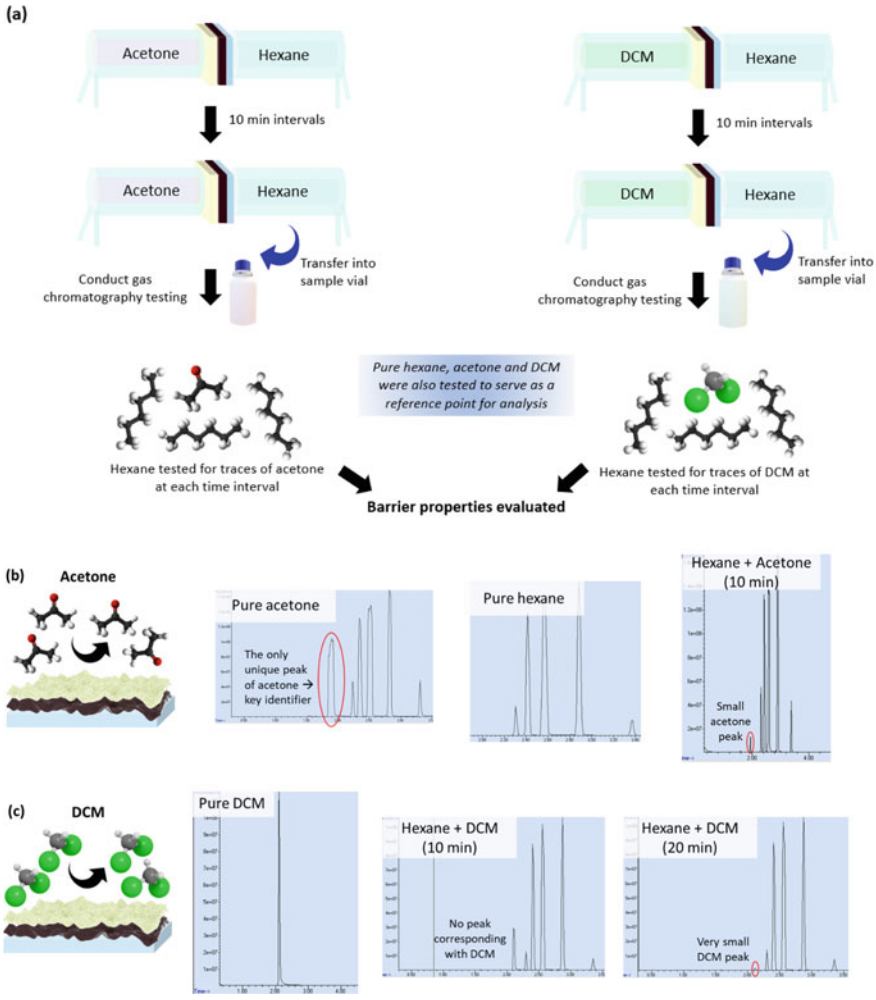

◀**Fig. 14** Procedure of chemical testing process and the corresponding results. **a** Chambers of acetone/DCM and hexane (the solvent, selected due to its commonplace usage) were prepared, separated in the middle by a small piece of our protective material (2 cm by 2 cm). At 10 min intervals, small amounts of solution on the right chamber (with primarily hexane) would be extracted into a solution vial. The components of this solution vial would then be determined using gas chromatography, as well as solutions of pure hexane, acetone and DCM, to detect the time at which trace amounts of acetone/DCM are detected in the solution, which implies the beginning of penetration. This allows us to better assess the chemical retardancy of our GO-MMT-elastomer hybrid. **b** Results for acetone, which involves comparison between the peaks of pure hexane and acetone. It shows that there is only one identifiable peak for acetone, as the other peaks of acetone coincide almost exactly with that of hexane. By analysing the hexane–acetone peaks, we found that our material was able to slow down acetone penetration by at least 10 min, as a small acetone peak only begins to appear at the 10 min mark. **c** Results for DCM, which show that our material was able to slow down DCM penetration by at least 20 min, as there are no DCM peaks appearing in the first 10 min, whilst a very small DCM peak only begins to appear at the 20 min mark. Overall, these results are promising as the chemical retardant properties are verified, meaning that users can buy time for seeking the necessary help in the event of direct chemical contact

References

1. Protective Clothing Market demand to grow at a CAGR of 6.1% during the forecast period 2019 to 2025. *The Express Wire* (2019). Available at: https://www.theexpresswire.com/pressrelease/The-global-protective-clothing-market-to-experience-an-expansion-due-to-the-demand-influx-from-the-manufacturing-and-healthcare-industries_10375772. (Accessed: 5th January 2020)
2. Ministry of Manpower. Workplace Safety and Health Report 2017.(2017).
3. Common office hazards—and how to reduce their risks. *Health & Safety Handbook* (2019). Available at: https://www.healthandsafetyhandbook.com.au/10-common-office-hazards-and-how-to-reduce-the-risk/. (Accessed: 5th January 2020)
4. Ashdown, S. P. *Sizing in clothing: developing effective sizing systems for ready-to-wear clothing*. (CRC, 2007).
5. Yu, W. *Advances in womens intimate apparel technology*. (Woodhead Publishing in association with The Textile Institute, Woodhead Publishing is an imprint of Elsevier, 2016).
6. Xiang, F., Givens, T. M., Ward, S. M. & Grunlan, J. C. Elastomeric Polymer Multilayer Thin Film with Sustainable Gas Barrier at High Strain. *ACS Applied Materials & Interfaces* **7,** 16148–16151 (2015).
7. Boutroy, N. *et al.* Hydrogenated amorphous carbon film coating of PET bottles for gas diffusion barriers. *Diamond and Related Materials* **15,** 921–927 (2006).
8. Nakaya, M., Uedono, A. & Hotta, A. Recent Progress in Gas Barrier Thin Film Coatings on PET Bottles in Food and Beverage Applications. *Coatings* **5,** 987–1001 (2015).
9. Corral, E. L. & Loehman, R. E. Ultra-High-Temperature Ceramic Coatings for Oxidation Protection of Carbon–Carbon Composites. *Journal of the American Ceramic Society* **91,** 1495–1502 (2008).
10. Jain, M. K. *Stretchable chemical protective material.*US8037550B2 (2011).
11. Pohanish, R. P. *Sittigs handbook of toxic and hazardous chemicals and carcinogens*. (Elsevier, William Andrew, 2017).
12. Su, Y. *et al.* Impermeable barrier films and protective coatings based on reduced graphene oxide. *Nat. Commun.* **5**, 1–5 (2014).
13. Malkappa, K., Bandyopadhyay, J. & Ray, S. S. Thermal degradation characteristic and flame retardancy of polylactide-based nanobiocomposites. *Molecules***23**, (2018).

14. Chang, T. H., Tian, Y., Wee, D. L. Y., Ren, H. & Chen, P. Y. Crumpling and Unfolding of Montmorillonite Hybrid Nanocoatings as Stretchable Flame-Retardant Skin. *Small* **14**, 1–9 (2018).
15. He, Y. *et al.* Alginate/graphene oxide fibers with enhanced mechanical strength prepared by wet spinning. *Carbohydrate Polymers* **88,** 1100–1108 (2012).
16. Hou, R. *et al.* Magnetic nanohydroxyapatite/PVA composite hydrogels for promoted osteoblast adhesion and proliferation. *Colloids and Surfaces B: Biointerfaces* **103,** 318–325 (2013).
17. Baker, M. I., Walsh, S. P., Schwartz, Z. & Boyan, B. D. A review of polyvinyl alcohol and its uses in cartilage and orthopedic applications. *Journal of Biomedical Materials Research Part B: Applied Biomaterials* **100B,** 1451–1457 (2012).
18. Gupta, P., Kakumanu, V. K. & Bansal, A. K. Stability and Solubility of Celecoxib-PVP Amorphous Dispersions: A Molecular Perspective. *Pharmaceutical Research* **21,** 1762–1769 (2004).
19. Kaynak, H. K. & Babaarslan, O. Breaking Strength and Elongation Properties of Polyester Woven Fabrics on the Basis of Filament Fineness. *Journal of Engineered Fibers and Fabrics* **10,** 155892501501000 (2015).
20. Azo Materials. Polyamide 6/6–6—Nylon 6/6–6—PA 6/6–6. *AZoM.com* (2001). Available at: https://www.azom.com/article.aspx?ArticleID=751. (Accessed: 5th January 2020)
21. Hsieh, Y. Chemical structure and properties of cotton. *Cotton* 3–34 (2007). https://doi.org/10.1533/9781845692483.1.3
22. Kim, M., Moon, B. U. & Hidrovo, C. H. Enhancement of the thermo-mechanical properties of PDMS molds for the hot embossing of PMMA microfluidic devices. *J. Micromechanics Microengineering***23**, (2013).

Monte Carlo Method in Chemical Engineering

Trivikram Mohan, Vinamr Athavle, Akshat Chaudhary, and Fook Choon Lee

Abstract Chemical reaction rates are described phenomenologically by differential equations. A fundamental limitation in the analytical study of chemical kinetics, however, is that it is generally not possible to solve more than two coupled differential equations, or to integrate analytically an integral of three dimensions or more. Monte Carlo is a class of stochastic algorithms designed to study the equilibria of such complex reactions by integrating the partial differential equations using random sampling. This project aims to determine the effectiveness of existing Monte Carlo methods using the 4th order Runge–Kutta algorithm as a benchmark. The Monte Carlo method was used to study the equilibria of a chemical reaction network consisting of three compounds and 4 elementary reaction steps. Equilibrium concentrations obtained using this method converge to the Runge–Kutta equilibrium concentrations with increasing simulation cycles, up to an observed 300,000 cycles. A pseudo-random number generator (PRNG) superior to Microsoft Excel's 'Rnd' function was used for improved accuracy and efficient debugging of the program.

Keywords Monte Carlo · Runge–Kutta · Chemical equilibria · Pseudo-random · Metropolis Monte Carlo

T. Mohan (✉) · V. Athavle · A. Chaudhary
School of Mathematics and Science, NUS High, 20 Clementi Avenue 1, Singapore 129957, Singapore
e-mail: h1610151@nushigh.edu.sg

V. Athavle
e-mail: h1610153@nushigh.edu.sg

A. Chaudhary
e-mail: h1610001@nushigh.edu.sg

F. C. Lee
School of Chemical and Life Sciences, Singapore Polytechnic, 500 Dover Rd, Singapore 139651, Singapore

H. Guo et al. (eds.), *IRC-SET 2020*,
https://doi.org/10.1007/978-981-15-9472-4_20

1 Introduction

It is difficult to solve reaction systems with two or more differential systems analytically. This causes us to use numerical approximation. Often, many approximations are applied, such as the Steady-State approximation, in an attempt to describe these complex, multi-reaction phenomena. The use of numerical simulations is crucial to obtain useful information regarding the kinetics of the reaction if the rate equations are not solvable using known analytical methods, such as direct integration and substitution. An example of such a reaction is the case of three generic chemical compounds that can interconvert by a first-order reaction rate law:

$$A \rightleftharpoons B \rightleftharpoons C \text{ (with rate constants } \mathbf{k}_{AB}, \mathbf{k}_{BC}, \mathbf{k}_{BA}, \mathbf{k}_{CB}) \tag{1}$$

Algorithms that integrate the rate equations sequentially in time are described collectively as *deterministic*. Once the integration is started, the concentrations of the compounds at fixed points of time are determined a priori. To obtain the equilibrium concentrations of a reaction rather than its detailed time dependence, alternative algorithms are required which integrate the partial differential equations by random sampling of their concentrations. Such algorithms are described as *stochastic*, since there is no time-dependence in the integrations; it is random and a priori, unpredictable. This helps to simulate and mathematically model the random collisions of the molecules.

Monte Carlo is the name given to a class of methods of solving complex numerical integrations by random sampling procedures involving pseudo-random numbers. The Monte Carlo Method is a stochastic algorithm which has no time dependence. Hence, it is extremely useful to calculate equilibrium concentrations and is versatile, having applications in Crystallization, Protein Folding, pharmaceutical powder mixing, drug molecule transport in the body, etc. where common deterministic algorithms including the Runge–Kutta algorithm may not be applied.

2 Materials and Methods

This project evaluated the effectiveness of Monte Carlo algorithms in analyzing complex chemical kinetics, while using the 4th order Runge–Kutta algorithm as a benchmark for equilibrium concentration. While keeping in consideration that Monte Carlo methods are far more versatile and applicable than Runge–Kutta algorithms, we first used the Runge Kutta algorithm to approximate equilibrium concentrations in (1), with various reactant concentrations.

2.1 Phase 1 (The Kinetics of $A \rightleftharpoons B \rightleftharpoons C$)

Introduced above, an example of how complex multi-reaction phenomena give rise to coupled differential equations that cannot be solved analytically, is the case of 3 generic compounds that can interconvert by the first-order reaction rate law.

There are three coupled first-order differential equations that express the change in concentrations of the three compounds, reactant A, product C and intermediate B, with time.

$$\begin{aligned}
\frac{\mathrm{d}}{\mathrm{d}t}[A] &= -k_{\mathrm{AB}}[A] + k_{\mathrm{BA}}[B] \\
\frac{\mathrm{d}}{\mathrm{d}t}[B] &= k_{\mathrm{AB}}[A] - k_{\mathrm{BA}}[B] - k_{\mathrm{BC}}[C] + k_{\mathrm{CB}}[C] \\
\frac{\mathrm{d}}{\mathrm{d}t}[C] &= -k_{\mathrm{CB}}[C] + k_{\mathrm{BC}}[B]
\end{aligned} \tag{2}$$

These equations are coupled because the rate of change of $[A]$ depends on $[B]$, and the rate of change of $[B]$ depends on both $[A]$ and $[C]$, etc. These reactions happen simultaneously, hence the results may only be obtained through numerical analysis via simulation. The analysis of interest are the Monte Carlo methods, which will be compared against the 4th order Runge–Kutta known for its high accuracy, but constrained applicability.

2.1.1 Brief Overview of the 4th Order Runge–Kutta Algorithm

The 4th order Runge–Kutta algorithm is a method of computing intermediate points given a differential equation to predict the Δy of the graph [1]. This is analogous to the computation of Δy from the truncation of the Taylor series of the function after the x^4 term. Hence, the error is of the magnitude of x^5, and while it is cumulative, it is extremely small and can be considered as trivial/negligible. Given the function $f(x, y)$, we compute the gradient at the initial, and intermediate points as follows:

$$\begin{aligned}
C_1 &= f'(x, y) \\
C_2 &= f'\left(x + \frac{\Delta x}{2}, y + \frac{C_1 \Delta x}{2}\right) \\
C_3 &= f'\left(x + \frac{\Delta x}{2}, y + \frac{C_2 \Delta x}{2}\right) \\
C_4 &= f'(x + \Delta x, y + C_3 \Delta x)
\end{aligned} \tag{3}$$

where C_1 is the value of the gradient at the start of the interval, C_2 and C_3 are predicted and corrected values of the slope at the midpoint of the interval $x + \Delta x/2$, and C_4 is the value of the gradient at the end of the interval $x + \Delta x$. The average gradient is computed by:

$$C_{\text{avg}} = \frac{C_1 + 2C_2 + 2C_3 + C_4}{6}$$
$$D_{\text{p}} = \Delta x \cdot C_{\text{avg}} \tag{4}$$

where D_{p} denotes predicted change in concentration.

The input data required to run a Runge–Kutta simulation are the initial concentration values $[A]_0$, $[B]_0$ and $[C]_0$, as well as the rate constants k_{AB}, k_{BC}, k_{BA}, and k_{CB}.

The differential equation (2) may then be solved using the 4th order Runge–Kutta algorithm, with a small time-step and many simulation cycles until the reaction reaches equilibrium.

As a simple test for the accuracy of the 4th order Runge–Kutta algorithm, since this is the premise for the main experiments using the Monte Carlo algorithms; we compared the 4th order Runge–Kutta, with (a) a crude approximation using local linear approximation, and (b) an analytical solution to a simple first order reaction, the gas phase conversion of cyclopropane to propene at 500 °C.

$$\text{cypropane} \rightarrow \text{propene}, \quad k = 0.0375\ \text{min}^{-1}, \quad \left[\text{cypropane}\right]_0 = 1\ \text{M}$$

Once this was complete, we performed numerical analysis using the 4th order Runge–Kutta on the complex reaction (1), using rate constants $k_{\text{AB}} = 1.0$, $k_{\text{BA}} = 0.5$, $k_{\text{BC}} = 0.5$, $k_{\text{CB}} = 0.25$ and $[A]_0 = 1$, $[B]_0 = 0$, and $[C]_0 = 0$. The reaction was simulated with a step size of 0.04 s, for 10,000 steps, yielding approximate equilibrium concentrations for the reaction, later used as benchmarks for the main experiments using Monte Carlo algorithms.

2.2 *Phase 2—Using the Monte Carlo Method*

Monte Carlo is the general name given to methods of solving complex integrations by random sampling procedures often using pseudo-random numbers, which are *deterministic sequences of numbers* generated from a *seed* value. A good pseudo-random number generator will appear statistically random, and their defining characteristics are repeatability and periodicity. The repeatability of the pseudo-random number sequence can be useful for debugging and simulation, since the program will calculate the same result every time it is run. While periodicity is hardly a useful characteristic, the periods of our generator are so large that they may be neglected.

2.2.1 Construction of a Pseudo-Random Number Generator

We used a classic pseudo-random generator which operated on a constant multiplier and additive principle. Using a real initial seed-value N_0, we obtain the recursive relation for all numbers in the pseudo random sequence (N_1 to N_{i}) as follows:

$$N_i = Z(N_{i-1} + Y) - Int[Z(N_{i-1} + Y)]$$

where Y is the constant additive and Z is the constant multiplier, where Y and Z are real but not natural numbers for an increased period. The output values of this pseudo-random number generator lie between 0 and 1, hence being useful for the Monte Carlo Method introduced later.

We then compare our pseudo-random function with the Excel Rnd function to test its randomness—a histogram was plotted to determine the uniformity of the distribution of both our pseudo-random series and a series generated by the Excel Rnd function. After this, the value of π was calculated 30 times using both series, and an average value was obtained, each with a different seed value. The value of π calculated using the Excel Rnd function was accurate to 2 decimal places, while that calculated using our pseudo-random generator was accurate to 3 decimal places.

2.2.2 Monte Carlo Methods

The pseudo-random sequences may be used in a simple Monte Carlo strategy, called the *rejection* method. Essentially, this method needs to count the number of times the random function hits or misses the target. Suppose we wish to evaluate the definite integral:

$$I = \int_a^b y(x)\mathrm{d}x \tag{5}$$

Putting a bounding box around the function *y(x)*, the integral of *y(x)* may be understood to be the fraction of the bounding box that is also within *y(x)*. Hence, if we choose a point at random uniformly within the bounding box, the probability that the point is within *y(x)* is given by the fraction of the area that *y(x)* occupies. Hence,

$$I = V\left(\frac{n}{N}\right) \tag{6}$$

where n is the number of points within $f(x)$, N is the total number of points generated, and V is the total area of the bounding box. However, this method is known to be inefficient and requires many points to be generated for (6) to converge to (5) with any degree of precision [2].

2.3 *Phase 3—Metropolis Monte Carlo*

A more precise and efficient approach, whose applicability to chemical kinetics has been limitedly tested. (5) can be written equivalently as an integral over the

probability of the point falling within y(x),

$$P(x) = y(x) \cdot f(x) \cdot V$$

where $f(x) = 1$ if x is inside the domain V and $f(x) = 0$ if x is outside V. Hence,

$$I = \frac{1}{V} \int_a^b (y(x) \cdot f(x) V) \mathrm{d}x$$

For the random x_i uniformly distributed within the domain, this gives us an approximate procedure which is highly applicable to kinetics;

$$I = \frac{1}{n} \cdot \sum_{x=0} P(x) = \frac{V}{n} \cdot \sum_{x=0}^{i} y(x_i)$$

This algorithm converges much more rapidly than estimates using the simple rejection method, since it uses a *1D domain* as compared to the latter, which uses a *2D domain*. According to classical thermodynamics, since all reactions are, to some degree, reversible; we can calculate their equilibrium concentrations using Metropolis Monte Carlo.

2.4 Phase 4—Obtaining Data

2.4.1 Metropolis Monte Carlo Applied to Multiple Equilibria

Using the initial conditions and differential equations describing the kinetics of (1) outlined in Phase 1, we may calculate the relative probabilities that a change in concentrations of the compounds in any of the 4 possible elementary reaction steps may occur:

$$i \text{ to } j \rightarrow P_{ij} = k_{ij}, \quad (i,\ j) \in \{(A,\ B),\ (B,\ C),\ (B,\ A),\ (C,\ B)\}$$

Using the pseudo-random number generating algorithm created, we initiated each Monte Carlo (MC) Cycle as follows;

1. Specify $[A]_0$, $[B]_0$, $[C]_0$ so that $[A] + [B] + [C] = 1$
2. Specify a step reaction concentration displacement $[\Delta]$
3. Select an elementary reaction step, using one pseudo-random function, depending on its value on the interval between 0 to 1; e.g. if it is between 0 and 0.25, reaction is $A \rightarrow B$.
4. Apply random change from $[A]$ to $[B]$ to obtain the tentative $[A]_1 = [A]_0 - \Delta$, and $[B]_1 = [B]_0 + \Delta$.

5. Obtain a random number R, using a second pseudo-random function from a uniform distribution between 0 to 1.
6. If the relative probability P_{ij} of that reaction is greater than R, we accept the change in concentrations. However, if $P < R$, we reject the changes.

The steps 1 through 6 were repeated until an equilibrium was established. Once equilibrium was established, we obtained the average concentrations of $[A]$, $[B]$ and $[C]$, if the fluctuations at equilibrium are wide.

A Monte Carlo program was written for (1), a complex equilibria problem which cannot be solved analytically for varying starting concentrations of each reactant. After a set number of cycles to reach equilibrium concentration, an average was taken upon the set of values revolving around equilibrium concentrations. These concentrations were compared against Runge–Kutta equilibrium concentrations to determine the accuracy of the Monte Carlo algorithm.

Factors affecting the accuracy and precision of the Monte Carlo program were investigated, including concentration displacement size and the number of MC Cycles. Time taken to run the program on an Intel i7 7th Gen CPU with 8 GB RAM and a 128 GB Solid-State Drive was measured, but not investigated in detail since with modern supercomputers it is trivial to run large, repetitive programs under a short timeframe.

3 Results and Discussion

3.1 Testing the Randomness of the PRNG Function

As a premise for this study it is crucial to determine whether our PRNG algorithm has a uniform random distribution, which requires an extremely large period for its periodicity. Due to the nature of our PRNG Algorithm, its periodicity will be very large, especially when using constant additives and multipliers that are not natural numbers. In our case, $Y = 2.923879492$ and $Z = 1199.199219$. To ensure that our results were uniform with a large periodicity, multiple scatter-plots were drawn for the first 1000 values in our PRNG output, and those with seed values $= 1$ and 2 may be found in Appendix 1. At a glance, we can see that the results look random and generally uniform, with minimal gaps and clustering.

To illustrate the uniformity of the pseudo-random function compared to the Rnd function, we drew a histogram for the first 100,000 values in the PRNG function, compared to the Excel's Rnd function. The bars are uniform, revolving around 2000 values per interval for 50 intervals. Finally, we calculated the value of π 30 times and used this to obtain an average calculated value of π for the PRNG, and Rnd Function. The value of π was accurate to 3 decimal places for our PRNG, while it was accurate to 2 decimal places for the Rnd Function, clearly illustrating the benefit of the use of our PRNG function over Rnd (Appendix 1).

In the Monte Carlo Simulation Runs, Tables 1, 2 and 3, the elementary reaction concentration displacement size (Δ) was varied between 0.001 in Table 1. 0.0005 in Table 2, and 0.00025 in Table 3. Since the displacement size determines the rate of progress towards equilibrium, a subset of the MC Cycles conducted in Table 1 had to be included in Tables 2 and 3.

Within each Tables 2, 3 or 4 (Appendix 3), the number of Monte Carlo Cycles were varied from 50,000 to 300,000 with regular intervals of 50,000. In Tables 3 or 4, if the reaction had not reached equilibrium yet, we would not measure the equilibrium concentrations in that number of MC Cycles. Neither of these 2 quantities (the no. of MC Cycles and concentration displacement size) have any physical reality since they are artefacts of the Monte Carlo Method.

In the deterministic integration of the differential rate laws using the 4th order Runge–Kutta algorithm, the reaction time step size (Δt) was varied, which affects the error margin and deviation of the algorithm from the actual value. Chemical equilibrium was obtained after 25 min in the deterministic simulation runs, and the accurate equilibrium concentrations for A, B and C are obtained, and are displayed in Table 1 (Appendix 3) for various timestep sizes.

3.2 Evolution of the Accuracy of the Metropolis Monte Carlo

Concentrations computed using the Metropolis Monte Carlo vary around the equilibrium concentrations in the deterministic simulations. Hence, when we take the average of these values, we obtain a value similar to that obtained in the deterministic simulations, at an accuracy of 2 decimal places compared to the actual values. Although CPU Time required to complete the Monte Carlo and Runge–Kutta simulations was not recorded, runtime for the code did not last more than 20 s even for 300,000 Monte Carlo Cycles. The selection for the average equilibrium concentration was made based on our heuristics, standardized to the average from the 50,000th to nth data value, where n is the total number of data points taken. For the row with 50,000 data points, this was varied to become the average from 45,000−50,000th data point.

3.3 Evaluation of the Factors Affecting the Accuracy of the Monte Carlo Method

There are 2 main determinants of the accuracy of the Monte Carlo Method—the concentration displacement size (Δ) and the number of Monte Carlo Cycles. First, we observed from the data in Appendix 3 that as the concentration displacement size decreases, it takes a larger number of Monte Carlo Cycles to reach the equilibrium. However, the magnitude of deviation around equilibrium concentrations

also decreases, since the step size is now smaller allowing randomness to have a lower effect. Next, having a larger number of Monte Carlo Cycles does not decrease the deviation around equilibrium. However, it provides us with a larger database to average from, minimizing error when computing concentrations.

3.4 Benefits and Caveats of the Monte Carlo Method in Chemical Engineering

In addition to the aforementioned factors, a good pseudo-random number generator is essential in obtaining accurate results using the Monte Carlo Method; this includes the crucial conditions of full periodicity and randomness [3]. Having tested this in our project, this premise is fulfilled. A common issue faced in Monte Carlo is the selection of results at equilibrium when fluctuations are encountered (which may be observed in Appendix 2). The method used in our report provides accurate results since we only select data ranges when the reaction concentration revolves around a flat line. Another possible method is to compute the derivative of the best fit curve, and find the value when it crosses zero to start computing the average equilibrium concentration from there.

Though deterministic simulations like the 4th order Runge–Kutta are more accurate and may be applied to chemical engineering, its scope is limited and there are numerous cases in chemical engineering, especially that in the biomedical field where results are neither accessible using analytical techniques nor deterministic simulations. Examples include crystallization, thermodynamic properties of petroleum products, pastes in the food industry, protein folding, pharmaceutical powder mixing, drug molecule transportation in the cardiovascular system, etc.

4 Conclusion and Future Work

The Monte Carlo method in chemical engineering is able to identify equilibrium concentrations of a superfluity of complex chemical reactions. Importantly, Monte Carlo methods are applicable in multiple scenarios where other numerical analysis methods may not be applied, giving it a great significance in biomedical engineering, particularly for protein folding, drug molecule transportation, etc. and other areas of chemistry. Unlike similar projects, our project provides a great degree of analysis into achieving a greater accuracy using Monte Carlo techniques in chemical engineering, by varying the number of Monte Carlo (MC) Cycles, and the Concentration Displacement Constant, Δ.

A crucial aspect of this project included the creation of our own pseudo-random number generator (PRNG) algorithm, which achieved better distribution and randomness than Microsoft Excel's Rnd Function, which is commonly used in

such projects. Our code which used this PRNG algorithm achieved accuracy to 2 decimal places compared to the 4th order Runge–Kutta, which is accurate but with limited applicability.

Further extensions include the application of the Monte Carlo technique to mutually exclusive problems which cannot be solved using other numerical analysis algorithms, particularly in the biomedical field. This allows us to demonstrate the direct application of the technique, after confirming its accuracy and applicability as we have done in this project.

Acknowledgements We would like to thank our research mentor Dr. Lee Fook Choon for his guidance and our teacher mentor Mr. Lim Teck Choow for his help in providing timely reminders on the deadlines.

Appendices

Appendix 1—PRNG and Rnd Scatterplots and Histograms

Sample PRNG Scatterplots for Seed Values 1 and 2.

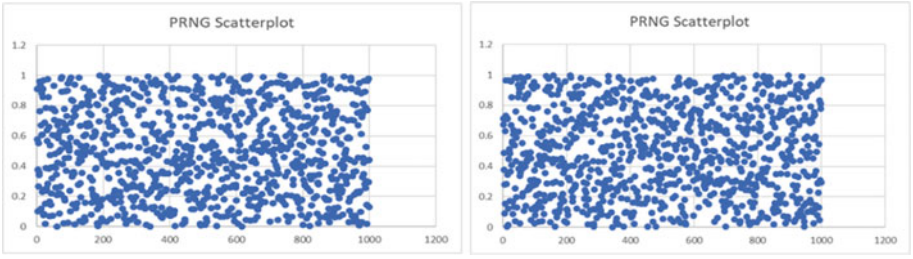

Appendix 2—Graphs of Deterministic Versus Monte Carlo Simulations

Runge Kutta Run for ($\Delta\ t$) = 0.04 min, Monte Carlo Run for 300 k MC Cycles (Δ = 0.001).

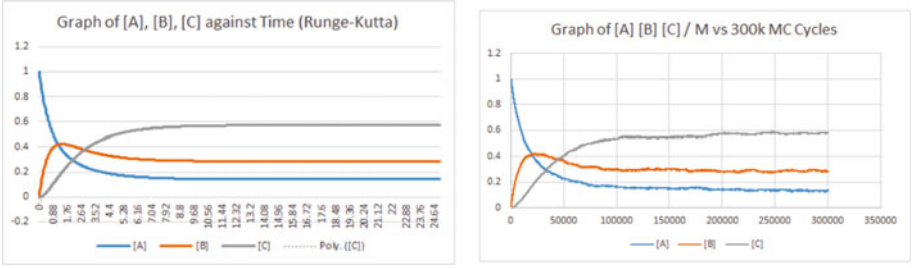

Appendix 3—Deterministic and Monte Carlo Simulation Results

See Tables 1, 2, 3 and 4.

Table 1 Deterministic simulation results

[Δ]/M	Number of steps	[A]/M	[B]/M	[C]/M
0.04	625	0.142723	0.285444	0.570882
0.02	1250	0.142789	0.285578	0.571156
0.01	2500	0.142823	0.285646	0.571292
0.005	5000	0.142840	0.285680	0.571360
0.002	12,500	0.142851	0.285700	0.571401
0.001	25,000	0.142854	0.285707	0.571414

Table 2 Monte Carlo simulation results ($\Delta = 0.001$)

[Δ]/M	Number of steps	[A]/M	[B]/M	[C]/M
0.001	50	0.130722	0.278157	0.591121
0.001	100	0.140638	0.27837	0.581092
0.001	150	0.151339	0.28534	0.563421
0.001	200	0.143146	0.290145	0.566709
0.001	250	0.140093	0.28556	0.574347
0.001	300	0.145130	0.28574	0.567134

Table 3 Monte Carlo simulation results ($\Delta = 0.0005$)

[Δ]/M	Number of Steps	[A]/M	[B]/M	[C]/M
0.0005	50	Reaction Mixture has not reached equilibrium		
0.0005	100	0.140187	0.282874	0.576939
0.0005	150	0.146067	0.289345	0.568106
0.0005	200	0.146256	0.285638	0.568106
0.0005	250	0.144590	0.285965	0.569445
0.0005	300	0.144550	0.289618	0.565833

Table 4 Monte Carlo simulation results ($\Delta = 0.00025$)

[Δ]/M	Number of Steps (thousands)	[A]/M	[B]/M	[C]/M
0.00025	50	Reaction mixture has not reached equilibrium		
0.00025	100	Reaction mixture has not reached equilibrium		
0.00025	150	0.145955	0.284559	0.590486
0.00025	200	0.148370	0.287119	0.564511
0.00025	250	0.146079	0.291990	0.561931
0.00025	300	0.144829	0.291148	0.564022

References

1. Lee, F.C. 2007. Research Notes: Phenomenological Scale - Rate Processes
2. Lee, F.C. 2007. Research Notes: Phenomenological Scale - Monte Carlo Methods
3. Park, S.K and Miller, K. W. 1988. Random Number Generators: good ones are hard to find. Communications of the ACM, 31(10):1192-1201

The Efficiency of Using Biowaste as a Greener Alternative to Conventional Fuel

Lim Kia Iag, Alicia Jocelyn Tjokro, and Debraath Pahari

Abstract Food waste and air pollution from fossil fuel consumption are environmental problems. This project aimed to investigate how age and type of fruit waste affects the extracted amount of ethanol. In this project, the efficiency and practicality of using biowaste-derived ethanol were examined. Various 0-week-old (freshest) fruit peels (watermelon, pineapple, orange) underwent yeast fermentation to produce ethanol. Ethanol was extracted via fractional distillation over 20 min. The results showed that fresh watermelon peels produced the most ethanol (15.4 ml), followed by orange (11.0 ml) and pineapple (7.6 ml). It was theorised that this is because of the varying pH levels of the fruits and their distances from the optimal range of efficient yeast fermentation. Then, different ages of watermelon peels, ranging from 0-week-old (freshest) to 3-weeks-old, underwent yeast fermentation to produce ethanol. The results showed that 0-week-old (freshest) watermelon peels still produced the most ethanol. It was theorised that the pH level of the watermelon increases with time, causing it to move further away from the optimal pH range mentioned above, so the 0-week old watermelon sample was still the most effective. Though the combustion of ethanol releases less energy compared to the same amount of petrol, ethanol combustion produces less soot and can reduce food waste, also being cost-efficient in the process as food waste is inexpensive. Our research shows how food waste-derived bioethanol can be a greener alternative to conventional fuel.

Keywords Biology · Chemistry · Distillation · Fermentation · Fuel · Green · Pollution

L. K. Iag (✉) · A. J. Tjokro · D. Pahari
NUS High School of Mathematics and Science, Singapore, Singapore
e-mail: h1810082@nushigh.edu.sg

A. J. Tjokro
e-mail: h1810005@nushigh.edu.sg

D. Pahari
e-mail: h1810030@nushigh.edu.sg

H. Guo et al. (eds.), *IRC-SET 2020*,
https://doi.org/10.1007/978-981-15-9472-4_21

1 Introduction

Our vehicles are major causes of fuel consumption and air pollution. Extracting petroleum for car fuel is an energy-intensive process that damages local ecosystems. Shipping fuels can also occasionally create environmental disasters such as oil spills. In the United States, vehicles produce one-third of all air pollution. Due to these negative effects of using car fuel, we have decided to examine the efficiency and practicality of using bioethanol, which we derived from yeast fermentation of fruit waste—namely orange, watermelon and pineapple. We are sure that these fruits have peels and skins that are inedible yet contain energy as the epicarp is made of cells that will definitely contain glucose in them, and this glucose can help in the production of ethanol carried out via anaerobic respiration of yeast. At the same time, it ensures that remaining energy in food waste does not go to waste. We believe this bioethanol is a possible greener alternative to traditional fossil fuels, and can effectively combat the problems of food waste and air pollution at the same time.

2 Literature Review

Fossil fuel consumption, partly used as a conventional car fuel, has disastrous impacts on the environment, including but not limited to global warming emissions and air pollution [1]. The biggest volume of food loss in Singapore involves fruit and vegetables and it remains a major problem in Singapore. This is another problem our research can be used for [2]. Bioethanol production from renewable sources to be used in transportation is now an increasing demand worldwide due to continuous depletion of fossil fuels, economic and political crises, and growing concern on environmental safety [3]. The requirement of an alternative clean energy source is increasing with the elevating energy demand of modern age. Bioethanol is considered as an excellent candidate to satiate this demand [4]. Using ethanol-blended fuel for automobiles can significantly reduce petroleum use and exhaust greenhouse gas emissions. An important advantage of crop-based ethanol is that it produces less greenhouse gases when combusted [5]. A possible way to produce ethanol is through the alcoholic fermentation of fruit and vegetable waste using the yeast *Saccharomyces cerevisiae*. It is an eco-friendly and green method as it also reduces food wastage [6].

3 Research Questions and Hypothesis

3.1 Research Questions

- From which type of fruit waste can the most amount of bioethanol be extracted?
- Does the amount of bioethanol in the fruit waste decrease as time passes?

- Is ethanol effective as a substitute for petrol?

3.2 Hypothesis, Engineering Goals and Expected Outcomes

Our goal is to find out how type and age of fruit waste affects the amount of ethanol produced, to see whether the production of bioethanol is viable in reality (we must take into consideration whether this method of producing ethanol is only effective and practical for a limited amount or age of fruit waste). We hypothesize that the most recent watermelon "shell" will contain the most glucose in it. We hypothesise that ethanol decreases with time. Since the watermelon "shell" has the greatest volume of biomatter per mass among the other "shells", the greatest volume of bioethanol can be extracted from it. As time passes, the amount of bioethanol that can be extracted from the food will decrease.

4 Methodology

4.1 Stage 1

The first stage aimed to test which type of fruit waste, of pineapples, watermelons, oranges, produced the greatest amount of ethanol when they were the freshest. Hence, fermentation mixtures were prepared in beakers for each type of fruit. The mixture consisted of 50 g of fruit waste, 5 g of yeast, and enough DI water to reach the 225 cm^3 mark on the beaker. A layer of oil was added at the top to prevent any loss of produced ethanol through evaporation. These mixtures were then allowed to ferment for 1 week in the laboratory.

After a week of fermentation, the layer of oil and any remaining bio-solids were removed from the fermentation mixture using plastic dropper and forceps. The remaining mixture then undergoes fractional distillation, where the temperature was maintained at around 78 °C for about 20 min. 78 °C is the approximate boiling point of ethanol. The distillate was collected in a tiny conical flask which rested in an ice bath, to ensure that the volatile ethanol would not evaporate as soon as it was collected [7–9].

To summarise, the constants in this experimental stage were the masses of fruit waste and yeast, duration of fermentation, temperature at which fractional distillation was carried out, and the duration of fractional distillation. The independent variable was the type of fruit used, and the dependent variable was the amount of ethanol extracted.

4.2 Stage II

It was discovered that the watermelon waste produced the greatest amount of ethanol. Hence, our second stage further investigated how the age of watermelon peels would affect the rate of ethanol production. The procedure remains identical to the first stage, however this time the independent variable has been changed to the age of the selected fruit. Watermelon peels with ages ranging from 0 weeks old (most fresh) to 3 weeks old (least fresh) were used for testing.

4.3 Stage III

In our final stage, we calculated the distance travelled by a car if it used the overall greatest amount of ethanol produced. Then, we calculated the amount of petrol needed for a car to travel the same distance, and compared the amounts of ethanol and petrol used.

4.4 Risk and Safety

Since carbon dioxide (CO_2) is also a by-product of anaerobic respiration of yeast, this means that we need to keep the set-up with the food waste and the yeast in a well-ventilated area. Otherwise, there might be a pressure build-up which will be a safety hazard.

While using the knife to cut fruits, we had to practice caution. We also wore goggles, gloves and covered shoes in the lab to protect ourselves from potentially harmful substances [10].

4.5 Methods for Data Analysis

To visualise and help analyse our data, we presented our data in the form of a table and bar graph (Stage 1) and in the form of a line graph over time (Stage 2). In Stage 3, we analysed our data using equations and calculations, to reach a final conclusion (Table 1 and Fig. 1).

5 Results

Stage 3 calculations (using 0 week old watermelon):

Table 1 Results of phase I and II

Phase I		Phase II	
Fruit waste	Week 0/ml (Fresh)	Week number	Ethanol/ml (Watermelon)
Pineapple	7.6	0	15.4
Watermelon	15.4	1	1.0
Orange	11	2	0.7
		3	0.5

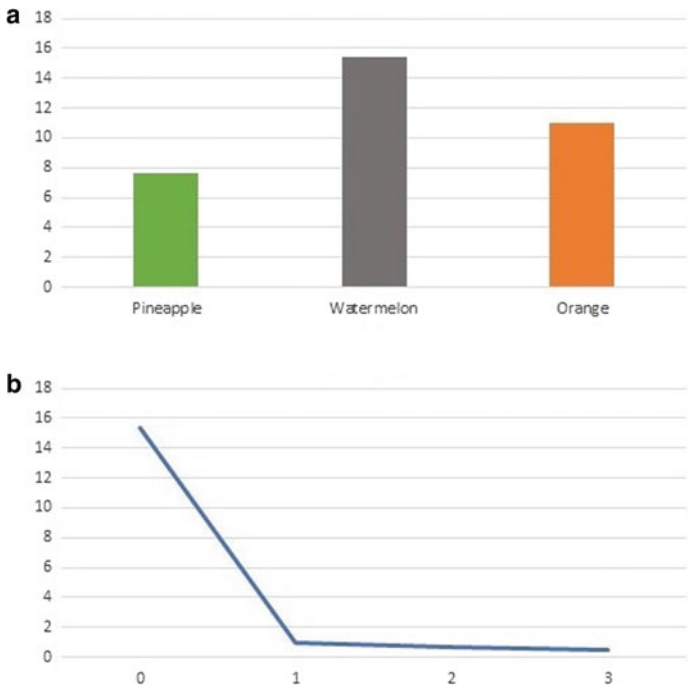

Fig. 1 **a** Volume of ethanol extracted from three different fresh fruit peels (ml). **b** Volume of ethanol produced (ml) over time (weeks)

Density of ethanol = *0.789* g/ml
Relative Molecular Mass of Ethanol = *46.068*
Energy released from combustion of ethanol = *277.7* kJ/mol
Average Fuel Efficiency of Cars = *25–50% (Assume Lower Bound)*
Average energy needed for cars = *720* kJ per km
Average distance travelled by combusting 1 l *of petrol* = *13* km
Amount of extracted ethanol = *15.4* ml

$$0.789 \text{ g/ml} * 15.4 \text{ ml} = 12.1506 \text{ g} \quad (1)$$

Hence, the mass of extracted ethanol is 12.1506 g.

$$12.1506\ \text{g}/46.068\ \text{g/mol}\ \approx\ 0.2638\ \text{mol} \tag{2}$$

Hence, the moles of extracted ethanol is 0.2638 mol.

$$0.2638\ \text{mol}\ *277.7\ \text{kJ/mol}\ \approx 73.26\ \text{kJ} \tag{3}$$

Hence, the total energy released from combustion of extracted ethanol is 73.26 kJ.

$$25\%\ *73.26\ \text{kJ}\ \approx 18.32\ \text{kJ} \tag{4}$$

Hence, the energy efficiency (energy as useful output) of cars is 18.32 kJ.

$$18.32\ \text{kJ}/720\ \text{kJ/km}\ \approx\ 0.02544\ \text{km} \tag{5}$$

Hence, the no. of kilometres travelled is 0.02544 km.

The volume of petrol needed to travel an equivalent distance is 1.96 ml.

In the results of our first stage, it was observed that watermelon produced the greatest amount of ethanol out of the three fruits we tested.

6 Discussions

6.1 Implications

The optimal pH range for yeast fermentation is 4.5–5.5.

In Stage 1, the Watermelon sample produced the most amount of ethanol as its pH was closest to the optimal pH range for yeast fermentation, followed by Orange and lastly Pineapple (Table 2).

In Stage 2, the changes in the amount of ethanol extracted from the fermentation of watermelon over time can be due to changes in its pH level. In our results, we observe that there is a general decreasing trend in the amount of ethanol produced over time. This may be due to the decrease in acidity of watermelon over time, as organic acids in fruits are converted to sugars as fruits ripen. Hence, as the pH level of the watermelon increased, the rate of yeast fermentation decreased [11, 12].

Table 2 pH values of fruits

Fruit	Pineapple	Watermelon	Orange
pH level	3.9	5.5	4.3
pH difference from range for optimum range	$4.5 - 3.9 = 0.6$	$5.5 - 5.5 = 0$	$4.5 - 4.3 = 0.2$

6.2 Limitations and Future Work

Some limitations of this experiment were that it was difficult to maintain the fractional distillation at around 78 °C, the heat settings of the electrical heater are difficult to control so we had to constantly readjust the heat settings to ensure that the temperature did not rise too much, and this resulted in numerous temperature fluctuations. There is a chance that not all the ethanol has been distilled out, or that other liquids may have distilled out along with the ethanol.

$$\begin{aligned} Q_{\text{energygivenbyheater}} &= Q_{\text{energytakenbyethanol}} \\ &= mc\Delta\theta + ml_{\text{vaporisation}} \\ &= (12.1506)(2.46)(78-30) + (12.1506)(841) \\ &= 11.65\,\text{kJ} \end{aligned} \tag{6}$$

$$\begin{aligned} Q_{\text{net}} &= Q_{\text{combustedethanol}} - Q_{\text{heater}} \\ &= 73.26 - 11.65 \\ &= 61.61\,\text{kJ} \end{aligned} \tag{7}$$

Since it was hard to maintain the temperature, we did not have any way to determine whether all of the ethanol had distilled out of the mixture, so we capped the duration of the fractional distillation at 20 min. There is a chance that not all of the ethanol has been distilled.

We also have to take into account the fact that the distillate is only at most 95–96% pure ethanol, as during distillation, a low-boiling water–ethanol azeotrope known as hydrous ethanol is distilled out.

As for this method of ethanol extraction, fractional distillation may not be energy-efficient as it takes up quite some energy for heating. However, we calculated and found out that it still is able to produce more energy when combusted.

This method of ethanol extraction is also not very practical in real life as it has been shown to yield the highest and only significant amounts of ethanol when the fruit waste is the freshest. Hence, aged fruit waste (likely constituting most of the fruit waste in Singapore) will not be very effective in producing ethanol.

As such, one possible solution is to use solar-derived energy as it is a renewable source of energy. We also have realized that carrying out fractional distillation at an industrial level is also very expensive. There are no solutions to this as fractional distillation is the only method to extract ethanol from plant-based sugars after going through fermentation.

Possible future research could include investigating how rate of fermentation changes as temperature changes, and further investigation into how rate of fermentation changes as pH changes. We could also investigate the conversion of biomass into electricity to charge electric vehicles as this may be a more "climate-friendly" transportation option than the conversion of biomass into ethanol fuel.

7 Conclusions

The 0-week old watermelon should be fermented to produce bioethanol as it produces the highest yield of ethanol. Since ethanol produces less soot when burned, it is a cleaner and greener alternative to conventional fuel. Although it was calculated that combustion of ethanol releases less energy compared to the same amount of petrol, it can reduce food waste by repurposing it as a renewable source of fuel. Since fruit waste is inexpensive, the cost of producing ethanol and using it as fuel is lower than using petrol. Thus, we believe bioethanol is a better alternative as it is more cost-efficient and environmentally-friendly.

Acknowledgements We thank our research mentors, Mr Yeo Shyh Yuan and Mr Lee Kim Hun, for their patient guidance and unending support in this research project. We also thank the Chemistry Lab officers in our school for their assistance in setting up the lab for us to carry out our experiments.

References

1. UCSUSA (Ed.). (2016, August 30). The Hidden Costs of Fossil Fuels. Retrieved from https://www.ucsusa.org/resources/hidden-costs-fossil-fuels.
2. Every Singaporean household throws away an average S$258 worth of food a year: Study. (2019, August 30). Retrieved from https://www.todayonline.com/singapore/every-singaporean-household-throws-away-average-s258-worth-food-year-study.
3. Zabed, H., Faruq, G., Sahu, J., Azirun, M., Hashim, R. and Boyce, A. (2014). Bioethanol Production from Fermentable Sugar Juice. [online] researchgate.net. Available at: https://www.researchgate.net/publication/261517718_Bioethanol_Production_from_Fermentable_Sugar_Juice.
4. Ahmed, M. (2013). Ethanol production from waste materials. [online] researchgate.net. unpublished Available at: https://www.researchgate.net/publication/248399563_Ethanol_production_from_waste_materials [Accessed 16 Oct. 2019].
5. Promon, S. K., Kamal, W., Rahman, S. S., Hossain, M. M., & Choudhury, N. (2018, March 5). Bioethanol production using vegetable peels medium and the effective role of cellulolytic bacterial (Bacillus subtilis) pre-treatment. Retrieved from https://www.ncbi.nlm.nih.gov/pmc/articles/PMC5968363/.
6. Demirbas, A. (2007, October 29). Producing and Using Bioethanol as an Automotive Fuel. Retrieved from https://www.tandfonline.com/doi/abs/10.1080/15567240600705466.
7. Khandaker, M. M., Qiamuddin, K., Majrashi, A., & Dalorima, T. (2018, July). Bio-ethanol production from fruit and vegetable waste by using saccharomyces cerevisiae. Retrieved from https://www.researchgate.net/publication/328233695_Bio-ethanol_production_from_fruit_and_vegetable_waste_by_using_saccharomyces_cerevisiae.
8. Jahid, M., Gupta, A., & Sharma, D. K. (2018, May 14). Production of Bioethanol from Fruit Wastes (Banana, Papaya, Pineapple and Mango Peels) Under Milder Conditions. Retrieved from https://www.omicsonline.org/open-access/production-of-bioethanol-from-fruit-wastes-banana-papaya-pineapple-and-mango-peels-under-milder-conditions-2155-9821-1000327-101834.html.
9. Baik, K. (n.d.). Extraction of Bio-Ethanol from Wasted Bio-Wastes. Unpublished Retrieved from https://www.sciencefairexperiments.org/Biochemistry/Extraction-of-Bio-Ethano-from-Wasted-Bio-Wastes.php.

10. CLEAPSS. (2019). Student Safety Sheets. Retrieved from https://science.cleapss.org.uk/Resource/SSS060-Ethanol.pdf.
11. Anthon, G. E., Lestrange, M., & Barrett, D. M. (2011, January 6). Changes in pH, acids, sugars and other quality parameters during extended vine holding of ripe processing tomatoes. Retrieved from https://cetulare.ucanr.edu/files/138169.pdf.
12. Taain, D. A. (2017, April 4). Why the organic acids in the most of fruits decrease at ripening stage? unpublished Retrieved from https://www.researchgate.net/post/Why_the_organic_acids_in_the_most_of_fruits_decrease_at_ripening_stage.

Plasma-Based Defect Engineering of Graphene for Optimised β-D-Glucose Sensing to Monitor Diabetes

Koo Min Seo, Angelina Wong, Jordan Low, and Joseph Vimal Vas

Abstract Diabetes is a growing heath concern in Singapore, resulting in the urgent need to develop sensitive and accurate glucose biosensors. In this project, we fabricated a graphene-based biosensor (GBB) via a quick and straightforward method with an enhanced immobilization of glucose oxidase (GOx). The graphene surface was subjected to various durations of radio-frequency (RF) plasma treatment to engineer defects onto the graphene interface, improving physical adsorption of GOx and thus sensitivity. Raman spectroscopy was used for the characterization of the graphene and to ascertain the presence of defects. GBB sensors fabricated using graphene with different durations of plasma treatments were then tested with differing concentrations of β-D-glucose solutions. The optimal GBB is obtained by employing 50 W RF plasma in a depressurized chamber of 0.7 mbar, of hydrogen gas with a flow rate of 27.5 SCCM and a treatment duration of 5 min. Our GBBs demonstrated balance between a wide detection range and high sensitivity for an improved detection of glucose levels in glucose solution.

Keywords Chemical vapour deposition (CVD) · Radio frequency (RF) plasma · Raman spectroscopy · Graphene-based biosensor · Glucose oxidase enzyme (GOx)

1 Introduction

Diabetes is a global epidemic that continues to plague the lives of many. It results from the deficiency of insigsulin as a result of damage to the beta cells in the pancreas or due to damaged target cells, causing elevated blood glucose levels, also known as hyperglycemia. A condition rapidly rising in prevalence, diabetes is expected to affect 592 million individuals by the year 2035 [1].

K. M. Seo (✉) · A. Wong · J. Low
School of Mathematics and Science, NUS High, Singapore, Singapore
e-mail: h1710067@nushigh.edu.sg

J. V. Vas
National Institute of Education (NIE), Nanyang Technological University (NTU), Singapore, Singapore
e-mail: joseph.vas@nie.edu.sg

H. Guo et al. (eds.), *IRC-SET 2020*,
https://doi.org/10.1007/978-981-15-9472-4_22

Diabetes is traditionally diagnosed and monitored by the detection of glucose levels in the blood. No cure has been found for diabetes, and constant monitoring of blood glucose levels is thus required to prevent complications which results from the activation of several metabolic pathways related to inflammation and apoptosis events [2]. Current commercially available glucose sensors typically utilise the enzyme glucose oxidase (GOx). Due to its high selectivity, GOx has an important role in the fast and accurate detection of glucose levels. The electrochemical biosensors produced with the immobilization of the enzyme can be used for a wide variety of samples.

The possible electrode surface for glucose biosensors have been widely studied, with many platforms investigated for the attachment of GOx to design sensitive and accurate biosensor. The predominantly used platform is graphene. Graphene is a monolayer of carbon atoms arranged in a hexagonal lattice, and its physical and chemical characteristics make it ideal for applications in biosensing. Being a relatively new nanomaterial, it has spurred great interest in the field of material science due to its large surface to volume ratio and high electrical conductivity. Its peculiar characteristics can be used for biosensing, with the manufacturing of graphene-based biosensors (GBBs). The band structure of graphene can be easily modified in the presence of activating or deactivating groups and this can be detected through IV characterisation.

The implementation of glucose biosensors involves the anchoring of GOx onto the surface of the graphene substrate via physical adsorption. The high specific action of GOx is tapped on to catalyse the breakdown of glucose to form gluconic acid and hydrogen peroxide. The effective attachment of GOx onto the graphene substrate is essential for the larger signal-to-noise ratio required for proper functioning of glucose biosensors.

The properties of graphene have demonstrated its promise in the amperometric sensing of biomolecules due to its ability to amplify signals [3]. However, challenges remain with ensuring the efficiency of the immobilisation of GOx onto the graphene surface. The novelty of this project lies in the improvement of the attachment of GOx with graphene by using different types of plasma to engineer defects on the surface. The electrical properties (resistance) of the graphene will be monitored using an IV probe station with increasing concentration of beta-D-glucose solutions and the quality of graphene will be ascertained using Raman spectroscopy.

2 Methodology

2.1 Graphene Synthesis by Chemical Vapor Deposition (CVD)

A 10 × 80 mm copper (Cu) strip, to be used as the growth substrate, was cleaned via sonication using isopropyl alcohol, acetone and DI water. The Cu substrate was

placed on a graphite boat and placed within a 25 mm diameter horizontal quartz tube which served as the CVD reaction chamber. The tube was then sealed and vacuumed to a base pressure of 3.0×10^{-3} mbar.

Hydrogen (H_2) gas with a flow rate of 2.0 standard cubic centimetres per minute (SCCM) was introduced into the tube, and subjected to a voltage of 50 V via a heating element. In 20-min intervals, the voltage was increased to 90 V and 110 V respectively to achieve the final temperature of around 1100 °C. In this process, H2 molecules are physically adsorbed and decompose due to the high temperature on the copper surface. The atomic hydrogen then removes any contamination on the Cu substrate, thereby allowing for a uniform growth of the graphene layer.

After 1 h, methane gas was introduced at 10.0 SCCM. The chemisorption of methane molecules results in methane molecules being bonded to the top layer of Cu atoms, which become successively de-hydrogenised and build the honeycomb pattern of graphene. As the graphene is minorly soluble in copper, the graphene growth process is self-limiting and ceases after a monolayer is formed. After another hour, the methane supply and the heater were turned off. The reaction chamber is cooled rapidly to room temperature with the constant flow of H2.

2.2 Graphene Transfer Process

Initially, the deposited graphene on the Cu substrate was transferred using the wet chemical etching method. Polymethyl methacrylate (PMMA) was spin-coated on top of the graphene/copper and baked at 100 °C for 2 min. The Cu layer was then removed by floating the PMMA/graphene/Cu stack in $FeCl_3$ solution for 5 h. The remaining PMMA/graphene stack was rinsed in DI water and transferred onto a glass slide cleaned via sonication, before it was kept in an incubator for around 8 h to remove moisture. An acetone bath was then used to remove the PMMA layer.

This method was observed to produce a non-uniform layer of graphene on the interface of the glass slide, as IV measurements failed to produce a linear graph. This was suspected to be due to the inability to remove the PMMA from the surface of graphene entirely. Subsequent transfer processes eliminated the PMMA spin-coating step, with the graphene/Cu stack floating directly in the $FeCl_3$ solution. The remaining graphene is carefully transferred onto the glass slides and baked in the incubator. The transferred graphene samples were characterised by Raman spectroscopy.

2.3 Designing and Implementation of Graphene-Based Glucose Biosensors

The designing and implementation of the required device structure involved 4 major steps. First, two silver ink droplets were placed on the graphene to act as metal

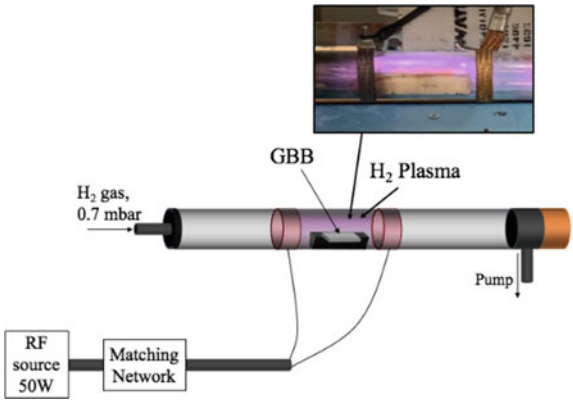

Fig. 1 Experimental setup of plasma engineering

contacts. Second, Cu wires were fixed onto the graphene on the metal contacts. Third, the metal contacts were insulated with water-insoluble Super Glue to minimize noise resulting from current through the glucose sample. Lastly, GOx was immobilized on the graphene interface by placing 1 droplet of 1 mg/dl GOx solution onto the surface for 10 min, before it was soaked in DI water for 5 min.

2.4 Defect Engineering via RF Plasma

For this project, 5 different types of GBBs were tested, each with different durations of exposure to RF plasma—0, 5, 10, 15 and 20 min.

Each GBB was placed within a 40 mm diameter horizontal quartz tube. Next, the quartz tube was sealed and evacuated to a base pressure of around 3.0×10^{-2} mbar. H_2 gas was introduced at a flow rate of 26.5 SCCM. After pressure reached 0.7 mbar, the capacitively coupled remote plasma was switched on at 50 W. The experimental setup is shown in Fig. 1. After the set period of time, the H_2 supply and RF power supply were turned off. The GBBs were then characterized with Raman spectroscopy to ascertain the presence of defects.

2.5 IV Measurements

The resistance of each GBB was measured using an IV probe station. Before plasma treatment, their IV properties were ascertained using the IV probe for each increasing concentration of glucose from 10 to 80 mg/dl. After each IV measurement, the graphene surface was washed by placing 1 droplet of DI water onto the surface for 2 min. IV measurements were then taken again. Different concentrations of glucose were tested with the GBBs and this process was repeated after plasma treatment.

3 Results

3.1 Raman Spectroscopy

From Fig. 2a, when the graphene sample obtained by CVD was characterised via Raman spectroscopy, the characteristic "G" peak was measured to be 1587.94 cm. The "G" peak's position is highly sensitive to the number of layers of graphene and is an extremely accurate way to determine the atomic thickness of the graphene. Using formula (1), it can be calculated that the graphene is a monolayer.

The "D" peak is negligible, which shows that the graphene was of few defects before being subjected to plasma treatment. The "2D" peak is the result of a two phonon lattice vibrational process. However, unlike the D peak, it does not require defects to be activated. It can also be used to determine the thickness of the graphene layer. The "2D" peak in Fig. 2a is sharp and symmetrical, which provides additional

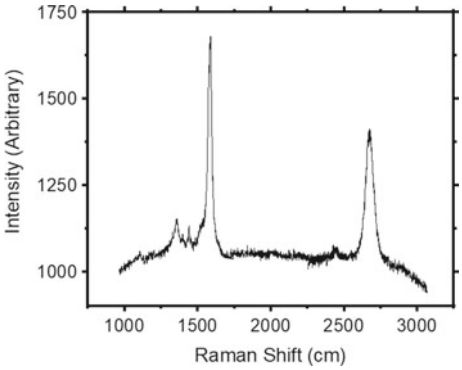

(a) obtained after CVD

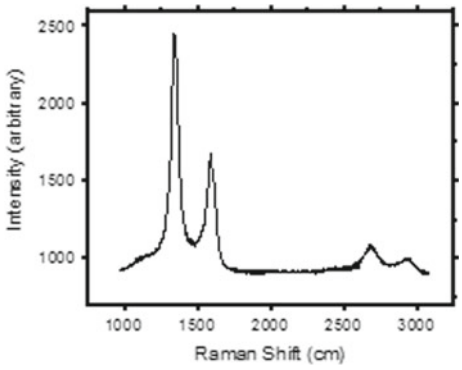

(b) obtained after 15min of plasma treatment

Fig. 2 Raman spectra for graphene samples

support that the graphene before plasma treatment is a monolayer.

$$\text{Raman shift of } "G" \text{ peak } = 1581.6 + 11/\left(1 + n^{1.6}\right) \quad (1)$$

From Fig. 2b, after the graphene sample had undergone 15 min of RF plasma treatment, there was a larger "D" peak, indicative of the presence of defects on the graphene surface. The "D" peak is known as the defect band and it represents a ring breathing mode from sp2 carbon rings within graphene, though to be active, the ring must be adjacent to a graphene edge or a defect. The peak is usually very weak in graphite and high-quality graphene. The significant "D" peak shows there were multiple defects in the material as the intensity of the "D" peak is directly proportional to the number of defects in the sample.

The "2D" peak remained symmetrical after plasma treatment, and did not split into several overlapping modes, which suggests that the graphene had remained a monolayer after RF plasma treatment. The loss of the sharp peak and the formation of a lower "2D" peak is the result of an increase in the number of defects on the graphene. The addition of the "D + D" peak is also indicative of the presence of defects on the graphene. The "G" peak remained at 1587.94 cm, indicating that the graphene remained a monolayer.

3.2 *Capability of Graphene for Glucose Sensing*

From Fig. 3, the current-measured voltage (IV) graph shows that the resistance of the graphene sample before immobilization was 40,449 Ω. After GOx was immobilised onto the graphene, the resistance was observed to increase to 104,380 Ω.

From Fig. 4, the IV measurements showed that the resistance of GBBs increased linearly with increasing concentrations of glucose.

For GOx to function as a catalyst, the presence of a redox cofactor is needed—in this case flavin adenine dinucleotide (FAD) is used, which is located within the

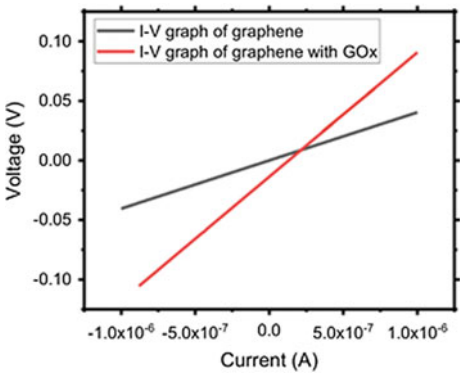

Fig. 3 IV characteristic curve for GBB with and without GOx

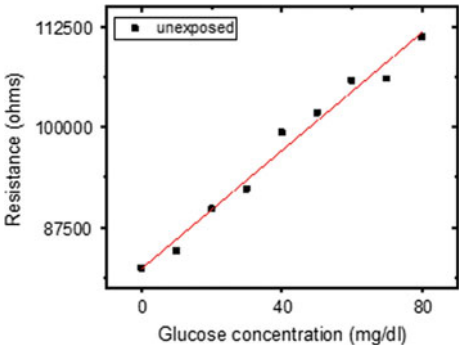

Fig. 4 Change in the resistance of GBB with increasing glucose concentration

GOx molecule [4]. For this project, the mechanism justifying the linear increase in resistance is as follows:

FAD present in GOx acts as the initial electron acceptor and is reduced to $FADH_2$ according to Eq. (3) [5]. $FADH_2$ then reacts with oxygen, forming hydrogen peroxide, in consonance with Eq. (2). The cofactor (FAD) is regenerated in the process, and will continue to catalyse the oxidation of other glucose molecules.

The equations are as shown below:

$$\text{GOx (FADH}_2\text{)} + \text{O}_2 \rightarrow \text{GOx (FAD)} + \text{H}_2\text{O}_2 \tag{2}$$

$$\text{Glucose} + \text{GOx (FAD)} \rightarrow \text{Gluconolactone} + \text{GOx (FADH}_2\text{)} \tag{3}$$

Hydrogen peroxide is a Lewis acid, with a pH of 4.5, which is due to partial dissociation of hydrogen peroxide as shown in reaction (4). The π-orbitals of graphene overlap with the π-orbitals of the GOx. The formation of the electrophilic hydroperoxyl ($HO_2^- HO_2^-$) and hydrogen (H^+) ions causes the electron cloud of graphene to skew towards the ions. The lower electron density at the surface of the graphene results in a lower number of mobile charge carriers to conduct electricity. Thus, the current is lower, leading to a higher resistance.

$$\text{H}_2\text{O}_2 \rightleftharpoons \text{H}^+ + \text{HO}_2^- \tag{4}$$

As the reaction continues to progress, the concentration of hydroperoxyl ions within the glucose solution increases, resulting in a higher resistance.

Comparing the graphs of the resistance of the GBB unexposed to plasma and that of the GBB exposed to 5 min of plasma in Fig. 5, the initial resistance of GBB increased after the RF plasma treatment.

This can be attributed to the increase in physical adsorption of GOx onto the GBB, which resulted from the plasma-engineered defects on the graphene surface. The defects increased the surface area for the adsorption of GOx. Each GOx molecule obstructs the movement of electrons, decreasing the electron mobility of

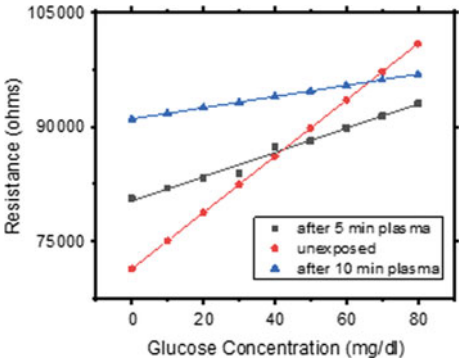

Fig. 5 Resistance of GBBs after different durations of exposure to RF plasma

the graphene. This results in an increase in resistance. This increase continues to be observed in GBBs exposed to 10, 15 and 20 min, suggesting that exposure to RF plasma is effective in aiding greater immobilization of GOx on the graphene surface, increasing the area of sensitivity of the GBBs.

A comparison of the slopes of the graphs also shows that a greater duration of RF plasma treatment results in a gentler gradient. This signifies that a smaller increase in resistance for every 10 mg/dl increase in glucose concentration is observed.

However, from Fig. 6, the GBBs exposed to 15 and 20 min of RF plasma were observed to have no increment with the increased glucose concentration. This suggests that the ions in RF plasma had resulted in defects to a degree that GOx molecules were no longer able to effectively bind to the surface of graphene.

It thus follows that GBBs exposed to 5 and 10 min of RF plasma treatment were the best candidates as effective biosensors. Although 10 min of plasma treatment were able to increase the immobilisation of GOx to a greater degree and is thus able to achieve a greater range of sensitivity, the lower gradient of the glucose concentration-resistance graph meant that there is a greater reliance on the specificity of GOx. As such, the GBB exposed to 5 min of plasma can be concluded to be the optimal GBB as it creates a balance between the range of sensitivity as well as room for error of the device.

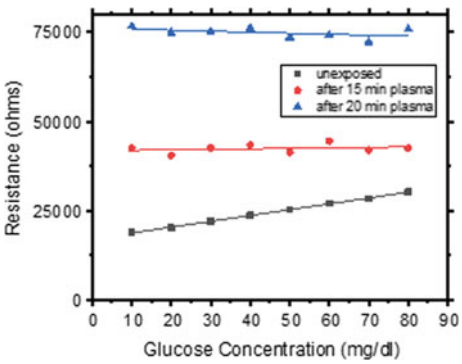

Fig. 6 Resistace of GBB after exposure to plasma for 15 and 20 min

4 Future Studies

In addition to taking IV measurements, the immobilisation of glucose oxidase could be ascertained more accurately with SEM characterisation techniques as a secondary check. The exact mechanisms of how the resistance of GBBs increases with increasing glucose concentration is also not known, and future studies could test the hypotheses for the mechanisms presented in this paper. Other types of plasma and effects of plasma on other nanomaterials suitable as electrodes for GBBs could also be studied further.

5 Conclusion

GBBs have shown to demonstrate biosensing capabilities. Exposure to RF plasma is able to introduce defects on the graphene surface, as shown by Raman characterisation, which increases the surface adsorption of the GOx enzyme. This increased binding of GOx then leads to a larger dynamic range of glucose sensing. Through the measurement of the GBBs' electrical properties, the most optimal duration of RF plasma treatment was found to be 5 min, as it was able to demonstrate balance between a wider detection range and high sensitivity, with its detectable range far surpassing current glucose biosensors. However, future work is necessary to confirm the mechanisms present in causing the resistance of GBBs to increase with the increase in glucose concentrations.

Acknowledgements The authors would like to gratefully acknowledge Dr. Joseph Vimal Vas for his expertise and teacher mentor Ms. Ng Tiong Eng for her guidance during every stage of our research. The authors would also like to thank the National Institute of Education for providing access to its facilities during data collection.

References

1. Ritesh K., Lakshmana P. N., Sadishkumar K., Jayaprakash S., and Muthupillai V. (2015). Evidence for current diagnostic criteria of diabetes mellitus *World J Diabetes. 7(17): 396–405.*
2. Scognamiglio, V. (2013). Nanotechnology in glucose monitoring: Advances and challenges in the last 10 years. *Biosens. Bioelectron.* 47, 12–25
3. Janire Peña-Bahamonde, Hang N. Nguyen, Sofia K. Fanourakis & Debora F. Rodrigues (2018) Recent advances in graphene-based biosensor technology with applications in life sciences Journal of Nanobiotechnology, volume 16, Article number: 75
4. Fritea, L., Tertis, M., Sandulescu, R., & Cristea, C. (2018). Enzymes–Graphene Platforms for Electrochemical Biosensors Design With Biomedical Applications. Methods in Enzymology. https://doi.org/10.1016/bs.mie.2018.05.010
5. Weibel MK, Bright HJ. The glucose oxidase mechanism. Interpretation of the pH dependence. J Biol Chem. 1971 May 10; 246(9):2734-2744.

Organic Solvent Nanofiltration Using Fish-Scale-Derived Membrane

Chua En Rui and Kannan Navaneethan

Abstract A Nanofiltration (NF) membrane derived from fish scales was developed for the treatment of textile wastewater. Sudan IV in Ethanol was used as the model dye. The membrane was developed by immersing the fish scales in sulfuric acid for an hour. The remaining solid mixed together with 2.00 ml of PVA (5%) is then applied onto the filter paper and pyrolyzed. The membrane was characterized by X-Ray Diffraction (XRD), Fourier Transform Infrared Spectroscopy (FTIR) and Thermogravimetric Analysis (TGA). Its surface morphology was mapped out by Scanning Electron Microscope (SEM). The membrane achieved a rejection rate as high as 85.56% for Sudan IV. The XRD and FTIR revealed that the membrane consisted of graphite with turbostratic structure and the SEM images revealed the flocculated structure of the membrane. The membrane works by adsorption and size rejection. The membrane was tested with Rose Bengal (RB) dye to investigate the relationship between the polarity of dyes and the effectiveness of the membrane. The adsorption test displayed a lower adsorption rate for RB as compared to Sudan IV. The separation results showed the membrane had a maximum rejection of only 43.57% for RB. This implies that the NF membrane has lower adsorption for RB as compared to Sudan IV. The NF membrane showed greater potential for the removal of non-polar dyes such as Sudan IV as compared to polar dyes.

Keywords Nanofiltration · Fish scales · Organic solvent nanofiltration

1 Introduction

Due to its wet processing methods, the textile industry is the main contributor of effluent waste which is largely toxic [1, 2]. An estimated 7×10^5 tons of synthetic dyes are produced annually and up to 2×10^5 tons of these dyes are lost to effluents

C. En Rui (✉) · K. Navaneethan
NUS High School of Mathematics and Science Singapore, Singapore, Singapore
e-mail: enruichua@gmail.com

K. Navaneethan
e-mail: h1510061@nushigh.edu.sg

H. Guo et al. (eds.), *IRC-SET 2020*,
https://doi.org/10.1007/978-981-15-9472-4_23

during the dying processes in the textile industry alone [3]. The textile industry often uses azo dyes like Sudan IV extensively due to its low cost and ease of synthesis [3, 4]. However, these are often mutagenic and/or carcinogenic thus it is of utmost importance that there are cheap and viable means of removing such organic pollutants from wastewater [3–6]. According to the Food and Agriculture Organization of the United Nations, global fish production in 2016 was reported to be 170.9 million tons [7]. As high as 30% of it was discarded as solid wastes, which consists of fish scales (FS), bones and skin [8]. The accumulation of such organic matter leads to acute environmental contamination [8]. By creating a Nanofiltration (NF) membrane made of FS, the pollution caused by the textile industry can be reduced by tapping into the organic waste material from fish farms as a sustainable raw material for membrane production.

Adsorption methods have been favored for textile wastewater treatment containing multiple dyes due to its decolorization efficiency [1]. However, it faces drawbacks in areas such as its regeneration and dumping [1]. These factors coupled together with the high price of adsorbents and sludge generation prompts for a more sustainable method of textile wastewater treatment method [1, 9]. NF generally has a lower energy consumption and have a higher flux as compared to Reverse Osmosis (RO) while maintaining a high rejection rate for organic molecules [10]. The treatment of textile wastewater by NF has been shown to achieve a high rejection rate and flux [10].

In this project, a new form of NF membrane was created based on FS and Polyvinyl Alcohol (PVA) for the selective and effective removal of Sudan IV. The membrane was tested against Rose Bengal (RB) as well. The membrane was characterized by SEM (Scanning Electron Microscope), XRD (X-Ray Diffraction), FTIR (Fourier Transform Infrared Spectroscopy) and TGA (Thermogravimetric Analysis). The efficiency of the membrane was measured by Ultraviolet–visible spectroscopy (UV–Vis). We hypothesize that the fish scale derived NF membrane works by adsorption and size rejection of the dye.

2 Materials and Methods

2.1 Materials

Sulfuric acid (95–98%, ACS reagent grade), Poly(vinyl alcohol) (Mw = 124–186 × 103, 98–99% hydrolyzed), Rose Bengal dye (95%) and Sudan IV dye (≥80%) was purchased from Sigma Aldrich. Characteristics and structure of both dyes are shown in Table 1 [11, 12]. Ethanol (99.8%+, Absolute) was purchased from Fisher Scientific. Millipore glass-fibre filters (Type 5, retention 0.7 μm), Stainless steel discs (316 L, 0.2 μm) purchased from Mott Corporation. Cellulose filtration paper (Diameter = 150 mm, thickness = 0.21 mm, pore size = 2 μm) purchased from Advantec. The raw fish scales of *Lates calcarifer* were obtained from Singapore.

Table 1 Characteristics and structure of Sudan IV and Rose Bengal dye

Compound (formula)	Structure	Molecular weight (g/mol)
Sudan IV ($C_{24}H_{20}N_4O$)	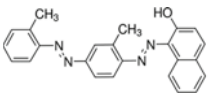	380.44
Rose Bengal ($C_{20}H_2Cl_4I_4Na_2O_5$)	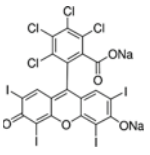	1017.64

These were repeatedly washed with distilled water to remove soluble impurities and stored in tightly sealed containers in a refrigerated environment.

2.2 Instruments

FTIR (with Bruker spectrometer) was used to observe the organic functional groups present within the FS and the FS derived membrane.

Thermogravimetric Analysis (TGA, Q50) by using a ramp of 10 °C/min to 400 °C under N2 purge (30 ml/min). This was to determine the thermal decompositions and aid in interpreting chemical properties and composition of the FS and membrane.

X-ray Diffractometer (Bruker D8 Advance), CuKα radiation $\lambda = 1.54$ Å was used to determine the structure of the membrane and its composition.

The surface morphologies of the membranes were imaged by JSM-7610Fplus Schottky Field Emission Scanning Electron Microscope.

UV–Vis spectrometer, Shimadzu 3600 was used to quantify separation and adsorption data.

2.3 **Prepa*ration of Dye Solutions***

The solutions of Sudan IV (10 ppm) and RB (10 ppm) were prepared by dissolving the required amount of dye in Ethanol. Batch experiments were conducted using these prepared solutions.

2.4 Preparation of Membranes

2.00 g of FS was stirred in 10.00 ml of Conc. H_2SO_4 for 1 h at 200 rpm. The acid-treated FS was separated from the mixture by vacuum filtration using a glass-fibre filter for 10 min. The retrieved acid-treated FS was then stirred with 2.00 ml of PVA (5% in DI water) for 1 h at 250 rpm. The resultant mixture was then applied onto a piece of filter paper using a paintbrush. The membrane was then allowed to air-dry at room temperature for 6 h followed by heating in a furnace to 350 °C at a rate of 2.5 °C/min and kept at 350 °C for 2 h. It was then cooled down at a rate of 2.5 °C/min till room temperature.

The control membrane was prepared by applying a 2.00 ml coating of PVA (5% in DI water), using a paintbrush onto a piece of filter paper. It was allowed to air-dry for 6 h at room temperature. The membrane was then pyrolyzed with the same heating cycle as the FS derived membrane.

2.5 Separation Set-Up

Dead-end filtration was used as the separation method. The set-up used a micro gear pump to feed the dye solution into the packing mechanism (Refer to Appendix 1 for set-up). The vial collecting the filtrate was changed every hour. The pressure was measured every hour. The volume of the filtrate collected in each vial was measured to calculate permeance according to Eq. (1),

$$\text{Permeance} = V/(A \times t \times P) \tag{1}$$

where V is the volume of filtrate in liters, A is the surface area of the membrane in m^2, t is time in hours and P is pressure in bar.

The rejection percentage was calculated using the absorbance data from the UV–Vis spectrometer according to Eq. (2),

$$\text{Rejection} = [(C_i - C_f)/C_i] \times 100\% \tag{2}$$

where C_i is the absorbance of the feed and C_f the absorbance of the filtrate.

3 Results and Discussion

3.1 FTIR Analysis

The FTIR spectrum of the fish scales in Fig. 1 shows bands at 3287, 1632, 1415, 1008 and 555 cm^{-1}. The 3287 and 1632 cm^{-1} bands correspond to Amide A and

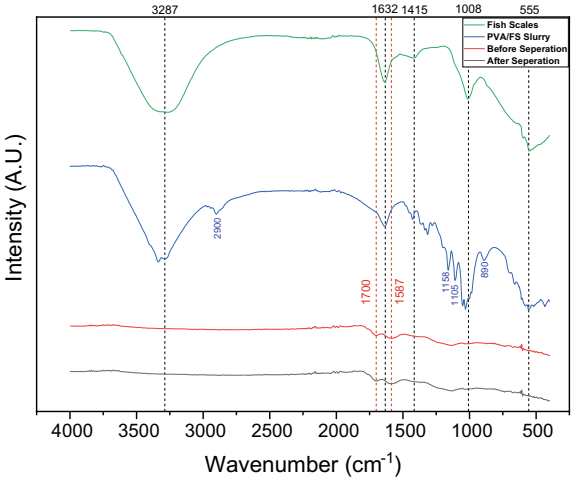

Fig. 1 ATR-FTIR results of fish scales, PVA/FS slurry, membrane before separation and membrane after separation

Amide I respectively from collagen in the FS. Amide A bands are due to the N–H stretching vibration [13]. The shift to a lower frequency in the results is due to the presence of hydrogen bonding of the NH group in the peptide. Amide I band is often due to C = O stretching vibration or H-bond with COO^- [13]. The latter is more likely due to the presence of the 1415 cm^{-1} band which is attributed to carbonate. Carbonate originates from substitution for hydroxyl or phosphate groups in hydroxyapatite (HA) [14, 15]. However, it is noted that the Amide II and III bands were not observed.

The 1008 and 555 cm^{-1} can be attributed to phosphate groups from HA [14–16]. The FTIR spectrum of the PVA/fish scale slurry produced show bands at 3287, 2990, 1632, 1427, 1158, 1105, 1008, 890 and 555 cm^{-1}. The Amide A, Amide I at 3287 cm^{-1} and 1632 cm^{-1} respectively can also be observed due to the collagen from the FS [13].

The band at 2900 cm^{-1} can be attributed to C–H broad alkyl stretching of PVA [17]. The band observed at 1427 cm^{-1} is due to carbonate from HA [14, 15]. The band at 1158 cm^{-1} is due to S=O symmetric stretching from sulfuric acid [18]. The 1105 cm^{-1} band can be attributed to the sulphate ion from sulfuric acid [18]. The 1008 and 555 cm^{-1} bands can be attributed to phosphate groups from HA [14–16]. The 890 cm^{-1} band is likely due to carbonate ion [14, 15]. This indicates the incorporation of PVA and FS treated with sulfuric acid.

The results also show 2 bands at 1700 and 1587 cm^{-1} for the membrane before and after the separation process. The similarities of both spectrums would suggest no change in the composition of the membrane due to the dye. The 1700 cm^{-1} band is likely due to a carboxyl group caused by C=O stretching [14–16].

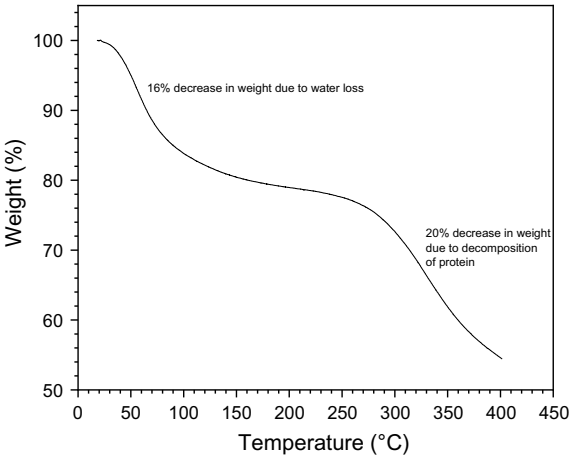

Fig. 2 TGA of fish scales of *Lates calcarifer*

3.2 TGA Analysis of Fish Scales

The TGA of the FS in Fig. 2 shows two slopes. The initial weight loss of about 16% up till 100 °C is largely due to the loss of water. The second weight loss of about 20% (from 270 to 350 °C) is due to the decomposition of protein (i.e. collagen) in the FS [16]. This backs the FTIR data where the collagen related Amide A and Amide I peaks from the FS is missing after pyrolysis. At 350 °C, most organic compounds due to the pyrolysis process combust to form carbon.

3.3 SEM Imaging

The SEM images in Fig. 3 shows the flocculated structure of the membrane. The smaller carbon fragments were scattered about the carbonized filter paper and held by the binding agent, PVA. This structure increases the surface area for adsorption and creates pores of varying sizes. The SEM images also confirm that the membrane is composed of carbon fragments.

3.4 XRD Analysis

The XRD shows a prominent diffraction peak at $2\theta = 26.21°$ which is of typical graphitic structure (002) [19, 20]. This confirms the FTIR results. Using Bragg's law, the interlayer spacing was calculated to be 3.40 Å. This is higher than the normal 3.35 Å of typical graphite sheets [19, 20]. This indicates that the graphite resultant from the pyrolysis process is more turbostratic in nature [19, 20]. This is

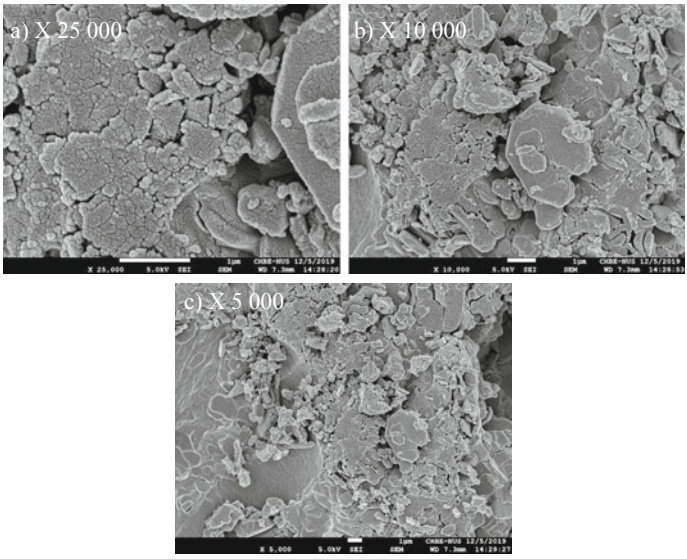

Fig. 3 SEM images of membrane surface at **a** 25,000 times magnification **b** 10,000 times magnification **c** 5000 times magnification

likely due to the local stacking faults and random shifts between adjacent layers as water and protein are lost during pyrolysis. The peak observed at 31.12° is proposed to represent fragmented developed crystallites [19, 20].

The diffraction peaks in the range around $2\theta = 42°$, are of weaker intensity and are slightly broader. This indicates less developed intragraphitic layers [19, 20]. The XRD results show no change in the structure of the membrane before and after the separation process (Fig. 4).

3.5 Separation Results for Sudan IV

The membrane had a relatively high rejection rate, peaking at 85.56% (Fig. 5). The average membrane permeance was 5.55 L h m^{-2} bar^{-1}. The general trend for both the membrane permeance and rejection rate was a slight increase till its peak at 180 min followed by a gradual decrease till the end. The control showed an initial rejection rate of about 76%. However, it drastically decreased to approximately 32% before allowing the feed to pass through.

The trend of the rejection data of the membrane would suggest that it possibly functions based on adsorption as the curve appears to be humped-shaped. We propose that as more dye molecules fill the pores of the top layers, the dye molecules would then be unable to pass through the blocked pores. This would result in size rejection of the dye molecules, aided by adsorption. The subsequent decrease in rejection is

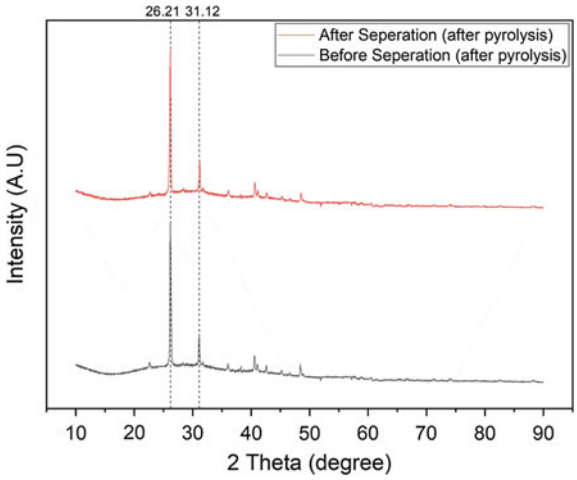

Fig. 4 XRD of membrane before and after separation

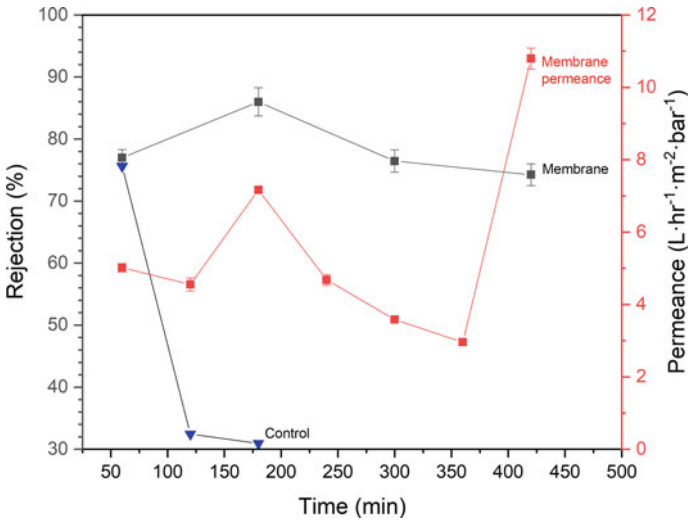

Fig. 5 Membrane permeance and rejection rate of Sudan IV for control and membrane

likely due to the dye molecules being pushed through the many layers of graphite over time and eventually being flushed out together with the solvent. 2 pieces of the membrane (0.0520 g) was stirred in 15 ml of Sudan IV feed at 250 rpm. The data of the Concentration (C) at time, t against the initial concentration (C_0) was plotted (Fig. 6). The results show the steady decline of the dye concentration as time passed. The membrane is able to effectively decolorize the dye by adsorption. This

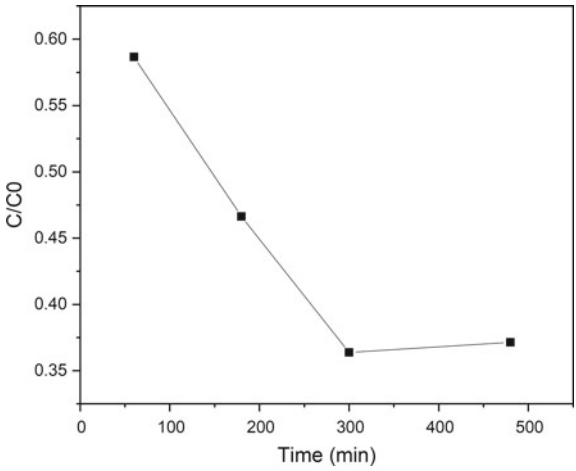

Fig. 6 Membrane adsorption test (Sudan IV)

further confirms the hypothesis that adsorption is at play for the membrane separation process.

3.6 Separation Results for Rose Bengal

The membrane had a peak rejection rate for RB at 43.57% (Fig. 7). The general trend of the separation results appears to be hump-shaped, though sharper as compared to

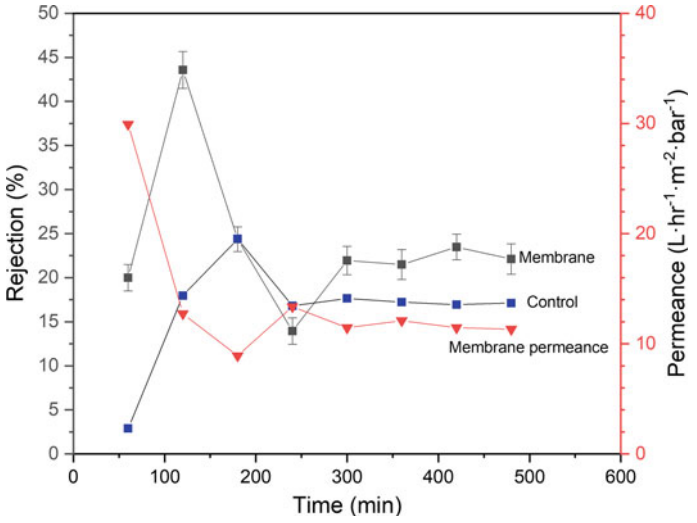

Fig. 7 Membrane permeance and rejection rate of Rose Bengal for control and membrane

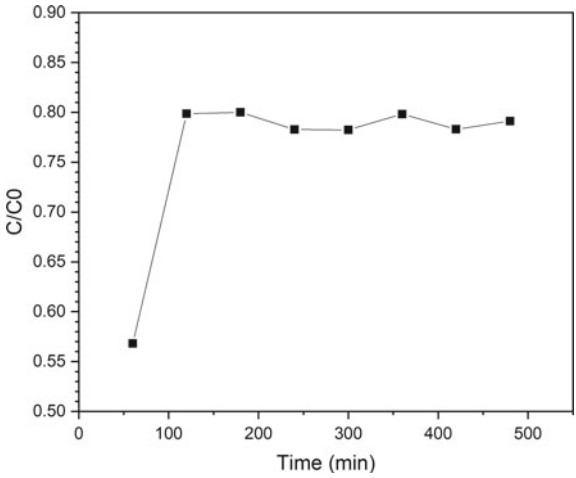

Fig. 8 Membrane adsorption test (Rose Bengal)

Sudan IV. Thus, the adsorption mechanism of the membrane of RB dye is likely to be similar to that of Sudan IV. However, there is a large disparity in the membrane's rejection rate between Sudan IV and RB.

2 pieces of the membrane (0.0520 g) was stirred in 15 ml of RB feed at 250 rpm (Fig. 8). Once again, the data of the Concentration (C) at time, t against the initial concentration (C_0) was plotted. The results show an initial ability of the membrane to adsorb the dye. However, the C/C_0 of the dye increased over time and plateaued at about 0.79. Overall, the membrane is unable to effectively adsorb the RB dye. This indicates that the membrane has a decreased ability to adsorb RB dye as compared to Sudan IV.

After looking at both the separation data and the adsorption test, we hypothesize that the membrane has a decreased ability to adsorb polar dyes like RB. This decrease in adsorption rate results in the membrane being able to reject polar dyes less effectively as compared to non-polar dyes. This affects the membrane's ability for size rejection as well due to the inability for it to adsorb the dye.

However, the mechanism of adsorption was not studied in this project and we are unable to definitively prove this hypothesis. Overall, these results show that the created FS derived NF membrane is able to carry out the filtration of dyes in organic solvents using Sudan IV as the model dye. The membrane is hypothesized to reject non-polar dyes more effectively due to its adsorption mechanism and membrane composition.

4 Further Studies

Further studies into characterizing the adsorption mechanisms of the membrane can be carried out. Analyses into the membrane preparation and the kinetics of dye

removal can be studied to better improve the membrane. Research to increase the permeance of the membrane and maximizing its rejection can also be done. The type of FS used to create the membrane and its effects can be studied. The membrane's effectiveness to reject dyes in polar solvents such as water can also be investigated.

5 Conclusion

The created FS derived membrane has a flocculated structure of graphite. Decolorization of Sudan IV in Ethanol was used as the model case. Overall, the data indicate that the created FS derived NF membrane is able to carry out the filtration of dyes in organic solvents using Sudan IV as the model dye. The membrane is hypothesized to be more effective in rejecting non-polar dyes due to its adsorption mechanism and membrane composition. Sudan IV was successfully removed by the NF membrane through adsorption and size rejection. The membrane shows promising results for the membrane to be used for textile wastewater treatment. The membrane can possibly be scaled up and used in textile wastewater treatment using flat sheet membranes. The production of the membrane using a sustainable and cheap material is cost-effective (refer to Appendix 2) and helps to reduce waste. This process of preparing and testing the membrane takes a maximum of 18 h.

Acknowledgements We would like to express our sincere thanks to Associate Professor Hong Liang from the Department of Chemical and Biomolecular Engineering, National University of Singapore, for introducing us to this project and also for his supervision and permission to conduct experiments in his lab. We would also like to thank Dr Teh Yun Ling from NUS High School of Mathematics and Science for her guidance.

Appendices

Appendix 1

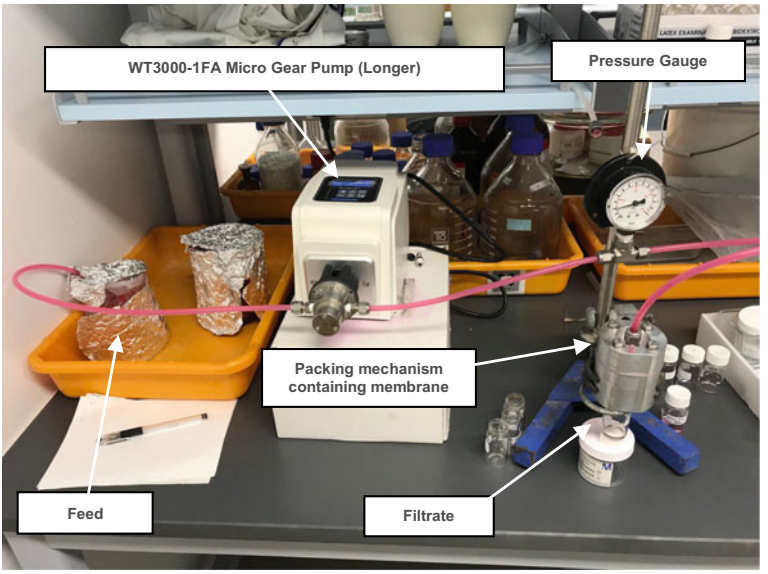

Appendix 2

See Table 2.

Table 2 Cost of production of membrane

Items	The amount required for 1 membrane	Unit price (SGD)	Cost of material per membrane (SGD)
Sulfuric acid	10.00 ml	$169/2.5 L	$0.68
PVA	0.10 g	$397/1 kg	$0.04
Fish scales	2.00 g	Nil	Nil
DI water	2.00 ml	$21.06/5 L	$0.009
Filter paper	1 piece (150 mm)	$19.02/100 pieces	$0.20
Total cost			$0.93

Price sourced from various distributors according to the materials used for this project

References

1. C. R. Holkar, A. J. Jadhav, D. V. Pinjari, N. M. Mahamuni, and A. B. Pandit, "A critical review on textile wastewater treatments: Possible approaches," Journal of Environmental Management, vol. 182, pp. 351–366, 2016.
2. X. Lu, L. Liu, R. Liu, and J. Chen, "Textile wastewater reuse as an alternative water source for dyeing and finishing processes: A case study," Desalination, vol. 258, no. 1-3, pp. 229–232, 2010.
3. F. M. D. Chequer, G. A. R. D. Oliveira, E. R. A. Ferraz, J. Carvalho, M. V. B. Zanoni, and D. P. D. Oliveir, "Textile Dyes: Dyeing Process and Environmental Impact," Eco-Friendly Textile Dyeing and Finishing, 2013.
4. K.-T. Chung and C. E. Cerniglia, "Mutagenicity of azo dyes: Structure-activity relationships," Mutation Research/Reviews in Genetic Toxicology, vol. 277, no. 3, pp. 201–220, 1992.
5. X. Sun, H. Ou, C. Miao, and L. Chen, "Removal of sudan dyes from aqueous solution by magnetic carbon nanotubes: Equilibrium, kinetic and thermodynamic studies," Journal of Industrial and Engineering Chemistry, vol. 22, pp. 373–377, 2015.
6. T. M. Fonovich, "Sudan dyes: are they dangerous for human health?," Drug and Chemical Toxicology, vol. 36, no. 3, pp. 343–352, May 2012.
7. The state of world fisheries and aquaculture 2018: meeting the sustainable development goals. Rome: Food and Agriculture Organization of the United Nations, 2018.
8. F. Marrakchi, M. J. Ahmed, W. Khanday, M. Asif, and B. Hameed, "Mesoporous carbonaceous material from fish scales as low-cost adsorbent for reactive orange 16 adsorption," Journal of the Taiwan Institute of Chemical Engineers, vol. 71, pp. 47–54, 2017.
9. M. T. Yagub, T. K. Sen, S. Afroze, and H. Ang, "Dye and its removal from aqueous solution by adsorption: A review," Advances in Colloid and Interface Science, vol. 209, pp. 172–184, 2014.
10. A. Mohammad, Y. Teow, W. Ang, Y. Chung, D. Oatley-Radcliffe, and N. Hilal, "Nanofiltration membranes review: Recent advances and future prospects," Desalination, vol. 356, pp. 226–254, 2015.
11. Sigma-Aldrich, "Rose bengal," CAS number 632-69-9. [Online]. Available: https://www.sigmaaldrich.com/catalog/product/aldrich/330000?lang=en. [Accessed: 04-Jan-2020].
12. Sigma-Aldrich, "Sudan IV," CAS number 85-83-6. [Online]. Available: https://www.sigmaaldrich.com/catalog/product/aldrich/198102?lang=en. [Accessed: 04-Jan-2020].
13. S. Chuaychan, S. Benjakul, and H. Kishimura, "Characteristics of acid- and pepsin-soluble collagens from scale of seabass (Lates calcarifer)," LWT - Food Science and Technology, vol. 63, no. 1, pp. 71–76, 2015.
14. M. Younesi, S. Javadpour, and M. E. Bahrololoom, "Effect of Heat Treatment Temperature on Chemical Compositions of Extracted Hydroxyapatite from Bovine Bone Ash," Journal of Materials Engineering and Performance, vol. 20, no. 8, pp. 1484–1490, 2010.
15. A. Boskey and N. Pleshkocamacho, "FT-IR imaging of native and tissue-engineered bone and cartilage," Biomaterials, vol. 28, no. 15, pp. 2465–2478, 2007.
16. S. Sankar, S. Sekar, R. Mohan, S. Rani, J. Sundaraseelan, and T. Sastry, "Preparation and partial characterization of collagen sheet from fish (Lates calcarifer) scales," International Journal of Biological Macromolecules, vol. 42, no. 1, pp. 6–9, 2008.
17. H. S. Mansur, R. L. Oréfice, and A. A. Mansur, "Characterization of poly(vinyl alcohol)/poly(ethylene glycol) hydrogels and PVA-derived hybrids by small-angle X-ray scattering and FTIR spectroscopy," Polymer, vol. 45, no. 21, pp. 7193–7202, 2004.
18. A. B. Horn and K. J. Sully, "ATR-IR spectroscopic studies of the formation of sulfuric acid and sulfuric acid monohydrate films," Physical Chemistry Chemical Physics, vol. 1, no. 16, pp. 3801–3806, 1999.
19. B. S. Girgis, Y. M. Temerk, M. M. Gadelrab, and I. D. Abdullah, "X-ray Diffraction Patterns of Activated Carbons Prepared under Various Conditions," Carbon letters, vol. 8, no. 2, pp. 95–100, 2007.

20. Z. Li, C. Lu, Z. Xia, Y. Zhou, and Z. Luo, "X-ray diffraction patterns of graphite and turbostratic carbon," Carbon, vol. 45, no. 8, pp. 1686–1695, 2007.

An Acoustic Study on the Dispersive Flexural Modes of Wave Propagation in a Helical Spring

Matthew Yar

Abstract Tapping a helical spring produces a sound of rapidly decreasing frequency resembling a "laser shot" in a science-fiction movie. This phenomenon is due to acoustic dispersion—when the helical spring is tapped, a wave packet is generated and propagates through the dispersive flexural mode of the helical spring. Higher frequency components travel faster than lower frequency components, hence a sound of rapidly decreasing frequency is perceived. A time–frequency analysis was used to investigate the sound produced experimentally. Variables such as number of coils (length of helical spring) and material (speed of sound) of helical spring as well as material used to tap the spring were varied. Theoretically, the helical spring was modelled as a dispersive Euler–Bernoulli beam; the derived dispersion relation correctly predicts the change in frequency over time for spring length and material. Tension and material used to tap the spring were shown to not affect the dispersion relation, although the material used to tap the spring/material of the spring were shown to affect the dominant frequency of the sound produced.

Keywords Beam theory · Acoustic dispersion · Flexural waves

1 Introduction

Acoustic dispersion is a common unique phenomenon; when sound waves pass through a certain medium, they may be separated into their many different component frequencies. It can be observed when one skates on thin ice or hits long steel cables (e.g. radio tower support cables). More interestingly, as first mentioned by Crawford [1], tapping a helical spring (also known as a 'slinky') can also produce such an interesting sound effect—a "laser shot" sound effect.

An excitation, in the form of tapping the slinky, will generate an impulse, comprising a wide range of superimposed frequencies. This impulse then travels through the slinky as a dispersive wave packet. The wave packet disperses, spreading

M. Yar (✉)
Raffles Institution, Singapore, Republic of Singapore
e-mail: 21ymatt818b@student.ri.edu.sg

H. Guo et al. (eds.), *IRC-SET 2020*,
https://doi.org/10.1007/978-981-15-9472-4_24

out as it propagates down the slinky. As the wave packet disperses, higher frequency components travel faster than lower frequency components; the higher the frequency, the faster the wave components will arrive at the other end of the slinky. Thus, higher frequency components are heard first and lower frequencies later, leading to a perceived decrease in frequency—the defining feature of a laser shot sound [2, 3].

Crawford was able to generate the laser shot sound using a crudely constructed experimental set-up, and compared simulated and experimentally recorded sounds by ear. For this research, a more rigorous method of data collection and sound analysis was used, which will be explained later. Additional and new insight was gained from varying the number of coils (different lengths) of the slinky, using different types of materials (different speed of sound) to excite the slinkys as well as using slinkys of different materials and dimensions.

An immediate application of this phenomenon would be as a cinematic sound effect (for example, a blaster gun sound in a "Star Wars" science-fiction movie). This research would also be useful in the music industry. Musicians would be able to make use of a slinky as an unconventional and innovative musical instrument with a distinct timbre. In doing so, more layers could be added to diversify the musical fabric, creating a richer tone colour and allowing a more unique and edifying listening experience. As can be seen, a precise transcription of the sound by being able to accurately predict the change in frequency over time of the "laser shot" sound effect would allow for fresh perspectives and developments in the arts and music industry. Thus, this research will attempt to conduct a detailed study on the joint time–frequency domain analysis of the sound, along with a quantitative account to accurately predict this change in frequency over time. A spectrogram was also used to identify two modes of wave propagation as well as reflected waves travelling through the slinky. Variables such as number of coils of the slinky, material of slinky, material used to tap the slinky will also be investigated to allow for a more complete understanding of the phenomenon of acoustic dispersion. The slinky shall be modelled as a Euler–Bernoulli beam (classical beam theory).

Further applications and detailed study on the propagation of flexural waves in dispersive beam structures (specifically, the dispersion relation [4]—how frequency affects the group velocity) could allow structural damage [5] of the beam to be identified, an important safety aspect under the study of structural mechanics.

2 Quantitative Account

2.1 Dispersion Relation

An alternative derivation of the dispersion relation is presented using Euler–Bernoulli beam theory. The slinky (of n coils, each of diameter D) is modelled by uncoiling and "stretching" it into an equivalent stiff, long straight and rectangular homogenous bar of length $L = \pi Dn$. The stainless-steel beam is a dispersive medium. The slinky

was modelled as a Euler–Bernoulli (EB) beam, as wavelength is much larger than its cross-sectional dimensions, governed by the following EB beam equation describing free vibration of a homogenous beam, with constants E (Young's modulus), I (second moment of area), ρ (density), A (cross-sectional area):

$$(EI/\rho A)\left(\partial^4 y\right)/\left(\partial x^4\right) = -\left(\partial^2 y\right)/\left(\partial t^2\right) \tag{1}$$

Substituting using an Ansatz trial solution $y = \sin(kx - \omega t)$, we can obtain the following dispersion relation:

$$\omega = k^2 cr \tag{2}$$

where ω is the angular frequency, k is the wave number, c is the speed of sound given by $c = (E/\omega)^{1/2}$ and r is the radius of gyration given by $r = (I/A)^{1/2}$.

The expression for group velocity can be given as:

$$v_g = \frac{d\omega}{dt} = 2kcr = 2(\omega cr)^{1/2} \tag{3}$$

Components of a flexural wave with higher wave number will result in bending with a lower radius of curvature, and due to the flexural rigidity of the Euler–Bernoulli Beam, the beam will respond in such a way that the restoring force increases more than proportionately to the wave number k. Therefore, waves with a higher wave number oscillate at a much higher frequency, and since based on the dispersion relation, group velocity is proportional to wave number, this explains why higher frequency components travel faster.

It is also observed that radius of gyration r is given as $d/(12)^{1/2}$, d is a cross-sectional dimension of the slinky. Since the slinky has a rectangular cross-section, there are two possible values of d depending on which dimension is excited, causing the 2 different modes of wave propagation (Fig. 1).

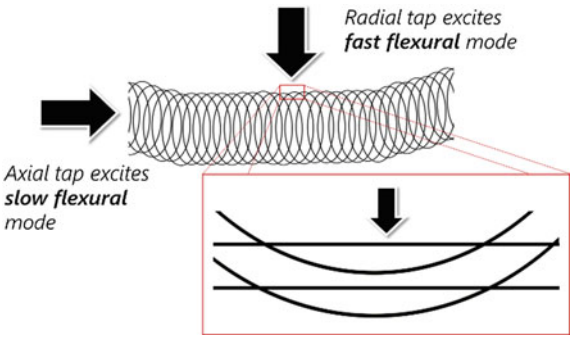

Fig. 1 Diagram illustrating flexural mode excited based on axis of tap

2.2 Frequency-Time Relation

Given distance = speed × time, $L = v_g \Delta t$ and by using substitutions of $v_g = 2(\omega cr)^{1/2}$, $L = \pi Dn$, $\omega = 2\ \pi f$, $r = d/(12)^{1/2}$ discussed earlier, the following equation can be obtained, showing how frequency of sound produced changes with time:

$$f = \left(N^2 D^2 \left(3\pi^2\right)^{1/2}\right) / \left(4cd\Delta t^2\right) \tag{4}$$

Note that the generated wave will be reflected back once it reaches the (output) end of the slinky, thus it will travel an extra 2 times the length of the slinky before it reaches the output end again. Thus, to account for reflected waves, the number of coils has to be multiplied by appropriate coefficients (first reflected wave $(3\ N)^2$, second reflected wave $(5\ N)^2$, etc.)

2.3 2 Modes of Wave Propagation

As discussed earlier, tapping each of the dimensions of the slinky excites different flexural mode. From the frequency-time relation derived earlier, exciting the short 'axial' dimension of the slinky ('slower' flexural mode) would yield a sound that arrives *later* ('late whistler'). Conversely, exciting the long 'radial' dimension of the slinky ('faster' flexural mode) would yield a sound that arrives *earlier* ('early whistler').

The frequency-time graph is plotted (Fig. 2) using Eq. (4); it is first observed that the late whistler has a longer duration than the early whistler. Zooming into the red area (Fig. 3), it is observed that at any given time, the late whistler has a higher frequency than the early whistler. Next, by comparing the slopes of the late and early

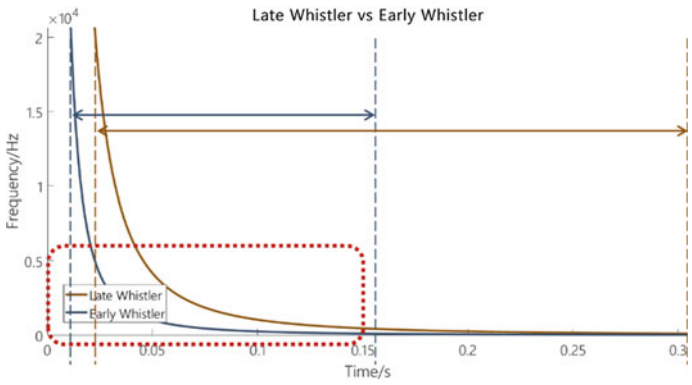

Fig. 2 Theory graph (frequency-time) for both the late and early whistler

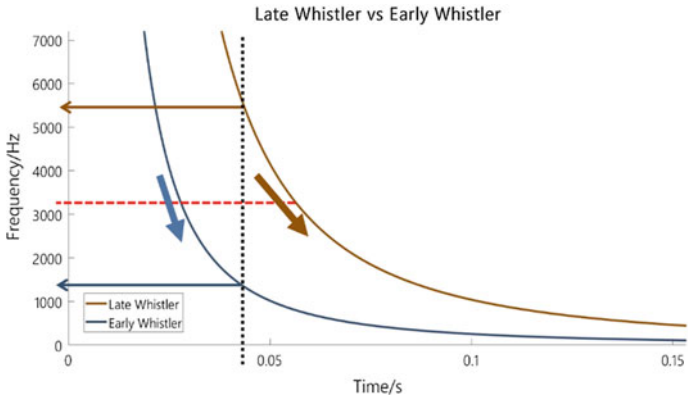

Fig. 3 Enlarged section of graph (identified as the red area of Fig. 2)

whistlers at the *same frequency*, the early whistler is seen to have a much steeper slope and faster rate of frequency decrease than the late whistler.

3 Methods and Results

3.1 Experimental Set-Up

Slinkys of different materials and sizes were used (Fig. 4). For experiments (Fig. 5), one end of the slinky was clamped tightly by a retort stand; the other was attached

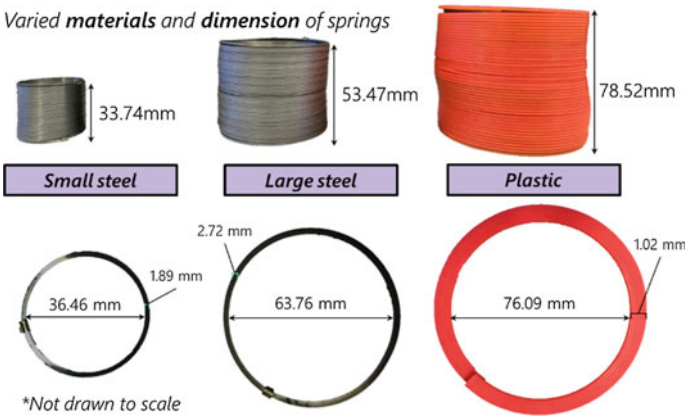

Fig. 4 Dimensions of small steel, large steel, and plastic slinkys used

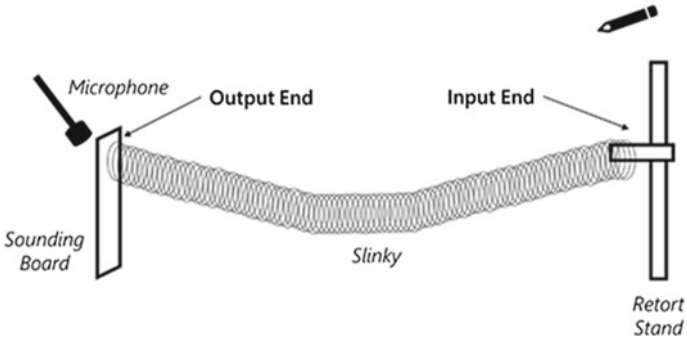

Fig. 5 Schematic of experimental set-up

to a sounding board near an acoustic microphone. When the input end was tapped, a laser shot sound was captured at the output end.

3.2 Determining Young's Modulus

To determine the Young's modulus of the different materials (of helical springs), the free vibration method was used to characterise Young's modulus (results in Fig. 6). From the frequency-time relation, a higher Young's modulus would lead to a higher speed of sound which would affect the change in frequency over time accordingly.

It is observed that experimental data lies well on fitted curve. For steel, the characterised value of 248 GPa is close to the literature value of 220 GPa. For further verification, a numerical simulation (finite element method) was conducted—corresponding frequencies were plotted for each length. A good correspondence indicates the validity of Euler–Bernoulli beam theory for helical coils. A full list of all experimentally determined material characteristics is provided in Table 1.

3.3 Method of Data Analysis

A time–frequency analysis was conducted using a short-time Fourier transform (STFT)[1] [6], allowing the dominant frequency identified for each small time window to be plotted on a frequency-time graph. Alternatively, the sound recorded was also displayed on a spectrogram (which visually illustrates the change in spectrum of frequencies against time). The spectrogram was then overlaid with the theoretically predicted change in frequency over time.

[1] 44,100 Hz sampling, hamming window (256 samples), 25% overlap.

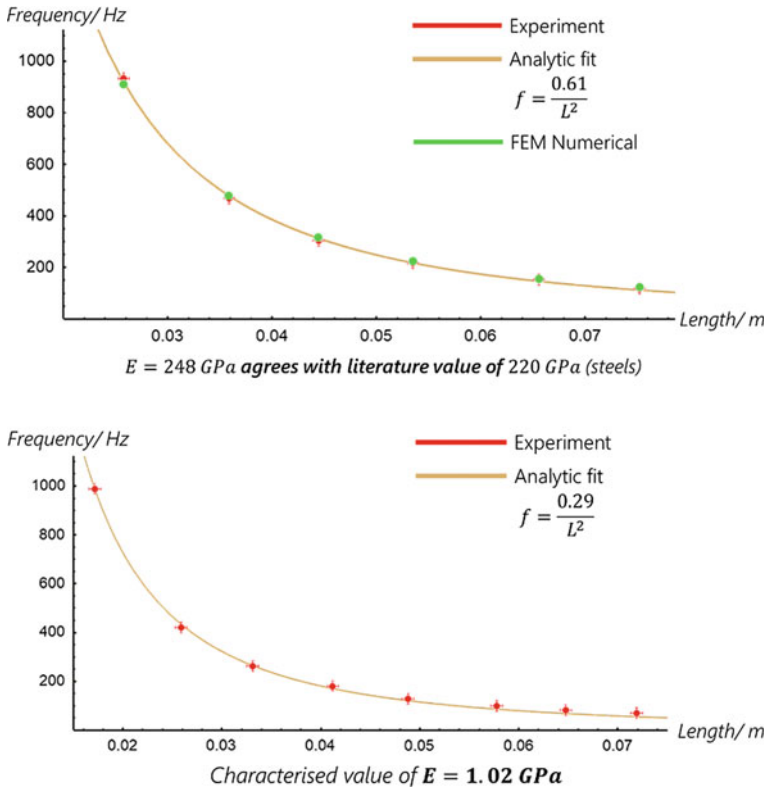

Fig. 6 Graph of natural vibrational frequency was plotted for each different length of a single coil section cut from the slinky. Top left: steel, top right: plastic

Table 1 Experimentally measured values

Parameter (method)	Measured value	
	Steel slinky	Plastic slinky
Young's modulus, E/GPa (free vibration method)	248 (*Literature: 220*)	1.02
Density, ρ/kg m^{-3} (calculated from measured mass and volume)	7510 (*Literature: 7700*)	220
Speed of sound, c/m s^{-1} (calculated using $c = (E/\rho)^{1/2}$)	5749 (*Literature: 5700*)	2151

3.4 Graphs of Steel Slinkys (Fig. 7, 8 and 9)

Overall, experimental results agree well with the theory.

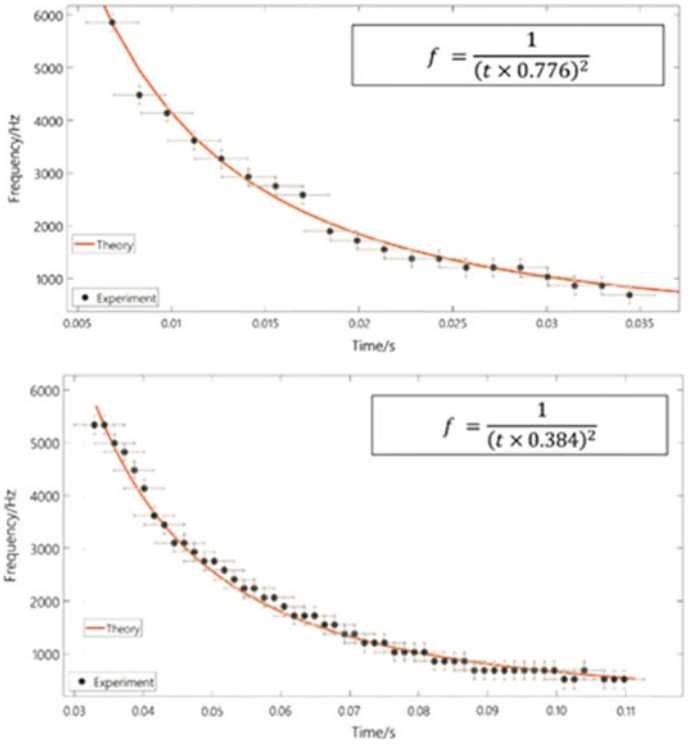

Fig. 7 Graph of frequency against time for both modes of excitation for a 67-coil large slinky. Long dimension (top) and short dimension (bottom)

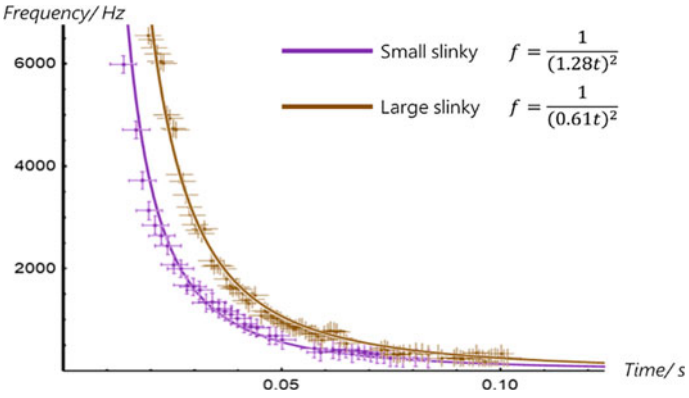

Fig. 8 Graph of frequency against time for the *slow* flexural mode of excited small and large 40-coil slinkys

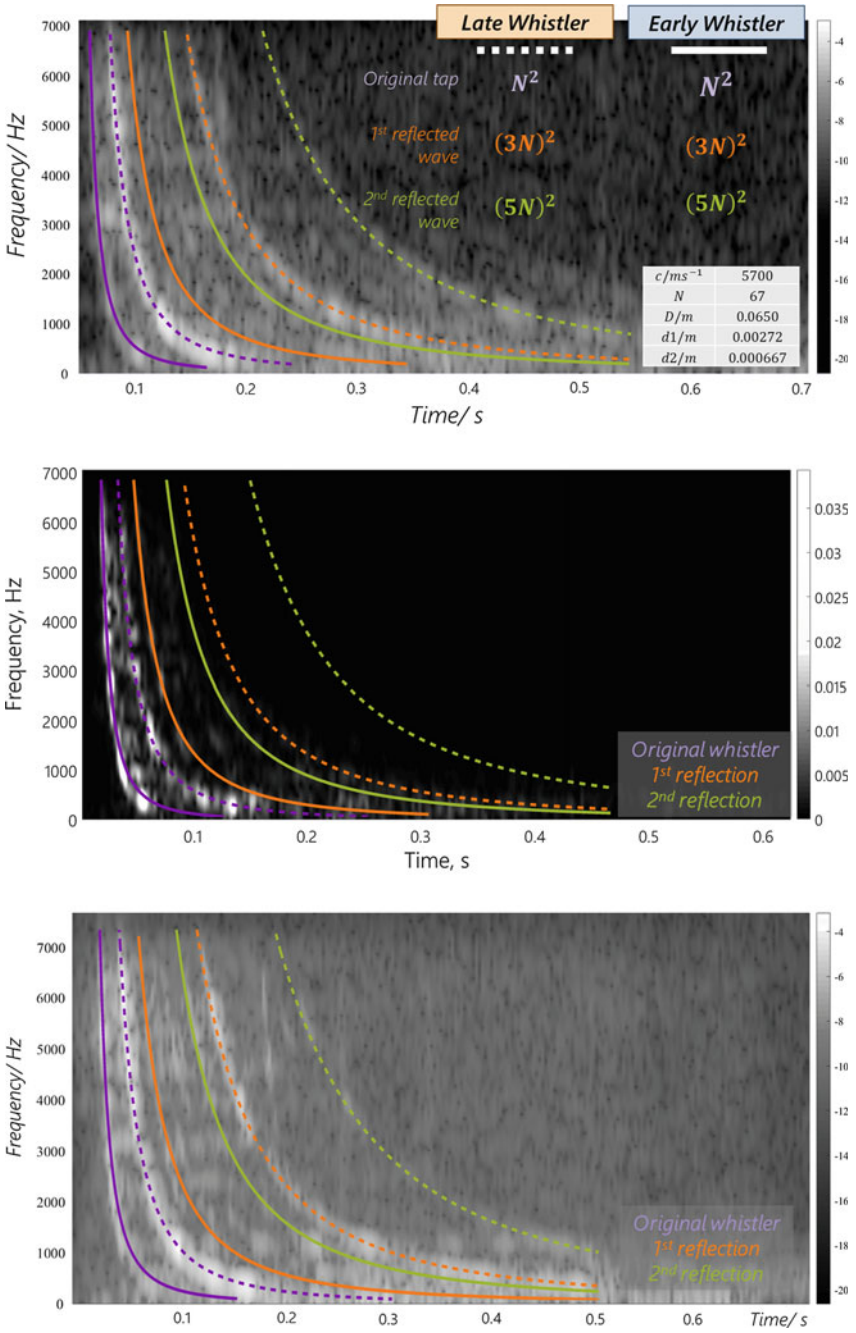

Fig. 9 Spectrograms of a 66-coil slinky (top), 57-coil slinky (middle) and 77-coil slinky (bottom). Reflected waves that arrive later and at lower intensity were also observed on the spectrogram and predicted, in addition to the original wave generated by the tap

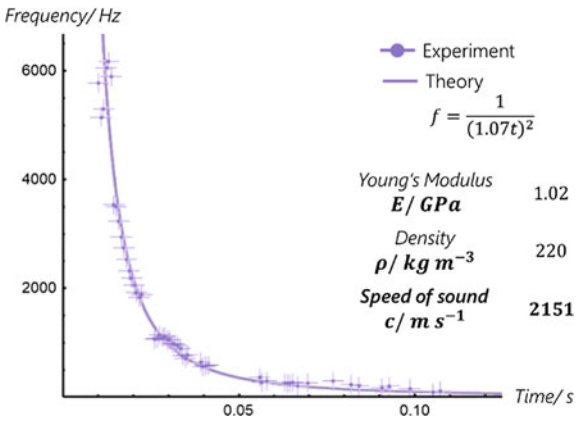

Fig. 10 Graph of frequency against time for *fast* flexural mode of excited 40-coil plastic slinky. Data corresponds well with theoretical curve

The small slinky shows an earlier and faster rate of frequency decrease as it is shorter than the large slinky (Fig. 8).

When coil length is increased, the whistler durations are longer, frequency decrease less rapid, and whistlers are further apart. The converse is observed for shorter coil lengths (Fig. 9).

3.5 Graph of Plastic Slinky (Fig. 10)

It can be seen that the dispersion theory presented is able to consistently give an accurate prediction when the material and coil dimensions are varied, showing a complete account of the frequency-time study of acoustic dispersion.

3.6 Spectrogram Comparison of Plastic Versus Metal (Fig. 11)

It is observed (Fig. 11) that metallic sounds have higher dominant frequencies because metal has a higher Young's modulus, so the restoring force when the slinky is excited would be greater for metal, thus sounds produced using a metal slinky are of a higher frequency and perceived to be brighter. Conversely, since plastic has a lower Young's modulus, sounds produced would have lower dominant frequencies, thus sounds produced using a plastic slinky are perceived to be duller.

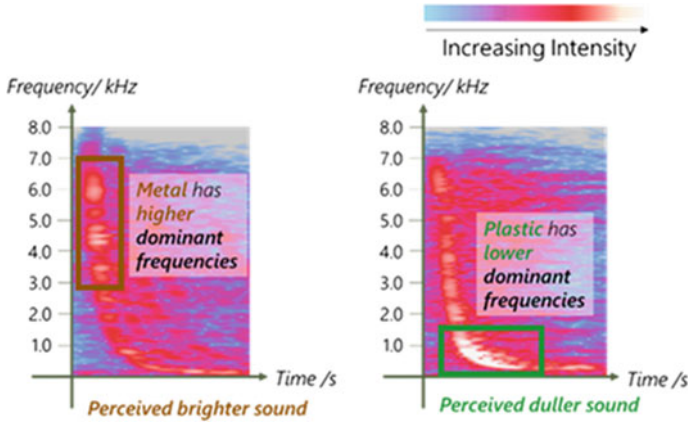

Fig. 11 Side-by-side comparisons of spectrograms of whistler sounds generated by metal (left) and plastic (right) slinkys

3.7 Further Insights (Figs. 12, and 13)

To investigate tension, frequency-time graphs (Fig. 12, next page) of a slack, stretched, and deformed slinky are overlaid. It is observed all 3 sounds agree with the theoretical prediction. Thus, tension does not affect the rate of frequency decrease. This is because a flexural wave travelling along a torsioned beam is simply a linear superposition of a torsioned beam and an untorsioned beam with flexural waves travelling along it. As such, deformation and wave propagation in the flexure mode remains uncharged by effects of torsion.

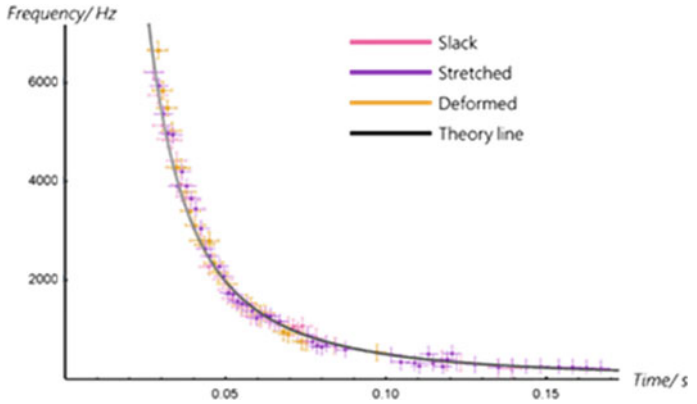

Fig. 12 Overlaid graphs of frequency against time for a slack, stretched and deformed slinky, showing that effects of tension are less relevant

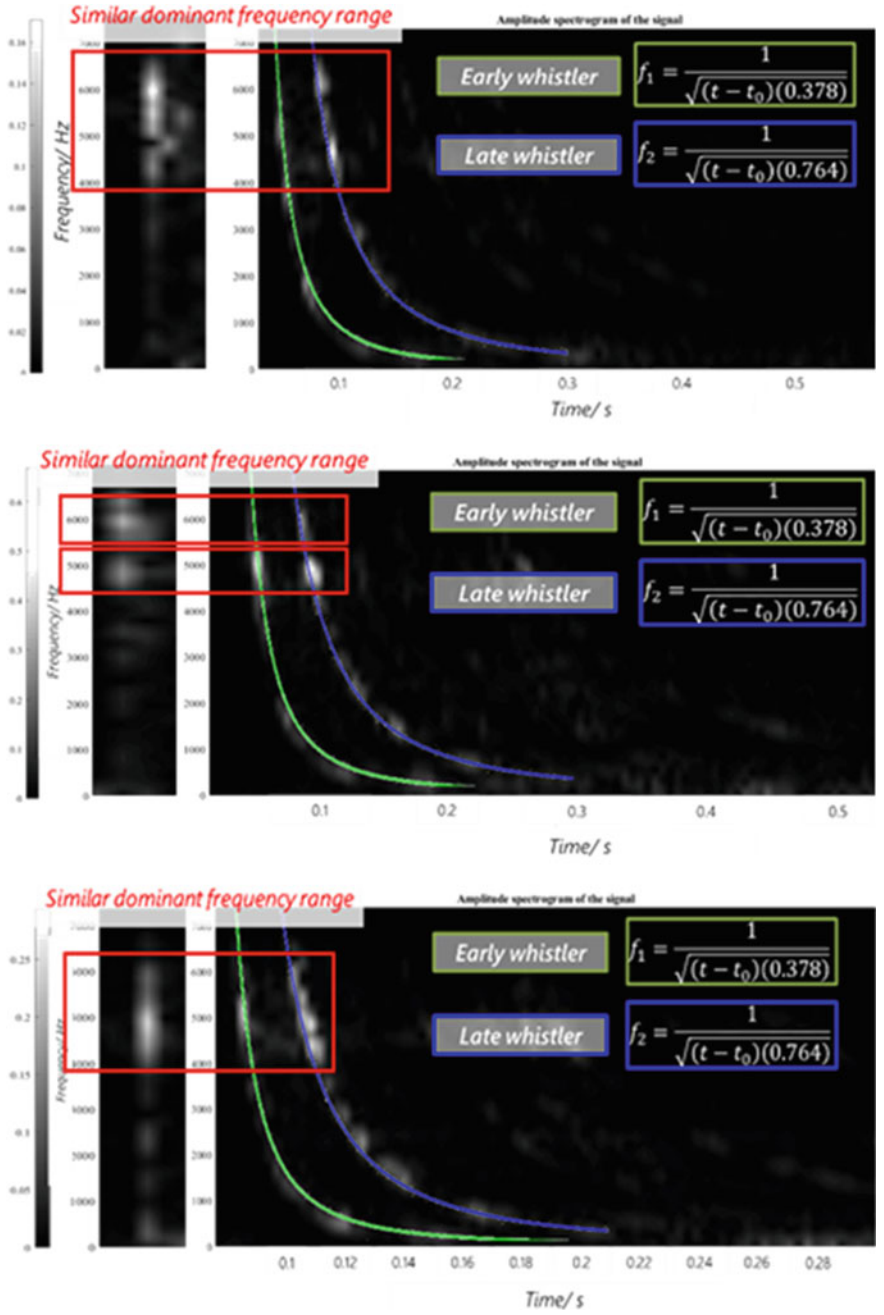

Fig. 13 Spectrograms of tap and corresponding whistler sounds by a metal rod (top), plastic pen (middle), and wooden pencil (bottom). Similar dominant frequency ranges for both the tap and whistler sounds are boxed in red

Finally, three different materials, metal rod, plastic pen and wooden pencil are used to tap a metal slinky (Fig. 13). Although the rate of dispersion and frequency decrease is not affected by the material used to tap the slinky, the initial dominant frequency of the excitation would appear more prominently in the whistler sound. For example, a wooden pencil tap produces a dominant frequency around 5000 Hz, which is observed in the whistler sound, which also has a dominant frequency around 5000 Hz.

4 Conclusion

A quantitative dispersion model using Euler–Bernoulli Beam theory predicted and explained both long and short dimensions/modes of wave propagation in the flexure mode—the excited long dimension produced waves that arrive earlier with a steeper frequency decrease, whereas the short dimension produced waves that arrive later with gentler frequency decrease. Young's modulus of slinkys made of different materials, steel and plastic was characterised (and a comparison was made between dominant frequencies of whistler sounds for both materials), and number of coils (length) and cross-sectional dimensions of slinky were also varied. Finally, tension was shown to have a negligible effect on the rate of frequency decrease, and it was shown that the dominant frequency of the tap would correspond to the dominant frequency of the whistler sound.

References

1. Crawford, F. S. (1987). Slinky whistlers. American Journal of Physics, 55(2), 130–134. https://doi.org/10.1119/1.15229
2. Hambric, S. (2006). Structural Acoustics Tutorial—Part 1: Vibrations in Structures. Acoustics Today,2(4). https://doi.org/10.1121/1.2961142
3. Parker, J & Henri, P & Bilbao, S & Abel, J. (2002). Modeling methods for the highly dispersive slinky spring: A novel musical toy.
4. Morin, D. (2010). Chapter 6: Dispersion.
5. Park, J. (2008). Identification of damage in beam structures using flexural wave propagation characteristics. Journal of Sound and Vibration, 318(4-5), 820–829. https://doi.org/10.1016/j.jsv.2008.05.008
6. Harris, F. J. (1978). On the use of windows for harmonic analysis with the discrete Fourier transform. Proceedings of the IEEE, 66(1), 51–83. https://doi.org/10.1109/proc.1978.10837

MicroRNA-Profiling Based Screening of Non-small-cell Lung Cancer in Plasma

Darren Wan-Teck Lim, Chee Keong Toh, Shevonne Chia, Shu Ying Nicole Tang, Yi Cheng, Kok Huei Seow, and Lihan Zhou

Abstract Current methods for screening and early diagnosis of lung cancer are limited to low-dose CT scans in high risk smokers, while other patients are typically diagnosed at later stages, leading to a higher mortality rate. Blood based biomarkers are needed to enrich this for at risk individuals, regardless of smoking status so as to detect early stage lung cancer. We studied potential biomarkers for early stage lung cancer using a microRNA (miRNA)-based panel. MiRNAs were isolated and quantified from the plasma of 67 patient samples (61 with lung cancer, 6 controls). 15 miRNAs were selected from a panel of 600 miRNAs based on previous work by the company MiRXES. These miRNAs were compared between patients with lung cancer and controls, as well as between different histological subtypes of lung cancer, stage and smoking history. Thus we evaluated their potential effectiveness as biomarkers for the screening of lung cancer. Specific miRNA levels were significantly different between lung cancer patients and controls: miR-618 ($p = 0.0249$) and miR-1290 ($p = 0.03192$). This was also true between different cancer types: miR-1290 ($p = 0.0110$), and between different smoking status: ($p = 0.00772$). 5 miRNAs (miR-618, miR-720 (V18), miR-1290, miR-214–3 and miR-28-5p) were identified as potentially suitable for a lung cancer screening panel, with the highest sensitivity and specificity (ROC AUC 0.915). Our panel of 5 miRNAs has the potential to be used as a non-invasive screening tool for lung cancer, with a reasonable degree of sensitivity and specificity. These results will have to be validated in further studies.

Keywords Non-small-cell lung cancer · miRNA · Early screening

D. W.-T. Lim · C. K. Toh
Department of Medical Oncology, National Cancer Centre of Singapore, Singapore, Singapore

S. Chia · S. Y. N. Tang · Y. Cheng
School of Mathematics and Science, NUS High, Singapore, Singapore
e-mail: h1710124@nushigh.edu.sg

K. H. Seow · L. Zhou (✉)
MiRXES Pte Ltd, Singapore, Singapore
e-mail: lihan_zhou@mirxes.com

H. Guo et al. (eds.), *IRC-SET 2020*,
https://doi.org/10.1007/978-981-15-9472-4_25

1 Introduction

Lung cancer is currently the leading cause of cancer-related mortality worldwide, having caused 1.8 million deaths in 2018 alone [1]. In Singapore, from 2011–2015, lung cancer has the highest mortality rate among all cancers in men (27.1%) and the second highest in women (16.6%), only exceeded by breast cancer (17.3%) [2]. There are two major subgroups of lung cancer: small-cell lung cancer (SCLC) and non-small-cell lung cancer (NSCLC). The majority of lung cancer cases are NSCLC, which can be further divided into various histological subtypes, the most common being adenocarcinomas and squamous cell carcinomas.

Lung cancer has a much lower mortality rate in its early stages, hence early detection is crucial. However, lung cancer largely becomes clinically evident only at advanced stages, thus the majority of lung cancers are diagnosed late [3]. The current process of diagnosing lung cancer in a patient involves low-dose computed tomography (LDCT) for screening and an invasive follow-up diagnostic procedure, typically a biopsy, to confirm the screening results. While LDCT is very sensitive, it has poor specificity, leading to a high chance of false positives.

In recent medical research, the use of biomarkers such as microRNAs (miRNAs) as a non-invasive tool for cancer screening and diagnosis has gained attention [4–6]. MiRNAs are small non-protein coding RNAs that inhibit gene expression, and their levels in body fluids (such as plasma and serum) have been shown to be different in some cancer patients compared to cancer-free patients. This makes them promising biomarkers for the early diagnosis and prognostication of cancer [4–7]. Therefore a miRNA blood test could potentially serve as an initial screening tool, prior to or in conjunction with the use of LDCT, to detect early stage lung cancer [8].

The primary aim of this study is to evaluate if a panel of miRNAs is able to differentiate between cancer and non-cancer patients (control). The secondary aims are to test if the levels of these miRNAs are different between i. smokers and non-smokers, ii. between subtypes of lung cancer, and iii. between early and late stage lung cancer.

2 Materials and Methods

2.1 Patients and Clinical Samples

Plasma samples used in this study were obtained from patients enrolled under the Lung Cancer Consortium Singapore (LCCS) study. This study was approved by the SingHealth Institutional Review Board (IRB) (2018/2963) with patients' written informed consent. Patient samples were classified based on their histological diagnosis (cancer type and stage) and patient interview record (smoking status).

Prior to analysis, samples were stored at − 80 °C. Of the 100 samples obtained, a total of 33 were excluded from this study. 19 of them were excluded from laboratory testing as they had a high sample age or degree of haemolysis. After laboratory testing, another 14 were excluded from statistical analysis due to various discrepancies occurring during experimentation, some of which were due to being stored differently in the plasma bank. In total, 67 samples were eventually used in analysis: 61 from cancer patients and 6 from controls.

2.2 MiRNA Selection

15 miRNAs were selected from a 600-miRNA panel based on previous work done by MiRXES involving 1700 patients of Asian or Caucasian ethnicity over the timeframe of 2014–2019 [9]. MiRNAs selected from this panel were previously shown to have a relatively small difference in Ct value across various factors such as histological subtype and stage of cancer [10]

2.3 MiRNA Extraction and Quantification

All the RNA, containing miRNAs, was extracted from 200 µl of each plasma sample using the Maxwell® RSC miRNA Plasma and Serum Kit (Catalogue number: AS1680, Promega, USA) on Maxwell® RSC 48 Instrument (Catalogue number: AS8500, Promega, USA) following the manufacturer's instructions.

Sixteen miRNAs, including candidate biomarkers and reference genes, were selected based on literature and in-house research. The expression levels of the 16 miRNAs in each sample were measured using miRNA-specific RT-qPCR assays (MiRXES, Singapore) according to manufacturer's instructions on Quantstudio 5 384-well Real-Time PCR System (Life Technologies, Singapore). Upon RT-qPCR assay completion, Ct values were determined using Quantstudio RUO software with automatic baseline setting and a 0.4 threshold. Candidate miRNA expression Ct values were normalized using an endogenous reference miRNA let-7a.

3 Results

The demographic profile of the 67 samples is summarized in Table 1. 56 out of 67 patient samples (83.6%) were from Chinese patients, approximately in line with the race distribution in Singapore where a majority (76.1%) of the population is Chinese [11].

Table 1 Sample demographics

Demographic Information		Normal (% of total controls)	Cancer (% of total cancer)		
			All	Adeno	Squamous
Age at collection	Median (year)	68	65	64	65
	Range	46–74	39– 90	39– 90	53–75
Gender	Male	3 (50.0%)	40 (65.6%)	25 (41.0%)	15 (24.6%)
	Female	3 (50.0%)	21 (34.4%)	16 (26.2%)	5 (8.2%)
Smoking History	Smoker	2 (33.3%)	18 (29.5%)	9 (14.8%)	9 (14.8%)
	Ex-smoker	3 (50.0%)	12 (19.7%)	8 (13.1%)	4 (6.6%)
	Non-smoker	1 (16.7%)	31 (50.8%)	24 (39.3%)	7 (11.5%)
Cancer Stage	Stage I		32 (52.5%)	26 (42.6%)	6 (9.8%)
	Stage II		11 (18.0%)	6 (9.8%)	5 (8.2%)
	Stage III		18 (29.5%)	9 (14.8%)	9 9 (14.8%)

3.1 Primary Outcome: Cancer Versus Non-Cancer

Normalized Ct values of each miRNA (total 15 miRNAs) were compared and depicted using box plots (Fig. 1) according to whether the samples were from cancer or non-cancer patients. The box plots show the distribution and median of relative concentrations of the miRNAs in the samples (Ct). The individual p-values of the 5 miRNAs used in the panel (miR-618, miR-720 (V18), miR-1290, miR-214–3, miR-28-5p) are 0.025, 0.657, 0.032, 0.074 and 0.392 respectively. All these miRNAs were upregulated in cancer patients with the exception of miR-28-5p, which was downregulated.

Based on these Ct values, the area under the ROC (Receiver Operating Characteristics) curve (AUC) (Fig. 2) was calculated using MATLAB. Multi-miRNA panels were tested and optimized using sequential forward selection algorithms to determine which miRNAs would be the most suitable to put in various panels. The AUC values obtained range from 0.5 to 1.0, with a higher value signifying greater accuracy of predictions. The Wilcoxon Rank Sum test was performed using Prism 8.2.0, where a p-value would be obtained. A p-value < 0.05 was considered statistically significant. The Wilcoxon Rank Sum test was selected over the Student's t-test due to the non-parametric nature of the data distribution, as well as the relatively small sample size.

All bar graphs and box plots were obtained using Excel 2016, in which the values for the bar graphs were obtained from the previous AUC values and the box plots plotted from the normalized Ct values.

The AUC increased from 0.773 using miRNA-618 alone to 0.842 using 2 miRNAs (miR-618 and miR-720 (V18) to 0.899 using 3 miRNAs (miR-618, miR-720 (V18) and miR-1290) to 0.910 when using 4 miRNAs (miR-618, miR-720 (V18), miR-1290 and miR-214-3p) and 0.915 when using a panel of 5 miRNAs. (miR-618, miR-720

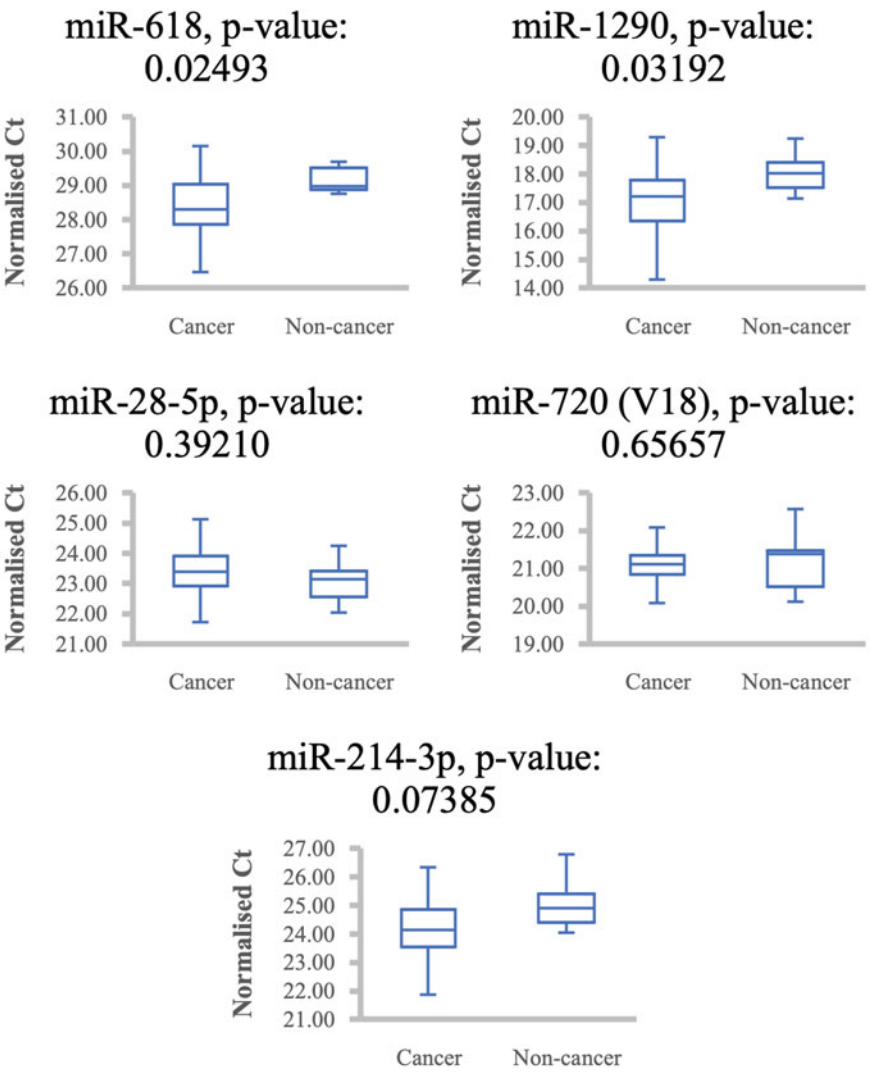

Fig. 1 Boxplots of Values of selected miRNAs

(V18), miR-1290, miR-214–3 and miR-28-5p) We limited the panel of miRNAs to 5 to prevent over-fitting.

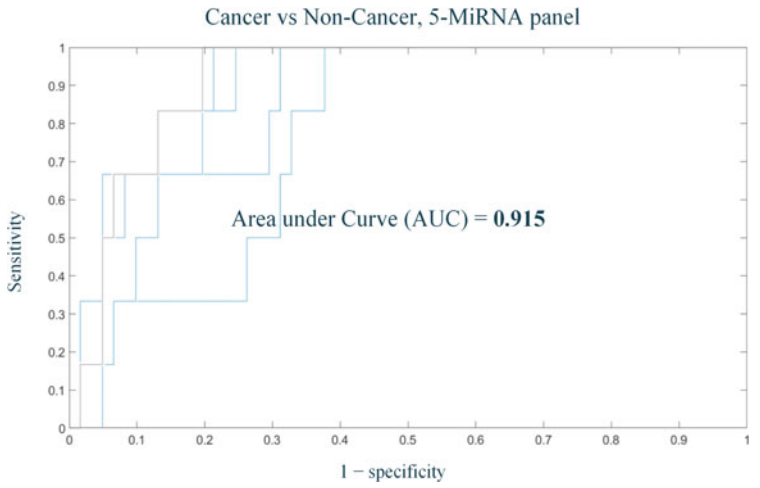

Fig. 2 ROC curves for optimal panels containing 1 to 5 miRNAs

3.2 Secondary Outcomes: Evaluation of MiRNA Levels in Patients Across Lung Cancer Histology, Stage and Smoking Status

The normalized Ct values of each miRNA were compared between i. patients diagnosed with adenocarcinoma and squamous cell carcinoma, ii. current/ex-smokers and non-smokers, and iii. those who had Stage I and Stage III cancer, and depicted using boxplots (Appendix). The AUC was calculated for each ROC curve comparing the various cohorts (Table 2). Bar graphs demonstrating the increasing AUC with increasing number of miRNAs can be found in the appendices. The best AUC values obtained for these cohorts are much lower than the cancer vs non-cancer cohort as the 15 miRNAs selected for testing were selected specifically for optimal accuracy of differentiation between cancer and non-cancer samples, while maintaining similar expression levels regardless of these other factors.

Table 2 AUC for distinction across various factors (identity of mirnas)

Comparison	miRNA	AUC
Cancer versus Non-Cancer	miR-618, miR-720 (V18), miR-1290, miR-214-3p, miR-28-5p	0.915
Adenocarcinoma versus Squamous cell carcinoma	miR-1290, miR-618, miR-20b-5p	0.735
Current and Ex-Smokers versus Non-Smokers	miR-1290, miR-1-3p, miR-618, miR-20b-5p, miR-143-3p	0.845
Stage 1 versus Stage 3	miR-28-5p, miR-451a, miR-144-3p	0.787

4 Discussion

4.1 Key Findings

Our study's key finding is that it is possible to differentiate between cancer and non-cancer patients by using a selected panel of 5 miRNAs. We determined the AUC values of the ROC of various miRNAs present in the plasma of cancer patients and controls and identified a panel of 5 miRNAs (miR-618, miR-720 (V18), miR-1290, miR-214–3 and miR-28-5p, AUC: 0.915) most suited for differentiating between cancer patients and non-cancer patients with a relatively high degree of certainty. This renders the miRNA panel potentially suitable as a lung cancer screening tool, which may be used in conjunction with the current standard methods.

The 5 miRNA panel does not effectively distinguish variations with factors such as cancer type, stage and smoking status, making it suitable for lung cancer screening for the general population, regardless of these factors. These findings align with ongoing research by MiRXES [9].

4.2 Roles of Identified MiRNAs

The roles of MiRNAs which differ in cancer and non-cancer patients are interesting and yet to be fully elucidated. This may be due to the complex roles of miRNA in the body and mechanistic differences in the pathology of various types of cancers.

MiR-618 was significantly upregulated in lung cancer patients ($p = 0.025$). There is not much literature on this particular microRNA, but some studies have found that miR-618 was downregulated in prostate cancer [12] and gastric cancer [13] cells, identifying that miRNA has functions in inhibiting cancer migration and invasion for these variants. It is possible that this discrepancy in results is due to a different mechanism in lung cancer which results in upregulation instead, or caused by experimental limitations.

MiR-1290 also had particularly interesting results: we found that it was significantly upregulated in lung cancer patients ($p = 0.031$), in current / ex-smokers, and in squamous cell carcinoma patients. This suggests that MiR-1290 plays a complex role in lung cancer and there are potential interactions between the type of cancer and smoking status. Prior literature has shown that the upregulation of this miRNA contributes to the proliferation of non-small-cell lung cancer and reducing its expression could suppress tumour growth [14]. In a study involving colon cancer cells, it was discovered that the upregulation of this miRNA impairs cytokinesis [15] which could increase the risk of cancer. As such, the high correlation between this miRNA and the occurrence of cancer concurs with findings from other literature. Another study [16] investigating this miRNA has found that 'miR-1290 expression levels were increased significantly in NSCLC tissues compared with non-tumour adjacent normal tissues, and higher miR-1290 expression levels were positively correlated

with high tumour stage ($p = 0.004$)', but has discovered no statistically significant correlation with smoking history ($p = 0.169$) or histology type ($p = 0.808$). This conflicts with our findings from this study.

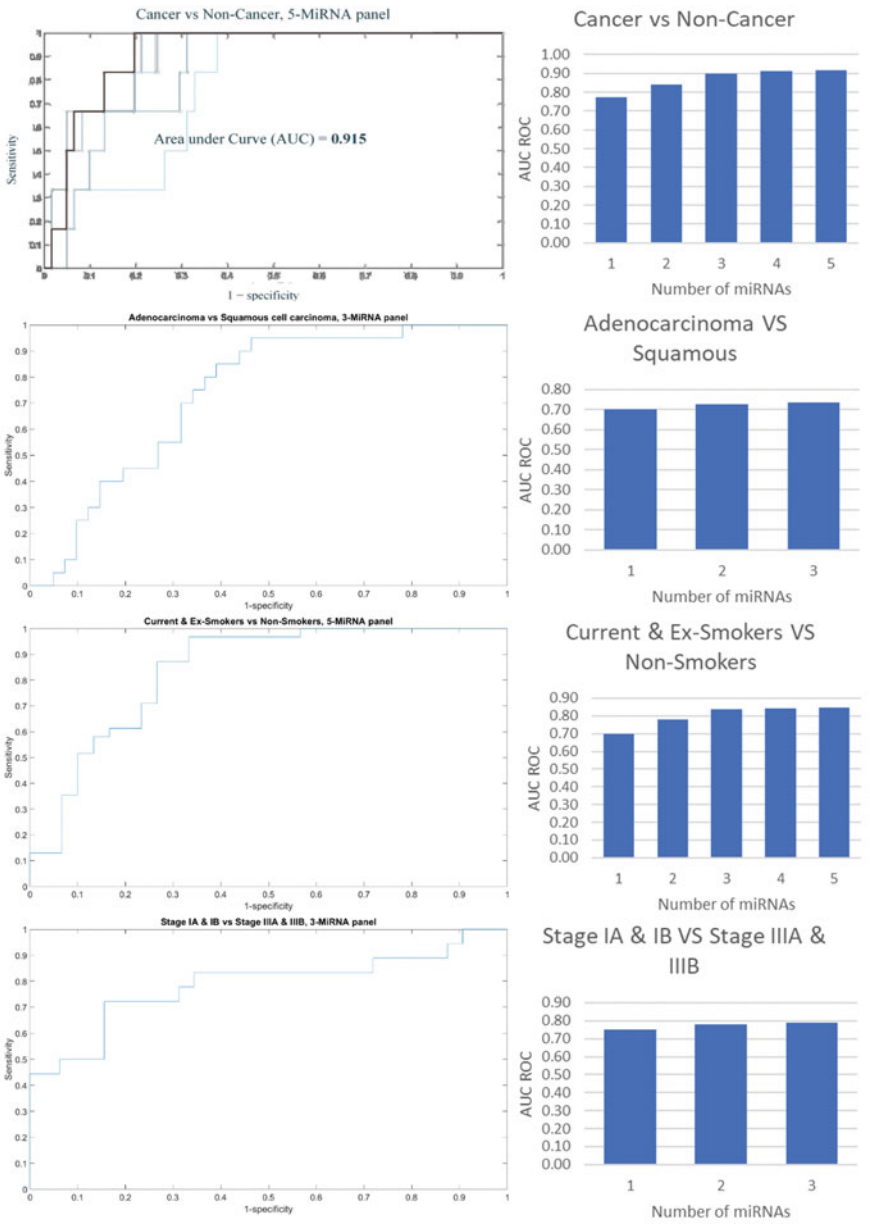

MiR-214-3p was also upregulated in cancer patients. ($p = 0.074$).

MiR-28-5p was downregulated in cancer patients ($p = 0.3921$); little literature is available on this regarding NSCLC, but a study [17] involving colorectal cancer cells concurs with our result, also showing that its overexpression promotes tumour metastasis in mice.

MiR-720 (V18) showed no statistically significant difference in expression levels between lung cancer and non-cancer patients. Yet used in conjunction with the above miRNAs, it improves the AUC for the screening tool. While there is little literature on it, a breast cancer study [18] found that it inhibits tumour formation and is generally downregulated in cases of breast cancer.

4.3 Limitations and Future Work

Our samples were obtained from local patients, each of whom had a definite histological diagnosis (with or without lung cancer): thus, we believe that the samples were sufficiently representative of the disease in the local population for an experiment of this scale. However our study is limited by a relatively small sample size, with only 6 control samples, making it difficult to achieve a high degree of confidence. This may have resulted in some limitation in identifying trends: although the AUC of ROC of our MiRNA panel is relatively high at 0.915, other studies have suggested that a typical AUC value for a panel of 4 or more miRNAs is 0.97 [19]. It is possible that we may have also missed out on some potentially important interactions. Most of the samples were obtained from males and there was a high correlation between gender and smoking status (with only 2 female smokers and 2 female ex-smokers), thus we were not able to fully explore the relationship between gender, smoking status and miRNA levels in lung cancer patients versus controls. However, an ongoing study by MiRXES has shown that gender has little impact on the degree of miRNA expression for the miRNAs involved in our study [9].

Based on previous work, we only investigated 15 out of a panel of 600 miRNAs to find a suitable panel of miRNAs as a tool for the screening of lung cancer. It is possible that there may be other more suitable biomarkers for the screening of lung cancers which were not investigated in this study. Thus, in order to refine our screening panel to ensure greater diagnostic accuracy, we will require further research on a larger sample size (possibly using other biomarkers) in both laboratory and clinical settings.

In conclusion, we have identified a panel of 5 miRNAs which are differentially expressed in lung cancer and non-lung cancer patients. This panel has the potential to be used as a non-invasive early screening tool with a reasonable degree of sensitivity and specificity. Further research involving a larger number of patient samples both in the laboratory and clinical setting and more miRNA assays is needed to refine the panel to obtain the optimal screening tool for lung cancer.

Acknowledgements We greatly appreciate and acknowledge the efforts of our mentors Dr Darren Lim of NCCS, Dr Lihan Zhou of MiRXES, and Dr Toh Chee Keong of NCCS in guiding and supporting us. We would like to thank Mr Terence and Ms Su Chin Tham from NCC for their

training and support, especially in lab work. From MiRXES, we would like to thank Mr Kok Huei for helping us with statistical analysis as well as other staff in MiRXES and NCC who guided us throughout our training and lab work. Last but not least, we would like to thank the teachers in NUS High School of Mathematics and Science as well as the staff at MOE for making this all possible.

Appendix

ROC Curves for Other Panels

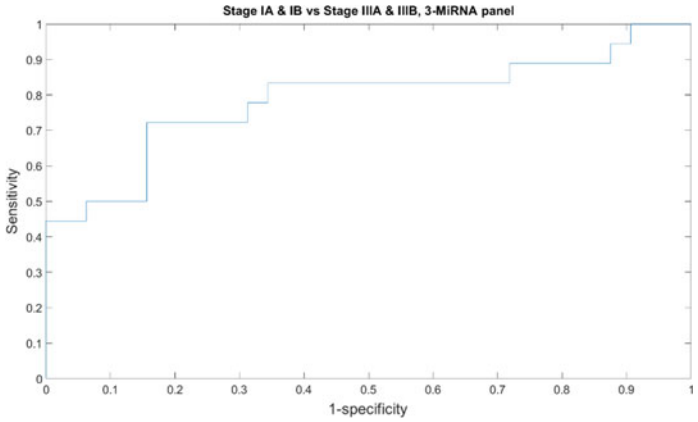

AUC Under ROC Curves for Panels Containing Different Numbers of MiRNAs

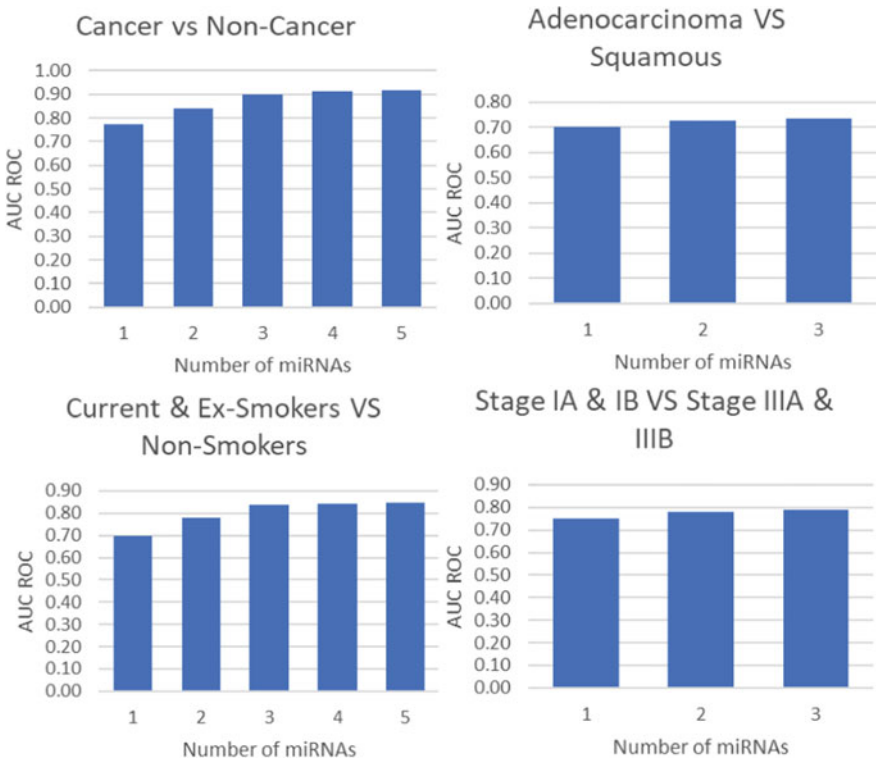

References

1. "Latest global cancer data: Cancer burden rises to 18.1 million new cases and 9.6 million cancer deaths in 2018.", Who.int, September 2018. [Online]. Available: https://www.who.int/cancer/PRGlobocanFinal.pdf.
2. "Singapore Cancer Registry Annual Registry Report 201", National Registry of Diseases Office (NRDO), June 2017. [Online]. Available: https://www.nrdo.gov.sg/docs/librariesprovider3/Publications-Cancer/cancer-registry-annual-report-2015_web.pdf?sfvrsn=10.
3. A. Jemal et al., "Cancer Statistics, 2008", CA: A Cancer Journal for Clinicians, vol. 58, no. 2, pp. 71–96, 2008. Available: https://doi.org/10.3322/ca.2007.0010.
4. P. Hennessey et al., "Serum microRNA Biomarkers for Detection of Non-Small Cell Lung Cancer", PLoS ONE, vol. 7, no. 2, p. e32307, 2012. Available: https://doi.org/10.1371/journal.pone.0032307.

5. D. Zheng et al., “Plasma microRNAs as novel biomarkers for early detection of lung cancer”, International journal of clinical and experimental pathology, vol. 6, no. 4, pp. 576-586, 2011
6. J. Shen et al., “Plasma microRNAs as potential biomarkers for non-small-cell lung cancer”, Laboratory Investigation, vol. 91, no. 4, pp. 579–587, 2010. Available: https://doi.org/10.1038/labinvest.2010.194.
7. Y. Zhang, Q. Yang and S. Wang, Cancer Chemother Pharmacol, vol. 74, p. 1105, 2014
8. G. Sozzi et al., “Clinical Utility of a Plasma-Based miRNA Signature Classifier Within Computed Tomography Lung Cancer Screening: A Correlative MILD Trial Study”, Journal of Clinical Oncology, vol. 32, no. 8, pp. 768–773, 2014. Available: https://doi.org/10.1200/jco.2013.50.4357.
9. Zhou et al., “Systematic development and multicohort validation of a serum miRNA biomarker panel for detection of early stage non-small cell lung cancer, accepted abstract”, in World Conference on Lung Cancer, IASLC, 2019.
10. L. Ying et al., “Abstract 4408: Development and validation of a serum miRNA biomarker panel for the detection of early stage lung cancer”, Molecular and Cellular Biology / Genetics, 2018. Available: https://doi.org/10.1158/1538-7445.am2018-4408.
11. “Population in Brief”, September 2018. [Online]. Available: https://github.com/isomerpages/isomerpages-stratgroup/raw/master/images/PublicationImages/population-in-brief-2018.pdf.
12. X. Song, Y. Tang, X. Lei, S. Zhao and Z. Wu, “miR-618 Inhibits Prostate Cancer Migration and Invasion by Targeting FOXP2”, Journal of Cancer, vol. 8, no. 13, pp. 2501–2510, 2017. Available: https://doi.org/10.7150/jca.17407.
13. Feng, X., Ji, D., Liang, C. and Fan, S., 2019. Does miR-618 rs2682818 variant affect cancer susceptibility? Evidence from 10 case–control studies. Bioscience Reports, 39(8).
14. J. Jin, Y. Liu, J. Si, R. Ni and J. Wang, “Overexpression of miR-1290 contributes to cell proliferation and invasion of non small cell lung cancer by targeting interferon regulatory factor 2”, The International Journal of Biochemistry & Cell Biology, vol. 95, pp. 113–120, 2018. Available: https://doi.org/10.1016/j.biocel.2017.12.017.
15. J. Wu et al., “Up-regulation of microRNA-1290 impairs cytokinesis and affects the reprogramming of colon cancer cells”, Cancer Letters, vol. 329, no. 2, pp. 155–163, 2013. Available: https://doi.org/10.1016/j.canlet.2012.10.038.
16. Mo et al., 2015. miR-1290 is a potential prognostic biomarker in non-small cell lung cancer. Journal of thoracic disease, 9(7), pp.1570-1579
17. Almeida, M., Nicoloso, M., Zeng, L., Ivan, C., Spizzo, R., Gafà, R., Xiao, L., Zhang, X., Vannini, I., Fanini, F., Fabbri, M., Lanza, G., Reis, R., Zweidler–McKay, P. and Calin, G., 2012. Strand-Specific miR-28-5p and miR-28-3p Have Distinct Effects in Colorectal Cancer Cells. Gastroenterology, 142(4), pp.886-896.e9
18. Li, L., Zhang, C., Liu, L., Yi, C., Lu, S., Zhou, X., Zhang, Z., Peng, Y., Yang, Y. and Yun, J., 2013. miR-720 inhibits tumor invasion and migration in breast cancer by targeting TWIST1. Carcinogenesis, 35(2), pp.469-478
19. Wang, Y., Guan, J. and Wang, Y., 2019. Could microRNA be used as a diagnostic tool for lung cancer?. Journal of Cellular Biochemistry, 120(11), pp.18937-18945
20. Yu, H., Guan, Z., Cuk, K., Brenner, H. and Zhang, Y., 2018. Circulating microRNA biomarkers for lung cancer detection in Western populations. Cancer Medicine, 7(10), pp.4849-4862

Low-Cost Draw-On Electronics: Investigation of Pen-Substrate Interaction

Saravanan Deepika and Soh Zhi Rong

Abstract Conductive pens are a cheaper alternative to expensive printing methods that offer conformal printing and helps to cut down development costs of electronics especially during prototyping. This study aims to investigate how different designs of pen affects the electrical conductivity of conductive traces drawn on various substrates and identify the most ideal design for a conductive pen. Characterisation of 4 different commercial conductive pens (carbon pressure pen, silver micro-tip pen, ballpoint pen and pressure pen) was conducted. Conductive traces were drawn on bandages, nitrile gloves, printing paper and polyethylene terephthalate film. It was observed that the width of the traces were affected by the design of the pen tip. Pens which discharge ink when the barrel of the pen is squeezed produced thicker lines. Scanning electron microscope pictures of the line samples were taken and it was found that the silver and carbon pressure pens produced conductive traces of better quality as compared to those drawn with the silver micro-tip pen and silver ballpoint pen. Cyclic folding was done on the conductive traces drawn on paper. Most of the carbon line samples underwent 25 folds before cracking while all of the silver underwent 20 folds before cracking. It was concluded that the design of the pressure pens were the most ideal. As proof of concept, 2 light emitting diode bulbs on a paper origami were lit up with a circuit fabricated with the silver pressure pen and a heater with its components fabricated using the silver and carbon pressure pens was tested with the use of an electric generator.

Keywords Conductive pen · Low-cost electronics · Draw-on electronics

S. Deepika · S. Z. Rong (✉)
National Junior College, Singapore, Singapore
e-mail: sohzhirongwut@gmail.com

S. Deepika
e-mail: sdeepika1610@gmail.com

H. Guo et al. (eds.), *IRC-SET 2020*,
https://doi.org/10.1007/978-981-15-9472-4_26

1 Introduction

In recent years, foldable electronics have developed new characteristics like low manufacturing cost, disposable and wearable style, environmentally sustainable production methods and lower energy consumption [1–3]. Various printing techniques have been developed to fabricate flexible electronics such as, gravure printing [4], flexo printing[5], offset printing [6], inkjet printing [7] and screen printing [8]. Though the new technology provides a potentially low-cost alternative for flexible electronics, many problems still exist, for example, some pollution and waste still can't be avoided during screen printing and printer setups are also quite expensive[9]. The introduction of conductive pens is a notable solution. Conductive pen provides one with circuit design freedom, can draw on a wide variety of surfaces and is a notable cheaper alternative to expensive printing methods that offer conformal printing.

Ali et al. (2015) [10] fabricated a printed circuit board (PCB) with the use of conductive silver pens. It was reported that after 10,000 cycles of bending printed silver conductive lines on the PCB, a 1.8% increase in the base resistance was observed. Following the bending on the printed silver conductive lines, no test was conducted to find out if the PCB was still able to allow the liquid crystal display (LCD) to function. Liu et al. [10, 11] also studied the effects of cyclic folding on AgNW-GO-Ink electrodes and tested its effect on the conductivity of the AgNW-GO-Ink electrodes. Scanning electron microscope (SEM) images showed that after being subjected to 1 folding cycle, nano-fractures were formed on the formed on the folded AgNW-GO-Ink electrode and these fractures remained fairly stable in the following 1000 folding–unfolding cycles, thus only introduced a very slight decline to the conductivity of the electrode was observed.

Electronics such as strain sensors for home healthcare [13], radio frequency identification (RFID) tags[14] have been fabricated using the conductive pen. showing the versatility of direct writing and potential in helping to further develop low cost electronics. A crucial component of developing them to be able to function as well as it's expensive counterparts and is further research into pen-substrate interaction.

In this study, commercial silver and carbon conductive pens loaded with silver and carbon conductive ink respectively were used to fabricate conductive circuits on various substrates such as PET films, nitrile gloves and commercial bandages as well as 3D printed substrates. The conductivity properties, mechanical flexibility and adhesion characterization of the circuit were also studied. Additionally, a paper-based electronic were fabricated using a conductive pen.

It is hypothesised that the silver and carbon pressure pens will perform better than the silver micro-tip pen and silver ballpoint pen as the barrel is easy to squeeze and the pen tip has a valve, allowing for easy discharge of ink.

2 Aims and Objectives

This study aims to investigate how different designs of pen affects the electrical conductivity of conductive traces drawn on various substrates and identify the most ideal design for a conductive pen.

3 Methodology/Materials

3.1 Materials and Sample Preparation

Commercial conductive silver and carbon pressure pens, specifically the MG Chemical 842AR-P Silver Conductive Pen (silver pressure pen), typical trace width of 1.00 mm and the MG Chemical 838AR-P Carbon Conductive Pen (carbon pressure pen), typical trace width of 1.00 mm. The valve tip of these pens opens when pressed against the surface, and the flow is controlled by squeezing the barrel. Commercial conductive silver pens were also obtained from CircuitScribe and Chemtronics, specifically the CircuitScribe Silver Conductive Ink Pen (silver ballpoint pen) and the Chemtronics Silver Conductive Adhesive Paint 7 g Pen (silver micro-tip pen). Smith & Nephew Opsite Flexifix bandages, SLG powder-free nitrile examination gloves and PET films were the substrates used. The flimsy nature of the bandages required it to be first pasted on a piece of masking tape for the line sample to be drawn. The sticky side of another piece of masking tape was then pasted onto the sticky side of the piece of masking tape with the bandage on it. A small rectangle was cut out from a nitrile glove. The nitrile glove was then held down with the fingers of one person while the line samples were being drawn. The carbon and silver line samples of varying line passes were drawn on the bandages, nitrile glove and PET film with the aforementioned conductive pens. All four pens were used to draw a line sample with one line pass on the bandage and on the PET film. Carbon and silver line samples were drawn on 10 3D printed substrates. The 3D printed substrates were rectangular blocks which were printed at varying degrees of 0°, 30°, 45°, 60° and 90° from the horizontal. Carbon line samples of 3 line passes were drawn on each of the 5 boards with varying degrees from the horizontal. The same procedure was done with the silver line passes. Two pieces of A6 white printing paper was folded into half and 5 line samples with one line pass were drawn on each one, one using the carbon pressure pen and the other using the silver pressure pen. All line samples were then dried for 10 min.

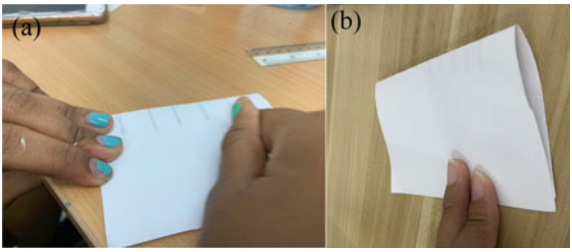

Fig. 1 **a** First folding method, **b** Second folding method

3.2 Instrumentation

The width, resistance and thickness of the line samples drawn on the bandage, nitrile glove and PET film. The width was tested with the use of an optical microscope. 5 measurements from different parts of each line were taken and the average width of the lines were then calculated. Using a Keithley parametric analyser, the resistance of the samples was measured. A laser microscope was used to measure the thickness of the sample. The circuits were hand drawn using commercial conductive pressure pens, causing the line samples to be subjected to random error. To reduce the random error, multiple measurements were taken for each line.

The width, resistance and surface roughness of the line samples on the 3D printed substrates were recorded. An optical microscope was used to test the width. The process of testing the resistance was done using a Keithley parametric analyser and the surface roughness of the 3D printed substrate was recorded using a Keyence focal microscope. The Sa (arithmetical mean height) of the various 3D substrates were recorded. The two pieces of A6 papers were folded 5 times. The Keithley parametric analyser was then used to measure the resistance of all 5 line samples. Two folding methods were used. The first involved compressing the crease of the sample and the second method involved folding the edge of the samples, until they touched each other. Figure 1 displays digital images of the two folding methods. This process was repeated until the line samples were no longer conductive due to cracks which would eventually form at the site of folding.

4 Results and Discussion

4.1 Width of the Line Samples

The width of the line samples were tested using an optical microscope. As seen in Fig. 2, the average width of the line samples drawn by the silver ballpoint pen are shortest at 502.75 μm on the bandage and 693.75 μm for the PET film. For both samples, the widest line samples were those of the carbon pressure pen. The error bar for the readings is the standard deviation.

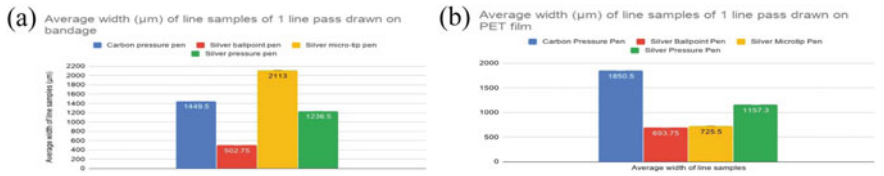

Fig. 2 Average width (μm) of line samples of 1-line pass drawn on the bandage **a** and PET film **b** with 4 different types of conductive pen—carbon pressure pen, silver ballpoint pen, silver microtip pen and silver pressure pen

The silver ballpoint pen had the thinnest pen tip, which thus resulted in lesser surface contact area between the pen tip and the substrates (bandage and PET film). The size of the silver ballpoint pen tip directly affects the width of the lines drawn by the pen, as ink flows based on surface area contact. Therefore the average width of the line samples on the two different substrates did not experience a sharp change.

4.2 Quality of Line Drawn

A SEM was used to observe the quality of the line samples. The line samples used were those of one line pass on the PET film. As seem in Fig. 3, cracks on the line sample were abundant on all the line samples drawn using the 4 different conductive pens.

The design of the pen tip had an effect on the severity of the cracks. Line samples drawn by the carbon pressure pen has the least amount of cracks, followed closely by those drawn with the silver pressure pen. The design of the two pens were similar, and both produced sufficient amount of ink to cover much of the perimeter of the line. The carbon pressure pen produced more ink as compared to its silver counterpart even with the same amount of pressure applied, justifying the slightly lesser amount of cracking observed on the line samples produced by the carbon pressure pen.

Extensive cracking was found on the line.

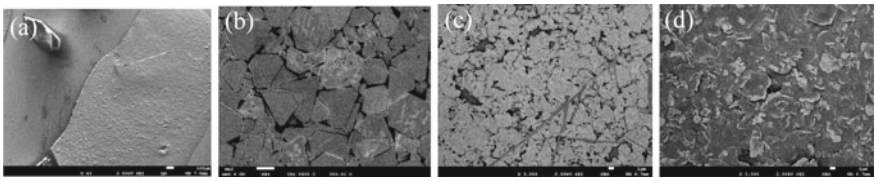

Fig. 3 SEM image of the cracks on a line sample drawn on PET film using the **a** carbon pressure pen, **b** silver ballpoint pen, **c** silver micro-tip and **d** silver pressure pen

samples drawn with the silver micro-tip pen and the silver ballpoint pen. Both pens produced lesser amount of ink as compared to the carbon and silver pressure pens and the lack of ink in the perimeter of the line resulted in many cracks formed.

The quality of the line included the production of homogenous lines. Production of homogenous lines was found to be rather challenging with the use of the silver micro-tip and ballpoint pen. The silver micro-tip pen had a small cylinder in the centre of the pen tip which resulted in the production of heterogeneous lines. The ink from the silver microtip pen dried almost immediately after it was squeezed onto the polyimide film. The friction between the cylindrical structure in the centre of the pen tip and the dried conductive ink caused a hole to form down the middle of the line. As for the silver ballpoint pen, the lines produced were thinner than those produced by 3 other conductive pens and were heterogeneous. This was a consequence of the lack of ink discharged when drawing the line. Homogeneous lines were easily produced with the use of the carbon and silver pressure pen as conductive inks loaded in the both pens dried slower compared to those of the silver micro-tip and ballpoint pen, allowing the small cylinder in the centre of the pens to pass through liquid conductive ink on the paper.

With the understanding that both the pressure pens work decently well on PET film (able to produce homogenous lines with little cracks) while the silver micro-tip pen and ballpoint pen work disappointingly on PET film (challenging to produce homogenous lines and heterogenous lines produced possess extensive cracking), it can be concluded that the carbon and silver pressure pens were suitable for use on PET film and the silver micro-tip and ballpoint pen were unsuitable.

4.3 Foldability of the Silver and Carbon Conductive Ink Electrodes on Paper

Photo paper as a flexible substrate is newly explored to produce flexible patterns. This is because photo paper has a set of advantages over conventional flexible substrate [15]. It was found that the substrate (A6 printing paper) was slightly conductive, thus the lines were considered non-conductive when the resistance for the was above 19.

When subjected to the first method of folding both the silver and carbon line samples were found to have become non-conductive after 10 folds. As seen in Fig. 4, both line samples showed poor foldability. Most of the carbon line samples underwent 25 folds before cracking while all of the silver underwent 20 folds before cracking. This shows that both the silver and carbon conductive ink electrodes have an equally poor foldability on paper as the difference is not substantial enough to be significant.

It is believed that the poor foldability of the silver and carbon conductive ink electrodes can be attributed to the components of the conductive ink - acrylic lacquer pigmented with highly conductive silver flakes. Acrylic lacquer is known to be susceptible to cracks with its most common applications include being used as coating for experimental samples which undergo cracking. This property of acrylic lacquer

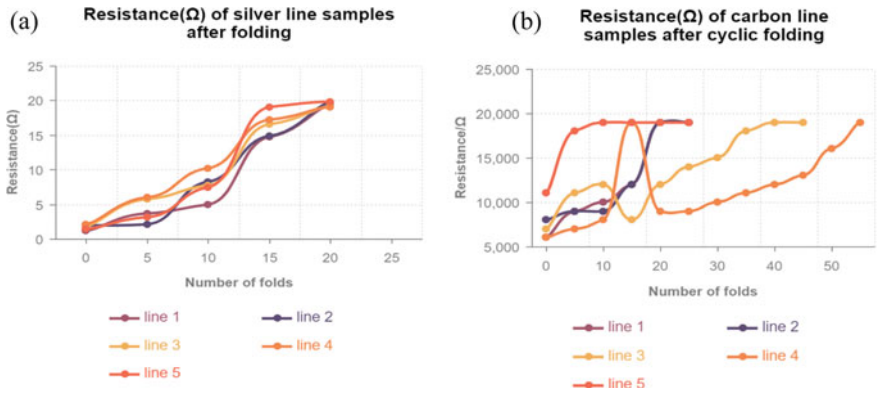

Fig. 4 Graphs showing the average resistance (Ω) of the line samples drawn using the **a** silver pressure pen and the **b** carbon pressure pen after being subjected to cyclic folding

resulted in the line samples cracking when subjected to the first method of folding as folding of the crease meant exerting a large amount of force onto the line sample, causing the acrylic lacquer to crack. The second method of folding exerted lesser force on the line samples and the line samples were able to undergo more folds before becoming non-conductive as the acrylic lacquer took a longer time to crack until the line samples became non-conductive.

4.4 Effects of Roughness of Substrate on Conductivity of Conductive Traces

3D printed structures are commonly used as substrates for conductive pens. An issue with 3D printed parts is that the surface roughness is poor and roughness varies with print direction, which might affect the quality of the line drawn.

As shown in Fig. 5., the silver line samples on the substrate printed at 45 ˚ had the greatest resistance at 4.07E-01 Ω while the carbon line samples on the substrate assembled at 90° had the greatest resistance at 418.75 Ω. As seen from Fig. 6., the 3D printed substrate assembled at 30° were the roughest with a Sa value of 70 μm, followed by 45°, 60°, 0° and 90*. It is expected that the rougher the surface, the less conductive the line samples would be. Line samples drawn on the substrate assembled at 90° had a higher resistance than the line samples drawn on the substrate assembled at 30° for both silver and carbon. A possible explanation for such a result would be that that the design of the pressure pens allowed ink to flow into the holes of the substrate, reducing the effect of surface roughness on the conductivity of the line samples. This is possible due to a few feature of the pressure pens. Firstly, the ink takes a while to dry, allowing it to flow into the cracks on the substrate. Secondly, the valve allows lots of ink to flow directly into the cracks at it acts like a tap. Lastly,

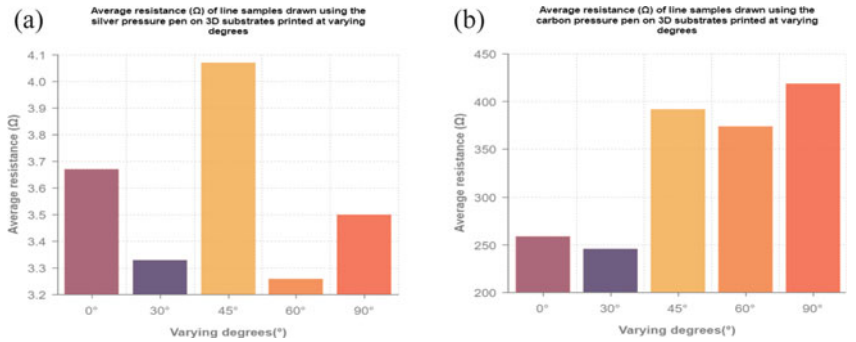

Fig. 5 Graph showing average resistance of the line samples drawn using the **a** Silver pressure pen and **b** Carbon pressure pen on 3D printed substrates assembled at various degrees

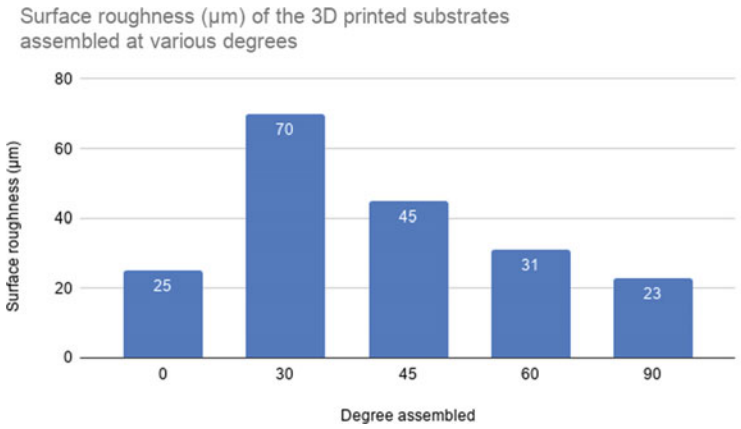

Fig. 6 Surface roughness (μm) of the 3D printed substrates assembled at various degrees

there is a possibility that the amount of pressure exerted when squeezing the barrel of the pen may differ from line to line as it is rather easy to squeeze and is therefore very sensitive to the amount of pressure applied on it, allowing a lot of ink to be discharged despite a slight difference in the amount of pressure used to squeeze the barrel.

4.5 Application

To demonstrate the application process of lighting an LED bulb on an origami, a circuit composed of a 3.0 V battery, a fabricated writing pattern, and 2 surface-mounted LEDs with a rated voltage of 1.9 V was drawn on the origami paper using silver conductive pen with three line passes. The conductive tracks were drawn by

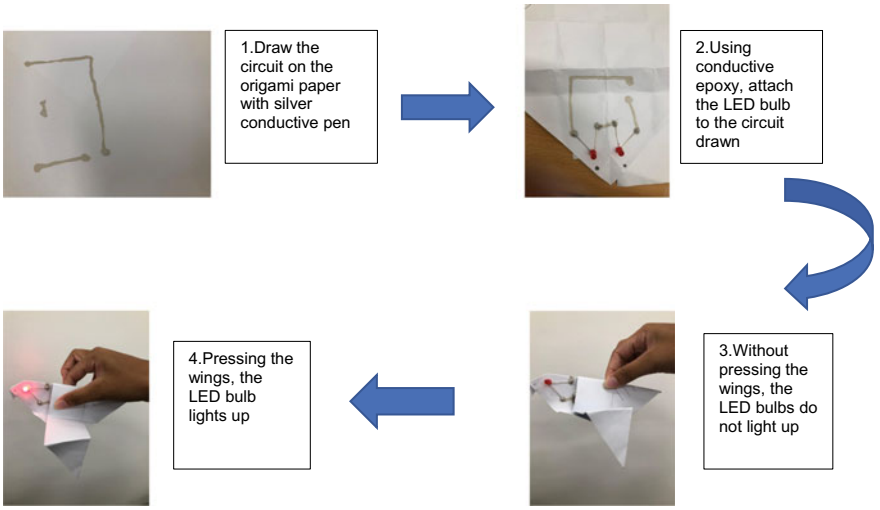

Fig. 7 Process of lighting up the LED bulb on the origami

silver pressure pens. The process of lighting up the LED bulb on the origami is shown in the illustration in Fig. 7. When the circuit is on, the LED is illuminated, and works rather well. This shows that the silver pressure pen works well on paper substrates for the fabrication of low cost lights. People living in isolated areas and in areas with no access to electricity.

5 Conclusion

In summary, the carbon and silver pressure pens are highly recommended for use as it was found to be suitable for use on the most amount of substrates which are the PET film, printing paper, 3D printed substrates and bandage. The silver micro-tip and ballpoint pen are both unsuitable for use on the PET film but with an increased amount of line passes, they have the potential to be able to fabricate conductive traces of quality similar to those produced by the 2 pressure pens. The design of the carbon and silver pressure pen's pen tip, which has a valve and easy ink flow control, makes it suitable for use on most substrates. The silver microtip pen lacks easy ink flow control as the barrel was challenging to squeeze and silver ballpoint pen had a pen tip which limits the amount of ink discharged as it is dependent on the surface contact area with the substrate.

Acknowledgements We would like to thank Assoc Prof. Yeong Wai Yee, Mr Goh Guo Liang, Mr William Phua and Ms Joey Goh for their advice and support throughout this programme.

References

1. A. C. Siegel, S. T. Phillips, M. D. Dickey, N. S. Lu, Z. G. Suo and G. M. Whitesides, Adv. Funct. Mater., 2010, 20, 28
2. K. Woo, D. Kim, J. S. Kim, S. Lim and J. Moon, Langmuir, 2009, 25, 429
3. X. F. Tang, Z. G. Yang and W. J. Wang, Colloids Surf., A, 2010, 360, 99.
4. M. M. Voigt, A. Guite, D. Y. Chung, R. U. Khan, A. J. Campbell, D. D. Bradley, F. Meng, J. H. Steinke, S. Tierney, I. McCulloch, *Adv. Funct. Mater.* **2010**, *20*, 239
5. H. Yan, Z. Chen, Y. Zheng, C. Newman, J. R. Quinn, F. Dötz, M. Kastler, A. Facchetti, *Nature* **2009**, *457*, 679
6. D. Zielke, A. C. Hübler, U. Hahn, N. Brandt, M. Bartzsch, U. Fügmann, T. Fischer, J. Veres, S. Ogier, *Appl. Phys. Lett.* **2005**, *87*, 123508
7. R. Vyas, V. Lakafosis, A. Rida, N. Chaisilwattana, S. Travis, J. Pan, M. M. Tentzeris, *IEEE Trans. Microwave Theory Tech.* **2009**, *57*, 1370
8. M. Härting, J. Zhang, D. Gamota, D. Britton, *Appl. Phys. Lett.*
9. Tai, Y.-L., & Yang, Z.-G. (2011). Fabrication of paper-based conductive patterns for flexible electronics by direct-writing. Journal of Materials Chemistry, 21(16), 5938https://doi.org/10.1039/C0JM03065A
10. Eshkeiti, A., Reddy, A., Emamian, S., Narakathu, B., Joyce, M., Joyce, M., Fleming, P., Bazuin, B. and Atashbar, M. (2015). Screen Printing of Multilayered Hybrid Printed Circuit Boards on Different Substrates. *IEEE Transactions on Components, Packaging and Manufacturing Technology*, 5(3), pp.415-421
11. Liu, S., Li, J., Shi, X., Gao, E., Xu, Z., Tang, H., … Chen, Y. (2017). Rollerball-Pen-Drawing Technology for Extremely Foldable Paper-Based Electronics. Advanced Electronic Materials, 3(7), 1700098https://doi.org/10.1002/aelm.201700098
12. Agarwala, S., Goh, G. L., Dinh Le, T.-S., An, J., Peh, Z. K., Yeong, W. Y., & Kim, Y.-J. (2018). Wearable Bandage-Based Strain Sensor for Home Healthcare: Combining 3D Aerosol Jet Printing and Laser Sintering. ACS Sensorshttps://doi.org/10.1021/acssensors.8b01293
13. Russo, A., Ahn, B. Y., Adams, J. J., Duoss, E. B., Bernhard, J. T., & Lewis, J. A. (2011). Pen-on-Paper Flexible Electronics. Advanced
14. Materials, 23(30), 3426–3430. doi:https://doi.org/10.1002/adma.201101328
15. Li, W., & Chen, M. (2014). Synthesis of stable ultra-small Cu nanoparticles for direct writing flexible electronics. Applied Surface Science, 290, 240–245https://doi.org/10.1016/j.apsusc.2013.11.057

Exploring the Use of Apple Skin to Boost the Energy Efficiency of Microbial Fuel Cells

Chescia Yi-Xin Lim, Hui Min Leong, Amanda Drea Chandra, and William Phua

Abstract The conundrum on exponentially accelerating excess food wastage and subsequent release of greenhouse gases from food decomposition has undeniably plagued various ecosystems on Earth. Microbial Fuel Cells (MFCs) has been contemplated as a prospective alternate source of renewable energy to resolve the aforementioned issue. Nevertheless, a notable challenge to overcome is the optimisation of catalytic activity for anaerobic substrate oxidation via economical constituents. This study primarily seeks to propose a novel approach for adopting epidermis of economical Malus domestica (apple) fruits in the operation of MFCs. The aptness of apple epidermis as cation exchange membranes and microbe anaerobic respiration substrate was subjected to quantitative electrochemical analysis. The combination of apple epidermis as both microbe substrate and a cation exchange membrane exhibited marginally higher peak voltage and voltage plateau stability relative to conventional Nafion® membranes upon electrochemical analysis. The higher component-specificity of apple epidermis MFCs comparative to conventional set-ups was evident through extensive MFC component optimisation experimentation. Supplementary structural analysis via Scanning Electron Microscope (SEM) characterisation on apple epidermis revealed additionally the significant pore formation on membrane surfaces upon cell usage, therefore rendering heightened cation permeation. The presence or lack thereof of wax on apple epidermis had negligible implications on the correlated electrochemical performance, reaffirming the viability of apple epidermis for economical MFCs under diverse conditions. The novel approach adopted in this study, which entailed incorporation of apple epidermis as paired cation exchange membranes and microbe substrates, could henceforth make provision for a robust avenue of economical MFC design.

Keywords Microbial fuel cells · Apple skin membrane · Alternative source of energy · Renewable energy

C. Y.-X. Lim (✉) · H. M. Leong · A. D. Chandra · W. Phua
National Junior College, Singapore, Singapore
e-mail: chescia@gmail.com

H. Guo et al. (eds.), *IRC-SET 2020*,
https://doi.org/10.1007/978-981-15-9472-4_27

1 Introduction

With climate change posing as a fundamental threat to the places, species and people's livelihoods, the rising demands for electricity globally for sources of renewable energy has called for research into Microbial Fuel Cells (MFCs). Microbial fuel cells (MFCs) exist as one of the most promising technologies which harness wastage for energy generation. MFCs are archetypical microbial Bio-Electrochemical Systems (BECs) that adopt microorganisms as catalysts to oxidize organic and inorganic matter and generate current. A preliminary contrast between MFCs and other fuel cells would reveal the ability of MFCs to generate clean energy at normal temperature, atmospheric pressure and neutral pH values while requiring minimal auxiliary maintenance. Given that the CO_2 emitted is biogenic, there is a lack of net carbon emission into the environment. MFCs can be primarily categorised into single-chambered and double-chambered configurations. The typical MFC used in experimentation is double-chambered, with a Cation Exchange Membrane separating the anode chamber and the cathode chamber in the MFC. Under anaerobic conditions, organic substrate is oxidised by a biocatalyst in the anode chamber, thereafter liberating electrons and protons separately. The electrons produced by the bacteria from these substrates are transferred to the negative anode electrode by a mediator, before passing through an external circuit and entering the positive cathode chamber.

Glucose oxidation reaction by the microbes in the anode chamber can be shown by the following equation:

$$C_6H_{12}O_2 + 6\,H_2O \rightarrow 6\,CO_2 + 24\,H^+ + 24\,e^-$$

The flow of electrons from one chamber to another will generate an electrical current, which by convention, flows from the positive to the negative terminal in the direction opposite to that of electron flow. While this process occurs, protons which are simultaneously liberated from the oxidation reaction diffuses from the anode chamber to the cathode chamber through a semipermeable Cation Exchange Membrane (CEM). These electrons would subsequently react with oxygen molecules in a redox reaction to form water molecules in the cathode chamber as shown by the following equation:

$$3\,e^- + MnO_4^- + 4\,H^+ \rightarrow MnO_2 + 2\,H_2O$$

The Nafion® membrane is the conventional CEM adopted in double-chambered MFCs. Nafion® membranes exists as a copolymer of fluoro 3,6-dioxo 4,6-octane sulfonic acid and polytetrafluorethylene (PTFE), which permits hydrogen ion/proton transport while preventing electron conduction. Despite its wide usage in MFCs, several prevalent issues have been associated with the membrane. The primary issues encompassed include the high costs of Nafion® membranes, and oxygen leakages between chambers. Given the objective of MFCs as a cost-effective green energy source, these concerns severely limit its applicability in the industry.

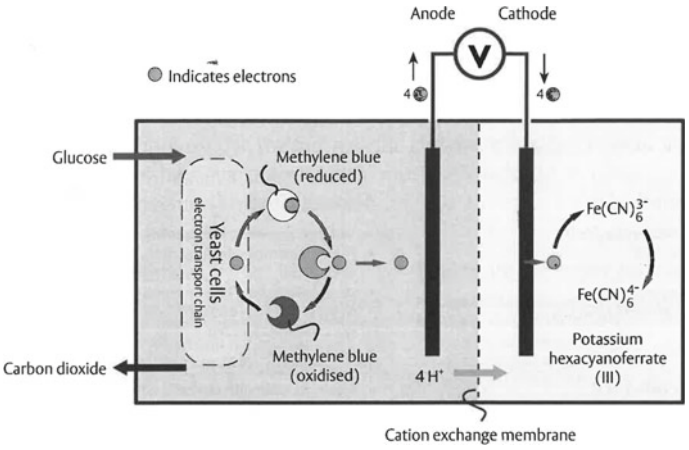

Fig. 1 How the microbial fuel cell works [4]

In view of food wastage, another rising global problem, our study focuses on combating this issue as well. Food waste disposed in landfills decompose and become a significant source of methane—a greenhouse gas with 21 times the global warming potential of carbon dioxide.

Hence, the usage of food waste as a potential cation exchange membrane to replace the conventional Nafion® membrane, as well as a microbe substrate to replace the current glucose substrate used, can tackle both critical global issues that directly impact our planet (Fig. 1).

2 Aim

2.1 Investigation Topic

This study investigates how the use of apple skins as MFC membranes and substrate affects the efficiency of the MFC. It delves into which is the most cost-efficient and commonly found material to act as the membrane that allows maximum efficiency for the MFC. The independent variable used is the type of organic membrane used in the set-up. Nafion® membrane is used as a control. The measured variable is the amount of voltage produced by the MFC. At the same time, it has also been investigated if higher voltage could be produced by replacing the glucose substrate with the apple skin powder substrate.

2.2 Motive

As the MFC is usually quite expensive to make and consists of materials that are hard to obtain, this study was conducted to see if there were alternative materials that would allow many people to make their own MFC. If successful, the alternative materials for the MFC could serve as a good replacement for energy sources around the world as it is a renewable source and is environmentally-friendly due to its prevalence around. Moreover, Nafion® is also a costly polymer to use as the membrane for MFCs in the current context. Additionally, the use of apple skins as MFC membranes in replacement of the Nafion® membrane has yet to be explored and is a novel method.

2.3 Hypothesis

Our hypothesis is that the voltage produced with the novel dried apple skin membrane would be comparable to that of the Nafion® membrane as it is permeable for cations and impermeable for anions. For proton transfer in the MFC, cations would have to pass through the Cation Exchange Membrane from the anode to the cathode, thus we think the apple skin would work better [5]. At the same time, dried apple skin would contain some glucose, coming from a plant source with photosynthetic properties, hence, it could serve as a substrate for bacterial anaerobic respiration to allow for greater efficiency of the MFC.

3 Methodology

3.1 Materials of Construction

Anode Yeast was used for anaerobic respiration (Saf-Instant Dry Baker's yeast, obtained from NTUC Fairprice), Methylene Blue was used as an electron mediator (obtained from Sigma-Aldrich), D-Glucose was used as a carbon source (obtained from Sigma-Aldrich), Carbon Electrode Paper was used as the anode electrode connected to the external circuit (obtained from Sigma-Aldrich).

Cathode $KMnO_4$ was used as an electron mediator (obtained from Sigma-Aldrich), Carbon Electrode Paper was used as the cathode electrode connected to the external circuit (obtained from Sigma-Aldrich).

Membrane Red Apple Skin was used as the organic membrane (Pasar Royal Gala Apples, obtained from NTUC Fairprice), Nafion® 115 Membrane (obtained from Fuel Cell Store, USA)

Instruments for measurement ADDeSTation Data Logger with Voltmeter (measures up to 6 V), Crocodile clips, Micropipette (measures up to 1 ml → 1000 μl)

3.2 Preparation of Materials/Chemicals Required

Membrane The flesh of the apple was removed using a scalpel, and it was ensured that the skin has no perforations. The skin was then wrapped in aluminium foil and dried in the drying oven for 15 min at 100 °C. It is then unwrapped and the inner part of the apple skin was allowed to dry for another 2 min. The membranes were then positioned in the centre of the 5 × 5cm acrylic block, with the rubber seal clamped down to secure the membrane in position.

1% Glucose Solution as Substrate 0.5 g of D-Glucose crystals were prepared. D-Glucose crystals were then mixed with 50 ml of water to obtain 1% Glucose Solution.

1% Apple Skin Powder Solution as Substrate The dried apple skin was blended into fine powder using a blender. 0.5 g of apple skin powder was then measured out and mixed with 50 ml of water to obtain 1% apple skin powder substrate solution.

Phosphate Buffer for Movement of Protons 5.52 g of Sodium Phosphate Monobasic crystals were prepared, along with 11.36 g of Sodium Phosphate Dibasic crystals. To prepare the stock solutions, the Sodium Phosphate Monobasic crystals were then dissolved in 200 ml of water, while the Sodium Phosphate Dibasic crystals were dissolved in 400 ml of water. Upon preparation of the stock solutions, 195 ml from the Sodium Phosphate Monobasic solution and 305 ml from the Sodium Phosphate Dibasic solution was extracted and mixed together. The mixture was then diluted with 500 ml of water to obtain 1 litre of Phosphate buffer (pH 6).

3.3 Construction of the MFC

The carbon electrode papers were first fitted into the anode and cathode chambers, followed by the screws and bolts through the four holes on one of the acrylic blocks. The prepared electrode chamber was then placed on top of the acrylic block, followed by a rubber seal on top of the electrode chamber. The membrane was positioned on top of the rubber seal, with the placement of another rubber seal over the membrane to secure it. The other prepared electrode chamber was then placed on top of the membrane with the final acrylic block at the end. The set-up should be properly aligned before tightening the screws fully. This will prevent possible leakage of the contents. The block will serve as the device for the MFC to function efficiently. The contents were then injected into the respective chambers, the anode chamber with 1.25 g of yeast, 2.5 ml of methylene blue ($C_{16}H_{18}ClN_3S$) and 0.2 ml of 1% glucose solution ($C_6H_{12}O_6$). The cathode chamber with 8 ml of potassium permanganate ($KMnO_4$) and 4.25 ml of Phosphate Buffer ($Na_2HPO_4 \bullet NaH_2PO_4$). Crocodile clips were then connected to the protruding electrode papers of the electrode chambers, black to anode and red to cathode, with the other end connected to the data logger to

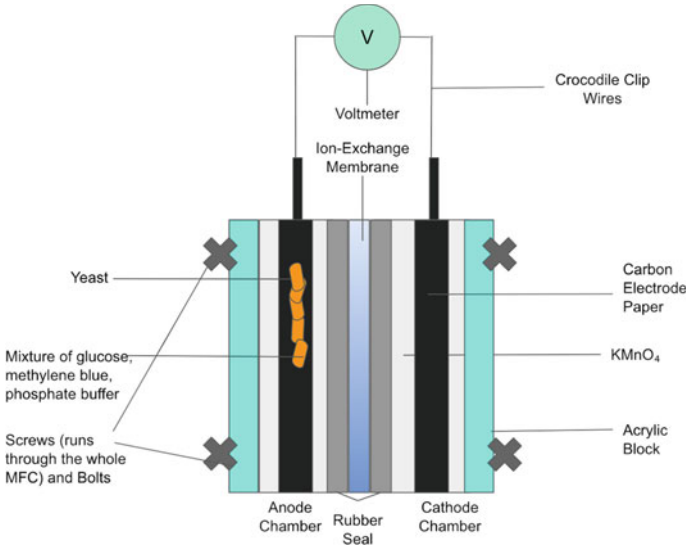

Fig. 2 Schematic diagram of MFC set-up (side-view)

collect substantial data. Repeat the procedure thrice for each set-up to heighten the accuracy of results obtained (Fig. 2).

4 Results and Discussion

Using Apple Skin as a Substitute for Nafion®

Apple skins have been found to be permeable to cations, and hence it has been investigated further in this study to determine if apple skin could be a good substitute for the conventional membrane used in MFCs.

From the data above, it is observed that apple skin membrane produced a similar trend to the Nafion® membrane. However, results have also shown that the voltage produced by the MFC with apple skin membrane is about half the voltage produced by the MFC with Nafion® membrane. The maximum voltage of the apple skin set-up was found to be 0.87 V while the Nafion® set-up was found to peak at 1.08 V. The minimum voltage produced was 0.26 V in the apple skin set-up and 0.41 V in the Nafion® set-up. The results obtained from the Nafion® set-up is also similar to another study done by other researchers, which was found to peak at 1.23 V [5]. It is likely that the yeast does not react well with a mixture of pure glucose and monosaccharides found within the apple skin, hence this combination is suboptimal. However, to be able to produce a significant amount of voltage, it proves that the apple skin is successful in acting as a Cation Exchange Membrane in the MFC set-up, allowing protons produced by the yeast in the anode chamber to pass through into

the cathode chamber. This shows that apple skin, while less efficient than Nafion® using conventional glucose substrate, serves as a good alternative for the conventional membrane used in MFCs in terms of the 1% glucose substrate (Fig. 3).

Using Apple Skin as a Substitute for 1% Glucose Solution

The apple substrate was used in two different set-ups, one with apple skin as the membrane and one with Nafion® as the membrane (Fig. 4).

The use of apple skin acting as a substrate was also novelly explored. The apple skin was used in the same concentration as glucose solution. In this study, it was tested against the efficiency of the waxed apple skin membrane and Nafion® membrane. Through graphs and voltage values obtained, it is deduced that the apple skin membrane is more efficient than the Nafion® membrane in the context of apple

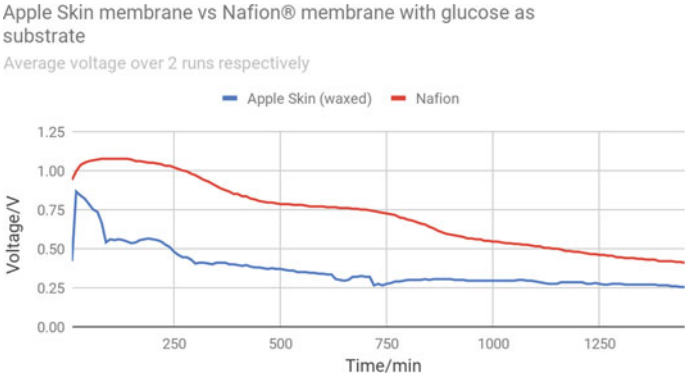

Fig. 3 Results of voltage/V of control membrane (Nafion) and experimental membrane (Apple Skin) using 1% glucose substrate against Time/min

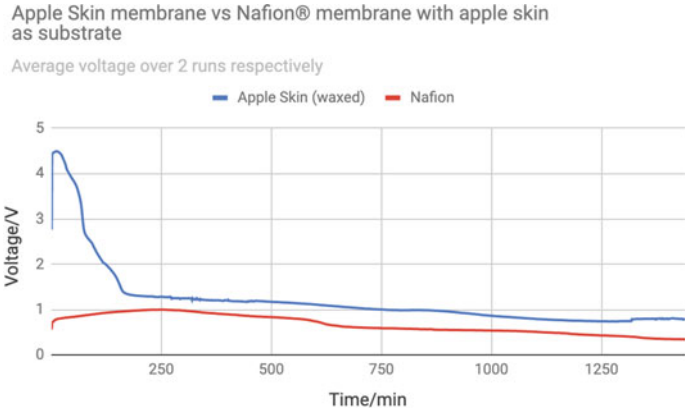

Fig. 4 Results of Voltage/V of Nafion® membrane and experimental membrane (Apple Skin) using apple skin powder substrate against Time/min

skin substrate. Comparing the efficiency of Nafion® membrane with 1% glucose substrate and 1% apple skin substrate, it has a similar trend and voltage regardless of the substrate used, proving its consistency in voltage produced despite the change in substrate. However, the main difference observed is the spike in voltage in the apple skin membrane set-up. The voltage obtained from 1% apple skin powder solution was about five times the voltage obtained from 1% glucose solution, with a peak of about 4.49 V compared to the glucose solution of about 0.87 V. It is likely due to the compatibility of the apple skin membrane and apple skin substrate, originating from the same source. It could also be due to the presence of greater amounts of reducing sugar in the apple skin powder substrate and within the apple skin membrane that aided in the anaerobic respiration of yeast in the MFC. This poses as a possible combination that could be used for greater efficiency of the MFC. The voltage also plateaus at a higher voltage than the Nafion® membrane, which proves that it is of greater energy efficiency than that of the conventional combination–Nafion® membrane and glucose substrate.

The Difference Between Waxed Apple Skin and Wax-Removed Apple Skin Membranes

The apple skin membrane was used in two different set-ups, one with apple skin with the production wax kept on and one with the wax removed using acetone (Fig. 5).

Comparing the voltage between waxed apple skin and wax-removed apple skin membranes, the trend of energy efficiency is similar, with a few fluctuations due to the anaerobic respiration of the different clusters of living yeast cells in each set-up. The maximum voltage produced by the waxed set-up was 0.87 V while the voltage produced by the wax-removed set-up was 0.85 V. The minimum voltage produced were 0.26 V and 0.20 V respectively in the waxed and wax-removed set-ups. Hence, it is concluded that regardless of whether the apple skin membrane contained wax,

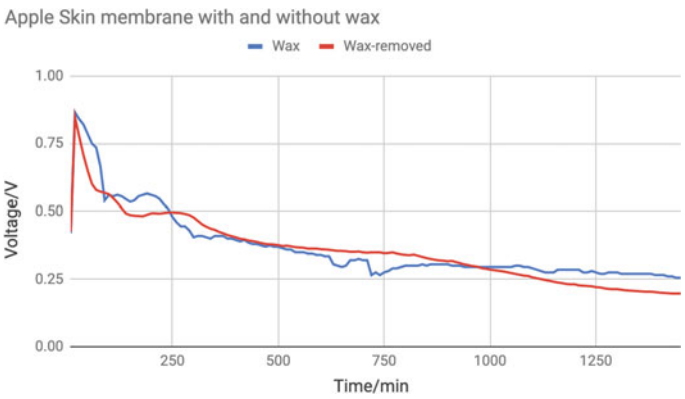

Fig. 5 Results of voltage/V of apple skin membrane, waxed and wax-removed using 1% glucose substrate against Time/min

it does not affect the results much and the voltage produced would be approximately the same (Table 1).

From the SEM figures above, it can be seen that the surfaces with and without wax were of similar surfaces before running the experiment. However, after running, openings could be observed in the SEM scans of the apple skin surfaces. This indicates traces of the cations permeating through the apple skin membrane, which proves that apple skin is a successful alternative membrane that could be used in replacement of Nafion® membrane in the MFC. With the results of the voltage produced by the 2 experiments of waxed apple skin and wax-removed apple skin membranes, it is also proven that the cations have managed to permeate through in order for both of the set-ups to produce significant, comparable voltage to that of Nafion® membrane during the experiment.

Table 1 Scanning electron microscope (SEM) imaging of apple skin membranes used (Image of × 300 magnification)

	Facing the anode	Facing the cathode
Waxed	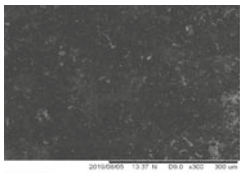	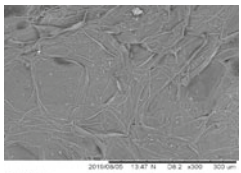
	Figure 6**a** Apple Skin (Outer) surface with wax, **b** Apple skin (Inner) surface with wax	
Waxed (After running)	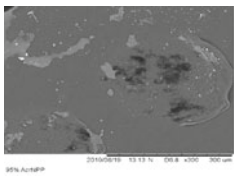	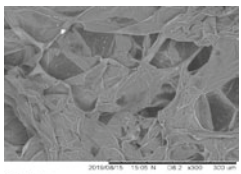
	Figure 7**a** Apple skin (Outer) surface with wax after running the MFC, **b** Apple skin (Inner) surface with wax after running the MFC	
Wax-removed	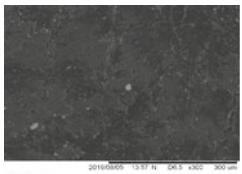	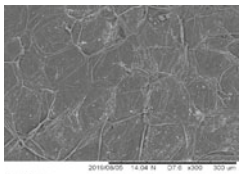
	Figure 8**a** Apple skin (Outer) surface without wax, **b** Apple skin (Inner) surface without wax	

5 Conclusion

In conclusion, it is shown that the apple skin membrane could serve as a good alternative to the current Nafion membrane used. Apple skin substrate is also a possible source of sugar for the yeast to conduct anaerobic respiration to generate electricity renewably. The apple skin membrane showed comparable voltage results to that of Nafion® membrane using 1% glucose substrate. Despite the halved voltage produced with 1% glucose substrate, apple skin membrane performed five times better than that of Nafion® membrane using apple skin substrate. Hence, it is deduced that apple skin membrane with apple skin substrate is the most compatible combination to produce the most efficient MFC, with the highest voltage using the same amount of starting materials due a higher sugar level present within the apple skin powder and in the apple skin membrane. It is also discovered that the apple skin will be permeable to cations regardless of the presence of wax left during production processes. Hence, apple skin will be a good replacement to the current Nafion® membrane and glucose substrate, opening the gateway to possible solutions that could solve the critical global issues of climate change and food wastage at the same time.

References

1. Chouler, J., Bentley, I., Vaz, F., O'Fee, A., Cameron, P., & Di Lorenzo, M. (2017). Exploring the use of cost-effective membrane materials for Microbial Fuel Cell based sensors. Electrochimica Acta, 231, 319-326. https://doi.org/10.1016/j.electacta.2017.01.195
2. Kalathil, S., Patil, S., Pant, D. (2017, August). Microbial Fuel Cells: Electrode Materials. Encyclopedia of Interfacial Chemistry, 309–318. https://doi.org/10.1016/b978-0-12-409547-2.13459-6
3. Logan, B., Hamelers, B., Rozendal, R., Schröder, U., Keller, J., & Freguia, S. et al. (2006). Microbial Fuel Cells: Methodology and Technology†. *Environmental Science & Technology*, *40*(17), 5181–5192. https://doi.org/10.1021/es0605016
4. Madden D. (2015). Microbial Fuel Cell Teacher's and technician's notes. United Kingdom: University of Reading
5. Michaelis, L. (1925). Contribution To The Theory Of Permeability Of Membranes For Electrolytes. The Journal of General Physiology, 8(2), 33–59. https://doi.org/10.1085/jgp.8.2.33
6. Parkash, A. (2016). Microbial Fuel Cells: A Source of Bioenergy. Journal of Microbial & Biochemical Technology, Volume 8(3): 247–255 (2016). https://doi.org/10.4172/1948-5948.1000293.
7. Santoro, C., Arbizzani, C., Erable, B., & Ieropoulos, I. (2017, April 06). Microbial fuel cells: From fundamentals to applications. A review. Journal of Power Sources, 356, 225–244. https://doi.org/10.1016/j.jpowsour.2017.03.109

Screening and Characterisation of Novel Environmental Phages

Cheng Yat Tan, Jason Han Meng Ong, and Juan Pablo Bifani

Abstract Bacteriophages (or simply 'phages') are viruses that replicate themselves within a host bacterial cell following infection of the host. For this project, environmental soil and water samples from around Singapore were collected to screen for phages, which have a myriad of purposes, due to their high specificity to their hosts. For instance, phages, coupled with genetic engineering of phage DNA, may provide an alternative to treating bacterial infections due to rapid replication times, and potential for non-intrusive therapy. Phages may also be used for diagnostics purposes, which allows scientists to potentially confirm the presence of a species of bacteria, and thus determine the need for the use of specific antibiotics. This research focuses on *Staphylococcus aureus* and Carbapanem-resistant *Enterobacteriaceae*, two of the species of the ESKAPE pathogens (*Enterococcus faecium*, *S. aureus*, *Klebsiella pneumoniae*, *Acinetobacter baumannii*, *Pseudomonas aeruginosa*, and *Enterobacter* species). The research aims to screen and isolate phages specific to these bacterial species (as they have high potential to achieve antibiotic resistance) and study them via purification, restriction enzyme digestion analysis and phenotypic characterisation. As a short summary, six distinct phages were found through the use of phenotypic and genotypic characterisation. Three of these phages targeted the Gram-positive *S. aureus* and *Streptococcus pneumoniae,* whereas the other three targeted Gram-negative *K. pneumoniae.* In particular, three of six studied phages targeted Carbapanem-resistant *K. pneumoniae.* The results of this study could provide insight into the species of phages present in Singapore, and whether they could be used for diagnostics and therapy Aslam (A Treatise on Electricity and Magnetism. Oxford, Clarendon, pp. 68–73, 2018 [1]), Dennehy (The Quarterly Review of Biology 85:109–109, 2010 [2])

C. Y. Tan (✉) · J. H. M. Ong
NUS High School of Mathematics and Science, Singapore, Singapore
e-mail: micpb@nus.edu.sg

J. P. Bifani
Department of Microbiology and Immunology, National University of Singapore, Singapore, Singapore

H. Guo et al. (eds.), *IRC-SET 2020*,
https://doi.org/10.1007/978-981-15-9472-4_28

1 Introduction

Bacteriophages (or simply 'phages') are viruses which infect bacterial cells and replicate using the host's cellular mechanisms, and have been used for treatment of bacterial diseases as early as 1920. Discovered in 1915, they became extensively used in phage therapy from 1920–1940, until they were replaced by antibiotics. However, with the emergence of pathogens resistant to antibiotics and other antimicrobials (with statistical analysis predicting up to 10 million deaths per year due to such infections by 2050), research industries are now looking towards possible alternatives to antibiotics.

ESKAPE pathogens (*E. faecium*, *S. aureus*, *K. pneumoniae*, *A. baumannii*, *P. aeruginosa*, and *Enterobacter* species) are bacterial pathogens commonly associated with antimicrobial resistance. That is, there are an increasing number of strains that are resistant to commonly used antibiotics, which is becoming increasingly common in today's healthcare sector. Of particular concern are ESKAPE pathogens resistant to Carbapanem, a class of antibiotics that are typically reserved for bacteria that are resistant to other drugs. Carbapanem-resistant bacterial infections are a growing concern due to increasing rates of incidence, and are especially problematic due to few therapeutic purposes.

The purpose of this research is to screen and characterise bacteriophages sourced from the environment within Singapore. In particular, we focused on samples from soil, seawater, sewage and water bodies. Such bacteriophages may target these ESKAPE pathogens and can be used for two main purposes- diagnostic and therapeutic. These phages can be modified such that they insert markers (typically green fluorescent protein gene) into the host bacterium. This can be used to detect the presence of specific bacteria, and is often quicker than growing bacteria cultures (which typically takes several days). In particular, a diagnostic array could be created such that each well has a different concentration of a different antibiotic, in order to quickly determine which (and at what concentration) antibiotics the bacteria-of-interest are susceptible to for a treatment plan.

Phage therapy, on the other hand, is a viable alternative to conventional antibiotics when treating bacterial infections, especially when the bacteria is resistant to said antibiotics. There has been some previous success with the use of engineered lytic phages for the treatment of a cystic fibrosis patient with a drug-resistant *Mycobacterium abscessus* infection [3].

2 Hypothesis

We hypothesise that Singapore's environment contains phages that are specific to members of the ESKAPE pathogens, and that these phages can be isolated for use in diagnosis and phage therapy.

3 Methodology and Results

3.1 Experimental Techniques

Growing of bacteria culture: Colonies of bacteria were removed from a plate culture which had undergone streaking using an inoculation loop. The bacteria were then suspended in Luria-Bertani broth (LB), in amounts varying between 1 ml and 20 ml, depending on the amount that was required. Alternatively, a thawed frozen sample of bacteria was spun at 11,500 RPM for 10 min, and the pellet was resuspended in 1 ml of LB. The bacterial culture was then allowed to grow in a shaking incubator at 37 °C, and 220 RPM. The culture is considered ready for use when its optical density (OD at 590 nm) was between 0.6 and 0.8. The typical doubling time for *S. aureus* is 20 min, and about 40 min for *K. pnuemoniae.*

Processing of samples: Solid samples (e.g. soil) were mixed with an appropriate amount of phosphate buffer solution (PBS) by vortex, whereas surface swabs were immersed in 10 ml of PBS. Solid samples were allowed to rest for at least 30 min for particulate to settle. The solutions were then transferred to a sterile syringe, and passed through a 0.220 μm filter in order to remove any bacteria/particulate, allowing only phages to remain in the filtrate.

Spiking (Optional step): In order to amplify the number of target-specific phages, 100 μl of the filtered sample in 1.5 ml of bacterial culture (0.6–0.8 OD) was mixed with 1.5 ml of phage buffer and 50 μl of 0.1 M $CaCl_2$ solution. The samples were incubated in a shaking incubator at 37 °C, and 220 RPM overnight. 1 ml of the spiked solution was then extracted and spun down at 13,000 RPM for 5 min. The supernatant was transferred to a new tube, along with 100 μl of chloroform (to kill remaining bacteria) and vigorously shaken. The tube was allowed to sit for 10 min, then spun down at 4000 RPM for 5 min. The supernatant (amplified phage sample) was then collected.

Bacteria Overlay: 0.5 ml of bacteria culture (0.6–0.8 OD) was mixed with 0.2 ml of 0.1 M $CaCl_2$ solution and 4 ml of warm 0.7% agarose solution. The mixture was poured onto an LB plate and allowed to cool and harden for 15 min. Such plates could be stored overnight in 4 °C, though it is best to use them immediately.

Spotting: Any amount of sample between 3 and 10 μl can be spotted onto a bacteria overlay. The plate was then incubated in 37 °C overnight. Plaques would then form if there were target-specific phages present in the sample.

Isolation: Using a micropipette tip, a plaque is gently stabbed, and swirled in small circular motions to collect phage-containing agar. The tip was then immersed into 100 μl of phage buffer and gently mixed with the pipette tip, to ensure that the phages were mixed into the phage buffer.

Serial dilution: A row of microcentrifuge tubes with 90 μl of phage buffer each was prepared. 10 µl of the *neat* (original) solution was then micro-pipetted into the '−1' tube (denoting a dilution factor of 10). The process was repeated, continually diluting the original phage buffer using dilution factors of 10 until our desired range for purification was obtained.

Purification: 10 µl of diluted phage solution was added into the bacterial overlay when preparing it, using solutions of 10^{-3} to 10^{-7} dilution factors (varying depending on the purification stage reached). Plates with less than twenty plaques were selected (as a general guideline), and the isolation step was repeated until all the plaque morphologies appeared similar.

Obtaining phage lysate: Using the purified phages, bacterial overlays were then prepared, tuning the amount of phage solution and dilution factor such that a web-like plate was achieved. This plate was soaked with 5 ml of phage buffer for 72 h, and the buffer is then transferred to a syringe where it will be passed through a 0.220 µm filter in order to remove any debris. The filtrate is known as the phage lysate.

DNA Extraction: To extract DNA from 1 ml of phage lysate, Promega's DNA extraction kit was used. Additionally, to increase DNA yields, 4 µl of Proteinase K (20 mg/ml; Invitrogen, Cat. 25530–049, Lot No. 356953; Promega, Cat. V3021, Lot No. 0000292336) was added and incubated at 55 °C for 30 min. Afterwards, NanoDrop was used to verify that the DNA sample was sufficiently pure, and to identify the concentration of DNA.

Gel Casting: For 50 ml of TAE buffer, 0.75 g of agarose powder was added. The solution was microwaved in pulses to dissolve the powder. It was then allowed to cool to about 55 °C, before 5 µl of SYBR-safe was added, and the gel was cast.

Gel Electrophoresis: DNA samples were loaded into the gel with an appropriate amount of loading dye. Gel electrophoresis was conducted at 100 V for 40 min to 1 h, and the results were visualised under UV lighting.

Restriction Enzyme Digestion: For restriction enzyme digestion, New England Biolab's products and protocols were used.

3.2 Storage of Samples

Samples: Samples were preserved at 4 °C.

Bacteria Cultures (short term): Bacteria cultures were diluted with LB to an optical density of 0.01 and allowed to rest at room temperature overnight.

Bacteria Cultures (long term): Bacteria cultures were streaked on an LB plate, incubated at 37 °C overnight to allow them to form colonies. Then, the plates were

wrapped with parafilm, and stored at 4 °C. Alternatively, the bacteria cultures were combined with an equal portion of 50% glycerol, and frozen at −80 °C.

Phage Lysates: Phage lysates were preserved at 4 °C.

Extracted DNA: Extracted DNA samples were preserved at −20 °C.

3.3 Methodology

44 samples were collected from the environment (soil, leaf litter, rivers, drains, sewage, markets, hospital surfaces, nasal swabs, poultry) and each of the samples was processed into a liquid form. In particular, samples from markets and poultry were spiked as they were of a diluted nature.

Following processing, the samples were spotted onto prepared bacteria overlays of interest in duplicates. This step was done in duplicate. Two samples in particular were discovered to have caused the formation of a plaque and those samples then underwent multiple (6–8) rounds of isolation and purification in order to obtain six different phages (A, B, C, X, Y, Z). These phages were then amplified and a phage lysate of each was obtained.

Phenotypic characterisation of the six phages was conducted by the spotting of the phage lysates onto bacteria overlays of differing strains. This was done in triplicates.

Genotypic characterisation of the six phages was conducted by first extracting the DNA, followed by restriction enzyme digestion of the extracted DNA. The resultant DNA fragments were then separated by gel electrophoresis and visualised under UV lighting.

3.4 Results

The phenotypic characterisation results are summarised in the following tables, where '+' denotes a lytic clearing (plaque formation), while '-' denotes absence of lytic clearing. 'T' denotes a turbid clearing (Tables 1, 2).

Noting that phages X, Y and Z could infect both strains KP30 and KP CRE, attempts were made to test KP30, a K. pneumoniae strain from Thailand, to see whether it too was Carbapanem-resistant. This was done by observing its growth

Table 1 Results for phenotypic characterisation of phages using *Staphylococcus aureus* strains

Bacterial Strain (*Staphylococcus aureus*)	A	B	C	X	Y	Z
SA33, SA36 RN4220, RN450, ATCC6538, MRSA252	+	+	+	–	–	–
LAC, SA31, SA32, SA37, MSSA476	+	+	T	–	–	–
S789B, SA34, SA35, SA38	+	+	–	–	–	–

Table 2 Results for phenotypic characterisation of phages using *K. pneumoniae* strains

Bacterial Strain (*Klebsiella pneumoniae)*	A	B	C	X	Y	Z
K3, K12, K13, K15, K21, BkA9, STVD, ESBL (+), ESBL (2), EC2778, SGH10	–	–	–	–	–	–
KP30, KP CRE	–	–	–	+	+	+

Table 3 Results for genotypic characterisation of phages using restriction enzymes

Restriction Enzyme	A	B	C	X	Y	Z
HindIII-HF	+	–	N.A.	–	–	–
SacI	–	–	N.A.	–	–	+
HindIII	–	–	+	N.A.	N.A.	N.A.
NdeI	+	–	–	N.A.	N.A.	N.A.
EcoRI	–	–	–	–	–	+
SmaI	–	–	–	–	–	+

in mediums containing varying amounts of Impipenem (0, 4, 16, and 50 g/ml). As a positive control, KP CRE was grown in mediums containing 0 and 50 g/ml of Impipenem. The result was that it was sensitive even at 4 g/ml.

The genotypic characterisation results are summarised in the table below, where '+' denotes presence of restriction enzyme activity, while '-' denotes absence of restriction enzyme activity, and 'N.A.' denotes no results (i.e. experiment not conducted) (Table 3).

4 Discussion and Implications

By examining the results obtained from the restriction enzyme digestion, and through restriction pattern analysis, it can be determined that most of the phages are genotypically distinct from one another, as different phages' DNA could be digested by different restriction enzymes. Phages X and Y are exceptions, as they appear to be similar.

By comparing the results of spotting of the bacterial strains, the lytic clearing (plaque formation) indicates that phages A, B, and C are phenotypically distinct from phages X, Y and Z, and in particular, phage C is phenotypically different from phages A and B.

It is especially interesting to note that phages X, Y and Z show specificity for Carbapanem-resistant *Kp* strains. However, they are not solely specific to such strains given that they may infect KP30, a non-resistant strain. It is unlikely that the mechanism of infection has much to do with any Carbapanem-resistance mechanisms.

These phages have a great potential to be used as new diagnostic tools in the future. For instance, *Kp* phages can be incubated with a sample that is suspected to be contaminated with a *Kp* strain. This would allow for the amplification (and replication of these phages) if the *Kp* strain is present, and an increase in phage numbers that can be detected. It is also possible that the receptor binding proteins found on the surface of these phages and phages' tails can be chemically and genetically modified. This has the potential to increase their affinity for binding to their hosts, or to hosts outside of their natural hosts' range.

One such application for diagnostics that has been widely suggested is the insertion of the green fluorescence protein (GFP) gene into the host's genome using lysogenic phages. When the gene is transcribed and translated, the proteins produced will serve as fluorescent markers, indicating the presence of the bacteria in question. This enables non-invasive screening of the bacteria by observing the presence of green fluorescence that is produced if the bacteria were present in a patient's body [4, 5].

It is also worth noting that the phages are extremely host-specific (due to the highly specific host-receptor-binding proteins), and will only infect bacteria that are within their range of specificity. As such, they have the potential to be used in non-invasive phage therapy, as they will target only the pathogens in question without infecting human cells [6, 7].

However, there are several limitations which can serve as topics for future research. Firstly, it must be noted that phages encounter bacterial hosts only by chance, and thus, infection of bacterial hosts will be a process determined by chance. Additionally, there is a possibility that the phages will be identified as foreign viral particles, and stimulate an immune response from the host. Thus, care must be taken to genetically engineer the phages for use in therapy and diagnostics, and in the present, it may be favourable to use phages in conjunction with antibiotics until further research on the issue is properly conducted [8, 9].

Acknowledgements We would sincerely like to thank Prof. Juan Pablo Bifani for offering us this opportunity, as well as for guiding us through the project. We would also like to thank Liew Jun Hao and Barry Choo for supervising and providing assistance during our research at the NUS Department of Microbiology and Immunology laboratories, as well as the laboratory staff and fellow researchers at the laboratories. Lastly, we would like to thank our research mentor, Dr. Tang Hock Chun from NUS High School of Mathematics and Science for his support throughout the entirety of this project.

References

1. Aslam, B., Wang, W., Arshad, M. I., Khurshid, M., Muzammil, S., Rasool, M. H., Nisar, M. A., Alvi, R. F., Aslam, M. A., Qamar, M. U., Salamat, M. K. F., & Baloch, Z. (2018, October 10). Antibiotic resistance: A rundown of a global crisis. Infection and Drug Resistance. https://doi.org/10.2147/IDR.S173867 J. Clerk Maxwell, A Treatise on Electricity and Magnetism, 3rd ed., vol. 2. Oxford: Clarendon, 1892, pp. 68–73. https://doi.org/10.2147/IDR.S173867
2. Dennehy, J. J. (2010). Bacteriophage ecology: Population growth, evolution, and impact of bacterial viruses. The Quarterly Review of Biology, 85(1), 109–109. https://doi.org/10.1086/650260

3. Dedrick, R. M., Guerrero-Bustamante, C. A., Garlena, R. A., Russell, D. A., Ford, K., Harris, K., Gilmour, K. C., Soothill, J., Jacobs-Sera, D., Schooley, R. T., Hatfull, G. F., & Spencer, H. (2019). Engineered bacteriophages for treatment of a patient with a disseminated drug-resistant *Mycobacterium Abscessus*. Nature Medicine, 25(5), 730–733. https://doi.org/10.1038/s41591-019-0437-z
4. Singh, A., Poshtiban, S., & Evoy, S. (2013). Recent advances in bacteriophage based biosensors for food-borne pathogen detection. Sensors, 13(2), 1763–1786. https://doi.org/10.3390/s130201763
5. Lee, J. H., Domaille, D. W., & Cha, J. N. (2012). Amplified protein detection and identification through dna-conjugated m13 bacteriophage. ACS Nano, 6(6), 5621–5626. https://doi.org/10.1021/nn301565e
6. O'Sullivan, L., Buttimer, C., McAuliffe, O., Bolton, D., & Coffey, A. (2016). Bacteriophage-based tools: Recent advances and novel applications. F1000Research, 5, 2782. https://doi.org/10.12688/f1000research.9705.1
7. Synthetic phages with programmable specificity. (n.d.). ScienceDaily. Retrieved June 28, 2020, from https://www.sciencedaily.com/releases/2019/11/191104112838.htm
8. Merwe, R. G. van der, Helden, P. D. van, Warren, R. M., Sampson, S. L., & Pittius, N. C. G. van. (2014). Phage-based detection of bacterial pathogens. *Analyst*, *139*(11), 2617–2626. https://doi.org/10.1039/C4AN00208C
9. Keen, E. C. (2012). Phage therapy: Concept to cure. Frontiers in Microbiology, 3. https://doi.org/10.3389/fmicb.2012.00238

Synthesis of Magnetic Carbonised Banana Peel as a Versatile and Reusable Adsorbent for Water Purification

Kiefer Ong, Pierre Yeap, and Brandon Ong

Abstract Discharge of industrial effluents containing dyes and heavy metal ions poses a serious threat to the environment but current methods such as adsorption by activated carbon are expensive. Banana peel is a widely available food waste that has potential to be used as a biosorbent for removal of pollutants. Carbonising banana peel enhances its adsorption capacity, while magnetising it renders the separation after adsorption simple and convenient via the use of a magnet. Magnetic carbonised banana peel (MCB) was prepared by dispersing 3 g to 5 g of carbonised banana peel into 15 ml of aqueous iron salts. The effectiveness of various MCBs in removing toxic pollutants like brilliant green and lead(II) ions were investigated. Results show that the percentage removal of the brilliant green and lead(II) ions by MCB was more than 95%. MCB also outperforms commercial activated carbon in lead(II) ion removal. The effectiveness of MCB in removing brilliant green and lead(II) ions did not drop significantly after progressive cycles of adsorption and desorption, unlike commercial activated carbon. More than 95% of MCB can be retrieved during the recovery process and reused, in contrast to commercial activated carbon where only about 60% could be retrieved. MCB shows great promise to be used as an eco-friendly, versatile and reusable adsorbent for water purification.

Keywords Magnetic · Eco-friendly · Water purification · Reusable · Banana peels

1 Introduction

With a rapid growth of industries, water pollution becomes a pertinent issue in today's context. Pollution is associated with about 9 million deaths a year, with water pollution contributing to 1.8 million deaths [1].

One common pollutant commonly discharged into water bodies is dye. In the textile industry, up to 200,000 tonnes of these dyes are lost to effluents every year due to the inefficiency of the dyeing process [2], presenting major environmental

K. Ong (✉) · P. Yeap · B. Ong
Hwa Chong Institution, Singapore, Singapore
e-mail: 171317B@student.hci.edu.sg

H. Guo et al. (eds.), *IRC-SET 2020*,
https://doi.org/10.1007/978-981-15-9472-4_29

problems for developing countries like Bangladesh [3]. One example of dye is brilliant green, a toxic cationic dye that is widely used in the textile industries [4]. Discharge of brilliant green into the hydrosphere has an adverse effect on humans, causing irritation to the gastrointestinal and respiratory tract, as well as symptoms such as nausea, vomiting and diarrhoea [5].

Common water pollutants also include heavy metal ions, such as lead(II) ions. Leakages of lead(II) ions into the water bodies generally occur as a result of corrosion of lead-containing plumbing systems and surface runoffs of lead-based materials like paints [6]. A recent example is the drinking water crisis that occurred in the post-industrial city of Flint in Michigan, US, which resulted in hundreds of people being poisoned by lead contaminated water [7]. Lead(II) ions are known to cause neurological diseases that impair basic mobility functions, growth defects and even death [8].

Current methods of removing toxic dyes include chemical coagulation, adsorption [9] and advanced oxidation processes [10]. Metal ions are removed by chemical precipitation, ion exchange and adsorption. Among these methods, adsorption by activated carbon is one of the most effective methods because of its efficiency and scalability for commercial usage [11]. However, synthesis of activated carbon requires high temperatures of up to 800 °C [12], leading to high energy and capital costs [13]. Retrievability is inefficient as it requires filtration or flocculation in order to remove the adsorbent-contaminant complex from water [6].

Banana peels have attracted attention as a widely available and inexpensive biological waste [14] to be used as eco-friendly adsorbents for water purification. The number of bananas consumed annually in the world is more than 100 billion, making it the fourth most important food crop after wheat, rice and corn [15]. Banana peels present a high adsorption capacity for metals and organic compounds [16], primarily due to the presence of the hydroxyl and carboxyl groups of the pectin [17]. Carbonisation of banana peel can potentially enhance its adsorption capacity [18] while magnetisation (via magnetite coating) serves as an easier and faster way of separating the adsorbent from the adsorbent-contaminant complex in place of filtration or flocculation.

Although there have been studies on the use of magnetised adsorbents such as waste tea and pollen grains to remove dyes and metal ions [6], to date, there have been limited studies on the use of magnetic banana peel to remove both dyes and metal ions. This study aims to synthesise magnetic carbonised banana peel (MCB) via co-precipitation, evaluate its effectiveness in removing brilliant green dye and lead(II) ions as compared to commercial activated carbon (AC), and investigate its reusability after progressive cycles of adsorption and desorption.

2 Materials and Methods

2.1 Materials

Iron(III) chloride hexahydrate, iron(II) sulfate heptahydrate, 25% (w/w) aqueous ammonia and lead(II) nitrate were procured from GCE Laboratory Chemicals; commercial activated carbon from Unichem; brilliant green from Sigma Aldrich. Banana peels were obtained from a fruit stall in school.

2.2 Synthesis of Magnetic Carbonised Banana Peel

Banana peels were washed with deionised water, dried and crushed. It was then carbonised in a furnace at 450 °C for 40 min under atmospheric conditions, and ground into powder. 6.66 g of iron(III) chloride hexahydrate and 13.39 g of iron(II) sulfate heptahydrate were dissolved in 45 ml of deionised water. Subsequently, carbonised banana peel (3, 3.5, 4, 4.5 and 5 g) was mixed and stirred in 15 ml of the iron salt solution. 25 ml of 25% (w/w) aqueous ammonia was added into the solution to induce co-precipitation of magnetite onto the carbonised banana peel. The mixture was stirred and left to stand for 30 min before being filtered using vacuum filtration. The residue was washed until neutral pH and dried at 60 °C until constant mass. The chemical reaction for the co-precipitation of magnetite is shown in Eq. (1).

$$Fe^{2+}(aq) + 2Fe^{3+}(aq) + 8OH^{-}(aq) \rightarrow Fe_3O_4(s) + 4H_2O(l) \quad (1)$$

The magnetic carbonised banana peels (MCB) were labelled according to the mass of carbonised banana peel used in the synthesis, as shown in Table 1.

Table 1 Sample IDs of MCB

Sample ID	Mass of carbonised banana peel used in synthesis/g	Volume of iron salt solution used/ml
MCB (3 g)	3.0	15
MCB (3.5 g)	3.5	15
MCB (4 g)	4.0	15
MCB (4.5 g)	4.5	15
MCB (5 g)	5.0	15

2.3 Batch Adsorption Studies on MCB

0.2 g of the various MCBs mentioned in Table 1 was added to 20 ml of brilliant green solution (50 mg/L) or lead(II) ion solution (50 mg/L) and shaken on an orbital shaker at 150 rpm for 24 h. A magnet was used to separate the MCB and the supernatant was obtained. Final concentration of brilliant green was analysed using a UV-VIS spectrophotometer (Shimadzu UV 1800) at 627 nm while that of lead(II) ions was analysed using an Atomic Absorption Spectrophotometer (AA 6300 Shimadzu). Pollutant solutions which do not contain any adsorbent served as the controls for the experiments. The adsorption studies were also conducted on commercial activated carbon (AC), carbonised banana peel and unmodified banana peel for comparison with MCB. These non-magnetic adsorbents were separated from the mixture using a centrifuge, whereas MCB was separated from the solution using a magnet. For each pollutant, out of the 5 MCBs synthesised, the MCB that could remove the highest percentage of pollutant while retaining its ability to be magnetically separated from the solution was selected for the subsequent reusability studies.

2.4 Reusability of Magnetic Carbonised Banana Peel (MCB)

After each adsorption study, 100 ml of 95% ethanol was added to the used adsorbent (MCB or commercial AC) to desorb the dye for 24 h, after which the adsorbent was separated and dried. The regenerated adsorbent was tested on its ability to re-adsorb brilliant green. The same procedure was conducted for lead(II) ions, except that 95% ethanol was replaced by deionised water.

3 Results and Discussion

3.1 Characterisation of MCB

Scanning Electron Microscope (SEM) images reveal that banana peel has a rough, uneven surface (Fig. 1) and becomes porous after carbonisation (Fig. 2).

Figure 3 shows magnetite particles. After magnetisation, a coating of magnetite particles can be seen blocking the pores on the surface of the carbonised banana peel (Fig. 4). The Scanning Electron Microscopy (SEM) images of MCB prepared by other masses of carbonised banana peel are similar to that seen in Fig. 4.

The X-Ray Diffraction (XRD) pattern of MCB (3 g) (Fig. 5) exhibits 2 theta peaks at 30.45°, 35.74°, 43.40°, 53.81°, 57.32°, 62.93° corresponding to crystal planes of (220), (311), (400), (422), (511) and (440) respectively, which are similar to that reported by Loh et al. in 2008 [19]. This suggests that magnetite has been successfully coated onto the carbonised banana peel.

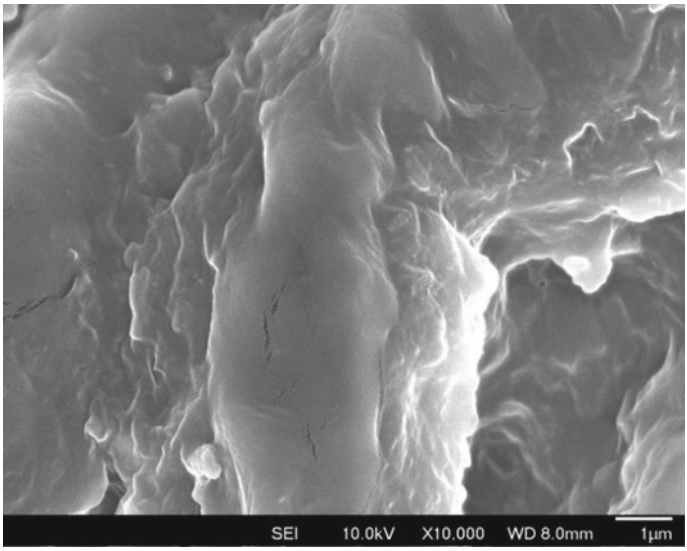

Fig. 1 SEM image of banana at 1000× magnification

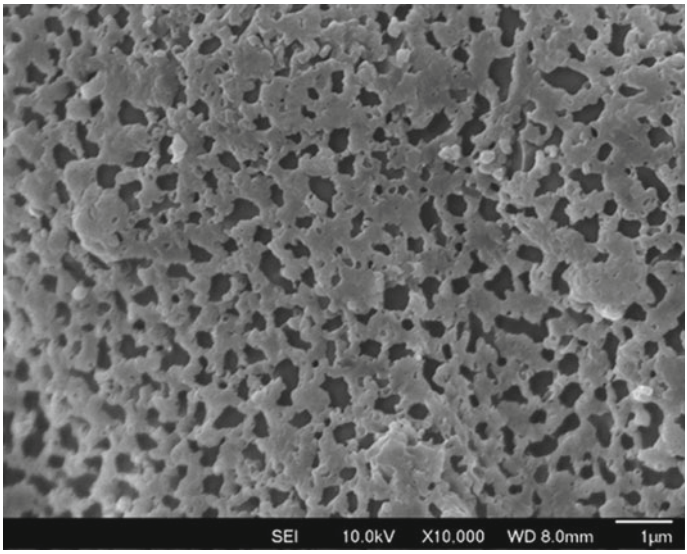

Fig. 2 SEM image of carbonised banana peel at 10,000× magnification

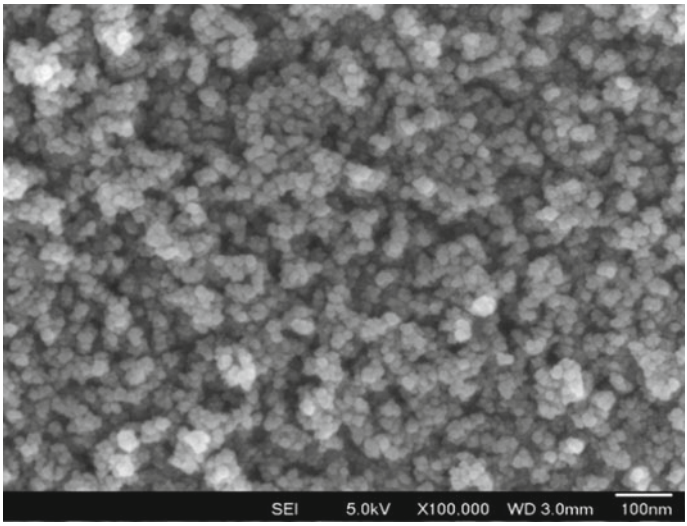

Fig. 3 SEM image of magnetite at 10,000× magnification

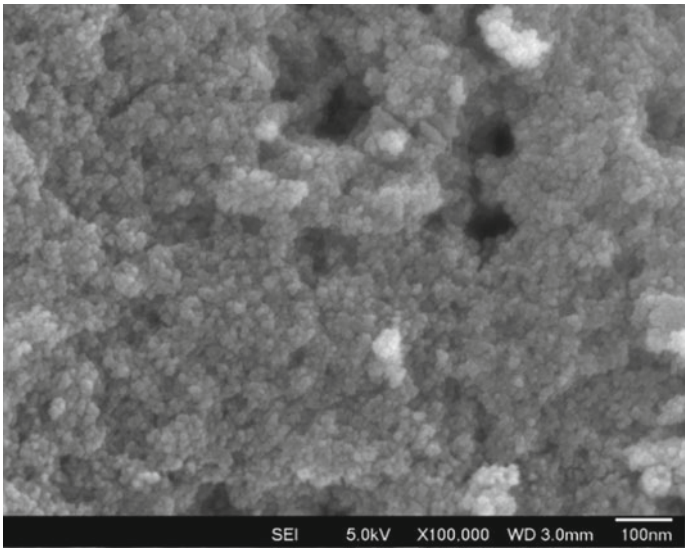

Fig. 4 SEM image of MCB (3 g) at 100,000× magnification

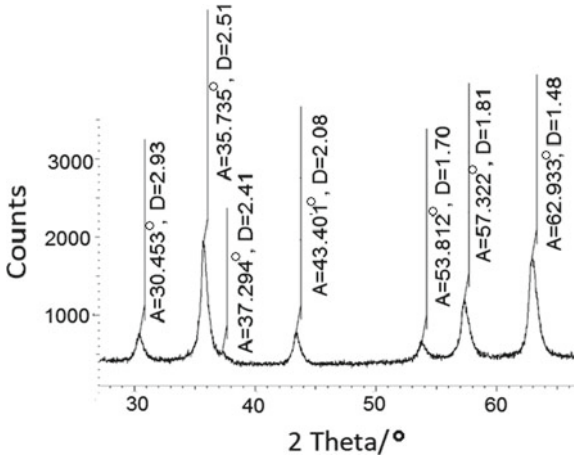

Fig. 5 XRD pattern of MCB (3 g)

3.2 *Batch Adsorption Studies of MCB*

Figure 6 shows that commercial AC has the highest adsorption capacity on brilliant green dye, followed by carbonised banana peel, the various MCBs and banana peel. This is likely due to the high porosity and surface area of both adsorbents (Fig. 2). Brilliant green is likely to be adsorbed via pi-pi interactions between aromatic rings of brilliant green and carbon, as supported by FTIR where a shift in peak (corresponding to C = C stretch of aromatic rings) from 1602 to 1583 cm^{-1} (Fig. 7) was observed, suggesting that the aromatic rings of MCB were likely to be involved in the adsorption of brilliant green. The proposed adsorption mechanism is in agreement with study by Calvete et al. 2010 [20].

Comparing the percentage removal of brilliant green by MCB (3 g) to MCB (5 g), it can be deduced that as the mass of carbonised banana peel used in the synthesis increases, the percentage removal of brilliant green increases (Figs. 7, 8).

To explain the trend, acid digestion was carried out by dissolving various MCBs in concentrated nitric acid to determine the mass of magnetite coating per gram of

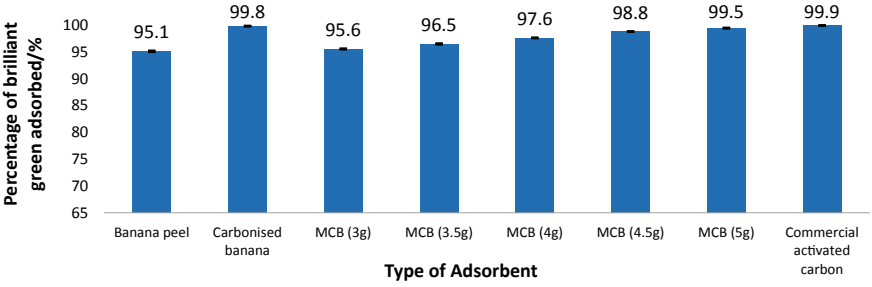

Fig. 6 Adsorption of brilliant green by different absorbents N = 5

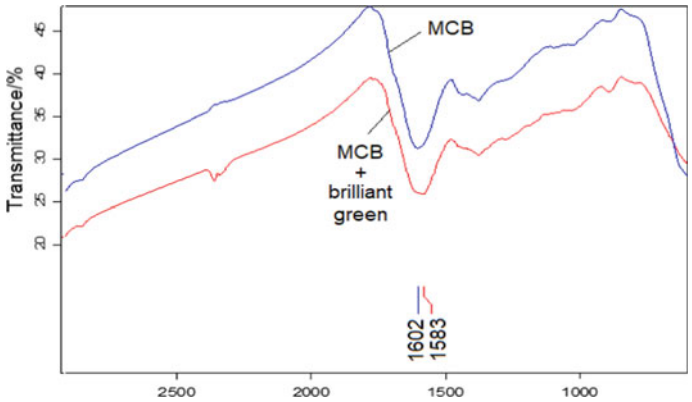

Fig. 7 FTIR spectrum of MCB before and after adsorption of brilliant green dye

Fig. 8 Adsorption of brilliant green by MCB (3 g) to (5 g) N = 5

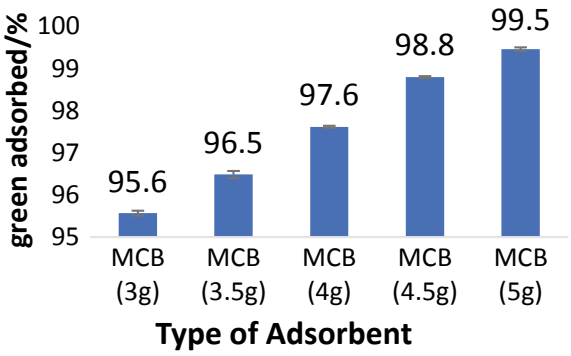

MCB. Interestingly, as the mass of carbonised banana peel used during magnetisation increases, mass of magnetite coating on the carbonised banana peel decreases (Fig. 9), and the percentage removal of brilliant green increases (Fig. 8). This suggests that the presence of magnetite coating compromises adsorption capacity of MCB by blocking

Fig. 9 Mass of magnetite coating in MCB (3 g) to (5 g) N = 3

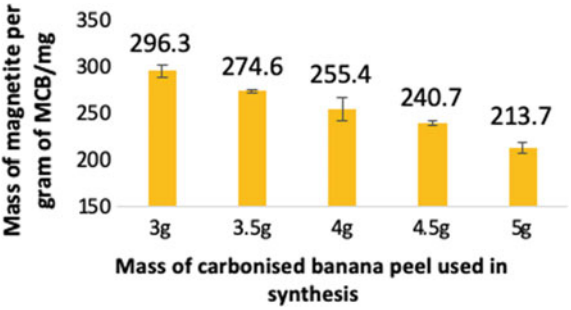

pores or binding sites in MCB, resulting in less area of contact for adsorption. MCB (3.5 g) was selected for subsequent tests on brilliant green as MCB (4 g) to MCB (5 g) were not as magnetic and not easy to retrieve using a magnet after adsorption.

Figure 10 shows that MCB synthesised using various masses of carbonised banana peel all have 100% or close to 100% adsorption for lead(II) ions. Commercial activated carbon (AC) has the next highest adsorption capacity, followed by carbonised banana peel, and lastly, banana peel. There is a significant difference in the results of MCB (3 g) and MCB (3.5 g) when compared to commercial activated carbon (Fig. 10). Energy Dispersive Spectroscopy (EDS) was then conducted to find out why.

Lead(II) ions are adsorbed via the formation of dative bonds between electron-deficient lead(II) ions and lone pairs of electrons of oxygen containing functional groups [21]. Figures 11 and 12 reveal that MCB has a greater oxygen content than

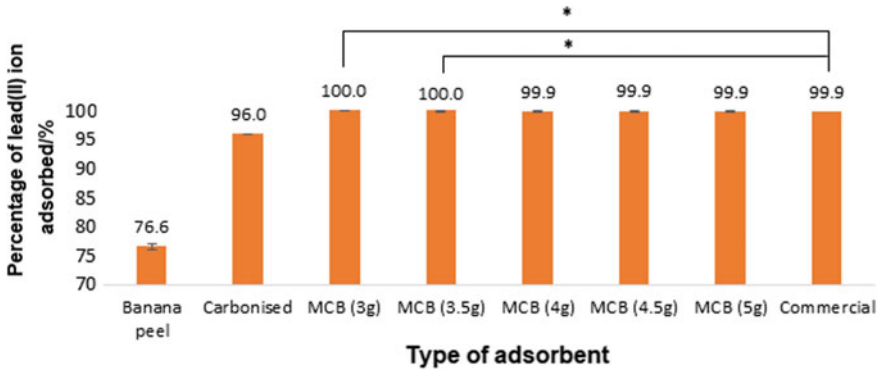

Fig. 10 Adsorption of lead(II) ions by MCB (3 g to 5 g)* denotes significant difference based on Mann-Whitney U test at significance level of 0.05 N = 5

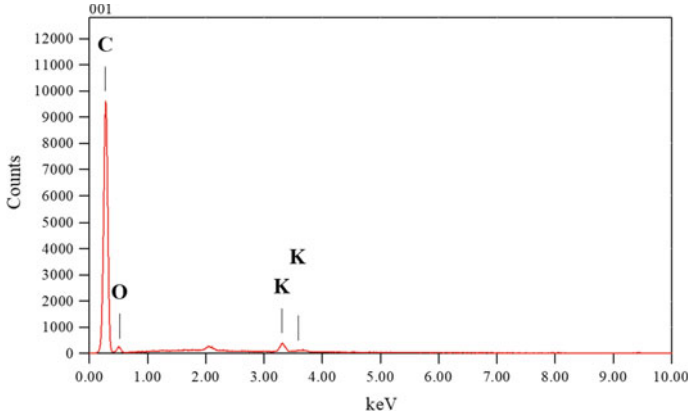

Fig. 11 EDS of commercial activated carbon

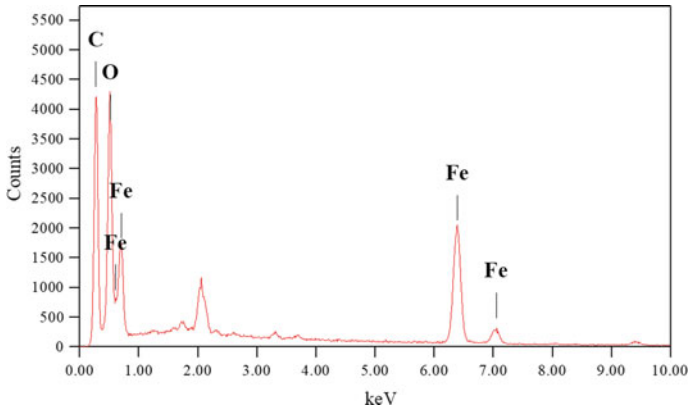

Fig. 12 EDS of MCB (3 g)

commercial activated carbon (AC), suggesting that there is more extensive dative bonding and thus more effective adsorption in MCB. MCB (3 g) was selected for future tests as it is most effective, requires the least carbonised banana peel for synthesis and yet magnetic.

3.3 Reusability of Magnetic Carbonised Banana Peel (MCB)

Figure 13 shows that after 3 cycles of adsorption and desorption, MCB is still able to effectively adsorb brilliant green, with the decrease in the percentage of dye removed being less than that of commercial AC. It is worth noting that in Cycle 3, there is

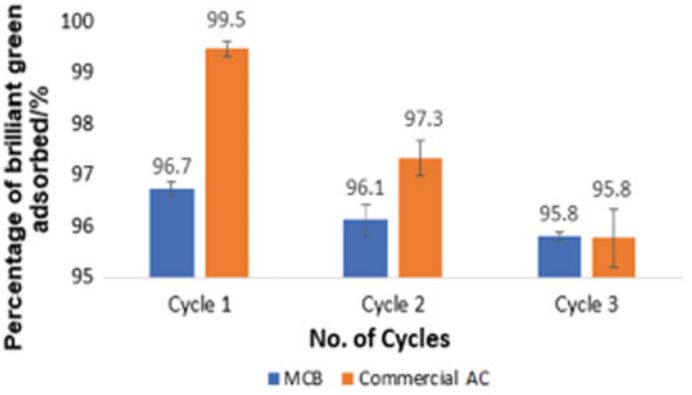

Fig. 13 Regeneration of MCB and commercial activated carbon for re-adsorption of brilliant green N = 5

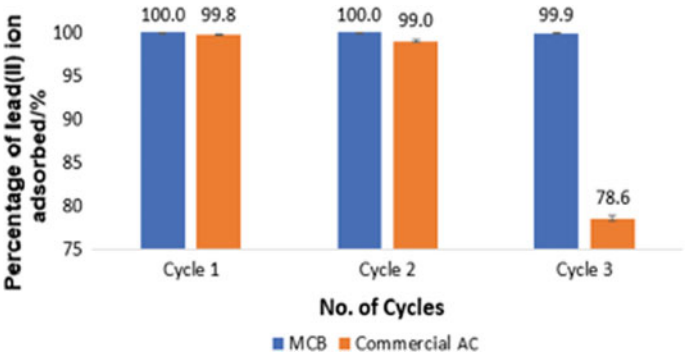

Fig. 14 Regeneration of MCB and commercial activated carbon for re-adsorption of lead(II) ions N = 5

no longer a significant difference in the results of AC and MCB (p-value of Mann-Whitney U test = 0.834 > 0.05). One possible explanation for this result is that the interactions between MCB and brilliant green are relatively weaker, thus allowing the dye to be easily desorbed. For lead(II) ions, Fig. 14 shows that MCB can adsorb lead(II) ions for 3 cycles of adsorption and desorption without a significant decrease in the percentage of lead(II) ions removed. However, there is a significant drop in percentage of lead(II) ions removed by AC from Cycle 2 to Cycle 3, suggesting that MCB has a greater potential than commercial AC in adsorbing lead(II) ions over multiple cycles of adsorption and regeneration. Another advantage of MCB over commercial AC is that as much as 97% of MCB could be retrieved after each cycle of adsorption via a magnet, while only about 60% of AC could be retrieved via filtration. Hence, MCB is able to outperform commercial AC in terms of reusability and sustainability and is much easier to retrieve after adsorption than commercial AC.

4 Conclusion and Future Work

Magnetic carbonised banana peel (MCB) was successfully synthesised via co-precipitation of magnetite onto carbonised banana peel. MCBs were effective in removing brilliant green dye and lead(II) ions, with the percentage removal being greater than 95%. Magnetising the carbonised banana peel lowers the adsorption capacity on brilliant green slightly but enhances the adsorption of lead(II) ions. The magnetic property of MCB allows for a rapid, simple, and convenient way of recovery by the use of a magnet, enabling it to be recycled effectively. MCB can be reused for at least 3 cycles of adsorption and desorption without a significant drop in effectiveness, potentially saving cost and making the use of it in water treatment even more eco-friendly.

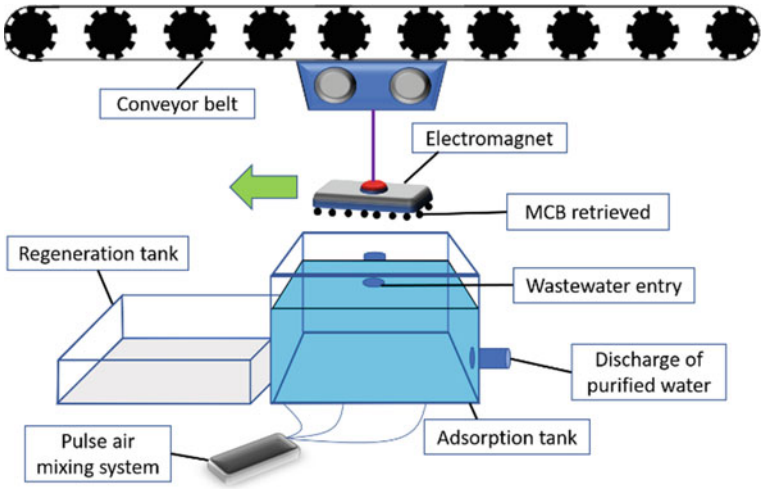

Fig. 15 Proposed model for real-life application of MCB

A model on how the MCB could be used in the industry was proposed (Fig. 15) and it can be designed to be fully automated using robotics technology. After adsorption, a magnet will be used to attract the MCB from the adsorption tank and transport it to a regeneration tank where the MCB can be desorbed. Such a system facilitates the rapid and efficient retrieval of MCB, making the purification process faster and more efficient. In the future, the effect of pH on the adsorption capacity of MCB can be studied and MCB can also be applied in the removal of other forms of pollutant like pesticides, anionic dyes and pharmaceuticals. Iron leaching tests can also be conducted in various types of wastewater to evaluate whether the iron leached out from MCB is within allowable limits to ensure the safety of utilising MCB to treat real-life industrial wastewater. An example would be the treatment of electroplating wastewater which contains lead(II) ions as well as other heavy metal ions like copper(II) ions [22].

Acknowledgements We would like to thank Mrs Sow-Peh Yoke Keow and Mdm Xia Ying for their guidance.

References

1. Mayor, S. (2017). Pollution is linked to one in six deaths worldwide, study estimates. *BMJ,* 2017, 359. https://doi.org/10.1136/bmj.j4844
2. Ogugbue, C.J., Sawidis, T. (2011). Bioremediation and Detoxification of Synthetic Wastewater Containing Triarylmethane Dyes by Aeromonas hydrophila Isolated from Industrial Effluent. *Biotechnology Research International*, 2011, 1–11. https://doi.org/10.4061/2011/967925.
3. Yardley, J. (2013). Bangladesh Pollution Told in Colours and Smells. *The New York Times.*

4. Chiou, M., & Li, H. (2002). Equilibrium and kinetic modeling of adsorption of reactive dye on cross-linked chitosan beads. *Journal of Hazardous Materials, 93*(2), 233–248. https://doi.org/10.1016/s0304-3894(02)00030-4
5. Kumar, R., & Barakat, M. (2013). Decolourization of hazardous brilliant green from aqueous solution using binary oxidized cactus fruit peel. *Chemical Engineering Journal, 226*, 377–383.
6. Yeo, S. Y., Choi, S., Dien, V., Sow-Peh, Y. K., Qi, G., Hatton, T. A.,… Thio, B. J. (2013). Using Magnetically Responsive Tea Waste to Remove Lead in Waters under Environmentally Relevant Conditions. *PLoS ONE*, 8.
7. Campbell, C., Greenberg, R., Mankikar, D., & Ross, R.D. (2016). A Case Study of Environmental Injustice: The Failure in Flint. *Int. J. Environ. Res. Public Health*, 13, 951. https://doi.org/10.3390/ijerph13100951.
8. Rosen, J. F. (1995). Adverse health effects of lead at low exposure levels: Trends in the management of childhood lead poisoning. *Toxicology, 97*(1–3), 11–17. https://doi.org/10.1016/0300-483x(94)02963-u
9. Gecgel, U., Ozcan, G & Gurpinar, G.C. (2013). Removal of Methylene Blue from Aqueous Solution by Activated Carbon Prepared from Pea Shells (Pisum sativum). *Journal of Chemistry*, 2013, 1–9.
10. Silva, C. R., Gomes, T. F., Andrade, G. C., Monteiro, S. H., Dias, A. C., Zagatto, E. A., & Tornisielo, V. L. (2013). Banana Peel as an Adsorbent for Removing Atrazine and Ametryne from Waters. *Journal of Agricultural and Food Chemistry*, 61, 2358–2363.
11. Mattson, J.S. & Mark, H.B. (1971). *Activated Carbon: Surface Chemistry and Adsorption from Solution*, New York: Marcel Dekker
12. Sabio, E., González, E., González, J., González-García, C., Ramiro, A., & Gañan, J. (2004). Thermal regeneration of activated carbon saturated with p-nitrophenol. *Carbon, 42*(11), 2285–2293. https://doi.org/10.1016/j.carbon.2004.05.007
13. Moreno-Castilla, C., Rivera-Utrilla, J., Joly, J., López-Ramón, M., Ferro-García, M., & Carrasco-Marín, F. (1995). Thermal regeneration of an activated carbon exhausted with different substituted phenols. *Carbon, 33*(10), 1417–1423. https://doi.org/10.1016/0008-6223(95)00090-z
14. Li, Y., Liu, J., Yuan, Q., Tang, H., Yu, F., & Lv, X. (2016). A green adsorbent derived from banana peel for highly effective removal of heavy metal ions from water. *RSC Advances, 6*(51), 45041–45048. https://doi.org/10.1039/c6ra07460j
15. Suparto, I., & Lin, M. (2016). Banana supply in Singapore'stable' despite fungus fears. Retrieved from https://www.asiaone.com/singapore/banana-supply-singapore-stable-despite-fungus-fears
16. Thirumavalavan, M., Lai, Y., Lin, L., & Lee, J. (2010). Cellulose-Based Native and Surface Modified Fruit Peels for the Adsorption of Heavy Metal Ions from Aqueous Solution: Langmuir Adsorption Isotherms. *Journal of Chemical & Engineering Data, 55*(3), 1186–1192. https://doi.org/10.1021/je900585t
17. Albarelli, J. Q., Rabelo, R. B., Santos, D. T., Beppu, M. M., & Meireles, M. A. (2011). Effects of supercritical carbon dioxide on waste banana peels for heavy metal removal. *The Journal of Supercritical Fluids, 58*(3), 343–351. https://doi.org/10.1016/j.supflu.2011.07.014
18. Ponou, J. (2016). Effect Of Carbonization On Banana Peels For Removal Of Cadmium Ions From Aqueous Solution. *Environmental Engineering and Management Journal*, 15, 851–860.
19. Loh, K., Lee, Y., Musa, A., Salmah, A., & Zamri, I. (2008). Use of Fe_3O_4 Nanoparticles for Enhancement of Biosensor Response to the Herbicide 2,4-Dichlorophenoxyacetic Acid. *Sensors,8*(9), 5775–5791. https://doi.org/10.3390/s8095775
20. Calvete, T., Lima, E. C., Cardoso, N. F., Dias, S. L., & Ribeiro, E. S. (2010). Removal of Brilliant Green Dye from Aqueous Solutions Using Home Made Activated Carbons. *CLEAN - Soil, Air, Water, 38*(5–6), 521–532. https://doi.org/10.1002/clen.201000027
21. Huang, Z., Zheng, X., Lv, W., Wang, M., Yang, Q., & Kang, F. (2011). Adsorption of Lead(II) Ions from Aqueous Solution on Low-Temperature Exfoliated Graphene Nanosheets. *Langmuir, 27*(12), 7558–7562. https://doi.org/10.1021/la200606r

22. Husain, A., Javed, I., Khan, N.A. (2014). Characterization and treatment of electroplating industry wastewater using Fenton's reagent. *Journal of Chemical and Pharmaceutical Research*, 6(1), 622–627

Improving B-Bit Minwise Hashing with Addition of Optimal Standard Vectors

Hengyue Wang, Hsin Wei Kuo, Ryan Nathaniel Thesman, and Keegan Kang

Abstract Minwise hashing has become a standard technique in estimating the resemblance between two sets of data and its high popularity can be attributed to the effective manner in which the estimations are done. b-Bit minwise hashing is an extension of this method where only the lowest b bits of each minwise hashed value is stored to reduce the data space needed. However, this will, in turn, cause a drop in accuracy. Our group took the main idea behind minwise hashing and wanted to develop a new method that needed less memory space and was still able to achieve higher accuracy. To accomplish this, we decided to use concepts behind b-Bit minwise hashing and add extra vectors to counter the drop in accuracy. By adding these extra data sets, we can do a comparison between the two unknown datasets and with known datasets, thus able to increase the accuracy of the estimation of similarity between 2 unknown data sets. The idea of adding extra vectors to increase accuracy was originally from the method sign random projections. After computation and passing data sets into our algorithm, the results show that our combined method had an increase in accuracy compared to b-Bit minwise hashing. We hence show that there is a better method for more accurate comparisons between 2 data sets which can be used to further improve the current methods for data comparison.

Keywords b-bit · Minwise · Hashing

H. Wang · H. W. Kuo (✉) · R. N. Thesman
NUS High School of Mathematics of Science, Singapore 129957, Singapore
e-mail: kathykuo11@gmail.com

H. Wang
e-mail: hengyue.wang04@gmail.com

K. Kang
Singapore University of Technology and Design, Singapore 487372, Singapore

H. Guo et al. (eds.), *IRC-SET 2020*,
https://doi.org/10.1007/978-981-15-9472-4_30

1 Introduction

Resemblance is a[1] number that represents how similar 2 vectors or datasets are.[2] This is calculated by the intersection of these vectors divided by their union and is also known as Jaccard Similarity. However, calculating the true resemblance with large datasets can be very slow, hence estimation algorithms like b-bit Minwise Hashing were developed to get an estimate in less time and memory complexity.

By only storing b bits of the (minwise) hashed value, the computational efficiency and usage of storage space are significantly improved as compared to the original Minwise Hashing. However, there are certain drawbacks such as higher variance in the estimated value. Therefore, in the hope of counteracting this effect, the addition of extra known vectors[3] should help in improving the accuracy of the estimated resemblances obtained from b-bit Minwise Hashing. [4] Recall that this method calculates the resemblance between 2 unknown data sets through comparison of a known data set and the 2 unknown data sets and calculating the unknown resemblance from there.

Our group thus hypothesises that our combined method will be have a higher accuracy than the individual methods. In this paper, we are going to discuss the steps and calculations in our method and how we make an estimator of resemblances by using one extra vector in b-bit Minwise Hashing.

2 One Extra Vector

Our idea is similar to the method mentioned in the paper Improving Sign Random Projections With Additional Information [1].

However, instead of using signed random projections, we are trying to apply the idea of an extra vector to b-bit Minwise Hashing to try and improve the accuracy of finding the Jaccard similarity between two data sets. In this paper, we will be trying to find the Jaccard similarity between two datasets.

2.1 Theoretical Resemblance

Given 2 unknown data sets v_1 and v_2 and 1 known data set v_e represented as e, the resemblance between v_1 and v_e will be represented as R_{v_1e}, the resemblance between v_2 and v_e represented as R_{v_2e} and the resemblance between v_1 and v_2 represented as $R_{v_1v_2}$.

[1] The Jaccard Similarity between two sets of data.

[2] Vectors and Datasets here represent ordered sets of data and mean the same thing.

[3] Refer to appendix for a more detailed explanation.

[4] Refer to appendix for a more detailed explanation.

The table below shows the different possibilities in which the 3 data sets, the two unknown and the one known data set, can be related where S means "same" and D means "different".

Cases	v_1	v_2	v_e
P_1	S	S	S
P_2	S	S	D
P_3	S	D	S
P_4	D	S	S
P_5	D	D	D

This S and D are obtained by checking if, after k number of random permutations, the obtained hashed value from the data sets are the same or different from one another.

Note that for 1-bit, the terms can only take up the value of 0 and 1 thus *Case 5* does not exist. Now, we can see that we have 5 cases. Given that R_{v_1e} is where v_1 and v_e are the same, the same can be said for the other resemblances. Hence, it can be concluded that

$$R_{v_1e} = P_1 + P_3$$

$$R_{v_2e} = P_1 + P_4$$

$$R_{v_1v_2} = P_1 + P_2$$

Our main goal is to find the value of $R_{v_1v_2}$ using values from R_{v_1e} and R_{v_2e}.

2.1.1 1-Bit

As mentioned earlier, only P_1 to P_4 is used in the calculations. Hence,

$$P_1 = \frac{N_1}{\Omega} \tag{1}$$

where Ω is equal to the total number of elements in the data set. Following that logic, we can state that

$$\Omega = N_1 + N_2 + N_3 + N_4 \tag{2}$$

The log-likelihood function is

$$l(P_1, P_2, P_3, P_4) = c + \sum_{i=1}^{4} N_i \log(P_1) \tag{3}$$

We already know the value of $P_1 + P_3$ and the value of $P_1 + P_4$ which is equal to R_{v_1e} and R_{v_2e} respectively. Thus, we will express the likelihood function in terms of P_1.

$$\begin{aligned} l(P_1) = N_1 \log(P_1) + N_2 \log(1 - R_{v_1e} - R_{v_2e} + P_1) \\ + N_3 \log(R_{v_1e} - P_1) + N_4 \log(R_{v_2e} - P_1) \end{aligned} \tag{4}$$

The first and second derivatives of the equation are given as follows

$$\begin{aligned} \frac{\mathrm{d}l}{\mathrm{d}P_1} = -\frac{N_1}{P_1} + \frac{N_2}{1 - R_{v_1e} - R_{v_2e} + P_1} \\ + \frac{N_3}{R_{v_1e} - P_1} - \frac{N_4}{R_{v_2e} - P_1} \end{aligned} \tag{5}$$

$$\begin{aligned} \frac{\mathrm{d}^2 l}{\mathrm{d}^2 P_1} &= -\frac{N_1}{(P_1)^2} + \frac{N_2}{(1 - R_{v_1e} - R_{v_2e} + P_1)^2} \\ &\quad + \frac{N_3}{(R_{v_1e-P_1)^2}} - \frac{N_4}{(R_{v_2e} - P_1)^2} \\ &= -\frac{k}{P_1} - \frac{k}{P_2} - \frac{k}{P_3} - \frac{k}{P_4} \end{aligned} \tag{6}$$

We can observe that the first and second derivatives are always equal to 0, giving us the maximum value of P_2. Expressing each of the probabilities in terms of R_{v_1e}, R_{v_2e} and $R_{v_1v_2}$. Recall that $P_1 + P_2 + P_3 + P_4 = 1$.

$$P_1 = \frac{(-1 + R_{v_1e} + R_{v_1e} + R_{v_1v_2})}{2}$$

$$P_2 = \frac{(1 - R_{v_1e} - R_{v_1e} + R_{v_1v_2})}{2}$$

$$P_3 = \frac{(1 + R_{v_1e} - R_{v_1e} - R_{v_1v_2})}{2}$$

$$P_4 = \frac{(1 - R_{v_1e} + R_{v_1e} - R_{v_1v_2})}{2}$$

The equations for 1-bit are highly similar to those in the b-bit Minwise Hashing paper.[5]

[5]Pin, Li., König, A.C. 'b-Bit-Minwise Hashing'.

2.1.2 B-Bit

The first few equations are highly similar to those presented in 1 - bit so we are going to examine the likelihood function straight away. A more in-depth explanation will be provided in the appendix.

For b-bit data, we have to consider all 5 different cases that were mentioned before.

We will now represent the likelihood equation in terms of P_1 and P_2

$$\begin{aligned} l(P_1, P_2) = {} & N_1 \log(P_1) + N_2 \log(P_2) \\ & + N_3 \log(R_{v_1 e} - P_1) + N_4 \log(R_{v_2 e} - P_1) \\ & + N_5 \log(1 - R_{v_1 e} - R_{v_2 e} - P_2 + P_1) \end{aligned} \tag{7}$$

As there are now 2 variables, we will do partial differentiation on P_1 and P_2 twice each and compare their values. P_1 and P_2 are used as they are needed in calculating the final resemblance.

We need to calculate the first and second derivatives for P_1 and P_2 and then use both the second derivatives to do partial differentiation.

$$\frac{\mathrm{d}^2 l}{\mathrm{d}P_1 \mathrm{d}P_2} = \frac{N_5}{(1 - R_{v_1 e} - R_{v_1 e} - P_2 + P_1)^2} \tag{8}$$

$$= \frac{k}{P_5} \tag{9}$$

$$\frac{\mathrm{d}^2 l}{\mathrm{d}P_2 \mathrm{d}P_1} = \frac{N_5}{(1 - R_{v_1 e} - R_{v_1 e} - P_2 + P_1)^2} \tag{10}$$

$$= \frac{k}{P_5} \tag{11}$$

After having the derivatives of the values, we can try to express one of the two values in the log likelihood function in terms of the other. We can substitute that into the other values derivatives. In the end, we can get P_2 in terms of P_1:

$$P_2 = \frac{N_2(1 - E_1 - E2 + P_1)}{N_2 + N5} \tag{12}$$

where E_1 and E_2 [6] are

$$E_1 = R_{v_1 e}(1 - C_{2b1e}) + C_{1b1e} \tag{13}$$

[6] E_1 and E_2 are referenced from the paper "b-Bit Minwise Hashing" by Li, P., Konig, A.C.

$$E_2 = R_{v_2e}(1 - C_{2b2e}) + C_{1b2e} \tag{14}$$

We will then get an equation which can be used for the Newton-Raphson method as well as its derivative, which are both shown below.

$$\begin{aligned} f(x) = {} & P_1^3(N_1 + N_2 + N_3 + N_4 + N_5) \\ & + P_1^2(N_4 - N_2(E_1) - 2N_4(E_1) \\ & - N_5(E_1) + N_1(1 - 2E_2 - 2E_2) - N_2(E_2) \\ & - N_4(E_2) - N_5(E2) - N_3(-1 + E1 + 2E_2)) \\ & + P_1((N_1 + N_4)(E_1)(-1 + E_1) \\ & + E_2(-N_1 - N_3 + E_1(3N_1 + N2 + N3 + N4 + N5) \\ & + E_2^2(N_1 + N3))) - N_1(E_1)(E_2)(-1 + E_1 + E_2) \end{aligned} \tag{15}$$

$$\begin{aligned} \mathrm{d}f(x) = {} & P_1^2(N_1 + N_2 + N_3 + N_4 + N_5) \\ & + P_1(N_4 - N_2(E_1) - 2N_4(E_1) - N_5(E_1) \\ & + N_1(1 - 2E_1 - 2E_2) - N_2(E_2) - N_4(E_2) \\ & - N_5(E_2) - N_3(-1 + E_1 + 2E_2)) \\ & + (N_1 + N_4)(E_1)(-1 + E_1) \\ & + E_2(-N_1 - N_3 + E_1(3N_1 + N2 + N3 + N4 + N5) \\ & + E_2^2(N_1 + N3)) \end{aligned} \tag{16}$$

By using this Newton Raphson method[7] on the equation received from the derivatives in terms of P_1, we can get the actual value of P_1. After getting the actual value of P_1, we can also get the actual values of P_3 and P_4 from substituting P_1 into R_{v_1e} and R_{v_2e} respectively. As for P_2, we have to use Eq. ((16)) to get the real value of P_2. For P_5, we know that $P_1 + P_2 + P_3 + P_4 + P_5 = 1$,[8] and since we know the actual values for P_1 to P_4, we can find the value of P_5.

2.2 Theoretical Variance

We can calculate the theoretical variance of the value calculated using Fisher Information in terms of P_2 for 1-bit and in terms of P_1 and P_2 for b-bit. After getting the equations, we can input the true values which we have gotten earlier for the probabilities and input them into the equations for both 1-bit and b-bit.
The theoretical variance is always equal to or lower than the empirical variance.

[7] More information can be found in the Appendix.

[8] From Eq. (5).

2.2.1 1-Bit

For 1-bit, to find the variance of our maximum likelihood estimator, we have to obtain the Fisher information of P_1 as the maximum likelihood function was expressed in terms of P_1. Below is the equation for the Fisher information of P_1:

$$I(P_1) = -E[\frac{d^2 l}{d^2 P_2}] \tag{17}$$

$$= -E[-\frac{k}{P_1} - \frac{k}{P_2} - \frac{k}{P_3} - \frac{k}{P_4}] \tag{18}$$

$$= k(\frac{1}{P_1} + \frac{1}{P_2} + \frac{1}{P_3} + \frac{1}{P_4}) \tag{19}$$

Hence, the variance we obtain is:

$$Var[P_1] = \frac{1}{k(\frac{1}{P_1} + \frac{1}{P_2} + \frac{1}{P_3} + \frac{1}{P_4})} \tag{20}$$

2.2.2 B-Bit

Below, we are solving for the expected Fisher information of P_1 and P_2, to find the variance for b-bit Minwise Hashing:

$$I(P_1, P_2) = -E[\begin{pmatrix} \frac{\mathrm{d}^2 l}{\mathrm{d}^2 P_1} & \frac{\mathrm{d}^2 l}{\mathrm{d}P_1 \mathrm{d}P_2} \\ \frac{\mathrm{d}^2 l}{\mathrm{d}P_2 dP_1} & \frac{\mathrm{d}^2 l}{\mathrm{d}^2 P_2} \end{pmatrix}]$$

$$= -E[\begin{pmatrix} -\frac{k}{P_1} - \frac{k}{P_3} - \frac{k}{P_4} - \frac{k}{P_5} & \frac{k}{P_5} \\ \frac{k}{P_5} & -\frac{k}{P_2} - \frac{k}{P_5} \end{pmatrix}]$$

$$= E[\begin{pmatrix} \frac{k}{P_1} + \frac{k}{P_3} + \frac{k}{P_4} + \frac{k}{P_5} & -\frac{k}{P_5} \\ -\frac{k}{P_5} & \frac{k}{P_2} + \frac{k}{P_5} \end{pmatrix}] \tag{21}$$

Here is the inverse of the Fisher Information obtained[9]:

$$I^{-1} = \frac{1}{(\frac{k}{P_1} + \frac{k}{P_3} + \frac{k}{P_4} + \frac{k}{P_5})(\frac{k}{P_2} + \frac{k}{P_5}) - \frac{k^2}{P_5^2}} \begin{pmatrix} \frac{k}{P_2} + \frac{k}{P_5} & \frac{k}{P_5} \\ \frac{k}{P_5} & \frac{k}{P_1} + \frac{k}{P_3} + \frac{k}{P_4} + \frac{k}{P_5} \end{pmatrix} \tag{22}$$

[9]This is used in the finding of the variance.

Hence, our reduced variance for b-bit obtained is:

$$Var[P_1, P_2] = \frac{\frac{k}{P_1} + \frac{k}{P_2} + \frac{k}{P_3} + \frac{k}{P_4} + \frac{4k}{P_5}}{(\frac{k}{P_1} + \frac{k}{P_3} + \frac{k}{P_4} + \frac{k}{P_5})(\frac{k}{P_2} + \frac{k}{P_5}) - \frac{k^2}{P_5^2}} \tag{23}$$

2.3 Results

Figure 1 shows the graph comparing the different bias obtained from the code. From Fig. 1, we can see that for the comparison for our method, we can see the bias are mostly converging to 0, which implies that the results obtained are fairly accurate. The extra vector causes a marked decrease in bias.

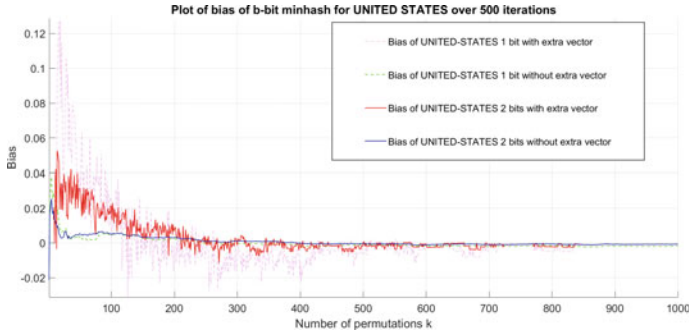

Fig. 1 The graph comparison between bias for the different functions

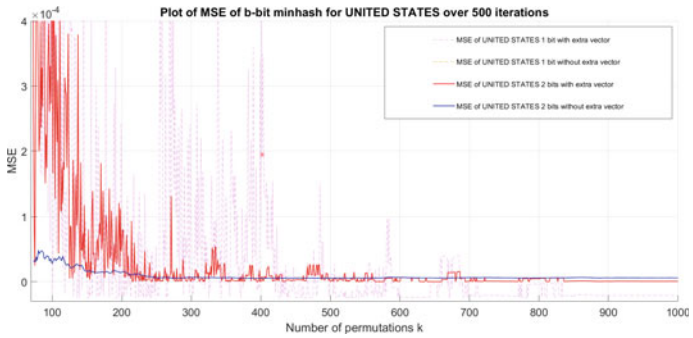

Fig. 2 Mean squared error graph

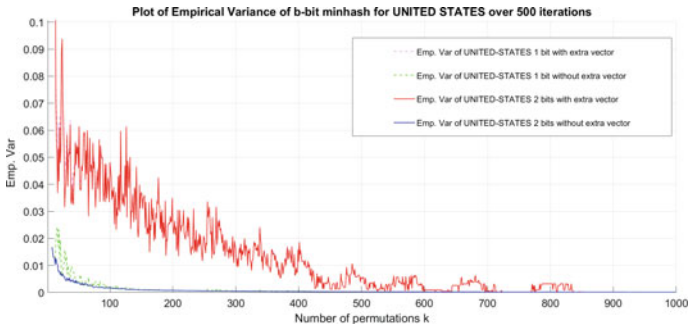

Fig. 3 Empirical variance where $b = 2$

Figure 2 shows that when less than 500 iterations have been run, the MSE is higher with an extra vector, however with more iterations the MSE of the modified algorithm is lower.

Figure 3 shows that at higher iterations, the variance is also reduced as compared to the unmodified equation.

3 2 Extra Vectors

With multiple extra vectors, there will be more comparison between the 2 known vectors which can allow greater accuracy. Thus, it is theorised that there will also be a corresponding decrease in variance. Due to certain time constraints, we only had time to do the calculations for the theoretical variance for b-bit.

The method is similar to 1 extra vector, but there are a lot more possibilities due to the addition of the extra known vector. Hence, we will go into detail with the more complicated calculations.

For 1 extra vector, P_1: SSS, P_2: SSD, P_3: SDS, P_4: DSS, P_{15}: DDD. However, with 2 extra vectors, the permutations are very different. The possible permutations are as shown below where the possible values are unlimited, for demonstration purposes, values 0, 1, 2 and 3 will be used to prevent ambiguity among same-number pairs. Take note that the possible values depend on the number of bits that are calculated.

Cases	v_1	v_2	v_{e_1}	v_{e_2}
P_1	1	1	1	1
P_2	1	1	1	0
P_3	1	1	0	1
P_4	1	0	1	1
P_5	0	1	1	1
P_6	0	0	1	2
P_7	1	2	0	0
P_8	1	0	2	1
P_9	1	0	0	2
P_{10}	0	1	2	0
P_{11}	1	0	2	2
P_{12}	0	1	2	3
P_{13}	0	0	1	1
P_{14}	0	1	0	1
P_{15}	0	1	1	0

Hence, it can be concluded.

$$R_{v_1e_1e_2} = P_1 + P_4$$

$$R_{v_2e_1e_2} = P_1 + P_5$$

$$R_{v_1e_1} = P_1 + P_2 + P_4 + P_8 + P_{14}$$

$$R_{v_2e_1} = P_1 + P_2 + P_5 + P_9 + P_{15}$$

$$R_{v_1e_2} = P_1 + P_3 + P_4 + P_{10} + P_{15}$$

$$R_{v_2e_2} = P_1 + P_3 + P_5 + P_{11} + P_{14}$$

$$R_{v_1v_2} = P_1 + P_2 + P_3 + P_6 + P_{13}$$

Now,

$$\Omega = N_1 + N_2 + N_3 + N_4 + N_5 \tag{24}$$

Implying that,

$$1 = P_1 + P_2 + P_3 + P_4 + P_5 \tag{25}$$

The log-likelihood function is now changed to

$$l(P_1, P_2, P_3, P_4, P_5, P_6, P_7, P_8, P_9, P_{10}, P_{11}, P_{12}, P_{13}, P_{14}, P_{15})$$

$$= c + \sum_{i=1}^{15} N_i \log(P_1)$$

We already know the value of the resemblances between the different vectors and can use these to represent the possibilities in terms of P_1, P_2, P_3, P_6, P_{13} and the resemblances. We can substitute these values into the likelihood function and we will get the following equation.

$$\begin{aligned} l(P_1, P_2, P_3, P_6, P_{13}) = {} & N_1 \log(P_1) + N_2 \log(P_2) \\ & + N_3 \log(P_3) + N_4 \log(R_{v_1e_1e_2} - P_1) \\ & + N_5 \log(R_{v_2e_1e_2}) + N_6 \log(P_6) \\ & + N_7 \log(R_{e_1e_2} - R_{v_1e_1e_2} + P_1 - P_{13} - R_{v_2e_1e_2}) \\ & + N_8 \log(R_{v_1e_1} - P_2 - R_{v_1e_1e_2} - P_{14}) \\ & + N_9 \log(R_{v_2e_1} - P_2 - R_{v_1e_1e_2} - P_{15}) \\ & + N_{10} \log(R_{v_1e_2} - R_{v_1e_1e_2} - P_3 - P_{15}) \\ & + N_{11} \log(R_{v_2e_2} - P_3 - R_{v_1e_1e_2} - P_{14}) \\ & + N_{12} \log(1 + P_2 + P_3 - P_6 + P_{14} + P_{15} - R_{e_1e_2} \\ & - R_{v_1e_1} - R_{v_1e_2} + 4R_{v_1e_1e2} - R_{v_2e_1} - R_{v_2e_2}) \\ & + N_{13} \log(P_{13}) + N_{14} \log(P_{14}) + N_{15} \log(P_{15}) \end{aligned} \tag{26}$$

To calculate the theoretical variance, we need to utilise the following equation:

$$\begin{aligned} Variance[P_1, P_2, P_3, P_6, P_{13}] = {} & \frac{d^2l}{d^2P_1} + \frac{d^2l}{d^2P_2} + \frac{d^2l}{d^2P_3} + \frac{d^2l}{d^2P_6} + \frac{d^2l}{d^2P_{13}} \\ & + 2\frac{d^2l}{d^2P_1d^2P_2} + 2\frac{d^2l}{d^2P_1d^2P_3} + 2\frac{d^2l}{d^2P_1d^2P_6} \\ & + 2\frac{d^2l}{d^2P_1d^2P_{13}} + 2\frac{d^2l}{d^2P_2d^2P_3} \\ & + 2\frac{d^2l}{d^2P_2d^2P_6} + 2\frac{d^2l}{d^2P_2d^2P_{13}} \\ & + 2\frac{d^2l}{d^2P_3d^2P_6} + 2\frac{d^2l}{d^2P_3d^2P_{13}} \\ & + 2\frac{d^2l}{d^2P_6d^2P_{13}} \end{aligned} \tag{27}$$

The final reduced variance is found by substituting in the second derivatives of the unknowns and the partial derivatives as required. The process is very similar to the one used in 1 extra vector. However, due to a large number of variable, the matrix for the Fisher Information will be extremely large. We used Mathematica programme to help us do the inverse calculations and the final equation will look like this.

$$\text{Variance} = \frac{\begin{array}{r}(P_1 + P_2 + P_3 - P_4 + 3P_5 + P_6 + P_7 + P_8 + \\ P_9 + P_{10} + P_{11} + P_{13} + P_{14} + P_{15} - 1)^2 \\ (N_1N_3N_6N_{13}(P_2)^2 + N_2(N_1N_6N_{13}(P_3)^2 + \\ N_3(N_1N_{13}(P_6)^2 + N_6(N_{13}(P_1)^2 + N_1(P_{13})^2))))\end{array}}{\begin{array}{r}N_2N_3N_6N_{12}N_{13}(P_1)^2 + N_1N_3N_6N_{12}N_{13}(P_2)^2 + \\ N_1N_2N_6N_{12}N_{13}(P_3)^2 + N_1N_2N_3N_{12}N_{13}(P_6)^2 + \\ N_1N_2N_3N_6N_{12}(P_{13})^2 + N_1N_2N_3N_6N_{13}(P_1 + P_2 + \\ P_3 - P_4 + 3P_5 + P_6 + P_7 + P_8 + P_9 + P_{10} + \\ P_{11} + P_{13} + P_{14} + P_{15} - 1)^2\end{array}} \tag{28}$$

4 Conclusion

Our proposed method of combining b - bit minwise hashing and sign random projections to reduce variance and thus increase accuracy has proven to be more effective than each of the individual methods. Recall that in sign random projections, only 1 extra vector was included. Hence, our group also proposed in theory that adding 2 extra vectors would reduce the variance even further. This has been proven through theoretical calculations but not yet proven with actual processing of data sets using our algorithm. It thus follows that our hypothesis is true and that combining the 2 methods will indeed have a higher accuracy when estimating the resemblances of 2 unknown data sets.

5 Future Work and Applications

From the work that has been completed so far, more research can be done as an extension in the future. One such possibility is trying to find out the optimal additional vector that can be used to return the best resemblance from b-bit Minwise Hashing. Another possible future work is by finding the full algorithm and thus, the empirical variance reduction for 2 extra vectors. Applications of Minwise Hashing range from information retrieval[10] and data management to social networks and computational advertising. This makes the project highly impactful on the current society as various applications of b-bit Minwise Hashing with extra vectors will be able to allow for more accurate information retrieval.

[10] Used in search engines such as in Google.

6 Appendix

6.1 Minwise Hashing and B-Bit

In the Minwise Hashing algorithm, a random permutation pi is performed upon Ω. Thus, it can be seen that

$$Pr(min(\pi(S_1)) = min(\pi(S_2))) = \frac{|S_1 \cap S_2|}{|S_1 \cup S_2|} = R$$

The estimate can thus be found after a number k independent permutations, which will give an estimate without bias. [11]

In the paper on Minwise Hashing, we have a random permutation performed on Ω. After k number of minwise independent permutations, we can find the estimated resemblance without bias. A hashed value in Minwise Hashing usually requires 64 bits to store it.

B-bit Minwise Hashing is an extension to Minwise Hashing in which instead of storing the entire hash, only the first b bits of the hash are stored. This allows for less memory and storage use, as well as fewer computations needed.

6.2 The Use of Extra Vectors

Extra Vectors are in theory meant to reduce the variance of the estimation with minimal time loss. Usually, this Extra Information is a known vector with pre-calculated resemblance values with the unknown values. This allows the calculation to take place in a similar time frame. The extra information given thus allows for some variance reduction.

6.3 1 Extra Vector

6.3.1 1 - Bit

Here is the full complete explanation and table for P_1 to P_4 to calculate the **Theoretical Variance of 1-bit**:

Here, with only 1-bit data, we have only 4 cases, P_1 to P_4 with the last case P_5 not included. This is because there are only two possible values since it is at 1-bit. The possible permutations are as shown below where there are only 2 possible values for each term, 0 and 1:

[11] b-Bit Minwise Hashing. Ping Li and Arnd Christian König.

Cases	v_1	v_2	v_e
P_1	1	1	1
P_2	1	1	0
P_3	1	0	1
P_4	0	1	1

We understand that P_1 is the probability that the element in the same position across all 3 vectors that fits into the criteria of "SSS". The same reasoning is used for P_2, P_3 and P_4.

6.3.2 B-Bit

Here is the full complete explanation and table for P_1 to P_5 to calculate the **Theoretical Variance of b-bit**

P_1: SSS, P_2: SSD, P_3: SDS, P_4: DSS, P_5: DDD with the last case P_5 included unlike 1-bit. The possible permutations are as shown below where the possible values are unlimited, for demonstration purposes, values 0, 1 and 2 will be used. Take note that the possible values depend on the number of bits that are calculated.

Cases	v_1	v_2	v_e
1	1	1	1
2	1	1	0
3	1	0	1
4	0	1	1
5	0	1	2

Now,

$$\Omega = N_1 + N_2 + N_3 + N_4 + N_5 \tag{29}$$

Implying that,

$$1 = P_1 + P_2 + P_3 + P_4 + P_5 \tag{30}$$

The log-likelihood function is now changed to

$$l(P_1, P_2, P_3, P_4, P_5) = c + \sum_{i=1}^{5} N_i \log(P_1) \tag{31}$$

The first and second derivatives of the two variables are as follows
The first and second derivatives of P_1:

$$\frac{dl}{dP_1} = -\frac{N_1}{P_1} - \frac{N_3}{R_{v_1e-P_1}} - \frac{N_4}{R_{v_2e} - P_1} + \frac{N_5}{1 - R_{v_1e} - R_{v_1e} - P_2 + P_1} \tag{32}$$

$$\begin{aligned}\frac{d^2l}{d^2P_1} &= -\frac{N_1}{P_1^2} - \frac{N_3}{(R_{v_1e} - P_1)^2} - \frac{N_4}{(R_{v_2e} - P_1)^2} \\ &\quad + \frac{N_5}{(1 - R_{v_1e} - R_{v_1e} - P_2 + P_1)^2} \\ &= -\frac{k}{P_1} - \frac{k}{P_3} - \frac{k}{P_4} - \frac{k}{P_5}\end{aligned} \tag{33}$$

The first and second derivatives of P_2:

$$\frac{dl}{dP_2} = \frac{N_2}{P_2} - \frac{N_5}{1 - R_{v_1e} - R_{v_1e} - P_2 + P_1} \tag{34}$$

$$\frac{d^2l}{d^2P_2} = \frac{N_2}{P_2^2} - \frac{N_5}{(1 - R_{v_1e} - R_{v_1e} - P_2 + P_1)^2} \tag{35}$$

$$= -\frac{k}{P_2} - \frac{k}{P_5} \tag{36}$$

6.4 2 Extra Vectors

Below are all the second derivatives and the partial derivatives substituted into the equation:

$$\begin{aligned}\frac{d^2l}{d^2P_1} &= -\frac{N_1}{(P_1)^2} - \frac{N_4}{(-P_1 + R_{v_1e_1e_2})^2} - \frac{N_5}{(-P_1 + R_{v_2e_1e_2})^2} \\ &\quad - \frac{N_7}{(P_1 - P_{13} + R_{e_1}e_2 - R_{v_1e_1e_2} - R_{v_2e_1e_2})^2}\end{aligned} \tag{37}$$

$$\frac{d^2l}{d^2P_2} = -\frac{N_2}{(P_2)^2} - \frac{N_8}{(-P_2 - P_{14} + R_{v_1e_1} - R_{v_1e_1e_2})^2} - \frac{N_9}{(-P_2 - P_{15} - R_{v_1e_1e_2} + R_{v_2e_1})^2} - \frac{N_{12}}{(1 + P_2 + P_3 - P_6 + P_{14} + P_{15} - R_{e_1e_2} - R_{v_1e_1} - R_{v_1e_2} + 4R_{v_1e_1e2} - R_{v_2e_1} - R_{v_2e_2})^2} \tag{38}$$

$$\frac{d^2l}{d^2P_3} = -\frac{N_3}{(P_3)^2} - \frac{N_{10}}{(R_{v_1e_2} - R_{v_1e_1e_2} - P_3 - P_{15})^2} - \frac{N_{11}}{(R_{v_2e_2} - P_3 - R_{v_1e_1e_2} - P_{14})^2} - \frac{N_{12}}{(1 + P_2 + P_3 - P_6 + P_{14} + P_{15} - R_{e_1e_2} - R_{v_1e_1} - R_{v_1e_2} + 4R_{v_1e_1e2} - R_{v_2e_1} - R_{v_2e_2})^2} \tag{39}$$

$$\frac{d^2l}{d^2P_6} = -\frac{N_6}{(P_6)^2} - \frac{N_{12}}{(1 + P_2 + P_3 - P_6 + P_{14} + P_{15} - R_{e_1e_2} - R_{v_1e_1} - R_{v_1e_2} + 4R_{v_1e_1e2} - R_{v_2e_1} - R_{v_2e_2})^2} \tag{40}$$

$$\frac{d^2l}{d^2P_{13}} = -\frac{N_7}{(P_7)^2} - \frac{N_7}{(P_1 - P_{13} + R_{e_1}e_2 - R_{v_1e_1e_2} - R_{v_2e_1e_2})^2} \tag{41}$$

The Newton Raphson method which was continuously looped until the estimates that are received all converge onto one value, which will be the root of the equation which we are finding for.

References

1. Kang, K., Wong, W.P. 'Improving sign random projections with additional information' URL http://proceedings.mlr.press/v80/kang18b/kang18b.pdf
2. Ping L., A. Christian König. 'b-Bit Minwise Hashing' WWW 2010

Biobutanol Biofuel Production via ABE Fermentation from Bread Waste for an Energy-Sustainable Singapore

Quek Shao-Yen Joseph, Koh Wen Jie Justin, Heok Yee Han Jovian, Su Guandong, and He Jianzhong

Abstract The generation of bread wastage due to an oversupply of bread products contributes significantly to Singapore's annual food waste, which is mainly incinerated or dumped in landfills. Both methods are highly energy-inefficient and harmful to the environment. Biofuel production from cheap substrates has been a focus for more than three decades with lignocellulosic biomass as the key substrate. However, it faces many limitations such as low butanol yield and high costs for obtaining the substrate. Here bread waste is identified as a viable substrate for butanol production via Acetone-Butanol-Ethanol (ABE) fermentation. It was found that using bread waste as a substrate, the fermentation process had a shorter acidogenesis phase and greater bacterial and enzyme activity as compared to using glucose as a substrate. This correlates to greater butanol production yields and a higher ABE productivity. In addition, local bakeries were surveyed on their daily bread production and handling of excess bread. Results show an overwhelming majority of the bakeries surveyed disposed of their excess bread, producing a substantial amount of bread waste. It can be concluded that bread waste is potentially viable for butanol production, thus providing a more efficient method for energy production to meet energy needs, and establishing a less- harmful, alternative method of treating bread waste.

Keywords Biofuel · ABE fermentation · Clean energy · Clostridium sp. strain BOH3

1 Introduction

Food waste is one of the biggest waste streams in Singapore and the amount of food waste generated has grown by around 30% over the last 10 years. 763 million kg

Q. S.-Y. Joseph (✉) · K. W. J. Justin · H. Y. H. Jovian
NUS High School of Math and Science Singapore, Singapore, Singapore
e-mail: h1710111@nushigh.edu.sg

S. Guandong · H. Jianzhong
Department of Civil and Environmental Engineering, National University of Singapore, Singapore, Singapore

H. Guo et al. (eds.), *IRC-SET 2020*,
https://doi.org/10.1007/978-981-15-9472-4_31

of food waste was generated in 2018 itself with rice, noodles and bread being the most wasted food items. Food waste in Singapore is mainly incinerated or dumped in landfills, with both methods being highly energy-inefficient and harmful to the environment. Though renewable energy sources are available globally, Singapore imports almost all its energy needs as it has limited renewable energy options. High population density and land scarcity limits our potential for sustainably grown domestic biomass and constraints the safe deployment of nuclear power in Singapore. Therefore, this experiment aims to find more energy-efficient methods of food waste disposal and cost- effective substrates for biobutanol production.

Biofuel production from cheap substrates has been a focus for more than three decades with lignocellulosic biomass as the key substrate. However, it faces many limitations such as low butanol yield and high costs for obtaining the substrate [1]. Through our experiment, the alternative use of bread waste as substrate has been surfaced. Not only is it economically efficient, it opens up another method of food waste disposal.

Acetone-Butanol-Ethanol (ABE) fermentation had been used in this experiment. It is a biphasic process which involves bacterial fermentation that converts carbohydrates such as starch and glucose into acids (acetate and butyrate) and solvents (acetone, n-butanol, ethanol) through a series of hydrolysis and reduction reactions. The bacteria often used in this process is Clostridia which is rod-shaped, spore-forming gram-positive and obligate anaerobe. During the first phase, acidogenesis, carbohydrates are depolymerized into soluble compounds by hydrolytic enzymes and fermented into volatile fatty acid. As the pH decreases, metabolism shifts to solventogenesis and the acids are assimilated into the ABE solvents [2, 3].

Butanol, a four-carbon alcohol with five isomeric structures produced from ABE fermentation is used for various purposes. The main reason for the demand for butanol is the usability of butanol as an efficient biofuel. Butanol has a high calorific value (29.2 MJ/dm), low heat of vaporization (0.43 MJ/kg) and is less corrosive compared to ethanol [4]. Butanol has many Industrial uses of butanol includes its usage in gasoline engines, lubricants, brake fluids and the synthesis of plastics, polymers, synthetic rubber. In this experiment, it has been concluded that bread is a feasible alternative to produce biobutanol of higher yield than traditional substrates. Hence, this will not only provide more energy-efficient methods of food waste disposal but also cost- effective substrates for biobutanol production.

2 Materials and Methods

2.1 Pretreatment

A wild-type *Clostridium* sp. Strain BOH3, isolated in a previous study [5], was used throughout this study. Medium composition for seed culture included bread of different concentrations, 0.2 g/L KH2PO4, 0.3 g/L NH4Cl, 0.5 g/L MgCl2·6H2O,

0.3 g/L KCl, 1.0 g/L NaCl. *Enriched Softmeaz* whole grain bread from *Sunshine* by *Auric* was obtained to represent bread waste as the carbon source in the fermentation process. Any trace of moisture in the bread was removed via heating in a furnace and the dried mass was rubbed together to produce a powdered substance.

The dried bread substance (100 g/L) was added into a bacteria culture bottle. Then, the bottle was autoclaved at 115 °C for 15 min to kill any bacteria possibly living within. The interior of the culture bottle was washed with nitrogen to displace any remaining oxygen to ensure an anaerobic environment. It was then sealed with a rubber stopper and strengthened with an aluminium ring. 30 mL of the prepared bacteria medium (Please see Appendix for full composition), mineral salts, plus a trace element solution were added into the fermentation medium. Anaerobic medium (pH 6.0) was prepared with an addition of 0.0242 g/L L-cysteine and 0.048 g/L Na2S·6H2O, respectively [6].

2.2 Experimental Set-up

A control set-up, identical to the first, was also prepared, with the only change being the use of a glucose solution (58.85 g/L) in the fermentation medium. This acted as the baseline of butanol production using the ABE fermentation process and served as a comparison for the effectiveness of bread waste conversion using this process. For a period of 6 days after the start of fermentation, the release of accumulated gaseous products and adjustment of medium's pH were conducted regularly every day. Adjustment of pH was carried out using 3.0 M NaOH solutions. The volumes of gases released, and solutions used for pH adjustment were recorded. Sampling of fermentation medium was also carried out every day. Samples were extracted into Eppendorf tubes and subsequently refrigerated till the last day of experimentation to carry out gas chromatography.

In addition to our experimentation, we conducted a survey at 25 small-to-mid sized bakeries, by asking a series of questions regarding their daily bread production and leftovers at the end of each day. Bakeries were also asked how they dealt with the wastage. The collated data was tabulated and used for further comparisons.

3 Results

The bread and bacterial medium were pre-treated as mentioned in 2.1 to (1) remove excess water from the bread and (2) create an anaerobic environment for the bacteria and (3) ensure to the best of our ability that only *Clostridium acetobutylicum* strain BOH3 was in each bacteria culture bottle. and underwent the fermentation process mentioned in 2.2. 3 parallel set-ups of ABE Fermentation in medium containing bread as the carbon source was conducted with pH adjustments done every day to test the feasibility of bread waste as a possible substrate for biobutanol production. It

is important to note that the amount of glucose used was chosen to match the amount of carbohydrates in the dried bread (Figs. 1, 2).

From Fig. 3, it is observed that in both graphs, the levels of organic acids (acetate and butyrate) increase from 0 h, and after a certain point, begins to decrease before maintaining at a certain level. The phase where the levels of organic acids increase is the acidogenesis phase and the decrease is the transition into solventogenesis. However, in can be noted in both the bread and glucose group, the acetate maintained at a relative constant level after acidogenesis with no significant decrease. From our results, the bread group had a shorter acidogenesis phase of 27.5 h compared to the glucose group who had an acidogenesis phase of 47.5 h hence it is safe to say that the glucose group only fully transitioned to the solventogenesis phase after 70 h while the bread group fully transitioned at 47.5 h.

The feasibility of bread waste as a possible substrate is dependent on the amount of ABE Solvents produced. Our second finding was, using bread as a substrate produced a maximum of 11.34 g/L of butanol using 100 g/L of bread at 70 h, while using glucose as a substrate with the same concentration only yielded a maximum

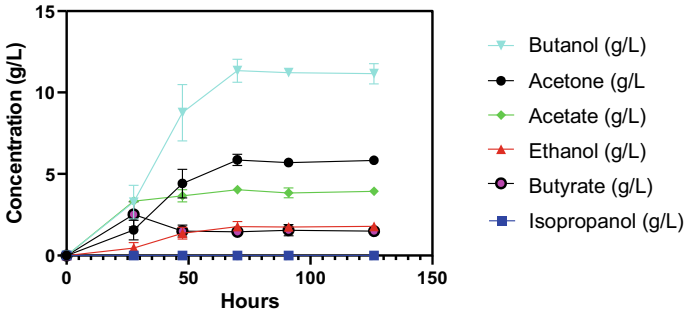

Fig. 1 Concentration of 6 organic solvents for bread group over 126 h for observation of acidogenic and solventogenic phases

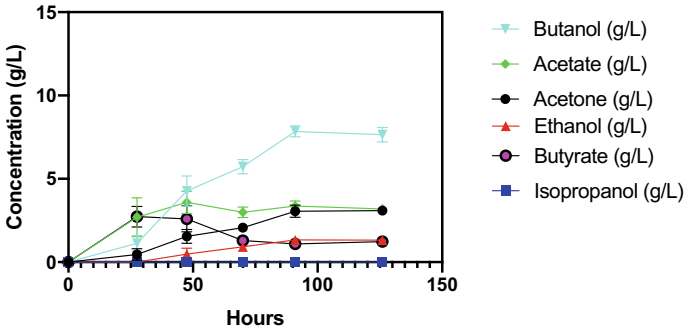

Fig. 2 Concentration of 6 organic solvents for glucose group over 126 h for observation of acidogenic and solventogenic phases

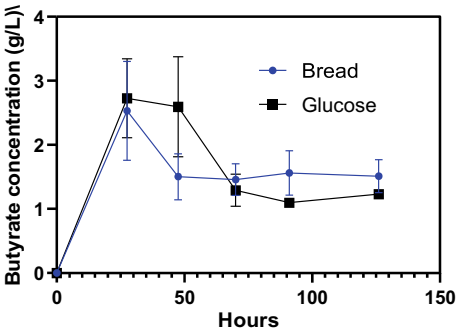

Fig. 3 Comparison of concentration of butyrate between bread group and glucose group over 126 h

of 7.85 g/L of butanol at 91 h. (Figure 3) Similarly, using bread as the substrate, a maximum of 5.87 g/L of acetone (Fig. 4) and a maximum of 1.80 g/L of ethanol was produced at 70 h (Fig. 5), as compared to the maximum of 3.06 g/L of acetone (Fig. 4) and the maximum of 1.33 g/L of ethanol (Fig. 5) produced at 91 h when glucose was

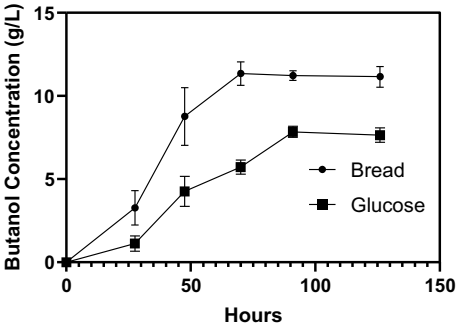

Fig. 4 Comparison of concentration of acetone between bread group and glucose group over 126 h

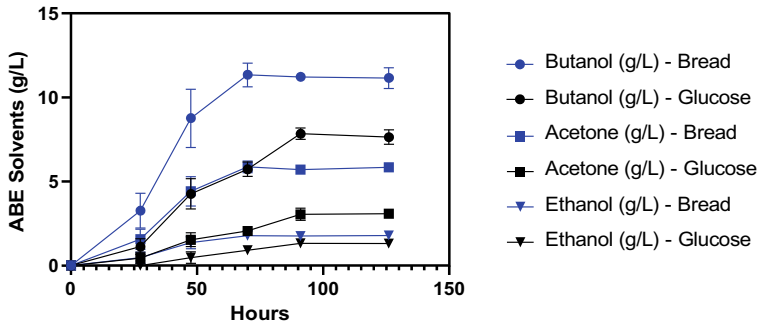

Fig. 5 Comparison of concentration of ABE Solvents between bread group and glucose group over 126 h

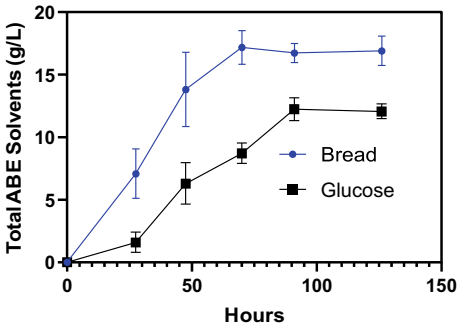

Fig. 6 Comparison of concentration of total ABE Solvents between bread group and glucose group over 126 h

the substrate. For all ABE, the bread group produced a greater amount compared to the glucose group and in a shorter time. The production of ABE Solvents in shorter time becomes important when we factor in the time cost trade-off (Fig. 6).

Our third finding was enzyme and bacterial activity was higher when bread was used as a substrate as compared to when glucose was used as a substrate. At specific timings, the gas in the culture bottle was collected. The gas collected consisted of hydrogen gas and carbon dioxide. The gas collected can be used as an indicator of enzyme and bacterial activity, but further tests have to be done to obtain the specific cell activity. From Fig. 7, at 47.5 h, both the gas collected for the bread group and the glucose group peaks. However, 327.7 mL of gas was collected from the bread group at 47 h, compared to the 146.3 mL of gas collected from the glucose group at 47.5 h. Hence this shows that there was greater enzyme and bacterial activity when bread was used as a substrate as compared to when glucose was used as a substrate (Fig. 8).

Our survey results showed that 84% of bakeries disposed of their leftover bread while 4% of bakeries donated excess bread to charities. The remaining 12% returned their excess bread back to their headquarters This was observed mostly for bakery

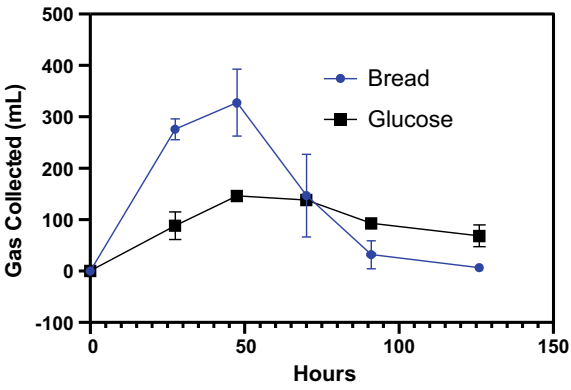

Fig. 7 Comparison of change in gas collected between bread group and glucose group over 126 h

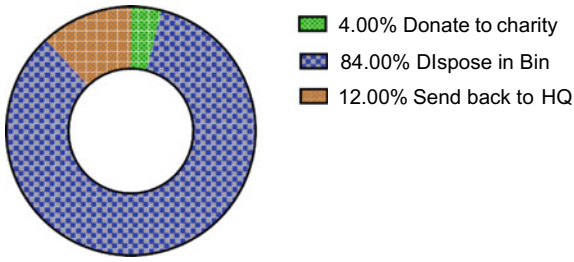

Fig. 8 Pie Chart of disposal methods of 25 bakeries in Singapore

chains. However, the results might not accurately reflect exact percentages as the survey was conducted locally and is small-scale (sample size of 25 bakeries).

Through the same survey, we found out that each bakery's amount of excess bread is 1%-10% of the total bread produced on that day. On average, the bakeries surveyed produced 1650pcs of bread per day (bakeries gave estimates to the nearest hundred), with some mentioning that production varied additionally according to demand. Using the data, we calculate that the daily bread waste per store sits at around 82.5 pcs (assuming that 5% of daily production is wasted). In Singapore, there are around 308 bakeries and only 84% of bakeries directly dispose waste and every piece of bread is estimated to weigh 0.45 kg we can estimate the annual bread waste produced as follows:

$$82.5 \times 365 \times 308 \times 84\% \times 0.45\text{kg}, = 3505817.7\,\text{kg}$$

Cross-referencing to data from *Statista* [7] which puts the annual volume of bread production in Singapore in 2019 at 77.34mkg (million kg). Using parameters from our survey findings (84% of bakeries directly dispose bread waste and 5% of daily production is wasted), the estimate of annual bread waste production is calculated at 3,533,801.96 kg. Evidently, the estimate we acquired is quite accurate and we will be using that number moving forward.

4 Discussion

AIn this study, we investigated (1) the feasibility of using bread as a substrate to produce biobutanol by ABE Fermentation using *C. acetobutylicum* strain BOH3 and (2) the extent of bread wastage in Singapore and predict an estimated amount of biofuel that can be produced using ABE Fermentation. Our results show that bread is a feasible substrate which produced greater yield and productivity of ABE Solvents is due to the presence of nutrients in the bread substrate which led to shorter acidogenesis phase and greater enzyme and bacterial activity.

Aforementioned, the bread group had a shorter acidogenesis phase compared to the glucose group and based on our findings, the bread group had increased enzyme and bacterial activity as compared to the glucose group which suggests that bread

waste supports the growth of *C. acetobutylicum.* Since bread had greater enzyme and bacterial activity than glucose despite having similar carbohydrate content, this points to there being other compositions in the bread substrate that on top of carbohydrate composition, possibly enhanced the cell growth and thereby increasing ABE production. A possible reason for this is the fact that bread waste contains nutrients that aid the growth of the bacteria whilst glucose does not. The bread we used - *Enriched Softmeal* whole grain bread from *Sunshine* by *Auric* – contained many such nutrients. Zhang et al. [8] has shown that Fe2 + from iron and Ca2 + from calcium exhibited strong positive correlation with butanol production, which could be a cause of increased ABE production. Calcium and iron which was in the bread support glycolysis, growth and ABE biosynthesis of solventogenic *Clostridium* species and together with the nitrogen content of the bread in protein (Table 1), played a pivotal role in cell growth on these substrate, especially in the early acidogenesis phase when starch hydrolysis may have been rate-limiting when compared to glucose. This allowed for greater cell and enzyme activity, leading to greater production and yield of ABE solvents, especially butanol. Li et al. [9–11] has also shown that cell growth and butanol concentration increased along with the increase of niacin concentration in the fermentation medium. The acidogenesis phase of *C. acetobut*ylicum strain BOH3's fermentation process is important as acetate and butyrate; precursors of ABE, and reducing cofactors (NADH and NADPH) are pivotal for starting and maintaining solventogenesis [7, 8, 12]. The pH of the fermentation media dropped with the increase in butyrate and acetate, both acidic in nature, during the acidogenesis phase *of C. acetobutylicum* strain BOH3 followed by an increase in pH and decrease in organic acid levels as *C. acetobutylicum* strain BOH3 transitioned to solventogenesis from acidogenesis. This observation of organic acid levels fluctuation is confirmed the typical behaviour in solventogenic *Clostridium*, which produce ABE solvents from a variety of carbon sources in a two-phase fermentation process referred to as biphasic fermentation.

Table 2 compares the performance of ABE fermentation between bread and traditional glucose as substrates. It shows that (1) bread outperforms glucose as a substrate in all performance indicators (butanol produced, butanol yield, ABE produced, ABE yield and ABE productivity). and (2) the efficiency of ABE fermentation obtained in this study with *C. acetobutylicum* strain BOH3 and bread as a substrate, in terms of ABE productivity, is higher than the results of previous works.

Comparing ABE fermentation from bread and from glucose, the butanol yield from bread (0.26 g butanol g bread-1 and 0.20 g butanol g bread-1) is much higher than the butanol yield of glucose (0.14 g butanol g glucose-1). It is also important to note that the carbon source used for the comparison were relatively similar in

Table 1 Content of certain nutrients in enriched softmeal whole grain bread from sunshine by Auric (nutrition information taken off nutrition facts label of product)

Nutrients	Proteins	Carbohydrates	Sodium	Iron	Calcium	Thiamine	Riboflavin	Niacin
Per 100 g	9.0 g	39.6 g	385 mg	6.5 mg	195 mg	0.56 mg	0.51 mg	5.20 mg

Table 2 Comparing production of acetone-butanol-ethanol by solventogenic Clostridium species using different carbon sources

Carbon source	Microorganism	Butanol produced (g/L)	Butanol yield (g butanol/g carbon source	ABE Produced (g/L)	ABE yield (g ABE/g carbonsource	ABE productivity (g/Lh)	References
Breading (92 g/L)	*C. beijerinckii* NCIMB 8052	10.5	0.26	14.8	0.36	0.20	[12]
Bread 100 g/L containing 56.85 g/L of carbohydrates	*C. acetobutylicum* Strain BOH3	11.34	0.20	17.2	0.30	0.25	This study
Glucose (56.85 g/L)	*C. acetobutylicum* Strain BOH3	7.85	0.14	12.23	0.22	0.13	This study

terms of amount and the large difference in butanol yield can be attributed to the type of substrate. The largest performance difference between using bread and glucose is the ABE productivity. Using bread as substrate performed 1.92 × better than using glucose as a substrate. Logically, this is due to shorter time or/and greater ABE production. In this case, using bread as a substrate produced significantly more ABE, up to 164% more in 23% less time as compared to when glucose was used as a substrate. Compared to previous studies, this study produced a relatively high butanol production of 11.34 g/L. However, the butanol yield was lower than the other study in Table 2. Ujor et al. [12] achieved a butanol yield of 0.26 with only a carbon source of 0.92 g/L of bread, from this we can infer that most likely, the study achieved a higher carbon source utilization than our study. However, compared to the same study, our study achieved a higher ABE productivity but a lower ABE yield which is a sign that a possible direction of future work could lie in increasing the carbon source utilization to achieve a greater'ABE yield and in turn a higher ABE productivity. It is important to note that current results of an ABE productivity of 0.25 is very promising and supports that bread waste is feasible and better than glucose as a substrate for biobutanol production to produce ABE solvents for usage.

Previous studies have also supported our results. Growth of solventogenic *Clostridium* species such as *C. beijerinckii* NCIMB 8052 and *C. acetobut*ylicum on inedible dough, bread and batter liquid-based culture media is characterized by short acidogenesis and rapid transition to solventogenesis, low accumulation of acids and better butanol titers relative to the glucose group (Table 2 and Figs. 1, 2 and 3), it is inferred that fermentation of bread, despite its polymeric nature, which leads to initial microbial hydrolysis to fermentable sugars [12], is feasible for ABE production.

In Singaporean context, the treatment of food wastes is not novel, however, the production of biofuel from bread waste is. The production of biofuels from food waste is not impossible, but the wide range of differing chemical compositions of food wastes makes it difficult to optimize biofuel production from them. Furthermore, the pre-treatment process for food waste includes sorting and blending, which are long and tedious, leading to additional costs and a decrease in productivity, thus reducing the feasibility of biofuel production in a modern Singapore due to the economic costs and time involved. However, there are policies in Singapore that encourage owners/operators of premises to sort their food waste. This would make it easier to implement biobutanol production from bread waste. Moreover, since most bread waste comes from bakeries, by only collecting from bakeries, we can ensure that we would only receive bread waste and remove the sorting phase of food waste pre-treatment. Using the data collected in this study, we can estimate the amount of butanol that can be collected in a year. Assuming we are able to recover 100% of the butanol, since the butanol yield previously calculated (Table 2) is 0.2, and the estimate of annual bread wasted is 3533801.96 kg, the butanol that can be produced a year is 707,000 kg of butanol.

Most investigations on the production of biobutanol from cheap substrates during the past three decades focused on lignocellulosic biomass. Hence investigating the feasibility of bread waste as a substrate was mostly ignored by researchers. Based on results from this study, the butanol production profile is comparable to that of other

solventogenic *Clostridium* species grown on related non-lignocellulosic substrates. And it is indeed feasible to use bread waste as a substrate for ABE fermentation for biobutanol synthesis.

5 Conclusion

In this study the feasibility of bread waste as a possible substrate was evaluated and ABE yields obtained on bread waste was better than those obtained when *C. acetobutylicum* was grown on glucose (this study). Furthermore, ABE productivity in this study fare well against previous studies by different solventogenic species. Put together, we have proven that bread waste is a feasible substrate for the production of biobutanol from ABE fermentation given the impact of traditional substrate costs on overall production costs of biobutanol. The abundance of bread waste makes it ideal as a substrate for use for a sustainable Singapore.

Using bread as a substrate for butanol production has key advantages over lignocellulosic biomass; bread not only produces higher butanol yield, it is also much cheaper to obtain since we are repurposing expired bread. In addition, bread has a short fermentation period of three days, which will further increase the feasibility of this method of waste treatment. With a low starting cost and short processing period, this method of waste treatment would be quite feasible in Singapore and go towards fulfilling Singapore's energy needs. From our theoretical model, we estimate an annual butanol production of 700,000 kg from Singapore's generated bread waste, which would be able to power 4% of Singapore's annual energy consumption, or roughly 14 days' worth of energy. This is a significant amount of energy that can be produced purely from bread waste alone. So significant in fact, that it would become Singapore's largest clean energy source, beating out solar energy which contributes less than 1% of Singapore's annual energy needs.

There would be an even higher potential, if this novel treatment of bread waste is expanded to other food types containing carbohydrates, like expired rice or noodles, allowing for higher production of clean energy. This will reduce the nation's reliance on natural gas for the production of electricity, and will introduce a cost-effective energy source into its arsenal.

Acknowledgements We would like to thank Mr. Guandong Su and Prof. He Jianzhong for their support and guidance throughout this project. We would also like to thank our teacher-in-charge, Ms Valarie Lim for her support and last but not least, Dr Chiam for is guidance along the way.

References

1. Gu, Y., Jiang, Y., Wu, H., Liu, X., Li, Z., Li, J.,… & Li, Y. (2011). Economical challenges to microbial producers of butanol: feedstock, butanol ratio and titer. *Biotechnology journal*, *6*(11), 1348–1357.
2. Atsumi, S., Hanai, T., & Liao, J. C. (2008). Non-fermentative pathways for synthesis of branched-chain higher alcohols as biofuels. *nature*, *451*(7174), 86.
3. Sun, C., Zhang, S., Xin, F., Shanmugam, S., & Wu, Y. R. (2018). Genomic comparison of *Clostridium* species with the potential of utilizing red algal biomass for biobutanol production. Biotechnology for biofuels, 11(1), 42.
4. KAMIŃSKI, W., Tomczak, E., & Gorak, A. (2011). Biobutanol- production and purification methods. *atmosphere*, *2*, 3.
5. Bramono, S. E., Lam, Y. S., Ong, S. L., & He, J. (2011). A mesophilic *Clostridium* species that produces butanol from monosaccharides and hydrogen from polysaccharides. *Bioresource technology*, *102*(20), 9558– 9563.
6. He, J., Ritalahti, K. M., Yang, K. L., Koenigsberg, S. S., & Löffler, F. E. (2003). Detoxification of vinyl chloride to ethene coupled to growth of an anaerobic bacterium. *Nature*, *424*(6944), 62.
7. Statista (https://www.statista.com/outlook/40050100/124/bread/singapore) visited 08/01/2020
8. Zhang, C., Li, T., & He, J. (2018). Characterization and genome analysis of a butanol–isopropanol-producing *Clostridium beijerinckii* strain BGS1. *Biotechnology for biofuels, 11(1), 280*
9. Li, T., Yan, Y., & He, J. (2014). Reducing cofactors contribute to the increase of butanol production by a wild-type *Clostridium* sp. strain BOH3. *Bioresource technology*, *155*, 220–228
10. Li, T., Yan, Y., & He, J. (2015). Enhanced direct fermentation of cassava to butanol by *Clostridium* species strain BOH3 in cofactor-mediated medium. *Biotechnology for biofuels*, *8*(1), 166.
11. Giacobbe, S., Piscitelli, A., Raganati, F., Lettera, V., Sannia, G., Marzocchella, A., & Pezzella, C. (2019). Butanol production from laccase-pretreated brewer's spent grain. *Biotechnology for biofuels, 12*(1), 47.
12. Ujor, V., Bharathidasan, A. K., Cornish, K., & Ezeji, T. C. (2014). Feasibility of producing butanol from industrial starchy food wastes. *Applied energy*, *136*, 590–598

EEG Based Multitasking Assessment Using Simultaneous Spatiotemporal Stimulus

Kay Hian Ng, Sean Ng, Xuan Hui Siew, and Aung Aung Phyo Wai

Abstract The use of Steady-State Visual Evoked Potential (SSVEP) and Rapid Serial Visual Presentation (RSVP) together with multitasking and different types of spatial attention is relatively new. This paper investigates how different spatial attention, overt or covert, could affect the results from the electroencephalogram when used with multitasking. We performed experiments with 15 subjects with overt and covert attention phases. We used a 4-channel EEG with 2 channels each at the occipital and prefrontal areas, and used canonical correlation analysis to perform feature extraction of the data from prefrontal positions, and used Bandpower separation to separate the data from the occipital positions into 6 bands. Using collected data, we determined that spatial attention affects some frequencies of SSVEP responses, and differing reaction time with different types of attention. Additionally, this model can be used in future studies into multitasking related attention type and effects of other external variables.

Keywords Covert attention · Overt attention · Spatial attention · Steady-state visual evoked potential · Rapid serial visual presentation · EEG

K. H. Ng (✉) · S. Ng · X. H. Siew
NUS High School of Mathematics and Science, Singapore, Singapore
e-mail: h1510098@nushigh.edu.sg

S. Ng
e-mail: h1510113@nushigh.edu.sg

X. H. Siew
e-mail: h1510117@nushigh.edu.sg

A. A. P. Wai
Computational Intelligence Lab, SCSE, Nanyang Technological University, Singapore, Singapore
e-mail: apwaung@ntu.edu.sg

H. Guo et al. (eds.), *IRC-SET 2020*,
https://doi.org/10.1007/978-981-15-9472-4_32

1 Introduction

1.1 Background

Brain-computer interfaces (BCI) are systems that allow communication between the brain and various machines. They work by collecting brain signals, interpreting them then reproducing the recordings of the brainwaves, or outputting commands to a connected machine according to the brain signal received. One of the most common methods is Electroencephalogram (EEG), a non-invasive technique, where sensors are placed on the scalp to measure the electrical potentials produced by the brain.

Multitasking is the ability to perform multiple activities at a time. As we multitask, the mental workload increases which often results in increased response time and/or error rates of the appropriate output required. Most research on multitasking has been focused on an active feedback demand, which could result in lower performance rates, instead of the role of attention.

Attention can be divided into Overt Attention and Covert Attention. Overt Attention is the obvious, saccadic eye movement (or quick, simultaneous movement of the eye) to a target. In contrast, Covert Attention is allowing the brain to mentally shifting one's focus without moving one's eyes, to focus on a target existing in one's peripheral vision.

1.2 Objective and Hypothesis

Studies have already been done where combination of two distinct BCI tasks are carried out to investigate cognitive flexibility, or multitasking, and is shown that healthy subjects are able to perform two independent cognitive tasks simultaneously with high accuracy [1].

Thus, in this research, we propose a Brain-Computer Interface (BCI) task comprising a combination of visual stimuli (rather than distinct tasks), implementing a 4-target Steady-State Visual Evoked Potential (SSVEP) and a single Rapid Serial Visual Presentation (RSVP), each at a different frequency. We aim to quantify the multitasking capabilities by measuring the speed at which attention is applied to a target with respect to covert and overt attention.

SSVEP is a visual target that flickers at a certain frequency, with a commonly used frequency range of 3−20 Hz, though some studies may use frequencies as low as 1 Hz or as high as 100 Hz for different purposes [2]. RSVP is a visual target that displays a series of images or text with presentation frequencies ranging from 3 to 20 Hz. The subjects' brain waves will resonate at the frequency of the target the subject has active overt and/or covert attention on and can be observed on the recordings of the brain waves produced by an Electroencephalogram (EEG).

Some recent studies have also shown that subjects that repeatedly carry out a cognitive task can show improvement in their cognitive performance [3]. Half the

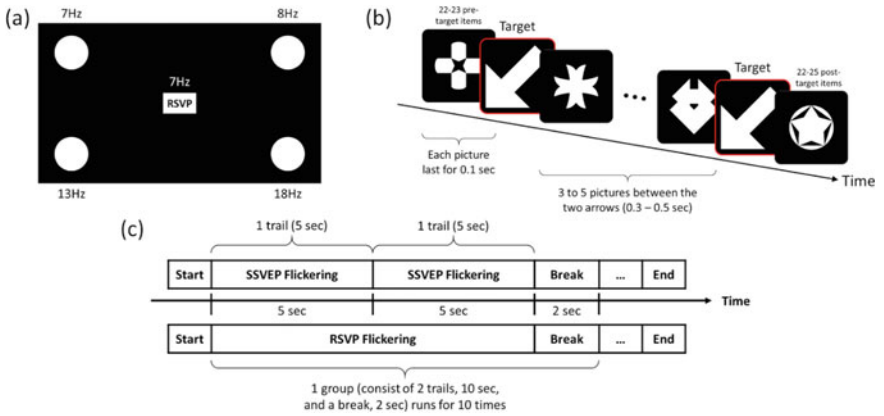

Fig. 1 **a** General trial structure and diagram of experimental setup (top left), consisting of 4 SSVEP in each corner and 1 RSVP in the center, each flickering at different frequencies. **b** (top right) For RSVP, each target is flashed twice with a short duration in-between, allowing 3 to 5 other images to flash. A total of 25 unique images (excluding 4 arrows used to indicate the targets) were used. For each target flashed, subjects attend to one of four SSVEP and press the spacebar to indicate that they notice the target. **c** (bottom) Every SSVEP trial last for 5 s and each group consist of 2 trials. Between each group is a 2 s break when the subject can rest their eyes. A total of 20 trials were run in each experimental session

subjects will be required to carry out the experiment on multiple occasions and results from different runs will be compared to quantify the cognitive improvements of the subjects. This could increase the efficiency of subjects in responding to the stimuli and minimize errors (looking at wrong target/looking at a different target before shifting attention to the right target).

We hypothesize that overt attention on SSVEP will allow subjects to perform better (pay better attention and have shorter reaction time) compared to covert attention [4].

2 Method

Fifteen healthy human subjects (15 right-handed, 13 males and 2 females, average age 17.6 ± 0.7 years) participated in this study, providing written consent to a protocol approved by the NUS High School of Math & Science Institutional Review Board. Of the fifteen participants, four has prior SSVEP BCI experience. Experienced users are deemed as acceptable participants as prior knowledge would not affect their capabilities in carrying out the task/experiment. We then collect data from the subjects and extract the data to segment it. We then use Canonical Correlation Analysis (CCA) to recognize target frequencies for analysis [5].

2.1 Experimental Setup

The BCI User Interface was presented on a laptop screen measuring 34 cm × 19 cm located approximately 60 cm in front of the subject. Four SSVEP components were used (Circles with a diameter of 3.1 cm), each positioned on each of the four corners of the interface and programmed to flicker at different frequencies [1]: top left −7 Hz, top right −8 Hz, bottom left −13 Hz, and bottom right −18 Hz (See Fig. 1a). Each SSVEP lies approximately at 25° view angle (lies 12.7 cm vertically and 25.4 cm horizontally away from the center), within the near-peripheral vision (~8° to 30°). A single RSVP (within 6 × 6 cm square) with a frequency of 10 Hz is also positioned in the center of the screen.

2.2 Experimental Design

Subjects participated in two experimental sessions composed of two conditions: Covert attention on SSVEP (or Overt attention on RSVP), Overt attention on SSVEP (or Covert attention on RSVP). Both conditions contained three runs each and the states of the RSVP were randomized.

2.3 Experimentation (Covert Attention on SSVEP)

Each run contained 20 trials (5 s each) in groups of 2 trials. (See Fig. 1c) Trials were structured as follows: a "go" period lasting 10 s (consisting of 2 trials), followed by a 2 s break period. During this "go" period, subjects were instructed to stay focused on the RSVP (in the center of the screen). For each trial, a target (an arrow pointing to one SSVEP/corner) was presented in the middle of the screen. Each arrow is flashed twice, with 3–5 other images between, or approximately 0.3–0.5 s separating them. (See Fig. 1b) The subject was instructed to attend to the corresponding SSVEP through their peripheral view whenever a target was presented without eye movements, as well as provide a keypress response to indicate that they have noted the target change. All four SSVEP flashed for the entire duration of the "go" period. The target was automatically determined in a pseudo-random fashion, ensuring that no two consecutive targets were the same.

2.4 Experimentation (Overt Attention on SSVEP)

The same structure was used for the second experimental setup, but a different set of instructions is provided. At the start of the session, the subjects start off by looking

at the RSVP. As soon as the first target was presented, subjects were instructed to stay focused on the SSVEP target until the next target is presented, during which the subject is instructed to change focus to the new SSVEP target, all while attending to the RSVP through their peripheral view; and this is repeated for the entire run.

Subjects will be told to make quick eye movements to the indicated target (for Overt attention experimental setup), or quickly shift peripheral attention to the indicated target (for Covert attention experimental setup). We will be using the time elapsed from the time the instructions (RSVP) are presented to the time the subject has his/her attention on the correct stimuli (SSVEP) for comparison [6, 7], shorter elapsed time indicates better attention on the instruction stimulus. The elapsed time will be obtained using the timing that the UI indicated (for when the instructions are displayed) and EEG readings timestamp.

2.5 Data Collection

We used a 4-channel Ganglion board with 6 gold-capped electrodes to collect the data. We collected occipital data from the O1 and O2 positions with electrodes connected to channel 3 and channel 4 of the ganglion and prefrontal data from the FP1 and FP2 positions with electrodes connected to channel 1 and channel 2 of the ganglion. The reference electrodes were connected to the A1 and A2 position. We then used Open BCI GUI to record the data from the ganglion. Using timestamps of our custom log file and the raw data of the open BCI GUI results, we split the data to be separated to the 15 subjects, 6 experiments and 10 pairs of trials.

2.6 Feature Extraction

In SSVEP research, CCA is a common approach to recognize target frequencies, which gives us the canonical correlation coefficient (CCC), which is the maximum linear relationship between two variables [8]. Using the equation above, we selected the ρ value that gives the highest canonical correlation between X and Y.

$$\rho = \frac{a^T \Sigma_{XY} b}{\sqrt{a^T \Sigma_{XX} a}\sqrt{b^T \Sigma_{YY} b}} \tag{1}$$

For the Bandpower analysis, we passed the raw EEG data through a 0.1–45 Hz bandpass filter to segment it into 6 different segments, delta (0.5–3 Hz), theta (3–8 Hz), alpha (8–12 Hz), low beta (12–25 Hz), high beta (25–38 Hz) and gamma (38–45 Hz). We then obtained the Bandpower ratio, $\beta/(\alpha + \theta)$ to quantify the subject's attentiveness. After this, we ran the data through an independent t test grouped by the type of spatial attention used (overt and covert).

For the reaction time analysis, we used the timestamps with each respective key press, and compared it with the timestamp of the last arrow shown to achieve the reaction time. We rejected any reaction time of less than 90 ms as it could be caused by the user accidentally hitting the key, and rejected any reaction time of greater than 1 s as it was likely that the subject did not react to the stimulus and accidentally pressed the key.

3 Analysis

First, we performed feature extraction (Fig. 2) from the EEG readings using CCA to classify the frequencies obtained [5], then using independent t-tests we analyzed our data for differences between the covert and overt experiments.

3.1 Canonical Correlation Coefficient (CCC)

Referring to Table 1, the 8 Hz ($p = 0.050$) and 10 Hz ($p < 0.001$) CCC results of the covert experiments compared to the overt experiments of the same frequency showed that covert attention caused higher CCC values in these frequencies. However, the remaining frequencies (7 Hz ($p = 0.93$), 13 Hz ($p = 0.21$) and 18 Hz ($p = 0.69$)) show no significant effect of the type of spatial attention on the results.

However, when the CCC results of individual subjects are compared, some showed differences. Referring to Table 2, using subject 14 as an example, the 7 Hz ($p = 0.018$), 8 Hz ($p = 0.018$), 13 Hz ($p = 0.012$) and 18 Hz ($p = 0.001$) CCC results of the covert experiments compared to the overt experiments of the same frequency showed that

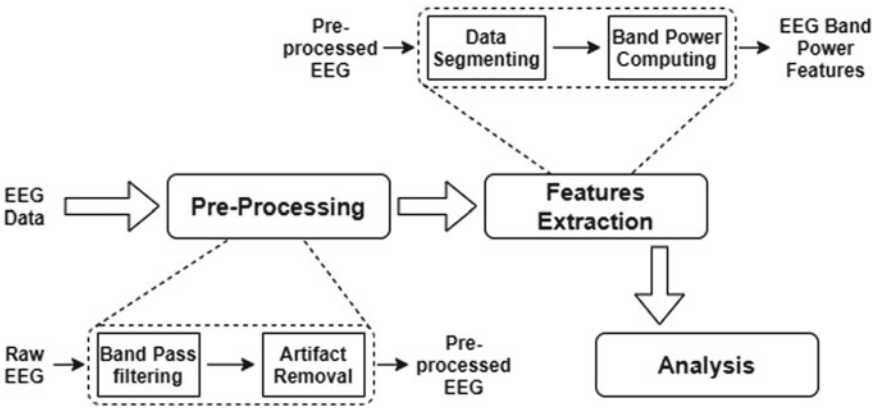

Fig. 2 Flow chart of data processing

Table 1 Independent sample T-test of subjects (CCC)

	t	df	p
7 Hz	-0.087	878.000	0.535*
8 Hz	1.650	878.000	0.050
10 Hz	4.991	878.000	< 0.001
13 Hz	-1.267	878.000	0.897*
18 Hz	-0.406	878.000	0.658*

Note Student's t-test
Note For all tests, the alternative hypothesis specifies that group covert is greater than group overt
* Levene's test is significant ($p < 0.05$), suggesting a violation of the equal variance assumption

Table 2 Independent sample T-Test of subject 14 (CCC)

	t	df	p
7 Hz	−2.148	58.000	0.018
8 Hz	−2.137	58.000	0.018
10 Hz	0.650	58.000	0.741
13 Hz	−2.321	58.000	0.012
18 Hz	−3.115	58.000	0.001

Note Student's t-test
Note For all tests, the alternative hypothesis specifies that group covert is greater than group overt

covert attention caused lower CCC values in these frequencies. However, the 10 Hz ($p= 0.52$) frequency showed no significant effect of type of spatial attention on the results.

3.2 Bandpower

Referring to Table 3, the Bandpower ratio (/(+)) for covert experiments (0.17 ± 0.032) compared to the Bandpower ratio for overt experiments (0.19 ± 0.044) showed no significant effect of type of spatial attention on the Bandpower ratio ($p = 0.11$).

3.3 Reaction Time

Referring to Table 4, the reaction time for the covert experiments (425.95 ± 113.48) compared to the reaction time for the overt experiments (439.26 ± 136.53) showed significance evidence that covert results in a lower reaction time compared to overt. ($p = 0.022$)

Table 3 Independent sample T-test of subjects (Bandpower)

	t	df	p
Theta	−5.727	58.000	< 0.001[a]
Alpha	−6.045	58.000	< 0.001[*]
Beta Low	−6.083	58.000	< 0.001[*]
Beta High	−5.637	58.000	< 0.001[*]
Bandpower ratio (/(+))	−1.606	58.000	0.114

Note Student's t-test
Note For all tests, the alternative hypothesis specifies that group covert is less than group overt
[*] Levene's test is significant ($p < 0.05$), suggesting a violation of the equal variance assumption

Table 4 Independent sample T-test of subjects (Reaction Time)

	t	df	p
Reaction time	−2.014	1434.000	0.022[*]

Note Student's t-test
Note For all tests, the alternative hypothesis specifies that group Covert is less than group Overt
[*] Levene's test is significant ($p < 0.05$), suggesting a violation of the equal variance assumption

3.4 Discussion

While certain categories indicated that covert attention had performed better overt attention, other categories had data that suggested that there was either no difference or that overt had perform better. The conclusion that covert attention performs better can only be applied to certain SSVEP frequencies based on the data collected.

Furthermore, with an uneven spread of gender in the volunteers, 13 males to 2 females, we should not conclude anything with regards to gender using only our data.

Although we took measures to increase the accuracy of the experiment, such as by decreasing the amount of possible distractions of the subject, the accuracy of the experiment could be improved.

(a) Hardware limitations

The SSVEP may not have been shown at the correct frequencies due to the refresh rate of the screen or the processing power of the computer, which may have caused errors in the CCA. Furthermore, the ganglion we used had 4 channels, which may have restricted the number of sites we could have collected data from. Furthermore, the electrodes may not have been secured tightly which could lead to incorrect data from shaking of the wires.

(b) User Input

As our reaction time analysis depends heavily on user input, some users may have pressed the key unintentionally or missed some of the stimuli, which would cause

inaccurate data. Although we tried to decrease the number of false data from incorrect presses, we have no way of determining whether the key was accidentally pressed, pressed very quickly or just pressed very late. Furthermore using subject 14 as an example, there was significant proof that CCC for overt is statistically significantly higher than that of covert for 7, 8, 13 and 18 Hz, while the overall shows that CCC for covert is statistically significantly higher than that of overt for 8 and 10 Hz. Some users have also stated that the covert experiment was more difficult than the overt experiment while some of the others stated the opposite.

The number of subjects tested in our study was small, and also limited to a specific population, our results may not generalize to all students of similar ages, and should also not be used to generalize subjects outside of the age group.

4 Conclusion

We have determined that overall, the covert experiments showed greater CCC values than the overt experiments for 8 and 10 Hz, showed no statistical significance on the Bandpower ratio, and showed less reaction time than the overt experiments. This suggests that covert attention is better when being used with SSVEP with frequencies of 8 and 10 Hz, does not affect the Bandpower, and is easier for the user to react to, compared to overt attention.

4.1 Practical Application

Our research could be used to improve security systems. With further development into this sector, the accuracy of such instruments could be improved which could make it easier for security guards to do their jobs. For instance, an EEG headset with electrodes on the correct positions of A1, A2, O1 and O2 could be used by the security guard when they are observing closed circuit television feeds, and while there is a main screen in the center, there are sub screens at the sides with SSVEP flickering around the borders of the sub screens with different frequencies. When something of interest turns up on a sub screen, the security guard could then observe the sub screens with covert attention and after the EEG reads a spike in the corresponding frequency of the SSVEP, the audio of the feed sub screen could then be played instead of the main screen, thus allowing the security guard to observe multiple screens with audio output. This could also allow for newer security guards to browse through the feeds more quickly as they would not need to spend time on manually entering a command or swapping the audio feed from one camera output to the other.

Acknowledgements We would like to thank the volunteers who willingly offered their time outside of school to allow us to collect and utilize their data. Finally, we would like to thank our school,

NUS High School of Mathematics and Science, for giving us this opportunity to do the project, as well as supporting us financially throughout the duration of our research.

References

1. Edelman, B., Meng, J., Gulachek, N., Cline, C. and He, B., 2018. Exploring Cognitive Flexibility With a Noninvasive BCI Using Simultaneous Steady-State Visual Evoked Potentials and Sensorimotor Rhythms. *IEEE Transactions on Neural Systems and Rehabilitation Engineering*, 26(5), pp. 936–947.
2. Norcia, A., Appelbaum, L., Ales, J., Cottereau, B. and Rossion, B., 2015. The steady-state visual evoked potential in vision research: A review. *Journal of Vision*, 15(6), p. 4.
3. Taya, F., Sun, Y., Babiloni, F., Thakor, N. and Bezerianos, A., 2015. Brain enhancement through cognitive training: a new insight from brain connectome. *Frontiers in Systems Neuroscience*, 9.
4. Treder, M. and Blankertz, B., 2010. (C)overt attention and visual speller design in an ERP-based brain-computer interface. *Behavioral and Brain Functions*, 6(1), p. 28.
5. Lin, Z., Zhang, C., Wu, W. and Gao, X., 2007. Frequency recognition based on canonical correlation analysis for SSVEP-based BCIs. *IEEE Transactions on Biomedical Engineering*, 54(6), pp. 1172–1176.
6. McCoy, B. and Theeuwes, J., 2018. Overt and covert attention to location-based reward. *Vision Research*, 142, pp. 27–39.
7. Vossel, S., Mathys, C., Daunizeau, J., Bauer, M., Driver, J., Friston, K. and Stephan, K., 2013. Spatial Attention, Precision, and Bayesian Inference: A Study of Saccadic Response Speed. *Cerebral Cortex*, 24(6), pp. 1436–1450.
8. Nakanishi, M., Wang, Y., Wang, Y. and Jung, T., 2015. A Comparison Study of Canonical Correlation Analysis Based Methods for Detecting Steady-State Visual Evoked Potentials. *PLOS ONE*, 10(10), p.e0140703.

The Effects of Vermicomposting Soybean Waste (Okara) Biostimulants on the Quality of Growth of Brassica Rapa Var. Parachinensis (Commonly Known as Choy Sum)

Investigating the Effect of Eco-friendly Vermicomposted Okara Biostimulants on the Health of Edible Produce- Choy Sum

Jun Lu Zhang, Victoria Dai Qi Ong, and Sean Chuan Zhou Lee

Abstract The overarching purpose of this study is to examine how soybean waste, okara, produced from soybean consumption can be managed in an environmentally-friendly manner by being converted into plant biostimulant. Our aim is to compare the effectiveness of vermicomposted and heat-composted okara as biostimulants on the growth of choy sum so as to produce higher quality vegetables. Our main hypothesis is that okara, when vermicomposted, can serve as a biostimulant that promotes plant health more effectively and sustainably than normal composting. We chose okara as it is nitrogen-rich and hence beneficial to plant growth, vermicomposting as worms can accelerate composting and produce casting which is nutritious for the plants. We grew three batches of choy sum in a greenhouse and applied soil with vermicompost, soil with compost, and soil alone to each of the three set-ups. We measured their initial height and after 28 days, their final height. We tested water retention by measuring the dry mass and wet mass of our plants. By using a refractometer, we measured the choy sum's Brix level, showing the amount of sucrose present. We also measured antioxidant levels using 2,2-diphenyl-1-picryl-hydrazyl-hydrate (DPPH) method of assay as DPPH scavenging effect is proportional to the antioxidant levels, which protects cells against free radicals. After analysing our results and comparing between set-ups, we can conclude the best method to produce biostimulants. Our experiments proved that vermicomposting biostimulant, specifically soybean pulp,

J. L. Zhang (✉) · V. D. Qi Ong · S. C. Z. Lee
National Junior College, Singapore, Singapore
e-mail: zhangjunlu01@gmail.com

V. D. Qi Ong
e-mail: victoriasailing237@gmail.com

S. C. Z. Lee
e-mail: seanlcz8172@gmail.com

H. Guo et al. (eds.), *IRC-SET 2020*,
https://doi.org/10.1007/978-981-15-9472-4_33

is useful for improving plant health and yield despite limitations like inability of keeping factors like humidity constant.

Keywords Biostimulants · Okara · Environmental-friendly · Choy sum; quality

1 Introduction

As global demand for soy products such as food and cosmetics increases, greater soybean cultivation leads to more okara (residue soybean pulp) generated, approximating 41 million tons yearly [1]. With such amounts of okara produced and the tendency for okara to putrefy [2], effective waste management methods are needed to recycle waste for maximum utility. Moreover, as the world develops, demand for higher-quality vegetables and fruit rises [3]. Therefore, we decided to research plant biostimulants, a substance enhancing plant growth and health [4]. In particular, we chose to focus on vermicompost biostimulant, a new composting method showing great innovation, i.e., global applicability to lower-income areas [5]. We produced the biostimulants: composted okara and vermicomposted okara, and tested their effects on plant health. We aim to find out if okara biostimulants improve plant health and which best improves plant health, and we hypothesize that vermicomposted okara is a more effective plant biostimulant than other okara biostimulants.

2 Methodology

Our experiment has 3 plant set-ups each grown for 28 days. The first set-up is the control without biostimulants, the second has composted okara biostimulant and the last has vermicomposted okara biostimulants. Biostimulants foster plant growth rates and render more efficient water use, enhancing quality attributes of products such as nutrient assimilation and more [6]. Thus, we used 4 methods to determine plant health and compare the efficacy of different biostimulants: plant height, plant biomass, Brix level, and antioxidant level. Vermicomposting is where earthworms, in our case African Nightcrawlers, ingest, digest and absorb organic waste, then excrete castings via their metabolic systems. This allows the final product, vermicompost, to have higher levels of major plant nutrients such as nitrogen [7].

2.1 Biostimulant Production

A major composting factor for biostimulant production is the carbon–nitrogen ratio of the compost material. As nitrogen is very important for plants (a major component of chlorophyll) [8] and research has shown that a low carbon–nitrogen ratio is preferred

for composting [9], we chose a common nitrogen-rich food waste that was little researched on as our main compost material to produce biostimulants. We sourced okara from Selegie Soya Bean. Every 2 days, we layered 400 g of okara on our heat-compost and vermicompost set-ups shown in the diagrams below, before turning them to increase oxygen flow and hasten the composting [10]. Heat-composting typically comprises decomposing organic waste by an aerobic process, which kills pathogens [11] and suits our timeline. After 45 days of composting and vermicomposting, the biostimulants matured sufficiently and biostimulants were applied to the germinated choy sum, adding 30 g of biostimulants per plant every 7 days for the 28 days the choy sum was grown (Figs. 1, 2, 3 and 4).

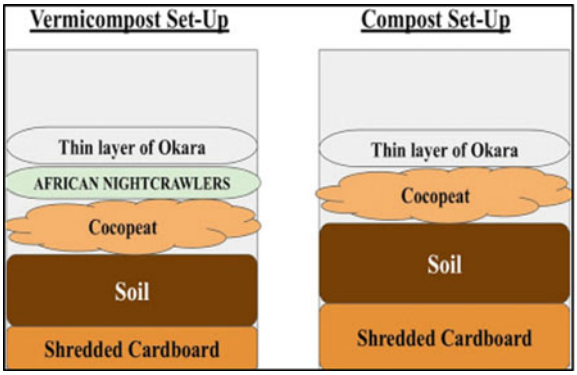

Fig. 1 Diagrams for comparison between simplified cross sectional diagram of vermicompost and compost okara biostimulants set-up

Fig. 2 Bird's eye view of top layer of vermicompost set-up

Fig. 3 Bird's eye view of top layer of heat compost set-up

Fig. 4 Image of African Nightcrawlers in turned over vermicompost

2.2 Plant Growth

We chose to test on choy sum growth as it germinates quickly and is feasible for various measurements. Each set-up comprises 40 choy sum plants growing in the same greenhouse, allowing for constant variables like surrounding temperature and light intensity (Figs. 5, 6, 7 and 8).

Fig. 5 Germinating batch of choy sun

Fig. 6 New transplanted choy sum seedling in greenhouse (compost batch)

We used 4 methods to measure how effectively our choy sum grew across set-ups against commercially-grown supermarket choy sum. First, we recorded the height of each plant before and after growth to obtain the change in plant height. Second, we measured the plants' water retention abilities by [12] subtracting the final dry biomass value from the initial wet biomass value to obtain their water mass. Third, we compared plant sucrose levels across set-ups. Sucrose level shows the photosynthesis rate in a plant, which determines plant health. It is also crucial for human growth as it contributes to energy production [13]. We extracted plant sap and placed it on a Hanna Instrumental digital refractometer [14] to obtain a Brix reading. Last, we measured plant antioxidant levels as high antioxidant levels decrease the toxicity of

Fig. 7 15 days (mid-period) choy sum in greenhouse (compost batch)

Fig. 8 28 Days (fully grown) choy sum in greenhouse (compost Batch)

free radicals, improve root and shoot growth for higher water content in leaves and low incidence of disease [15]. We used the 2,2-diphenyl-1-picryl-hydrazyl-hydrate (DPPH) method of antioxidant assay [16]. DPPH solution was prepared by dissolving 0.0788 g of DPPH in 1000 ml of methanol. Next, we added a 1 g slice of choy sum and 10 ml of methanol per test tube which was placed in a 50 °C water bath for the alcohol to absorb the antioxidant properties. The test tube solution containing 8 ml of DPPH and 2 ml of plant solution was transferred to a UV–VIS spectrophotometer at 517 nm wavelength to measure absorbance. We followed the procedure provided by

Tailor C. S. et al. to find the DPPH scavenging effect, which is directly proportional to antioxidant levels. The equation provided was A0 − (A1 / A0) × 100, where A0 is the absorbance for the control reaction involving Trolox, and A1 is the absorbance measured after the test samples have reacted with the DPPH [17].

3 Results and Discussion

We grew 15 choy sum for each control, compost and vermicompost set-up, and compared them against the supermarket-bought commercial choy sum for final plant height, Brix level and antioxidant level. The data of 15 plants per set-up are collated (e.g. Table 1, average plant heights) and used to plot graphs (Figs. 9, 10 and 11).

As seen from Graph 1a and 1b, the final height of the plants with vermicompost biostimulant is higher than commercially-grown supermarket plants. Although the final height of the compost choy sum was shorter than the supermarket choy sum's final height, we postulate this is because supermarket choy sum undergo selection for the best-grown produce to satisfy consumers [18], thus it is expected that they are physically large. However, our other results like antioxidant levels show that supermarket choy sum may not be more nutrient-rich than those with biostimulants applied (Fig. 12).

Table 1 Table of sample data for change in plant height for control batch of choysum

Table of average change in height for control plants during growth			
Initial height (cm)	Final height (cm)	Change in height (cm)	Average change in heigt (cm)
6.8	39.4	32.6	23.6 (to 3 s.f.)
6.5	18.3	11.8	
4.2	29.8	25.6	
6.4	40.7	34.3	
5.4	16.1	10.7	
7	27.5	22.5	
4.3	42.5	37.8	
4.7	32.3	27.6	
6.3	28	21.7	
6.2	34.7	28.5	
5.3	14.6	9.3	
5.2	30.2	25	
5.3	28.1	22.8	
5.3	27.3	22	
4.4	25.7	21.3	

Table of average change in height for control plants during growth			
Initial height/cm	Final height/cm	Change in height/cm	Average change in height/cm
6.8	39.4	32.6	23.6 (to 3s.f.)
6.5	18.3	11.8	
4.2	29.8	25.6	
6.4	40.7	34.3	
5.4	16.1	10.7	
7	27.5	22.5	
4.3	42.5	37.8	
4.7	32.3	27.6	
6.3	28	21.7	
6.2	34.7	28.5	
5.3	14.6	9.3	
5.2	30.2	25	
5.3	28.1	22.8	
5.3	27.3	22	
4.4	25.7	21.3	

a.Table of sample data for change in plant height for control batch of choysum

Fig. 9 Table for values of control batch of choy sum

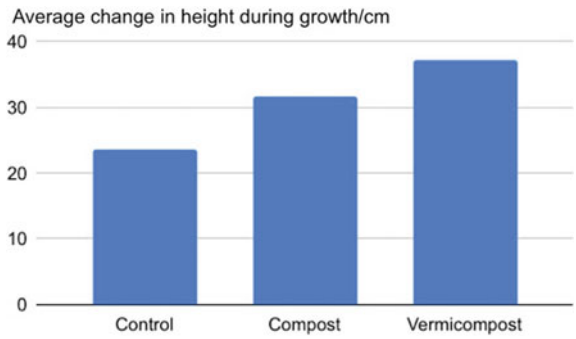

Fig. 10 Graph 1a: Average change in height of 15 control, compost and vermicompost choy sum after 28 days of growth

Graph 2 (above) shows the choy sum with vermicompost containing the highest water mass amongst the set-ups. Unexpectedly, the control choy sum had a higher reading than both the compost and commercial choy sum, which does not cohere with our hypothesis that compost choy sum should have better water retention than the control. In Graph 2, we can see that water retention is highest in plants with vermicompost biostimulant and the supermarket choy sum has a lower value than

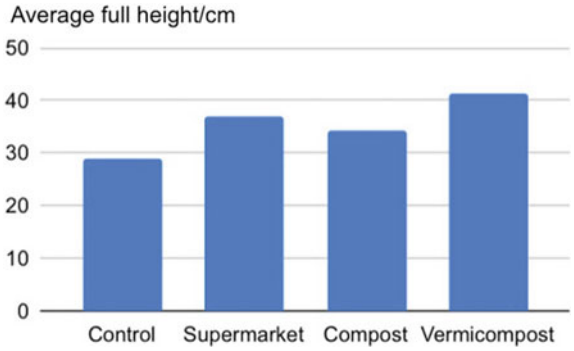

Fig. 11 Average actual height of 15 control, compost and vermicompost choy sum after 28 days of growth

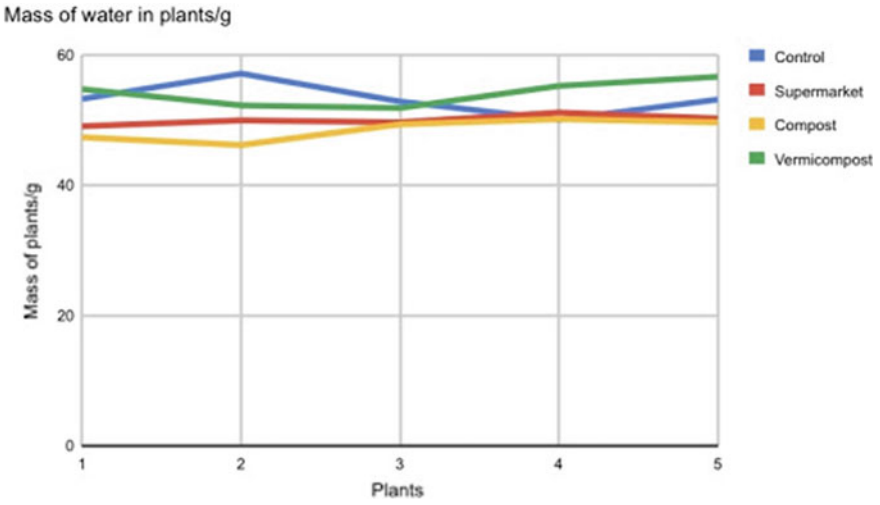

Fig. 12 Graph 2: Amount of water absorbed by control, compost, vermicompost and commercially-grown supermarket batches of choy sum after 28 days of growth

the control. We conclude this is because supermarkets hold vegetable produce to high aesthetic standards so as to appeal to consumers, rather than non-aesthetic traits such as the amount of water, which is our focus. Unexpectedly, the compost choy sum had lower water mass than the control as well. This may be because our compost biostimulants had bigger particle size than both vermicompost biostimulants and soil. Although it still provides the supplements that a biostimulant would to the plants, this impacted the hydraulic conductivity of the soil, a main factor that affects the amount of water in plants [19] (Fig. 13).

As seen from Graph 3, the Brix levels of 4 plants are highest for the vermicompost set-up at an average of 2.3 degree brix, followed by the supermarket set-up, control,

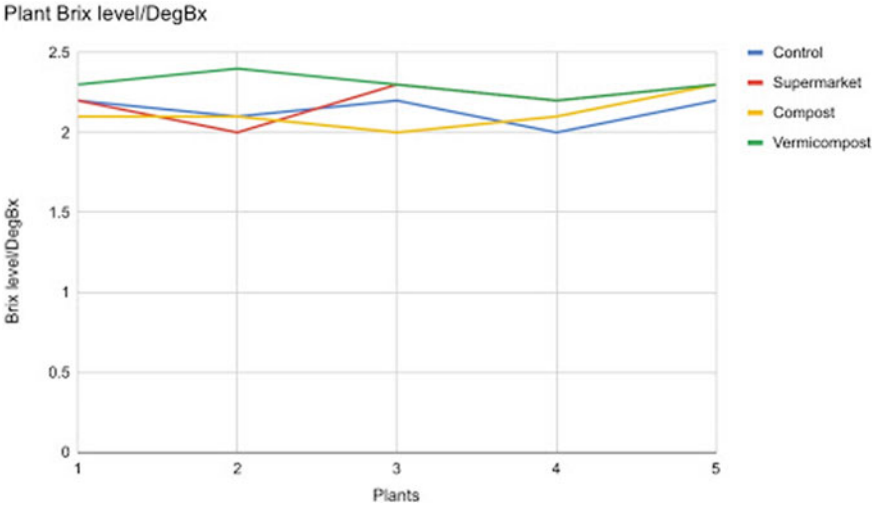

Fig. 13 Average actual height of 15 control, compost and vermicompost choy sum after 28 days of growth

and compost set-ups with an average of 2.12. The results confirm our hypothesis that vermicompost biostimulants are most effective in improving plant health, yet composted biostimulants caused plant sucrose concentration to be lowest. This could be a limitation of composted okara compared to vermicomposted okara in promoting plant health, as sucrose level shows the plant's rate of photosynthesis and plant health (Fig. 14).

From Graph 4 we observe the choy sum with vermicompost applied had the highest DPPH scavenging effect at 32.1%, followed by the compost batch, control batch and last, the supermarket choy sum, which is lower than vermicomposted choy sum by 5.3%. We can see that choy sum with vermicompost has the highest DPPH scavenging effect, followed by compost, control and supermarket last. DPPH scavenging effect is directly proportional to plant antioxidant level as antioxidants protect cells from free radicals like DPPH [20]. Despite performing better than the compost choy sum and control choy sum for some of our experiments like water retention ability, our tests have proven that supermarket choy sum had the lowest antioxidant levels, while choy sum with vermicompost had the highest. This shows that plants with biostimulants processed through vermicomposting were the healthiest and therefore benefit human health most.

4 Conclusion and Future Work

In the experiments conducted, the plants grown with vermicomposted okara biostimulant performed better, both physically and health-wise, compared to the other

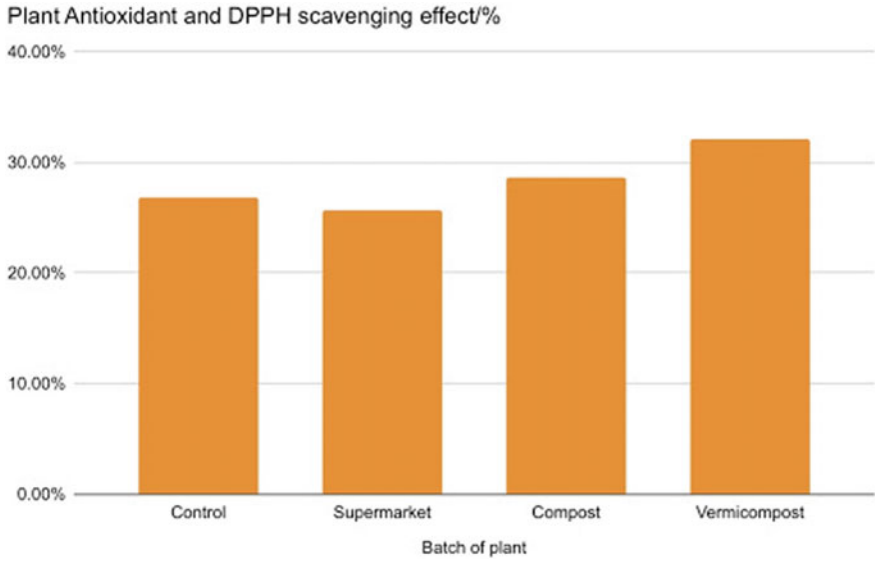

Fig. 14 Graph 2: Amount of water absorbed by control, compost, vermicompost and commercially-grown supermarket batches of choy sum after 28 days of growth

three types in terms of the four factors we established to define plant health. Thus, it can be concluded that not only is okara a viable base for good biostimulants as it has a low carbon–nitrogen ratio, but also that vermicomposting increases the biostimulants' effectiveness, as it increases the number of microorganisms involved in the production of biostimulants. With our vermicomposted okara biostimulants, we can contribute to recycling nitrogen-rich organic wastes and improve Singapore's food security by producing higher yield of healthier plants, bringing our nation one step closer to our 30-by-30 food self-sustainability goal [21].

Our project was limited by the space allocated to grow our plants in the greenhouse as we could only grow 1 batch of choy sum at a time. This proved a limitation as although the greenhouse keeps various factors such as soil type and substrate type constant, differences in the amount of sunlight and humidity levels caused deviations in the conditions for each batch. However, these deviations are minimal as the greenhouse is ventilated and controls temperature and humidity, ensuring that our plants do not lose too much water via transpiration. Thus our results pertaining to the mass of water retained by choy sum are unaffected. Moreover, to eliminate variables like pests, we visited the greenhouse as much as possible to get rid of weeds and pests and check our plants. More research can focus on a potentially feasible alternative for composting to produce biostimulants: the use of black soldier fly larvae. Black soldier fly larvae composting may be faster than vermicomposting. Other modes of action of biostimulants other than carbon–nitrogen ratio and microorganisms, such as particle size, can be further researched on. Furthermore, there may be potential in substituting okara with other kinds of food waste as compost material, especially

nitrogen-rich waste to implement this project on a larger scale, manage more food waste and produce fruit and vegetables with higher water retention and sucrose levels.

Acknowledgements We would like to thank our mentor Ms Lee Shan Shan from National Junior College for her constant support and guidance for this research, as well as Sekine Sensei from Ritsumeikan Keisho Junior & Senior High School, for his insights during the research exchange conducted in Hokkaido, Japan. We are also honoured and grateful to have collaborated with Ritsumeikan Keisho Senior High School students Reo Dohi, Yoh Natsuizaka and Hinata Mamesuke, who provided assistance over the course of our experimentation in Japan. Lastly, we would like to thank all our friends and family, who have been nothing but supportive and understanding during our research journey.

References

1. Martins et al. (2019). Soybean waste in particleboard production. Retrieved 3 November 2019 from https://www.researchgate.net/publication/326022270_Soybean_waste_in_particleboard_production
2. Zhang et al. (2013). Soybean Curd Residue: Composition, Utilization, and Related Limiting Factors. Retrieved 3 November 2019 from https://www.hindawi.com/journals/isrn/2013/423590/
3. CBI Ministry of Foreign Affairs. (2018). What is the demand like for fresh fruit and vegetables in the European market? Retrieved from https://www.cbi.eu/market-information/fresh-fruit-vegetables/what-demand/
4. Interagro. (2019). Stress levels: Fighting abiotic stress with amino acid biostimulants. Retrieved from https://www.interagro.co.uk/yield-boosting-biostimulant-available-for-conventional-and-organic-crops/.
5. Jjagwe et al. (2019). Assessment of a Cattle Manure Vermicomposting System Using Material Flow Analysis: A Case Study from Uganda. Retrieved from https://www.mdpi.com/2071-1050/11/19/5173/htm
6. European Biostimulants Industry Council. (n.d.). About Biostimulants and the Benefits of Using Them. Retrieved from https://www.biostimulants.eu/about/what-are-biostimulants-benefits/.
7. Pattnaik, S., & Reddy, M. V. (2009). Nutrient Status of Vermicompost of Urban Green Waste Processed by Three Earthworm Species—Eisenia fetida, Eudrilus eugeniae, and Perionyx excavatus. Retrieved from: https://www.hindawi.com/journals/aess/2010/967526/
8. The Mosaic Company. (n.d.). Retrieved from https://www.cropnutrition.com/efu-nitrogen.
9. Gullickson, Gil. (2015). Here's Why the Carbon-Nitrogen Ratio Matters. Retrieved from https://www.agriculture.com/crops/cover-crops/heres-why-carbonnitrogen-ratio-matters_568-ar48014.
10. Golueke, C. G., & Diaz, L. F. (1996). Historical Review of Composting and its Role in Municipal Waste Management. Retrieved from https://link.springer.com/chapter/https://doi.org/10.1007/978-94-009-1569-5_1
11. Comesaña, D. A., Comesaña, I.V., & de la Iglesia, S. M. (n.d.). Municipal Sewage Sludge Variability: Biodegradation through Composting with Bulking Agent. Retrieved from https://www.intechopen.com/predownload/60184
12. McElrone, A. J., Choat, B., Gambetta, G. A. & Brodersen, C. R. (2013). Water Uptake and Transport in Vascular Plants. Retrieved from https://www.nature.com/scitable/knowledge/library/water-uptake-and-transport-in-vascular-plants-103016037/
13. International Food Information Council Foundation. (2009). Questions and Answers About Sugars. Retrieved from https://foodinsight.org/questions-and-answers-about-sugars/

14. GPS Instrumentation Ltd. (n.d.). Retrieved from https://www.gpsil.co.uk/our-products/refractometers/measuring-pri/#affixMenu3
15. de Vasconcelos, A. C. F. & Chaves, L. H. G. (2019). Biostimulants and Their Role in Improving Plant Growth under Abiotic Stresses. Retrieved from https://www.intechopen.com/online-first/biostimulants-and-their-role-in-improving-plant-growth-under-abiotic-stresses
16. Singh, R. P., & Jen, J. J. (2011). Vegetable processing. Retrieved from https://www.britannica.com/technology/vegetable-processing
17. Tailor C.S. et al. 2014Antioxidant Activity by DPPH Radical Scavenging Method of Ageratum conyzoides Linn. Leaves. Retrieved from https://www.researchgate.net/publication/285525623_Antioxidant_Activity_by_DPPH_Radical_Scavenging_Method_of_Ageratum_conyzoides_Linn_Leaves
18. United States Department of Agriculture. (2010). Soil Survey Technical Note 6. Retrieved from https://www.nrcs.usda.gov/wps/portal/nrcs/detail/soils/ref/?cid=nrcs142p2_053573.
19. Shekhar, T.C. & Anju, G. (2014). Antioxidant Activity by DPPH Radical Scavenging Method of Ageratum conyzoides Linn. Leaves. Retrieved from https://citeseerx.ist.psu.edu/viewdoc/download?doi=10.1.1.678.4869&rep=rep1&type=pdf
20. Kedare, S. B., & Singh, R. P. (2011). Genesis and development of DPPH method of antioxidant assay. Retrieved from https://www.ncbi.nlm.nih.gov/pubmed/23572765
21. Ai-Lien, C. (2019). Singapore sets 30% goal for home-grown food by 2030. Retrieved from https://www.straitstimes.com/singapore/spore-sets-30-goal-for-home-grown-food-by-2030.

Novel Combination of Plantar Pressure and Lower Limb Rotation Measurements Towards Monitoring and Early Detection of Diabetic Foot Ulcers

Yuan Zhe Wen and Jovan Liau Yi Jun

Abstract Diabetes is a chronic illness with severe impacts on the patient's health. Specifically, diabetes may lead to other complications, such as diabetic foot ulcerations. Diabetic foot ulcers progressively deteriorate without proper treatment, with infections leading to hospitalization and amputation. However, loss of sensation resulting from diabetic neuropathy and other complications may result in these foot ulcers going unnoticed. One of the preventing strategies is to use monitoring devices to detect early onset of diabetic foot ulcers. Previous studies used plantar pressure or joint mobility as indicators to design such devices. However, very few studies combined both measurements. The measuring systems involved are also difficult to operate. The aim of this paper is to present a non-invasive household tool prototype for monitoring and early detection of diabetic ulcers by combining plantar pressure measurements from TEKSCAN HUGE MAT and hip range of motion measurements from a gyroscope sensor installed in smartphones. This new prototype models the situation where a patient walks on a floormat while the phone is located within the front pants pocket at home, which requires minimal human intervention to predict the risk of diabetic ulcerations. Further testing shows that this prototype can obtain measurements with reasonable accuracy.

Keywords Diabetic foot ulceration · Loss of sensation · Monitoring device · Combined measurements · Non-invasive household tool

1 Introduction

A diabetic foot ulcer is an open sore or wound commonly located at the bottom of the foot [1], which are difficult to treat. This is especially so in later stages where infection of the wound may occur, leading to the need for amputation. Early detection

Y. Z. Wen (✉) · J. L. Y. Jun
NUS High School of Math and Science, Singapore, Singapore
e-mail: jennyyuan0204@gmail.com

J. L. Y. Jun
e-mail: h1510057@nushigh.edu.sg

H. Guo et al. (eds.), *IRC-SET 2020*,
https://doi.org/10.1007/978-981-15-9472-4_34

and treatment can help reduce the chances of surgical intervention. One issue faced for early detection is diabetic neuropathy, where damage to the nerves results in inability of diabetic patients to detect the diabetic foot ulcers. In addition, many diabetic patients suffer from poor vision as a result of diabetic complications. Thus, it is difficult for diabetic patients to check foot conditions themselves. A household monitoring tool for diabetic ulceration would be desirable.

Diabetic patients are at risk of developing diabetic foot ulcers due to a variety of reasons, amongst which diabetic peripheral neuropathy is the most important etiologic factor, but there is a complex interplay between a number of other contributory factors, such as limited joint mobility and altered foot pressures [2]. Past studies have been done on identifying diabetic groups by using joint mobility or plantar pressure as indicators. It was reported that peak foot pressure is significantly higher in diabetic ulceration and diabetic neuropathy groups [3]. A reduction in joint mobility is also observed among diabetic patients [4]. However, no previous study has been done to combine these two measurements together to assess diabetic foot condition. Evaluating two parameters at the same time allows us to have a deeper understanding of gait dynamics and monitor foot conditions more effectively. Recently there are diabetic foot assessment systems using image analysis [5], in-shoe sensors [6] or thermal imaging system [7]. Image analysis and thermal imaging systems require the patient to use smart devices to scan their foot regularly. In-shoe sensors have a high chance of slipping while walking and have low spatial resolution for the data, leading to unsafety and inaccuracies in measurements. Clinically, the hip rotation angle is measured with a goniometer, which is a highly specialized equipment. Hence, the patients are unable to complete the measurements on their own. Given the fact that the elderly comprise a large proportion of diabetic patients, it is essential to develop a combination of devices to be able to be implemented as a non-invasive method of tracking the disease progression of individuals, with little human intervention to operate and lower cost compared to clinical devices.

In this paper, the plantar pressure is measured with a device designed similarly to a floormat, whereas tracing of the angular motion of the hip would be conducted by a phone with a built-in gyroscope placed near hip joint to model the situation where the phone is located within the right front pocket. Patients can put the pressure measuring device outside the toilet door at home or a location where he will step on barefoot on a regular basis to take pressure measurements. With algorithm to synchronize gyroscope with the pressure measuring device, the system can record down angular velocity concurrently. Data will be analysed and the system can evaluate the risk of getting diabetic ulceration or determine if ulcers are likely to exist already. Such data analysis would require machine learning based on large datasets. Relevant factors such as age, ethnicity, gender, past medical history, and even foot size need to be taken into account to give a fair evaluation on the risk of getting diabetic ulcers. Thus some preliminary data that allows us to do simple classification would be helpful in designing the algorithm in a later stage.

The aim of this paper is to construct such a prototype to measure and investigate the combination of plantar pressure and the hip rotation to allow for the classification

of individuals as healthy versus diseased, particularly towards early detection of diabetic foot ulcers. As such, a commercially-available device could be developed.

2 Methodology

Tekscan HUGEMAT (0.35 sensel per sq-cm and a frame rate of 8 frames per second) was used for plantar pressure measurements. The angular velocity of hip was measured a gyroscope built into a HUAWEI p20 with a sampling rate of 546 data points per second. Android app IMU+GPS-Stream was used for data logging. 34 non-diabetic volunteers participated in this study. Age, gender, weight, height and past foot conditions were collected.

In experiment, individuals began walking barefooted at a non-controlled, steady pace from 2 meters away from the Tekscan Mat, and hold the phone used approximately 5cm away from the right hip joint vertically (Fig. 1). Subjects were given time to familiarize themselves with the test settings. Each individual was asked to walk across the mat barefooted in the same direction for 20 runs. The angular velocity of hip rotation in the sagittal plane (Fig. 2) was also measured concurrently**.** Maximum peak plantar pressure and the hip range of motion in the sagittal plane within each

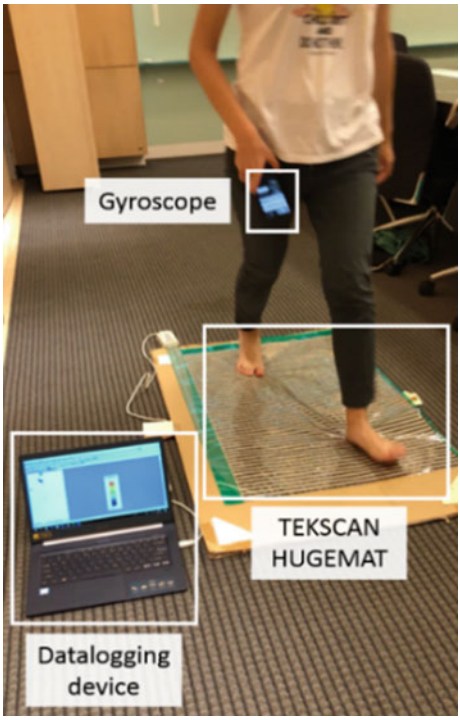

Fig. 1 Setup used to record measurements

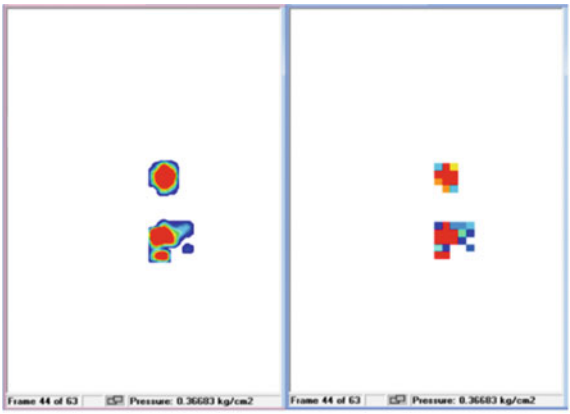

Fig. 2 Output from Tekscan Software

run were invesitagted. One full gait cycle begins at the heel strike of one foot and continues until the heel strike of the same foot in preparation for the next step [8] (Fig. 4). The peak plantar pressure is defined as the highest pressure recorded by the sensors over a full gait cycle; the hip rotation angle is the angle that hip rotates from extension to flexion in one gait cycle, obtained by integrating angular velocity over time processed by python (Fig. 3).

3 Results

The experimental data demonstrates that this prototype can collect measurements with a reasonable accuracy. As expected, all volunteers' data falls into healthy range, indicating that they do not have foot conditions that affect gait. BMI is the most important risk factor for diabetic ulceration.

The raw data obtained from measuring instrument were plotted for the gyroscope (Fig. 5) and the pressure mat (Fig. 6).The hip range of motion in the sagittal plane was computed by integrating the angular velocity (Fig. 7). Two distinct peaks can be observed in peak plantar pressure record over one gait cycle (Fig. 6). These two distinct peaks occur at two different instances: the first occurring where the heel comes into contact with the pressure mat (heelstrike), the second occurring at the toe region when the foot leaves the mat (pushoff) [11]. This proves that this measuring system is sensitive enough to detect a full gait cycle.

The raw data of the volunteers was collected and maximum peak plantar pressure against range of motion in the sagittal plane was plotted (Fig. 8). The conservative threshold for peak pressure of 40 N/cm^2 for diabetic patients is taken from literature [12]. All volunteers' peak pressure values are within normal range. For the hip range of motion, different studies show different threshold values, ranging from 25.99 (SE: 3.63) degrees [13] to 44.7 (SE: 1.3) degrees [14]. Here we focus on investigating people who are less flexible, so the threshold was set to be 25.99°. All our volunteer

Fig. 3 Diagram of the sagittal plane (pink) [9]

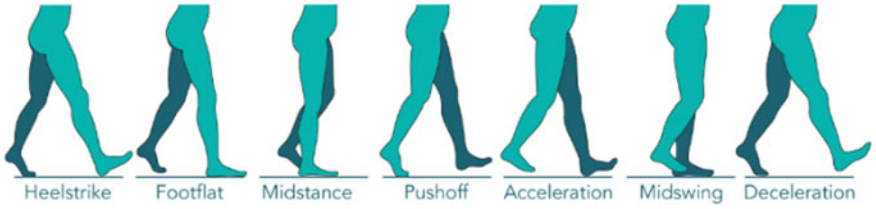

Fig. 4 Stages in a gait cycle [10]

data is within the healthy range. Thus reasonable numbers can be picked up using this simple device.

We tried to classify the data based on gender, BMI and age using peak plantar pressure and hip rotation angle by performing t-tests. From the graphs (Figs. 9 and 10), we observe that for both range of motion and the maximum peak plantar pressure, there is no significant difference for different genders ($p > 0.05$). People with high

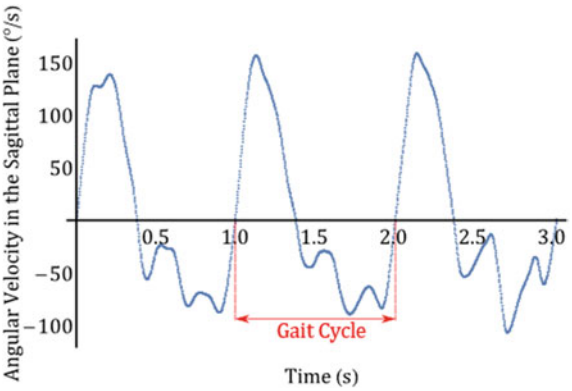

Fig. 5 Angular velocity (°/s) against time (s)

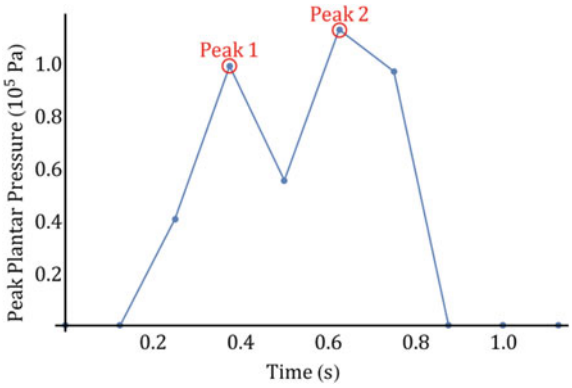

Fig. 6 Peak plantar pressure (10^5 Pa) against time (s)

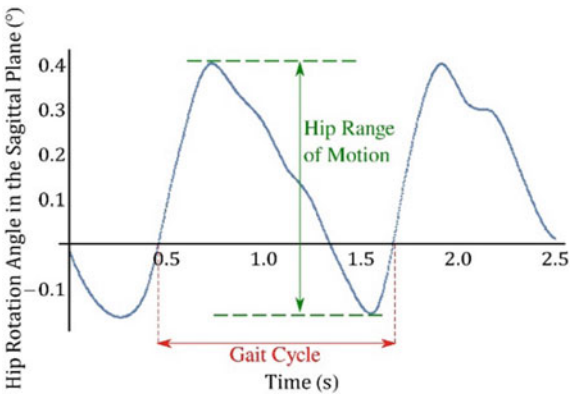

Fig. 7 Hip rotation angle (°) against time (s)

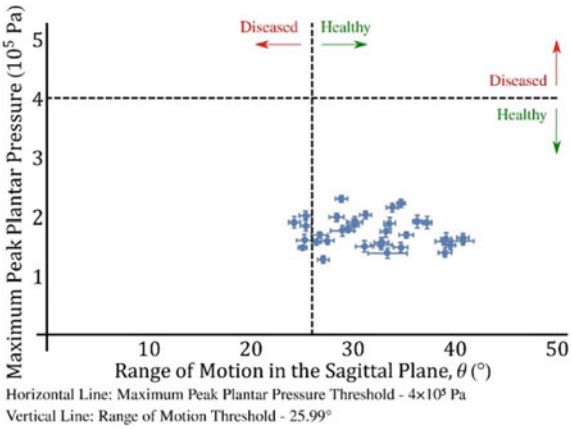

Fig. 8 Peak plantar pressure (10^5 Pa) against hip rotation angle (°)

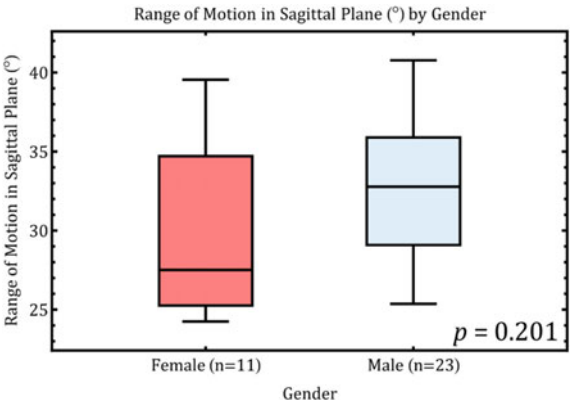

Fig. 9 Range of motion in sagittal plane by gender

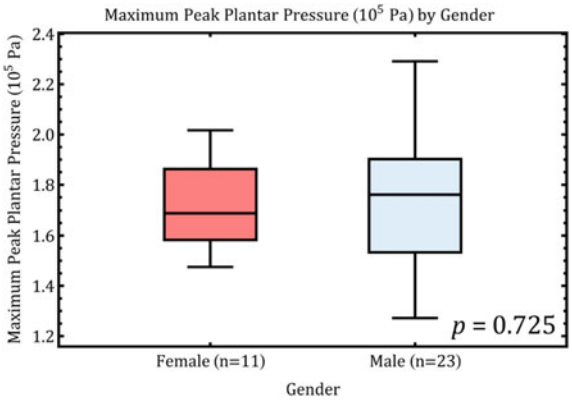

Fig. 10 Maximum peak plantar pressure by gender

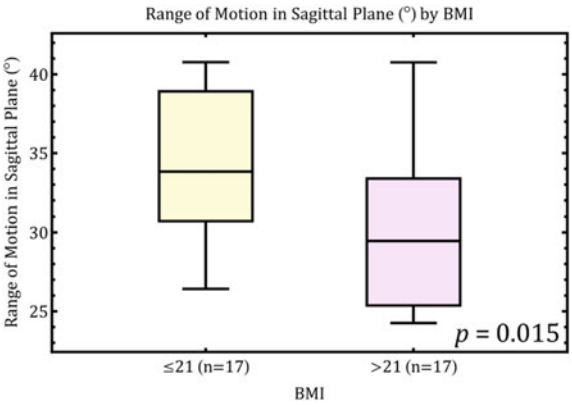

Fig. 11 Range of motion for different BMI

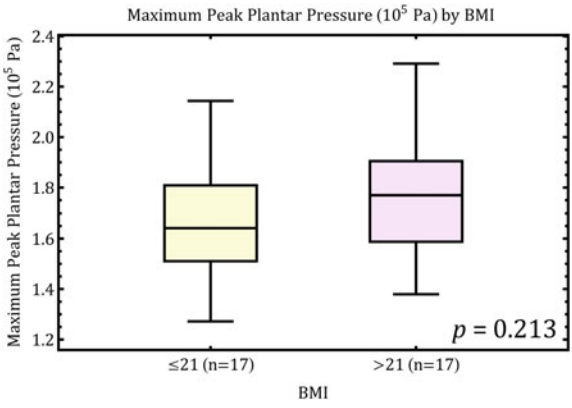

Fig. 12 Maximum peak plantar pressure for different BMI

BMI have a smaller range of motion (Fig. 11, $p < 0.05$), but BMI is not a predictor for peak plantar pressure (Fig. 12, $p > 0.05$). Based on our data, age does not affect range of motion and peak plantar pressure significantly as well (Figs. 13 and 14, $p > 0.05$). In this case, age and gender do not play a role in determining the range of motion and peak plantar pressure. One possible reason is that the age difference between volunteers is small and all the volunteers are considered very young (all below 35) for disease to develop. Thus, only BMI is the main determinant.

4 Discussion

With our measuring system, we can classify individuals under 2 sets of conditions using maximum peak plantar pressure and range of motion. The plot of maximum peak plantar pressure against range of motion allows for a classification of individuals into 4 categories (Fig. 15). (I) inflexible and high plantar pressure; (II) flexible and

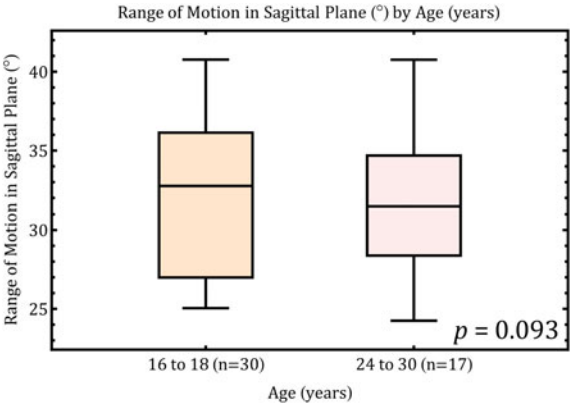

Fig. 13 Range of motion for different ages

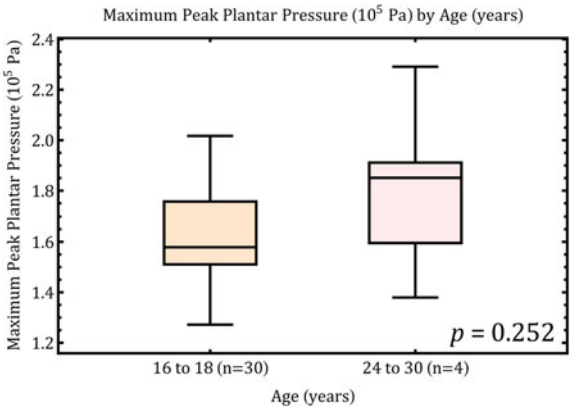

Fig. 14 Maximum peak plantar pressure for different ages

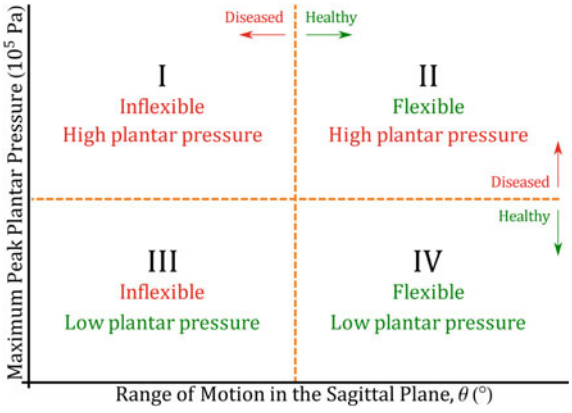

Fig. 15 Four categories for individuals

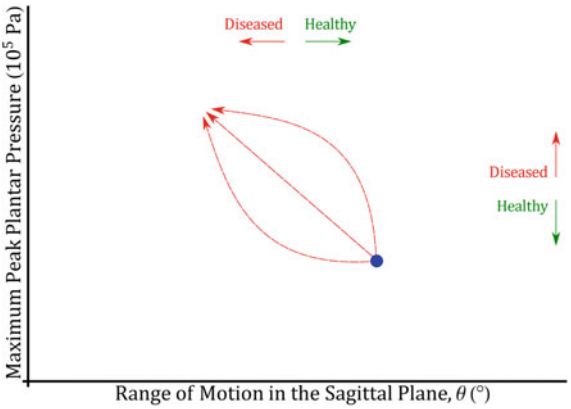

Fig. 16 Deterioration of health over time for individual (indicated by red dashed arrow)

high plantar pressure; (III) inflexible and low plantar pressure; and (IV) flexible and low plantar pressure. These four categorisations allow us to track the health of the individual, and particularly disease progression for diabetic patients. A shift in these points over a long period of time can be used to determine the rate of change of an individual's flexibility and plantar pressure, which indirectly signifies the health of the individual. If an individual's diabetes has deteriorated, data points are expected to shift towards region (I) (Fig. 16).

The fact that peak plantar pressure and joint mobility allow for a risk prediction for the development of diabetic ulcers is proven biomechanically in past literature. Elevated glucose levels among diabetic patients cause sugar to stick to collagen in bones, cartilage and tendons. When collagen becomes glycosylated, it thickens, resulting in stiffness and preventing bones from moving smoothly through the full range of motion [15]. Thus, the low range of motion of the hip in the sagittal plane can be attributed to a decrease in flexibility of the individual caused by diabetes. Subsequently, the reduced joint mobility causes elevated foot pressure. During gait in healthy individuals, muscles help to distribute plantar pressures generated in response to mechanical loading on the ground [16]. However, for diabetic patients, limited ankle dorsiflexion and subtalar joint mobility may reduce the foot's ability to absorb shock. The smaller contact area caused by foot deformities, which is prevalent among diabetic patients, further contributes to the development of tissue breakdown that can precede ulceration in patients without foot sensitivity. Research has shown that ulcers develop at sites of maximum pressure [17]. Thus, this measuring system can also be used to predict the location of foot ulcers.

This novel measuring system allows us to investigate other possible parameters for a more comprehensive outlook on the risk of diabetic ulcerations like walking speed, stride length, contact area and plantar force that may be further extended for the prediction and monitoring of the health conditions.

5 Conclusions

Within this paper, a non-invasive prototype to monitor disease progression via a combination of a plantar pressure measuring floormat and the tracking of angular rotation of the hip has been proposed. The plantar pressure and the hip rotation in the sagittal plane were investigated, and a categorisation of individuals can be drawn from the results obtained. Possible reasons for such observations are also proposed. This may be further extended for the prediction and monitoring of the health conditions of individuals.

Acknowledgement The authors would like to thank Dr. Chiam Keng-Hwee for supervising this project. We would also like to appreciate ASTAR BII for providing TEKSAN mat and NUS High School of Mathematics and Science for supporting this research project.

References

1. Diabetic Wound Care: Foot Health: Patients. (n.d.). Retrieved from https://www.apma.org/diabeticwoundcare
2. The Role of Limited Joint Mobility in Diabetic Patients With an At-Risk Foot. (2003). *Diabetes Care*, *27*(4).
3. Fawzy, O. A. (2014). Plantar Pressure as a Risk Assessment Tool for Diabetic Foot Ulceration in Egyptian Patients with Diabetes. *Clin Med Insights Endocrinol Diabetes*, *7*. doi: https://doi.org/10.4137/CMED.S17088
4. History, Prevalence and Assessment of Limited Joint Mobility, from Stiff Hand Syndrome to Diabetic Foot Ulcer Prevention: A Narrative Review of the Literature. (2018). *Curr Diabetes Rev*, *14*(5). doi: https://doi.org/10.2174/1573399813666170816142731
5. An Automatic Assessment System of Diabetic Foot Ulcers Based on Wound Area Determination, Color Segmentation, and Healing Score Evaluation. (2015). *J Diabetes Sci Technol*, *10*(2). doi: https://doi.org/10.1177/1932296815599004
6. Abdul, A. H. (2012). Foot Plantar Pressure Measurement System: A Review. *Sensors (Basel)*, *12*(7). doi: https://doi.org/10.3390/s120709884
7. Diabetic foot ulcer mobile detection system using smart phone thermal camera: a feasibility study. (2016). *Biomed Eng Online*, (16). doi: https://doi.org/10.1186/s12938-017-0408-x
8. Kawalec, J. S. (2017). Mechanical testing of foot and ankle implants. *Mechanical Testing of Orthopaedic Implants*, 231–253. Retrieved from https://doi.org/https://doi.org/10.1016/B978-0-08-100286-5.00012-3
9. Mike, M. W. (2019, Octobr 16). Planes Of Motion - Sagittal Plane, Transverse Plane, Frontal Plane. Retrieved from https://www.teachpe.com/anatomy-physiology/planes-of-movement.
10. The Gait Cycle: Phases, Parameters to Evaluate & Technology. (2019, August 23). Retrieved from https://www.tekscan.com/blog/medical/gait-cycle-phases-parameters-evaluate-technology.
11. Deursen, R. V. (2004). Mechanical Loading and Off-Loading of the Plantar Surface of the Diabetic Foot. *Clinical Infectious Diseases*, *39*(Supplement_2). doi: https://doi.org/10.1086/383268
12. 12. Stess, R. M., Jensen, S. R., & Mirmiran, R. (1997). The Role of Dynamic Plantar Pressures in Diabetic Foot Ulcers. *Diabetes Care*, *20*(5), 855–858. doi: https://doi.org/10.2337/diacare.20.5.855

13. 13. Gomes, A. A., Onodera, A. N., Otuzi, M. E., Pripas, D., Mezzarane, R. A., & Sacco, I. C. N. (2011). Electromyography and kinematic changes of gait cycle at different cadences in diabetic neuropathic individuals. *Muscle & Nerve*, *44*(2), 258–268. doi: https://doi.org/10.1002/mus.22051
14. 14. Raspovic, A. (2013). Gait characteristics of people with diabetes-related peripheral neuropathy, with and without a history of ulceration. *Gait & Posture*, *38*(4), 723–728. doi: https://doi.org/10.1016/j.gaitpost.2013.03.009
15. 15. Schie, C. H. V., Vermigli, C., Carrington, A. L., & Boulton, A. (2004). Muscle Weakness and Foot Deformities in Diabetes: Relationship to neuropathy and foot ulceration in Caucasian diabetic men. *Diabetes Care*, *27*(7), 1668–1673. doi: https://doi.org/10.2337/diacare.27.7.1668
16. Plantar pressure and gait in patients with diabetes. (n.d.). Retrieved from https://lermagazine.com/article/plantar-pressure-and-gait-in-patients-with-diabetes.
17. Hughes, R. (n.d.). *Patient Safety and Quality: An Evidence-Based Handbook for Nurses.*

IoT Smart Trolley System for Healthcare

Jiaqiang Yeow, Yongqing Zhu, Paul Horng Jyh Wu, and Fang Liu

Abstract Technological advances in Internet of things (IoT) have brought the technology well within the reach of many small and medium enterprises as well as consumer markets in recent years. Food preparation in the healthcare industry is generally labor intensive and there are safety standards to adhere to. There is great potential in applying IoT technologies to improve food preparation and streamline the process in hospitals. In this paper, an IoT smart trolley system is proposed to automate the process of temperature tracking of food trolleys in hospitals. The system targets to reduce the time and labor needed to record temperatures of food trolleys, and improve the accuracy of the data collected, thereby resulting in cost-savings in the long run and allowing real-time monitoring of temperatures in food trolleys. Various hardware and software technologies are applied in the system, including Raspberry Pi for data collection, MQTT via Wi-Fi for data transmission, and Firebase cloud backend for data store and process, etc. After design and implementation, the IoT smart trolley system has undergone different levels of testing. The system can achieve its objective to automatically record and monitor temperatures for food trolleys with improved data accuracy and reduced time and labor.

Keywords Temperature tracking · Real-time monitoring · IoT · Healthcare

J. Yeow · Y. Zhu (✉) · P. H. J. Wu · F. Liu
School of Science and Technology, Singapore University of Social Sciences, 463 Clementi Road, Singapore 599494, Singapore
e-mail: yqzhu@SUSS.edu.sg

J. Yeow
e-mail: jqyeow001@SUSS.edu.sg

P. H. J. Wu
e-mail: paulwuhj@SUSS.edu.sg

F. Liu
e-mail: liufang@SUSS.edu.sg

H. Guo et al. (eds.), *IRC-SET 2020*,
https://doi.org/10.1007/978-981-15-9472-4_35

1 Introduction

The Dietetics and Catering Services of a hospital is responsible for meeting the nutritional and dietary requirements of the patients. The quality objectives of hospital food services are to provide the right food to the right patient at the right time while avoiding food wastage. Not only must the food provided be safe for consumption, it must also be palatable. To meet these objectives, heated food trolleys are used in hospitals to keep the portioned food trays at a desired temperature before they are delivered to the wards.

Harmful bacteria can grow in food at a temperature range from 5 to 60 °C. This temperature range is known as the Temperature Danger Zone [1]. Hospitals are required to maintain the correct temperature of food outside of this Temperature Danger Zone before serving to patients. Currently, hospitals are portioning food into food trays and putting those trays into heated food trolleys that maintain the food temperature at 70 °C. These heated food trolleys, with the food trays inside, are then delivered to the wards at mealtimes.

As part of audit requirements, the hospital must record these temperature readings in the heated food trolleys before the food is served to patients [2]. Currently, there is no system available for recording the temperature of food trolleys. Hospital staff have to rely on pen and paper to manually record temperature readings taken from analog thermometers which are placed inside the heated food trolleys. These temperature readings are then manually keyed into excel spreadsheets. The whole process, involving multiple staff from the kitchen, ward and the administrative teams, is very laborious and time-consuming.

In this paper, we propose an Internet of things (IoT) smart trolley system to automate the process of temperature monitoring and recording for food trolleys in hospitals. The proposed IoT system target to reduce the human labors required in the traditional process of temperature recording, while obtain highly accurate and consistent temperature data at the same time. This paper is organized as follows. Section 1 is the introduction, followed by literature review in Sect. 2. Design of the IoT smart trolley system is presented in Sect. 3. Section 4 introduces the system implementation, including hardware setup, software development, and security processes. Section 5 discusses different levels of testing on the system, and Sect. 6 concludes the whole paper.

2 Literature Review

IoT has introduced new ways to utilize technologies to provide better business solutions and add values to many industries, including healthcare and food supply chain management. In the healthcare industry, implementation of IoT technologies has largely revolved around patient care applications and mobile IoT devices, which

face energy challenges such as energy constraints, limited battery or accessing to energy resources [3].

Research has been done on the use of LoRaWAN [4], 6LoWPAN [5] and Sigfox [6] networks for hospital networks [3, 7]. Although these technologies have a better range than Wi-Fi [8], the hefty infrastructure and subscription costs would outweigh the financial benefits if these technologies were considered for the proposed IoT system. There was also research done on successfully creating a user friendly and low maintenance system that transfers sensor data (such as temperature) through Message Queuing Telemetry Transport (MQTT) publish and subscribe protocol in a Smart hospital setting [9].

In food supply chains, IoT devices are already being used in farming and food manufacturing. A study has shown that the introduction of IoT technologies has benefited food production. However, IoT technologies are currently mostly available to larger corporations but still out of reach of smaller businesses [10]. Despite the limitations imposed by high costs, a small-scaled and successful proof-of-concept experiment had created an automated system to monitor humidity and temperature data in a cold food storage [11]. This was shown to be an effective way of monitoring and could translate into savings in terms of labor cost.

In hospital food preparation, meals are increasingly being cooked in advance through cook-chill and cook-free systems which offer better flexibility when preparing and serving large quantities of food in a hospital. According to [12], food should be cooked at temperatures 70 °C or above for at least two minutes to eliminate micro-organisms. Proper cooling is used to prevent bacterial spores that survive the cooking process from growth. The cooked food should be: (1) consumed immediately; or (2) kept for a short duration of time at a temperature of 63 °C or higher; or (3) cooled rapidly and kept at 3 °C or below to prevent micro-organism growth, and reheated to an internal temperature of above 70 °C for more than 2 min before consumption.

3 Design of IoT Smart Trolley System

This paper proposes an IoT smart trolley system, to automate the process of temperature monitoring and recording of food trolleys in hospitals. The system targets to reduce the time and labor needed to record temperatures of food trolleys, and improve the accuracy of the data collected at the same time.

3.1 Architecture of IoT Smart Trolley System

System architecture of the proposed IoT smart trolley system is shown in Fig. 1. It includes Temperature Recording Devices, IoT Gateway Device, Firebase cloud backend, web application front-end, and email service. In the system, Raspberry

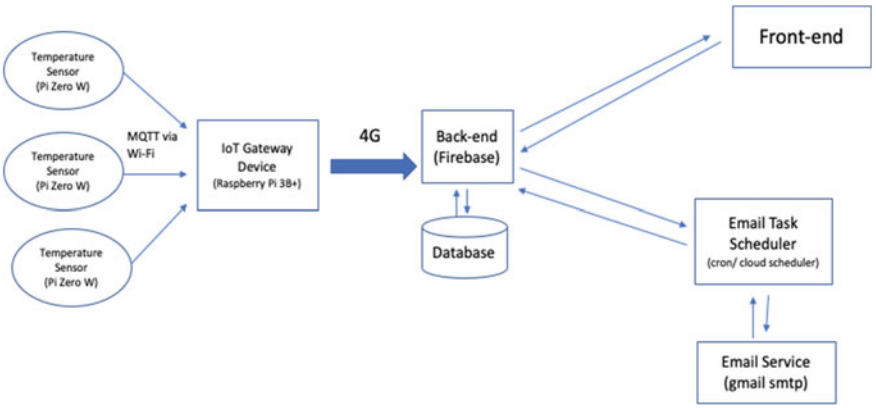

Fig. 1 Architecture design of IoT smart trolley system

Pi Zero W is deployed in the sensor units that attached to the food trolleys for data collection purpose. These sensor units relay temperature readings using MQTT over a Wi-Fi network to a Raspberry Pi 3B+ gateway, and transmit to the IoT Gateway Device. The gateway device uploads the temperature recordings to a Firebase backend database (Cloud Firestore) through a 4G cellular network. The Firebase backend can be accessed by both a web application front-end as well as a scheduler which periodically sends emails to the users' email addresses [13].

3.2 Related Technologies

Various software and hardware technologies are used to achieve the IoT smart trolley system. In order to collect data, there must be a sensor attached to each food trolley to record the temperature readings. A processor or "brain" is required to interpret the temperature data received from the sensor. Raspberry Pi Zero W [14] is adopted here which comes with built-in Wi-Fi and Bluetooth capabilities. Considering the power consumption, there are electrical charging points above each food trolley in the trolley docking bay that can charge the battery or use power bank to charge the sensor unit. In this work, a power bank can be used to power the Raspberry Pi. A 10,400 mAh power bank has the capacity to power a Raspberry Pi Zero W for a minimum of 6 h on continuous usage, and around 46 h on standby [15]. Raspberry Pi 3B+ is used for the IoT gateway device that is responsible for collecting data from multiple sensors.

Raspbian Operating System (OS) [16] is a Debian-based [17] and lightweight operating system used by Raspberry Pi. Raspbian Lite is installed on the temperature recording Raspberry Pi Zero W devices, whereas Raspbian Desktop is selected for the IoT Gateway Device. Third party open-source libraries are installed on the Raspbian OS. These include the CircuitPython library [18] for working with the hardware

modules such as temperature sensors, as well as the Eclipse Paho Python client library [19] for enabling python scripts to use MQTT.

For wireless protocol, Wi-Fi [8] is chosen for data transmission from temperature sensors to the IoT gateway device. Wi-Fi is favorable due to its longer range comparing to Bluetooth that can cover the kitchen loading bay area and its ability to support large amount of cell nodes. Moreover, Wi-Fi is a well-established technology, and there are many devices and software libraries that can support Wi-Fi. Considering the transmission distance between IoT gateway devices and the backend, a wireless protocol supporting long range (e.g. 4G) is required for data transmission.

MQTT [20] is used for transmitting the temperature data from the devices attached to the trolleys to the central IoT gateway device located in the kitchen. Eclipse Mosquitto [21], an open source implementation of MQTT protocol, is implemented to perform messaging through a publish/subscribe model. It is lightweight, thus making it feasible for the small transmission bandwidth capacity of IoT applications.

In the backend, Firebase cloud [22] is deployed to store and process the temperature data after receiving from the IoT gateway devices. As a real-time database, Firebase is very useful as it can display temperature data in real-time so that data can be monitored and actions can be taken quickly in the case of abnormalities. Besides, the documentation is comprehensive and easy to read. Firebase is also cost effective. Firebase backend can be accessed by both a web application front-end and a scheduler which periodically emails reports to the users' email addresses. This scheduler service can be provided by Firebase cloud backend.

4 System Implementstion

Implementation of the IoT smart trolley system includes various hardware setup and software development for data store, process, and presentation.

4.1 Hardware Setup

Hardware setup of the system mainly includes the Temperature Recording Devices and IoT Gateway Devices. These devices are made up of multiple components such as DHT temperature sensor, Raspberry Pi, LCD screen, and casing.

Temperature Monitoring Unit is designed to be mobile and powered by a power bank. As shown in Fig. 2, the Temperature Monitoring Unit includes the following components: Temperature and Humidity Sensor, Potentiometer, Real-Time Clock Module, Raspberry Pi Zero W, and LCD screen.

The IoT Gateway Device collects temperature data from Temperature Recording Units and uploads these data to a Firebase backend which is accessible by a Web Application. Components of the IoT Gateway Device include: Raspberry Pi 3B+, LCD screen, and 4G USB Dongle.

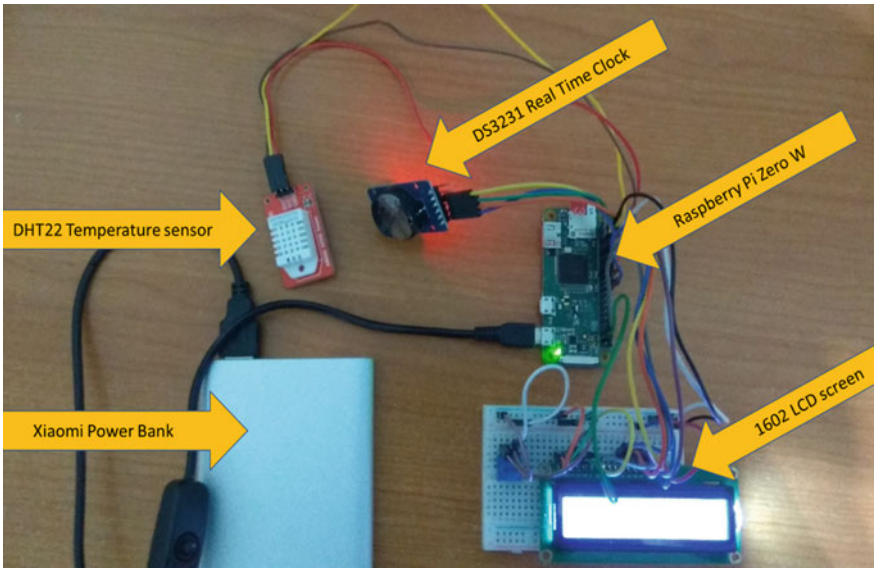

Fig. 2 Breadboard setup of temperature monitoring unit

4.2 Software Development

Besides hardware setup, various software are implemented in the system to support data store, process, and presentation as well. One main effort in this work is web application development. Web application provides the front-end interfaces that allow the user to interact with the data gathered. The application is developed using Angular 8 [23] which is a client-side framework that uses JavaScript and Typescript to create dynamic web applications.

The Web Application provides four main functionalities: Dashboard, Account Management, Email Configuration, and Download (Fig. 3). The Web Application uses an Operational Dashboard to give a quick overview of the operations to the end-user who is either in an administrative or operational position. Account Management provides two functionalities. First, it allows the user to change his password. Second, if the user is an Admin or Supervisor role, it allows the user to grant levels of privileges to other users. The system monitors and records the temperature readings. If a recorded temperature falls outside of a threshold range in the given period of time, the system will send an email notification to the user. Furthermore, the system can also send periodic emails with attached reports to the user. The user can configure the frequency of email that the system will send the report. In addition, the user can export data from the system in the form of an excel spreadsheet through the Download view. The user interface design improves the user experience and satisfaction, and ultimately aids in user acceptance of the system. An intuitive design allows for quick and efficient retrieval of desired information.

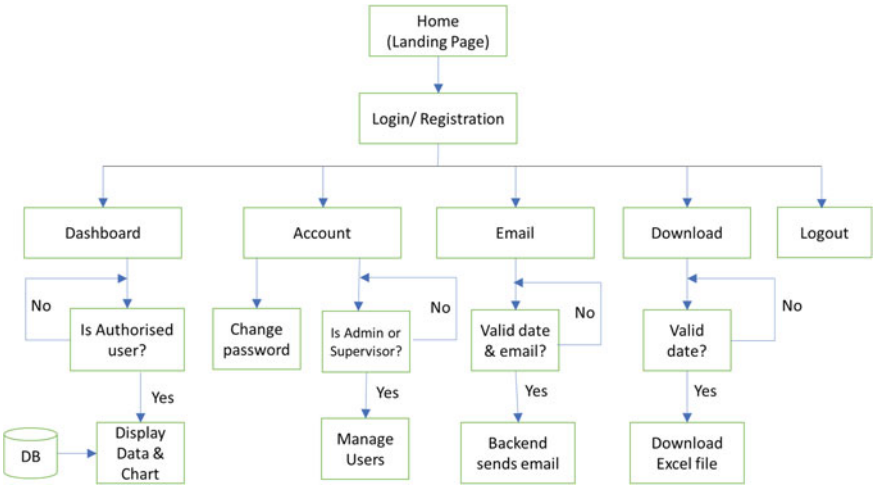

Fig. 3 System architecture diagram of web application

Cloud functions serve to run backend code and perform computations in response to events that are triggered by the Angular Web Application front-end. The cloud functions used by the Web Application include: *app*,*createNewUser*,*createRecording*,*deleteUser*,*dispatchMail*, etc. Since the code is stored on the cloud in a managed environment, it is not run on the user's computer or revealed to the user on the front-end. This provides several benefits, such as being able to run sensitive code on the cloud backend without the risk of modifications from the user, as well as avoiding the need to scale and manage a server.

The Cloud Firestore data model provides the web application the flexibility to store data in hierarchical structure, which is organized into collections and can contain nested documents or further sub-collections. The primary advantage of using Cloud Firestore is its data synchronization capability to update data on any connected device. This is very useful on a system that monitors data in real-time. Furthermore, the Cloud Firestore database is designed to scale with the cloud infrastructure, making it easier to scale the database in a cost-effective way.

4.3 Security Processes

In order to ensure that a valid user is able to access the web application and prevent unauthorized access, authorization is required to determine which level of access should be granted to a user based on his user credentials. Figure 4 shows the authorization process flow of the Angular Web Application.

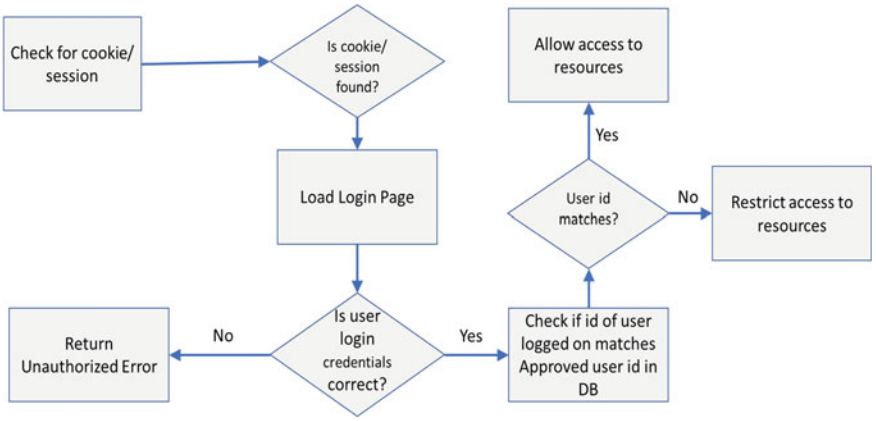

Fig. 4 Authorization flow of web application

To secure the MQTT server on the IoT Gateway Device, encrypted MQTT communication is implemented to prevent information leakage during data transmission. In this system, the free OpenSSL [24] utility is used to generate the certificates for the MQTT server to enable Transport Layer Security (TLS) with Mosquitto. A generated digital certificate confirms that a specific public key belongs to the subject included within the certificate. The scripts on the Temperature Monitoring Unit uses the generated files in conjunction with the paho-mqtt library to transmit secured MQTT messages over Wi-Fi.

5 Testings

After implementing the IoT smart trolley system prototype, the system underwent different levels of testing including modular testing, integration testing, and system testing.

5.1 Modular Testing

Modular Testing is a type of software testing that checks individual components in a software. In this level, the entire software application is divided into smaller "building blocks" and tested individually instead of testing the whole software application at once. The main objective is to spot errors and bugs in a module, rather than to show that the module is functioning properly. This level of testing allows multiple components to be tested concurrently in parallel, thereby speeding up the process of testing.

5.2 Integration Testing

Integration Testing combines and integrates modules of a system logically and tests them as a group. As systems generally comprised multiple modules built for different purposes, it is crucial for Integration Testing to expose bugs and defects when modules are integrated. The focus of Integration Testing is the interfaces and data communication amongst these modules.

During Integration Testing, testing is conducted by joining two or more modules which are logically linked. Additional modules are subsequently added to test for proper functionality. This process is continued until all of the modules are integrated and successfully tested.

5.3 System Testing

The IoT smart trolley system comprises hardware and software modules. The objective of System Testing is to validate the complete system from end-to-end.

Regression Testing is done to confirm that a change made during the coding process has not created issues or bugs. It is done by re-executing the test cases to ensure that existing features are functioning properly and no previous bugs re-surface from adding new modules over the time. The test cases are prioritized according to critical functionalities and requirements, and not all the test cases are re-executed.

Recovery Testing verifies whether the system can recover failures such as hardware or software crashes, or even network failure. Both the Temperature Monitoring Unit and IoT Gateway Device have shell scripts which run on startup. These scripts start up the software (e.g. MQTT server on IoT Gateway Device) as well as python programs automatically. During the test, when a device is brought down by failure and restarted, the shell script in the respective device can run and start up the relevant software on boot. In the event of failure on the Wi-fi Router or 4G Mobile Data Network, Temperature Monitoring Unit and IoT Gateway Device can store the data locally and retransmit the data when network connectivity is re-established.

6 Conclusions

This paper proposes an IoT smart trolley system to automate the process of temperature recording and monitoring for food trolleys in hospitals. Various technologies are used in the system including MQTT, Raspberry Pi, and Firebase backend. Data collected are stored in the Firebase backend and the results are generated in reports which are accessible through an Angular Web Application. Temperature Recording Devices and IoT Gateway Devices are setup with different hardware components. Software implementation includes front-end and backend, where web application

development is the main effort. Authorization and encrypted MQTT communication are implemented to control access to the data as well as secure data transmission.

After the proper design and implementation, the IoT smart trolley system has been tested under different levels. The system can achieve its objective to automatically record and monitor temperatures for food trolleys. Not only does the system improve quality and accuracy of the temperature data collected, it also saves the time and effort in collecting this information and minimizes the risk of food contamination.

In the future, Machine Learning applications can be incorporated into the IoT smart trolley system. Additional data parameters, such as humidity data, can be collected and analyzed together with the temperature data. Predictions can be made in advance to recommend whether a food trolley requires preventive maintenance. Besides applications in a hospital kitchen environment, the system can be deployed in other environments within the business domains of healthcare and F&B. These can include other non-medical devices in hospitals, food manufacturing, catering, vending machines, food storage and food transportation.

References

1. Singapore Food Agency, 2019. Guidelines on Proper Storage of Food in Refrigerators and Maintenance of Refrigerators. [Online] Available at: https://www.sfa.gov.sg/docs/default-source/food-retailing/practices-and-guidelines/guidelines-on-proper-storage-of-food-in-refrigerators.pdf
2. Joint Commission International, 2017. Joint Commission International Accreditation Standards for Hospitals. *6th ed. Oak Brook: Joint Commission Resources.*
3. Shahamabadi, M. S., Ali, B. B. M., Varahram, P. & Jara, A. J., 2013. A network mobility solution based on 6LoWPAN hospital wireless sensor network (NEMO-HWSN). *Proceedings - 7th International Conference on Innovative Mobile and Internet Services in Ubiquitous Computing, IMIS 2013,* pp. 433–438.
4. Angular 8. [Online] Available at: https://angular.io/
5. LoRaWAN. [Online] Available at: https://lora-alliance.org/
6. LoWPAN. [Online] Available at: https://datatracker.ietf.org/wg/6lowpan/charter/
7. Dumka, A., 2019. Smart information technology for universal healthcare. In: *Healthcare Data Analytics and Management.* s.l.:Elsevier, pp. 211–226.
8. Eclipse Paho Python client. [Online] Available at: https://www.eclipse.org/paho/clients/python/-cloud-functions-firebase-cron.html
9. Jaisree, K., Sharmila, J., Jeevitha, J. & Chandrakala, K., 2017. Smart Hospitals Using Internet of Things (IoT). *International Journal of Trendy research in Engineering and Technology (IJTRET),* 1(3), pp. 1735-1737.
10. Dolci, R., 2017. IoT solutions for precision farming and food manufacturing. *IEEE 41st Annual Computer Software and Applications Conference,* pp. 384–385.
11. Karim, A. B., Hassan, M. Z., Akanda, M. M. & Mallik, A., 2018. Monitoring food storage humidity and temperature data using IoT. *MOJ Food Processing & Technology,* 6(4), pp. 400-404.
12. Lund, B. . M. & O'Brien, S. J., 2009. Microbiological safety of food in hospitals andother healthcare settings. *Journal of Hospital Infection,* Volume 73, pp. 109-120.
13. The Firebase Blog, 2019. Scheduling Cloud Functions for Firebase (cron). [Online] Available at: https://firebase.googleblog.com/2019/04/schedule

14. Sahoo, N., Lin, H. W. & Chang, Y. H., 2019. Design and implementation of a walking stick aid for visually challenged people. *Sensors (Switzerland),* 19 (1).
15. Raspberry Pi. [Online] Available at: https://www.raspberrypi.org/
16. Sigfox. [Online] Available at: https://www.sigfox.com/en
17. Raspbian OS. [Online] Available at: https://www.raspberrypi.org/downloads/raspberry-pi-os/
18. CircuitPython. [Online] Available at: https://circuitpython.org/
19. Wi-Fi. [Online] Available at: https://www.wi-fi.org/
20. Message Queuing Telemetry Transport (MQTT). [Online] Available at: https://mqtt.org/
21. Eclipse Mosquitto. [Online] Available at: https://mosquitto.org/
22. Firebase cloud. [Online] Available at: https://firebase.google.com/
23. Debian. [Online] Available at: https://www.debian.org/
24. OpenSSL. [Online] Available at: https://www.openssl.org/

Portable Precision Ellipsometer for Analysis of Molecular Layers

Han Lin Li, Keith Hong Xun Ong, and Nikolai L. Yakovlev

Abstract Precision ellipsometry (PREL) is an analytical technique that measures changes of light polarisation that reflects off the surface of a sample. It can be used to determine molecular layering or bonding between chemicals. A new portable PREL system has been designed and made. It contains a polarisation modulator which has a self-tuning generator for it to oscillate at the resonance frequency, a photodetector which has its signal current amplified by transistors and an Arduino programmed with phase lock function. The work of the system has been examined by measuring adsorption of propanol to oxidized silicon in air and attachment of small molecules and polymers in water. It is shown that this system has sensitivity down to the molecular level. This portable PREL system is energy efficient, cheap, light, while maintaining high sensitivity and can be applied for the analysis of molecular layers in the lab and in the field.

Keywords Precision ellipsometry · Polarisation modulation · Adsorption · Molecular binding

1 Introduction

The precision ellipsometry (PREL) is a tool used to analyse molecular layers using optics. It measures the polarization of light reflected off a surface of a material [1]. It can model a system that can be used to find out the thickness, surface roughness, and optical constant of various films that are usually hard to measure as they are smaller than the wavelength of light. It is also able to detect bonding within 2 molecular layers through the signal received that indicates a change of polarization of reflected light. Changes in polarization are measured using modulation of polarisation. It creates AC component of the light passing through the modulator. This AC component is

H. L. Li · K. H. X. Ong
NUS High School, Singapore, Singapore

N. L. Yakovlev (✉)
Institute of Materials Research and Engineering, A*STAR, Singapore, Singapore
e-mail: niko-y@imre.a-star.edu.sg

H. Guo et al. (eds.), *IRC-SET 2020*,
https://doi.org/10.1007/978-981-15-9472-4_36

extracted by a lock-in amplifier which creates a signal proportional to the rotation of polarization, which is in turn proportional to the thickness of the layer. It has various applications, from analysis of water to analysing molecular layers.

Previous tabletop precision ellipsometry system is bulky and requires socket power supply. We aim to create a precision ellipsometry system, one that is portable but equally as precise as the original tabletop system. To enable the sensitivity, we use polarisation modulator. To enable the portability, we make self-tuning generator for the modulator and realise the phase-lock function in Arduino microcontroller.

2 Materials and Methodology

The ellipsometry system consists of 3 main parts, optical part, fluidic part, and optical cuvette that holds substrate and molecules in the study. It includes laser, cuvette holder, retarder, modulator, and a photodetector (Fig. 1).

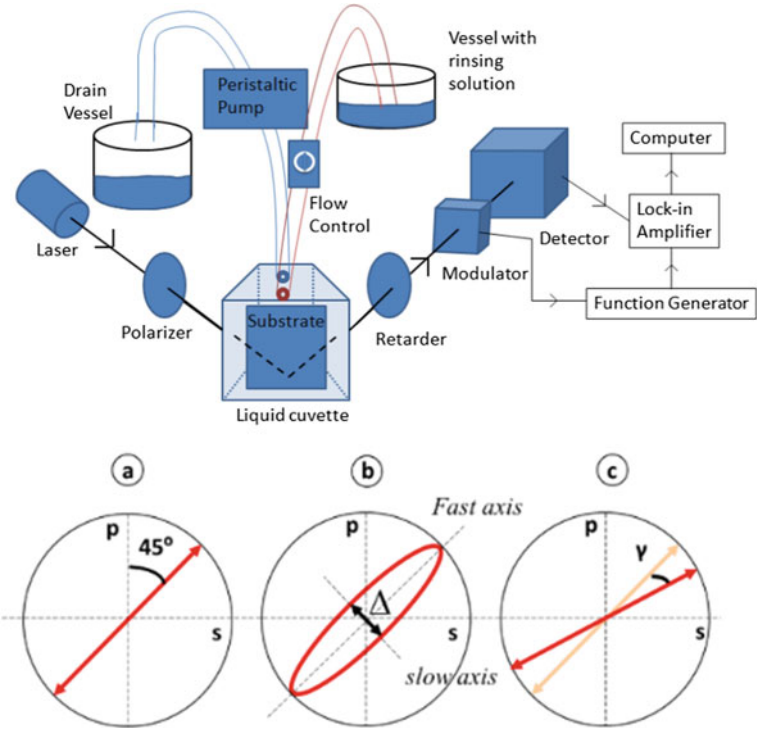

Fig. 1 Set-up of a liquid precision ellipsometry system (top) and states of polarisation: **a** original, **b** after reflection off the sample, **c** after passing through the retarder (bottom)

Light from the laser contains some diffused light and passes through a polarizer to be linearly polarised and removes diffused light as only light that is perpendicular to the polariser can pass through. After it hits the sample, it is elliptically polarized and passes through the retarder which causes it to be linearly polarised by angle gamma. The light then passes through a modulator that modulates it and a photodetector then converts the light signal to a current. From these, we can obtain the amplitude of modulation, the light intensity, and the voltage from the photodetector which is used to determine the thickness of the layers.

2.1 Modulator

The modulator consists of a polariser combined to 4 springs which are in turn connected to 4 piezo-transducers, Fig. 2. When the piezo is at positive voltage it vibrates downwards and rotates the polariser slightly anti-clockwise. Conversely, at a negative voltage, the polarizer rotates slightly clockwise. This rotation modulates the light: the light intensity is at the minimum as modulator axis is perpendicular to the polarisation of reflected light. When it rotates clockwise or anti-clockwise, more light can pass through. This also provides an alternating current in photodetector output as the axis of polariser rotates left and right [2]. The resonance frequency of our modulator was 239 Hz and was set to be away from multiples of 50 Hz. This was first determined using an oscilloscope through manual tuning and the self-tuning generator can accommodate this frequency.

The circuit on the modulator is connected to the sensing and driving piezo. The aim is to use this circuit and the 4 piezo located in the modulator to make a self-tuning generator so that the modulator will continuously oscillate in its resonance frequency. It also provides a reference signal to the lock-in amplifier in the Arduino which is important in reducing noise. The voltage from sensing piezo also provides a feedback signal to the Arduino to record the amplitude of modulation.

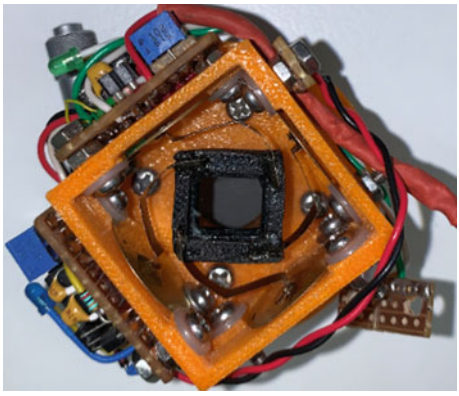

Fig. 2 Photo of the modulator

2.2 Self-tuning Generator

For the circuit to work, the sensing signal must be amplified and phase-shifted while the driving signal is amplified. To achieve resonance, the driving signal (periodic force) must be phase-shifted 90 degrees from sensing signal (displacement). This will lead to a higher and higher voltage which is resonance.

First, when 5 V is applied, the amplitude of the oscillation of sensing piezo is small. It will be amplified by 20 times using integrated circuit ICL7621D, Fig. 3. The amplified signal is subsequently phase-shifted by 90 degrees from sensing signal to achieve resonance. To perform phase-shifting, a resistor and capacitor are used. The circuit MAX662A creates 12 V for driving signals. The phase-shifted signal is amplified by the first transistor, T1, and then inverted by the second transistor, T2, and is used as a driving voltage for the driving piezo, Figs. 4 and 5. Such a circuit allows the self-tuning modulator to tune to the natural frequency of different modulators as they have different resonance frequency depending on the shape and type of springs. With a 5 V power source, we can produce a peak to peak voltage of 24 V.

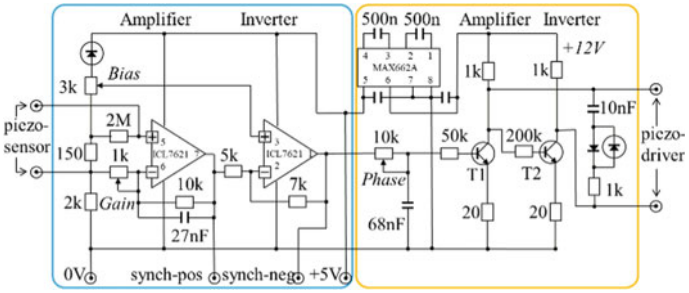

Fig. 3 Schematic for self-tuning generator realized on two circuit boards: amplifier of sensing signal (blue) and amplifier of driving signal (yellow) placed on the modulator itself

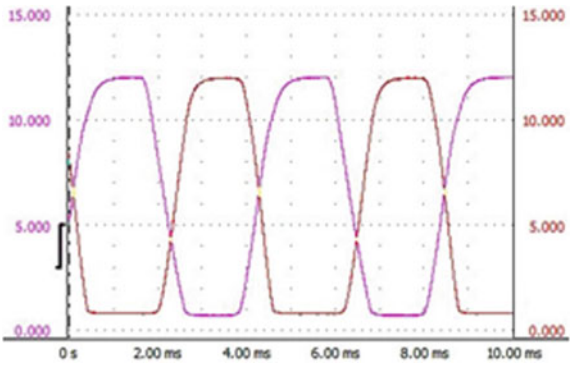

Fig. 4 Driving voltage from T1 (purple) and from T2 (red)

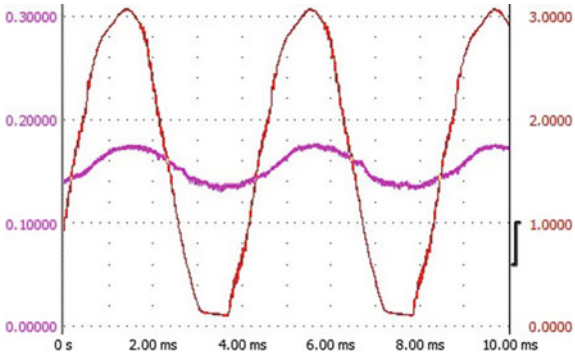

Fig. 5 Signal from photodetector (purple) and sensing voltage (red) as reference for phase lock function

2.3 *Photodetector and Digital Lock-In Detection*

To achieve the highest current signal proportional to the laser intensity, the photodiode must be aligned linearly with the incident laser. This allows for maximum conversion from light to electrical current which would result in maximum collector current after amplification by transistors. This is different from the self-tuning generator, as the generator uses an integrated circuit. Our objective is to amplify current, whereas the integrated circuit in the generator provides amplification of voltage. Hence, transistors are ideal for amplification of current, which is proportional laser intensity going into the photodiode.

As light is received by the photodiode, it is converted into current within the circuit, Fig. 6. The direct current is amplified 300 times by transistor T1. The current then flows to the 2 outer transistors on the right, which are responsible for voltage amplification. Here a small AC voltage at the transistor base generates a small base-emitter current which is amplified by the transistor to give a larger AC collector current. This amplified collector current through the collector resistor creates an AC voltage that is greater than the input voltage, in this case, 20 times the original. The

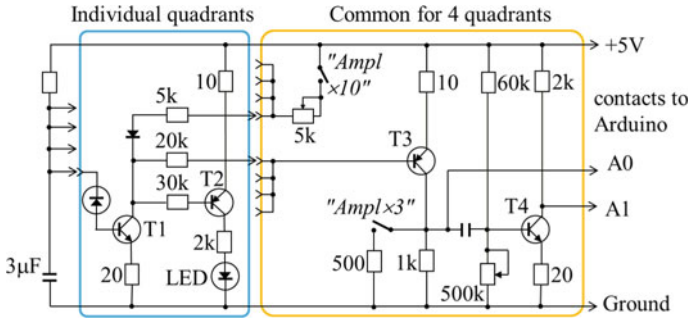

Fig. 6 Schematic for quadrant photo-detector amplifier

transistor T3 amplifies both DC and AC, where transistor T4 further amplifies only AC.

In addition to these, there are 3 switches on the top side of the detector box, which are meant to further change the amplification coefficient. The 10× and 3× switches are responsible for amplification of current, using a very basic concept of adding or removing resistors in parallel to reduce or increase effective resistance with the on–off of switches to change the magnitude of the current.

A four-quadrant photodiode is chosen to connect with a set of four LEDs, which each represent the 4 quadrants (top left to bottom right) of the photodiode. The current from each quadrant is amplified and goes to respective LED. This allows the user to tell the alignment based on the brightness of the LEDs, Fig. 7. When all LEDs have equal brightness, the incident laser is centred onto the photodetector (Fig. 7).

Digital lock-in detection is realized in the Arduino processor to send intensity and polarisation data to a computer. The data are presented on a graph during the acquisition and saved using a python program. The whole system is shown in Fig. 8.

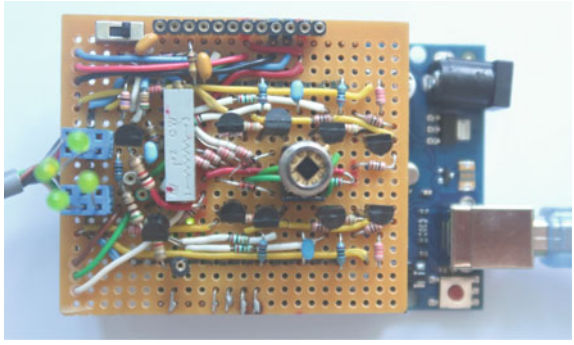

Fig. 7 Photo of quadrant detector amplifier on Arduino board

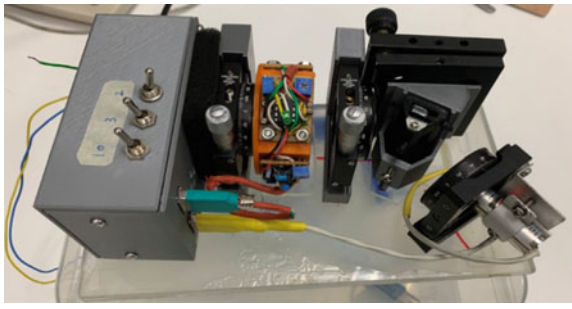

Fig. 8 Photo of portable PREL. From right to left: laser, cuvette with a substrate, retarder, modulator and photodetector

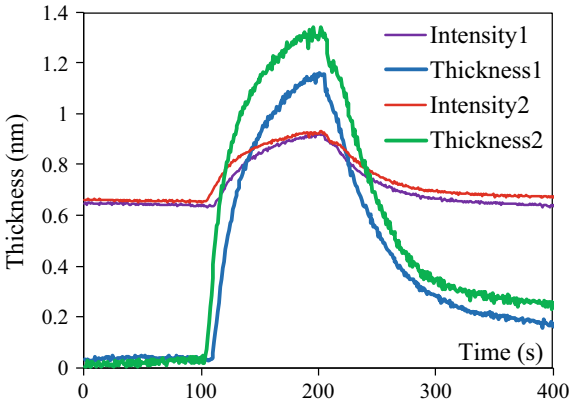

Fig. 9 Two consecutive records of propanol attachment to oxidized silicon surface in air

3 Results

Before any experiments, all substrates are cleaned using wet chemistry depending on what they were used for. Firstly, the modulator must be removed to ensure the laser is centred on the photodetector. The system then must achieve extinction, and this is done by rotating the modulator. To measure the full scale, we rotate the modulator and record the corresponding milliradians needed for a change of 1000 units in intensity. Measurement is started when all the above conditions are done, and the system is at extinction state.

3.1 Experiments in Air

Simple experiment to examine the work of PREL system is to measure adsorption of propanol molecules on oxidised and dried silicon substrate. The substrate was placed in the optical cuvette, light beam was aligned and data acquisition started, Fig. 9.

A sponge soaked with propanol was placed in the cuvette near the substrate at 100 s, molecules evaporated and adsorbed on the substrates as seen in increase of the thickness. At around 200 s, the sponge was removed and the molecules desorbed. Using standard ellipsometric formulae [1], one can calculate the proportion between the layer thickness and polarisation rotation, which is 4 mrad for 1 nm of organic molecules on silicon in air. Same in water gives 2 mrad for 1 nm.

3.2 Experiments in Water

For experiments in water, optical system is equipped with a fluidic system [3]. Usually, we will start with the flow of water to ensure all is going well. A typical

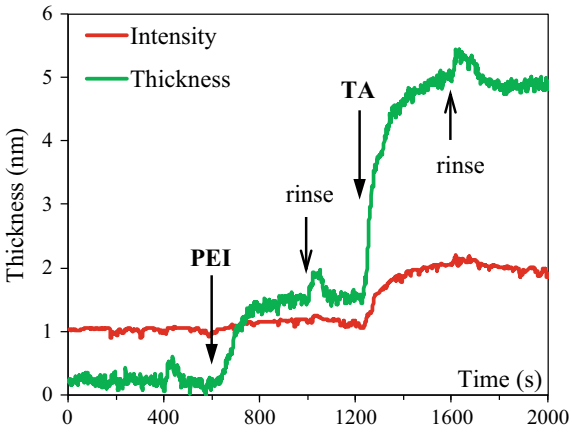

Fig. 10 Attachment of PEI on the oxidised silicon substrate and subsequently TA

experiment would start water flow, it is stopped at 200 s, and flow again at 400 s. Then at 600 s, the flow is stopped and a solution of molecules is injected into the cuvette. After the insertion of chemicals, we must check the strength and extent of bonding between the substrate and the chemical, and this is done through the rinsing of water typically at 400 s after the injection to allow more time for bonding to occur if we know the bonding will be quite weak. We will then stop water flow after about 200 s of rinsing, inject the next solution and wait for 400 s. Same can be repeated with subsequent solutions and multilayer attachment can be measured in one run.

In the experiment in Fig. 10, 5 mM of polyethyleneimine (PEI) was added at 600 s and 5 mM of tannic acid (TA) was added at 1200 s. There is an increment of 1.5 nm after PEI was added and 3.5 nm after TA was added. They are not removed after rinsing; thus the attachment is permanent. Using such a system, we can accurately get the thickness of the layers and kinetics of attachment.

In the experiment in Fig. 11, 5mM of aminopropyl silane (silane) added at 600 s, 10 mM of polystyrene sulfonate (PSS) added at 1400 s and 1 mg/ml of bovine serum albumin (BSA) added at 2200 s. There are increments of 0.8 nm for silane, 0.7 nm for PSS and 1 nm for BSA. Thus also bio-molecules can be measured using PREL.

4 Further Discussion and Possible Improvements

Other applications of PREL include and drug testing. PREL can test for the ability of attachment of layers of molecules onto a substrate. Using this feature, PREL can test for the affinity of antibodies towards antigens in the human body, and thus the effectiveness of the drug. To do so, a possible way is that we use the antigen as the substrate and place it in the cuvette, then dissolve the drug into bodily fluids and place the set-up in a setting of 38 °C to simulate conditions within the body. From the polarisation, we can measure the thickness of the layer, which corresponds to the

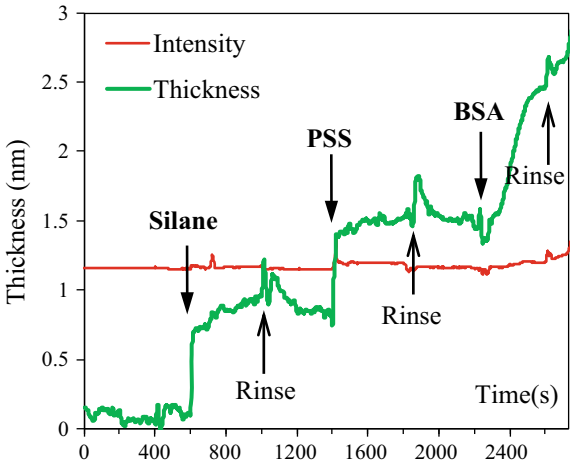

Fig. 11 Attachment of aminosilane, subsequently PSS and BSA

effectiveness of bonding between antibodies and antigens, and hence the effectiveness of the drug.

5 Conclusion

A new portable PREL system has been designed and made. It contains a modulator which has a self-tuning generator for it to oscillate at the resonance frequency, a photodetector which has its signal current amplified by transistors and an Arduino programmed with phase lock function. It is shown that this system has sensitivity down to the molecular level. Being able to work in both air and liquid allows it to be very useful as it can analyse samples in different states. It is convenient to bring the new PREL around to test for water quality or the affinity of certain molecules.

With the new modulation system, our PREL is energy efficient, cheaper, lighter, and more compact than tabletop PREL, while maintaining high sensitivity. With the portable PREL, we can expect new generation of technology that is capable of engaging high precision metrology. Our very own model would be pioneering this engagement and participate proactively in all fields of modern technology.

Acknowledgements The authors are grateful to Dr. Chiam Sher-Yi for his help and encouragement in the course of the project. The authors are also grateful to other students in PREL lab who provided help for the authors to understand the concepts.

References

1. S.N.Jasperson, S.E.Schnatterly, “An Improved Method for High Reflectivity Ellipsometry Based on a New Polarisation Modulation Technique” The Review of Scientific Instruments, v.40 (6), 761-767 (1969).
2. N.L.Yakovlev, Hou Chin Quek, Karol M. Dabrowski , William R Birch, Kinetics of Small Molecule Adsorption Studied Using Precision Ellipsometry, Surface and Interface Analysis, v.51(7), p.697 (2019).
3. Hooi Hong Lau, Regan Murney, N.L. Yakovlev, et al., Protein-tannic acid multilayer films: A multifunctional material for microencapsulation of food-derived bioactive, J. Colloid and Interface Science, v.505, p.332 (2017).

Incorporating Dilemma Reasoning into Modern SAT Solvers

Yue Chen Li, Kian Ming A. Chai, and Vincent Boon Chin Seng

Abstract The Boolean SATisfiability Problem (SAT) is an important intractable problem in computer science with numerous theoretical and industrial applications. With the growing availability of multi-core and multi-processor systems, parallel algorithms are increasingly important and useful. Yet, state-of-the-art parallel SAT solvers are mostly portfolio solvers that exchange learn't clauses to achieve knowledge sharing. We describe some novel extensions to using Stalmårck's method to create a parallel SAT solver. This includes two new knowledge sharing methods across solvers, $t\text{-}BFD$ and $c\text{-}BFD$ merging. We prove that $t\text{-}BFD$ and $c\text{-}BFD$ merging are distinct, and experimentally show that they occur significantly. In fact, $t\text{-}BFD$ merging occurs more frequently at deeper levels of the problem decomposition tree. Within the problem subtree, $t\text{-}BFD$s merging gives unit clauses, and $c\text{-}BFD$ merging gives clauses that are empirically short. Such short clauses are likely useful in simplifying the problem. Also, we introduce a more flexible problem decomposition method than naive splitting on N variables to form 2^N subproblems. Based on the Dilemma Rule, it picks branching literals independently at every vertex in the decomposition tree. In addition, we engineered a method to avoid processor starvation in the parallelisation. We benchmarked a preliminary implementation of our modified solver against Glucose-Syrup 4.1 and show that certain configurations of restart and runtime budgets allow our solver to outperform Glucose-Syrup 4.1 on SAT instances. Furthermore, $t\text{-}BFD$ merging significantly improved our solver's performance on UNSAT benchmarks, suggesting that $t\text{-}BFD$ and $c\text{-}BFD$ merging are effective.

Y. C. Li (✉)
NUS High School of Mathematics and Science, Singapore, Singapore
e-mail: h1610073@nushigh.edu.sg

K. M. A. Chai · V. B. C. Seng
INFO Division, DSO National Laboratories, Singapore, Singapore
e-mail: ckianmin@dso.org.sg

V. B. C. Seng
e-mail: sboonchi@dso.org.sg

H. Guo et al. (eds.), *IRC-SET 2020*,
https://doi.org/10.1007/978-981-15-9472-4_37

Keywords SAT solver · Boolean satisfiability problem · Parallel algorithms · Stålmarck's method · Dilemma rule · Problem decomposition

1 Introduction

The *Boolean SATisfiability Problem* (SAT) is a classic intractable (NP-Complete) problem that is important to many computer scientists and industries as it can be used to model many real-world problems. Currently, state-of-the-art solvers are mostly based on the *Davis-Putnam-Logemann-Loveland* (DPLL) and *Conflict-Driven Clause Learning* (CDCL) algorithms [1], and they are significantly faster than *Look-Ahead* solvers [2].

Sequential solvers can take a long time to tackle difficult mathematical problems expressed as SAT. Hence, parallel SAT solvers are useful to trade computing resources for a shorter solving time [3]. The vast majority of parallel SAT solvers presently are *portfolio solvers*, which are solvers that run multiple instances of a sequential solver with different configurations on the same problem concurrently, hoping that one of them will be able to solve the problem quickly as different configurations can have significantly varying performance on different problems [4]. This is because DPLL + CDCL is not inherently parallelisable. Efforts to improve parallel solvers have resulted in the sharing of learnt clauses across solvers, for instance in Glucose-Syrup [5].

Stalmårck's method [6], an alternative algorithm to the DPLL + CDCL algorithm, is better able to lend itself to parallelisation as its *Dilemma Rule* involves partitioning of the search space. Recently, a solver based on it, *Dissolve* [7], was created. In this paper, we present another approach inspired by this relatively new development for *decomposition* and *knowledge sharing*, two challenges in parallel SAT solving suggested by Hamadi and Wintersteiger [8].

This paper has three contributions. First, we give a novel way to approach problem decomposition inspired by the Stålmarck's method and *Dissolve*, which provides greater flexibility than homogeneous decomposition. Second, we present two additional ways of merging information from splits ($t\text{-}BFD$ and $c\text{-}BFD$ merging) and prove that they are different. Third, we also engineer a method to avoid *starvation*, a challenge encountered when designing parallel algorithms. An implementation of our algorithm is benchmarked against Glucose-Syrup 4.1, showing that some configurations of our solver are able to outperform Glucose-Syrup in certain SAT instances. We find that $t\text{-}BFD$ and $c\text{-}BFD$ merging occur to a significant extent, especially when we are deeper in the search tree, to derive potentially useful clauses. Furthermore, we show experimentally that $t\text{-}BFD$ merging improves the performance on certain UNSAT benchmarks for our solver.

2 Preliminaries

2.1 Boolean Satisfiability Problem

We begin with definitions [10]. A **Boolean variable**, x, is a variable which can take on the values *True* and *False*. For simplicity, we refer to boolean variables as variables. A **literal**, l, is a variable x (positive literal) or its negation $\neg x$ (negative literal). A **clause** C of length N is a disjunction of N literals: $C = l_1 \vee l_2 \vee l_3 \vee \ldots \vee l_N$. A **Conjunctive Normal Form (CNF)** formula F of size M is a conjunction of M clauses: $F = C_1 \wedge C_2 \wedge C_3 \wedge \ldots \wedge C_M$. In propositional logic, the Boolean Satisfiability Problem (SAT Problem) asks whether it is possible to assign a *True/False* value to all variables in a formula so that it will evaluate to *True*. A formula for which that is possible is termed *satisfiable*, otherwise it is termed *unsatisfiable*.

2.2 DPLL+CDCL Solvers

The DPLL+CDCL algorithm can be summarised as follows. The solver guesses the value of a variable (such a guess is termed a *decision*) and simplifies the formula as much as possible using **Boolean Constraint Propagation (BCP)** after each guess, that is, if a literal is true, then all clauses containing it are satisfied and its negation can be removed from all clauses. If any clause ends up with only one literal, a similar simplification is applied. This is repeated until either there is no clause containing only one literal, or the solver arrives at a contradiction, which is termed a *conflict*. If the latter occurs, the solver analyses the conflict to determine the reason and creates a *learnt clause*, which expresses the condition that must be true to avoid that conflict—this is the CDCL algorithm. By doing so, the CDCL algorithm is able to prune the search space to avoid arriving at the same conflict. After that, it backtracks to a state before the conflict. In either case, it then continues to guess the values of other variables. Eventually, if the solver is able to guess the values of all the variables without arriving at a contradiction, the formula is satisfiable. In contrast if the solver arrives at an inherent contradiction in the formula, the formula is unsatisfiable.

2.3 Stalmårck's Method

Stalmårck's method [6] is a system using deductions on parts of the formula to prove whether a propositional logic formula is a tautology (a formula which is true under every possible assignment of values to its variables). The key idea involved is termed the *Dilemma Rule*. In brief, two parts of the formula are first assumed to either have the same or distinct truth values. Next, the relationships between the parts are simplified based on a set of *propagation rules*. Finally, the two sets of relationships

are intersected: if a relationship is true in both cases, it is true all the time since the two cases form a partition of the entire search space. This can be repeatedly applied to simplify the formula to eventually arrive at a conclusion.

3 Parallel SAT-Solvers with Dilemma Reasoning

In this section, we describe the three contributions of problem decomposition, knowledge sharing and starvation avoidance.

3.1 Decomposition

To create new subproblems for each sequential solver to work on, one straightforward way is to pick k decision variables and split on them as done in *Dissolve*, which is shown in Fig. 1a. In contrast, to increase the flexibility of our search, we pick the decision variables to split on independently and randomly at each node. This way, we build an incomplete binary tree which is as balanced as possible that has the same number of leaves as solvers we have, with the root-to-leaf path representing a set of assumptions for each solver, as shown in Fig. 1b. Extensions to this idea is part of our future work as we did not fully exploit this flexibility presently.

Since each split forms a partition of the current search space, then for any chosen vertex all the leaf vertices in its subtree form a partition of its search space by induction. This is an important property that will be required in the next section.

3.2 Knowledge Sharing

Given a certain set of assumptions, let us first introduce the following definitions: The **trail-before-first-decision**, denoted $t\text{-}BFD$ is the set of literals that are implied to be true by BCP on the assumptions before any decisions are made. The **clauses-before-first-decision**, denoted $c\text{-}BFD$ is the set of clauses that are simplified and not yet satisfied (have literals deleted) due to BCP on the assumptions before any decisions are made. These different types of derived facts are summarised in Fig. 2. With that, we present the following two observations.

Observation 1 If any implication is derived from BCP on the assumptions in all the solvers represented by a set of leaves in the subtree of a vertex, it must be true for the set of assumptions represented by this vertex. (Intersection, analogous to the Dilemma Rule)

Thus, we see that for a vertex in the decomposition binary tree, we can take the intersection of the $t\text{-}BFD$ and $c\text{-}BFD$ each of all the solvers represented by its

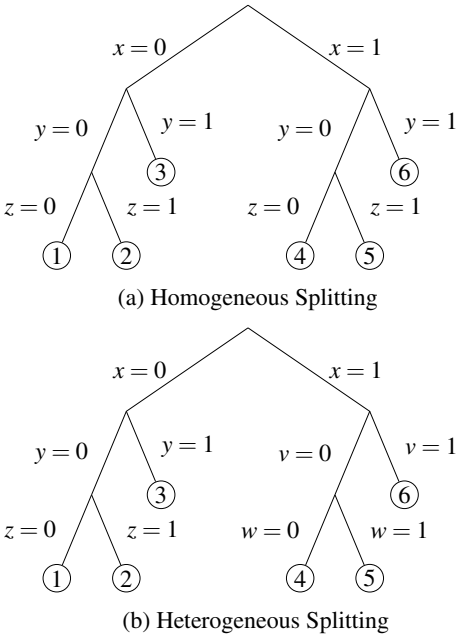

Fig. 1 Problem decomposition with $N = 6$ solvers

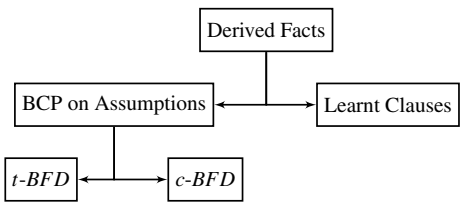

Fig. 2 Types of facts derived in solvers

children to be true in this subtree. For the $c\text{-}BFD$, we can get rid of any clause that it subsumes (derived or otherwise) since for any three clauses A, B and C, if $A \subseteq B$ and $B \subseteq C$, then $A \subseteq C$. However, if we obtain an UNSAT result after clause simplification, we cannot determine whether it is inherent or a consequence of the assumptions. This is as the CDCL algorithm will give a top-level conflict in both cases.

Observation 2 Since learnt clauses are independent of the assumptions [7], we can bring any of learnt clauses up the tree. (Union, similar to Glucose-Syrup)

Observation 2 allows all the solvers to share learnt clauses just like in portfolio solvers. Together, these observations should help to prune the search space further. Merging the $t\text{-}BFD$s is especially useful since we learnt the equivalent of unit clauses, which we can employ BCP on. Ideally, longer $t\text{-}BFD$s are desired as they are more likely to overlap. This applies similarly to $c\text{-}BFD$s. To achieve that, we postulate the following:

Hypothesis 1 The deeper we are in the binary tree, the more literals we will be able to merge from our children's $t\text{-}BFD$s.

Hypothesis 2 The deeper we are in the binary tree, the more clauses we will be able to merge from our children's $c\text{-}BFD$s.

Hypothesis 1, but not hypothesis 2, is supported by our experimental observations. Hence, for problems that give long trails, this may be a useful heuristic, especially since trail merging is a relative cheap operation that can be done in $O(N)$ time and $O(N)$ space, where N is the number of variables in the problem. On the other hand, merging the $c\text{-}BFD$s is an expensive process if we loop through all the modified clauses naively, which can take up to $O(NM)$ time, where N is number of variables and M is the number of clauses. However, with efficient data structures to identify the modified clauses and determine whether clauses are identical, perhaps through hashing, we may be able to reduce the overhead. Yet, one would have hoped that merging $t\text{-}BFD$ is sufficient to derive any facts derivable by merging $c\text{-}BFD$, but that is unfortunately incorrect.

Proposition 1 *Both the sets of learnt clauses from merging $t\text{-}BFD$ and merging $c\text{-}BFD$ do not imply each other.*

Proof Suppose otherwise, that at least one of the sets implies the other. Let A be the set of learnt clauses from merging clauses and B be the set of learnt clauses from merging trails. Then either $A \subseteq B$ or $B \subseteq A$. Figure 3a, b are two counterexamples to each of the case. This is a contradiction. □

3.3 Maximising Computing Resources

After the problem is decomposed, each solver is assigned a subproblem to work on for a limited amount of wall-clock time, termed a *budget*. This allows us to both merge and use the information derived in the subproblems from a split as well as recover from possibly ineffective splits of the problem. However, if we wait for both children to terminate and return the derived information before commencing the merging, we may encounter *starvation* [8]. That is, if the solver of one leaf vertex continues running for an extended period of time until it reaches the maximum allowed running time (time budget) but all other solvers have terminated earlier, we may have up to $N - 1$ idle solvers. An illustration is given in Fig. 4.

To remedy this, we first build a tree which is equivalent to the recursion tree created by problem decomposition. On this shared tree data structure, we introduce a $hurry$ flag at each vertex, which will cause the vertex to terminate as soon as possible and return the information derived so far.

When one vertex terminates, it will reset its $hurry$ flag and set the $hurry$ flag of its sibling (if said sibling has not terminated) and propagate the flag down the

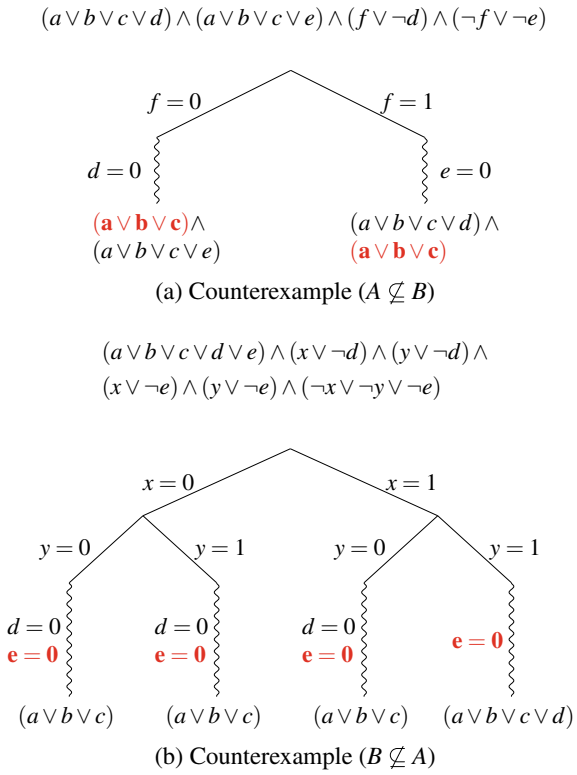

Fig. 3 Counterexamples showing that merging *t-BFD* and *c-BFD* give different results

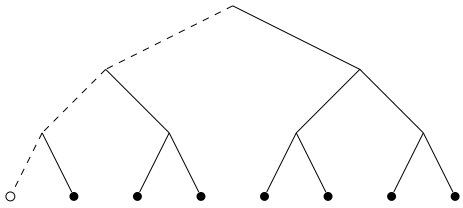

Fig. 4 Dashed edges show the uncompleted path; Solid edges show the completed and idle paths

sibling's subtree. This way, we are able to propagate the termination signal down to all solvers blocking a branch. In the implementation, it is important to check the status of the sibling in a thread-safe manner (e.g. by using mutexes/locks) to avoid race conditions. Alternatively, the tree can be implemented as a lock-free data structure to improve performance.

This effectively solves the issue of many solvers idling for a possibly long time (if the time budget given is long).

3.4 Pseudocode

Algorithm 1 shows the pseudocode for our idea. It takes the following as parameters: N, the corresponding node in tree data structure; P, the set of unused variables; A, the set of assumptions for this subtree; C, the set of merged clauses for this subtree; R, the number of restarts allowed at each depth; T, the time budget allowed for a solver. In the pseudocode, the **threadSafe** keyword denotes the need to guard against race conditions when processing the statement (e.g. by using mutexes), the **parallel do ... done** construct denotes that the statements within the block are executed in parallel until both are done, and the **break** statement denotes exit of the innermost loop containing the statement.

Algorithm 1 Dilemma Main Procedure

```
1: procedure DILEMMA(N, P, A, C, R, T)
2:     threadSafe N.done ← false
3:     learnts ← {trail : {}, clauses : {}, result : undefined}
4:     if N.solversAssigned > 1 then
5:         for i = 0 to R[N.depth] − 1 do
6:             if N.hurry then break
7:             x ← PICKRANDOMVAR(P)
8:             P ← P \ {x}
9:             parallel do
10:                r1 ← DILEMMA(N.l, P, A ∪ {¬x}, C, R, T)
11:                r2 ← DILEMMA(N.r, P, A ∪ {x}, C, R, T)
12:            done
13:            r ← COMBINE(r1, r2)
14:            if job is done by any solver then
15:                r.result ← jobStatus
16:            if r.result ≠ undefined then
17:                learnts.result ← r.result
18:            P ← P ∪ {x}
19:            add r.trail to learnts.trail
20:            add r.clauses to learnts.clauses
21:    else
22:        Add C to N.solver
23:        for i = 0 to R[N.depth] − 1 do
24:            if N.hurry then break
25:            learnts.result ← N.solver.SOLVEWITHBUDGET(A, N, T)
26:            add N.solver.t-BFD to learnts.trail
27:            add N.solver.modifiedClauses to learnts.clauses
28:        Remove C from N.solver
29:    threadSafe N.done ← true
30:    if N.sibling exists then
31:        threadSafe N.sibling.PROPAGATEHURRYIFNOTDONE
32:    threadSafe N.hurry ← false
33:    return learnts
```

Table 1 Comparison of solvers

Heuristics	Glucose-Syrup	Dissolve	Our Solver
Problem decomposition	Yes	No	No
Branch literal heuristic	Yes	No	Yes[a]
Clause sharing	No	No	No
$t\text{-}BFD$ merging	Yes	Yes	No
$c\text{-}BFD$ merging	Yes	Yes	No

[a]See future work

4 Methods and Results

Combining the ideas in Sect. 3, we arrive at our modified algorithm. Table 1 compares our solver with *Dissolve* and the unmodified Glucose-Syrup 4.1 based on MiniSat [11]. Our solver is implemented in C++ based on Glucose-Syrup 4.1, a portfolio solver with good performance in recent SAT competitions. To evaluate our modified solver, we selected the 23 largest benchmarks from the Agile Track of the SAT 2017 Competition and all 26 benchmarks related to van der Waerden numbers[1] from the SAT 2011 Competition. The solver is run against each benchmark for a maximum of 5000 s and 64 GB memory with 8 threads on an Intel(R) Xeon(R) computing system (CPU: E5-2620 v4, 2.10 GHz; 64 hyper-threaded cores), exceeding which it is prematurely terminated. Statistics of the solver are logged and the run-times are represented in a cactus plot [9]. Figure 5 shows the performance of our solver compared to Glucose-Syrup, while Fig. 6a, b show the normalised number of literals and clauses merged (from the $t\text{-}BFD$s and $c\text{-}BFD$s of the children vertices) respectively with respect to the number of merges at each depth—this is important as the number of merges are greater at greater depths. Regression lines are plotted to show the difference in gradients.

4.1 Results and Discussion

There is evidence that intersections of $t\text{-}BFD$s and $c\text{-}BFD$s do derive a significant number of facts. In fact, Hypothesis 1 is supported by the graph shown in Fig. 6a. Interestingly, the average merged clause length appears to be rather short ($\approx$4) compared to the maximum clause lengths ($>$20) (refer to Table 2), suggesting that merging $c\text{-}BFD$ may allow us to obtain useful clauses.

[1]A van der Waerden number $W(c, k)$ is the minimum natural number such that if the integers $\{1, 2, \ldots, W(c, k)\}$ are assigned colours from the set $\{1, 2, \ldots, c\}$, then there are at least k integers in an arithmetic progression which all have the same colour. Finding such numbers is an unsolved problem in Ramsey Theory in general.

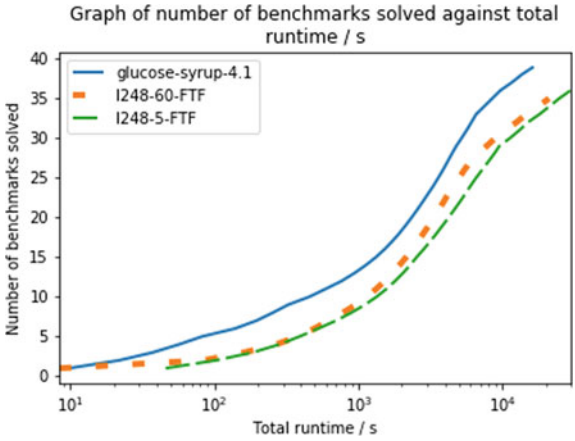

Fig. 5 Comparison of overall performance of our solver with trail merging and glucose-syrup

Overall, our solver performed worse than Glucose-Syrup by a constant time factor as seen in Fig. 5. This is likely due to the greater overhead from the splitting and merging, which appears to be especially significant for UNSAT instances, particularly for hard UNSAT instances (related to van der Waerden numbers). In fact, with only our modified decomposition, some configurations of our solver solve SAT instances faster than Glucose-Syrup. With $t\text{-}BFD$ merging turned on, our solver solves an additional van der Waerden instance and the Agile instances faster.

Although these are only preliminary tests with only a small number of benchmarks, we believe that these results show that these new heuristics are worth investigating further.

5 Conclusion and Future Work

We described a novel way to approach problem decomposition inspired by the Stålmarck's method and *Dissolve*. Beyond merely splitting the problem on N variables at a time with Dilemma rule, we explored heterogeneous splitting for about k times instead, which provides greater flexibility. Furthermore, we presented two more ways of merging information from splits ($t\text{-}BFD$ and $c\text{-}BFD$ merging) in addition to the commonly used sharing of learnt clauses. Moreover, we proved that $t\text{-}BFD$ and $c\text{-}BFD$ are distinct. Finally, we discussed a method to avoid *starvation*, a challenge encountered when designing parallel algorithms.

We implemented our modified algorithm and ran a set of tests to benchmark its performance against an existing state-of-the-art solver, Glucose-Syrup 4.1, as well as against one another with different configurations. We showed that some configurations of our solver are able to outperform Glucose-Syrup in SAT instances and (a) $t\text{-}BFD$ and $c\text{-}BFD$ merging occur to a significant extent and (b) $t\text{-}BFD$

Fig. 6 Graph of number of merged $t\text{-}BFD$ and $c\text{-}BFD$ against total number of merges for tests with ∞-2-4-8 restart pattern and a time budget of 600 seconds

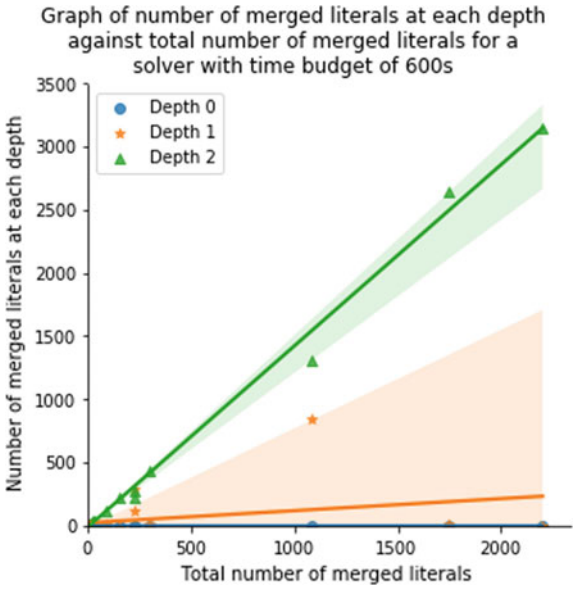

(a) Graph showing a greater number of merged literals at greater depths.

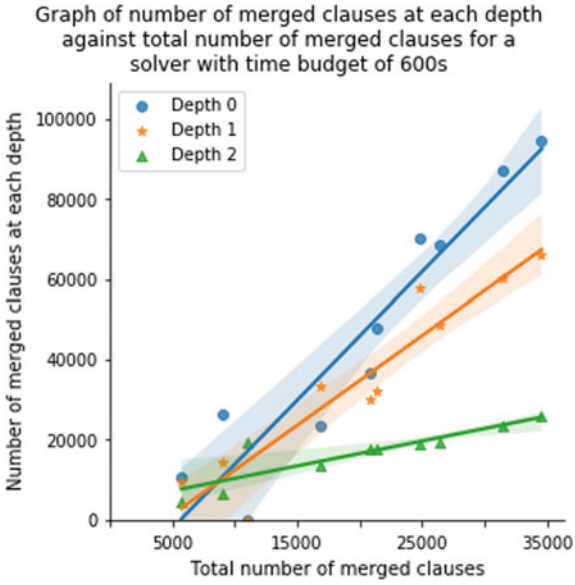

(b) Graph showing a smaller number of merged clauses at greater depths.

Table 2 Length of merged clauses for the cases (#) which our solver solved. All minimum lengths are 0

Budget = 60			Budget = 600		
#	Average	Maximum	#	Average	Maximum
0	3.958164	12	0	3.981017	12
1	3.758052	19	1	3.934512	13
2	3.746337	20	2	3.721468	19
3	3.798731	20	3	3.718266	20
4	3.980227	21	4	3.843215	20
5	3.751489	21	5	3.935537	21
6	3.790726	21	6	3.759932	21
7	4.024393	22	7	3.995705	21
8	4.268452	22	8	3.896167	22
9	3.843114	23	9	3.899929	22
			10	3.866584	23
			11	4.157838	24

merging occurs more frequently at greater depths in the decomposition tree. Finally, we showed that the $c\text{-}BFD$ merged are rather short.

In the future, we hope to optimise the implementation of our algorithm to minimise the overheads, as well as implement a heuristic for the picking of decision variables like *Dissolve*. In addition, we hope to exploit the flexibility of heterogeneous splitting. Furthermore, we hope to fully implement and optimise our $c\text{-}BFD$ merging idea, after working out how to distinguish between cases of UNSAT due to assumptions and UNSAT due to the problem itself as explained after Observation 1. Finally, due to the promising preliminary results, we hope to run more detailed tests with more benchmarks.

Acknowledgements Yue Chen thanks DSO National Laboratories for hosting her for this Young Defence Programme (2019) internship project.

References

1. J. P. Marques-Silva and K. A. Sakallah, "GRASP: a search algorithm for propositional satisfiability," *IEEE Transactions on Computers*, vol. 48, pp. 506 – 521, 1999.
2. M. J. H. Heule and H. Maaren, "Look-ahead based SAT solvers," in *Handbook of Satisfiability*, vol. 185 of *Frontiers in Artificial Intelligence and Applications*, Amsterdam, The Netherlands, The Netherlands: IOS Press, 2009.
3. M. J. H. Heule, O. Kullmann, S. Wieringa, and A. Biere, "Cube and conquer: guiding CDCL SAT solvers by lookaheads," in *Hardware and Software: Verification and Testing*, (Berlin, Heidelberg), pp. 50 – 65, Springer Berline Heidelberg, 2011.

4. A. E. J. Hyvärinen and N. Manthey, "Designing scalable parallel SAT solvers," in *Theory and Applications of Satisfiability Testing – SAT 2012* (A. Cimatti, ed.), (Berlin, Heidelberg), pp. 214 – 227, Springer Berlin Heidelberg, 2012.
5. G. Audemard and L. Simon, "On the Glucose SAT solver," *International Journal on Artificial Intelligence Tools*, vol. 27, no. 01, p. 1840001, 2018.
6. J. Nordstrom, "Stålmarck's method versus resolution: A comparative theoretical study," Master's thesis, Stockholm University, Stockholm, Sweden, 2001.
7. J. Henry *et al.*, "Dissolve: A distributed SAT solver based on Stålmarck's method," tech. rep., University of Wisconsin-Madison, Madison, Wisconsin, United States of America, 2017.
8. Y. Hamadi and C. Wintersteiger, "Seven Challenges in Parallel SAT Solving," *AI Magazine*, vol. 34, 2012.
9. M. N. Brain, J. H. Davenport, and A. Griggio, "Benchmarking solvers, SAT-style," in *Satisfiability Checking and Symbolic Computation* (M. England and V. Ganesh, eds.), (Kaiserslautern, Germany), Springer Berlin Heidelberg, 2017.
10. C. Sinz and T. Balyo, "Practical SAT solving." https://baldur.iti.kit.edu/sat/, 2019. Accessed on 2019.
11. N. Eén and N. Sörensson, "An extensible SAT-solver," in *Theory and Applications of Satisfiability Testing* (E. Giunchiglia and A. Tacchella, eds.), (Berlin, Heidelberg), pp. 502 – 518, Springer Berlin Heidelberg, 2003.

Evaluating the Effectiveness of Audio, Visual and Behavioural Calibrations on EEG-Based Relaxation Training

Rachel Hui-Min Yeo, Minyue Zhang, and Aung Aung Phyo Wai

Abstract In this fast-paced world, stress becomes more prevalent in our daily lives. Thus, mental health is of increasing importance. In our experiment, we aim to compare the effects of different relaxation methods, namely audio, visual and behavioural (deep breathing). Brain-Computer Interface (BCI) makes use of an electroencephalogram (EEG) to record brain waves to test the effectiveness of relaxation methods. Data was collected from 13 subjects using 3 relaxation paradigms. Participants carried out alternating non-relaxed tasks and relaxed tasks. We used 6 EEG band-power features extracted from EEG data in performance evaluation. From accuracy analysis results, we carried out statistical analysis using paired-sample t-test to test the effectiveness of each calibration method. The accuracy performance shows $71.09 \pm 5.79\%$ with tenfold cross validation, $71.00 \pm 5.33\%$ with leave-1-subject-out and $53.53 \pm 6.44\%$ with leave-1-task-out cross validation. The mean accuracy of tenfold cross validation for all feature bands $72.02 \pm 5.82\%$ is statistically different from that for only across theta, alpha and gamma band features $70.15 \pm 5.83\%$; $p < 0.001$, implying that all bands should be used for a more accurate analysis of relaxation results, not just theta, alpha and gamma bands, being more significantly changed according to some papers. Our findings show that audio calibration has the highest mean accuracy $74.02 \pm 9.44\%$ as compared to behavioural $73.12 \pm 9.94\%$ and visual calibration $69.07 \pm 8.77\%$. However, the significance between audio and behavioural relaxation calibration is not significant ($p = 0.47$). Thus, we concluded that audio and behavioural calibrations are the most effective forms of relaxation. We believe this will improve the range and quality of relaxation and anxiety management therapies to benefit people of our society.

R. H.-M. Yeo (✉) · M. Zhang
Nanyang Girls' High School, Singapore, Singapore
e-mail: rachelyeohm@gmail.com

M. Zhang
e-mail: melanie.zhangmy@gmail.com

A. P. W. Aung
Nanyang Technological University, Singapore, Singapore
e-mail: apwaung@ntu.edu.sg

H. Guo et al. (eds.), *IRC-SET 2020*,
https://doi.org/10.1007/978-981-15-9472-4_38

Keywords Relaxation methods · Calibration · EEG

1 Background

Past research in translational medical science is disease-targeted, and most research discuss physical illnesses. However, as mental health issues are becoming more prevalent in today's world, it is important to look at methods to address them. In particular, we are focusing on stress and anxiety issues. In the 2019 Cigna 360 Well-Being Survey, 84% of participants globally reported feeling stressed, while 13% considered their stress unmanageable. This issue is even worse in Singapore, where 92% of participants said they felt stressed [1]. Thus, we feel that it is important to develop relaxation techniques to manage stress levels.

One common method to evaluate the effectiveness of such relaxation techniques is by using Brain Computer Interface (BCI). BCI is a platform that allows users to connect and control external devices by their brain signals [2]. Electrodes of an electroencephalogram (EEG) are used to detect the brain waves of the user. BCI has also been incorporated in research studies regarding meditation.

There have been experiments showing that meditation has a positive impact on BCI performance [3–5], allowing more accurate responses to be recorded and inhibits subjects from mind-wandering when carrying out a task. Studies have also been carried out to investigate the effects of meditation using different methods such as music [6], aromatherapy [7] and deep breathing. Breathing meditation also reduces rumination through distraction, and reduces negative mood [8]. However, few have compared the effectiveness of different relaxation techniques.

The use of EEG is still unable to help in short-term stress reduction as compared to unassisted relaxation [9]. Thus, we are trying to address this knowledge gap. Finding the most effective relaxation technique will allow more specific and effective stress therapies and anxiety management techniques.

We aim to find out the most effective relaxation method between audio, visual and behavioural calibrations, where behavioural calibration refers to deep breathing exercises. We hypothesise that the different stimuli would have different degrees of impact on the user, where audio stimuli would be the most effective method, followed by behavioural stimuli and lastly, visual stimuli. This is because the use of visual stimuli as a form of a relaxation technique is not as common and has little research done on it. Whereas, audio and behavioural relaxation methods are more commonly used in current relaxation therapies. However, audio relaxation is more easily utilised in daily life by listening to music whereas a dedicated time needs to be set aside to effectively carry out deep breathing exercises.

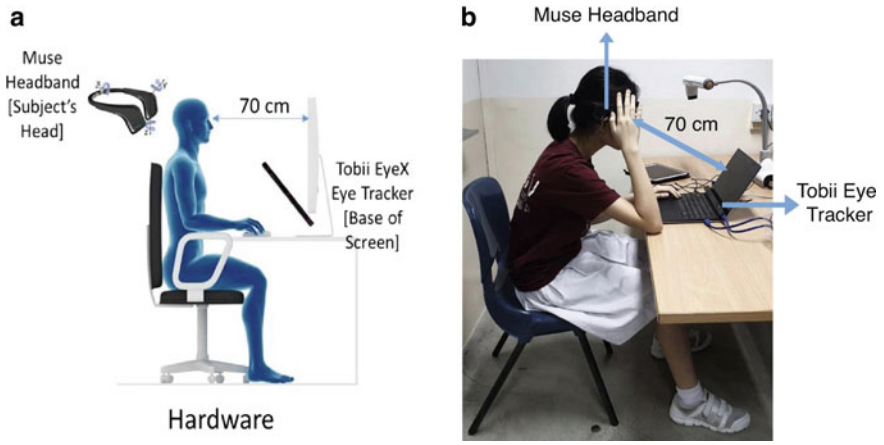

Fig. 1 **a** Planned experimental set-up, **b** Actual experimental set-up

2 Research Methodology and Experiment

2.1 Experimental Set-Up

Participants are seated 70 cm away from a computer screen, within the suggested range for screen usage [10]. A Muse headband (Muse 2016) is fitted on their head to collect EEG data. A Tobii EyeX Eye Tracker is attached below the computer screen to track subjects' eye movements (Fig. 1).

2.2 Experimental Sequence

Prior approval was obtained by the Institutional Review Board (IRB) before conducting our experiment. Our participants have also consented to taking part in our experiment by acknowledging what the experiment entails, what they are required to do during the experiment and signed consent forms sent to them. 14 participants, aged 14.5 ± 0.91 years old from our school took part in our experiment.

Before the experiment, participants filled up a pre-experiment form, arranging 7 genres of music from the most relaxed to least relaxed in their opinion (Fig. 2).

At the start of the experiment, for 30 s each, participants close their eyes, then stare at a dot in the centre of the screen, to capture EEG data at resting stage without execution of any specific tasks, acting as the base-line so subsequent data collected is accurate.

The experiment consists of 2-min long alternating non-relaxed tasks and relaxed tasks.

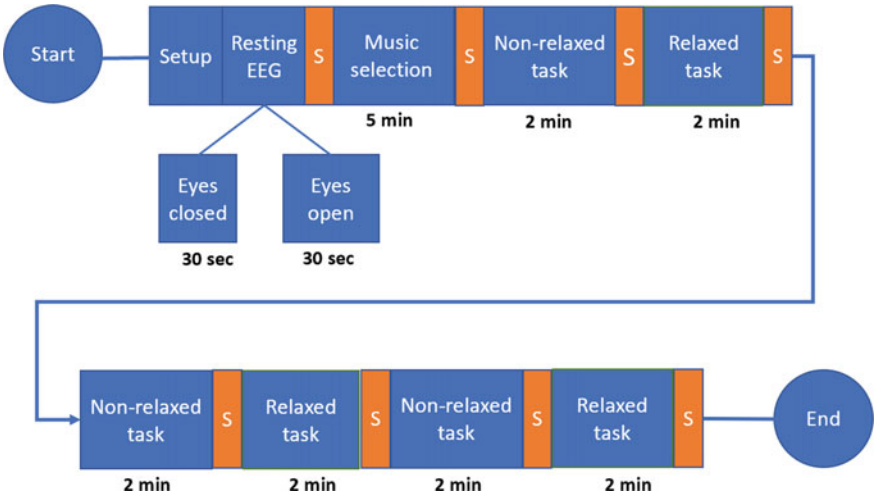

Fig. 2 Experiment sequence diagram

We alternated non-relaxed and relaxed tasks, so that the non-relaxed task would induce a non-relaxed state in the subject. Then, by making the participant go through the relaxed task afterwards, we could find out the effectiveness of the relaxed task in transforming the participants from a non-relaxed state to the relaxed state. The alternating non relaxed and relaxed task was also to simulate real-life situations where a user transitions from the non-relaxed state to the relaxed state, rather than from a neutral state.

The three non-relaxed tasks comprise of listening to audio in the most non-relaxed genre (pre-experiment survey), a mental arithmetic task and a FLANKER test.

The FLANKER test is used as a non-relaxed task in our experiment. During the test, a row of 5 arrows will be shown on the computer screen in randomly-chosen directions ("<" or ">") for a maximum of 2 s.

Participants would have to press the arrow on the keyboard that corresponded to the middle arrow on the screen. Their keystrokes will be recorded by the program and it will identify if they have pressed the direction of the arrow correctly or not. It will then proceed to the next sequence. This test induces stress by requiring participants to stay alert throughout the task and answering within a time limit.

The three relaxed tasks consist of listening to audio in the most relaxed genre (pre-experiment survey), looking at images of scenery and deep breathing. During deep breathing exercises, participants were asked to follow instructions displayed on the computer screen to breathe in, hold their breath, and exhale for 4 s each.

Music excerpts in the audio calibration was obtained by taking a popular song from each genre to ensure that it was conventional. The songs are all of recognisable characteristics that clearly define it as its genre (Fig. 3).

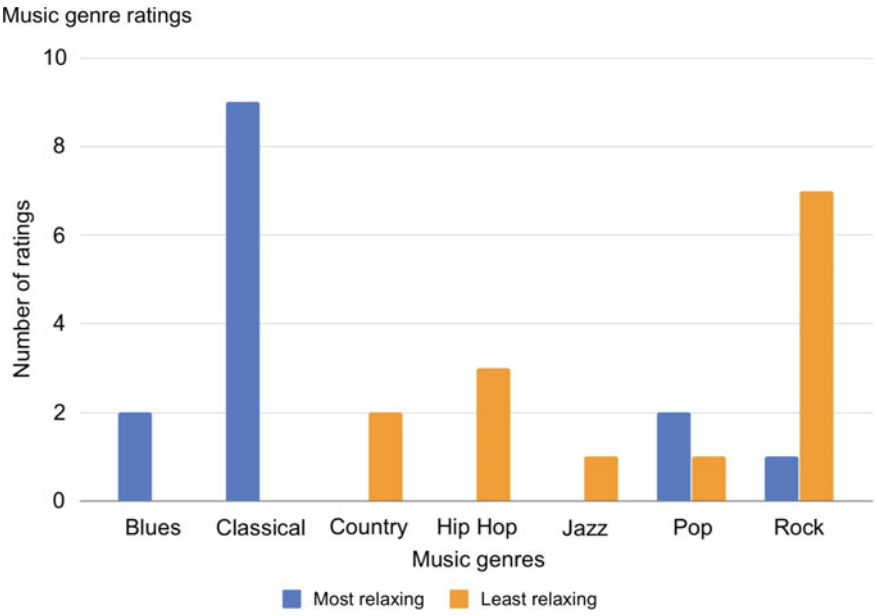

Fig. 3 Distribution of music genres rated as "most relaxing" and "least relaxing" by participants in the pre-experiment survey

For visual calibration, images displaying nature, like that of forests and beaches were used in our experiment. This is because nature imagery has been shown to be effective in physiological relaxation [11] (Fig. 4).

Order of tasks for each participant is randomised as a standard operational procedure to ensure that results are not affected by combination of tasks, thus able to obtain the effect of the particular task. Baselines of 30 s before each task allows participants to return to resting stage to ensure data collected is accurate.

3 Analysis and Results

EEG data collected from the 4-channel EEG Muse headband with a sampling rate of 256 Hz first goes through feature extraction. In feature extraction, they are passed through a band-pass filter, Butterworth Type II filter, to filter for significant frequencies (0.5–45 Hz). Artifacts, which are data flaws, are then removed through a set of multiple moving average filters with different filter width. The data is then segmented into different bandpower ranges, based on the 6 features in each EEG channel, namely Delta (0.5–3.5 Hz), Theta (3.5–7 Hz), Alpha (7–13 Hz), Low Beta (13–21 Hz), High Beta (21–30 Hz) and Gamma (30–45 Hz), resulting in a total of 24 features from all 4

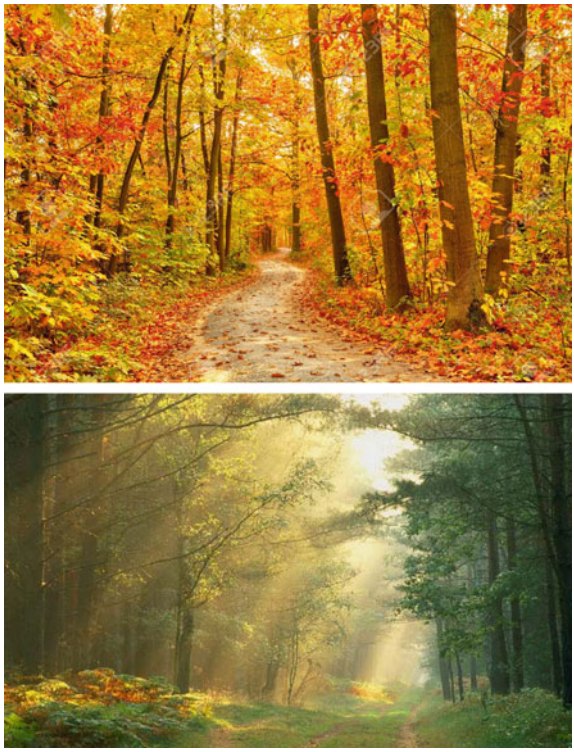

Fig. 4 Two of the images used during visual calibration

channels. Lastly, data collected was segmented based on the timestamps of different tasks carried out during the experiment to be used for analysis (Fig. 5).

The Support Vector Machine (SVM) training algorithm [12] was used to classify the data into non-relaxed tasks and relaxed tasks, and checks whether its classification is correct, producing an accuracy score. The accuracy of the data from different tasks of individuals was obtained using tenfold cross validation, leave-1-subject-out and leave-1-task-out. MATLAB online and JASP was used to analyse our data.

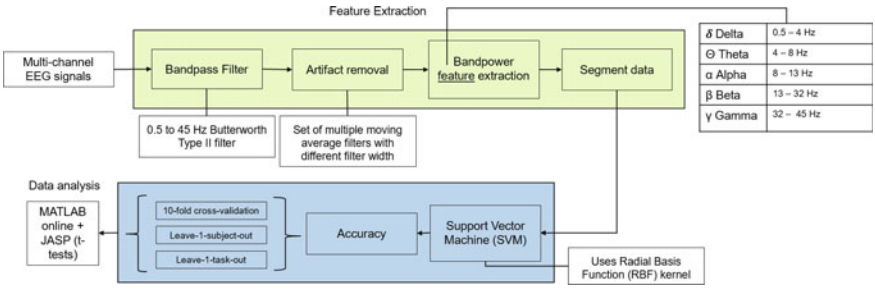

Fig. 5 Outline of steps for data analysis

We compared the mean accuracy and standard deviation obtained using tenfold cross validation, leave-1-subject-out and leave-1-task-out classification methods to evaluate which classification method yields the highest accuracy. When a relaxed task obtains a higher accuracy, it means the SVM can distinguish it from non-relaxed tasks better, because data from this task has a more significant difference from data from the "non-relaxed" task. This suggests that the relaxation technique is more effective in causing participants to transition from the non-relaxed state to the relaxed state.

In Fig. 6a, accuracy derived from both all bands and theta, alpha and gamma bands is used to achieve a fairer comparison. Figure 6b shows an averaged result from each band to obtain a total mean accuracy.

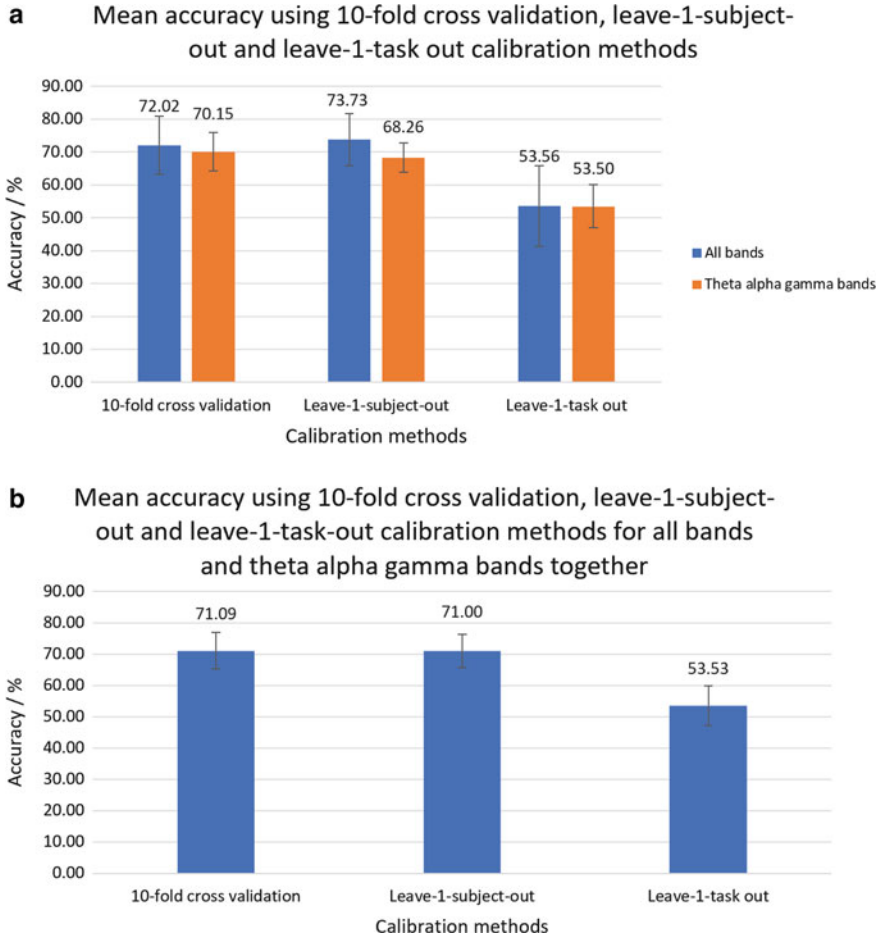

Fig. 6 **a** Comparison of mean accuracy between classification methods using all bands and theta, alpha, gamma bands, **b** Comparison of mean accuracy between classification methods together

Figure 7 shows the mean accuracy and standard deviation of each subject for all band features and theta, alpha and gamma bands. We differentiated out theta, alpha and gamma band features as they were suggested to be significantly different in relaxed and non-relaxed states, thus likely to produce higher accuracy than using all band features [13–15]. However, our results seemed to suggest otherwise (Table 1).

We also conducted a paired sample t-test to compare each subject's accuracy in all bandpowers and in the theta, alpha and gamma band powers using tenfold cross validation classification. This is to determine if the difference in mean accuracy is significant, thus better understanding which method is more effective. We could then use the more effective method to compare the mean accuracies of the different combinations of relaxed and non-relaxed tasks (Table 2).

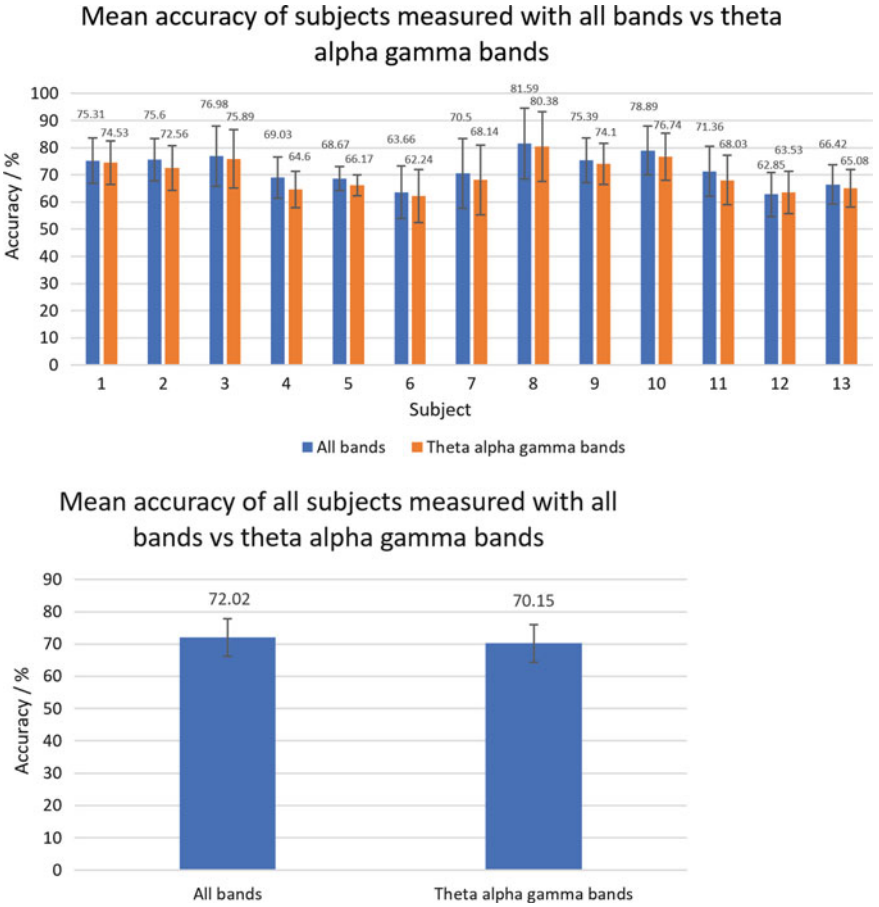

Fig. 7 Comparing accuracy obtained using all band features and theta, alpha and gamma band features. using tenfold cross validation

Table 1 Paired-sample t-test of accuracy between using all band features and theta, alpha and gamma band features, using tenfold cross validation

Paired sample t-test of accuracy of all bands versus theta alpha gamma bands		
Subject	t-value	*p*-value
1	2.027	0.077
2	2.927	0.019
3	1.834	0.104
4	3.376	0.010
5	8.055	<0.001
6	2.853	0.021
7	2.538	0.035
8	1.069	0.316
9	1.675	0.133
10	4.231	0.003
11	3.140	0.014
12	−1.537	0.163
13	1.989	0.082
Mean	5.169	<0.001

Table 2 Labelled non-relaxed and relaxed calibration for easy identification

A: Audio calibration	1: Audio calibration
B: Mental arithmetic test	2: Visual calibration
C: FLANKER test	3: Deep breathing

For ease of reading, we have assigned values to each non-relax and relaxed calibration as listed above. Henceforth, we will refer to each pair of non-relaxed and relaxed calibration as A1 to C3.

Figure 8 shows the mean accuracy and standard deviation for every combination of non-relaxed and relaxed tasks, from A1 to C3. In Fig. 9, the mean accuracy for each relaxation method was determined by averaging all the accuracies of non-relaxed and relaxed calibration pairs involving the particular relaxed task to find the relaxation method with the highest accuracy.

4 Discussion

From Fig. 6b, the accuracy of classification methods, tenfold cross validation $71.09 \pm 5.79\%$ and leave-1-subject-out $71.00 \pm 5.33\%$ did not have any significant difference, while leave-1-task-out $53.53 \pm 6.44\%$ was lower than both. Thus, we believe both tenfold cross validation and leave-1-subject-out are suitable for statistical analysis.

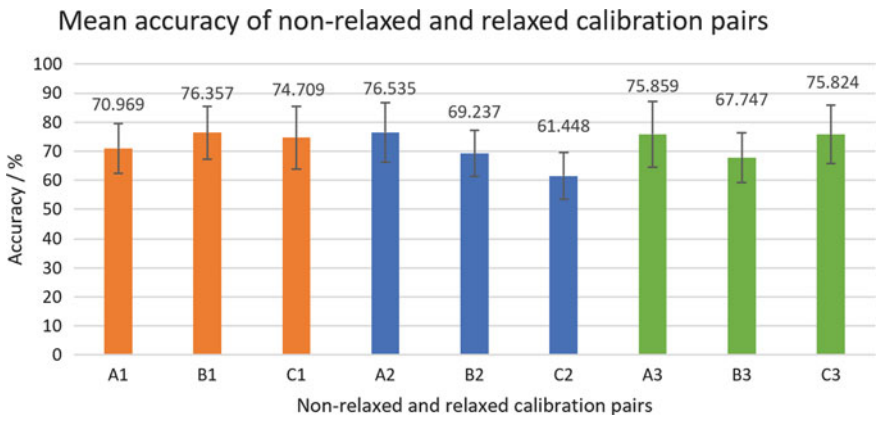

Fig. 8 Comparison of mean accuracy of non-relaxed and relaxed calibration pairs

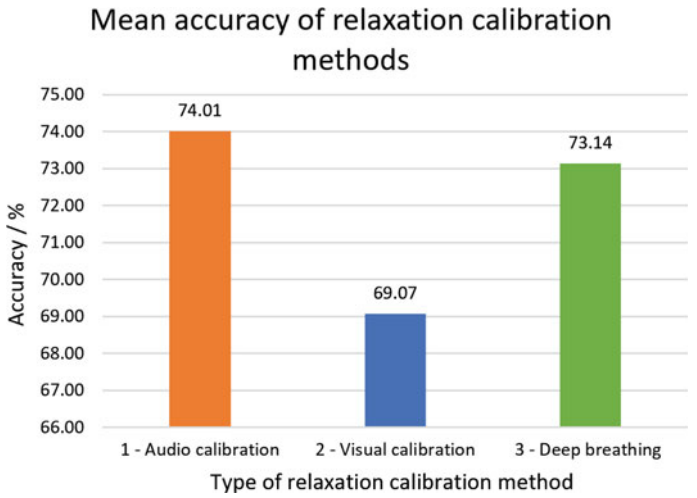

Fig. 9 Comparison of mean accuracy of relaxation calibration methods

However, as accuracy of tenfold cross validation is slightly higher, we will use it for subsequent analysis.

As shown in Fig. 7 using the paired t-test, there was a highly significant difference in mean accuracy for all bandpowers 72.02 ± 5.82% and bandpowers including only theta, alpha and gamma bands 70.15 ± 5.84% conditions; $t(12) = 5.169$, $p < 0.001$.

The average accuracy of all subjects for all bandpowers, 72.02% is higher than the average accuracy of all subjects for theta, alpha and gamma bands 70.15%. This shows that when measuring relaxation level, all bands, not just theta, alpha and gamma need to be measured to achieve higher accuracy of results, contradicting other sources [13–15].

Figure 8 compares the average accuracies and standard deviations of all possible relaxed and non-relaxed calibration combinations. Non-relaxed audio and relaxed visual calibration (A2) has the highest mean accuracy of 76.5 ± 10.2%. Thus they are the most effective pair of non-relaxed and relaxed calibration. This will be useful in trials where it is important that the participant needs to relax fully.

We will also determine the most effective overall relaxation calibration. From Fig. 9, we can see that while visual relaxation 69.07 ± 8.77% has the lowest accuracy, from a paired-sample t-test, there is no significant difference between accuracy of audio relaxation 74.02 ± 9.44% as compared to behavioural relaxation 73.12 ± 9.94%. $t(2) = 0.892$, $p = 0.47$.

A higher accuracy of a relaxed task suggests that the SVM can distinguish the relaxed state from the non-relaxed state better as data from this task has a more significant difference from data from the non-relaxed task, hence being more effective as a relaxation calibration. Thus, audio and behavioural relaxation are the most effective relaxation calibrations overall and enable subjects to feel the most relaxed. Thus, we can use both methods in a variety of relaxation therapies and anxiety management therapies.

5 Conclusion

In our experiment, we have collected EEG data to compare the effectiveness of different forms of relaxation, namely audio relaxation, visual relaxation and deep breathing against different non-relaxed tasks. We have got the mean accuracies of each relaxed task when paired with the non-relaxed tasks. Using the paired t-test analysis, we found that audio and behavioural calibrations were the most effective methods of relaxation since they have the highest mean accuracy. Our findings might help in areas such as relaxation therapies and stress and anxiety management by focusing on audio stimuli as a form of relaxation.

Acknowledgements We would like to express our gratitude to our teacher-mentor, Mr. Ang Joo Liak, for helping us with administrative matters throughout the duration of our research. We would also like to thank an NTU alumni Goh Shi Yong for his assistance in teaching us how to use various softwares needed to carry out our experiment. Lastly, we greatly appreciate the effort and cooperation of all our participants to take time off their busy schedules in order to take part in our experiment.

References

1. Sean Lim. (26 March 2019). *A whopping 92% of working Singaporeans are stressed - and Women are prioritising families over themselves, study finds.* https://www.businessinsider.sg/a-whopping-92-of-working-singaporeans-are-stressed-and-women-are-prioritising-families-over-themselves-study-finds/#. Retrieved on 6 December 2019.

2. Cincotti F, Mattia F, Aloise F, Bufalari S, Schalk G., Oriolo G., Cherubini A., Marciani M.G., Babiloni F. (2008) Non-invasive brain–computer interface system: Towards its application as assistive technology *Brain Research Bulletin Volume 75, Issue 6, 15 April 2008*, 796–803.
3. Tan LF., Dienes Z., Jansari A., Goh SY. (2014). Effect of mindfulness meditation on brain-computer interface performance. *Consciousness and Cognition Volume 23, January 2014*, 12–21.
4. Eskandari P., Erfanian A. (2008). Improving the performance of brain-computer interface through meditation practising. *2008 30th Annual International Conference of the IEEE Engineering in Medicine and Biology Society.*
5. Tan Y.Q., Tan L.F, Mok S.Y., and Goh S.Y.(2015) Effect of Short Term Meditation on Brain Computer Interface Performance. *Journal of Medical and Bioengineering Vol. 4, No. 2, April 2015.*
6. Lin S., Chih-Fang H., and Bo-Yuan L. (2016). A Pilot Study on the Portable EEG-Based Music Effects. *Journal of Biomusical Engineering.*
7. Miguel A. Diego, Nancy Aaron Jones, Tiffany Field, Maria Hernandez-reif, Saul Schanberg, Cynthia Kuhn, Mary Galamaga, Virginia McAdam and Robert Galamaga (1998) Aromatherapy Positively Affects Mood, Eeg Patterns of Alertness and Math Computations. *International Journal of Neuroscience, Volume 96, 1998 - Issue 3–4* 217–224.
8. Barnhofer T., Chittka T., Nightingale H., Visser C., Crane C. (2010). State Effects of Two Forms of Meditation on Prefrontal EEG Asymmetry in Previously Depressed Individuals. *Mindfulness, March 2010, Volume 1, Issue 1*, 21–27.
9. Artem S. Svetlov, Melanie M. Nelson, Pavlo D. Antonenko, Joseph P. H. McNamara and Regina Bussing. Commercial mindfulness aid does not aid short-term stress reduction compared to unassisted relaxation. *Heliyon, Volume 5, Issue 3, E01351, March 1, 2019.*
10. Ergotron. *Monitor tips.* Retrieved from https://www.osha.gov/SLTC/etools/computerworkstations/components_monitors.html.
11. Jo, H., Song, C.,; Miyazaki, Y. (2019). Physiological Benefits of Viewing Nature: A Systematic Review of Indoor Experiments. International Journal of Environmental Research and Public Health, 16(23), 4739. doi:https://doi.org/10.3390/ijerph16234739
12. Chang C-C., Lin C-J. (2011) LIBSVM: A library for support vector machines. *ACM Transactions on Intelligent Systems and Technology*, *Volume 2. No. 3, 2011*
13. Gregg D. Jacobs and Richard Friedman. (2004). EEG Spectral Analysis of Relaxation Techniques. *Applied Psychophysiology and Biofeedback, Volume 29, December 2004.*
14. Minguillon J., Miguel A., Lopez-Gordo and Francisco Pelayo. (22 September, 2016). Stress Assessment by Prefrontal Relative Gamma. *Frontiers in Computational Neuroscience.*
15. Sushil Chandra, Amit Kumar Jaiswal, Ram Singh, Devendra Jha and Alok Prakash Mittal. (2017). Mental Stress : Neurophysiology and Its Regulation by Sudarshan Kriya Yoga. *International Journal of Yoga, Volume 10, Issue 2, May-August 2017*.

Empirical Evaluation of Perimetry and Electrophysiology Methods in Visual Field Assessment

Yueh Yang Vince Tan, Deepankur John Njondimackal, and Aung Aung Phyo Wai

Abstract Visual field defects often go unnoticed by patients, making early diagnosis especially important. However, the commonly used Standard Automated Perimetry (SAP) assessment relies on manual user input. As such, we consider utilizing Steady-State Visual Evoked Potential (SSVEP) to provide accurate and objective results. We believe that SSVEP can produce more reliable data than SAP, given the same conditions. To test this, we created an SSVEP based program with the same layout as an existing SAP program. Subjects were then tested with both programs under two conditions—blocked and unblocked vision. SSVEP data was collected using a portable Brain Computer Interface and processed using canonical-correlation analysis. We constructed contour plots of the visual field for all sets of data, allowing us to easily compare the two methods. SAP ended up being more accurate than SSVEP, but SSVEP managed to approximate the visual field fairly well. A paired-samples t-test indicated that there was no significant difference in the Canonical-Correlation Coefficient values for blocked and unblocked visual fields ($p = 0.492$). We hope that our work can encourage greater development for SSVEP-based visual field assessment. In the future, we can use SSVEP for each stimulus at the same time but at different frequencies, allowing testing time to be cut down threefold. Another realm of inquiry would be the use of Virtual Reality to present the SSVEP stimuli, creating a completely portable diagnostic system.

Keywords Component · SSVEP · BCI · Visual field

Y. Y. V. Tan (✉) · D. J. Njondimackal
NUS High School of Math and Science, Singapore, Singapore
e-mail: vince.tanyy@gmail.com

D. J. Njondimackal
e-mail: jdeepankur@outlook.com

A. A. Phyo Wai
Nanyang Technological University, Singapore, Singapore
e-mail: apwaung@ntu.edu.sg

H. Guo et al. (eds.), *IRC-SET 2020*,
https://doi.org/10.1007/978-981-15-9472-4_39

1 Background

Medical conditions such as scotoma and glaucoma [1] reduce the visual field of individuals, slowly creating blind spots that increase in size unknowingly until near blindness. In order to diagnose the onset of these conditions therefore, an objective method of assessing the visual field of a patient is necessary. Visual field assessment for such conditions is typically conducted in clinical settings through Standard Automated Perimetry (SAP) [2, 3]. However, this assessment relies heavily on user input, meaning that its effectiveness is subject to the irregularities of the patient's responses to the stimuli.

Instead, we may use a Brain Computer Interface (BCI), which is a biosensing device that can detect Electroencephalogram (EEG) signals from the brain. These EEG signals are typically invoked by exposing the patient to flickering Steady-State Visual Evoked Potential (SSVEP) stimuli.

When a visual stimulus that a person is observing flickers at a constant frequency, an EEG signal of the exact corresponding frequency can be picked up in the visual cortex of the brain. A BCI can then easily evaluate whether an individual has seen a stimuli, without relying on them physically pressing a button in response. This can reduce response time, and indeed speeds up the procedure as a whole.

2 Objective and Methodology

In this research project, we aim to provide a more effective alternative method to determine the visual field of a patient and thus diagnose his condition better. We will compare two different types of visual field assessment - the industrial standard, SAP, and a self-designed SSVEP-based assessment. We will compare the effectiveness of an existing SAP program, Specvis [4], to our SSVEP stimuli technique.

For SSVEP data collection, we designed and coded a Unity-based application that displays a 4 by 6 grid. This grid is the same as the one we use in SpecVis, except the stimulus is larger. To evoke SSVEP responses, each stimulus flickers at 10 Hz one at a time, with breaks in between for the subject to rest.

This comparison between SSVEP and SpecVis is used to empirically establish the efficiency of this new system. We hypothesized that our method of SSVEP-based perimetry will more accurately predict the shape of the visual field compared to SAP.

3 Experiment Design and Data Collection

We would conduct the experiment on ten participants, all of the age of 17. The participants will be seated about 20 cm away from a 22″ monitor. The user is tested

with 2 conditions, one with unrestricted vision, and another with parts of the screen covered.

During the SSVEP assessment, the biosensing device and EEG electrodes are connected according to the "10–20 System". This biosensing device will be able to record the EEG signals received from the electrodes. The stimuli will be presented on the same screen as the previous test but a break will be provided to allow the user to recuperate and prevent fatigue from affecting our results.

Figure 1 shows the layout of our unblocked screen. All 24 of the stimuli are clearly visible, with no blockages at all. In our SSVEP-based Unity program, a cross is placed in the centre for the user to focus on.

Similarly, Fig. 2 shows the layout of out blocked screen. Specific parts of the screen are blocked by a piece of place paper, with certain regions being cut out.

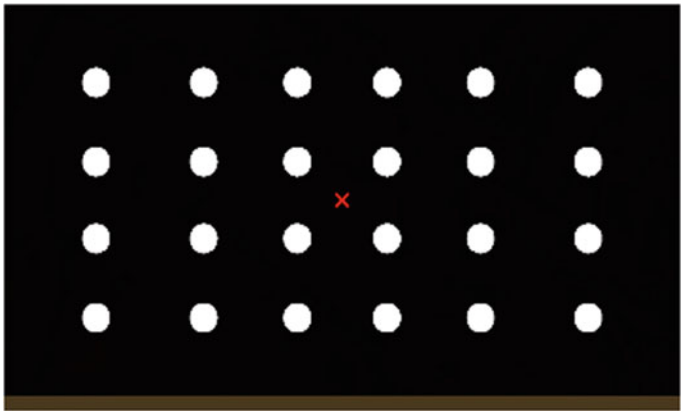

Fig. 1 Unblocked screen

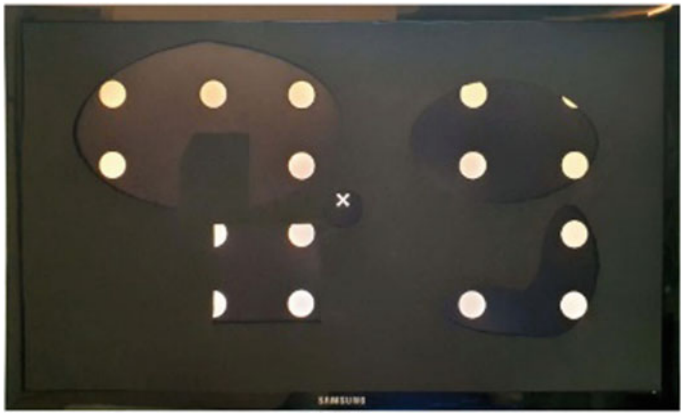

Fig. 2 Blocked screen

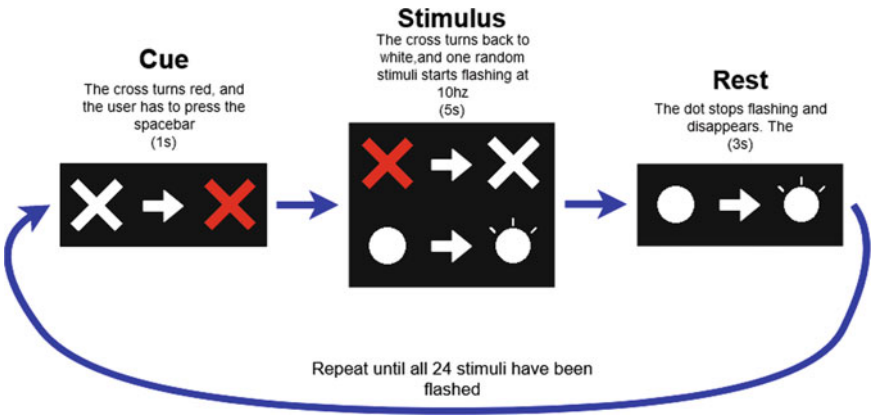

Fig. 3 Stimuli presentation

These designs are intended to simulate visual field loss and feature various designs that are prevalent in real life visual field loss [5, 6].

For SSVEP test, we will detect the brain activity at the primary visual cortex using EEG from occipital electrodes O1 and O2. A1 and A2 are used as ground and reference electrodes, and Fp2 will be used by us to measure subject attentiveness.

Before each stimulus flickers, the cross which the participant is supposed to focus on will turn red and the user has to press the spacebar. This ensures that the user is focusing directly on the cross in the middle. The stimuli will then flicker at a frequency of 10 Hz for that will evoke SSVEP when observed, that can be extracted from the EEG readings from O1 and O2.

Figure 3 shows the design of our SSVEP-based perimetry experimentation. We have three stages – cue, stimulus and rest. The procedure is described as follows.

(1) *Cue*

In the cue stage, the middle cross turns red and the subject has to press the spacebar. This ensures that the subject is focusing on the cross. The time the subject takes to press the cross is also collected. The cross remains red for 1 s.

(2) *Stimulus*

Next, the cross turns back to white. One of the stimuli is randomly selected to start flashing at 10 Hz. The subject is to remain focusing on the cross while keeping the flashing stimulus in the peripheral vision. The stimulus will continue flashing for 5 s.

(3) *Rest*

After the 5 s of flashing, the dot stops flashing and disappears. 2 s of rest time is given to the user to prevent fatigue.

This procedure goes on until all 24 stimuli have been selected to flash, and then the SSVEP test is complete. A logfile is generated with the specific time that each

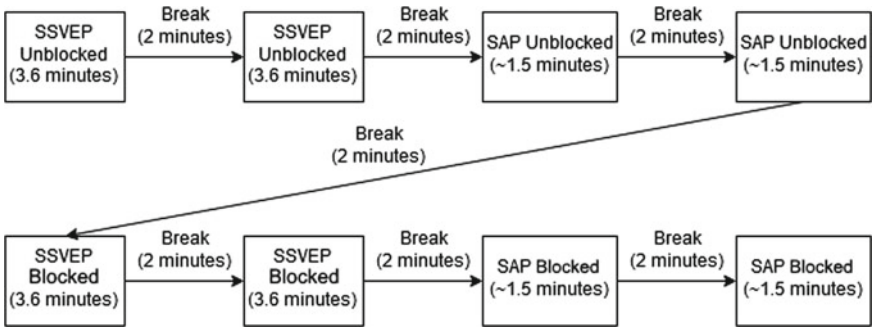

Fig. 4 Experiment timeline

event occurs, allowing us to sync the EEG data with the SSVEP-based perimetry app.

In SpecVis, small stimuli will appear on the screen at different locations upon which the user is expected to press a key. The timestamps of the stimuli presentation and the key press, and the visual field angle of the stimuli are compared to produce an evaluation of the user's visual field. This is similar to the logfile generated in the SSVEP-based perimetry app.

Figure 4 shows the experiment timeline for each subject. All the tests are conducted in one sitting. We start with our unblocked screen, conducting the SSVEP and SAP test twice each. Afterwards, we add the black piece of paper to form our blocked screen and repeat the same tests under the new conditions. Sufficient rest time of 2 min is put in between each test so as to prevent fatigue of the subject.

4 Statistical Analysis and Results

For the SSVEP-based assessment, specific features will be extracted using Canonical-Correlation Analysis [7] (CCA) and EEG bandpowers. We first synchronized the EEG and Unity events data, segmenting out the timings during which the stimulus was flashing. After sorting out everything, we have 24 sets of segmented data for each trial. The Canonical-Correlation Coefficient (CCC) for each stimulus in each trial is derived by the above mentioned CCC, which is a form of multivariate analysis.

As shown in (1), we aim to maximise ρ, which measures the canonical correlation between x and y with respect to maximizing spatial weights W_x and W_y. x and y correspond to response EEG and ideal reference signal using stimulus frequency respectively. In our experiment, a higher CCC value would indicate better SSVEP responses with respect to the flickering frequency [8].

$$\rho = \frac{{W_x}^T C_{xy} W_y}{\sqrt{{W_x}^T C_{xx} W_x W_y^T C_{yy} W_y}}. \tag{1}$$

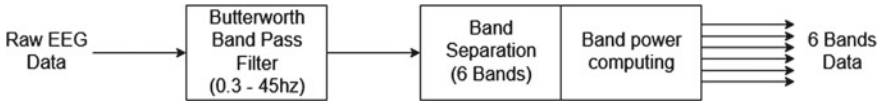

Fig. 5 Bandpower processing

Butterworth band pass filter was also applied to the raw EEG data with a 0.3–45 Hz passband. The delta, theta, alpha, low beta, high beta and gamma frequency bandpowers were then extracted from each of the segmented EEG data [9].

To obtain the frequency bandpower data, the EEG data was collected and then processed using MATLAB. Figure 5 shows the processing we applied to the raw EEG data. The steps are taken as follows:

(1) *Pre-processing*

A Butterworth band pass filter was also applied to the raw EEG data with a 0.3 to 45 Hz passband. Artifact removal is done by subtracting smoothed references from the EEG. These smoothed references are obtained through the use of moving averaging with multiple moving windows.

(2) *Feature Extraction*

We then segment the data into its own epochs with a 200 ms shift between them. This analysis is done for various epoch lengths (1 s, 2 s, 3 s, 4 s) and accuracy in each is computed. The delta (1–4 Hz), theta (4–8 Hz), alpha (8–12 Hz), low beta (12–18 Hz), high beta (18–30 Hz) and gamma (30–45 Hz) frequency band powers were then extracted from each of the segmented EEG data.

We have thus obtained the 6 frequency bandpowers, and this data is later used to ascertain the engagement of the subject.

Since we have all the CCC values of each stimulus in each trial, we can then average them out for each subject and plot them on a contour plot. Similarly, for SpecVis, an averaged contour plot is created depending on whether the subject pressed the spacebar for each stimulus. Since the layout for both Specvis and the SSVEP-based assessment program are the same, we can easily compare the two. We have selected 2 of our subjects which have the most similar pattern to the actual blocked layout to showcase.

Figure 6 shows the actual blocked layout that we simulated. The hole in the middle is to allow the subject to see the cross which they are supposed to focus on.

Figure 7 and 8 show the SAP results for subject 5 and 8 respectively. These contour plots have a very similar layout to the actual one. Most, if not all, of the blocked spots are correctly identified and match up with the actual layout.

Figures 9 and 10 show the SSVEP results for subject 5 and 8 respectively. These contour plots have similarities between them and the actual layout. However, they are not entirely accurate as not all identified blocked spots correspond to the actual layout. There are a few regions that have been correctly identified.

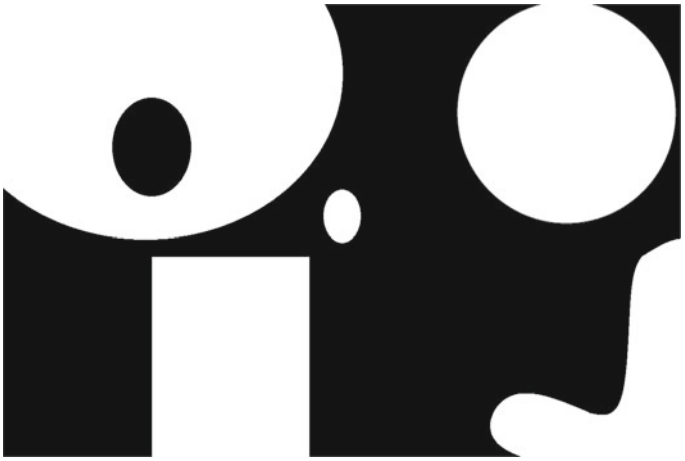

Fig. 6 Actual blocked layout

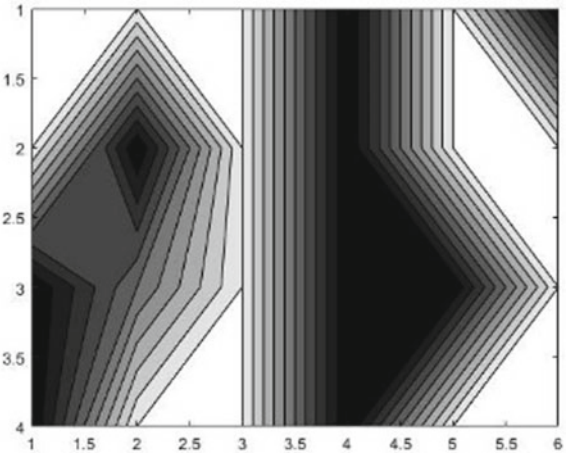

Fig. 7 SAP subject 5 contour plot

For our SSVEP trials, we conducted a paired samples t-test to compare the CCC values for unblocked and blocked conditions. There was no significant difference in the CCC values for unblocked (0.18 ± 0.065) and blocked (0.18 ± 0.062) conditions; $t(398) = -0.688$, $p = 0.492$.

We also conducted a Pearson correlation matrix to evaluate the correlation between the CCC value and bandpower ratio $\beta/(\alpha + \theta)$. This ratio is an indication of the subject's engagement [10, 11]. This was performed on Subject 5, one of our 2 best subjects in terms of the SSVEP contour map. For blocked trials, there was no significant correlation between the CCC value and bandpower ratio, $r = 0.10$, $n = 47$, $p = 0.49$. For unblocked trials, there was no significant correlation between the CCC value and bandpower ratio, $r = -0.16$, $n = 48$, $p = 0.27$.

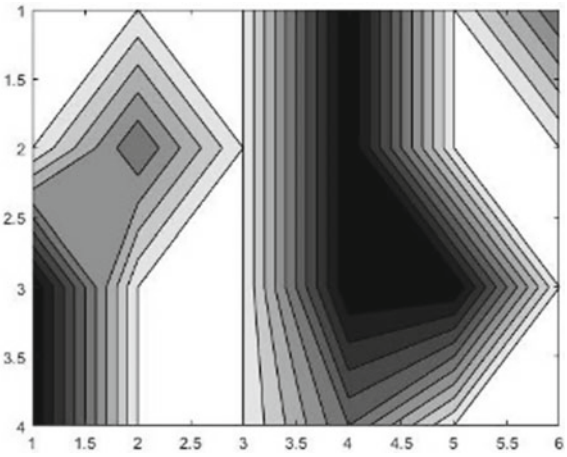

Fig. 8 SAP subject 8 contour plot

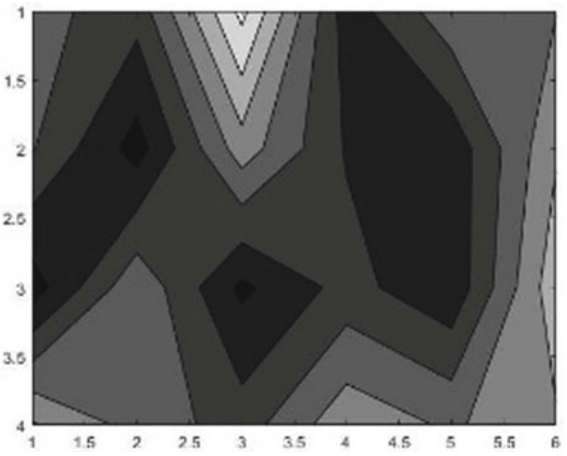

Fig. 9 SSVEP subject 5 contour plot

5 Discussion

The contour maps generated by the alignment of CCC values of the SSVEP measurements to the position of the stimuli at the corresponding time are roughly similar to those generated by SAP. This indicates that the SSVEP can potentially be used as a alternative method of testing in place of SAP. The presence of artifacts and irregularity in shape can be explained by the difficulty of enforcing total concentration on the presented stimuli as well as the low frequency of stimuli used in comparison to conventional SSVEP. Although SSVEP has not outdone SAP in this experiment as initially hypothesised, we still believe that our primary objective of establishing a viable alternative method to determine the visual field of a patient has been achieved. There are a few vindicating factors towards this surmise. When considering the CCC

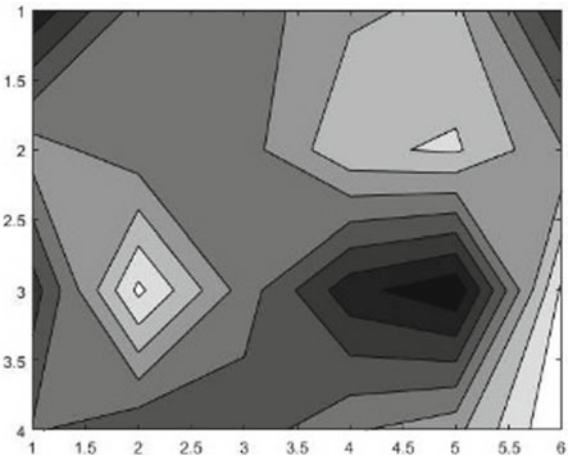

Fig. 10 SSVEP subject 8 contour plot

values—which measure the similarity of our measured EEG signals to a "perfect" 10 Hz reference signal, and thereby the "strength" of the Steady State Visual Evoked Potential (SSVEP)—we see that the use of visual blocks does not significantly alter the strength of SSVEP evocation in the subject. This means that the reliability of this method does not differ even as the severity of the patient's visual defect intensifies. Another reason would be the limited reliability of our equipment, particularly due to heavy mains current interference.

6 Conclusion

As discussed, we have managed to prove that the use of SSVEP is feasible for the diagnosis even of complex visual field blockages. It should be noted that for the purpose of proving our proposed alternative under the most vigorous assessment we used visual blocks that consisted of multiple complex polygons, whereas in reality visual defects like glaucoma largely consist of peripheral blockages or random spots. The detection of conventional visual defects will surely be easily achieved in medical conditions using professional environmental control and equipment. For future studies, we hope to execute an assessment of the feasibility of presentation of SSVEP stimuli through VR with the added benefit of making the entire system portable and accessible outside the lab. We also aim to also reduce the assessment duration by presenting different frequency SSVEP stimuli at once.

References

1. Albert, D. M., & Gamm, D. M. (2017, July 6). Visual field defect. Retrieved from https://www.britannica.com/science/visual-field-defect.
2. Medeiros, F., & Alencar, L. (2011). The role of standard automated perimetry and newer functional methods for glaucoma diagnosis and follow-up. Indian Journal of Ophthalmology, 59(7), 53. doi:https://doi.org/10.4103/0301-4738.73694
3. Johnson, C. A., Sample, P. A., Cioffi, G. A., Liebmann, J. R., & Weinreb, R. N. (2002). Structure and function evaluation (SAFE): I. criteria for glaucomatous visual field loss using standard automated perimetry (SAP) and short wavelength automated perimetry (SWAP)11Internet Advance publication at ajo.com June 17, 2002. *American Journal of Ophthalmology, 134*(2), 177–185. doi:https://doi.org/10.1016/s0002-9394(02)01577-5
4. Dzwiniel, P., Gola, M., Wójcik-Gryciuk, A., & Waleszczyk, W. J. (2017). Specvis: Free and open-source software for visual field examination. Plos One, 12(10). doi: https://doi.org/10.1371/journal.pone.0186224
5. Trick, G., Trick, L., Morris, P., & Wolf, M. (1995, January 01). Visual field loss in senile dementia of the Alzheimer's type. Retrieved June 29, 2020, from https://n.neurology.org/content/45/1/68.abstract
6. Liu, G., Volpe, N., & Galetta, S. (2018, March 19). Visual Loss: Overview, Visual Field Testing, and Topical Diagnosis. Retrieved June 29, 2020, from https://www.sciencedirect.com/science/article/pii/B9780323340441000031
7. Wai, A. A. P., Goh, Z., Foo, S. D., & Guan, C. (2018). A Study of SSVEP Responses in Case of Overt and Covert Visual Attention with Different View Angles. 2018 IEEE International Conference on Systems, Man, and Cybernetics (SMC). doi: https://doi.org/10.1109/smc.2018.00652
8. Wai, A. A., Lee, M., Lee, S., & Guan, C. (2019). Improving the Performance of SSVEP BCI with Short Response Time by Temporal Alignments Enhanced CCA. *2019 9th International IEEE/EMBS Conference on Neural Engineering (NER).* doi:https://doi.org/10.1109/ner.2019.8716985
9. Bilgin, P., Agres, K., Robinson, N., Wai, A. A. P., & Guan, C. (2019). A Comparative Study of Mental States in 2D and 3D Virtual Environments Using EEG. 2019 IEEE International Conference on Systems, Man and Cybernetics (SMC). doi: https://doi.org/10.1109/smc.2019.8914326
10. Chaouachi, M., Chalfoun, P., Jraidi, I., & Frasson, C. (2010). Affect and Mental Engagement: Towards Adaptability for Intelligent. Retrieved from https://www.researchgate.net/publication/221438970_Affect_and_Mental_Engagement_Towards_Adaptability_for_Intelligent
11. Sandhu, V., Wai, A. A., & Ho, C. Y. (2017). Evaluation of learning performance by quantifying users engagement investigation through low-cost multi-modal sensors. *2017 International Conference on Orange Technologies (ICOT).* doi:https://doi.org/10.1109/icot.2017.8336117

Improving the Performance of Lithium-Ion Batteries Using Silicon-Metal Based Anodes

William Chia

Abstract Lithium-ion rechargeable batteries (LIB) have high energy densities and are thus widely used in portable electronic devices and they show great potential for more demanding applications like electric vehicles. However, LIB have short cell lives due to capacity loss. To build higher performance batteries, this project will synthesise Si-metal Alloys and investigate their properties as an anode material in Lithium-ion Batteries (LIB). Silicon is chosen as it has a high theoretical specific capacity (4200 mAh/g) (Yao et al. in Nano Letters 11:2949–2954, 2011). The structure of the active materials was characterised by Scanning Electron Microscopy (SEM) and X-ray diffraction (XRD) while Galvanostatic Cycling (GC) was used to analyse the cells. Results show that batteries using $Al_{55}Si_{40}Zr_5$ (a Si-metal Alloy) as an anode material have lower percentage of capacity fading (8.44%) as compared to batteries using only Si (99.6%). This means that we should leverage on the potential of $Al_{55}Si_{40}Zr_5$ as a promising high capacity anode material that would best reduce the capacity fading of Si-based LIBs. For future work, the electrochemical properties of $Al_{55}Si_{40}Zr_5$ and alloys of Al, Si and Zr with different compositions as the anode material could be investigated in greater scope.

Keywords Battery · Lithium-ion · Zirconium · Rechargeable battery · Silicon · Anode

1 Introduction

Lithium-ion batteries (LIB) are a key component of personal portable devices such as mobile phones. LIBs possess high energy density, high power density, long service life and environmental friendliness and thus have found wide application in the area of consumer [1]. LIBs also possess higher operating voltages than most other batteries. For example, LIBs operate at 2.5–4.0 V as compared to Nickel Cadmium batteries (1.0–1.25 V) or Lead Acid batteries (1.10–1.25 V). A battery with a higher operating

W. Chia (✉)
NUS High School of Math and Science, Singapore, Singapore
e-mail: williamchia2012@gmail.com

H. Guo et al. (eds.), *IRC-SET 2020*,
https://doi.org/10.1007/978-981-15-9472-4_40

voltage means that more power can be delivered within the same period of time as opposed to a battery with a lower operating voltage and the appliance would be more efficient. The ever increasing demand for energy storage has thus stimulated more research on LIBs.

Silicon has a low discharge potential and the highest theoretical specific capacity (4200 mAh/g) [2] as compared to 372 mAh/g for graphite, which is currently used in LIBs. Thus, silicon has the potential to replace graphite as an anode material. A battery using Silicon may be able to run for longer periods of time as opposed to a similar battery that uses graphite. However, electrode volume expansion of approximately 400% during lithiation places a large strain on the material. This strain causes cracks in the silicon nanoparticles, thus causing them to break down and creating spaces between particles. This results in poor conductivity and the LIB would have low cycle life [3, 4]. This is supported by an investigation conducted by Jung et al. which showed that Silicon anode-based LIBs experienced rapid capacity decay after 20 cycles [5]. In addition, silicon has low electrical conductivity and low diffusivity for lithium ions.

Hence, the aim of this project is to find a suitable Si-metal alloy that has high capacitance and high cycle life using the solid state precursor method. A high capacitance implies that the battery can have a larger power output while a high cycle life means that the battery can last longer. The solid state precursor method can be suitable for bulk production. X-ray diffraction (XRD) was carried out to analyse the structure of the compounds and Scanning Electron Microscopy (SEM) was used to characterise the materials. TOPAS software was also used to analyse the data collected while Galvanostatic Cycling (GC) was used to analyse the cells.

From my literature review, I came up with 2 hypotheses.

(1) The batteries with Si-metal alloys as the anode have higher energy density and reduced capacity fading as compared to the battery with Si as the anode. In this project, I will create 3 different combinations of Si-metal alloys.
(2) The battery with $Al_{55}Si_{40}Zr_5$ as the anode has the highest energy density. This is because zirconium is highly resistant to corrosion and the battery can a high cycle life.

2 Methodology

2.1 Synthesising Active Compounds

The Si-metal alloys were synthesised using the carbothermal precursor method. This method was chosen as it is simple and can be used for bulk production. All starting materials were ensured to be of high purities from suppliers. The starting materials were mixed together, ground up and heated in a furnace for 6 hours at 900 degrees Celsius. Samples were heated in the tube furnace in argon as argon provides an inert atmosphere and removes unwanted side reactions that may occur with other gases

Table 1 Masses of starting materials for active compounds

Sample	Active compound	Starting materials	Mass (g)
1	$Al_{55}Si_{40}Mn_5$	Al	1.53
		Si	0.16
		Mn	0.31
2	$Al_{55}Si_{40}Zr_5$	Al	1.45
		Si	1.10
		Zr	0.45
3	$SiO_2 + Co_3O_4 + 5C$	SiO_2	1.33
		Co_3O_4	1.33
		C	0.33
4	Si	Si	0.62
		SiO_2	1.32
		C	1.27

in an air furnace. Table 1 shows the masses of starting materials used to obtain the active compounds.

2.2 Electrode Fabrication

Slurries were then made using the active compounds. Samples 1 and 2 were mixed with Polyvinylidene fluoride (PVDF), carbon fibre and Super P Carbon in a 60%–15%–15%–10% weight ratio, with N-Methyl-2-pyrrolidone (NMP) as a solvent. Samples 3 and 4 were mixed with PVDF and Super P Carbon in a 70%–15%–15% weight ratio, with NMP as a solvent [6]. PVDF was used for its binding properties, Super P Carbon as a conductive additive, carbon fibre as it possesses low thermal expansion and NMP as its low toxicity and flammability results in safer battery usage. The slurries were placed in a magnetic stirrer until fully mixed. They were then coated onto separate copper foils using the doctor blade technique to obtain a consistent coating of 20 micrometres, left to dry in an air oven at 90 degrees Celsius for 6 hours and pressed between twin rollers to increase contact area. The coated copper foil was cut into circular disks of radius 8.0 mm. Table 2 summarises the

Table 2 Weight ratios of samples

Sample	Components	Weight ratio of components
1	Active compound, Polyvinylidene fluoride (PVDF), carbon fibre, Super P Carbon	60%–15%–15%–10%
2		
3	Active compound, Polyvinylidene fluoride (PVDF), Super P Carbon	70%–15%–15%
4		

weight ratio of components of the samples.

2.3 Battery Fabrication

Electrodes with a uniform layer of active compound were chosen and weighed. The electrodes were then placed in a vacuum oven at 80 degrees Celsius for 12 hours to remove moisture and contaminants from the electrodes. The cells were assembled in an argon filled glove box in the following order cell cap, electrode, electrolyte ($LiFePO_4$), Whatman filter paper (as a separator), lithium metal and cell base. The lithium metal was scraped to remove any oxides that had formed. A coin cell press was used to assemble the cell, ensuring contact between cell components.

3 Results and Discussion

3.1 Structure and Morphology

Sample 4 seems to comprise of smaller particles than samples 1 and 3. Smaller particles allow for better lithium-ion intercalation as total surface area of the particles increases. Sample 1 seems to have a flaky structure while samples 3 and 4 seem to have a coral-like structure. As such, sample 3's and 4's high total surface area may aid lithium intercalation but prevent deintercalation. All samples are black in colour. A possible reason why sample 1 has larger particles than samples 3 and 4 is that sample 1 has a higher metal content and thus have larger particles. We were unable to obtain SEM images for sample 2 (Figs. 1, 2 and 3).

3.2 X-Ray Diffraction (XRD)

Figures 4 and 5 show the XRD data for $Al_{55}Si_{40}Co_5$ and sample 4. XRD was carried out to measure the purity of compounds produced and to check the crystallinity of the materials. The XRD data for samples 1, 2 and 3 could not be obtained. As the structure of $Al_{55}Si_{40}Co_5$ is similar to the structures of samples 1 and 2, the XRD data of $Al_{55}Si_{40}Co_5$ was used as a reference for samples 1 and 2. As sample 3 and 4 had similar structures, the XRD data of sample 4 was used as a reference for sample 3. Peaks at similar areas for Sample 4 high purity of the sample, thus showing that carbothermal precursor method, a bulk preparation method, can be used to produce silicon and its alloys.

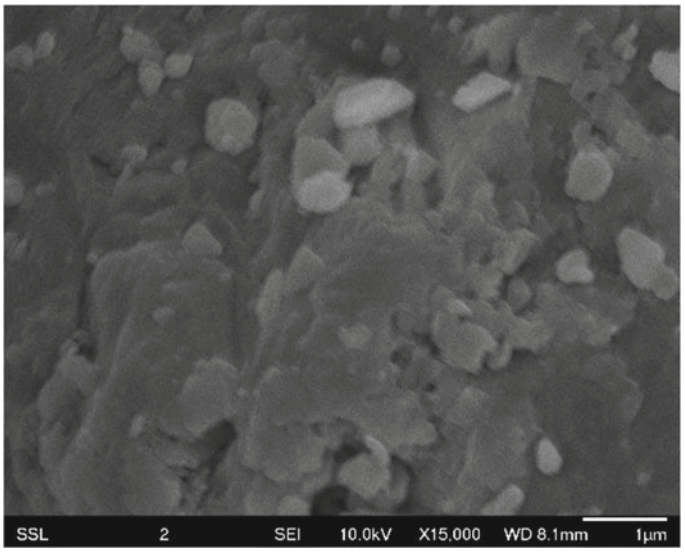

Fig. 1 SEM image of sample 1 with 15,000 magnification

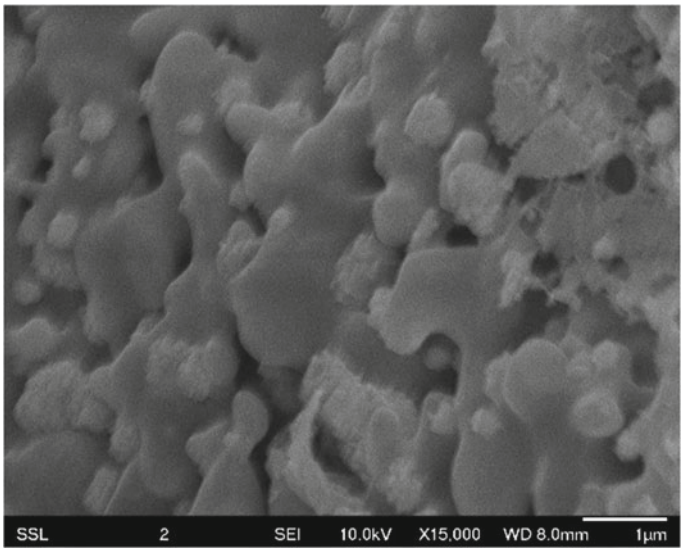

Fig. 2 SEM image of sample 3 with 15,000 magnification

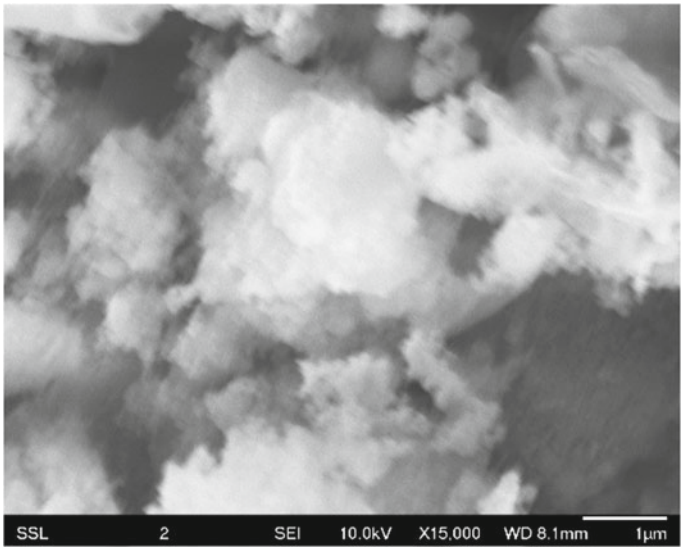

Fig. 3 SEM image of sample 4 with 15,000 magnification

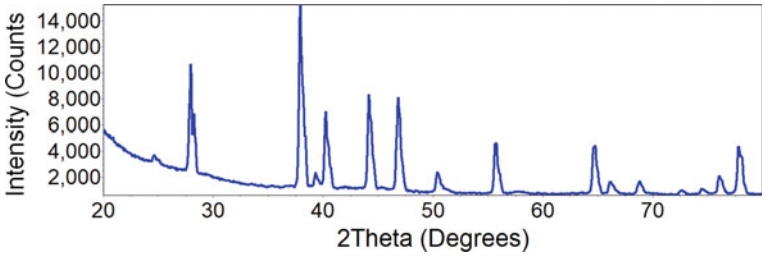

Fig. 4 XRD Pattern of $Al_{55}Si_{40}Co_5$

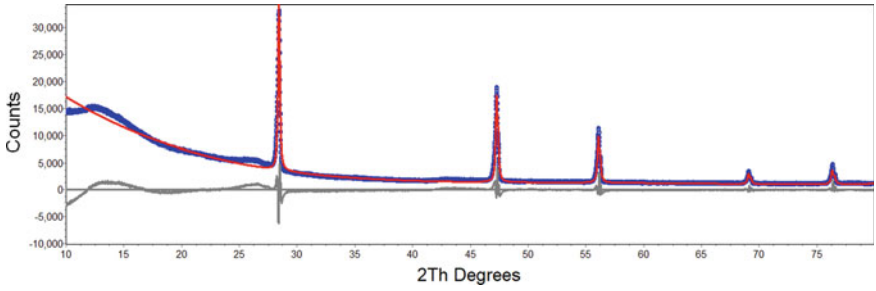

Fig. 5 XRD Pattern of Sample 4

3.3 Galvanostatic Cycling (GC)

GC was carried out on all samples to analyse the capacity and coulombic efficiency of the cells. This is done by charging and discharging the cells at a constant current rate at a voltage range of 0.02–3.0 V while measuring the cell's specific capacity. The current rate used was 100 mA/g and cycled in the voltage range 0.02–2.0 V versus Li. The graphs of the GC are shown in Fig. 6.

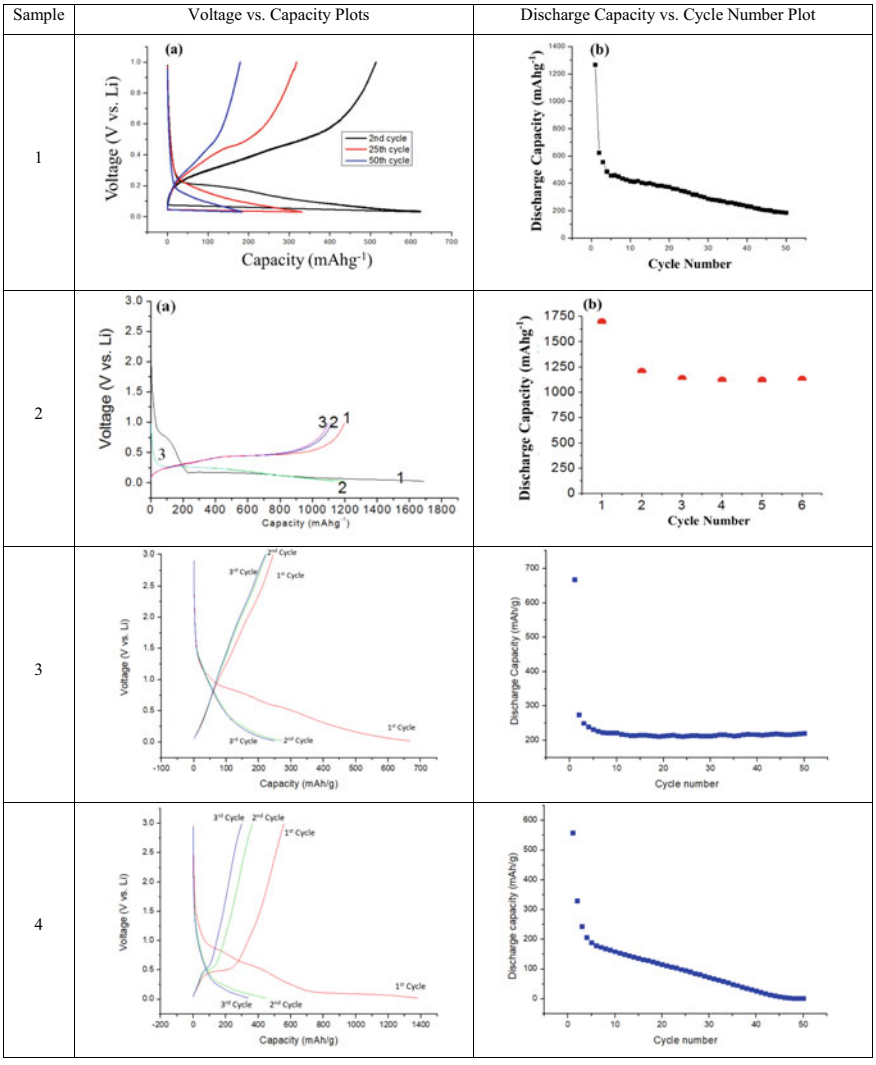

Fig. 6 Plots of voltage versus capacity and discharge capacity versus cycle number

Sample 1 had an initial discharge capacity of 1263 mAh/g. For the subsequent cycles, a substantial decline in the discharge capacity was observed, where the discharge capacity reached a lowest value of 183 mAh/g. No plateaus were observed throughout the charge cycles. Therefore, the magnitude of capacity fading experienced by sample 1 is 1080 mAh/g.

Sample 2 had an initial discharge capacity of 1681 mAh/g. For the subsequent cycles, a moderate decline in the discharge capacity was observed, before they plateaued at an average discharge capacity value of approximately 1117 mAh/g. Therefore, the magnitude of capacity fading experienced by sample 2 is given by 564 mAh/g.

Sample 3 had an initial discharge capacity of 667 mAh/g. For the subsequent cycles, a moderate decline in the discharge capacity was observed, before they plateaued at an average discharge capacity value of approximately 218 mAh/g. Therefore, the magnitude of capacity fading experienced by sample 3 is given by 449 mAh/g.

Sample 4 had an initial discharge capacity of 558 mAh/g. For the subsequent cycles, a substantial decline in the discharge capacity was observed, where the discharge capacity reached a lowest value of 1.59 mAh/g. No plateaus were observed throughout the charge cycles. Therefore, the magnitude of capacity fading experienced by sample 4 is given by 556.41 mAh/g.

The theoretical capacity is given as

$$(C_2 - C_{50}) \div C_2 \times 100\% \tag{1}$$

where C_n is the capacity of the battery at the nth cycle.

Using (1), the capacity fading experienced in percentages by sample 4 is the highest (99.6%), followed by sample 1 (70.5%), sample 3 (20.4%) and sample 2 (8.44%).

Table 3 summarises the results of the GC.

Table 3 Results of GC

Sample	Initial discharge capacity (mAh/g)	Magnitude of capacity fading (mAh/g)	Percentage of capacity fading (%)
1	1263	1080	70.5
2	1681	564	8.44
3	667	449	20.4
4	558	566.41	99.6

4 Conclusion and Future work

In conclusion, the research analysed the performance of Li-ion batteries with anode material made of different Si-Al-based alloys. GC tests were conducted for all four new Li-ion batteries which were created for this research and it was determined that the battery fabricated with $Al_{55}Si_{40}Zr_5$ as the anode material exhibited the optimal electrochemical performance, with the lowest percentage of capacity fading of 8.44%. Out of the four samples, sample 4 had the highest percentage of capacity fading of 99.6%.

Thus, from the GC results the first hypothesis that the batteries with Si-metal alloys as the anode have higher energy density and reduced capacity fading as compared to the battery with Si as the anode was true.

The second hypothesis that the battery with $Al_{55}Si_{40}Zr_5$ as the anode has the highest energy density and least capacity fading was also true. It has the lowest capacity fading at 8.44%. The next best battery is sample 3 which has a capacity fading at 20.4%. Thus, $Al_{55}Si_{40}Zr_5$ has the potential as a promising high capacity anode material that would best suppress the capacity decay of Si metal.

For future work, the electrochemical properties of $Al_{55}Si_{40}Zr_5$ and alloys of Al, Si and Zr with different compositions as the anode material could be investigated in greater scope.

Acknowledgment I would like to thank my parents, expert mentor Dr M.V. Reddy, teacher mentor Mr Lim Teck Choow and laboratory staff at Department of Physics, National University of Singapore for their help and support.

References

1. L. Lu, X. Han, J. Liu, J. Hua, and M. Ouyang, "A review on the key issues for lithium-ion battery management in electric vehicles," *Journal of Power Sources*, vol. 226, pp. 272–288, November 2012.
2. Y. Yao, M. T. McDowell, I. Ryu, H. Wu, N. Liu, L. Hu, W. D. Nix, and Y. Cui, "Interconnected Silicon Hollow Nanospheres for Lithium-Ion Battery Anodes with Long Cycle Life," *Nano Letters*, vol. 11, no. 7, pp. 2949–2954, June 2011.
3. A. Casimir, H. Zhang, O. Ogoke, J. C. Amine, J. Lu, and G. Wu, "Silicon-based anodes for lithium-ion batteries: Effectiveness of materials synthesis and electrode preparation," *Nano Energy*, vol. 27, pp. 359–376, July 2016.
4. A. A. Istratov and E. R. Weber, "Electrical properties and recombination activity of copper, nickel and cobalt in silicon," *Applied Physics A*, vol. 66, no. 2, pp. 123–136, September 1997.
5. H. Jung, M. Park, Y. Yoon, G. Kim, and S. Joo, "Amorphous silicon anode for lithium-ion rechargeable batteries," *Journal of Power Sources*, vol. 115, no. 2, pp. 346–351, December 2002.
6. S. Vivet, J. M. Joubert, B. Knosp, and A. Percheron-Guégana, "Effects of cobalt replacement by nickel, manganese, aluminium and iron on the crystallographic and electrochemical properties of AB5-type alloys," *Journal of Alloys and Compound*, vol. 356–357, pp. 779–783, December 2002.

Enhancing the Capabilities of a Water Dielectric Resonator Antenna to Support Wireless Charging

William Chia

Abstract ANSYS High-frequency Structure Simulator (HFSS) was used in the design of a compact water dielectric antenna (water DRA) for wireless charging of mobile devices. We evalauted the performance of water DRAs using a coaxial probe feeding method for rectangular, cylindrical and hemispherical shaped dielectric resonators. We have found that a rectangular sea water dielectric antenna has good omnidirectionality and the best gain performance compared to our other models.

Keywords Water dielectric resonator antenna · Wireless charging · High-frequency structure simulator (HFSS)

1 Introduction

Dielectric resonator antennas (DRAs) possess the following characteristics—A small size when using a high permittivity dielectric material, a high radiation efficiency, and the ability to adjust its operating bandwidth by suitably choosing the operating parameters [1–5]. Liquid DRAs open up new possibilities for antenna design—the dielectric material can be easily modified to the desired shape and there are no air gaps between the probe and the dielectric material [6]. Water has become the most popular dielectric material recently because it is cheap, easily accessible, safe, and eco-friendly [1, 7]. In addition, water has a high permittivity ($\varepsilon_r = 80$). As such, a DRA antenna using water as its dielectric material can have its size reduced by $\sqrt{\varepsilon_r}$ (i.e. $\sqrt{80}$) [1, 8, 9].

An application of antennas is wireless charging of mobile phones. The charger is the transmitting antenna and the current induced in the receiving antenna in the phone can be used for charging. Wireless charging has its benefits. Wireless chargers are superior to charging cables as a wireless charger can charge multiple types of phones while different charging cables (e.g. Micro-USB, USB-C) are needed for different types of phones. However, most wireless phone chargers can only operate

W. Chia (✉)
NUS High School of Math and Science, Singapore, Singapore
e-mail: williamchia2012@gmail.com

H. Guo et al. (eds.), *IRC-SET 2020*,
https://doi.org/10.1007/978-981-15-9472-4_41

over short distances of <1 cm, meaning that the phone usually needs to be placed on top of the charger. Small movements that move the phone away from the charger can interrupt the charging process, thus making the process of wireless charging very cumbersome. Recently, the Qi standard has also been developed, but wireless charging is still limited to 4 cm.

Hence, the concept of water DRAs can be implemented wireless phone chargers. Water DRAs can create an oscillating magnetic field which will induce a current in mobile phones. As water DRAs are superior to traditional antennas in areas such as size and efficiency, water DRAs may outperform traditional wireless phone chargers which use copper coils. There are many factors that determine the performance of antennas. Different shapes have different properties which can affect the performance of antennas while different types of water used have different conductivities which affect the radiation efficiency of antennas. In this project, we will focus on these factors in evaluating 9 diffferent water DRA models.

2 Aims

We aim to compare different shapes of water DRAs and types of water used as dielectric material to determine a model that is best suited for wireless charging based on gain and omnidirectionality.

3 Methodology

We have used the ANSYS high-frequency structure simulator (HFSS) software to create 9 computer models of DRAs. The antennas were fed by a coaxial cable. 3 different shapes of antenna models were created—hemispherical, cylindrical and rectangular [10]. For each shape, 3 separate models are created implementing distilled water, freshwater and seawater. Distilled water has a conductivity of 0.002 S/m, freshwater has a conductivity of 0.01 S/m and seawater has a conductivity of 4 S/m. Table 1 summarises the list of antenna models we have simulated while Figs. 1, 2 and 3 describe the dimensions in detail of the different antenna shapes used.

In the HFSS software, we analysed our models with a Fast sweep using LinearCount with a start of 0–3 GHz and a count of 150. Then, 3 graphs were plotted and analysed for each model. Table 2 summarises the graphs plotted and the reasoning behind them.

A 2D graph of the radiation pattern in function of dB was plotted at angles $\phi = 0°$, $\phi = 90°$, and $\theta = 90°$. This gives the gain in the x–z, y–z and x–y planes respectively. The directivity of the computer models could be determined by comparing the gain vs angle of the computer models.

Similarly, a 2D gain plot was generated in function of dB. This was done to investigate the power efficiency of the antennas at different directions.

Table 1 Shapes and types of water used for the models

Model	Shape	Type of water used
(a)	Cylinder	Distilled water
(b)		Freshwater
(c)		Seawater
(d)	Hemisphere	Distilled water
(e)		Freshwater
(f)		Seawater
(g)	Rectangle	Distilled water
(h)		Freshwater
(i)		Seawater

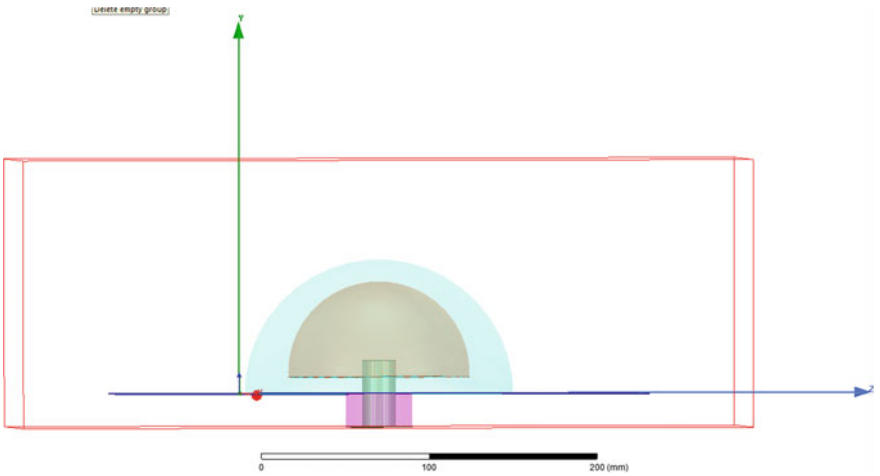

Fig. 1 Hemispherical water DRA: dielectric region with radius of 5.43 mm; encased in a foam container ($\varepsilon_r = 1.03$) with radius of 80.5 mm; ground plane (perfect E) size 161 mm × 318 mm. Feeding using a coaxial cable with outer ring (wave port on bottom surface) made of Teflon ($\varepsilon_r = 2.10$) with radius 20.0 mm and height 20.0 mm connected to ground plane; inner ring made of "perfect conductor" ($\varepsilon_r = 1.00$) with radius 10.0 mm and height 40.0 mm. Vacuum boundary region with dimensions such that there is a 60.0 mm distance from all points of the antenna

A graph of the S11 parameter was then plotted in function of dB to measure the power reflected from the model. Hence, the performance of the computer model can be determined over a specific bandwidth (the S11 parameter for a good model should be less than −10 dB for the required bandwidth).

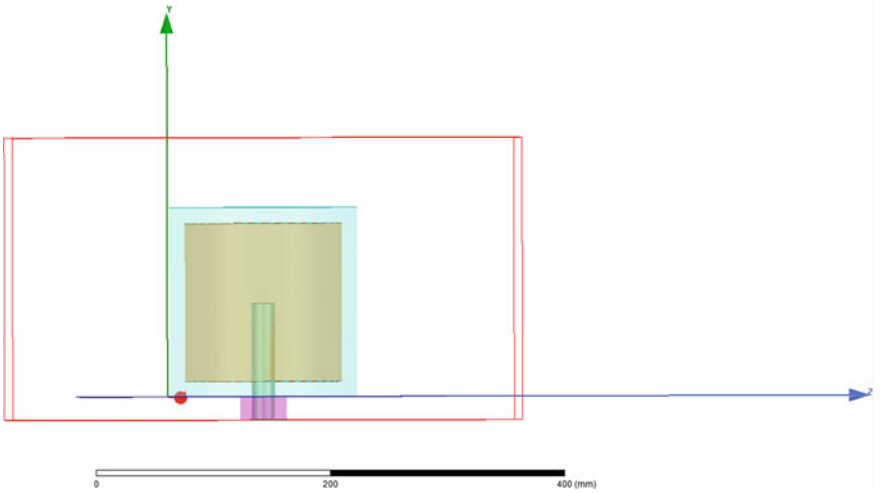

Fig. 2 Cylindrical water DRA: dielectric region with radius of 67.4 mm, height 135.8 mm; encased in a foam container ($\varepsilon_r = 1.03$) with radius of 80.5 mm, height 162.5 mm; ground plane (perfect E) size 161.0 mm × 318.0 mm. Feeding using a coaxial cable with outer ring (wave port on bottom surface) made of Teflon ($\varepsilon_r = 2.10$) with radius 20.0 mm and height 20.0 mm connected to ground plane; inner ring made of "perfect conductor" ($\varepsilon_r = 1.00$) with radius 10.0 mm and height 100 mm. Vacuum boundary region with dimensions such that there is a 60.0 mm distance from all points of the antenna

4 Results and Discussion

A. Graph of Radiation Patterns

From the results of Fig. 4, the radiation pattern in the y–z and x–y plane is relatively omnidirectional for all models where the curves almost coincide with each other. However, the radiation pattern in the x–z plane of antennas using distilled water Fig. 4a, d, g have multiple irregular side lobes.

The radiation pattern of antennas using freshwater Fig. 4b, e, h or seawater Fig. 4c, f, i have a slightly more omnidirectional shape with fewer huge drops in gain at various directions. The nodes for these antennas are found at 90° and −90°. However, the other directions have relatively low loss in gain roughly ≥ -10 dB. Hence, models Fig. 4b, c, e, f, i, h are shortlisted as directions and is especially important since longer range wireless mobile phone chargers should be able to supply power to phones in all directions.

B. Graph of Gain Plots

In graph 2, we have specifically looked at the gain plot and half power beamwidths of the shortlisted antennas from the analysis of the radiation pattern: Table 2b, c, e, f, h, i. The majority of the gain in the models that are above −3 dB is located on the upper left and lower left of the graphs. The 2 main lobes are relatively the same size so the top lobe is used in the identification of the half power beamwidth.

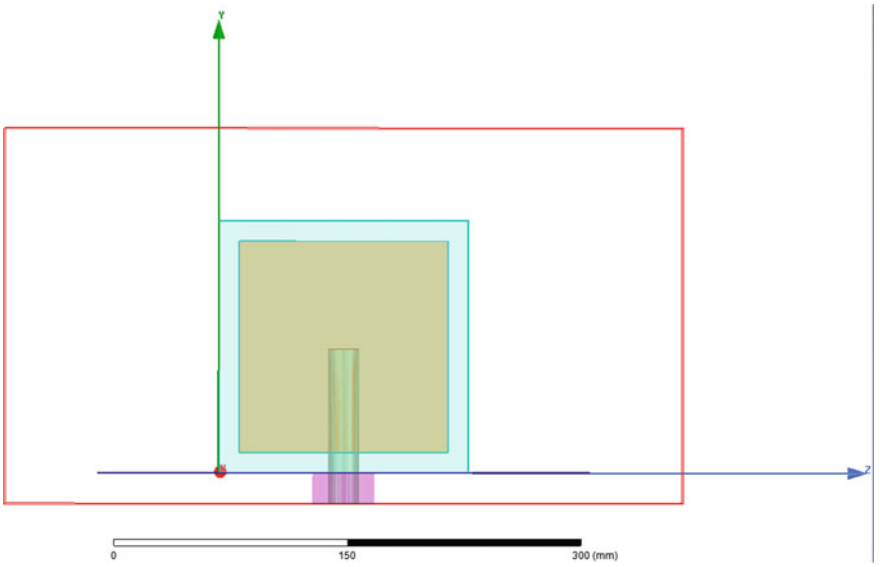

Fig. 3 Rectangular DRA: dielectric region with sides of equal length of 135 mm; encased in a foam container ($\varepsilon_r = 1.03$) with sides of equal length of 161 mm; ground plane (perfect E) size 161.0 mm × 318.0 mm. Feeding using a coaxial cable with outer ring (wave port on bottom surface) made of Teflon ($\varepsilon_r = 2.10$) with radius 20.0 mm and height 20.0 mm connected to ground plane; inner ring made of "perfect conductor" ($\varepsilon_r = 1.00$) with radius 10.0 mm and height 100.0 mm.Vacuum boundary region with dimensions such that there is a 60.0 mm distance from all points of the antenna

Table 2 Applications of graphs plotted using HFSS

Model	Application
2D radiation pattern	Determine the directivity of the antennas
Gain plot	
S11 parameter	Determine the model's performance over a particular bandwidth

In models b) and c) which are cylindrically shaped, there is an almost negligible half power beamwidth. In model i), which is rectangular sea, however, it has the highest half power beamwidth at approximately 50°. The half power beamwidth of the hemispherical models are also quite respectable at approximately 40°. Thus we have further shortlisted the models to 2e, f, h, i. The half power beamwidth is important to consider in order to identify the set of directions where there is less power loss for greater power efficiency.

C. Graph of Return Loss (S11 Parameter)

In Table 3, we have specifically looked at the shortlisted antennas from the previous analysis of the gain plot: Table 3e, f, h, i. We can observe that the bandwidths and resonant frequencies of the models are very similar. The rectangular fresh model

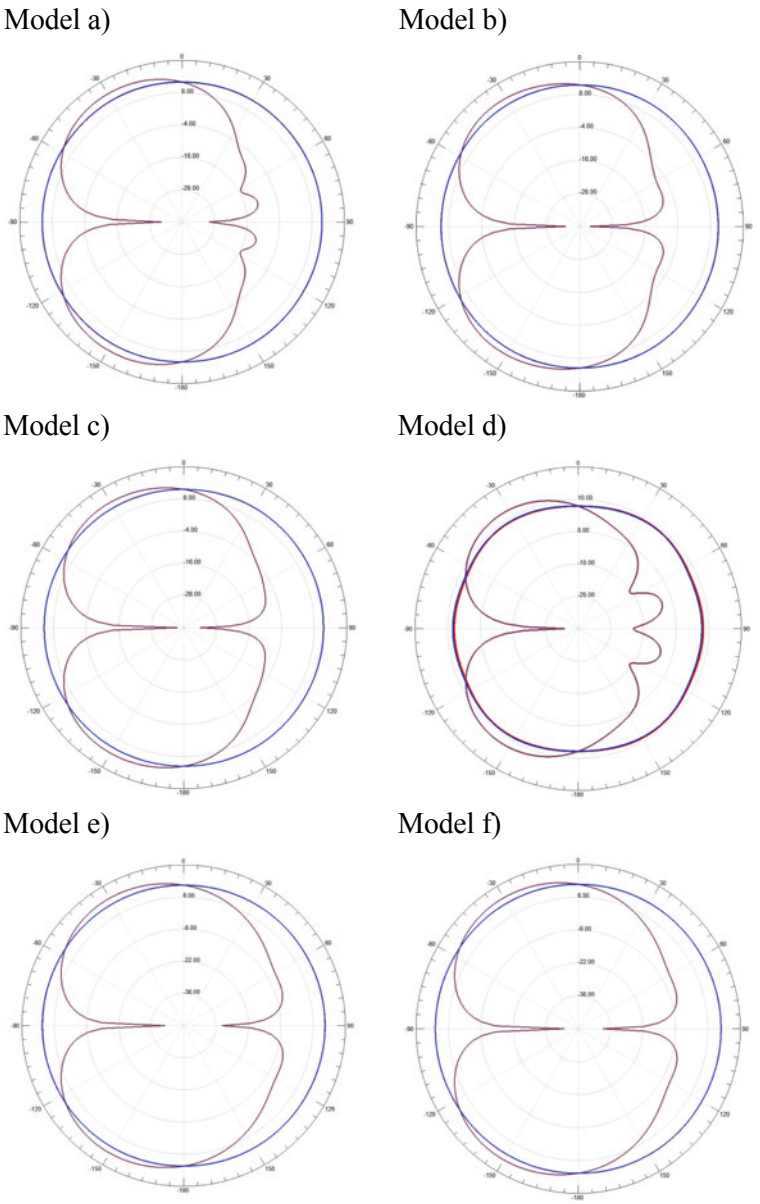

Fig. 4 Graphs of radiation patterns of models. The brown line shows the radiation pattern in the x–z plane, the blue line shows the radiation pattern in the y–z plane, and the red line shows the radiation pattern in the x–y planes

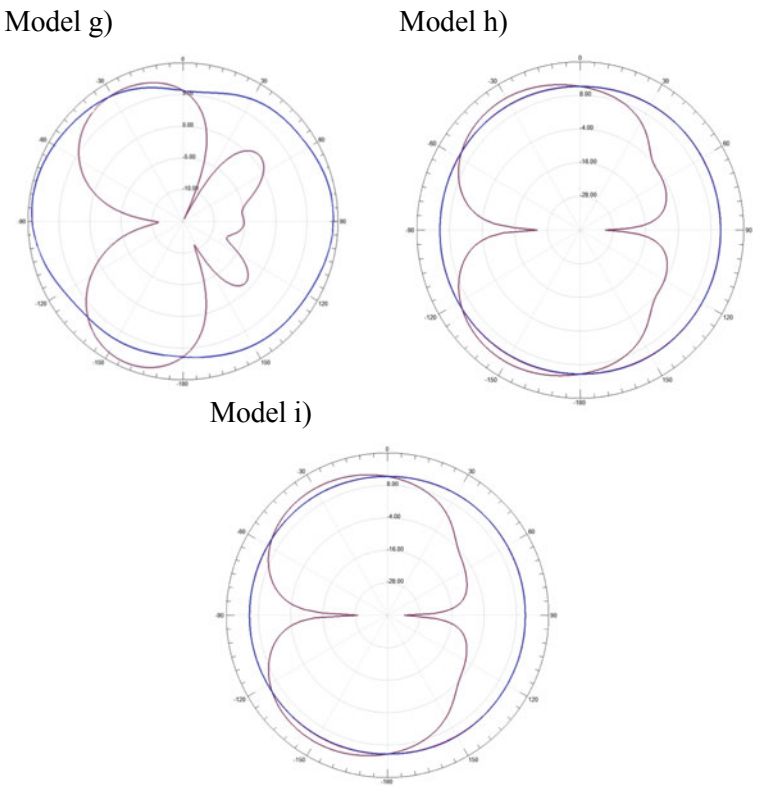

Fig. 4 (continued)

Table 3 Half power beamwidth (at −3 dB) approximates of the various models for comparison

Model	Half power beamwidth (at −3 dB)
b)	0
c)	0
e)	40
f)	40
h)	35
i)	50

h) has the largest absolute bandwidth at 0.915 GHz while hemispherical sea model f) has the smallest absolute bandwidth of 0.818 GHz. Overall, we have noticed that the models using freshwater consistently have a larger bandwidth than antennas using seawater. This is because freshwater has a models using freshwater consistently have a larger bandwidth than antennas using seawater. The bandwidth is important to consider because a larger bandwidth is more accommodating of various transmitting

and receiving frequencies to minimise the interference with other antennas such as Wi-Fi and Bluetooth connections (Fig. 5).

The resonant frequency is also noted to tune the antenna input with the highest possible transmitting and receiving gain for greater power transmission efficiency (Table 4).

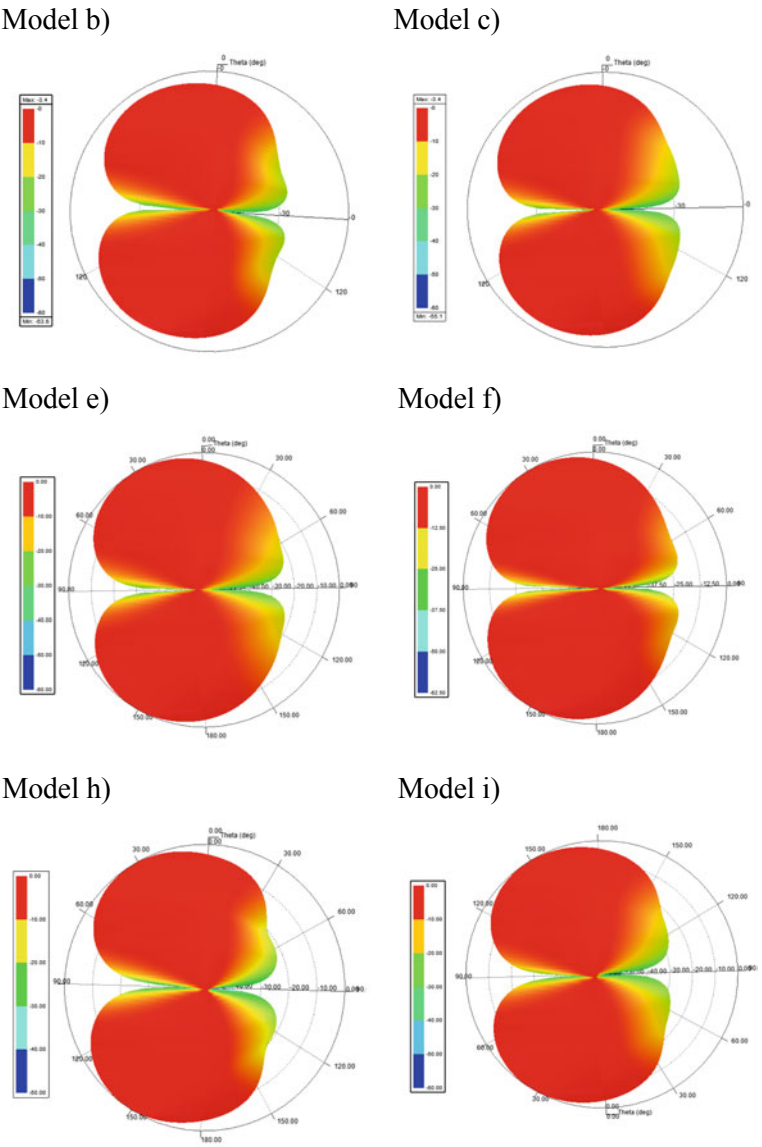

Fig. 5 Gain plots of models b, c, e, f, h, i

Table 4 Graph of return loss, absolute bandwidth and resonant frequency of models e, f, g, h

Model	Graph	Absolute bandwidth/GHz	Resonant frequency/GHz
e)	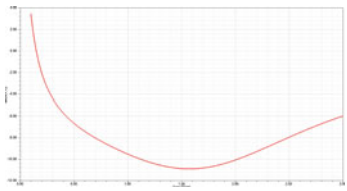	0.895 (1.105–2.000)	1.58
f)	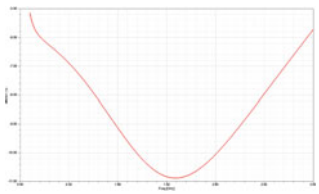	0.818 (1.189–2.007)	1.61
h)	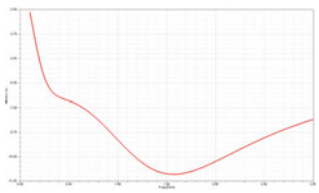	0.915 (1.169–2.084)	1.57
i)	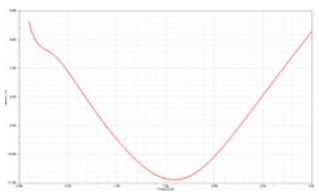	0.863 (1.146–2.009)	1.59

5 Conclusion

Taking into consideration the radiation pattern, gain plot, and absolute bandwidth of the models, we have come to a conclusion that model i), which is rectangular sea, has the best overall performance for our application.

Absolute bandwidth is a less important factor than the directionality and gain of the antenna for the purposes of wireless charging. Therefore despite model i) not having the largest absolute bandwidth, its good performance in the omnidirectionality shown in the radiation pattern, and especially the half power beamwidth shown in the gain plot makes model i) the most desired antenna design for the purposes of wireless power transmission and reception.

For future works, more research could be done on different shapes of antennas. We can also work towards increasing the gain of the models and improving on the

omnidirectionality of the models. A physical prototype of the wireless charger using the design of model i) or other optimised models can also be constructed for testing in real-life circumstances.

Acknowledgements I would like to thank my parents, research partner Ng Yu Hung, expert mentor Prof Shen Zhongxiang, teacher mentor Ms Ng Tiong Eng and laboratory staff at School of Electrical and Electronic Engineering, Nanyang Technological University for their help and support.

References

1. T. A. Denidni, Y. Coulibaly, and H. Boutayeb, "Hybrid Dielectric Resonator Antenna With Circular Mushroom-Like Structure for Gain Improvement," *IEEE Transactions on Antennas and Propagation*, vol. 57, no. 4, pp. 1043–1049, April 2009.
2. R. K. Mongia and P. Bhartia, "Dielectric resonator antennas—A review and general design relations for resonant frequency and bandwidth," *Int. J. Microw. Millimeter-Wave Comput.-Aided Engineering*, vol. 4, no. 3, pp. 230–247, July 1994.
3. T. A. Denidni and R. Qinjiang, "Hybrid dielectric resonator antenna with radiationg slot for dual-frequency operation," *IEEE Microw. Guided Wave Lett.*, vol. 3, pp. 321–323, December 2004.
4. R. K. Mongia, A. Ittipibon, and M. Cuhaci, "Measurement of radiation efficiency of dielectric resonator antennas," *IEEE Antennas Wireless Propag. Lett.*, vol. 4, pp. 80–82, March 1994.
5. R. Qinjiang, T. A. Denidni, and A. R. Sebak, "A hybrid resonator antenna suitable for wireless communication applications at 1.9 and 2.45 Ghz," *IEEE Microw. Guided Wave Lett.*, vol. 4, pp. 341–343, December 2005.
6. W. Huang and A. A. Kishk, "Compact Dielectric Resonator Antenna Array for Microwave Breast Cancer Detection," *2007 IEEE Region 5 Technical Conference*, pp. 9–12, April 2017.
7. S. Keyrouz and D. Caratelli, "Dielectric Resonator Antennas: Basic Concepts, Design Guidelines, and Recent Developments at Millimeter-Wave Frequencies," *International Journal of Antennas and Propagation*, vol. 2016, September 2016.
8. L. Xing, Y. Huang, S. S. Alja'afreh, and S. J. Boyes, "A monopole water antenna," *2012 Loughborough Antennas & Propagation Conference (LAPC)*, pp. 1–4, November 2012.
9. Y. Li and K. Luk, "A Water Dense Dielectric Patch Antenna," *IEEE Access*, vol. 3, pp. 274–280, April 2015.
10. S. P. Kingsley and S. G. O'Keefe, "Beam steering and monopulse processing of probe-fed dielectric resonator antennas," *IEEE Proceedings - Radar Sonar and Navigation*, vol. 146, no. 3, pp 121–125, July 1999.

Protective Effect of Bacopasides on 7-Ketocholesterol Induced Damage in Human Brain Endothelial Cells

Xingkai Yang, Vernice Teo, and Kristie Eliana Ramli

Abstract Alzheimer's disease (AD) is an irreversible, progressive brain disorder which leads to severe dementia. It is estimated to affect more than 100,000 people in Singapore and cost more than S$8 billion for its treatment for all Singaporeans by 2030. Recent studies demonstrated that altered cholesterol metabolism, which has been suggested to be caused by cholesterol autoxidation and oxidative stress in the brain, have been involved in AD progression. 7-Ketocholesterol (7KCh), abundantly found in deep-fried and over-cooked food, is a highly oxidised cytotoxic cholesterol which induces cell apoptosis and inflammation and is proven to result in AD. Previous researches demonstrated various pathway to inhibit 7KCh inflammation in human endothelial cells. However, there is a limited investigation on usage of phytochemical in botanical drugs against 7KCh. Bacopa monnieri has been used by Ayurvedic medical practitioners for centuries for a variety of purposes, including improving memory, reducing anxiety, and reducing inflammation. In this research, Bacopaside I (BI) and Bacopaside II (BII), two types of chemical extracts of Bacopa monnieri, are used to investigate the protective effect of BI and BII on 7KCh induced damage in human brain endothelial cells. HCMEC/d3 cell line is used as a model of the human blood–brain barrier. Cell culture is exposed to 7KCh, after which BI and BII were introduced. Cell viability test and quantitative real-time polymerase chain reaction test for pro-inflammatory cytokines, interleukin-6 and tumour necrosis factor-α were conducted. Results show that there is a significant protective effect of Bacopaside I on 7KCh damage in hCMEC/D3 cells, while Bacopaside II is deemed as ineffective against 7KCh induced damage. Therefore, Bacopa monnieri has the potential to become an effective medicinal approach to treat or mitigate AD.

X. Yang (✉) · V. Teo · K. E. Ramli
National Junior College, Singapore, Bukit Timah, Singapore
e-mail: sunnyjackyang@gmail.com

V. Teo
e-mail: teovernice14@gmail.com

K. E. Ramli
e-mail: kristie.ramli@gmail.com

H. Guo et al. (eds.), *IRC-SET 2020*,
https://doi.org/10.1007/978-981-15-9472-4_42

Keywords Bacopasides · Alzheimer's disease · hCMEC/d3 · 7KCh · Blood–brain barrier

1 Background and Purpose of Research

A. Significance of Research

Alzheimer's disease (AD), an irreversible, progressive brain disorder caused by neuroinflammation that leads to severe dementia. Currently, AD affects 82,000 people in Singapore and this number continues to rise with the increasing life expectancy. By 2030, this number is expected to hit 100,000. Furthermore, in Singapore, an estimated S$2.8 billion was spent in 2015 locally and is estimated to almost triple by 2030 [1, 2]. Current methods of treating AD using immunotherapy may result in intense adverse reactions within patients and this may hinder the treatment. Due to the rapidly increasing clinical and financial burden caused by AD, an effective approach to preventing and mitigating AD is of carinal significance to our society.

B. Background

Previous research has shown that 7-Ketocholesterol (7KCh), abundantly found in deep-fried and over-cooked food, is a highly oxidised cytotoxic cholesterol which induces cell apoptosis and inflammation in places such as the blood–brain-barrier (BBB) [3–5]. Hence, it can be concluded that the progression of AD can be induced by 7KCh.

C. Rationale for Research

Bacopa monnieri has been used in Indian Ayurvedic medicine to treat various mental illnesses such as anxiety, epilepsy, and insomnia. It is an Ayurvedic nootropic for poor cognition, and lack of concentration, and has been widely researched by scientists as a natural alternative to synthetic drugs [6, 7]. Bacopaside, a group of triterpene saponins isolated from Bacopa monnieri, has been well documented to possess anti-inflammatory, antioxidative, and Amyloid-β (Aβ) aggregation inhibition properties [8–11]. This study aims to determine the protective effect of Bacopaside I (BI) and Bacopaside II (BII), two members of Bacopaside chemicals, on 7KCh induced damage on the human cerebral microvascular endothelial cell (hCMEC/D3) to simulate the process in BBB in vitro for an effective medicinal approach to protect brain endothelial cells and hence prevent or treat AD caused by aggregation of 7KCh [12, 13]. This project would greatly contribute to the research of novel anti-Alzheimer drugs that are becoming increasingly relevant in the Singaporean society.

2 Hypothesis

We hypothesised that the presence of Bacopaside I and II will protect hCMEC/D3 cells from the harmful effects of 7KCh. The introduction of Bacopasides may result

in a higher survival rate of hCMEC/D3 cells and a reduction in inflammation sites among the cells.

3 Methodolody

A. Cell Culture

To simulate the BBB environment in vitro, the human cerebral microvascular endothelial cell line (hCMEC/D3) were cultured in EBM-2 medium (Applied Biological Materials Inc., Canada) and seeded onto flasks previously coated with collagen. They were maintained at 37 °C in 95% air and 5% CO_2 until confluence.

B. Preparation of Materials

hCMEC/D3 cell cultures were seeded on collagen-coated 6-well and 12-well culture plates at a concentration of 5×10^5 cells per millilitre. 7KCh (Cayman Chemical Company, USA) was dissolved in 5% ethanol, then mixed with EBM2-medium to form a 50 μM solution. Bacopasides, both Bacopaside I (BI) (Merck, USA) and Bacopaside II (BII) were dissolved in methanol to form a 1 mM solution, then mixed with EBM2-medium to form 0.1 μM, 1 μM and 10 μM solutions respectively. Cell culture medium (EBM-2), PBS solution, trypsin EDTA were all warmed up to 37 °C before treatment to the cell.

C. Treatment of Cells

Cells were pretreated with BI or BII for 1 h, followed by addition of 7KCh for 24 h. Nine different methods of treatment were applied to the cells: Control (EBM-2 culture medium), Vehicle Control (30 μM methanol), 7KCh (50 μM), 0.1 μM Bacopasides, 1 μM Bacopasides, 10 μM Bacopasides, 0.1 μM Bacopasides + 7KCh (50 μM), 1 μM Bacopasides + 7KCh (50 μM) and 10 μM Bacopasides + 7KCh (50 μM). [Bacopasides refer to either BI or BII].

D. Cell Viability Test

Cells were pretreated with BI or BII for 1 h, followed by addition of 7KCh for 24 h. Nine different methods of treatment were applied to the cells: Control (EBM-2 culture medium), Vehicle Control (30 μM methanol), 7KCh (50 μM), 0.1 μM Bacopasides, 1 μM Bacopasides, 10 μM Bacopasides, 0.1 μM Bacopasides + 7KCh (50 μM), 1 μM Bacopasides + 7KCh (50 μM) and 10 μM Bacopasides + 7KCh (50 μM). [Bacopasides refer to either BI or BII].

E. Quantitative Real Time Polymerase Chain Reaction

Total RNA extraction and sample purification were also carried out using the RNeasy Mini Kit (Qiagen, Germany) according to the manufacturer's protocol. The RNA samples were reverse transcribed using High-Capacity complementary DNA Transcription Kit (Applied Biosystems, USA) at 25 °C for 10 min, 37 °C for

120 min, then 85 °C for 5 min in the T-Personal Thermocycler (Biometra, Germany). The 7500 Real-time PCR System (Applied Biosystems, USA) were employed to carry out real-time PCR amplification using TaqMan Universal PCR Master Mix (Applied Biosystems, USA) and TaqMan Gene Expression Assay Probes for IL-1β (Hs01555410_ml), IL-6 (Hs00174131_ml) and β-Actin (Hs99999903_ml) (Applied Biosystems, USA). The PCR reaction conditions would be 95 °C for 10 min, followed by 40 cycles of 95 °C for 15 s and 60 °C for 1 min.

4 Results and Discussion

A. Cell Viability Test

From Fig. 1, the living cell count for vehicle group (treated with 10 μM methanol) (97.2%) did not vary greatly with the untreated cells (100%). Hence it can be deduced that methanol does not greatly affect the survival of endothelial cells.

From Fig. 1a, it can be seen that there is a higher percentage of alive cells when the cells are treated with 0.1 and 1.0 μM of BI (128.3% and 148.8% respectively) as compared to the control group (100%). This may be because BI triggers cell proliferation, resulting in a higher cell count.

However, when the cells are treated with 10 μM of BI (98.6%), the percentage of alive cells is slightly lower than that of cells from control group (100%). This may imply that an overly concentrated BI solution may lose its ability to cause cell proliferation, yet the mechanism of such overdose effect is still undetermined.

For cells treated with 50 μM 7KCh, around 50% cell death rate is observed compared to cells in the control group. This validates the theory that 7KCh induces cell death.

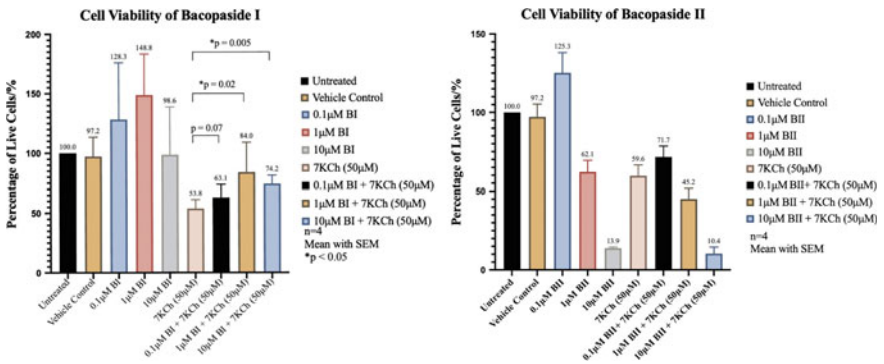

Fig. 1 **a** Graph of cell viability of hCMEC/D3 cells after treatment with BI and 7KCh (n = 4, Standard Error of Mean), **b** graph of cell viability of hCMEC/D3 cells after treatment with BII and 7KCh (n = 4, standard error of mean)

However when 7KCh is added to cells pretreated with 0.1 μM, 1 μM and 10 μM of BI, there is a 10% to 20% rescue (up to 63.1%, 84.0% and 74.2% respectively) as compared to sample where only 7KCh is treated to the cells (53.8%). At 0.1 μM concentration of BI (63.1%), the concentration of BI may not have been high enough to show significant protection against the effects of 7KCh, and shows a lower percentage of live cells as compared to at 1 μM concentration of BI (84.0%). However, at higher concentrations of 10 μM of BI, while some rescue was shown, the concentration of Bacopaside I may have been too high, resulting in a small amount of cell death. Regardless, both 1 μM and 1 μM of Bacopaside I + 7KCh treatment have shown a significantly higher percentage of live cells as compared to when only 7KCh is treated to the cells, showing that the protective effect of Bacopaside I on 7KCh induced damage is significant ($p < 0.05$).

One way ANOVA with Bonferroni post hoc correction test was carried out. As eta squared = 62.3, it means that 62.3% of the difference between the percentage of live cells was because of the treatment used on the cells. Hence, the treatment of the cells is affecting the percentage of live cells, not because of chance or any other factor. Furthermore, between 1 μM of BI + 7KCh and only 7KCh treatment and between 10 μM of BI + 7KCh and only 7KCh treatment, statistically, the p value is less than 0.05. Therefore, there is a less than 5% chance that the 2 groups belong to the same population, showing that it is statistically significant that 1 and 10 μM of BI have protective effects against 7KCh.

For Bacopaside II, Fig. 1b shows that the percentage of live cells of the 0.1 μM BII treated cells (125.3%) is slightly higher than that of the control group(100%). This shows that BII may also stimulate cell proliferation to some extent. However, as BII concentration increases up to 1 and 10 μM, cells (62.9%, 13.9%), the percentage of live cells were lower than that of the untreated cells (100%). It is also notable that the percentage of live cells of the 1 μM BII treated cells (62.9%) is higher than that of 10 μM BII treated cells (13.9%). A possible reason for this is an overdose of BII, leading to increased cell death due to higher concentration of BII, mechanism of overdose remains unclear.

When 7KCh is treated on the cells, the 0.1 μM BII + 7KCh treated cells (71.7%) had a higher percentage of live cells as compared to the 7KCh treated cells (59.6%). However, based on the one way ANOVA post hoc correction test, the rescue of the cells was not significant, it could be due to other factors or by chance. The percentage of live cells for 1 μM BII + 7KCh treated cells and 10 μM BII + 7KCh (45.2, 10.4%) treated cells showed to be lower than that of the 7KCh treated cells (59.6%). The percentage of live cells of the 1 μM BII + 7KCh treated cells (45.2%) is higher than that of 10 μM BII + 7KCh treated cells (10.4%). These trends are similar to that of only BII treated cells. Therefore, similarly, a reason for these trends could be an overdose of BII, leading to increased cell death as higher concentrations of BII. Again, mechanism of overdose is unclear. It can also be concluded that BII has little to none protective effect on 7KCh induced damage on hCMEC/D3 cells. However, it may also be possible that BII will show protective effect on the cells at a concentration lower than 0.1 μM.

Comparing Bacopaside I and II, it is evident that BI has a greater potential of being an effective medicinal approach to treat AD since it has shown better rescue of the hCMEC/D3 cells. Hence, qRT-PCR was conducted with cells that were treated with 1.0 μM of BI as it had continually shown the best rescue of cells among all 3 concentrations.

B. Quantitative Real-time PCR

The delta delta CT method was used to analyse the data from the 7500 Real Time PCR System (Applied Biosystems, USA) using β-Actin as the housekeeping gene. IL-6 is an endogenous chemical that is active during inflammation and is produced in wherever part of the body which has inflammation. It produces inflammatory effects by inducing the transcription of factors in multiple pathways of inflammation [14]. Hence when the expression levels of IL-6 increases, inflammation increases. TNF-α plays a pivotal role in orchestrating the production of a pro-inflammatory cascade and is rapidly released after trauma, infection, or exposure to bacterial-derived LPS [15]. Thus, the expression of TNF-α can show inflammation as it stimulates an inflammatory response.

Figure 2 shows that IL-6 mRNA levels for 7KCh treated cells (8.4-fold) were higher as compared to untreated cells (1.0-fold) while TNF-α mRNA levels for 7KCh treated cells (3.3-fold) were also higher compared to untreated cells (1.0-fold). This further proves that 7KCh induces inflammation as it increases the expression levels of pro-inflammatory genes IL-6 and TNF-α.

Figure 2 shows that Bacopaside I has a significant protective effect against inflammation caused by 7KCh. IL-6 mRNA levels for 1uM Bacopaside I + 7KCh treated cells (2.4-fold) were lower as compared to that of 7KCh treated cells (8.4-fold),

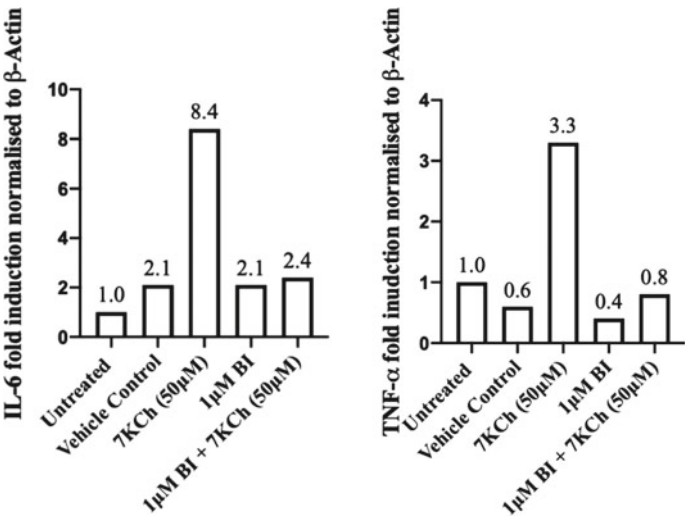

Fig. 2 Expression levels of IL-6 and TNF-α for 7KCh and BI

which is a 75% decrease in the expression of the IL-6 pro-inflammatory gene. TNF-α mRNA levels for 1uM Bacopaside I + 7KCh treated cells (0.8-fold) were also lower as compared to that of the cells that were only treated with 7KCh (3.3-fold). That shows a decrease in TNF-α expression levels by 76%.

These data corroborates with the cell viability data, where cells treated with 1uM Bacopaside I managed to revive the cells that were then treated with 7KC by 44%. As inflammation leads to cell necrosis, the decrease in expression levels of pro-inflammatory genes, IL-6 and TNF-α, shows that the reduced inflammation has helped to rescue cells.

5 Conclusion

From our results, it can be concluded that Bacopaside I has very significant protective effect against 7KCh induced damage to brain endothelial cells while such effect is absent in Bacopaside II. High fat diet causes unhealthy cholesterols such as 7KCh to aggregate in our body. This will induce inflammation and damage the integrity of the blood–brain barrier, allowing toxins entering the brain. Consumption of a small amount of Bacopaside I may reduce inflammation caused by 7KCh in the BBB, leading to a lower risk of development of AD.

5.1 Future Works

qRT PCR should be repeated a few more times so as to ensure reliability of data. In our results, high dosages, of Bacopaside I may not be very protective and it may even be harmful to the endothelial cells. Hence it is important to determine the optimal concentration of BI treatment for the endothelial cells for a targeted and effective clinical usage. Only in vitro experiments were conducted by model the blood–brain barrier with hCMDE/d3 cell line. This model may not be so accurate compared to the actual blood–brain barrier. Extensive in vivo clinical trials on mice or human subjects is still required for the development of anti-Alzheimer drug using Bacopasides.

References

1. Tay, R. (2019, April 30). 82,000 people in Singapore today have dementia—and 3 in 4 feel ashamed and rejected because of the illness. Retrieved from https://www.businessinsider.sg/82000-people-in-singapore-today-have-dementia-and-3-in-4-report-feeling-ashamed-and-rejected/.
2. Alzheimer's Disease Association. Dementia in Singapore. Retrieved from https://alz.org.sg/dementia/singapore/.

3. Anderson, A., Campo, A., Fulton, E., Corwin, A., Jerome, W.G. III, O'Connor, M.S. (2019, September 27). 7-Ketocholesterol in disease and aging. Retrieved from https://www.sciencedirect.com/science/article/pii/S2213231719311759.
4. Gamba, P., Testa, G., Gargiulo, S., Staurenghi, E., Poli, G., Leonarduzzi, G., (2015, June 19). Oxidised cholesterol as the driving force behind the development of Alzhemier's disease. Retrieved from https://www.frontiersin.org/articles/10.3389/fnagi.2015.00119/full.
5. Huang, Jiahn-Dar & Amaral, Juan & Lee, Jung Wha & Rodriguez, Ignacio. (2014). 7-Ketocholesterol-Induced Inflammation Signals Mostly through the TLR4 Receptor Both In Vitro and In Vivo. Retrieved from https://www.researchgate.net/publication/264053513_7-Ketocholesterol-Induced_Inflammation_Signals_Mostly_through_the_TLR4_Receptor_Both_In_Vitro_and_In_Vivo.
6. Nemetchek, M. D., Stierle, A. A., Stierle, D. B., & Lurie, D. I. (2017). The Ayurvedic plant Bacopa monnieri inhibits inflammatory pathways in the brain. Retrieved from https://www.ncbi.nlm.nih.gov/pmc/articles/PMC5269610/.
7. Abdul Manap, A. S., Vijayabalan, S., Madhavan, P., Chia, Y. Y., Arya, A., Wong, E. H., Koshy, S. (2019, July 31). Bacopa monnieri, a Neuroprotective Lead in Alzheimer Disease: A Review on Its Properties, Mechanisms of Action, and Preclinical and Clinical Studies. Retrieved from https://www.ncbi.nlm.nih.gov/pmc/articles/PMC6669844/.
8. Liu, X., Liu, F., Yue, R., Li, Y., Zhang, J., Wang, S., Zhan, S., Wang, R., Shan, L., Zhang, W. The antidepressant-like effect of bacopaside I: Possible involvement of the oxidative stress system and the noradrenergic system. Pharmacol Biochem Behav. 2013. Retrieved from https://www.ncbi.nlm.nih.gov/pubmed/23872136.
9. Liu, X., Yue, R., Zhang, J., Shan, L., Wang, R., Zhang, W. Neuroprotective effects of bacopaside I in ischemic brain injury. Restor Neurol Neurosci. 2013. Retrieved from https://www.ncbi.nlm.nih.gov/pubmed/23160060.
10. Li, Y., Yuan, X., Shen, Y., Zhao, J., Yue, R., Liu, F., He, W., Wang, R., Shan, L., Zhang, W. (2016, Jan 20). Bacopaside I ameliorates cognitive impairments in APP/PS1 mice via immune-mediated clearance of β-amyloid. Retrieved from https://www.ncbi.nlm.nih.gov/pmc/articles/PMC4833143/#R16.
11. Rauf, Khalid & Subhan, Fazal & AM, Al-Othman & I, Khan & Zarrelli, Armando & MR, Shah. (2012). Preclinical Profile of Bacopasides From Bacopa monnieri (BM) As An Emerging Class of Therapeutics for Management of Chronic Pains. Current Medicinal Chemistry. 20. Retrieved from https://www.researchgate.net/publication/233842854_Preclinical_Profile_of_Bacopasides_From_Bacopa_monnieri_BM_As_An_Emerging_Class_of_Therapeutics_for_Management_of_Chronic_Pains.
12. Lopez-Ramirez, M. A., Male, D. K., Wang, C., Sharrack, B., Wu, D., & Romero, I. A. (2013). Cytokine-induced changes in the gene expression profile of a human cerebral microvascular endothelial cell-line, hCMEC/D3. Fluids and barriers of the CNS, 10(1), 27. Retrieved from https://www.ncbi.nlm.nih.gov/pmc/articles/PMC3849656/.
13. Biemans, E. A. L. M., Jäkel, L., de Waal, R. M. W., Kuiperij, H. B., & Verbeek, M. M. (2017, July). Limitations of the hCMEC/D3 cell line as a model for Aβ clearance by the human blood-brain barrier. Retrieved from https://www.ncbi.nlm.nih.gov/pmc/articles/PMC5484315/.
14. Cojocaru, I.M., Cojocaru, M., Miu, G., Sapira, V. (2011). Study of interleukin-6 production in Alzheimer's disease. Retrieved from https://www.ncbi.nlm.nih.gov/pubmed/22026253il6.
15. Parameswaran, N., Patial, S. (2010). Tumor Necrosis Factor-α Signaling in Macrophages. Retrieved from https://www.ncbi.nlm.nih.gov/pmc/articles/PMC5436834/tnfa.

Using Sorbents for Subsurface Oil Spill Cleanups Study in Saline and Fresh Water Using Optical Techniques

Lucas Tan, Pavan Singh, and Srivathsan Ram

Abstract Crude oil spills in freshwater are more frequent and potent than oil spills in the sea due to the formation of emulsions, affecting marine life below the surface. Yet little research has been conducted in this area investigating the stark differences between oil spills in seawater and freshwater. This project pioneers the first steps aiming to demonstrate the danger of crude oil spills in freshwater conditions and provide a viable solution to clean up the spills. Precision Ellipsometry is an optical analysis technique that can detect the binding of molecules to a substrate, this will be used to investigate the adsorption of oil to various sorbents. Sorbents tested included Bovine Serum Albumin (BSA), hydrophobic surfaces and Glutaraldehyde. The salinity of the water was also varied to emulate fresh and salty water conditions to investigate the differences in the emulsification of oil. From the results, all the sorbents exhibited binding with crude oil in freshwater conditions. From data of a colorimeter, it was observed that crude oil emulsifies throughout the freshwater, giving it ample time to penetrate to subsurface marine life, demonstrating its hazardous effects to the environment. BSA showed a strong affinity for binding to oil and hence inexpensive proteins similar in structure to BSA can be utilised to effectively adsorb the subsurface oil emulsions. Hence it is evident that oil spills in freshwater is indeed potent to marine life below the surface and sorbents such as proteins can be developed to adsorb the oil.

Keywords Oil spills · Sorbents · Subsurface contamination · Optical techniques · Precision ellipsometry · Colorimetry · Freshwater oil spills

L. Tan (✉) · P. Singh · S. Ram
School of Math and Science, NUS High School of Math and Science, Garden City, Singapore
e-mail: h1710131@nushigh.edu.sg

P. Singh
e-mail: h1710109@nushigh.edu.sg

S. Ram
e-mail: h1710128@nushigh.edu.sg

H. Guo et al. (eds.), *IRC-SET 2020*,
https://doi.org/10.1007/978-981-15-9472-4_43

1 Introduction

Several million tonnes of crude oil must be transported across the ocean every year. Oil spills occur due to accidents, natural disasters or terrorism. In July 1979, two super tankers, Atlantic Empress and Aegean Captain collided during a tropical storm. More than 88.3 million tons of crude oil was spilled into the ocean which devastated the marine wildlife present and it contaminated precious water resources with oil. Cleaning up oil spills can be a very challenging task as it is extremely difficult to separate the large amounts of oil from the water. Oil spills can cause the death of marine life such as fish due to asphyxiation. Many avian species die due to the oil sticking to their down feathers incapacitating their ability to insulate the birds against extreme temperatures. Several other marine species are killed during oil spills and during invasive clean-ups. This results in a detrimental imbalance in the ecosystem which results in the irreversible destruction of several habitats for the marine organisms. This can even result in contamination of fish and the oil spills near coasts and shorelines could affect the human population directly in addition to the indirect effects of the traditional oil spills. Another breed of oil spills that is less heard of but more dangerous is oil spills in freshwater. An example would be the Kalamazoo oil spill in which 1 million gallons of oil were discharged. The clean-up took 5 years and around 30–50 households were evacuated while the water quality of nearly double that number of households was compromised.

2 Methods of Cleaning Up Oil Spills

A. *Burning*

Burning the oil results in severe pollution due to the release of carbon monoxide during incomplete combustion. This can result in the deaths of several avian species and can contribute to global warming too.

B. *Oil Booms and Skimmers*

Using oil booms and skimmers for preliminary clean-ups to contain the oil spill before further action is taken to clean up the oil spills. This method is usually ineffective and does not work well in turbulent sea conditions or for an oil spill that is too large.

C. *Emulsifiers*

Emulsifiers result in the emulsification of oil causing the oil to form an emulsion which usually is suspended in the seawater for prolonged periods resulting in greater rates of fish contamination.

D. *Sorbents*

Table 1 Comparison of methods

	Methods			
	Burning	Containment	Emulsifiers	Sorbents
Does it prevent harm to marine life?	✗	✓	✗	✓
Is it environmentaly safe/feasible?	✗	✓	✓	✓
Does it remove the oil from the water?	✓	✗	✗	✓
Can the oil be recovered?	✗	With the help of skimmers	✗	✓
Speed of method	Very fast	Very slow	Slow	Medium

a. Speed of methods are taken to be relative to each other

Sorbents are currently being developed for cleaning up oil spills. They work by binding to the oil using intermolecular forces of attraction. The oil and sorbent then sink passively to the bottom of the sea and cause little or no harm to marine life.

E. *Comparison of Different oil Recovery Methods*

See Table 1.

3 Analysis of Sorbents

Hence from these methods, we can gather that the option that offers the most reasonable trade-offs is the use of sorbents. Sorbent technology is currently being developed as the current sorbents are extremely expensive and cheaper alternatives are being researched.

Oil is an organic molecule; hence it will be attracted to other organic molecules with similar intermolecular forces (IMF). To determine the type of intermolecular forces, we must look at the polarity of the oil molecule. Oil molecules used in cooking are made up of triglycerides. There is a glycerol part of the molecule connected to three fatty acid molecules. There are carboxyl groups present and the structure is asymmetrical. The structure of a castor oil molecule is shown below (Fig. 1):

The carboxyl groups are polar and there are hydroxyl groups present as well. Since the molecule is asymmetrical, the dipole moments are not cancelled out. The hydroxyl groups allow hydrogen bonding to take place as well. However, most of the oil molecule is made up of non—polar hydrocarbon chains and it makes up a more significant part of the molecule. Therefore, the more dominant intermolecular force is London dispersion forces (LDF), due to its large molecular mass.

Therefore, we can see that sorbents with non-polar groups will make for better sorbents.

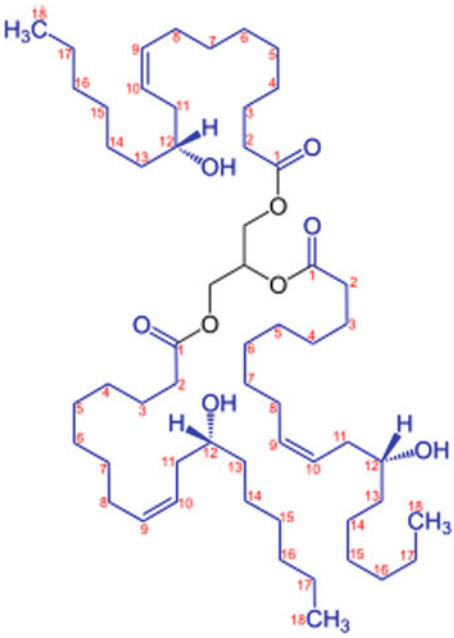

Fig. 1 Crude oil molecule structure

4 Materials

A. *Light Oil*

Light crude oil was obtained from Malaysia and diluted in a 1:1 ratio with water.

B. *Units*

Several active layers were made on silicon surface to catch crude oil. A variety of sorbents were experimented to test their effectiveness in freshwater conditions.

- Aminosilane binds very well to the SiO_2 substrate as a Si–O–Si covalent bond can be formed. Hence, when PSS binds to Aminosilane that is bound to the substrate, it allows BSA to attach to the substrate so it can be tested.
- Bovine Serum Albumin (BSA) is a globular protein that we used for testing throughout our experiment as it is used as a protein concentration standard in lab experiments, and it is very stable. It is made up of amino acids, some of which are non-polar. This will cause there to be London Dispersion interactions with the oil and the protein can "wrap" around the oil molecules [5].
- Polystyrene Sulfonate (PSS) is widely used as ion-exchange resins to remove ions such as Potassium, Calcium and Sodium from solutions. We did do an experiment testing how well BSA binded to any foreign substances from the crude oil that dissolved in the water below it, to test for the presence of any ions but the results showed there were not many ions present. Another crucial feature of PSS us the

fact that it is a linker layer that allows BSA to bind to aminosilane that is bound to the substrate.

- Glutaraldehyde is a commercial disinfectant, medication, preservative, and fixative. It is an organic molecule with 2 aldehyde groups at its ends. Glutaraldehyde contains two aldehyde groups: one of them attaches to amino-silane the other is exposed and can react with compounds from oil, e.g. mercaptanes. While the aldehyde groups are polar, since they are on opposite ends, the polarity largely cancels out in the horizontal direction. There is however a net dipole moment due to its 3d structure. However, it is still able to exhibit London Dispersion Interactions with non-polar molecules due to its carbon chain. It is a possible candidate for a sorbent due to its stability and ability to attract non-polar oil molecules.
- Polyethylenimine is a polymer with repeating unit composed of the amine group and two carbon aliphatic CH_2CH_2 spacer. It has multiple nitrogen groups sticking out of the molecule, hence allowing it to exhibit hydrogen bonding. Polyethylenimine can be used to detect for the presence of ions such as fluorine, chlorine and nitrogen. While it is unlikely that Polyethylenimine binds to oil due to its lack of London dispersion interactions, it is used as a negative control to ensure that the substance binding to the sorbents is oil and not ions sticking onto them instead.
- Phenylsilane, also known as Silylbenzene, is a colorless liquid, and is one of the simplest organosilanes with the formula $C_6H_5SiH_2$. It is a hydrophobic molecule; hence it exhibits London dispersion force with other hydrophobic molecules. Phenylsilane is a possible sorbent due to its high affinity to the hydrophobic oil molecules as well its stability which is evident in its uses in cross linkages between proteins.
- Hydrogen terminated silicon (Si–H) is a chemically passivated silicon substrate whose silicon atoms are covalently bonded to hydrogen. This surface was obtained by immersing silicon into solution of HF for 20 s. Si–H is also hydrophobic surface and is a possible candidate for a sorbent due to its high stability and ability to exhibit London dispersion interactions with non-polar, hydrophobic oil molecules.

5 Equipment and Methods

The equipment used include primarily the Precision Ellipsometer [6, 7] and the Colorimeter. The Precision Ellipsometer was used to determine the degree of binding of the crude oil to the different substrate [10, 11]. The Colorimeter was used to determine for how long oil emulsions persisted in waters of varying salinities. This is done to evaluate how much subsurface contamination occurs in freshwater as compared to saline water.

A. *Precision Ellipsometer*

To observe the binding of Bovine Serum Album (BSA), Glutaraldehyde, hydrogen terminated silicon (Si–H) and phenylsilane to the crude oil in the water, Precision Ellipsometry (PREL) was employed (see Appendix A). It is chosen for its ability

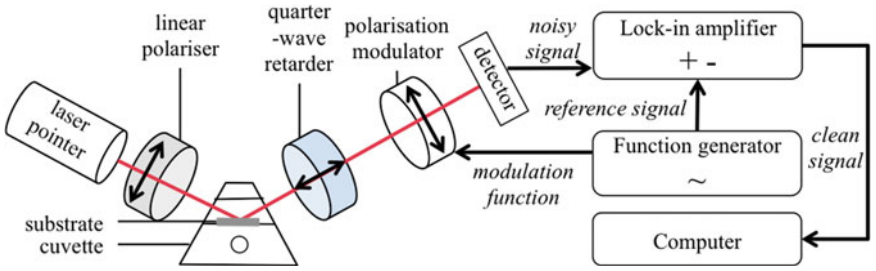

Fig. 2 Electro-optical set-up of liquid-phase precision ellipsometry

to monitor chemical reactions in real time and sensitive measurements capable of detecting molecular layers just a few nanometres thick [1, 9]. PREL is very portable and can be used on-site when testing chemicals far out in natural environments where certain conditions are needed to be met, at a small footprint of less than an A4-sized page (Fig. 2).

In the precision ellipsometry system, a 650 nm laser is utilized. The beam passes through a polarizer at 45º anticlockwise from the y-axis. This causes the initially unpolarized light (Fig. 3a) beam to be linearly polarized (Fig. 3b). The polarized light then enters the cuvette perpendicularly and reflects off the substrate with incident and reflection angles of 45°. This reflection at 45º causes the s component of the light to rotate 180º. After reflection, the reflected beam is elliptically polarized due to the phase shift in the s and p components (Figs. 3c and 4).

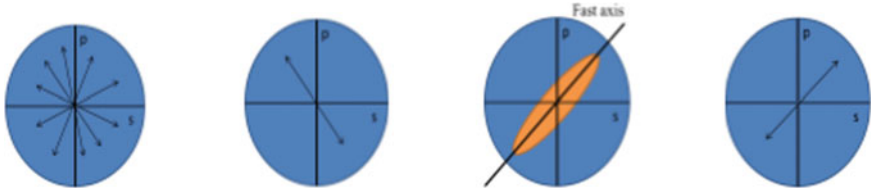

Fig. 3 Figures 3a (left) through 3d (right) depicting polarization of the laser light

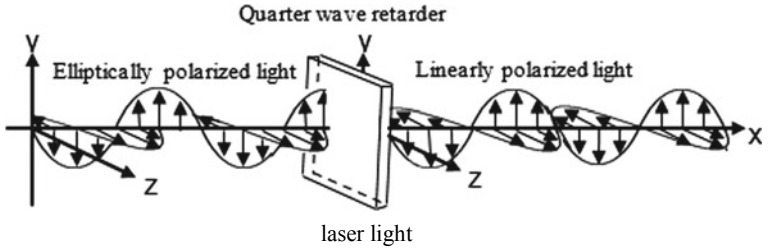

Fig. 4 Quarter wave retarder adjusting elliptically polarised light

6 Colorimeter

The question at issue is are crude oil spills in freshwater more detrimental than spills in salt/seawater. To investigate this, it was noted that mixing of oil with water creates an emulsion, hence an analysis of the segregation of oil and water can be conducted to test if the oil emulsifies throughout the water which would indicate that it is detrimental to sea life below the surface. To analyse the rate of segregation, an optical setup was assembled as shown in Fig. 5 (See Appendix B).

Oil was mixed with water in different ways. Homogeneous mixing occurs when the oil is mixed only on the water–oil boundary, for example in waves. This was imitated by shaking a bottle containing oil and water. Heterogeneous mixing occurs when oil is mixed with water in presence of solid bodies, for example on rocks or stones of coast line. This was imitated by mixing with rotating wire in the bottle. Both fresh and salty water were used for this experiment. Within seconds after the mixing, 2 mL of the emulsion was placed into an optical cuvette and inserted into transmission measurement setup (Fig. 6).

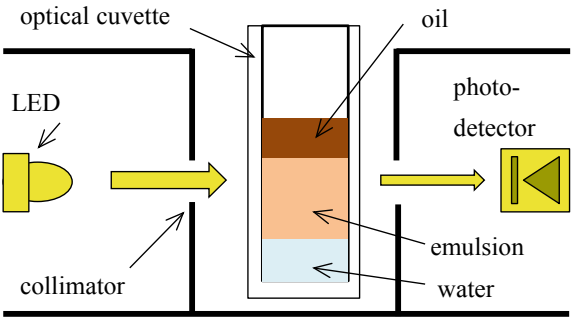

Fig. 5 Schematic of optical setup for light transmission measurements, light emitting diode (LED) shines the light through optical cuvette and transmitted light is measured by photo-detector

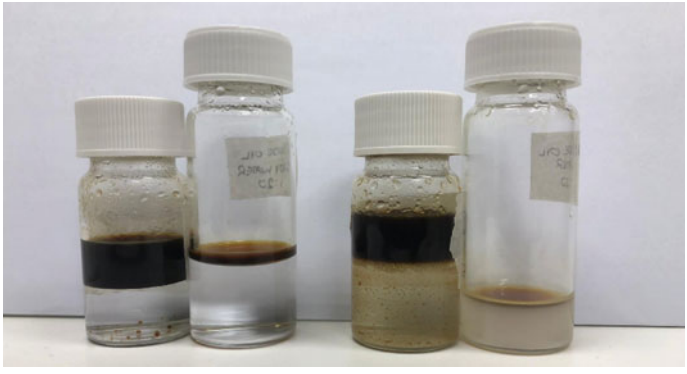

Fig. 6 Photos of oil water emulsions in saline (left) and fresh water (right)

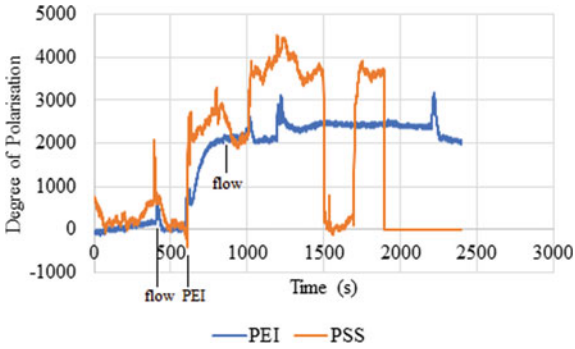

Fig. 7 Binding of crude oil on PEI and PSS—negative control

7 Results

See Figs. 7, 8, 9 and 10.

8 Discussion

A. *Negative Control*

From Fig. 7, it can be seen that there is no attachment of any substances on Polyethylenimine and polystyrene sulfonate. Hence it serves as a negative control to show that there is no other soluble compound in crude oil which could possibly have attached to the sorbents, and thus any attached substance on the sorbents is definitely crude oil.

B. *Effectiveness of BSA and Glutaraldehyde*

From Fig. 8, it can be inferred that both BSA and Glutaraldehyde had successful attachments to oil even after washing. BSA is a protein that binds to a large variety of substances, it is not surprising that it can bind to crude oil as well. BSA is made up of many smaller amino acids of which some are hydrophobic which is characteristic of a protein. Hence these hydrophobic groups had London dispersion interactions with the crude oil, allowing BSA to bind to crude oil. Furthermore, the London dispersion interactions between the 2 molecules was very extensive as both oil and BSA have a large mass and contain many hydrophobic components. Glutaraldehyde also had a successful attachment due to binding of aldehyde with inclusions of nitrogen, or phosphorus, or sulfur atoms in carbon chain. While glutaraldehyde may not be as hydrophobic as BSA, it's carbon skeleton likely provided a place for London dispersion forces to form between it and the crude oil, hence allowing crude oil to stick to glutaraldehyde. From these results it can be concluded that proteins and organic molecules (with a long carbon backbone) are able to be effective sorbents underwater.

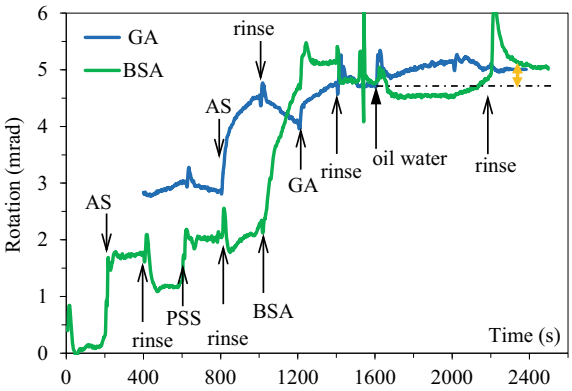

Fig. 8 Attachment of contaminants from oil water on sorbent layers consisting of amino-silane (AS), poly-styrene-sulfonate (PSS) and bovine serum albumin (BSA) green curve, and amino-silane (AS) and glutaraldehyde (GA) blue curve. Orange arrow shows increment around 0.5 mrad due to contaminants in the oil water

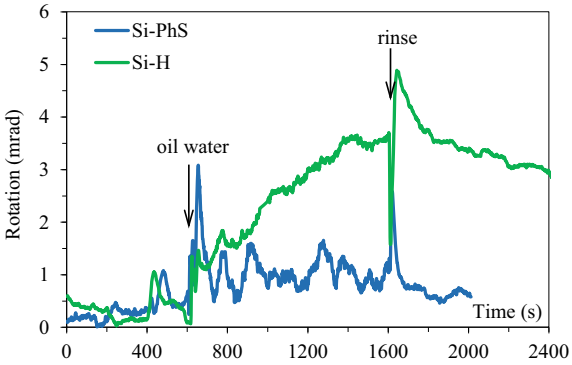

Fig. 9 Attachment of contaminants from oil water to hydrophobic surfaces of silicon covered with phenylsilane (Si–PhS) and hydrogen terminated silicon (Si–H)

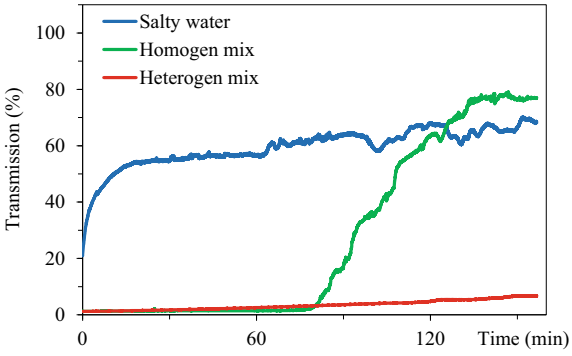

Fig. 10 Change in transmission of oil-water emulsion mixed in different was: homogeneous mixing in fresh water, heterogeneous mixing in fresh water and heterogeneous mixing in saline water

C. *Effectiveness of hydrophobic surfaces*

For the experiment conducted for Fig. 8, instead of using a new substrate and adding chemicals/substances to bind onto it to test it, we used a substrate that was left in

phenylsilane to make it hydrophobic. As the oil is also non-polar (hydrophobic), they interact well together and bind to each other, as can be easily seen by comparing the point of the graphs at 500 s and at 2000 s.

The hydrogen terminated silicon surface graph (in green) had a very large increase, showing a lot of attachment of chemicals from the water below the oil to it, but the phenylsilane-coated substrate only had a slight increase between 500 and 2000s. This is a much more efficient and quick way of testing, as not much needs to be done to conduct the experiment. It supported our hypothesis that the oil would bind to a non-polar hydrophobic substance due to the dominant London Dispersion Forces acting on them, and it also confirms our main hypothesis, showing the presence of small emulsified oil in the water below the main layer of oil.

D. *Emulsification of crude oil in waters of different salinities*

From Fig. 10 of the colorimeter, it can be seen that transmission of light recorded for salty water increases very quickly, so the mixture segregates during several minutes. It can be concluded that emulsion in fresh water is more stable: after homogeneous mixing, it segregated in around two hours. Heterogeneous mixing creates (most likely) smaller oil droplets and the emulsion is stable even during several days. Thus it shows that oil emulsifies and permeates through freshwater, likely seeping down to marine life deep under the surface. Whereas for oil in salty water, it quickly segregates at the top, affecting only sea birds and fishes coming up to breathe.

E. *Applications*

In Singaporean context, we can utilise soybean derived proteins as sorbents. With more advanced sorbents, we can utilise a spinning drum to allow the oil to be harvested and purified for later use. The drum will be coated with a protein-based sorbent which adhere to the drum, to the oil but not to water. Hence by having the drum submerged in the water, we can create more efficient skimmers for secondary clean-ups after majority of the oil has been cleared up (Fig. 11).

9 Conclusion

This study has shown that oil spills in freshwater are much more threatening to marine life than that of oil spills in seawater. The crude oil permeates through the surface into deep waters in a freshwater environment, which results in the poisoning of fishes underneath the surface. These results can be concluded from the colorimeter data where the emulsification of oil in pure water remained there for days, however, when oil was mixed with salty water, the oil–water mixture quickly separated into their distinct layers where the oil remained at the surface which would not harm marine life. Furthermore, commercial sorbents mainly target adsorption of oil at the surface and are ineffective at adsorbing oil under the surface, we propose using natural proteins instead to adsorb oil beneath the surface of the water. Our results showed

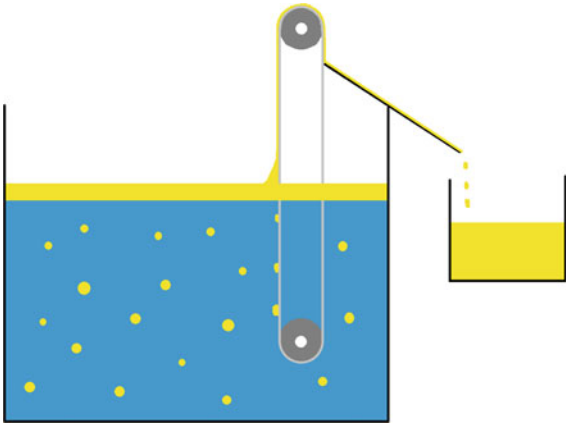

Fig. 11 Schematic of a proposed skimmer which could aid in subsurface oil recovery

significant binding of Bovine Serum Albumin (BSA—a protein) with crude oil and its harmful soluble components. Proteins such as BSA or other natural proteins can be quickly sprinkled on the water in the event of an oil spill and will readily adsorb the crude oil, 'pulling' the oil-protein compound to the seabed where it poses no threat to marine life. By doing so, the threats the oil poses to marine life are quickly neutralised resulting in more effective oil-spill clean-ups.

Acknowledgements We would like to express our deepest gratitude to Dr. Nikolai Yakovlev who has assisted us greatly in all aspects of the planning and execution of this project. We would also like to thank all students working under his lab for their support and assistance, especially Joshua for taking the time to help us complete some of the experiments in this report.

Appendix

A. *Precision ellipsometer "PREL17QdetG"*

The Precision Ellipsometer PREL17QdetG was assembled by research mentor Dr. Nikolai Yakovlev and parts were sourced from Thorlabs, Inc.

Wave length used 650 nm, incidence angle 60 deg, substrate silicon with n = 3.8; frequency of polarisation modulation 288 Hz; digitiser is Arduino Uno, and recording with 1 data point per second.

B. *Colorimeter "CLM3"*

The Colorimeter apparatus CLM3 was assembled by research mentor Dr. Nikolai Yakovlev and parts were sourced from Thorlabs, Inc.

Wave length used are 520 nm for green, 580 nm for yellow, 650 nm for red, and the intensity shown on the graph is the sum of intensities of all three colours; optical

path through the liquid 1 cm; digitiser is Arduino Uno, recording with 1 data point per second.

References

1. H. Arwin, Thin Solid Films, 519, 2589 (2011).
2. H. Tan, S. Huang, and K. Yang, *Langmuir 2007*, 23, 8607–8613 "Transferring Complementary Target DNA from Aqueous Solutions onto Solid Surfaces by Using Affinity Microcontact Printing".
3. T. Berlind, M.Poksinski, O.Tengvall, H.Arwin, *Colloids and Surfaces B: Biointerfaces*, 75, 410 (2010). "Formation and cross-linking of fibrinogen layers monitored with in situ spectroscopic ellipsometry".
4. Kim, J., Seidler, P., Wan, L. S., & Fill, C. (2009). *Journal of colloid and interface science*, *329*(1), 114–9. "Formation, structure, and reactivity of amino terminated organic films on silicon substrates".
5. T. M. Byrne, S. Trussler, M.A. McArthur L.B. Lohstreter, Zhijun Bai, M.J. Filiaggi, J.R. Dahn, *Surface Science 603*, 2888–2895 (2009).
6. Azzam, R. M. A. Oscillating-analyzer ellipsometer. *Review of Scientific Instrument*. 47(5), 624-628 (1976)..
7. J.A. Woollam Co., Inc. A Short Course in Ellipsometry. 2.
8. CH Instruments, Inc. Model 400A Time-Resolved Electrochemical Quartz Crystal Microbalance. http://chinstruments.com/chi400.html accessed Dec 27, 2009 (2009)
9. Lawrence, C. R., Martin, A. S., Sambles, J. R. Surface plasmon polariton studies of highly absorbing Langmuir- Blodgett films. *Thin Solid Film.* 208 (1992) 269-273
10. Vörös J., Textor M. Optical Waveguide Lightmode Spectroscopy (OWLS) Evanescent Field Detection of Surface Processes on Transparent, Metal-Osxide-Type of Surfaces. http://www.surface.mat.ethz.ch/research/biointerfaces/instrumental_developments/optical_waveguide accessed Dec 27, 2009 (2005)
11. Swann, M.J., Freeman, N.J., Cross, G.H. Dual Polarization Interferometry: A Real-Time Optical Technique for Measuring (Bio) Molecular Orientation, Structure and Function at the Solid/Liquid Interface. *Handbook of Biosensors and Biochips*, 2 (2007) 549–568.

Investigation on the Effects of Different Concentrations of Nitrogen on the Growth of Ocimum Basilicum

Nallapuraju Ananya

Abstract For such an economically important plant, the basil plants need to be grown quickly and efficiently. To accomplish this, farmers add fertilisers to the soil in which the basil plants are grown in. A primary component of these fertilisers is nitrogen. The aim of this experiment was to find out how different concentrations of nitrogen in the soil affect the plant's growth, measured through the change in the height of the plant, number of leaves on the plant and colour of its leaves.

Keywords Ocimum basilicum · Plants · Basil · Leaves · Nitrogen · Fertiliser

1 Introduction

A. *Ocimum Basilicum*

Among the various species of basil, sweet basil (*Ocimum Basilicum)* is the most economically important, and it is grown and used around the world. Basil has been used in folk medicine, as an insecticide and as a remedy for snake, scorpion and insect bites. Furthermore, the basil plant's leaves are used frequently in the food and spice industries. The essential oil of the basil plant is also used in food industries, perfumery, dental and oral products and in traditional rituals and medicines.

For such an economically important plant, the basil plants need to be grown quickly and efficiently. To accomplish this, farmers add fertilisers to the soil in which the basil plants are grown in. A primary component of these fertilisers is nitrogen.

B. *Nitrogen*

Nitrogen plays a significant role in plant growth as it is part of the chlorophyll molecule, the compound plants require to undergo photosynthesis, and which gives plants their green colour [1].

N. Ananya (✉)
NUS High School of Mathematics and Science, 20 Clementi Avenue 1, Singapore 129957, Singapore
e-mail: h1810111@nushigh.edu.sg

H. Guo et al. (eds.), *IRC-SET 2020*,
https://doi.org/10.1007/978-981-15-9472-4_44

Nitrogen is also a major component of amino acids, the building blocks of proteins that act as structural units in plant cells while others act as enzymes. Nitrogen is also a component of energy-transfer compounds such as adenosine triphosphate (ATP), which allows cells to conserve and utilise energy released during metabolism. In addition, nitrogen is a key component of nucleic acids such as deoxyribonucleic acid (DNA) which allows cells to grow and reproduce.

A lack of nitrogen appears as general yellowing of the plant. On the other hand, too much nitrogen may damage plants and cause leaf burn. Leaf burn is caused by dehydration of the roots or crown due to the high concentrations of nitrogen that cause the foliage to turn brown or yellow [2].

Plants that receive too much nitrogen might produce a lot of new leafy growth. However, this new growth is often feeble and sappy, attracting various pests and making the plant unable to survive the stress of drought. Furthermore, aromatic plants such as basil lose much of their fragrance.

Nitrogen in the soil is often absorbed by the plants' roots in the form of nitrate salts and healthy plants often contain 3–4% nitrogen in their above ground tissues. However, nitrate is easily drained from the soil by heavy rain, resulting in soil acidification. Thus, fertilisers containing nitrogen need to be applied to the soil.

2 Aim and Hypothesis

The aim of this experiment was to find out how different concentrations of nitrogen in the soil affect the plant's growth, measured through the change in the height of the plant, number of leaves on the plant and colour of its leaves. It was hypothesized that a higher concentration of nitrogen in the soil increases the growth of the plant i.e. change in the height of the plant, number of leaves on the plant and the colour of the plant.

3 Literature Review

According to the New South Wales Government Department of Primary Industries website, Agricultural sector, nitrogen is a key element in plant growth and is found in many plant proteins, hormones and chlorophyll. According to the Oxford Academic Journal of Experimental Botany, there was a study conducted by I.G. Burns [4] in which the nitrogen supply was not steady. It was conducted to find out how the relative growth rate was affected by the nitrogen concentration. Another similar study was conducted after that to find out about the response of plants to nitrogen supply [3]. Hydroponic experiments were carried out with young lettuce plants (*Lactuca sativa* L.) to compare responses to an interruption in external nitrogen supply. In this experiment, they interrupted the external nitrogen supply to find out how the relative growth rate of the plant affects the amount of nitrogen given to it. However, for this

investigation, hydroponic is not a suitable method for the basil seedlings as too much exposure to water may cause the roots of the basil seedlings to rot.

4 Materials

1. Small flower pots—25
2. Basil Seeds—75
3. Anhydrous calcium nitrate— ~ 60 g
4. D.I. water
5. Garden Soil— ~ 5 kg
6. Electronic analytical mass balance—1
7. Spray bottle/mister—6
8. 1 L measuring cylinder—1
9. 500 mL beakers—6
10. 1 L white plastic bottles—6
11. Spatula—5
12. Ruler—1

5 Methodology

A. *Phase 1: Preparing the nitrate solutions*

Measure out 0.9448 g of hydrated calcium nitrate using a weighing boat and an electronic mass balance. Pour these nitrate crystals into a beaker. Measure out 1000 mL of DI water using a 1 L measuring cylinder. Pour the DI water into the beaker containing the nitrate crystals. Stir the solution using a spatula to produce a 8.00 mmol L^{-1} of nitrate solution (label as B). Repeat steps 1–5 using 1.8892 g, 2.8340 g, 3.7788 g and 4.7232 g of anhydrous calcium nitrate to produce a 16.00 mmol L^{-1} (C), 24.00 mmol L^{-1} (D), 32.00 mmol L^{-1} (E) and 40.00 mmol L^{-1} (F) of nitrate solution respectively.

B. *Phase 2: Planting the basil seeds*

Fill two-thirds of each pot with garden soil. Plant 3 basil seeds in each of the 25 flowerpots, 3 for each kind of the 6 concentrations and extras. If more than one of the basil seeds germinates in each pot, remove the other basil seedlings in the pot to reduce competition for nutrients.

C. *Phase 3: Watering the basil seeds/seedlings*

Before germination, mist the soil damp daily with a mister/spray bottle (~20 sprays).

After germination, water the basil seedlings with nitrate solution daily (50 ml daily).

6 Results and Discussions

Firstly, seedlings watered with the highest concentration of nitrate solution, 40.00 mmol/L died after the first week, as seen in Figs. 1 and 2. They also had yellowish-brown leaves, showing significant signs of leaf burn. The high concentration of nitrates in the soil could have also made the soil hypertonic, reducing the water potential of the soil. Hence, it might have caused the seedlings to dry up as water in the soil is unable to enter the roots via osmosis.

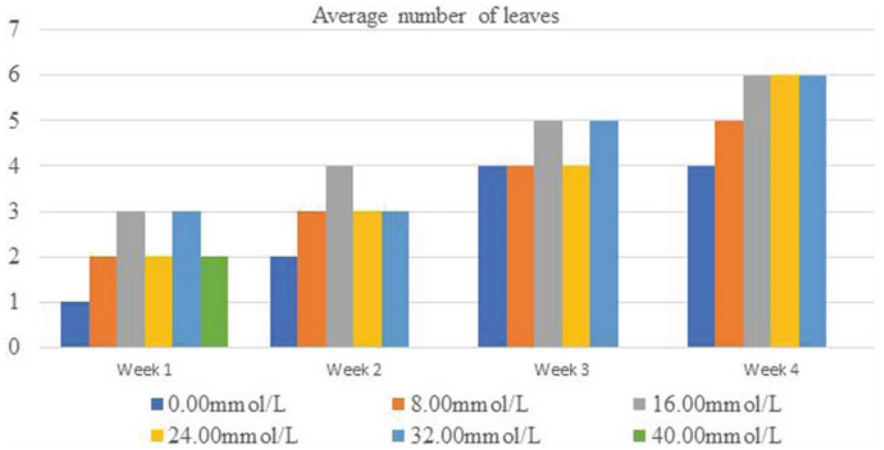

Fig. 1 Histogram of the average increase in the number of leaves on each plant by the concentration of nitrate solutions that they are watered with over four weeks

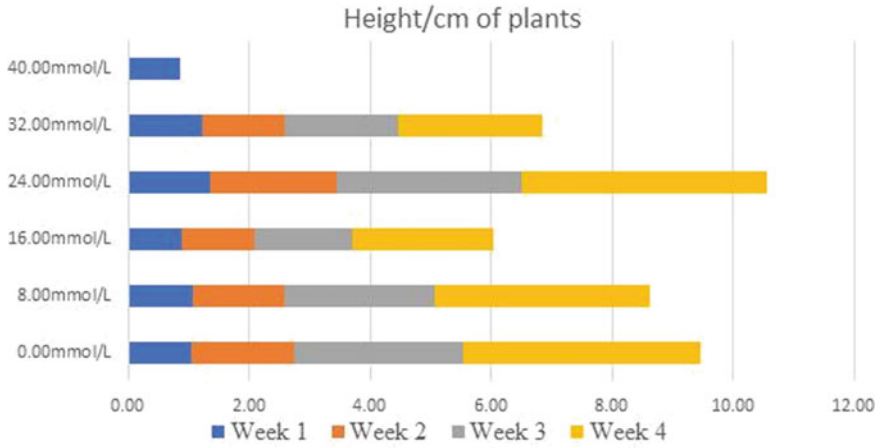

Fig. 2 Bar graph of the average increase in the height (cm) of each plant by the concentration of nitrate solution that they were watered with over the four weeks

Table 1 Average increase in the height of the seedlings

	Week 1	Week 2	Week 3	Week 4
A	1.05	1.70	2.80	3.90
B	1.08	1.50	2.48	3.57
C	0.90	1.18	1.63	2.33
D	1.37	2.08	3.07	4.05
E	1.22	1.38	1.87	2.438
F	0.87	0.00	0.00	0.00

Secondly, seedlings watered with 24.00 mmol/L of nitrate solution have the greatest increase in mean height, based on Fig. 2. The seedlings watered with 16.00, 24.00 and 32.00 mmol/L all had the greatest mean number of leaves according to Fig. 1. Hence, it can be seen that 24.00 mmol/L is the optimum concentration for basil seedlings to have the greatest height and the most number of leaves.

Lastly, although the seedlings watered with D.I. water grew the second best in terms of height according to Table 1, it had the dullest coloured leaves. From this, it can be inferred that nitrogen also contributes to the production of the green pigments in the leaves of plants (i.e. chlorophyll) significantly.

7 Conclusion

The seedlings watered 16.00 mmol/L of nitrate solution had the least height but the highest number of leaves. The control, which was watered with D.I. water (0.00 mmol/L), grew the second most in terms of height but it had duller coloured leaves.

The seedlings watered with 24.00 mmol/L of calcium nitrate had the greatest increase in number of leaves, and the greatest average height at the end of 4 weeks.

Thus, increasing the concentration of the nitrate solution increases the growth of basil seedlings up till the optimum concentration (24.00 mmol/L) after which an increasing concentration of nitrate solution decreases the growth of basil seedlings.

Therefore, 24.00 mmol/L is the optimum concentration for the growth of basil seedlings with healthy leaves.

8 Limitations

In Phase 1, as small amounts of hydrated calcium nitrate are required, the measurements could not be exactly accurate.

In Phase 2, as the seeds were very small, they could not be planted at the same depths, which may have led to the roots of some seedlings growing deeper and more widespread than those of other seedlings.

In Phase 3, when the seedlings are watered, the concentration of nitrates in the soil may not have been evenly spread throughout the soil. However, this had been minimized as the watering of the seedlings was attempted to be done in similar circular motions around the plant.

As this experiment was conducted with seedlings, which may not be as strong as mature adult plants, they may not be able to withstand the high concentration of nitrates in the soil as well as the adult plants. Hence the results are not an

accurate indicator of the optimum concentration of nitrates for adult basil plants.

Lastly, as this investigation was conducted over only four weeks, only four data points could be collected, which may have caused the growth pattern graphed in Figs. 1 and 2 to be inaccurate. If the investigation could be carried on for a longer period of time, the differences in the growth patterns of the seedlings could be more significant.

9 Future Work

Similar experiments can be done to find out how the concentration of other essential ions, potassium and phosphorus, in the soil affects the growth of plants. Plants of different species and age can also be used instead of the young basil seedling that has been used in this study.

Another study can also be conducted to find out how the concentration of different types of natural fertilisers can affect plant growth instead of the chemical fertilisers that have been used in this study.

References

1. Plant nutrients in the soil. (1970, January 1). Retrieved from https://www.dpi.nsw.gov.au/agriculture/soils/improvement/plant-nutrients.
2. Nitrogen. (n.d.). Retrieved from https://www.cropnutrition.com/efu-nitrogen.
3. *Journal of Experimental Botany*,Volume 52, Issue 355, February 2001, Pages 309–317, https://doi.org/10.1093/jexbot/52.355.309.
4. *Annals of Botany*, Volume 74, Issue 2, August 1994, Pages 143–157. https://doi.org/10.1006/anbo.1994.1104.

From Waste to Worth: Silver Recovery and Its Electrochemical Transformation to Nanoparticles

Baskaran SreeHarin, R. Manideepan, and Divyesh SenthilKumar

Abstract Obtaining the Chemical Oxygen Demand (COD) is extremely important to waste water analysis, as it can show the level of contamination. Thus, this is a common process that takes place in wastewater treatment laboratories, producing large amounts of COD waste. Among the chemicals contained in COD waste, silver is present in high concentrations and can be easily recovered by precipitation. Furthermore, silver has many practical applications such as antibacterial and wastewater treatment. Silver recovery from COD waste, was carried out through a precipitation process using NaCl to produce AgCl. The concentration of NaCl was optimized, obtaining silver removals above 95% from the COD waste, while ensuring minimal NaCl usage. Subsequently, the AgCl powder was converted to AgNO3 in order to have a water-soluble compound, which was used to synthesize silver nanoparticles supported on Granular Activated Carbon (GAC) through a novel electrochemical set up. Different experimental conditions such as applied current and silver solution concentration were studied, obtaining activated carbon materials with different loadings of silver particles and diameters ranging from 50 to 1000 nm. The effectiveness of the materials developed as water treatment agents, was evaluated through its antibacterial potential and phenol removal of a synthetic wastewater. We found that GAC with silver nanoparticles was able not only to increase the phenol adsorption capacity from 174 to 191 mg of phenol per gram of GAC but also inhibited E. Coli bacteria growth. These results showed that it is possible to recover silver from COD waste and transform it into a promising antibacterial material for wastewater treatment.

Keywords COD – chemical oxygen demand · GAC – granular activated carbon · Silver nanoparticles · Antibacterial · Electrochemical

B. SreeHarin (✉)
#05-630, Block 658D, Jurong West Street 65, Singapore 644658, Singapore
e-mail: sreeharin02@gmail.com

R. Manideepan
Block 180, Yung Sheng Road, #04-111, Singapore 610180, Singapore

D. SenthilKumar
Toh Guan Road Block 266, #07-25, Singapore 60026, Singapore

H. Guo et al. (eds.), *IRC-SET 2020*,
https://doi.org/10.1007/978-981-15-9472-4_45

1 Introduction

COD refers to chemical oxygen demand as referenced from article on COD [1], this parameter allows to determine the amount of oxygen that is necessary to decompose the organic matter and oxidize inorganic chemicals such as ammonia and nitrite, therefore it is related to the level of contamination in the water. Therefore, the measurement of COD is a common process that takes place in all laboratories related to wastewater treatment, producing large amounts of COD waste. Silver ions are present among the compounds used during the COD determination; this metal is added in excess to overcome interferences from other oxidants different than oxygen. For that reason, silver ions are present in considerable amounts in the COD waste, however, despite the ease which this metal can be recovered (Eq. 1) and reused, this waste is commonly only disposed by laboratories.

$$Ag^{+} + Cl^{-} \rightarrow AgCl(s) \tag{1}$$

Silver is a precious metal well known for its antibacterial activity and photocatalytic properties which can enhance wastewater treatment processes, especially in the form of Silver nanoparticles. Although, there is a debate regarding its toxicity in humans, low concentrations (<1 ppm) do not show adverse effects (World Health Organization 1996). For this reason, silver nanoparticles usually are supported on a material, preventing its release into the environment and ensuring human health. Hence, in this work the main objective was not only to determine the feasibility of silver recovery from COD waste, but also transform it into an environmental technology used for wastewater treatment. Specific objectives include the optimization of reagent amount used for the silver recovery, the transformation of silver into silver nanoparticles supported into activated carbon and the evaluation of the produced material as an antibacterial agent and wastewater treatment technology.

2 Methodology

The overall methodology can be synthesized in 3 steps (Fig. 1), which correspond to the specific objectives of this work. Detailed processes are described below.

2.1 Silver Recovery from COD Waste

Before we start extracting the Silver from the COD waste by precipitating Silver Chloride (AgCl), we needed and approximation of the concentration of silver (Ag^{+}) ions present in the COD waste. To assess this, we used the following procedure (Fig. 2).

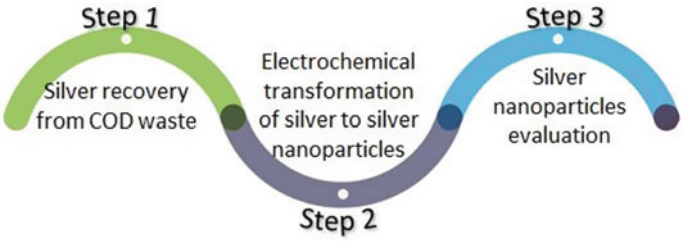

Fig. 1 Methodology summary of the present work

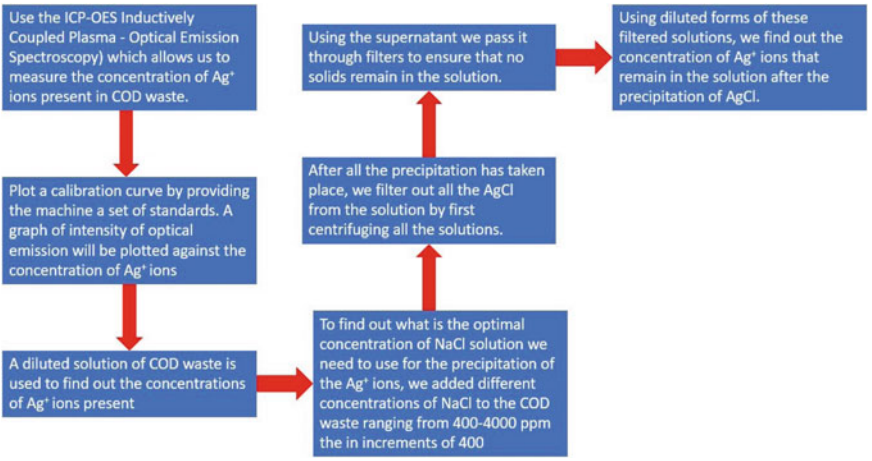

Fig. 2 Process diagram to determine silver concentration using ICP

We managed to conclude that using 2000 ppm concentration of NaCl in the reaction's solution is the most optimal to obtain the most amount of precipitate while ensuring that we don't waste too much of NaCl especially when it is being done in a large scale.

4 L of COD waste were obtained and 1 L of 2000 ppm NaCl solution was prepared. Then we poured the COD waste and NaCl solution into a 5 L beaker inside the fume hood. Then with the aid of a magnetic stirrer we sped up the precipitation of AgCl from COD waste. After that in multiple batches we centrifuged the solution to settle the precipitated AgCl at the bottom of the test tube. Then with the supernatant, we passed it through filters to ensure there was no more AgCl precipitate in the solution. Following that we diluted a sample of that solution and used the ICP-OES to calculate the experimental yield. We then scraped the AgCl off the bottom of the test tubes that were centrifuged and collected them in a beaker and placed it in a sealed jar which had desiccant to absorb the moisture.

The obtained AgCl residue is added to a beaker along with concentrated ammonium solution, copper turnings, and hot distilled water. The mixture is then stirred

rapidly using a magnetic stirrer for 5–10 min. Following that, the precipitated silver is then allowed to settle and the blue solution was decanted off with distilled water. The copper remains were then removed and nitric acid was added, to obtain $AgNO_3$ Solution. This entire process was carried out in the fume hood. This process is referenced from the article of recovering silver nitrate from silver chloride [2].

2.2 *Electrochemical Synthesis of Silver Nanoparticles on Activated Carbon*

GAC and GAC-Cu were used as substrates and coated with silver in order to provide a material with antimicrobial properties that can be used to disinfect water and carry out adsorption processes. Embedding nanoparticles on GAC also can improve the adsorption properties of the GAC due to an increase in the specific surface area. To impregnate the GAC with Ag nanoparticles, we used and electrochemical method which consisted in the reduction of silver ions to metallic silver (Eq. 2) by applying a negative potential and using the GAC as electrode material, in this way we avoided the use of toxic chemical reducing agents, commonly used in this process, referencing from the article cathodic polarising effect [3] on GAC and also the article on electrochemically prepared Iron-Modified GAC [4].

$$Ag^{+} + e^{-} \rightarrow Ag(s) \tag{2}$$

The novel reactor (Fig. 3) was composed by carbon cloth as anode, while the cathode comprised the GAC and a stainless steel mesh. To aid in compressing the GAC so as to increase conductivity of the reactor, the electrolysis was conducted in a syringe.

Electrolysis was conducted on both GAC and GAC-Cu. The electrolysis was repeated 3 times each for both the types of GACs in different concentrations of $AgNO_3$ solutions. The concentrations that were used are 1000 ppm, 5000 ppm

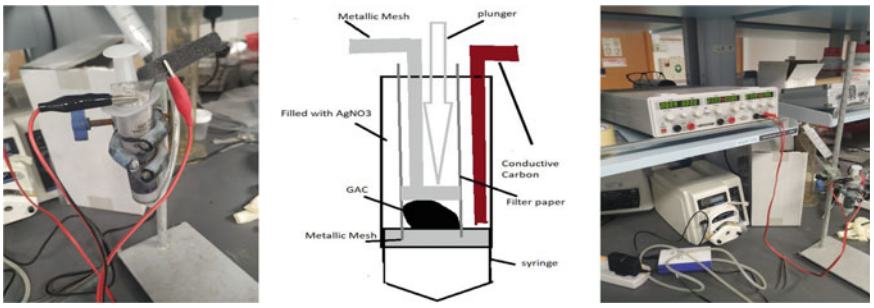

Fig. 3 Experimental set-up, **a** image of the electrochemical reactor, **b** electrochemical reactor materials and **c** power supply connection to the electrochemical reactor

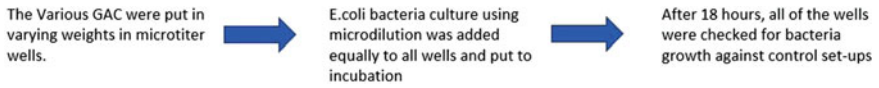

Fig. 4 Process diagram to evaluate the antibacterial potential

and 10,000 pm. These samples were then removed from the syringe and washed with Deionized water and dried over a few days in a closed container with desiccants. Scanning Electron Microscope pictures of the 6 different samples (3 different concentrations of $AgNO_3$ for GAC, GAC-Cu) were taken together with standards of the 2 different types of GACs. The 8 samples were labelled. For activated carbon nomenclature, please refer to appendix.

2.3 Evaluation of Activated Carbon for Antibacterial Potential

There are more than 25 infectious diseases related to water contamination from pathogenic microbial agents such as bacteria, virus, protozoa etc. Due to the various complexities in microbial agents, to test the effectiveness of the silver coated GACs in preventing the microbial replication we used *Escherichia coli* to test for the growth due to the high replication rate and reactivity of it. The used microdilution process can be found in the appendix. In short, we followed the next procedure (Fig. 4):

2.4 Evaluation of Activated Carbon for Adsorption Capacity

The following diagram was used to obtain the adsorption data, which was fitted to the Langmuir and Freundlich isotherm models in order to obtain the adsorption capacity of the different materials. The full methodology can be found in the appendix (Fig. 5).

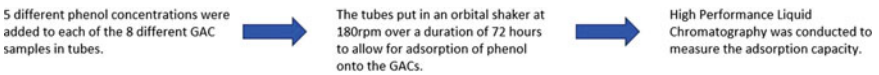

Fig. 5 Process diagram to evaluate the adsorption capacity

3 Results and Discussion

3.1 Silver Recovery from COD Waste

Following that we conducted experiments with NaCl concentrations ranging from 400 to 4000 ppm and we reached 99.32% yield at 2000 ppm. From results in Fig. 6 we were able to conclude that 2000 ppm was the optimum amount of NaCl that yielded the highest percentage of Ag precipitated while ensuring minimal NaCl usage.

The precipitated AgCl and obtained $AgNO_3$ was then tested with Energy Dispersive X-Ray Spectroscopy (EDS) to find out the composition of the solid that we obtained. From Fig. 7, we can see that $AgNO_3$ was indeed produced and the reason for the high level for Oxygen is due to the oxidation of AgCl which oxidises very readily.

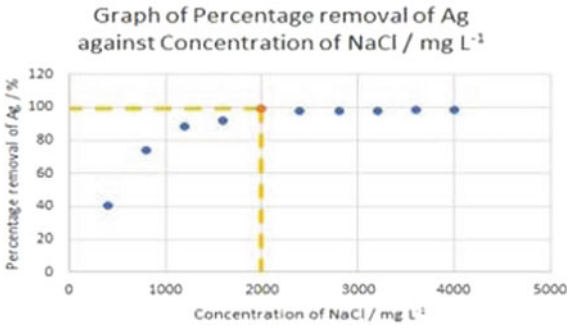

Fig. 6 Graphs of percentage removal of silver against concentration of NaCl added to COD waste, NaCl concentration from 400–4000 ppm

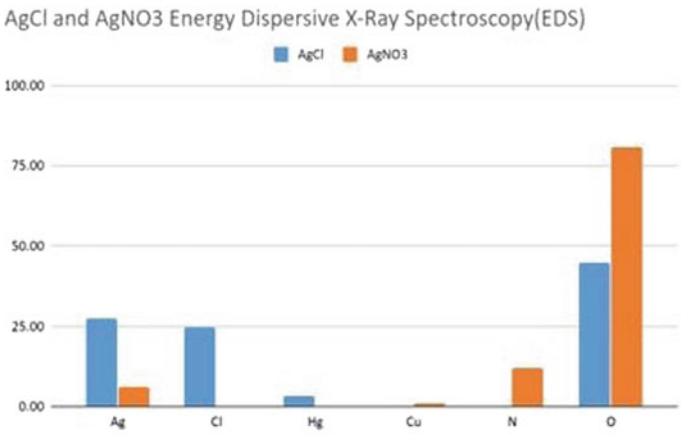

Fig. 7 Graph of energy dispersive X-ray spectroscopy for atomic % of the elements on AgCl and $AgNO_3$

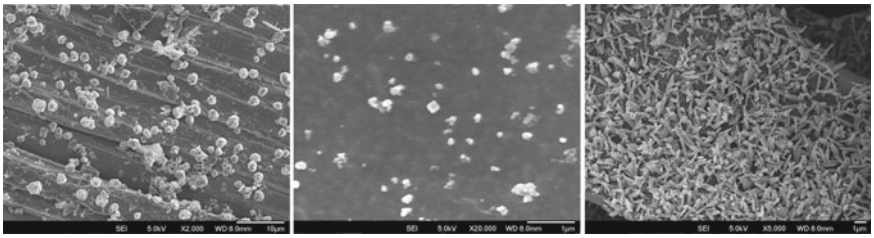

Fig. 8 Scanning electron Microscope images of all the 8 different GACs were taken after electrochemical deposition of silver, **a** silver microparticles on GAC-10000, **b** silver nanoparticles on GAC-1000, **c** needle structures representing Cu on GAC-Cu-5000

3.2 Electrochemical Synthesis of Silver Nanoparticles on Activated Carbon

From the SEM images, we found that when using a larger concentration of $AgNO_3$, due to the abundance of Ag^+ ions, there were larger molecules of Ag reduced on the surface of AC while when using a lower concentration of $AgNO_3$ in the electrolysis, the reduction from Ag^+ ions to Ag was slower due to the lower availability of Ag^+ ions and as such fewer big lumps of larger molecules formed and the more desired nanoparticles were deposited on the surface of the GAC. It was observed in the pictures of GAC-Cu that needle-like structure were formed, indicating that the oxidized Cu on the GAC reduced to form metallic copper on the GAC. The nanoparticles have higher reactivity as well as excellent adsorption rates in comparison to larger clumps of molecules. One factor that we had to take note was the toxicity that silver posed when induced in water for water treatment (Fig. 8).

We can infer from Fig. 9 that with increasing concentration of $AgNO_3$ the mass percentage of Ag also increases for the GAC samples. For the GAC-Cu samples, the percentages of Cu did not have a correlation due to the unpredictability of the copper oxide reducing to form metallic copper. However, increasing amounts of Silver may not be a good thing as they form larger silver particles instead of silver nanoparticles that are more desired.

3.3 Evaluation of Activated Carbon for Wastewater Treatment and Antibacterial Potential

From Fig. 10, we can see that the presence of a silver coating itself ensures that bacterial growth is inhibited, and the solution remains clear. As seen from the GAC-Cu-STD we can also conclude that the presence of a copper coating also actually inhibits bacterial growth. Therefore, the only row that has cloudy solution is the GAC-STD row where neither silver nor copper is present to inhibit bacterial growth and thus allowing for the growth of bacteria. However, in that there seems to be an

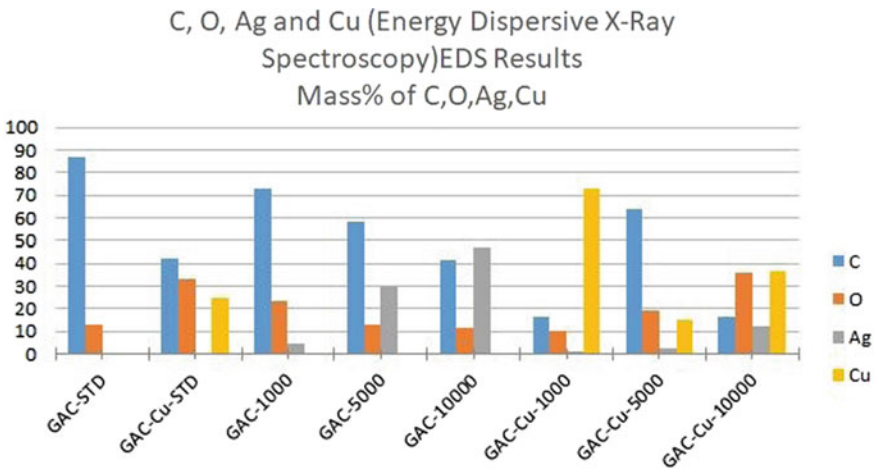

Fig. 9 Energy dispersive X-Ray results of the mass% components of the 8 various GACs

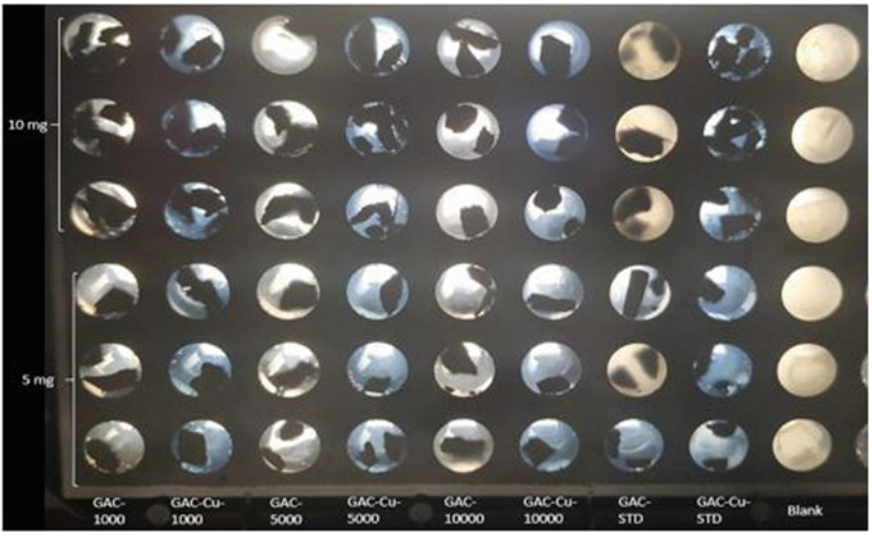

Fig. 10 Results from the microdilution test after being left to incubate for 18 h

anomaly where 2 of the wells are bluish and clear. We believe that there may have been some contamination or experimental error that may have led to the presence of copper hence the blue colour of Cu^{2+} ions as well as the absence of bacteria due to the inhibition of bacteria from copper. Thus, we in overall conclude that GACs coated with silver particles are indeed effective in inhibiting bacterial growth specifically that *E.Coli* and can indeed act as antimicrobial agents.

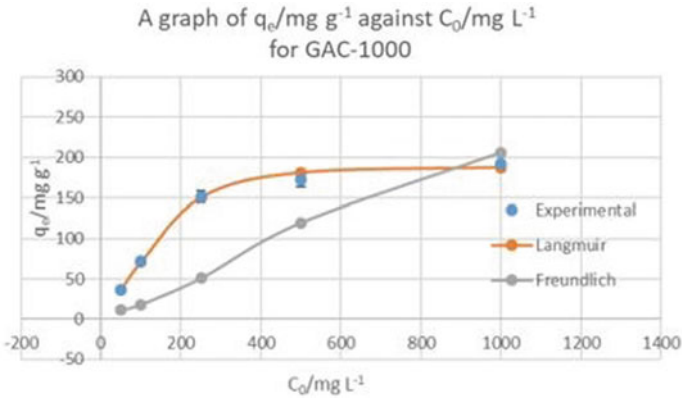

Fig. 11 A graph to illustrate how the experimental data points fit the Langumir model better

3.4 Effectiveness in Improving the Adsorption Capacity of GAC

The Langmuir isotherm model is representative of a monolayer adsorption onto the AC while the Freundlich is representative of a multilayer adsorption instead. The linear equations of the Langmuir and Freundlich Isotherm Models are shown here. qmax and K from the Langmuir and Freundlich model respectively are measures of the adsorption capacity of the different samples of GAC which can be found from the intercepts of the linear equation after the data is plotted in the respective isotherms. After fitting the data in the linear form of the isotherm models, we can see from the larger R^2 values in the langmuir linear graphs (See Appendix part 4) are much closer to 1 than those observed in the freundlich isotherm graphs (See Appendix part 5). Thus, we can conclude that the adsorption in this case is a monolayer adsorption. The non-linear graphs of the isotherm models also agree with this conclusion as the experimental data points match those of the Langmuir Model (Fig. 11). Then, from the line equation of the linear langmuir graphs we can obtain the qmax values of each of the 8 different GACs allowing us to compare the adsorption capacity of each activated carbon. The comparison of the qmax values is shown in Fig. 12. From the adsorption capacity values, we can see that when GAC-Cu were used regardless of the concentration of $AgNO_3$ it was electrolysed it resulted in the Adsorption Capacity of to be lower than the GAC-STD. This is probably due to the GAC-Cu having large needle-like structures forming during the electrolysis and thus blocking the small pores present in the activated carbon. This reduced the surface area of the adsorption surface available for the adsorption of phenol. The same can also be said for the GAC in 5000 and 10,000 mg L^{-1} concentrations which caused the formation of large silver microparticles which also blocked the small pores and thus they also have Adsorption Capacities that are lower than the GAC-STD. Only the GAC that was electrolysed in 1000 ppm of $AgNO_3$ formed silver nanoparticles that were not too big in size

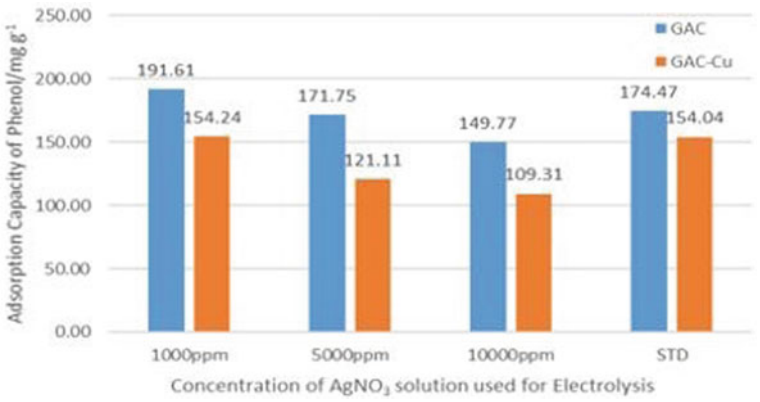

Fig. 12 Absorption capacities of the types of activated carbon electrolysed in different concentrations of $AgNO_3$ solution

and thus helped to improve the surface area of the Adsorption surface allowing for a higher adsorption capacity that the that of the GAC-STD. Thus, in this case we can conclude that only the GAC that was electrolysed in 1000 ppm of $AgNO_3$ solution is effective in increasing the adsorption capacity of the GAC to improve the adsorption of phenol. We can also conclude that only silver nanoparticles that are small enough help to increase the adsorption capacity when coated on the GAC and larger silver particles actually end up decreasing the adsorption capacity.

4 Conclusion and Future Work

There are a few major conclusions. The first being that the optimal concentration for precipitation of silver from the COD waste is 2000 ppm. The second major conclusion is that the most suitable concentration to conduct electrolysis for coating of silver nanoparticles on the GAC is 1000 ppm of $AgNO_3$. The third conclusion is that the presence of copper coating does not improve the coating process of Silver nor does it improve its effectiveness in treating water contamination. Even though Ag NPs have antimicrobial properties they can still have negative effects in cellular processes in which we Ag-NPs set off toxic processes in cells such disruption of cell transport and local depletion of glutathione and other antioxidants. Hence, we took ICP readings for the leaching of Ag as well as Cu while performing the adsorption experiment. It was observed that the smaller nanoparticles, found in 1000 ppm concentration of GAC, did not leach onto the phenol solution, while in larger particles found in 5000 ppm and 10000 ppm, leaching was observed for Ag. Cu was leached for all concentrations of GAC-Cu. All the activated carbon coated with silver had antibacterial activity regardless the silver concentration used to carry out the electrodeposition, although the mechanism of bacteria deactivation is not well understood, some researchers

have proposed that NPs smaller than 5 nm can penetrate cell walls and membranes, referenced from the Guidelines for drinking-water quality, 2nd ed. Vol. 2 [5]. Hence in our future work we could experiment more on the ideal concentration of $AgNO_3$ to use so that we can produce NPs which are most effective with high antimicrobial and adsorption capabilities and at the same time does not pose a health risk in leached into drinking water. Another thing that we can consider is that during the recovery of AgCl from the COD waste there was Hg present in small amounts in the solid that we recovered and tested. This could be due to the presence of Hg ions in COD waste that may have precipitated out as

Hg_2Cl_2 upon addition of NaCl solution. Also in the $AgNO_3$ that we tested, there were traces of copper present in the sample and this could be due Copper being one of the reagents that were used in the conversion of AgCl into $AgNO_3$ and thus this may have resulted in the copper not being removed properly at the end of the procedure. Thus, we could on methods to purify these samples to get a more pure sample. The last thing we could do is use different kinds of contaminants other than just phenol or other forms of bacteria apart from *E. Coli* to check for the silver coated GAC's effectiveness in treating them.

One of the main disadvantages of using precious metals is the cost such as silver, so obtaining silver from waste could diminish the cost. Furthermore, the electrochemical deposition of silver into activated carbon is a novel procedure, usually they do it in a chemical way which implies the use of toxic chemicals, electrochemical is a "green and safe procedure" which mainly uses electricity to carry out the needed reactions. This is also more cost effective in comparison to procedures like vacuum impregnation. Hence, we have developed a method which is very cost effective, hence easier to implement in a large scale to carry out water treatment.

References

1. Chemical Oxygen Demand (COD) in Wastewater I Real Tech Water. (n.d.). Retrieved from https://realtechwater.com/parameters/chemical-oxygen-demand/.
2. Thomas, N. C. (1990). Recovering silver nitrate from silver chloride residues in about thirty minutes. *Journal of Chemical Education*, *67*(9), 794. https://doi.org/10.1021/ed067p794.
3. Bañuelos, J. A., García-Rodríguez, O., Rodríguez-Valadez, F. J., Manríquez, J., Bustos, E., Rodríguez, A., & Godínez, L. A. (2015). Cathodic polarization effect on the electro-Fenton regeneration of activated carbon. *Journal of Applied Electrochemistry*, *45*(5), 523–531. https://doi.org/10.1007/s10800-015-0815-2.
4. Bañuelos, J. A., García-Rodríguez, O., Rodríguez-Valadez, F. J., & Godínez, L. A. (2015). Electrochemically Prepared Iron-Modified Activated Carbon Electrodes for Their Application in Electro-Fenton and Photoelectro-Fenton Processes. *Journal of The Electrochemical Society*, *162*(9). https://doi.org/10.1149/2.0581509jes.
5. Guidelines for drinking-water quality, 2nd ed. Vol. 2. Health criteria and other supporting information.

Isolation and Characterization of *Pseudomonas Aeruginosa* Phages from the Environment

Sahel Xunwei Tan, K. V. Samyukktha, Clara Guoting Quek, and Pablo Juan Bifani

Abstract Phage therapy is the use of lytic bacteriophages, which are the natural enemy of bacteria, to treat pathogenic bacterial infections. It is a field that has been gaining interest recently as a promising complement with antibiotics to treat bacteria, given increasing antimicrobial-resistance of bacteria. Reported cases of lives saved with isolated environmental phages, such as that of Isabelle Carnell-Holdaway, proves the potential of phage therapy. In this study, we focus on *Pseudomonas aeruginosa,* which is a Gram-negative pathogenic bacterium that is commonly found in soil and water. It is a frequent cause of nosocomial infections, which are complicated and can be life threatening. *P. aeruginosa* is notorious for its resistance to antibiotics and is associated with a mortality rate ranging from 18 to 61%. Hence, treatment for *P. aeruginosa*-caused diseases is challenging and of utmost importance. As such, we aim to isolate environmental phages that target *P. aeruginosa* and can be used in phage therapy. Nine sewage samples were collected from Singapore's Water Reclamation Plants and processed. Nine phages of different morphology were isolated and characterised through phenotypic and genotypic methods. They were proven to be genotypically distinct with different *Eco*RI and *Hind*III digestion patterns, and were tested for infectivity in 13 different clinical strains of *P. aeruginosa,* proving to be phenotypically distinct. The phages isolated from this study provide possible therapeutic treatments for *P. aeruginosa* in clinical patients, as well as diagnostic purposes in identifying specific *P. aeruginosa* strains of patients.

Keywords Phage therapy · Bacteriophage · Antimicrobial · Environmental · Pseudomonas · Diagnostics

S. X. Tan (✉) · K. V. Samyukktha · C. G. Quek
NUS High School of Mathematics and Science, Singapore, Singapore
e-mail: h1510130@nushigh.edu.sg

K. V. Samyukktha
e-mail: h1510130@nushigh.edu.sg

P. J. Bifani
Department of Microbiology and Immunology, National University of Singapore, Singapore, Singapore

H. Guo et al. (eds.), *IRC-SET 2020*,
https://doi.org/10.1007/978-981-15-9472-4_46

1 Introduction

A. *Phage therapy and its uses*

There is a large number of infectious diseases that are caused by pathogenic bacteria. Bacteriophages, or phages, are viruses that target, infect and replicate within bacteria. Phage therapy is the use of natural or genetically modified lytic bacteriophages to treat pathogenic bacterial infections, usually complementary alongside antibiotic treatment. It is a field that has been gaining interest recently as a promising alternative to mono antibiotic therapy, although the discovery of bacteriophages and the existence of phage therapy has been around for about a century. First used therapeutically in 1919 by microbiologist Felix d'Herelle, phage therapy progressed briefly for two decades before the arrival of antibiotics in the 1940s, which were much easier and effective to use, eliminated potential interest of the U.S. and most of Europe in further development of phage therapy [1]. However, by the 1980s, the continual evolution of bacterial antimicrobial resistance caused the health industry to relook into phage therapy [2]. Phage therapy proves its benefits over traditional antibiotics, with its specificity in bacterial infection minimising collateral damage to good bacterial and human cells and the auto-dosing effect, where phage number multiplies in bacterial-killing process [3, 4]. The superabundance of natural environmental phages also allows for a copious supply of phages that can infect a bacteria, even if mutation and resistance to some of those phages occur.

B. *Background of Pseudomonas aeruginosa*

Pseudomonas aeruginosa (Pa) is a common, Gram-negative bacterium found in the environment (e.g. soil, water). It is an opportunistic pathogen that causes severe illness by infection of many parts of the body (gastrointestinal, tissue, respiratory, bone and joint, etc.) in humans and especially those who are immunocompromised [5]. A significant and notable trait of this bacteria species is its advanced intrinsic antibiotic resistance mechanisms, and as such, extremely high antibiotic and drug resistance. They are resistant to multiple commonly used antibiotics and are thus of increasing threat. In fact, the World Health Organisation (WHO) published a list of bacteria of urgent need for new antibiotics in 2017, with *P. aeruginosa* being labelled 'critical' as a top priority [6].

C. *Hypothesis and experimental aims*

In this study, we hypothesize that there are many different types of phages capable of infecting *P. aeruginosa* that can be isolated from the environment for therapeutic and diagnostic purposes. Phages that infect *P. aeruginosa* are found where *P. aeruginosa* lives in the environment (e.g. soil, water), and can be purified and isolated from the environment for therapeutic and diagnostic purposes. As such, the purpose of this project is to identify and isolate different bacteriophages that infect *P. aeruginosa* from environmental sewage samples around Singapore, and perform genomic and host range characterisation tests on the isolated phages. We aim to understand the

host target range of the isolated phages against different *P. aeruginosa* bacterial strains, if any, can potentially be used for therapeutic purposes. We also anticipate that the isolated phages that are highly specific in infecting certain *P. aeruginosa* strains could be utilised as a diagnostic tool for rapid detection of drug resistant *P. aeruginosa* infection.

2 Materials and Methods

A. *Sewage sample collection and filtering*

Nine sewage samples were collected from Singapore's Water Reclamation Plants and left to settle for 30 min to settle solid particles before passing the supernatant through a 0.22 μm filter membrane (Fig. 1).

B. *Making overlay plates and phage hunting*

The top agar consisted of 4.0 mL of 0.7% agar, 500 μL of the respective bacterial cultures and 200 μL of 0.1 M $CaCl_2$ was prepared over a Luria Bertani (LB) agar (bottom agar). 10 μL of each phage sample was spotted onto the respective overlay plates and incubated at 37 °C overnight. Plaque formation (a clear area formed in the opaque overlay plate) indicates the presence of phages targeting the respective bacteria (Fig. 2).

C. *Isolation, purification, phage stocks and titer calculation of bacteriophage*

Isolation: *P. aeruginosa* ATCC Strain (#27853) and 12 clinical strains previously collected in the lab were used. Bacteria cultures were grown to an optical density (OD) at 590 nm to 0.6–0.8 (log phage), and were mixed at 1:10 ratio with each sewage sample in the presence of a final concentration of 4 mM $CaCl_2$ for adsorption. The mixture was serially diluted and 10 μl of the serial diluted mixture (up to 10^{-3} if the original phage titre is too high) were used to make overlay plates to allow observation of secluded plaques forming units (PFU).

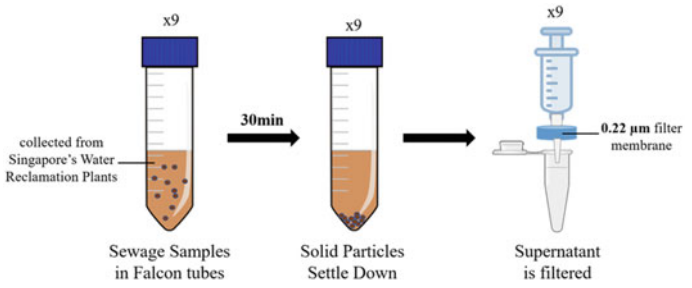

Fig. 1 Collection and filtering of sewage samples

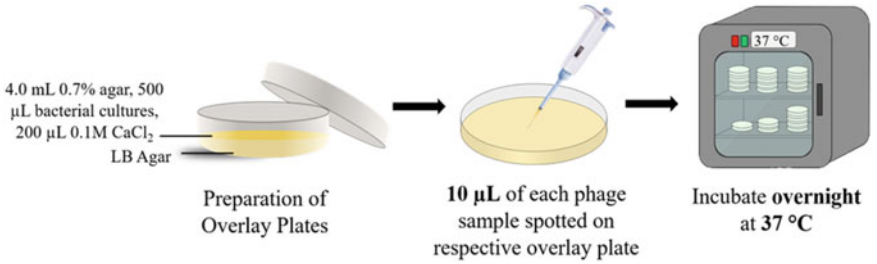

Fig. 2 Making overlay plates and finding phages to purify

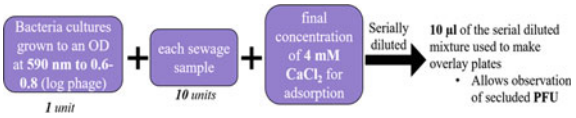

Purification: Plaques with different morphologies were picked with a pipette tip and mixed into 100 µL of phage buffer (40 mM Tris-HCl of pH 7.4, 150 mM NaCl, 10 mM $MgSO_4$, 1 mM $CaCl_2$) to form a neat solution, followed by serial dilutions to obtain overlay plates with isolated plaques. A total of four rounds of such purification step was performed to obtain identical phage morphology (plaques) across the plate, as seen in Fig. 3.

Phage stocks: Amplification of phage was done by soaking overlay plates with web-like appearance with phage buffer. Upon incubation at room temperature, the buffer was collected and filtered through a 0.22 µm membrane to obtain purified phage lysate.

Phage titer: Phage titer was determined by spotting serial dilutions of the purified phage stock onto respective overlay plates and upon incubation, only lysate spots with isolated countable plaques were used to determine phage titer with the following formula:

$$\text{Number of plaques}/10\mu\text{L Dilution factor } 10^3\ \mu\text{L/mL} = \text{Number of PFU/mL}.$$

D. *Genotypic Characterisation*

Fig. 3 Purification process of isolated phage samples

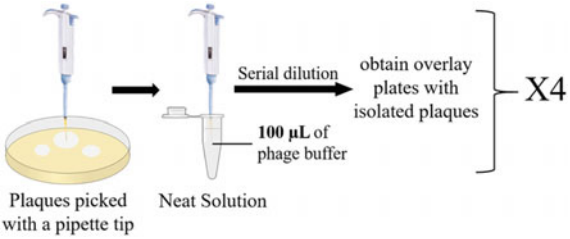

Phage DNA was purified using Phage DNA Isolation Kit (Product #46850) from NORGEN BIOTEK CORP according to the manufacturer's protocol except the following. The titer for some phage filtrates exceeded the upper recommended limit of the kit, and was diluted with phage buffer. Milli-Q water was used in place of Elution Buffer B provided in the kit. DNA purity and concentration was measured and recorded using NanoDrop Spectrophotometer. The DNA was then subjected to restriction enzyme digestion using EcoRI or HindIII according to New England Biolabs (NEB)'s protocol. The digested phage DNA, including the uncut DNA were loaded onto a 1.4% agarose gel stained with SYBR Safe dye and ran at 100 V for 80 min. The gel was visualised using a Chemidoc Imaging System (Bio-rad).

E. *Phenotypic Characterisation*

The nine phage lysates were spotted onto the 13 different *P. aeruginosa* bacterial strain overlay plates, to determine the range of infection of the isolated and purified phage samples. Upon incubation at 37 °C overnight, clearings on the overlay plates were recorded down.

3 Results and Discussion

A. *Bacteriophage isolation and purification*

Nine sewage samples were collected from Singapore's Water Reclamation Plants (WRP) from Changi, Jurong, Kranji and Ulu Pandan. Each sewage sample was mixed with 13 strains of *P. aeruginosa* bacterial culture (12 clinical strains and 1 commercial ATCC strain) and cultured at 37 °C for overnight as described in Materials and methods. From the total of 117 solution mixtures, 78 of them showed clearings on the overlay plates, plaques, suggesting the presence of phages specific to the particular *P. aeruginosa* strain. Each of the 78 solutions were then spotted again on the 13 different strains of *P. aeruginosa* overlay plates. Of these 78 solutions, three samples, sample 41, 64 (from Changi WRP) and sample 78 from (Kranji WRP), which had phages that targeted most of the 13 bacterial strains were selected for further purification to isolate individual types of phages.

Phage isolation was done on the three selected solutions through serially diluted overlay plates and morphologically different plaques were selected. An example of the serially diluted overlay plates (ranging from 10^{-3} to 10^{-6}) that give isolated plaques a round of purification is shown in Fig. 4a. We observed 2–4 morphological different plaques for each solution and an example of two morphologically distinct plaques (clear white vs cloudy turbid) is shown in Fig. 4b. From the incubated agar plates, two different morphologies of isolated plaques was observed for solution 64 (ΦA64, ΦB64), three for solution 41 (ΦA41, ΦB41, ΦC41) and three for solution 78 (ΦA78, ΦB78, ΦC78). Purification was then carried out on the isolated plaques of different morphologies. The isolated plaques were picked and mixed with phage buffer to form a neat solution, after which serial dilution was carried out on the neat

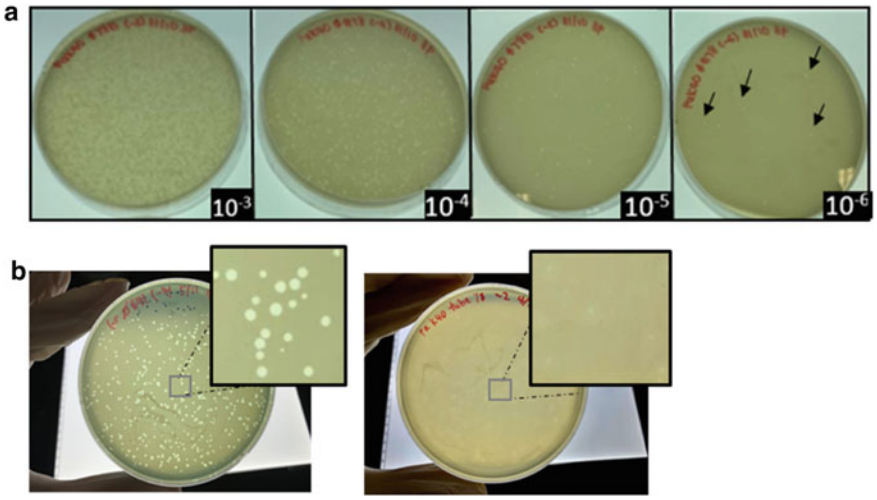

Fig. 4 **a** Third round of purification of phage ΦB78 from solution 78. Isolated palques (shown in arrows) were picked from the most diluted plate (10^4) for the next round purification, **b** examples of distinct plaque morphology: ΦB41 (left panel, clear white) and solution 78 (right panel, turbid cloudy)

solutions in the phage buffer to obtain dilutions from 10^{-1} to 10^{-12} and the overlay plates were incubated overnight.

Four rounds of purification was done. Two morphologies were observed in the ΦA78 purification plates after the first round of purification, as such they were further purified (ΦAi78, ΦAii78). In summary, nine different phage samples were collected after isolation and four rounds of purification and is shown in Fig. 5.

B. *Genotypic characterisation of the isolated phages*

For genotypic characterisation, DNA was extracted from the isolated nine phages and restriction enzymes analysis was performed. Gel electrophoresis of the uncut DNA, EcoR1 enzyme digests and HindIII enzyme digests of the phage samples are shown in Fig. 6. As the phage samples were isolated from three different sewage solutions, it is expected that there should be different phages across the three solutions. Interestingly, it appears that phages isolated from Kranji WRP (ΦAi78, ΦAii78, ΦB78 and ΦC78) exhibits more similar patterns than those isolated from Changi WRP (Solution 64: ΦA64, ΦB64 and Solution 41: ΦA41, ΦB41 and ΦC41).

When looking at the digestion patterns of the isolated phages, it is of note that the enzyme digested bands by *Eco*RI or *Hind*III for ΦA64 is very distinct from that of ΦB64. On the other hand, the gel bands of ΦB41 and ΦC41 look similar, as well as that of ΦAi78 and ΦB78, and that of ΦAii78 and ΦC78. This may suggest that the pairs of phages highlighted are genetically very similar or even identical. However, DNA sequencing of these phages DNA needs to be done in order to confirm their genetic features. Apart from using A-T base pair rich restriction enzymes like EcoR1

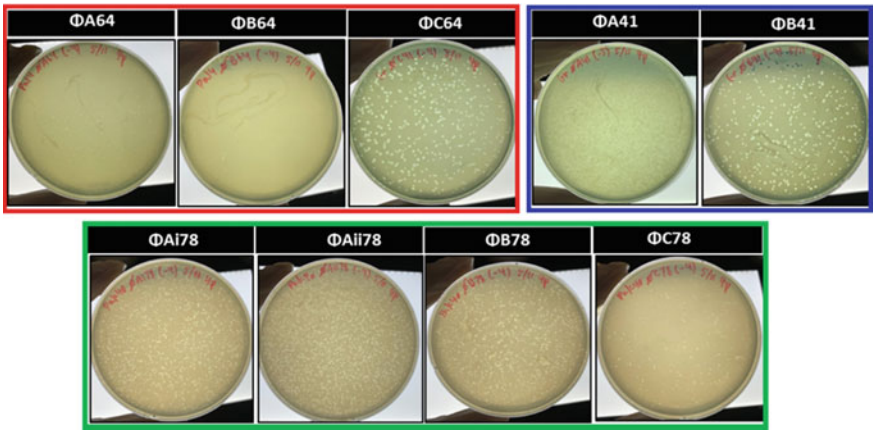

Fig. 5 Plaque morphology of nine isolated phages (three from solution 64: A64, B64, and C64; two from solution 41: A41 and B41; four from solution 78: Ai78, Aii78, B78 and C78)

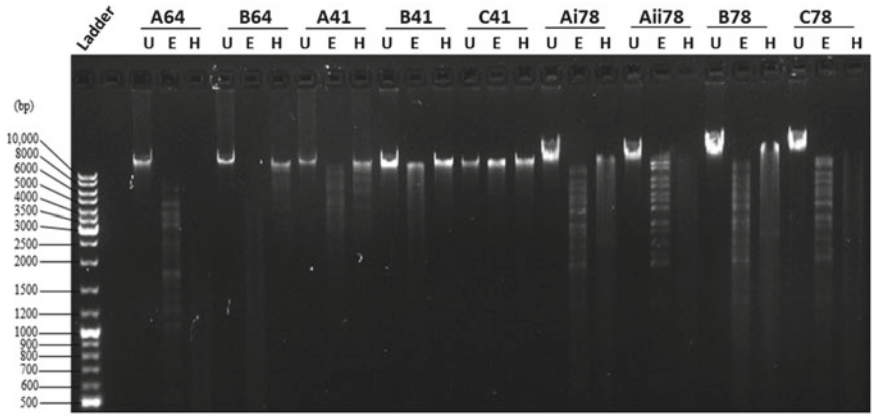

Fig. 6 DNA analysis of uncut DNA (U), *EcoR*1 enzyme digests (E) and *Hind*III enzyme digests (H) of the nine phages by agarose electrophoresis

and HindIII, C-G base pair rich restriction enzymes like BamH1, Xmal and SacII can also be used to further characterise the phages' genotypes.

C. *Phenotypic characterisation of the purified phages*

Phenotypic characterisation is done by spotting our 9 phage samples onto different bacteria overlay plates. The characterisation results are summarised in the table in Fig. 7, with a '+' indicating plaque formation and '−' indicating absence of plaques (no clearings). The phenotypic characterisation shows the different range of infectivity of the phages against the *P. aeruginosa* bacterial strains. From this table

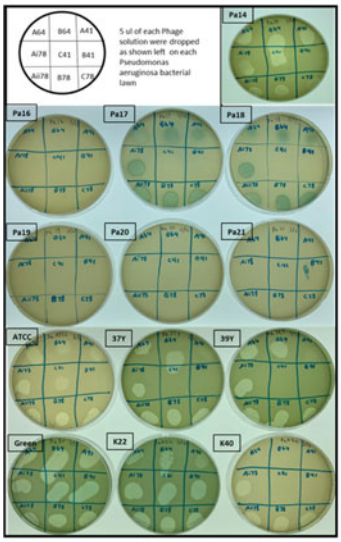

P. aeruginosa	A64	B64	A41	B41	C41	Ai78	Aii78	B78	C78
14	+	+	+	-	+	+	+	+	+
16	-	-	-	-	-	-	-	-	-
17	+	+	+	-	-	+	+	+	+
18	+	+	+	-	-	+	+	+	+
19	-	-	-	-	-	-	-	-	-
20	-	-	-	-	-	-	-	-	-
21	-	-	-	-	-	-	-	-	-
ATCC	+	+	+	-	+	+	+	+	+
37Y	+	+	+	-	-	+	+	+	+
39Y	+	+	+	-	-	+	+	+	+
K22	+	+	+	+	+	+	+	+	+
K40	-	-	-	-	-	+	+	+	+
Green	+	+	+	+	+	+	+	+	+

Fig. 7 Characterisation results for the nine isolated phages against 13 Peudomonas aeruginosa strains. '+' indicates palque formation and '–' indicates absence of plaques

we can determine the host specificity and activity of the phage samples. Phages from solution 78 show a wide range of infectivity against the bacterial strains.

4 Future Studies

A. *Uses for phages with wide range of infectivity*

As phages from solution 78 show a wide range of infectivity against bacterial strains, it may thus be used in making phage cocktails in phage therapy for treating patients with *P. aeruginosa,* provided the patient isolate is first screened for an ideal lytic phage treatment. These phages that are selected for therapeutic treatment would then have to be genetically modified to exclude their DNA coding for lysogenic incorporation mechanism. This is to prevent the immunity against lysis that the prophage confers to host bacterium against homologous phages [7].

B. *Uses for phages with specific infectivity*

Conversely, phages such as ΦB41 and ΦC41 are much more strain-specific in infectivity against *P. aeruginosa.* These phages can be further modified for diagnostic purposes in identifying particular strains of *P. aeruginosa* in clinical patients. For phages selected for diagnostic purposes that are tested to be lysogenic, the insertion of a reporter Green Fluorescent Protein (GFP) gene into the phage genome allows the phage to act as a marker for the specific strains they infect, when the GFP gene is

inserted as prophage into the host genome [8]. This allows for non-invasive screening of GFP produced for identification of specific *P. aeruginosa* strains in patients. It is worthy to mention that the nine phage samples showed no clearing for the *P. aeruginosa* strains 19, 20 and 21. A continuation of the experiment is to isolate more phages from the other 78 solutions to find isolated phages that infect those strains, as well as new strains of *P. aeruginosa* from other clinical sources.

5 Conclusion

This study demonstrates that there are indeed many bacteriophages present in the world around us that target many kinds of bacteria, and these phages are unique in both their genotype and phenotype. Bacteriophages from the environment are shown to be effective in reducing bacterial population through inducing bacterial lysis, and different phages do have a unique range of infectivity against different types of bacterial strains. Our study has attained phages that are specific as well as phages which have wide ranges. Depending on this range of infectivity, phages can be further modified genetically to be used in phage therapy complementary to antibiotic treatment as well as for diagnostics.

Acknowledgements We would like to thank Dr. Pablo Bifani, Barry Choo, Ayuni Norman, Liew Jun Hao (National University of Singapore) and Ms. Verlyn Woo (NUS High School of Mathematics and Science) for their guidance and mentorship throughout the project.

This work was supported by NUS High School of Mathematics and Science and the Ministry of Education, Singapore.

References

1. Summers, W. C. (1999). Felix d'Herelle and the Origins of Molecular Biology. Yale University Press.
2. Sulakvelidze, A., Alavidze, Z., & Morris, J. (2001). Bacteriophage Therapy. Antimicrobial Agents and Chemotherapy, 45(3), 649–659.
3. Bhaskaran, N., Quigley, C., Paw, C., Butala, S., Schneider, E., & Pandiyan, P. (2018). Role of Short Chain Fatty Acids in Controlling Tregs and Immunopathology During Mucosal Infection. Frontiers in Microbiology, https://doi.org/10.3389/fmicb.2018.01995.
4. Loc-Carrillo, C. & Abedon, S. (2011). Pros and Cons of Phage Therapy. Bacteriophage, 1(2), 111–114.
5. Moradali, M.F., Ghods, S., & Rehm, B. (2017). *Pseudomonas aeruginosa* Lifestyle: A Paradigm for Adaptation, Survival, and Persistence. Front Cell Infect Microbiol, 7(39).
6. World Health Organization. (2017). WHO publishes list of bacteria for which new antibiotics are urgently needed. World Health Organization.
7. Boyd, J. (1956). Immunity of Lysogenic Bacteria. Nature, 178(141).
8. Pires, D., Cleto, S., Sillankorva, S., Azeredo, J., & Lu, TK. (2016). Genetically engineered phages: a review of advances over the last decade. Microbiol Mol Biol Rev 80, 523–543.

FTIR and SEM Study on the Degradation of Microplastics

William Chia, Yu Hung Ng, and Chong Yuan Ong

Abstract Microplastic, plastics that are smaller than 5 mm in size, can be directly manufactured or formed from the breakdown of larger plastics. The aim of this project is to research on the effects of temperature, humidity and UV light on the degradation of microplastics. We would also propose ways to counter the harmful effects brought about by microplastic breakdown. Using Attenuated Total Reflectance Fourier Transform Infrared Spectroscopy (ATR FTIR) and Scanning Electron Microscopy, we found that an increase in temperature and humidity and the presence of UV light would speed up the degradation of plastics. This is a cause of concern as global warming will intensify these conditions, thus accelerating the production of microplastics.

Keywords Microplastic · Doegradation · FTIR · SEM

1 Introduction

Plastics have been mass produced since the 1950s and the annual production exceeds 288 million tonnes [1]. With the invention of plastics comes microplastics—tiny plastics that are smaller than 5 mm and are invisible to the naked eye [2]. Microplastics can be intentionally produced (primary microplastics) or can result from everyday items like plastic bags, straws and bottles that break down into smaller pieces over time (secondary microplastics) [3]. As plastics flowed into oceans, they become persistent organic pollutants in the water [4]. These microplastics may contain hazardous chemical ingredients and have adverse impacts on us [5, 6].

W. Chia (✉) · Y. H. Ng · C. Y. Ong
NUS High School of Math and Science, Singapore, Singapore
e-mail: williamchia2012@gmail.com

Y. H. Ng
e-mail: brandon.ngyuhung@gmail.com

C. Y. Ong
e-mail: ongchongyuanh1610105@gmail.com

H. Guo et al. (eds.), *IRC-SET 2020*,
https://doi.org/10.1007/978-981-15-9472-4_47

More importantly, studies showed that microplastics can be found in a large, remote, mountain Lake Hovsgol in Mongolia, alps and even artic snow [7]. While microplastics in the sea and shoreline were comprised largely of plastic bottles, microbeads, household plastics and bags, the most abundant microplastic types in the alps and artic are fragments and films. These lightweight plastic fragments have become airbourne and could heavily pollute freshwater systems and the artic [8].

Some people have proposed that we use biodegradable plastics instead as it is deemed to be more eco-friendly than traditional plastics. However, the use of biodegradable plastics could also result in environmental pollution. Rujnic-Sokele and Pilipovic [9] pointed out that when biodegradable plastics enter the water, biodegradation is slowed down and microplastics may be formed due to incomplete degradation. Also, the rate of composting is greatly reduced during periods of cold weather and high humidity.

The breakdown of microplastics is dependent on many factors—UV light intensity (photoreactive degradation), surrounding temperature (thermal degradation), humidity, presence of enzymes (biodegradation) and pH of surroundings. When microplastics break down, they produce even more microplastics, thus aggravating the situation and causing a vicious cycle.

Hence, we aim to study how the breakdown of microplastics is affected by our surrounding conditions. As Singapore has a high air temperature all year round, humid climate and high UV intensity, we decided to confine our research to these three factors. We chose to conduct tests on two types of plastic - Low Density Polyethylene (LDPE) and Polyvinyl chloride (PVC). This is because these plastics are very commonly used in our everyday activities. PVC can be used to make pipes, doors, windows, bottles and cards while LDPE is mainly used for manufacturing containers such as plastic bags [10]. In addition, we would also discuss ways to mitigate the harmful effects brought about by these microplastics.

2 Methodology

The experiment was split into 2 parts—Degradation Testing and Characterisation. In Degradation Testing, the samples were set up to observe the degradation of beads over a period of 4 weeks. In Characterisation, Attenuated Total Reflectance Fourier Transform Infrared Spectroscopy (ATR FTIR) and Scanning Electron Microscopy (SEM) were used to determine the extent of degradation of beads.

A. *Degradation testing*

There were a total of 12 batches of samples (Table 1). To prepare the samples, the beads were dried for 20 min at 55 °C to remove any excess water. 10 g of plastic beads was placed in a glass bottle and sealed for each sample. Samples 5 and 10 simulated the natural environment of Singapore and were placed on the rooftops. Samples 11 and 12 were exposed to UV light with wavelength 365 nm (UVC) by

Table 1 Conditions for the 12 samples

Sample	Type of plastic	Temperature (°C)	Humidity	UV light
1	PVC	45–50	Low	Absent
2	PVC	45–50	High	Absent
3	PVC	65–70	Low	Absent
4	PVC	65–70	High	Absent
5	PVC	25–30	Low	Present
6	PVC	25	Low	Present
7	LDPE	45–50	Low	Absent
8	LDPE	45–50	High	Absent
9	LDPE	65–70	Low	Absent
10	LDPE	65–70	High	Absent
11	LDPE	25–30	Low	Present
12	LDPE	25	Low	Present

using a UV lamp with a power of 40 W. The remaining samples were placed in water baths to ensure relatively constant temperature.

Every week, 20 beads were removed from the samples placed in centrifuge tubes. These tubes were stored in the cold room to stop degradation.

B. *Characteriasation*

Infrared spectra from 400 to 4000 cm^{-1} with a data interval of 2 cm^{-1} and resolution of 16 cm^{-1} was collected using Perkin-Elmer FTIR Frontier model. Each sample was compressed with a force of about 100 N and background scans were conducted for every sample. Plastic beads made of LDPE were cut into smaller pieces using a penknife to facilitate the compression of the samples. The transmittance (%T) of each sample was measured for each spectra and a graph of transmittance against spectra was plotted. For SEM, the morphologies of the surfaces of some samples were observed by using a field emission scanning electron microscopy (FESEM) (JSM-7600F), where the reference foils and functionalized foils were analysed at an accelerating voltage of 1 kV and variable working distance using a 10 m-sized aperture.

3 Results and Discussion

Figures 1, 2, 3, 4, 5, 6, 7, 8, 9, 10, 11 and 12 shows the FTIR spectra for the 12 samples before and after degradation. The orange lines show the initial %T while the purple lines show the final %T of the samples. The x-axis is the wavenumbers (cm^{-1}) and y-axis is the %T.

A. *Comapring the FTIR spectra for samples 1–4 (PVC)*

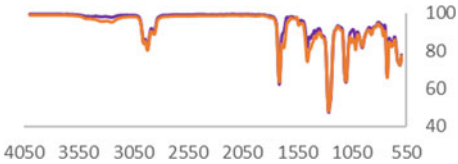

Fig. 1 Before (orange) and after (blue) degradation FTIR spectra for sample 1

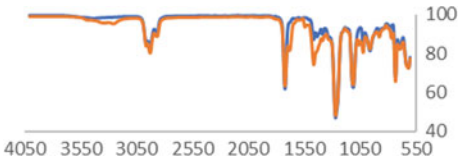

Fig. 2 Before (orange) and after (blue) degradation FTIR spectra for sample 2

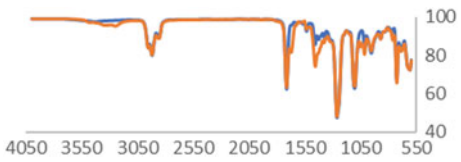

Fig. 3 Before (orange) and after (blue) degradation FTIR spectra for sample 3

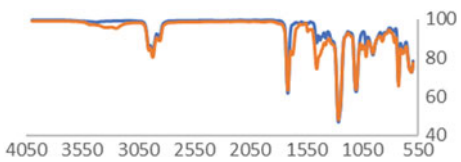

Fig. 4 Before (orange) and after (blue) degradation FTIR spectra for sample 4

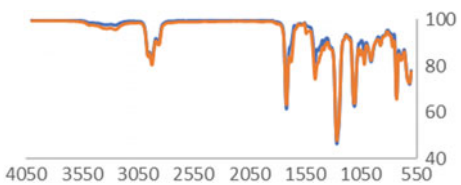

Fig. 5 Before (orange) and after (blue) degradation FTIR spectra for sample 5

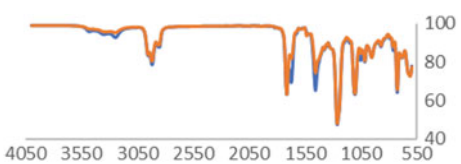

Fig. 6 Before (orange) and after (blue) degradation FTIR spectra for sample 6

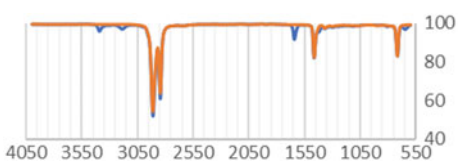

Fig. 7 Before (orange) and after (blue) degradation FTIR spectra for sample 7

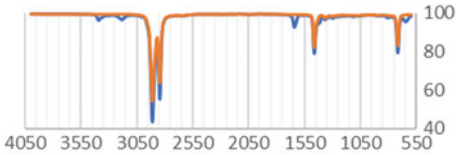

Fig. 8 Before (orange) and after (blue) degradation FTIR spectra for sample 8

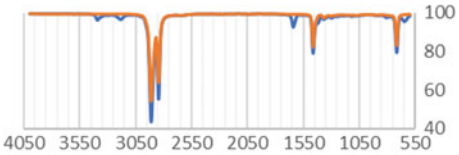

Fig. 9 Before (orange) and after (blue) degradation FTIR spectra for sample 9

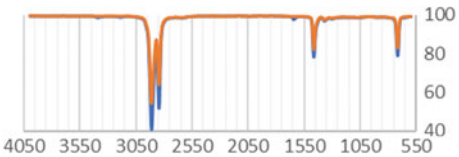

Fig. 10 Before (orange) and after (blue) degradation FTIR spectra for sample 10

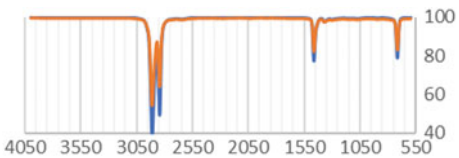

Fig. 11 Before (orange) and after (blue) degradation FTIR spectra for sample 11

From the FTIR spectra (Figs. 1, 2, 3 and 4), PVC samples 1–4 showed significant changes after degradation. There are some new peaks at 3250, 3350 and 3500 cm^{-1}. The peaks that appear conspicuously at 3400–3100 cm^{-1} are hydroxyl regions H–O–H [11, 12], which occur because the sample adsorbs moisture easily. High temperature and high humidity environment accelerated the chemical degradation of PVC.

B. *Comparing the FTIR spectra for samples 7–10 (LDPE)*

From the FTIR spectra (Figs. 7, 8, 9 and 10), LDPE samples 7–10 showed significant changes after degradation. There are some new peaks at 1100, 1645, 3192 and 3400 cm^{-1}. The peak at 1100 cm^{-1} represents –C–O stretch while the peaks at

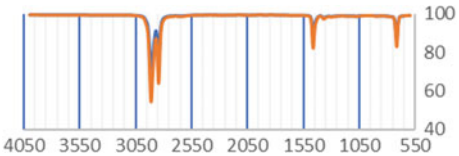

Fig. 12 Before (orange) and after (blue) degradation FTIR spectra for sample 12

1645 and 1465 cm^{-1} represents the –C=O stretch of erucamide and characteristic $–CH_2–CH_2$—stretch in polyolefin respectively.

The peaks appear conspicuously at 3400–3100 cm^{-1} are hydroxyl regions H–O–H, which imply that the sample adsorbs water easily. High temperature and high humidity environment accelerated the chemical degradation of LDPE.

C. *Comparing the FTIR spectra for samples 6 and 12 (effect of UV light on both PVC and LDPE)*

From Fig. 12, LDPE sample 12 showed significant changes after degradation. From Fig. 6, PVC sample 6 also showed significant changes when compared to the initial PVC sample. Larger peaks are observed and this means that UV light accelerated the chemical degradation of both PVC and LDPE.

D. *Comparing the SEM images of sample 5 (PVC) and sample 11 (LDPE) at the beginning of the experiment and at week 4*

Figure 13a is slightly rough while Fig. 13b is very rough and has many bumps. Figure 1b also has small protrusions on its surface. This shows that surface crack of LDPE has taken place after 4 weeks of outdoor exposure.

Figure 14a is smooth and flat while Fig. 14b is rougher and has a noticeable bump at the bottom right part. This shows that surface crack of PVC has taken place after 4 weeks of outdoor exposure.

However, the extent of change in structure is more severe and noticeable in Fig. 14 than Fig. 13. Hence Fig. 14 experienced more degradation than Fig. 13. This implies that LDPE degrades faster than PVC which can be explained by examining the molecular structure of the two types of plastics.

For both PVC and LDPE, the primary force of attraction between the polymer chains are London Dispersion Forces (LDF). However, the presence of polar C–Cl bonds along the length of each polymer chain of PVC results in the presence of dipole-dipole forces of attraction (DDF) along with the pre-mentioned LDF, while LDPE only has LDF between the polymer chains. Chang [11] and Burrows et al. [12] pointed

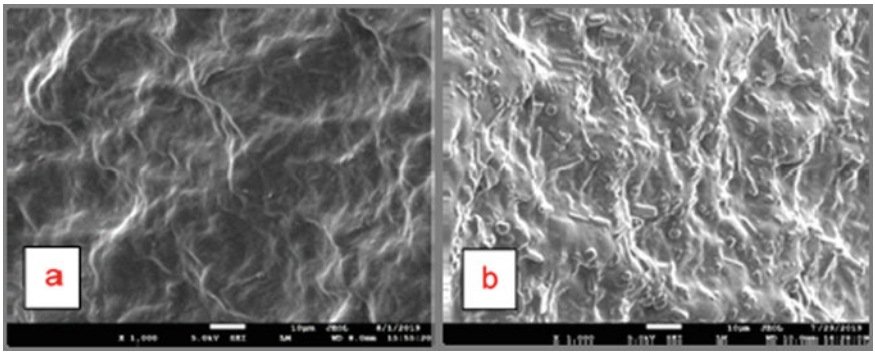

Fig. 13 Before (**a**) and after (**b**) degradation SEM images of sample 5 (PVC)

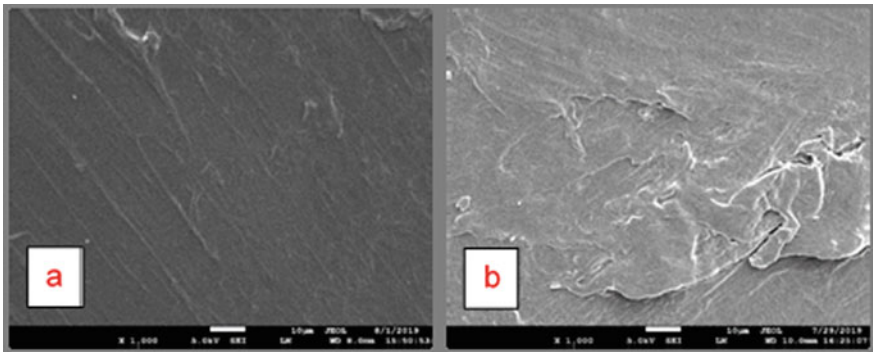

Fig. 14 Before (**a**) and after (**b**) degradation SEM images of sample 11 (LDPE)

out that DDF is stronger than LDF. The effect of the additional DDF between PVC polymer chains is not negligible since the C–Cl bonds are present along the whole length of the long polymer chains. Thus, PVC has an overall stronger intermolecular force of attraction between the polymer chains than LDPE, therefore allowing PVC is more resistant to degradation as more energy is required to overcome the stronger attractive forces between the polymer chains.

4 Implications and Conclusions

Our research project demonstrated that increased humidity and temperature and prolonged exposure to UV light cause microplastics to degrade faster. This is quite ominous as global warming exacerbates such conditions. The increase in global temperature would increase the rate of water evaporation and result in an increase in humidity. Thus, plastics would degrade faster, resulting in more extensive pollution and adversely impacting biota. From our study, LDPE produces more microplastics in the environment than PVC.

Acknowledgements We would like to express our appreciation to our research mentor Assistant Professor Fei Xunchang, our teacher mentor Mr Murali Krishnaswamy, research student Miss Lu Xuhong, the laboratory staff at School of Civil and Environmental Engineering, Nanyang Technological University, our parents and all others who have helped us in the course of this project for their guidance and unwavering support.

References

1. PlasticsEurope. (2013). Plastics—the Facts 2013: An analysis of European latest plastics production, demand and waste data. Retrieved from https://www.plasticseurope.org/applic

ation/files/7815/1689/9295/2013plastics_the_facts_PubOct2013.pdf.
2. Mathalon, A., & Hill, P. (2014, March 17). Microplastic fibers in the intertidal ecosystem surrounding Halifax Harbor, Nova Scotia. *Marine Pollution Bulletin*, 81(1), 69–79. https://doi.org/10.1016/j.marpolbul.2014.02.018.
3. Anderson, A.G., Grose, J., Pahl, S., Thompson, R.C. & Wyles, K.J. (2016, November 08). Microplastics in personal care products: Exploring perceptions of environmentalists, beauticians and students. *Marine Pollution Bulletin*, 113(1–2), https://doi.org/10.1016/j.marpolbul.2016.10.048454–460.
4. Andrady, A. L. (2011, July 13). Microplastics in the marine environment. *Marine Pollution Bulletin*, 62(8), 1596–1605. https://doi.org/10.1016/j.marpolbul.2011.05.030.
5. Rochman, C. M., Hoh, E., Kurobe, T., & Teh, S. J. (2013, November 21). Ingested plastic transfers hazardous chemicals to fish and induces hepatic stress. *Scientific Reports*, 3(3263), 2013. https://doi.org/10.1038/srep03263.
6. Teuten, E. L., Rowland, S. J., Galloway, T. S., & Thompson, R. C. (2007, October 20). Potential for Plastics to Transport Hydrophobic Contaminants. *Phil. Trans. R. Soc. B*, 364, 2027–2045. https://doi.org/10.1021/es071737s.
7. Free, C. M., Jensen, O. P., Mason, S. A., Eriksen, M., Williamson, N. J., & Boldgiv, B. (2014, June 24). High-levels of microplastic pollution in a large, remote, mountain lake. *Marine Pollution Bulletin*, 85(1), 156–163. https://doi.org/10.1016/j.marpolbul.2014.06.001.
8. Cox, K.D., Covernton, G.A., Davies, H.L., Dower, J.F., Juanes, F. & Dudas, S.E. (2019). Human Consumption of Microplastics. *Environmental Science & Technology*, 2–19 https://doi.org/10.1021/acs.est.9b01517.
9. Rujnic-Sokele, M. & Pilipovic, A. (2017). Challenges and opportunities of biodegradable plastics: A mini review. *Waste Management and Research*, 35(2), 132–140.
10. Kershaw, P. (2016). Marine plastic debris and microplastics - global lessons and research to inspire action and guide policy change. Retrieved from https://www.researchgate.net/publication/309735731_Marine_plastic_debris_and_microplastics_-_global_lessons_and_research_to_inspire_action_and_guide_policy_change.
11. Chang, R. (2010).*Chemistry (10th Edition).* New York, NY: McGraw-Hill.
12. Burrows, A., Holman, J., Parsons, A., Pilling, G., & Price, G. (2009). *Chemistry3: introducing inorganic, organic and physical chemistry*. Oxford: Oxford University Press.

Membrane Synthesis for Commercially Viable Osmotic Power Generation by Pressure Retarded Osmosis (PRO)

Cheng Yi, Yu Sutong, Liang Canzeng, and Wan Chunfeng

Abstract Water and energy are crucial resources for humans. Current energy and water demands are on the rise and it is necessary to find new avenues to obtain these resources. Osmotic power is an increasingly well-studied form of energy. Our research is on focused on pressure retarded osmosis (PRO) because it is the most prominent way of generating osmotic energy. Past applications of PRO have largely ended in failure due to limitations of the membrane. Our research is focused on developing new membranes that can generate commercially viable osmotic power. The power generated from the PRO process can compensate for the high energy consumption in the desalination processes. In this project, we have successfully fabricated membranes that are strong (i.e., high maximum tensile stress and high burst pressure), possess high water permeability as well as high salt rejection of over 95% (i.e., low salt permeability) through direct phase inversion and interfacial polymerization. We have achieved a peak power density of 12 W/m^2 which is higher than 3 W/m^2. This shows that our membrane can generate commercially viable energy. We have outperformed the early membranes developed for power generation. PRO is especially applicable in Singapore which relies heavily on desalination for potable water. To the best of our knowledge, we have synthesized the strongest inner selective hollow fiber thin film composite PRO membrane.

Keywords Thin film composite · Hollow fiber · Pressure retarded osmosis · Osmotic energy

C. Yi (✉) · Y. Sutong
NUS High School of Mathematics and Science, Singapore, Singapore
e-mail: h1510020@nushigh.edu.sg

Y. Sutong
e-mail: h1510166@nushigh.edu.sg

L. Canzeng · W. Chunfeng
NUS Department of Chemical and Biomolecular Engineering, Singapore, Singapore
e-mail: chelian@nus.edu.sg

W. Chunfeng
e-mail: chunfeng.wan@nus.edu.sg

H. Guo et al. (eds.), *IRC-SET 2020*,
https://doi.org/10.1007/978-981-15-9472-4_48

1 Introduction

The total amount of energy consumed globally is predicted to rise to 240 kTWh in 2040 [1]. On top of that, we face the depletion of non-renewable fossil fuels and climate change. As we face tight environmental regulations as well as high energy production cost, we are incentivized to explore other alternative renewable energy sources. The existing desalination processes face two main challenges: high energy consumption and the generation of highly concentrated brine after the desalination process which induces additional disposal issues. There are a variety of opportunities to co-produce energy and water and to harvest the benefits of synergies. Our project uses pressure retarded osmosis (PRO) to generate clean energy while treating wastewater. The energy generated from PRO can compensate for the energy consumed during desalination. Several technologies have been researched on to generate osmotic power, but PRO is deemed as the most explored and developed process due to efficiency of power generation as well as high obtainable power density [2–8]. In PRO, the water travels across a semipermeable membrane from a low salt concentration feed solution (i.e. freshwater) to a high salt concentration draw solution (i.e. saltwater) against a pressure applied on the feed solution, ΔP. The pressure we applied is less than the osmotic pressure difference, $\Delta\pi$, so that spontaneous water flux between the two solutions is maintained as shown in Fig. 1.

PRO extracts the osmotic energy, which is converted into the diluted draw solution with an increased volumetric flow rate as shown in Fig. 2 [2–9].

We can convert osmotic power into electrical energy by passing the water through a turbine or mechanical energy through a pressure exchanger. Every day, 86.8 million

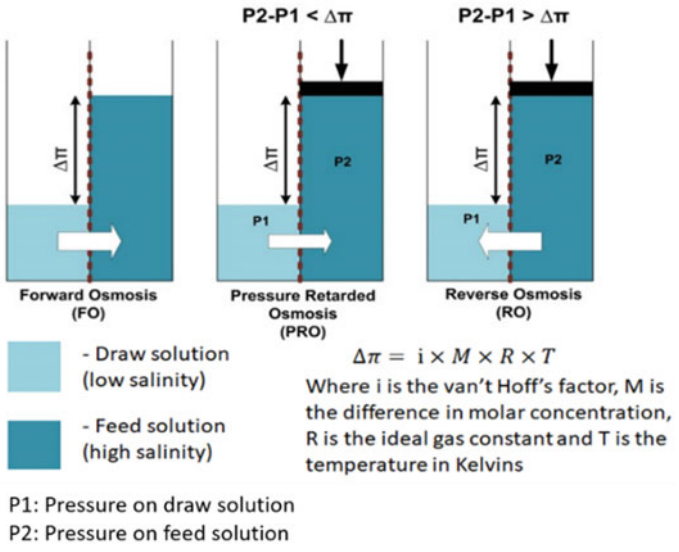

Fig. 1 Schematic depicting the three osmotic processes

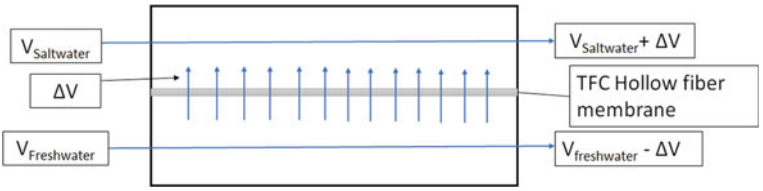

Fig. 2 Diagram of the PRO process

m^3 of water are desalinated [10, 11]. The product of desalination is concentrated brine that can harm the marine environment if it is being discharged indiscriminately. The brine has high salinity and it can generate high energy output. Therefore, we can utilize the seawater brine to not only generate high osmotic power but also cut cost for the treatment of seawater brine for disposal [12, 13]. Membranes are the core of PRO technologies; however, research progress was slowed down as it lacks effective and efficient membrane. There were pioneers in using the PRO process to generate energy. One of them is Statkraft of Norway, they used seawater and river water as feed and draw solutions respectively and built the first PRO prototype plant in 2009. However, in 2014, they terminated the plant. This might be due to technology immaturities at that point of time i.e. lack effective membrane, membrane fouling, and limited salinity gradient between the draw and feed solutions that results in small power output. According to analysis done by Stakraft, we need to generate at least 3 W/m^2 of power density for hollow fiber membranes so that the process is commercially viable [3, 14]. Figure 3 shows the theoretical profile of osmotic power density against operating pressure. The theoretical power density is the highest when the operational pressure is around half of the osmotic pressure difference. Therefore,

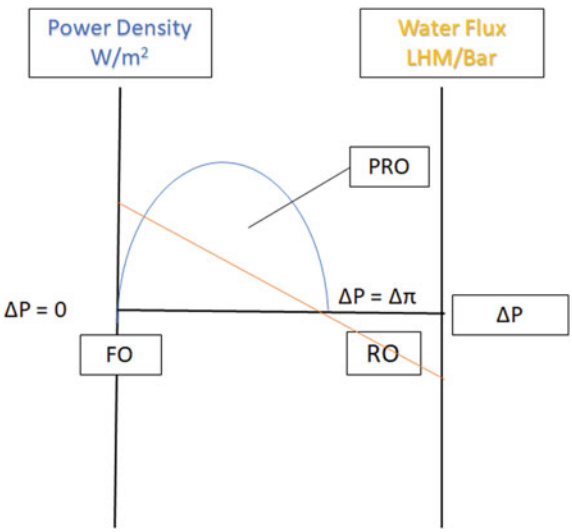

Fig. 3 Graphs of PRO water flux and power density against operating pressure

novel PRO membranes are required to withstand the high operational pressure and achieve high power density output.

We used phase inversion and interfacial polymerization in the fabrication of PRO membranes. These 2 methods result in the formation of the hollow fiber substrate layer and the ultrathin polyamide selective layer. This layer is above the porous and robust support layer. This allows us to achieve high water flux and high salt rejection. Our aim of our project is to develop TFC hollow fiber membranes that can generate commercially viable energy.

2 Experimental

A. *Chemicals and materials*

For the preparation of the polymer dope, we used polyethersulfone (PES), n-methyl-2-pyrrolidone (NMP) and polyethylene glycol 400 (PEG 400) as solvents. The polymer dope is used to form the hollow fiber membrane substrate layer. After that, we treated the as-spun hollow fiber substrates with 50/50 weight percentage of glycerol solution. Isopropanol (IPA) was used to wet the membrane substrates in advance before proceeding with interfacial polymerization [15]. We used trimesoyl chloride (TMC), m-phenylenediamine (MPD), sodium dodecyl sulphate (SDS) for interfacial polymerization. In our membrane characterizations and test for PRO performance, we used sodium chloride (NaCl).

B. *Fabrication of TFC-PES hollow fiber membranes*

The dried PES polymer was added in batches to a mixture of NMP and PEG 400 in a round-bottom flask to make the polymer dope. This mixture is continuously stirred overnight under heating until all PES polymers have dissolved and a homogenous solution was obtained. The solution was then degassed and loaded into a syringe pump, ready for the Dry-jet wet spinning process.

C. *Dry-jet wet-spinning process*

Phase inversion is a demixing process where a homogeneous solution of a polymer and solvent is immersed in a coagulation bath containing a nonsolvent. The polymer solution is converted into two phases: (1) a polymer-rich phase, which is the membrane with an asymmetric structure and (2) the liquid-rich phase. The membrane substrate layer was then fabricated via the dry-jet wet-spinning process using a single layer spinneret.

As shown in Fig. 4, the spinneret consists of a needle and an annulus flow channel. Water is ejected through the lumen of the needle to induce the internal coagulation and give the “hollow” part of the hollow fiber, while the polymer dope is ejected through the annulus channel so that the forming membrane has a hollow cylindrical shape. As the forming hollow fiber enters the coagulant bath of water, it solidifies and forms a solid hollow fiber through the phase inversion process. The properties of the

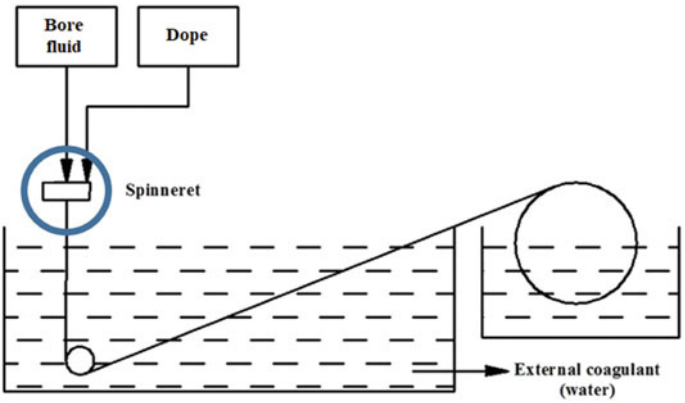

Fig. 4 Dry-jet wet-spinning schematic diagram

as-spun hollow fiber, such as morphology, average pore size, membrane thickness could be manipulated by changing the spinneret dimension, air gap distance as well as take-up speed. After that, we soaked the hollow fiber substrate in water for two days to remove any NMP residues [16]. The hollow fiber substrate was then treated in a 50/50 by weight glycerol aqueous solution. After that, the hollow fiber substrate was dried at ambient temperature.

D. *Interfacial polymerization*

Three PES membrane substrates hollow fibers were assembled in a parallel configuration into lab scale test modules as depicted in Fig. 5.

We wetted the module with isopropanol alcohol on the inner side of the hollow fiber substrate for 30 s and then soaked it in DI water for an hour before carrying out interfacial polymerization [17]. Firstly, the hollow fibers were wetted by 2% aqueous solution containing 0.1% SDS for 3 min on their lumen side. The module

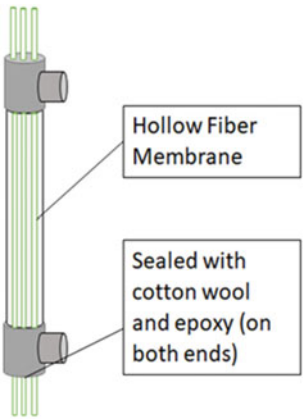

Fig. 5 Schematic of lab scale module

was then purged with air to remove excess MPD solution for 5 min. Next, the hollow fiber substrates were wetted with hexane solution containing 0.15% TMC for 5 min. This results in the formation of a thin polyamide selective layer [17]. The TFC-PES hollow fibre membrane was then purged with air to remove any residual hexane before being stored completed membranes in DI water to prevent breakdown of the selective layer.

E. *Characterization of PES hollow fiber substrates*

We used field emission scanning electron microscopy to obtain membrane morphologies. We used Instron tensiometer to obtain the tensile strengths of our hollow fibers. The eleongation rate is 10 mm/min and the initial length of the membrane substrate is 50 mm.

F. *Characterization of TFC-PES hollow fiber membrane*

Pure water permeability (PWP) (L/(m^2 h bar), LMH/bar) testing is carried out to determine the permeability of the hollow fibre membrane. In this test, DI water is used for both the lumen and shell side. The membrane module first undergoes a conditioning phase at 30 bar. After conditioning, pressure is reduced to 10 bar and the change in mass of water on the shell side is measured against time. The PWP (A) is calculated as:

$$A = \frac{\Delta V}{M \Delta t \Delta P} \tag{1}$$

ΔV (L) is the change in volume of water in the draw solution. Δt (h) is the time period of the test. M (m^2) is the effective membrane area. ΔP (bar) is the operating pressure [17]. Salt rejection testing is conducted to test membrane rejections (R). In this test, 2000 ppm NaCl solution is used at the lumen side while DI water is used at the shell side. This test does not have a conditioning phase. The membrane module is directly subjected to 10 bar of pressure and the change in conductivity and mass at the shell side is measured against time. We calculate R by measuring the change in conductivity of the draw and feed solutions using the following equation:

$$R = \left(1 - \frac{C_p}{C_f}\right) \times 100\% \tag{2}$$

where C_f is the concentration of the feed solution and C_p is the concentration of the permeate solutions.

G. *Osmotic power generation* via *the PRO process*

The PRO tests are conducted by running 1.0 M NaCl draw solution at the lumen side and DI water as feed solution at the shell side. The experimental conditions are summarized in Fig. 6. The membrane module first undergoes a conditioning phase at 30 bar. After conditioning, the pressure is reduced to 10 before increasing up to

Fig. 6 PRO experimental conditions

Lumen side draw solution		Shell side feed solution	
Flowrate (ml/min)	200	Flowrate (ml/min)	200
Pressure (bar)	0 - 30	Pressure (bar)	0 - 30
Temperature (°C)	25	Temperature (°C)	25

30 bar at fixed intervals. At each interval, the change in conductivity at both the shell and lumen side and change in mass of water at the shell side is measured against time.

The water permeation flux J_w (LMH) is calculated with the formula below

$$J_w = \frac{\Delta V_f}{M \Delta t} \tag{3}$$

The theoretical osmotic power density, W, is calculated from

$$W = \frac{J_w}{36} \tag{4}$$

3 Results and Discussion

A. *Morphology of PES hollow fiber substrate*

The morphologies of the PES hollow fiber substrates are shown in Fig. 7. Since we used water as both the bore fluid and external coagulant, dense skins are formed on both the inner and outer surfaces. We can observe 3 layers in the PES hollow fiber substrate. The outer layer is very irregular and porous. The layer in between has short macrovoids near the inner skin. The inner layer is a very thin, dense and it is a sponge-like layer with small surface pores. The inner layer is good for interfacial polymerization. This membrane substrate acts as a porous and robust support layer

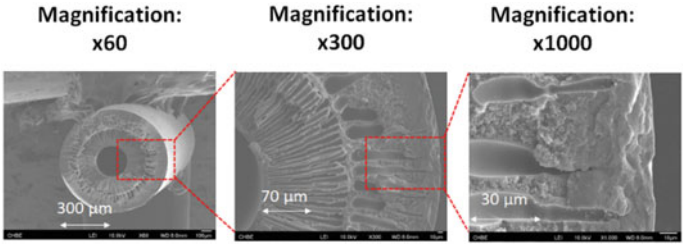

Fig. 7 FESEM images of the cross-sections of PES hollow fiber substrates

for the ultrathin polyamide selective layer on top to achieve high water flux and high salt rejection. Table 2 shows the dimensions of the two PES hollow fiber substrate fabricated.

B. *Mechanical strengths of the PES hollow fiber substrates*

Barlow's equation is used to calculate the burst pressure [15].

$$P \approx \frac{2x\tau}{OD} \tag{5}$$

In this equation, x is wall thickness, τ is the tensile stress, OD is the outer diameter of the membrane and P is the burst pressure. As tensile strength increases burst pressure increase. Membrane A's tensile strength is 5.11 MPa and its burst pressure is 61.9 bar. Membrane B's tensile strength is 5.97 and its burst pressure is 63.9 bar.

C. *PRO performances*

Both membranes possess a high NaCl rejection which are listed in Fig. 8. Since both the thin film composite membranes have the same thickness of the selective layer, their PWP decreases as the thickness of the hollow fiber increases. Membrane B has a thinner hollow fiber support layer, therefore it has a higher PWP.

As the operating pressure increases, the water flux and PWP for both membranes decrease as depicted in Fig. 9. This is consistent with the theoretical graph of water flux against operating pressure in Fig. 3. Figure 10 shows the power density against operating pressure of the TFC hollow fiber membranes. Membrane A has achieved a peak power density of 6 W/m^2 at 15 bar while membrane B has achieved a peak power density of 12 W/m^2 at 15 bar. This is consistent with the parabolic profile of power density against operating pressure in Fig. 3. The power density against operating pressure graph for Membrane A has apparent outliers, but due to limitations, we are unable to repeat the test. The difference in power density between these two membranes can explained by the thickness of hollow fiber membrane. However, a thinner wall has other implications and we need to optimize these parameters. For example, thin hollow fiber support layer in B results in a larger drop in water flux and PWP as the operating pressure increases, as compared to A. A small outer diameter

Fig. 8 Properties of membrane A and B

Parameter	Membrane A	Membrane B
Inner diameter (μm)	310.4	295.9
Outer diameter (μm)	1101.6	1053.0
Effective area (m²)	0.0004388	0.0004183
Salt rejection (%)	89.4965	95.7057
PWP (LMH/bar)	4.8767	5.2352
Maximum tensile stress (MPa)	5.11	5.97
Burst pressure (bar)	61.9	63.9

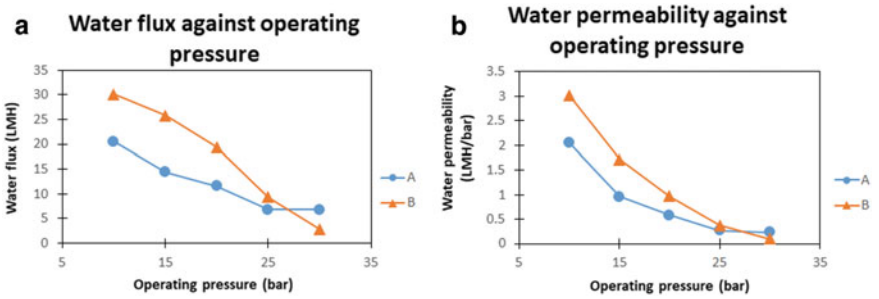

Fig. 9 Graphs of water flux against operating pressure and water permeability against operating pressure for membrane A and B

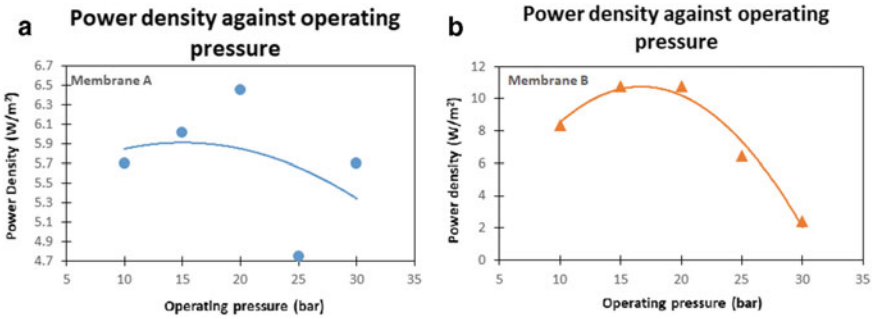

Fig. 10 Graphs of power density against operating pressure for membrane A and B

favours a high burst pressure, but it might induce severe pressure drop along the membrane module and this will greatly increase the operational costs.

D. *PRO-RO System*

PRO is especially applicable in Singapore which relies heavily on desalination. Two scenarios are depicted in Fig. 11. In the first scenario of an integrated PRO-RO system, the concentrated brine from desalination can be used as the saltwater for PRO. The seawater brine from RO possesses a high pressure and a high concentration of salts, but it has fewer foulants because of the preceding seawater pretreatment. The pressurized concentrated brine will first pass through an energy recovery device to lower the pressure to the PRO operating pressure and the osmotic energy can be harvested from PRO. The energy generated can compensate for the energy consumed during desalination. In the second scenario, PRO can be used first to dilute and treat the seawater used for desalination, harvesting osmotic energy and diluting the seawater feed to RO at the same time. With PRO pre-dilution, seawater RO can operate at a much lower pressure to achieve the same seawater recovery.

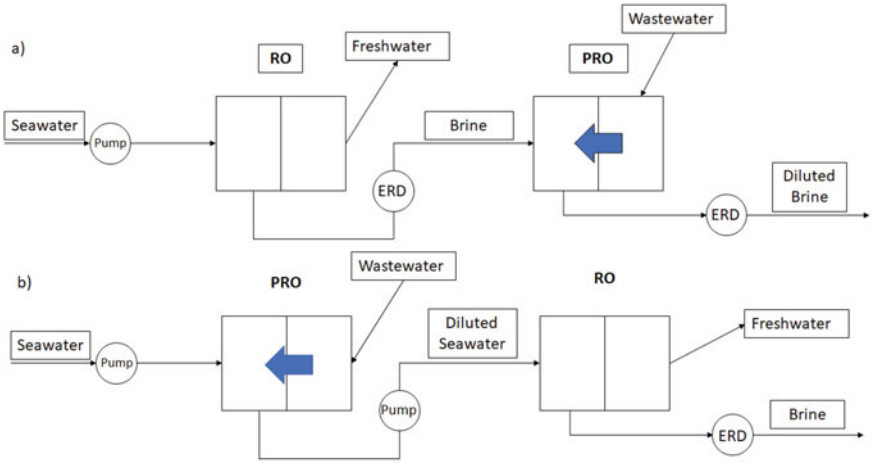

Fig. 11 **a** Schematics for RO-PRO and **b** PRO-RO integrated processes

4 Conclusion

PRO is a technology with significant potential in harvesting clean energy. In this project, we have successfully fabricated membranes that are strong, highly permeable with high salt rejection through direct phase inversion and interfacial polymerization. We have achieved a peak power density of 12 W/m^2 which is higher than 3 W/m^2 for PRO to be commercially viable. We have also synthesised the strongest inner selective hollow fiber thin film composite membrane for PRO thus far. However, there are apparent limitations in our project. Our PRO performance was calculated theoretically without using turbines. Instead of using actual wastewater and seawater, we synthetically created NaCl solutions. It should be noted that the actual power output depends on both the membranes' efficiency as well as turbine design and the efficiency of energy recovery devices. PRO is an exciting technology and future studies can investigate the possibility of large-scale operation in PRO-RO plants for commercial energy production.

Acknowledgements We would like to thank of our mentor Dr Wan Chunfeng, Professor Chung Tai-Shung Neal from NUS Department of Chemical and Biomolecular Engineering as well as our teacher mentor Dr Teh Yun Ling for their continuous support throughout this journey. Additionally, this research study is supported by the National Research Foundation, Prime Minister's Office, Republic of Singapore, under its Environmental and Water Technologies Strategic Research Programme and administered by the Environment and Water Industry Programme Office (EWI) of the PUB. This research work was funded by the projects entitled "Development of 8 inch Novel High Efficiency Pressure Retarded Osmosis (PRO) Membrane Modules towards Potential Pilot Testing and Field Validation" (USS-IF-2018-1) and NUS grant number of R-279-000-555-592. Special thanks would be given to Separation Technologies Applied Research and Translation (START) Centre, Singapore for their kind help.

References

1. World Energy Outlook 2013. (2013). World Energy Outlook. https://doi.org/10.1787/weo-2013-en.
2. Skilhagen, S. E., Dugstad, J. E., & Aaberg, R. J. (2008). Osmotic power—power production based on the osmotic pressure difference between waters with varying salt gradients. Desalination, 220(1–3), 476–482. https://doi.org/10.1016/j.desal.2007.02.045.
3. Thorsen, T., & Holt, T. (2009). The potential for power production from salinity gradients by pressure retarded osmosis. *Journal of Membrane Science*, *335*(1–2), 103–110. https://doi.org/10.1016/j.memsci.2009.03.003.
4. Achilli, A., Cath, T. Y., & Childress, A. E. (2009). Power generation with pressure retarded osmosis: An experimental and theoretical investigation. *Journal of Membrane Science*, *343*(1–2), 42–52. https://doi.org/10.1016/j.memsci.2009.07.006.
5. Logan, B. E., & Elimelech, M. (2012). Membrane-based processes for sustainable power generation using water. Nature, 488(7411), 313–319. https://doi.org/10.1038/nature11477.
6. Chung, T.-S., Li, X., Ong, R. C., Ge, Q., Wang, H., & Han, G. (2012). Emerging forward osmosis (FO) technologies and challenges ahead for clean water and clean energy applications. Current Opinion in Chemical Engineering, 1(3), 246–257. https://doi.org/10.1016/j.coche.2012.07.004.
7. Chung, T.-S., Zhang, S., Wang, K. Y., Su, J., & Ling, M. M. (2012). Forward osmosis processes: Yesterday, today and tomorrow. Desalination, 287, 78–81. https://doi.org/10.1016/j.desal.2010.12.019.
8. Han, G., Zhang, S., Li, X., & Chung, T.-S. (2015). Progress in pressure retarded osmosis (PRO) membranes for osmotic power generation. Progress in Polymer Science, 51, 1–27. https://doi.org/10.1016/j.progpolymsci.2015.04.005.
9. Tedesco, M., Scalici, C., Vaccari, D., Cipollina, A., Tamburini, A., & Micale, G. (2016). Performance of the first reverse electrodialysis pilot plant for power production from saline waters and concentrated brines. Journal of Membrane Science, 500, 33–45. https://doi.org/10.1016/j.memsci.2015.10.057.
10. Wan, C. F., & Chung, T.-S. (2016). Energy recovery by pressure retarded osmosis (PRO) in SWRO–PRO integrated processes. Applied Energy, 162, 687–698. https://doi.org/10.1016/j.apenergy.2015.10.067.
11. Wan, C. F., & Chung, T.-S. (2015). Osmotic power generation by pressure retarded osmosis using seawater brine as the draw solution and wastewater retentate as the feed. Journal of Membrane Science, 479, 148–158. https://doi.org/10.1016/j.memsci.2014.12.036.
12. Palacin, L. G., Tadeo, F., Prada, C. D., & Touati, K. (2012). Evaluation of the recovery of osmotic energy in desalination plants by using pressure retarded osmosis. Desalination and Water Treatment, 51(1–3), 360–365. https://doi.org/10.1080/19443994.2012.715130.
13. J.L. Prante, J.A. Ruskowitz, A.E. Childress, A. Achilli, RO-PRO desalination: an integrated low-energy approach to seawater Desalination, Appl. Energy 120 (2014) 104–114.
14. Achilli, A., & Childress, A. E. (2010). Pressure retarded osmosis: From the vision of Sidney Loeb to the first prototype installation—Review. Desalination, 261(3), 205–211. https://doi.org/10.1016/j.desal.2010.06.017.
15. Oberg, E., & Green, R. E. (1997). Machinerys handbook: a reference book for the mechanical engineer, designer, manufacturing engineer, draftsman, toolmaker, and machinist. New York: Industrial Press.
16. Cheng, Z. L., Li, X., Feng, Y., Wan, C. F., & Chung, T. (2017). Tuning water content in polymer dopes to boost the performance of outer-selective thin-film composite (TFC) hollow fiber membranes for osmotic power generation. *Journal of Membrane Science, 524*, 97–107. https://doi.org/10.1016/j.memsci.2016.11.009.
17. Wan, C. F., Yang, T., Gai, W., Lee, Y. D., & Chung, T. (2018). Thin-film composite hollow fiber membrane with inorganic salt additives for high mechanical strength and high power density for pressure-retarded osmosis. *Journal of Membrane Science, 555*, 388–397. https://doi.org/10.1016/j.memsci.2018.03.050.

Bioremediation of Arsenic-Contaminated Water Through Application of Bioengineered *Shewanella oneidensis*

Hong Meng Yam, Sean Kar Weng Leong, Xinzhi Qiu, and Norazean Zaiden

Abstract This study aims to determine the bioremediation potential of bioengineered *Shewanella oneidensis* as a cost-effective alternative for arsenic (As) removal from groundwater, as opposed to the current complex and hazardous chemical and physical methods. Herein we present a novel filtration method, by bioengineering a bacterium with bioremediation potential, *S. oneidensis* MR-1, to express As-binding protein, ArsR, as it adopts a biofilm lifestyle. The recombinant *S. oneidensis* (M) was compared to its wild-type MR-1 (WT) across a range of As concentrations (0–800 μM) and time (0–48 h) in its planktonic and biofilm form. Analyses of As-sorption in the wild-type MR-1 and recombinant indicated significant sequestration which increased with time incubated, while As-sorption did not plateau even at high As concentrations of 800 μM. The recombinant displayed significantly higher As sequestration than the wild type ($p < 0.0001$; cohen's $d = 122.4$), with higher sequestration observed in the planktonic compared to the biofilm form ($p < 0.0001$; cohen's $d = 4.262$). Filtration efficiencies of 87% and 94% were obtained for As(III) and As(V) respectively using our system, showing a significant improvement over current commercial systems. With applications in potable water and industrial wastewater filtration, especially for rural and underdeveloped countries given the lack of reliance on specialized equipment, this system represents a powerful potential next-generation Arsenic filtration method.

H. M. Yam (✉) · S. K. W. Leong · X. Qiu
NUS High School of Mathematics and Science, Singapore, Singapore
e-mail: h1510158@nushigh.edu.sg

S. K. W. Leong
e-mail: h1510112@nushigh.edu.sg

X. Qiu
e-mail: h1510108@nushigh.edu.sg

N. Zaiden
Singapore Centre for Environmental Life Sciences Engineering, Nanyang Technological University, Singapore, Singapore

H. Guo et al. (eds.), *IRC-SET 2020*,
https://doi.org/10.1007/978-981-15-9472-4_49

Keywords Arsenic · Bioremediation · Bacteria · Biofilms · Planktonic · Bioengineer · Filtration · Rural · Underdeveloped · Simple · *Shewanella oneidensis* · Water · Contaminate · Groundwater

1 Introduction

1.1 Global Issue of Arsenic-Contamination in Consumable Water

The contamination of groundwater with arsenic (As) is a current global crisis. Arsenic sources include geological (e.g. volcanic eruptions, leaching of natural ores) and anthropogenic sources (e.g. pesticides and fertilizers in agriculture, textile dyeing processes) [1]. Among all its forms, the As(III) and As(V) species are predominant.

In some areas (such as parts of Bangladesh), As levels in groundwater were determined to be above 5000 μg/l, far exceeding WHO guide limits of 10 μg/l [2]. Unlike other organic contaminants which can degrade into harmless constituents, inorganic As cannot be degraded. This is detrimental to the health of those consuming the contaminated groundwater, leading to arsenicosis, carcinogenesis and skin lesions [3].

1.2 Current Strategies of As-Removal

Conventional As-removal strategies include coagulation-flocculation, sorption and ion exchange techniques [4], as well as membrane techniques such as reverse osmosis [5]. However, most of these filtration systems are complex and expensive to install and maintain, making them impractical for rural use.

Current research has tried to involve the use of microbes which play key roles in geochemical cycles [6]. They act as geoactive agents that can transform several metal species via solubilization and immobilization. When exposed to As, they detoxify it via enzymatic reactions [7] and biomethylating arsenite to the less toxic trimethylarsine [8]. Many of such traditional strategies involve the oxidation of As(III) to As(V), followed by the removal of the less water-soluble As(V). For example, removal of As in polystyrene bead filtration systems by iron-reducing bacteria reduced the As(III) levels from 60 to 10 μg/l in 4 days and is effective for long term use [9]. Nonetheless, these strategies are still unable to outperform conventional filtration methods in terms of efficacy and cost, and as such, are still unsuitable for widespread usage in rural areas.

1.3 Biofilms as a Bioremediation Strategy for As-Removal

While current microbial bioremediation strategies may display low efficacy, the exploitation of the biofilm forms of microorganisms may ameliorate this disadvantage. Microorganisms in natural systems can exist in either the planktonic or the biofilm form. Planktonic cells are free-moving, while biofilms are aggregates of microorganisms encased in a self-produced matrix termed the extracellular polymeric substances (EPS) [10].

Various components in the EPS may function as electron-donors or electron-acceptors, permitting redox reactions to occur in the biofilm matrix and aiding the detoxification process of several toxic metal ions. For example, once positively charged heavy metal ions are sequestered effectively due to the net anionic makeup of the EPS biopolymer, groups of proteins (pili and nanowires in the EPS) and humic substances can oxidize or reduce these metal ions [11].

1.4 Genetic Fusion to Exploit MR-1 Biofilm Advantages

In this study, we bioengineered a novel *Shewanella oneidensis* (MR-1) bacteria and investigated its efficacy for the bioremediation of As in both biofilm and planktonic forms. MR-1 was chosen due to its ability to reduce heavy metals and form biofilms on metal oxides [12], as well as methylate inorganic arsenic into less toxic organo-arsenic compounds which can be metabolised by the bacterium [11].

This study involves the genetic fusion of *arsR* to Biofilm-Promoting Factor A gene (*bpfA*), resulting in the genes being translated into a single chimeric protein during biofilm formation, which is then exported out of the cell as the EPS matrix develops [13].

arsR is a structural gene of the ars operon that is responsible for As detoxification. This structural gene encodes a transcriptional repressor that regulates expression of the ars operon. Thiol groups of ArsR cysteine residues (of the transcriptional repressor) are able to bind reversibly to inorganic arsenic, initiating transcription of the operon. [13] The ars operon also contains the structural gene arsC which encodes Cytoplasmic As reductase, allowing the reduction of As(V) to As(III).

The other component, *bpfA*, is essential for biofilm formation in MR-1 as extracellular BpfA is a predominant EPS matrix component that holds the EPS matrix together [13]. Putatively, this presents extracellular ArsR for the sequestration of extracellular inorganic As. Extracellular ArsR bound to the biofilm may thus serve as a competent As-binding module that can immobilise As.

Therefore, instead of oxidizing As(III) to As(V) as in traditional bioremediation methods, M reduces As(V) to As(III), removing As(III) via the ArsR-BpfA chimeric protein due to the greater binding affinity of ArsR to As(III) than As(V) [14]. This leads to potential development of a novel, sustainable, competent and cost-effective

As removal solution, reducing reliance on complicated physical systems and omitting the increased environmental burden of chemical application.

1.5 Our Study

Herein we developed and and characterised the efficacy of our MR-1 mutation in increasing sorption of both As(III) and As(V) to facilitate their removal from groundwater. Additionally, we explored the use of two different filtration systems for the removal of arsenic. Firstly, using a biofilm system, allowing for the complete formation of an EPS matrix with ArsR-BpfA chimeric protein embedded in it. The second method would be using MR-1 in the planktonic form, where the constant disruption of the biofilm formation to facilitate continuous secretion of the ArsR-BpfA chimeric protein into the synthetic groundwater environment.bind to arsenic in significant amounts, sequestering it and facilitating its removal from groundwater.

2 Methodology

2.1 Conditions

Reaction was conducted in synthetic groundwater (SGW) (Appendix 1). To obtain mutant MR-1, arsR was fused to bpfA (Appendix 3). The use of planktonic and biofilm (Appendix 6) forms of M and WT MR-1 were compared through As-sorption capacity determination and As-binding isotherm.

Each experiment was performed with 3 biological and 3 technical replicates and the total protein amount of the initial biomass was measured using Qubit Protein Assay (Life Technologies) to derive results as sorped As nmol/mg of protein.

Equivalent aliquots of abiotic control (Ab), planktonic WT and M (both OD 0.2 600 nm biomass) were pelleted at 14,000 rpm for 2 min before being washed with SGW of pH 7. The bacteria was pelleted again. For As-sorption capacity determination, the pellet was resuspended in SGW spiked with As(III) or As(V) of varying concentrations (μM): 0.0,0 6.25, 12.5, 25.0, 50.0, 100.0, 200.0, 400.0, 800.0. Reactions were performed at 30 °C, 200 rpm for 1 h.

For As-binding isotherm, the pellet was resuspended in SGW spiked with 10 μM As(III) or As(V). Reactions were performed at 30 °C, 200 rpm for different timepoints (h): 0, 10, 24, 48.

The bacteria were spun down and [As(III)] and [As(V)] remaining in the supernatant was determined using Molybdenum-blue As-colorimetric assay [15] (Appendix 5).

2.2 Biofilm

Equivalent aliquots of the harvested biofilms (biomass OD 0.2) in SGW pH 8.5 were spiked with 10 μM As(III) or As(V) in a reaction volume of 15 ml. Reactions were performed at 30 °C, 200 rpm over 48 h. Samples of the supernatant were collected at time-points (h): 0, 4, 10, 24, 48. All samples were diluted 10 × in distilled water, and syringe filtered (0.2 μm) before being analysed using ICP-MS. The amounts of sorped As was derived from the difference between the analysed supernatant and the initial spiked arsenic concentration.

3 Results

3.1 As-Sorption in Planktonic State

As-Sorption Increases as Concentration Increases
From Fig. 1a, b, we observe significant increases in As-Sorption as concentration of As in environment increases. Sorped As/Protein is proportional to As concentration ($r^2 = 0.996$) and it can be observed that As-Sorption does not plateau and thus the system does not reach capacity even at 800 μM of As(III) and As(V), which is almost 6000 times the WHO safe limit [16]. This is testament to this system's ability to even filter industrial wastewater, which has an average As concentration of only around 130 μM. [17]

As-Sorption Increases Over Time (Planktonic)
As-Sorption is also observed to increase with time in Fig. 2a, b, showing that constant uptake of arsenic it is observed that M displays a higher saturation point than WT for As-sorption in increasing As concentrations. However, this increase in sorption for As(III) is less than for As(V).

Mutant Displays Higher As Sorption than Wild Type, Increased Affinity for As(V)
The As-sorption potential for M is higher than WT ($p < 0.0001$; cohen's d = 122.4), with M showing As Sorption of around 1.5× that of WT after 48 h.

High basal As-sorption rates were seen, proving that background As-sorption of WT is high. For As(III), there was no significant difference in As-sorption between WT and M, while a substantial difference was observed for As(V), genetic fusion of arsR to bpfA had a greater effect on As(V) sorption than As(III) sorption ($p = 0.0007$; cohen's d = 1.988).

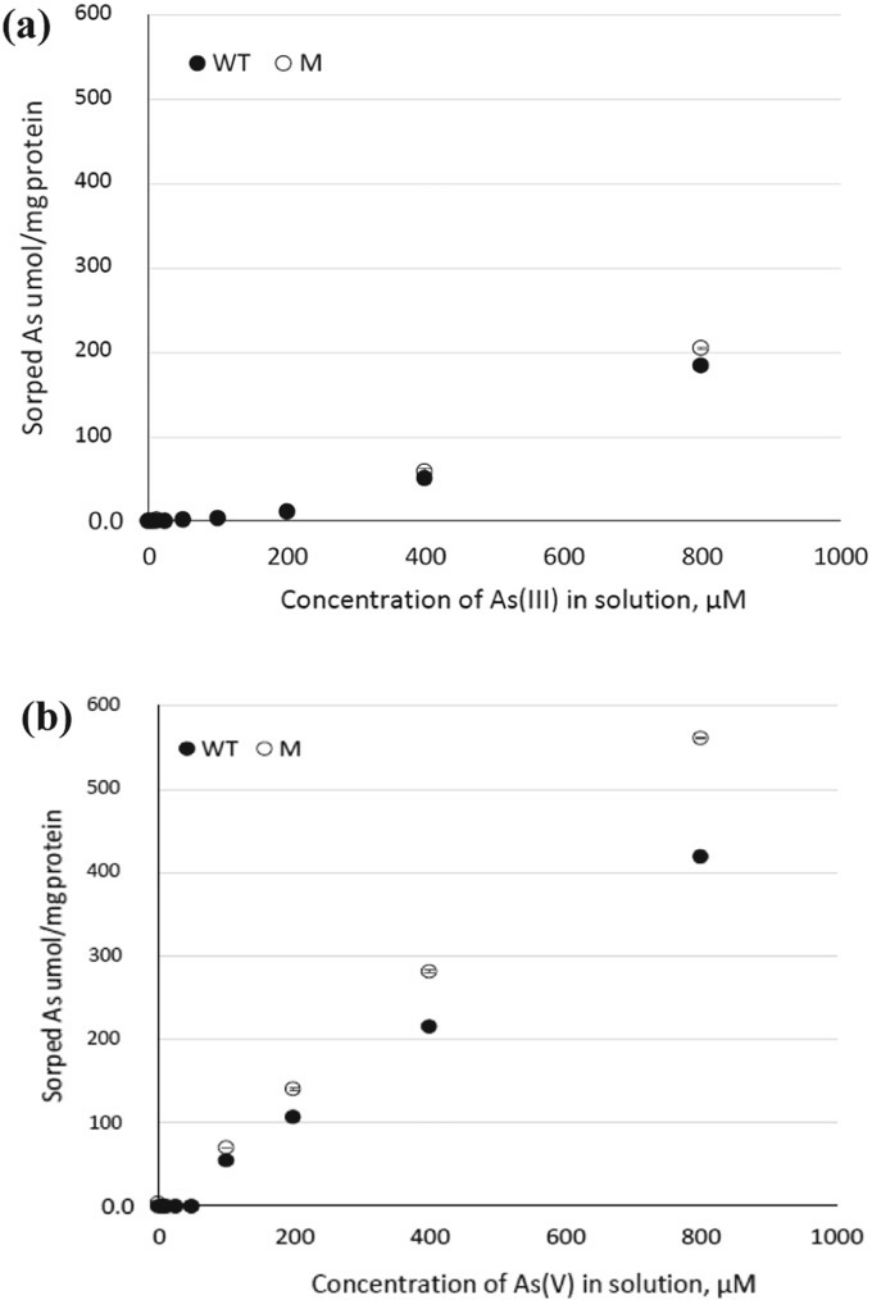

Fig. 1 **a** As(III) and **b** As (V) sorption capacity of wild type (WT) and mutant (M) bacteria in the planktonic state. Reactions were performed at 30 °C, 200 rpm for 1 h. All data is shown as mean ± standard error (n = 9)

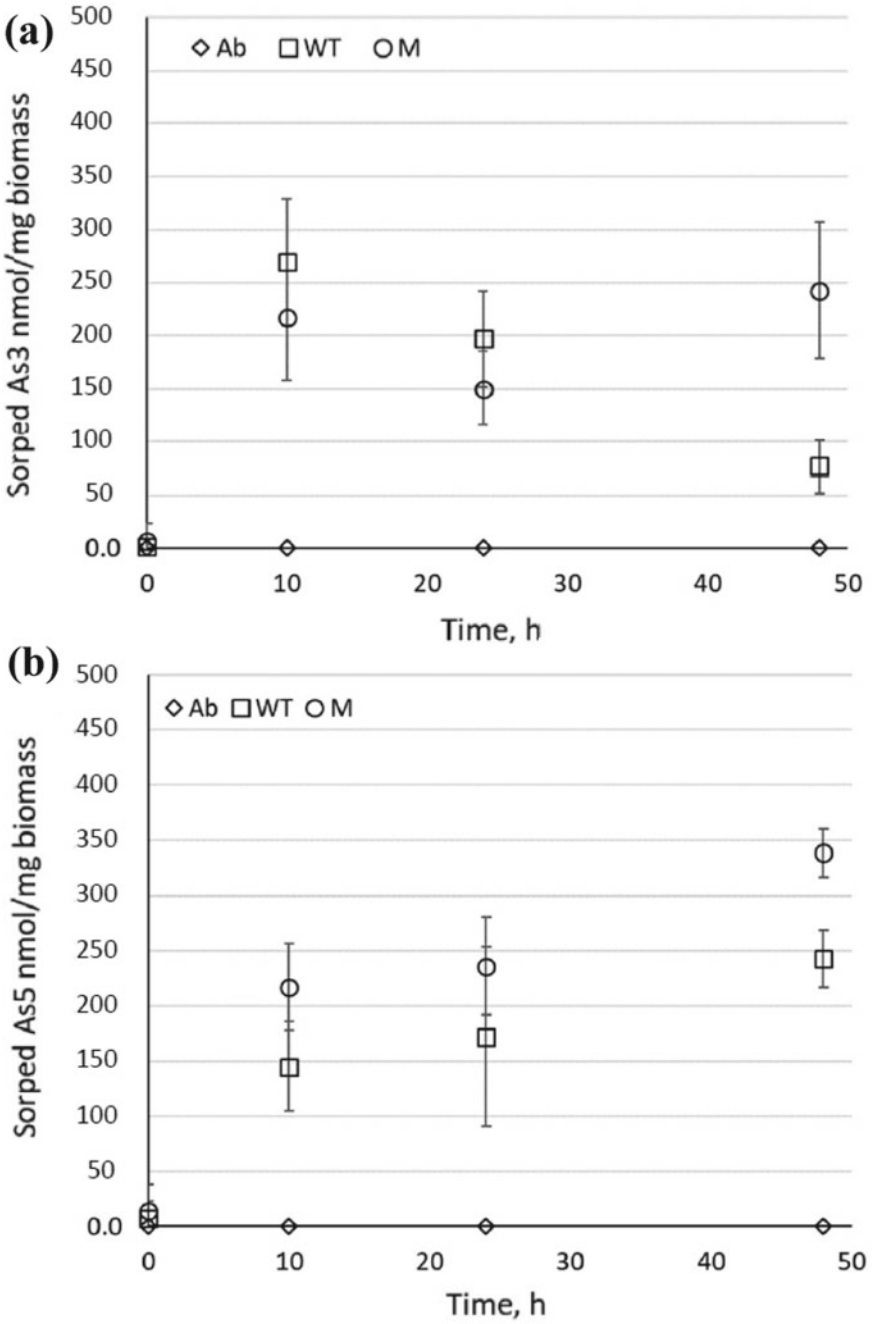

Fig. 2 **a** As(III)-binding isotherm and **b** As(V)-binding isotherm of wild type (WT) and mutant (M) bacteria in the planktonic form for a period of 48 h in solution spiked with 10 μM As. Reactions were performed at 30 °C, 200 rpm for different time-points (h): 0, 10, 24, 48. All data is shown as mean ± standard error (n = 9)

3.2 As-Sorption in Biofilm State

As-Sorption Increases Over Time (Biofilm)
Likewise, As-Sorption is shown to increase over time for bacterial in biofilm form. This shows that continued secretion of arsR into biofilm is likely to have taken place despite prior biofilm formation (Fig. 3).

4 Discussion

4.1 As-Sorption Analyses in M Show Potential in Enhanced as Sequestration

The hypothesis that the bioengineered MR-1 would have a greater As-sorption capacity was supported by the data collected.

In the planktonic form, as M MR-1 adopts a biofilm lifestyle, BpfA is co-expressed with ArsR, depositing Bpfa-ArsR proteins in the EPS matrix. This is evident from the higher As-sorption seen in M than WT for the planktonic MR-1 in both the binding isotherm and the sorption capacity determination.

The hypothesis was also supported by data collected for MR-1 in the biofilm form, with the binding isotherms showing increased sorption of both As(III) and As(V) for M as compared to WT, although this increase was less significant than the planktonic MR-1 experiments.

For both the biofilm and planktonic form, as well as M and WT, MR-1 shows a greater sorption of As(V) than As(III). This is likely due to MR-1 being able to better sequester As(V) in the EPS, as the hydrated form of As(III) is neutral while hydrated As(V) is an oxyanion [18]. As a result, As(III) is less able to participate in hydrogen bonding with the other components of the EPS, which may explain the lower As(III) sequestration than As(V).

Thus, in addition to As(V) being converted to As(III) by Cytoplasmic As reductase and then pumped out of the cell by the As efflux pump to be captured by the ArsR-BpfA chimeric protein, this sequestration likely increases the sorption of As(V) as compared to As(III), which is shown in the results collected.

4.2 Higher as Sequestration in Planktonic Than Biofilm State

The data indicates that M bacteria sequester more As(III) and As(V) in the planktonic state than in the biofilm state ($p < 0.0001$, cohen's $d = 4.262$). This may suggest that some of the Bpfa-ArsR chimeric protein may diffuse freely throughout the groundwater, instead of just being trapped in the EPS matrix. These free-diffusing

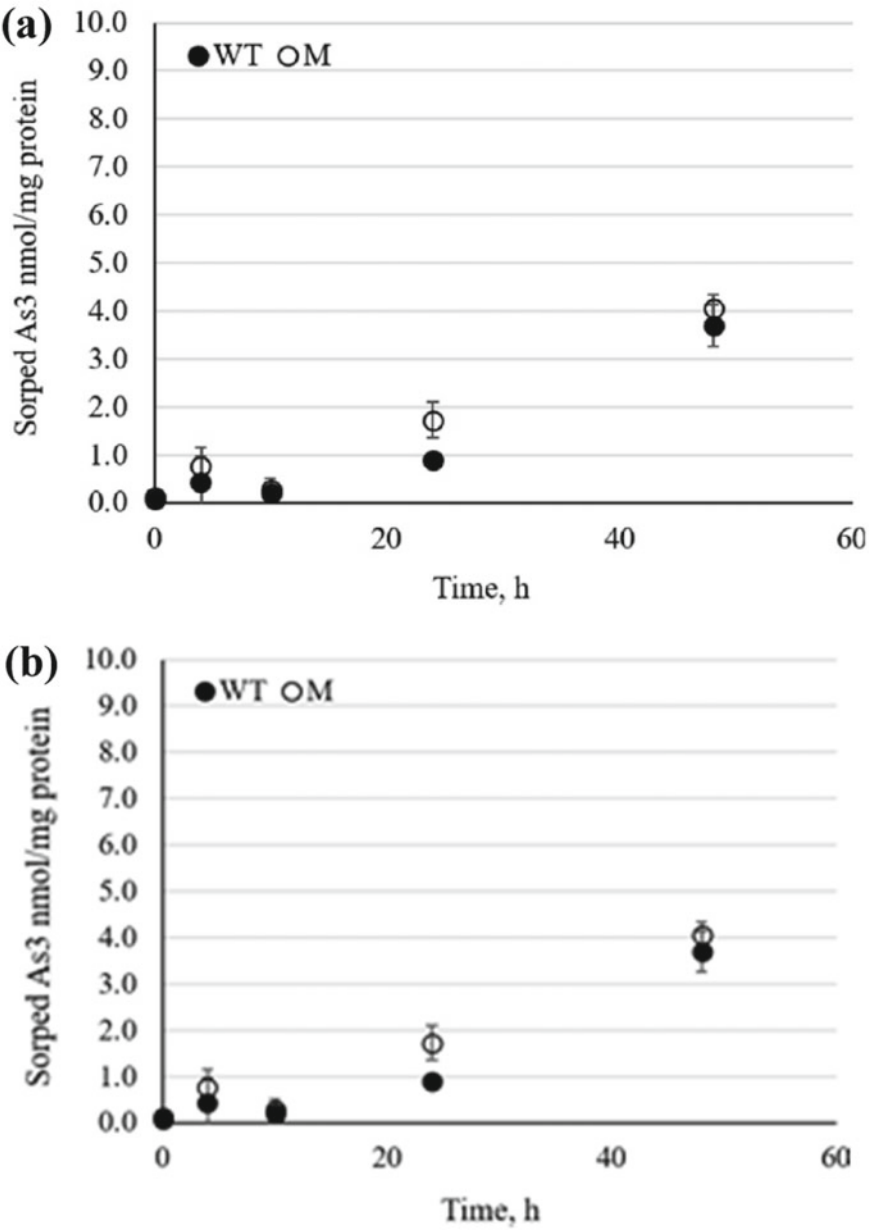

Fig. 3 **a** As (III)-binding isotherm and **b** As(V)-binding isotherm of wild type (WT) and mutant (M) bacteria in the biofilm form for a period of 48 h. Reactions were performed at 30 °C, 200 rpm for different time-points (h): 0, 10, 24, 48. All data is shown as mean ± standard error (n = 9)

proteins come into direct contact with As for binding, allowing an increased surface area and resulting in a higher As sequestration in planktonic form.

In addition, the biofilm macrostructure may also limit diffusion, as prior research has found that EPS can bar diffusion of anti-microbial agents [19] as well as retard the diffusion of heavy metals through the biofilm [20]. This may result in decreased access of BpfA-ArsR to As in the synthetic groundwater.

Nevertheless, the recombinant MR-1 displays better efficacy in As-sorption than WT in both forms. Hence, it is a better candidate for bioremediation of As-contaminated groundwater in the polystyrene bead filtration system than existing techniques using wild type bacterial strains.

4.3 Comparison with Conventional Filtration Techniques

From Fig. 4, the recombinant MR-1 (left) has an As(III) and As(V) filtration efficiency of 87% and 94% respectively, significantly higher than conventional filtration methods [21–24]. This is significantly better than the co-precipitation method used in specialized Arsenic removal plants in Bangledesh [25] and even Reverse Osmosis treatments to create potable water used in developed countries like the United States. [26]

Not only does our system show greater filtration efficiency, it possesses huge advantages in its simplicity. It does not suffer from the drawbacks of other high-efficiency methods due to their reliance on inorganic metals which may cause algal blooms. It also does not require heavy and expensive specialized equipment, and can function without electricity as bacterial can be cultivated at room temperature and removed through village slow sand filtration, and thus is suitable for use in rural and underdeveloped areas.

5 Future Studies

In addition to testing how the As-sorption of the M and WT bacteria in planktonic and biofilm forms varies with pH, future studies can test other physicochemical factors such as temperature, varying chemical compositions of the SGW and the addition of fine particulate matter, which will more accurately mimic the varying conditions of actual groundwater. Optimistically, varying physicochemical factors within the range of the real -life conditions would not affect As-sorption efficacy significantly. Another study that could be carried out can involve the testing and optimisation of the growth and As-sorption of planktonic bacteria placed into a sand filter and allowed to develop into a biofilm in the sand filter. SGW can then be cycled in from the top and out from the bottom of the sand filter. The process of biofilm formation is expected to produce BpfA-ArsR chimeric proteins that freely diffuses in the groundwater, giving a greater surface area to capture more As in groundwater before being trapped in

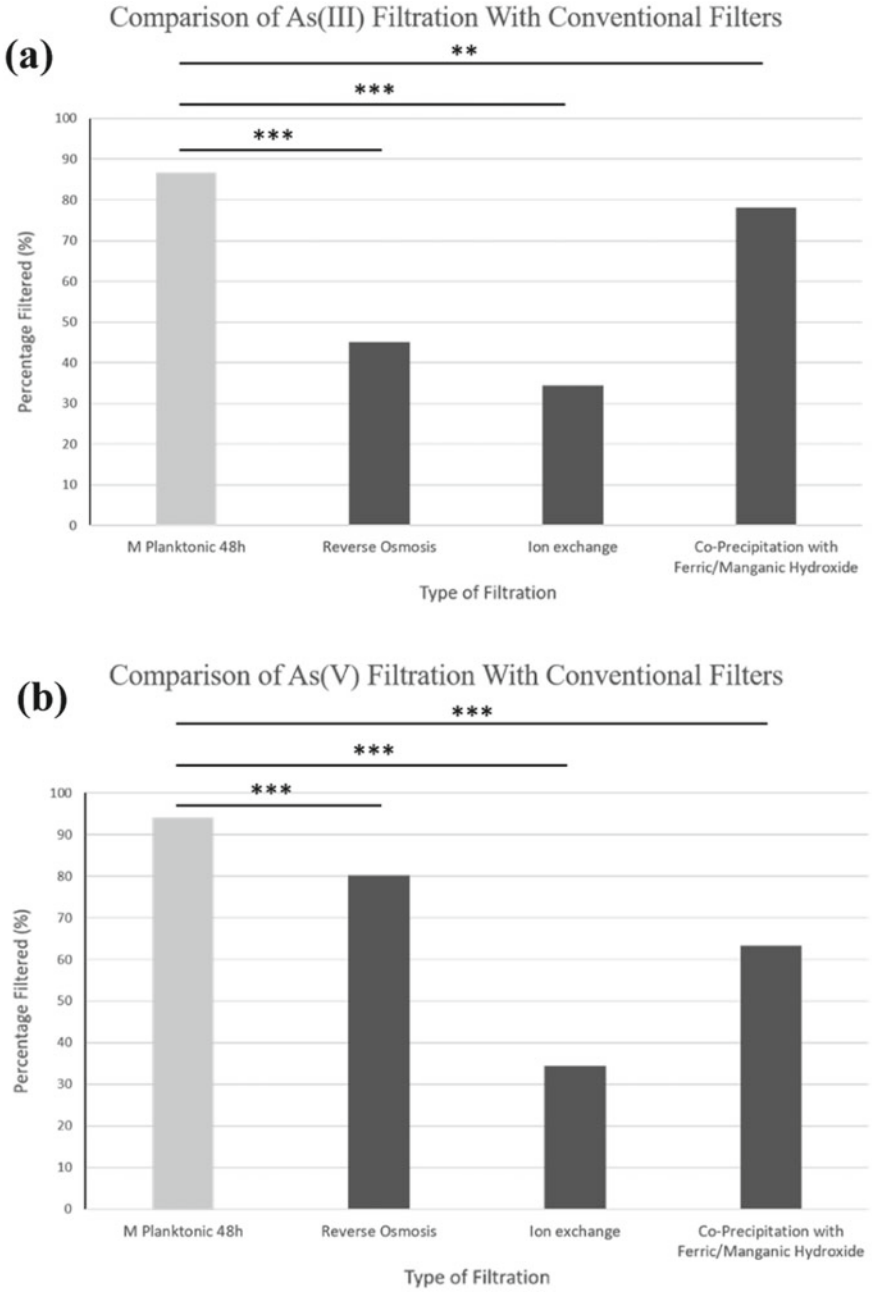

Fig. 4 Comparison of **a** As(III) and **b** As (V) filtration with conventional filters. A time period of 48 h is used for the M bacteria, bacteria in planktonic form. ***$p < 0.005$ **$p < 0.01$ *$p < 0.05$ (one tailed t-test)

the EPS rather than using a fully developed biofilm which has BpfA-ArsR trapped within the EPS.

6 Conclusion

The recombinant S.oneidensis MR-1 co-expressing arsR with chromosomal bpfA enabled it to sequester high amounts of As, particularly in the sorption of As(V). Additionally, the planktonic form sequestered more As than the biofilm form. Planktonic bacteria corresponding to an OD200 of 0.2 is capable of sorping high percentages of arsenic, comparable to or even higher than conventional methods. Thus, it has great potential for future applications in filters which capitalise on the efficacy of As-sorption of planktonic bacteria. The EPS matrix of the biofilm itself showed good capacity in As-sorption, of which incorporation of ArsR generated minimal difference in As-sorption enhancement since each ArsR has a capacity for binding only a single As element. Further improvement of biofilm-mediated As-sorption may require designing multiple binding domains to increase As sequestration.

The recombinant S.oneidensis MR-1 co-expressing arsR with chromosomal bpfA enabled it to sequester high amounts of As, particularly in the sorption of As(V). Additionally, the planktonic form sequestered more As than the biofilm form. Planktonic bacteria corresponding to an OD200 of 0.2 is capable of sorping high percentages of arsenic, comparable to or even higher than conventional methods. Thus it has great potential for future applications in filters which capitalise on the efficacy of As-sorption of planktonic bacteria, and can filter groundwater with varying pH effectively. The EPS matrix of the biofilm itself showed good capacity in As-sorption, of which incorporation of ArsR generated minimal difference in As-sorption enhancement since each ArsR has a capacity for binding only a single As element. Further improvement of biofilm-mediated As-sorption may require designing multiple binding domains to increase As sequestration.

With significantly greater As filtration efficiencies as compared to commercially used conventional filtration methods, both in developing and developed countries, coupled with removed reliance on inorganic metals and specialized equipment, herein we thus presented and established a filtration system with high potential for use in bioremediation of arsenic contaminated water.

Acknowledgements We would like to thank Ms Norazean Zaiden (Singapore Centre of Enviornmental Life Science Engineering) and Ms Lim Suat Fong Valerie (NUS High School of Mathematics and Science) for their guidance and mentorship.

This work was supported by NUS High School of Mathematics and Science, the Science Mentorship Programme, and the Ministry of Education, Singapore.

Appendix 1: Synthetic Groundwater (SGW) Recipe

SGW was prepared with the following chemicals (and their concentrations): $CaCl_2$ (2.500 mM), $MgSO_4$ (1.246 mM), NH_4Cl (0.168 mM), KNO_3 (replaced with $NaNO_3$ in this study) (0.059 mM), H_3PO_4 (0.032 mM), $SrCl_2.6H_2O$ (0.008 mM), $NH_46Mo_7O_{24}.4\,H_2O$ (0.016 mM),, $MnCl_2.4H_2O$ (0.091 mM), $NaHCO_3$ (7.799 mM), $FeSO_4.7\,H_2O$ (0.010 mM). Arsenic was then added. (Refer to Appendix 4).

Appendix 2: Standard Curves of As(III) and As(V) Methodology

Molybdenum blue As-colorimetric assay [15] was carried out on samples of known concentrations of As(III) and As(V), to obtain a standard curve that is able to convert absorbance read by the spectrophotometer (at 880 nm) to the concentration of As(III) or As(V) in the solution.

Appendix 3: Preparation of Wild-Type and Recombinant *S. oneidensis* MR-1 Methodology

Polymerase chain reaction (PCR) procedures were performed to fuse the *arsR* of wild-type (WT) MR-1 to the 5′-end of *bpfA*, before ligated to pUC57 vector to incorporate a kanamycin resistance gene and *aggC*, which is a gene downstream to the chromosomal *bpfA*. With these complementary sequences of chromosomal *bpfA* and *aggC*, the linearised fused gene product was transformed into MR-1 by electroporation procedure for homologous recombination to its chromosomal DNA. The starting culture was prepared in Luria–Bertani medium (LB) for 16 h at 30 °**C**, shaken at 200 rpm. Addition of antibiotic (kanamycin) is used for selection of M. The WT MR-1 was prepared without kanamycin addition.

Appendix 4: Preparation of As in Synthetic Groundwater Methodology

Arsenic stock solutions of As(III) and As(V) were prepared in distilled water using Sodium (meta) arsenite (Sigma Aldrich, S7400) and Sodium arsenate dibasic heptahydrate (Sigma Aldrich, S6756). The As(III) and As(V) concentrations in synthetic groundwater (SGW, refer to Supporting Document 1 [15]) were varied by serial diluting the stock solutions. The pH of SGW was manually adjusted using a pH meter by adding acid (HCl) or base (KOH).

Appendix 5: Calculation of As-Sorption Using the Molybdenum Blue As-Colorimetric Assay Method Methodology

As-colorimetric assay [14] was used to determine the amount of As(III) and As(V) remaining in the solution by reading using a spectrophotometer (at 880 nm). By using standard curves (Appendix 2), the absorbance was converted to the corresponding concentrations of As(III) and As(V) remaining in the solution, determining As sorped by WT and M. The steps for the colorimetric assay are as follows:

1. Use a micropipette to transfer 600 μL of reaction mixture to 3 sets of Eppendorf tubes; set T, set X and set R.
2. Add 18 μL of $KMnO_4$ solution to set X and 18 μL of 5% L-cysteine solution to set R, and mix the tubes using a vortex machine.
3. Heat set R at 80 °C for 1 h.
4. To all sets, add 30 μL of ascorbic acid, then 90 μL of acetone, and finally 120 μL of mixed reagent, mixing with a vortex machine after each addition. 100 mL of mixed reagent contains 5 mL antimony potassium tartrate, 50 mL 20% sulfuric acid, 15 mL ammonium molybdate and 30 mL of distilled water.
5. Use a micropipette to add 3 × 200 μL of the mixture to a 96-well plate, creating 3 technical replicates, and read the plate using a spectrophotometer at OD880.

Appendix 6: Preparation of WT and M Biofilms Methodology

Biofilms of MR-1 wild-type (WT) and *bpfA-arsR* recombinant (M) were allowed to form within a 15 cm silicone tubing of 0.3 mm inner diameter connected to a continuous supply of Minimal Medium 1 (MM1) pH 7.4 supplemented with 10 mM sodium lactate as carbon source. A starting inoculation volume of 1 ml from a 16 h culture at biomass of OD 1.0 prepared in Luria–Bertani medium (LB) at 30 °**C**, 200 rpm, were used. Attachment of the inoculated volumes were allowed for 2 h before initiating the pump flow of 3 ml/h. The biofilms were accumulated in the tubing for 1 week before harvested with 3 ml SGW pH 8.5 for downstream experiments.

References

1. Ferguson, J. F., & Gavis, J. (1972). A review of the arsenic cycle in natural waters. *Water research*, *6*(11), 1259-1274.
2. Mukherjee, A., Sengupta, M. K., Hossain, M. A., Ahamed, S., Das, B., Nayak, B., ... & Chakraborti, D. (2006). Arsenic contamination in groundwater: a global perspective with emphasis on the Asian scenario. *Journal of Health, Population and Nutrition*, 142–163.

3. Hong, Y. S., Song, K. H., & Chung, J. Y. (2014). Health effects of chronic arsenic exposure. *Journal of preventive medicine and public health*, *47*(5), 245.
4. Choong, T. S., Chuah, T., Robiah, Y., Koay, F. G., & Azni, I. (2007). Arsenic toxicity, health hazards and removal techniques from water: An overview. *Desalination, 217*(1-3), 139-166.
5. Ning, R. Y. (2002). Arsenic removal by reverse osmosis. *Desalination*, *143*(3), 237-241.
6. Tourney, J., & Ngwenya, B. T. (2014). The role of bacterial extracellular polymeric substances in geomicrobiology. *Chemical Geology*, *386*, 115-132.
7. Gadd, G. M. (2010). Metals, minerals and microbes: geomicrobiology and bioremediation. *Microbiology*, *156*(3), 609-643.
8. Gadd, G. M. (1993). Microbial formation and transformation of organometallic and organometalloid compounds. *FEMS Microbiology Reviews*, *11*(4), 297-316.
9. Zouboulis, A. I., & Katsoyiannis, I. A. (2005). Recent advances in the bioremediation of arsenic-contaminated groundwaters. *Environment international*, *31*(2), 213-219.
10. Laspidou, C. S., & Rittmann, B. E. (2002). A unified theory for extracellular polymeric substances, soluble microbial products, and active and inert biomass. *Water research*, *36*(11), 2711-2720.
11. Flemming, H. C., & Wingender, J. (2010). The biofilm matrix. *Nature Reviews Microbiology*, *8*(9), 623.
12. Myers, J and Myers, C. 2001. "Role for Outer Membrane Cytochromes OmcA and OmcB of Shewanella putrefaciens MR-1 in Reduction of Manganese Dioxide." Appl and Env Microbiology. 67(1):260-69
13. Zhou, G., Yuan, J., & Gao, H. (2015). Regulation of biofilm formation by BpfA, BpfD, and BpfG in Shewanella oneidensis. *Frontiers in Microbiology, 6*. https://doi.org/10.3389/fmicb.2015.00790
14. Saltikov, C. W., Cifuentes, A., Venkateswaran, K., & Newman, D. K. (2003, May). The ars detoxification system is advantageous but not required for As(V) respiration by the genetically tractable Shewanella species strain ANA-3. Retrieved from https://www.ncbi.nlm.nih.gov/pubmed/12732551
15. Carvalho, L., De Koe, T., & Tavares, P. (1998). An improved molybdenum blue method for simultaneous determination of inorganic phosphate and arsenate. *Restoration*, *1*(1).
16. World Health Organization. (2018). Arsenic. Retrieved from https://www.who.int/news-room/fact-sheets/detail/arsenic#:~:text=The%20current%20recommended%20limit%20of,removing%20arsenic%20from%20drinking%2Dwater.
17. Harper, T. R., & Kingham, N. W. (1992). Removal of arsenic from wastewater using chemical precipitation methods. Water Environment Research, 64(3), 200-203.
18. Ramírez-Solís, A., Mukopadhyay, R., Rosen, B. P., & Stemmler, T. L. (2004). Experimental and Theoretical Characterization of Arsenite in Water: Insights into the Coordination Environment of As−O. Inorganic Chemistry, 43(9), 2954-2959. doi:https://doi.org/10.1021/ic0351592
19. Harimawan, A., & Ting, Y. P. (2016). Investigation of extracellular polymeric substances (EPS) properties of P. aeruginosa and B. subtilis and their role in bacterial adhesion. *Colloids and Surfaces B: Biointerfaces*, *146*, 459-467.
20. Teitzel, G. M., & Parsek, M. R. (2003). Heavy metal resistance of biofilm and planktonic Pseudomonas aeruginosa. *Applied and environmental microbiology*, *69*(4), 2313-2320.
21. George, C. M., Smith, A. H., Kalman, D. A., & Steinmaus, C. M. (2006). Reverse osmosis filter use and high arsenic levels in private well water. Archives of environmental & occupational health, 61(4), 171-175.
22. Duarte, A. A., Cardoso, S. J., & Alçada, A. J. (2009). Emerging and innovative techniques for arsenic removal applied to a small water supply system. Sustainability, 1(4), 1288-1304.
23. Lara, F., Cornejo, L., Yáñez, J., Freer, J., & Mansilla, H. D. (2006). *Solar-light assisted removal of arsenic from natural waters: effect of iron and citrate concentrations. Journal of Chemical Technology & Biotechnology, 81(7), 1282–1287.*doi:https://doi.org/10.1002/jctb.1547
24. Vaaramaa, K., & Lehto, J. (2003). Removal of metals and anions from drinking water by ion exchange. Desalination, 155(2), 157-170.

25. Rahman, M. H., Rahman, M. M., Watanabe, C., & Yamamoto, K. (2003). Arsenic contamination of groundwater in Bangladesh and its remedial measures. In Arsenic Contamination in Groundwater-Technical and Policy Dimensions. Proceedings of the UNU-NIES International Workshop, United Nations University, Tokyo, Japan (pp. 9–21).
26. Walker, M., Seiler, R. L., & Meinert, M. (2008). Effectiveness of household reverse-osmosis systems in a Western US region with high arsenic in groundwater. Science of the Total Environment, 389(2-3), 245-252.

Analyzing Recursive Sequences by Big Data Technologies

Trivikram Mohan, Yen Jun Hung, and Vivian Jiang Zewei

Abstract In this project we investigate the application of Big Data—the collection of data points which characterizes a recursive relation—to find meaningful approximations of the general formula of these relations. We develop a methodology for application through its application in a new derivation for Binet's Formula for the Fibonacci Sequence, as well as a novel refinement of Stirling's Approximation of $n!$ which closely matches Ramanujan's approximation for $n!$. We find our methodology and analysis to be highly applicable to complex, modern recursive sequences which cannot be easily solved for analytically.

Keywords Big data · Recursive sequences · Trend analysis · Fibonacci sequence · Binet's formula · Ramanujan's approximation · Factorial

1 Introduction: The Fibonacci Sequence and Conventional Proof of it's General Formula

Named [1, 2] after Fibonacci, also known as Leonardo of Pisa or Leonardo Pisano, Fibonacci numbers were first introduced in his Liber Abaci in 1202. The son of a Pisan merchant, Fibonacci traveled widely and traded extensively. Math was incredibly important to those in the trading industry, and his passion for numbers was cultivated

T. Mohan (✉) · Y. J. Hung
NUS High School of Mathematics of Science, 20 Clementi Avenue 1, Singapore 129957, Singapore
e-mail: h1610151@nushigh.edu.sg

Y. J. Hung
e-mail: h1610165@nushigh.edu.sg

V. J. Zewei
Department of Mathematics, Statistics and Computing at NUS High School of Mathematics and Science,Singapore, Singapore

H. Guo et al. (eds.), *IRC-SET 2020*,
https://doi.org/10.1007/978-981-15-9472-4_50

in his youth. The term "Fibonacci numbers" is used to describe the series of numbers generated by the pattern

$$0, 1, 1, 2, 3, 5, 8, 13, 21, 34, 55, 89, 144 \ldots,$$

where each number in the sequence is given by the sum of the previous two terms. Fibonacci numbers are of interest to biologists and physicists because they are frequently observed in various natural objects and phenomena. Mathematically, they can be represented by the recurrence relation:

$$F_n = F_{n-1} + F_{n-2}$$

where $F_0 = 0$ and $F_1 = 1$.

To find the general formula for the Fibonacci Sequence, we will first define a linear homogeneous relation as follows;

Definition 1.1 A linear homogeneous relation is defined as;

$$a_n = c_1 a_{n-1} + c_2 a_{n-2} + c_3 a_{n-3} + \cdots + c_d a_{n-d},$$

whose Characteristic Equation is defined as;

$$x^d = c_1 x^{d-1} + c_2 x^{d-2} + \cdots + c_d$$

By this definition, the characteristic equation of the Fibonacci Sequence (a linear homogeneous relation) is;

$$x^2 - x - 1 = 0$$

Lemma 1.2 *If the characteristic equation* $x^2 - c_1 x - c_2 = 0$ *of the defining formula* $a_n = c_1 a_{n-1} + c_2 a_{n-2}$ *has:*

1. *two distinct roots* s_1,s_2, *then the general formula for term* a_n *is*

$$u s_1^n + v s_2^n$$

2. *a single root s, then the explicit formula for* a_n *is"*

$$u s^n + v n s^n$$

where u and v are determined by its the sequence's initial conditions.

Since the characteristic equation of the Fibonacci Sequence $x^2 - x - 1 = 0$ has 2 distinct linear roots;

$$(s_1, s_2) = \left(\frac{1 + \sqrt{5}}{2}, \frac{1 - \sqrt{5}}{2} \right)$$

Theorem 1.3 *([3]) The general formula for F_n of the Fibonacci Sequence is given by;*

$$F_n = \frac{1}{\sqrt{5}}\left(\left(\frac{1+\sqrt{5}}{2}\right)^n - \left(\frac{1-\sqrt{5}}{2}\right)^n\right)$$

Proof From Lemma 1.2,

$$F_n = u\left(\frac{1+\sqrt{5}}{2}\right)^n + v\left(\frac{1-\sqrt{5}}{2}\right)^n$$

Given the initial conditions $F_1 = F_2 = 1$, hence we have $u = \frac{1}{\sqrt{5}}$ and $v = -\frac{1}{\sqrt{5}}$. Substituting these values in the above equation, we have the general formula for F_n. This formula is also known as Binet's Formula.

Big Data in this report refers to a collection of data points of a recursive relation F_n with respect to n to better understand and formulate easier-to-derive yet accurate approximations for the general formulae of recursive sequences.

In the next section, we will prove Theorem 1.3 using Big Data, which involves looking at the general trends ofF_n versus n, linearizing the graph, and finding deviation within our estimated formula.

2 Proof of Fibonacci Sequence General Formula using Big Data Technologies

To obtain a general formula for the Fibonacci Sequence, we must observe the general trends in its values; hence, we will plot a graph of F_n versus n. We want to observe trends in the values of F_n with as many values as possible to obtain more accurate graphs. For a conservative estimate, we use 1000 data points to plot the data. Clearly, the graphs are exponential.

Lemma 2.1 *The estimated general formula for the Fibonacci Sequence F_n is given by;*

$$F_{n(est.)} = \frac{1}{\sqrt{5}}\left(\frac{1+\sqrt{5}}{2}\right)^n$$

Proof To make it easier to interpret data graph from these graphs, we need to linearize it by using $\ln F_n$ versus n instead with the same 1000 data points. The graphs are clearly not straight lines, however they may be approximated as such and we can interpolate it with a best-fit line to yield the equation;

$$\ln F_n = 0.4812n - 0.8039$$

It is a good fit since the R^2 value of this interpolation is 1. Now, let $\ln F_n = an + b$. Then, $F_n = kr^n$ where $r = e^a$ and $k = e^b$. By definition of the Fibonacci Sequence, we have;

$$kr^n = kr^{n-1} + kr^{n-2},$$

and hence $r = \frac{1+\sqrt{5}}{2}$ since $r > 0$. Furthermore,

$$k = e^{-0.8039} \approx \frac{1}{\sqrt{5}}$$

Therefore

$$F_{n(est.)} = \frac{1}{\sqrt{5}}\left(\frac{1+\sqrt{5}}{2}\right)^n$$

However, this could not be the general formula of the Fibonacci Sequence, as there are still discrepancies which are more prominent for lower values of n.

Definition 2.2 We let the discrepancy between F_n and $F_{n(est.)}$, T_n be defined as

$$T_n = F_n - F_{n(est.)} = F_n - \frac{1}{\sqrt{5}}\left(\frac{1+\sqrt{5}}{2}\right)^n$$

Now, we graph T_n with respect to n, and we find that as n approaches infinity, T_n approaches 0. Indeed, our estimate for F_n becomes more accurate as the number of terms in the Fibonacci Sequence increases. However, the value of T_n alternates between negative and positive values for each alternate n. Hence we graph T_n^2 versus n, and we find that the graph is one of exponential decay. By plotting $\ln T_n$ versus n, we can linearize it to obtain the best fit line;

$$\ln(T_n^2) = -0.9623n - 1.6112$$

Hence, we have $T_n^2 = cn + d = pq^n$, where $p = e^d$ and $q = e^c$. Hence,

$$T_n^2 = 0.2 * 0.382^n = \frac{1}{5} \times 0.382^n$$

Again, the estimate is good since the R^2 value of this interpolation is 1. Now,

$$T_n = \pm\frac{1}{\sqrt{5}} \times (\pm 0.618)^n \approx \pm\frac{1}{\sqrt{5}} \times \left(\pm\frac{\sqrt{5}-1}{2}\right)^n;$$

Now, we have;

$$F_n = T_n + F_{n(est.)} = \frac{1}{\sqrt{5}}\left(\frac{1+\sqrt{5}}{2}\right)^n \pm \frac{1}{\sqrt{5}} \times \left(\pm\frac{\sqrt{5}-1}{2}\right)^n$$

Trying out all 4 possibilities to see which one works as a general formula for the Fibonacci Sequence, we find that the formula that works out of the 4 is;

$$F_n = \frac{1}{\sqrt{5}}\left(\frac{1+\sqrt{5}}{2}\right)^n - \frac{1}{\sqrt{5}} \times \left(\frac{1-\sqrt{5}}{2}\right)^n = \frac{1}{\sqrt{5}}\left(\left(\frac{1+\sqrt{5}}{2}\right)^n - \left(\frac{1-\sqrt{5}}{2}\right)^n\right)$$

Hence, we have derived Binet's formula using trends in the Fibonacci Sequence, and some insight in the way we had worked to the final result. If we had been satisfied and stopped at Lemma 2.1, we would have ended up with an incomplete version of the final formula. The applications of Big Data are not limited to simple proofs like the above for the Fibonacci Sequence. Rather, it can be used as a powerful tool to sharpen available approximations for complex recursive relations, as we will demonstrate in the next section.

3 Deriving Ramanujan's Approximation from Stirling's Approximation for the Factorial

Definition 3.1 Abraham De Moivre discovered that $n!$ may be approximated as;

$$n! \approx cn^{n+\frac{1}{2}}e^{-n},$$

where c is a positive, real constant and n is an integer. Stirling[4] later contributed to this formula by discovering the the constant c may best be approximated as $\sqrt{2\pi}$. Hence, Stirling's approximation for $n!$ is given as;

$$n! \approx \sqrt{2\pi} * n^{n+\frac{1}{2}}e^{-n} = \sqrt{2\pi n} \times \left(\frac{n}{\mathrm{e}}\right)^n$$

In this section, we will use *Big Data* to derive a more accurate approximation for Factorials. The creative approach to this problem will be to use a polynomial best fit curve instead of a linear best-fit line which we used in the previous section, so as to replace the linear function within the square-root in Stirling's Approximation with a more accurate polynomial function within an ath-root.

Let us simplify the setup for Stirling's Approximation to;

$$n! \approx \left(\frac{n}{\mathrm{e}}\right)^n \times c[g(n)]^a = \left(\frac{n}{\mathrm{e}}\right)^n \times [f(n)]^a$$

where $c > 0$, $\frac{1}{a}$ is a positive integer and $f(n)$ and $g(n)$ are polynomials in n.

Lemma 3.2 *The polynomial $f(n)$ within the may be defined as;*

$$f(n) = \left[\frac{n!e^n}{n^n}\right]^{\frac{1}{a}}$$

Proof Now, to make a polynomial best-fit curve we need the Right-Hand-Side of Stirling's Approximation to be a polynomial in n.

$$\frac{n!}{\left(\frac{n}{e}\right)^n} \approx [f(n)]^a$$

Hence,

$$\frac{n!}{\left(\frac{n}{e}\right)^n}^{\frac{1}{a}} = f(n)$$

Now, if we graph $f(n)$ versus n at various a, we find the $f(n)$ directly as the polynomial approximation for the best-fit curve. For example, for $a = \frac{1}{2}$, we find that the $f(n)$ for which $R^2 = 1$ is

$$f(n) = 6.2748n + 1.0993$$
$$f(n) = 2\pi(n + 7/20)$$

Hence,

$$\left[\frac{n!e^n}{n^n}\right]^2 = 2\pi(n + 7/20)$$

$$n! \approx \left(\frac{n}{e}\right)^n \sqrt{2\pi(n + 7/20)}$$

This is very similar to Stirling's Formula. We will now graph for $a = \frac{1}{2}, a = \frac{1}{3}, \ldots$ for positive integer denominators.

Proposition 3.3 For even values of $\frac{1}{a}$ up to $\frac{1}{a} = 10$, the polynomial $f(n)$ will be of order $\frac{1}{2a}$. For odd values of $\frac{1}{a}$, up to $\frac{1}{a} = 10$, no such statement can be made about the order of $f(n)$.

This Proposition is made on the basis of best-fit curves made on the graphs of all $f(n)$ for all positive integers a where $0 < a < 11$. For example, at $a = \frac{1}{4}$, the polynomial $f(n)$ where $R^2 = 1$ becomes;

$$f(n) = 39.476n^2 + 13.193n + 2.0053$$
$$f(n) = \pi^2\left(4n^2 + \frac{4}{3}n + \frac{1}{5}\right)$$

Hence,

$$\left[\frac{n!e^n}{n^n}\right]^4 = \pi^2\left(4n^2 + \frac{4}{3}n + \frac{1}{5}\right)$$

$$n! \approx \left(\frac{n}{e}\right)^n \sqrt[4]{\left(4n^2 + \frac{4}{3}n + \frac{1}{5}\right)}$$

Definition 3.4 ([5]) Ramanujan's Approximation for $n!$ is given by;

$$n! \approx \left(\frac{n}{\mathrm{e}}\right)^n \times \sqrt{\pi} \times \sqrt[6]{8n^3 + 4n^2 + n + 1/30}$$

Ramanujan's Approximation is more accurate than Stirling's Approximation even for all n. However, as n increases the deviation between the actual value of $n!$ and the approximation becomes more error-prone.

Theorem 3.5 *Ramanujan wrote the inequality;*

$$\left(\frac{n}{\mathrm{e}}\right)^n \times \sqrt{\pi} \times \sqrt[6]{8n^3 + 4n^2 + n + 1/100} <$$
$$n! < \left(\frac{n}{\mathrm{e}}\right)^n \times \sqrt{\pi} \times \sqrt[6]{8n^3 + 4n^2 + n + 1/30}$$

Proposition 3.6 Using Big Data as a basis, we may approximate $n!$ as follows;

$$n! \approx \left(\frac{n}{\mathrm{e}}\right)^n \times \sqrt{\pi} \times \sqrt[6]{8n^3 + 4n^2 + n + 1/50}$$

Proof By applying Proposition 3.3 for $\frac{1}{a} = 6$, the polynomial $f(n)$ for which $R^2 = 1$ becomes;

$$f(n) = 248.05n^3 + 124.026n^2 + 31.1n + 0.6062$$
$$f(n) = \pi^3\left(8n^3 + 4n^2 + n + 1/50\right)$$

By applying Lemma 3.2, we have;

$$\left[\frac{n!e^n}{n^n}\right]^6 \approx \pi^3\left(8n^3 + 4n^2 + n + 1/50\right)$$

Hence,

$$n! \approx \left(\frac{n}{\mathrm{e}}\right)^n \times \sqrt{\pi} \times \sqrt[6]{8n^3 + 4n^2 + n + 1/50}$$

A Concluding Note for this Proof: We must note that the polynomial $f(n)$ in our approximation is almost exactly the average of the two polynomials within the 6th-root of the polynomials within the upper and lower bounds of the inequality in Theorem 3.5.

4 Creating a Higher-Order Approximation for $n!$ using Big Data Technologies

Through our considerations in Proposition 3.3, we have ruled out odd values of $\frac{1}{a}$. Now, we can consider even values such as $\frac{1}{a} = 8$ or $\frac{1}{a} = 10$. Now, the polynomial $f(n)_8$ and $f(n)_{10}$ respectively are;

$$f(n)_8 = \pi^4\left(16n^4 + \frac{32}{3}n^3 + 3.556n^2 + 0.394n + 1.275\right)$$

$$f(n)_{10} = \pi^5\left(32n^5 + \frac{80}{3}n^4 + 11.112n^3 + 2.234n^2 - 5.804n + 234\right)$$

To compare and contrast the accuracy of the various approximations in this section and the last, we will be measuring the discrepancies between $n!$ and the estimate from Ramanujan's Approximation R_n, the lower bound in Theorem 3.5 L_n, Stirling's Approximation S_n, our approximation in Proposition 3.6 $a6_n$, and the two above approximations $a8_n$ and $a10_n$ respectively (Fig. 1).

From our results above, an interesting result is that the accuracy of the approximation need not depend on the order of the polynomial within the ath-root. Rather, it depends on the n in the approximation. For example, $a6_n$ approximates $n!$ better for small n, however R_n approximates the factorial function best at high n. This makes R_n the most useful approximation, because there is no need to approximate $n!$ at small n.

	3!	5!	10!	20!	50!
N! – S(N)	0.164	1.98	$3.04*10^{4}$	$1.012*10^{16}$	$5.065*10^{61}$
N! – L(N)	$4.32 * 10^{-5}$	$2.75*10^{-4}$	1.366	$1.303*10^{11}$	$1.125*10^{56}$
N! – R(N)	$-4.83*10^{-5}$	$-1.47*10^{-4}$	-0.312	$-1.37*10^{10}$	$-4.554*10^{54}$
N! – A6(N)	$3.99*10^{-6}$	$9.43*10^{-5}$	0.647	$6.861*10^{10}$	$6.236*10^{55}$
N! – A8(N)	$5.77*10^{-4}$	$1.54*10^{-3}$	-2.69	$-8.556*10^{10}$	$-1.734*10^{55}$
N! – A10(N)	$-2.36*10^{-2}$	$-2.10*10^{-2}$	-18.9	$-3.225*10^{11}$	$-4.514*10^{55}$

Fig. 1 Table of Discrepancy for $R(n)$, $S(n)$, $L(n)$, $a6_n$, $a8_n$, and $a10_n$

5 Conclusions

In Conclusion, we have applied Big Data—a collection of data points of a recursive relation F_n with respect to n to better understand and formulate easier-to-derive yet accurate approximations for the general formulae of recursive sequences. Specifically, we have derived exactly the Binet's Formula for the Fibonacci Sequence. We have also formulated our unique approximation of $n!$ by leveraging Big Data upon already existing formulae such as Stirling's Approximation. We can verify our results by comparing it with the actual values of the recursive relation, or by comparing its accuracy with pre-existing results—similar to how our unique approximation for $n!$ was similar in nature to Ramanujan's approximation for $n!$.

This similar pedagogy may be used outside the context of problems like these—the general application of Big Data requires some prior insight about the function so as to figure out how to linearize or 'polynomialize' the function, as we had done in the latter sections. Once finding approximate values through a best-fit curve, we simplify them to fractions and surds and factorize out irrational numbers like π and e. If the problem allows for it, we may back-substitute our approximation and characterize the difference between the approximation and the true value to further increase the accuracy of our estimation of the general formula of F_n. This back-substitution process is very similar to what we did in Definition 2.2.

Acknowledgements We would like to express our sincerest thanks to our teacher-mentor Ms Vivian Jiang Zewei for her careful reading of the manuscript and valuable advice and suggestions throughout this project.

References

1. Elaine J. Hom. What is the Fibonacci Sequence?Livescience, 2013. [Online; accessed 29-June-2020].
2. Tyler Clancy. The Fibonacci Numbers.
3. A Proof of Binet's formula.Milefoot. [Online; accessed 30-June-2020].
4. Conrad, Kieth. STIRLING'S FORMULA. 2015, kconrad.math.uconn.edu/blurbs/analysis/stirling.pdf.
5. Hirschhorn, M. D. (2012). (PDF) A Refinement of Ramanujan's Factorial Approximation. Retrieved June 30, 2020, from https://www.researchgate.net/publication/233846996 A Refinement of Ramanujan's Factorial Approximation

Machine Learning Using Satellite Remote Sensing to Predict Agricultural Yield of Cash Crops in USA

Lakshmi Sirisha Kommareddi and Luo Sha

Abstract Remote sensing on satellite images enables us to obtain more information than what is seen by the human eye. Applying Machine Learning on the data obtained from satellite remote sensing makes it possible to gain better insights by performing analysis and understanding trends. Some applications of remote sensing are fire detection, crop yield prediction, deforestation detection etc. According to studies done by the Food and Agricultural Organization (FAO) of the United Nations, the world's population is growing at an immense rate and is expected to reach 9.1 billion by 2050, which is a 34% increase from the current population [7]. This forecasted growth highlights the importance of having higher agricultural yield and accurate crop information. Hence, crop yield prediction is a very useful tool that will validate better management of agricultural resources. This paper explores Machine Learning applications using Satellite Remote Sensing to predict Agricultural Yield. Support Vector Machine Simple Linear Regression and Multiple Linear Regression models were used to build the prototype. Model validation and testing was done to determine the accuracy of the prediction. This prototype was built using Landsat-8 images as Landsat-8 has high spatial resolution whereas many existing research papers use satellites like MODIS with higher temporal resolution. The prototype predicts Corn and Soybeans yield in Iowa and Illinois, USA with an accuracy ranging from 70–90%. These yield prediction models will allow researchers to better understand crop patterns.

Keywords Machine learning · Satellite remote sensing · Data analysis

L. S. Kommareddi (✉)
Computer Engineering, National University of Singapore (NUS), Singapore, Singapore
e-mail: sirishakommareddi@gmail.com

L. Sha
Department of Electrical and Computer Engineering, National University of Singapore (NUS), Singapore, Singapore
e-mail: eleluos@nus.edu.sg

H. Guo et al. (eds.), *IRC-SET 2020*,
https://doi.org/10.1007/978-981-15-9472-4_51

1 Introduction

Satellite Image Processing and its applications have a significant role in Astronomical Research and Development. The aim of this paper is to use Machine Learning on satellite images to build a model that uses vegetation indices such as Normalized Difference Vegetation Index (NDVI) and Enhanced Vegetation Index (EVI) obtained from the satellite images to predict crop yield in certain areas of interest. This will aid researches to better understand crop yield patterns.

In the future, this model could be integrated into Satscope, which is an existing web application that serves as a platform for the research engineers at NUS Satellite Technology and Research Centre (STAR) to collect, store, process and view the satellite imagery captured by Galassia-II and Landsat-8. This will enhance Satscope's current capabilities and allow users to perform remote-sensing operations such as crop yield prediction on satellite images.

The objective is to use Machine Learning on Satellite Imagery to predict Agricultural Yield for cash crops. Firstly, Corn in Iowa, USA is selected to develop a proof-of-concept model and test accuracy of yield prediction. The end goal is to develop an accurate model for yield prediction of corn, and extend this to other crops and regions. The model has currently been extended to different states as well as crops, such as Corn and Soybeans in Iowa and Illinois.

A study on Palm Oil Yield by the paper "Estimating oil palm yields using vegetation indices derived from QuickBird", uses regression analysis to create empirical yield estimation models using Palm Oil Yield and NDVI values [2]. The paper "Crop Yield Assessment from Remote Sensing" uses a crop model to extract information from satellite images such as vegetation indices and simulate yield of wheat crops in the south eastern counties of North Dakota State in the US [5]. This model uses simple regression analysis as well. The paper "Near real-time prediction of U.S. corn yields based on time-series MODIS data" uses a simple regression model to estimate crop yield for various crops such as soybean, wheat etc. Different vegetation indices such as NDVI, RVI, EVI, GNDVI etc. are used for correlation [13].

MODIS satellite has lower spatial resolution than Landsat-8, so in this research paper, Landsat-8 imagery was used which has high spatial resolution. This makes it possible to observe the crop plantation landscape in detail and accurately calculate vegetation indices from the image [3, 11].

Hence, from most of the relevant literature, it can be determined that a regression model correlating crop yields and vegetation index values derived from satellite images is a suitable approach to estimate crop yields in different regions.

2 Support Vector Machine (SVM) Model

2.1 Simple and Multiple Linear Regression Models

In statistics, linear regression attempts to model the relationship between a dependent and independent variable [9]. If there is only one independent variable, it is called simple linear regression. If there is more than one such variable, it is called multiple linear regression. A strong correlation indicates that there is a significant relation between the variables.

Scikit-learn is a machine learning library for the Python language. It contains numerous regression and classification algorithms. In this research, the Linear Regression Model from the Scikit-learn library is used [14].

A SVM Linear Regression Model is used to build simple linear correlation models of Yield versus NDVI and Yield versus EVI. The average NDVI values per year are the independent variables (x-axis) whereas the yearly crop yield data values are the dependent variables (y-axis).

In the implementation, once the accuracy of the simple regression models of Crop Yield versus NDVI and Crop Yield versus EVI is established, a multiple regression model is used to further enhance accuracy. The multiple regression model using NDVI and EVI as the independent variables and crop yield as the dependent variable will be more accurate than the simple regression model. The multiple regression model generally has higher correlation than the simple linear regression models.

2.2 Evaluation Metrics

There are various regression error metrics that can be used to examine the model. These metrics provide insight into the quality of the model. Mean Square Error (MSE), Root Mean Square Error (RMSE), Mean Absolute Error (MAE) and R-Square are some of the commonly used metrics for linear regression models [11].

MSE basically measures the average squared error of our predictions. For each data point, it calculates the difference between the predictions and the target, squares this difference and then takes the average of those values.

- Range of MSE is from 0 to infinity.
- Lower values of MSE indicate better model fit.

RMSE is the square root of MSE. It can be interpreted as the standard deviation of the unexplained variance, and has the useful property of being in the same units as the response variable. The square root brings the scale of the errors to the same level as the scale of the targets.

- Range of RMSE is from 0 to infinity.
- Lower values of RMSE indicate better model fit.

MAE is a linear score which means that all the individual differences are weighted equally in the average. The error is calculated as an average of absolute differences between the actual values and the forecasted values.

- Range of MAE is from 0 to infinity.
- Lower values of MAE indicate better model fit.
- Not as sensitive to outliers as MSE.

The coefficient of determination, or R^2, is a scale-free metric used to gauge a model. It is a statistical measure of how close the data values are to the fitted regression line. It determines correlation strength. Whether the output values are extremely large or small, the R^2 value will still be within their range.

- Range of R^2 is from 0 to 1.
- Higher R^2 value indicates higher correlation.

3 Implementation

The implementation consists of the following summary of steps, which are explained in detail later in this section.

Example— Selected crop: Corn, Year: 2017, State: Iowa

1. Developed a Python Script to obtain the actual yield data from United States Department of Agriculture (USDA) database for Corn in all the counties in Iowa for the year 2017.
2. Obtained Corn crop masks from USDA CropLand Data Layer (CDL) website for all the counties in Iowa.
3. Selected a county from Iowa and obtain Landsat–8 Images for 2017 using Earth Explorer Feature Collection function.
4. Mosaicked the obtained images to form a single composite image.
5. Visualized NDVI and EVI layers for the selected county.
6. Analyzed the NDVI and EVI layers for different time periods to confirm June–September as the most accurate period to choose for training the model.
7. Filtered the obtained Landsat-8 Images to the chosen period of June–September.
8. Used a reducer function on the composite image to obtain NDVI and EVI time-series charts
9. Averaged these charts to obtain the NDVI and EVI values for the selected county in Iowa.
10. Repeated Steps 1–9 for all counties in Iowa.
11. Once all NDVI and EVI values were obtained for all counties, fed it into the Support Vector Machine Regression Model to obtain the regression graphs as well as evaluation metrics.
12. Steps 1–11 were repeated for obtaining the yield prediction models for other states and crops such as Soybeans in Illinois, Corn in Illinois etc.

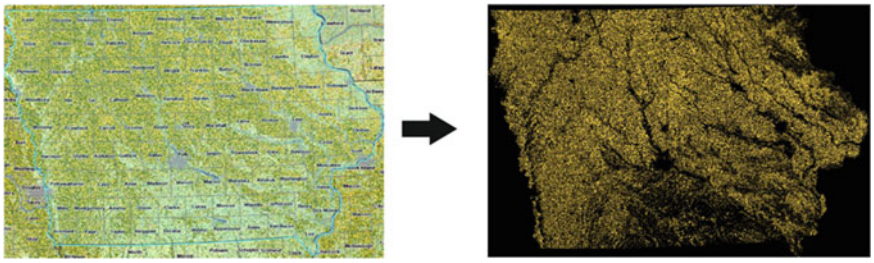

Fig. 1 Image of region before mosaicking

3.1 USDA Yield Data and Crop Masks

The United States Department of Agriculture (USDA) website has annual yield data of various crops in the USA which can be filtered by state and further narrowed down by county [16]. To make it more automated, a python script was written to query from USDA Quickstats for all the counties based on the state and crop selected for the model.

The USDA CropLand Data Layer (CDL) website has a Crop mask raster for corn and soy plantations in Iowa and Illinois [4, 17]. Applying this mask on the image of the selected state shows only the chosen crop plantations in that state and masks everything else.

For example, applying the corn mask on the image of Iowa shows only corn plantations in Iowa state and masks the rest. The left image in Fig. 1 is a map of Iowa state showing all plantations and crops. Once the crop mask is applied, the non-corn plantations are masked out. The yellow pixels in the right image of Fig. 1 denote only corn plantations/farms. These crop masks make it possible to build models for selected crops in selected regions.

3.2 Landsat-8 Images and Mosaicking

Mosaicking refers to the process of spatially assembling image datasets to produce a spatially continuous image. Mosaicking allows us to obtain the highest quality image with least cloud cover for the given region in the specified date range.

In Fig. 2, from the Landsat-8 images obtained, the highest quality pixels from these images are stitched together to form one composite image for the selected regions.

This composite image in Fig. 3 reduces bias from cloud cover, and provides an accurate representation of NDVI and EVI values for the region.

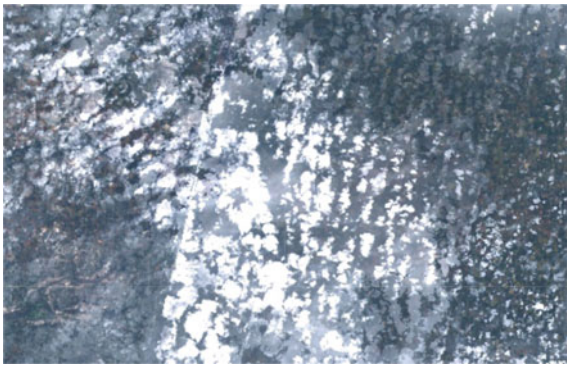

Fig. 2 Image of region before mosaicking

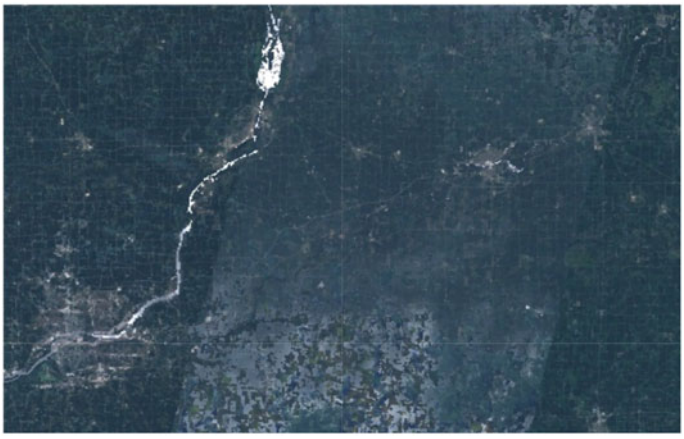

Fig. 3 Image of same region after Mosaicking

3.3 Visualization and Analysis of NDVI and EVI Layers

A strong positive correlation exists between vegetation indices and crop yields. Among vegetation indices, Normalized Difference Vegetation Index (NDVI) and Enhanced Vegetation Index (EVI) showed the best correlation with corn yield [1].

The NDVI and EVI layers are computed after applying the crop mask to the images. After applying the Crop Mask, the only visible pixels in the image are of the selected crop plantations. Hence the NDVI and EVI visualization layers only show the selected crop plantations in the selected states. Visualizing county boundaries, NDVI Layers and EVI Layers provides more insight into understanding the growth of crops in a region (Fig. 4).

For Corn crop, months from early June to end September have an accurate representation of potential yield using NDVI and EVI indices as it would clearly measure the Vegetation Index during plantation and growth stages of the crop only [9].

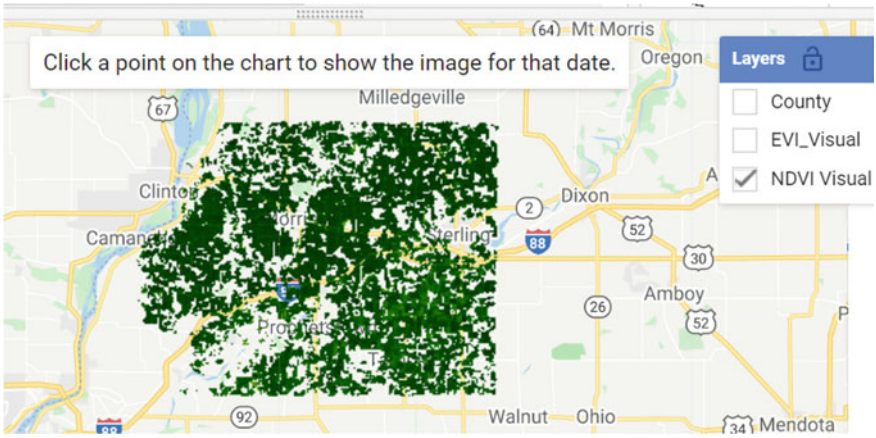

Fig. 4 NDVI layer visualization

3.4 Reducer Function and Time Series Charts

The reducer function will composite all the images in the collection to a single image representing the min, max, mean or standard deviation of the images. The mean is selected in this research.

After mosaicking all these images, a composite image is obtained. The reducer processes the image collection and obtains the individual composite based on mean values for each day in the year for a time series chart (Fig. 5).

This chart shows the NDVI values over the selected growth phase period of the crop which is averaged to obtain the mean NDVI for the county.

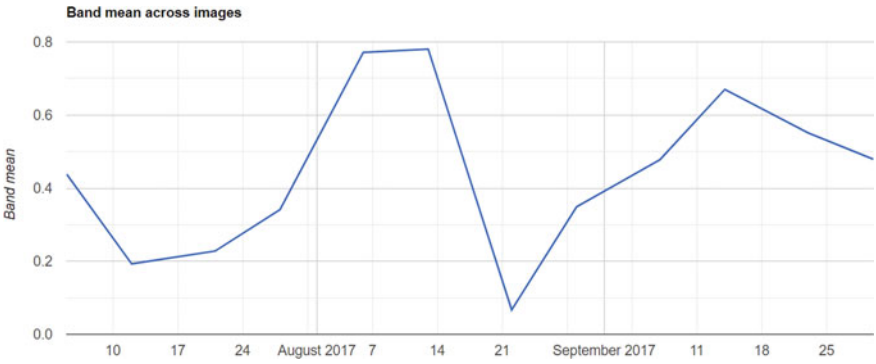

Fig. 5 NDVI time-series chart

3.5 SVM Linear and Multiple Regression Models

SVM Linear Regression Model is used to build simple linear correlation models of Yield versus NDVI and Yield versus EVI. In Fig. 6, the average NDVI/EVI values per year are the independent variables (x-axis) whereas the yearly crop yield data are the dependent variables (y-axis).

The predicted yield values for the multiple regression model are compared with the actual yield values to evaluate the model (Fig. 7). It can be seen that the predicted values are close to the actual values, which validates the accuracy of the model.

4 Results

The SVM Linear and Multiple Regression Models are built, and the evaluation metrics are obtained for different states and years. The results are summarized in this section.

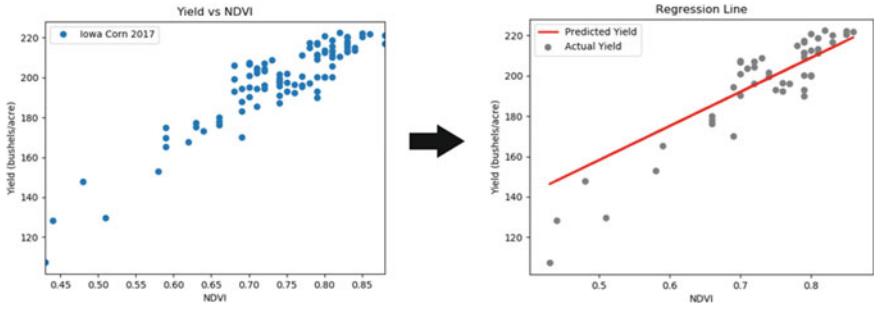

Fig. 6 Corn yield vesus NDVI regression plot (Iowa, 2017)

Fig. 7 Actual versus predicted yield (multiple regression model)

	Actual	Predicted
0	200.1	204.773846
1	147.9	157.551668
2	190.5	190.055487
3	216.6	213.308884
4	211.6	205.940361
5	200.3	204.706045

Table 1 R^2 summary

Crop	State	Year	Yield versus NDVI	Yield versus EVI	Multiregression
Corn	Iowa	2017	0.79	0.88	0.90
Corn	Illinois	2017	0.79	0.74	0.81
Corn	Illinois	2018	0.76	0.70	0.84
Corn	Illinois	2017-18	0.78	0.72	0.79
Corn	Iowa and Illinois	2017	0.60	0.70	0.70
Soy	Illinois	2017	0.60	0.74	0.80

4.1 R^2 Summary Table

The summary of the R^2 values for different states and years provide insight into the variations in different regions and crops (Table 1). The R^2 values represent the correlation strength of the models. Hence comparing the values for different criteria such as varying states, years and regions helps to analyze the strength of the different models, and identify outliers.

It can also be observed that the Multiregression R^2 values are higher compared to individual Yield versus NDVI or Yield versus EVI R^2 values for all the cases as Multiregression model generalizes the regression line over more data points.

4.2 Control Experiment

Independent Variable—Crop: The Crop is varied between Corn and Soy while the year and region are kept constant. The year used is 2017 for Illinois State to compare differences between Corn and Soy Yield.

Figure 8 is a comparison of actual Corn Yield versus Soy Yield in Illinois for 2017. It is seen that Corn and Soy result in very different yield amounts as they are different crops.

Figure 9 shows the Yield versus NDVI and Yield versus EVI plots for Corn and Soy, and it is observed that both crops have a very different trend.

Independent Variable—Year: The Year is varied between 2017 and 2018 while the crop and region are kept constant. The crop used is Corn for Illinois State to compare differences between 2017 and 2018 Yield.

Figure 10 is a comparison of actual 2017 Yield versus 2018 Yield in Illinois for Corn. It is seen that even though different years are used, since it is the same crop, the yield is in the same range.

Figure 11 shows the Yield versus NDVI and Yield versus EVI plots for 2017 and 2018, and it is observed that both years have a similar trend as the same crop and region are used.

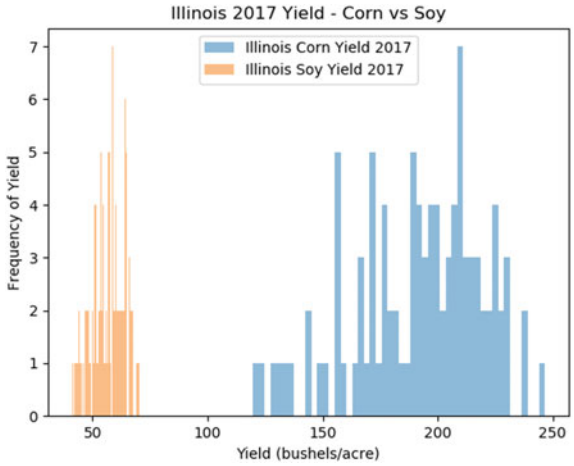

Fig. 8 Illinois 2017 yield—Corn versus Soy Histogram

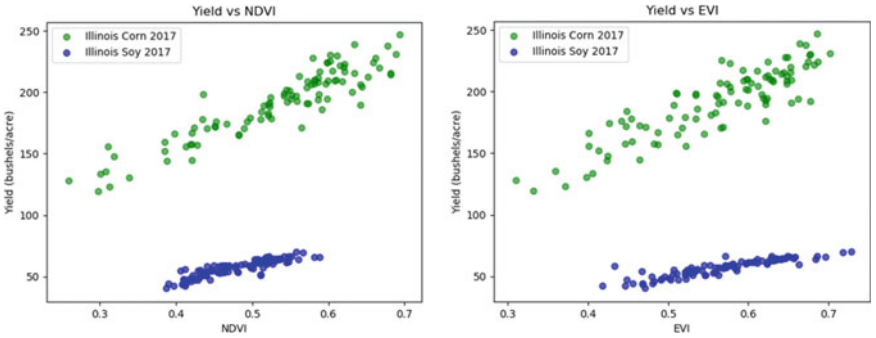

Fig. 9 Yield versus NDVI (left) and yield versus EVI (right) plots for Illinois 2017 yield—Corn versus Soy

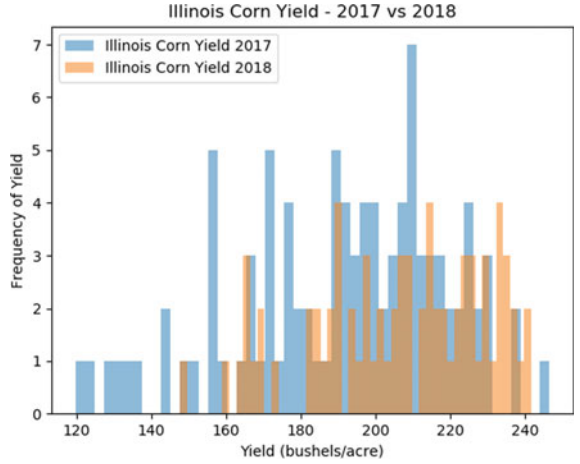

Fig. 10 Corn yield—2017 versus 2018 histogram

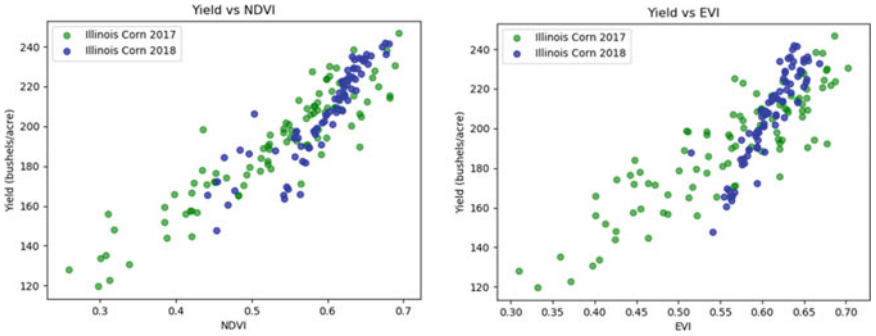

Fig. 11 Yield versus NDVI (left) and yield versus EVI (right) plots for Illinois Corn yield—2017 versus 2018

Independent Variable—Region: The Region is varied between Iowa and Illinois states while the crop and year are kept constant. The crop used is corn for 2017 year to compare differences between Iowa and Illinois Yield.

A comparison of actual Iowa Yield versus Illinois Yield for Corn in 2017 is shown in Fig. 12. Even though different regions are used, since it is the same crop and year, the yield is in a similar range.

Figure 13 shows the Yield versus NDVI and Yield versus EVI plots for Iowa and Illinois. It is observed that for Yield versus NDVI, both regions have a slightly different trend even though the same crop and year are used. On the other hand, for Yield versus EVI, both regions appear more similar.

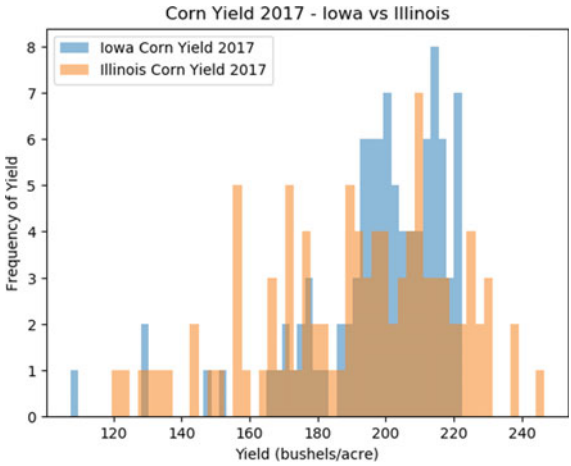

Fig. 12 Corn 2017 yield—Iowa versus Illinois histogram

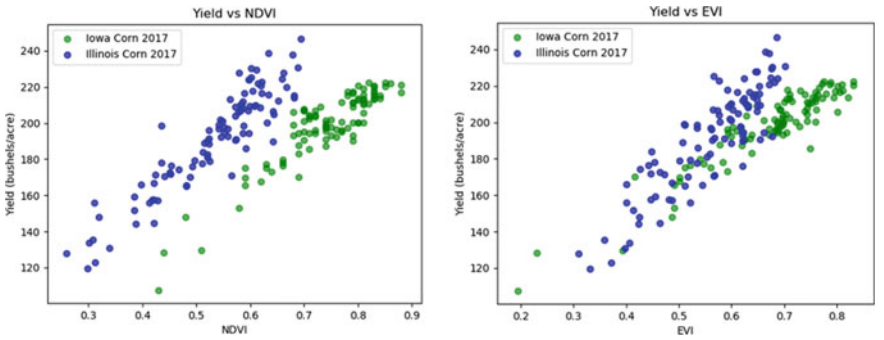

Fig. 13 Yield versus NDVI (left) and yield versus EVI (right) plots for Illinois 2017 yield—Corn versus Soy

4.3 Experiment Results and Observations

Different Crops have different growth phases, harvest periods, and varying crop structures, so although NDVI is a general representation of the green vegetation, there might be slight differences in the yield. The density of vegetation cannot be taken into account with NDVI. Since the same crop will represent NDVI in a similar way, and the region is the same which means the soil type, and atmospheric conditions are same, there is not much yearly variation. Even though the crop and year are same, there could be differences between different regions due to varying climate, soil conditions, harvest period etc. The effect of the different independent variables is shown in Table 2.

This research uses vegetation indices such as NDVI and EVI obtained from satellite images to predict crop yield in certain areas of interest. The analysis of vegetation indices has shown that these indices (such as NDVI and EVI) have good correlation with the crop yield when the yield relies directly on the leaves (2D Crop Structure). The indices are not relevant when the yield depends on small fruits or tree crops

Table 2 Control experiment results

Independent variable	Details	NDVI	EVI	Multiregression
Crop	Illinois, 2017: Corn versus Soy	0.79 versus 0.60	0.74 versus 0.74	0.81 versus 0.80
Year	Illinois, Corn: 2017 vesus 2018	0.79 versus 0.76	0.74 versus0.70	0.81 versus 0.84
Region	Corn, 2017: Iowa versus Illinois	0.79 versus 0.79	0.88 versus 0.74	0.90 versus 0.81

as the density of the vegetation in these crops cannot be taken into account with vegetation indices such as NDVI and EVI.

Based on the experiments, it can also be noted that EVI seems to be a better indicator of crop yield compared to NDVI. EVI has lesser variations, and is more consistent even when the years and region are changed.

The following observations have been made from the control experiment:

- Combining various years for same crop and region will not reduce accuracy.
- Combining different regions into same model might reduce accuracy.
- Combining various crops into the same model will reduce accuracy.

5 Conclusion

The objective of this paper is to use Machine Learning on Satellite Imagery to predict Agricultural Yield. Corn in Iowa, USA was selected to first develop a proof-of-concept model and test accuracy of yield prediction.

Once an accurate yield prediction model was built for corn, the end-goal was to extend it to other crops and regions. The model has currently been extended to different states as well as crops, such as Corn in Illinois, and Soy in Illinois.

In this paper, Support Vector Machine Simple Linear Regression and Multiple Linear Regression models were used to predict crop yield for Corn and Soy in Iowa and Illinois states in the USA. The models were evaluated and the results had a good accuracy with R^2 values in the range of 0.70–0.90.

From the experiments, results and observations, it can be concluded that to get a yield prediction model with the best accuracy, it would be ideal to use the same region and crop, and a wider range of years.

More indices such as Green Vegetation Index (GVI), Soil Adjusted Vegetation Index (SAVI), Ratio Vegetation Index (RVI), Perpendicular Vegetation Index (PVI) etc. can be used to build a more accurate model. The PVI index measures the changes from the bare soil reflectance caused by the vegetation. This may be a good index to use for different regions to deal with the problem of varying soil conditions.

The models could be combined with more variables such as temperature, precipitation, soil data etc. to further enhance accuracy and prevent bias between varying regions and years [13].

Lastly, deep neural networks such as Convolutional Neural Networks or Bayesian models could be tested to enhance the current prediction accuracy [16].

References

1. Antognelli, S. NDVI and NDMI vegetation indices. Retrieved 4 November 2019, from https://www.agricolus.com/en/indici-vegetazione-ndvi-ndmi-istruzioni-luso/

2. Balasundram, S., Memarian, H., & Khosla, R. (2013). Estimating oil palm yields using vegetation indices derived from QuickBird [Ebook]. Life Science Journal. Retrieved from https://www.researchgate.net/publication/281508567_Estimating_oil_palm_yields_using_vegetation_indices_derived_from_QuickBird/link/57dee23308ae72d72eac154e/download
3. Butler, K. (2013). Band Combinations for Landsat 8. Retrieved 4 November 2019, from https://www.esri.com/arcgis-blog/products/product/imagery/band-combinations-for-landsat-8/
4. CropScape - Cropland Data Layer. (2019). Retrieved 4 November 2019, from https://nassgeodata.gmu.edu/CropScape/
5. Doraiswamy, P., Moulin, S., Cook, P., & Stern, A. (2003). Crop Yield Assessment from Remote Sensing [Ebook]. Retrieved from https://pdfs.semanticscholar.org/16bd/56b570aabfbe812f5e1c6e342abfd4d8aae1.pdf
6. Feng, G., Anderson, M., Daughtry, C., & Johnson, D. (2018). Assessing the Variability of Corn and Soybean Yields in Central Iowa Using High Spatiotemporal Resolution Multi-Satellite Imagery [Ebook]. MDPI. Retrieved from https://www.mdpi.com/2072-4292/10/9/1489
7. Food and Agriculture Organization of the United Nations. (2017). The future of food and agriculture: Trends and challenges [Ebook]. Rome. Retrieved from http://www.fao.org/3/a-i6583e.pdf
8. Kowalski, C. (2019). Planting and Harvesting Seasons for Corn Crops. Retrieved 4 November 2019, from https://www.thebalance.com/corn-planting-and-harvest-seasons-809309
9. Linear Regression. (2019). Retrieved 4 November 2019, from http://www.stat.yale.edu/Courses/1997-98/101/linreg.htm
10. Loyd, C. (2013). Landsat 8 Bands. Retrieved 4 November 2019, from https://landsat.gsfc.nasa.gov/landsat-8/landsat-8-bands/
11. Pascual, C. (2018). Understanding Linear Regression and Regression Error Metrics. Retrieved 4 November 2019, from https://www.dataquest.io/blog/understanding-regression-error-metrics/
12. Phongpreecha, J. (2018). Early Corn Yields Prediction Using Satellite Images. Retrieved 4 November 2019, from https://tpjoe.gitlab.io/post/croppredict ion/
13. Sakamoto, T., Gitelson, A., & Arkebauer, T. (2014). Near real-time prediction of U.S. corn yields based on time-series MODIS data [Ebook]. Elsevier. Retrieved from https://www.sciencedirect.com/science/article/abs/pii/S0034425714000790
14. sklearn.linear_model.LinearRegression — scikit-learn 0.21.3 documentation. (2019). Retrieved 4 November 2019, from https://scikit-learn.org/stable/modules/generated/sklearn.linear_model.LinearRegression.html
15. Teresa, P., Soni, P., & C, M. (2018). Agricultural Crop Yield Prediction Using Artificial Intelligence and Satellite Imagery [Ebook]. Eurasian Journal of Analytical Chemistry. Retrieved from http://www.eurasianjournals.com/Agricultural-Crop-Yield-Prediction-Using-Artificial-Intelligence-and-Satellite-Imagery,105697,0,2.html
16. USDA. (2019). Iowa Ag News—2018 Crop Production [Ebook]. Iowa. Retrieved from https://www.nass.usda.gov/Statistics_by_State/Iowa/Publications/Crop_Report/2019/IA-Crop-Production-Annual-01-19.pdf
17. USDA - National Agricultural Statistics Service—Research and Science—CropScape and Cropland Data Layer—Announcements. (2019). Retrieved 4 November 2019, from https://www.nass.usda.gov/Research_and_Science/Cropland/SARS1a.ph

DNA Proximity Circuit a Universal Platform for Analyzing Biomarkers

Xinzhi Qiu, Hong Meng Yam, Ningjing Wu, Yan Shan Ang, and Lin-Yue Lanry Yung

Abstract Advanced diagnostic techniques, such as PCR and ELISA, are widely used in well-equipped laboratories. However, they are expensive and are not accessible in resource-limited settings. With growing evidence that point-of-care testing (POCT) improves clinical outcomes, there exists a need for simple, fast, low cost, yet sensitive POCT technique. We present a single pot "molecular adaptor", which we name DNA split proximity circuit (SPC), that can be used as an isothermal, enzyme-free and wash-free diagnostics platform. SPC consists of a pair of "plug-and-play" DNA initiators readily adaptable to various biomarkers ranging from nucleic acids to protein complexes, which then triggers a signal amplification readout based on Hybridization Chain Reaction (HCR). We first improved the kinetics and the sensitivity of HCR by refining HCR hairpin designs. Using biomarkers related to breast cancer as model systems, we applied the optimized HCR to our SPC system and demonstrated its capability to detect microRNA (miRNA) and cell surface receptors. SPC demonstrated good limit of detection in the femtomolar range within 30 min for all miRNA targets tested. It also showed high specificity and an ability to differentiate between different cell surface protein markers. Being isothermal and enzyme-free, our system is less sensitive to temperature and buffer conditions, making it highly robust, thus showing great potential for bedside use. With applications in biomarker analysis, cell visualization and disease diagnostics, herein we improved and established the potential of SPC as a powerful next-generation POCT assay.

X. Qiu · H. M. Yam · N. Wu (✉)
NUS High School of Mathematics and Science, Singapore, Singapore
e-mail: h1510154@nushigh.edu.sg

X. Qiu
e-mail: h1510108@nushigh.edu.sg

H. M. Yam
e-mail: h1510158@nushigh.edu.sg

Y. S. Ang · L.-Y. L. Yung
Chemical and Biomolecular Engineering, National University of Singapore, Singapore, Singapore

H. Guo et al. (eds.), *IRC-SET 2020*,
https://doi.org/10.1007/978-981-15-9472-4_52

Keywords DNA · DNA circuit · Synthetic biology · Biomolecular engineering · Disease diagnostics · Circuit · Hybridization chain reaction · Split proximity circuit · Biomarker detection · Breast cancer

1 Introduction

Diagnostics is an integral component of healthcare systems today, with time and accuracy being pressing concerns [1]. Recently, point-of-care testing (POCT) devices gained traction as it streamlines healthcare processes and improves clinical outcomes. This is reflected by an expanding POCT devices market that is predicted to have an annual compound growth of 10.4% to reach a total of US$46.7 billion in 2024 from just US$28.5 billion in 2019 [2]. With such enormous growth, the World Health Organization has introduced the ASSURED (Affordable, Sensitive, Specific, User-friendly, Rapid and Robust, Equipment-free and Deliverable to end-users) criteria to guide the development of new POCT devices [3].

This push towards POCT applications has led to the development of new isothermal signal amplification technologies like Rolling Circle Amplification (RCA) and Loop-mediated Isothermal Amplification (LAMP) that are rapid and efficient in detecting nucleic acid-based biomarkers even without the thermocycling step necessary in Polymerase Chain Reaction (PCR) [4–6]. Nonetheless, these techniques involve the use of enzymes which demand for controlled reaction conditions e.g. temperature and buffer composition. As such, a recent method called the Hybridization Chain Reaction (HCR) stands out for being both isothermal and enzyme free [7].

HCR operates using a of a pair of metastable DNA hairpins (HP1 and HP2) that are trapped kinetically in their stem-loop structure, of which HP1 is modified with a Fluorophore-Quencher (F-Q) label. Upon the introduction of a trigger sequence, a linear chain reaction cascades via the alternating opening of HP1 and HP2 to produce a nicked double-stranded DNA which fluoresces as the fluorophore and quenchers are separated (Fig. 1a). This enzyme-free property of HCR makes it less sensitive to storage and reaction conditions as compared to RCA or LAMP [8, 9]. However, HCR still faces limitations of washing steps and long processes of HCR hairpin redesigns which thus far limits its application as a POCT technology [10, 11].

Here, we present a platform called the DNA Split Proximity Circuit (SPC), a fast and low-cost "plug and play" molecular "adaptor" for HCR that is enzyme-free, wash-free and can be applied universally for biomarkers such as nucleic acids and proteins. This expanded on the types of biomarkers that HCR can detect, creating a simple, fast and universal POCT by mitigating existing limitations of HCR.

Our HCR circuit design comprises of two DNA initiator strands (I1 and I2) that can be freely modified to incorporate antibodies, aptamers or nucleic acid sequences to analyze the desired targets (Fig. 1b). In the absence of targets, they exist as separate metastable entities as the trigger sequence is split between I1 and I2 (and protected by a hairpin loop on I1), reducing non-specific signal generation. Upon binding to

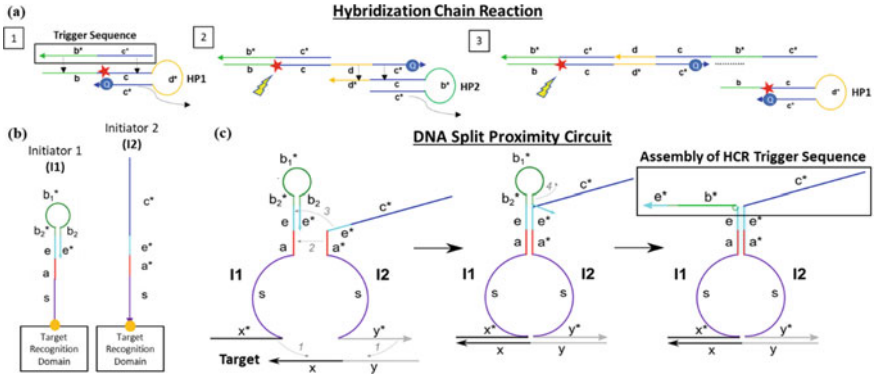

Fig. 1 **a** Mechanism for the Hybridization Chain Reaction (HCR) which works via the basis of DNA strand displacement attached with Fluorophore-Quencher (F-Q) labels **b** Initiators for the DNA Split Proximity Circuit (SPC) (c) The activation of our SPC system involves 3 steps: (1) The two initiators bind to respective complementary sites on the target, (2) unlocking of the hairpin lock, leading to (3) the formation of trigger sequence (b*c*) and a HCR reaction

targets, however, I1 and I2 will held in proximity, promoting the assembly of the trigger sequence via the opening of the hairpin loop on I1, which triggers HCR (Fig. 1c). As only the recognition domains are modified, our SPC system retains optimal designs of the trigger sequence, HP1 and HP2 in all applications.

In this project, we first aimed to minimize the background leakage and to improve the kinetics and the sensitivity of HCR through improved hairpin designs using Nupack software (computer simulations) and experimental data, before applying this optimized HCR to our SPC system. We then tested its capability to universally detect different biomarkers. Specifically, we characterized the assay's kinetics, sensitivity, specificity (discrimination of single nucleotide polymorphism) and performance in different biological matrices. Biomarkers related to breast cancer will be used as model systems.

As miRNAs are emerging biomarkers in the field of diagnosis due to their differential expressions in various diseases, including cancer, we will be using miRNA targets that are upregulated in triple-negative breast cancer (TNBC) [12–16]. In addition, to demonstrate the application of our SPC system on protein complexes, we will be detecting and visualizing human epidermal growth factor receptor (HER) protein dimers (HER1:HER1, HER2:HER2 and HER2:HER3 dimers) in TNBC and HER2 + cell lines [17–19]. The differential expression of HER receptors is helpful in the diagnosis and categorization of Breast Cancer [20].

2 Methodology

2.1 Preparation of Working Solutions for SPC and HCR

The reaction buffer comprises of 10 mM Tris (pH 7.0), 5 mM MgCl2 and 140 mM NaCl. Stock DNA (100 μM) was diluted to 1 μM working concentration. All oligonucleotides were heated at 95 °C for a total of 5 min and then snap cooled on ice cubes for 30 min in separate tubes.

2.2 Real-Time Fluorescence Measurement for Fluorophore Quencher (F–Q) HCR and SPC

All reactions were conducted at 24 °C in 20 μl of reaction buffer which contains a final reaction concentration of 24 nM for HP1, 16 nM for HP2 for HCR and 20 nM of I1 and I2 and a corresponding dilution of targets as stated in the text.

The reactions were conducted in a single one-pot format where all components were added together. All fluorescence measurements were carried out in 384-well black Nunc microwell plate with a Tecan Spark 10 M plate reader with excitation wavelength of 485 nm and emission wavelengths of 530 nm.

2.3 Cell Culture Andimaging

AU565 (ATCC CRL-2351) and MDA-MB-231 (triple negative, ATCC HTB-26) breast cancer cells were cultured in RPMI 1640 media and supplemented with additional 10% FBS. Cell cultures were maintained in a sterile environment of 5% CO_2 and 37 °C. The cells were seeded overnight at a density of 5000–10,000 cells in 96-well chamber slides. After a 24 h post plating process (confluency ~70%), the cell medium was extracted, and the slides were washed once with warm 1 × PBS. The cells were then fixed for 10 min with 4% ice-cold paraformaldehyde.

2.4 Cell Lysate Analysis

The split proximity circuit was added into a reaction buffer of 1 × PBS (pH 7.4) and 10 mM MgCl2 which was the added one-pot to the cell lysate in order to detect HER1:HER2 heterodimers, HER2:HER2 homodimers and HER2:HER3 heterodimers. Fluorescence measurement was taken at 30 min in Tecan Spark M200 reader to monitor the kinetics of signal evolution.

After an additional 3 rounds of washing, the cells were blocked with 1% BSA and 0.1 mg/ml salmon sperm DNA in 1 × PBS for 30 min shaking (100 rpm). After this, the blocking buffer was extracted, and the chamber was washed once with 1 × PBS. Next, the cells were stained with 50 mL of 1000 × dilute DAPI (diluted with 1 × PBS from a concentration of 1 mg/mL) for 5 min in the dark, followed by washing twice with 1 × PBS. The SPC reagents were then mixed (120 nM HP1, 80 nM HP1 and 20 nM I1 and I2) and incubated with the cells for 30 min in 0.1 mg/ml salmon sperm DNA, 0.05% Tween-20, 1% BSA and 10 mM KCl in 1xPBS (SPC reaction buffer). We used Olympus Epifluorescence IX73 microscope to capture florescent cell images.

3 Results

We improved our HCR hairpin design using Ang and Yung's original guidelines [21].

After some optimization of buffer, annealing condition, hairpin ratio and salt (NaCl and $MgCl_2$) concentrations, our HCR hairpin design achieved good signal and low background leakage (Fig. 2a). This drastically improved the limit of detection (LOD), defined to be the background plus 3 standard, to 0.3 fM, (Fig. 2b, c) which was better than several HCR assays reported including those which require another separation step or enzymatic amplification steps [22–27] . In addition, our HCR

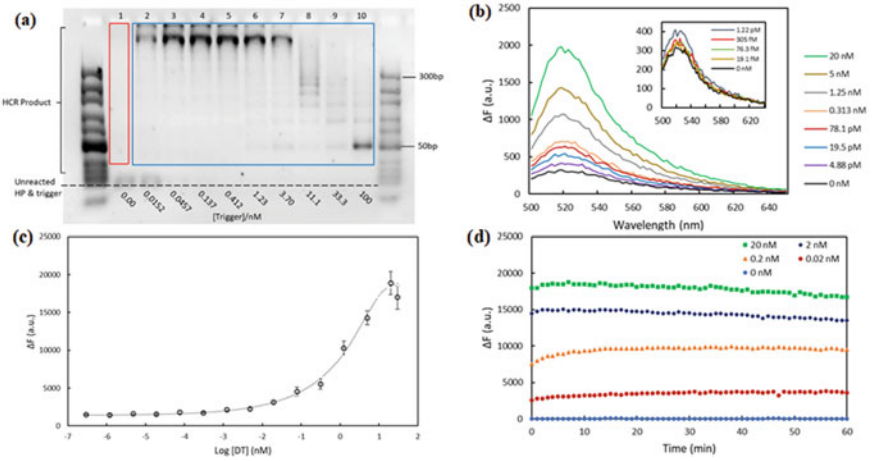

Fig. 2 **a** Gel electrophoresis of our improved DNA HP design. Low background was observed (red) and there was signal propagation (blue) visible even at [Trigger] = 15.2 pM **b** Fluorescence emission spectrum when increasing concentrations for trigger sequences was measured. **c** Characterization of the limit of detection (LOD) for the F-Q HCR system. A LOD of < 0.3 fM was achieved. **d** The kinetics of the HCR F-Q system was improved across all trigger concentrations tested. Equilibrium was reached within minutes. All data is shown as mean ± standard deviation (n = 3)

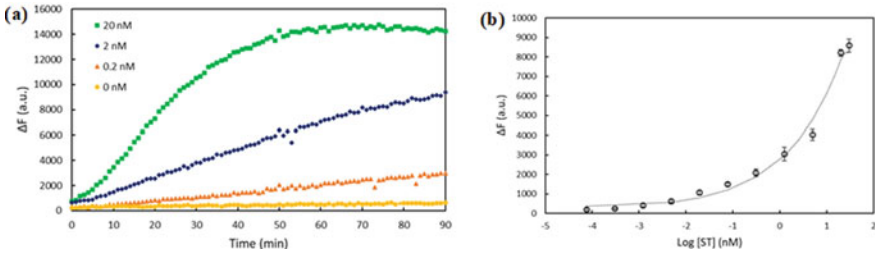

Fig. 3 **a** Characterization of the kinetics of the SPC system. Equilibrium was reached within an hour, with clear trends observable within 30 min. **b** Characterization of the LOD for the SPC system. The LOD of < 19fM was achieved. Results are shown as mean ± standard deviation (n = 3)

system showed improved kinetics, with equilibrium being reached in minutes across all target concentrations tested (Fig. 2d).

3.1 Evaluating SPC Circuit Performance

We applied our improved HCR hairpin designs into the SPC system. After going through a substantial design and optimization process, we first characterized the kinetics, sensitivity and the specificity of the SPC system with a Synthetic Target (ST). We observed that the SPC retained reasonably fast signal generation (Fig. 3a) and a detection limit well within femtomolar range in 30 min (Fig. 3b).

3.2 MiRNA Detection Using SPC

By changing our target recognition domain, we demonstrate that our SPC is able to detect miRNA targets which are upregulated in TNBC: mir9, mir21 and mir29[15] as well as let7a. We demonstrated that our SPC system continues to maintain good limit of detection ranging from 61fM to 336fM. This is well within the femtomolar range across all miRNA targets tested while using initiators designed in a plug-and-play manner.

3.3 Receptor Dimer Detection and Visualization

By changing the recognition domains, we demonstrate that our SPC can be used to detect HER receptor dimers (Fig. 4a). Here, we used two cell lines: breast cancer cell line AU565, which over-express HER2 and HER3 [28], while showing low levels of HER1 [29] and breast cancer cell line MDA-MB-231 which shows low

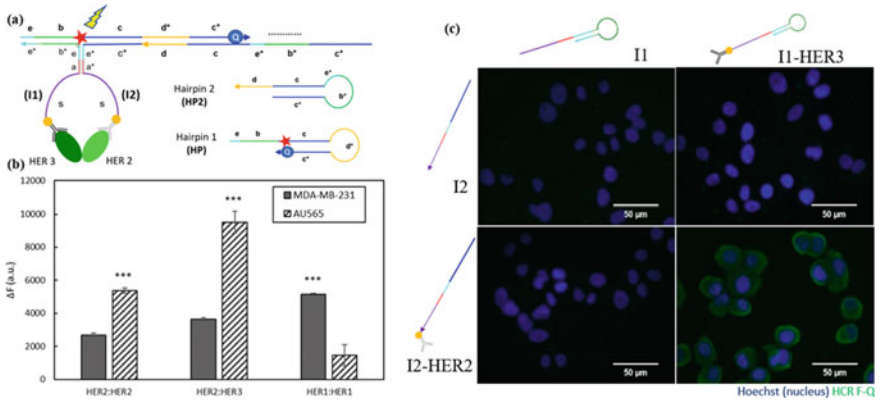

Fig. 4 **a** Binding of initiators to HER2:HER3 dimers on fixed AU565 HER2 + cells triggers HCR. **b** Detection of HER2:HER2, HER2:HER3 and HER1:HER1 dimers in cell lysate. The total protein content in the cell lysate was adjusted to 50 μg/mL **c** Fluorescence readout was achieved only when both initiators are in proximity with one another when binded to HER2:HER3 heterodimers. Nonspecific fluorescence is low even in the presence of one antibody-conjugated initiator. One sided t-test was carried out against the negative cell line (MDA-MB-231 for HER2:HER2 and HER2:HER3, AU565 for HER1:HER1). Results are shown as mean ± standard deviation (n = 5). ***$p < 0.001$

levels of HER2 and HER3 [30] but over-expresses HER [31]. In cell lysate, we observed statistically significant fluorescence signal for HER2:HER2, HER2:HER3 and HER1:HER1 dimers as compared to their respective negative cell lines (Fig. 4b). This demonstrates the high specificity displayed by our SPC system even in the complex cell lysate environment.

On fixed cells, we observed very clear signal being generated within 30 min in the detection of HER2:HER3 dimers, with no signals visible in the negative control (Initiators without antibody conjugated) (Fig. 4c). Our method is quicker than the traditional immunohistochemistry techniques used in clinical diagnosis and also shows a potential to profile strong binding interactions with extended binding times, such as the binding between T-cell and antigen presenting cells. [32]

3.4 Comparison with Common Signal Amplification Methods

In Table 1, we compare various characteristics of our SPC system with various other commonly used methods of signal amplification. SPC possesses major advantages in its ease and simplicity, showing potential for point-of-care use.

Table 1 Table summarizing the various characteristics of different signal amplification methods

Categories	SPC	PCR [33]	ELISA [34]	LAMP [33]	RCA [33, 34]	Lateral Flow [35]
Enzyme-free	+	–	–	–	–	+
Assay Design	Simple	Simple	Simple	Complex	Complex	Complex
Isothermal	+	–	+	+	+	+
Temperature(s) °C	RT (22–24)	94, 55–60, 72	RT (22–24)	60–65	37	RT (22–24)
No washing	+	+	–	+	–	+

4 Conclusion

Here, we present the DNA Split Proximity Circuit, a robust and adaptable assay which achieved a low LOD in the femtomolar range within 30 min at room temperature without the need for enzymes and intermediate washing steps. In this work, we refined the design for HCR hairpin monomers and applied this improved design to our DNA Split Proximity Circuit system. We then demonstrated the universality of our assay through the characterization of sensitivity, specificity and robustness of the assay in the detection of biomarkers like miRNA and proteins both in buffered and more complex biological environments such as cell lysate and serum. Here, we put forth our SPC system as a platform with immense potential to be used for miRNA profiling and protein complex detection in point of care applications.

Acknowledgements We would like to thank Dr Ang Yan Shan and A/P Lanry Yung Lin Yue (NUS Department of Chemical and Biomolecular Engineering) and Dr Seow Nianjia (NUS High School of Mathematics and Science) for their guidance and mentorship.

This work was supported by the National University of Singapore and NUS High School of Mathematics and Science.

References

1. Price, C. P., & Christenson, R. H. (2008). Evaluating new diagnostic technologies: perspectives in the UK and US. *Clinical Chemistry*, 54, 1421
2. ltd, R. and M. (n.d.). Point of care diagnostics market by product (glucose, infectious disease (hepatitis C, influenza, respiratory), coagulation), platform (microfluidics, immunoassays), mode (prescription & OTC), end-user (hospitals, home care) - global forecast to 2024. Retrieved from https://www.researchandmarkets.com/reports/4859240/point-of-care-diagnostics-market-by-product.
3. Kosack, C. S., Page, A. L., & Klatser, P. R. (2017). A guide to aid the selection of diagnostic tests. *Bulletin of the World Health Organization*, 95, 639.
4. Saiki, R., Gelfand, D., Stoffel, S., Scharf, S., Higuchi, R., Horn, G., Erlich, H. (1988). Primer-directed enzymatic amplification of DNA with a thermostable DNA polymerase. *Science*, 239, 487.

5. Ali, M. M., Li, F., Zhang, Z., Zhang, K., Kang, D.-K., Ankrum, J. A., Le XC., Zhao, W. (2014). Rolling circle amplification: a versatile tool for chemical biology, materials science and medicine. *Chem. Soc Rev.*, 43, 3324.
6. Zhang, X., Lowe, S. B., & Gooding, J. J. (2014). Brief review of monitoring methods for loop-mediated isothermal amplification (LAMP). *ACS Sym. Ser.*, 61, 491.
7. Dirks, R. M., & Pierce, N. A. (2004). Triggered amplification by hybridization chain reaction. *P. Natl. Acad. Sci.*, 101, 15275.
8. Li, L., Feng, J., Liu, H., Li, Q., Tong, L., & Tang, B. (2016). Two-color imaging of microRNA with enzyme-free signal amplification via hybridization chain reactions in living cells. *Chem. Sci.*, 7, 1940.
9. Gill, P., & Ghaemi, A. (2008). Nucleic acid isothermal amplification technologies—a review. *Nucleosides, Nucleotides and Nucleic Acids*, 27, 224.
10. Choi, H. M. T., Beck, V. A., & Pierce, N. A. (2014). Next-generation in situ hybridization chain reaction: higher gain, lower cost, greater durability. *ACS Nano.*, 8, 4284.
11. Choi, J., Routenberg Love, K., Gong, Y., Gierahn, T. M., & Love, J. C. (2011). Immuno-hybridization chain reaction for enhancing detection of individual cytokine-secreting human peripheral mononuclear cells. *Anal. Chem.*, 83, 6890.
12. Radojicic, J., Zaravinos, A., Vrekoussis, T., Kafousi, M., Spandidos, D. A., & Stathopoulos, E. N. (2011). MicroRNA expression analysis in triple-negative (ER, PR and Her2/neu) breast cancer. *Cell Cycle*, 10, 507.
13. D'Ippolito, E., Plantamura, I., Bongiovanni, L., Casalini, P., Baroni, S., Piovan, C., … Iorio, M. V. (2016). miR-9 and miR-200 Regulate PDGFRβ-mediated endothelial differentiation of tumor cells in triple-negative breast cancer. *Cancer Res.*, 76, 5562.
14. Jiang, H., Zhang, G., WU, J.-H., & Jiang, C.-P. (2014). Diverse roles of miR-29 in cancer (Review). *Oncol. Rep.*, 31, 1509.
15. Piasecka, D., Braun, M., Kordek, R., Sadej, R., & Romanska, H. (2018). MicroRNAs in regulation of triple-negative breast cancer progression. *J. Cancer Res. Clin.*, 144, 1401.
16. Barh, D., Malhotra, R., Ravi, B., & Sindhurani, P. (2010). MicroRNA let-7: an emerging next-generation cancer therapeutic. *Curr. Oncol. (Toronto, Ont.)*, 17, 70.
17. Spears, M., Taylor, K. J., Munro, A. F., Cunningham, C. A., Mallon, E. A., Twelves, C. J., … Bartlett, J. M. S. (2011). In situ detection of HER2:HER2 and HER2:HER3 protein–protein interactions demonstrates prognostic significance in early breast cancer. *Breast Cancer Res. Tr.*, 132, 463.
18. Sergina, N. V., Rausch, M., Wang, D., Blair, J., Hann, B., Shokat, K. M., & Moasser, M. M. (2007). Escape from HER-family tyrosine kinase inhibitor therapy by the kinase-inactive HER3. *Nature*, 445, 437.
19. Green, A. R., Barros, F. F. T., Abdel-Fatah, T. M. A., Moseley, P., Nolan, C. C., Durham, A. C., … Ellis, I. O. (2014). HER2/HER3 heterodimers and p 21 expression are capable of predicting adjuvant trastuzumab response in HER2 + breast cancer. *Breast Cancer Res. Tr.*, 145, 33.
20. Barros, F. F. T., Powe, D. G., Ellis, I. O., & Green, A. R. (2010). Understanding the HER family in breast cancer: interaction with ligands, dimerization and treatments. *Histopathology*, 56, 560.
21. Ang, Y. S., & Yung, L. Y. L. (2016). Rational design of hybridization chain reaction monomers for robust signal amplification. *Chem. Commun.*, 52, 4219.
22. Ma, C., Wang, W., Mulchandani, A., & Shi, C. (2014). A simple colorimetric DNA detection by target-induced hybridization chain reaction for isothermal signal amplification. *Anal. Biochem.*, 457, 19.
23. Dong, J., Cui, X., Deng, Y., & Tang, Z. (2012). Amplified detection of nucleic acid by G-quadruplex based hybridization chain reaction. *Biosensors and Bioelectronics.*, 38, 258.
24. Liu, P., Yang, X., Sun, S., Wang, Q., Wang, K., Huang, J.,… & He, L. (2013). Enzyme-free colorimetric detection of DNA by using gold nanoparticles and hybridization chain reaction amplification. *Anal. Chem.*, 85, 7689.
25. Niu, S., Jiang, Y., & Zhang, S. (2010). Fluorescence detection for DNA using hybridization chain reaction with enzyme-amplification. *Chem. Commun.*, 46, 3089.

26. Wang, X., Lau, C., Kai, M., & Lu, J. (2013). Hybridization chain reaction-based instantaneous derivatization technology for chemiluminescence detection of specific DNA sequences. *Analyst.*, 138, 2691.
27. Guo, J., Mingoes, C., Qiu, X., & Hildebrandt, N. (2019). Simple, amplified, and multiplexed detection of microRNAs using time-gated FRET and hybridization chain reaction. *Anal. Chem.*, 91, 3101.
28. Holliday, D. L., & Speirs, V. (2011). Choosing the right cell line for breast cancer research. *Breast Cancer Res.*, 13, 215.
29. DeFazio-Eli, L., Strommen, K., Dao-Pick, T., Parry, G., Goodman, L., & Winslow, J. (2011). Quantitative assays for the measurement of HER1-HER2 heterodimerization and phosphorylation in cell lines and breast tumors: applications for diagnostics and targeted drug mechanism of action. *Breast Cancer Res.*, 13, R44.
30. Okita, R., Mougiakakos, D., Ando, T., Mao, Y., Sarhan, D., Wennerberg, E.,… & Kiessling, R. (2012). HER2/HER3 signaling regulates NK cell-mediated cytotoxicity via MHC class I chain-related molecule A and B expression in human breast cancer cell lines. *J. Immunol.*, 188, 2136.
31. Jeong, H., Kim, J., Lee, Y., Seo, J. H., Hong, S. R., & Kim, A. (2014). Neuregulin-1 induces cancer stem cell characteristics in breast cancer cell lines. *Oncol. Rep.*, 32, 1218.
32. Chakraborty, A. K. (2002). How and why does the immunological synapse form? Physical chemistry meets cell biology. *Sci. Signal*., 2002, pe10.
33. Fakruddin, M., Mannan, K. S. B., Chowdhury, A., Mazumdar, R. M., Hossain, M. N., Islam, S., & Chowdhury, M. A. (2013). Nucleic acid amplification: Alternative methods of polymerase chain reaction. *J.* Pharm. *& Bioallied Sci.*, 5, 245.
34. Mégraud, F. (1996). Advantages and disadvantages of current diagnostic tests for the detection of Helicobacter pylori. *Scand. J. Gastroentero.*, 31,57.
35. Park, K. W., Lee, C. Y., Batule, B. S., Park, K. S., & Park, H. G. (2018). Ultrasensitive DNA detection based on target-triggered rolling circle amplification and fluorescent poly (thymine)-templated copper nanoparticles. *RSC. ADV.*, 8, 1958.

Wireless Interface for Electrical Impedance Tomography

Dhanabalan Jeevakaarthik, Adrian Luah Jun Kang, Krishnan Nithesh, David Liang Tai Wong, Lei Zeng, and Chun-Huat Heng

Abstract Electrical Impedance Tomography (EIT) is a non-invasive medical imaging technique, in which the bio-impedance of a part of the body is inferred from surface electrode measurements and used to form a tomographic image of that part. EIT is particularly useful for monitoring lung function because the resistivity of the lung tissue is higher than most other soft tissues in the thorax. Lung tissue resistivity also decreases several folds between inhalation and exhalation, which explains why monitoring ventilation is currently the most promising clinical application of EIT. EIT plays a crucial role in monitoring patients aided by mechanical ventilation, as the usage of mechanical ventilation frequently results in ventilator-associated lung injury (VALI). To enable portability and continuous remote monitoring of patients, it is desirable to incorporate wireless transmission capability to the EIT device. The main objective of this research is to design and establish a wireless interface for the transmission of bio-impedance data from the human body, to obtain real-time tomographic imaging.

Keywords Wireless interface · EIT (Electrical impedance Tomography) · ESP32-PICO-KIT · Surface electrodes · SPI interface · TCP/IP · FFT · Tomographic imaging

D. Jeevakaarthik (✉) · A. L. J. Kang · K. Nithesh
NUS High School of Math and Science, Singapore, Singapore
e-mail: jeeva.kaarthik@gmail.com

A. L. J. Kang
e-mail: adrian.luahjk@gmail.com

K. Nithesh
e-mail: nitheshkrishnan.kn@gmail.com

D. L. T. Wong · L. Zeng · C.-H. Heng
Department of Electrical and Computer Engineering, National University of Singapore, Singapore, Singapore

H. Guo et al. (eds.), *IRC-SET 2020*,
https://doi.org/10.1007/978-981-15-9472-4_53

1 Introduction

Advances in clinical telemetry medical systems in recent years have shown their usefulness in meeting the healthcare demands. In Singapore, healthcare is the third-largest spending by the ministry, behind education and defense. In the Financial Year of 2018, the government has spent 9 billion SGD on healthcare. Following Singapore's aging population, their deployment will aid in enhancing the quality of healthcare while reducing the cost [1].

Medical devices, such as medical ventilators, are designed to aid patients with respiratory problems. These life-saving devices provide mechanical ventilation by moving air into and out of the lungs to simulate inhalation and exhalation of the patient. In Singapore, a major cause of hospital admissions and 20% of death is due to respiratory disorders, such as Chronic Obstructive Pulmonary Disease (COPD). A large proportion of people affected by these disorders require assistive respiratory techniques such as lung ventilation. Electrical Impedance Tomography (EIT) is potentially a viable method for continuous monitoring of lung ventilation. By processing the collected bio-impedance signals from surface electrode measurements, imaging could be obtained subsequently with the help of well-established signal processing software. In this research, we have incorporated wireless transmission capability between the EIT device, and the computer used for imaging, to enhance the portability of the device.

2 Existing Solution and Need for Evolution

Currently, medical EIT devices are large, complex, wired systems that require the intervention of skilled personnel to collect bio-impedance data from patients. Therefore, it would be advantageous to make these devices portable and efficient for continuous monitoring purposes. With this objective, we embark on incorporating wireless transmission capability to in-house developed EIT devices. Besides, with the real-time collection of EIT data on the internet-enabled platform, real-time analysis by healthcare professionals can be made feasible to further enhance the quality of healthcare.

3 Tools

The hardware and software tools used in the development of the EIT device is shown in Table 1.

Table 1 Tools used [2–4]

Hardware	Software
Cmod A7	Arduino IDE v1.8.9
ECG device	Python 2.7 Spyder
Electrodes	Python 3.7 IDLE
ESP32-PICO-KIT	MATLABR2018b
ADS1292r	

4 System Design and Description

Figure 1 shows the functional flow diagram of the system. This functional flow is described in the subsections that follow.

4.1 Data Acquisition by EIT Device

The BIO-IMP1811 board consists of two chips, Cmod A7 and Bio-impedance analog front-end (AFE), mounted on it. Bio-impedance data from surface electrode measurements will be collected by Bio-impedance AFE, which functions as interface sensors. Data received by Bio-impedance AFE are subsequently read by Cmod A7. Cmod A7 then continuously streams data to ESP32-PICO-KIT through the SPI interface.

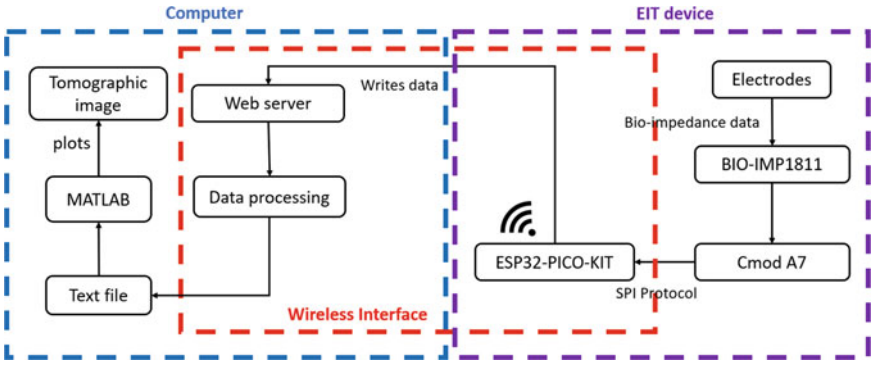

Fig. 1 Functional flow diagram of the system (EIT device, computer and wireless interface between them)

4.2 Data Transmission Through Wireless Interface

The computer hosts the web server. This server program has been written in Python 2.7 on Spyder IDE. The ESP32-PICO-KIT has an inbuilt Wi-Fi module, allowing us to incorporate wireless transmission capability into our wireless EIT system. The Arduino program running in ESP32-PICO-KIT has been designed to collect data from BIO-IMP1811 through the SPI interface, and send data to the web server over the wireless interface.

For each state of electrodes, 8192 bytes of data are written into the web server over the wireless interface. Thus, for one complete cycle of measurements, 16 sets of 8192 bytes of data are written into the web server, as there are 16 electrodes.

4.3 Data Processing and Imaging in Computer

The server program reads 8192 bytes of data from the web server. These data then undergo processing and are stored in a text file on the computer. Processed data in the text file are then read by the MATLAB program. The MATLAB program performs several computations, before plotting the final tomographic image.

The Unified Modeling Language (UML) sequence diagram of a typical interaction between various components in the EIT Device is shown in Fig. 2. The sequencing explained in Fig. 2 assumes the pre-condition that wireless connection between ESP32-PICO-KIT and the web server has been established. The numbered sequences in Fig. 2 are explained as follows:

(1) Acquisition of Bio-impedance data by surface electrodes attached to patient's body, and subsequent transmission of these data to BIO-IMP1811
(2) Data transmission to Cmod A7
(3) Data transfer from Cmod A7 to ESP32-PICO-KIT through the SPI interface

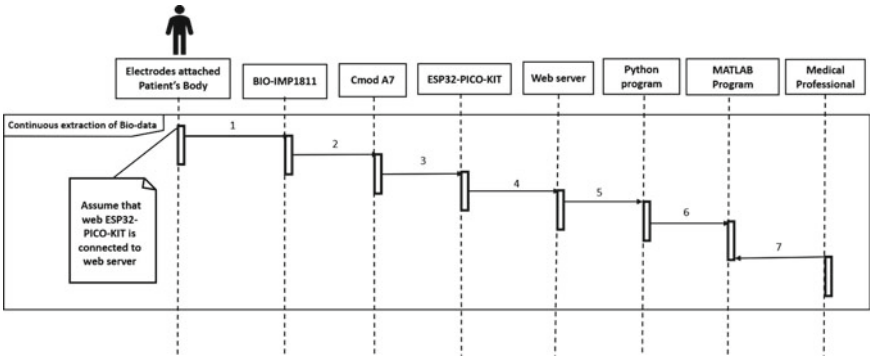

Fig. 2 UML sequence diagram of a typical interaction between various components in the EIT device

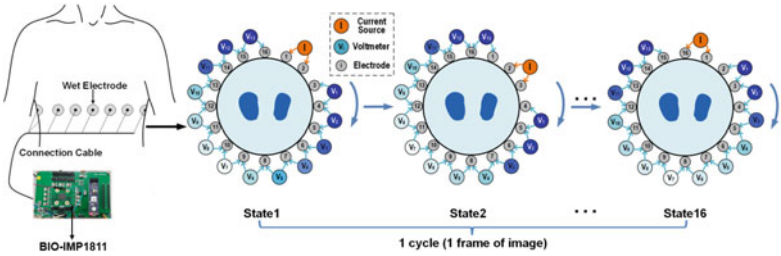

Fig. 3 Surface electrode measurements in the human body

(4) Data transfer from ESP32-PICO-KIT to the web server over the wireless interface
(5) Data processing by Python program
(6) Data processing and tomographic imaging by MATLAB program
(7) Analysis of tomographic image by healthcare professional

4.4 Surface Electrode Measurements

Surface electrode measurements are illustrated in Fig. 3. Wet electrodes are used for better contacts and signal acquisition quality. As shown in Fig. 3, signals from all 16 states are required to construct a tomographic image. During each state, a high-frequency current signal is injected into a pair of electrodes, and corresponding voltage signals are captured at the remaining 13 pairs of electrodes. This process is repeated for all 16 electrodes through successive rotations, to create one frame of the high-resolution tomographic image.

4.5 Architecture of EIT Device

The general architecture of the wireless EIT device is described in Fig. 4. The Wireless EIT device consists of the following - 'Electrodes' block for collecting electrical signals from patients body, 'Amplifier & ADC' block for amplifying and converting analog signals to digital signals, the 'Micro Controller Unit (MCU)' for overall system control and coordination, the 'Transceiver' block for transmitting the EIT data obtained, and the 'Power Source' block to power the wireless EIT device.

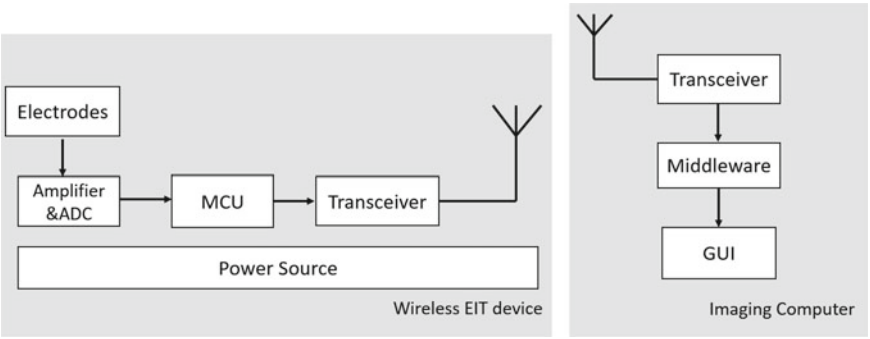

Fig. 4 General architecture of a wireless EIT device

4.6 SPI Protocol

The Serial Peripheral Interface (SPI) is a 4-wire synchronous serial communication interface specification used primarily in embedded systems [5]. Figure 5 shows the basics of how the SPI protocol works. Since the communication is synchronous, a clock signal is sent along with the data to help synchronize the two or more communicating elements. SPI devices communicate in full-duplex mode using master-slave architecture. Any data transmission through the SPI interface, specifically, through the MISO (Master In Slave Out) and MOSI (Master Out Slave In) lines, is controlled solely by the master. In our system, the master is ESP32-PICO-KIT, while the slave is Cmod A7.

An interrupt occurs when the DRDY (Data Ready) pin drops low. During each interrupt, 64 bytes of data are read from Cmod A7 by ESP32-PICO-KIT. During data transmission, the CS (Chip Select) pin must be set low. A signal in SCLK (Serial

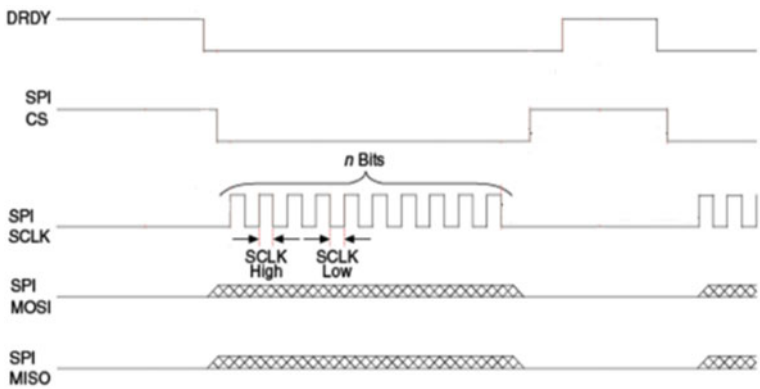

Fig. 5 SPI analog signals in each wire of the SPI protocol

Clock) pin toggles during transmission of data, to synchronize the data transfer between master and slave.

4.7 Data Transmission Using Wireless Interface

In the development of the wireless interface between the computer and the EIT Device, TCP/IP (Transmission Control Protocol/ Internet Protocol) has been established using socket programming, as shown in Fig. 6. TCP/IP is used on top of the 802.11b Wireless Interface.

Firstly, a socket object is instantiated by the Python Server Program, which binds to the IP address of the host computer. This server then listens for connection requests from clients. The client in our system will be ESP32-PICO-KIT, which uses a socket to establish a connection with the web server. Once the connection is accepted by the server program, successful connection is established between the client and server, and the client starts writing data into the server continuously. The server program will be reading these data for processing.

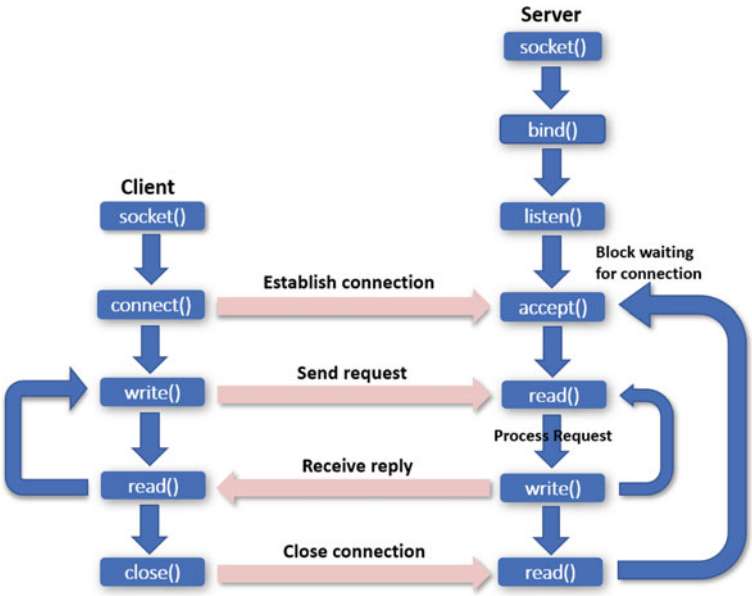

Fig. 6 Data transmission using the wireless interface

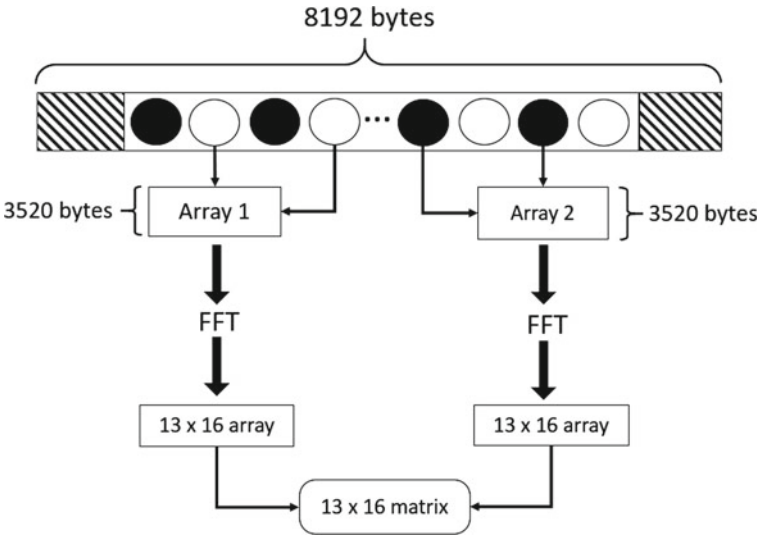

Fig. 7 An analogy of the data processing done in computer

4.8 Data Processing

As the Python server program reads each array of data from the web server, data trimming is done to ensure accuracy and reliability of the data being processed. The portion of data in each array that is used for processing is then separated into 2 arrays. FFT (Fast Fourier Transform) is carried out on each of these arrays to give an output array, containing 13 sub-arrays of 16 bytes each. Corresponding elements of every two consecutive sub-arrays are then added, giving a resultant array, that similarly has 13 sub-arrays of 16 bytes each. This 13 **x** 16 matrix is then written into a text file. An analogy of this process is shown in Fig. 7.

4.9 MATLAB Program and Tomographic Imaging

MATLAB is a multi-paradigm numerical computing environment used for technical computing, such as matrix manipulation and plotting of functions and data. The MATLAB program reads a processed array of data from the text file and performs several computations. The plotting of a tomographic image of the human chest or chest model is then done.

5 Procedure and Results

Over the course of this project, we set out a step-by-step approach to achieve the objective. Before embarking on developing the actual wireless EIT system, we have divided the project into multiple phases as follows:

5.1 Connecting ESP32-PICO-KIT to Local Wi-Fi Network

Starting with the basics, we established the connection of ESP32-PICO-KIT to the local Wi-Fi network, using an Arduino Program. Thus, ESP32-PICO-KIT can either host or connect to a web server, to transfer data through the wireless interface.

5.2 Familiarizing and Controlling GPIO of ESP32-PICO-KIT Using Web Interface

To familiarize with interfacing GPIO (General-Purpose Input/Output) pins, we connected 2 LEDs to a couple of GPIO pins. A program is run on the Arduino IDE to host a web server. Using the Graphical User Interface (GUI) designed on the web server, LEDs connected to the GPIOs of ESP32-PICO-KIT could be controlled independently.

5.3 Determining Roles of ESP32-PICO-KIT and Computer in Wireless Data Transfer

In data transfer, there exist two roles, i.e. server and client. The server is responsible for hosting a web server into which data can be written, and the client is responsible for connecting to the server to either read or write data. To determine the roles of ESP32-PICO-KIT and computer in the client-server communication, we carried out an experiment to record the time delay involved in data transfer between ESP32-PICO-KIT and computer in 2 different set-ups:

Set-up 1 - ESP32-PICO-KIT as client and computer as server; Set-up 2 - ESP32-PICO-KIT as server and computer as client.

As illustrated in Fig. 8, our results conclude that Set-up 1 results in a much faster data transfer than Set-up 2. Hence, Set-up 1 will be adopted for the development of the wireless EIT system to minimize data latency, therefore enabling continuous imaging and monitoring of real-time data.

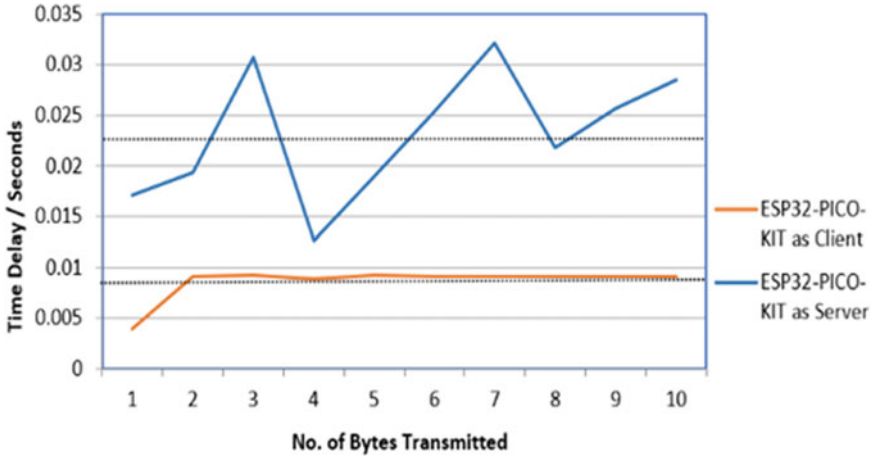

Fig. 8 Graph of time delay involved in data transfer against the number of bytes transmitted, when ESP32-PICO-KIT is: 1) client and 2) server

5.4 Transfer and Plotting of ECG Data

Testing with ECG (electrocardiogram) data helps to design our targeted wireless EIT system due to the following reasons – processing and plotting of ECG data are simpler as compared to generating an image based on EIT data, and the process of obtaining data from the ECG Device is analogous to the EIT Device [5].

Data from the ECG Device are first transferred to ADS1292r. ESP32-PICO-KIT sends a specific set of commands to obtain ECG data from ADS1292r, through the SPI interface. ESP32-PICO-KIT then writes ECG data into the connected web server. The Python server program reads data from the web server and plots a graph of ECG data, as shown in Fig. 9.

5.5 Transfer, Processing and Tomographic Imaging of Data from EIT Device

Based on the experience and knowledge gained from previous phases, the actual set-up for the EIT system has been made to retrieve data from the EIT device for tomographic imaging.

ESP32-PICO-KIT sends a specific set of commands through the SPI interface to Cmod A7, to obtain data from surface electrodes attached to the patient's body. These data, that are written into the web server by ESP32-PICO-KIT, are then processed by the Python program. The MATLAB program subsequently displays a tomographic image using the processed data.

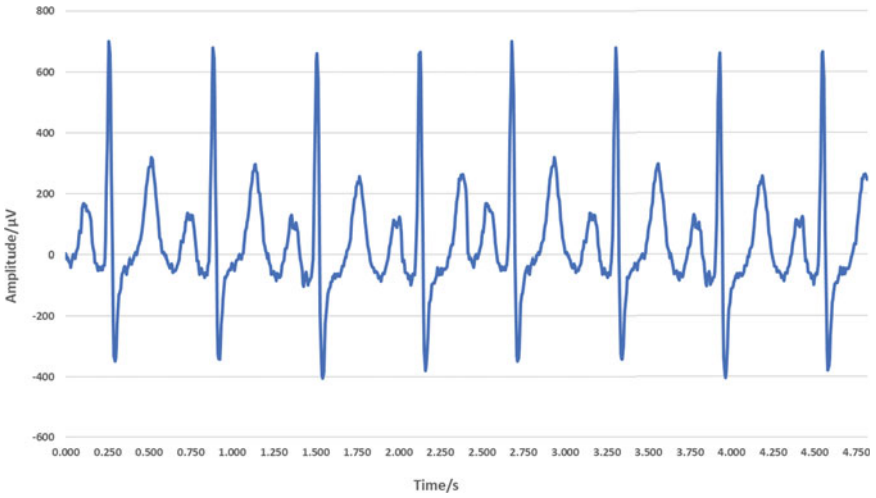

Fig. 9 Plot of ECG data

Figure 10 shows the experimental set up for the wireless EIT system and the tomographic images that are to be obtained.16 electrodes placed around the human chest, as well as the chest model. The chest model is simulated using a water tank with two cylindrical test objects placed within the tank to model the human lungs [6].

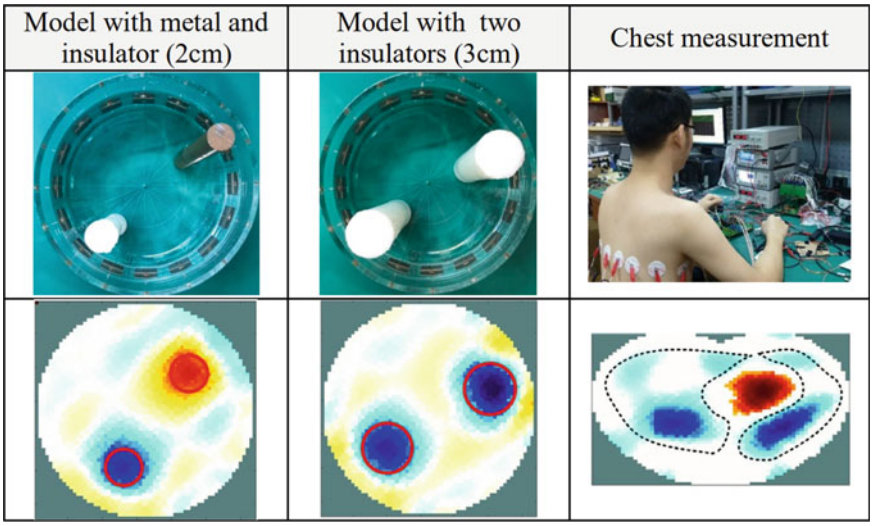

Fig. 10 Tomographic images of human chest and chest model [6]

Bio-impedance data from these surface electrode measurements are collected through BIO-IMP1811 and Cmod A7. These data are transferred to ESP32-PICO-KIT through the established SPI Protocol, and subsequently to the computer over the wireless interface. Data processing and tomographic imaging will then be done, to generate the corresponding images as shown in Fig. 10 (Images in the second row). In these tomographic images, blue color indicates low conductivity, while the color intensity represents the relative conductivity measured within the region.

6 Future Works

6.1 Enhancing Web-Based GUI (Graphical User Interface)

There is scope to improve the GUI to make it more user friendly. Creating a web-based GUI enables the continuous monitoring of patients via the Internet and Mobile app.

6.2 Power Management and Optimisation

In this configuration, the wireless EIT device transmits real-time data continuously to the computer, and so the optimization of the power consumption of different components would enhance the power efficiency of the device.

6.3 Testing the EIT Device Using Different Chest Models

Accuracy and reliability of the tomographic images generated from the data transmitted by the EIT device can be improved by testing more chest model samples.

6.4 Automation of Data Imaging

The web GUI can be improved to configure data collection and generation of imaging at regular intervals, to further automate the continuous monitoring of patients.

7 Conclusion

As stated in the objective of this research, the major application of the EIT Device is to provide a continuous monitoring technique of lung ventilation of patients with respiratory problems. The current devices used in hospitals are not as sophisticated. We are doing this research to devise a portable wireless EIT Device, which assures the quality of healthcare due to its remote monitoring capability and portability. This EIT Device helps to collect data from surface electrodes attached to the patients and transmits data to the web server through the wireless interface, for processing and tomographic imaging. This enables the medical professional to monitor the patient's condition via GUI, to provide prompt medical assistance. This is surely a leap in the advancement of Electrical Impedance Tomography Devices.

Acknowledgements We would like to thank our mentor, Professor. Heng Chun Huat, for providing us with this opportunity and his valuable guidance, Mr. David Wong Liang Tai for overseeing our research journey and providing us his best support to overcome the hurdles faced during research, and Mr. Zeng Lei for helping us with the hardware setup and to resolve hardware issues.

References

1. Singapore Government, "Injecting More Into Singapore's Healthcare As We Age," Budget 2018, 2018. [Online]. Available: http://www.singaporebudget.gov.sg/budget_2018/DoYouKnow/BudgetFeatures/InjectingmoreintoSingaporeshealthcareasweage.aspx. [Accessed: -Mar-2018]
2. Texas Instruments, ADS129x Low-Power, 2-Channel, 24-Bit Analog Front-End for Biopotential Measurements [Online]. Available: https://www.ti.com/lit/ds/symlink/ads1292r.pdf?ts=1595646820797&ref_url=https%2525253A%2525252F%2525252Fwww.google.com%2525252F
3. Espressif Systems, ESP32 Series Datasheet [Online]. Available: https://www.espressif.com/sites/default/files/documentation/esp32_datasheet_en.pdf
4. Espressif Systems, ESP32-PICO-D4 Datasheet [Online]. Available: https://www.espressif.com/sites/default/files/documentation/esp32-pico-d4_datasheet_en.pdf
5. D. L. T. Wong, "Embedded Hardware And Software Design For Low-power Wireless ECG Device," National University of Singapore, 2014.
6. B. Liu, G. Wang, Y. Li, L. Zeng, H. Li, Y. Gao, Y. Ma, Y. Lian, and C.-H. Heng, "A 13-Channel 1.53-mW 11.28-mm2 Electrical Impedance Tomography SoC Based on Frequency Division Multiplexing for Lung Physiological Imaging," IEEE Transactions on Biomedical Circuits and Systems, vol. no. c, pp. 1–1, 2019.

Wearable Physiological Stress Monitoring System—A Proof-of-Concept Study

Siew Woon Ong, Raghav Sundar, Aishwarya Bandla, and Noori Kim

Abstract Monitoring physiological responses to stressors is critical for both mental and physical health management. Different methods of physiological monitoring can early detect and prevent onset of mental disorders. Various methods and tools are commercially available to assess physiological parameters such as smartwatches and smartphones. However, only a few are used specifically for stress detection purposes. Moreover, in general, research on emotions and physiological stress is performed traditionally in a lab environment, causing results to not reflect accurately in real life, despite various sensors being used. In this paper, we design a proof-of-concept wearable stress monitoring system that assesses physiological responses to common stressors—physical activity thermal pain. The proposed stress monitoring system consists of two sensors, a pulse sensor, and a skin conductivity sensor. An early feasibility study has been carried out with multiple sensor locations implemented and analyzed including the finger, wrist and ankle. Various stressor conditions such as rest, thermal pain and physical activity were carried out. Compared to being at rest, the pulse rate and skin conductance increased following physical activity. These initial findings warrant further studies involving a larger sample size and broader stressor conditions.

Keywords Component stress · Pain · Skin conductance · Pulse rate · Wearable monitoring system

S. W. Ong
Electrical Power Engineering, Singapore Institute of Technology, Singapore 567739, Singapore

R. Sundar
Department of Haematology-Oncology, National University Hospital, Singapore, Singapore

R. Sundar · A. Bandla (✉)
The N.1 Institute for Health, National University of Singapore, Singapore 117456, Singapore
e-mail: aishwarya.bandla@nus.edu.sg

N. Kim (✉)
Electrical and Electronic Engineering, Newcastle University in Singapore, Singapore 567739, Singapore
e-mail: noori.kim@newcastle.ac.uk

H. Guo et al. (eds.), *IRC-SET 2020*,
https://doi.org/10.1007/978-981-15-9472-4_54

1 Introduction

The term stress was first explained in 1936 by the endocrinologist Hans Selye. Stress is defined as "the non-specific response of the body to any demand for change" [1]. Stress causes the mind to be in a state of fear or anxiety. In modern society, stress has become a significant problem many countries face. This condition is the way the body or mind responds to a situation or an event. However, the reason for acute or chronic stress varies hugely from person to person and differs from an individual's social and economic conditions [2].

Pain can be defined as a collection of emotional and sensory aspects, along with motor behaviors which will result from the activations of nociceptive pathways in response to harmful stimuli. Researchers have found that pain and stress are adaptive as a protection for on our bodies, for example, from physical injury or starvation. Pain and stress can be related in two ways; the pain can appear when an individual is in a state of excessive stress and/or stress can arise when an individual is experiencing severe pain [3].

Many studies on stress are divided into two categories: psychological questionnaires and physiological measurements. For this project, we focus on physiological measures. Stress monitoring can differ in healthy people and those with health conditions. The experiences of a healthy person compared to a person suffering from chronic pain are different physiologically and psychologically and it is essential to consider them while monitoring stress.

When an individual is in pain or in a condition of stress, their physiological measures differ. We hypothesize that the physiological parameters of pulse rate and skin conductivity will increase drastically as a sign of stress or pain. This was investigated using a setup consisting of a pulse sensor and a Galvanic Skin Response (GSR) sensor to measure pulse rate and skin conductivity, respectively.

When an individual undergoes physical activity, energy is being consumed, converted to heat and result in a rise in body temperature. This also initiates sweating [4]. Pulse rate also increases with exercise [5]. The pulse rate also increases in response to thermal stimuli such as when in contact or immersion in ice [6]. With the evidence of change of pulse rate and sweating, the activity of sports and thermal stimulus, in this study these stressors were used to simulate pain and physical stress.

The current state of the art emotional research is commonly conducted in lab conditions. Finger measurements are usually for skin conductance testing for psychological research. This method requires the subject to be in the lab for extended hours to obtain a sufficient amount of data.

Devices such as smartphones or smartwatches can detect multiple physiological parameters at the same time. However, the obtained results might not be accurate. For the research environment, sensors are designed to undertake experiments from an individual without leaving the lab at stationary conditions. This could cause inconvenience to the subject and hamper conditions, especially if the measurement has to be taken over a longer period [7].

In this paper, we describe a proof-of-concept study investigating the effect of stressors (physical activity and thermal pain) on physiological measures of stress including pulse rate and GSR. We talk about the system design and experiment testing method. We also discuss the obtained results and possibilities for future studies.

2 System Design and Testing Method

2.1 Design Implementation

An illustration of the system design is found in Fig. 1. The sensors used should be able to detect the parameters accurately and be highly sensitive. As mentioned, we are focused on skin conductivity and pulse readings. Figure 2 shows the early

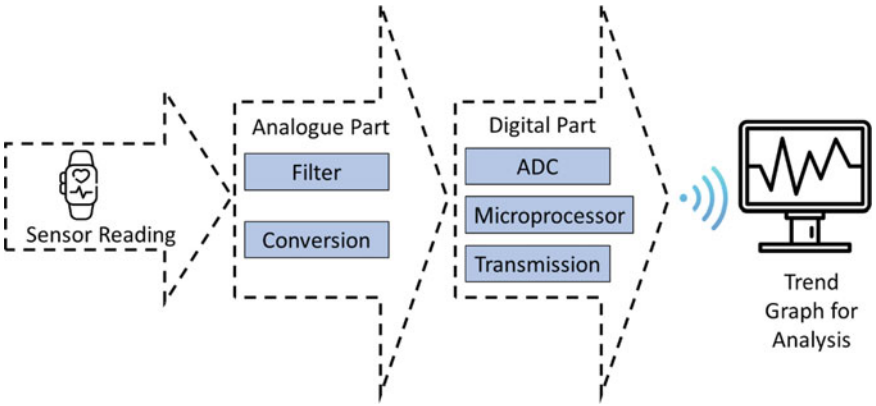

Fig. 1 Overview of system design

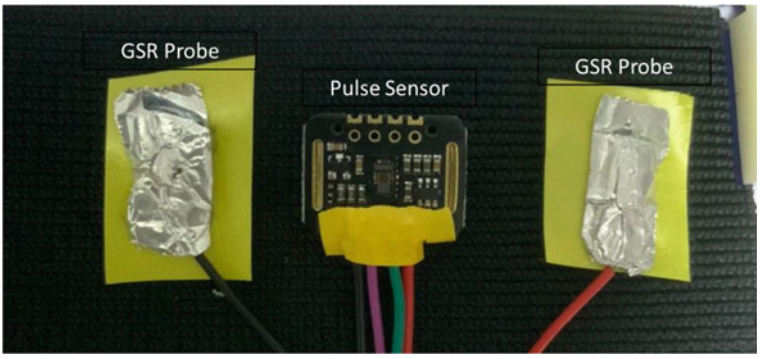

Fig. 2 Experimental set-up of sensor probes

feasibility set-up of the experiment.

Arduino Nano was used as a development board. An Arduino board is readily available. The available input and output pins are suitable to be scalable in the future with more sensor.

To measure the pulse rate, Max30102 was used as the pulse sensor, using Inter-Integrated Circuits (I2C) communication. The basic principle of the pulse oximeter is to have the ability to continuously monitor the functional oxygen saturation of haemoglobin in arterial blood (SaO_2). The pulse oximeter uses red and infrared (IR) light to differentiate oxygenated and deoxygenated blood via varying levels of light absorption [8]. Green light is used for pulse measurement for the wrist and ankle as the wavelength is shorter for better penetration through the skin. For the sensor to be accurate and sensitive, conditions such as the Light Emitting Diode (LED) light, sample size, sample rate, pulse width and range are to be adjusted. The intensity of the light setting is ranged from 0–255 steps, 0 being 0A and 255 being 50 mA. The mode of the light was red and IR for finger reading and green for wrist and ankle reading. Brightness intensity was 70, approximately using 13.73 mA.

An average of 4 samples were taken as one reading and the sampling rate was 1 s. The pulse width was set at 69 ms. The Analogue-Digital Converter (ADC) range was set at 8bits. The mode and intensity of the light were adjusted to get a better reading for different conditions but for this experiment, the settings reminded the same.

To create the GSR sensor, we used the concept of an ADC and a low-pass filter. To simulate the probes of the GSR sensor, we used aluminum foil. The low-pass filter rejects high-frequency noise. A 10 kΩ resistor and 0.1μF capacitor were used to design the cut-off frequency is 159.2 Hz. A simple first-order filter was used.

The GSR signal consisted of two components, skin conductance level (SCL) and skin conductance response (SCR). SCL is known as the tonic level and SCR is known as the phasic response [9]. SCR are short fluctuations in the skin conductance that last for a few seconds and usually follows a pattern of a steep rise, a short peak and followed by a slow return to a baseline [7]. For this study, we recorded the mean skin conductance response. Velcro straps were used to secure the sensors and probes to various locations on the skin. The Velcro strap ensures that the sensor probes maintain close contact to the skin. A pictorial representation of the GSR system is illustrated in Fig. 3.

Conductivity (G) is obtain by the reciprocal of Resistance (R) [10]. By reading the resistance of the skin, we were able to calculate the skin conductance.

$$G = \frac{1}{R}$$

Three locations were tested to determine the most suitable placement of a wearable sensor, the center wrist (1 cm from the end of palm), and ankle and the fingers (index finger and middle finger for skin conductance reading and index finger only for pulse reading). A representative example of skin conductance positions on one subject is illustrated in Fig. 4.

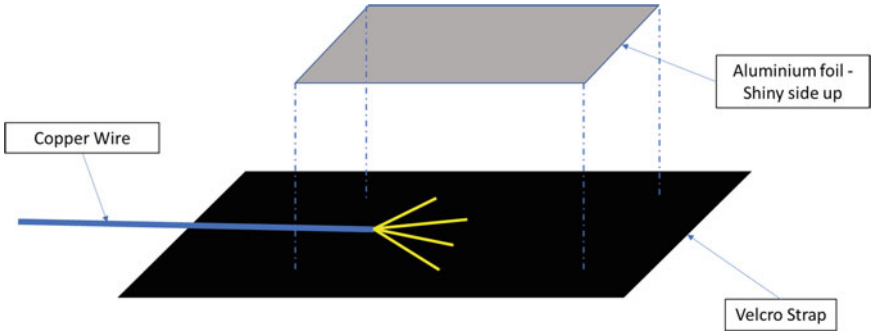

Fig. 3 Skin conductivity probe

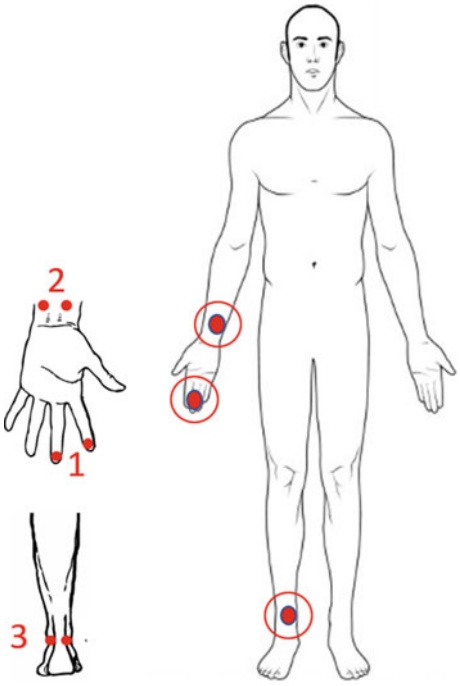

Fig. 4 Measurement locations: (1) Fingers (2) Wrist (3) Ankle

The values collected in the first 30 s will not be used to ensure that the values obtained are in a stable state. As the motivation of this project was to create a wearable stress monitoring system, the data was set to restart when the user removes the sensor from his/her skin.

The GSR data is acquired over a longer time period, and hence there was no need to obtain sensor reading every second. The values of pulse rate and skin conductance were averaged over the entire duration of the study. Skin resistance decrease with

time of contact and exposure. The resistance of dry and wet skin becomes equal overtime, at around 2/3 of the wet skin resistance [10].

We used the Parallax Data Acquisition (PLQ-DAQ) Tool to convert the sensor readings into graph form in real-time. With the graphs, we could observe the stability of the sensor and the changes.

2.2 Experiment Testing

As we tested for feasibility at an early stage, there was only one subject and the data were collected under different stressor conditions. The subject was a healthy female, aged 24 years.

For each skin sensor location, results were taken at different stressor conditions. The aim of these conditions was to simulate and create physiological changes and stress to the body to investigate the change in pulse rate and skin conductance due to these changes and stress. The conditions were at rest, exposure to thermal stimulus (ice) and after physical activity (continuous jumping for 4 min). Pulse rate was recorded in Beats Per Minute (bpm) and skin conductivity in micro-siemens (μS).

The simulations of pain were done by exposure to thermal stimulus (ice) on the right hand for 4 min. The skin temperature changes rapid when exposed to cold, typically in a minute. Ice compression are most effective when it is done for below 10 min [11]. Within 4 min, the subject will feel pain.

For each stressor condition, the subject was started of being seated in a comfortable position for 1 min, followed by completion of stress condition and another rest for 5 min to conclude the experiment. Each experiment will be at least 1 h apart to ensure the start conditions were as similar as possible.

3 Results

As mentioned, PLQ-DAQ was able to show the readings in form of a graph for each experiment. Figures 5 and 6 shows examples of the readings when three activities are placed in a single graph.

3.1 Skin Response Reading

For GSR reading, the values tabulated in table are averages during each activity (Tables 1, 2, 3, 4, 5, 6).

During rest, the SCR reading decreases with time. As for the jumping condition, the results in the first minute were the highest, followed by a dip and gradually increase.

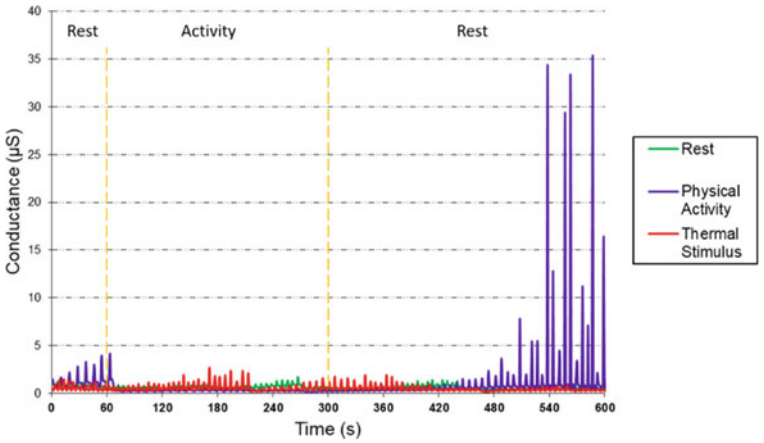

Fig. 5 Skin conductance at the fingers

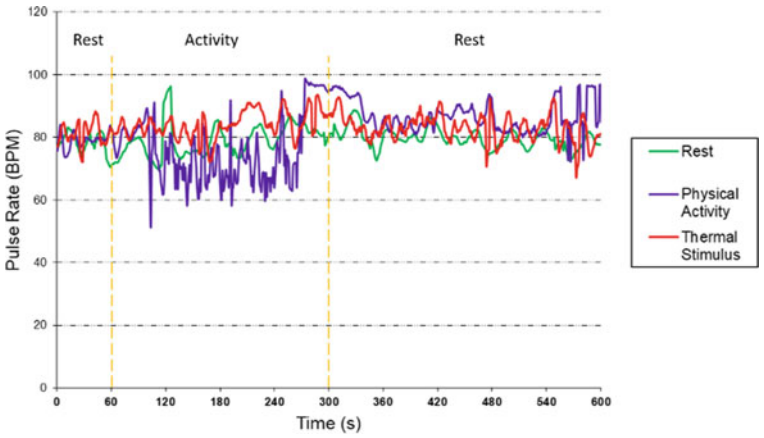

Fig. 6 Pulse rate at the finger

Table 1 Skin conductance response reading from the finger

Activity	Skin conductance (μS)		
	First minute rest	Activity	5 min Rest
At rest	0.66	0.62	0.52
Exercise	1.16	0.29	1.21
Thermal stimulus	0.56	0.59	0.45

Table 2 Skin conductance response reading from the wrist

Activity	Skin conductance (μS)		
	First minute rest	Activity	5 min Rest
Rest	2.86	2.64	1.40
Exercise	2.04	0.54	1.84
Thermal stimulus	2.29	1.88	1.84

Table 3 Skin Conductance Response Reading from the Ankle

Activity	Skin conductance (μS)		
	First minute rest	Activity	5 min Rest
Rest	4.87	4.89	3.90
Exercise	5.34	1.80	3.45
Thermal stimulus	4.38	5.21	5.11

Table 4 Pulse rate reading from the finger

Activity	Pulse rate (BPM)		
	First minute rest	Activity	5 min Rest
Rest	79.6	78.9	80.0
Exercise	80.4	75.9	86.1
Thermal stimulus	82.7	83.3	84.1

Table 5 Pulse rate reading from the wrist

Activity	Pulse rate (BPM)		
	First minute rest	Activity	5 min Rest
Rest	83.5	82.0	80.4
Exercise	83.9	78.3	87.7
Thermal stimulus	83.1	81.0	84.3

Similar to being at rest, the skin conductance did not change when on exposure to thermal stimulus.

The different skin sensor locations had different SCR sensitivity and detected SCR differently. The range of SCR readings differ from sensor locations.

Table 6 Pulse rate reading from the ankle

Activity	Pulse rate (BPM)		
	First minute rest	Activity	5 min Rest
Rest	78.7	80.1	78.7
Exercise	78.4	82.4	82.5
Thermal stimulus	78.8	80.66	78.24

3.2 Pulse Reading

Similarly, for pulse rate, the values tabulated in table are averages during each activity.

The pulse rate increased after going through exercise. However, the pulse rate did not increase exposure to thermal stimulus, similar to the results on comparison with the rest condition.

4 Discussion

The results for skin conductance show that consist of small fluctuation and takes a relatively long time to change. The difference in responsiveness is due to several conditions of the skin such as amount of sweat glands density and electrodermal activity [7]. During physical activity, the body becomes dehydrated [5] and our results showed that when the subject started exercising, SCR is the lowest. However, when the subject stopped, the SCR reading started to increase.

From the pulse rate results we noticed that, only after exercise, the pulse increased slightly. However, during the experiment, while exercising, the sensor readings were the most unstable compared to being at rest and thermal stimulus of the hand. This could be due to instability due to physical activity.

Comparing to our hypothesis, we predicted that the pulse rate and SCR will increase when in pain and physical activity. The results confirmed that there is no significant increase of SCR and pulse rate when going through a thermal pain.

Literature evidences that resistances from various body parts vary. For example, the left wrist and right wrist have a slight difference in resistance [7]. In our study, the sensors were tested on the left side of the body to reduce variation due to potential lateralization influence.

Fingers were included as finger measurements are traditionally used in labs to measure emotional research. Wrist and ankle are body parts that are commonly exposed and easily accessed. The wrist and ankle were also selected because it can be integrated into a product that is commonly found. The wrist measurement can be incorporated in a watch while the ankle measurement can be incorporated for an anklet or socks.

In some studies, subjects were asked to refrain from moving to reduce skin conductance changes due to physical activity [7]. We should take this into consideration when reviewing the results in the future.

At rest, the hearts pump the least amount of blood thorough the rest of the body therefore the pulse rate should be the lowest here. According to the Singapore Heart Foundation, for an average adult, the resting pulse rate can vary from 60–90BPM and can vary from person to person [12]. Our results correspond to the standard given with 79.6BPM at rest for 10 min.

As this was a proof-of-concept study, this does not have enough evidence to show a significant difference and comparison of different living and health conditions.

Further studies would entail bigger sample size and over a longer duration. Also, the conditions employed represent only a certain aspect of stress and are not exhaustive. Future work could also explore development of this proof-of-concept study into a wearable device, with several physiological measures such a temperature and also including wireless data transfer.

5 Conclusion

From this study, GSR and pulse reading are affected due to physical activity. Readings from skin conductance and pulse rate are found to be higher when during physical activity compared to being at rest. However, when undergoing thermal stimulus, GSR and pulse reading did not have drastic changes compared to being at rest.

Acknowledgements We would to show our gratitude to the institutes, Singapore Institute of Technology for providing us the platform to carry out our studies and experiment.

The authors would also like to thank the support of the National University of Singapore through its N.1 Institute's Translational Core.

We would like to thank Choong Zi Jie and Rezwana Binte Mohsin for their help with development the skin conductance sensors. We would also like to thank Joslyn Lim and Shawn Ting for their helpful advice and comments during the experiment period.

Additionally, the authors like to thank the reviewers for their kind comments and we have taken them in o consideration and made some adjustments in the manuscript.

References

1. H. Selye, Stress without Distress, Springer, Boston, MA, 1976, pp. 137–146.
2. M. R. Salleh, "Life Event, Stress and Illness," October 2018. [Online]. Available: https://www.ncbi.nlm.nih.gov/pmc/articles/PMC3341916/.
3. C. G. Abdallah and P. Geha, "Chronic Pain and Chronic Stress: Two Sides of the Same Coin?," *Chronic Stress,* Vols. 1: 1–10, 2017.
4. T. McMorris, P. D. Tomporowski and M. Audiffren, "Exercise, Dehydration and Cognitive Function," in *Exercise and Cognitive Function*, John Wiley & Sons, Ltd, 2009, pp. 135–151.
5. B. Fitzgerald, A. Weldon and G. Scalia, "The Normal Heart Rate Response to Treadmill Exercise," *Heart Lung and Circulation,* vol. 25, p. 653, 2016.
6. C. C. W. G. Bongers, T. M. H. Eijsvogels, D. H. J. Thijssen and M. T. E. Hopman, "Thermoregulatory, Metabolic, and Cardiovascular Responses During 88 min of Full-body Ice Immersion – A Case Study," *Physiological Reports,* vol. 7, no. 24, p. 6, 2019–12.
7. M. v. Dooren, J. (.-J. d. Vries and J. H. Janssen, "Emotional sweating across the body: Comparing 16 different skin conductance measurement locations," *Physiology & Behavior,* no. 106(2), p. 298–304, 2012.
8. E. D. Chan, M. M. Chan and M. M. Chan, "Pulse oximetry: Understanding its Basic Principles Facilitates Appreciation of its Limitations.," *Respiratory Medicine,* no. 107(6), p. 789–799, 2013.
9. M. E. Dawson, A. M. Schell and D. L. Filion, The Electrodermal System, Handbook of Psychophysiology, p. 217–243.

10. P. E. Sutherland, "Electrical Safety Aspects of the Resistance Property of Materials, Circuit Model of the Human Body, Effect of Current on the Human Body," in *Safety, Principles of Electrical*, The Institute of Electrical and Electronics Engineers, Inc., 2015, pp. 90–100, 101-117.
11. S. L. Michlovitz, J. W. Bellew and T. P. Nolan, Modalities for Therapeutic Intervention, 5 ed., F. A. Davis Company, 2011, pp. 19–278.
12. "Singapore Heart Society," 2019. [Online]. Available: https://www.myheart.org.sg/.

Fabrication of Microbial Fuel Cells Powered by Soil-Based Electrogenic Microbes and Wastewater as a Novel Method for Electricity Generation and Wastewater Purification Via a Novel Hybrid Process

Ng Yan Bin Lucas and Peng Zikang

Abstract Microbial Fuel Cell (MFC) is a promising renewable energy source through the use of biofuels. This study involves the testing of Microbial Fuel Cells with potting soil, burnt soil and garden soil, before evaluating the efficacy of lime compost, grapefruit compost and strawberry compost (made from recycled fruit waste) in generating electricity. The MFC's maximum voltage output and maximum power output at various ohmic resistances were then determined. Among the 3 common soils tested, potting soil produced the highest voltage and power output. It produced an open circuit voltage of 137 mV. Grapefruit compost had greatest voltage and power output among the compost soils with an open circuit voltage of 152 mV. The simultaneous nitrification-denitrification (SNdN) process was utilized by the introduction of ammonia-oxidizing bacteria (AOB) and nitrite-oxidizing bacteria (NOB). The use of aquarium wastewater was in the cathodic chamber produced greater voltage than the control set-up (burnt soil). In addition, ammonium and nitrate levels in the wastewater dropped drastically. Finally, to maximize the efficiency of the MFC, grapefruit was composted with potting soil (to achieve the best voltage), and also used alongside with aquarium wastewater, producing a maximum voltage of 310 mV and removing ammonium and nitrates by over 80%.

Keywords Microbial fuel cell · Compost · Nitrification · Denitrification · Ammonia-oxidizing bacteria

1 Introduction

Fossil fuels provide a valuable source of energy but is being depleted and will eventually run out. Consumption of fossil fuels has also severely imperiled human life

N. Y. B. Lucas (✉) · P. Zikang
Hwa Chong Institution (High School), Singapore, Singapore
e-mail: lucasnyb@gmail.com

P. Zikang
e-mail: pengzikang@gmail.com

H. Guo et al. (eds.), *IRC-SET 2020*,
https://doi.org/10.1007/978-981-15-9472-4_55

through its drastic aftermaths, such as global warming and atmospheric pollution [1]. Furthermore, in 2016, about 2.5 kg of food waste is thrown away by an average Singaporean household each week [2], showing the severity of food wastage in Singapore. Hence there is a need to explore cleaner alternative sources of energy, as well as to promote recycling to manage wastage at the same time.

Driven by the increasing concern over the energy-climate crisis and environment pollution, recently, there has been growing interest in the double chambered Microbial Fuel Cells (MFCs). MFCs put forward the possibility of harvesting electricity from organic waste and renewable biomass and are hence a renewable energy source. MFC is a bio-electrochemical system that utilizes microbes to consume and degrade nutrients to release energy in the form of electrons, protons and carbon dioxide [3]. An MFC (Fig. 1) comprises an electron acceptor, a cathode and an anode, a proton exchange membrane or salt bridge and the medium with microbial populations [4]. The anodic chamber is connected to the cathodic chamber by a salt bridge, which transfers protons via the salt ions in the salt bridge. These protons will then meet with the electrons that travelled through the external circuit across the multimeter to the cathodic chamber, resulting in a current produced [5].

This study aims to explore a more environmentally friendly method to generate electricity using MFC. Previous studies have found that microbes found in soil mainly come from the *Geobacteraceae* family [6], resulting in a limited diversity of microbial populations, which could be accountable for low electricity produced. Thus, this study proposes introducing fruit waste to enrich soil with nutrients like carbohydrates, and the low pH level of the fruit could also introduce a new microbial population known as Acidophiles, which are exoelectrogens [7]. However, fruit waste is difficult to obtain in large quantities. Therefore, creating soil compost with fruit waste to reduce the amount of resources needed while maximizing power output, by introducing both bacteria found in fruits and soil will be more ideal. In this study, the effect of different types of soil (burnt soil, garden soil and potting soil) and fruit waste (lime, grapefruit and strawberry) on power output of a self-constructed double chamber MFC was investigated.

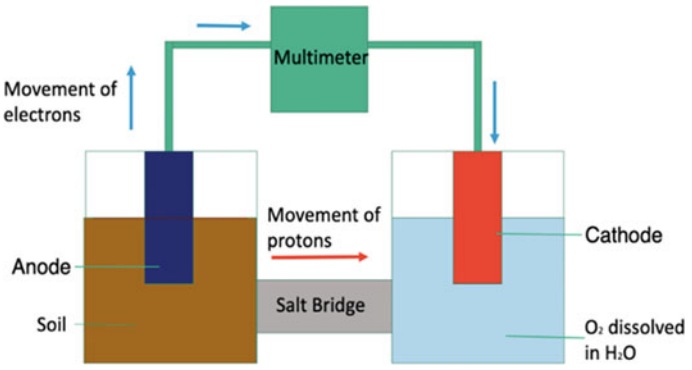

Fig. 1 Set-up of a microbial fuel cell (MFC)

Based on several studies, the most common Terminal Electron Acceptor used is oxygen dissolved in water due to its high redox potential, yet it poses challenges due to its poor contact with electrode surface [4]. Oxygen is the most common electron acceptor utilized in the cathode compartment due to its high oxidation potential and that it yields a clean product (water) after reduction. However, most studies show that the oxygen supply to the cathode compartment is energy consuming [4]. Some studies use MFCs that reduces oxygen from atmosphere by using an air cathode, but contact difficulties of oxygen at the air cathode is pertinent and expensive catalysts such as platinum is needed for reduction using an air cathode. Hence, there is a need to explore alternative electron acceptors. Research has shown that MFC can remove ammonium and metal ions when electrons and protons reduce them to less toxic forms, serving as alternative electron acceptors [8]. In a conventional MFC used to treat wastewater, wastewater from leachates, brewery and sewages have been utilized but is used only in the anodic chamber, which only allows ammonia-oxidizing bacteria (AOB) and nitrite-oxidizing bacteria (NOB) to remove harmful pollutants in wastewater by cellular redox reactions, without being able to utilize fully the electrochemical reactions of the fuel cell to reduce the level of these pollutants [9].

Unlike most studies which rely on biological methods for ammonium and nitrate removal, this study proposes introducing these bacteria into the aquarium wastewater first, before adding the effluent to the cathodic chamber, such that removal of these pollutants would be made more efficient by the redox reactions from both the bacteria and fuel cell.

2 Materials and Methods

2.1 Materials

Burnt, potting and garden soil were purchased from Corona Florist and Nursery. Potassium chloride (99% purity) and agar powder were procured from Sigma Aldrich. Wastewater was obtained from fish tanks.

2.2 Construction of a Double-Chamber Microbial Fuel Cell

A 3.0 cm hole was drilled at the side of each of the 2 containers. Soil (1 L), premixed with 350 ml of 0.28 moldm^{-3} of glucose solution was added to the anodic chamber.

$$\text{Percentage of pollution removal: } Q_d = \frac{C_b - C_a}{C_b} \times 100\%$$

where Q_d is the percentage of ammonium or nitrate removed;

Fig. 2 Actual set up of MFC

C_a is the final concentration of ammonium or nitrate/mgL^{-1},
C_a is the initial concentration of ammonium or nitrate/mgL^{-1}

Volume rather than mass of soil was kept constant as different types of soil have different densities and using the same mass of soil would result in the volume being very different. Three types of soil were studied—burnt, potting and garden. A salt bridge which was prepared from potassium chloride and agarose powder was connected tightly to the two ends. 4 graphite electrodes were obtained from spent batteries and coiled with copper wires which were soldered together to form one set of electrodes. Electrodes in soil were 3 cm above the base while electrodes in water were fully submerged. An electric air pump was used to introduce oxygen into the water in the cathodic chamber (Fig. 2).

Power output and current were first calculated after measuring the voltage output when an external resistance was applied. Resistors were ranged from 100 ohms to 470 k ohms, taking a total of 15 points to plot the power density curve and polarization (Voltage versus current density) curve. Subsequently, the set-up was left for 7 days to generate electricity and voltage trends were recorded using a SparkVue datalogger.

2.3 Preparation of Compost

Discarded fruits (lime, grapefruit and strawberry) which were bruised or disfigured were collected from fruit stalls. The fruits were sliced into quarters and arranged evenly on 2 L of burnt soil, before adding another 2 L of burnt soil on top. The containers were then placed in an eco-garden with constant shade for 90 days. The power output of the different types of compost was determined as described in section B.

2.4 Removal of Ammonium and Nitrate from Wastewater via the MFC

1 L of aquarium wastewater was mixed with 500 ml of burnt soil and left for 2 h to allow the essential bacteria in soil to mix with the wastewater. The levels of ammonium and nitrate in the wastewater were measured using a colorimeter (HACH DR 890) before and after the experiments. The suspension was then filtered under vacuum to obtain the filtrate which was placed in the cathodic chamber of MFC for redox reactions to occur. The efficiency in removing the pollutant was calculated using the formula:

3 Results and Discussion

3.1 Characterization of MFC Using Varied External Resistances

Maximum power outputs were obtained from power density graphs while maximum voltage outputs were obtained from polarization graphs. Out of the 3 types of common soils, potting soil showed the most ideal power density curve (Fig. 3), with the highest power output of 130 W m^{-2}, highlighting that its electrochemical reactions and electron transfer rates are the greatest. It also has the highest maximum voltage output (Fig. 4) of 118.3 mV. Among the 3 types of compost soils, grapefruit showed the greatest power output of 71.3 W m^{-2} (Fig. 5) and also the greatest maximum voltage output of 151.3 mV (Fig. 6).

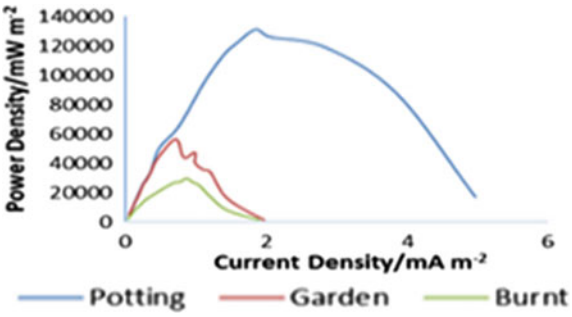

Fig. 3 Power density curves of the common soils

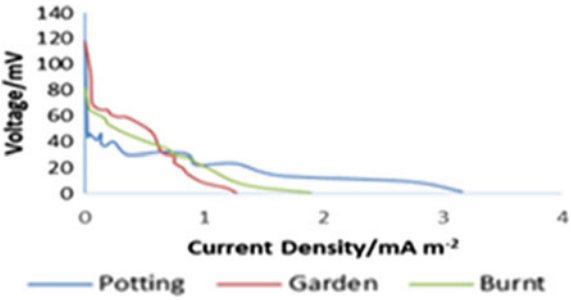

Fig. 4 Polarisation curves of the common soils

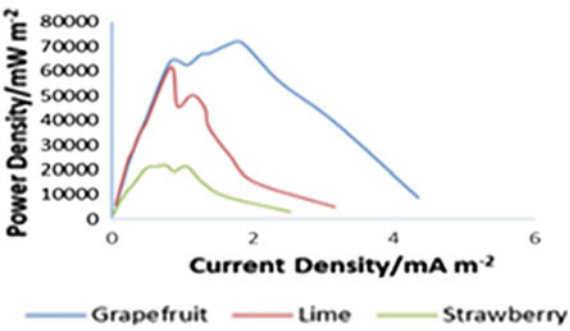

Fig. 5 Power density curves of the compost soils

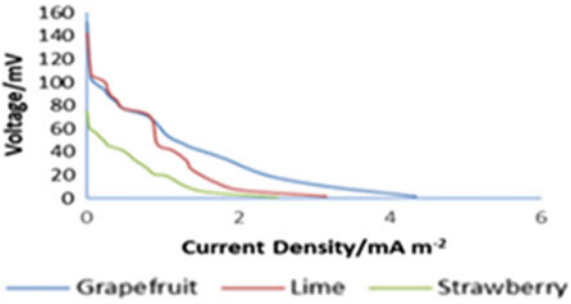

Fig. 6 Polarisation curves of the compost soils

3.2 Gram Staining of Soils

Gram-positive bacteria were identified based on its unique purple color because of the staining of peptidoglycan cell wall while red stains from safranin are characteristic of gram-negative bacteria. Burnt soil (Fig. 7) and garden soil (Fig. 8) showed communities of gram-negative bacteria and a few isolated groups of gram-positive bacteria while potting soil (Fig. 9) showed the presence of both gram-negative and gram-positive bacteria. Among the compost soils, grapefruit compost (Fig. 10) contains both gram-negative and gram-positive bacteria, while lime compost and strawberry compost contain mainly gram-positive bacteria. Gram-negative bacteria rely on

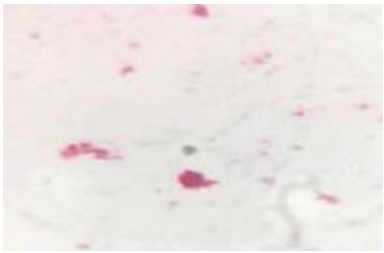

Fig. 7 Bacteria in burnt soil

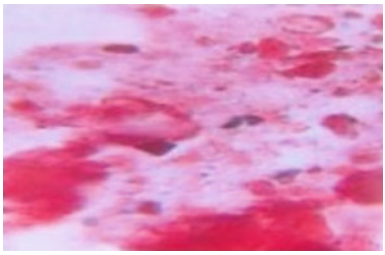

Fig. 8 Bacteria in garden soil

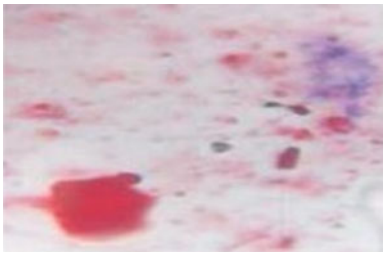

Fig. 9 Bacteria in potting soil

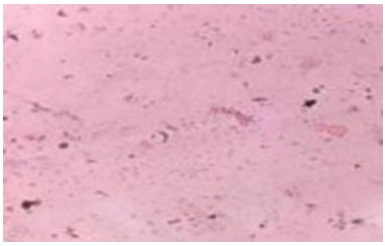

Fig. 10 Bacteria in grapefruit compost

cell surface exposed cytochromes for the oxidation and reduction of minerals and organic material extracellularly and thus could generate a higher voltage than gram-positive bacteria [10]. This suggests that potting soil and grapefruit compost that have more gram-negative and gram-positive bacteria can produce a greater voltage output (Figs. 11, 12, 13).

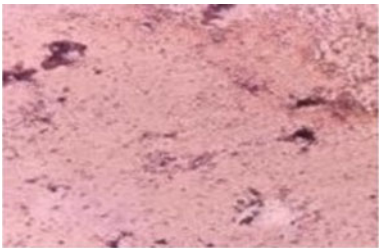

Fig. 11 Bacteria in lime compost

Fig. 12 Bacteria in strawberry compost

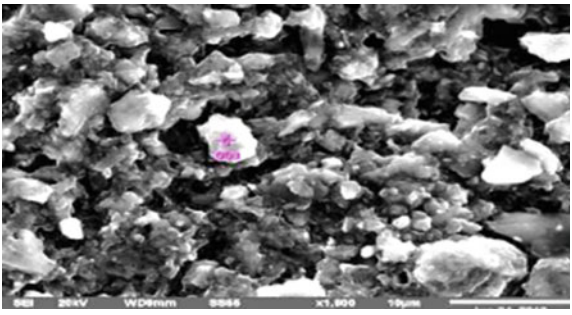

Fig. 13 SEM image of control electrode

3.3 Analysis of Electrodes by SEM

SEM images of the electrodes from burnt, garden and potting soil (Figs. 14, 15 and 16) revealed a much smoother surface as compared to the surface of the control electrode (a new graphite rod cleansed with ethanol), which showed a rougher surface with discrete particles. This suggests that a layer of biofilm had formed over the graphite electrodes of the soil, thus increasing the voltage of the MFC. Biofilm comprises mainly gram-negative bacteria, which are more adaptable than gram-positive bacteria in the soil conditions [11], therefore they are able to reproduce more rapidly compared to gram-positive bacteria. Furthermore, bacteria like *Geobacter sulfurreducens* in soil show the best extracellular electron transfer (EET) performance because the biofilm grown on the electrode undergoes direct electron transfer due to its multiheme cytochromes [12]. Thus, the gram-negative bacteria found in the biofilm that could

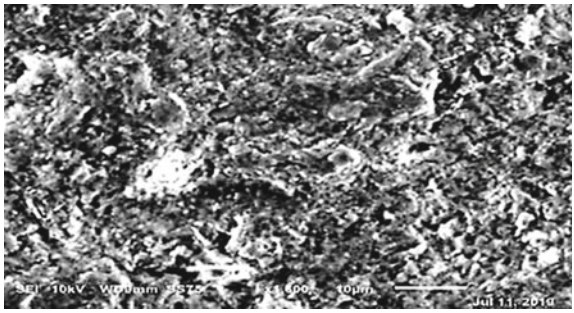

Fig. 14 SEM image of burnt soil eletrode

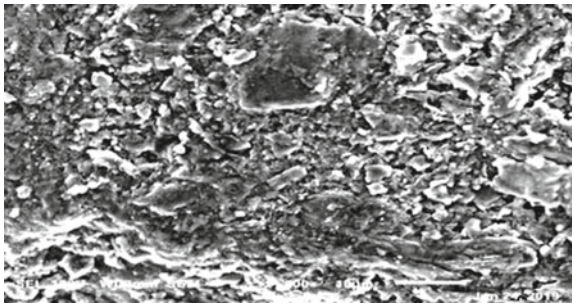

Fig. 15 SEM image of garden soil electrode

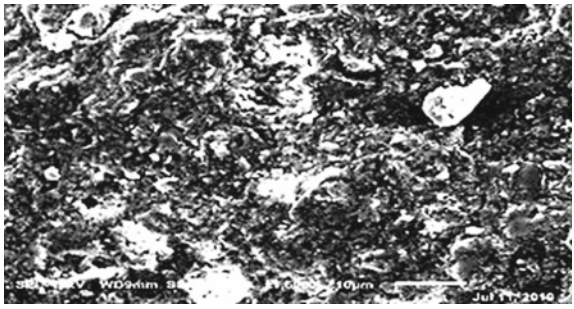

Fig. 16 SEM image of potting soil electrode

oxidize the minerals in the soil could also contribute to the high voltage produced by potting soil (Figs. 17, 18).

3.4 Characterization of Common Soils by EDS

The analysis of the EDS spectrum showed that potting soil (Fig. 19) contained the highest concentration of aluminum (1.70%) and silicate ions (1.08%), followed by garden soil (Fig. 18), with 0.59% aluminum and 0.29% silicate ions and burnt soil

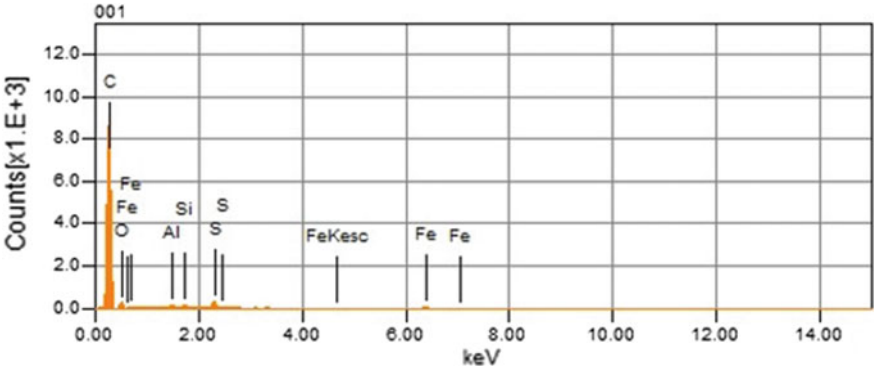

Fig. 17 EDS image of burnt soil (control)

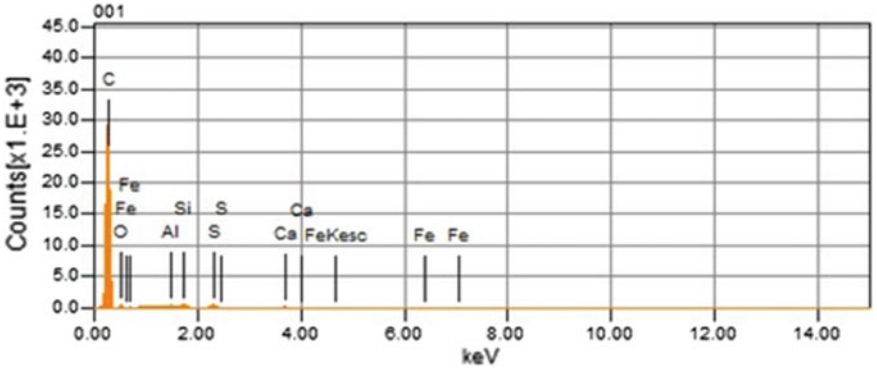

Fig. 18 EDS image of garden soil

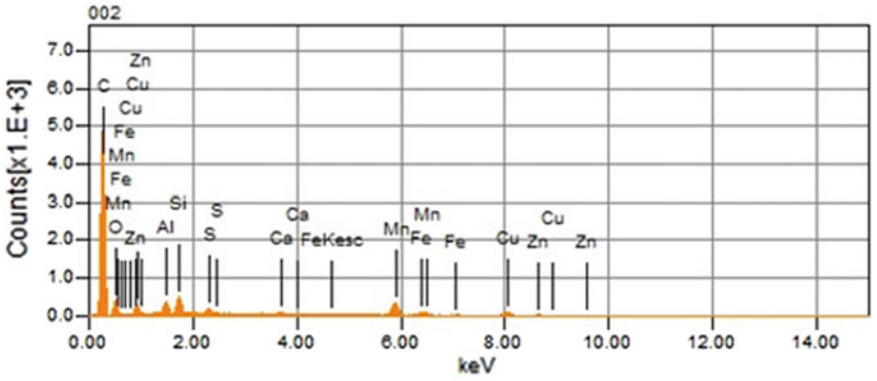

Fig. 19 EDS image of potting soil

(Fig. 17) with 0.41% aluminum and 0.26% silicate ions. Potting soil contains other minerals in higher concentrations as compared to garden and burnt soil, like calcium (1.50%) and iron (0.36%) [11], in which the gram-negative bacteria present in it can thrive. This is because the mineral respiring gram-negative bacteria in potting soil can work by the redox active molecules in their outer membrane to oxidize minerals extremely efficiently [13]. This further supports why potting soil has high voltage output (Fig. 4) which is similar to grapefruit compost in terms of its bacterial communities, which also produced highest voltage out of the 3 compost soils (Fig. 6).

3.5 Comparison of Voltage Output Between Different Terminal Electron Acceptors Used at the Cathode

From Fig. 20, the wastewater set-ups containing ammonium and nitrate ions as terminal electron acceptors had a peak voltage of 172 mV while the control set up with only oxygen as the terminal electron acceptor only attained 138 mV. Hence, ammonium and nitrates in wastewater are suitable alternatives to oxygen as terminal electron acceptors.

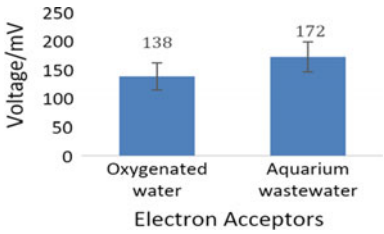

Fig. 20 Type of terminal eletron acceptor against voltage produced

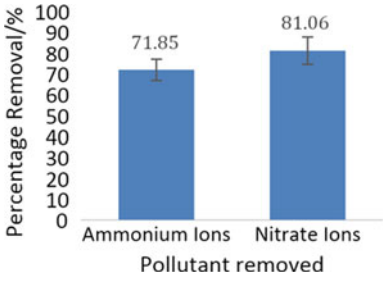

Fig. 21 Removal of ammonium and nitrate ions by MFC

3.6 *Efficiencies of Ammonium and Nitrate Removal*

As shown from Fig. 21, 71.85% of ammonium ions and 81.06% of nitrate ions had been removed when aquarium wastewater is used in the cathode chamber of MFC, and burnt soil in the anode chamber. The efficient removal of ammonium and nitrates was made possible due to the novel hybrid method of incorporating three rounds of purification processes.

The first stage of wastewater treatment occurs when soil is first mixed with the wastewater. This allows ammonium ions to be adsorbed by the soil as organic matter in soil contain negatively charged silicates, carboxyl and phenolic groups [14] which attract positively charged ammonium ions. The mineral soils that this study investigated have a net negative charge because of the substitution of silica by aluminum in the mineral structure of the soil. This replacement is termed as isomorphous substitution, and the result is the soils having a negative surface charge which enables it to attract positively charged ions.

The second stage of the water treatment occurs after bacteria in soil diffuses into the wastewater. This allows simultaneous nitrification-denitrification (SNdN) process to occur. Ammonia-Oxidizing Bacteria (AOB) would participate in the oxidation of ammonium ions to nitrite ions while Nitrite-Oxidizing Bacteria would participate in the oxidation of nitrites to nitrate ions. During denitrification, nitrate ions being formed as a result of nitrification would undergo a chain series of redox reactions before nitrogen is finally evolved as the end product. The nitrogenous end product is much less toxic than the nitrate ions initially present [15].

Nitrification

$$NH_4^+ + 3/2\,O_2 \xrightarrow{\text{ammonia oxidizers}} NO_2^- + 2H^+ + H_2O \tag{1}$$

$$NO_2^- + 1/2\,O_2 \xrightarrow{\text{nitrite oxidizers}} NO_3^- \tag{2}$$

Denitrification

$$2NO_3^- + 4H^+ + 4e^- \rightarrow 2NO_2^- + 2H_2O \tag{3}$$

$$2NO_2^- + 4H^+ + 2e^- \rightarrow 2NO + 2H_2O \tag{4}$$

$$2NO + 2H^+ + 2e^- \rightarrow N_2O + H_2O \tag{5}$$

$$N_2O + 2H^+ + 2e^- \rightarrow N_2O + H_2O \tag{6}$$

In the third stage of successive water treatment, when the effluent of wastewater is placed into the cathodic chamber, the transfer of electrons and constant movement of protons across the external circuit and the salt bridge respectively would cause the

rate of denitrification to increase. Hence, nitrates and ammonium ions are removed more effectively in this novel hybrid process.

3.7 Optimization of MFC for Simultaneous Wastewater Treatment and Power Generation

3.7.1 Comparison of Maximum Voltage of Optimized MFC with Other Set Ups

Due to potting soil, grapefruit compost and wastewater-fueled burnt soil displaying best voltage outputs, combination of Grapefruit-Potting-Compost-Wastewater (GPCW) was used for the MFC, which is a 3 in 1 optimization of the MFC, where the cathode contains the aquarium wastewater while the anode contains the grapefruit composted with potting soil. The optimization involved selecting the best soil medium, best fruit for composting, as well as the best Terminal Electron Acceptor to be used in the cathode. Such a combination is able to generate power and at the same time treat wastewater. Figure 22 reveals that GPCW indeed displayed the highest maximum voltage output among all other set ups, attaining 310 mV. The maximum voltage output of GPCW is significantly higher than the cathode control (burnt soil) and anode control (Wastewater-fueled burnt soil), based on Mann-Whitney U test at a significance level of 0.05.

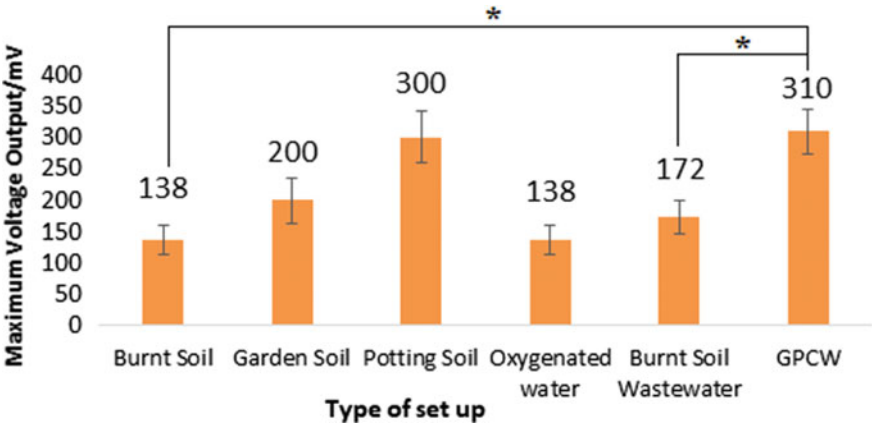

Fig. 22 Comparison of maximum voltage output of optimized MFC with other set ups.* denotes statistical significance based on Mann-Whitney U test at a significance level of 0.05

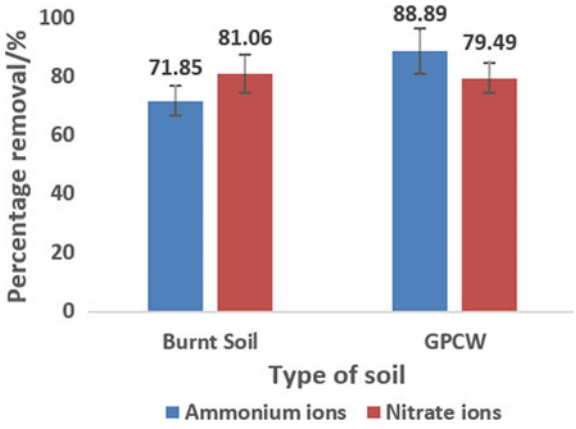

Fig. 23 Comparison of removal of ammonium and nitrate ions

3.7.2 Comparison of Wastewater Treatment Capabilities of Optimized MFC

Compared to the burnt soil-powered wastewater set up, GPCW is able to remove 17% more ammonium ions but is slightly less effective in removing nitrate ions (Fig. 23). Most ammonia-oxidizing bacteria (AOB) are gram-negative while nitrite-oxidizing bacteria (NOB) are mostly gram- positive [16], and thus GPCW having the most gram-negative bacterial communities due to the presence of potting soil is likely to have more AOB but lesser NOB being involved in the nitrification process.

4 Conclusion

Among the 3 types of soil tested, potting soil produced the highest maximum voltage and power output while grapefruit compost produces the highest maximum voltage and power output compared to lime and strawberry compost. Wastewater containing ammonium and nitrate ions was determined to be a suitable replacement for the conventional electron acceptors such as oxygen, producing higher voltages. Hence, not only is MFC able to generate electricity, it is effective in removing ammonium and nitrate ions from aquarium wastewater via the SNdN process. On the other hand, the SNdN process was also proven to be more effective when this process is facilitated by the MFC.

A combination of potting soil, with grapefruits composted in it and powered by aquarium wastewater (GPCW set-up) improved the amount of electricity generated and at the same time led to higher percentage removal of ammonium ions. Compared to conventional technologies of producing energy which utilizes fossil fuel, MFC is a greener alternative. MFCs have great potential to simultaneously generate electricity and treat wastewater, and its power can be increased significantly by stacking it in series.

In the future, MFCs can be fabricated using a greener method by recycling even its container and delve into more types of pollutant removal like metal ions and dyes, helping to save the environment. More types of soil can also be used to explore how different bacterial species in soil contributes to power production by the MFC. Ultimately, it has the potential to be used to meet future clean water and energy demand by upscaling it.

Acknowledgements We would like to thank Mdm Loh Yih Huey and Mrs Sow-Peh Yoke Keow for their guidance and support.

References

1. M. Rahimnejad., A. Ghoreyshi, G. Najafpour, H. Younesi and M. Shakeri, "A novel microbial fuel cell stack for continuous production of clean energy," Int. J. Hydrogen Energy, vol. 37, pp. 5992–6000, April 2012.
2. L.M. Zhang, "2.5 kg Of Food a Week Wasted by Each Household, Equal to Half of All Household Waste: NEA Study," 2017.
3. S. Imologie, O.A. Raji, A. Gbabo, and S. Okoro, "Performance of a single chamber soil microbial fuel cell at varied external resistances for electric power generation," Journal of Renewable Energy and Environment, vol. 3, pp. 53–58, February 2017.
4. D. Ucar, Y. Zhang, and I. Angelidaki, "An overview of electron acceptors in microbial fuel cells". Frontiers in Microbiology, vol. 8, pp. 643, April 2017.
5. B.E. Logan, S. Cheng, and B. Min, "Electricity generation using membrane and salt bridge microbial fuel cells," Water Research, vol. 39, pp. 1675–1686, May 2005.
6. E. Fosso-Kankeu, S. Marx, F. Waanders, and V. Jacobs, "Impact of soil type on electricity generation from a Microbial Fuel Cell," in 7th International Conference on latest Trends in Engineering and Technology, 978–93-84422-58-2, pp. 73-77, November 2015.
7. A.M. Khan and M. Obaid, "Comparative bioelectricity generation from waste citrus fruit using a galvanic cell, fuel cell and microbial fuel cell," in Journal of Energy in Southern Africa, vol. 26(3), 2015, pp. 90–99.
8. U. Daalkhaijav, "Removal of Ammonia (nitrification) in conventional and Microbial Fuel Cell bioreactors" (Master Thesis). University of Saskatchewan, Saskatoon, Canada, 2012.
9. I. Alabiad, et al. "Ammonia removal via microbial fuel cell (MFC) dynamic reactor," in IOP Conf. Series: Materials Science and Engineering 206, 2017.
10. M. Hernandez and D. Newman, "Extracellular electron transfer," in CMLS, Cell. Mol. Life Sci, 2001,vol. 58.
11. S. Read, et al. "Initial development and structure of biofilms on microbial fuel cell anodes.", 2010.
12. J. Zhou, and Z. He, (2009). "The Shewanella Federation: Functional Genomic Investigations of Dissimilatory Metal-Reducing Shewanella," 2009.
13. R. Arbianti, T. S. Utami, V. Leondo, Elisabeth, S.A. Putri, and H. Hermansyah, "Effect of biofilm and selective mixed culture on microbial fuel cell for the treatment of tempeh industrial wastewater," in IOP Conference Series: Materials Science and Engineering, 2018.
14. D. Jaremko and D. Kalembasa, "A Comparison of Methods for the Determination of Cation Exchange Capacity of Soils. Ecol Chem Eng," vol.21(3), 2014, pp. 487–498.
15. Alabiad., et al. "Ammonia removal via microbial fuel cell (MFC) dynamic reactor.", IOP Conf. Ser: Mater. Sci. Eng, 2017.
16. I. Shmidt, O. Sliekers, M. Schmid, I. Cirpus, M. Strous, E. Bock, J.G. Kuenen, and M. Jetten, "Aerobic and anaerobic ammonia oxidizing bacteria – competitors or natural partners," in FEMS Microbiology Ecology, vol. 39 (3). 2002, pp. 175–181.

Synthesis of Photocatalytic Iron(III) Fumarate Metal Organic Framework Microrods for the Degradation of Organic Dyes

Shao Jun Neo, Keith Koh, and Wei Sheng Low

Abstract Metal Organic Frameworks (MOFs) have been gaining attention as emerging photocatalysts that can degrade organic pollutants in water. In this study, Iron(III) Fumarate MOF was successfully synthesized using a simple hydrothermal method by refluxing a mixture of iron(III) chloride and fumaric acid, with water as the solvent. The Iron(III) Fumarate MOF was then characterized using both Scanning Electron Microscopy and X-ray Diffraction. 60 mM of both iron(III) chloride and fumaric acid resulted in the Iron(III) Fumarate MOF with the optimum morphology. Iron(III) Fumarate MOF synthesized was able to photocatalytically degrade methylene blue, brilliant green and methyl orange dyes by radical generation, which was confirmed using Mass spectra and Photoluminescence spectra analysis. Iron(III) Fumarate MOF degraded methyl orange, an azo dye, via demethylation, desulfonation followed by deamination and the cleavage of the azo bond. The band gap of Iron(III) Fumarate MOF was determined to be 1.49 eV, which was lower than that of conventional photocatalysts such as titanium dioxide and zinc oxide. The effect of the presence of visible light and hydrogen peroxide on the amount of dye degraded was investigated. It was found that Iron(III) Fumarate MOF outperformed conventional photocatalysts, titanium dioxide and zinc oxide, in degrading all the dyes tested when both visible light and hydrogen peroxide were present, removing at least 97% of all dyes. Hence, Iron(III) Fumarate MOF is a promising alternative to conventional photocatalysts in degrading organic dyes.

Keywords Iron(III) fumarate MOF · Photocatalysis · Radical generation · Band gap · Photoluminescence

S. J. Neo (✉) · K. Koh · W. S. Low
Science Department, Hwa Chong Institution, Singapore, Singapore
e-mail: 161742b@student.hci.edu.sg

K. Koh
e-mail: 161674n@student.hci.edu.sg

W. S. Low
e-mail: 161726e@student.hci.edu.sg

H. Guo et al. (eds.), *IRC-SET 2020*,
https://doi.org/10.1007/978-981-15-9472-4_56

1 Introduction

In recent years, the rapid development of industries has generated an increasing amount of wastewater. With over 10,000 types of dyes that are commercially available, and factories that produce over 70 million kg of dyes per year [1], severe environmental problems will arise if these dyes are disposed into wastewater. Dyes are highly toxic and mutagenic [2], and the introduction of organic dyes into aquatic ecosystems interferes with bacteria growth, preventing them from degrading pollutants [3]. Wastewater treatment technologies that are currently available for industries, such as adsorption and coagulation, only concentrate or separate the organic pollutants from water [4]. They are not completely degraded into biodegradable or less toxic compounds [5]. Other water treatment methods, including membrane technologies such as reverse osmosis, are expensive [6].

Among various methods used to remove organic pollutants, photocatalysis is increasingly adopted to remove organic contaminants from wastewater, due to their high efficiency, good reproducibility, and their relative ease of handling [5]. In general, photocatalysis involves the generation of highly reactive chemical oxidants (such as radicals) under light to degrade toxic organic substances [7]. In advanced oxidation processes (AOPs), the heterogeneous photocatalytic removal of organic pollutants using semiconductor catalysts (such as TiO_2 and ZnO) has been demonstrated to be highly efficient in degrading a wide range of organic pollutants [7]. However, one typical drawback is that the photocatalysts are not stable in aqueous medium—the illumination of these catalysts leads to their corrosion, introducing metal ions into water [7].

On the other hand, Metal Organic Frameworks (MOFs), a class of metal–organic hybrid porous materials, have recently caught the attention of researchers due to their diverse and easily tailored structures. MOFs are composed of metal-containing nodes connected by organic ligands through strong coordinate bonds. Some MOFs behave as semiconductors when exposed to light, implying that they can be used as photocatalysts [8]. Compared to reported photocatalysts, photocatalytic MOFs have more versatile synthesis strategies and a large surface area [9]. Iron(III) Fumarate MOF is a 3D metal organic framework formed from trimers of iron(III) octahedral linked to fumarate anions (Fig. 1), forming cages with open channels running along the z-axis [10]. Iron(III) Fumarate MOF swells by 85% after being exposed to a polar solvent, while fully maintaining its open-framework topology. This large increase in surface area of Iron(III) Fumarate MOFs is very favorable for photocatalysis.

Currently, titanium dioxide (TiO_2) is commonly used as a photocatalyst to degrade dyes [11]. However, photocatalysts such as TiO_2 are only responsive to UV light, which merely accounts for 3% of the energy of the sunlight arriving on the Earth's surface [12]. This reduces its effectiveness in a large-scale setting. Therefore, this project aims to synthesize Iron(III) Fumarate MOF and investigate its ability to degrade both cationic dyes (brilliant green and methylene blue) and anionic dyes (methyl orange) in the presence of hydrogen peroxide and visible light. Hydrogen peroxide can be activated by iron complexes to generate hydroxyl radicals, which

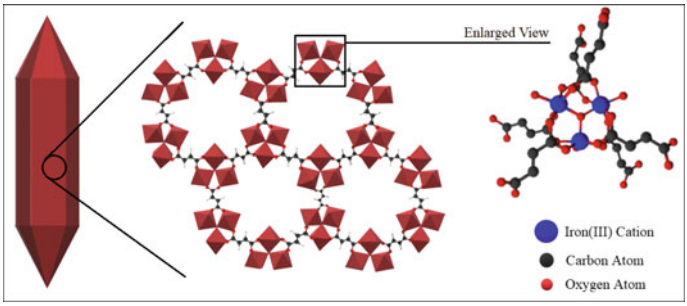

Fig. 1 Structure of Iron(III) Fumarate MOF, Hydrogen omitted for clarity

are non-selective oxidants that could potentially degrade a wide variety of organic contaminants.

2 Materials and Methods

Iron(III) chloride, fumaric acid, brilliant green, methyl orange, terephthalic acid, titanium dioxide and zinc oxide were purchased from Sigma Aldrich. Hydrogen peroxide and methylene blue were purchased from GCE Chemicals and Unichem respectively.

2.1 Synthesis of Iron(III) Fumarate MOF

200 ml of both iron(III) chloride and fumaric acid solutions were mixed with a mole ratio of 1:1 and refluxed for 2 h under continuous stirring at 100 °C. The concentration of reactants used was set at 20 mM or 60 mM. The resulting precipitate was then centrifuged, washed and dried until constant mass.

2.2 Determination of Effectiveness of Iron(III) Fumarate MOF in Degrading Dyes

0.050 g of Iron(III) Fumarate MOF and 1 ml of 6% hydrogen peroxide was added to 20 ml of 25 ppm dye solution and stirred for 24 h in darkness or under the irradiation of visible light by a 14 W fluorescent tube. After which, the final absorbance of dye was measured using a UV–Vis Spectrophotometer at $\lambda = 664$ nm for methylene blue, at $\lambda = 625$ nm for brilliant green and at $\lambda = 464$ nm for methyl orange. A control with no Iron(III) Fumarate MOF and hydrogen peroxide was included in the

set up. The experiments were repeated with conventional photocatalysts, titanium dioxide and zinc oxide. Five replicates were conducted for each photocatalyst. The formula below was used to calculate the percentage removal of dye:

$$P_{\mathrm{d}} = \frac{C_i - C_f}{C_i} \times 100\%$$

where

P_d Percentage of dye removed
C_i Initial concentration of dye
C_f Final concentration of dye.

2.3 Analysis of the Photocatalytic Generation of Hydroxyl Radicals by Iron(III) Fumarate MOF

Varying amounts of Iron(III) Fumarate MOF and 6% hydrogen peroxide were added to 20 ml of a mixture of 0.2 mM terephthalic acid and 1.4 mM sodium hydroxide and stirred for 15 min. After which, the photoluminescence of the resulting solution was measured using a Spectrofluorophotometer. The excitation wavelength was set at 310 nm. In the presence of hydroxyl radicals, terephthalic acid reacts with the radicals to form 2-hydroxyterephthalic acid, which emits a florescence signal at a wavelength of around 425 nm. A control with no Iron(III) Fumarate MOF and hydrogen peroxide was included in the set up.

3 Results and Discussion

3.1 Characterization of Iron(III) Fumarate MOF by X-Ray Diffraction (XRD)

Iron(III) Fumarate MOF was successfully synthesized, as confirmed by the XRD pattern of the MOF where 2-Theta peaks at 10.2°, 10.9° and 13.3°, characteristic of Iron(III) Fumarate MOF [9], were identified (Fig. 2).

3.2 Effect of Concentration of Reactant Solutions on Iron(III) Fumarate MOF

MOF synthesized using 20 mM precursors (iron(III) chloride and fumaric acid) yielded small, spherically-shaped MOF (Fig. 3c) while MOF synthesized using

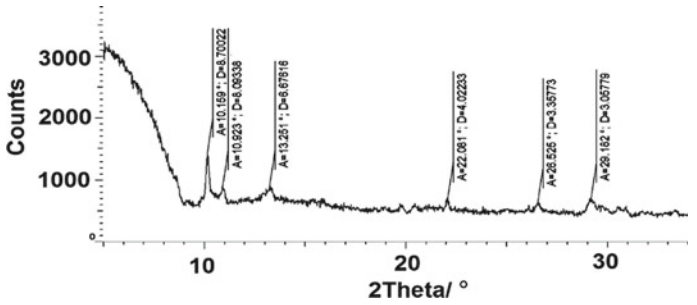

Fig. 2 XRD pattern of Iron(III) Fumarate MOF

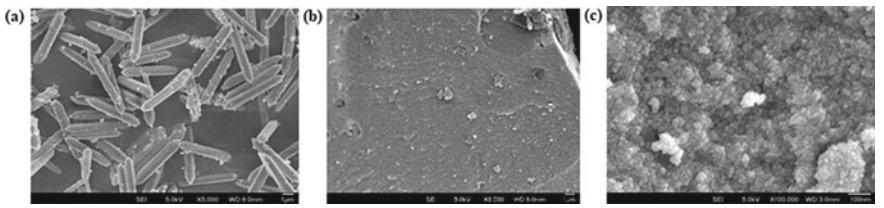

Fig. 3 Scanning Electron Micrographs (SEM) of MOF synthesized using **a**) 60 mM precursors at 5000× magnification, **b**) 20 mM precursors at 5000× magnification, and **c**) 20 mM precursors at 100,000× magnification. Total volume of both reactant solutions was kept constant at 200 ml

60 mM precursors yielded large, hexagonally-shaped rods (Fig. 3a), which was the reported structure of Iron(III) Fumarate MOF [9]. This is because higher concentrations of reactants allowed for a more complete crystallization of MOF.

3.3 Effect of Presence of Visible Light and Hydrogen Peroxide on Degradation of Dyes

Figure 4 reveals that the presence of hydrogen peroxide enhanced the degradation of all three dyes by Iron(III) fumarate MOF, with the percentage of dyes removed being greater than 97%. Based on Mann Whitney U-Test, it was shown that there was a significant difference in the amount of all the 3 dyes degraded when hydrogen peroxide was present.

The presence of visible light significantly enhanced the effectiveness of the MOF to degrade the three dyes (Fig. 5a). The reason why the degradation of dyes by the MOF was enhanced by both visible light and hydrogen peroxide (H_2O_2) is because it is a photocatalyst. Under visible light, electrons would be promoted from the valence band to the conduction band of Iron(III) Fumarate MOF, reducing dye molecules. The electron holes formed as a result acted as an oxidizing agent (Fig. 5b). Together, they can take part in redox reactions to generate radicals which degraded the dyes.

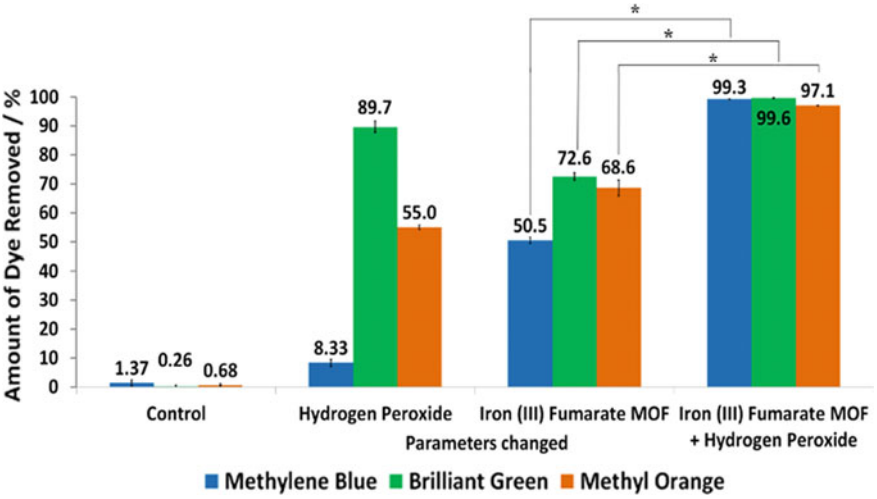

Fig. 4 Effect of the presence of hydrogen peroxide on the percentage of dye degraded. * denotes statistical significance based on Mann Whitney U-Test at a significance level of 0.05

H_2O_2 could also be reduced and oxidized to generate radicals, thereby enhancing the ability of the MOF to degrade dyes.

3.4 Comparison of Iron(III) Fumarate MOF with Conventional Photocatalysts

Remarkably, in the presence of visible light, MOF synthesized in this study was more effective than both ZnO and TiO_2 in degrading all 3 dyes (Fig. 6). However, based on the Mann Whitney U-Test, only methylene blue and methyl orange showed a significant difference on the percentage of dye removed as compared to ZnO and TiO_2. The reason why Iron(III) Fumarate MOF was more effective in degrading dyes may be due to its lower band gap.

3.5 Determination of the Band Gap of Iron(III) Fumarate MOF Synthesized

The band gap of semiconductor photocatalysts is a crucial factor in determining their photocatalytic efficiency, since it shows how much energy from the visible light region (photon energy of 1.7–3.0 eV) they could capitalize. Zinc oxide and titanium dioxide both have high band gaps of 3.2 eV [13], which limit their ability to initiate photocatalytic reactions using visible light. However, MOF synthesized in this study

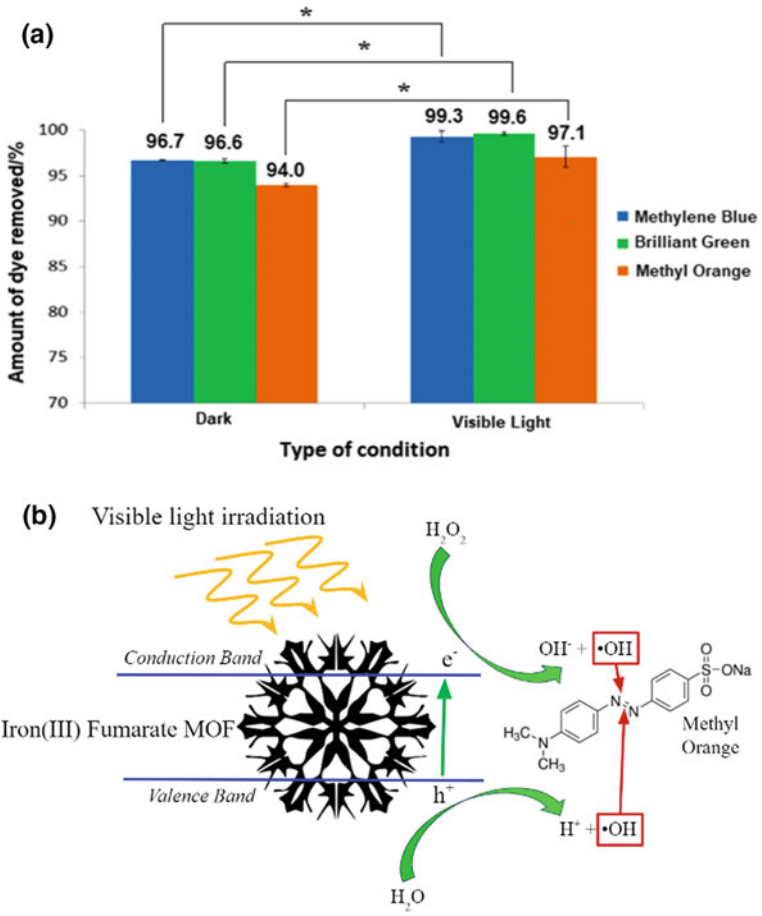

Fig. 5 **a**) Effect of presence of visible light on the degradation of dyes by Iron(III) Fumarate MOF. * denotes statistical significance based on Mann Whitney U-Test at a significance level of 0.05. **b**) Proposed mechanism of how Iron(III) Fumarate MOF degrades methyl orange dye

was determined to have a band gap of 1.49 eV (Fig. 7), which means that even light in the near infrared region could be used to initiate the photocatalytic reaction, unlike the conventional photocatalysts which can only harness UV radiation.

3.6 Photocatalytic Generation of Hydroxyl Radicals by Iron(III) Fumarate MOF

It is commonly established that terephthalic acid can react specifically with hydroxyl radicals in alkaline conditions to form 2-hydroxyterephthalic acid, which emits a

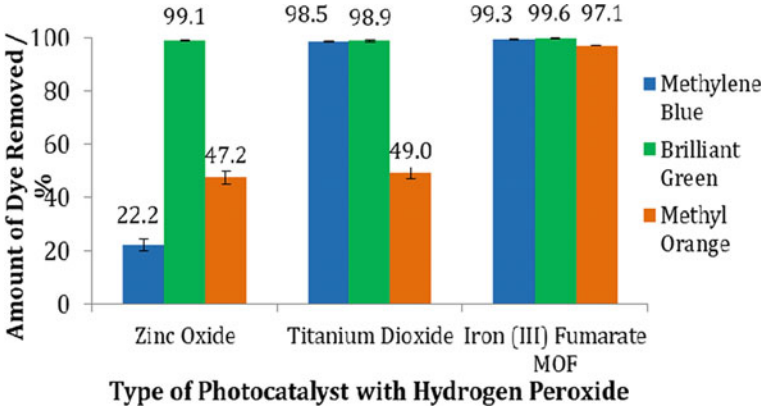

Fig. 6 Comparison of Iron(III) Fumarate MOF with conventional photocatalysts on the percentage of dye degraded under visible light irradiation

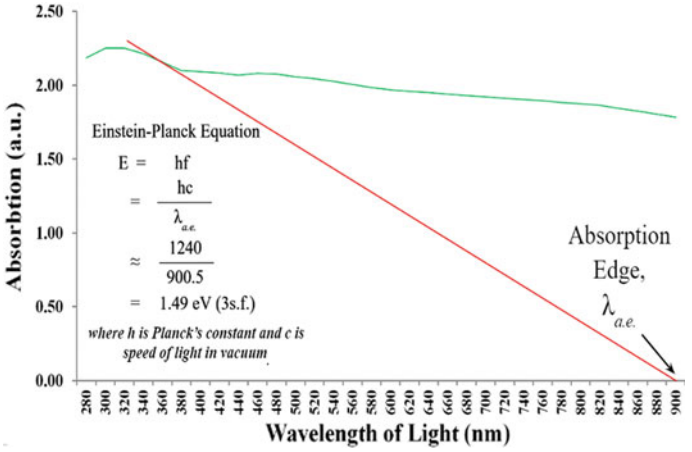

Fig. 7 UV–Vis Spectrum of MOF and determination of optimum band gap E of the MOF

strong fluorescence signal at 425 nm [9]. Thus, this reaction was used to qualitatively determine the difference in the amount of hydroxyl radicals generated when differing amounts of MOF (Fig. 8a) or hydrogen peroxide (Fig. 8b) were added. Peaks of higher intensity were obtained when a larger amount of MOF or hydrogen peroxide was added into the terephthalic acid solution, suggesting that the amount of hydroxyl radicals photocatalytically generated increased when the amount of MOF or H_2O_2 added increased.

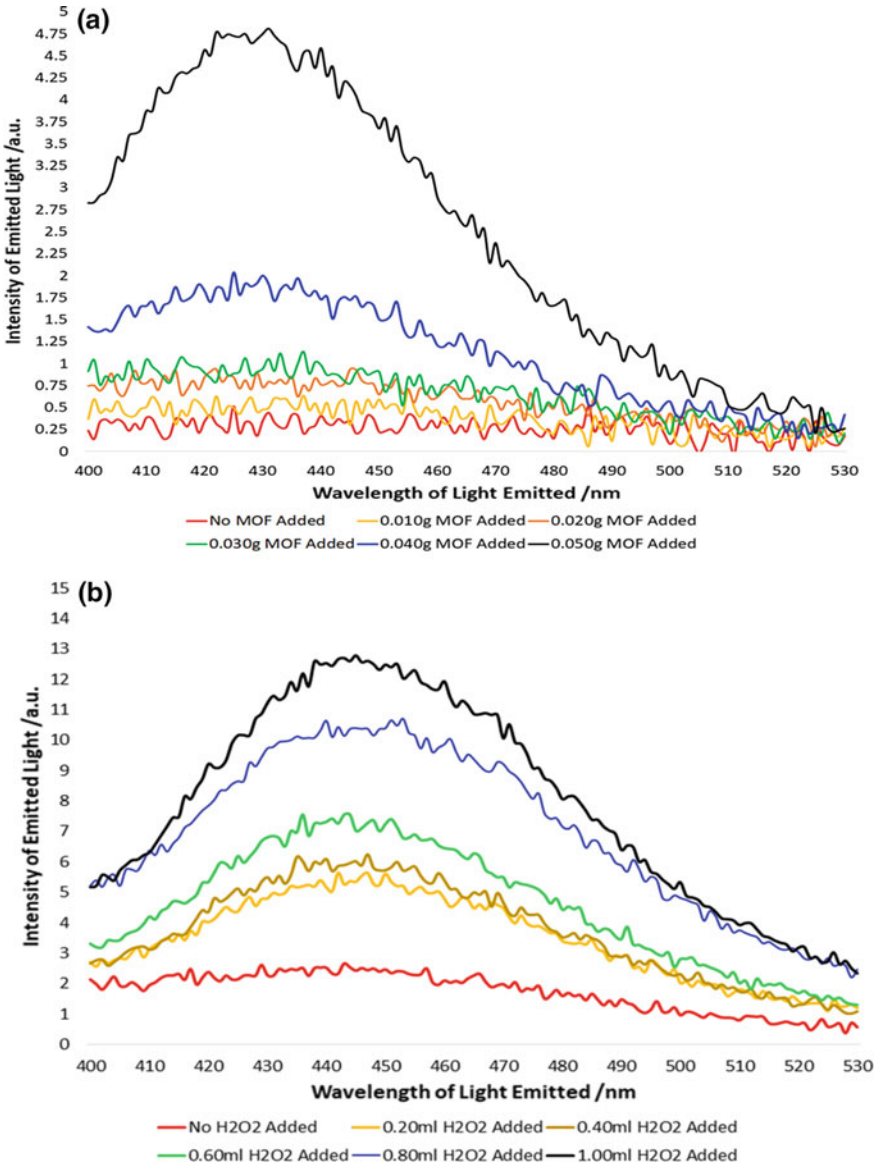

Fig. 8 **a**) Photoluminescence spectra as differing amounts of MOF were added. **b**) Photoluminescence spectra as differing amounts of H_2O_2 were added

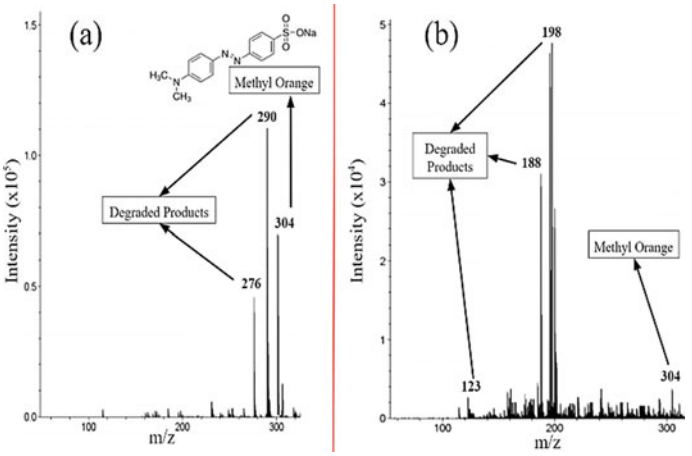

Fig. 9 Mass Spectra of methyl orange residue in **a**) absence of H_2O_2, **b**) presence of H2O2

3.7 Proposed Mechanism of Photocatalytic Degradation of Methyl Orange Dye

Figure 9 shows the different mass spectra obtained with and without the presence of hydrogen peroxide. The intensity of methyl orange at peak 304 was more than 30 times lower when hydrogen peroxide was added, implying that much more methyl orange was degraded in the presence of hydrogen peroxide. Furthermore, many more peaks were observed when H_2O_2 was added, further suggesting that the photodegradation was more complete with more intermediates.

Considering the different types of radicals generated and the masses of the degraded products, the mechanism of photodegradation of methyl orange by Iron(III) Fumarate MOF is proposed. Without H_2O_2, demethylation occurs, removing the 2 methyl groups of methyl orange (Fig. 10a). However, with H_2O_2, the presence of more radicals resulted in desulfonation and deamination of methyl orange (Fig. 10b). Remarkably, methyl orange was also degraded by the cleavage of the azo group (Fig. 10c), which suggests that the MOF has the potential to break down persistent azo compounds.

4 Conclusion and Recommendations for Future Work

Iron(III) Fumarate MOF was synthesized with a simple hydrothermal process from iron(III) chloride and fumaric acid. The Iron(III) Fumarate MOF had a micro-rod morphology when it was synthesized with a reactant concentration of 60 mM. Additionally, Iron(III) Fumarate MOF could degrade at least 97% of the tested dyes in

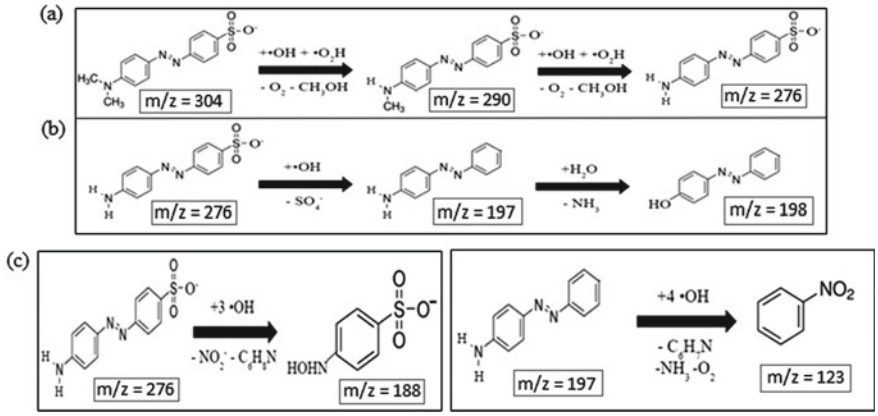

Fig. 10 Proposed degradation pathways of methyl orange: **a**) demethylation, **b**) desulfonation followed by deamination, and **c**) 2 ways the azo group is cleaved

the presence of visible light and hydrogen peroxide. Iron(III) Fumarate MOF outperformed zinc oxide and titanium dioxide in degrading the 3 dyes. The band gap of Iron(III) Fumarate MOF was determined to be 1.49 eV, suggesting that light in the near-infrared and visible region can be used to initiate the photocatalytic reaction, unlike conventional catalysts which could only harness UV. Iron(III) Fumarate MOF degraded methyl orange, an azo dye, via demethylation, desulfonation followed by deamination and the cleavage of the azo bond. Iron(III) Fumarate MOF is therefore a very promising photocatalyst that can be used against azo pollutants, with its remarkable ability to degrade azo compounds through different pathways.

In the future, the Iron(III) Fumarate MOF can be tested against other organic pollutants, such as pesticides, drug residues and azo compounds. Kinetic studies could also be conducted to investigate the rate of dye degradation. The toxicity of the organic pollutant residues could be evaluated and compared with the organic pollutants itself.

Acknowledgements We would like to sincerely thank our mentor, Mrs Sow Yoke Keow, for her invaluable advice and dedication in helping us do our best for this project, whilst wishing nothing in return. We would also like to thank the Science Research Centre Lab Staff, Mdm Xia Ying, for her guidance and help in carrying out the procedures for this project. Without their help, this project would not come into fruition.

References

1. H. Zollinger, "Colour Chemistry: Syntheses, Properties, and Applications of Organic Dyes and Pigments," New York: VCH Publishers, 2003.

2. A.A. Adeyemo, I. O. Adeoye, and O. S. Bello, "Metal organic frameworks as adsorbents for dye adsorption: overview, prospects and future challenges," Toxicological & Environmental Chemistry, 94(10), 1846-1863, 2012.
3. S. J. Allen and B. Koumanova, "Decolourisation of water/wastewater using adsorption," Journal of the University of Chemical Technology and Metallurgy, 40(3), 175-192, 2005.
4. P. V. A. Padmanabhan et al, "Nano-crystalline titanium dioxide formed by reactive plasma synthesis," Vacuum, 80(11-12), 1252-1255, 2006.
5. U. I. Gaya and A. H. Abdullah, "Heterogeneous photocatalytic degradation of organic contaminants over titanium dioxide: a review of fundamentals, progress and problems," Journal of Photochemistry and Photobiology C: Photochemistry Reviews, 9(1), 1-12, 2008.
6. F. M. D. Chequer, G. A. R. de Oliveira, E. R. A. Ferraz, J.C. Cardoso, M. V. B. Zanoni, D. P. de Oliveira, "Textile dyes: dyeing process and environmental impact," In: Gunay M (ed). Eco-friendly textile dyeing and finishing (pp. 152), 2013.
7. M. N. Chong, B. Jin, C. W. Chow, and C. Saint, "Recent developments in photocatalytic water treatment technology: a review," Water research, 44(10), 2997-3027, 2010.
8. C. G. Silva, A. Corma, and H. García, "Metal–organic frameworks as semiconductors," Journal of Materials Chemistry, 3141–3156, 2010.
9. W. T. Xu et al, "Metal–organic frameworks MIL-88A hexagonal microrods as a new photocatalyst for efficient decolorization of methylene blue dye," Dalton Transactions, 43(9), 3792-3798, 2014.
10. T. Chalati, P. Horcajada, R. Gref, P. Couvreur, and C. Serre, "Optimisation of the synthesis of MOF nanoparticles made of flexible porous iron fumarate MIL-88A," Journal of Materials Chemistry, 21(7), 2220-2227, 2011.
11. J. Fisher and T. A. Egerton, "Titanium Compounds, Inorganic," Kirk-Othmer Encyclopedia of Chemical Technology, 24, 225–274, 1997.
12. A. M. Umabala, P. Suresh, A. V. Prasada Rao, "Visible light assisted photocatalytic degradation of 2-aminophenol using H_2O_2 sensitized $BiVO_4$," Der Pharma Chemica, 8(6), 1–7, 2016.
13. A. Dodd, A. Mckinley, T. Tsuzuki, and M. Saunders, "Tailoring the photocatalytic activity of nanoparticulate zinc oxide by transition metal oxide doping," Materials Chemistry and Physics, 114(1), 382-3, 2009

Aerosol Jet Printed Temperature Sensor for Wireless Healthcare Monitoring

Joslyn Jun Wei Lim, Noori Kim, Seung Ki Moon, Joonphil Choi, and Haining Zhang

Abstract Temperature sensor are ubiquitous and essential electronics that provide thermal feedback to users: one of the vital physiological parameters—the body temperature. During this year global pandemic outbreak, COVID-19, the temperature sensor has become a triggering detection kit for all those who may be infected. In this study, a Three-Dimensional (3D) printed temperature sensing prototype with a wireless function has been developed. The designed sensor has high flexibility and accuracy to be used for practical healthcare applications. The 3D-printed flexible electronic can sense and transmit an user's body temperature to the cloud platform, ThingSpeak, for real-time monitoring purpose. Due to its flexibility in term of design and material choice, Aerosol Jet Printing (AJP) technique is used for sensor fabrication. This paper highlights (1) the importance of monitoring an individual's body temperature, (2) the strength and limitations on various type of 3D printing methods and materials, and (3) the development of the printed sensing prototype design is discussed. The system has been suggested to be implemented and tested in any thermal-sensitive application or clinical environment for healthcare application purpose.

Keywords Aerosol jet printing · Temperature sensor · Healthcare application · IoT

J. J. W. Lim · N. Kim (✉)
Electrical and Electronic Engineering, Newcastle University in Singapore, Singapore 567739, Singapore
e-mail: noori.kim@newcastle.ac.uk

J. J. W. Lim
Electrical Power Engineering, Singapore Institute of Technology, Singapore 567739, Singapore

S. K. Moon · J. Choi · H. Zhang
School of Mechanical and Aerospace, Nanyang Technology University, Singapore 639798, Singapore

H. Guo et al. (eds.), *IRC-SET 2020*,
https://doi.org/10.1007/978-981-15-9472-4_57

1 Introduction

Body temperature is one of the most crucial and essential parameters in reflecting the physiological activities and well-being of a human. One such example, changes in temperature can assist the medical professionals or an individual to in analyzing the pathological symptoms, such as infections, inflammation, hyperthermia, and hypothermia [1]. Real-time mornitoring of an individual's body temperature is crucial for identifying sudden adverse conditions, such as cardiovascular condition (e.g., heart attack, heart failure, and arrhythmias), wound healing, pulmonary diagnostics (e.g., asthma), and syndrome prediction [2]. Additionally, temperature monitoring is vital for a soldier and an athlete, where physical activity is directly related to their accomplishments [1], and for the elderly and chronic diseases patients. Continuous temperature monitoring and supervison are vital for those who are in vulnerable positions [3].

Among the commercially available printing techniques for developing flexible sensors, some commonly used ones are: photolithography, screen printing (SP), laser cutting, contact printing, contact printing, and Three-Dimensional (3D) printing [4]. A 3D printing technique, which also referred to as Additive Manufacturing (AM), is one of the most revolutionary technologies in the twenty-first century and has been studied extentively and explored for its distinct advantages over other mentioned techniques [5].

Comparatively, 3D printing can reduce fabricating process steps, chemical waste, lowering fabrication cost [6], and manual labour to complete the prototypes than to other traditional printing techniques, such as photolithography. For example, once a designed sensing prototype is imported to the printer system, the sensor is developed accordingly without much human interference. Secondly, the developed sensors can be configured thus to suit any particular application of the device. Thirdly, the simple fabricating principle of the 3D printed flexible sensor allows the prototype to be developed with high accuracy, repeatability, and resolution. Lastly, the range of materials available in this printing technique is significantly more extensive than other methods like lithography. With this printing technique, it has made the fabrication process of a sensor with multifunctional attributes so much easier [4].

In recent years, electrically printed devices such as semiconductors, and circuits like thin-film transistors, Light-Emitting Diodes (LEDs), sensors and solar cells with 3D non-contact printing technology have gained many attentions and interests from the researchers [6].

The two primary methods used in this technology consists of InkJet Printing (IJP) and Aerosol Jet Printing (AJP), and both printing methods have their pros and cons in fabricating flexible electronic devices. The primary technical specification comparison between IJP and AJP are shown in Table 1. In contrast, AJP has an adjustable working height of 1–5 mm and can print conductive inks with a wide range of viscosities from 1 to 2500 cP onto complex non-planar substrates with high resolution of 10 μm. Besides, it has a clog-resistant nozzle and can print with a low processing temperature [6, 7].

Table 1 Basic technical specification comparison of non-contact printing technique

Characteristic	IJP [6]	AJP [6]
Printing Principle	Electrostatic	Aerodynamic
Tip height (mm)	1	1–5
Ink viscosity (cP)	10–20	1–2500
Tip diameter (μm)	10–50	100–300
Process speed (mm/s)	Up to 5000	Up to 200
Dynamic accuracy (μm)	N/A	± 6
Droplet size (pl)	1–8	0.001–0.005
Line thickness (nm)	5–500	100–5000
Particle diameter (nm)	<100	10–700
Feature size (μm)	>30	10–200
Surface tension (mN/m)	<60	<30
Metal loading (wt.%)	<20	>60
Throughput (m^2/s)	0.01–05	0.01–05

In this paper, we will be reviewing the state-of-art of the various types of printing techniques and materials used by many other researchers, in comparison with the fabricating methods and materials that the project employees. We will also be describing the designing process and implementation of the wireless sensor network system and discussing on the printed temperature sensor related results. The conclusion associated with this projected is provided in Sect. 4.

2 Materials and Methods

2.1 Overall System Description

Figure 1 explains the design and development process flow of our proposed work. The fabrication of the sensing prototype starts with designing the model in Two-Dimensional (2D) and 3D format with a Computer-Aided Design (CAD) software. During the design process, the pattern and the dimensions—width, length, and height of the ink, resistance value, alterations that may occur during the flexing or stretching of the electronics should be taken into account.

Whereas, Fig. 1b illustrates the working principle of the AJP technique. In this process, an atomizer is used to atomize the functional ink, and the aerosol droplets produced are transported by the carrier Nitrogen (N_2) gas to the deposition head. The entrained ink is then cylindrically enwrapped in the print head by sheath gas flow. Due to the aerodynamic interaction between the sheath gas stream and the carrier gas stream, the droplet will exit the tip of the nozzle and impact the substrate with

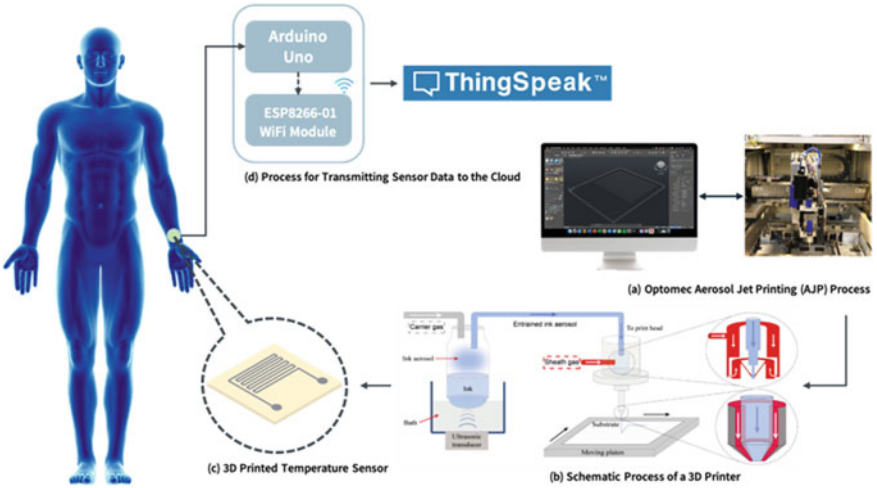

Fig. 1 A conceptual representation depicting the overall system description. **a** Printing steps for flexible electronics fabrication; Design with CAD software to printing the results with an AJP 3D printer. **b** Schematic explanation of the AJP printing technique process. **c** The AJP printed temperature sensor placed under the arm for body temperature. **d** Schematic procedure of the wireless function in the Microcontroller Unit (MCU) for transmitting data to the cloud for real-time monitoring

high speed. The line with high density and resolution is printed onto the selected substrates [6].

Figure 1d explains the procedure of the wireless sensor network system. The system is deployed to collect user's body temperature and transmit the collected data to the cloud platform, ThingSpeak, for real-time monitoring and visualization.

2.2 Prototype Design and Material Choice

The schematic representation of the designed temperature sensor is illustrated in Fig. 2; materials used for electronics development are indicated. Substrate material, polyimide (PI) is selected for fabricating such temperature sensors due to its flexibility, transparency, good surface roughness, and combability to silver (Ag) ink [3].

When fabricating of printed electronics, substrates have played a significant role in shaping the physical, mechanical, and electrical features of the devices. Additionally, the substrate's properties such as chemical inertness, thermal, electrical insulations, as well as, combability of conductive ink, are essential and should be taken into accordingly for the printing of the flexible devices and electrical development to suit a particular application [3, 8]. The flexible electronics require a degree of bendability, foldability, and stretchability of the substrates [3]. The commonly used thin

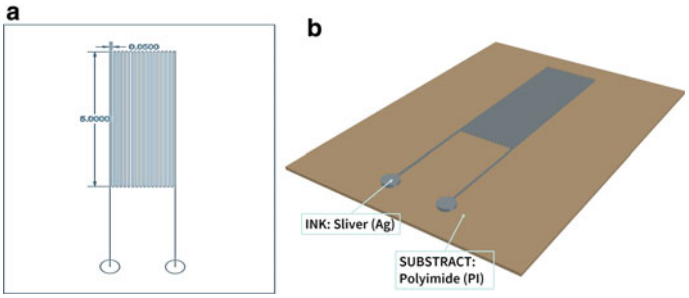

Fig. 2 CAD design of the temperature sensor created with Autodesk, AutoCAD. **a** Design and dimensions used for a printed temperature sensor in 2D. **b** Design and material used in this project in 3D

polymeric substrates include polyetherimide (PEI), polycarbonate (PC), polyacrylate (Pacr), PI, polyethylene (PE), polyurethane (PU), and polyethylene terephthalate (PET) [3, 8]. Some popular substrates used for integrating sensitive nanomaterials are PET, PC, and PU for its excellent deformability and optical transparency, and polydimethylsiloxane (PDMS) films for its superb elasticity and biocompatibility [8]. In comparison with the mentioned substrates, in this project, PI is used as the substrate material for printing the sensing prototype, as discussed above.

Functional lines printing is a crucial influence in fabricating printed electronics devices. Its high controllability and excellent uniformity should fulfil with Morphology Control (MC) and Uniform Control (UC) [6]. Conductive inks used for printing are usually composed of organic and/or inorganic materials. Organic inks are referred to as carbon-based nanomaterials, and it exhibits good sensitivity and excellent mechanical and electrical properties. Additionally, it is straightforward and inexpensive to develop printed electronics on different types of flexible polymer. Some widely used organometallic ink includes graphene, Carbon Nanotubes (CNT), and carbon black [8]. Whereas, nanowires or nanofibers of inorganic materials are extensively studied among the advanced materials used in the manufacture of printed electronics like sensors due to properties such as high sensitivity, high durability device performance and stability, and simple assembly [8]. Inorganic metallic inks consist of Ag, and silver nanoparticles (AgNP) and in the field of this project, we will be using Ag as the conductive ink over the substrate, PI. The specification of the ink used in this framework is stated in Table 2.

The approach for designing the temperature sensing prototype illustrated at Fig. 2 is to use semi-circle or semi-hemisphere as the cross-sectional area (A) shape, and 50 μm as the minimum width or diameter for each microchannel. As the diameter of the semi-circle is 50 μm, the radius (r) will be 25 μm. Thus, the cross-sectional area for the sensing prototype can be obtained from the equation:

$$A = \frac{\pi r^2}{2} \tag{1}$$

Table 2 Specification of Ag Ink

Characteristics	Specification
Particle size (mm)	3–10
Viscosity (cP)	4–5
Resistivity (μΩ-cm)	10–50
Solvent	Water or organic based
Solid content (wt%)	~45
Sintering temperature (°C)	200

From the given specification stated in Table 2, the resistivity (ρ) of Ag is 10–50 μΩ-cm. The average resistivity of the conductive ink can be obtained by adding both values together and divided by 2. Giving the average resistivity of the ink to be 30 μΩ-cm. The resistance (R) of the ink and the total number of microchannels (n) used in this framework are 620 Ω and 100, respectively. The length (L) of each microchannel can be calculated with the following formulas:

$$R = \frac{\rho \ell}{A} \tag{2}$$

and

$$\ell = 2n(L + \pi r) + \pi r \tag{3}$$

3 Results and Discussion

3.1 Wireless Network System

From the given circuit diagram, Fig. 3, it showcases the wireless sensor network system. In this work, it comprises of an Arduino Uno board, a Negative Temperature Coefficient (NTC) thermistor, an ESP8266: ESP-01 Wi-Fi module, four resistors with the value of 1 KΩ, 2.2 KΩ, 100 Ω, and 47 Ω each.

In this wireless network system, the Arduino Uno board act as a Microcontroller Unit (MCU). It is capable of sending actions and data and collecting the temperature from the device.

A thermistor, which is also known as a thermal resistor is an electronic temperature sensing device, has a characteristic to alter its physical resistance accordingly when exposed to changes in temperature. In the thermistor family, it consists of two types of thermistors: Positive Temperature Coefficient (PTC) thermistor and NTC thermistor. Due to its high accuracy and flexibility, an NTC thermistor is used in this framework to measure temperature. NTC thermistor is a commonly used sensing devices as

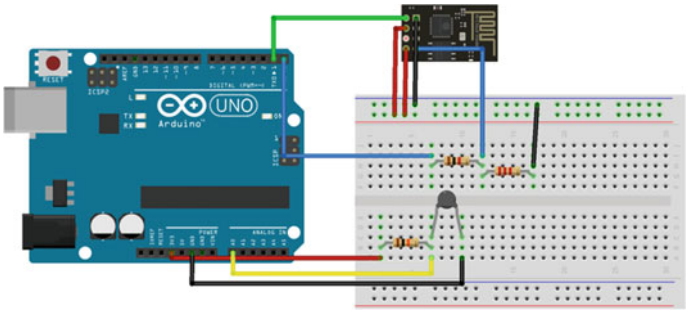

Fig. 3 Wireless sensor network system circuit diagram

they can be used in almost in any type of equipment where temperature plays a role. The characteristic of such components is that the resistance value will decrease as the operating temperature around them increases, and it can be observed in Fig. 6, Sect. 3.2.

The Wi-Fi module, ESP-01, can grant access for the MCU to the internet like a Wi-Fi shield, and communication between the module and another device via transmitting and receiving data. According to the ESP-01 datasheet from AI-Thinker, the operating voltage of the module is stated to be ranging from 3.0 to 3.6 V. However, the typical nominal voltage used by Arduino Uno board is 5 V, a voltage divider is implemented into the circuit to avoid damaging the ESP-01 during the serial communication between the module and the MCU, as shown in Fig. 3. Resistors used for the voltage divider are a 1 KΩ and a 2.2 KΩ at the RX pin of the ESP-01 and the Arduino Uno board. It is to ensure that the voltage across the two resistors to be 3.44 V.

3.2 Printing Related Results

From the given photograph, Fig. 4, it depicts the printed sensing prototype that was fabricated with AJP technique.

Figure 5 illustrates the temperature detected by the printed temperature sensor, shown in Fig. 4, on the cloud platform, ThingSpeak. This experiment has proved that the wireless sensor network system can send the up-to-date data with the desired duration time set for collecting the temperature data.

The experiment setup: are to place the sensing prototype in a room environment, the first reading is sent to the cloud after the temperature come to stable, the readings are transmitted to the cloud every 10 s.

Two resistance tests were performed to check the sensor's non-linearity: heating and cooling. As observed in Fig. 6, both graphs are overlapping with each other, which supports the system's linearity. The experiment was conducted by applying a heat pack onto the printed electronics for 10 min. Additionally, the printed sensing

Fig. 4 Example of aerosol jet printed temperature sensor

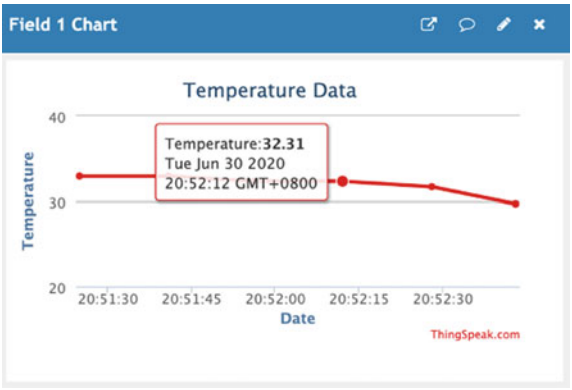

Fig. 5 The temperature detected by the printed temperature sensor on the cloud platform, ThinkSpeak

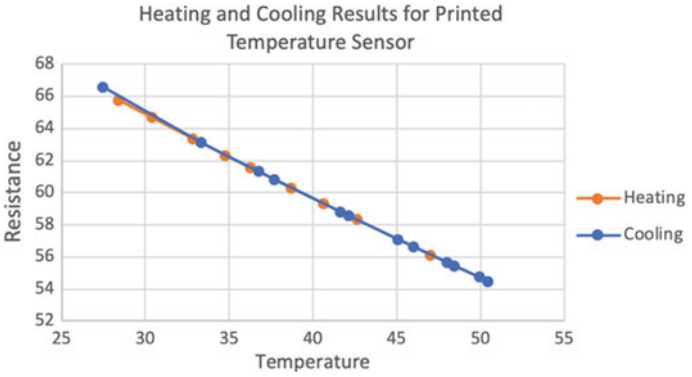

Fig. 6 Resistance versus temperature for the heating and cooling process of the printed temperature sensor

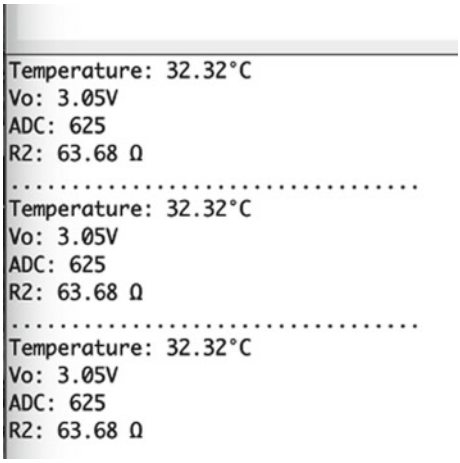

Fig. 7 Results obtained from Arduino Wirelessly

prototype we used for the test experiment has a resistance of 70 Ω at room temperature (usually 25 °C). Thereby, from the given graph, it has proved that the printed electronics can to detect a wide range of temperature ranging from 28 to 51 °C, while keeping the resistance value within the range set.

Taking Fig. 8 as a reference, and assuming that the Analog-to-Digital (ADC) reading is done in the MCU; the physical output voltage of the printed sensor can be verified with the theoretical output voltage by:

$$V_{out} = \frac{V_{in} \times ADC\ value}{1023} = 3.05\ \text{V} \tag{4}$$

Thereby, the resistance of the printed electronic, R2, can be obtained by using the simple voltage divider network formula, then substituting the V_{out} into the formula (Fig. 7):

$$R_{th} = R \times \left(\frac{V_{in}}{V_{out}} - 1\right) = 63.93\ \Omega \tag{5}$$

3.3 Discussion

The morphology of printed lines can be determined by the spreading and drying of the ink after the printing process is done. The spreading of the ink on a solid surface is influenced by the wetting properties and can be expressed with Young's equation [9, 10]:

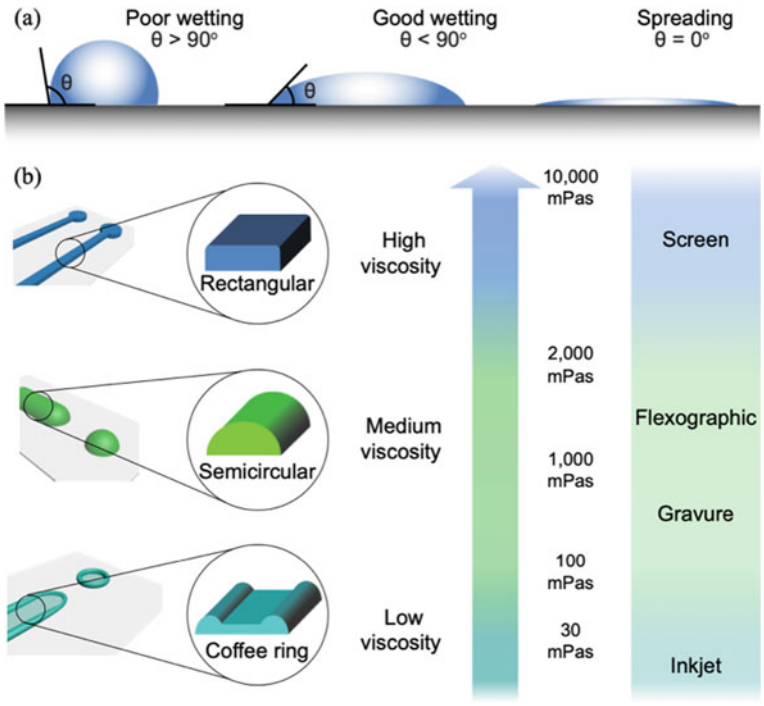

Fig. 8 Ink wetting and drying. **a** Various type of wetting behaviour of the ink droplet on substrates. **b** Typical cross-sectional area profile of the printed line [9]

$$\gamma_{sv} = \gamma_{sl} + \gamma_{lv} \cos\theta \tag{6}$$

where γ_{sl} represents the solid/ liquid interfacial free energy, γ_{sv} and γ_{lv} are the surface energy of the substrates and the ink droplets respectively, and θ is the angle between the contacted surfaces. Figure 8a depicts different wetting behaviour of the ink droplet on the substrate during the spreading process. Good wetting is suggested when the contact angle is small or lesser than 90°, while a large angle between the contacted surface is greater than 90° indicates a poor wetting [9, 10]. For example, when the contact angle is 0°, it is suggested to be a perfect wetting and spreading, while 180° represented a perfect-non wetting scenario [9]. In other words, a favorable wetting described that the ink is capable of spreading over and maintaining its contact with the solid surface for a continuous feature. It is of crucial for functional printing as constant deposition of the functional material is required for fabricating the reliable device. Whereas, a poor wetting means that the ink cannot remain in contact with the surface and tends to retract and bead up, causing it to a discontinuous material deposition [9].

The morphology of the printed pattern is further described by the ink viscosity, assuming reliable ink spreading. Based on the ink's specification in Table 2, the ink's viscosity is only 4–5 cP, causing the cross-sectional area profile of the printed line to

be in the shape of a coffee ring. The coffee ring shape happens when the deposited material dries up and concentrates on the periphery of the print, leaving a concave at the central area, as shown in Fig. 8b. Note that the coffee ring effect is a very common but an unwanted phenomenon due to this effect would lead to non-uniform solvent evaporations across the droplet during the drying process [9].

4 Conclusion and Future Work

This paper highlights the importance of monitoring an individual's body temperature in real-time. The state-of-art of the various type of fabrication methods and material chosen for manufacturing flexible electronics are reviewed. The wireless sensor network system implementation and the derivation of the sensing prototype design are described with printed results from feasibility tests.

In this study, we have demonstrated a wireless health monitoring system with the use of an aerosol jet printed temperature sensor. The flexible electronics can detect a wide range of temperature of 28–51 °C. The system is suggested to be implemented and tested in any thermal-sensitive application or clinical environment for healthcare application purpose.

In future studies, we will investigate further the performance of the printed temperature sensor in comparison with the commercially available temperature sensor. Additionally, we could develop the printed temperature sensor into a portable or wearable device, with several physiological parameters such as strain and humidity.

Acknowledgements This research work was collaborated with and supported by School of Mechanical and Aerospace of Nanyang Technological University (NTU). The authors would like to thank all professors involved in this study from Singapore Institution of Technology, Newcastle University, and NTU.

In addition, we would like to thank the reviewers for their kind comments and suggestions. We have taken all the comments into account and all the amendments have been made accordingly in the manuscript.

References

1. An, B., Shin, J., Kim, S.-Y., Kim, J., Ji, S., Park , J., … Park, J.-U. (2017). Smart Sensor Systems for Wearable Electronic Devices. *Polymers, 9*(12), 303.
2. Di Novo, N., Cantù, E., Tonello, S., Sardini, E., & Serpelloni, M. (2019). Support-Material-Free Microfluidics on an Electrochemical Sensors Platform by Aerosol Jet Printing. *Sensors, 19*(8), 1842.
3. Han, T., Kundu, S., Nag, A., & Xu, Y. (2019). 3D Printed Sensors for Biomedical Applications: A Review. *Sensors, 19*(7), 1706.
4. Hu, G., Kang, J., Ng, L., Zhu, X., Howe, R., Jones, C., … Hasan, T. (2020). *Functional inks and printing of two-dimensional materials.* Retrieved June 30, 2020

5. Khan, S., Ali, S., & Bermak, A. (2019). Recent Developments in Printing Flexible and Wearable Sensing Electronics for Healthcare Applications. *Sensors, 19*(5), 1230.
6. Senthil Kumar, K., Chen, P.-Y., & Ren, H. (2019). A Review of Printable Flexible and Stretchable Tactile Sensor. *Research , 2019*, 1-32.
7. Sreenilayam, S., Ahad, I., Nicolosi, V., Acinas Garzon, V., & Brabazon, D. (2020). Advanced materials of printed wearables for physiological parameter monitoring. *Materials Today, 32*, 147-177.
8. Wang, Y.-F., Sekine, T., Takeda, Y., Yokosawa, K., Matsui, H., Kumaki, D., . . . Tokito, S. (2020). Fully Printed PEDOT:PSS-based Temperature Sensor with High Humidity Stability for Wireless Healthcare Monitoring. *Scientific Reports, 10*(1).
9. Xu, Y., Wu, X., Guo, X., Kong, B., Zhang, M., Qian , X., . . . Sun, W. (2017). The Boom in 3D-Printed Sensor Technology. *Sensor, 17*(5), 1166.
10. Zhang, H., Moon, S., & Ngo, T. (2019). 3D Printed Electronics of Non-contact Ink Writing Techniques. *International Journal of Precision Engineering and Manufacturing-Green Technology, 7*(2), 511-524.

Facile and One-Step Synthesis of Zirconium Oxide Nanoparticles for Removal of Phosphate and Lead(II) Ions

Lim Dillion, Ho Shanley, and Bryan Lee Chong Han

Abstract Water pollution, caused by toxic pollutants such as lead(II) and phosphate ions, results in a lack of safe drinking water. Zirconium oxide nanoparticles show great promise as an adsorbent in water purification. However, the conventional method of synthesizing zirconium oxide nanoparticles involves calcination. Although it is effective, it is extremely energy-intensive and economically unfriendly. In the present study, zirconium oxide nanoparticles were synthesized using a facile precipitation method involving zirconium oxychloride, sodium hydroxide and banana peel extract. The zirconium oxide nanoparticles synthesized were evaluated in terms of their adsorption capabilities on lead(II) and phosphate ions and by varying the initial concentration and pH of phosphate and lead(II) ion solutions. Results showed that zirconium oxide nanoparticles synthesized using banana peels are spherical in shape and have a significantly lower diameter than that without banana peel extract. Zirconium oxide nanoparticles are also comparable to calcium oxide (lime) and commercial activated carbon in the removal of phosphate and lead(II) ions respectively, removing 99.7% of phosphate ions and 99.5% of lead(II) ions. The simple, one-step proposed method of synthesizing zirconium oxide nanoparticles could potentially reduce cost of synthesis of zirconium oxide, rendering its use to purify water feasible.

Keywords Zirconium oxide · Nanoparticles · Facile · Phosphate · Lead(II) ions

1 Introduction

Due to pollution from farms, dissolution of rocks and wastewater discharge from factories, the elevated amounts of phosphate in water bodies have been a big threat to the environment [1]. Elevated amounts of phosphate in water bodies could cause eutrophication which is harmful to aquatic life and reduces oxygen content in water,

L. Dillion (✉) · H. Shanley · B. L. C. Han
Hwa Chong Institution, Singapore, Singapore
e-mail: dillionlim2004@gmail.com

H. Guo et al. (eds.), *IRC-SET 2020*,
https://doi.org/10.1007/978-981-15-9472-4_58

and even be perilous to humans. Phosphate often causes fatal cardiovascular calcification because it leads to the deposits of calcium phosphate in various tissues [2].

Another pollutant commonly found in water is lead(II) ions which may cause many serious ailments such as becoming anemic, kidney failure and even resulting in death [3]. Infants, for example, are largely affected by extremely low lead levels, which could lead to impaired neurobehavioural development in young children [4].

Conventional methods to remove phosphate from wastewater include precipitation, biological methods, reverse osmosis and adsorption [5]. On the other hand, current treatment methods for removal of lead(II) ions from industrial wastewater include precipitation, ion-exchange, separation using membranes, as well as adsorption [6]. Among these methods, adsorption is promising to treat wastewater containing both phosphate and lead(II) ions, due to its high efficiency, low cost and ease of execution [7]. Although activated carbon is the most popular adsorbent used throughout the world for the removal of pollutants, its generation is difficult and is costly, which restricts its application in developing countries [8].

Zirconium oxide has been increasingly researched upon in recent years, with applications including artificial jewellery, insulating materials, light shutters and stereo television glasses. Zirconium oxide nanoparticles possess good adsorption capacities for metal ions, even in the presence of large amounts of competing ions, hence being a promising adsorbent for industrial wastewater treatment [9]. In addition, zirconium loaded materials such as zirconium loaded reduced graphene oxide [10] and zirconium loaded activated carbon [11] have a high affinity for phosphate. As zirconium oxide is very resistant to extreme pH values, oxidizing and reducing agents [12], it is a promising adsorbent for both phosphate and lead(II) ions.

Based on several studies, the conventional way of synthesising zirconium oxide nanoparticles involves calcination [7, 13], which is highly energy-intensive and hence limits its use as an adsorbent.

Hence, this study aims to investigate the synthesis of zirconium oxide nanoparticles using a facile, simple and one-step synthesis via precipitation and the use of plant extracts as capping agents, and to evaluate the effectiveness of the synthesized zirconium oxide nanoparticles in removing phosphate and lead(II) ions.

2 Materials and Methods

2.1 Materials

Sodium hydroxide, sodium dihydrogen phosphate and lead(II) nitrate were procured from GCE Chemicals. Zirconium oxychloride and Folin–Ciocalteau agents were purchased from Sigma Aldrich. Banana peels were obtained from local fruit stalls.

2.2 Preparation of Banana Peel Extract

Banana peels were washed with deionised water, dried and blended. Dried banana peel (30 g) was then boiled with 100 ml of water for 15 min. The mixture was then filtered and stored at 4 °C before use.

2.3 Total Polyphenol Content of Banana Extracts

The total polyphenol content of banana peel was found using the Folin–Ciocalteau method with gallic acid as a standard [14]. 1 ml of banana peel extract was added to a 25 ml volumetric flask and 9 ml of deionised water was added. A reagent blank was also prepared using deionised water. Next, 1 ml of the Folin–Ciocalteau's reagent was added to the mixture. It was then shaken. 10 ml of 7% (w/v) Na_2CO_3 solution was added to the mixture after 5 min. The solution was diluted to 25 ml with deionised water and shaken. After the solution was incubated at room temperature for 90 min, the absorbance against the prepared blank mixture was determined at 750 nm with a UV–VIS Spectrophotometer (Shimadzu UV1800). Calibration curve was prepared using gallic acid from 20 to 100 mg/l with 20 mg/l intervals. The total polyphenol contents of the extracts were then expressed as milligrams of gallic acid equivalents (GAE) per kg of banana peel (mg GAE/kg).

2.4 Synthesis of Zirconium Oxide Nanoparticles

With stirring, banana peel extract (1 ml) was added to aqueous zirconium oxychloride (0.3 M). The pH of the mixture was adjusted to 7.5 with 1 M sodium hydroxide, followed by forceful stirring for 16 h. The precipitate formed was centrifuged and washed with deionised water until the electrical conductivity of the supernatant was lower than 1 mS cm^{-2}. The final product was oven-dried at 60 °C until constant mass was attained and crushed into fine powder using a pestle and mortar. The reaction which leads to the formation of zirconium oxide nanoparticles is proposed to be:

$$ZrOCl_2 + 2NaOH \rightarrow ZrO_2 + 2NaCl + H_2O \quad (1)$$

Polyphenols present in banana peel extract act as capping agents to stabilize the nanoparticles by preventing them from aggregating.

The zirconium oxide nanoparticles synthesized were characterised with the Scanning Electron Microscope (SEM), Energy Dispersive Spectroscope (EDS) and X-Ray Diffraction (XRD).

2.5 *Effect of Initial Concentration*

The adsorbate solutions were made through the dissolution of different amount of AR grade $NaH_2PO_4{\cdot}H2O$ and $Pb(NO_3)_2$ in deionized water respectively to achieve solutions of concentration from 50 to 250 mg/L of phosphate or lead(II) ion. Batch adsorption studies were conducted with beakers containing 20 ml of phosphate or lead(II) ion solution of different concentrations and 0.10 g of zirconium oxide. The mixtures were stirred for 24 h, after which they were centrifuged and the supernatant analysed for residual phosphate and lead(II) ion using a colorimeter (HACH DR 890) and an Atomic Absorption Spectrophotometer (Shimadzu 6300) respectively. The set-ups also included a control without any zirconium oxide. Five replicates were conducted for each concentration.

The equilibrium concentration data were fitted into Langmuir and Freundlich linearised isotherms as given in Eqs. 2 and 3 respectively to determine the adsorption mechanisms, where C_e refers to the concentration of the pollutant at equilibrium (mg/L), Q_e is the adsorption capacity (mg/g) while Q_{max} is the maximum adsorption capacity (mg/g), b is the Langmuir constant, indicating the sorption intensity. K_F is a constant corresponding to sorption capacity while n corresponds to sorption intensity.

$$\frac{C_e}{Q_e} = \frac{1}{bQ_{\max}} + \frac{C_e}{Q_{\max}} \tag{2}$$

$$\log Q_e = \log K_F + \frac{1}{n} \log C_e \tag{3}$$

Adsorption of phosphate and lead(II) was evaluated in terms of adsorption capacity (Q) and removal efficiency (R). The adsorption ion capacity (Q) was calculated in mg/g according to the following formula:

$$Q = \frac{(C_i - C_f)V}{M}$$

C_i intial concentration
C_f final concentration
V volume of solution
M mass of ZrO_2.

Removal efficiency (R) was calculated in % according to the following formula:

$$R = \frac{C_i - C_f}{C_i} \times 100\%$$

C_i initial concentration
C_f final concentration.

2.6 *Effect of pH*

The effect of pH on phosphate and lead(II) ion uptake can throw light on the mechanism of how zirconium oxide adsorbs both ions. The initial concentration of the pollutant ion was standardised at 50 mg /l and the mass of zirconium oxide was fixed at 0.1 g while the pH was varied between 2–12 for phosphate and pH 2–6 for lead(II) ions using dilute hydrochloric acid or sodium hydroxide.

2.7 *Comparing the Performance of Zirconium Oxide with Lime and Activated Carbon*

The effectiveness of zirconium oxide was compared with lime, a conventional coagulant used to remove phosphate and with commercial activated carbon, a conventional adsorbent used to remove lead(II) ions.

3 Results and Discussion

3.1 *SEM Images of Zirconium Oxide Nanoparticles*

Zirconium oxide nanoparticles synthesized were spherical in shape (Figs. 1 and 2). Using ImageJ, zirconium oxide nanoparticles synthesized without the banana peel extracts were determined to have an average size of 24.85 nm which is about twice as large as the ones synthesized with banana peel extract which have an average size of 12.18 nm (Fig. 3). Total polyphenol test on banana peel extract shows that it contains 107 mg GAE/kg of peel which is comparable to most fruit peels such as blueberry and strawberry [15]. It was postulated that polyphenols present in the banana peel extract act as capping agents for the zirconium oxide nanoparticles (Fig. 4), stabilizing them and preventing them from aggregating, hence resulting in particles with much smaller sizes.

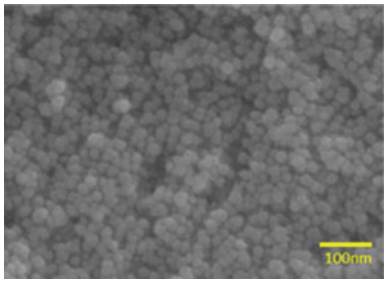

Fig. 1 Image of ZrO_2 nanoparticles synthesized with banana peel extracts from SEM (left)

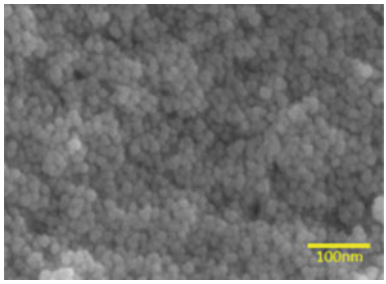

Fig. 2 Image of ZrO_2 nanoparticles synthesized without banana peel extracts from SEM (right)

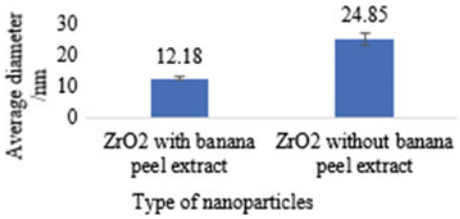

Fig. 3 Diameter of zirconium oxide nanoparticles with and without banana peel extract

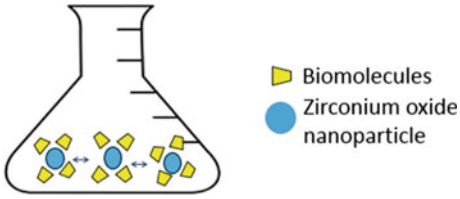

Fig. 4 Polyphenols in plant extracts acting as capping and stabilizing agents for zirconium oxide nanoparticles

3.2 Energy-Dispersive Spectroscopy (EDS)

The presence of zirconium and oxygen confirms the identity of zirconium oxide (Fig. 5). Carbon present is due to the polyphenols from the banana peel extract.

3.3 X-Ray Diffraction (XRD)

The 2-theta peak at 31.3° (Fig. 6) is characteristic of zirconium oxide. The XRD pattern of zirconium oxide synthesized is similar to those reported in literature [7]. The broad peak indicates that the zirconium oxide is non-crystalline and amorphous.

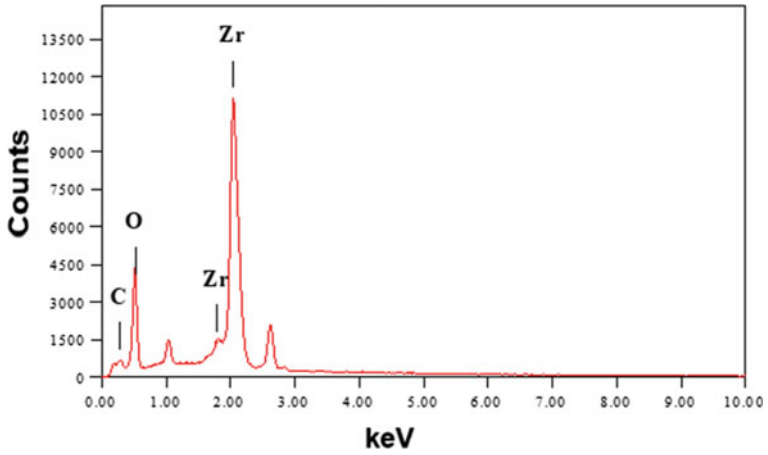

Fig. 5 EDS of zirconium oxide nanoparticles synthesized

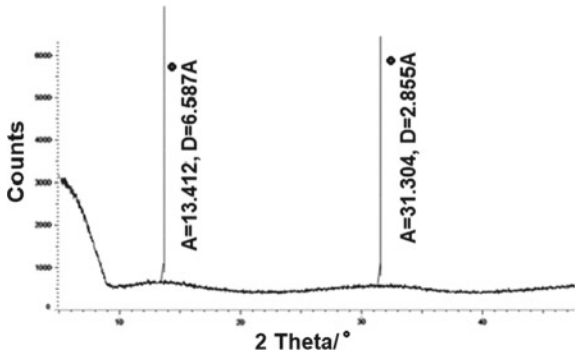

Fig. 6 XRD pattern of zirconium oxide nanoparticles

3.4 Comparison of Adsorption of Phosphate Using ZrO_2 Nanoparticles and CaO

Zirconium oxide is effective in adsorbing phosphate, removing more than 99% of phosphate (Fig. 7). There is no significant difference in the percentage removal by zirconium oxide and lime as the p-value of Mann–Whitney test is 0.203 (>0.05). As illustrated by Fig. 8, phosphate ions are being adsorbed via ion exchange with the surface hydroxyl groups present in zirconium oxide nanoparticles [10]. On the other hand, lime (CaO) removes phosphate via precipitation, as illustrated by Eq. 4:

$$10Ca^{2+}(aq) + 6PO_4{}^{3-}(aq) + 2OH^-(aq) \rightarrow Ca_{10}(PO_4)_6(OH)_2(s) \quad (4)$$

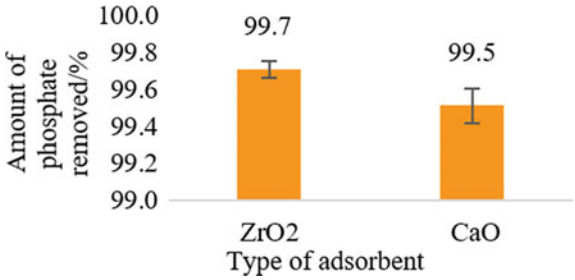

Fig. 7 Adsorption of phosphate by zirconium oxide as compared to lime

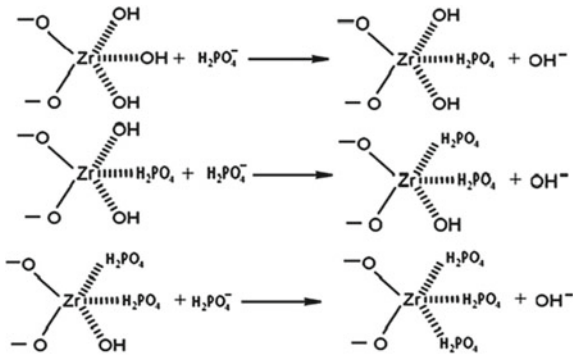

Fig. 8 Removal of phosphate by ZrO_2 via ion exchange

3.5 Comparison of Adsorption of Pb^{2+} Using ZrO_2 Nanoparticles and Activated Carbon

ZrO_2 nanoparticles synthesized with the use of banana peel extract removes close to 100% of lead(II) ions. There is no significant difference in the adsorption of lead(II) ions by zirconium oxide and commercial activated carbon (p-value of Mann–Whitney test = 0.209 > 0.05).

The high percentage of adsorption of lead(II) ions by zirconium oxide nanoparticles can be accredited to the –OH groups present in zirconium oxide forming dative bonds with the lead(II) ions [16], thus adsorbing the lead(II) ions.

Activated carbon, however, contains functional groups containing oxygen such as –OH, phenol and ether groups which allow it to datively bond to lead(II) ions (Fig. 9) [17].

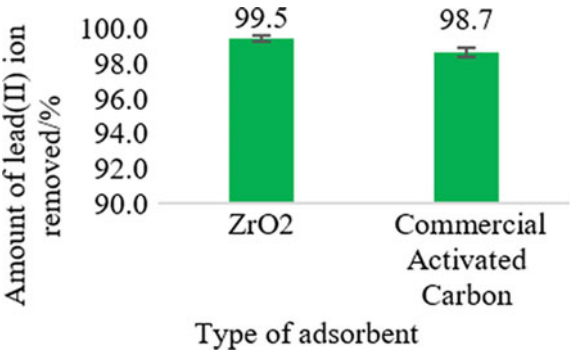

Fig. 9 Adsorption of Pb^{2+} ions by ZrO_2 in comparison with commercial activated carbon

3.6 *Effect of pH on Adsorption of Phosphate by ZrO_2 Nanoparticles*

The adsorption of PO_4^{3-} by zirconium oxide nanoparticles were evidently dependent on the pH (Fig. 10). At low pH, the percentage of adsorption increased from pH 2 to 6, with the optimum pH being 6. As pH increases beyond 6, percentage adsorption drops. A low pH causes poorer adsorption capabilities to drop because of electrostatic repulsion between the anionic OH^- and PO_4^{3-} groups [2]. However, at a pH of about 6, the predominant chemical species is $H2PO_4^-$ (Fig. 11) which has the same charge as hydroxyl groups, hence they are able to replace the hydroxyl groups favourably via ion exchange (Fig. 11). This explains why the best pH for removal of phosphate is pH 6.

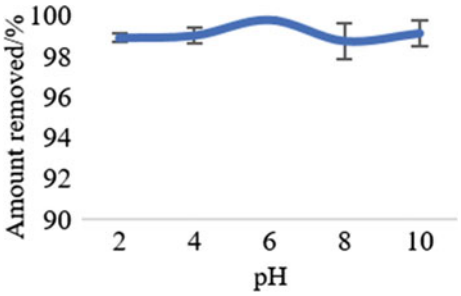

Fig. 10 pH's effect on adsorption of phosphate ions Adsorption of Pb^{2+} ions by ZrO_2 in comparison with commercial activated carbon

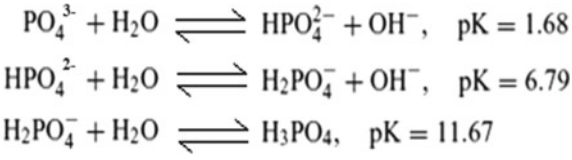

Fig. 11 Predominant chemical species at different pK values

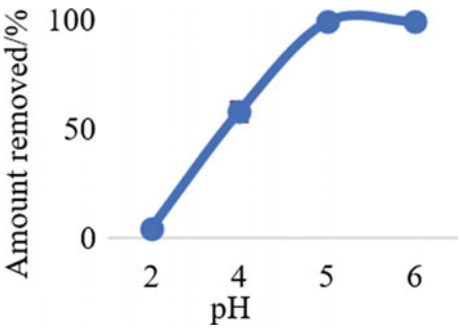

Fig. 12 pH's effect on adsorption of lead(II) ions

3.7 Effect of pH on Adsorption of Pb^{2+} Ions by Zirconium Oxide Nanoparticles

The pH's effect on Pb^{2+} adsorption by ZrO_2 nanoparticles was demonstrated in Fig. 12. Under the acidic pH conditions, the adsorption performance increased significantly from pH 2 to pH 6. To avoid the spontaneous precipitation of lead(II) hydroxide, a pH beyond 6 was not tested. Evidently, the removal of Pb^{2+} was poor at a low pH, which will result in H^+ and Pb^{2+} ions to compete for adsorption sites due to protonation of ZrO_2 at lower pH values, thus having a poorer adsorption capability [18]. The optimal pH for adsorption is determined to be between pH 5 to 6.

3.8 Isotherm Studies

The equilibrium concentration data of both PO_4^{3-} and Pb^{2+} fit Langmuir isotherms, suggesting that the adsorption is monolayer on a homogeneous surface. Maximum adsorption capacities on phosphate and lead(II) ions were derived and compared with other adsorbents (Tables 1 and 2). The maximum adsorption capacity (Q_{max}) of zirconium oxide on phosphate is higher than that on lead(II) ions. Compared to zirconium oxide without plant extracts and several other adsorbents reported in literature, the Q_{max} of zirconium oxide synthesized using banana peel extracts on both pollutants are higher, suggesting that it is an adsorbent with great potential to be used in water treatment.

Figure 13 shows the plot of the linearized Langmuir isotherm, and its gradient was used in the calculation of the maximum adsorption capacity (Q_{max}), which has been tabulated in Table 3. Figure 14 shows the linearized Freundlich plot. A higher correlation coefficient (R^2) indicates that the Langmuir isotherm fits the adsorption data better. The Q_{max} for phosphate was determined to be 106 mg g^{-1}.

Figure 15 shows the linearized Langmuir plot, where its gradient was used to calculate the Q_m (maximum adsorption capacity), which are tabulated in Table 4. Figure 16 shows the linearized Freundlich plot. The correlation coefficients (R^2)

Table 1 Comparing The maximum adsorption capacity of different adsorbents on PO_4^{3-}

Adsorbent	Maximum adsorption capacity (mg/g)	Reference
Zirconium oxide with plant extract	106	This study
Zirconium oxide without plant extract	30	[2]
Nobium oxide	13	[2]
Iron hydroxide-Eggshell waste	14	[2]
Red mud	1	[2]
Fe–Mn binary oxide	23	[2]

Table 2 Comparing the maximum adsorption capacity of different adsorbents on PB^{2+}

Adsorbent	Maximum adsorption capacity (mg/g)	Reference
Zirconium oxide with plant extract	31.8	This study
Zirconium oxide without plant extract	25.0	[19]
Groundnut husk modified with guar gum	9.76	[20]
Activated carbon	26.6	[19]
Pinewood biochar	3.00	[19]

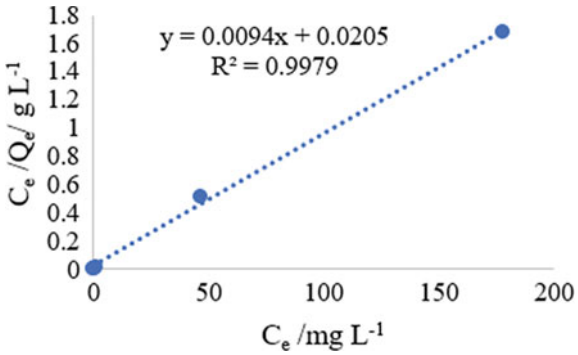

Fig. 13 Langmuir isotherm for phosphate

Table 3 The parameters of the isotherm for the adsorption of $PO_4^{3-}$by zirconium oxide nanoparticles

Pollutant	Langmuir			Freundlich
	Q_{max} (mg g^{-1})	b (L mg^{-1})	R^2	R^2
PO_4^{3-} ions	106	0.46	0.9979	0.8598

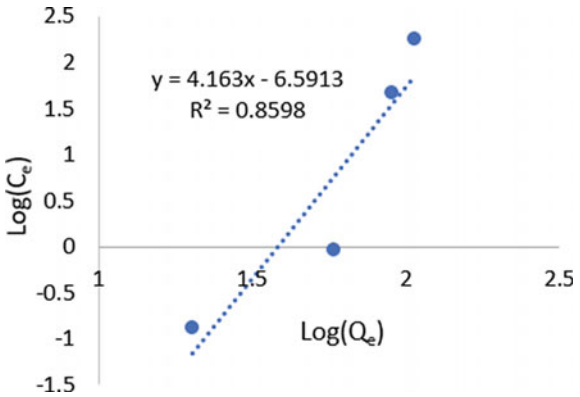

Fig. 14 Freundlich isotherm for phosphate ions

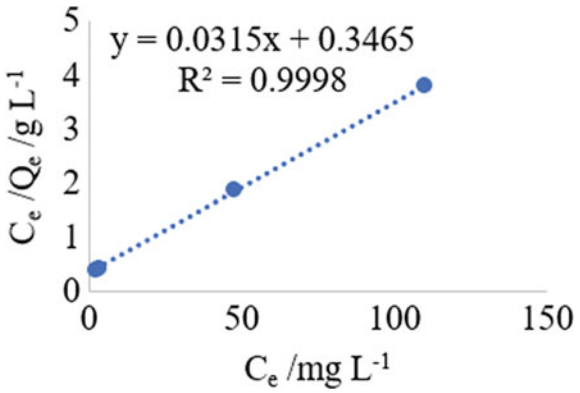

Fig. 15 Langmuir isotherm for lead(II) ions

Table 4 The parameters of the isotherm for the adsorption of lead(II) ions by zirconium oxide nanoparticles

Pollutant	Langmuir			Freundlich
	Q_{max} (mg g^{-1})	b (L mg^{-1})	R^2	R^2
Pb^{2+}	31.8	0.08	0.9998	0.9830

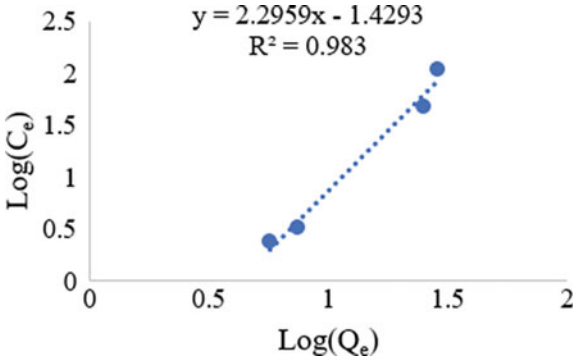

Fig. 16 Freundlich isotherm for lead(II) ions

indicate that the Langmuir model once again was a better fit for the adsorption data. Maximum adsorption capacity on Pb^{2+} was determined to be 31.8 mg g^{-1}.

4 Conclusion and Future Work

Zirconium oxide nanoparticles have been successfully synthesized using banana peel extracts via a simple and one-step precipitation reaction. Compared to zirconium oxide synthesized without banana peel extract, the ones synthesized using banana peel extracts are smaller in size. The zirconium oxide nanoparticles synthesized using banana peel extract are also comparable to conventional adsorbents, lime and activated carbon, in adsorbing phosphate and lead(II) ions respectively. The removal of phosphate and lead(II) ions by zirconium oxide highly depends on the pH. The optimum pH for adsorption of both phosphate and lead(II) ions is 6. The equilibrium data is a good fit for Langmuir isotherm, showing that the adsorption of both phosphate and lead(II) ions by zirconium oxide is monolayer. The maximum adsorption capacity of ZrO_2 for phosphate and lead(II) ions was determined to be 106 mg g^{-1} and 32 mg g^{-1} respectively. The simple, one-step method of synthesizing zirconium oxide nanoparticles proposed in this study is a promising and more eco-friendly alternative to current method of synthesizing zirconium oxide nanoparticles.

Possible extensions to this study include investigating the kinetics of the removal of phosphate and lead(II) ions by zirconium oxide. In real life, wastewater contains multiple anions and hence it would be relevant to study whether the presence of other anions would affect the adsorption of phosphate by zirconium oxide. Finally, for practical usage, zirconium oxide nanoparticles can be embedded into calcium alginate beads for easier retrieval and the possibility of reusability.

Acknowledgements We would like to thank Mrs Sow-Peh Yoke Keow and Mdm Xia Ying for their guidance.

References

1. Bai, L., Yuan, L., Ji, Y. & Yan, H. (2018). Effective Removal of Phosphate from Aqueous by Graphene Oxide Decorated with αα-Fe_2O_3 αα-Fe_2O_3: Kinetic, Isotherm, Thermodynamic and Mechanism Study. *Arab J Sci Eng*, 43, 7, 3611–3620.
2. Razzaque, M. S. (2011) Phosphate toxicity: New insights into an old problem. *Medical Science*, 120, 3, 91–97.
3. Naseem, Z. (2012). Lead Removal from Water by Low Cost Adsorbents: A Review. *Pak. J. Anal. Environ. Chem.*, 2013, 13, 1–8.
4. Wani, A., Ara, L. A. & Usmani, J. A. (2015). Lead toxicity: A review. *Interdisciplinary Toxicology*, 8, 2, 55–64.
5. Jiang, J. Q. & Wu, L. (2010). Preliminary study of calcium silicate hydrate (tobermorite) as crystal material to recovery phosphate from wastewater. *Desalination and Water Treatment*, 23, 1-3, 49–54.

6. Dakhil, I. B. (2005). Adsorption of lead from industrial effluents using rice husk. *International Journal of Engineering and Management Research.* 5, 1, 109–116.
7. Keiteb, S., Saion, E., Zakaria, A. & Soltani, N. (2016). Structural and Optical Properties of Zirconia Nanoparticles by Thermal Treatment Synthesis. *Journal of Nanomaterials*, 2016, 1, 1–6.
8. Kyriakopoulos, G. & Doulia, D. (2016) Adsorption of pesticides on carbonaceous and polymeric materials from aqueous solutions: A review. *Separation and Purification Reviews*. 2016, 35, 97–191.
9. Wang, C., Liu, X., Chen, J. P. & Li, K. (2015). Superior removal of arsenic from water with zirconium metal-organic framework UiO-66. *Scientific Reports.* 5, 16613, 1–10.
10. Luo, X., Wang, X., Bao, S., Liu, X., Zhang, W. & Fang, T. (2016). Adsorption of phosphate in water using one-step synthesized zirconium-loaded reduced graphene oxide. *Scientific Reports*, 2016, 6, 39108.
11. Wajima, T. (2016). Phosphate Adsorption on Zirconium-Loaded Activated Carbon, and its Application for Phosphate Recovery from Deep Seawater. *International Journal of Chemical Engineering and Application*, 7, 6, 1–4.
12. Suzuki, T. M., Bomani, J. O., Matsunaga, H. & Yokoyama, T. (2000). Preparation of porous resin loaded with crystalline hydrous zirconium oxide and its application to the removal of arsenic. *React. Funct. Polym*, 2000, 43, 165–172.
13. Salehpour, M. & Ghanbary, F. (2016). Synthesis of cellulose / zirconium oxide nanocomposite and the study of its activity in the removal of pollutants. *IIOABJ*, 7, 5, 401–408.
14. Song, F-L., Gan, R-Y., Zhang, Y., Xiao, Q., Kuang, L. & Li, H-B. (2016). Total Phenolic Contents and Antioxidant Capacities of Selected Chinese Medicinal Plants. *Int. J. Mol. Sci*., 2016, 11, 2362–2372. Doi:https://doi.org/10.3390/ijms11062362
15. Manach, C., Scalbert, A., Morand, C., Rémésy, C. & Jime´nez, L. (2004). Polyphenols: food sources and bioavailability. *The American Journal of Clinical Nutrition*, 79, 5, 727–747.
16. Yung, A., Lim, S. F., Chua, D., Sanaullah, D., Baini, R. & Abdullah, M. O. (2017). Adsorption equilibrium for heavy metal divalent ions (Cu^{2+}, Zn^{2+}, and Cd^{2+}) into zirconium-based ferromagnetic sorbent. *Advances in Materials Science and Engineering*, 2017, 121067, 1–4.
17. Chen, J. P. & Shunnian. (2004). Acid/Base-Treated Activated Carbons: Characterization of Functional Groups and Metal Adsorptive Properties. *Langmuir*, 20, 6, 2233–2242.
18. Su, Y., Cui, H., Li, Q., Gao, S. & Shang, J. K. (2011). Strong adsorption of phosphate by amorphous zirconium oxide nanoparticles. *Water Research*, 4, 7, 5018–5026.
19. Ogunlala, O. U., Aderibigbe, A. D., Oluwasina, O. O. & Amoo, I. A. (2017). Adsorption studies of Pb^{2+} from aqueous solutions using unmodified and citric acid - modified Plantain (Musa paradisiaca) Peels. *IOSR Journal of Applied Chemistry*, 10, 2, 30–39.
20. Rahman, S. & Sathasivam, K. V. (2015). Heavy Metal Adsorption onto Kappaphycus Sp. From Aqueous Solutions: The Use of Error Functions for Validation of Isotherm and Kinetic models. *BioMed Research International*, 2015, 126298, 1–13.

A Novel Electrochemical Enhancement of Activated Carbon Fibres for the Purification of Contaminated Pharmaceutical Effluents

Low Jeen Liang, Yiu Yi Hin Kinsey, and Tan Wei An

Abstract Industrial discharge of pharmaceutical effluents has rapidly increased over the last decade and poses severe environmental threats. Activated carbon is the most prevalent adsorbent for wastewater treatment because of its efficiency and scalability for commercial usage, however, its application in treating pharmaceutical wastewater is unsustainable. This is due to the presence of several pharmaceutical organics in the wastewater, such as acetone, which are harder to purify. To overcome this limitation, the electrochemical enhancement of activated carbon fiber (ACF) for the treatment of acetone-contaminated pharmaceutical wastewater was explored. It was found that at an applied voltage of −1.0 V, electro-sorption at an optimum electrolyte concentration of 0.001 M increased ACF's adsorption capacity for acetone by up to 107%. An improvement in adsorption capacity after electrochemical enhancement was consistent across a wide range of wastewater salinities. Freundlich and Langmuir isotherm studies also revealed that the maximum adsorption capacity of electrochemically enhanced ACF greatly outperformed that of unenhanced ACF and other well-known adsorbents. When electrochemically regenerated, ACF retained over 90% of its original adsorption capacity while the unenhanced ACF lost 39% of its initial adsorption capacity over three back-to-back cycles of adsorption and regeneration. Therefore, electrochemical enhancement increases the reusable lifespan of ACF, decreasing the amount of new ACF needed during treatment. Furthermore, electro-sorption and electrochemical regeneration have no lag time between each process, potentially allowing for a cyclic treatment process. This was explored in the construction of a working prototype. Electrochemically enhanced ACF holds immense promise as an effective and waste-minimizing technology for pharmaceutical wastewater purification.

Keywords Acetone · Activated carbon fibre · Electrochemical enhancement · Electro-sorption · Adsorption capacity · Regeneration · Isotherms · Prototype

L. J. Liang (✉) · Y. Y. H. Kinsey · T. W. An
Hwa Chong Institution (High School), Singapore, Singapore
e-mail: 171423y@student.hci.edu.sg

H. Guo et al. (eds.), *IRC-SET 2020*,
https://doi.org/10.1007/978-981-15-9472-4_59

1 Introduction

In recent years, increased demand for healthcare has accelerated the growth of the pharmaceutical industry. Singapore's vibrant pharmaceutical sector has seen rapid growth over the past half-century due to several factors, including a growing population and the development of new and innovative drug therapies to treat infectious and chronic conditions [1]. Globally, each and every individual that requires medication—a universal necessity—contributes to total water expenditure during pharmaceutical production, and its subsequent disposal as wastewater. Consequently, the discharge of pharmaceutical effluents containing numerous organic pollutants has risen worldwide. These pollutants pose a dire threat to the environment and even to human health.

Acetone is a prominent example of the organic pollutants found in pharmaceutical wastewater. Acetone, a polar organic with a low molecular weight, is often used as a solvent in pharmaceutical manufacturing [2]. For example, acetone is used as a solvent in the wet granulation process in the formulation of tablets or capsules [3]. Acetone is highly volatile at room temperature and causes acute or chronic poisoning to humans by prolonged contact. In high concentrations, acetone is also toxic to wildlife and contributes to air pollution [4].

Conventional purification methods, such as reverse osmosis and electrochemical oxidation, are costly [5] and unsustainable for the prolonged treatment of pharmaceutical wastewater. Activated carbon is widely hailed as the most prevalent adsorption material used for the removal of toxic organics from wastewater due to its effectiveness, capacity and scalability for commercial usage. In particular, activated carbon fibres (ACFs), which are a hybrid of carbon fibre and activated carbon have gained prominence. ACF is a promising microporous material with a fibre shape and well-defined porous structure. It has a high specific surface area (800–3000 m^2/g), fast adsorption and desorption rate and is easy to regenerate [6].

However, activated carbon remains unsuitable for pharmaceutical wastewater treatment. Activated carbon adsorbents are quickly saturated with organic pollutants found in wastewater and lose their adsorption ability. Current regeneration efforts of activated carbon for its reusability are also expensive and time consuming. Furthermore, activated carbon is less efficient in its adsorption of polar organics with a low molecular weight such as acetone, many of which are present in pharmaceutical wastewater [7]. An estimated 300,000 tonnes of activated carbon are disposed yearly as secondary waste [8]. Activated carbon is largely produced from the carbonization of lignocellulosic materials [9], such as rice husk and coal. Large-scale production of activated carbon depletes natural resources and is expensive.

Electro-sorption (also known as electrochemical enhancement) has attracted attention as a promising technology that is primarily known to effectively desalinate seawater using activated carbon electrodes. Upon the passage of a potential difference through electrically conductive adsorbents, the adsorption capacity for ionic salts and heavy metal ions was enhanced by over 40% [7]. Recent forays have found

that applying a second voltage on the activated carbon after adsorption could potentially enhance its regeneration for future reuse. These enhancements would make the use of activated carbon more meaningful.

However, despite the urgent need to develop more efficient technologies for pharmaceutical wastewater purification, there are currently, to this study's knowledge, no studies on the electro-sorption of pharmaceutical pollutants. Electro-sorption has the unique features of low cost, does not cause pollution, environmentally friendly and simple operation [8], making it a suitable technology for pharmaceutical wastewater treatment. Acetone as a pharmaceutical pollutant is uniquely both volatile and resistant to biodegradation, suggesting a need for greater understanding of new available methods in order to efficiently remove it from pharmaceutical effluents. This study aims to explore and fill up this lack of material in the current field.

By utilizing a novel electrochemical enhancement of activated carbon fibre (ACF), this study aims to enhance ACF's performance as an attractive and promising treatment technology for the minimization of pharmaceutical wastewater pollution.

2 Experimental

2.1 Materials

Acetone and sodium sulfate were procured from Sigma Aldrich. ACFs were ordered from Guangdong, China.

2.2 Electro-sorption by ACF

1.3 g of ACF was suspended by a working electrode holder in a 1000 mg/L 250 ml acetone solution of varying salinities (0.01, 0.001 and 0.0001 M of sodium sulfate) (Fig. 1). A bias potential of −1.0 V was applied onto the ACF for the duration of the adsorption using a potentiostat. An AgCl reference electrode was used to detect voltage applied, while a platinum plated electrode as the auxiliary electrode,

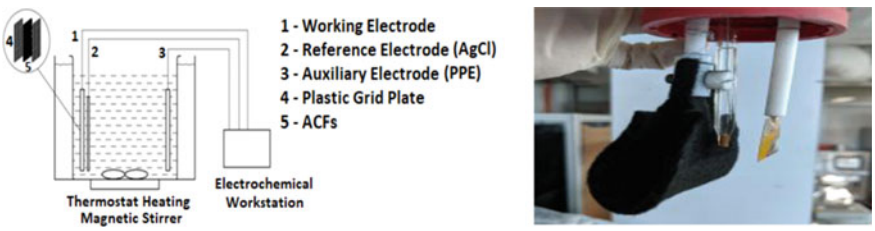

Fig. 1 Electro-sorption setup

completing the circuit. Electro-sorption was not carried out at a positive voltage as acetone may be reduced to form either propane or isopropanol instead of being adsorbed [8].

A similar setup, without a bias potential applied onto the ACF, served as the control. Finally, to account for volatilization of acetone, another setup with neither ACF nor bias potential applied was employed.

UV–Vis spectroscopy at a wavelength of 267 nm was used to determine the final concentration of acetone after adsorption and electro-sorption.

2.3 Isotherm Studies on ACF and Electrochemically Enhanced ACF

1.3 g of ACF and electrochemically enhanced ACF were submerged in a setup similar to the one mentioned in section B with a salinity of 0.001 M sodium sulfate and varying acetone concentration (200, 400, 600, 800 and 1000 mg/L). The equilibrium concentrations of acetone were then fitted into Langmuir and Freundlich isotherms. The Langmuir isotherm, which assumes monolayer adsorption onto a homogeneous surface, was plotted using the linearized equation:

$$\frac{C_e}{Q_e} = \frac{1}{bQ_{\max}} + \frac{C_e}{Q_{\max}} \tag{1}$$

where C_e is the final concentration of acetone at equilibrium in mg/L, Q_eQ_e is the adsorption capacity at equilibrium in mg/L, Q_{max} is the maximum adsorption capacity and b is a constant. The inverse of the gradient allows one to derive Q_{max}

The Freundlich isotherm, which in contrast to the Langmuir isotherm, assumes multilayer adsorption onto a heterogeneous surface, was plotted using the linearized equation:

$$\lg Q_e = \lg K_f + \frac{1}{n} \lg C_e \tag{2}$$

where $C_e$is the final concentration of acetone at equilibrium in mg/L, Q_e is the adsorption capacity at equilibrium, K_F is a constant proportional to the maximum adsorption capacity and $\frac{1}{n}$ is another constant which determines favourability of adsorption.

2.4 Reusability Studies on ACF

After adsorption or electro-sorption, ACF from both set ups were submerged in 100 ml of 0.001 M sodium sulfate solution. A voltage of +0.6 V was applied on the

electrochemically enhanced ACF for 30 min. ACF and electrochemically enhanced ACF was subjected to three consecutive cycles of adsorption/electro-sorption and regeneration with their adsorption capacity at the end of each cycle determined.

3 Results and Discussions

3.1 Electrochemical Enhancement of the Adsorption Capacity of ACF for Acetone

A wide range of salt concentration is naturally found in pharmaceutical wastewater. Figure 2 shows that the electrochemically enhanced ACF removed more acetone than the unenhanced ACF across all wastewater salinities, with the greatest increase being 107% when sodium sulfate concentration is 0.001 M.

Similar to ACF, the adsorption capacity of electrochemically enhanced ACF increased as salinity increased from 0.0001 to 0.001 M of sodium sulfate. This is likely due to the "salting out" of acetone [10] where the solubility of acetone decreases as more sodium sulfate is dissolved in the solution, resulting in more acetone being retained on the surface of ACF. However, at 0.01 M of sodium sulfate, the adsorption capacity of electrochemically enhanced ACF decreases, as the excess ions occupy adsorption sites on ACF due to electrostatic attraction from the voltage applied [6].

It is proposed that ACF adsorbs acetone due to dipole–dipole interactions and hydrogen bonding between its surface functional groups and acetone molecules (Fig. 3).

To explain the increase in adsorption capacity, Scanning Electron Microscopy (SEM) and Energy Dispersive Spectroscopy (EDS) analysis were conducted on ACF before and after electro-sorption. Both SEMs in Fig. 4 were performed at an eV of 5.0 kV and aperture working distance of 8.0 mm.

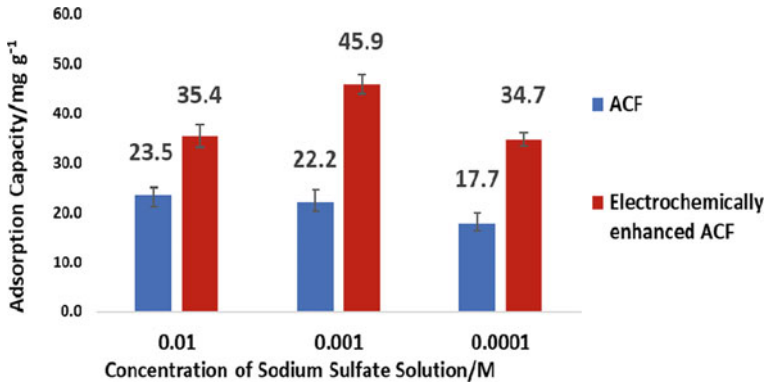

Fig. 2 Removal of acetone by ACF and electro-sorption

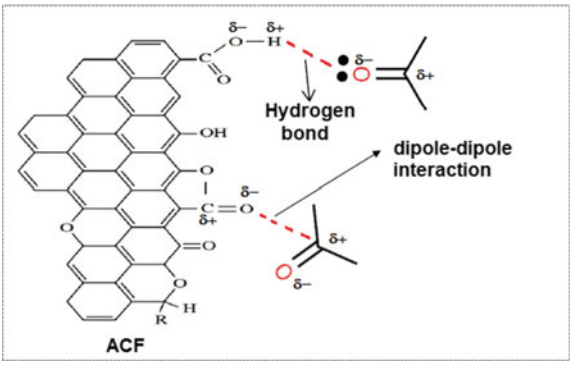

Fig. 3 Proposed adsorption mechanism of acetone by ACF

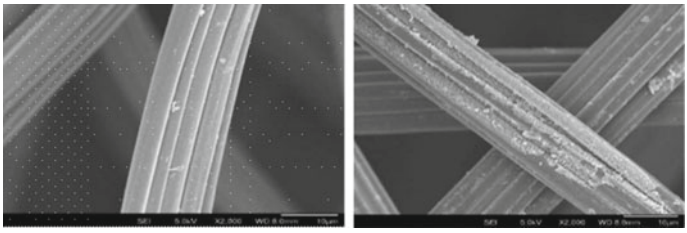

Fig. 4 SEM of ACF before electro-sorption at 2000 × magnification (left) and SEM of ACF after electro-sorption at 2000× magnification (right)

Figure 4 reveals that ACF after electro-sorption has a rougher and more uneven surface, possibly due to electrochemical polarization, which is attributed to electrostatic repulsion between surface functional groups [11], inducing inelastic deformation on the surface of the ACF. This increases the number of adsorption sites available on ACF's surface, enhancing its adsorption capacity. EDS data also suggests an increase in the oxygen containing functional groups of ACF after electro-sorption (Table 1), which improves the hydrophilicity of ACF, thereby allowing ACF to better adsorb acetone via dipole–dipole interactions. At a negative voltage applied during electro-sorption, active oxidising free hydroxyl radicals are generated on the surface of the ACF, causing it to be oxidized [12, 13].

Table 1 EDS of oxygen content in ACF and ACF after electro-sorption

Oxygen content (%)	
ACF before electro-sorption	ACF after electro-sorption
6.71	9.70

3.2 *Isotherm Studies*

The equilibrium concentration data of ACF and electro-sorption were fitted into the Langmuir and Freundlich isotherms. By analysing the plot of the Langmuir isotherm, the maximum adsorption capacity (Q_{max}) of ACF and electrochemically enhanced ACF can be derived. This can be compared with the Q_{max} of other adsorbents from different studies. Table 2 reveals that electrochemically enhanced ACF not only has a much higher maximum adsorption capacity (Q_{max}) than unenhanced ACF, but also outperforms other adsorbents like zeolite and silica.

By comparing R^2 (Coefficient of determination) of isotherm plots, mechanisms of adsorption and electro-sorption of acetone were compared (Table 3). The respective isotherms determined are shown below (Figs. 5, 6, 7 and 8). The Freundlich isotherm is a better fit for electrochemically enhanced ACF as its R^2 is greater, suggesting multilayer and heterogeneous adsorption. In contrast, adsorption by unenhanced ACF fits Langmuir model better, suggesting that adsorption is predominantly monolayer and homogeneous. A visual model of both forms of adsorption can be seen in Fig. 9.

Table 2 Maximum adsorption capacity (Q_{max})

Adsorbent	Q_{max} (mg g^{-1})	Source
Enhanced ACF	189	This study
Unenhanced ACF	50	This study
Zeolite	57	[10]
Silica	68	[11]

Table 3 Isotherm parameters

Type of ACF	R^2 values	
	R^2 Freundlich	R^2 Langmuir
Enhanced ACF	0.994	0.952
Unenhanced ACF	0.864	0.880

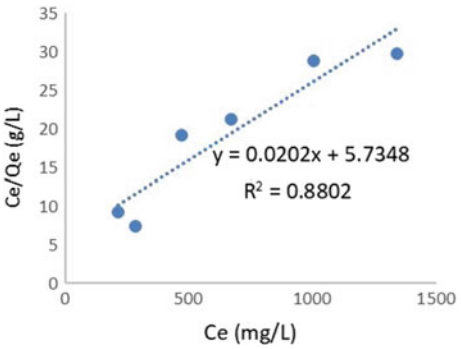

Fig. 5 Langmuir Isotherm for ACF

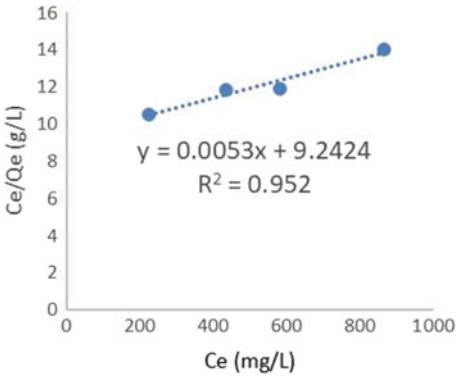

Fig. 6 Langmuir Isotherm for electrochemically enhanced ACF

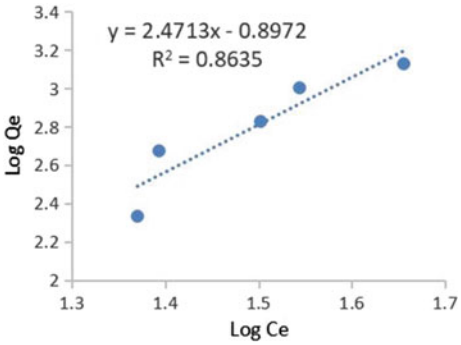

Fig. 7 Freundlich Isotherm for ACF

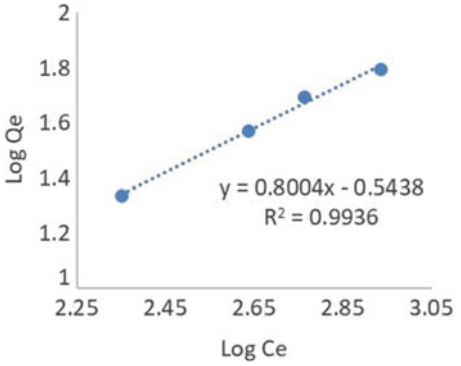

Fig. 8 Freundlich Isotherm for electrochemically enhanced ACF

3.3 Regeneration and Electrochemical Regeneration of ACF

Figure 10 reveals that after three cycles of adsorption and regeneration, the electrochemically enhanced and regenerated ACF maintained over 90% of its original adsorption capacity, while that of ACF plunged by 39.2% in the third cycle. Therefore,

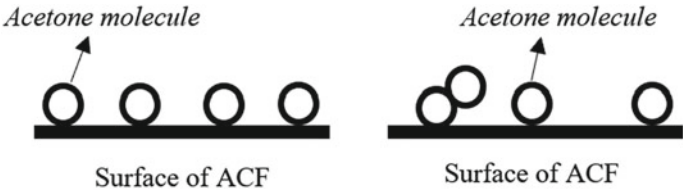

Fig. 9 Representation of homogeneous and monolayer adsorption (left) and representation of heterogeneous and multilayer adsorption (right)

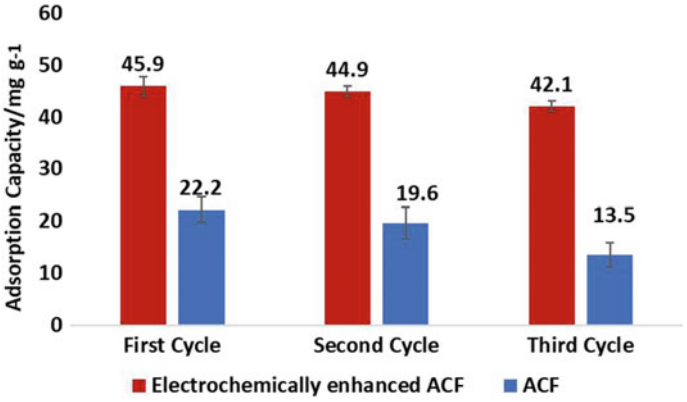

Fig. 10 Regeneration and Electrochemical Regeneration of ACF

electrochemical enhancement increases the reusable lifespan of ACF, decreasing the amount of new ACF needed during treatment. Under a positive voltage applied, H^+ ions are produced at the ACF functioning as an anode, causing local pH to decrease [14]. As H^+ ions protonate acetone, the hydrogen bonds between acetone and ACF are weakened, promoting the desorption of acetone into the solution and rendering the regeneration of ACF efficient.

Notably, electro-sorption was carried out immediately after regeneration, with no time in between cycles. In comparison, commercial chemical regeneration of activated carbon typically requires up to several hours between cycles for the drying of adsorbents [13]. This suggests that electro-sorption and electrochemical regeneration can be conducted immediately after each another, rendering a cyclic process. Thermal regeneration, a widely used commercial regeneration method, is energy intensive as it requires high temperatures up to 800°C during its pyrolytic stage [5]. In contrast, electrochemical regeneration, which has a low energy consumption as it operates in low direct current voltages [5], is potentially a cost-effective alternative to conventional chemical or thermal regeneration.

3.4 *Construction of Prototype for Integrated Treatment of Pharmaceutical Wastewater*

A prototype was designed for the large-scale treatment of pharmaceutical wastewater. The prototype consists of three containers, two of which are containers for the wastewater and regeneration solutions with the third being the central electrochemical cell. The containers were constructed using 5.0 mm thick acrylic sheets cut out using a laser cutter joined together with acrylic glue. A 10 mm hole was drilled in each of the reagent containers to attach a pipe by which the container would be drained. In the electrochemical cells, a 40 mm circle was cut out from the top to fit the electrodes in, in addition to two 10 mm holes which would be attached to pipes leading from the reagent containers. To control the flow of solution, two electronic ball valves were installed at the reagent containers. A third ball valve was installed at the bottom of the electrochemical cell to drain away the solution after electro-sorption and regeneration cycles. With the use of the electronic ball valves, the process is fully automated (Fig. 11).

With the flick of a button, wastewater from Tank 1 drains into the central cell where electro-sorption of pharmaceutical wastes occurs. After electro-sorption, the treated effluent will be drained. Regeneration solution from Tank 2 will then be channelled into the central cell to desorb the adsorbed pollutants so that the ACF could be regenerated. This process can be visualized in Fig. 12. After desorption, the spent regeneration solution will be drained, and the cycle repeats. The process is automated, rapid and efficient.

Our prototype demonstrates the potential for electro-sorption and electrochemical regeneration to be combined as a cyclic treatment process. This process allows for a single batch of ACF to potentially treat tonnes of pharmaceutical wastewater without human intervention, as well as minimize lag time between electro-sorption

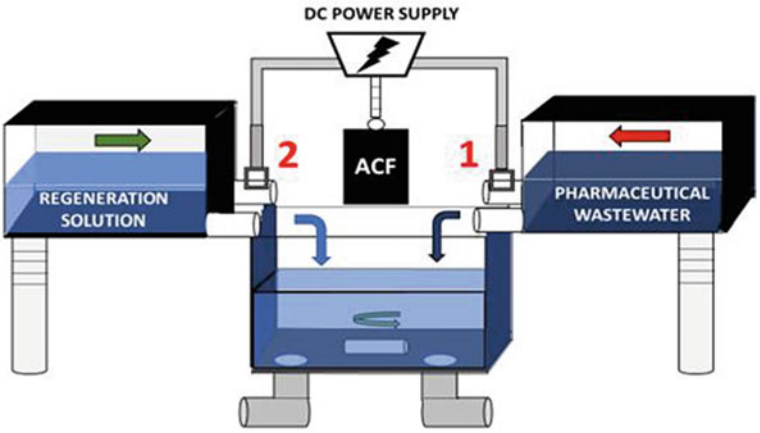

Fig. 11 Prototype blueprint

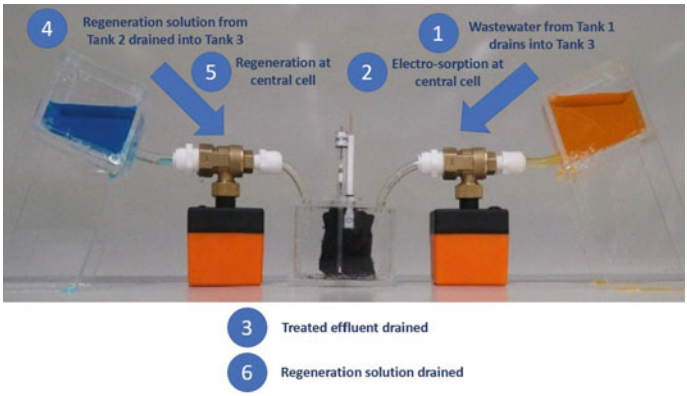

Fig. 12 Actual Prototype

and electrochemical regeneration. In an industrial setting, the prototype can be upscaled, rendering the treatment of pharmaceutical wastewater by electro-sorption and electrochemical regeneration even more attractive and convenient.

4 Conclusion

Electro-sorption successfully increases the adsorption capacity of ACF, a prevalent commercial adsorbent, for acetone up to 107% across a wide range of wastewater salinity. The maximum adsorption capacity of ACF was enhanced from 50 to 189 mg g^{-1}. Furthermore, electrochemical regeneration can retain over 90% of ACF's adsorption capacity over three continuous cycles of adsorption and regeneration. The cyclic nature of electro-sorption and electrochemical regeneration allows for a rapid, simple and convenient treatment process. Electro-sorption and electrochemical regeneration are attractive and promising methods to enhance the performance of ACF as a more cost-efficient and waste minimizing option for pharmaceutical wastewater purification.

A model on how electrochemically enhanced ACF can be used in industrial wastewater treatment plants has been proposed and constructed. The prototype has been fully automated to continuously channel wastewater and regeneration solvent into its central electrochemical cell for wastewater treatment and ACF regeneration respectively. The solutions are then drained from the central cell, and the process repeats itself again. In this way, electro-sorption and electrochemical regeneration can be integrated in situ without any manual intervention required, effectively reducing transport and labour costs. On an industrial scale, such a prototype could potentially be used for a large-scale cyclic treatment process for the purification of acetone-contaminated pharmaceutical wastewater, allowing for a facile treatment process.

In the future, the study could be extended to include a wider range of ions and other pharmaceutical pollutants such as ethylene glycol and dimethyl sulfoxide. A synthetic form of pharmaceutical wastewater containing a mixture of these solvents, together with a high concentration of ions such as Cl^- and NO_3^- could be used to mimic real-life pharmaceutical wastewater. Further investigations would ensure the effectiveness of electrochemically enhanced ACF in real life wastewater treatment, so that electrochemically enhanced ACF can be an even more eco-friendly, sustainable and widely applicable product. Studies could also be conducted to determine the maximum amount of times electrochemically enhanced ACF can be reused while retaining over 90% of its adsorption capacity, as our study only investigated this up to three consecutive cycles.

The process of electrochemical enhancement lends itself easily to being used for other adsorbents. Electrochemical enhancement could be employed as a low-cost, eco-friendly method to enhance the performances of other electrically conductive adsorbents such as carbon nanotubes or reduced graphene oxide. With the development of more cost-efficient and environmentally friendly adsorbents, electrochemical enhancement has the potential to be a versatile method which can be adapted to complement innovative adsorbent materials for the treatment of pharmaceutical wastewater. Therefore, electrochemical enhancement shows enormous potential in the field of water purification, and can be applied in a wide range of industrial settings.

Acknowledgements We would like to thank our teacher-mentor, Mrs Sow-Peh Yoke Keow, for her invaluable support and guidance.

References

1. W.S. Ho, "Overview of the Singapore PharmBio Sector. Singapore PharmBio Guide 2019/2020," Retrieved on 20 May from https://vcf.mycareersfuture.sg/resources/content/0b87b993ce809dddd521c3088c3c4bcf.pdf, 2020.
2. C. Gadipelly, A. Pérez-González, G. D. Yadav, I. Ortiz, R. Ibáñez, V.K. Rathod, and K. V. Marathe, "Pharmaceutical industry wastewater: review of the technologies for water treatment and reuse," Industrial & Engineering Chemistry Research, Vol. 53(29), pp. 11571-11592, 2014.
3. K. Grodowska and Parczewsk, "Organic solvents in the pharmaceutical industry," Acta Poloniae Pharmaceutica, Vol. 67(1), 3–12, 2010.
4. L. Tang., L. Li, R. Chen, C. Wang, W. Ma, and X. Ma, "Adsorption of acetone and isopropanol on organic acid modified activated carbons," Journal of Environmental Chemical Engineering, vol. 4, pp. 2045–2051, 2010.
5. K. Foo and B. Hameed, "A short review of activated carbon assisted electro-sorption process: An overview, current stage and future prospects," Journal of Hazardous Materials, vol. 170(2-3), pp 552-559. 2009.
6. L. Wang, M. Zhang, Q. Huang, C. Zhao, K. Luo, and M. Lei, "Fabrication of ACF/GO/PEI Composite for Adsorption of Methyl Orange from Aqueous Solution," Journal of Nanoscience and Nanotechnology, vol. 18, pp 1747-1756, 2018.
7. Y. Han, X. Quan, X. Ruan, and W. Zhang, "Integrated electrochemically enhanced adsorption with electrochemical regeneration for removal of acid orange 7 using activated carbon fibers," Separation and Purification Technology, vol. 59(1), pp. 43-49, 2008.

8. W. Li, L. Zhang, J. Peng, N. Li, and X. Zhu, "Preparation of high surface area activated carbons from tobacco stems with K_2CO_3 activation using microwave radiation," Industrial Crops and Products, Vol. 3, pp. 341-347, 2008.
9. J. Menéndez-Díaz and I. Martín-Gullón, "Chapter 1 Types of carbon adsorbents and their production," Interface Science and Technology Activated Carbon Surfaces in Environmental Remediation, pp 1–47, 2006.
10. C. E Matkovich., and G. D Christian, "Salting-out of acetone from water. Basis of a new solvent extraction system," Analytical Chemistry, 1973.
11. X. Su, and T.A. Hatton, "Electro-sorption at functional interfaces: From molecular-level interactions to electrochemical cell design", Physical Chemistry Chemical Physics, vol. 19(35), pp 23570-23584, 2017.
12. Y. Han, X. Quan, S. Chen, S. Wang, and Y. Zhang, "Electrochemical enhancement of adsorption capacity of activated carbon fibers and their surface physicochemical characterizations," Electrochimica Acta, vol. 52(9), pp 3075-308, 2007.
13. Y. Han, X. Quan., S. Chen, H. Zhao, C. Cui, and Y. Zhao, "Electrochemically enhanced adsorption of aniline on activated carbon fibers. Separation and Purification Technology," vol 50(3), pp. 365–372, 2006.
14. M. P Mehta and J. R. V Flora, "Effects of electrochemical treatment of granular activated carbon on surface acid groups and the adsorptive capacity for phenol," Water Research, vol. 31 (9), pp. 2171–2176, 1997.

Investigating the Use of Phosphate Removing Organisms in Bioremediation

Lim Chern Howe Ryan, Tan Wei Liang Darrius, and Tay Hock Jun

Abstract This study aims to investigate the use of phosphate removing organisms in bioremediation, testing the phosphate removal capabilities of 3 microorganisms, *Bacillus subtilis*, *Pseudomonas putida* and *Saccharomyces cerevisiae* under various conditions. To determine the concentration of residual phosphates, phosphate test kits were used along with a colorimeter. The findings revealed that all 3 microorganisms were capable of phosphate removal, although *S. cerevisiae* performed the best at 84% removal. In general, synergistic effects between the microorganisms were found to be present. Additionally, immobilisation of *S. cerevisiae* within calcium alginate beads was found to reduce phosphate removal capability, although *S. cerevisiae* still managed to achieve a significant percentage of phosphate removal. Immobilised *S. cerevisiae* cells were able to remove phosphates after being reused, albeit at a lower percentage. Dead *S. cerevisiae* cells were also found to be capable of removing phosphates. Our findings suggest that *S. cerevisiae* is the microorganism best suited for bioremediation, and that immobilisation can be a viable technique given the benefits it provides, such as allowing for cell reuse and protecting cells against hazardous conditions, as well as not disrupting the marine ecosystem by introducing *S. cerevisiae* cells directly into water.

Keywords Phosphates · Phosphate removal · Microorganisms · *S. cerevisiae* · Immobilisation

L. C. H. Ryan · T. W. L. Darrius (✉) · T. H. Jun
High School Section, Hwa Chong Institution, Singapore, Singapore
e-mail: hci.darriustan@gmail.com

L. C. H. Ryan
e-mail: 171263m@student.hci.edu.sg

T. H. Jun
e-mail: 1712711@student.hci.edu.sg

H. Guo et al. (eds.), *IRC-SET 2020*,
https://doi.org/10.1007/978-981-15-9472-4_60

1 Introduction

Eutrophication is a serious problem worldwide, threatening natural aquatic ecosystems, especially in suburban areas and developing countries [1]. Eutrophication induces hypoxia, depleting oxygen levels in water and causing marine life to die off, as well as reduces water quality [14]. Eutrophication is mainly caused by excess nutrient loading which promotes excessive algal growth [15]. This is especially so for phosphates, which are considered the limiting factor for the growth of algae [12]. Sources of excess nutrients include excessive use of fertilisers and pesticides in agriculture [11] and excessive soil erosion caused by unrestricted deforestation (DebRoy et al. [7].

Status quo methods to control eutrophication include chemical precipitation [10] and the use of powerful algaecides [6]. However, these methods have been found to be expensive, ineffective and to cause second-hand pollution. The use of bioremediation as an alternative has become increasingly prevalent as a cheaper and more effective alternative to control eutrophication. Bioremediation involves the use of phosphate removing organisms (PAO), a group of microorganisms that are capable of removing phosphates by accumulating phosphates within their cells as polyphosphates [13].

In particular, *Bacillus subtilis*, a gram-positive bacteria strain, has shown capability for phosphate removal. Anyako and Obot [2] found that *B. subtilis* was capable of removing up to 66% of phosphates present in iron ore, even considering that the iron ore had anti-microbial properties which caused the *B. subtilis* population to drop significantly over the course of the 7 week experiment. Similarly, *Pseudomonas putida*, a Gram-negative bacteria strain, has also demonstrated the ability to remove phosphates. Cai et al. [4] showed that *P. putida* was capable of quick and efficient phosphorus removal. They found that in one hour under anaerobic conditions, *P. putida* managed to remove 96% of phosphorus from activated sludge. The yeast *Saccharomyces cerevisiae* has also previously demonstrated the ability to remove phosphates. Breus et al. [3] reported that cells of *S. cerevisiae* removed 40% of phosphates from the media containing concentrations of phosphate and glucose, and this percentage increased up to 80% upon addition of 5 mM magnesium sulfate.

Immobilisation is a technique widely used in bioremediation, as it offers various advantages [16]. These include allowing for cell reuse, reducing the need for costly cell recovery and recycle, as well as providing resistance to extreme conditions such as extreme pH, temperature, presence of toxic chemicals and heavy metal ions, etc. Lau et al. [9] and Chevalier and De la Noue [5] reported that immobilisation does not inhibit the function of microorganisms in terms of bioremediation, but in fact catalyses it, due to numerous reasons including providing high flow rates, allowing high volumetric productivities, and providing suitable micro environmental conditions.

2 Objectives and Hypotheses

2.1 Objectives

Our objectives are to screen the effectiveness of different species of bacteria and yeast in the removal of phosphate, to investigate the effect of pH on the rate of removal of phosphates, investigate the possible synergistic effects of co-inoculating different combinations of bacteria on the amount of phosphates removed, to investigate the effectiveness of immobilised bacteria and yeast in phosphate removal, as well as to determine if living and non-living cells remove phosphates to the same extent.

2.2 Hypotheses

Our hypotheses are that different species of bacteria and yeast can remove phosphates to varying degrees, that bacteria show the highest rate of removal of phosphates at their optimal pH of growth, that co-inoculation of a mixture of bacteria demonstrates a synergistic effect in the removal of phosphates, higher than the summation of their individual phosphate removal effects, that immobilised bacteria and yeast are capable of removing phosphates from wastewater with efficiency similar to that of non-immobilised bacteria, and that living cells remove phosphate at a higher rate than non-living cells.

3 Methods and Materials

3.1 Experimental Variables

See Table 1.

Table 1 Experimental variables

Independent variables	Dependent variable	Controlled variables
Species of bacteria and yeast used	Final concentration of phosphates	Initial concentration of phosphates
pH value of phosphate medium		Absorbance of microorganism precultures at 600 nm
		Temperature of incubation

3.2 Procedure

3.2.1 Growth of Microorganism Precultures

Bacteria required (*Bacillus subtilis* ATCC19659 & *Pseudomonas putida* ATCC31800) were inoculated into 10 ml LB broth and grown overnight at 30 °C in a shaking incubator. The yeast (*Saccharomyces cerevisiae* Carolina) was inoculated into 10 ml potato dextrose broth and likewise grown overnight at 30 °C in a shaking incubator. The absorbance of each microorganism culture at 600 nm was then standardised at 0.800 using a UV–vis spectrophotometer.

3.2.2 Preparation of Phosphate Medium

Phosphate medium was prepared containing (per litre): 10 g glucose, 0.1 g KH_2PO_4, 0.5 g $(NH_4)_2SO_4$, 0.2 g NaCl, 0.1 g $MgSO_4.7H_2O$, 0.2 g KCl, 0.5 g yeast extract, 0.002 g $MnSO_4{\cdot}H_2O$ and 0.002 g $FeSO_4{\cdot}7H_2O$.

3.2.3 Phosphate Removal Test

In test setups, microorganism precultures were inoculated into phosphate medium at a final concentration of 20% (v/v). In the control setups, the same volumes of LB broth and potato dextrose broth were inoculated into phosphate medium. 3 replicates of each setup were prepared. Setups were then incubated at 30 °C for 1 day in a shaking incubator, and concentration of residual soluble phosphates were determined using the phosphate test kits (Hach) and a colorimeter. 0.1 ml of each setup mixture was added to 9.9 ml of deionized water to dilute phosphate concentration by a factor of 100. The contents of one sachet from the phosphate test kit (Hach) was then added to the diluted sample. The sample was then thoroughly shaken and left for 2 min, before concentration of phosphates was measured by a colourimeter (a part of the phosphate test kit).

3.2.4 Investigating Effects of pH on Removal of Phosphates

The pH value of the phosphate medium was then adjusted to 6 and 8 using the pH probe and sodium hydroxide/hydrochloric acid. Microorganism precultures were then added to phosphate medium of varying pH values as described above, with phosphate medium at pH 7 serving as control. 3 replicates of each setup were prepared. Then, the phosphate removal test as described above was carried out to determine the concentration of residual soluble phosphate.

3.2.5 Testing for Synergistic Effects in Phosphate Removal

In test setups, various combinations of microorganism precultures were inoculated into phosphate medium at a total final concentration of 20% (v/v). The following combinations were tested: equal volumes of *B. subtilis* and *P. putida* (10% each), equal volumes of *B. subtilis* + *S. cerevisiae* (10% each), equal volumes of *P. putida* + *S. cerevisiae* (10% each), and equal volumes of *B. subtilis* + *P. putida* + *S. cerevisiae* (6.67% each). In control setups, similar volumes of LB broth/potato dextrose broth were inoculated into phosphate medium with similar volumes as shown in the setups above. 5 replicates of each setup were prepared. The phosphate removal test as detailed earlier was again carried out to determine the concentration of residual soluble phosphate.

3.2.6 Removal of Phosphates by Cells Immobilised in Calcium Alginate Beads

5 ml of broth culture of *Saccharomyces cerevisiae* was mixed with 2% sodium alginate solution in equal volumes. The mixture was then added dropwise into 0.1 M calcium chloride solution to produce calcium alginate beads containing entrapped cells. In test setups, beads were added into 4 ml phosphate medium. In control setups, beads containing entrapped potato dextrose broth, non-immobilised *S. cerevisiae* broth culture and non-immobilised potato dextrose broth were added into similar volume of phosphate medium as in the test setups. 5 replicates of each setup were prepared. Phosphate removal test as described earlier was then carried out to determine the concentration of residual soluble phosphate.

3.2.7 Removal of Phosphates by Living and Non-living Cells

Half the volume of the *S. cerevisiae* preculture was removed and immersed into a boiling water bath for 10 min. Boiled and unboiled precultures of *S. cerevisiae* were inoculated separately into phosphate medium at a final concentration of 50% (v/v) for test setups. In control setups, potato dextrose broth was added to phosphate medium at a final concentration of 50% (v/v). 5 replicates of each setup were prepared. Absorbance of each setup at 600 nm was measured. Phosphate removal test as described earlier was then carried out to determine the concentration of residual soluble phosphates.

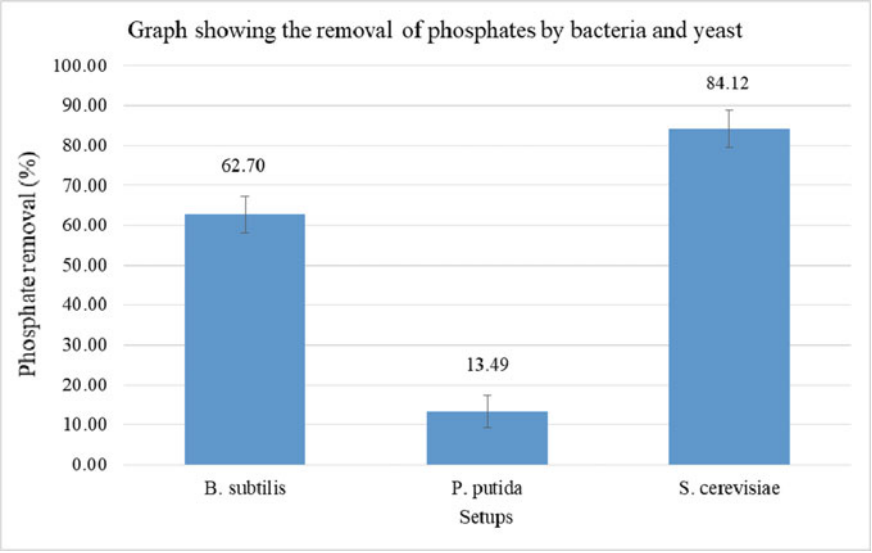

Fig. 1 Graph showing phosphate removal by various microorganisms

4 Results

4.1 Phosphate Removal Test

Figure 1 shows our results from the initial screening test for phosphate removal capability. Phosphate removal as a percentage was calculated by finding difference between phosphate concentration in the control setup (LB broth for bacteria, PDB broth for yeast) and test setup, divided by the phosphate concentration in the control setup.

B. subtilis and *P. putida* achieved 62.7% and 13.5% phosphate removal respectively in our initial screening tests. *S. cerevisiae* outperformed both the bacteria, achieving 84.1% phosphate removal. Thus, we decided to focus on *S. cerevisiae* in the tests for immobilisation and reusability, as well as the tests for phosphate removal by living and non-living cells.

4.2 Effect of pH on Phosphate Removal

Figure 2 and Table 2 illustrate the results of our phosphate removal tests carried out on the 3 microorganisms at various pH.

B. subtilis achieved optimal phosphate removal at pH 7, and was significantly affected by any change in pH. *P. putida* achieved optimal phosphate removal at pH 8,

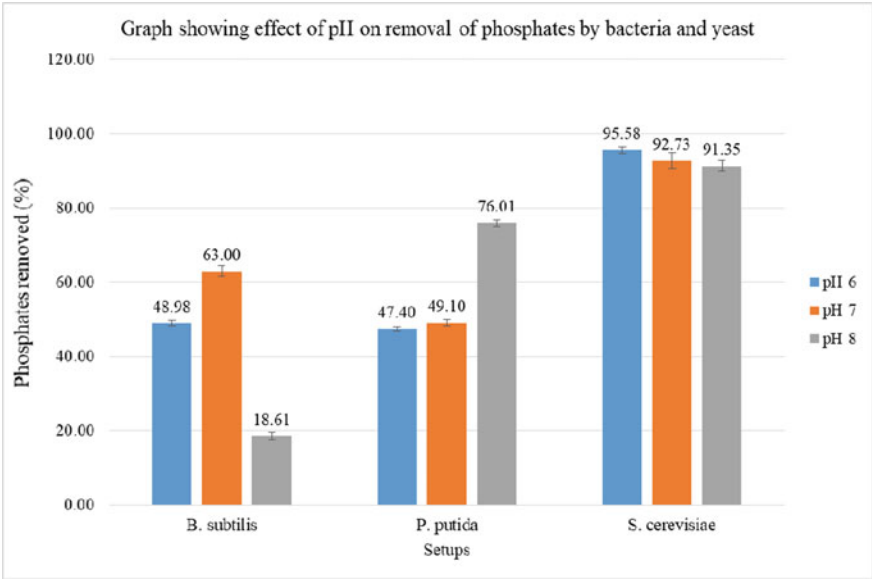

Fig. 2 Graph showing effect of pH on phosphate removal by various microorganisms

Table 2 Effect of pH on phosphate removal

Microorganism	Removal at pH 6/%	Removal at pH 7/%	Removal at pH 8/%
B. subtilis	47.6	63.0	18.6
P. putida	45.9	49.1	76.0
S. cerevisiae	95.6	92.7	91.7

and was similarly affected by a drop in pH. *S. cerevisiae* achieved optimal phosphate removal at pH 6, and was not significantly affected by an increase in pH, remaining consistent at around above 90% removal, indicating that *S. cerevisiae* is resistant to pH variations.

4.3 Synergistic Effects in Phosphate Removal

Table 3 demonstrates how we compared the different setups to show if there was a synergistic effect.

To determine if synergistic effect was present, we calculated the average removals of setups with individual microorganisms (expected removal), and compared it to the actual phosphate removal by the setup with a mixture. As can be seen from the table, the actual removal by the combined setup exceeded average removal by individual setups, showing a synergistic effect. As the Kruskal–Wallis p value was below 0.05

Table 3 Synergistic effects in phosphate removal

Combination	Removal by combined setup/%	Average removal of individual setups	Kruskal–Wallis p value
B. subtilis + *P. putida*	9.8	6.8	0.01729
B. subtilis + *S. cerevisiae*	87.9	52.3	0.00192
P. putida + *S. cerevisiae*	81.6	50.6	
B. subtilis + *P. putida* + *S. cerevisiae*	69.5	36.6	

for all mixtures, it indicates a significant difference in percentage phosphate removal, demonstrating a clear synergistic effect.

4.4 Phosphate Removal by Immobilised S. cerevisiae *Cells*

Figure 3 shows the phosphate removal by both immobilised and non-immobilised yeast cells.

Compared to the non-immobilised yeast cells, the immobilised yeast cells achieved 73.4% phosphate removal capability. The Mann–Whitney U test p value was 0.011, showing that there is a significant difference between percentage removal of immobilised and non-immobilised yeast. However, most of the phosphate removal

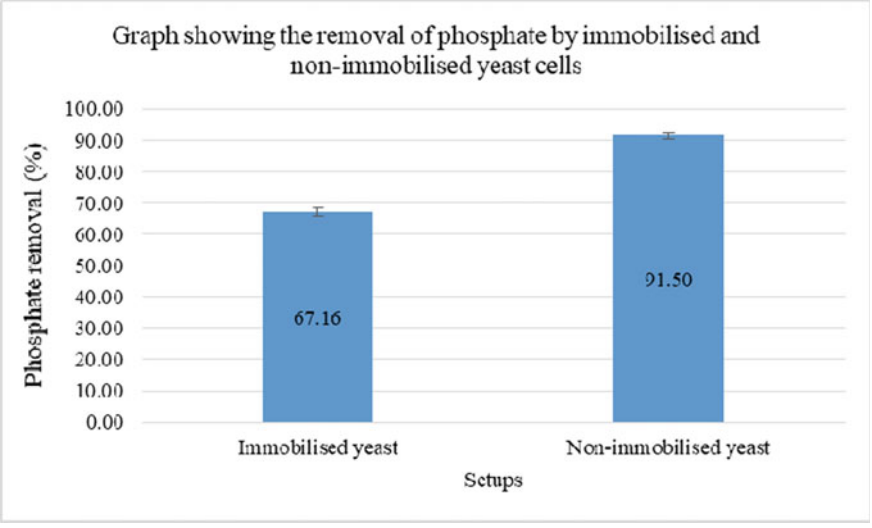

Fig. 3 Graph showing effect of immobilisation on phosphate removal by *S. cerevisiae*

capability is preserved when *S. cerevisiae* is immobilised, and immobilisation is still a viable technique for phosphate removal.

4.5 Phosphate Removal by Living/Non-living Cells

Phosphate removal values were divided by absorbance at 600 nm to account for cell division in the unboiled culture, as shown in Table 4. The adjusted phosphate removal values are also shown in Fig. 4.

After adjusting for absorbance, it can be seen that both the boiled and unboiled cultures achieved relatively similar phosphate removal, suggesting that even boiled

Table 4 Removal of phosphates by boiled and unboiled cultures, adjusted for absorbance

	Boiled culture	Unboiled culture
Average phosphate removal (%)	30.2	56.8
Average absorbance at 600 nm	0.942	1.538
Adjusted phosphate removal (%)	32.1	36.9

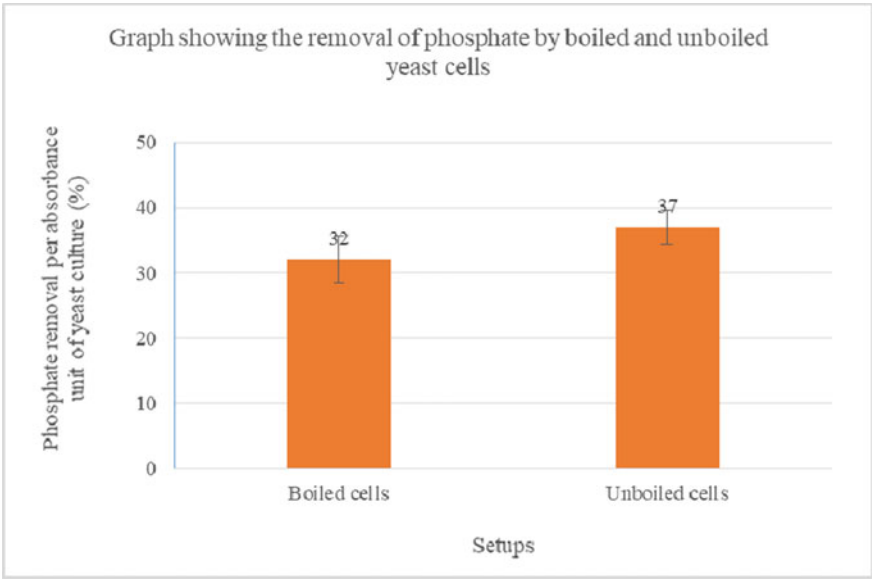

Fig. 4 Graph showing phosphate removal by boiled and unboiled *S. cerevisiae* cells

S. cerevisiae was capable of significant phosphate removal. The Mann–Whitney U-test p value was 0.4009, demonstrating that there was no significant difference in phosphate removal capability of living and non-living *S. cerevisiae* cells.

4.6 Reusability of Immobilised S. Cerevisiae

Figure 5 shows the results of phosphate removal by reused immobilised yeast cells and fresh immobilised yeast cells.

Compared to fresh immobilised yeast, the reused immobilised yeast achieved 80.4% phosphate removal capability. The Mann–Whitney U test *p* value was 0.209, showing that there was no significant difference in percentage phosphate removal of fresh and reused immobilised yeast cells. However, given that phosphate removal capability only decreased by about 20% with each reuse of the immobilised yeast cells, immobilisation of yeast cells could allow reuse for a few cycles, showing the potential benefit of immobilisation.

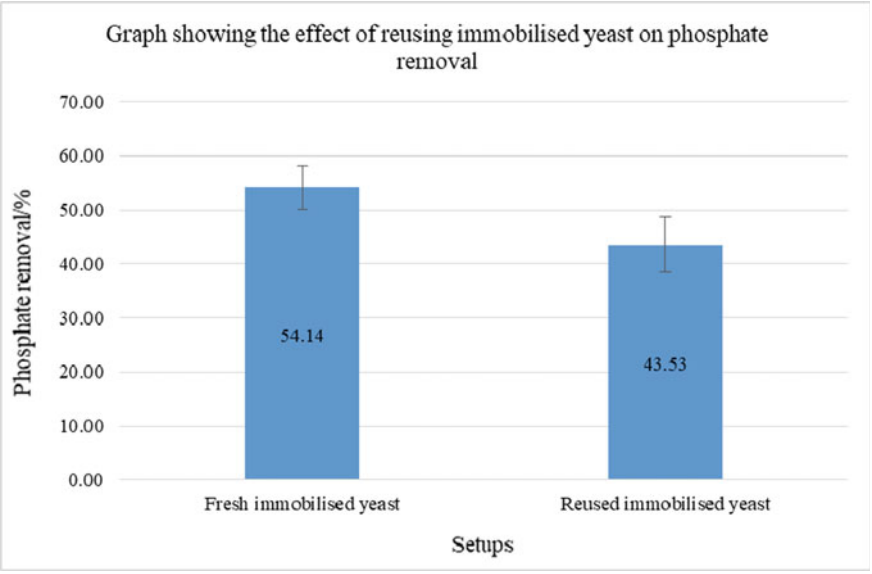

Fig. 5 Graph showing phosphate removal by freshly immobilised yeast cells and reused immobilised yeast cells

5 Conclusion and Discussion

Our project discovered that *S. cerevisiae* was the most efficient microorganism for phosphate removal, and that it also demonstrated a resistance to pH changes. We also found that immobilisation of *S. cerevisiae*, although impacting phosphate removal capability, remained a viable option for bioremediation, and that dead *S. cerevisiae* cells were still capable of phosphate removal. Lastly, we found that *S. cerevisiae* demonstrated a synergistic effect in phosphate removal when co-inoculated with *B. subtilis* and/or *P. putida.*

Other researchers have found that phosphate transport and signaling in *S. cerevisiae*, specifically by the PHO84 and PHO87 transporters, does not require ATP or metabolism to be activated, only a presence of glucose [8]. This would allow dead *S. cerevisiae* cells to remove phosphates in the presence of glucose and phosphates in phosphate medium by transporting them into the cell to be stored as polyphosphates, which supports our findings.

In general, although this was not supported by our findings, other researchers have found that immobilisation could in fact promote the removal of phosphates. Nakamura et al. (1995) found that bacterium strain *Microlunatus phosphovorus* NM-1, when immobilised in polyacrylamide gel, rapidly took up phosphates present in the medium under aerobic conditions, with a phosphate take-up rate of about 10–20 mg-P/g-cell·h. Similarly, Swe Cheng et al. (2017) found that *Scenedesmus bijugatus* when immobilised still achieved a rapid phosphate removal rate of 0.25 mg L^{-1} d^{-1}.

Even though immobilisation was shown to negatively impact phosphate removal, the effect of immobilisation on phosphate removal was shown to not be very severe. Immobilisation confers numerous benefits onto the bioremediation process, such as protecting microorganisms from toxic pollutants and heavy metal ions, as well as granting increased resistance to temperature and pH changes. It also improves efficacy of bioremediation by allowing for cell reuse in multiple batches, and also ensures that microorganisms do not contaminate the final treated product. As such, the tradeoffs of bioremediation indicated by our project appear to be worth it in real-life application of bioremediation.

Some limitations of our research include that the cell counts of bacteria/yeast may differ between setups and experiments due to differing growth rates, which would result in varying degrees of phosphate removal both within experiments and between experiments. Immobilised and non-immobilised yeast cells may also have reproduced at different rates, affecting final cell count which could not be accounted for using absorbance (unlike our experiment involving boiled and unboiled cells).

For further work, more investigation into the optimal conditions (temperature and concentration of nutrients) for *S. cerevisiae* to remove phosphates is needed, along with investigation into other potential synergistic effects in phosphate removal following co-immobilisation of *S. cerevisiae* with other microorganisms.

References

1. Anderson, D.M., Gilbert, P.M., & Burkholder, J.M. (2002). Harmful algal blooms and eutrophication: nutrient sources, composition, and consequences. Estuaries and Coasts, 25(4), 704–726. Retrieved March 11, 2019 from https://link.springer.com/article/10.1007/BF02804901
2. Anyako, C.N. & Obot, O.W. (2010) Phosphorus removal capability of Aspergillus terreus and *Bacillus subtilis* from Nigeria's Agbaja iron ore. Journal of Minerals & Materials Characterisation and Engineering, 9(12), 1131–1138. Retrieved July 7, 2019 from https://www.researchgate.net/publication/277926405_Phosphorus_Removal_Capability_of_Aspergillus_Terreus_and_Bacillus_Subtilis_from_Nigeria's_Agbaja_Iron_Ore
3. Breus, N.A., Ryazanova, L.P., Dmitriev, V.V., Kulakovskaya, T.V., & Kulaev, I.S. (2012). Accumulation of phosphate and polyphosphate by Cryptococcus humicola and *Saccharomyces cerevisiae* in the absence of nitrogen. FEMS Yeast Research, 12(6), 617–624. Retrieved March 11, 2019 from https://www.ncbi.nlm.nih.gov/pubmed/22591314
4. Cai, T.M., Guan, L.B., Chen, L.W., Cai, S., Li, X.D., Cui, Z.L., & Li, S.P. (2007). Enhanced biological phosphorus removal with *Pseudomonas putida* GM6 from activated sludge. Pedosphere, 17(5), 624–629. Retrieved March 11, 2019 from https://www.sciencedirect.com/science/article/abs/pii/S1002016007600745
5. Chevalier, P. & De la Noue, J. (1985). Wastewater nutrient removal with microalgae immobilised in carrageenan. Journal of Enzyme of Microbial Technology, 7(12), 621–624. Retrieved March 11, 2019 from https://www.sciencedirect.com/science/article/pii/0141022985900032
6. Chislock, M. F., Doster, E., Zitomer, R. A. & Wilson, A. E. (2013). Eutrophication: Causes, Consequences, and Controls in Aquatic Ecosystems. Nature Education Knowledge 4(4). Retrieved March 11, 2019 from: https://www.nature.com/scitable/knowledge/library/eutrophication-causes-consequences-and-controls-in-aquatic-102364466
7. DebRoy, S., Das, S., Ghosh, S., Banerjee, S., Chatterjee, D., Bhattacharjee, A., Mukherjee, I., & RayChaudhuri, S. (2012). Isolation of nitrate and phosphate removing bacteria from various environmental sites. Online Journal of Biological Sciences, 12(2), 62–71. Retrieved March 11, 2019 from https://thescipub.com/pdf/10.3844/ojbsci.2012.62.71
8. Giots, F., Donaton, M.C.V., Thevelein, J.M. (2003, February 6) Inorganic phosphate is sensed by specific phosphate carriers and acts in concert with glucose as a nutrient signal for activation of the protein kinase A pathway in the yeast *Saccharomyces cerevisiae*. Molecular Microbiology, Volume 47, Issue 4, Pages 1163–1181. Retrieved July 1 2019 from https://onlinelibrary.wiley.com/doi/full//10.1046/j.1365-2958.2003.03365.x
9. Lau, P.S., Tamb, N.F.Y., & Wong, Y.S. (1998). Effect of carrageenan immobilisation on the physiological activities of Chlorella vulgaris. Journal of Bioresource Technology, 63(2), 115–121. Retrieved March 11, 2019 from https://www.sciencedirect.com/science/article/pii/S0960852497001119
10. Lenntech Water Solutions (n.d.). Phosphorus removal from wastewater. Retrieved March 11, 2019 from https://www.lenntech.com/phosphorous-removal.htm
11. Oram, B. (2018). Phosphates in the environment. Retrieved March 11, 2019 from https://www.water-research.net/index.php/phosphates
12. Scannone F. (2016, 3 November). What is eutrophication? Causes, effects and control. Retrieved June 23, 2019 from https://www.eniscuola.net/en/2016/11/03/what-is-eutrophication-causes-effects-and-control/
13. Seviour, R.J., Mino, T., & Onuki, M. (2003). The microbiology of biological phosphorus removal in activated sludge systems. FEMS Microbiology Reviews, 27(1), 99–127. Retrieved March 11, 2019 from https://www.ncbi.nlm.nih.gov/pubmed/12697344
14. Tammi, J., Lappalainen, A., Mannio, J., Rask, M., & Vuorenmma, J. (2001). Effects of eutrophication on fish and fisheries in Finnish lakes: a survey based on random sampling. Fisheries Management and Ecology, 6(3), 173–186. Retrieved March 11, 2019 from https://onlinelibrary.wiley.com/doi/full/https://onlinelibrary.wiley.com/doi/full/10.1046/j.1365-2400.1999.00152.x

15. Yamashita, T. & Yamamoto-Ikemoto, R. (2014). Nitrogen and phosphorus removal from wastewater treatment plant effluent via bacterial sulfate reduction in an anoxic bioreactor packed with wood and iron. International Journal of Environmental Research and Public Health, 11(9), 9835–9853. Retrieved March 11, 2019 from https://www.ncbi.nlm.nih.gov/pmc/articles/PMC4199053/
16. Zeynab B., Mehdi H. & Simone C. (2015, July 31) Immobilisation of Microbes for Bioremediation of Crude Oil Polluted Environments: A Mini Review. Open Microbiology Journal, Volume 9, Pages 48–54. Retrieved June 30, 2019 from https://doi.org/10.2174/1874285801509010048

Security Development with an Industrial Device for SCADA System

Clifton Perth Link Choo, Wang Ling Goh, and Huaqun Guo

Abstract It is not a normal occurrence that Supervisory Control and Data Acquisition (SCADA) system encountered cyberattacks. However, there has been an increase in the number of security threats as the world is progressing into Industry 4.0. As such, cyber security becomes more prominent and it is paramount to safeguard valuable information from cybercriminals as well as preventing disruptive events that can lead to devastating outcomes. This paper addresses the integration of an industrial Single Board Computer (SBC) with firewall implemented, enhancing the security of SCADA systems overall. The paper presents the details to design and implement using various software and methods to overcome the challenges/issues during the implementation. A series of performance tests have been conducted, and the results obtained have shown the good functionality and reliability of the installed firewall with SBC.

Keywords SCADA systems · Single board computer · Firewall · Security

1 Introduction

1.1 Background

The adoption of Supervisory Control and Data Acquisition (SCADA) systems is one of the several types of industrial control applications that is used to manage industrial

C. P. L. Choo (✉) · W. L. Goh
School of Electrical & Electronic Engineering, Nanyang Technological University, Singapore, Singapore
e-mail: clif0003@e.ntu.edu.sg

W. L. Goh
e-mail: ewlgoh@ntu.edu.sg

H. Guo
Cybersecurity Department, Institute for Infocomm Research, A*STAR Entities, Singapore, Singapore
e-mail: guohq@i2r.a-star.edu.sg

H. Guo et al. (eds.), *IRC-SET 2020*,
https://doi.org/10.1007/978-981-15-9472-4_61

operations. As technology advances, new capabilities are added to these automated systems which can constitute to a significant part of the current safety-critical infrastructures [1]. SCADA systems are usually operated in distribution systems such as water distribution networks, electrical utility transmission systems, and public transportation facilities [2]. They are constructed to retrieve and process field information through the integration of data transmission system as well as a human machine interface software to create a centralised monitoring system [2]. This allows the user to oversee and operate the entire system from a central location in real time.

The automated systems discussed above are generally insecure as they are primarily designed for performance, reliability, and safety. The need for cyber security measures becomes even more prominent when there is an increased demand in the market for efficient large-scale SCADA systems. In addition, SCADA security is essential to prevent any forms of attacks and threats in the present digital world. One example is the malicious computer worm known as Stuxnet Virus which was discovered in 2010 [3]. The virus particularly targets the programmable logic controllers that regulated both the machinery and technical mechanisms of the Iranian nuclear centrifuges. This resulted in the malfunction of the SCADA systems, causing a huge investment of time and money to rectify the problem. Similarly, the WannaCry ransomware attacked the United Kingdom's National Health Service in 2017 [4]. This hindered medical procedures as medical workers were unable to access critical patient details. Given the success of both viruses penetrating the SCADA environment, it is important to acknowledge the vulnerabilities of the current security system and that the traditional security measures are inadequate in providing a complete protection of the infrastructures.

1.2 Work Scope

The objective of this work is to implement a firewall between devices operated in SCADA systems using an industrial grade Single Board Computer (SBC), to provide attack detection and prevention to the security platform. Existing firewall security features are executed on the Linux operating system computer before migrating to the industrial grade SBC. A series of quantitative tests will then be conducted to determine the performance and functionality of the firewall. This proposed solution enables the firewall to manage the network traffic while detecting and intercepting any unwanted data packets. Furthermore, the SBC comes with an inbuilt bypass functionality that inhibits the interruption of data traffic flow in the event of an inline network device failure. As such, the proposed systematic approach can help to protect against computer malwares and viruses, to ensure a secure and sustainable network in SCADA systems.

The remainder of this paper is organized as follows. Section 2 provides the literature review on the related technologies. Section 3 describes the details of our design and implementation, while our experimental tests and results are presented in Sect. 4. Finally, Sect. 5 outlines our conclusions and future work.

2 Literature Review

2.1 Firewall Technology

A firewall is hardware, software, or a combination of both that monitors the transmission of packets of digital information that attempts to pass through the perimeter or a network. Based on a predefined set of security rules called firewall policies, the firewall inspects each packet and determines whether it should be allowed or blocked upon arriving at the firewall. This helps to block unwanted traffic from entering or leaving the network and this is crucial as it can ward off harmful attacks that cause unavailability of an operation that hinders network performance. The access control lists that are capable of accepting or dropping network packets can be implemented to enhance the security features of the system. This is usually done by checking the port numbers at the specified source and destination. A notable difference between a software firewall and a hardware firewall is the entity they protect. Software firewall protects endpoint systems whereas hardware firewall protects the whole network infrastructure. Also, hardware firewalls are more costly and complicated to configure as compared to their peers. They can then be further categorised into several different types like static packet filtering, stateful packet inspection, application gateways, and circuit gateways.

In a SCADA network, the number of rules required by an organisation tend to be large and this can affect the performance of the firewall. In other words, the factor of firewall rule matching speed plays an important role in optimal operation network performance [5, 6]. A study shows that Hash Table Search Algorithm has the smallest execution time and becomes faster when the number of rules increases exponentially as compared to its peers like the Binary Search algorithm and the Linear Search Algorithm [5, 6]. Hence, the optimum firewall rules to be engaged must be carefully considered.

SCADAWall will be introduced in this work as the firewall software to filter industrial control commands that flows within the network. Its functionality includes the use of a comprehensive packet inspection (CPI) feature that inspects the entire protocol payload and a proprietary industrial protocols extension algorithm (PIPEA) that enables users to customise their CPI configurations for extended capability of SCADAWall [7]. Besides that, it provides out-of-sequence command detection algorithm that detects and blocks irregular behaviours in the SCADA system, for instance, a different order of commands that does not follow the correct sequence [7].

2.2 Modbus

Modbus protocol is a request-response protocol that maintains client/server communications between devices connected on different types of networks [8]. A master-slave relationship is usually used to depict the communication between the SCADA

system (Master) and the PLC device (Slave). To initiate an interaction, the master will send a query and wait for a response from the slave. The content of these queries and responses as well as the network layers are determined by the different layers of protocol.

To understand Modbus protocol, the protocol framework and its functionality will be explained in detail. In general, the Modbus frame shown in Fig. 1 consists of the Application Data Unit (ADU) and the Protocol Data Unit (PDU) [9]. The Modbus PDU is defined as a function code that comprises the size and value of the function code, followed by an associated set of data. When a message is sent to the recipient, a function code for the action to perform is allocated to the slave device. This code can be in the range of 1–255 whereby each unique function code has a specific behaviour except for 128–252 which are reserved for exception responses. The Modbus ADU initiates a Modbus transaction and helps establish the format of request initiated by client. It consists of additional addresses such as the discrete and register addresses and the capacity of handled items for server to operate. The error check component exists to alert any error in a given action.

Shown in Fig. 2 is the typical Modbus/TCP payload on the SCADA system where it incorporates a seven bytes Modbus Protocol Header and Modbus payload. The transaction identifier distinguishes each transaction where each identifier is designated for the same request and reply. As mentioned above, the function code delivers instructions to the slave to execute a particular action. It can also be an indication of successful execution when used in a reply. In SCADA system, the function code together with the data field of Modbus message are important to get inspected. Significant attacks such as intruding the SCADA system by manipulating some Modbus commands can cause imperative outcomes. Hence, the Modbus message must be

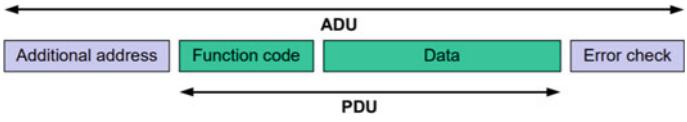

Fig. 1 Modbus frame

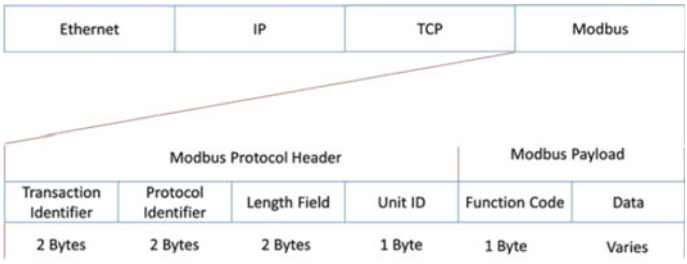

Fig. 2 Modbus/TCP message

carefully monitored using a firewall to prevent attackers for making full use of this vulnerability.

2.3 *Iptables*

Iptables is an open-source firewall that has been extensively used for protecting safety-critical systems by providing packet filtering capabilities [10]. This user-space module operates at network and transport layers, and permits users to define firewall rules, conduct network address translation, and packet mangling. As both IP and TCP have different header lengths, a feature called u32 match was introduced to resolve this issue.

The u32 match extracts four bytes (32 bits) of the packet and compares with the values of interest. For those with less than 32 bits, masking and shifting will be applied to the indicated value. The problem of the variable header-length was overcome by calculating the header length of header-length field. A summarised series of steps using u32 match [10] will be described below:

1. To obtain header length of IP field in bytes, extract it from the header length field.
2. Value obtained will be used to return to the beginning of the TCP header.
3. Repeat step (1) on TCP header length field.
4. Value obtained will be used to return to the beginning of the SCADA message.
5. Indicate an offset on beginning of SCADA message and match against the desired value.

For IP header (see Fig. 3), the header length field can be extracted from bits 4–7 of the first byte by using the command "0≫22&0x3C". The number 0 in the command indicates the location of the header length and number 22 specifies the

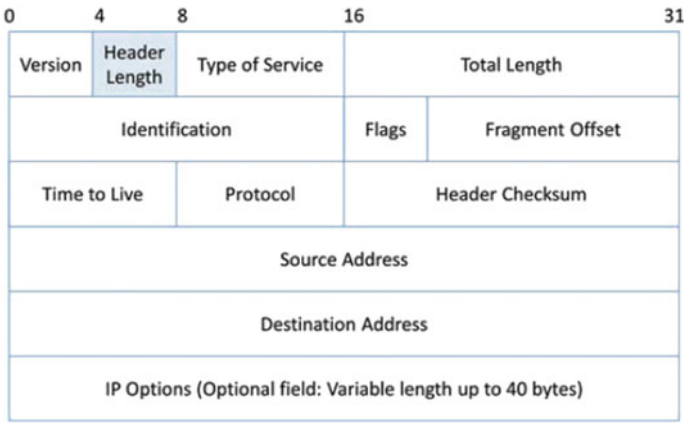

Fig. 3 IP header

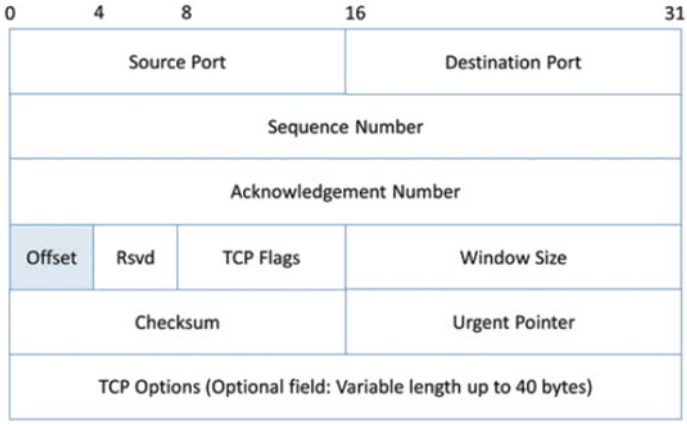

Fig. 4 TCP header

number of times the bit must shift to reach the last bit. The hexadecimal "0x3C" represents the header length mask. To allow the operation of jumping to the beginning of the message, the "@" sign is added to the back of the command, forming "0≫22&0x3C@".

Similarly, this can be done on the TCP header as shown in Fig. 4. For TCP, it is easier to obtain the length of the TCP header field because of the offset field. A simple command "12≫26&0x3C" will then complete the operation and proceed to the checking of SCADA message.

Configuring the firewall rules in iptables is essential to manage the traffic flow in and out of the system. Before constructing personalised rules sets, the type of rules must be addressed. There are three distinct rule sets: Input, Output, and Forward [11]. The Input rule set defines the acceptable incoming traffic and state the data to be explicitly blocked. The Output rule set filters the outgoing traffic and the Forward rule set establishes various configuration settings such as port forwarding where it reroutes the incoming packets to another intended port number. Without indicating any of the three rule sets above, the default configuration rule set will first be applied which basically allows all traffic coming in and out of the network. The default rule set [11] is shown below:

```
:OUTPUT ACCEPT [0:0]
:FORWARD ACCEPT [0:0]
:INPUT ACCEPT [0:0]
-A INPUT -I lo -j ACCEPT
-A INPUT -p icmp -j ACCEPT
-A INPUT -m state –state NEW -m tcp -p tcp –dport 22 -j ACCEPT
-A INPUT -m state –state ESTABLISHED, RELATED -j ACCEPT
-A INPUT -j REJECT –reject-with icmp-host-prohibited
-A FORWARD -j REJECT –reject-with icmp-host-prohibited
```

COMMIT

The components of the syntax commands above will be outlined in bullet forms to explain the significance.

- "-A" syntax appends to the existing rule set
- "-m state –state NEW" pairs with connection state of NEW
- "-m tcp -p tcp" matches the protocol type of TCP
- "-j ACCEPT" or "-j REJECT" gives the decision of accepting or dropping if all items match.

To sum it up, iptables with feature of u32 match is a powerful security tool that will be use on SCADA system to protect against malicious threats conducted by attackers. Furthermore, firewall rule sets introduced in iptables will only allow desired traffic and block unwanted packets.

3 Design and Implementation

3.1 Single Board Computer

An industrial level Single Board Computer (SBC) with functional computer components such as microprocessor and input/output that acts as a small computer device capable of performing multiple computing tasks has been implemented on a SCADA system. The SBC supports Linux based operating system (OS) and has built in function of advanced Local Area Network (LAN) bypass. The bypass functionality guarantees connectivity between two devices in the absence of power or when the SBC is under non-operational state. There are four connectivity modes (see Fig. 5) in the system, and the bypass mode is supported by advanced LAN bypass.

Connect mode—This mode connects the bypass system to the host systems. For instance, device A and device B are connected to their respective network ports of the Network Interface Cards (NIC).

Disconnect mode—This mode disconnects the bypass system such that both devices A and B are isolated from each other and from their respective NICs.

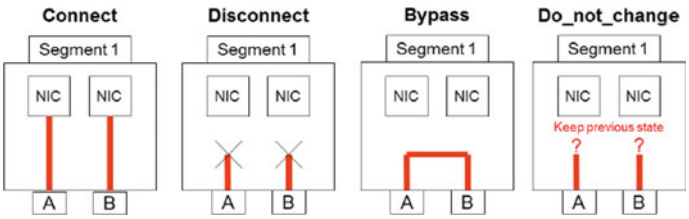

Fig. 5 Bypass action and related connectivity codes

Bypass mode—In this mode, both devices A and B are connected to each other while being isolated from the SBC. Network traffic between both ports maintain flowing in the network but bypass the SBC.

Do_not_change mode—This action states that the current state of the SBC will not be changed when a specific event takes place. As such, network connectivity remains as it is.

Given the information above, the SBC is connected in between the SCADA server and client and has two main operational modes, i.e., Connect mode and Bypass mode. Under normal circumstances, the Connect mode will be active and the Bypass mode will only be activated when there is a power failure.

3.2 Installation and Configuration of Operating System

Due to the lack of Operating System in the SBC, the only way to install the OS is to aid in the creation of a bootable stick. The solution is to use Rufus which is an application to format USB flash drives and insert the ubuntu ISO image into the thumb drive. Thus, a bootable stick created by Rufus was used to install the Linux OS. To enable the installation of the OS, hold the 'delete' button before powering on of the SBC to enter the BIOS (basic input/output system) of the SBC. In the BIOS configuration, the primary boot priority was changed to allow the USB stick to be at the first position. This will ensure the boot up of the program in the USB to run instead of others.

1. *Booting Issues*

An error message "Error: no suitable video mode found. Booting in blind mode." was displayed after the booting of the SBC. To solve this problem, the settings at the grub.cfg file had to be modified and the codes of the text file of Isolinux are represented below to allow smooth running of installation.

```
Original as below
menuentry "Install Ubuntu Server" {

    set gfxpayload=keep
    linux/install/vmlinuz file=/cdrom/preseed/ubuntu-server.seed quiet---
    initrd/install/initrd.gz

}
is updated with the following:
menuentry "Install Ubuntu Server" {

    set gfxpayload = keep
    linux/install/vmlinuz  file=/cdrom/preseed/ubuntu-server.seed  vga=normal
    console=tty0 console=ttyS0, 115200n8---
    initrd/install/initrd.gz
```

}

2. *Internet Connectivity Issues*

Another issue faced is that there is no connection to the Internet as the Ethernet had not been configured during the initialisation of configurating the OS. In the case of SBC, Dynamic Host Configuration Protocol (DHCP) instead of static IP was utilised to obtain Internet connection.

Depending on which management port (mgt) is connected to the router, the commands entered in the Linux shell will vary. "ifconfig" command checks for ongoing connections to the SBC. This will verify the availability of Internet connection should the Ethernet routing procedure operated.

To bring up connection of mgt1 port: Type "sudo ifconfig enp2s0 up". The light on the SBC will indicate that it has been successfully connected. To bring down connection of mgt1 port: Type "sudo ifconfig enp2s0 down". Lights will be turned off.

To bring up connection of mgt2 port: Type "sudo ifconfig enp3s0 up". You will see lights to show that it is connected. To bring down connection of mgt2 port: Type "sudo ifconfig enp3s0 down". Lights will be turned off.

Upon bringing up the connection of the mgt1/mgt2 port, the next step is to enter the command "sudo nano -w/etc./network/interfaces". We then replace "eth0" with "enp2s0" after entering the file as shown below. Note that iface is an internal variable for ifup and ifdown.

```
{
auto eth0

    allow-hotplug eth0
    iface eth0 inet dhcp

}
```

3.3 Migration of Firewall

SCADAWall is configured to be a layer 2 transparent firewall dedicated to increase the overall security of the system. It will be transferred to the SBC using the Linux terminal. Afterwards, users operate the SCADAWall by applying "$ sudo python3 scadawall.py" command. SCADAWall provides various settings to configure firewall rules and sequence rules, retrieve log information, define proprietary protocols, and upload firewall settings via the graphical interface of the SCADAWall configurator. Ultimately, the SCADAWall differentiates the configurated packets from normal network traffic and applies decryption technique where it updates the firewall rules automatically. An alert or message will be sent to the administrator's computer if the SCADAWall detects a malicious command.

The network bridge had to be established before the downloading of SCADAWall program. This is done by typing the following commands in the terminal:

```
$ sudo apt-get update
$ sudo apt-get install bridge-utils
$ sudo brctl addbr br0 # note that this and below settings will be reset after reboot
$ sudo brctl addif br0 eth0 # change to the name of your network interface accordingly
$ sudo brctl addif br0 eth1 # change to the name of your network interface accordingly
$ sudo ifconfig br0 up
```

4 Results and Evaluation

4.1 Bypass Functionality Check

The bypass function of the SBC should be activated when there is power loss, allowing packets to flow within the network. Ping, a network administrator utility to test for reachability of host or IP network, will be used to measure connectivity of the targeted networks. It operates by sending Internet Control Message Protocol (ICMP) echo request packets and waits for the host to reply. A statistical summary of results such as round-trip times, errors, and packet loss will be displayed on the command prompt terminal as shown in the figures below.

To show that the bypass mode of SBC is working, a ping request was made and sent to the server. Figure 6 shows the results whereby the client has successfully reached the server without any packet loss.

An additional test was carried out to determine that the client was unsuccessful in reaching the server when the connect mode was activated. Figure 7 validated that the connect mode of SBC is working.

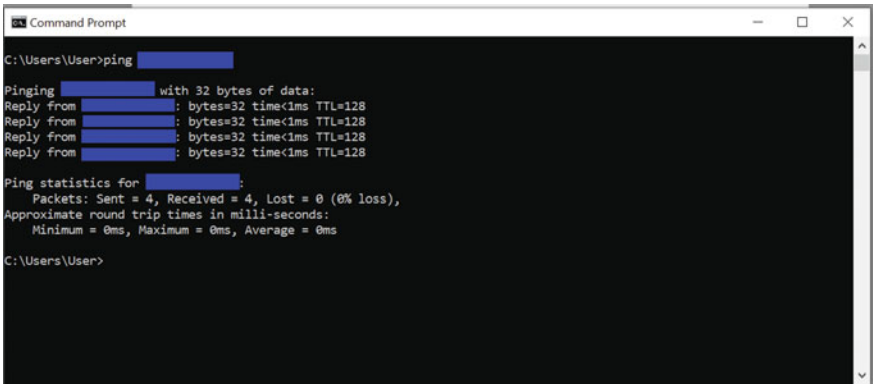

Fig. 6 Ping test on bypass mode

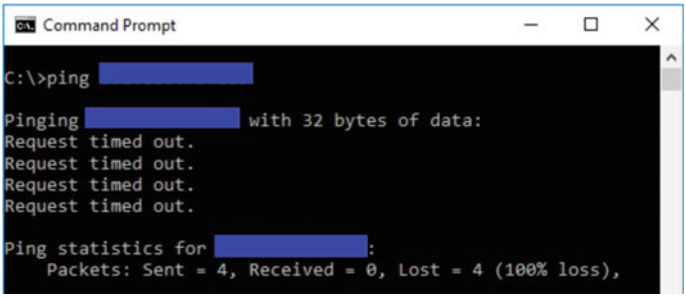

Fig. 7 Ping test on connect mode

4.2 Firewall Performance

1. *System Testing Results*

Constructing proper test environment as shown in Fig. 8 will help to justify that an accurate and reasonable outcome is attained. Table 1 shows the relevant tests conducted on the firewall to validate its functionality. These tests include Comprehensive Packet Inspection assessment, Out-of-sequence command detection, Proprietary industrial protocol extension, and Tunnelling communication technology evaluation.

2. *Latency*

To determine the speed and accuracy of the firewall, time stamping using Wireshark will be performed with the same system setup shown (Fig. 8). Two Wireshark terminals will be operated simultaneously to detect the two network interfaces that is connected to the SCADA system. The time difference observed between the two network interfaces are tabulated in Table 2.

It is important to consider both the number of inspected payload fields and the number of firewall rules as variables in this assessment to measure the CPI latency so that it can yield a fair and accurate outcome. Also, all conditions of the experiment are the same when measuring the latency of both the "No Firewall Rules" and "100 Non-CPI Rules" categories to provide unbiased comparisons. These firewall rules consist of 100 non-CPI rules and CPI rules to inspect various payload fields of

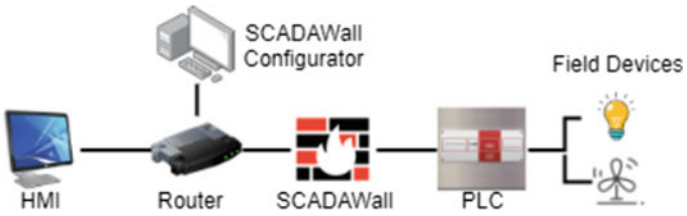

Fig. 8 System setup for testing

Table 1 Results of firewall function tests

Index	System testing analysis		
	feature to be tested	Testing details	Results
1	Comprehensive packet inspection	Set firewall rules to block control commands by the prevention of allocating value "1" to specific address	SCADAWall can block such commands and sends an alert to the log configurator
2	Out-of-sequence command detection	Set sequential firewall rules that only allows specific sequence of control commands (For example, device 2 can only be activated after device 1 has been switched on). Injection of out-of-sequence commands using Metasploit module will be applied for testing purposes	SCADAWall can block out-of-sequence commands
3	Proprietary industrial protocol extension	Using the interface to setup user-defined protocol and apply comprehensive packet inspection	SCADAWall can extend its ability to check the new proprietary protocols
4	Tunnelling communication technology	Sniffing and checking the communication between the SCADAWall and the SCADAWall Configurator. Also, it is to check on whether SCADAWall is in transparent mode	SCADAWall is in transparent mode (configured as a network bridge without IP address). All traffic is encrypted

Table 2 Latency of firewall tests

Without CPI rules	No firewall rules (μs)		100 Non-CPI rules (μs)	
Latency for command	10.10		10.17	
Latency for response	11.07		11.06	
With 100 CPI rules	4 fields (μs)	6 fields (μs)	8 fields (μs)	10 fields (μs)
Latency for command	25.20	20.49	24.51	26.71
Latency for response	13.07	12.82	13.57	13.78
With 10 checked fields	25 rules (μs)	50 rules (μs)	75 rules (μs)	100 rules (μs)
Latency for command	12.81	18.14	20.50	26.71
Latency for response	12.32	12.99	12.29	13.78

control command. For each configuration, ten thousand commands and responses are transmitted by the devices to produce the best results.

The latency results in Table 2 show that the additional latency with CPI rules are in the range of less than 17 μs in our experiments.

From the bypass function test, various firewall functions tests and latency tests, the results obtained have shown the good functionality and reliability of the installed firewall with SBC.

5 Conclusion and Future Works

The current SBC model has proved its usefulness in the security development for SCADA system. Not only it supports the integration of firewall, but also its bypass functionality has demonstrated that network traffic between two end-users hosts continue to flow in the event of a power failure. The firewall performance tests have been conducted to review its feasibility and functionality. To sum it up, the implementation of the SBC with firewall and bypass functions to the SCADA system can be considered a success. Further improvements and works on increasing firewall complexity can be carried out to achieve higher degree of security level. One possible suggestion is to introduce an intrusion detection system to the SCADA system. It is a networking structure that scans and monitors network traffic for unusual behaviours and reports them via a management system. When such activity is discovered, an alarm sound will be generated to indicate that a cyberattack may have occurred. This alerts the administrators to investigate the network quickly to devise an effective solution to terminate the attack. As compared to current circumstances where network administrators have to regularly inspect the log file for unusual activities, the proposed solution will be more efficient.

References

1. V. L. Do, L. Fillatre, I. Nikiforov and P. Willett, "Security of SCADA systems against cyber–physical attacks," IEEE Aerospace and Electronic Systems Magazine, vol. 32, no. 5, pp. 28–45, May 2017.
2. K. Stouffer, J. Falco, and K. Kent, "Guide to Supervisory Control and Data Acquisition (SCADA) and Industrial Control Systems Security". Retrieved on September 15, 2019 from https://www.dhs.gov/sites/default/files/publications/csd-nist-guidetosupervisoryanddataccquisition-scadaandindustrialcontrolsystemssecurity-2007.pdf.
3. S. Karnouskos, "Stuxnet worm impact on industrial cyber-physical system security", IECON 2011 – 37th Annual Conference of the IEEE Industrial Electronics Society, Melbourne, VIC, 2011, pp. 4490–4494.
4. C. Graham, "NHS cyber attack: Everything you need to know about 'biggest ransomware' offensive in history". The Telegraph. Retrieved on September 15, 2019 from https://www.telegraph.co.uk/news/2017/05/13/nhs-cyber-attack-everything-need-know-biggest-ransomware-offensive/.
5. Pabilona Jime Lee, Huaqun Guo, and Bharadwaj Veeravalli. "Enhancing CII Firewall Performance Through Hash Based Rule Lookup," IEEE TENCON 2017, Penang, Malaysia, November 2017.

6. Elvira Febiani, Huaqun Guo, Wang Ling Goh. “An Advanced Firewall Rule Matching Algorithm,” IEEE International Conference on Service Operations and Logistics and Informatics (SOLI), Singapore, 31 July -2 August 2018.
7. Dong Li, Huaqun Guo, Jianying Zhou, Luying Zhou, and Jun Wen Wong. “SCADAWall: A CPI-Enabled Firewall Model for SCADA Security,” Computers & Security Journal, Volume 80, January 2019, Pages 134–154.
8. “The Modbus Protocol In-Depth” National Instruments. Retrieved on September 15, 2019 from https://www.ni.com/en-sg/innovations/white-papers/14/the-modbus-protocol-in-depth.html.
9. “MODBUS APPLICATION PROTOCOL SPECIFICATION V1.1b” Modbus. Retrieved on September 15, 2019 from http://www.modbus.org/docs/Modbus_Application_Protocol_V1_1b.pdf.
10. J. Nivethan and M. Papa, “On the use of open-source firewalls in ICS/SCADA systems”. Information Security Journal: A Global Perspective, 25: 1–3, 83–93, 2016. https://doi.org/10.1080/19393555.2016.1172283.
11. “IPTables Firewall (Basic)” serverpronto. Retrieved on April 10, 2019 from https://www.serverpronto.com/kb/page.php?id=IPTables+Firewall+%28Basic%29.

Investigating the Effect of Phytoextracts on Protecting *Saccharomyces cerevisiae* from Oxidative Stress

Jun Yuan Koo, Ryan Teoh, and Sheng Hao Zong

Abstract Environmental stressors can lead to an increased generation of reactive oxygen species (ROS) which can lead to oxidative stress when ROS levels exceed detoxification mechanisms. Addition of antioxidant-rich phytoextracts to stressed cells would be beneficial as the antioxidants would scavenge free radicals, thus protecting the yeast cells and increasing cell viability and thus fermentation efficacy. In the present study, UV radiation, hydrogen peroxide, and ethanol were found to exert oxidative stress on *Saccharomyces cerevisiae*, and yeast cells revealed a significant decrease (86%, 83%, and 95% respectively) in colony forming units (CFUs). However, addition of 10% concentration aqueous extracts of *Zingiber officinale* and *Capsicum annuum* showed significant ameliorative effects on yeast cells, restoring the CFU with only a loss of 17% and 4% for UV, 11% and 37% for hydrogen peroxide, and 44% and 35% for ethanol. Mixture of aqueous extracts was not found to exhibit synergistic effects in ameliorating stressed yeast cells.

Keywords *S. cerevisiae* · Oxidative stress · ROS · Phytoextracts · *Z. officinale* · *C. annuum*

1 Introduction

Saccharomyces cerevisiae has many industrial uses. However, in these processes, *S. cerevisiae* experiences oxidative stress resulting from environmental stresses. In the brewing process, optimal oxygen levels are required for fermentation to take place. Thus, yeast is constantly exposed to oxygen in brewery propagation as well as in fermentation vessels [3]. Serial repitching, a process whereby yeast cropped at the end of the fermentation is reused in subsequent fermentations and re-exposed to oxygen as before, can only be conducted a finite number of times before fermentation performance deteriorates [5]. Due to the fact that reactive oxygen species (ROS) results in cellular aging [7] and replicative lifespan in yeast is correlated to the

J. Y. Koo (✉) · R. Teoh · S. H. Zong
High School Section, Hwa Chong Institution, Singapore, Singapore
e-mail: 171291a@student.hci.edu.sg

H. Guo et al. (eds.), *IRC-SET 2020*,
https://doi.org/10.1007/978-981-15-9472-4_62

cell's antioxidant potential [1, 10], the amount of oxygen exposure of a certain batch of yeast and its ability to mitigate the effects of ROS generation might be used to determine how many times serial repitching can be carried out [5]. In wine-making, yeast cells experience processes involving aeration, nutrient deprivation, and dehydration, which can induce oxidative stress [4]. As for baking, cells of *S. cerevisiae* often go through freeze-thawing, high-sucrose, and air-drying, leading to denaturation of antioxidant enzymes and damaging the mitochondrial membrane, causing *S. cerevisiae* cells to experience oxidative stress [9]. Oxidative stress can lead to the deterioration of fermentation efficacy in *S. cerevisiae*. By exogenously adding antioxidants, yeast cells would be aided in the free radical scavenging, and be more resistant to environmental stresses [2], thus possessing increased replicative lifespan, fermentation capacity, viability, leading to higher fermentation efficacy, and lower production costs.

2 Objectives and Hypotheses

2.1 Objectives

In the present study, UV light, hydrogen peroxide, and ethanol were the chosen inducers of oxidative stress. This study aims to investigate whether aqueous extracts of *Zingiber officinale* and *Capsicum annuum* would be able to restore the CFUs of stressed cells, and whether a mixture of these phytoextracts would exhibit synergistic effect in protecting yeast cells.

2.2 Hypotheses

We hypothesise that the extracts are able to protect yeast cells against UV radiation, hydrogen peroxide, and ethanol, and a synergistic effect would be observed with a combination of extracts.

3 Methods and Materials

3.1 Experimental Variables

See Table 1.

Table 1 Experimental variables

Independent variables	Dependent variable	Controlled variables
Type of plant extract	Number of colony forming units of yeast Absorbance at 517 nm in the DPPH test	Temperature of growth of yeast Initial number of cells in yeast preculture Concentration of plant extract Duration of exposure of yeast cells to ultraviolet light Concentration of hydrogen peroxide solution Concentration of ethanol

3.2 Procedure

1. *Growth of yeast cells (preparation of yeast preculture)*

S. cerevisiae cells were inoculated into 10 ml potato dextrose broth and grown overnight at 30 °C in a shaking incubator. The number of cells were determined using a haemocytometer and standardised at approximately 1×10^7 cells ml^{-1}.

2. *Preparation of plant extracts*

1 g of plant sample was ground in 10 ml of deionised water using a mortar and pestle. The entire mixture was then transferred to a 50-ml centrifuge tube and heated to 48 °C for 20 min in a water bath. The mixture was centrifuged at 7000 rpm for 10 min, the supernatant was collected and was filter-sterilised through a microfilter.

3. *Investigating effect of plant extracts on yeast cells exposed to ultraviolet light*

Four mixtures were prepared and left to stand at room temperature for 20 min. Control setups 1 (C1) and 2 (C2) each consisted of 3 ml of yeast preculture and an equal volume of sterile water. The mixture in C2 was transferred into a Petri dish for UV exposure for 30 s. This tested the effect of UV light on the growth of yeast cells in the absence of antioxidants. Control setup 3 (C3) consisted of 3 ml of yeast preculture and an equal volume of plant extract. This tested the effect of antioxidants on the growth of yeast cells. The test setup (T) contained 3 ml of yeast preculture and an equal volume of plant extract. This mixture was exposed to UV for 30 s to test if the antioxidants protected the cells from damage caused by free radicals from UV light. Five replicates of each setup were prepared. Mixtures from C1, C3 and T setups were serially diluted to 10^{-4} with saline solution, while mixtures of C2 were diluted to 10^{-2}. 0.1 ml of the diluted cultures were spread evenly with a sterile spreader on potato dextrose agar. The plates were incubated at 30 °C and the number of yeast colony forming units was determined after 24 h.

4. *Investigating effect of plant extracts on yeast cells treated by hydrogen peroxide*

Three setups were prepared. Control setup 1 (C1) contained 2 ml of yeast preculture with 3 ml of sterile water. Control setup 2 (C2) consisted of 2 ml of yeast preculture with 2 ml of sterile water and 1 ml of 2 mM hydrogen peroxide solution. This tested the effect of hydrogen peroxide on the growth of yeast. The test setup (T) had 2 ml of yeast preculture added with 2 ml of plant extract and 1 ml of 2 mM hydrogen peroxide solution. This tested the effect of antioxidants on the growth of yeast treated with hydrogen peroxide. Five replicates of each setup were prepared. The set-ups were incubated at 30 °C for 60 min. Serial dilution, plating and incubation of plates were done according to that previously described.

5. *Investigating effects of plant extracts on yeast cells treated with ethanol*

Three setups were prepared. Control setup 1 (C1) contained 3 ml of yeast preculture with 3 ml of sterile water. Control setup 2 (C2) contained 3 ml of yeast preculture with 1.8 ml of sterile water and 1.2 ml of absolute ethanol to give a final concentration of 20% (v/v) ethanol. This tested the effect of ethanol on the growth of yeast cells in the absence of antioxidants. The test setup (T) was made up of 2 ml of yeast preculture added with 1.8 ml of plant extract and 1.2 ml of absolute ethanol. This tested the effect of antioxidants on the growth of yeast cells treated with ethanol. Five replicates of each setup were prepared. Serial dilution, plating and incubation of plates were done according to that previously described.

6. *DPPH antioxidant test*

1,1-diphenyl-2-picryl-hydrazil (DPPH) is a free radical which produces a purple solution when dissolved in methanol. When it is reduced by antioxidants, a change in colouration from purple to yellow is observed. The negative control consisted of 1.0 ml of DPPH, 1.9 ml of methanol and 0.1 ml of sterile water. In the test set-up, plant extract replaced sterile water. Five replicates were prepared. For the respective blanks for each set-up, methanol was added instead of DPPH solution. The initial absorbance was measured at 517 nm against the respective blanks and the mixtures were then left to stand in the darkness for 20 min, before the final absorbance readings were measured. The radical scavenging activity (in %) was then calculated based on the following formula:

$$\frac{Final\ absorbance\ of\ control - final\ absorbance\ of\ test}{Final\ absorbance\ of\ control} \times 100\%$$

4 Results

4.1 Effect of Phytoextracts on Yeast Cells After UV Exposure

Exposure of *S. cerevisiae* cells to UVC light for 30 s was found to decrease colony forming units by 86%, but addition of aqueous extract of *Zingiber officinale* showed

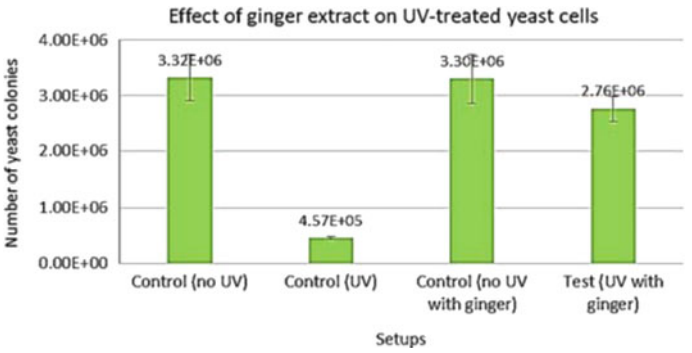

Fig. 1 Graph showing the effect of ginger extract on UV-treated yeast cells

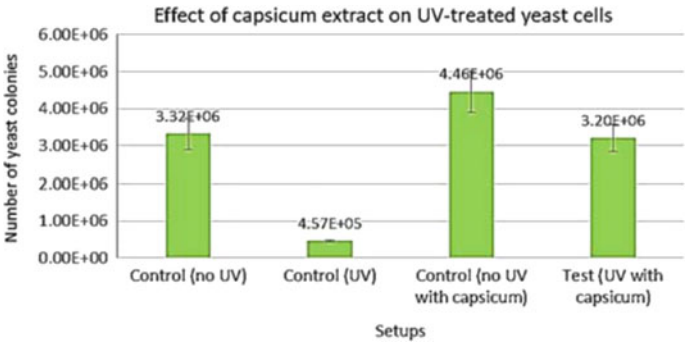

Fig. 2 Graph showing the effect of capsicum extract on UV-treated yeast cells

significant ameliorative effects, reducing loss of CFUs to only 17% (Fig. 1). Addition of aqueous extract of *Capsicum annuum* showed even stronger ameliorative effects, restoring CFUs with only a loss of 4% (Fig. 2). However, mixture of both extracts did not restore CFUs at a significantly higher rate than the individuals extract, thus it was not found to exhibit synergistic effect (Fig. 3). The Kruskal-Wallis test p value was 0.00547 for setups with ginger, 0.00896 for capsicum, and 0.0015 for the mixture, showing that the differences in number of colony forming units were statistically significant. The plates are shown in Fig. 4.

4.2 Effect of Phytoextracts on Yeast Cells Treated with Hydrogen Peroxide

Treatment of *S. cerevisiae* cells with hydrogen peroxide decreased CFUs by 83%, but addition of aqueous extract of *Capsicum annuum* restored the CFUs with a

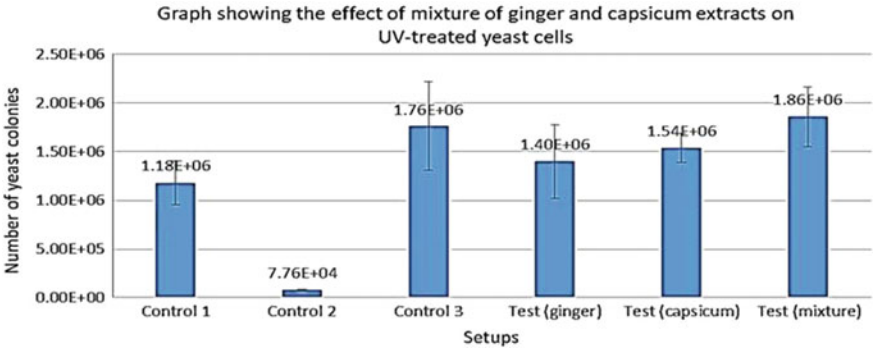

Fig. 3 The effect of a mixture of ginger and capsicum extracts on UV-treated yeast cells

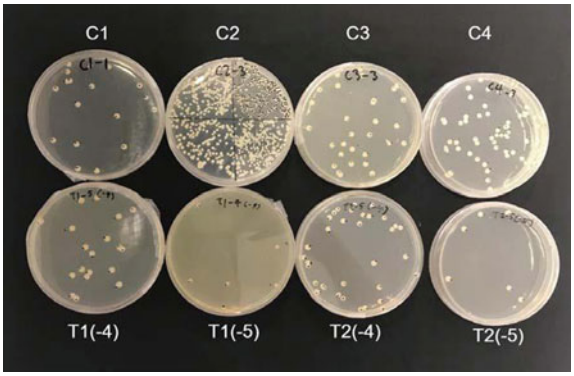

Fig. 4 Plates with yeast colonies. C1 and C2 represent control 1(no UV) and control 2 (UV), respectively. C3 and C4 represent control 3 (ginger extract) and control 4 (capsicum extract), respectively. T1 and T2 represent test 1 (ginger extract with UV) and test 2 (capsicum extract with UV), respectively. Dilution factors for all setups were 10^{-4} or 10^{-5}, but 10^{-2} for control 2

loss of 37%, while the addition of aqueous extract of *Zingiber officinale* restored the CFUs with a loss of only 11% (Fig. 5). A mixture of extracts was not found to exhibit synergistic effect (Fig. 6). The *p* values in the Kruskal-Wallis test were 0.0062 and 0.0023 for individual extracts, and the mixture, respectively, showing statistical significance in the number of yeast colonies among setups (Fig. 7).

4.3 Effect of Phytoextracts on Yeast Cells Treated with Ethanol

Treatment of *S. cerevisiae* cells with ethanol decreased CFUs by 95%, but addition of aqueous extract of *Zingiber officinale* restored the CFUs with a loss of 44%, while

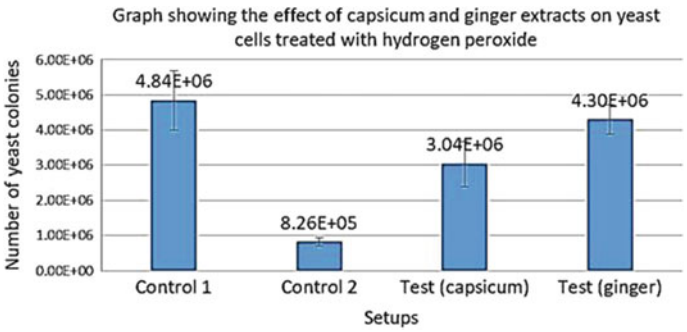

Fig. 5 Graph showing the effect of capsicum and ginger extracts on yeast cells treated with hydrogen peroxide

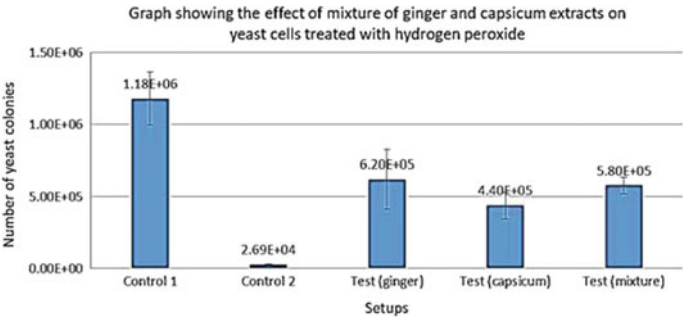

Fig. 6 Graph showing the effect of mixture of capsicum and ginger extracts on yeast cells treated with hydrogen peroxide

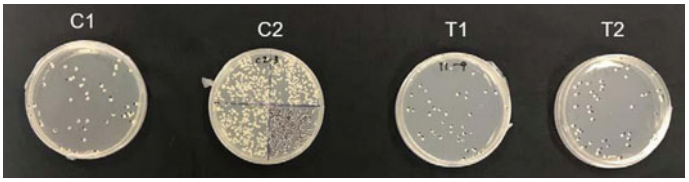

Fig. 7 Plates with yeast colonies. C1 and C2 represent control 1 (no hydrogen peroxide) and control 2 (hydrogen peroxide), respectively. T1 and T2 represent test 1 (ginger extract with hydrogen peroxide) and test 2 (capsicum extract with hydrogen peroxide), respectively. Dilution factors for all setups were 10^{-4}, but 10^{-2} for control 2

the addition of aqueous extract of *Capsicum annuum* restored the CFUs with a loss of only 35% (Fig. 8). The Kruskal-Wallis test p value was 0.00151, indicating that the difference in the mean number of yeast colonies in setups was statistically significant (Fig. 9).

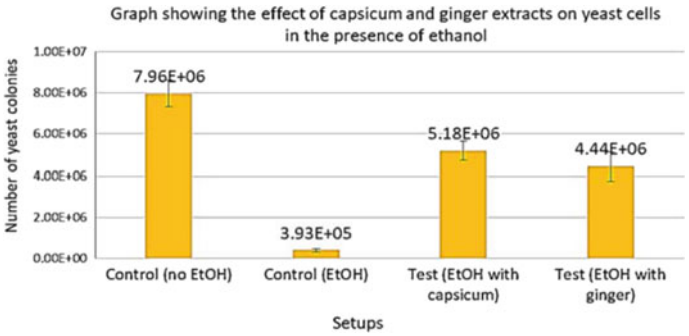

Fig. 8 Graph showing effect of capsicum and ginger extracts on yeast cells in the presence of ethanol

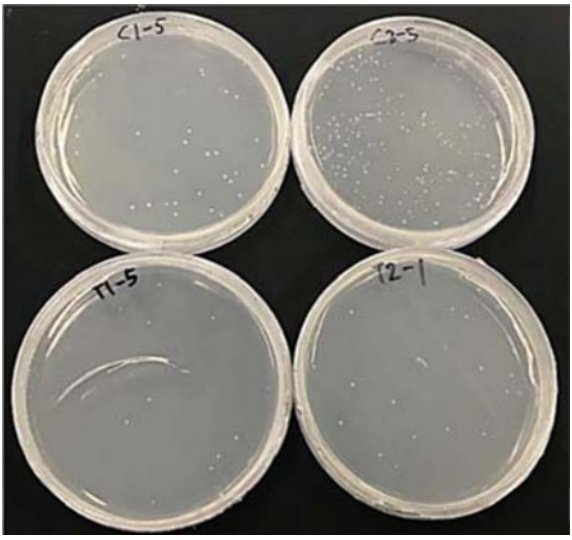

Fig. 9 Plates with yeast colonies. C1 and C2 represent control 1 (no ethanol) and control 2 (ethanol), respectively. T1 and T2 represent test 1 (ginger extract with ethanol) and test 2 (capsicum extract with ethanol), respectively. Dilution factor was 10^{-4}, except 10^{-2} for control 2

4.4 DPPH Antioxidant Assay

DPPH antioxidant assay was carried out to quantify the radical scavenging activities of both extracts. The radical scavenging activity of *Zingiber officinale* was determined to be 60.33% whereas that of *Capsicum annuum* was 65.45% (Fig. 10). The Mann-Whitney U test gave a *p*-value of 0.01208, showing that the differences in final absorbance of the control and test were statistically significant.

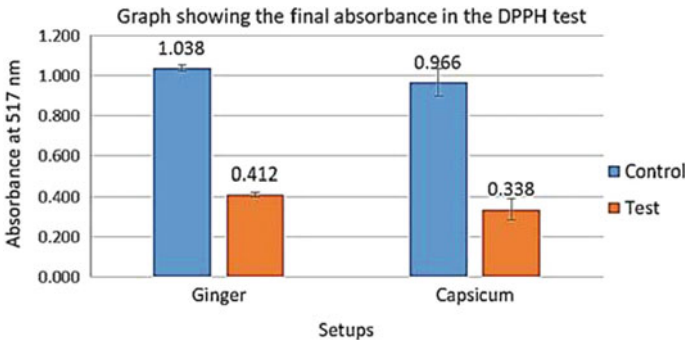

Fig. 10 Graph showing final absorbance in the DPPH test

5 Conclusion and Discussion

In the present study, oxidative stress was induced on *Saccharomyces cerevisiae* via exposure to UV light, hydrogen peroxide, and ethanol, resulting in significant loss of colony forming units (CFUs). However, loss of CFUs was greatly restored with the addition of aqueous extract of ginger (*Zingiber officinale*) and red capsicum or red bell pepper (*Capsicum annuum*), which can be attributed to the antioxidant compounds present in both plants. This is supported by the results from the DPPH assay showing the strong free-radical scavenging properties of both extracts. However, no synergistic effect was found for the ginger-capsicum mixture.

Hydrogen peroxide is a reactive oxygen species itself, so the loss in CFUs after treatment with hydrogen peroxide can be attributed to the action of ROS which causes oxidative stress, directly leading to cell death. UV light induces oxidative stress by releasing inflammatory cytokines which results in the generation of ROS [6]. As for ethanol, the process of oxidative stress is much more complicated as it is induced via multiple pathways such as damage to the cell membrane leading to increased cell membrane permeability, as well as depletion of antioxidant enzymes and release of inflammatory cytokines [11]. The reduction in loss of CFUs can be attributed to the plant antioxidant compounds found in the phytoextracts which scavenge free radicals, therefore protecting yeast cells from oxidative stress.

Both capsicum and ginger extracts showed strong ameliorative effects, which also corresponds with the high antioxidant levels found in these extracts. One in vivo study reported that ginger essential oil increased antioxidant marker enzymes like catalase and glutathione peroxidase, and hence the cells' viability of hydrogen peroxide-induced oxidative stress [8]. As for capsicum, compounds like ascorbate, as well as gallic acid, which are both found in high amounts in *Capsicum annuum*, could have been the main factor behind the restoration of yeast CFUs. One study by Wu et al. [12], showed that ascorbate and gallic acid scavenged hydrogen peroxide by mitigating the oxidant-induced growth arrest of the yeast cells.

A limitation in this study was the difficulty in standardising the antioxidant content in the extracts of ginger and capsicum each time a fresh batch of extract was prepared, thus leading to varying concentrations of antioxidants. Further research could be conducted using other inducers of oxidative stress apart from those used in the present study, and also investigate whether other solvents could be used to effectively extract antioxidants from the plants.

References

1. Barker, M. (1999). Effect of Cu, Zn superoxide dismutase disruption mutation on replicative senescence in *Saccharomyces cerevisiae*. *FEMS Microbiology Letters,* 177(2), 199–204.
2. Biradar, S., Tamboli, A., Patil, T., Khandare, R., Govindwar, S., & Pandwar, P. (2017). Phytoextracts protect *Saccharomyces cerevisiae* from oxidative stress with simultaneous enhancement in bioremediation efficacy. *Indian Journal of Experimental Biology,* 55, 469–478.
3. Briggs, D.E., Boulton, C.A., Brookes, P.A., & Stevens, R. (2004). Brewing: science and practice. *Journal of the Science of Food and Culture*, 86(1). https://doi.org/10.1533/9781855739062.
4. Garre, E., Raginel, F., Palacios, A., Julien, A., & Matallana, E. (2010). Oxidative stress responses and lipid peroxidation damage are induced during dehydration in the production of dry active wine yeasts. *International Journal of Food Microbiology,* 136(3), 295–303. https://doi.org/10.1016/j.ijfoodmicro.2009.10.018.
5. Gibson, B.R., Lawrence, S.J., Leclaire, J.P., Powell, C.D., & Smart, K.A. (2007). Yeast responses to stresses associated with industrial brewery handling. *FEMS Microbiology Reviews,* 31(5), 535–569. https://doi.org/10.1111/j.1574-6976.2007.00076.x.
6. Goswami, S., Sharma, S., & Haldar, C. (2013). The oxidative damages caused by ultraviolet radiation type C (UVC) to a tropical rodent *Funambulus pennanti*: Role of melatonin. *Journal of Photochemistry and Photobiology B: Biology*, 125, 19–25. https://doi.org/10.1016/j.jphotobiol.2013.04.008.
7. Halliwell, B. & Gutteridge, J.M.C. (1999). Free radicals in biology and medicine. Oxford: Oxford University Press. https://doi.org/10.1016/s0378-1097(99)00308-0 March 11, 2019 from https://thescipub.com/pdf/10.3844/ojbsci.2012.62.71.
8. Höferl, M., Stoilova, I., Wanner, J., Schmidt, E., Jirovetz, L., Trifonova, D., . . . Krastanov, A. (2015). Composition and comprehensive antioxidant activity of ginger (*Zingiber officinale*) essential oil from Ecuador. *Natural Product Communications*, 10(6), 1085–1090. https://doi.org/10.1177/1934578x1501000672.
9. Takagi, H. & Shima, J. (2015). Stress tolerance of baker's yeast during bread-making processes. *Stress Biology of Yeasts and Fungi,* 23–42. https://doi.org/10.1007/978-4-431-55248-2_2.
10. Van Zandycke, S.M., Sohier, P.J., & Smart, K.A. (2002). The impact of catalase expression on the replicative lifespan of *Saccharomyces cerevisiae*. *Mechanisms of Ageing and Development*, 123(4), 365–373. https://doi.org/10.1016/s0047-6374(01)00382-7.
11. Wu, D., & Cederbaum, A.I. (2003). Alcohol, oxidative stress, and free radical damage. *Alcohol Research & Health*, 27, 277–284.
12. Wu, M.J., Odoherty, P.J., Fernandez, H.R., Lyons, V., Rogers, P.J., Dawes, I.W., & Higgins, V.J. (2011). An antioxidant screening assay based on oxidant-induced growth arrest in *Saccharomyces cerevisiae*. *FEMS Yeast Research*, 11(4), 379–387. https://doi.org/10.1111/j.1567-1364.2011.00726.x.

Development of a First-Aid Smart Assistant Device Using IoT Technology and Augmented Reality

Cheng Zhi Ying

Abstract The objective of this project is to build a system software that could assist any first responder irrespective of their background in first-aid. The system software employs a combination of Internet of Things (IoT) technologies to dial for emergency medical assistance as well as make a diagnosis of the first-aid treatment needed. A custom Image Recognition (IR) service is trained using IBM Watson's deep machine-learning to assess the casualty's primary condition based on data analytics of the photo taken. Training phrases are fed into Dialogflow to construct a voice and text-based conversational interface for Google Assistant's Artificial Intelligence (AI) to give a secondary first-aid diagnosis. Vuforia's Augmented Reality (AR) engine in Unity is then enlisted via Target Detection to display a superimposed visual-aid of a virtual assistant applying first-aid on the casualty. The various components are amalgamated using the AI's autonomous control over the IR and AR applications to create the proposed end-to-end system software. Lastly, XCode, an app-building engine, develops the components built in the various software into prototype mobile applications. Future prototyping could assist first responders during an actual emergency and complement SCDF's efforts of promoting high standards of first-aid through the myResponder application.

Keywords Augmented reality · Image recognition · First-aid

1 Introduction

1.1 Internet of Things (IoT)

The Internet of Things (IoT) is the neural internetworking of web-enabled devices and has hence emerged as the paradigm shift of future Internet applications because of its two key attributes. Firstly, IoTs are embedded with Artificial Intelligence (AI) that allows for autonomous control over many devices. Thus, time spent as a result

C. Z. Ying (✉)
Raffles Girls' School (Secondary), 20 Anderson Road, Singapore 25997, Singapore
e-mail: zhi.ying252@gmail.com

H. Guo et al. (eds.), *IRC-SET 2020*,
https://doi.org/10.1007/978-981-15-9472-4_63

of human intervention to toggle and navigate between different control systems is minimised. This radically improves users' convenience and an evident example of this is the development of smart home controls such as Amazon Alexa. Secondly, IoTs leverages on machine learning. Therefore, given enough training datasets, IoTs are highly trainable and opportunities such as Image Recognition (IR) services are presented by IoT's capability to analyse and employ the data received.

1.2 Augmented Reality (AR)

Augmented reality (AR) is the integration of digital information with the end-user's real-world environment. As such, when AR is used in educational tools, it has the aptitude of enhancing visual learning and it has hence given rise to many visual-aid applications in the healthcare sector [1]. By bringing life-saving information into the medics' field of vision with the assistance of AR, the administration of medical treatment can be executed with greater precision in a significantly shorter duration [1].

1.3 IoT and AR Integrated Application in First-Aid

First-aid is the simple medical assistance given to prevent the degradation of a person's health condition before professional medical care is made available. Despite its vitality in lifesaving, the importance of first-aid is often undervalued. According to research done by St John, an organisation well-versed in providing first-aid and ambulance services, the lack of first-aid expertise endangers an average of 150,000 lives a year [2]. Heart attack emergencies where first-aid would have made a difference kill at least 29,000 yearly and 70% of these deaths occur before the victim reaches the hospital [3]. A research paper from the University of Warwick revealed that one-in-eight cardiac arrest patients could not be saved as the rate of bystanders with CPR knowledge was very low [3]. Without prior first-aid knowledge, bystanders are uncertain of the type of first-aid to administer as there could be similar or overlapping symptoms. Furthermore, they are also unsure of how to carry out proper first-aid procedures even if they knew the type of first-aid to administer. Evidently, the need to equip people with basic first-aid skills has become increasingly apparent over the years but the time-consuming nature of professional first-aid courses is a major deterrent. With a time allowance of as short as six minutes to save a life [4], current first-aid tutorials online would likewise be ineffective during an actual emergency as they are used as teaching material before the emergency and not during the emergency itself, making them relatively lengthy. Moreover viewers may also find these tutorials confusing because of the angling of the videography. Learning from a third person point-of-view (POV) demonstration does pose as a learning barrier, especially for more complicated first-aid procedures [1]. Hence, this project

aims to create a software, the First-aid Aider, that will respond with useful first-aid information presented in an easily comprehensible manner for real-time and proper administration of first-aid by any first responder, regardless of their proficiency in first-aid.

2 Method

2.1 Design Thinking Process

A general concept of the software was first formulated by tapping on the useful characteristics of IoTs and AR technologies. The empowerment of an IR service could resolve issues on uncertain diagnoses by inexperienced first responders as an IR service could be trained to identify the symptoms of the casualty using deep machine learning and thus propose a primary diagnosis to the first responder. On the other hand, an AR service could serve as a visual-aid to teach first-aid in a clear and concise manner by showing an "AR virtual assistant" performing first-aid on the casualty itself from a first person POV. To create this effect, an AR video player will be created. A first person POV first-aid video with a transparent background will be played such that only the hands of the first-aider in the video can be viewed. This is so that the video can be superimposed on the casualty. In doing so, even amateur first-aiders can quickly replicate the same actions displayed by the AR and administer the necessary treatment. This is because unlike watching online tutorials, the first responder need not have to spend time understanding the first-aid tutorials in the third person POV before applying this understanding to the casualty from their first person POV.

However, the IR and AR services are built on two different platforms. Thus, incorporating a suitable IoT's AI is imperative to merge the separate IR and AR platforms into one complete end-to-end system by having the AI toggle between the two different platforms with the AI's autonomous control over them. Furthermore, the AI will also help give a more contextualised secondary diagnosis by asking the user more questions after the IR's primary diagnosis is given (Fig. 1).

2.2 Actuation and Prototyping Process

Different development tools were used to create, test and finalise the various AI, IR and AR components. After building the individual components with the respective platforms, the prototyping stage of unifying them into a single application system that can be used on mobile devices commenced. This was done with an application building engine, XCode.

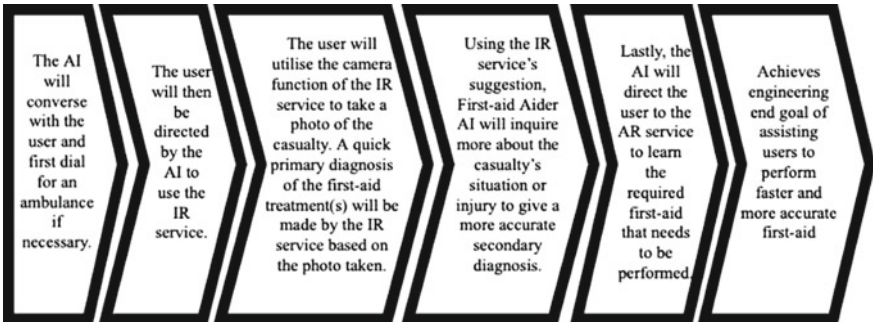

Fig. 1 Workflow of the first-aid aider application system

3 Methodology and Results

3.1 Google Assistant and Dialogflow

For the purpose of the prototype, the Google Assistant was chosen as a suitable AI due to the fact that it allows custom tailoring of conversations between the user and the Google Assistant using the Dialogflow console. As such, it can be easily trained to give useful and appropriate replies in response to all kinds of emergency situations.

The Dialogflow console operates on a fundamental call and response principle in the form of intents and responses. Intents refer to the wants of the user and in this context, they are the verbal first-aid procedures required by the user. Responses refer to the utterances spoken and displayed back to the user by the Google Assistant (Annex, Fig. 2).

The training of the Google Assistant constituted of two processes. The first was charting the dialogue succession between Google Assistant and the user to call for an ambulance and to teach the respective first-aid scenarios based on the intent of the user after they have used the IR component (Annex, Figs. 3, 4, 5 and 6). The second was training the Google Assistant to recognise the intent of the user. As the same intent would have infinite variations of phrasing, Google Assistant had to be trained to comprehend the intent and invoke the correct corresponding response. Hence, training phrases, different ways of how a user's intent can be worded, were fed and processed by the Google Assistant (Annex, Fig. 7). With Dialogflow's machine learning, Google Assistant can understand similar user utterances to the training phrases and this increases the accuracy of Google Assistant returning the right response.

3.2 Result of AI Development

Testing of the Google Assistant showed that it was able to recognise the intents of the user well and respond accordingly. The Google Assistant was also useful in giving a secondary diagnosis by asking important clarifying questions to assess if the correct diagnosis has been made. For instance, the first responder was able to better discern if the injury is a sprain and fracture, which is commonly hard to tell apart, when asked by the Google Assistant to check for the presence of the differentiating symptoms of the casualty (Annex, Fig. 6). As the voice of the Google Assistant is computer generated, it was helpful in reading out a steady count when the user's intent was to perform Cardiopulmonary resuscitation (CPR). The speed of the Google Assistant's speech delivery is also tailored close to a rate of 100 bpm, the appropriate rate for delivering CPR [5], which increased the user's success rate in performing it.

3.3 IBM Watson Visual Recognition

IBM Watson Visual Recognition is an IR service that relies on high-performing convolutional neural networks and deep learning algorithms by Python Keras libraries in Jupyter Notebook. Apart from its reliability and accuracy as a service, IBM Watson Visual Recognition gives users the option of developing custom IR classifiers with their own image collection. Hence, IBM Watson was selected for the IR service for the First-aid Aider.

To begin with, training images were prepared for each type of first-aid treatment needed (Annex, Fig. 8). The minimum training data size of a classification class is ten images. Thus, an average of 30 images for each class was used to improve the accuracy of the customised IR service (Annex, Fig. 9). After the custom IR service was trained, test images that were not part of the training image datasets were used to evaluate the accuracy of the IR service. Fine tuning and retraining of the IR service began after some of the test images were wrongly identified. After which, the IR service was downloaded as a compatible Core ML model file type to develop the IR application with the application building engine, XCode.

3.4 Xcode

The building of the IR application comprised of two steps. The first was writing the script for the IR service in Swift. Taking reference from James Rochabrun's project for an IBM Watson Objects Identifier Application [6], the script was modified to suit the needs of the IR service for the First-aid Aider (Annex, Fig. 10). The second step was to design the interface of the application design in Xcode's Main.storyboard. A UIButton was included at the bottom of the application for the user to take a photo

of the casualty. An UIImageView was added next for the photo taken to be displayed in the IR application. Lastly, a UILabel was used to display the classification of the first-aid treatment to be shown on the phone screen. The iOS application was then built and downloaded for testing on an iPhone (Annex, Fig. 11).

3.5 Result of IR Application

Experimenting with the IR application showed that it was capable of identifying the correct first-aid treatment needed. It was also proven to be useful in identifying multiple injuries on a casualty so that it covered all the necessary first-aid that needed to be performed.

3.6 Vuforia and Unity AR Application

Unity is a 2D and 3D development engine that is commonly used to build virtual graphics. Using Unity with Vuforia AR Support, an AR video player with play, pause and scrubbing functions was easily created.

Vuforia AR Support was selected as its AR technology relies on Target Images to superimpose the AR object in the real world. This means that the AR object will only be displayed when a specific image is detected. Hence, using this concept of Target Images, the Target Image was set as the casualty's injuries. This way the AR video player with the first-aid animation can be overlaid over the casualty's injury directly.

To build the video player, a 3D plane was used Play and Pause UIButtons were created below the plane. Unity's VideoPlayer.Play and VideoPlayer.Pause functions were attached to the respective UIButtons. Finally, A UISlider was introduced to the video player with a script written in C++ to allow the user to scrub the video (Annex, Fig. 12).

3.7 Adobe Premiere Pro CC

Adobe Premiere Pro CC is a video editing software that removes the backgrounds of videos with the use of green screens. After editing the videos with Adobe Premiere Pro CC, the background of the first-aid tutorial was removed and added to Unity's video player for the intended effect of an "AR virtual assistant" (Annex, Fig. 13).

3.8 XCode

Xcode was used again to build the iOS application on the iPhone for testing.

3.9 Result of AR Application

The AR video was successfully superimposed in the real-world and all three play, pause and scrubbing functions worked well. The superimposed first person POV demonstration was also significantly simpler for a first responder with no first-aid experience.

Unfortunately, with the current AR technology, Vuforia was only able to display AR objects with a static 2D Target Image or miniscule 3D Target Images. Larger 3D Target Images such as human body parts were not recognised. Therefore for the purpose of the prototype, 2D printed images were used as Target Images to demonstrate this concept (Annex, Fig. 13). With further development of Vuforia's Target Image technology however, such an AR application can be created to recognise real human body parts as Target Images.

4 Conclusion

In conclusion, the prototype shows that the concept of utilizing useful characteristics of IoT and AR technologies significantly helps inexperienced first responders to firstly, identify the symptoms of the casualty using machine learning data analytics and secondly, learn first-aid in a clear and concise manner using AR as a visual-aid. Although the prototype had a limitation of not being able to detect 3D objects like human body parts with the current Vuforia AR technology, but further prototyping of this project will allow the convergence of IR and AR technologies to potentially revolutionise the administration of first-aid to save more lives.

Acknowledgements I would like to express my utmost gratitude to everyone who has helped me in my research in one way or another.

Annex

See Figs. 2, 3, 4, 5, 6, 7, 8, 9, 10, 11, 12 and 13.

ANNEX

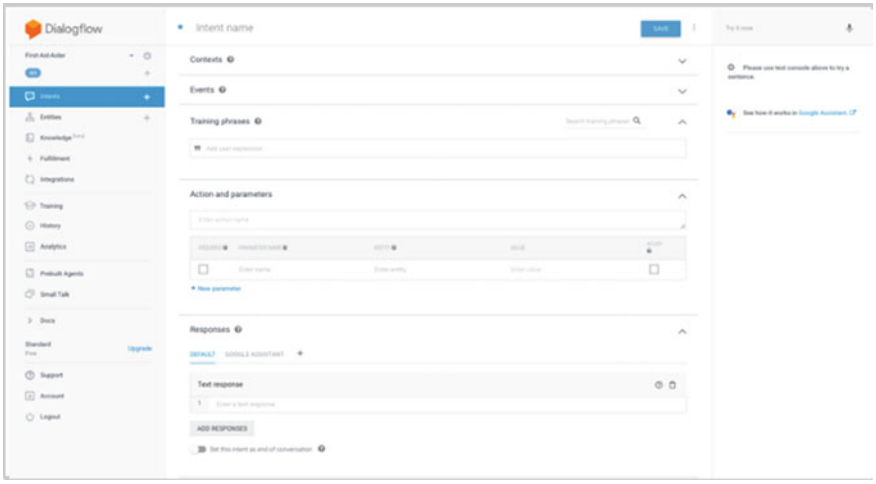

Fig. 2 Dialogflow console and its operations

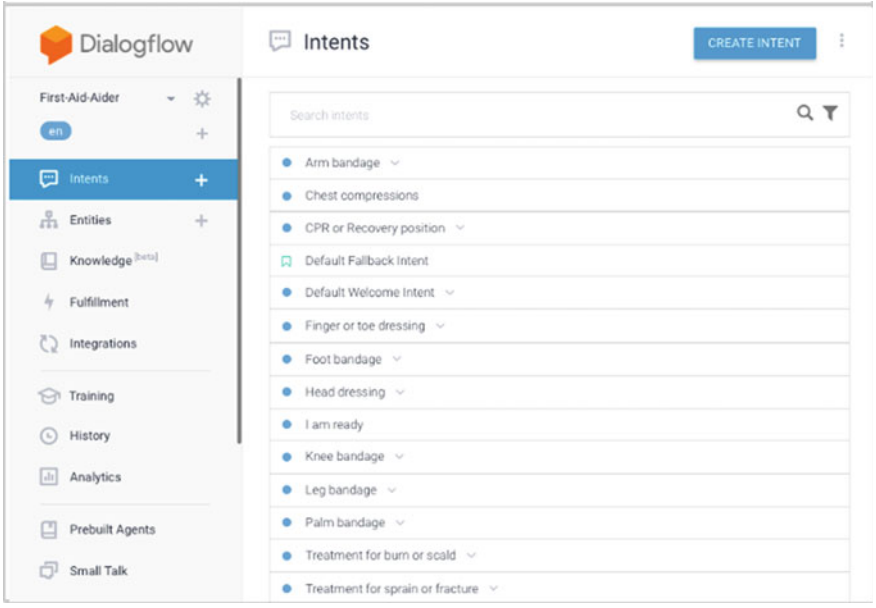

Fig. 3 Dialogue successions created for each intent for the respective first-aid treatments

1. **Default Welcome Intent**
    a. **Google Assistant:** Hi I am your First-aid Aider! Do you need to call for an emergency or non-emergency ambulance?
        i. **User:** Yes
            1. **Google Assistant:** Ask Siri to call 995 if it's an emergency or 1777 if it's a non-emergency. After which I will teach you how to administer the necessary first aid. Say "I am ready" once you've contacted SCDF.
                a. **User:** I am ready.
                    i. **Google Assistant:** Please open the IR app with Siri and take a picture of the casualty. Ensure that the entire body is in the camera frame. I will generate my top first aid suggestions for you. What first aid treatment would you like to know?
        i. **User:** No
            1. **Google Assistant:** In that case please open the IR app with Siri and take a picture of the casualty. Ensure that the entire body is in the camera frame. I will generate my top first aid suggestions for you. What first aid treatment would you like to know?

Fig. 4 Default welcome intent and response from Google assistant

2. **Default Fallback Intent**
    a. **User:** says a response that Google Asssistant does not understand
        i. **Google Assistant:**

	Text response
1	I didn't get that. Can you say it again?
2	I missed what you said. What was that?
3	Sorry, could you say that again?
4	Sorry, can you say that again?
5	Can you say that again?
6	Sorry, I didn't get that. Can you rephrase?
7	Sorry, what was that?
8	One more time?
9	What was that?
10	Say that one more time?
11	I didn't get that. Can you repeat?
12	I missed that, say that again?

Fig. 5 Default fallback intent and response from Google assistant

5. **Treatment for sprain or fracture Intent**
    a. **User:** Treatment for sprain or fracture.
        i. **Google Assistant:** Firstly, identify if the injury is a fracture or a sprain. If the casualty has pain around the soft tissue areas, no deformity on the foot, no numbness and the injured limb is still movable, it is more likely to be a sprain. If not it is more likely to be a fracture. May I know if it's a sprain or fracture?
            1. Sprain
                a. Enter the AR app to learn the sprain first aid tutorial. Press on the play and pause buttons to operate it.
            2. Fracture
                a. Enter the AR app to learn the fracture first aid tutorial. Press on the play and pause buttons to operate it.

Fig. 6 Dialogue succession under the treatment for the sprain or fracture treatment intent

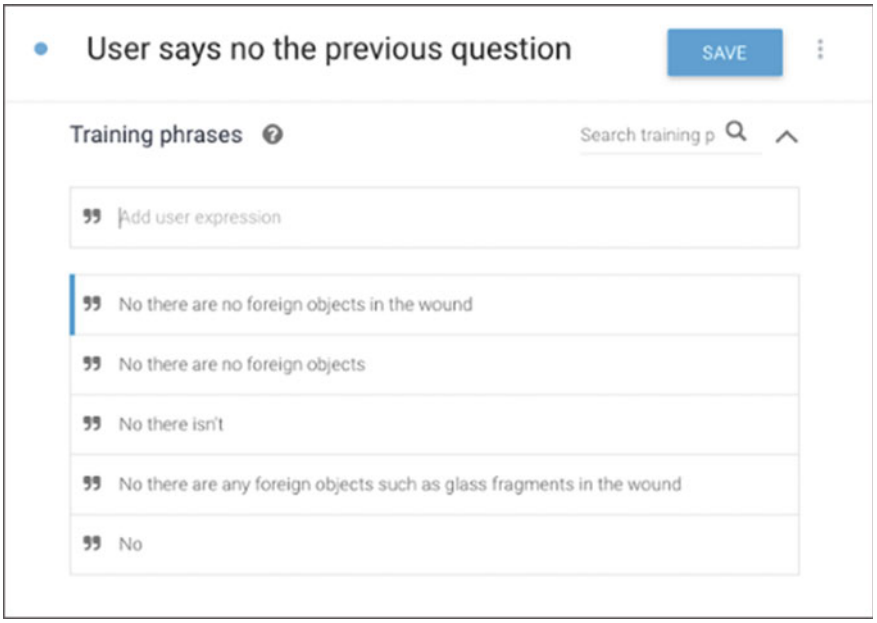

Fig. 7 Training phrases for different utterances by the user but with the same intent

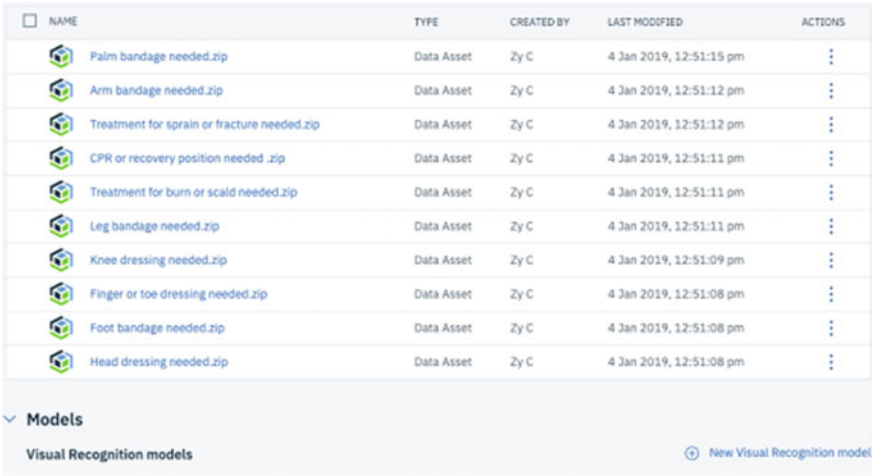

Fig. 8 IBM Watson training images

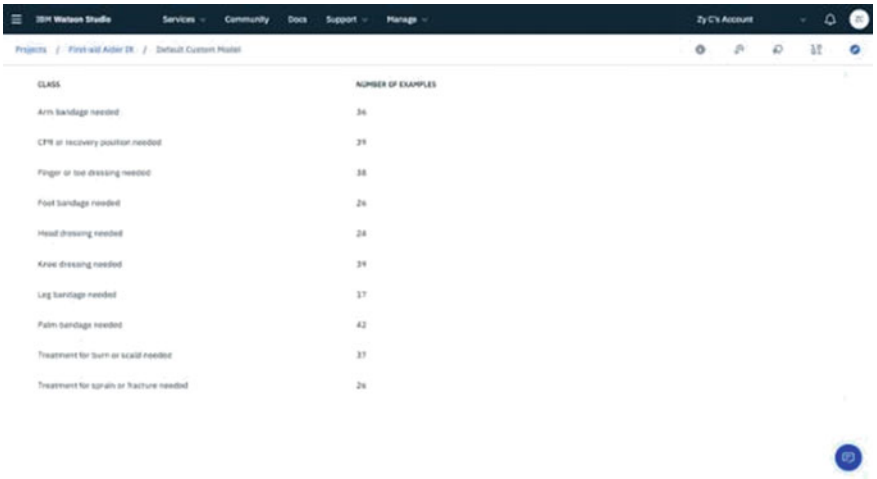

Fig. 9 Training image sizes for each classification class

```
//
//  ViewController.swift
//  ObjectsIdentifier
//
//  Created by james rochabrun on 4/13/18.
//  Copyright © 2018 james rochabrun. All rights reserved.
//

import UIKit
import CoreML
import Vision
import ImageIO
import Photos

class ImageClassificationViewController: UIViewController {
    // MARK: - IBOutlets

    @IBOutlet weak var imageView: UIImageView!
    @IBOutlet weak var cameraButton: UIButton!
    @IBOutlet weak var classificationLabel: UILabel! {
        didSet {
            classificationLabel.layer.cornerRadius = 10
            classificationLabel.layer.masksToBounds = true
        }
    }
    @IBOutlet weak var themeLabel: UILabel! {
        didSet {
            themeLabel.layer.cornerRadius = 10
            themeLabel.layer.masksToBounds = true
        }
    }

    // MARK: - Image Classification

    /// - Tag: MLModelSetup
    lazy var classificationRequest: VNCoreMLRequest = {
        do {

            let model = try VNCoreMLModel(for: firstAidAider().model)

            let request = VNCoreMLRequest(model: model, completionHandler: { [weak self] request, error in
                self?.processClassifications(for: request, error: error)
            })
            request.imageCropAndScaleOption = .centerCrop
            return request
        } catch {
            fatalError("Failed to load Vision ML model: \(error)")
        }
    }()

    /// - Tag: PerformRequests
    func updateClassifications(for image: UIImage) {
        classificationLabel.text = "Classifying..."

        let orientation = CGImagePropertyOrientation(image.imageOrientation)
        guard let ciImage = CIImage(image: image) else { fatalError("Unable to create \(CIImage.self) from \(image).") }

        DispatchQueue.global(qos: .userInitiated).async {
            let handler = VNImageRequestHandler(ciImage: ciImage, orientation: orientation)
            do {
                try handler.perform([self.classificationRequest])
            } catch {

                print("Failed to perform classification.\n\(error.localizedDescription)")
            }
        }
    }

    /// Updates the UI with the results of the classification.
    /// - Tag: ProcessClassifications
    func processClassifications(for request: VNRequest, error: Error?) {
        DispatchQueue.main.async {
            guard let results = request.results else {
                self.classificationLabel.text = "Unable to classify image.\n\(String(describing:
                    error?.localizedDescription))"
                return
            }
            // The `results` will always be `VNClassificationObservation`s, as specified by the Core ML model in this
                project.
            let classifications = results as! [VNClassificationObservation]

            if classifications.isEmpty {
                self.classificationLabel.text = "Nothing recognized."
            } else {
                // Display top classifications ranked by confidence in the UI.
                let topClassifications = classifications.prefix(10)
```

Fig. 10 Script in swift for the IR application

```
                let descriptions = topClassifications.map { classification in
                    // Formats the classification for display; e.g. "(0.37) cliff, drop, drop-off".
                    return String(format: "  (%.2f) %@", classification.confidence, classification.identifier)
                }
                self.classificationLabel.text = "Classification:\n" + descriptions.joined(separator: "\n")
            }
        }
    }

    // MARK: - Photo Actions

    @IBAction func takePicture() {

    /// - Tag: PerformRequests
    func updateClassifications(for image: UIImage) {
        classificationLabel.text = "Classifying..."

        let orientation = CGImagePropertyOrientation(image.imageOrientation)
        guard let ciImage = CIImage(image: image) else { fatalError("Unable to create \(CIImage.self) from \(image).") }

        DispatchQueue.global(qos: .userInitiated).async {
            let handler = VNImageRequestHandler(ciImage: ciImage, orientation: orientation)
            do {
                try handler.perform([self.classificationRequest])
            } catch {

                print("Failed to perform classification.\n\(error.localizedDescription)")
            }
        }
    }

    /// Updates the UI with the results of the classification.
    /// - Tag: ProcessClassifications
    func processClassifications(for request: VNRequest, error: Error?) {
        DispatchQueue.main.async {
            guard let results = request.results else {
                self.classificationLabel.text = "Unable to classify image.\n\(String(describing:
                    error?.localizedDescription))"
                return
            }
            // The `results` will always be `VNClassificationObservation`s, as specified by the Core ML model in this
                project.
            let classifications = results as! [VNClassificationObservation]

            if classifications.isEmpty {
                self.classificationLabel.text = "Nothing recognized."
            } else {
                // Display top classifications ranked by confidence in the UI.
                let topClassifications = classifications.prefix(10)
                let descriptions = topClassifications.map { classification in
                    // Formats the classification for display; e.g. "(0.37) cliff, drop, drop-off".
                    return String(format: "  (%.2f) %@", classification.confidence, classification.identifier)
                }
                self.classificationLabel.text = "Classification:\n" + descriptions.joined(separator: "\n")
            }
        }
    }

    // MARK: - Photo Actions

    @IBAction func takePicture() {
        // Show options for the source picker only if the camera is available.
        guard UIImagePickerController.isSourceTypeAvailable(.camera) else {
            presentPhotoPicker(sourceType: .photoLibrary)
            return
        }

        let photoSourcePicker = UIAlertController()
        let takePhoto = UIAlertAction(title: "Take Photo", style: .default) { [unowned self] _ in
            self.presentPhotoPicker(sourceType: .camera)
        }
        let choosePhoto = UIAlertAction(title: "Choose Photo", style: .default) { [unowned self] _ in
            self.presentPhotoPicker(sourceType: .photoLibrary)
        }

        photoSourcePicker.addAction(takePhoto)
        photoSourcePicker.addAction(choosePhoto)
        photoSourcePicker.addAction(UIAlertAction(title: "Cancel", style: .cancel, handler: nil))

        present(photoSourcePicker, animated: true)
    }

    func presentPhotoPicker(sourceType: UIImagePickerControllerSourceType) {
        let picker = UIImagePickerController()
        picker.delegate = self
        picker.sourceType = sourceType
```

Fig. 10 (continued)

```
        present(picker, animated: true)
    }
}

extension ImageClassificationViewController: UIImagePickerControllerDelegate, UINavigationControllerDelegate {
    // MARK: - Handling Image Picker Selection

    func imagePickerController(_ picker: UIImagePickerController, didFinishPickingMediaWithInfo info: [String: Any]) {
        picker.dismiss(animated: true)

        if let asset = info[UIImagePickerControllerPHAsset] as? PHAsset  {

            print("KMPHASSET \(asset.localIdentifier)/*)
            print("KMPHASSET \(asset.creationDate)/*) ⚠ String interpolation produces a debug description for an optional value; did you...

        }

        // We always expect `imagePickerController(:didFinishPickingMediaWithInfo:)` to supply the original image.
        let image = info[UIImagePickerControllerOriginalImage] as! UIImage
        imageView.image = image
        updateClassifications(for: image)
    }
}
```

Fig. 10 (continued)

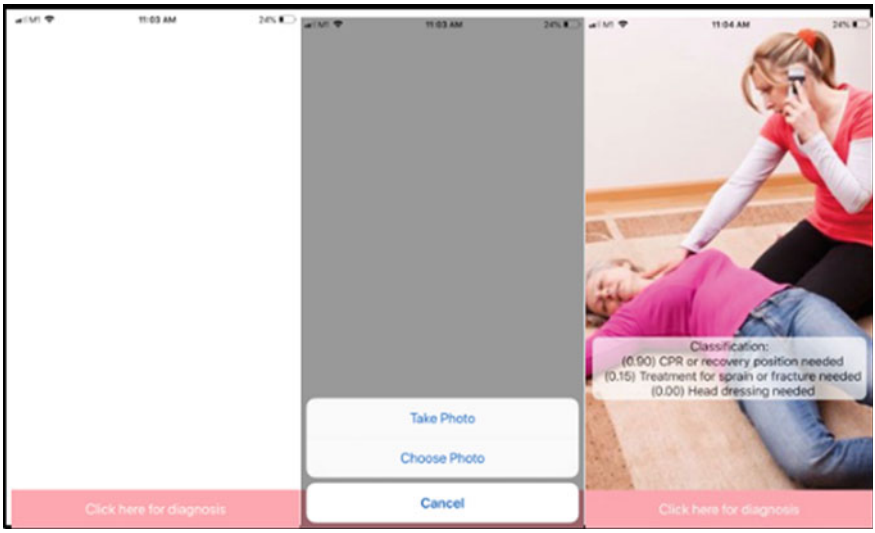

Fig. 11 IR application prototype

```
using System.Collections;
using System.Collections.Generic;
using UnityEngine;
using UnityEngine.UI;
using UnityEngine.Video;
using UnityEngine.EventSystems;

public class Slidertrack : MonoBehaviour, IPointerDownHandler, IPointerUpHandler {
    public VideoPlayer video;
    Slider tracking;
    bool slide = false;
    // Use this for initialization
    void Start () {
        tracking = GetComponent<Slider>();
    }

    public void OnPointerDown(PointerEventData a){
        slide = true;
    }


    public void OnPointerUp(PointerEventData a){
        float frame = (float)tracking.value * (float)video.frameCount;
        video.frame = (long)frame;
        slide = false;

    }

    // Update is called once per frame
    void Update () {
        if (!slide && video.isPlaying) {
            tracking.value = (float)video.frame / (float)video.frameCount;
        }

    }
}
```

Fig. 12 Script written in C++ for the UISlider

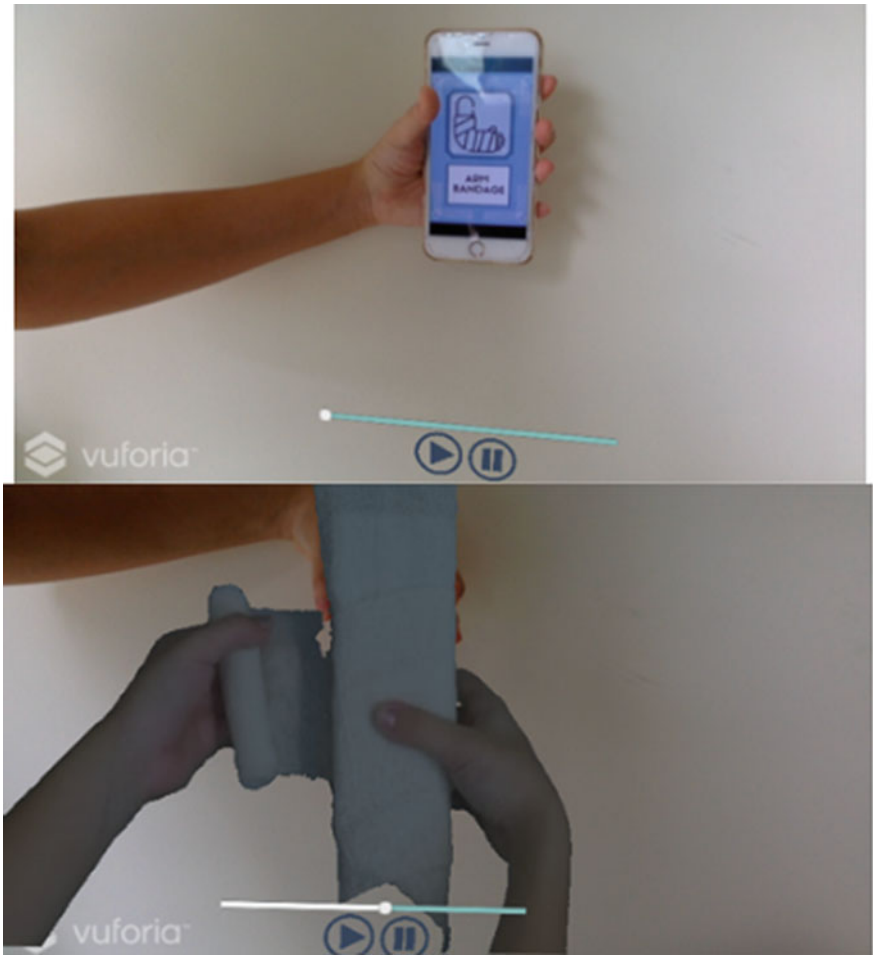

Fig. 13 Arm bandage tutorial displayed by the AR application prototype using a 2D Target Image on the iPhone

References

1. Rochlen, L. R., Levine, R., & Tait, A. R. (2016). First-Person Point-of-View–Augmented Reality for Central Line Insertion Training. Simulation in Healthcare: The Journal of the Society for Simulation in Healthcare, 1. https://doi.org/10.1097/sih.0000000000000185.
2. Association, P. (2010, April 12). Lack of first aid skills endangers up to 150,000 lives. Retrieved January 9, 2019, from https://www.theguardian.com/society/2010/apr/12/first-aid-skills-deaths.
3. First Aid 101. (n.d.). Retrieved January 9, 2019, from https://www.emssafetyservices.com/how-to/first-aid-101/#G.
4. Harvard Health Publishing. (n.d.). Six minutes to save a life. Retrieved January 9, 2019, from https://www.health.harvard.edu/newsletter_article/Six-minutes-to-save-a-life.

5. Paul.samwise.martin. “Chest Compressions: At What Rate Do You Perform CPR Compressions?” ProCPR Blog, 20 Oct. 2018, https://www.procpr.org/blog/training/cpr-chest-compression-rate.
6. Jamesrochabrun. (2018, June 05). Jamesrochabrun/ObjectRecognizer. Retrieved January 9, 2019, from https://github.com/jamesrochabrun/ObjectRecognizer.

The Synthesis and Design of Nanoparticles for Measuring Traction Forces in Living Cells

Su Minn Jeilene Ho, Ming Guo, Nicolas Fang, Satish Kumar Gupta, and Zheng Zhang

Abstract In the cytoplasm of mammalian cells, there are diverse and continuous intracellular movements essential for cell physiology, such as the transport of vesicles and other organelles. It is crucial to determine varied mechanical behaviours of the cell from viscous, viscoelastic, and poroelastic to pure elastic for differing physiological cell processes. In this project, poly(*N*-isopropylacrylamide), PNIPAM nanoparticles were synthesised and designed to measure traction forces in living cells via the passive microrheology method. Confocal microscopy was used for characterisation of the nanoparticles such as its size and shape. Subsequently, the nanoparticles were injected into a living cell's cytoplasm and intracellular movement was observed. The video was then analysed to determine the traction forces in the cells using the passive microrheology method. The nanoparticles were found to be non-toxic to the cells and were able to successfully permeate through the cell membrane. Thus, these nanoparticles can be used to further comprehend the mechanics of cells. By expanding on our knowledge of the intricacies of cell physiology, nanoparticle-based monitoring of cells paves the way for understanding the effect of cancer mutations on normal cells.

Keywords Nanoparticles · PNIPAM · MDCK cells · Confocal microscopy · Cell mechanics

1 Introduction

In the cytoplasm of mammalian cells, there are diverse and continuous intracellular movements essential for cell physiology, such as the transport of vesicles and other

Under the guidance of Mr. Zheng Zhang and Mr. Satish Kumar Gupta.

S. M. J. Ho (✉)
National Junior College, Singapore, Singapore
e-mail: jeileneho@gmail.com

M. Guo · N. Fang · S. K. Gupta · Z. Zhang
Mechanical Engineering Department, Massachusetts Institute of Technology, Cambridge, MA, USA

H. Guo et al. (eds.), *IRC-SET 2020*,
https://doi.org/10.1007/978-981-15-9472-4_64

organelles. While biological motors and enzymatic processes provide key driving forces for these activities, the mechanical properties determine the mechanical resistance that cellular compartments experience. Hence, in order to understand living cellular machinery, it is paramount that the active driving force and appropriate mechanical environment to overcome for transport [1] is determined. Furthermore, previous research has shown that cells have both viscoelastic [2] and poroelastic [3] properties. Viscoelasticity is defined as the property of a material that exhibits both viscous and elastic properties during deformation: Elastic materials deform instantaneously when stretched and return back to their original configuration instantly after the removal of stress, whereas viscous materials deform at a constant rate under constant stress while exhibiting time-dependent behaviour [4]. In the context of cells, those with viscoelastic properties deform under constant stress while demonstrating time-dependent behaviour and are able to fully recover to their original form once stress is removed. Poroelastic materials are porous mediums in which pore volume changes when an external load is exerted onto the material, resulting in the deformation of the solid. Hence, it is crucial to determine varied mechanical behaviours of the cell from viscous, viscoelastic, and poroelastic to pure elastic for differing physiological cell processes. To date, little groundwork has been made in the study of mechanical properties of the cytoplasm as compared to the research for the force that molecular motors generate both individually and collectively [5, 6].

This project aims to synthesise and design poly(*N*-isopropylacrylamide), PNIPAM nanoparticles in living cells for the measurement of traction forces by using the passive microrheology method. PNIPAM nanoparticles was mixed with fluorescein O-methacrylate (FMA) dye to enable inverted confocal microscopy to study surface morphology. Subsequently, the nanoparticles will be injected into a living cell's cytoplasm and a video of its movement within the cell is taken. Thereafter, the speed at which the nanoparticle moves in the cell and its diameter is obtained. These values can then be used to deduce the varied mechanical behaviours of the cell for physiological cell processes.

2 Methods

2.1 Synthesis of PNIPAM Particles

N-isopropylacrylamide (NIPAM, 6 g) monomer, N0-methylene-bisacrylamide (BIS, 150 mg) crosslinker and 2-Aminoethylmethacrylate hydrochloride (AEMA, 25.8 mg) [7] are dissolved in 150 mL deionized (DI) water and stirred under nitrogen flow at 60 °C. Subsequently, 10 mg of fluorescein O-methacrylate (FMA) dye was dissolved in 5 mL DI water and added into the mixture. 30 mL of mixture and 60 mL of DI water were added to a double-walled glass reactor coupled to a water circulation thermostat (Fig. 1). The reactor was then fitted with a reflux condenser, a mechanical stirrer, a septum and a nitrogen gas inlet. Under nitrogen and stirring,

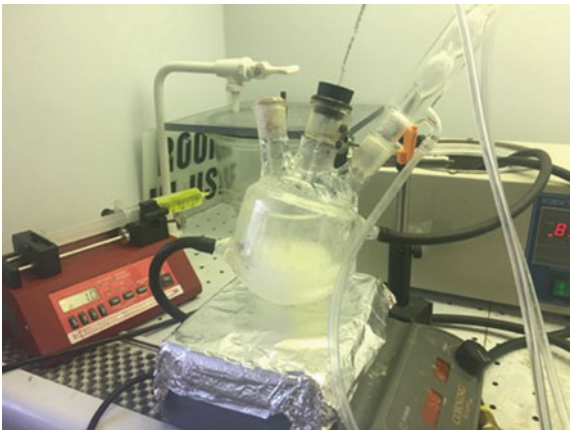

Fig. 1 Synthesis of PNIPAM nanoparticles with the use of a double-walled glass reactor

the reaction mixture is heated to 80 °C [8]. Then, 31.2 mg of ammonium persulfate catalyst dissolved in 6 mL of water is added into the reactor. The rest of the mixture was added into the reactor at 1 mL/min using a syringe pump at the rate of 1 mL/min. After a few hours, the reaction mixture was allowed to cool before centrifugation.

2.2 Inverted Confocal Microscopy

An inverted confocal microscope (Leica, Leica TCS SP8 MP) was used for its distinctive ability to control field depth and eliminate or reduce background information away from the focal plane which results in image degradation [10]. Inverted confocal microscopy was used to evaluate 3 characteristics of the nanoparticles. Firstly, it was used to check if the fluorescence of the nanoparticles came through. Secondly, if the sample is too dense and needs to diluted, this is determined when clustering of the nanoparticles is observed. Lastly, the spherical shape and size of the nanoparticles is verified. Furthermore, the inverted confocal microscope is used to determine if the nanoparticles have successfully entered the cells while a video is recorded. A schematic of the inverted confocal microscope can be found in Fig. 2.

2.3 Cell Culture

Madin-Darby Canine Kidney (MDCK) cells were cultured in DMEM medium [10% Fetal bovine serum (FBS), 1% Penicillin-Streptomycin (PS)]. As the cells were transfected with Green Fluorescent Protein (GFP), they were able to fluoresce under the inverted confocal microscope. As the nuclei of the cells are very large (~10 μm)

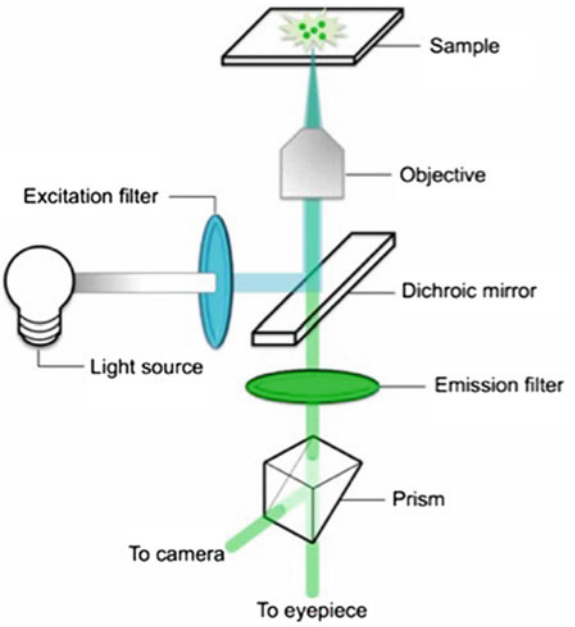

Fig. 2 Schematic of inverted confocal microscope [9]

relative to the size of the PNIPAM nanoparticles synthesised, it is easy to differentiate between the cells and the nanoparticles during imaging.

2.4 Dynamic Light Scattering

Dynamic Light Scattering (DLS) (Wyatt, DynaPro NanoStar) was used to determine the size of the nanoparticles across a series of temperatures from 25 °C to 45 °C in intervals of 5 °C. Each data set consisted of 10 acquisitions with the time interval of 5 s while the set temperatures used were 25 °C, 30 °C, 32 °C, 35 °C, 40 °C and 45 °C (Fig. 3a). Solvent specific parameters were set to that of water as the samples had densities close to that of water (Fig. 3b).

A stability test was also performed to deduce the stability of the PNIPAM molecules between 30 °C and 35 °C. This verifies PNIPAM's ability to reform into its original size after contraction at temperatures above 32 °C.

2.5 FIJI

FIJI was used to track the movement of the nanoparticles in the cell using the plugin, *TrackMate*. The parameters were set as shown in Fig. 4a.

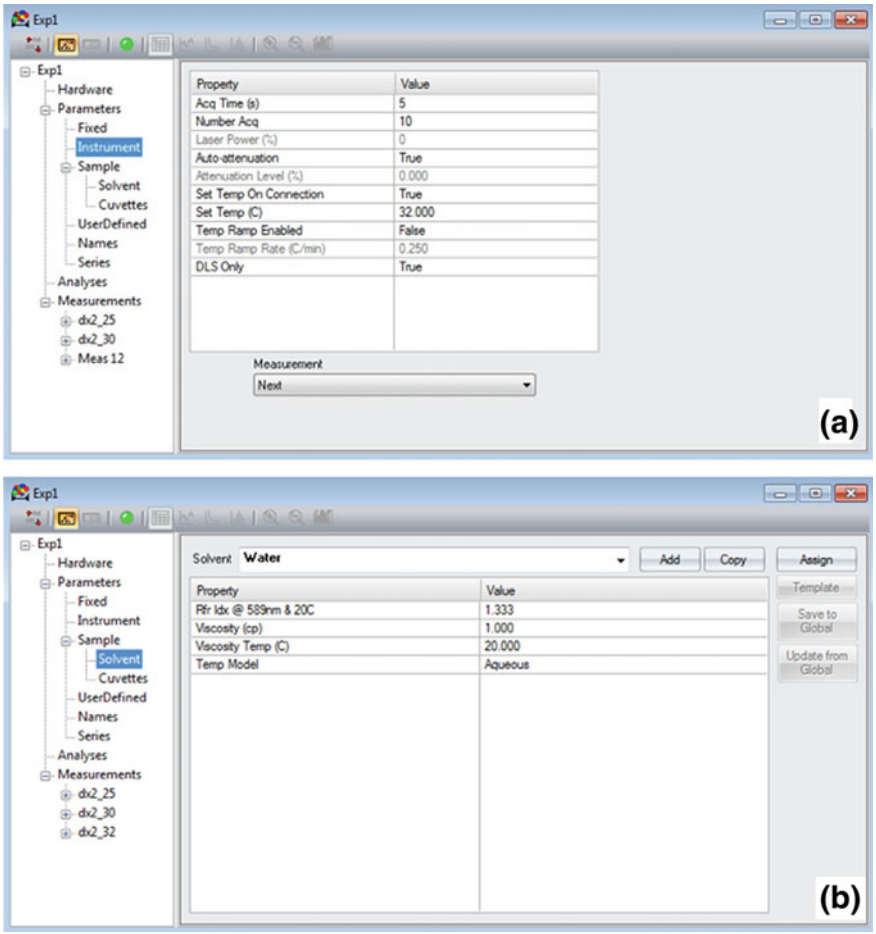

Fig. 3: **(a)** Instrumental and **(b)** solvent parameters for DLS

3 Results

Two sizes of spherical PNIPAM particles are used. During the synthesis of Batch A of nanoparticles, the surfacant, Sodium Dodecyl Sulfate (SDS) was added to form smaller particles of the average size of 700 nm at room temperature which is determined through DLS from preliminary results (Fig. 4b(i)). In Batch B, surfacant was not added and it was found that the size of the nanoparticles was an average of 1067 nm at room temperature (Fig. 4b(ii)). Additionally, it was observed that the radius of the particles decreases drastically after 32 °C which verifies its expected thermoresponsiveness.

Furthermore, the stability of the PNIPAM nanoparticles from Batch B was also analysed. From Fig. 4c, it was observed that there was no significant variation of the particle radius throughout the three runs for each temperature (30 °C and 35 °C).

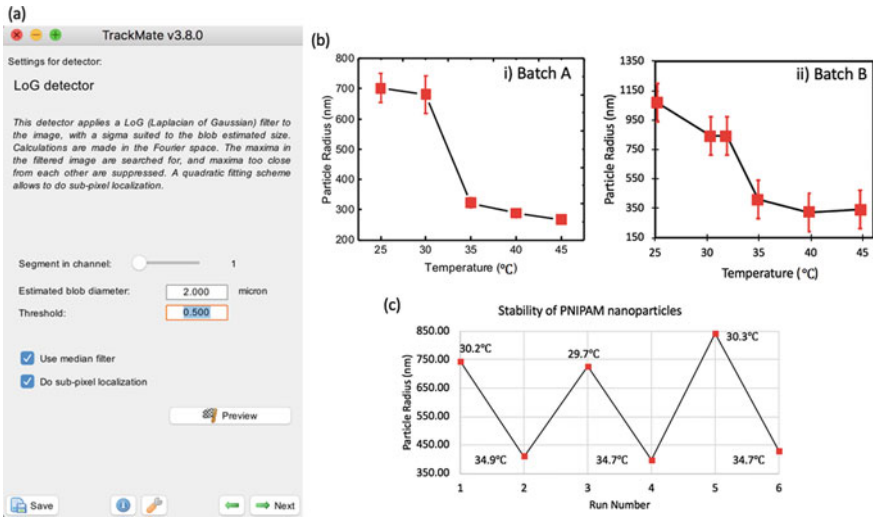

Fig. 4 **(a)** Parameters for *FIJI* **(b)** Dynamic Light Scattering of **i)** Batch A nanoparticles **ii)** Batch B nanoparticles **(c)** Stability test between 30 °C and 35 °C

Hence, we deduce that the PNIPAM nanoparticles are relatively stable. However, it was observed that in comparison to the first and second runs (Run 1–4) for each temperature, the third run (Run 5–6) had a greater variation. Thus, increased repetition of readings will enable the verification of nanoparticle stability.

To add on, it was discovered that the nanoparticles had inconsistent sizes as shown in **Appendix**. This is possibly due to the lack of surfactant added during the synthesis of the particles from Batch B which results in inconsistent sizes of PNIPAM nanoparticles.

For Batch A, it was deduced that the particles had fluoresced and there was no clustering when diluted (Fig. 5b, c). Images collected from the inverted confocal microscope confirmed that the nanoparticles were spherical. However, for batch B, it was discovered that the nanoparticles emitted fluorescence weakly and many that

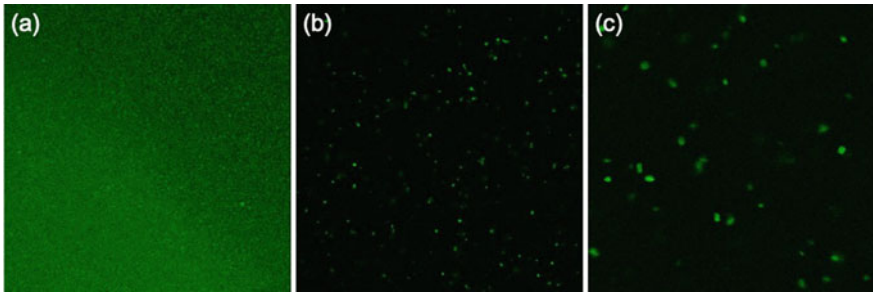

Fig. 5 Inverted confocal microscopy of batch A **(a)** dense sample (184.88 × 184.88 microns) **(b)** dilute sample (184.88 × 184.88 microns) **(c)** dilute sample (69.76 × 69.76 microns)

were present in the bright-field image (Fig. 7b) was not seen in the fluorescent image (Fig. 7a). This is possibly due to the FMA dye in the nanoparticles no longer being excited due to constant exposure to visible light.

To verify the proposed non-toxicity of the nanoparticles, 50 μL of nanoparticles from Batch A was added to the DMEM medium of the sub-cultured cells. It was discovered that the nanoparticles did not affect cell growth in the culture and thus were deemed non-toxic to the living MDCK cells as illustrated in Fig. 6.

Subsequently, with the use of the inverted confocal microscope, it was deduced that the nanoparticles had successfully entered the cells. This is determined by adding varying amounts of nanoparticles from both batches into the sub-culture of the cells in a (35 mm × 10 mm) petri dish. The cells are left in the incubator for at least a day to grow and attach to the bottom of the petri dish. Once taken out, the solution is poured out and the samples are washed 3 times with 2 mL of Phosphate-Buffered Saline (PBS) each time. In Fig. 6, it is observed that there are green specks in the

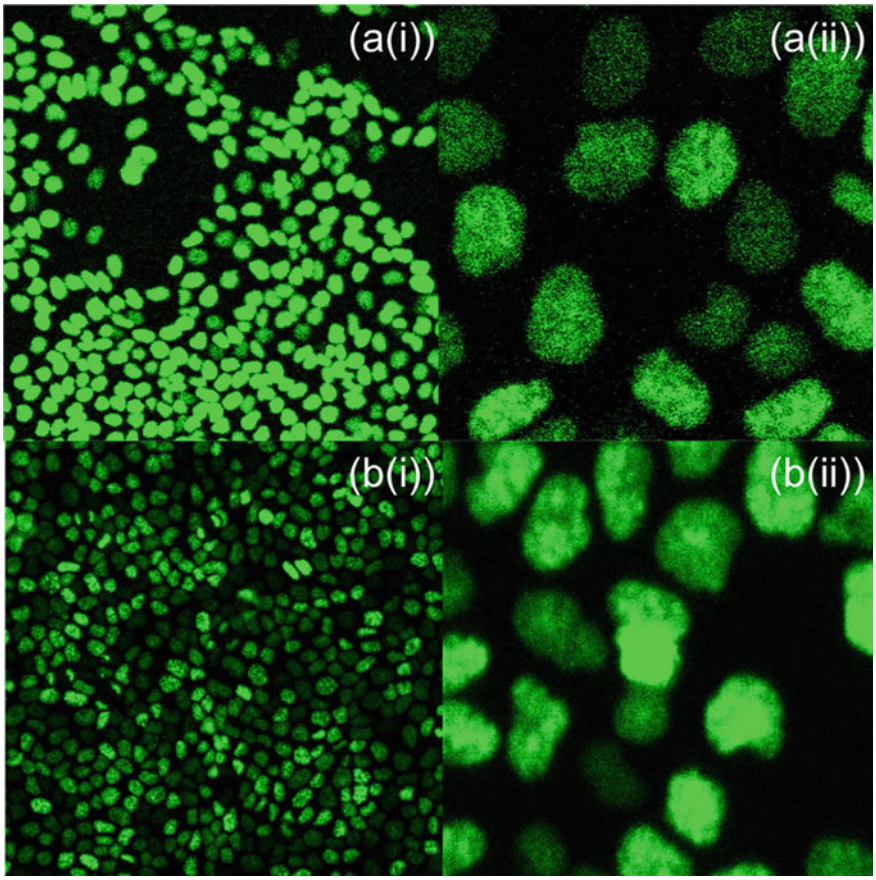

Fig. 6 **(a)** MDCK cells with 50 μL of Batch A **i)** zoomed out image **ii)** zoomed in image. **(b)** MDCK cells with no nanoparticles **i)** zoomed out image **ii)** zoomed in image

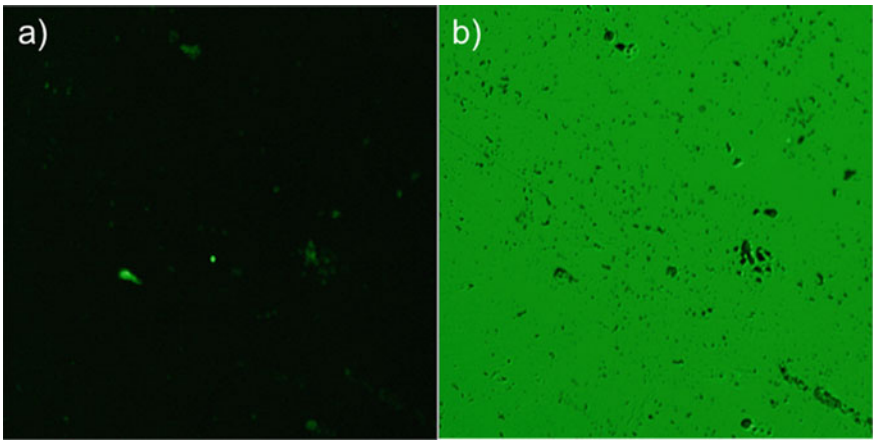

Fig. 7 Inverted confocal microscopy of Batch B (482.23 × 482.23 microns) **(a)** under fluorescence **(b)** bright-field

image for the MDCK cells with nanoparticles (Fig. 6a(ii)) which is not found in the images taken of just MDCK cells (Fig. 6b(ii)). The green specks are known to be the nanoparticles. As additional nanoparticles that did not enter the MDCK cells would have been washed away previously, it is determined that the nanoparticles have successfully entered the cells.

The MDCK cells with 100 μL of Batch B were analysed with the use of *FIJI*. The yellow pathways of the particles previously marked by the software with purple circles (Fig. 8a) were drawn (Fig. 8b). However, it is known that the particles did not travel as much as the pathways suggested from the video taken. Thus, this method of tracking the cells is inaccurate. However, the accuracy of this measurement can

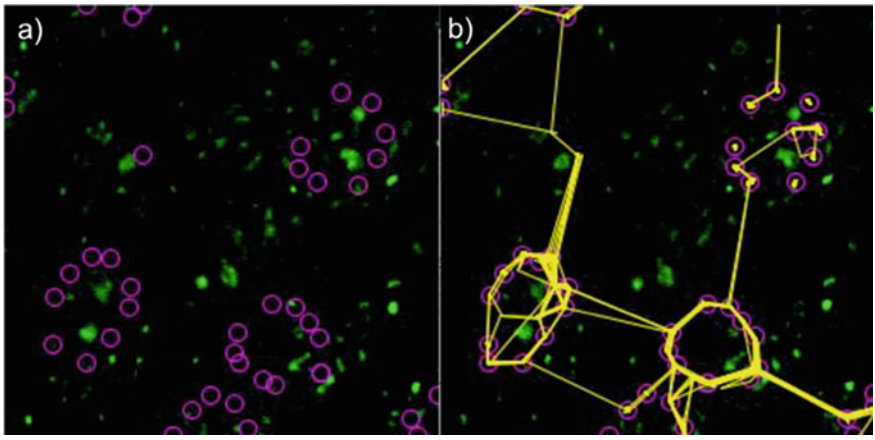

Fig. 8 **(a)** Particles marked by *FIJI* are demarcated by the purple cells **(b)** Path of particles is represented by yellow lines for MDCK cells with 100 μL of Batch B

be improved by increasing the fluorescence of the nanoparticles such that it is more easily detected by the software.

4 Discussion

This work aimed to synthesise and design poly(*N*-isopropylacrylamide), PNIPAM nanoparticles to measure traction forces in living cells. It was found that Poly-NIPAM particles of sizes 700nm and 1067 nm were able to successfully permeate the cells' membrane and were not toxic to the cell. This can have many further applications as it is a non-invasive method to understand the cells physiology.

PNIPAM particles also have thermoresponsive properties which can be explored further. It is known that PNIPAM has a volume phrase transition temperature of 32 °C. Below 32 °C, PNIPAM particles are clear and transparent (Fig. 9a). Above 32 °C, the nanoparticles will contract and become cloudy white instead (Fig. 9b). Hence, they can potentially be used to sense the internal temperature of the living cell.

Furthermore, PNIPAM particles have also been found to have pH-responsive properties by incorporating a weak acid or base into the NIPAM network through co-polymerisation [11]. Thus, this concept can be further explored by testing for weak acid/base and NIPAM combinations that are non-toxic to the cells. Consequently, PNIPAM particles can also serve as pH-sensors of the cells' cytoplasm.

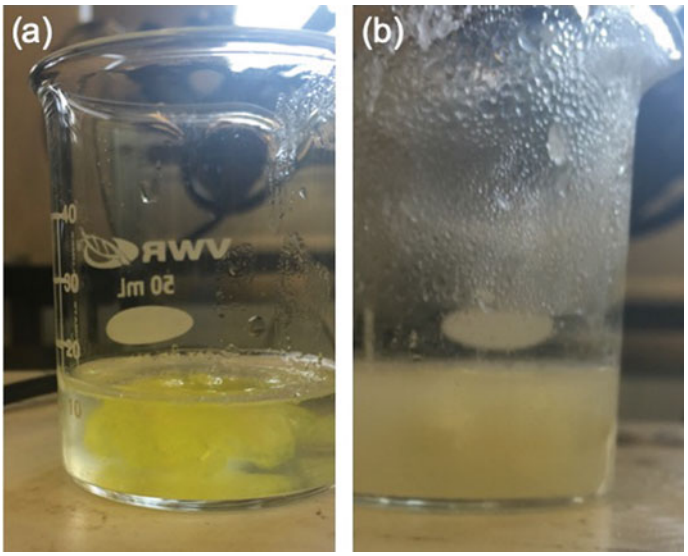

Fig. 9 **(a)** Clear PNIPAM solution with yellow cluster below 32 °C **(b)** Cloudy white PNIPAM solution with white cluster above 32 °C

Another possible advancement of the project is by manipulating the nanoparticles in the cell with optical tweezers. The nanoparticles can be dragged unidirectionally with constant forces exerted on them with the aid of optical tweezers through optical trapping [1].

Lastly, different characteristics of the nanoparticles can be further explored such as a greater size range and even varying shapes such as cylindrical or pyramidal shapes. The effect of cancer mutations on the cells can also be investigated by injecting nanoparticles into a cancerous cell and a normal cell. This can be determined by evaluating the difference in mechanical properties of the living cells cytoplasm.

Acknowledgements First and foremost, I will like to thank both Professor Ming Guo and Professor Nicholas Fang from the Department of Mechanical Engineering, Massachusetts Institute of Technology, for giving me the opportunity to work on this amazing project. Additionally, I will like to thank my mentors, Mr. Zheng Zhang and Mr. Satish Kumar Gupta for providing me guidance throughout this project. I will also like to thank my tutor Nathan Siegel for his assistance in this project and the first week teaching assistants for their dedication in teaching us how to operate LaTeX. Additionally, I am grateful for the feedback I received from Michael Fraczek, Grace Sun and the last week teaching assistants. I will like to thank the Centre of Excellence in Education and Massachusetts Institute of Technology for providing us with this wonderful opportunity. I am eternally grateful for the Ministry of Education, Singapore for sponsoring me for this programme and for Mr. Leonard Ngoei, my secondary school teacher who introduced me to scientific research and has guided me all these years. Last but not least, my greatest thanks to my family for supporting me throughout my life and my journey to pursue my passion.

Appendix: Dynamic Light Scattering

See Fig. 10, 11, 12, 13, 14 and 15.

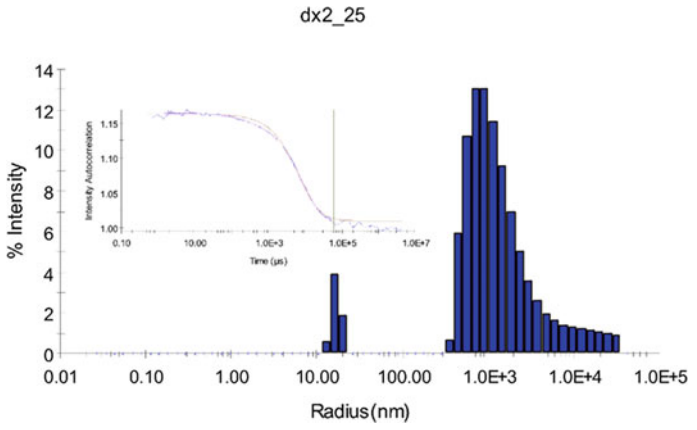

Fig. 10 DLS readings at 25 °C

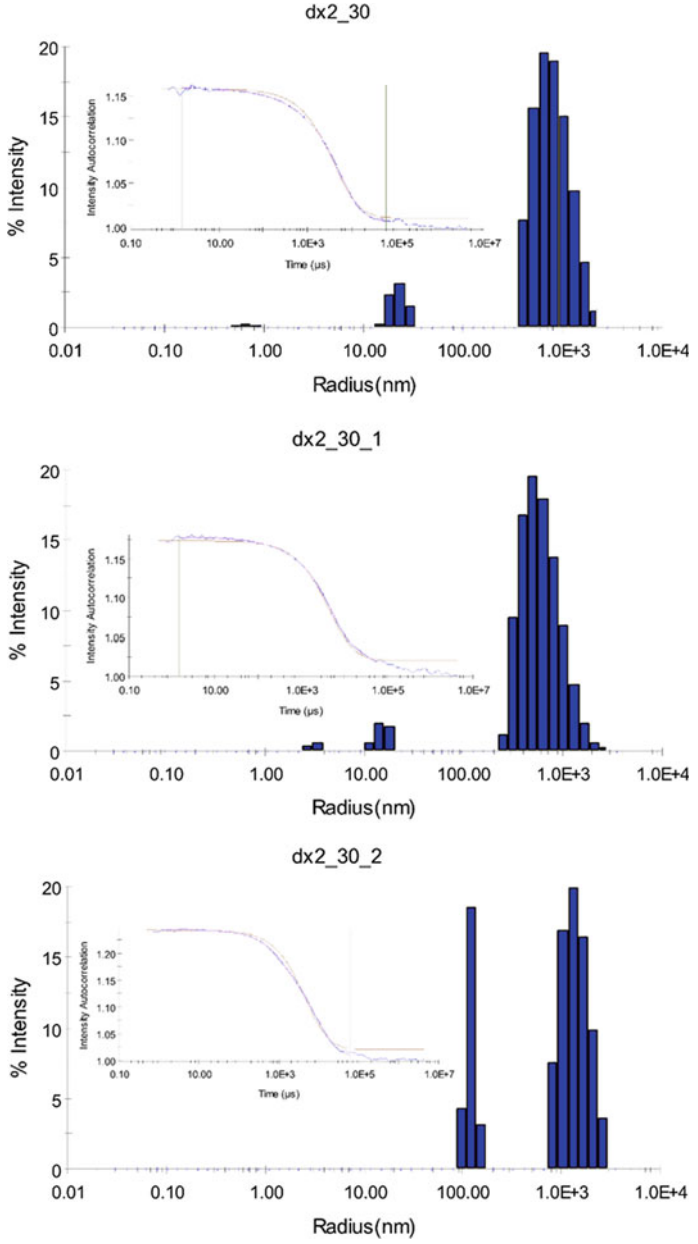

Fig. 11 DLS readings for all 3 runs at 30 °C

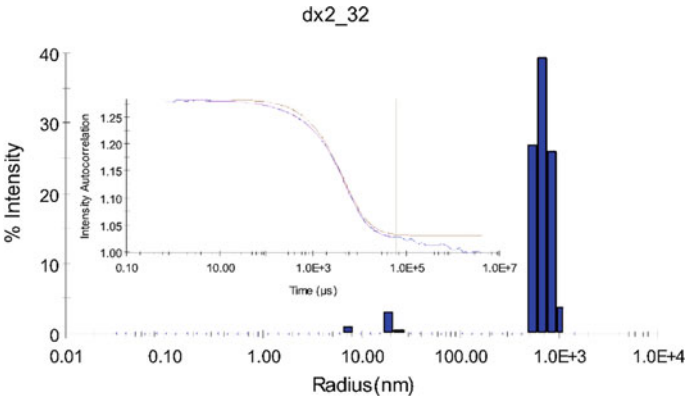

Fig. 12 DLS readings at 32 °C

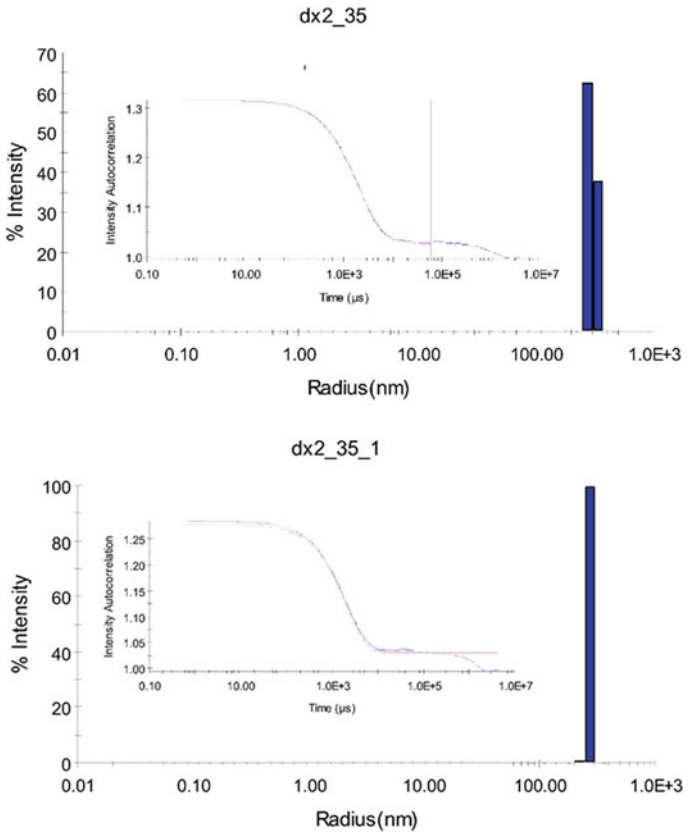

Fig. 13 DLS readings for all 3 runs at 35 °C

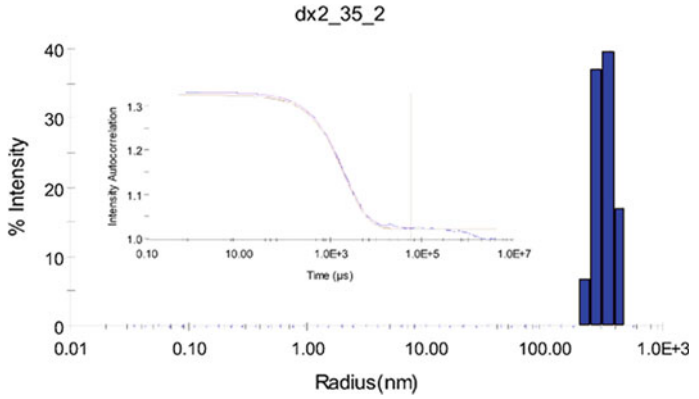

Fig. 13 (continued)

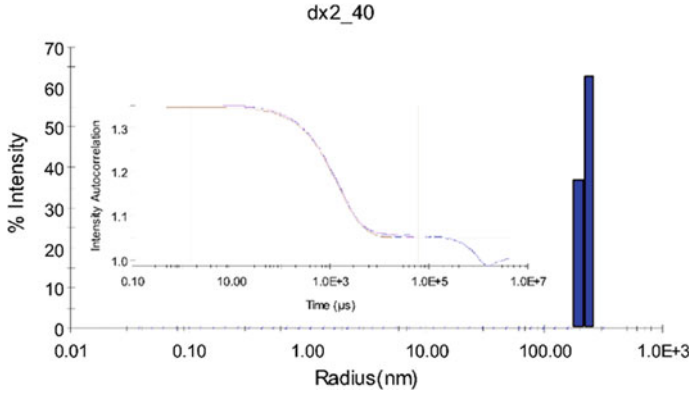

Fig. 14 DLS readings at 40 °C

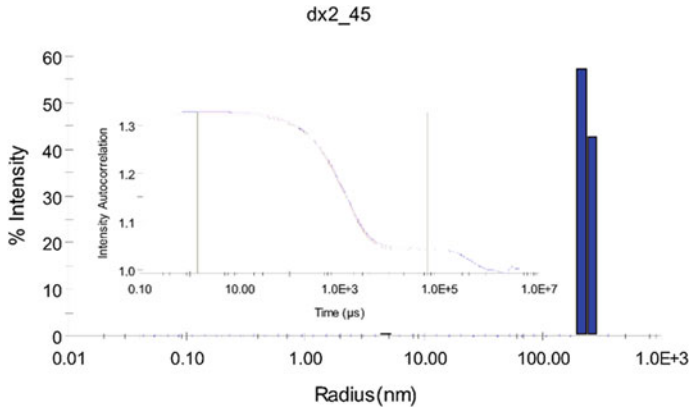

Fig. 15 DLS readings at 45 °C

References

1. J. Hu, S. Jafari, Y. Han, A. J. Grodzinsky, S. Cai, and M. Guo. Size-and speed-dependent mechanical behavior in living mammalian cytoplasm. *Proceedings of the National Academy of Sciences*, 114(36):9529–9534, 2017.
2. A. R. Bausch, W. M¨oller, and E. Sackmann. Measurement of local viscoelasticity and forces in living cells by magnetic tweezers. *Biophysical journal*, 76(1):573–579, 1999.
3. E. Moeendarbary, L. Valon, M. Fritzsche, A. R. Harris, D. A. Moulding, A. J. Thrasher,E. Stride, L. Mahadevan, and G. T. Charras. The cytoplasm of living cells behaves as a poroelastic material. *Nature materials*, 12(3):253, 2013.
4. G. Papanicolaou and S. Zaoutsos. Viscoelastic constitutive modeling of creep and stress relaxation in polymers and polymer matrix composites. In *Creep and fatigue in polymermatrix composites*, pages 3–59. Elsevier, 2019.
5. A. G. Hendricks, E. L. Holzbaur, and Y. E. Goldman. Force measurements on cargoes in living cells reveal collective dynamics of microtubule motors. *Proceedings of the National Academy of Sciences*, 109(45):18447–18452, 2012.
6. M. Guo, A. J. Ehrlicher, M. H. Jensen, M. Renz, J. R. Moore, R. D. Goldman, J. Lippincott-Schwartz, F. C. Mackintosh, and D. A. Weitz. Probing the stochas-tic, motor-driven properties of the cytoplasm using force spectrum microscopy. *Cell*,158(4):822–832, 2014.
7. T. Still, K. Chen, A. M. Alsayed, K. B. Aptowicz, and A. Yodh. Synthesis of micrometer-size poly (n-isopropylacrylamide) microgel particles with homogeneous crosslinker den-sity and diameter control. *Journal of colloid and interface science*, 405:96–102, 2013.
8. M. Wang, A. M. Mihut, E. Rieloff, A. P. Dabkowska, L. K. M ̊ansson, J. N. Immink, E. Sparr, and J. J. Crassous. Assembling responsive microgels at responsive lipid mem-branes. *Proceedings of the National Academy of Sciences*, 116(12):5442–5450, 2019.
9. global fluorescence microscope market top players 2019 – 2025: Bruker, olympus, leica, zeiss, thermo fisher scientific inc., picoquant, May 2019.
10. T. J. Fellers and M. W. Davidson. Introduction to confocal microscopy.
11. A. Ahiabu and M. J. Serpe. Rapidly responding ph-and temperature-responsive poly(n-isopropylacrylamide)-based microgels and assemblies. ACS Omega, 2(5):1769–1777, 20.

An Investigation into the Ability of Mesocarp of Durian, Lemon, Pomelo and Sweet Orange in Reducing Residual Nitrite Content in Processed Meat Products

Wei Le Lim, Zong Hon Justyn Lae, Zhi Yuan Melvin Loh, and Conrad Zheng

Abstract Sodium nitrite is a preservative used in processed meat which can react with compounds found in the meat to form carcinogenic products.Research has shown that the mesocarp (the middle layer of the peel) of some citrus fruits is able to reduce the nitrite content of processed meat when incorporated in the meat during the manufacturing process. Hence, we investigated the effectiveness of the mesocarp of Durian (*Durio zibethinus*), Lemon (*Citrus limon*), Pomelo (*Citrus maxima*) and Sweet Orange (*Citrus sinensis*) in reducing nitrite content. In our experiment, fruit mesocarp was mixed with processed chicken sausages. The concentration of sodium nitrite in the sausages was measured before and after the mixing. The type of mesocarp, mesocarp concentration and duration of reaction between the mesocarp and sausages were varied in our experiments. The mesocarp concentrations we used were 5% and 10%, while the duration of reaction was 1 day and 1 week. We found that at 10% concentration of mesocarp and after 1 week of reaction, lemon was the most effective at reducing residual nitrite content, followed by durian, pomelo and sweet orange.

Keywords Mesocarp · Nitrite · Processed meats · Food science · Cancer

W. Le Lim (✉) · Z. H. J. Lae · Z. Y. M. Loh · C. Zheng
Raffles Institution, Singapore, Singapore
e-mail: 20YLIMW143A@student.ri.edu.sg

Z. H. J. Lae
e-mail: 20YLAEZ761E@student.ri.edu.sg

Z. Y. M. Loh
e-mail: 20YLOHZ095A@student.ri.edu.sg

C. Zheng
e-mail: conrad.zheng@ri.edu.sg

H. Guo et al. (eds.), *IRC-SET 2020*,
https://doi.org/10.1007/978-981-15-9472-4_65

1 Introduction

Nitrites and nitrates are used in the manufacturing of meat products. Sodium nitrite is a preservative that fights harmful bacteria in ham, salami and other processed and cured meats and also gives them their pink colouration. However, extra nitrite, or residual nitrite that is not involved in preservation might be harmful. During the manufacturing process of certain meats, sodium nitrite combines with naturally present amines in the meat to form carcinogenic N-nitroso compounds. When ingested, these compounds are associated with the cause of cancer [1].

Through research, we found that the mesocarp of citrus fruits such as lemon and orange can reduce nitrite levels in meat products. Mesocarp is defined as the middle layer of pericarp, or the fleshy part of certain fruits. Mesocarp of certain fruits might contain biologically active compounds that could reduce sodium nitrite [2]. Moreover, the biologically active compounds, such as flavonoids and vitamin C, contain antioxidant properties that may exert higher health promoting effects [3].

Hence, we investigated the effectiveness of the mesocarp of durian, lemon, pomelo and sweet in reducing residual nitrite content in sausages. Pomelo was chosen as it is a tropical citrus fruit that was untested, and durian as it is a tropical, non-citrus fruit that could be a potential alternative to citrus mesocarp. Tropical fruits could potentially be easier to obtain given Singapore's tropical climate.

We evaluated the effectiveness of the four fruit mesocarp in reducing residual nitrite content by using a colourimetric procedure to test for nitrite reduction levels in cured chicken sausages that had been treated with the four different types of mesocarp. Nitrite reacts with NEDA-Sulfa in acidic solutions to produce a purple-coloured solution according to the equation below. The more intense the colour of the solution, the higher the concentration of nitrite present [4].

$$\begin{aligned} &C_{12}H_{14}N_2(\text{NEDA}) + C_6H_8O_2N_2S\ (\text{sulfa}) + NO_2^-(\text{nitrite}) + H^+(\text{acid}) \\ &\quad \rightarrow C_{18}H_{19}O_2N_5S(\text{purple colour}) + 2\,H_2O \end{aligned}$$

We measured the absorbance reading of the samples using a microplate spectrophotometer and plotted a calibration graph against concentration of sodium nitrite, thereby concluding which mesocarp was most effective in reducing residual nitrite content.

From our background reading, all citrus fruit albedo (mesocarp) contains the biologically active compounds responsible for reducing nitrite content [2]. Hence, we hypothesised that lemon, orange, pomelo mesocarp, being citrus fruits, are more effective in reducing residual nitrite content than durian. However, currently not all the biologically active compounds that are responsible for reducing nitrite content have been identified and we could not hypothesise which fruit mesocarp amongst the citrus fruits might be able to reduce the greatest amount of nitrite content.

We hope that through our research, manufacturers are able to use fruit mesocarp to effectively reduce residual nitrite content in processed meat products for the benefit of consumers' health.

2 Materials and Methods

2.1 Materials

The materials and chemicals used in our project are: cured chicken sausages, sweet orange, pomelo, lemon and durian mesocarp, potassium ferrocyanide, zinc acetate, borax solution, sulfanilamide, hydrochloric acid, *N*-1-naphthalenediamine dihydrochloride (NEDA) and sodium nitrite.

The equipment used in our project include a microplate spectrophotometer, an electronic balance, micropipettes, a blender and other common laboratory apparatus like filter funnels, filter paper, beakers, glass rods, test tubes and measuring cylinders.

2.2 Method

Preparing the mesocarp

1. Cut out lemon mesocarp from the fruit and place the mesocarp in a beaker and immediately keep it in the freezer. When needed, the lemon mesocarp is thawed at room temperature.
2. Use a blender to obtain a powdery form of mesocarp. Then, put it in an oven on low heat for 2 days so as to remove water content.

Mixing the dry cured chicken sausages with the fruit mesocarp

1. Weigh out about 1 g of cured chicken sausages into three beakers each.
2. Add lemon mesocarp separately (0 g, 0.05 g and 0.1 g) into cured chicken sausages of the three beakers. The sample with 0% mesocarp by mass is the control sample. Mix the meat with the mesocarp using a glass stirring rod. This is the first set of samples.
3. Repeat Steps 1 and 2. This is the second set of samples.
4. Leave the two sets of samples (one for 1 day and the other for 7 days) respectively in the freezer for the reaction between the compounds in mesocarp and nitrite in the sausage to take place.

Deproteination

The purpose of deproteination is to precipitate the proteins. This is necessary because proteins have a certain UV absorption and could give a false reading as we are using a colourmetric method (nitrite test) to measure the results. Moreover, proteins are colloids which make the solution turbid and difficult to read on the microplate spectrophotometer [5].

1. Remove samples from freezer (after 1 day/7 days respectively) to stand at room temperature for 10 min with occasional swirling.

2. Add 1 cm^3 of saturated borax solution into all the beakers and heat the beakers for 15 min on a boiling water bath.
3. Allow all the beakers and its contents to cool to room temperature and add successively 200 μl of potassium ferrocyanide and 200 μl of zinc acetate. Mix thoroughly after each addition.
4. Allow all the beakers to stand for 30 min at room temperature for full precipitation of proteins before filtering the solution into a test tube so as to obtain a clear solution.

Nitrite Test

1. Prepare 0, 2.5, 5.0, 7.5 and 10.0 mg/dm^3 of standard sodium nitrite for calibration.
2. After the deproteination of samples, add 100 μl of sample solutions, standard sodium nitrite solutions and water each into separate wells of the microplate.
3. Repeat Step 2 on the other rows of wells of the microplate. The repetition is for the averaging of the absorbance readings for reliability of results.
4. Add 600 μl of water, 100 μl of sulphanilamide and 60 μl of hydrochloric acid each to every well of the microplate. Then leave the cuvettes for 5 min in the dark as light might interfere with the reaction.
5. Add 20 μl of *N*-1-naphthylethylenediamine dihydrochloride (NEDA) to each well and leave for 5 min in the dark. NEDA reacts with nitrite in the solution to give a purple coloured solution. Then, add 120 μl of water to each well, making the volume of the wells 1 ml each.
6. Dispose of all NEDA containing waste in the waste bottles in the fume hood.

Calculation nitrite level in the sausage

1. Measure the absorbance of the standard solutions and samples at 538 nm using a microplate reader.
2. Plot a calibration graph of concentration of nitrite against absorbance readings. The data obtained from the standard nitrite solutions is used for this plot. Average the absorbance readings obtained for each of the known
3. Concentrations. After plotting the points, draw a best fit line on the graph (Fig. 1).
4. Estimate the nitrite concentration in the samples by comparing the absorbance of each sample to the nitrite concentration on the graph.
5. Repeat the procedure with pomelo, sweet orange and durian mesocarp.

Comparison of the effectiveness of the different fruit mesocarp

Using the results, determine the effectiveness of the different types of mesocarp by calculating the percentage reduction in nitrite concentration in each sample. This is done by comparing the nitrite concentration in each sample to the control.

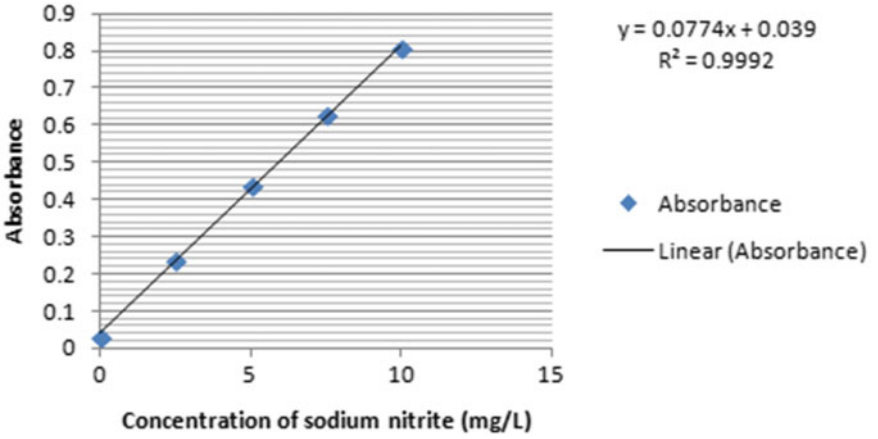

Fig. 1 A sample of a sodium nitrite calibration graph from one of our experiments

3 Results

The experiment was performed three times and the absorbance readings from the microplate spectrophotometer were used to determine the nitrite concentration in the sausages. A computer programme was used to correct the readings by doing a pathlength correction. This was done to ensure that the random errors made during the experiments were minimised to get a more reliable and accurate reading. The average nitrite concentrations from the three experiments are summarised in the table (Tables 1, 2). More detailed data from each experiment, including absorbance readings, can be found in Appendix.

Table 1 Average reduction of sodium nitrite in meat mixed with mesocarp for 1 day

		Duration: 1 day	
Percentage of mesocarp (%)	Mesocarp	Average nitrite concentration after reaction (mg/L)	Percentage of nitrite concentration reduced (%)
0	Control	1.25	0
5	Lemon	1.13	9.90
10		0.948	24.3
5	Orange	1.18	5.81
10		0.995	20.5
5	Pomelo	1.08	13.7
10		0.995	20.5
5	Durian	1.12	10.6
10		1.04	16.7

Table 2 Average reduction of sodium nitrite in meat mixed with mesocarp for 1 week

		Duration: 1 week	
Percentage of mesocarp (%)	Mesocarp	Average nitrite concentration after reaction (mg/L)	Percentage of nitrite concentration reduced (%)
0	Control	1.15	0
5	Lemon	0.544	52.7
10		0.467	59.5
5	Orange	0.742	35.5
10		0.699	39.3
5	Pomelo	0.833	27.7
10		0.695	39.6
5	Durian	0.786	31.8
10		0.665	42.3

According to our results, the average nitrite concentration in the samples after reaction all ranged below the average nitrite concentration of the control, showing that each mesocarp did reduce nitrite content.

4 Discussion

The average percentage of nitrite concentration reduction for the four fruit mesocarp in Experiments 1, 2 and 3 is summarised in Fig. 2.

Our discussion will focus on three areas:

1. **Trends in Nitrite Reduction**

Type of Mesocarp

At 10% concentration and 1 week, the higher concentration and longer reaction time we experimented with, lemon was the most effective mesocarp, by a large margin, at reducing residual nitrite content. The differences in nitrite reduction levels between orange, pomelo and durian mesocarp at the same concentration and reaction time were not significant. Lemon is also the most effective mesocarp at 10% concentration and 1 day, and at 5% concentration and 1 week. At the lower concentration and shorter reaction time, 5% and 1 day, pomelo was the most effective mesocarp.

This difference in the effectiveness may be caused by the varying amounts of the biological active compounds responsible for reducing nitrite content among the fruit mesocarp, with lemon likely having the most.

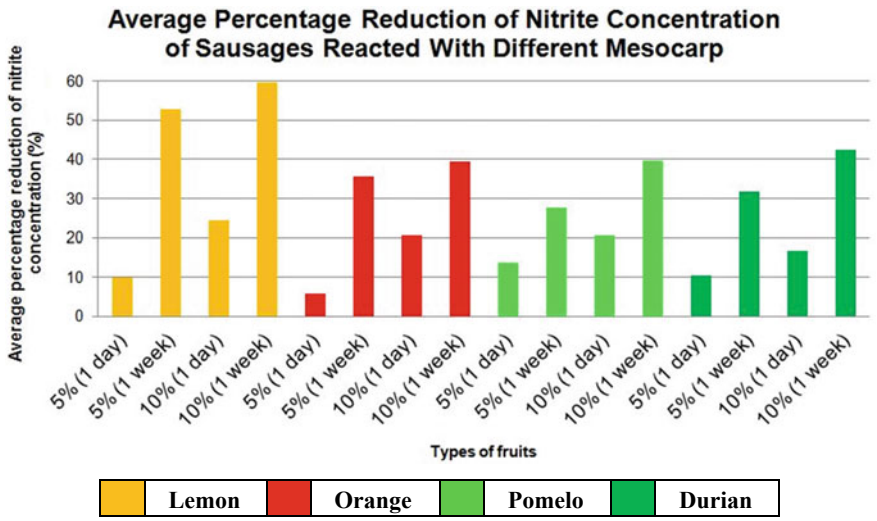

Fig. 2 Graph of average percentage reduction of nitrite concentration of sausages reacted with different mesocarp of different concentrations (5 and 10%) and over different periods (1 day and 1 week)

Concentration of Mesocarp (5 and 10%)

From Fig. 3, we see that the higher the percentage of mesocarp used, the greater the reduction in nitrite concentration.

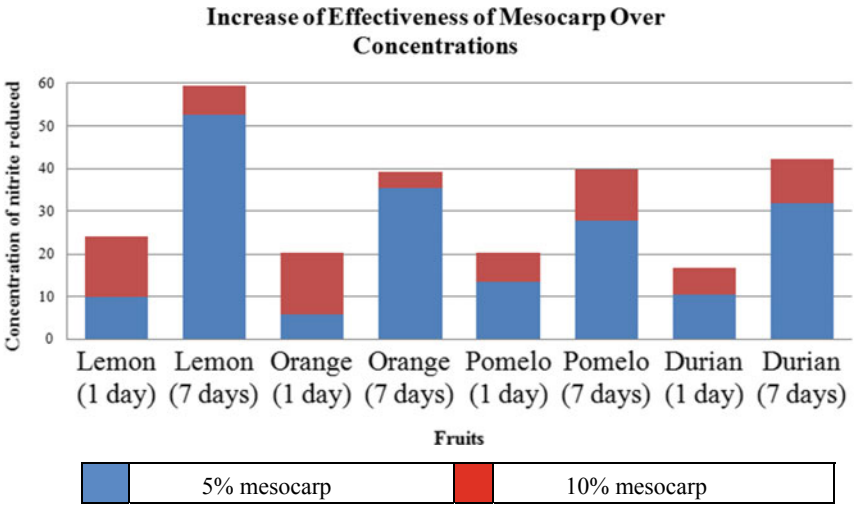

Fig. 3 Graph showing the effectiveness of mesocarp in reducing nitrite when different fruit mesocarp concentrations are changed

The increase in concentration of mesocarp provided more active biological compounds for the same volume, which can speed up the rate of the reaction, causing more nitrite to be reduced in the same amount of time.

However, the longer the reaction time, the nitrite reduction due to an increase in mesocarp concentration becomes less significant. Doubling the concentration of mesocarp from 5 to 10% reduced a greater percentage of nitrite content for the 1 day samples compared to the 1 week samples, especially for orange and lemon mesocarp. For example, for the 1 day reaction, doubling the orange mesocarp concentration from 5 to 10% increases nitrite reduction levels by about 19%. However, for 1 week of reaction, doubling the mesocarp concentration of orange by the same amount only increases the percentage nitrite reduction by about 4%. This might be due to the reaction time becoming the limiting factor at 1 week, hence little nitrite content could be further reduced.

Duration of reaction (1 day and 1 week)

The longer the time of reaction between the mesocarp and the meat, the greater the reduction in nitrite concentration (Fig. 4).

Increasing the duration of the reaction from 1 day to 1 week consistently increased the percentage nitrite concentration reduction by about two times or more across all fruits. The increase in reaction time gave the active biological compounds a longer time period to reduce residual nitrite concentration, so more time would mean more residual nitrite reduced.

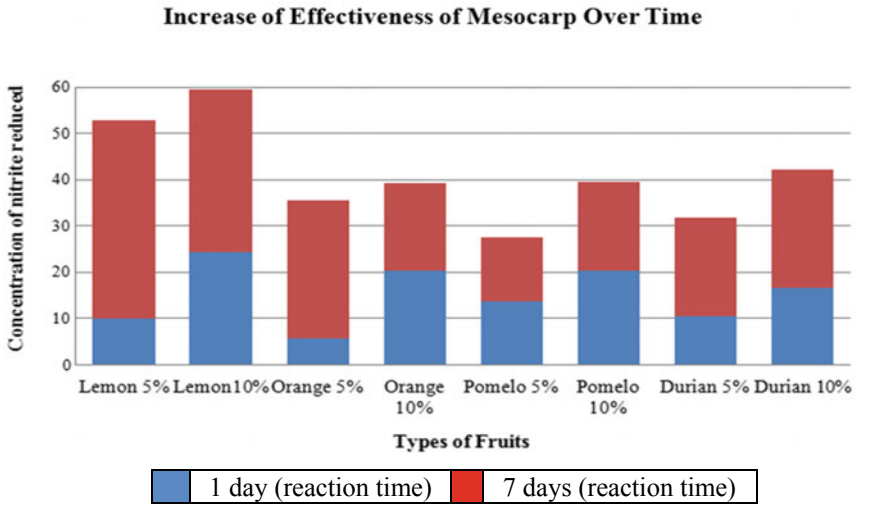

Fig. 4 Graph showing the nitrite reduced when the duration for reaction of mesocarp with the processed meats are changed

2. Possible Reasons for Variations in Results

There were significant variations in results during individual experiments (Appendix).

Firstly, there were certain variables regarding the growth of Sweet Orange, Pomelo, Lemon and Durian trees which were not possible for us to keep constant, such as the humidity, temperature, and amount of sunlight received by those fruit trees, the freshness of the fruits, which will then affect the quality of the fruit and its peels.

Secondly, the ripeness of each fruit at harvest might have been different. This may have affected our results because harvesting the fruits at different stages of ripeness may have resulted in a difference of the quality of their mesocarp. Also, different parts of the mesocarp might have different amounts of the biological active compounds, which could lead to variations in results.

Thirdly, the temperature may be a factor. The mesocarp was dried in an oven and stored in a freezer. This could have affected the biological compounds in the citrus mesocarp, which could possibly vary the results.

Lastly, the reason why some mesocarp showed zero percent or even negative reduction in nitrite levels is due to experimental errors with equipment as the scales involved are small, such as with the electronic balance or the micropipettes. Hence the results were not very precise and were averaged (Tables 1 and 2) to get more reliable results.

3. Relevance to Practical Applications

The Agri-Food and Veterinary Authority of Singapore (AVA) has set a standard for the amount of sodium nitrite in the finished meat product not to exceed 125 mg/L, [6] while the Codex General Standard for Food Additives (GSFA) mandates that food products containing sodium nitrite cannot contain more than 80 mg/L [7]. The most effective mesocarp we tested, lemon mesocarp at 10% concentration, had 0.467 mg/L of nitrite content at the end of 1 week of reaction whereas the control had 1.25 mg/L of nitrite content (Fig. 5).

The concentration of nitrite in our control was within the range of both standards, although the nitrite content could be further reduced with the use of mesocarp. However, even at the low concentrations of nitrite in our product, processed meat reacted with nitrite can still form significant levels of carcinogenic compounds. For

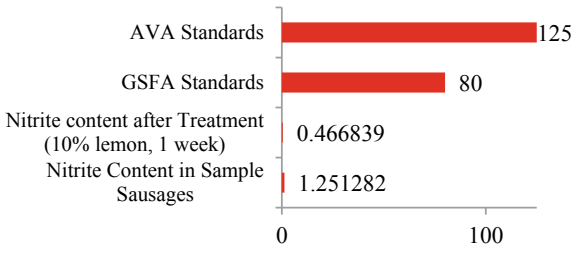

Fig. 5 Graph of concentration of nitrite as compared to other standards

example, experts concluded that each 50 g portion of processed meat eaten daily increases the risk of colorectal cancer by 18% [8]. Therefore, although the current concentration of nitrite in permitted meat products is much lower than the AVA and GSFA standards, these standards may be revised in future due to current studies showing the dangers that nitrites pose even at such low concentrations.

We have also shown that durian, despite not being a citrus fruit, is about as effective at reducing nitrite content as orange, and has the potential to be incorporated in processed meat depending on the desired final levels of nitrite in the meat. The durian fruit is itself rich in antioxidants, which adds to the benefits using the mesocarp, as it not only helps to reduce nitrite levels, but also reduces cancer risks in other ways [9].

Incorporating mesocarp into the manufacturing process of meat products is highly feasible in Singapore's context, as pomelo and durian are tropical and hence accessible in Singapore, while orange and lemon can also be obtained easily. Secondly, fruit peels can be recycled to obtain mesocarp, reducing wastage. Manufacturers could get the fruit peels from fruit juice or fruit ice-cream companies, which make these fruits easy to obtain. Thirdly, the mesocarp is also cleaner and more free from pesticides compared to the outer layer of the fruit (exocarp). Lastly, the mesocarp does not need to be in high concentrations to produce effective reduction in nitrite content and hence would not affect the colour, taste or texture of the fruits, and can even increase the fibre content in sausages.

5 Conclusion

As the concentration of mesocarp and duration of the reaction (between mesocarp and processed meat) increases, the more nitrite content is reduced, although diminishing returns will set in and manufacturers have to strike a balance between nitrite content and texture of the meat. From our results, we concluded that lemon mesocarp was the most effective in reducing nitrite content, followed by durian, pomelo and sweet orange. Pomelo and durian have also been shown to be potential alternatives.

Due to time constraints, our project was limited. Further extensions to this project would be to experiment with other non-citrus fruits so as to raise the awareness of the effectiveness of non-citrus mesocarp in reducing nitrite content. Secondly, we could experiment with a greater variety of concentrations of mesocarp and further vary the reaction time between the mesocarp and the meat as well as find out if there are other factors affecting the colour of the sample solutions that have been reacted with NEDA.

Lastly, we hope that our research helps to raise awareness of the possible dangers of sodium nitrite in our food as well as the benefits of recycling mesocarp from fruit peels, which are commonly thrown away. They could be useful in reducing residual nitrite content and could be implemented by manufacturers, thus slowing down the rising cancer rates in Singapore.

Acknowledgements We would like to thank the following people:
1. Our teacher-mentor, Mr. Conrad Zheng
2. Our school's chemistry laboratory technician, Mr. Goh Chun Lian
3. Our parents who gave us their unwavering support and everyone who has helped us in one way or another.

Appendix—Data from Findings

See Tables 3, 4, 5, 6, 7 and 8.

Table 3 Reduction of sodium nitrite in meat mixed with mesocarp to react for 1 day (experiment 1)

Substance tested	Absorbance	Concentration of sodium nitrite left after reaction (mg/L) (3 s.f.)	Percentage of nitrite reduced (%)
5% Lemon	0.148	1.07	13.5
10% Lemon	0.137	0.931	24.8
5% Orange	0.151	1.11	10.4
10% Orange	0.143	1.01	18.6
5% Pomelo	0.151	1.11	10.4
10% Pomelo	0.148	1.07	13.5
5% Durian	0.150	1.10	11.4
10% Durian	0.138	0.95	23.8
Control	0.161	1.24	0

Table 4 Reduction of sodium nitrite in meat mixed with mesocarp to react for 1 week (experiment 1)

Substance tested	Absorbance	Concentration of sodium nitrite left after reaction (mg/L) (3 s.f.)	Percentage of nitrite reduced (%)
5% Lemon	0.092	0.411	64.2
10% Lemon	0.088	0.359	68.7
5% Orange	0.112	0.669	41.7
10% Orange	0.115	0.708	38.3
5% Pomelo	0.120	0.773	32.7
10% Pomelo	0.109	0.630	45.1
5% Durian	0.114	0.695	39.4
10% Durian	0.110	0.643	43.9
Control	0.149	1.15	0

Table 5 Reduction of sodium nitrite in meat mixed with mesocarp to react for 1 day (experiment 2)

Substance tested	Absorbance	Concentration of sodium nitrite left after reaction (mg/L) (3 s.f.)	Percentage of nitrite reduced (%)
5% Lemon	0.148	1.07	16.9
10% Lemon	0.137	0.931	27.8
5% Orange	0.165	1.29	0
10% Orange	0.14	0.969	24.9
5% Pomelo	0.139	0.956	25.8
10% Pomelo	0.136	0.918	28.8
5% Durian	0.155	1.16	9.94
10% Durian	0.151	1.11	13.9
Control	0.165	1.29	0

Table 6 Reduction of sodium nitrite in meat mixed with mesocarp to react for 1 week (experiment 2)

Substance tested	Absorbance	Concentration of sodium nitrite left after reaction (mg/L) (3 s.f.)	Percentage of nitrite reduced (%)
5% Lemon	0.103	0.553	50.7
10% Lemon	0.098	0.488	56.5
5% Orange	0.123	0.811	27.7
10% Orange	0.114	0.695	38.0
5% Pomelo	0.123	0.811	27.7
10% Pomelo	0.115	0.708	36.9
5% Durian	0.127	0.863	23.0
10% Durian	0.105	0.579	48.0
Control	0.147	1.12	0

Table 7 Reduction of sodium nitrite in meat mixed with mesocarp to react for 1 day (experiment 3)

Substance tested	Absorbance	Concentration of sodium nitrite left after reaction (mg/L) (3 s.f.)	Percentage of nitrite reduced (%)
5% Lemon	0.161	1.24	−1.05
10% Lemon	0.141	0.982	19.9
5% Orange	0.153	1.14	7.32
10% Orange	0.143	1.01	17.8
5% Pomelo	0.156	1.18	4.18
10% Pomelo	0.142	0.995	18.8
5% Durian	0.150	1.10	10.5
10% Durian	0.148	1.07	12.6
Control	0.160	1.23	0

Table 8 Reduction of sodium nitrite in meat mixed with mesocarp to react for 1 week (experiment 3)

Substance tested	Absorbance	Concentration of sodium nitrite left after reaction (mg/L) (3 s.f.)	Percentage of nitrite reduced (%)
5% Lemon	0.112	0.669	43.6
10% Lemon	0.103	0.553	53.4
5% Orange	0.118	0.747	37.0
10% Orange	0.114	0.695	41.4
5% Pomelo	0.131	0.915	22.9
10% Pomelo	0.118	0.747	37.0
5% Durian	0.122	0.798	32.7
10% Durian	0.120	0.773	34.6
Control	0.152	1.19	0

References

1. The link between sodium nitrites and cancer. (2013). Retrieved June 16, 2016, from http://www.cancercenter.com/discussions/blog/the-link-between-sodium-nitrites-and-cancer/
2. Utilization of lemon albedo in dry-cured sausages. (n.d.). Retrieved June 16, 2016, from http://eurekamag.com/research/004/379/004379963.php
3. Anticarcinogenic Activity of Phytochemicals In Citrus Fruits And Their Juice Products. (n.d.). Retrieved June 17, 2016, from http://fshs.org/proceedings-o/1992-vol-105/162-168(NAGY).pdf
4. DETERMINATION OF NITRITE IN PROCESSED MEAT(n.d.). Retrieved February 09, 2016, from http://web.williams.edu/wpetc/chemistry/epeacock/EPL_AP_GREY/LABS/NITRITEs.pdf
5. CRAIC Technologies Microspectrophotometer & Microspectrometer. (n.d.). Retrieved August 16, 2016, from http://www.microspectra.com/component/content/article/35-technical-support/185-protein-absorbance

6. Agri-Food and Veterinary Authority of Singapore(n.d.). AVA Food Regulations. Retrieved August 16, 2016, from https://www.ava.gov.sg/docs/default-source/default-document-library/food-regulations-2-feb-2016
7. Codex General Standard for Food Additives (GSFA) Online Database. (n.d.). Retrieved August 16, 2016, from http://www.fao.org/fao-who-codexalimentarius/standards/gsfa/en/
8. IARC Monographs evaluate consumption of red meat and processed meat. (2015, October 26). IARC Monographs Evaluate Consumption of Red Meat and Processed Meat. Retrieved August 16, 2016, from https://www.iarc.fr/en/media-centre/pr/2015/pdfs/pr240_E.pdf
9. Health Benefits of Durian| Organic Facts. (2013). Retrieved August 02, 2016, from https://www.organicfacts.net/health-benefits/fruit/health-benefits-of-durian.html

Novel Therapeutic Strategy Suppresses Mosquito Saliva-Enhanced CHIKV Infection

Ting Qi Yong and JiaXin Xiao

Abstract Chikungunya virus (CHIKV) is one of the most important emerging infectious diseases and is responsible for significant global public health problems due to its recent outbreaks which was associated with severe morbidity. Transmission of CHIKV occurs through a bite by infected *Aedes aegypti* or *Aedes albopictus*. As such mosquito saliva, may contain active components to promote the transmission of CHIKV. The effect of a specific mosquito salivary protein (Protein X) on human skin fibroblast (BJ) cells, which is the first line of cells in contact with the virus and protein as well as the primary virus replication site, is being studied. Through analysis on viral load and infectivity coupled with studies on antiviral gene expression, we found that this mosquito salivary protein enhanced CHIKV infection in BJ cells through interrupting host antiviral response by binding to a specific host cell receptor. Further research was done to investigate the effect of blocking the receptor with antagonists to bring down the infection. Both antagonists A and antagonist B restricted enhancement of CHIKV infection in human skin fibroblast cell by mosquito salivary protein. Our data highlights the potential use of these antagonists for prophylaxis and treatment of CHIKV infection in humans.

Keywords Immunology · CHIKV · Flow cytometry · qRT-PCR · Mosquito saliva · Antagonist

T. Q. Yong (✉) · J. Xiao
Singapore Immunology Network, Agency for Science, Technology and Research, Singapore (A*STAR), Singapore 138648, Singapore
e-mail: tiffany.yong@mail.mcgill.ca

J. Xiao
e-mail: B200018@e.ntu.edu.sg

H. Guo et al. (eds.), *IRC-SET 2020*,
https://doi.org/10.1007/978-981-15-9472-4_66

1 Introduction

1.1 Background

Chikungunya virus (CHIKV) is a mosquito-transmitted alphavirus that has in recent years, emerged in many new locations all over the world, including South America, and Southeast Asia [1]. Symptoms include fever and joint pain, and in severe cases, it may result in death. As of yet, there is no commercial vaccine or antiviral agent to protect against or treat for CHIKV [2].

1.2 Rationale

CHIKV is primarily transmitted by infected female mosquitoes, typically by *Aedes aegypti* and *Aedes albopictus* [3]. During blood feeding, these mosquitoes inject both virus and their saliva into the human host. This mosquito saliva is shown to have pharmacologically active substances, that have many effects on the human body [4]. These effects include vasodilation—which helps prevent blood clots and helps the mosquito in blood feeding—and it also affects the human host immune response [5]. This effect on the host immune response enhances CHIKV in multiple ways, favouring CHIKV infection spreading [6]. Previous studies only analysed the effect of mosquito saliva as a whole, or other components of mosquito saliva on CHIKV infectivity [6–9]. In this study, we focused on a specific protein X that is abundantly expressed in the female mosquito's saliva and studied both its effect on CHIKV infection and how to reverse it.

The skin fibroblasts are the initial cells in contact with both virus and mosquito saliva [9] during CHIKV infection. They also serve as the primary site for virus replication [10] in the skin, which is why we choose to use human skin fibroblast (BJ) cells for our in vitro testing. We studied the effect of Protein X on CHIKV infection and discovered the mechanism behind its effect. From there, we designed a strategy to antagonise the effect of Protein X to control CHIKV infection in human skin fibroblast cells.

2 Methodology

2.1 Cell Culture and Cell Seeding [11, 12]

HEK 293T cells (ATCC Cat No. CRL-11268) were cultured in filter sterilised Gibco™ Dulbecco's Modified Eagle Medium (DMEM) supplemented with 10% fetal bovine serum. BJ (human skin fibroblast) cells were cultured in filter sterilised

GibcoTM Dulbecco's Modified Eagle Medium supplemented with 10% fetal bovine serum with 100 units of penicillin and 100 μg of streptomycin. 40,000 cells/well was seeded in 6-well culture plate and incubated at 37 °C for 18 h.

2.2 Cell Viability Assay [13]

The CellTiter-Glo® Luminescent Cell Viability Assay was performed to evaluate the cytotoxicity of mosquito salivary protein and antagonists against HEK-293T cells according to the manufacturer's protocol. Briefly, monolayers of HEK-293T cells were grown in 96-well plate and were treated with different concentrations of mosquito salivary protein/antagonists. The plate was then incubated at 37 °C with 5% CO_2 for 24 h before the CellTiter-Glo® Luminescent Cell Viability Assay was performed.

2.3 Virus Infection and Protein X Treatment

For CHIKV infection, the human skin fibroblast cells were treated with Protein X during the infection with CHIKV strain LR2006 OPY1 tagged with ZsGreen at multiplicity of infection, MOI 2. The infected but untreated cells were served as controls in this case. The cells were then incubated at 37 °C for 24 h. At 24 hpi, the cells were harvested and the culture supernatant was collected for infectivity checking.

2.4 Blocking of Host Receptors with Antagonists [14]

For receptor blocking, the human skin fibroblast cells were pre-treated with antagonists for 30 min before CHIKV infection and Protein X treatment. The cells were then harvested at 24 hpi for infectivity checking.

2.5 Flow Cytometry [15]

Fluorescent Activated Cell Sorting (FACS) was carried out to determine the percentage of CHIKV infected cells between treated and non-treated cells. After 24 h incubation at 37 °C and 5% CO_2, the cells were harvested and transferred into FACS tube to proceed to staining and fixation for FACS analysis. The cells were stained with live dead Amcyan dye and fixed with BD FACS Lysing solution before

being analysed using FACSCanto II. The ZsGreen tag in CHIKV allowed the infected cells to be detected through FITC channel.

2.6 Viral Load Determination

Viral RNA was extracted from 140 μL of cell supernatant using Qiagen RNeasy Mini Kit. Manufacturer's protocol was used to obtain the viral RNA. To determine the viral load present, quantitative real-time polymerase chain reaction (qRT-PCR) was carried out using the Taqman probe.

2.7 Gene Expression Study [16]

Total cellular RNA were extracted using TRIzol (Invitrogen). Samples were reverse-transcribed using random primers at 37 °C for 30 min. qPCR was performed using SYBR Master Mix with primers the target genes of GAPDH, IFN-β, RIG-I, ISG 54 and ISG 56.

3 Results

To define a non-cytotoxic concentration range, we tested the cytotoxicity of Protein X at 6 concentrations (10 fold dilution starting from 100 μM) in HEK-293T cells by measuring the cell viabilities. After 24 h incubation, cell viability was observed to have dropped at more than 10% in viability compared to no treatment control at 100 μM. We chose 10 μM and lower doses of Protein X for all subsequent experiments (Fig. 1a) [17]. To determine the effect of Protein X on CHIKV infection, we treated BJ cells with different concentrations of Protein X during infection. Our experimental results showed that Protein X had an enhancing effect on CHIKV infection in human skin fibroblast cells at concentrations of 10 μM, 1 μM and 0.1 μM. The percentage of infected cells and also the viral load in culture supernatant were significantly higher in treated cells compared to non-treated cells (Fig. 1b).

To further analyse the effect of Protein X, the expression levels of a few important antiviral genes in type I interferon pathway were studied in CHIKV infected BJ cells. It was observed that upon CHIKV infection, there was upregulation of antiviral gene expression in human skin fibroblast cells. When cells were treated with various concentrations of Protein X, it was observed that across all the antiviral genes tested, expression was lowered. This lowering of antiviral gene expression was observed most significantly in the cells treated with 1 μM concentration of Protein X (Fig. 1c).

By looking into carboxyl terminal sequence of Protein X, we speculated that this protein is capable of acting as an agonist at a specific human host receptor. In order

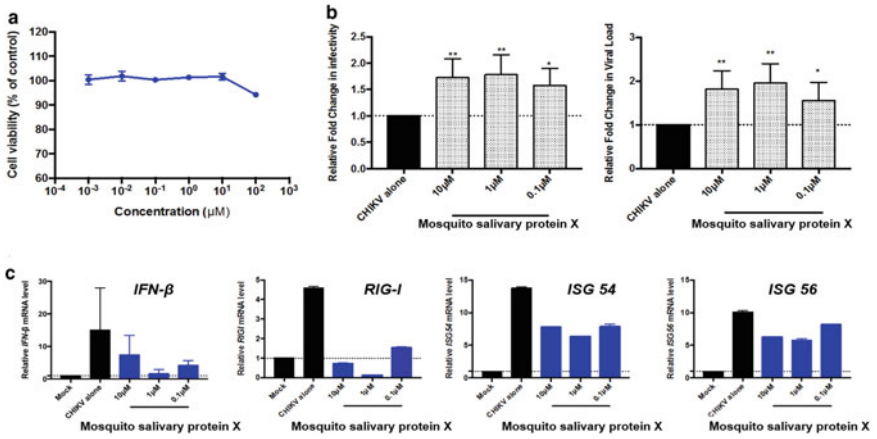

Fig. 1 Mosquito salivary protein X enhances CHIKV infection in human skin fibroblast (BJ) cells. **a** The CellTiter-Glo® Luminescent Cell Viability Assay to determine the toxicity of different concentrations of mosquito salivary protein x on HEK-293T cells 24 h post-treatment. **b** BJ cells were either mock infected, infected with CHIKV alone (MOI 2), co-treated with 10-different concentrations of mosquito salivary protein x with concomitant CHIKV infection. Cells were harvested for infectivity checking using FACs analysis and qRT-PCR. Relative levels of infectivity and viral load were normalized to CHIKV alone infected control. Data represent averages of 4 independent experiment. **c** Total RNA was extracted from the cells and gene expression study was performed to determine mRNA expression levels of anti-viral. Data represent averages of 3 independent experiments

to check whether its enhancing effect on CHIKV infection in BJ cells is dependent on the specific host receptor, we blocked the receptors with either antagonist A or B. These antagonists are designed to bind to the specific host receptor and block its activation. From cell viability testing, after 24 h incubation, we observed a drop at more than 40% in cell viability compared to no treatment control at 100 μM concentration of these antagonists (Fig. 2a). Thus, we decided to pre-treated the BJ cells with 10 μM of these antagonists before incubation with Protein X and CHIKV.

Our results showed that the block of specific host receptor by either antagonist A or antagonist B neutralised the enhancing effect of Protein X on CHIKV infection in BJ cells. Both antagonists were able to bring down CHIKV infection in human skin fibroblast cells, with antagonist B showing better potency in neutralising enhancing effect of Protein X than antagonist A (Fig. 2b). When we looked into expression level of antiviral genes, we also found that both antagonist A and B restricted downregulation of these genes by Protein X during CHIKV infection (Fig. 2c). Data suggested that the enhancing effect of Protein X on CHIKV is dependent on its binding to specific receptor expressed on human skin fibroblast cells.

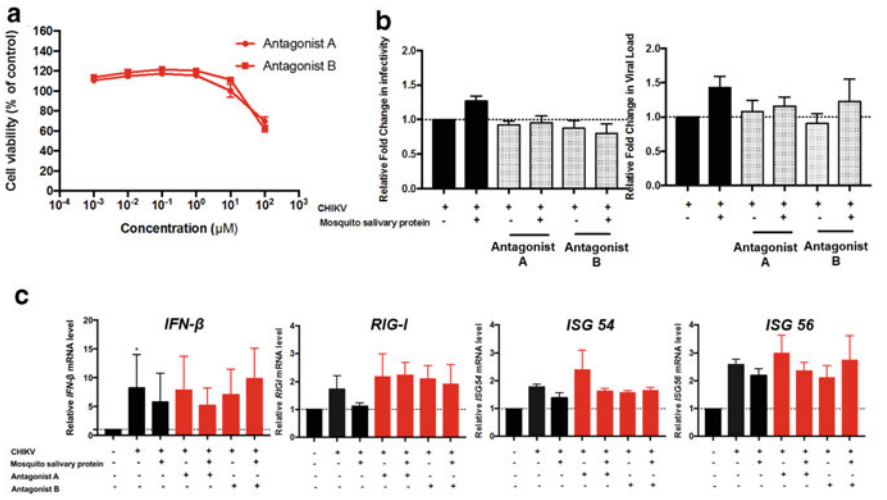

Fig. 2 Enhancing effect of mosquito salivary proteinx on CHIKV infection in human skin fibroblast cells is dependent on host cell receptors. **a** The CellTiter-Glo® Luminescent Cell Viability Assay to determine the toxicity of different concentrations of antagonist A and B on HEK-293T cells 24 h post-treatment. **b** BJ cells were pre-treated with 10 μM of antagonist A/B before CHIKV infection in the presence or absence of mosquito salivary protein x. Cells were harvested for infectivity checking using FACs analysis and qRT-PCR. Relative levels of infectivity and viral load were normalized to CHIKV alone infected control. **c** Total RNA was extracted from the cells and gene expression study was performed to determine mRNA expression levels of anti-viral. Data represent averages of 3 independent experiments

4 Discussion

In this study, we have demonstrated that Protein X enhanced CHIKV infection in human skin fibroblast cells. Upon CHIKV infection, the antiviral response will be activated to control virus infection in human host cells. As such, the activation of antiviral response is crucial for human host to control CHIKV infection. However, Protein X treated cells has lower antiviral response following CHIKV infection, bringing an increase in infectivity and viral replication across all samples treated with this protein. Hence, we believe that Protein X interrupts the activation of antiviral response in human skin fibroblast cells, creating an environment more favourable for CHIKV infection and replication [18]. This highlights the importance of Protein X in enhancing CHIKV infection and replication. Therefore, we went on to determine whether the enhancement of Protein X on CHIKV infection in BJ cells is dependent on human host cell receptor.

Our data showed that both antagonists potently inhibit enhancing effect of Protein X on CHIKV infection in human skin fibroblast cells. This antagonism of specific host cell receptor also restricted downregulation of antiviral genes following treatment with Protein X. The observed inhibition is the consequence of the interruption of

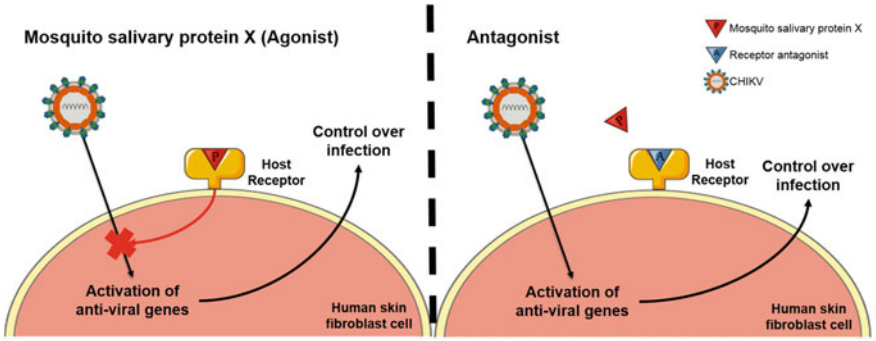

Fig. 3 Without receptor antagonist, mosquito salivary protein X will bind to the host receptor, interrupting the activation of anti-viral genes following CHIKV infection, and making the host unable to control the infection. However, with the introduction of receptor antagonists, these antagonists will bind to the host receptor in place of mosquito salivary protein X, without activating it. This prevents mosquito salivary protein X from disrupting the immune pathway

pathway activation downstream of specific host cell receptor through antagonism of Protein X-receptor interaction on the cell membrane.

Our data strongly supported the following hypothesis: (i) mosquito Protein X enhances CHIKV infection in human skin fibroblast cells (ii) mosquito Protein X acts as an agonist to a specific cell receptor to interrupt activation of antiviral response following CHIKV infection, and subsequently making the host cells more susceptible to virus infection (iii) the blocking of host cell receptor by antagonist A or antagonist B prevents mosquito Protein X from binding to the cell receptor. As such, they neutralise the effect of Protein X (Fig. 3).

5 Conclusion

Characterisation of virus-vector-host interactions allows development of arthropod-based therapeutics. Targeting mosquito Protein X may enhance current therapeutic strategies that are directed at virus. Our data highlights the potential use of host cell receptor antagonist in controlling mosquito saliva-assisted CHIKV infection. There are many novel therapeutic and prophylactic uses of these receptor antagonists. By adding the receptor antagonists to commonly used mosquito related products, we are able to either weaken the viral infection, or prevent it from spreading altogether (Fig. 4). The addition immune system, thereby controlling the replication of the virus at the bite site.

Some limitations of our work include the fact that all testing was done in vitro. In order to develop a product that can be used on humans to control CHIKV infection, these antagonists must go through both animal testing and clinical trials [19, 20], before a fully-fledged product is created. However, we have isolated these antagonists

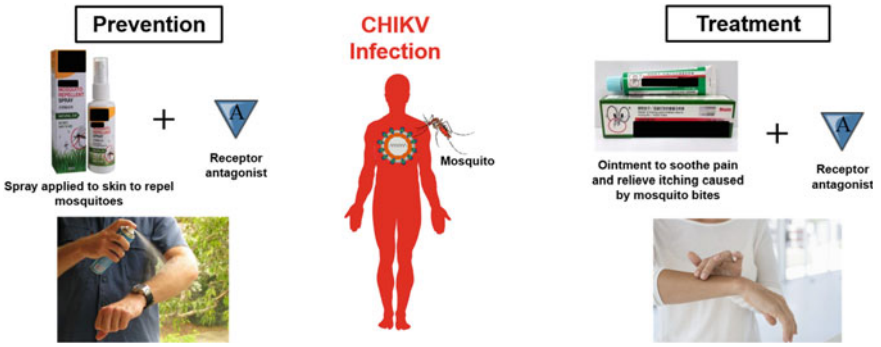

Fig. 4 Novel therapeutic and prophylactic uses of receptor antagonist

as a good candidate for both prophylactic and therapeutic antiviral drugs to control CHIKV infection in humans.

References

1. Morrison, T. E. (2014, 07). Reemergence of Chikungunya Virus. *Journal of Virology,88*(20), 11644–11647. https://doi.org/10.1128/jvi.01432-14
2. Parashar, D., & Cherian, S. (2014). Antiviral Perspectives for Chikungunya Virus. *BioMed Research International,2014*, 1–11. https://doi.org/10.1155/2014/631642
3. Chikungunya Virus. (2016, August 13). Retrieved from https://www.cdc.gov/chikungunya/transmission/index.html
4. Ribeiro, J. M., & Francischetti, I. M. (2003). ROLE OFARTHROPODSALIVA INBLOOD-FEEDING: Sialome and Post-Sialome Perspectives. *Annual Review of Entomology,48*(1), 73–88. https://doi.org/10.1146/annurev.ento.48.060402.102812
5. Vogt, M. B., Lahon, A., Arya, R. P., Kneubehl, A. R., Clinton, J. L., Paust, S., & Rico-Hesse, R. (2018, 05). Mosquito saliva alone has profound effects on the human immune system. *PLOS Neglected Tropical Diseases,12*(5). https://doi.org/10.1371/journal.pntd.0006439
6. Fong, S., Kini, R. M., & Ng, L. F. (2018, 03). Mosquito Saliva Reshapes Alphavirus Infection and Immunopathogenesis. *Journal of Virology,92*(12). https://doi.org/10.1128/jvi.01004-17
7. Thangamani, S., Higgs, S., Ziegler, S., Vanlandingham, D., Tesh, R., & Wikel, S. (2010). Host Immune Response to Mosquito-Transmitted Chikungunya Virus Differs from That Elicited by Needle Inoculated Virus. *PLoS ONE,5*(8). https://doi.org/10.1371/journal.pone.0012137
8. Maharaj, P. D., Widen, S. G., Huang, J., Wood, T. G., & Thangamani, S. (2015). Discovery of Mosquito Saliva MicroRNAs during CHIKV Infection. *PLOS Neglected Tropical Diseases,9*(1). https://doi.org/10.1371/journal.pntd.0003386
9. Briant, L., Desprès, P., Choumet, V., & Missé, D. (2014). Role of skin immune cells on the host susceptibility to mosquito-borne viruses. *Virology,464–465*, 26-32. https://doi.org/10.1016/j.virol.2014.06.023
10. Tang, B. L. (2012). The cell biology of Chikungunya virus infection. *Cellular Microbiology,14*(9), 1354–1363. https://doi.org/10.1111/j.1462-5822.2012.01825.x
11. Jing, L. (2012). Cell Culture Transfection for Production and Purification of Wnt Ligands. *Bio-Protocol,2*(2). https://doi.org/10.21769/bioprotoc.176
12. Yang, J., Shi, G., Bei, J., Wang, S., Cao, Y., Shang, Q., . . . Wang, W. (2002). Fabrication and surface modification of macroporous poly(L-lactic acid) and poly(L-lactic-co-glycolic acid)

(70/30) cell scaffolds for human skin fibroblast cell culture. *Journal of Biomedical Materials Research,62*(3), 438–446. https://doi.org/10.1002/jbm.10318
13. Promega. (2015, March). CellTiter-Glo® Luminescent Cell Viability Assay Technical Bulletin. Retrieved December 13, 2018, from https://www.promega.sg/resources/protocols/technical-bulletins/0/celltiter-glo-luminescent-cell-viability-assay-protocol/
14. Sourisseau, M., Schilte, C., Casartelli, N., Trouillet, C., Guivel-Benhassine, F., Rudnicka, D., . . . Schwartz, O. (2007). Characterization of Reemerging Chikungunya Virus. *PLoS Pathogens,3*(6), 804–817. https://doi.org/10.1371/journal.ppat.0030089
15. Manak, M. M., Moshkoff, D. A., Nguyen, L. T., Meshki, J., Tebas, P., Tuluc, F., & Douglas, S. D. (2010). Anti-HIV-1 activity of the neurokinin-1 receptor antagonist aprepitant and synergistic interactions with other antiretrovirals. *Aids,24*(18), 2789–2796. https://doi.org/10.1097/qad.0b013e3283405c33
16. Tamassia, N., Bazzoni, F., Moigne, V. L., Calzetti, F., Masala, C., Grisendi, G., . . . Cassatella, M. A. (2012). IFN- Expression Is Directly Activated in Human Neutrophils Transfected with Plasmid DNA and Is Further Increased via TLR-4-Mediated Signaling. *The Journal of Immunology,189*(3), 1500–1509. https://doi.org/10.4049/jimmunol.1102985
17. Gangalum, R. K., Atanasov, I. C., Zhou, Z. H., & Bhat, S. P. (2010). αB-Crystallin Is Found in Detergent-resistant Membrane Microdomains and Is Secreted via Exosomes from Human Retinal Pigment Epithelial Cells supplemental information. Journal of Biological Chemistry, 286(5), 3261–3269. https://doi.org/10.1074/jbc.m110.160135-1
18. Battcock, S. M., Collier, T. W., Zu, D., & Hirasawa, K. (2006). Negative Regulation of the Alpha Interferon-Induced Antiviral Response by the Ras/Raf/MEK Pathway. Journal of Virology, 80(9), 4422–4430. https://doi.org/10.1128/jvi.80.9.4422-4430.2006
19. Elhassa, G. O. (2015). Drug Development: Stages of Drug Development. Journal of Pharmacovigilance, 03(03). https://doi.org/10.4172/2329-6887.1000e141
20. Introduction to Clinical Trials. (n.d.). Retrieved from https://www.hsa.gov.sg/content/hsa/en/Health_Products_Regulation/Clinical_Trials/Overview/Introduction_to_Clinical_Trials.html